VOLUME 1: CONFERENCE PAPERS

12TH International Conference on Permafrost

PROCEEDINGS

EDITED BY RYLEY BEDDOE AND KUMARI KARUNARATNE

WHITEHORSE · YUKON · CANADA

16-20 June 2024

INTEGRATING PERSPECTIVES OF PERMAFROST THAW, CHANGE, AND ADAPTATION

Proceedings of the 12th International Conference on Permafrost
Whitehorse, Canada
16-20 June 2024

12th International Conference on Permafrost

Volume 1: Conference Papers

Edited by Ryley Beddoe and Kumari Karunaratne

Co-editors:
Karen MacFarlane, Sarah Gervais, Derek Cronmiller, Élise Devoie, Simon Dumais & Earl de Guzman

Recommended citation

Beddoe, R.A. and Karunaratne, K.C. (Eds.). 2024. 12th International Conference on Permafrost. 16-20 June 2024, Whitehorse, Canada: International Permafrost Association.

Cover Photo: Lake in ice-rich terrain in tundra uplands northwest of Inuvik, Northwest Territories. Ice wedge polygons are visible adjacent to the lake (Photo: Rachelle Landriau).

Cover Design: Inkit Communications Ltd.

12TH INTERNATIONAL CONFERENCE ON PERMAFROST
2024
XII
WHITEHORSE YUKON

INTEGRATING PERSPECTIVES OF PERMAFROST THAW, CHANGE, AND ADAPTATION

Preface

We are thrilled to share the contributions submitted for the 12th International Conference on Permafrost (ICOP2024) held 16-20 June 2024 in Whitehorse, Yukon, Canada. ICOP2024 is hosted by the Canadian Permafrost Association and is the first hybrid conference for the International Permafrost Association with live-streaming of oral presentations, a virtual poster hall, and facilitated online discussions. This innovative approach allows us to connect with participants from around the world, both in person and virtually, broadening the reach and impact of our collective knowledge.

The journey to ICOP2024 began with a call for solicited sessions 18 months before the conference. Session proposals required that the Session Chairs were from different countries and include an early career member. This community-driven approach encouraged international collaboration, mentoring, and the inclusion of both the classic permafrost topics as well as emerging issues in adjacent disciplines that are crucial to advancing permafrost science and engineering. We received a total of 50 session proposals. These submissions were evaluated by the International Scientific Committee and the Technical Program Committee and were organized into 13 distinct focus areas, which beautifully captured the ICOP2024 theme "Integrating Perspective of Permafrost Thaw, Change, and Adaptation".

We offered two conference submission options for ICOP2024: Full Papers (6-8 pages) and Extended Abstracts (2 pages). The response was impressive, receiving 72 Full Papers and over 450 Extended Abstracts. The session chairs were essential to the program development as they assigned two external reviewers to each paper, reviewed the extended abstracts, and made recommendations for presentation type. Following review of the submissions and confirmation of author registration, the ICOP2024 Conference Proceedings were compiled with Volume 1 comprising 64 Full Papers, and Volume 2 comprising 429 Extended Abstracts, organized according to the respective sessions. The ICOP2024 program included 227 oral presentations, 199 in-person posters, and 67 virtual posters. The keynote presentations and five concurrent sessions were live-streamed for virtual participants and recorded, allowing information to be shared for years to come.

We extend our heartfelt gratitude to everyone who contributed to the success of ICOP2024 program. Special thanks to Karen MacFarlane and Sarah Gervais, for their exceptional efforts in copyediting and formatting the proceedings, and the Technical Program Committee (Élise Devois, Derek Cronmiller, Simon Dumais, and EARL de Guzeman), whom we relied on to screen all submissions, complete reviews, draft instructions for authors and presenters, and advise on challenging decisions. And last, but not least, Lukas Arenson, our ICOP2024 Conference Chair. Lukas did a remarkable job convening an oversubscribed event in a small Northern city and we are extremely grateful for all his guidance, support, and camaraderie throughout this adventure.

Ryley Beddoe and Kumari Karunaratne

ICOP 2024 Organizing Committees

National Organizing Committee

Lukas Arenson, Chair, BGC Engineering

Ryley Beddoe, Technical Program Committee Chair, Royal Military College

Barb Fortin, Treasurer, Tetra Tech Canada Inc.,

Brian Horton, Local Organizing Committee Chair, Yukon University

Fabrice Calmels, Field Trips Committee Chair, Yukon University

Peter Morse, Secretary, Geological Survey of Canada

Nick Brown, Communications Committee Chair, Carleton University

Joseph Young, Early Career Representative, University of Alberta

Kumari Karunaratne, Publications Committee Chair, Northwest Territories Geological Survey

Technical Program Committee

Ryley Beddoe (Chair), Royal Military College
Élise Devoie, Queens University
Simon Dumais, Université Laval
Derek Cronmiller, Yukon Geological Survey
Earl de Guzman, Tetra Tech Canada Inc.
Kumari Karunaratne, NWT Geological Survey

Publication Committee

Kumari Karunaratne (Chair), NWT Geological Survey
Sarah Gervais, NWT Geological Survey
Karen MacFarlane, Yukon Geological Survey (retired)
Ryley Beddoe, Royal Military College

Local Organizing Committee

Brian Horton (Chair), Yukon University
Moya Painter, Yukon Geological Survey
Aaron Weber, BGC Engineering
Jay Dobson, Yukon University
Panya Lipovsky, Yukon Geological Survey
Muhammad Idrees, Yukon Government

Fieldtrip Committee

Fabrice Calmels (Chair), Yukon University
Louis-Philippe Roy, Yukon University
Duane Froese, University of Alberta
Steve Kokelj, NWT Geological Survey
Alice Wilson NWT Geological Survey
Jennifer Humphries, Aurora Research Institute

Communications Committee

Nick Brown (Chair), Carleton University
Astrid Schetselaar, Yukon Government

Sponsorship Committee

Robin McKillop, Palmer (SLR)
Emmanuel Herault, Université Laval
Lukas Arenson, BGC Engineering

International Advisory Committee

Antoni Lewkowicz (Chair), Canada
Anne Morgenstern, Germany
Karina Schollaen, Germany

ICOP 2024 Session Chairs

Lukas Arenson
Natalie Arpin
Michel Baraer
Prashant Baral
Helena Bergstedt
Frédéric Bouchard
Vincent Boulanger-Martel
Francesco Brardinoni
Sam Bratsman
Heather Brooks
Nick Brown
Fabrice Calmels
Bastien Charonnat
Lin Chen
Alexandre Chiasson
Derek Cronmiller
Julian Dann
Margaret Darrow
Earl de Guzman
Élise Devoie
Geoff Eichhorn
Saskia Eppinger
Jessica Ernakovich
Louise Farquharson
Daniel Fortier
Samuel Gagnon
Isabelle Gärtner-Roer
Sarah Gauthier
Raquel Granados Aguilar
Ed Grozic
Christopher Gruben
Stephan Gruber
Mauro Guglielmin
Charlotte Haugk
Liam Heffernan
Teddi Herring
Jennifer Humphries
Cornelia Inauen
Thomas Ingeman-Nielsen
Elchin Jafarov
Benjamin M. Jones
Andreas Kääb
Brandon Karchewski
Kaytan Kelkar
Anna Klene
Charles Klengenberg
Steve Kokelj
Michael Krautblatter
Julius Kunz
Emmanuel L'Hérault
Yuanming Lai
Mark Lara
Emma Lathrop
Mary-Cathrine Leewis
Susanne Liebner
Zhanju Lin
Rachel Mackelprang
Mahsa Malmir
Shawn Marshall
Jeffrey McKenzie
Robin McKillop
Burke Minsley
Lexi Mollica
Peter Morse
Marc Oliva
Laurent Orgogozo
Santosh Panda
Silvio Pastore
Anna Pekinasova
Cécile Pellet
Louis-Philippe Roy
Regina Plasken
Stefano Ponti
Youhua Ran
Mahya Roustaei
Line Rouyet
Pascale Roy-Léveillée
Wolfram Rühaak
Remya S.N.
Lutz Schirrmeister
Fabian Seemann
Antoine Séjourné
Ted Shuur
Ylva Sjöberg
Elliott Skierszkan
Sharon L. Smith
Andrea Soellinger
Emma Street
Tazio Strozzi
Matt C. Strzelecki
Dmitry A. Streletskiy
Zuzanna Swirad
Andy Take
Jing Tao
Carla Tapia Baldis
John Thornley
Claire Treat
Dario Trombotto Liaudat
Eole Valence
Aleksandra Veremeeva
Marja Vuorio
Anna Wagner
Ziyi Wang
Melissa Ward Jones
Niels Weiss
Juliane Wolter
Stephanie Wright
Mousong Wu
Ming Xiao
Brett Young
Joseph Young
Wenxin Zhang
Simon Zwieback

ICOP 2024 Sponsors, Partners, and Supporters

Arctic Foundations of Canada
Canadian National Committee for the IPA
NSERC PermafostNet
WSP
BGC Engineering Inc.
KGS Group
LogR Systems Inc.
Tetra Tech Inc.
TREK Geotechnical Inc.
Adaptive Baseline Geotechnical Ltd.
Arctic Gateway Group LP
Chance Oil and Gas Ltd.
Klondike Placer Miners' Association
Palmer Environmental Consulting Group
Permafrost Pathways
Hatch Ltd.
beadedstream Inc.
Center for Northern Studies
Mobile Augers and Research Ltd.
Quantum Machine Works Ltd.
Air North, Yukon's Airline
AM2 Geotechnical Inc.
Casino Mining Corporation
Core Geoscience Services Inc.
Winterlong Brewing Co.
Yukon Brewing
Yukon Government
Government of Northwest Territories
Transport Canada
Environment and Climate Change Canada
Natural Resources Canada
Canadian Geotechnical Society
Canadian Permafrost Association

International Scientific Committee

Andreas Kääb, Denmark
Andreas Kellerer-Pirklbauer, Austria
Anna Liljedahl, USA
Annett Bartsch, Germany
Antoine Sejourne, France
Arne Instanes, Norway
Britta Sannel, Sweden
Christian Hauck, Switzerland
Dario Trombotto Liaudat, Argentina
Ed Yarmak, USA
Francesca Casini, Italy
Frederick Nelson, USA
Gonçalo Vieira, Portugal
Guido Grosse, Germany
Hanne Christiansen, Norway
Hugues Lantuit, Germany
Isabelle Gärtner-Roer, Switzerland
Jambaljav Yamkhin, Mongolia
Jeanette Noetzli, Switzerland
John Zarling, USA
Lothar Schrott, Germany
Margaret Darrow, USA
Mauro Guglielmin, Italy
Megan Balks, New Zealand
Michael Krautblatter, Germany
Norikazu Matsuoka, Japan
Paul Overduin, Germany
Pavel Talalay, China
Phlippe Schöneich, France
Regula Frauenfelder, Norway
Thomas Douglas, USA
Thomas Ingeman-Nielsen, Denmark
Vladimir Romanovsky, USA
Ylva Sjöberg, Denmark

Table of Contents

Preface

Intrusive origin of a 4.8-meter-thick ground ice body within a polygonal peatland along the Inuvik-Tuktoyaktuk Highway, NWT

Alejandro Alvarez[1], Jordan Harvey[1], Alexandre Chiasson[1], Joseph M. Young[1], Steven V. Kokelj[2], Peter D. Morse[3] & Duane Froese[1]

[1]*PACS Lab, Department of Earth and Atmospheric Science, University of Alberta, Edmonton, Canada*

[2]*Northwest Territories Geological Survey, Government of the Northwest Territories, Yellowknife, Canada*

[3]*Geological Survey of Canada, Natural Resources Canada, Ottawa, Canada*

ABSTRACT

A seemingly unusual 4.8-m-thick ground ice body between 2.1 m and 6.9 m depth, within a polygonal peatland adjacent to the Inuvik-Tuktoyaktuk Highway (ITH), was recovered by the Sentinel drill program in 2017. Characterizing the nature of large ground ice bodies is necessary for predicting the potential effects of ground ice thaw on highway embankment stability. Here, we characterize the ground ice body and hosting sediments using Computed Tomography (CT), radiocarbon dating, geochemistry (δD, δ^{18}O, and d-excess), and cryostratigraphy. CT scanning was performed to quantify ice textures, including bubble content, shape, size, and orientation. The ice has a milky-white to clear horizontal tabular appearance with consistent vertical bubble train dispersals. Stable isotopes range from -27‰ to -18‰ (δ^{18}O) and -219‰ to -149‰ (δD), comparable to modern isotope values and a co-isotope slope similar to the local meteoric water line. This indicates ice formation likely derived from atmospheric water sources, with little evaporative transformation, in the Late Holocene. Given the thickness, sharp upper contact with the peat, and tabular appearance, we interpret this ground ice body as being of injection ice origin. Injection ice is typically not associated with peatlands, but has been observed in isolated occurrences in the area. The results here indicate that polygonal peatlands, widespread throughout the western Arctic and along the ITH, may have higher ground ice contents and potential for subsidence than previously inferred.

1 INTRODUCTION

The Inuvik-Tuktoyaktuk Highway (ITH) traverses ice-rich, continuous permafrost with a wide range of vegetation, surficial geology, and ground ice types. Ice-rich terrain, and in particular large bodies of ground ice, can pose considerable risk to infrastructure due to the terrain implications associated with thaw. Understanding the origin of ground ice types and their associated geomorphic context provides insight into variation in terrain sensitivity and potential hazards associated with permafrost thaw. One common type of ground ice found within the area is injection (or intrusive) ice. Injection ice is formed by the pressurized intrusion of water into soils or rock, uplifting the overlying materials and freezing to form bodies of ice (Mackay 1972). Typical cryostructures of injection ice are described in Pollard (1990) and Mackay (1990), which include layered, suspended, and solid (pure) ice, while typical cryotextures include tubular bubbles, long bubble trains, stratified bubbles and potential inclusion of small bubbles and crystals along chill margins. Injection ice is usually found at shallow depths, within the former active layer (Mackay 1972; Pollard and French 1985); however, injection ice has also been observed deeper within permafrost, whereby water is injected deep along fractures (Mackay 1989). Previous work has described injection ice as a driver of frost blister formation (Pollard and French 1985; Pollard 1990; Morse and Burn 2014), ice dykes (Mackay 1989; Mackay and Dallimore 1992), sill ice (Mackay, 1972), and pingo ice (Mackay, 1990). Here, we characterize a 4.8-m-thick body of ice from a borehole (NTGS 17-01; Figure 1) in a polygonal peatland that does not conform to traditional wedge ice or pool ice structural or geochemical characteristics. Our interpretation of the origin of this ground ice body is based on cryostratigraphy, cryotextures, and isotopic analyses that provide insight into processes of ground ice formation. We propose a conceptual model involving multiple episodes of injection ice forming an unusually thick body of ground ice in a peatland setting.

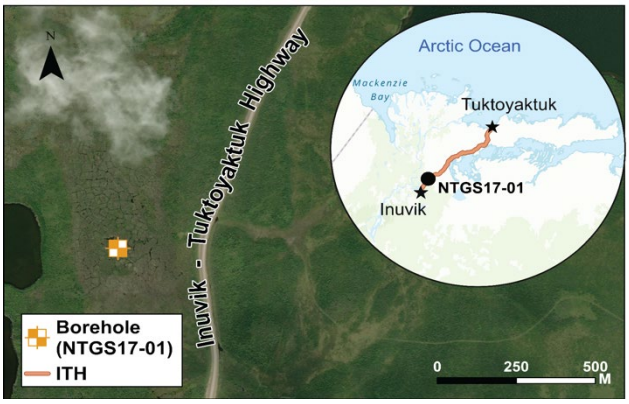

Figure 1. Location of study area. NTGS17-01 is located within a high-centred polygonal peatland west of the ITH.

2 STUDY AREA

The polygonal peatland hosting the 4.8-m-thick ground ice body is located ~20 km north of Inuvik, 260 m west of the ITH, NT, Canada (68.54°N, -133.77°W). This site lies within the continuous permafrost zone and is in tall-shrub tundra within the limits of the northern boreal treeline. The vegetation at this peatland is mainly low shrub (*Salix spp.*)

https://doi.org/10.52381/ICOP2024.232.1

with heath ground cover. The peat deposit overlies hummocky Pleistocene till of the Laurentide Ice Sheet ca. 18,000 to 13,100 ^{14}C years BP (Rampton 1988; Lacelle et al. 2004; Kennedy et al. 2010). The mean annual air temperature in Inuvik is -6 °C (Kokelj et al. 2017) and mean annual ground surface ground temperature (MAGST) and mean annual ground temperature (MAGT) at a depth of 2 m are -0.7 °C and -1.8 °C, respectively (Rudy et al. 2020). The active layer is ~0.8 m thick (Figure 2B). This site is at a polygonal peatland with mainly high-center polygons within an old lake basin. The polygons are predominantly non-orthogonal in shape (120°, Y-junction), with high connectivity of ice-wedge troughs, several of which exhibit active thermokarst degradation and host small trough ponds.

3 METHODS

A collaborative drilling program funded by the Government of Northwest Territories was carried out along the ITH in March 2017 (for details on the program see Ensom et al. 2020). Our study analyzes borehole NTGS17-01, drilled in a polygonal peatland to a depth of 11.2 m. All core samples were sectioned in the field, logged, and transported frozen to the University of Alberta's Permafrost Archives Science (PACS) Lab. In the laboratory, cores were scraped to reveal textures, photographed, and characterized following the cryostructure classification of Murton and French (1994). Subsequently, cores were subsampled at ~20 cm intervals to analyze for water isotopes (δ^{18}O and δD) using a Picarro L2130-i water isotope analyzer. Two reference waters, USGS 45 and USGS 46, were used to calibrate measurements to the Vienna Standard Mean Ocean Water (VSMOW) – Standard Light Antarctic Precipitation (SLAP) scale with internal precisions of ± 0.5‰ and ± 0.1‰ for δD and δ^{18}O. Additionally, some of the core segments were sampled at higher resolution (~2 cm) to sample different cryotextures. One radiocarbon date was determined on a mixed terrestrial plant material sample, pretreated following a standard acid-base-acid preparation (c.f., Reyes et al. 2010) at the university of Alberta, and shipped to the A.E Lalonde AMS Laboratory, University of Ottawa.

Computed tomography (CT) scans were used to determine core characteristics and statistical analysis were done on segmented images to characterize gas inclusions (gas bubbles). The scans were carried out at the PACS lab with a Nikon XTH 225 ST Industrial CT scanner using an insulated container containing dry ice to hold samples below -10ºC. The CT scans used a beam energy of 150 Kv and an exposure time of 8fps, resulting in an effective voxel size of ~60µm. The primary TIFF images were reconstructed into three-dimensional volume files using Nikon CT Pro 3D software and imported into ORS Dragonfly 3D visualization software (ver. 2022.1.0.1249). Representative boxes were selected within each core to avoid edge effects. Within each box, regions of interest (ROIs) were defined for ice and bubbles using Dragonfly's Otsu splitting method, enabling automatic segmentation (c.f., Roustaei et al. 2022). Gas bubble ROIs were further processed using Dragonfly's multi-ROI analyses, where bubble characteristics and statistics, including sphericity (degree of how close a bubble resembles a sphere, where a sphericity of 1 is a perfect sphere), Feret diameter (diameter of longest bubble axis), orientation and volume, were calculated. In some cases, multi-ROIs were refined by removing gas bubbles smaller than 10 voxels to allow for greater visual clarity. CT scan ROIs and water isotopes were sampled in the middle of the core to mitigate any biases from the core sampling method.

4 RESULTS AND ICE CHARACTERISTICS

The NTGS17-01 borehole is distinguished by three main stratigraphic deposits that were subdivided into six units based on differences in cryostratigraphic characteristics (Figure 2A). A peat deposit with a thickness of 2.1 m, overlies a ground ice deposit of 4.8 m (2.1 to 6.9 m depth). The ice body displays a mostly milky white tabular appearance and has a sharp lower contact with an underlying ice-poor diamict. The ice-poor diamict deposit, which extended from 6.9 m to the full depth of the borehole at 11.2 m, is dark grey and matrix-supported with clasts, varying in size between pebbles and cobbles. One radiocarbon date was collected from NTGS17-01 at the upper peat-ice contact, at a depth of 2.0 m (Figure 2A). The water isotope (δ^{18}O and δD) values in the NTGS17-01 borehole have values that are similar to modern precipitation in Inuvik (Fritz et al. 2022). The uppermost peat unit has average δ^{18}O and δD (± standard deviation) values of -18.9 ± 0.8‰ and -152.7 ± 6.2‰, respectively (Figure 2A). The underlying ground ice deposit is more depleted, with average δ^{18}O and δD values of -23.5 ± 3.1‰ and -189.5 ± 22.4‰, respectively, but shows a greater range in values than the underlying diamict or overlying peat deposits. By comparison, the local meteoric water line (LMWL) at Inuvik has a slope of 7.4 (Fritz et al. 2022). In contrast, the regression slope of the ice-poor diamict is lower, at 3.2 (Figure 4). Below we describe six units within the three main deposits (peat, ice and diamict) at this site

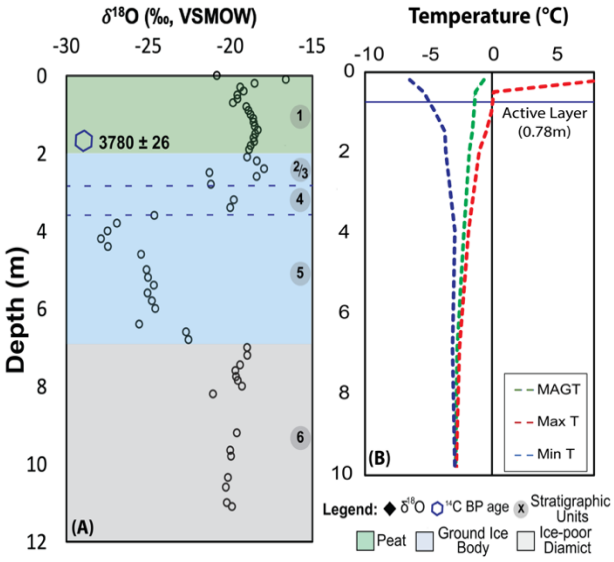

Figure 2. NTGS17-01 summary. (A) δ^{18}O profile, radiocarbon, three stratigraphic deposits (peat, ground ice body, and ice-poor diamict), and the six units. (B) Mean, maximum and minimum annual ground temperatures.

based on variations in cryostructures, and cryotextures, which comprise microscopic textures and features, including bubble shape, orientation, and volume.

4.1 Unit 1: Peat Unit

The peat unit (0 m to 2.1 m) has a dark-brown massive appearance, predominantly composed of organic-matrix and rare crustal cryostructures (Figure 3a). The CT scan statistics show a low concentration of gas bubbles within the peat, with an average of 4%. This value represents the volume of gas bubbles relative to the volume of the sample within an ROI. Gas bubbles within the peat unit have a mean Feret diameter of 0.56 mm, a mean volume of 0.05 mm^3, and a mean sphericity of 0.81. Towards the base of the peat unit, sitting above the basal ice contact, there are tubular bubbles which tend to narrow downwards and have a maximum Feret diameter between 6 and 10 mm (Figure 5A).

4.2 Unit 2: Contact Unit

The contact unit (2.1 to 2.3 m) includes the contact of the ice body and the overlying peat (Figure 3a). The ice portion has a milky-white appearance with layered and suspended cryostructures, including angular organic inclusions (Figure 3a). A radiocarbon date of 3,780 ± 26 (UOC-5201) was obtained at 2.0 m depth, right above the peat–ice contact. A bimodal distribution of bubbles is present at the soil–ice contact, with large downward-tapering bubbles from the overlying peat unit and small bubbles within the ice (Figure 5A). This unit has a high concentration of small gas bubbles, whereby 21% of this unit is composed of gas bubbles, illustrated by the opaque nature of the ice and CT images (Figure 5A). The gas bubbles within the ice have a mean Feret diameter of 0.33 mm, a mean volume of 0.01 mm^3, and a mean sphericity of 0.88. Tubular bubbles with a maximum Feret diameter between 5 and 7 mm are present within the suspended peat inclusions and tend to narrow downwards (Fig. 5a).

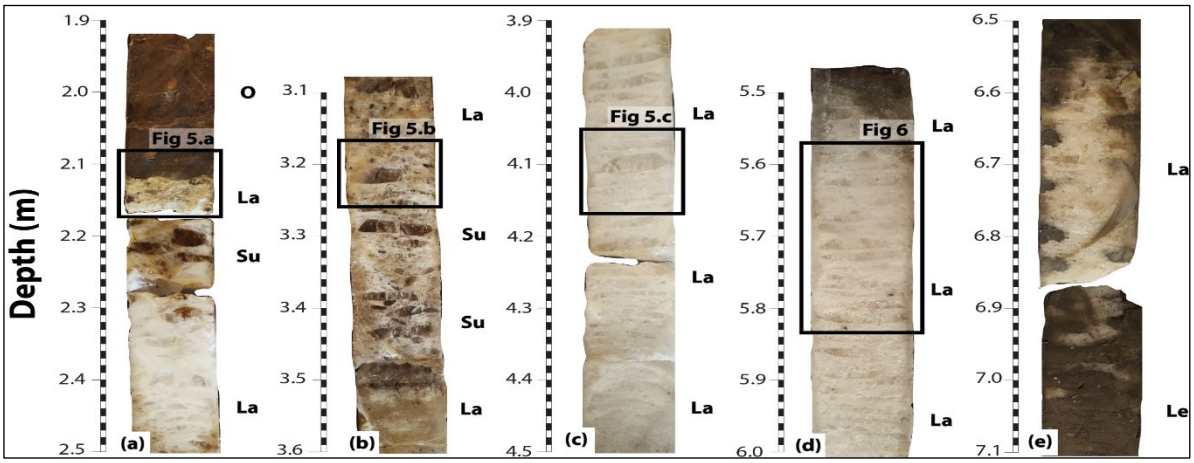

Figure 3. Representative core segments of borehole NTGS17-01 highlighting different cryostratigraphic units and cryostructures. The black boxes represent inset figures of scanned CT images in Figure 5 and 6. (a) Peat unit (0 to 2.1 m), contact unit (2.1 to 2.3 m), and upper layered unit (2.3 to 2.5 m). (b) Brecciated unit (3.1 to 3.5 m). (c–d) Lower layered unit (3.5 to 6.9 m), including location of CT scan in Figure 6. (e) Lower sharp contact between ground ice (unit 5 lower layered unit) and ice-poor diamict unit (6.8 to 11.2 m). Cryostructures shown to the right of the core segments include Layered (La), Suspended (Su), Organic-Matrix (O), and Lenticular (Le).

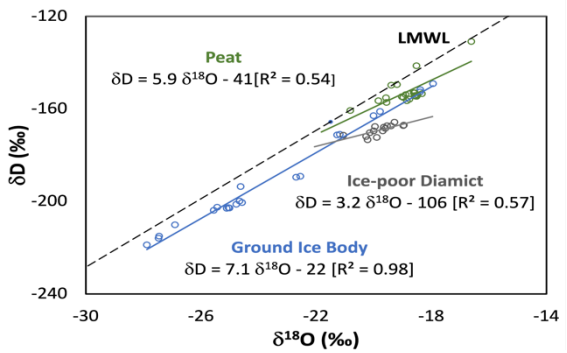

Figure 4. Co-isotope diagram of the three deposits in the NTGS17-01 borehole, along with the LMWL (s = 7.4).

4.3 Unit 3: Upper Layered Unit

This upper layered unit (2.3 to 2.7 m) displays a tabular appearance (i.e., flat, sheet-like appearance) with alternating translucent and opaque ice layers (Figure 3a). This tabular ice unit has layered cryostructures, with translucent layers varying in thickness between 0.5 and 1.5 cm. The CT scan statistics show similar statistics to unit 5 (lower layered unit) between the opaque and translucent layers (Table 1).

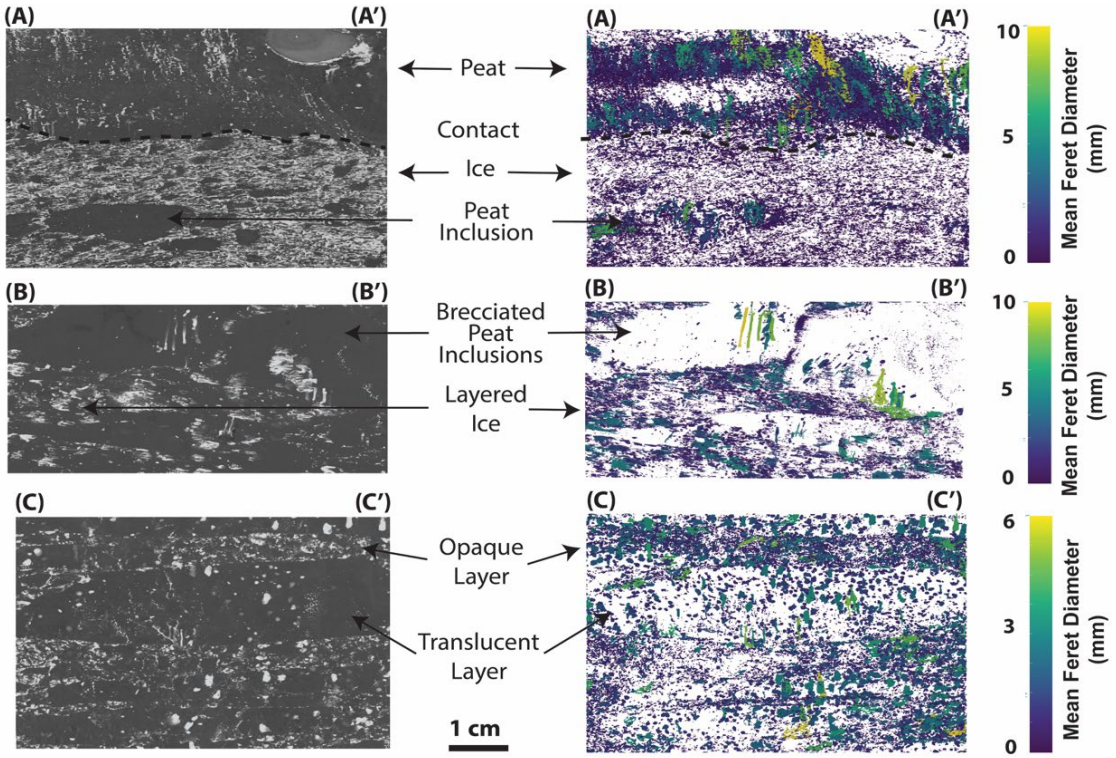

Figure 5. CT scans of the ice body with stratigraphic positions are indicated in Figure 3. The left figures show gas bubbles in white relative to ice and peat in black, while the right figures show the mean Feret diameter and orientations of gas bubbles, for the same field of view at the left figures. (A) Contact unit. High concentration of very small bubbles below the contact and long tubular bubbles above the contact and within peat inclusions (B) Brecciated unit. Bimodal distribution of bubbles with long tubular bubbles within peat inclusions and small bubbles within the layered ice. (C) Layered unit showing bimodal distribution of bubbles with upwards-tapering elongated bubbles within translucent layers and a high concentration of small bubbles in the opaque layer.

4.4 Unit 4: Brecciated Unit

The brecciated unit (2.7 to 3.5 m) has milky-white ice with brecciated (angular) organic inclusions (Figure 3b). This sediment-poor ice unit has lenticular, layered and suspended cryostructures. The organic inclusions vary in size, with larger inclusions between 1 and 3 cm thick and 7–10 cm wide (larger inclusions were as wide as the 10 cm diameter core). These angular organic inclusions are fractured but occur roughly parallel to the underlying layered ice unit. Gas bubbles within the peat inclusions vary between small spherical bubbles and long tubular bubbles, with a maximum Feret diameter of 9 mm.

These long tubular bubbles thin downwards and occur normal to the base of the angular inclusions, consistent with the overlying peat unit (Figure 5B). There is a bimodal distribution of bubbles within this unit, with gas bubbles within the peat inclusions having an average gas bubble concentration of 1%, despite being ~200% larger than bubbles in the sediment-poor layered ice (Figure 5B). The gas bubbles within the peat inclusions have a mean Feret diameter of 0.46 mm, a mean volume of 0.06 mm^3, and a mean sphericity of 0.88. The gas bubbles concentration within the ground ice layers is 11%. The gas bubbles within the layered ice have a mean Feret diameter of 0.34 mm, a mean volume of 0.03 mm^3, and a mean sphericity of 0.87.

4.5 Unit 5: Lower Layered Unit

The lower layered unit (3.5 m to 6.9 m) has a tabular appearance with alternating layers of translucent and opaque ice (Figure 3c,d). The translucent ice layers, or lenses, vary in thickness between 0.5 and 2 cm, with a low concentration of bubbles (average gas bubble concentration 4%). Some translucent layers show upward-tapering bubble trains, elongated bubbles, and vertical tubular bubbles (Figure 5C). Gas bubbles within the translucent layers have a mean Feret diameter of 0.52 mm, mean volume of 0.07 mm^3, and a mean sphericity of 0.85. The opaque, milky-white layers vary in thickness between 0.1 and 0.6 cm, with a greater concentration of fine bubbles (average gas bubble concentration of 11%) and no bubble trains. Gas bubbles within the opaque layers have a mean Feret diameter of 0.27 mm, mean volume of 0.01 mm^3, and mean sphericity of 0.90. The opaque layers tend to host a higher concentration of smaller bubbles with higher sphericity (Figure 6; Table 1). This contrast between translucent and opaque layers leads to a banded appearance, overall. In total, between units 3 and unit 5

there are a total of ~120 banded-pair layers. Additionally, for this layered unit we a tested the isotopic signatures of a few core segments at a higher resolution between the layers (Figure 6). Overall, the translucent layers have a slight $\delta^{18}O$ depletion (~-0.2‰) relative to the opaque layers.

4.6 Unit 6: Ice-poor Diamict Unit

An ice-poor diamict unit is present from 6.9 m to the base of the borehole at 11.2 m (Figure 3e). This unit has a sharp contact with the overlying ground ice deposit. This unit is mostly ice-poor with rare lenticular and vein cryostructures varying in thickness between 1 and 5 cm.

5 Interpretation and Discussion

Several cryostratigraphic and isotopic features of the NTGS17-01 ground ice body, peat, and diamict deposits preclude common ground ice types in the region. First, this body of ice, 2.1 m below the ground surface, and about 1.3 m below the permafrost table, comprises relatively pure ice, without significant mineral inclusions. This suggests that it's not aggradational ice of segregated origin (i.e., a rising permafrost table in the near surface) due to the absence of near-surface mineral soil with many small (mm to cm thick), segregated lenses (Kokelj and Burn 2003). As it is a peatland that lacks any significant slope, and there's an absence of mass wasting or alluvial sediments in the core, the possibility of a rapid burial mechanism for surface ice preservation (i.e., aufeis, lake ice, or snowbank) is unlikely. Another common ice type within peatlands is wedge ice, but negative d-excess values and the absence of vertical foliations preclude a wedge ice origin. Lastly, this ice type does not exhibit the typical characteristics of segregated ice, which include massive appearance, i.e., homogenous without structure, translucent without mineral inclusions, and gradational contacts with adjacent material (Mackay 1989; Pollard 1990; French and Harry 1990). Buried glacier ice is a common feature in permafrost-preserved Pleistocene till deposits of the Laurentide Ice Sheet (French and Harry 1990; Murton et al. 2005; Kokelj et al. 2017) and locally, in the moraine demarcating the Sitidgi Stade ice limit (Rampton 1988). In addition, large, tabular segregated-intrusive ice bodies, interpreted to be of Laurentide Ice sheet meltwater origin have been described for areas of the Tuktoyaktuk Coastlands by Dallimore and Wolfe (1988) and Mackay and Dallimore (1992). However, these ice bodies are typically underlain by sandy deposits, and often associated with positive relief known as involuted hills (Dallimore and Wolfe 1988). However, the relatively high isotopic values of the ice body and the lower diamict, rule out its origin as a buried glacier or segregated ice of glacier-meltwater origin. The average $\delta^{18}O$ value is -23.5‰, which is enriched relative to Pleistocene values in the region and most similar to Holocene waters with minor evaporative enrichment (e.g., Lacelle et al. 2004). The regression line with a slope of 7.1, similar to the LMWL, suggests a meteoric water source (Figure 4). Further, $\delta^{18}O$ values, range from –-27‰ to -18‰, suggest the ice layers capture seasonal variations in precipitation and coupled with the age of the basal peat and the presence of peat inclusions, indicate the ice body formed during the late Holocene.

Another possibility is that the thick ice body is of pool ice origin (also sometimes termed thermokarst cave ice), which can be found within ice-wedge polygon networks (Mackay 1988, 1997). Pool ice can have a banded structure similar to injection ice (Mackay 1988). However, the ground ice body in NTGS17-01 lacks common pool ice characteristics of reticulate-chaotic cryostructures at sediment contacts (Fortier et al. 2008) or radial bubble train dispersion from lateral freezing processes (Mackay 1997; Kotler and Burn 2000). Despite this, some 'injection ice' can form if water within the ice-wedge troughs is pushed or "injected" into the active layer of adjacent polygon ridges by cryostatic pressure (Mackay 2000). This type of ice developed by injection processes has been observed in poorly drained ice-wedge terrain similar to this study site by Mackay (2000), who refers to it as a type of 'pool ice'.

We interpret the 4.8-m-thick NTGS17-01 ground ice body as injection ice based on several lines of evidence. First, the stratigraphy of the ground ice body displays distinct sharp horizontal contacts that are concordant with the diamict and peat deposits. Where a concordant ice body is an ice body that is aligned parallel to host deposits. The water is likely injected at the interface between the frozen peat and underlying mineral soil. Van der Sluijs et al. (2018) describe a similar scenario, with injection ice occurring between the

Table 1. Summary of gas inclusions (bubbles) characteristic for all the ice deposit units, including sphericity, Feret diameter, volume, and gas bubble concentration (volume of gas over the total volume) with standard deviations (SD).

Peat Unit & Inclusions	**Mean Feret Diameter** [± SD] **(mm)**	**Mean Volume** [± SD] **(mm^3)**	**Mean Sphericity** [± SD]	**Gas Bubble Concentration (%)**
Unit 1: Peat	0.56 ± 0.54	0.05 ± 0.17	0.81 ± 0.15	5
Unit 2 (Contact) Peat Inclusions	0.49 ± 0.46	0.03 ± 0.08	0.85 ± 0.14	9
Unit 4 (Brecciated) Peat Inclusions	0.46 ± 0.83	0.06 ± 0.24	0.88 ± 0.14	1
Ground Ice Units	**Mean Feret Diameter** [± SD] **(mm)**	**Mean Volume** [± SD] **(mm^3)**	**Mean Sphericity** [± SD]	**Gas Bubble Concentration (%)**
Unit 2: Contact	0.33 ± 0.24	0.01 ± 0.03	0.88 ± 0.11	21
Unit 4: Brecciated	0.34 ± 0.32	0.03 ± 0.09	0.87 ± 0.14	11
Unit 3/5: Layered: Translucent Layers	0.52 ± 0.41	0.07 ± 0.21	0.85 ± 0.14	4
Unit 3/5: Layered: Opaque Layers	0.27 ± 0.25	0.01 ± 0.06	0.90 ± 0.12	11

uplifted peat and mineral soil interface. Whereby, water flow is impeded by physical obstacles (including road embankments and frozen culverts) or frozen soil, it results in hydrostatic and cryostatic pressure. This, in turn, causes the injection of ice, and the upwards displacement of the overlying frozen material (van der Sluijs et al. 2018). Moreover, this concordant interpretation is further highlighted in the bubble size and orientation at the contact between the ground ice and peat deposits. The contact unit (depth 2.1 to 2.3 m) features opaque, milky-white ice characterized by a high gas bubble concentration of 11% and small air bubbles (mean Feret diameter and volume of 0.33 mm and 0.01 mm^3, respectively). While the peat unit shows long downward-tapering bubble trails towards the contact. We interpret the ice at the contact between unit 1 and unit 2, as having frozen rapidly with a downward freezing front. The small bubbles in the contact unit are likely caused by a chill zone by the overlying frozen peat deposit, similar to Pollard (1990), which would reflect rapid downward freezing of pressurized water.

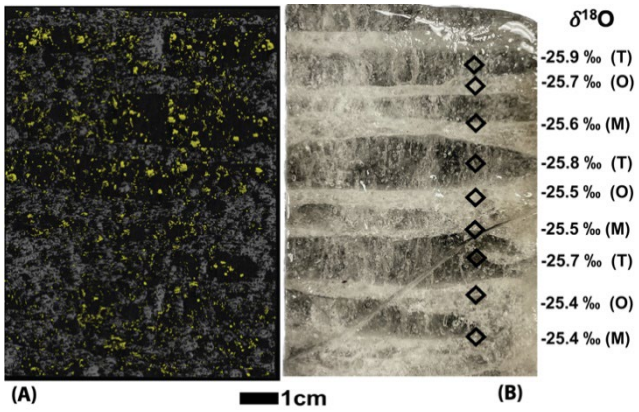

Figure 6. Layered unit with the stratigraphic position indicated in Figure 3d. (A) CT scan showing ice in black relative to small gas bubbles (white) and large elongated bubbles (yellow) with a mean Feret diameter of 0.27mm and 0.52mm, respectively. (B) Photo of layered ice with high resolution isotope sampling between translucent (T), opaque (O) and mixed (M) layers.

Second, the water isotope record highlights at least some seasonal variation, with $\delta^{18}O$ ranging from -17.9‰ to -27.9‰, indicative of modern summer and winter/spring precipitation (Fritz et al. 2022). Water that makes up injection ice bodies should comprise late-season precipitation with perhaps some snowmelt. Moreover, the co-isotope slope of the ice body is 7.1, similar to the LMWL. In contrast, the co-isotope slope of the peat deposit and ice-poor till are 5.9 and 3.2, respectively (Figure 4). These data are consistent with water sourced from an open reservoir, suggesting an accumulation of the ice body and surface heave within winter months, rather than segregation from the overlying or underlying deposits.

Third, the most common cryostructures within the ground ice body are layered, underlining the horizontal tabular form within units 2 and 4. This layered appearance is governed by bubble sphericity, bubble size and gas bubble concentration. Within these units, there are alternating layers highlighting a banded nature to the ice with distinct cryotextures. Thinner, opaque layers contain smaller, spherical bubbles (mean Feret diameter of 0.27 mm) and a gas bubble concentration of 11%, while translucent layers have larger elongated and upward-tapering bubbles (mean Feret diameter of 0.52 mm), aligned parallel to freezing directions. This banded appearance with elongated bubbles parallel to the freezing direction is similar to injection ice reported by Mackay (1972, 1990, 1998), and Pollard and French (1985), and it is attributed to multiple generations of injection ice whereby upward tapering bubbles align in the direction of heat flow. In addition, the opaque and translucent layers display differing bubble concentrations. We interpret the layering as first-ice and last-ice processes. This process is based on the notion that the initial ice tends to be clear, as it expels dissolved solutes, thereby reducing impurities and gas bubbles. This succeeded by the freezing of the remaining water containing a higher concentration of gases and impurities. First-ice and last-ice processes has been observed by Mackay (1990), within a seasonal time frame, whereby he suggests that clear ice bands with large gas bubble trails represent fast freezing ice in winter months, meanwhile the opaque, gas-rich bands represent slow freezing ice in summer months. These forms are similar to the banded ice described by Mackay (1988, 1990) in pingos, and Pollard and French (1985) in frost blisters, whereby the layering is governed by multiple generations of seasonal first-ice and last-ice processes. However, the isotopic differences within the layers of the ice body in NTGS17-01 do not align with first-ice and last-ice processes at seasonal timescales (Figure 6B). Instead, we interpret this banding as a first-ice and last-ice process within a rapid freezing environment. Therefore, we interpret that the translucent layers freeze first and have a lower bubble concentration (4% gas bubble concentration) leading to their greater light penetration. In contrast, the last-ice formation typically consists of opaque, bubble-rich layers (11% gas bubble concentration).

Lastly, this ice deposit has peat inclusions within the contact and brecciated units. These peat inclusions feature long (up to 9 mm) tubular bubbles that narrow downwards. Brecciated inclusions have also been observed in some segregated ice bodies (Shumskii 1964; Pollard 1990). However, the long downward-tapering bubbles within the peat inclusions contrast bubble trends throughout the ice deposit, including upward-tapering bubbles in some of the translucent layers of unit 4 or the absence of bubble trails within the other ice units. Therefore, the downward-tampering bubbles, which go against the direction of heat flow within the ice, suggest a downward displacement of fragmented frozen peat, brittle deformation, from the overlying peat deposit. This displacement is likely a result of pressurized water lifting the frozen peat and integrating brecciated fragments prior to freezing (Figure 7).

5.1 Layered Intrusive Ice Conceptual Model

Given the available evidence, the likely origin of the ground ice body is as intrusive ground ice. Our hypothesis is that the injected water originates from meteoric sources based on the isotope data. This injected water likely comes from a combination of two meteoric sources: (1) pond water within

ice-wedge troughs, which if truncated by thaw can exceed 2 m depth relative to the surface of the adjacent polygon centers, and (2) a riparian zone located ~10 m uphill, whereby a constant water source routed through an ice-wedge trough network provides a hydraulic head. These two water sources allow for hydraulic pressure coupled with last-to-freeze pond water sitting adjacent to the peat-diamict interface (Figure 7). Similar forms of injection ice, governed by cryostatic pressures, have been observed by Mackay (2000) in ice-wedge polygons, adjacent to stream banks (Kane 1981), and due to road embankments and blocked culverts along the Dempster (van der Sluijs et al. 2018) and Inuvik-Tuktoyaktuk Highway. Cryostatic pressure can build in pockets of unfrozen material between the downward-freezing active layer and the permafrost table, typically during the winter freeze-back (Mackay and Mackay 1976). The rhythmic alternation between the bubble-rich opaque and translucent ice is interpreted to record multiple episodes of water injection, perhaps within a single year. Notably, the thickness of band-pairs (translucent and opaque layers) in the ice body ranges from ~3 cm to 5 cm

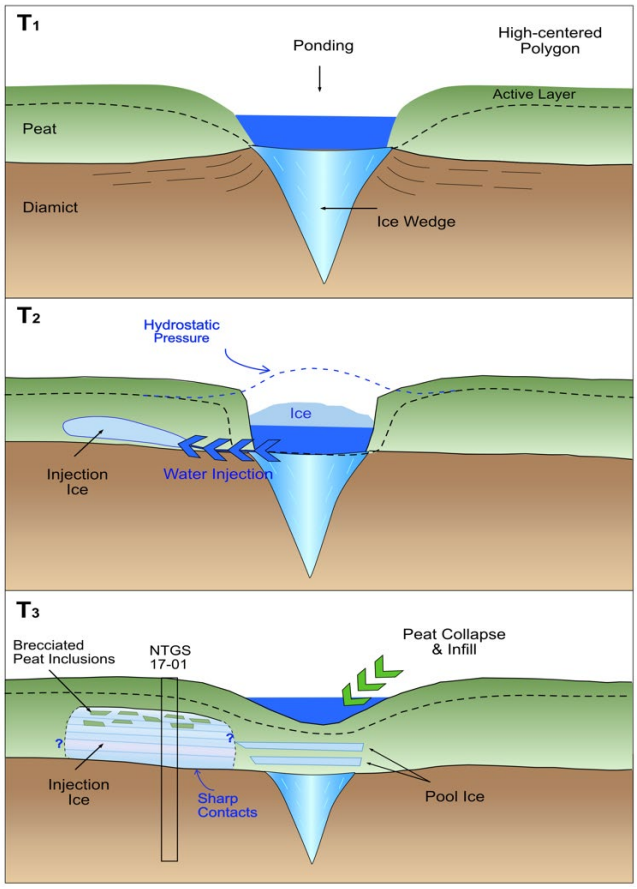

Figure 7. Conceptual model of layered intrusive ice formation in a high-centered ice-wedge polygon, based on Kane (1981) and Mackay (2000). (T1) Active layer expansion and ponding in ice wedge. (T2) Development of injection ice lens from hydrostatic head due along the peat and diamict contact. (T3) Growth of banded ice body from repeated injection events. Resulting uplift causes peat infilling troughs coincident with pool ice formation.

which differs significantly from the band-pairs in pingo ice (10 to 60 cm). This variation is noteworthy because Mackay (1990) interprets each pingo band-pair to represent 1 year of growth, with the translucent layers indicating fast-freezing winter injections, while opaque layers are interpreted as slower-freezing summer injections. In contrast, the NTGS17-01 intrusive body likely does not conform to this yearly seasonal pattern within the bands; rather, we suggest these ~120 band pairs may correspond to distinct ice growth pulses. It is challenging to determine the exact number of years it took to form the banding; however, the isotopic evidence coupled with freezing cryostatic pressure suggests that these periods of growth primarily occur during the winter season.

6 CONCLUSIONS

This study assesses the origin of an anomalously thick layered ice body at the interface between the peat and underlying diamict in a 11.2 m peatland core adjacent to the ITH highway. We interpret the 4.8-m-thick ground ice body as concordant intrusive ice based on: (1) sharp contacts and a chill zone within the upper contact with the overlying peat; (2) winter isotopic signature with a co-isotope slope suggestive of open-source water; (3) tabular appearance with distinct band-pair layering indicative of first-ice and last-ice processes; and (4) peat inclusions within the ice, indicative of pressurized frozen peat displacement. This intrusive ice is, therefore, likely formed by hydrostatic pressure in ice-wedge troughs (where water tends to freeze last), forcing water under pressure laterally into permafrost at the interface between the peat and the ice-poor diamict. This observation provides additional evidence that tabular ice bodies may comprise and important but underappreciated ice type in polygonal peatlands.

7 ACKNOWLEDGEMENTS

We gratefully acknowledge the Inuvialuit, whose land (Inuvialuit Settlement Region) this borehole was drilled on and material was retrieved from. This work has been supported by the Natural Sciences and Engineering Research Council (NSERC), UAlberta North, and Indigenous partners, including the Inuvialuit Land Administration. Additionally, we acknowledge the Government of Northwest Territories – Department of Infrastructure, the Aurora Research Institute, for their support of the Sentinel Drilling Program.

8 REFERENCES

Dallimore, S.R. and Wolfe, S.A. 1988. 'Massive ground ice associated with glaciofluvial sediments, Richards Island, N.W.T. Canada', in K. Senneset (ed.), *Fifth International Conference on Permafrost*, Trondheim, Norway, volume 1, pp. 132–136.

Ensom, T., Morse, P.D., Kokelj, S.V., MacDonald, E., Young, J., Tank, S., Subedi, R., Grozic, E. and Castagner, A. 2020. 'Permafrost geotechnical borehole data synthesis: 2013–2017 Inuvik-Tuktoyaktuk region', *Northwest Territories Geological Survey* NWT Open Report 2019-012 (also Geological Survey of Canada Open File 8652). doi:10.4095/321869.

Fortier, D., Kanevskiy, M., and Shur, Y. 2008. 'Genesis of Reticulate-Chaotic Cryostructure' in *Permafrost, Proceedings of the Ninth International Conference on Permafrost*, Fairbanks, Alaska, United States, volume 1, pp. 451–456. doi:10.13140/2.1.4703.3929.

French, H.M. and Harry, D.G. 1990. 'Observations on buried glacier ice and massive segregated ice, western arctic coast, Canada', *Permafrost and Periglacial Processes* 1, pp. 31–43, doi:10.1002/ppp.3430010105.

Fritz, M., Wetterich, S., Mcalister, J., and Meyer, H. 2022. 'A new local meteoric water line for Inuvik (NT, Canada)', *Earth System Science Data* 14**,** pp. 57–63. doi:10.5194/essd-14-57-2022.

Kane, D.L. 1981. 'Physical mechanics of aufeis growth', *Canadian Journal of Civil Engineering* 8, pp. 186–195. doi:10.1139/l81-026.

Kennedy, K.E., Froese, D.G., Zazula, G.D., and Lauriol, B. 2010. 'Last Glacial Maximum age for the northwest Laurentide maximum from the Eagle River spillway and delta complex, northern Yukon', *Quaternary Science Reviews* 29, pp. 1288–1300. doi:10.1016/j.quascirev.2010.02.015.

Kokelj, S. V. and Burn, C.R. 2003. 'Ground ice and soluble cations in near-surface permafrost, Inuvik, Northwest Territories, Canada', *Permafrost and Periglacial Processes* 14, pp. 275–289, doi:10.1002/ppp.458.

Kokelj, S.V., Palmer, M.J., Lantz, T.C., and Burn, C.R. 2017. 'Ground Temperatures and Permafrost Warming from Forest to Tundra, Tuktoyaktuk Coastlands and Anderson Plain, NWT, Canada', *Permafrost and Periglacial Processes* 28, pp. 543–551, doi:10.1002/PPP.1934.

Kotler, E. and Burn, C.R. 2000. 'Cryostratigraphy of the Klondike "muck" deposits, west-central Yukon Territory', *Canadian Journal of Earth Sciences* 37, pp. 849-861, doi:10.1139/e00-013.

Lacelle, D., Bjornson, J., Lauriol, B., Clark, I.D., and Troutet, Y. 2004. 'Segregated-intrusive ice of subglacial meltwater origin in retrogressive thaw flow headwalls, Richardson Mountains, NWT, Canada', *Quaternary Science Reviews* 23, pp. 681–696. doi:10.1016/j.quascirev.2003.09.005.

Mackay, J.R. 1972. 'The World of Underground Ice', *Annals of the Association of American Geographers* 62, pp. 1–22. doi:10.1111/j.1467-8306.1972.tb00839.x.

Mackay, J.R. 1988. 'Catastrophic lake drainage, Tuktoyaktuk Peninsula area, District of Mackenzie'**,** *Geological Survey of Canada* Paper 83-1D, pp. 83–90. doi:10.4095/122663.

Mackay, J.R. 1989. 'Massive ice: some field criteria for the identification of ice types', *Geological Survey of Canada* Paper 89-1G, pp. 5–11.

Mackay, J.R. 1990. 'Seasonal growth bands in pingo ice', *Canadian Journal of Earth Sciences* 27, pp. 1115–1125. doi:10.1139/e90-116.

Mackay, J.R. 1997. 'A full-scale field experiment (I 978 - I 995) on the growth of permafrost by means of lake drainage, western Arctic coast: a discussion of the method and some results', *Canadian Journal of Earth Sciences* 34, pp. 17–33. doi.org/10.1139/e17-002.

Mackay, J.R. 1998. 'Pingo growth and collapse, Tuktoyaktuk Peninsula area, western arctic coast, Canada: A long-term field study', *Geographie Physique et Quaternaire* 52, pp. 271–323. doi:10.7202/004847ar.

Mackay, J.R. 2000. 'Thermally induced movements in ice-wedge polygons, western arctic coast: A long-term study', *Geographie Physique et Quaternaire* 54, pp. 41–68. doi:10.7202/004846ar.

Mackay, J.R. and MacKay, D.K. 1976. 'Cryostatic pressures in nonsorted circles (mud hummocks), Inuvik, Northwest Territories', *Canadian Journal of Earth Sciences* 13, pp. 889–897.

Mackay, J.R. and Dallimore, S.R. 1992. 'Massive ice of the Tuktoyaktuk area, western Arctic coast, Canada', *Canadian Journal of Earth Sciences* 29, pp. 1235–1249. doi:10.1139/e92-099.

Morse, P.D. and Burn, C.R. 2014. 'Perennial frost blisters of the outer Mackenzie Delta, western Arctic coast, Canada', *Earth Surface Processes and Landforms* 39, pp. 200–213. doi:10.1002/esp.3439.

Murton, J.B. and French, H.M. 1994. 'Cryostructures in permafrost, Tuktoyaktuk coastlands, western Arctic Canada', *Canadian Journal of Earth Sciences* 31, pp. 737–747. doi:10.1139/e94-067.

Murton, J.B., Whiteman, C.A., Waller, R.I., Pollard, W.H., Clark, I.D. and Dallimore, S.R. 2005. 'Basal ice facies and supraglacial melt-out till of the Laurentide Ice Sheet, Tuktoyaktuk Coastlands, western Arctic Canada', *Quaternary Science Reviews* 24, pp. 681–708

Pollard, W. 1990. 'The nature and origin of ground ice in the Herschel Island area, Yukon Territory', in M. Burgess, D. Harry, and D. Sego (eds.), Proceedings of the fifth Canadian Conference on Permafrost, Québec City, Québec, pp. 23–30. Available at: http://pubs.aina.ucalgary.ca/cpc/cpc5-23.pdf.

Pollard, W.H. and French, H.M. 1985. 'The Internal Structure and Ice Crystallography of Seasonal Frost Mounds', *Journal of Glaciology* 31, pp. 157–162. doi:10.3189/s0022143000006407.

Rampton, V.N. 1988. 'Quaternary Geology of the Tuktoyaktuk Coastlands, Northwest Territories', *Geological Survey of Canada* Memoir 423. Available at: https://doi.org/10.4095/126937.

Reyes, A. V, Jensen, B.J.L., Zazula, G.D., Ager, T.A., Kuzmina, S., La Farge, C., and Froese, D.G. 2010. 'A late-Middle Pleistocene (Marine Isotope Stage 6) vegetated surface buried by Old Crow tephra at the Palisades, interior Alaska', *Quaternary Science Reviews* 29, pp. 801–811. doi:10.1016/j.quascirev.2009.12.003.

Roustaei, M., Pumple, J., Harvey, J., and Froese, D. 2022. 'Estimating ice and unfrozen water in permafrost samples using industrial computed tomography scanning', in *GeoCalgary 2022*. Calgary, Alberta, Canada.

Rudy, A.C.A., Kokelj, S.V., Morse, P.D., and Ensom, T. 2020. 'Permafrost Ground Temperature Report: Inuvik to Tuktoyaktuk Highway Sentinel sites', *Northwest Territories Geological Survey* NWT Open Report 2019-017. Available at: https://doi.org/10.46887/2019-017.

Shumskii, P.A. 1964. 'Ground (subsurface) ice', *National Research Council of Canada* Technical Translation. doi.org/10.4224/20386780.

van der Sluijs, J., Kokelj, S.V., Fraser, R.H., Tunnicliffe, J., and Lacelle, D. 2018. 'Permafrost terrain dynamics and infrastructure impacts revealed by UAV photogrammetry and thermal imaging', *Remote Sensing* 10, 1734. doi:10.3390/rs10111734.

A conceptual carbon budget for an icy riverine corridor

Suzanne P. Anderson, Cole Cochran, Robert S. Anderson, Marisa Repasch, Josie Arcuri & Irina Overeem

Institute of Arctic and Alpine Research, University of Colorado, Boulder, Colorado, United States

ABSTRACT

The contribution of river corridors to the global carbon budget exceeds their small areal footprint, yet our understanding of fluvial carbon dynamics is incomplete, particularly in periglacial settings. Frequent disturbance and lateral fluxes are key attributes of carbon budgets in riparian corridors. Climate change affects the pace and style of fluvial and biogeochemical processes in periglacial settings. The effects of these can be assessed with a carbon budget, a statement of all fluxes in and out of a control volume, which we outline for a river corridor.

We are generating data from a field campaign of the carbon stock in select river corridor segments of the Canning River, Alaska. This gravel-bedded river drains continuous permafrost from glaciated headwaters in the Brooks Range to its delta in the Beaufort Sea. Fluvial erosion and deposition generate distinct, mappable geomorphic surfaces in the river corridor that accumulate carbon over time. Carbon stocks on surfaces are summed across the river corridor to compute the total carbon stock. Characterizing the depth of alluvium is a poorly constrained component of the carbon stock. Lateral bank erosion hews away geomorphic surfaces, while sediment deposition buries carbon and generates new surfaces. Deposition of uprooted willows or turf mats augment the carbon stock and can jump-start plant succession. All fluxes in the carbon budget are sensitive to warming and arctic hydrologic intensification. Analyzing how these fluxes may change and affect the carbon stock in icy river corridors will advance our understanding of their contribution to the global carbon budget.

1 INTRODUCTION

Permafrost regions hold a large reservoir of organic carbon (Tarnocai et al. 2009; Hugelius et al. 2014) that has accumulated over thousands of years and is vulnerable to decomposition upon thaw (Schuur et al. 2015; McGuire et al. 2018). Although warming raises permafrost temperatures, increases active layer depths, changes hydrology, and instigates abrupt thaw features (Meredith et al. 2019), the implications of these physical processes for carbon cycling in a fluvial system are unclear. The most recent IPCC Assessment Report places low confidence on knowledge of decadal trends in carbon fluxes between permafrost regions and the atmosphere (Canadell et al. 2021), due to sparse observations and incomplete process models. Fluvial systems are one component of land surfaces that are not well represented in global carbon budgets (e.g., Friedlingstein et al. 2022), and are understudied in permafrost regions (Wrona et al., 2016). Nevertheless, there is growing understanding that significant carbon processing occurs in rivers, lakes, and coastal oceans (Regnier et al. 2013, 2022).

The carbon stock in periglacial river corridors is particularly dynamic and vulnerable to effects of climate warming. The stock of carbon in Arctic fluvial systems is large: Hugelius et al. (2014) estimate that the deltas of 12 major Arctic rivers store 91 Pg of carbon in frozen sediment layers below 3 m depth. The deep carbon reservoirs in these 12 deltas alone contain one-tenth of the total soil organic carbon in northern polar permafrost regions, despite the surveyed deltas occupying less than 1% of the area of permafrost soils and not including other significant occurrences of deltas or upstream river corridors in the Arctic (Hugelius et al. 2014). Data are limited on the volume (particularly the depth of deposits) and carbon content of alluvium (Hugelius et al. 2014).

Warming is increasing productivity across the tundra biome. From 1980–2010, tundra vegetation increased in height and shrubs became more abundant (Elmendorf et al. 2012). Shrub and tree expansions are linked to particular geomorphic settings, especially those subject to disturbance such as fluvial corridors (Tape et al. 2012; Frost and Epstein 2014). Even without treating differences across geomorphic settings, warming-induced increased vegetation productivity was found to offset carbon emissions from permafrost in the modeling scenarios explored by McGuire et al. (2018).

Finally, the physical effects of climate change on rivers are large. Extreme warming in the Arctic is driving hydrologic intensification, which increases freshwater fluxes (Stuefer et al. 2017; Lafrenière and Lamoureux 2019). Discharge in large rivers has risen by 0.22% per year across the Arctic over the last three decades (Feng et al. 2021). Decreasing snow cover and snow cover duration (Meredith et al. 2019) are leading to an earlier spring freshet in some areas (Zheng et al. 2019; Feng et al. 2021) and earlier river ice breakup (Cooley and Pavelsky 2016). Changes in precipitation, evapotranspiration, snowmelt, and active layer depth affect runoff generation in dissimilar ways and have resulted in an increase in interannual variability in river discharge (Stuefer et al. 2017). Together, these shifts in hydrologic intensity are expected to produce profound impacts on ecological systems (Wrona et al. 2016) that may significantly impact the carbon budget of river corridors.

The large carbon stock, rapid increases in productivity, and changes in fluvial processes make it difficult to predict the trend in carbon fluxes in river corridors under changing climate regimes. Developing a carbon budget that

https://doi.org/10.52381/ICOP2024.161.1

addresses these processes can help evaluate the significance of river corridors in regional carbon budgets.

1.1 Riverine Landscapes

The riverine landscape is the area occupied by the river corridor. Larger than the channel itself, it encompasses the terrain created by a river and its sediment load (e.g., Ward et al. 2002; Wymore et al. 2023). A primary component of a river corridor is the floodplain, which is the flat area adjacent to the channel constructed by the river under the present climate and is frequently subject to overflow (Leopold and Dunne 1978). The floodplain, in other words, is part of the present hydroclimatic conditions and undergoes recurrent disturbance (Nanson and Croke 1992). Terraces are floodplain surfaces that are rarely inundated, due to channel entrenchment or migration. As such, river corridors comprise a mosaic of surfaces distinguished by varying frequency of fluvial inundation and disturbance (Wolman and Leopold 1957) and states of plant succession (Bliss and Cantlon 1957). These variations produce a range of environments that support diverse ecological communities (Naiman and Décamps 1997: Hauer et al. 2016). On Alaska's Arctic coastal plain for example, the Canning River corridor (Figure 1) includes sparsely vegetated gravel bars, transitory aufeis, and fully vegetated terraces. The interplay between vegetation growth (modulated by proximity to water) and flow disturbance governs both the distribution of biomass within the river corridor and the evolution of channel morphology (Gurnell et al. 2012). Our goal in this paper is to outline a carbon budget for a river corridor under rapidly changing periglacial conditions, with a focus on the interactions of physical processes and storage of organic carbon within the system.

2 Previous Work on Riverine C Budgets

Cole et al. (2007) first suggested that rivers play an active and significant role in the carbon cycle at global or regional scales, rather than serving as passive pipes that transmit carbon from terrestrial ecosystems to the sea. In their analysis, aquatic systems are both net sources of gaseous carbon to the atmosphere and net accumulators of stored organic matter because they receive inputs of organic carbon from surrounding terrestrial ecosystems. This situation contrasts with terrestrial environments, where gross primary production (GPP) is the main pathway to introduce carbon into the system (aside from minor abiotic sources like weathering). In the terrestrial ecosystem, fluxes to the atmosphere, storage, and exports cannot collectively exceed GPP. Cole et al. (2007) compiled a global freshwater aquatic ecosystem carbon budget to show that carbon fluxes to gaseous carbon efflux, storage, and export (all losses to the aquatic ecosystem) require large carbon inputs (both GPP and organic carbon from the land); carbon inputs into freshwater systems exceed the global export of carbon to the ocean by at least a factor of two. The carbon "subsidy" from terrestrial landscapes supports aquatic ecosystems as simultaneous C sources and sinks.

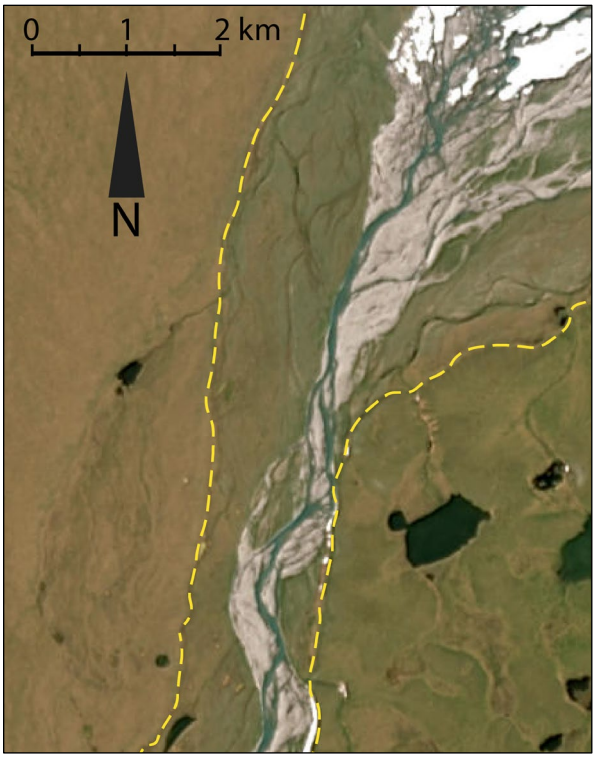

Figure 1. The Canning River in northern Alaska illustrates the heterogeneity in carbon stocks and surface age across an active river corridor in contrast with the surrounding tundra. The river corridor between the dashed yellow lines spans a shifting mosaic of vegetation communities in different stages of growth and whose carbon stock has been augmented and/or depleted by fluvial processes. The example here includes gravel bars, vegetated channels, vegetated terraces, and bodies of aufeis. (Landsat image.)

The land-ocean aquatic continuum (LOAC) model of Regnier et al. (2013) builds a more detailed carbon budget for inland waters. Like the Cole et al. (2007) mass budget, carbon fluxes to the inland waters section (rivers, lakes, and reservoirs) of the LOAC (Figure 2) are bracketed by the total C delivered into inland waters from surrounding terrain ($C_{tot,in,}$) and the total C delivered out to estuaries ($C_{tot,out}$). The difference between these is balanced by fluxes arising from processes within the inland waters system: net primary production within the aquatic ecosystem (GPP-plant respiration), C_{NPP}; gases released by respiration and decomposition of organic matter, C_{CO2} and C_{CH4}; dissolved inorganic carbon from weathering, $C_{inorg,w}$; rock-derived petrogenic carbon, $C_{petro,}$ (Hilton and West 2020); and organic carbon burial C_{sed}. The fluxes at the top of the box (C_{NPP}, C_{CO2}, and C_{CH4}) reflect plant growth, decay, and microbial activity within the inland waters system. The fluxes at the bottom of the box ($C_{inorg,w}$, C_{petro}, and C_{sed}) arise from physical and (in the case of weathering) chemical interactions with sediments and bedrock. Because this is a budget, all fluxes sum to 0.

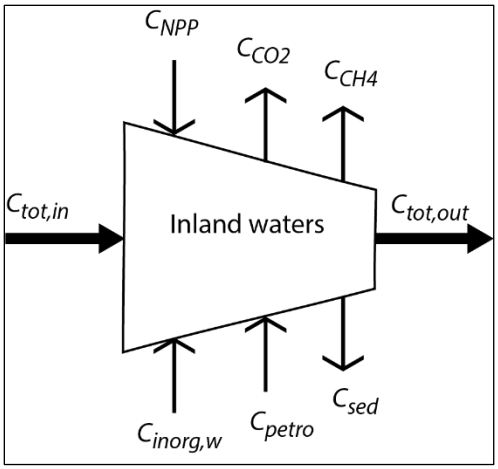

Figure 2. C budget of inland waters (modified from Regnier et al. 2013, inspired by Cole et al. 2007). The trapezoid mirrors the funneling of input ($C_{tot,in}$) from the surrounding watershed to the aquatic system. Fluxes across the top of the box are direct exchanges with the atmosphere, fluxes at the bottom of the box arise from groundwater ($C_{inorg,w}$) and production or deposition of sediment. C inputs from the terrestrial landscape ($C_{tot,in}$) generally exceed fluvial exports to the sea ($C_{tot,out}$).

Several conceptual carbon models address processes unique to fluvial systems. Wohl et al. (2017) treat the active river channel and surrounding riparian area as separate linked systems. In twin mass balance equations, fluvial erosion and deposition are implicitly included in organic carbon mass flux terms into and out of each system. Lininger and Wohl (2019) elaborate that in permafrost regions these fluxes are affected by the ratio of "erosive force to erosional resistance". Sutfin et al. (2016) conclude that organic carbon retention in river systems is optimized by cool, wet conditions and wide river corridors with complex channel forms.

3 Tailoring a Carbon Budget for an Icy Riverine Corridor

The Icy Landscapes project addresses fluvial processes and their carbon budget implications in a riverine corridor in continuous permafrost terrain (Anderson et al. 2022). This report outlines how the data we are generating will inform a riverine corridor carbon budget.

Our field site is the Canning River in northern Alaska (Figure 3), which drains a catchment area of 7,142 km^2 and flows ~200 km through continuous permafrost from glaciated headwaters in the Brooks Range to its delta in the Beaufort Sea. Its multi-thread channel is gravel-bedded and flows in a river corridor that tends to widen from ~0.5 km in the mountains to ~1.5 km in the foothills and widens further in the delta on the coastal plain. The vegetation in the watershed ranges from prostrate shrub tundra in the mountains to graminoid tundra in the foothills to sedge wetlands in the delta (Raynolds and Walker, 2022), but the river corridor as distinct from the surrounding landscape is dominated by willow shrub communities (Schickhoff et al. 2002; Bockheim et al. 2003).

Our study focuses on a few sites along the channel (Figure 3), each representing different hydrologic and ecological environments within the watershed. At each site, we define a control volume that spans the breadth of the river corridor and extends downstream one to several kilometers. In these sites, we have collected samples to characterize organic carbon stocks and constrain deposit ages within the river corridor segment, and we have made spot measurements of river sediment and solute fluxes (Repasch et al. 2024). Data from these samples are still being generated. We complement these data with studies of fluvial erosion processes (Arcuri et al. 2022).

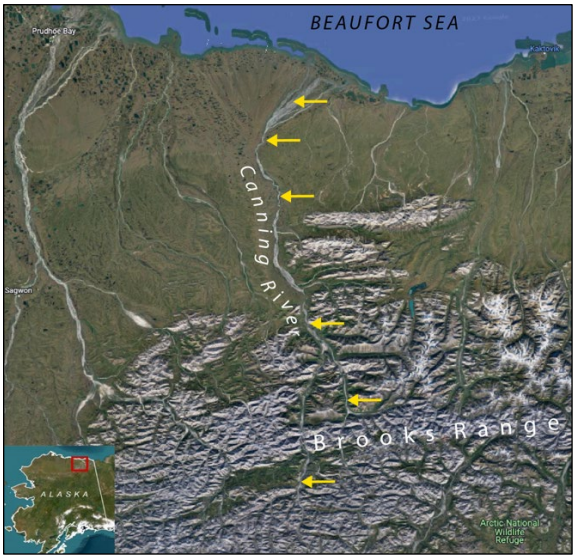

Figure 3. Riverine corridors cross the continuous permafrost terrain of the North Slope of Alaska. Yellow arrows show sites on the Canning River where we have sampled to assess the carbon stock. Inset shows location in Alaska. (Landsat image)

Although the carbon budgets outlined thus far (see Figure 2) focus on carbon fluxes, in campaign-style field work it is more practical to collect data on carbon stock. Figure 4 shows an adaptation of the carbon budget to analyze the carbon stock (S_{Ctot}) in a river corridor segment. The fluxes from weathering processes ($C_{inorg,w}$ and C_{petro}) are now included in the fluvial flows in and out ($C_{tot,in}$ and $C_{tot,out}$). Bicarbonate from weathering reactions ($C_{inorg,w}$) and recalcitrant carbon from rock organic carbon (C_{petro}) both tend to pass through the channel system unchanged and the fluxes are small relative to those of organic matter (Regnier et al. 2013). The remaining fluxes (C_{NPP}, C_{CO2}, C_{CH4}, and C_{sed}) directly affect the standing carbon stock. The challenge is to discover how these fluxes are changing and may affect the carbon stock. To do so, we next consider how to compute the C stock across the heterogeneous river corridor, the accumulation of organic carbon on a fluvial surface, and the fluvial processes that both create and destroy floodplain surfaces.

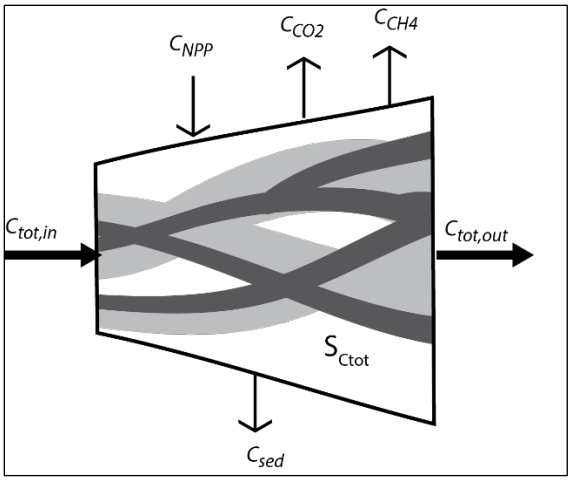

Figure 4. Carbon budget refined to analyze carbon stocks (S_{Ctot}) in a braided river corridor segment. River corridors often widen downstream, as suggested with the widening trapezoid shape. Dark gray lines represent channels within the river corridor. Light gray and white areas represent different age geomorphic surfaces on which carbon stocks differ due to the time-integrated effects of C_{NPP}, C_{CO2}, C_{CH4}, and C_{sed}. The fluxes $C_{inorg,w}$ and C_{petro} are now included in $C_{tot,in}$ and $C_{tot,out}$.

3.1 Geomorphic Surfaces

Fluvial erosion and deposition processes regularly create, modify, and destroy landforms that comprise the river corridor, producing a heterogeneous landscape of abandoned channels, meander scrolls, bars, islands, and terraces (Figure 4; see also Figure 1). These geomorphic surfaces can be mapped from aerial imagery (Wellstein et al. 2003), surveys of vegetation communities (e.g., Kalliola and Puhakka 1988), or detailed stratigraphic study (Mann et al. 1995). Pioneer vegetation species establish on newly exposed surfaces and succession proceeds until a sufficiently large flood removes or buries the community. Although disturbance is a defining characteristic of river corridors, some surfaces remain stable for decades or more. Cross-cutting relationships, vegetation stages, and age-dating techniques can be used to identify a chronosequence of geomorphic surfaces that span a range of development.

3.2 Carbon Stock

The carbon stock (S_{Ctot}) on a geomorphic surface is the total of soil organic matter, above ground biomass, and below ground biomass (roots), integrated over the depth of the deposit. Soil organic matter generally forms the largest part of the total carbon stock, particularly in arctic soils where decomposition rates are low. The carbon stock on a fluvial geomorphic surface reflects inputs from plant growth (C_{NPP}), losses from microbial respiration (C_{CO2}) and methanogenesis (C_{CH4}), and the net fluvial deposition and erosion of organic matter (C_{sed}).

Growing plant communities can sequester carbon rapidly (Cole et al. 2007). Primary succession on alluvial surfaces on Alaska's North Slope progresses from pioneering herbaceous species, through a succession of shrub (predominantly willow) species, and, if undisturbed, ultimately to a wet tundra meadow community (Bliss and Cantlon 1957; Bliss and Peterson 1992). These changes are associated with an increase in soil organic matter and in permafrost, a decrease in active layer thickness. Among arctic vegetation types, riparian willow shrubs have the highest productivity (Shaver and Chapin 1991), suggesting that there is an increase in the input flux, C_{NPP}, on riparian surfaces with surface age up through the shrub stages. The efflux of carbon from a surface due to microbial respiration, C_{CO2}, should increase along with the carbon stock, assuming a fixed rate of microbial respiration per unit mass of organic matter. The net effect of these time-varying fluxes is expected to produce an asymptotic increase in the carbon stock on an undisturbed fluvial geomorphic surface (i.e., C_{sed} = 0) over time (Figure 5 top). The development of carbon stock on a surface may be punctuated by flood events that deposit organic matter, producing a step increase in the stock, or remove organic matter, producing a step decrease. These processes are not included in the idealized scenario shown in Figure 5, but their occurrence is seen in truncated soil profiles and buried organic layers in floodplain deposits (e.g., Mann et al. 1995).

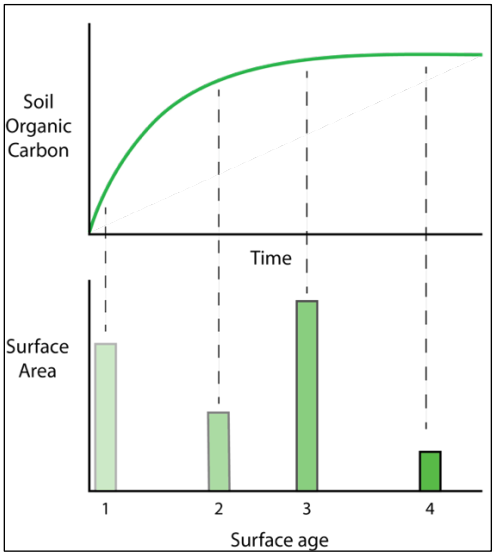

Figure 5. (Top) Hypothetical accumulation of soil organic carbon (SOC) over time on an undisturbed geomorphic surface. (Bottom) Areas (A_i) of four surfaces, numbered 1–4, of different ages that might be used in Equation 1 to compute total carbon stock in a reach (S_{Ctot}).

The carbon stock for a reach of a river corridor (e.g., Figure 4) must account for the mosaic of different surface areas and states of vegetation succession and organic matter accumulation. The total carbon stock in a reach, S_{Ctot}, is therefore computed as the sum of the carbon stocks on all geomorphic surfaces:

$$S_{Ctot} = \Sigma A_i SOC_i \quad [1]$$

where A_i is the area and SOC_i is the carbon stock of the i^{th} geomorphic surface (Figure 5).

An unknown in measuring the carbon stock on a geomorphic surface is the depth over which to integrate. The depths of arctic alluvial deposits are poorly constrained (Hugelius et al. 2014). Alluvium of North Slope rivers probably ranges from 5–8 m in depth and increases to 15–20 m in deltaic areas (Carter et al. 1986). The gravel and sand-dominated deposits are poor candidates for auger or core sampling.

3.3 Dynamics of Periglacial River Corridors

Channel migration, gravel bar formation, bank incision, and overbank deposition are among the fluvial processes that create and destroy alluvial geomorphic surfaces. Collectively these processes control the areas of geomorphic surfaces (A_i in Equation 1) on which plants grow and soil organic matter accumulates (SOC_i; Ward et al. 2002). Therefore, understanding fluvial processes and rates and their control are important for predicting future carbon budget changes. We consider three aspects of fluvial processes in floodplain ecosystems under warming whose effects need to be incorporated into a carbon budget analysis: channel erosion rates, changing hydrology, and vegetation feedbacks.

3.3.1 Channel erosion

A recent analysis of riverbank erosion found that, on average, permafrost riverbank erosion rates are nine times lower than non-permafrost rivers (Rowland et al. 2023). They conclude that permafrost limits bank erosion and infer that bank erosion rates will increase as warming degrades permafrost. A second study of Arctic rivers by Ielpi et al. (2023), however, showed declining channel lateral migration rates since 1970. They suggest that the northward-advance of shrubs and deepening of their root systems under warming conditions strengthens riverbanks and limit bank erosion. Both studies focus on lateral bank erosion and channel migration, processes that reduce the areas of geomorphic surfaces (A_i) adjoining an active channel.

Floodplains are also affected by vertical accretion by sediment deposition in bars, overbank deposits, and channel fills, processes that act as episodic C_{sed} flux events. Douglas et al. (2021) found that particulate organic carbon (POC) deposition at least partially offsets current bank erosion rates. Non-organic sediment deposition also plays a role by burying peat, wood, and leaves, common components of arctic floodplain stratigraphy (Carter et al. 1986; Mann et al. 1995). The deposits that entomb organic carbon, also serve as new surfaces (A_i) on which vegetation growth and soil organic matter accumulation restarts.

As climate warms, the question arises whether periglacial river systems will undergo net aggradation or net incision. Early Holocene warming apparently triggered an increase influx of sediment into fluvial systems from thawing hillslopes, which drove aggradation in floodplains on the North Slope (Mann et al. 2010). That history suggests that a full understanding of likely carbon budget trajectories for arctic river systems is connected to processes that deliver sediment from hillslopes.

3.3.2 Hydrologic change

Rivers like the Canning in continuous permafrost are subject to arctic hydrologic intensification effects that may influence bank erosion and overbank flows. Stream gauge data on the Canning River are limited, but data on the nearby Kuparuk River are probably representative of the region. The Kuparuk has shown an increase in discharge of 35% since the 1970s, an earlier arrival of the spring freshet, and rising river water temperatures (Zheng et al. 2019). The mechanisms of ice breakup during the freshet and their impacts on flooding and erosion are difficult to observe, particularly where extensive aufeis fields develop (Overeem et al. 2023). If the freshet arrives before riverbanks have thawed substantially, lateral bank erosion might be reduced. This effect would be countered, however, by warming river waters. Ice-cemented banks in the Canning River are most prominent along the edges of the river corridor in the delta region. We measured river water temperatures of 11–17 °C in July of 2022 and 2023, which suggests that the summer flows are capable of considerable thermal erosion in reaches with ice cemented banks. Observations and measurements during the challenging conditions of the spring freshet are needed to understand these competing processes and how they are changing.

Another hydrologic change is a possible increase in frequency and severity of convective storms (e.g., Poujol et al. 2020). The potential impact of these events is illustrated by observations of Repasch et al. (2024). During convective storms in 2022 and 2023 on the Canning River the discharge roughly doubled, suspended sediment flux increased 30-fold, and particulate organic carbon flux increased 90-fold. It will take more work to determine the source and fate of the sediments mobilized in such events. At the same time, increasing active layer depths may increase subsurface water storage capacity on hillslopes and limit storm runoff peaks as warming continues, an effect that would reduce storm erosion.

3.3.3 Vegetation feedbacks

Throughout the tundra biome, increased temperatures are causing an increase in plant canopy height and abundance of shrubs (Elmendorf et al. 2012). In the Canning and other north-flowing rivers on the North Slope, the riparian vegetation canopy height is greatest in the Brooks Range foothills and decreases downstream with increasing latitude. Riparian willows interact with flood waters in more ways than simply providing bank strength (Gurnell et al. 2012). Bank scour (and probably ice jam breakup) can erode well-established willow clumps from banks during floods and redeposit (i.e., strand) them on gravel bars downstream. Cursory observations along the Canning River suggests that sharp outer bends in channels are prone to this type of scour, and that willow clump deposition is most likely on the upstream edge of the next gravel bar. Even so, we observed willow clumps (several meters in length) rolling down the channel in the coastal plain, far from obvious erosional sources. Deposited willow clumps can re-sprout and form a living anchor for a growing bar. Alternatively, the willow does not survive, but adds to the

carbon stock of the surface on which it is deposited. In both cases, deposited willow clumps form obstacles that interact with water flow and sediment deposition, in some places inciting scour and in other places supporting deposition. These complex interactions are not unique to periglacial systems (Gurnell et al. 2012). The habitat expansion and rapid growth of shrubs are introducing new vegetation-channel dynamics to arctic river corridors.

While willow shrubs are important players in channel dynamics in the upper reaches of the Canning River, graminoid and wet sedge tundra dominate the vegetation in the coastal plain. In these areas, the active layer is often a strongly rooted turf mat, and the bank is peat rich. The river can incise into this vegetation community and mobilize the carbon stock it contains. Our summertime observations show that these banks erode by fluvial thermal undercutting, followed by cantilevered block collapse (Arcuri et al. 2022), mirroring the erosion of coastal bluffs along the Beaufort Sea (e.g., Barnhart et al. 2014). Blocks of strongly rooted turf are typically < 1 m thick (typically 10s of cm, essentially the active layer where roots thrive), and several meters in breadth. Often, the turf block does not cleanly break at the surface, but instead drapes over the riverbank, armoring it for some period. The blocks that break free may lie stranded on the channel edge close to the bank from which it fell or may be trundled some distance downstream. Like willow clumps, turf blocks are deposited on the upstream edges of bars and can either re-sprout or not. On one gravel bar we surveyed > 100 turf blocks with dimensions of ~0.3 m x 1 m x 1 m in an area < 200 m^2. The blocks serve as an important addition to the carbon stock and can initiate plant growth on barren bars. Understanding these contributions to the carbon budget deserves more study.

4 Summary

We have reviewed aquatic system carbon budgets with an eye toward understanding the role of riverine corridors on carbon exchange with the atmosphere in a changing climate. River corridors characteristically contain a mosaic of surfaces shaped by fluvial inundation and disturbance and colonized by successional plant communities. It is therefore practical to assess the carbon stock on multiple geomorphic surfaces and deduce the impacts of changing processes and their rates on that stock. An understudied component of the carbon stock is the depth of alluvium within river corridors. Every flux that affects carbon stocks is likely to be impacted by climate warming, from plant growth rate to microbial degradation, to the size of floods and their timing relative to timing of bank thawing. Organic matter deposition on the floodplain, in the form of large willow clumps or intact turf blocks, has received little attention yet appears to play important roles that have yet to be elucidated.

5 Acknowledgements

The Icy Landscapes project is funded by NSF 2001225; MR supported by NSF OPP Post-Doctoral Fellowship. We thank Sue Aikens (Kavik River Camp), Cyn Merrow and Kyle Milne (Arctic Wild), Justin Hill and Faustine Bernadac (Polar Field Services), and Scott (Alpine Air). We thank J. Koch and two reviewers for their input.

6 References

Arcuri, J., Overeem, I., Repasch, M.N., Anderson, S.P., Anderson, R.S., and Koch, J. 2022. 'Permafrost riverbanks shaped by thaw-dependent fluvial erosion', in *American Geophysical Union Fall Meeting*. Chicago, Illinois, United States: 12–16 December, 2022.

Anderson, S.P., Repasch, M.N., Overeem, I., Arcuri, J., Anderson, R.S., and Koch, J. 2022. 'Icy riverine landscapes: mobilization and fate of carbon-rich sediment in a periglacial braided river corridor', in *American Geophysical Union Fall Meeting*. Chicago, Illinois, United States: 12–16 December, 2022.

Barnhart, K.R., Anderson, R.S., Overeem, I., Wobus, C., Clow, G.D. and Urban, F.E. 2014. 'Modeling erosion of ice-rich permafrost bluffs along the Alaskan Beaufort Sea coast', *Journal of Geophysical Research - Earth Surface* 119(5), pp. 1155–1179, doi:10.1002/2013JF002845.

Bliss, L.C. and Cantlon, J.E. 1957. 'Succession on river alluvium in northern Alaska', *The American Midland Naturalist* 58(2), pp. 452–469. Available at: https://www.jstor.org/stable/2422628/.

Bliss, L.C. and Peterson, K.M. 1992. 'Plant succession, competition, and the physiological constraints of species in the Arctic', in F.S. Chapin III, R.L. Jefferies, J.F. Reynolds, G.R. Shaver, J. Svoboda, and E.W. Chu (eds.), *Arctic Ecosystems in a Changing Climate: An Ecophysiological Perspective*. San Diego, California, United States: Academic Press, pp. 111–136.

Bockheim, J.G., O'Brien, J.D., Munroe, J.S., and Hinkel, K.M. 2003. 'Factors affecting the distribution of *Populus balsamifera* on the North Slope of Alaska, U.S.A', *Arctic, Antarctic, and Alpine Research* 35 (3), pp. 331–340. doi:10.1657/1523-0430

Canadell, J. G., Monteiro, P. M. S., Costa, M. H., Cotrim da Cunha, L., Cox, P. M., Eliseev, A. V., et al. 2021. 'Global carbon and other biogeochemical cycles and feedback', in V. Masson-Delmotte, et al. (eds.), *Climate Change 2021: The Physical Science Basis, Contribution of Working Group I to the Sixth Assessment Report of the IPCC*. Cambridge, United Kingdom and New York, New York, United States: Cambridge University Press, pp. 673–816, doi:10.1017/9781009157896.007.

Carter, L.D., Ferrians, O.J., Jr., and Galloway, J.P. 1986. 'Engineering-geologic maps of northern Alaska coastal plain and foothills of the Arctic National Wildlife Refuge', *United States Geological Survey* Open-File Report 86–334.

Raynolds, M. and Walker, D. 2022. *Raster Circumpolar Arctic Vegetation Map*. Mendeley Data, version 2. doi:10.17632/c4xj5rv6kv.2.

Cole, J.J., Prairie, Y.T., Caraco, N.F., McDowell, W.H., Tranvik, L.J., Striegl, R.G., Duarte, C.M., Korelainen, P., Downing, J.A., Middelburg, J.J., and Melack, J. 2007. 'Plumbing the global carbon cycle: Integrating inland waters in the terrestrial carbon budget', *Ecosystems* 10, pp. 171–184. doi:10.1007/s10021-006-9013-8.

Cooley, S.W. and Pavelsky, T.M. 2016. 'Spatial and temporal patterns in Arctic river ice breakup revealed by automated ice detection from MODIS imagery', *Remote Sensing of Environment* 175, pp. 310–322. doi:10.1016/j.rse.2016.01.004

Douglas, M.M., Li, G.K., Fischer, W.W., Rowland, J.C., Kemeny, P.C., West, A.J., Schwenk, J., Piliouras, A.P., Chadwick, A.J., and Lamb, M.P. 2021. 'Organic carbon burial by river meandering partially offsets bank erosion carbon fluxes in a discontinuous permafrost floodplain', *Earth Surface Dynamics* 10, pp. 421–435. doi:10.5194/esurf-10-421-2022

Elmendorf, S.C., Henry, G.H.R., Hollister, R.D., et al. 2012. 'Plot-scale evidence of tundra vegetation change and links to recent summer warming', *Nature Climate Change* 2, pp. 453–457. doi:10.1038/nclimate1465.

Feng, D., Gleason, C.J., Lin, P., Yang, X., Pan, M., and Ishitsuka, Y. 2021. 'Recent changes to Arctic river discharge', *Nature Communications* 12, 6917. doi:10.1038/s41467-021-27228-1

Friedlingstein, P. et al. 2022. 'Global carbon budget 2022', *Earth System Science Data* 14, pp. 4811–4900. doi:10.5194/essd-14-4811-2022.

Frost, G.V. and Epstein, H.E. 2014. 'Tall shrub and tree expansion in Siberian tundra ecotones since the 1960s', *Global Change Biology* 20, pp. 1264–1277. doi:10.1111/gcb.12406.

Gurnell, A.M., Bertoldi, W., and Corenblit, D. 2012. 'Changing river channels: The roles of hydrological processes, plants and pioneer fluvial landforms in humid temperate, mixed load, gravel bed rivers', *Earth-Science Reviews* 111, pp. 129–141. doi:10.1016/j.earscirev.2011.11.005.

Hauer, F.R., Locke, H., Dreitz, V.J., Hebblewhite, M., Lowe, W.H., Muhlfeld, C.C., Nelson, C.R., Proctor, M.F., and Rood, S.B. 2016. 'Gravel-bed floodplains are the ecological nexus of glaciated mountain landscapes', *Science Advances* 2, e1600026. doi:10.1126/sciadv.1600026.

Hilton, R.G. and West, A.J. 2020. 'Mountains, erosion and the carbon cycle', *Nature Reviews - Earth and Environment* 1, pp. 284–299. doi:10.1038/s43017-020-0058-6.

Hugelius, G., Strauss, J., Zubrzycki, S., Harden, J.W., Schuur, E.A.G., Ping, C.-L., Schirrmeister, L., Grosse, G., Michaelson, G.J., Koven, C.D., O'Donnell, J.A., Elberling, B., Mishra, U., Camill, P., Yu, Z., Palmtag, J., and Kuhry, P. 2014. 'Estimated stocks of circumpolar permafrost carbon with quantified uncertainty ranges and identified data gaps', *Biogeosciences* 11, pp. 6573–6593. doi:10.5194/bg-11-6573-2014.

Ielpi, A., Lapôtre, M.G.A., Finotello, A., and Roy-Léveillée, P. 2023. 'Large sinuous rivers are slowing down in a warming Arctic', *Nature Climate Change* 13, pp. 375–381. doi:10.1038/s41558-023-01620-9.

Kalliola, R. and Puhakka, M. 1988. 'River dynamics and vegetation mosaicism: A case study of the River Kamajohka, northernmost Finland', *Journal of Biogeography* 15, pp. 703–719. Available at: https://www.jstor.org/stable/2845334.

Lafrenière, M.J. and Lamoureux, S.F. 2019. 'Effects of changing permafrost conditions on hydrological processes and fluvial fluxes', *Earth-Science Reviews* 191, pp. 212–223. doi:10.1016/j.earscirev.2019.02.018.

Leopold, L.B. and Dunne, T. 1978. *Water in Environmental Planning.* San Francisco, California, United States: W.H. Freeman and Co.

Lininger, K.B. and Wohl, E. 2019. 'Floodplain dynamics in North American permafrost regions under a warming climate and implications for organic carbon stocks: A review and synthesis', *Earth-Science Reviews* 193, pp. 24–44.

Mann, D.H., Fastie, C.L., Rowland, E.L., and Bigelow, N.H. 1995. 'Spruce succession, disturbance, and geomorphology on the Tanana River floodplain, Alaska', *Écoscience* 2(2), pp. 184–199. Available at: https://www.jstor.org/stable/42900819.

Mann, D.H., Groves, P., Reanier, R.E., and Kunz, M.L. 2010. 'Floodplains, permafrost, cottonwood trees, and peat: What happened the last time climate warmed suddenly in arctic Alaska?', *Quaternary Science Reviews* 29, pp. 3812–3830. doi:10.1016/j.quascirev.2010.09.002

McGuire, A.D., Lawrence, D.M., Koven, C., Clein, J.S., Burke, E., Chen, G., et al. 2018. 'Dependence of the evolution of carbon dynamics in the northern permafrost region on the trajectory of climate change', *PNAS* 115(15), pp. 3882–3887, doi:10.1073/pnas.1719903115.

Meredith, M., Sommerkorn, M., Cassotta, S., Derksen, C., Ekaykin, A., Hollowed, A., Kofinas, G., et al. 2019. 'Polar Regions', in H.-O. Pörtner, et al. (eds.), *IPCC Special Report on the Ocean and Cryosphere in a Changing Climate*. Cambridge, United Kingdom and New York, New York, United States: Cambridge University Press, pp. 203–320. doi:/10.1017/9781009157964.005.

Naiman, R.J. and Décamps, H. 1997. 'The ecology of interfaces: Riparian zones', *Annual Review of Ecological Systems* 28, pp. 621–658, doi:10.1146/annurev.ecolsys.28.1.621.

Nanson, G.C. and Croke, J.C. 1992. 'A genetic classification of floodplains', *Geomorphology* 4, pp. 459–486.

Overeem, I., Arcuri, J., Repasch, M., Anderson, R.S., Anderson, S.P., Urban, F., Koch, J., Vachon, R., and Cochran, C. 2023. 'Thermal state controls coupling discharge and sediment transport in Arctic rivers', in *AGU23—Wide. Open. Science*. San Francisco, California, United States: 11–15 December, 2023.

Poujol, B., Prein, A.F., and Newman, A.J. 2020. 'Kilometer-scale modeling projects a tripling of Alaskan convective storms in future climate', *Climate Dynamics* 55 (11–12), pp. 3543–3564. doi:10.1007/s00382-020-05466-1.

Regnier, P., et al. 2013. 'Anthropogenic perturbation of the carbon fluxes from land to ocean', *Nature Geoscience* 6, pp. 597–607. doi:10.1038/NGEO1830.

Regnier, P., Resplandy, L, Najjar, R.G., and Ciais, P. 2022. 'The land-to-ocean loops of the global carbon cycle', *Nature* 603, pp. 401–410. doi:10.1038/s41586-021-04339-9.

Repasch, M., Arcuri, J., Overeem, I., Anderson, S.P., Anderson, R.S., and Koch, J.C. 2024. 'Impacts of convective storms on runoff, erosion, and carbon export in a continuous permafrost landscape', in *ICOP 2024 12th International Conference on Permafrost*. Whitehorse, Yukon, Canada: 16–20 June, 2024.

Rowland, J.C., Schwenk, J.P., Shelef, E., Muss, J., Ahrens, D., Stauffer, S., et al. 2023. 'Scale-dependent influence of permafrost on riverbank erosion rates', *Journal of Geophysical Research-Earth Surface* 12, e2023JF007101. doi:10.1029/2023JF007101.

Schickhoff, U., Walker, M.D., and Walker, D.A. 2002. 'Riparian willow communities on the Arctic Slope of Alaska and their environmental relationships: A classification and ordination analysis', *Phytocoenologia* 32(2), pp. 145–204. doi:10.1127/0340-269X/2002/0032-0145.

Schuur, E.A.G., McGuire, A.D., Schädel, C., Grosse, G., Harden, J.W., Hayes, D.J., et al.. 2015. 'Climate change and the permafrost feedback', *Nature* 520, pp. 171–179. doi:10.1038/nature14338

Shaver, G.R. and Chapin, F.S. 1991. 'Production: biomass relationships and element cycling in contrasting Arctic vegetation types', *Ecological Monographs* 61(1), pp. 1–31. doi:10.2307/1942997.

Stuefer, S.L. Arp, C.D., Kane, D.L., and Liljedahl, A.K. 2017. 'Recent extreme runoff observations from coastal arctic watersheds in Alaska', *Water Resources Research* 53, pp. 9145–9163. doi:10.1002/2017WR020567

Sutfin, N.A., Wohl, E., and Dwire, K.A. 2016. 'Banking carbon: a review of organic carbon storage and physical factors influencing retention in floodplains and riparian ecosystems', *Earth Surface Processes and Landforms* 41, pp. 38–60. doi:10.1002/esp.3857.

Tarnocai, C., Canadell, J.G., Schuur, E.A.G., Kuhry, P., Mazhitova, G., and Zimov, S. 2009. 'Soil organic carbon pools in the northern circumpolar permafrost region', *Global Biogeochemical Cycles* 23, GB2023. doi:10.1029/2008GB003327

Tape, K.D., Hallinger, M., Welker, J.M., and Ruess, R.W. 2012. 'Landscape heterogeneity of shrub expansion in Arctic Alaska', *Ecosystems* 15, pp. 711–724. doi:10.1007/s10021-012-9540-4.

Ward, J.V., Tockner, K., Arscott, D.B., and Claret, C. 2002. 'Riverine landscape diversity', *Freshwater Biology* 47, pp. 517–539. doi:10.1046/j.1365-2427.2002.0893.x.

Wellstein, C., Uehlinger, U., and Zah, R. 2003. 'Terrestrial floodplain vegetation', in J.V. Ward and U. Uehlinger (eds.), *Ecology of a Glacial Flood Plain*. Dordrecht, Netherlands: Springer Science+Business Media.

Wohl, E., Hall, R.O, Jr., Lininger, K.B., Sutfin, N.A., and Walters, D.M. 2017. 'Carbon dynamics of river corridors and the effects of human alteration', *Ecological Monographs* 87, pp. 379–409. doi:10.1002/ecm.1261/full

Wolman, M.G. and Leopold, L.B. 1957. 'River flood plains: Some observations on their formation', *US Geological Survey* Professional Paper 282-C. US Government Printing Office, Washington, D.C., United States, 28 p.

Wrona, F.J., Johansson, M., Culp, J.M., Jenkins, A., Mård, J., Myers-Smith, I.H., Prowse, T.D., Vincent, W.F., and Wookey, P.A. 2016. 'Transitions in Arctic ecosystems: Ecological implications of a changing hydrologic regime', *Journal of Geophysical Research: Biogeosciences* 121, pp. 650–674. doi:10.1002/2015JG003133

Wymore, A.S., Ward, A.S., Wohl, E., and Harvey, J.W. 2023. 'Viewing river corridors through the lens of critical zone science', *Frontiers in Water* 5, 1147561. doi:10.3389/frwa.2023.1147561

Zheng, L., Overeem, I., Wang, K., and Clow, G.D. 2019. 'Changing Arctic river dynamics caused localized permafrost thaw', *Journal of Geophysical Research-Earth Surface* 124. doi:10.1029/2019JF005060.

Mobility of an ancient buried ice mass, Transantarctic Mountains, Antarctica

Marie Bergelin[1], Jaakko Putkonen[2], Daniel Morgan[3] & Greg Balco[1]

[1]*Berkeley Geochronology Center, Berkeley, California, United States*

[2]*Department of Geology and Geological Engineering, University of North Dakota, Grand Forks, North Dakota, United States*

[3]*Department of Earth and Environmental Science, Vanderbilt University, Nashville, Tennessee, United States*

Abstract

We determined the stability of an ancient, buried ice mass in Ong Valley, Transantarctic Mountains, Antarctica. The buried ice underlies the two younger of the three successively older drifts, dated at 11–13 kyrs, 2.9 Myrs, and 4.3–5.1 Myrs, making this some of the oldest ice on Earth. The middle drift contains two stacked ice masses, which are covered by a meter-thick layer of supraglacial debris. Ice of such antiquity has the potential to extend and reveal information about the paleoclimate, that is currently poorly known. To utilize these drifts for paleoclimatological and geomorphological analyses, it is important to determine their stability. Therefore, we measured high-precision markers (~0.5 mm resolution) over a period of seven years on eight surface boulders lodged in the drifts to determine their mobility/stability. We find the stability of the three drifts to increase with distance from the currently exposed ice sheet at the valley mouth. The youngest drift, containing buried ice, appears dynamic and exhibits surface boulder movement between 0.79 and 1.10 cm/yr down the valley over the seven-year period. The middle drift and ice are considered stable, but the surficial debris is still subject to slow erosion and/or patterned ground formation. The old drift is void of buried ice and shows no signs of movement.

1 Introduction

In Antarctica, debris-covered ice is one of three main sources of old glacial ice (Bergelin et al. 2022; Bibby et al. 2016; Schäfer et al. 2000), which also includes basal ice at ice sheet domes (Jouzel et al. 2007) and blue ice at the Transantarctic Mountains (TAM) margin (Yan et al. 2019). Ice, older than 1 Myrs has the potential to extend and reveal information about the Antarctic paleoclimate, that is currently poorly known. However, to utilize these ancient, buried ice masses for paleoclimatological and geomorphological analyses, it is important to determine their long-term stability.

A debris-cover thicker than a few centimeters is known to thermally insulate glacial ice and decrease the effect of ablation (Evatt et al. 2015; Kowalewski et al. 2011; Mihalcea et al. 2006; Östrem 1959). In Alpine settings, surface features such as ice cliffs, water channels, and ponds can enhance ablation (Ragettli et al. 2016), causing the stability of debris-covered glaciers to greatly vary (Moore 2017). However, the occurrences of these surface features are limited in Antarctica due to its cold and arid climate, resulting in the preservation of old buried ice near the surface (e.g., Bibby et al. 2016).

Many buried ice masses have been identified throughout the Transantarctic Mountains, in Antarctica, with a few having the potential to harbor ancient ice (Putkonen and Mahmood 2022), and only two ancient buried ice masses have been studied in greater detail. One is found in Beacon Valley in McMurdo Dry Valleys. This buried ice mass was initially dated to be 8 Ma (Sugden et al. 1995) but its age was later questioned due to Beacon Valley's complex glacier system and potential recharge of ice (Hindmarsh et al. 1998; Ng et al. 2005; Stone et al. 2000; Van der Wateren and Hindmarsh 1995). The other is located in Ong Valley in Miller Range and dated to be 3–5 Ma (Bergelin et al. 2022). These buried ice masses are found to be remnants of the once more extensive continental ice sheet during its previous high stand. They are formed when the continental ice sheet retreats and leaves behind isolated and stagnant smaller ice masses. As the isolated ice mass sublimates, the englacial debris within the sublimating ice slowly accumulates on the surface as supraglacial debris and begins to insulate the underlying ice from further melting.

In Ong Valley, the buried ice mass is part of a glacial drift system of debris deposited by glacial ice, separated by lateral and end moraines. The youngest two of the drifts have massive, buried ice under a thin (< 1 m) layer of loose debris completely concealing the ice. The oldest drift appears to be devoid of buried ice, which, presumably, has sublimed over extended exposure. The youngest drift has been dated to be 11–13 kyrs (Bibby et al. 2016), the middle > 1.1 Myrs (Bibby et al. 2016), and recently determined to be 2.95 Myrs (Bergelin et al. 2022). The oldest drift was initially dated to be > 2.6 Myrs (Bibby et al. 2016) and was recently determined to be 4.3–5.1 Myrs (Bergelin et al. 2022). Each drift system exhibits various age stages of patterned ground formation that appear to correlate to its age. All three drifts have related lateral moraines up on the valley walls that trace the original elevation of the expanded and elevated continental ice sheet surface during deposition. The oldest drift also has a distinct end moraine close to the head of the valley.

The long-term stability of such drifts observed in Ong Valley has been studied elsewhere in Antarctica (Putkonen et al. 2008). However, no comparable studies have been done in the central TAM. Therefore, to evaluate the stability of the drift system in Ong Valley we use high-precision GPS positioning to map the glacial moraines and drift boundaries, and the current boundary of the two buried ice masses. Mapping the distribution of glacial features and

https://doi.org/10.52381/ICOP2024.229.1

deposits can aid in understanding the behavior of past glacial advancements, such as the extent and dimensions, locally and potentially continental-wide. Further, we measure high-precision markers (~0.5 mm resolution) on eight surface boulders located on the drifts over a period of seven years (2010–2017) to determine the mobility and stability of these drifts and buried ice masses.

2 METHODOLOGY

Differential high-precision positioning allows for the determination of an accurate location of an object by making use of a reference point to correct for transient errors and attains a precision level of centimeter to millimeter scale. In Ong Valley, we use GPS and differential correction schemes between two receivers to acquire a high-accuracy position for (i) mapping the glacial moraines and drift boundaries and (ii) detecting surface movement to evaluate the stability of this buried ice mass and associated drift system.

2.1 Data Collection and Processing

During the 2017/2018 Antarctic field season, we mapped the crests of multiple glacial moraines throughout Ong Valley. Each moraine was measured using stop-and-go kinematic surveying. The moraines were mapped by following the crest or perimeter and measuring the positions for approximately 15 seconds, every 5–15 m. The moraine positions were collected using a Trimble receiver, with an antenna mounted to a 2 m survey pole with an attached leveler.

Six visible moraines were not accessible for direct GPS measurements because of their location up on steep valley walls. Instead, the positions of these moraines were determined using a laser ranger and a reference location on the valley floor that was mapped by a handheld GPS. A reference point was found perpendicular to each moraine crest (valley-wall) and 100–500 m away towards mid-valley, from which the distance and elevation difference between the moraine and reference point was measured.

To evaluate the stability of each of the three drifts and determine if any movement has occurred in Ong Valley, we repeatedly measured the position of eight boulders from the three drifts. The positions of the surface boulders were originally measured during the Austral summer 2010, and again in 2011 and 2017.

During the Austral summer, 2010/2011, bolts were installed in eight boulders found on the surface of the three Ong Valley drifts (Figures 1 and 2). These bolts are ~30 cm long and were manually drilled and mounted as close to vertical orientation as possible, into the upper surface of the boulders. The measurement point is a small (~2 mm diameter) dimple stamped on the middle of the flat, top surface of the rock bolt. To perform the final leveling of the antenna, a leveling mount of known shaft dimensions was screwed on the rock bolt. Once the mount was leveled the antenna was attached to the mount for determining the exact position of the stamped dimple.

Two boulders were chosen from the youngest drift, three from the middle drift, two from the oldest drift, and one near

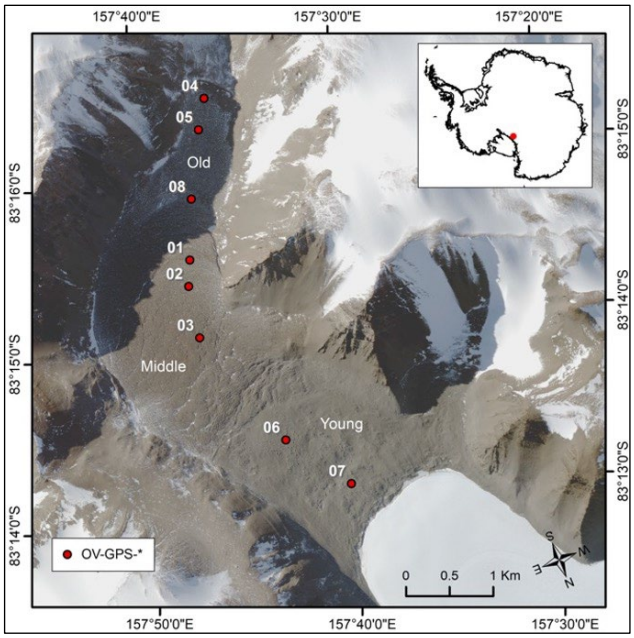

Figure 1. Satellite image of Ong Valley, Antarctica (WV2 satellite image © 2016 Maxar. Red dots indicate the locations of the 8 surface boulders. The legend shows the prefix for the boulder names.

the boundary between the middle and old drift. The boulders were originally selected based on their evidence for stability in the drift. Each boulder was > 1.5 m in the longest dimension and partially submerged in the supraglacial debris, such that any movement is assumed to be caused by either ice movement or active polygons (Figure 2). However, no ideal boulder was available at the boundary between the middle and old drift, and therefore boulder OV-GPS-08 was chosen although it is entirely perched above the drift.

The installed bolts in each boulder were revisited twice over the years. On these re-occupations, we followed the original antenna mounting procedure described above and determined the exact locations of the 2 mm diameter dimples at the top end of the stationary rock bolts. We were able to attach the antenna to a horizontal accuracy of < 1°, resulting in a centered offset of < 0.2 cm of the antenna between the years of repeating measurement. Each boulder location was recorded for a duration of 18–60 minutes for optimal accuracy.

During the initial 2010/2011 field season, a base station bolt was established in Ong Valley on an elevated bedrock outcrop central to the valley and less than 3 km from any of the eight boulders and moraines. The base station antenna was installed at the beginning of each field expedition in Ong Valley and disassembled at the end of each expedition, continuously collecting data in between.

All GPS data collected were processed using the Trimble Business Center (TBC) v5.20 software package provided by UNAVCO. The 2017/2018 Ong Valley base station was set to record daily and hourly (1Hz1Hr) positioning. The collected moraine data were processed against 1Hz1Hr hourly base data, with a horizontal and vertical precision

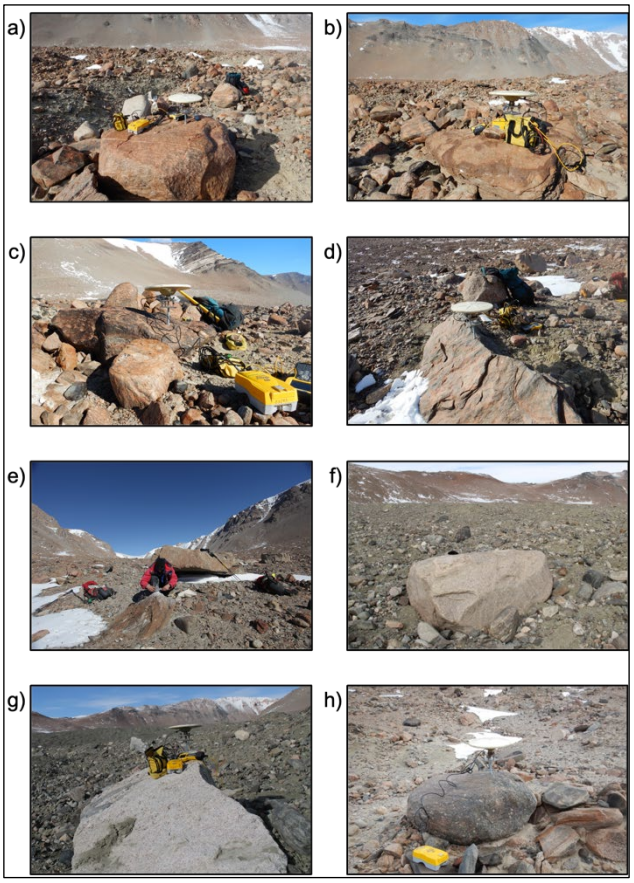

Figure 2. Photographs of surface boulders used for GNSS high-precision movement analysis. (a) OV-GPS-01, (b) OV-GPS-02, (c) OV-GPS-03, (d) OV-GPS-04, (e) OV-GPS-05, and (f) OV-GPS-06, (g) OV-GPS-07, and (h) OV-GPS-08.

failure set at 0.50 m. During field season 2010 and 2011, only daily data files were available (as opposed to hourly), and therefore only daily data files from the base station were used for all baseline processing of the boulder position.

2.2 Moraine Position Analysis

The moraine data point was imported and analyzed using ArcGIS Desktop 10.7.1. To analyze the moraine data, a 1-m resolution, Digital Surface Model (DSM) of Ong Valley was obtained from the Polar Geospatial Center's (PGC) Reference Elevation Model of Antarctica (REMA; Howat et al. 2019). Further, an 8-band multispectral, high-resolution (1.9 m) WorldView2 satellite imagery was obtained for Ong Valley. The satellite image was overlaid and visually georeferenced to the DSM hillshade raster imagery, resulting in a 2-m resolution satellite image of Ong Valley overlaying a 1-m resolution elevation data. The laser-measured moraines were manually added to the moraine point data, based on field measurements, satellite imagery, and raster elevation values.

To correlate glacial features across the valley walls in Ong Valley, an elongated two-dimensional profile of Ong Valley was created. First, a smooth curved profile line was drawn along the center of the valley, using the DSM raster for elevation values. Then all moraine data points were projected, in planar view, onto the profile line based on the nearest analysis. The resulting profile of Ong Valley is then plotted with the projected moraine points.

2.3 Boulder Movement Analysis

The movement of a boulder is determined by its change in position between the repeated measurements from 2010 to 2017. That is, we can calculate the distance between the measured location for a boulder between the years 2010–2011, 2011–2017, and 2010–2017. If the distance exceeds that of the uncertainty between two points in time, then the boulder is assumed to have moved. The position of the point is measured over a processing period in which multiple positions are continuously being recorded. The position after baseline processing is the calculated mean of x (Easting), y (Northing), and z (elevation) position during the measured period. The vertical precision is a one-dimensional component in the z-direction at the 95% confidence interval and is found by scaling the estimated 1-sigma standard deviation of all measured z-values by the coverage factor of 1.960 (Trimble 2019). The associated horizontal precision value is a two-dimensional standard error circle at the 95% confidence interval, representing the local accuracy. That is, the uncertainty in the x and y direction is represented by an error ellipse with semi-major and semi-minor axis and is combined into one horizontal precision value during baseline processing.

The calculated distance a boulder moved is that of the distance between the mean x, y, and z estimated for two separate years. Since the distance between the points is assumed to be < 10 cm, the spherical effect of Earth's curvature can be ignored, and the distance moved is calculated by the Euclidean distance between two points. The uncertainty in the Euclidean distance between the two points is that of the combined standard uncertainty expressed as the positive root of the combined covariance and is determined through error propagation using summation in quadrature, following that of Eq. B15 in Farrance and Frenkel (2012).

3 RESULTS

3.1 Moraine Mapping

It is evident from the mapping of the lateral and terminal moraines in Ong Valley that the Argosy Glacier has, during glacial advancement, expanded up and into the valley at least three times, leaving behind glacial drifts; previously identified by Bibby et al. (2016) as the old, middle and young drift (Figure 3). Using both field observations, moraine mapping, two-dimensional profile, and DSM, we can correlate between the mapped lateral and terminal moraines and assign inferred boundaries. We find that majority of the moraines can be continuously traced across the valley walls (Figure 3).

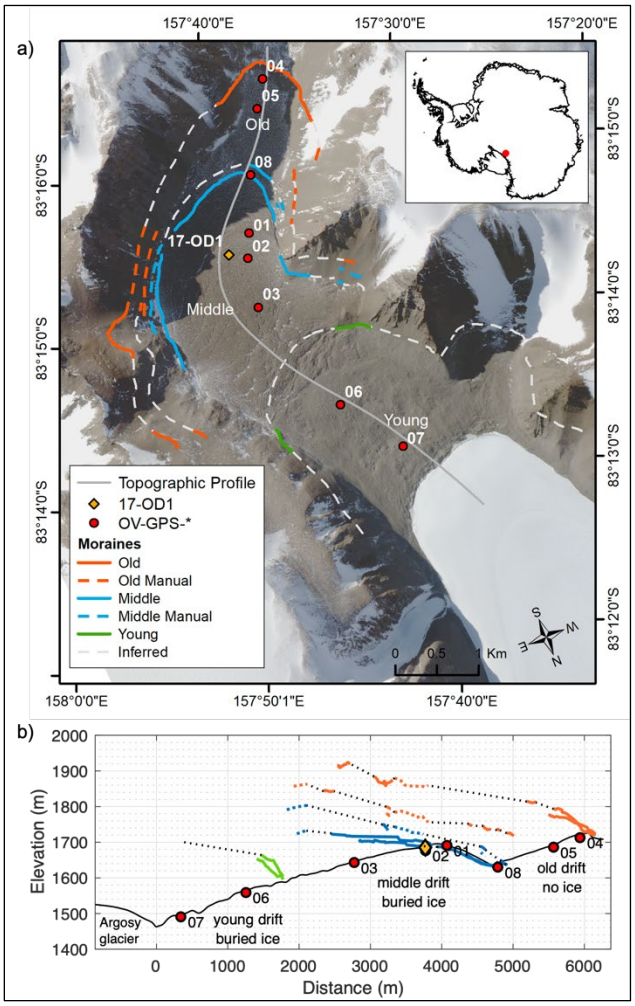

Figure 3. Moraine and drift boundaries mapped in Ong Valley, Antarctica (WV2 satellite image © 2016 Maxar). Solid lines indicate the lateral and end moraines traversed for the old drift (orange), middle drift (blue), and young drift (green). Dashed lines indicate the respective moraines mapped by laser ranger and reference point. Dashed grey (a) and black (b) lines are inferred moraine positions.

The current exposed Argosy Glacier lobe in Ong Valley is found at the valley mouth at an elevation of 1480 m a.s.l. The farthest advancement observed in the valley is that of the old drift. This advancement is well defined by a 1.8 km long, uninterrupted terminal moraine near the valley head. The old terminal moraine is found 6.2 km up valley from the Argosy Glacier lobe and at an elevation of 1725 m a.s.l. This results in at least a 245 m increase of ice surface elevation above the current in Ong Valley during the deposition of the old drift. The highest lateral moraine that can be correlated to the old terminal moraine is found at 1920 m a.s.l. on the East valley wall close to the valley mouth and is 440 m above the current ice elevation.

The extent of the middle drift is defined by a 330 m-long terminal moraine positioned on the western side of the drift. This terminal moraine is found 4.9 km from the Argosy Glacier lobe at an elevation of 1645 m a.s.l., and therefore, 165 m above current ice elevation. The current extent of the middle ice, buried below supraglacial debris, is located 110 m down valley from the middle terminal moraine at an elevation of 1636 m a.s.l., indicating that this part of the middle drift is depleted of ice. Further, we find that the highest point of the middle ice (along the topographic profile) is at 1695 m a.s.l., providing a minimum increase in elevation of the Argosy Glacier of 215 m above current during the deposition of the middle ice.

The drill site 17-OD1, used to date the age of the middle ice (Bergelin et al. 2022), is located centrally within the middle drift and found at 1685 m a.s.l., using the DSM (Figure 3). From the drill site and directly perpendicular to the valley wall, the current middle ice boundary is found at an elevation of 1699 m a.s.l. and 1694 m a.s.l. for the East and West valley walls, respectively. This results in the current boundary of the middle ice being 9–14 m above the drill site. Further, the lateral moraines associated with the emplacement of the middle ice are 1722 m a.s.l. This provides an ice surface lowering, local to the drill site, of at least 37 m since emplacement.

The most recent advancement has been dated to occur during the LGM (11–13 kyr; Bibby et al. 2016). During the LGM, the Argosy Glacier lobe expanded 2.3 km up valley reaching an elevation of 1600 m a.s.l. and, therefore, a 120 m increase in ice surface elevation above current.

3.2 Boulder Movement

We find that four of the eight boulders (OV-GPS-03, 06, 07, and 08) indicate movement in both the horizontal plane and three-dimensional space between the different periods of measurement (Table 1 and Figure 4). An additional boulder OV-GPS-01 indicates movement in the three-dimensional space only since no horizontal movement can be distinguished from the uncertainty (Table 1). The most movement was determined between 2010 and 2017, and 2011 and 2017, which are the two longest time intervals. The only movement between 2010 and 2011 occurs for boulder OV-GPS-03 and recorded in the horizontal plane only.

The young drift appears dynamic and exhibits surface movement (Table 1). The two boulders OV-GPS-06 and OV-GPS-07, located on the young drift, show distinct movement of 5.78 ± 0.91 cm and 4.85 ± 2.91 cm between the longest time interval, 2010-2017. The direction of movement is generally NNW, towards down valley (Figure 5). In three-dimensional space, the uncertainty has increased > 3 cm, resulting in a greater but less distinct movement for OV-GPS-07 (2010–2017, 7.73 ± 7.20 cm; and 2011–2017, 5.63 ± 7.89 cm), caused by the increased uncertainty in the vertical direction when measuring GPS positioning.

Table 1. Boulder movement results. The distances are reported for both horizontal and three-dimensional space, including the azimuth direction (Az.) and degrees from horizontal (From h.) representing the degree move in either upward (positive) or downward (negative) direction. Bold/grey shaded values indicate distance that are greater than the 95% uncertainty and where movement is considered.

		2010 - 2011				**2011 - 2017**				**2010 - 2017**			
Drift	Boulder OV-GPS-*	Horizontal distance (cm)	3D distance (cm)	Az. (deg.)	From h. (deg.)	Horizontal distance (cm)	3D distance (cm)	Az. (deg.)	From h. (deg.)	Horizontal distance (cm)	3D distance (cm)	Az. (deg.)	From h. (deg.)
Old	04	1.39 ± 5.68	6.37 ± 13.18	245	-77	1.87 ± 4.38	2.2 ± 8.27	40	31	0.84 ± 3.59	5.15 ± 11.95	356	-81
	05	0.68 ± 2.71	0.83 ± 6.58	139	35	0.87 ± 0.94	2.19 ± 4.49	299	-67	0.33 ± 2.41	1.56 ± 8.96	254	-78
	08	-	-	-	-	**0.96 ± 0.78**	**1.68 ± 1.50**	**298**	**55**	-	-	-	-
Middle	01	0.35 ± 1.43	1.32 ± 3.87	52	-75	0.14 ± 0.51	**1.94 ± 1.39**	**293**	**86**	0.31 ± 1.35	0.73 ± 3.67	29	65
	02	0.56 ± 0.84	1.76 ± 2.11	180	71	0.65 ± 1.19	0.66 ± 1.41	3	9	0.09 ± 1.4	1.77 ± 2.22	22	87
	03	**1.29 ± 1.28**	2.77 ± 3.46	49	-62	**0.78 ± 0.77**	**2.69 ± 1.86**	**327**	**73**	**1.6 ± 1.21**	**1.61 ± 1.32**	**20**	**4**
Young	06	0.51 ± 1.81	2.13 ± 4.71	23	-76	**5.55 ± 1.78**	**6.6 ± 3.75**	**318**	**33**	**5.78 ± 0.91**	**5.97 ± 1.25**	**322**	**15**
	07	1.36 ± 3.62	7.67 ± 11.04	171	80	**6.14 ± 3.12**	**7.73 ± 7.20**	**334**	**-37**	**4.85 ± 2.91**	5.63 ± 7.89	330	31

The middle drift shows a less definite movement in the surface boulders. Boulder OV-GPS-02 is located on the highest area of the middle drift and displays no movement to a position accuracy of < 1 cm. Boulder OV-GPS-01 and OV-GPS-03 are positioned on either side of the highpoint (up and down valley, respectively), and both indicate movement (Figure 5). Further, these two boulders are the only ones that display a vertical movement greater than the combined vertical uncertainty from 2011–2017 (Table 1). The vertical movement for boulders OV-GPS-01 and OV-GPS-03 is 1.94 ± 1.38 cm and 2.57 + 1.86 cm, respectively, in an upward direction. In addition, OV-GPS-03 shows horizontal movement in the NW direction and a maximum distance of 2.69 ± 1.86 cm in three-dimensional space (Table 1).

None of the boulders on the old drift surface (OV-GPS-04 and OV-GPS-05) show movement (Table 1). However, boulder OV-GPS-08 located at the boundary between the middle and old drift indicates a movement of 0.96 ± 0.78 cm and 1.68 ± 1.50 cm in the horizontal and three-dimensional space, respectively. The direction of movement is towards WNW (Table 1 and Figure 5). It should be noted that no GPS data was available for 2010, and therefore only movement analysis from the period 2011–2017 exists.

4 DISCUSSION

Each of the three drifts in Ong Valley shows varying degrees of boulder movement and, therefore, variation in their stability. However, generally stability of the three drifts increases with distance from the valley mouth and, the age (Bibby et al. 2016; Scarrow et al. 2014).

4.1 Young drift

Movement analysis of surface boulders indicates a dynamic young drift with an average movement of 4.9–7.8 cm between 2010 and 2017 for boulders OV-GPS-06 and OV-GPS-07. We measured a supraglacial debris thickness of 14–26 cm for the young drift near these boulders. From field observations (Figures 2f and 2g), this would suggest that both boulder OV-GPS-06 and OV-GPS-07 are partially embedded in the ice and frozen in place. Therefore, any movement of the boulders is assumed to be a direct reflection of ice movement. The cause of this movement is speculative. However, from field observations, we find two possible scenarios that could lead to this distinct movement of the young drift surface boulders.

One possible scenario would suggest a stagnant ice mass, in which cryoturbation causes active movement of the supraglacial debris and surface of the buried ice. Thermal contraction of the ice during a cooling phase causes cracks to form in the ice and become filled with supraglacial debris. During a warming phase, thermal expansion of the ice causes compressive stresses and produces uplift along the crack. Over time, these cracks deepen and expand by the in-filling of supraglacial debris (Sletten et al. 2003). Such cryoturbation leads to polygon formation on the surface with an upward force of the underlying ice. A boulder on the surface of an active polygon can therefore experience movement caused by cryoturbation. However, the magnitude of movement for supraglacial debris on a polygon is dependent on its developmental stage and is unknown for the drifts in Ong Valley. Further, since the movement is caused by localized upward force of ice movement below the polygon, the direction of movement would be related to the boulder location relative to the

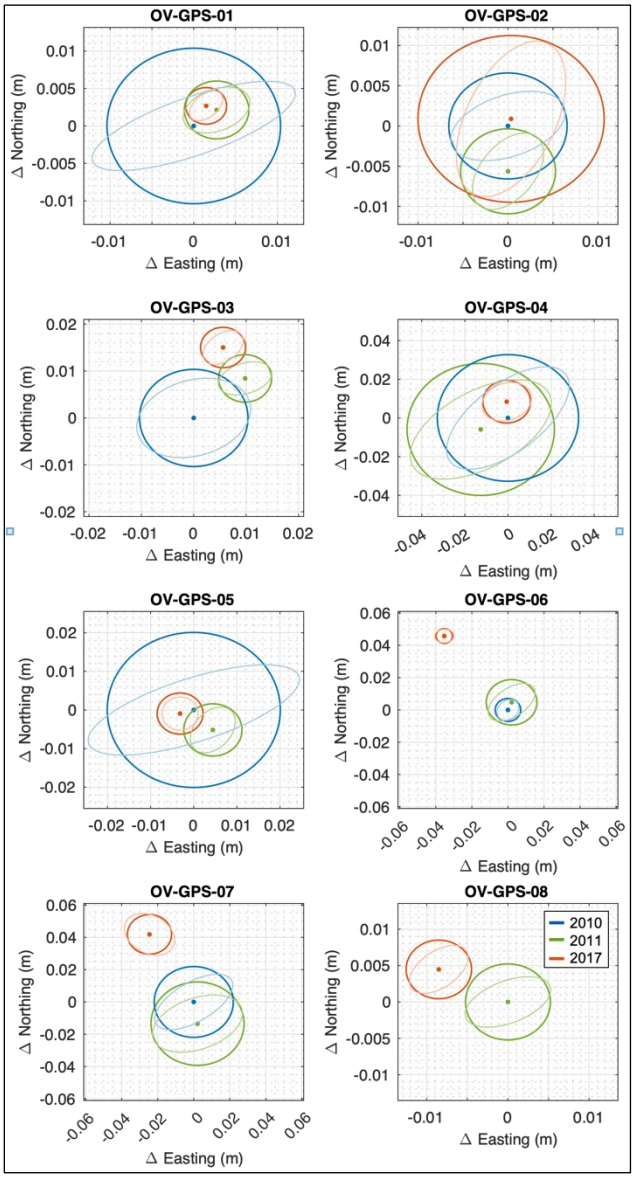

Figure 4 Horizontal boulder GNSS positions. An initial zero position is assigned to the 2010 boulder location, with 2011 and 2017 being the position relative to the initial point. Thick line represents the 95% error circle with a radius being the horizontal precision. Thin line represents the 95% error ellipse.

polygon's center. However, both boulder OV-GPS-06 and OV-GPS-07 are centered within the polygon, and therefore the direction of movement could be considered coincidental.

A second possible scenario would suggest that the young ice mass below the young drift is retreating and, therefore, not stagnant. Advancement of the Argosy Glacier deposited the young drift during the LGM, 11–13 kyrs ago (Bibby et al. 2016). During deposition, the Argosy Glacier extended 2.3 km farther into Ong Valley at an elevation of 120 m higher than the current. Since then, retreat and sublimation

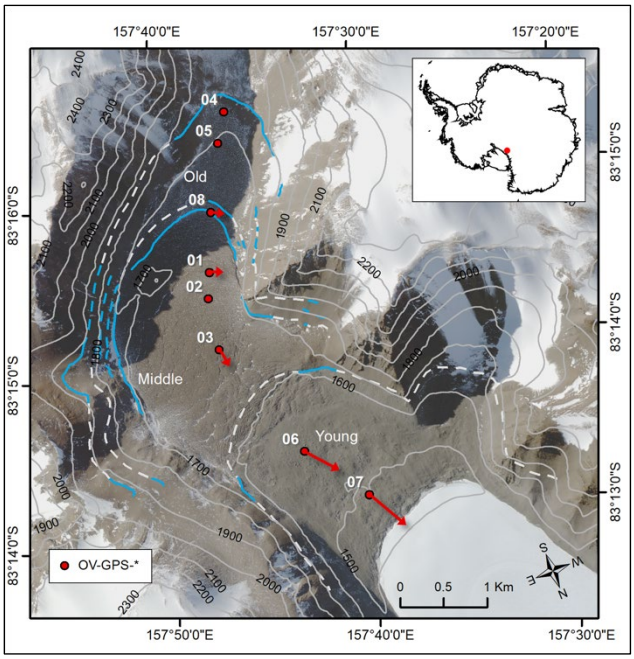

Figure 5 Directional movement of surface boulder in Ong Valley, Antarctica (WV2 satellite image © 2016 Maxar). Red arrows indicate the average direction of movement for the period 2010-2017 and 2011-2017, with arrow length indicating the average relative magnitude moved. Lines indicate lateral and end moraines mapped from traverses (blue solid line), elevation laser measurements (blue dashed line), and inferred from continuously tracing the moraines (white dashed line). Contour lines are shown in solid grey.

of the glacier lobe have created a buried ice mass experiencing an elevation difference between the maximum extent of the young drift buried ice and the current exposed glacial ice at the valley mouth (Figures 3 and 5). Boulders OV-GPS-06 and OV-GPS-07 both show movement in the NNW direction. This direction coincides with the direction of the slope gradient towards down valley, caused by a downward surface slope of ~5%. Therefore, the movement of boulders OV-GPS-06 and OV-GPS-07 could be caused by a downward flow of this young, buried ice towards the valley mouth. However, the movement is not considered an average flow rate of the ice. If this were the case, then this would suggest that the ice has moved several km since its deposition 11–13 kyrs ago and disagrees with observations in Ong Valley.

Whether or not the movement of boulders OV-GPS-06 and OV-GPS-07 was caused by flow of the young ice or a shift/tilt in the position of the boulders due to cryoturbation is unclear. From the available field data, the cause of movement observed in boulders 10-OV-GPS-06 and OV-GPS-07 could be either one of the above scenarios or more likely a combination of the two.

4.2 Middle Drift

The middle ice is assumed to be stable and stagnant as it has been preserved for ~3 Ma, and also the primary assumption for cosmogenic nuclide dating of the middle ice (Bergelin et al. 2022). With a supraglacial debris thickness of ~60 cm for the middle drift, all boulders found on the surface of the middle drift are assumed to be completely detached from the buried ice. Boulders OV-GPS-01 and OV-GPS-02 are located near drill site 17-OD1 (Bergelin et al. 2022) and are considered the most stable part of the middle drift. The calculated distances between the measured boulder positions are < 1.94 cm. The distance between 2011 and 2017 for boulder OV-GPS-01 is the only distance greater than the uncertainty of 95% by ~0.55 cm, and therefore an indication of movement.

While the middle drift is considered stable, the presence of desert pavement on the surface of the middle drift polygon formations provides evidence for an active debris surface. In addition, an active surface can also be explained by a partial mixing of the supraglacial debris as observed in the cosmogenic nuclide inventory (Bergelin et al. 2022). Therefore, it is not surprising that minimal movement could be observed for any boulder from the stable middle drift. Further, Bergelin et al. (2022) find the surface erosion rate for the middle drift to be ~0.0002 mm yr^{-1}. While such low erosion rates are not detectable within a decadal time scale, it is still indicative of an active surface. Whether or not a slowly eroding surface or active polygon formations caused this movement or shift in bolt positions is unclear.

In contrast, boulder OV-GPS-03 shows a maximum movement of 1.6 ± 1.21 cm and 2.69 ± 1.86 cm for horizontal and three-dimensional movement, respectively. Boulder OV-GPS-03 is located farther down valley near a transition zone between the young and the middle drift. From field observations, this zone shows recent disturbance caused by the deposition of the young drift 11–13 kyrs. Here, the polygon formations have increased high relief (Figure 3b). The surface exhibits larger-scale extensional crevasses perpendicular to the valley direction, with a down-sloping trend toward the Argosy Glacier, as observed in the topographic profile in Figure 3b. During the deposition of the young drift into Ong Valley, the upward pushing force of the advancing Argosy Glacier lobe would potentially cause the lower part of the middle drift, the transition zone, to be compressed. Since then, a retreat of the Argosy Glacier would cause relaxation and extension of this zone. As discussed above, if the young ice below the young supraglacial debris is active and moving down valley, this could potentially influence the middle ice found in this zone as an elevation difference is created from a recently (11–13 kyrs) retreating glacial deposit, causing a gravitational relaxation of the ice topography.

Boulder OV-GPS-08 is located near the boundary between the middle and old drift. More specifically, this boulder is positioned on the middle drift but beyond the current extent of the middle ice. Therefore, boulder OV-GPS-08 is part of the middle drift surface that has been depleted of ice and is considered to be relict. The stability of boulder OV-GPS-08 is questionable, as it is positioned on top of a debris mound and not partially embedded in the debris (Figure 2h). These debris mounds are left behind when the ice below polygon formations completely sublimates. On a million-year timescale, these debris mounds are expected to erode and flatten slowly, as observed on the surface of the old drift. Given the instability of boulder OV-GPS-08, such erosion could contribute to a tilting in the bolt position and result in a general upward movement of 1.68 ± 1.50 cm. However, this is speculative.

4.3 Old Drift

The old drift is completely depleted of buried ice based on the field observations and the valley cross-sectional profiles (Figure 3b). If the separate, older ice mass below the middle ice is that of the old drift deposit (Bergelin et al. 2022), then the oldest drift was deposited 4–5 Myrs ago and is considered an ancient, relict surface. Boulder OV-GPS-04 and OV-GPS-05 agree with such, as no movement is detected.

5 Conclusions

We evaluated the stability of an ancient, buried ice mass and its associated drift system in Ong Valley, Transantarctic Mountains, Antarctica. The glacial drift system comprises three successively older drifts, dated at 11–13 kyrs, 2.9 Myrs, and 4.3–5.1 Myrs, in which buried ice underlies the two youngest. We used high-precision GPS positioning to map the glacial moraines and drift boundaries, and the current boundary of the two buried ice masses. Further, we measured high-precision markers on eight surface boulders located on the drifts over a period of seven years (2010–2017) to determine the mobility and stability of these drifts and buried ice masses.

We find the stability of the three drifts to increase with distance from the valley mouth. The youngest drift appears to be dynamic and exhibits surface boulder movement between 0.79 and 1.10 cm/yr down the valley over the seven-year period, indicating active movement of the ice below the supraglacial debris. The middle drift and ice are considered stable with a potential boundary relaxation and adjustment because of the loss of buttressing by the now retreating Argosy Glacier since the LGM. The middle drift surface is still subject to slow erosion and/or polygon formations. However, no ice movement was detected during the observed seven-year period. The old drift is void of buried ice and shows no signs of movement.

Our differential GPS-based analyses of the three drift surfaces of which two younger ones are still underlain by glacial ice supports and enhances our understanding of the slowly evolving Antarctic landscape. The oldest surface on the valley floor has entered a more sedentary phase as no ice from a 4–5 Myrs old ice sheet expansion exist there any more. However, the middle drift (2.95 Myrs old) is still underlain by slowly sublimating ice and thus, currently shows signs of intermittent shifts on surface boulders. And the youngest drift is in a stage of relatively rapid landscape evolution as attested by relatively large boulder movements within the 7-year study period.

6 ACKNOWLEDGEMENTS

We thank Theodore Bibby, Collin Giusti, and Andrew Grant who assisted in data collection during the various field seasons. Further, we thank UNAVCO Polar Engineers Thomas Nylen and Marianne Okal, who provided assistance in processing the GPS data for increased accuracy. Satellite imagery of Ong Valley was provided by the Polar Geospatial Center under NSF-OPP awards 1445205, 1445168, and 1445169.

7 REFERENCES

Bergelin, M., Putkonen, J., Balco, G., Morgan, D., Corbett, L.B., and Bierman, P.R. 2022. 'Cosmogenic nuclide dating of two stacked ice masses: Ong Valley, Antarctica', *The Cryosphere* 16, pp. 2793–2817.

Bibby, T., Putkonen, J., Morgan, D., Balco, G., and Shuster, D.L. 2016. 'Million year old ice found under meter thick debris layer in Antarctica', *Geophysical Research Letters* 43, pp. 6995–7001.

Evatt, G.W., Abrahams, I.D., Heil, M., Mayer, C., Kingslake, J., Mitchell, S.L., Fowler, A.C., and Clark, C.D. 2015. 'Glacial melt under a porous debris layer', *Journal of Glaciology* 61, pp. 825–836.

Farrance, I. and Frenkel, R. 2012. 'Uncertainty of Measurement: A Review of the Rules for Calculating Uncertainty Components through Functional Relationships', *The Clinical Biochemist Review* 33, pp. 49–75.

Hindmarsh, R.C.A., Van der Wateren, F.M., and Verbers, A.L.L.M. 1998. 'Sublimation of ice through sediment in Beacon Valley, Antarctica', *Geografiska Annaler, Series A, Physical Geography* 80(3/4), pp. 209–219.

Howat, I.M., Porter, C., Smith, B.E., Noh, M.-J., and Morin, P. 2019. 'The Reference Elevation Model of Antarctica', *The Cryosphere* 13, pp. 665–674.

Jouzel, J., Masson-Delmotte, V., Cattani, O., Dreyfus, G., Falourd, S., Hoffmann, G., et al. 2007. 'Orbital and millennial Antarctic climate variability over the past 800,000 years', *Science* 317, pp. 793–796.

Kowalewski, D.E., Marchant, D.R., Swanger, K.M., Head, J.W., 2011. Modeling vapor diffusion within cold and dry supraglacial tills of Antarctica: Implications for the preservation of ancient ice', *Geomorphology* 126, pp. 159–173.

Mihalcea, C., Mayer, C., Diolaiuti, G., Lambrecht, A., Smiraglia, C., and Tartari, G. 2006. 'Ice ablation and meteorological conditions on the debris-covered area of Baltoro glacier, Karakoram, Pakistan', *Annals of Glaciology* 43, pp. 292–300.

Moore, P.L. 2017. 'Stability of supraglacial debris', *Earth Surface Processes and Landforms* 43, pp. 285–297.

Ng, F., Hallet, B., Sletten, R.S., and Stone, J.O. 2005. 'Fast-growing till over ancient ice in Beacon Valley, Antarctica', *Geology* 33, pp. 121–124.

Östrem, G. 1959. 'Ice Melting under a Thin Layer of Moraine, and the Existence of Ice Cores in Moraine Ridges', *Geografiska Annaler* 41, pp. 228–230.

Putkonen, J., Balco, G., and Morgan, D. 2008. 'Slow regolith degradation without creep determined by cosmogenic nuclide measurements in Arena Valley, Antarctica', *Quaternary Research* 69, pp. 242–249.

Putkonen, J. and Mahmood, T.H. 2022. 'Twenty-four buried ice masses remotely mapped in Transantarctic Mountains, Antarctica', *Geocarto International* 38.

Ragettli, S., Bolch, T., and Pellicciotti, F. 2016. 'Heterogeneous glacier thinning patterns over the last 40 years in Langtang Himal, Nepal', *The Cryosphere* 10, pp. 2075–2097.

Scarrow, J.W., Balks, M.R., and Almond, P.C. 2014. 'Three soil chronosequences in recessional glacial deposits near the polar plateau, in the Central Transantarctic Mountains, Antarctica', *Antarctic Science* 26, pp. 573–583.

Schäfer, J.M., Baur, H., Denton, G.H., Ivy-Ochs, S., Marchant, D.R., Schlüchter, C., and Wieler, R. 2000. 'The oldest ice on Earth in Beacon Valley, Antarctica: new evidence from surface exposure dating', *Earth and Planetary Science Letters* 179, pp. 91–99.

Sletten, R.S., Hallet, B., and Fletcher, R.C. 2003. 'Resurfacing time of terrestrial surfaces by the formation and maturation of polygonal patterned ground' *Journal of Geophysical Research* 108.

Stone, J., Sletten, R.S., and Hallet, B. 2000. 'Old ice, going fast: Cosmogenic isotope measurements on ice beneath the floor of Beacon Valley, Antarctica', *Eos Transactions American Geophysical Union* 81, pp. 15–19.

Sugden, D.E., Marchant, D.R., Potter, N., Souchez, R.A., Denton, G.H., Swisher, C.C., and Tison, J.L. 1995. 'Preservation of Miocene Glacier Ice in East Antarctica', *Nature* 376, pp. 412–414.

Trimble 2019. *Trimble Business Center v5.0 – Processing and Adjusting GNSS Survey Control Networks.* Sunnyvale, California, United States.

Van der Wateren, D. and Hindmarsh, R. 1995. 'Stabilists strike again', *Nature* 376.

Yan, Y., Bender, M.L., Brook, E.J., Clifford, H.M., Kemeny, P.C., Kurbatov, A.V., Mackay, S., Mayewski, P.A., Ng, J., Severinghaus, J.P., and Higgins, J.A. 2019. 'Two-million-year-old snapshots of atmospheric gases from Antarctic ice', *Nature* 574, pp. 663–666.

Observing social-ecological design of permafrost landscapes: Grounding urban planning in Utqiaġvik, Alaska

Hannah Bradley

Department of Engineering and Society, University of Virginia, Charlottesville, Virginia, United States

ABSTRACT

How can Utqiaġvik develop new strategies of urban design on changing permafrost? Ongoing ethnographic analysis of the University of Virginia's project, "Understanding the Changing Natural-Built Landscape: An Integrated Urban Sensor Network in Utqiaġvik, AK," provides insight into how "design process" can help develop adaptive urban permafrost landscapes. Anthropological analysis of designers provides insight into how interdisciplinary practices create social-ecological change, and this paper builds on previous ethnographic work of the socio-political aspects of infrastructure and urban space. This UVA project uses design process, a collaborative approach common in architecture and other fields, in partnership with utilities and public services in Utqiaġvik, to co-develop relationships between urban planning, micrometeorological and ecological data, and permafrost. I analyze preliminary ethnographic observations of the cooperative dynamics of this project, including cross-disciplinary data collection structure, a "design studio" course's production of data-informed design proposals, developing discussions of water, snow, and thermal management, and input from community partners. Local residents have clear relationships of savvy renegotiation of the built environment, and snow removal maintenance emerged as a potential crux of designed change connecting hydrological data, ground temperatures, infrastructural impacts, and public services. Visualization of potential design solutions provides an accessible projection of possibilities for change that allow reconceptualization of relationships between city and permafrost. I argue that this project's work, as an iterative design process, integrates data, community experiences, and creative ideation. This integration allows Arctic urban residents and planners to redesign interactions with the land grounded in conceptions of permafrost as a social-ecological infrastructure and malleable architecture, potentially promoting senses of lived engagement with the changing land.

1 INTRODUCTION

1.1 Change toward adaptable landscapes

Utqiaġvik is growing. A friend of a friend, a retired nurse, walked me around her house pointing out changes inside and out: the new addition built in the 90s, that one spot in the floor that never seems to be level, and all her good friends and neighbors living up and down the street. None of these neighbors' homes were built when she moved to this house in the 80s, decades before the new hospital facilities were built two blocks away. She remembered the open tundra that used to surround her home: "Oh, it was beautiful, but you know, they [Utqiaġvik residents] need the space!".

Two days later, just a few blocks to the south, I hiked across tundra with my aquatic scientist colleagues toward their last years' pond sites. Looking out over the area, slated for future subdivision and development evidenced by new survey markers dotting the broad drained-lake basin, our bear guard talked of how he used to play out here as a kid—his uncle lived nearby—back when the old ice cellar near our sample ponds seemed miles and miles away to his short kid legs. A new road to the nearby gravel pit had sprung up since our study began: the aquatic scientists weren't sure until they reached their sites whether the road had disrupted them. We heard often from project partners at the utilities co-op how plans for a new college campus, new police station, would soon be needing new electrical substations to meet new demand. Utqiaġvik grows and expands, always on a dynamic permafrost substrate.

Utqiaġvik is the northernmost community in the U.S. Arctic, located on the Chukchi Sea. The town is built entirely on continuous, ice-rich permafrost, with maximum active layer depths of 35 to 50 cm (Klene et al. 2013). Residents of Utqiaġvik are aware of the infrastructural issues facing their city: frost-jacking, subsidence, standing water, snowdrifts, coastal erosion, and disrupted utilities are all problems encountered at varying degrees of severity every year. Providing strategies to plan sustainable futures for Utqiaġvik's built environment is the goal of the University of Virginia's (UVA) National Science Foundation (NSF) "Navigating the New Arctic" (NNA) project of which I am a part. I study the work of my colleagues at UVA and in Utqiaġvik to understand the social effects of their collaborations. In this preliminary analysis of this ongoing project, I provide emerging insights of how a group of researchers and community partners are using iterative "design process" (a collaborative approach common in design fields like architecture) to synchronize urban planning with permafrost dynamics.

An ethnographic analysis of a project aimed at improving design of Arctic cities must ask what does "doing design process" *do?* How can this interdisciplinary approach affect the relationships between designers, planners, residents, scientists, and the Arctic environment? Toward further understanding the social role of research in the Arctic built environment, this paper asks: What is the social effect of this project, if the project itself is not leveling buildings, repairing infrastructure, or building houses? The deliverables of the project include urban design suggestions, data to support best practices, and computer models of sample sites, but a further effect of the project is

https://doi.org/10.52381/ICOP2024.203.1

conceptual. The process of sketching new ideas and connecting different kinds of knowledge provides an opportunity to reconceptualize permafrost from a natural infrastructure to adaptable, negotiable social-ecological architectures which can be designed and coproduced, operationalizing relationships between the social and material aspects of the permafrost landscape. By looking at 1) the way that the project coalesces around water management as a central engagement, 2) how the project reflects local ideals of creative manipulation of the built environment, and 3) the projection of creatively-visualized ideas as products, my ethnography of this interdisciplinary collaboration describes how the design process creates conceptual space for urban design that is synchronized with the rhythms of the permafrost landscape.

1.2 Project Structure and Partners

The possibility of the design process changing social relationships to permafrost in Utqiaġvik begins in the structure of the project analyzed in this paper: the University of Virginia's National Science Foundation – funded Navigating the New Arctic five-year research grant, entitled "Understanding the Changing Natural-Built Landscape: An Integrated Urban Sensor Network in Utqiaġvik, AK" which began work in 2021. The project aims to improve understanding of the relationships between Utqiaġvik built environment—including buildings, utilities, and roads—and the surrounding air, ground, and water. By understanding how the town's infrastructures affect permafrost, the project team aims to propose changes to urban planning and design which can mitigate existing impacts on infrastructure, and increase the resilience of communities' future planning and design in the face of climate change. Though engineered solutions to problems of Arctic infrastructure already exist[1], and adaptations to climate impacts including permafrost thaw have been considered in the North Slope Borough (NSB) Comprehensive Plan (2019–2039) the project aims to ground these solutions in fine-scale definition of the interactions between built structures and permafrost stability, in recombination of existing practices, and in the social aspects of living, working, and knowing in this place.

The project aims for interdisciplinary structure and collaboration with local partners along three main branches of the project: sensor data, urban design, and social science. The PI's come from terrestrial ecology (Howie Epstein), aquatic science (Claire Griffin) architecture and geophysics (Matthew Jull), landscape architecture (Leena Cho), anthropology and data science (Luis Felipe Murillo), and science and technology studies (STS; Caitlin Wylie). The project contracts its project logistical support with TRIBN, Inc. (Lars Nelson) in Utqiaġvik, and works locally with Barrow Utilities and Electric Cooperative, Inc. (BUECI), Arctic Slope Native Association (ASNA), the Tagiuġmiullu Nunamiullu Housing Authority (TNHA), the NSB Planning Department, NSB Capital Improvement Program Management (CIPM) and NSB Public Works, and partners with the Cold Climate Housing Research Consortium (CCHRC) of the National Renewable Energy Lab (NREL) and the USACE Cold Regions Research and Engineering Laboratory (CRREL). Preliminary meetings with local partners both guided the delineation of research questions, as well as eventual site selections, and their participation continues to shape the interests and outcomes of the research.

The project has three ongoing strands of activity. The first is collection of micrometeorological, geophysical (LiDAR, ERT, and GPR) and hydrological data in the urban area of Utqiaġvik, and analysis of correlations in the time series data. The second is the translation of scientific data and related findings into a potential list of actionable design factors to improve the management of the built environment, including 3D spatial modelling and hosting two "design studio" field courses in Utqiaġvik. The third simultaneous project is that of ongoing ethnographic observation of cooperation both among the team and with community partners, seeking best practices for collaborative projects in the Arctic.

Over the first two years of the project, sensor installation has concentrated on the sites of the project's main community partners: the BUECI water and sewage treatment facility, the Samuel Simmonds Memorial Hospital (SSMH) run by ASNA, the "29-Unit" residential building managed by the TNHA, and a tundra control site on the Barrow Environmental Observatory (BEO) "Scientific Research District" managed by UIC Science, a subsidiary of the local Ukpeaġvik Iñupiat Corporation (UIC). Remotely monitored sensor stations monitor multiple variables at different aspects of each site[2]. Aquatic sampling and hydrologic analysis also concentrated on sets of urban-connected ponds intersecting with terrestrial sampling sites, additionally intersecting GPR and ERT sampling contracted through CRREL.

Figure 1. UVA aquatic scientists locating pond sampling sites, with Utqiaġvik neighborhoods in the distance.

[1] See CCHRC, CCREL

[2] Wind speed, wind direction, gust speed, air temperature, relative humidity, solar radiation, snow depth, ground temperature

1.3 Anthropology of infrastructural design

This paper analyzes the outcomes of a project which uses, in part, "design process" to find new solutions to permafrost problems. Design process, loosely defined, is an iterative, collaborative method used in many fields of architecture, engineering, etc. to address complex problems (Brown 2008). The UVA NNA project creates a design process through its multidisciplinary structure requiring digestion of multiple kinds of data, through multiple rounds of data collection, studio, proposition, and redirection.

Anthropological analysis of design process is a multifaceted subfield addressing multiple scales of "design" (Murphy 2016): there is anthropology of designed spaces, anthropology of designers, and anthropology through design which uses design process in its research methodology, sometimes in turn "for" design to improve design process. Some seek to bridge between anthropology and design to analyze development of new knowledge categories over the course of unfolding design process in a team including anthropologists (e.g., Gunn and Donovan 2012).

Interest in architecture and infrastructure reflects classically anthropological interests in space and place in anthropological literature (Low 2009), as well as renewed interest in the social roles of materials and objects. Anthropologists have focused in on architecture as a form of material culture, such as indigenous architectures (Lee and Reinhardt 2003), or as an expression of ideology (Humphrey 2005; Stender 2017). Caroline Humphrey (1988) points out that architecture has been less examined by anthropologists than other forms of "studying up," perhaps because of its many overlaps, though anthropological analyses of planning processes work to outline the politics and social practices of urban form and function (Holston 1989; Rutheiser 2008; Sadana 2018).

1.4 Studying Arctic Infrastructure

My theoretical stance in this project joins in anthropological analyses of how infrastructures include both material and relational or symbolic processes to structure social landscapes (Larkin 2017; Star 1999). Other ethnographies of infrastructure (Anand 2015; Harvey and Knox 2015; Nielsen 2022) further trouble the false dichotomy between built and natural environments and bring the unseen structures of infrastructure to the fore (Carse "Keyword: Infrastructure" 29). As an example, in Alaska, Elizabeth Marino's (2015) *Fierce Climate, Sacred Ground* links colonial ideologies of home, city, and education to the insufficiency and instability of rural Alaskan Native villages, especially those now requiring relocation due to fast-eroding coasts and riverbanks, further exacerbated by climate change.

Growing interest in the impacts of infrastructure on permafrost, and of changing climates on infrastructure's permafrost setting, has included other anthropologists' analysis of arctic infrastructure. Schweitzer, Povoroznyuk, and Schiesser (2017) argue specifically for re-centering social and landscape analyses of the Arctic away from naturalized concepts of wilderness toward the important social roles of the built environment.

Architectural studies, such as Jull's overview of the "microrayon" (2016) and Sheppard and White's (2017) *Many Norths* show the cultural, historical, and material parameters of Arctic architecture. Steinberg (2019) points out how the Arctic's land, water, ice material dynamism resists typical binaries of architecture, politics, governance from temperate areas (in Cho and Jull 2019, pp. 52–55). These extreme material differences of the polar climate Cho and Jull describe as forcing designers—resident or otherwise—to "innovate cultural and material linkages" (p. 23). Design process becomes an opportunity to re-think relationships to material environments.

Cho and Jull compiled their 2019 *Mediating Environments* to communicate routes toward "new relationships to environments" (p. 24). In this book they describe that design

> "has the capacity to act as an intervening agency and to reify the link between the living and the environment that envelops it. Its capacity to bring about change, subtle or radical, can fundamentally restructure the relationships among things, and the modes by which our beliefs and ways of living are materialized." (p. 22)

Here I describe the practice of this restructuring through ethnographic analysis of the project's activities.

2 Methodology

This paper is based on ongoing participant observation of the UVA NNA project activities from June 2022 to August 2023, during installation and subsequent maintenance of micrometeorological sensor arrays and aquatic sampling sites in the Utqiaġvik urban zone and the BEO tundra control site. Though born and raised in Alaska, this was my first trip north of Anaktuvuk Pass and thus my first introduction to the community of Utqiaġvik. Besides these field visits, I also participated in biweekly project meetings, terrestrial sensor meetings, outreach committee meetings, geophysical data meetings, and fieldwork planning meetings with UVA team members over Zoom and telephone. The corpus of my data also included reading publications by team members and partners, and any intra-project email correspondences. I performed preliminary follow-up interviews with team members and project partners, with research ongoing.

My participation and observation in the project's associated "design studio" course in architecture and landscape architecture—taught by PI's Cho and Jull—was an important part of my understanding how design process and ideation fit into the goals and outputs of the NNA project. All architecture and landscape architecture students at UVA take "design studio" courses, intensive courses which include important professionalization and training toward their future careers. Cho has written of the important role of embodied experience for studio students (Cho 2022). I participated in the "pin-up" of the students' in-class research (visual and oral presentation of draft pages literally pinned to a wall), their project proposal "review" presentation, and then accompanied their visit to Utqiaġvik in February 2023. During the visit I observed and participated in their group debriefs and site visits, and their scheduled meetings with BUECI, TNHA, and NSB

representatives. Later in the semester I then participated in the “final review” of their final projects.

Working toward understanding the impacts of the project’s structure required considerable “language acquisition” of the vocabulary of permafrost ecology, architecture, design, and landscape architecture. I arrived in Utqiaġvik with the design studio students still asking endless questions to try to understand what a “design studio” really was, unveiling my lack of comprehension of terms of “design” and “design tools” and “sketch” among others. Sharing terms was important for understanding the social frictions of design: NSB employees later teased Jull for his discipline’s use of “charette” to describe seawall plans, “CCREL uses those words too” they roared with laughter. Besides vocabulary, my ethnography also serves as a kind of translation of the visual work of the design process into my own analysis.

The interdisciplinary, intercultural, multi-sited context of my ethnography provided friction between backgrounds which increases the visibility of changes in relationships to material and immaterial landscapes. Explaining the role of an ethnographer to my colleagues promoted a further iteration of describing how relationships are made and shifted. Just before departing with the studio class, I was reminded by Jull that he was “still totally in the dark” and needing clarification of my intentions in observing the trip. Gunn and Donovan (2012, p. 7) describe that ethnography of design practice can “reveal differences and crossovers in order to allow people to have a more sophisticated way of knowing what they do, and to make many different understandings present,”. One such understanding which I describe in this paper, is that of interpersonal engagements building toward common reconceptualizations of landscape.

3 Results

The themes I identify here as emergent across the project’s first few field seasons, mark an ongoing articulation of multiple forms of data—from sensors to conversations—toward more malleable relationships between permafrost and built environment. The processes I follow in this paper that trace this shift are the project’s refocusing on maintenance, and modes of proposing creative but practical ideas and visualizations, both converging with local definitions of re-design.

3.1 Local forms of design

Interactions between permafrost, urban planning, public services, and community members are shaped by local concepts of change and utility in the material environment: local processes of design. The social analysis of the project’s activities through the commentaries of local partners and community members were often made in the down time of the project, just after a presentation or discussion, or while problem-solving the many technical issues of the sensor arrays.

A hardware store employee commented that “people up here, we are good at working with what we have”. He patiently fielded our questions of how best to protect a deep-cycle battery we were rigging to get our solar-powered data-loggers through to spring, describing a potential workaround of bagging the battery in plastic and using spray-foam inside a plastic tote. A day later a member of the NSB planning department riffed on description of the “interdisciplinary” strengths of our NNA project, commenting that even beyond interdisciplinarity and survival, “elders are the original MacGyvers!”

Figure 2. UVA Design Studio students discuss culvert drainage and snow removal at North Slope Borough Public Works garage.

Similarly, standing in the unfinished hallway of an apartment renovation project as Design Studio students explored the airflow and lighting of the space, a TNHA manager chatted about the goals of our NNA project, which includes a set of “design tools”, ending the conversation by relating how people across agencies were wary of “overengineered” solutions: they weren’t going to “go out on a limb” for something that hadn’t been tried and true somewhere else. The comment was a bit of a warning against anything beyond local capacity.

Such comments show not only how rural Alaskans are open to rearranging their relationships to material objects, but also the importance of humble simplicity when approaching future-oriented solutions for local problems.

3.2 Maintenance

Snow removal strategies and other forms of water management maintenance emerged as an important intersection of terrestrial, aquatic, and community

datapoints. Standing water is a known amplifier of active layer thaw, and a highly visible problem in Utqiaġvik neighborhoods and along roadways. As the aquatic scientists focused their interests on both original plans for tracking water movement through tundra ponds, they also shaped transects to pick up impacts associated with increased snow-depths near snow fences. Terrestrial sensors' metadata also reflected potential early signals of correlations between relative distances to nearby lagoons and annual snowdrifts—both naturally occurring due to building configuration and man-made due to snow removal piling.

Though "maintenance" does not appear in any of the UVA NNA project's proposal text, it is an increasingly recognized aspect of process-oriented landscape architecture (Raxworthy 2018), the category began to take on importance as a key word over the course of the design studio class. When students arrived at TNHA 29-unit, they were confronted with a massive snowdrift in the lee of the building, as well as a big pile by the lagoon, where Public Works amasses snow from surrounding roads.

At a meeting with NSB representatives, from NSB Planning, Public Works, and Capital Projects, Jull and Cho presented a brief overview of the NNA project's goals, and the studio students introduced themselves and spoke about some of the research they did to prepare to visit Utqiaġvik. The discussion ranged from the seawall, to construction trends, to Point Lay's infrastructure disruptions, and the students asked questions: "why is the hospital built in a bowl?" and "what do you do with the snow". Public Works director Scott Danner described the snow removal, and Jull saw the opportunity to extend the students' experience in this direction: "Hey can we come visit?" "Sure" was the hospitable response, "What do you want to see?" The next day, the class filled the spaces between snow removal machines in the NSB shop. One group's final project, titled "Water in the Desert: Experimental maintenance as a socio-ecological practice in the Arctic Tundra" catalogued snow management strategies that might both increase outdoor social space and minimize snow-depth and melt impacts on ground temperatures.

Months later at the studio's final review presentation, when Cho and Jull were introducing the NNA project to invited architecture reviewers, visitors including Nelson, and partners in Utqiaġvik who were able to join via Zoom, Cho interjected "and maintenance regimes" to the list that Jull was naming of the goals of the project: maintenance had moved toward the center of the project.

3.3 Social role of ideas and visualization

At the final studio "review," the presentation of the students' final projects, comments from reviewers, including Lars Nelson, circulated around practicality and budgeting of these projects. This tension underlines both the importance of practicality, as well as the role of creative speculation in the design studio. Several questioned the costs associated with the students' ideas, and Nelson noted that the presentations were high quality but "What's missing is the money."

Figure 3. Winter snow dumpsite at the edge of Utqiaġvik with standing water beside road.

Besides design propositions for new structures—a boardwalk, a greenhouse—the students' designs reflected programmatic elements, such as coordinating snow management, and visualized relationships between the project's scientific data and community concerns such as subsidence or flooding. Another project visualized a strategy of aligning new subdivisions along ice wedges rather than a standard grid. Nelson noted that streets are already oriented to advantage scouring, and that snow compaction is a known best practice already: the work of the studio lay in the visualization and conceptualization of future urban groundings.

While in Utqiaġvik, Nelson had emphasized the power of the visualizations, how "people want to see" new ideas. Remembering the results of past studios, he commented that "if you showed a drawing of an indoor playground to an elder they'd be like wow, I've been thinking about that my whole life." Before their departure to Utqiaġvik, in discussion about presenting their research to the project's community partners, Cho had cautioned the students about the precarity of balancing others' expectations with the aesthetics of their visual products. Having drawings look "finished" has weight, implies certainty which promotes a more "top-down" design process rather than remaining open to the input of the community.

Visual aids further develop relationships to permafrost soil dynamics that will aid in future planning, promoting conceptual synchronization with permafrost whether along ice wedge lines or meltwater timing. In the example of the studio project centered on the SSMH hospital, Jull noted how the students' project created dozens of drawings, analysis, and considerations which could help further conversations or help the facilities manager create future plans.

4 Discussion and Conclusion

Ethnographic attention to interactions of researchers, partners, and residents with the UVA NNA project's design process helps understand how the structure of

interdisciplinary inquiry can synchronize social, municipal, and ecological rhythms to produce visualized ideas that enact new, cooperative relationships to Arctic environments. Through flexibility, humility, visual communication, and digestion of both qualitative and quantitative data, the design process creates opportunities to pursue more interactive conceptual relationships between infrastructural development and permafrost soils.

Permafrost is an integral foundation of many Arctic cities, and by revealing—and changing—relationships to the material ground, permafrost can be considered a social-ecological infrastructure in the expanded anthropological definition. As Larkin (2013, p. 329) writes, "What distinguishes infrastructures from technologies is that they are objects that create the grounds on which other objects operate, and when they do so they operate as systems,". The design propositions grounded by scientific data collection and visualized into a haptic reality further produce permafrost as a manipulable architecture. "We haven't really considered this other field, of 'landscape architecture'" stated Lars Nelson in his NSB Assembly Member role during a workshop with the Assembly following an interdisciplinary "Permafrost & Infrastructure Symposium" in early August, 2023[3]. He described how "We need to terraform our community" so that building homes is still possible in the future.

Conceptualizing urban planning and design as seeking to synchronize with permafrost—as planning *with* permafrost rather than against—may have potential to increase the resilience of future development of the built environment in the Arctic. Though changes due to climate change increase the difficulties of building and developing infrastructure on permafrost, by grounding designs in deep understanding of social entanglement with permafrost dynamics, residents may feel fewer negative perceptions of impacts of permafrost thaw (Ramage et al. 2022), or less solastalgia, emotional distress due to environmental change (Albrecht 2010). By reflecting a more-than-human definition of fellow life in the landscape (Povinelli 2016), a more holistic metaphysical landscape can be affirmed along local cultural values of co-constitution of human and nonhuman (Tallbear 2011), such as Iñupiat Iḷitqusiat values of respect for nature and cooperation (Itchuaqiyaq et al. 2021). Perhaps synchronizing the creative use of urban space—from maintenance to building to planning—in synchrony with permafrost dynamics will promote a closer sense of lived engagement with the changing land, rather than only reactionary measures against permafrost degradation.

5 Acknowledgements

This project is supported by NSF award #2022639. Enormous thanks to the community of Utqiaġvik, everyone who ever offered their house as a potential sensor site, everyone who stopped to ask what we were measuring. Thanks to all my project colleagues, both Utqiaġvik partners and UVA academic partners, and the UVA Design Studio course: I appreciate your patience with my presence and questions. Thanks to the North Slope Borough and UIC Science for permitting our study and their ongoing support.

6 References

Albrecht, G. 2010. 'Solastalgia and the creation of new ways of living', in S. Pilgrim and J.N. Pretty (eds.) *Nature and Culture: Rebuilding Lost Connections*. London, UK: Routledge, pp. 207–234.

Anand, N. 2015. 'Leaky States: Water Audits, Ignorance, and the Politics of Infrastructure', *Public Culture* 27, pp. 305–330. Available at: https://doi.org/10.1215/08992363-2841880.

Brown, T. 2008. 'Design Thinking', *Harvard Business Review* June 2008, pp. 1–10.

Cho, L. 2022. 'Climate Inquiries from Arctic Fieldwork', in R. Monicella and B. Keane (eds.) *Designing Landscape Architectural Education: Studio ecologies for unpredictable futures*. London, United Kingdom: Routledge, pp.179–189.

Cho, L. and Jull, M. 2019. *Mediating Environments*. Applied Research + Design Publishing.

Gunn, W. and Donovan, J. (eds.) 2012. *Design and Anthropology*. 1st edition. New York, New York, United States: Routledge.

Harvey, P. and Knox, H. 2015. *Roads: An Anthropology of Infrastructure and Expertise*. 1st edition. Ithica, New York, United States: Cornell University Press.

Holston, J. 1989. *The Modernist City: An Anthropological Critique of Brasilia*. 1st edition. Chicago, Illinois, United States: University of Chicago Press.

Humphrey, C. 2005. 'Ideology in Infrastructure: Architecture and Soviet Imagination', *Journal of the Royal Anthropological Institute* 11, pp. 39–58. Available at: https://doi.org/10.1111/j.1467-9655.2005.00225.x.

Humphrey, C. 1988. 'No Place Like Home in Anthropology: The Neglect of Architecture', *Anthropology Today* 4, pp. 16–18. Available at: https://doi.org/10.2307/3032875.

Itchuaqiyaq, C.U. 2021. 'IÑUPIAT IḶITQUSIAT', in R. Walton and G.Y, Agboka (eds.) *Equipping Technical Communicators for Social Justice Work: Theories, Methodologies, and Pedagogies*. Logan, Utah, United States: Utah State University, pp. 33–48. Available at: https://doi.org/10.7330/9781646421084.c002.

Jull, M. 2016. 'Toward a Northern Architecture: The Microrayon as Arctic Urban Prototype', *Journal of Architectural Education* 70, pp. 214–222. Available at: https://doi.org/10.1080/10464883.2016.1197672.

Klene, A., Nelson, F. and Hinkel, K. 2013. 'Urban–rural contrasts in summer soil-surface temperature and active-layer thickness, Barrow, Alaska, USA', *Polar Geography* 36(3), pp. 183–201. Available at: https://doi.org/10.1080/1088937X.2012.706756.

[3] https://permafrostcoasts.org/activities/symposium

Larkin, B. 2013. 'The Politics and Poetics of Infrastructure', *Annual Review of Anthropology* 42, pp. 327–343. Available at: https://doi.org/10.1146/annurev-anthro-092412-155522.

Lee, M. and Reinhardt, G. 2003. *Eskimo Architecture: Dwelling and Structure in the Early Historic Period*. 1st edition. Fairbanks, Alaska, United States: University of Alaska Press.

Low, S.M. 2009. 'Towards an anthropological theory of space and place', *Semiotica* 2009(175), pp. 21–37. Available at: https://doi.org/10.1515/semi.2009.041.

Marino, E.K. 2015. *Fierce climate, sacred ground: an ethnography of climate change in Shishmaref, Alaska*. Fairbanks, Alaska, United States: University of Alaska Press.

Murphy, K.M. 2016. 'Design and Anthropology'. *Annual Review of Anthropology* 45, pp. 433–449. Available at: https://doi.org/10.1146/annurev-anthro-102215-100224.

Nielsen, M. 2022. 'Speculative cities: housing and value conversions in Maputo, Mozambique', *Housing Studies* 37(6), pp. 889–909. Available at: https://doi.org/10.1080/02673037.2021.1935770.

Nielsen, M. and Pedersen, M.A. 2015. 'Infrastructural Imaginaries: Collapsed Futures in Mozambique and Mongolia', in M. Harris and N. Rapport (eds.) *Reflections on Imagination: Human Capacity and Ethnographic Method*. London, United Kingdom: Routledge.

North Slope Borough 2019. *NSB Comprehensive Plan 2019-2039*. Available at: https://www.north-slope.org/departments/planning-community-services/comprehensive-plans/.

Povinelli, E.A. 2016. *Geontologies: a requiem to late liberalism*. Durham, North Carolina, United States: Duke University Press.

Ramage, J., Jungsberg, L., Meyer, A. and Gartler, S. 2022. ''No longer solid': perceived impacts of permafrost thaw in three Arctic communities'', *Polar Geography* 45(3), pp. 226–239. Available at: https://doi.org/10.1080/1088937X.2022.2105973.

Raxworthy, J. and Harrisson, F. 2018. *Overgrown: Practices between Landscape Architecture and Gardening*. Cambridge, Maine, United States: The MIT Press.

Rutheiser, C. 1997. 'Beyond the Radiant Garden City Beautiful: Notes on the New Urbanism', *City & Society* 9, pp. 117–133. Available at: https://doi.org/10.1525/ciso.1997.9.1.117.

Sadana, R. 2018. '"We Are Visioning It": Aspirational Planning and the Material Landscapes of Delhi's Metro', *City & Society* 30, pp. 186–209. Available at: https://doi.org/10.1111/ciso.12163.

Schweitzer, P., Povoroznyuk, O. and Schiesser, S. 2017. 'Beyond wilderness: towards an anthropology of infrastructure and the built environment in the Russian North', *The Polar Journal* 7, pp. 58–85. Available at: https://doi.org/10.1080/2154896X.2017.1334427.

Sheppard, L. and White, M. 2017. *Many Norths: Spatial Practice in a Polar Territory*. New York, New York, United States: Actar Publishers.

Star, S.L. 1999. 'The Ethnography of Infrastructure'. *American Behavioral Scientist* 43, pp. 377–391. Available at: https://doi.org/10.1177/00027649921955326.

Steinberg, P. 2019. 'Land-Water-Ice: Making Space for Architecture in the Arctic', in L. Cho and M. Jull (eds.) *Mediating Environments*. Applied Research + Design Publishing.

Stender, M. 2017. 'Towards an Architectural Anthropology—What Architects can Learn from Anthropology and vice versa', *Architectural Theory Review* 21, pp. 27–43. Available at: https://doi.org/10.1080/13264826.2016.1256333.

TallBear, K. 2011. 'Why Interspecies Thinking Needs Indigenous Standpoints', *Fieldsights,* Society for Cultural Anthropology. Available at: https://culanth.org/fieldsights/why-interspecies-thinking-needs-indigenous-standpoints (Accessed February 22, 2023).

An integration approach to combine land cover products for improved ecosystem modeling across the pan-arctic

Valeria Briones[1], *Elchin E. Jafarov*[1], *Brendan M. Rogers*[1], *Susan Natali*[1] & *Hélène Genet*[2]

[1]*Woodwell Climate Research Center, Falmouth, Massachusetts, United States*

[2]*Institute of Arctic Biology, University of Alaska Fairbanks, Fairbanks, Alaska, United States*

ABSTRACT

Rapid warming across the Arctic is a main driver of observed permafrost thaw, which has significant implications for the global climate system. Land cover is a critical component of the spatial heterogeneity of the permafrost carbon climate-feedback, as vegetation structure and composition affect ecosystem carbon and nutrient turnovers, energy balance, soil environment, and ecosystem vulnerability to disturbance. An exponential increase in ecological investigations provides the necessary data for parameterization of ecosystem models for an increasing number of land cover classes in the arctic-boreal regions. However, most global land cover products do not provide classifications that match the level of detail to represent the diversity and specificity of land cover types across the pan-arctic.

We present our use of data integration using machine learning to improve validation techniques of classification systems of existing global and regional land cover products to create a hybrid map designed specifically to represent high-latitude land cover diversity in ecosystem model simulations at a 1 km spatial resolution. As a base layer we used a global land cover map and incorporated finer-resolution regional maps to capture the diversity of land cover types, in this study focused across the arctic-boreal region of North America, with the final map extending across the pan-arctic. This approach ensured comprehensive coverage while incorporating representative vegetation communities at a country level. We further show that land cover maps can be improved and tailored for use by ecosystem models at large spatial scales, while maintaining the level of detail needed to accurately represent landscape heterogeneity.

1 INTRODUCTION

Across high-latitude regions, changes in climate are altering the complex interactions between biophysical and biogeochemical processes of terrestrial ecosystems (Heimann and Reichstein 2008; Jia et al. 2019). It is critical that ecosystem models represent these complex processes and feedback to accurately forecast how these systems will respond to projected changes in climate and disturbance regimes (Fisher and Koven 2020; Heimann and Reichstein 2008). Land cover mapping of high-latitude systems is of great importance as Arctic warming results in changes in vegetation dynamics and accelerated thawing of underlying permafrost in the arctic regions (Horvath et al. 2021; Kåresdotter et al. 2021). Land cover is an important indicator of surficial changes across the pan-arctic and can have subsequent impacts on terrestrial ecosystems such as above and below-ground carbon dynamics (Poulter et al. 2015). Such impacts are the changes in albedo linked to the expansion of shrubs and the northward advancement of the treeline (Betts 2000; Miller and Smith 2012). This reduction in albedo and occurrence of arctic shrubification may further accelerate warming in these regions (Bonfils et al. 2012). Land cover information is a key input and feature for many terrestrial ecosystem models and the availability of reliable land cover data is critical for accurate estimations of carbon pools and fluxes, and permafrost dynamics (Gasser et al. 2020; Liu et al. 2023). A land cover product should thus consist of a dynamic classification scheme that allows users to tailor the products for model-specific applications at a spatial resolution which captures important vegetation community dynamics (Townsend et al. 1992).

Remotely sensed data serve as a major data source for land cover mapping, allowing monitoring across global systems (Joshi et al. 2016; Rogan and Chen 2004). There are few maps which contain a comprehensive classification of land cover across the Arctic region with one of the most comprehensive and consistent maps across the Arctic (e.g. the Circum-Arctic Vegetation Map (CAVM)), representing the area north of treeline at a 1 km spatial resolution (Raynolds et al. 2019). Because CAVM is representative of strictly the Arctic zone, its application is limited and thus not representative of land cover types within the transitional Boreal region, which falls within the main area represented in our study region.

There are multiple process-based earth system models (i.e., LPJ-GUESS, DVM-DOS-TEM, FATES), which incorporate vegetation cover to assess regional feedbacks to ecosystem structure and function across the arctic-boreal region (Euskirchen et al. 2009, 2014; Genet et al. 2018; Fisher et al. 2015; Smith et al. 2001), however many models do not often incorporate adequately detailed information on vegetation community type(s) or plant functional types represented within a given community, which may influence the accuracy of vegetation-climate feedback (Isabelle et al. 2012; Miller and Smith 2012). Thus, improved vegetation products are important for these models to project the impacts of future climate change across the arctic-boreal region. Especially important are products which contain detailed information on vegetation cover and characteristics spatially explicit to the area of interest (Miller and Smith 2012; Pearson et al. 2013; Zou et al. 2022). Modeling of permafrost is strongly linked to accurate surface data, of

https://doi.org/10.52381/ICOP2024.201.1

which vegetation is one of the most important as it strongly influences the soil-thermal hydrological regime (Grünberg et al. 2020; Raynolds and Walker, 2008). Thus, using the most updated sources of vegetation maps and products to drive ecosystem models is essential to provide the high accuracy level of information for the multiscale modeling needs across the high-latitude systems (Langford et al. 2019).

While there is a growing number of land cover products at both regional and global scales at varying resolutions, there is a gap for wall-to-wall land cover products, which are representative of high-latitude vegetation communities and designed specifically to meet the needs of pan-arctic ecosystem models. These products should be compatible with existing global and regional maps and be representative of the diverse land cover types within the arctic-boreal region. Here, we discuss the technique and tools we used to develop a hybrid land cover map using and leveraging existing land cover products to develop a representative map for use within ecosystem models across the arctic-boreal region.

The purpose of this paper is to assess limitations and opportunities to further improve land cover maps designed specifically to represent high-latitude terrestrial systems. We present our use of a multi-step workflow incorporating data integration, validation techniques and harmonization of classification systems of existing global and regional land cover products to create a hybrid map at a 1 km spatial resolution tailored specifically for use within a terrestrial ecosystem model, applied and tested for North America with the goal to extend across the pan-arctic region. We integrate machine learning methods to integrate and reclassify vegetation map indices to better suit our modeling needs.

2 Materials and Methods

2.1 Study Area

Our study region encompassed the Arctic-Boreal Zone (ABZ) of North America, which is characterized by spatially diverse vegetation composition and consists of northern tundra and boreal biomes (Virkkala et al. 2021). For this study, we will focus our study sites to the arctic-boreal region of Alaska and Canada. These sentinel sites were carefully selected to represent the arctic-boreal region and diverse vegetation community types. These sites provide unique land cover information for each location and provide a diverse range of vegetation community types represented within DVM-DOS-TEM (Muchoney et al. 1999). In total, we selected 17 sites across North America (Alaska, Canada; Figure 1).

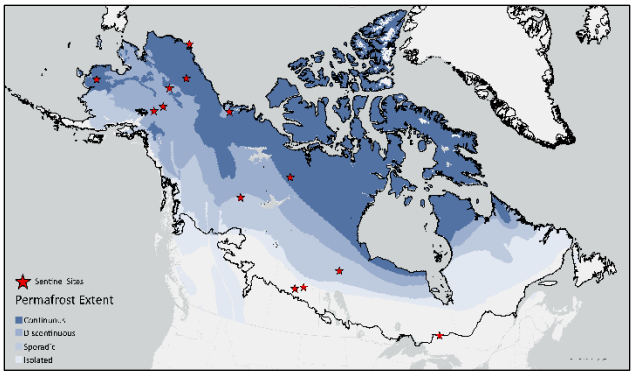

Figure 1. Our study locations shown by red stars within the Arctic Boreal extent of the study region in addition to the permafrost extent map. Modified after (Brown et al. 1997).

2.2 Methods Overview

Our goal is to form a hybrid map that merges existing land cover products to reclassify land cover indices specific to our modeling needs. Our workflow was developed to address inconsistencies across land cover datasets and produce a final harmonized pan-arctic product. Five major steps comprised the workflow (1) pre-processing and re-projecting land cover products to a 1 km grid using a majority rule approach, (2) reclassifying and combining global and regional products to a common final legend based on agreement between global and regional products, (3) finalize reclassifying remaining pixels where no condition was met using random forest machine learning algorithm in addition to input including the reclassified and harmonized products as well as ancillary data variables (i.e., fire occurrence, NDVI), (4) post classification comparison, and (5) final product compilation at 1 km resolution. The general schematic can be seen in Figure 2. This further refines the classification to the final target legend of the hybrid map for a region.

2.3 Land Cover Products

To create our hybrid land cover map, we used a global map as the base layer to provide a globally consistent land cover classification scheme. Then, we selected and integrated more region-specific land cover maps to provide a fine-scale detailed land cover classification scheme used to inform the reclassification of land cover classes to the final product (Table 1). The European Space Agency (ESA) Climate Change Initiative land cover map was selected as the global base map to be used for the creation of the composite DVM-DOS-TEM land cover map. We selected the ESA map for the year 2016 at 300 m resolution (Lamarche et al. 2017). It was used as the primary base map across the boreal region. To represent arctic vegetation community types, we incorporated the Circumpolar Arctic Vegetation Map (CAVM) which was produced in 2003 (Raynolds et al. 2019). The CAVM map includes 15 vegetation types, which we further grouped to five major land cover types based on the arctic bio climate subzones: Barrens, Graminoid tundra, Prostrate-shrub tundra, Erect-shrub tundra, and wet-sedge tundra.

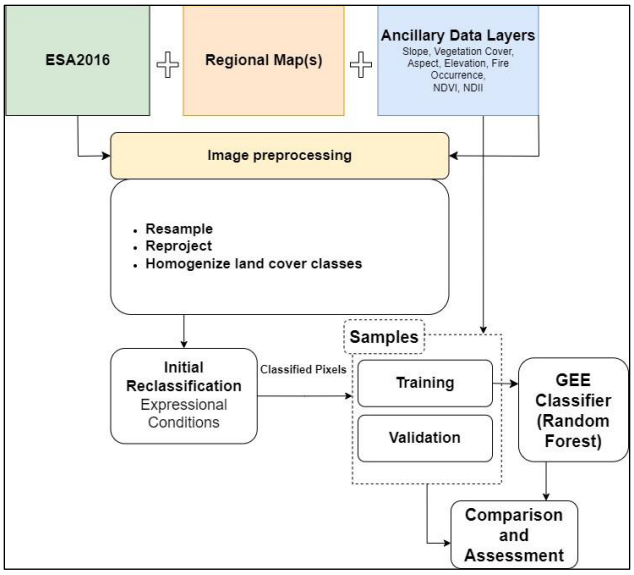

Figure 2. Flowchart of the study highlighting the major inputs, output and major steps.

We chose not to alter the circumpolar region encompassed within the CAVM map as it provides a detailed and accurate classification of arctic vegetation. We thus focused our analysis to the region below the treeline or that which excludes the CAVM extent.

2.4 Pre-Processing

Each land cover product was re-projected to a 1 km resolution using a majority-rule approach. A majority rule is used to aggregate the finer scale resolution maps into the corresponding coarser land cover map. Non-overlapping square windows, each representing one pixel in an output image, are overlaid and assigned to the class that comprises the majority in a given window. To have a one-to-one comparison of land cover classes between global and regional products, we reclassified original land cover classes to align with the classification of the global land cover map. This reclassification created a harmonized classification scheme, while maintaining the main representative land cover classes. These classes included: forest, shrubland, herbaceous/grassland, barren, and wetland. This general reclassification of land cover classes was also used to estimate the level of agreement between each regional map to the global base map.

2.5 Random Forest classification

Random Forest is one of the most widely used supervised machine learning algorithms for land cover mapping and classification because of its ability to handle noisy and multi-source datasets (Jin et al. 2018; Maxwell et al. 2019). The random forest method is an ensemble-based classifier which uses decision trees for training and prediction. In Google Earth Engine, we used the function ee.ClassifiersmileRandomForest, which is based on the random forest method. We set the hyperparameter, number of trees (ntrees), based on the value which produced the best resulting accuracy for each region. The rest of the hyperparameters were left at their default values, which is the square root of the total number of features.

To build the random forest model, we compiled a dataset with ancillary variables further detailing landscape characteristics and disturbance history to further aid in the prediction of land cover classes including fire occurrence, canopy cover, elevation, slope, and aspect, which are further detailed in (Hermosilla et al. 2022; Matasci et al. 2018). In addition, classified pixels from the initial classification based on overlap agreement between the global and regional dataset were compiled into the ancillary dataset to provide the model with training data on successfully classified land cover classes. We created a collection of samples that were then randomly split into two groups of training (80%) and testing (20%). In total between 500–1,000 samples per land cover class were collected within each region (Alaska, Canada), with the number of samples determined based on the max sample number of a given class in each region. A separate random forest model was trained for each study region (Alaska, Canada) to be region-specific to map the distribution of natural land cover by conducting a supervised classification process, integrating ancillary variables.

The first step of reclassification is based on the overlap or agreement of major land cover classification between global and regional maps. A given pixel is grouped as one of the following classes if both the global and regional map pixels agree: forest (evergreen, deciduous, mixed), shrubland, herbaceous, barren or wetland. The

Table 1. Characteristics of the land cover products used in this study.

Dataset	Spatial Resolution	Extent	Date	Reference
ESA CCI Land Cover 2016	300 m	Global	2016	Lamarche et al. 2017
Circumpolar Arctic Vegetation Map (CAVM)	1 km	Circumpolar	2022	Raynolds et al. 2019
LANDFIRE	30 m	Alaska	2016	Rollins, 2009
Alaska Vegetation and Wetland Composite (AKVWC)	30 m	Alaska	Multi-year-not explicit	Flagstad et al. 2018
Leading Tree Species	30 m	Canada	2019	Hermosilla et al, 2022
Canada Virtual Land Cover Engine (VLCE)	30 m	Canada	2016	Hermosilla et al. 2018
Wetland Map for Canada	30 m	Canada	2000-2016	Wulder et al. 2018

classification rules are further refined to then reclassify the pixels of agreements of the major land cover classes into more specific classes using various conditional statements. For example, if both the global and regional maps classify the pixel as evergreen and an overlapping ancillary regional map classifies it as a White Spruce Forest, then it gets classified as White Spruce Forest.

After this initial classification step, if a condition is not met, the pixel is left unclassified. We then incorporate our random forest model, train the model on pixels successfully classified in addition to ancillary datasets and use machine learning to classify the remaining pixels within a region. This multi-step process ensures that we are using points of agreement between maps to inform the reclassification process.

2.6 Assessment, Comparison and Testing

Model performance, which varies across regions, dictated the level of success in creating an integrated reclassified land cover map. The success or accuracy of this process was dependent on the quality of the input data and assessed based on the composition of each new land cover class for the hybrid map to the composition of its corresponding class of the regional and global maps to ensure the percentage of a given land cover type fell within the range of composition of both maps. We estimated percent coverage of each land cover class of the newly developed hybrid map for Alaska and Canada This composition estimation is straightforward yet allows us to better understand the range of accuracy of the final product.

3 RESULTS

Our workflow shows the ability to reclassify global and regional land cover maps utilizing machine learning as an additional tool to produce a final hybrid map with updated land cover classes specifically designed to meet our modeling needs. When assessing the overall agreement between global and regional land cover products, we see that across the boreal region of Alaska, the LANDFIRE and ESA showed a total 55.57% agreement in major land cover classifications, while the Canadian VLCE map and ESA showed a total of 49.68% agreement across Canada. Our assessment shows that across Alaska and Canada the land cover class with the greatest point of agreement was in classification of forest at 44% and 33% of the total area, respectively as shown in Figure 3. The greatest disagreement in land cover classification between the global ESA and regional maps occurred between wetlands and shrubland classification across both Alaska and Canada.

For each region, our combined final hybrid map (Figure 4a) was able to represent the general land cover classes for each region of focus, while maintaining and representing the fine-scale land cover classes we targeted for the final legend. Across Alaska, our final map resulted in a forest composition of 42.6% in comparison to 37.1% and 42.3% for the LANDFIRE and ESA2016 maps respectively (Figure 4b), while the final hybrid map for Canada resulted in a total forest composition of 60.6% compared to 56.8% and 71.8% for the VLCE and ESA2016 maps respectively (Figure 4c). Similarly, across Alaska shrublands represented 35.9% of the total vegetation cover, compared to 44.4% and 26.7% represented in both LANDFIRE and ESA. Total shrublands were less prominent across Canada at 12.6% within the hybrid map, compared to 15.9% and 7.6% across the VLCE and ESA maps respectively.

Since we are not creating a new land cover map, but utilizing existing land cover products, we still have to further assess the accuracy of the newly reclassified land cover scheme for each region. A method in which we do so is through comparing percent coverage of each major land cover class between the global, regional, and final hybrid map as well as using the sentinel site locations to further ground truth.

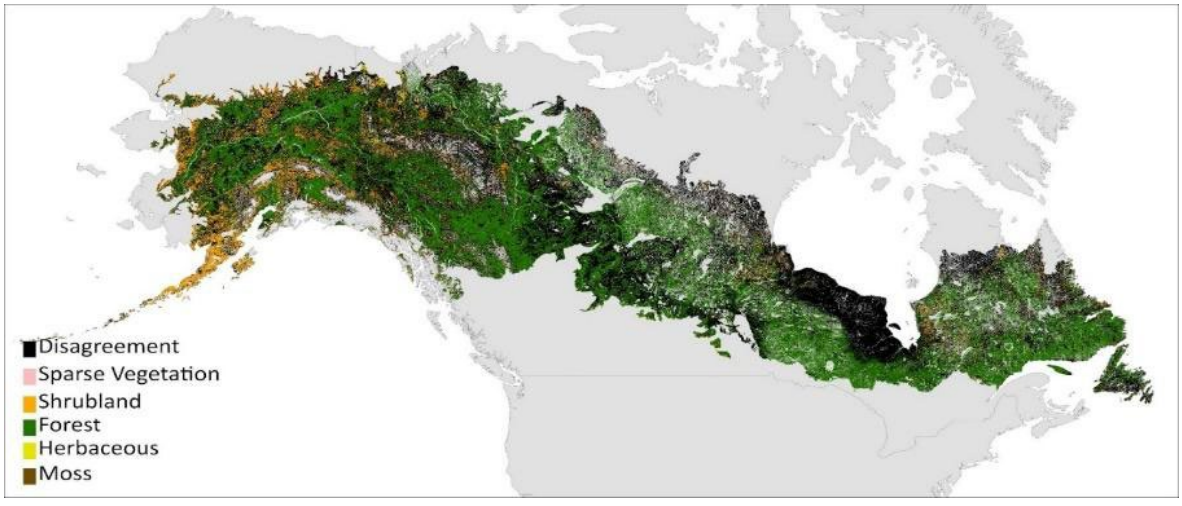

Figure 3. Agreement between the global ESA2016 map to each region-specific land cover products across Alaska and Canada highlighting the areas of classification agreement at a 1 km spatial resolution.

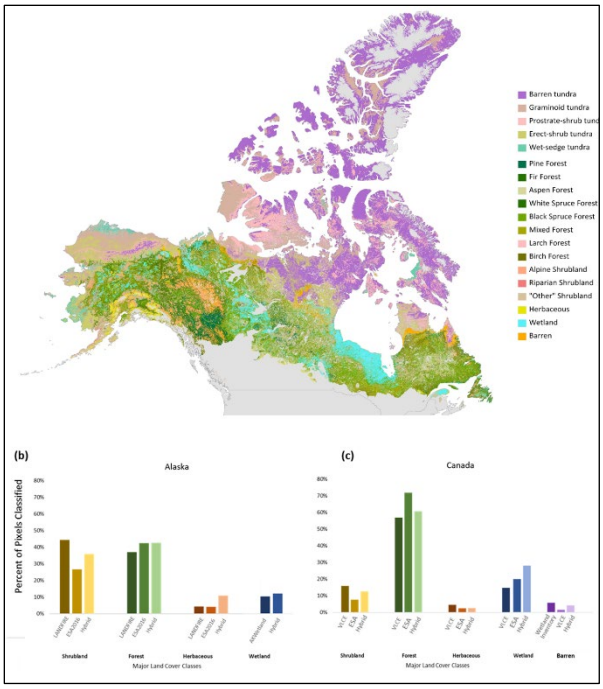

Figure 4. Final Hybrid map at 1 km resolution across the study region, in addition to the Circumpolar Arctic Vegetation Map (CAVM) across the arctic (a). Comparisons of the percent composition of each major land cover class across the major land cover products used for the study for both Alaska and Canada (b,c).

The final hybrid map is able to capture the presence of more shrubland dominant land cover types particularly in the top left quadrant of the grid.

Figure 5 shows the comparison of land cover products and their classification of an upland boreal site located outside of Fairbanks, Alaska encompassing a 10 x 10 km grid. This site is characterized by both black spruce and deciduous birch dominated forests.

4 Discussion

In this study, we present an integration approach to generate a hybrid land cover map at a 1 km spatial resolution, specifically tailored to community types parameterized within DVM-DOS-TEM. One of the primary challenges in comparing land cover products lies in the variations in resolution or detail of the land cover classes, making it difficult to ensure direct interpretation across different datasets. Our main objective is to introduce an adaptable approach that enables the combination of multiple land cover datasets with varying spatial resolutions, thematic content, and sources, resulting in a unified hybrid classification system. This method can be applied to harmonize existing global land cover datasets of moderate resolution, ultimately yielding the most accurate land cover product possible for any location worldwide.

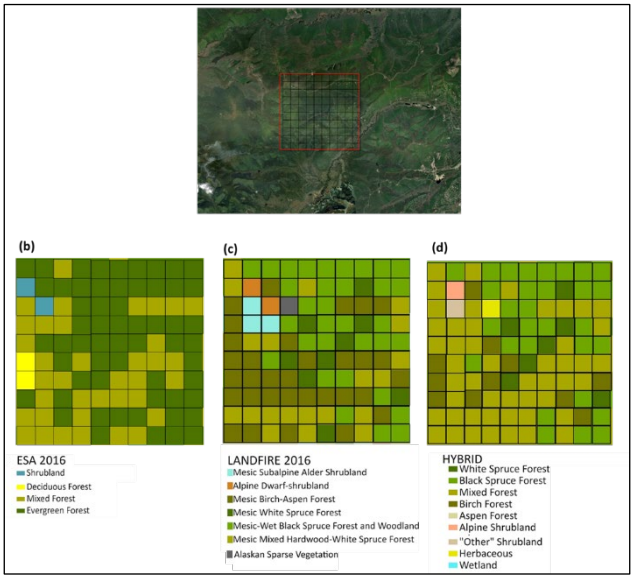

Figure 5. Comparison of land cover products: ESA2016(b), LANDFIRE2016(c), and the final hybrid map (d) classification of a 10 x10 km grid encompassing one of the boreal study sites located near Fairbanks, AK.

Throughout the study, we utilized a random forest model, incorporating four ancillary variables primarily related to topography and disturbance, as additional predictors to improve the accuracy of the hybrid map. Our results demonstrated that the hybrid map exhibited reasonable accuracy across regions when compared to both the global and corresponding regional maps, although slight variations were observed due to differences in model hyperparameters. We compile the most relevant and detailed regional land cover maps that encompassed our study region and included the target land cover classes required for reclassifying our final hybrid map. Utilizing existing global and regional products, our approach successfully generated a hybrid land cover map through a merging scheme that emphasized areas of agreement between the two types of maps. This ensured that the final product effectively represented the target classes and fell within the composition range of each class derived from both global and regional sources, capturing the general composition of land cover while accommodating new target classifications tailored to our modeling needs.

Our approach is reproducible and can be applied to other study regions at both regional and global levels. Additionally, it is versatile enough to be customized for various purposes, including modeling, allowing users to tailor land cover classes according to their specific requirements. Moreover, its adaptability permits the integration of new or updated regional and global products, facilitating ongoing revisions and improvements to the final hybrid product and allowing for the incorporation of more detailed land cover classifications.

We build our approach upon existing agreements across validated and tested land cover products rather than introducing a new product. This emphasis on existing agreements ensures the reliability and credibility of the final hybrid map. To accurately represent the diverse vegetation communities of the circumpolar arctic-boreal region, integrating multiple land cover maps derived from remotely sensed products is essential, particularly when the final product serves multiple applications in ecosystem modeling. Employing a multi-step approach, which includes a machine learning model, ensures the accurate representation and composition of the hybrid map concerning the original land cover products used in its creation. As new or updated regional and global products become available, our approach remains flexible enough to incorporate these data, leading to continuous refinement and enhancement of the final product and providing more detailed land cover classifications as needed.

To further improve our workflow, we can focus on exploring and utilizing additional ancillary datasets such as NDVI and NDII, which we have integrated into our revised workflow to enhance the precision of our findings. By incorporating these datasets, we aim to address issues such as unequal or unrepresentative sampling rates and scaling discrepancies, which may introduce biases in our results. Leveraging recently developed databases for the validation of global land cover products (e.g., Friedl et al. 2010; Pérez-Hoyos et al. 2012) could prove instrumental in overcoming these limitations and further improving the reliability of our presented outcomes. In summary, our study showcases a robust and adaptable methodology for generating a comprehensive hybrid land cover map, addressing the challenges posed by varying land cover datasets and offering valuable insights for ecosystem modeling and other applications.

5 Conclusions

Our study underscores the significance of accurate land cover mapping in high-latitude regions, where climate-induced changes are reshaping ecosystem dynamics. The integration of diverse land cover datasets using a multi-step approach and machine learning techniques has resulted in the creation of a versatile hybrid land cover map tailored to the specific needs of ecosystem models across the arctic-boreal region. Our final hybrid map not only integrates existing global and regional land cover products but also introduces refinements to better represent the unique vegetation communities in the study area. By leveraging agreements between validated land cover products, our approach ensures the reliability and credibility of the final map, enhancing its utility for diverse applications, particularly in ecosystem modeling.

While our methodology demonstrates its effectiveness in generating accurate land cover maps, future efforts should focus on incorporating additional validation datasets to further refine and enhance the precision of our findings. These datasets can help address potential biases and scaling issues, ultimately bolstering the reliability of our results. Our future product will include validation sites across Eurasia. In summary, our study offers a robust and adaptable framework for producing comprehensive land cover maps, addressing the complexities of varying datasets, and providing valuable insights for high-latitude ecosystem modeling and other related endeavors.

6 Acknowledgements

This project was made possible with funding through the Audacious Project and Quadrature Climate Foundation Prime Grant Number 01-21-000094 (to SMN and BR).

7 References

Betts, R.A. 2000. 'Offset of the potential carbon sink from boreal forestation by decreases in surface albedo', *Nature*, 408(6809), pp. 187–190. doi:10.1038/35041545.

Brown, J., Ferrians, O.J., Heginbottom, J.A., and Melnikov, E.S. 1997. Circum-Arctic map of permafrost and ground-ice conditions. Available at: https://doi.org/10.3133/cp45.

Euskirchen, E.S., Edgar, C.W., Turetsky, M.R., Waldrop, M.P., and Harden, J.W. 2014. 'Differential response of carbon fluxes to climate in three peatland ecosystems that vary in the presence and stability of permafrost', *Journal of Geophysical Research: Biogeosciences* 119(8), pp. 1576–1595. doi:10.1002/2014JG002683.

Euskirchen, E.S., McGuire, A.D., Chapin III, F.S., Yi, S., and Thompson, C.C. 2009. 'Changes in vegetation in northern Alaska under scenarios of climate change, 2003–2100: implications for climate feedbacks', *Ecological Applications* 19(4), pp. 1022–1043. doi:10.1890/08-0806.1.

Fisher, R.A. and Koven, C.D. 2020. 'Perspectives on the Future of Land Surface Models and the Challenges of Representing Complex Terrestrial Systems', *Journal of Advances in Modeling Earth Systems* 12(4), e2018MS001453. doi:10.1029/2018MS001453.

Fisher, R.A., Muszala, S., Verteinstein, M., Lawrence, P., Xu, C., McDowell, N.G., Knox, R.G., Koven, C., Holm, J., Rogers, B.M., Spessa, A., Lawrence, D., and Bonan, G. 2015. 'Taking off the training wheels: the properties of a dynamic vegetation model without climate envelopes, CLM4.5(ED)', *Geoscientific Model Development*, 8(11), pp. 3593–3619. doi:10.5194/gmd-8-3593-2015.

Flagstad, L., Steer, M.A., Boucher, T., Aisu, M., and Lema, P. 2018. 'Wetlands across Alaska: Statewide wetland map and Assessment of rare wetland ecosystems', *Alaska Natural Heritage Program, Alaska Center for Conservation Science*, University of Alaska Anchorage.

Friedl, M.A., Sulla-Menashe, D., Tan, B., Schneider, A., Ramankutty, N., Sibley, A., and Huang, X. 2010. 'MODIS Collection 5 global land cover: Algorithm refinements and characterization of new datasets', *Remote Sensing of Environment* 114(1), pp. 168–182. doi:10.1016/j.rse.2009.08.016.

Gasser, T., Crepin, L., Quilcaille, Y., Houghton, R.A., Ciais, P., and Obersteiner, M. 2020. 'Historical CO_2 emissions from land use and land cover change and their uncertainty', *Biogeosciences* 17(15), pp. 4075–4101. doi:10.5194/bg-17-4075-2020.

Genet, H., He, Y., Lyu, Z., McGuire, A.D., Zhuang, Q., Clein, J., et al. 2018. 'The role of driving factors in historical and projected carbon dynamics of upland ecosystems in Alaska', *Ecological Applications* 28(1), pp. 5–27. doi:10.1002/eap.1641.

Grünberg, I., Wilcox, E.J., Zwieback, S., Marsh, P., and Boike, J. 2020. 'Linking tundra vegetation, snow, soil temperature, and permafrost', *Biogeosciences* 17(16), pp. 4261–4279. doi:10.5194/bg-17-4261-2020.

Heimann, M. and Reichstein, M. 2008. 'Terrestrial ecosystem carbon dynamics and climate feedbacks', *Nature* 451(7176), pp. 289–292. doi:10.1038/nature06591.

Hermosilla, T., Bastyr, A., Coops, N.C., White, J.C., and Wulder, M.A. 2022. 'Mapping the presence and distribution of tree species in Canada's forested ecosystems', *Remote Sensing of the Environment* 282, 113276. doi:10.1016/j.rse.2022.113276.

Hermosilla, T., Wulder, M.A., White, J.C., Coops, N.C., and Hobart, G.W. 2018. 'Disturbance-Informed Annual Land Cover Classification Maps of Canada's Forested Ecosystems for a 29-Year Landsat Time Series', *Canadian Journal of Remote Sensing* 44(1), pp. 67–87.doi:10.1080/07038992.2018.1437719.

Horvath, P., Tang, H., Halvorsen, R., Stordal, F., Tallaksen, L.M., Berntsen, T.K., and Bryn, A. 2021. 'Improving the representation of high-latitude vegetation distribution in dynamic global vegetation models', *Biogeosciences* 18(1), pp. 95–112. Copernicus GmbH. Doi:10.5194/bg-18-95-2021.

Isabelle, B., Pauline, P., Sylvain, A., Roland, D., Luc, G., Sébastien, L., Sandra, L., Jérémie, V.E., Pascal, V., and Wilfried, T. 2012. 'Improving plant functional groups for dynamic models of biodiversity: at the crossroads between functional and community ecology', *Global change biology* 18(11). doi:10.1111/j.1365-2486.2012.02783.x.

Jia, G., Shevliakova, E., Artaxo, P., Brazil, N., De Noblet-Ducoudré, F., Houghton, R., Anderegg, W., et al. 2019. 'Land-Climate interactions', in *Special Report on climate change, desertification, land degradation, sustainable land management, food security, and greenhouse gas fluxes in terrestrial ecosystems*.

Jin, Y., Liu, X., Chen, Y., and Liang, X. 2018. 'Land-cover mapping using Random Forest classification and incorporating NDVI time-series and texture: a case study of central Shandong', *International Journal of Remote Sensing* 39, pp. 1–21. doi:10.1080/01431161.2018.1490976.

Joshi, N., Baumann, M., Ehammer, A., Fensholt, R., Grogan, K., Hostert, P., Jepsen, M.R., Kuemmerle, T., Meyfroidt, P., Mitchard, E.T.A., Reiche, J., Ryan, C.M., and Waske, B. 2016. 'A Review of the Application of Optical and Radar Remote Sensing Data Fusion to Land Use Mapping and Monitoring', *Remote Sensing* 8(1), pp. 70. doi:10.3390/rs8010070.

Kåresdotter, E., Destouni, G., Ghajarnia, N., Hugelius, G., and Kalantari, Z. 2021. 'Mapping the Vulnerability of Arctic Wetlands to Global Warming', *Earth's Future* 9(5), e2020EF001858. doi:10.1029/2020EF001858.

Lamarche, C., Santoro, M., Bontemps, S., D'Andrimont, R., Radoux, J., Giustarini, L., Brockmann, C., Wevers, J., Defourny, P., and Arino, O. 2017. 'Compilation and Validation of SAR and Optical Data Products for a Complete and Global Map of Inland/Ocean Water Tailored to the Climate Modeling Community', *Remote Sensing* 9.

Le Quéré, C., Moriarty, R., Andrew, R.M., Canadell, J.G., Sitch, S., Korsbakken, J.I., et al. 2015. 'Global Carbon Budget 2015', *Earth System Science Data* 7(2), pp. 349–396. doi:10.5194/essd-7-349-2015.

Liu, A., Moore, J.C., and Chen, Y. 2023. 'PInc-PanTher estimates of Arctic permafrost soil carbon under the GeoMIP G6solar and G6sulfur experiments', *Earth System Dynamics* 14(1), pp. 39–53. doi:10.5194/esd-14-39-2023.

Matasci, G., Hermosilla, T., Wulder, M.A., White, J.C., Coops, N.C., Hobart, G.W., and Zald, H.S.J. 2018 'Large-area mapping of Canadian boreal forest cover, height, biomass and other structural attributes using Landsat composites and lidar plots', *Remote Sensing of Environment* 209, pp. 90–106

Maxwell, A.E., Strager, M.P., Warner, T.A., Ramezan, C.A., Morgan, A.N., and Pauley, C.E. 2019. 'Large-Area, High Spatial Resolution Land Cover Mapping Using Random Forests, GEOBIA, and NAIP Orthophotography: Findings and Recommendations', *Remote Sensing* 11(12), 1409. doi:10.3390/rs11121409.

Miller, P.A. and Smith, B. 2012. 'Modelling Tundra Vegetation Response to Recent Arctic Warming', *AMBIO* 41(3), pp. 281–291. doi:10.1007/s13280-012-0306-1.

Muchoney, D., Strahler, A., Hodges, J., and LoCastro, J. 1999. 'The IGBP DISGover Confidence Sites and the System for Terrestrial Ecosystem Parameteilzation: Tools for Validating Global Land-Gover Data', *Photogrammetric Engineering & Remote Sensing* 65(9), pp. 1061–1067.

Pearson, R.G., Phillips, S.J., Loranty, M.M., Beck, P.S.A., Damoulas, T., Knight, S.J., and Goetz, S.J. 2013. 'Shifts in Arctic vegetation and associated feedbacks under climate change', *Nature Climate Change* 3(7), pp. 673–677.doi:10.1038/nclimate1858.

Pérez-Hoyos, A., García-Haro, F.J., and San-Miguel-Ayanz, J. 2012. 'A methodology to generate a synergetic
land-cover map by fusion of different land-cover products', *International Journal of Applied Earth Observation and Geoinformation* 19, pp. 72–87. doi:10.1016/j.jag.2012.04.011.

Raynolds, M. and Walker, D. 2008. 'Circumpolar Relationships Between Permafrost Characteristics, NDVI, and Arctic Vegetation Types', in *Ninth International Conference on Permafrost*. Fairbanks, Alaska, United States.

Raynolds, M.K., Walker, D.A., Balser, A., Bay, C., Campbell, M., Cherosov, M.M., et al. 2019. 'A raster version of the Circumpolar Arctic Vegetation Map (CAVM)', *Remote Sensing of Environment* 232, 111297. doi:10.1016/j.rse.2019.111297.

Rogan, J. and Chen, D. 2004. 'Remote sensing technology for mapping and monitoring land-cover and land-use change', *Progress in Planning* 61(4), pp. 301–325. doi:10.1016/S0305-9006(03)00066-7.

Rollins, M.G. 2009. 'LANDFIRE: a nationally consistent vegetation, wildland fire, and fuel assessment', *International Journal of Wildland Fire* 18(3), pp. 235–249.doi:10.1071/WF08088.

Smith, B., Prentice, I.C., and Sykes, M.T. 2001. 'Representation of vegetation dynamics in the modelling of terrestrial ecosystems: comparing two contrasting approaches within European climate space', *Global Ecology and Biogeography* 10(6), pp. 621–637. doi:10.1046/j.1466-822X.2001.t01-1-00256.x.

Townsend, A.R., Vitousek, P.M., and Holland, E.A. 1992. 'Tropical soils could dominate the short-term carbon cycle feedbacks to increased global temperatures', *Climatic Change* 22(4), pp. 293–303. doi:10.1007/BF00142430.

Virkkala, A.-M., Natali, S.M., Rogers, B.M., Watts, J.D., Savage, K., Connon, S.J., et al. 2022. 'The ABCflux database: Arctic–boreal CO_2 flux observations and ancillary information aggregated to monthly time steps across terrestrial ecosystems', *Earth System Science Data* 14(1), pp. 179–208. doi:10.5194/essd-14-179-2022.

Wulder, M.A., Coops, N.C., Roy, D.P., White, J.C., and Hermosilla, T. 2018. 'Land cover 2.0', *International Journal of Remote Sensing* 39(12), pp. 4254–4284.doi:10.1080/01431161.2018.1452075.

Zou, D., Zhao, L., Liu, G., Du, E., Hu, G., Li, Z., Wu, T., Wu, X., and Chen, J. 2022. 'Vegetation Mapping in the Permafrost Region: A Case Study on the Central Qinghai-Tibet Plateau', *Remote Sensing* 14(1), 232. doi:10.3390/rs14010232.

Multi-technical study of retrogressive thaw slumps at km 1456 of the Alaska Highway, Yukon

Fabrice Calmels, Philip Sedore, Fanny Amyot, Louis-Philippe Roy, Cyrielle Laurent, Casey Buchanan & Cathy Koot

YukonU Research Centre, Yukon University, Whitehorse, Yukon, Canada

ABSTRACT

The presence of active retrogressive thaw slumps (RTSs) adjacent to the Alaska Highway at km 1456 have created a unique opportunity for permafrost characterization, monitoring, and climate change impact analysis in the greater Whitehorse area. An intensive research program was established to act before serious damage occurs and acquire a better understanding of retrogressive thaw slumps that impact northern road corridors. The study addresses key knowledge gaps in mapping of RTS formation and evolution processes, as well as methodological gaps in the monitoring of such geohazards. To acquire this new knowledge about RTS processes, the study focuses on frozen soil properties, ground thermal regime, ground movements, and ground water dynamics. Research activities included geotechnical borehole investigations, ground temperature monitoring, ground surface movement monitoring with differential GPS, imaging and topography monitoring using unmanned aerial vehicle photogrammetry, and electrical resistivity tomography surveying. The multi-technical monitoring approach was used to inform an approach to mitigate the threat caused by RTSs on road corridors.

1 INTRODUCTION

Retrogressive thaw slumps (RTSs) occur in areas of ice-rich permafrost. They develop on hillslopes and usually occur along the shorelines of lakes, rivers and coastlines (Ramage et al. 2017). Thaw slumps consist of a headwall made predominantly of ice and a muddy slump floor. Slumps grow as melting ground ice in the headwall turns material into a muddy slurry that flows downslope to the base of the exposure (Kokelj and Jorgenson 2013; Armstrong et al. 2018; Ballantyne 2018). Melting of the exposed ground ice causes the headwall to retreat upslope and the disturbance grows. A headwall may migrate by several metres in a single summer, and over time a slump can impact several hectares of terrain. The rate of headwall movement is linked to several environmental factors, but generally, rates of slump growth are most rapid when the temperature is warmest (Bernard et al. 2021). Retrogressive thaw slump activity has increased in the Arctic in recent decades (Ward Jones et al. 2019; Lewkowicz and Way 2017), and their occurrence is projected to intensify in magnitude and frequency with a changing climate (Turner et al. 2021).

Retrogressive thaw slumps can represent permafrost thaw-related geohazards that may lead to widespread damage or lead to failure of northern transportation infrastructure. The development of some of these geohazards can be attributed to the thermal disturbances induced by the construction and presence of the very infrastructures themselves (Bliss and Ross 1971). Other thaw processes that are occurring naturally or as a function of climate change in the vicinity of infrastructures, sometimes even hundreds of meters away, can eventually impact them. Such an occurrence was reported along the Dempster Highway on the Peel Plateau (Kokelj et al. 2021; van de Sluijs et al. 2018).

Two retrogressive thaw slumps formed close to the Alaska Highway at km 1456, approximately 30 km west of Whitehorse (Figure 1). They are located within a forested area surrounded by the Takhini River to the north and the Alaska Highway to the south. The first RTS (RTS 1) was discovered in April 2019, while the second (RTS 2) initiated in September 2021.

The headwall of RTS 1 was approximately 80 m away from the road in May 2019. Given the RTS proximity to the Alaska Highway and the risk posed to road safety, a multi-technical study and monitoring program were implemented to address this hazard and provide the Transportation Engineering Branch of Yukon Highway and Public Works department with the information needed to address the issue. The study also provided the opportunity to investigate RTS formation and evolution processes in sporadic discontinuous permafrost zones.

This paper presents and discusses results obtained using a methodological approach combining Unmanned Aerial Vehicle (UAV) surveys, borehole geotechnical and temperature data, and electrical resistivity tomography (ERT) geophysical surveys that were used to develop a better understanding of the RTS processes in the area.

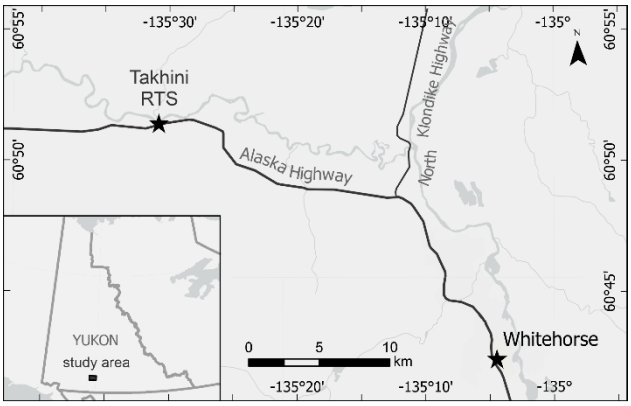

Figure 1. Study area map.

2 STUDY SITE

This section of the Alaska Highway is in the Southern Lakes Ecoregion (Yukon Ecoregions Working Group 2004). The

https://doi.org/10.52381/ICOP2024.177.1

climate is subarctic with large seasonal variations in temperature and a mean annual air temperature (MAAT) of -3.0 °C, which is 2.3 °C cooler than the Whitehorse airport (Burn 1998). This area is also characterized by low precipitation and low humidity due to the rain shadow of the Coast Mountains. The site is covered by a deciduous mixed forest consisting of lodgepole pine, white spruce, and trembling aspen. Shrubs such as willow and soapberry are present throughout much of the site. Common plant species are forbs such as fireweed and alpine sweet-vetch, mosses, and lichens. The site lacks a thick organic cover.

The surficial geology and landscape features of the study site are largely a product of the most recent (Late Wisconsinan) McConnell Glaciation, which occurred between 24,000 and 11,000 years ago. At this location in the Ibex Valley, Glacial Lake Champagne deposited up to 75 m of silt and clay between 10,000 and 9,000 years ago (Yukon Ecoregions Working Group 2004). After the drainage of the lake, permafrost was able to aggrade in this sediment. In the Ibex Valley, glaciolacustrine silt and clay often contains massive ice bodies, which are prone to RTSs and general thermokarst degradation when disturbed by river erosion, forest fires, or other changes in surface conditions (H.M. French 2017).

The Takhini River RTSs were likely initiated by erosion on the outer bend of a meander of the Takhini River. Though studies began at this site in the spring of 2019, satellite and aerial imagery show the RTS 1 to have been active since at least 2014. The RTS 2 initiated in September 2021, during the monitoring program.

A similar failure had already occurred only 180 m east of this site. Aerial photography revealed that a 40,000 m^3 RTS was initiated in 1979 by river bank erosion and stayed active until 1986, causing 112 m of headwall retreat to approximately its present position. Since 2004, that thaw slump stabilized a few meters short of the highway.

The study site is in sporadic discontinuous permafrost zone (Hegginbottom et al. 1995). Research led by Burn (1987, 1998) in a nearby forested site found a 1.4 m thick active layer, and 17 m thick permafrost, the temperature at the top of permafrost (TTOP) being -0.7 °C. When the site RTS 1 was first assessed in May 2019, the then 50 m wide and 5 m high headwall provided an outstanding natural exposure of ice-rich permafrost with ice lenses that were up to 20 cm thick. The other noticeable signs of permafrost degradation on the study site were meter-wide tension cracks and split trees due to ground movements. Along the road in the cleared area, some shallow ponds are present, which probably have thermokarstic origins. A noticeable feature is groundwater that frequently seeps from the headwall of the slump during the thaw season and icings in winter.

3 METHODOLOGY

3.1 Below surface investigations

A total of four boreholes of various depths were drilled at the site (locations shown in Figure 2). Borehole 1 (BH1) and 2 (BH2) were drilled by a contractor using a CRREL corer

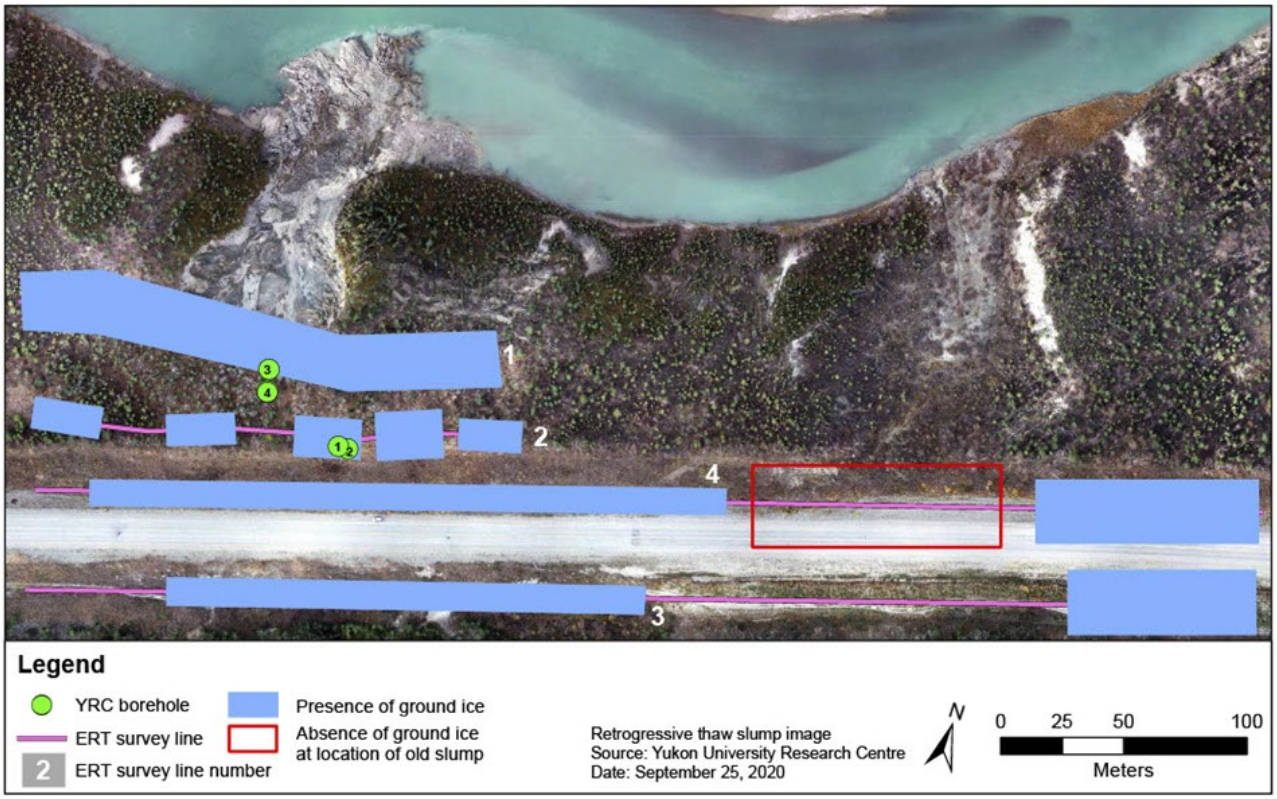

Figure 2. Boreholes and ERT line locations, with approximate position of ground ice based on ERT profiles.

for BH1 and destructively for BH2 on October 16 and 23, 2019, reaching 10 m and 25 m depths respectively.

Two shallow boreholes, BH3 and BH4, were drilled May 13 and May 22, 2020, by the research team with a portable core-drill system using a diamond-carbide corer, reaching 6 m and 3 m depth, respectively. Once drilling was completed, the boreholes were cased with 1-inch PVC conduits and backfilled to the surface. Groundwater was encountered at approximatively 3 m depth in boreholes BH1, BH2, and BH4. It resulted in the collapsing of BH1 and BH4, and the termination of drilling.

Cores from BH1 and BH3 were brought frozen to the laboratory where grain-size, cryostructures, volumetric ice content, gravimetric ice content and settlement potential were analysed. A log for each permafrost borehole was then created. BH2 was outfitted with a 16-channel LogR Systems thermistor and logger, and BH3 with two 4-channel Hobo UX120 loggers to record ground temperatures. The two boreholes also were outfitted with MeasureAnd SAAV Shape Array inclinometer to monitor deformation and slope movements every 50 cm from the surface to the base.

Electrical resistivity surveys were performed using an ABEM Terrameter LS electrical resistivity and tomography system. Two 200 m ERT lines, profiles 1 and 2, were surveyed in the forested slump area using Wenner and dipole-dipole arrays with 2.5 m spacing between electrodes. Two 500 m ERT lines, profiles 3 and 4, were surveyed on each side of the road, at the base of the embankment, using a dipole-dipole array with 2.5 m spacing between electrodes (Figure 2). ERT 1 survey was completed on June 14, 2019. It ran from east to west, through a dense undisturbed deciduous mixed forest 12 m away from the RTS 1 headwall. ERT 2 was conducted on July 16, 2019. This transect ran east to west in a deciduous mixed forest, along the cleared portion of the right-of-way of the Alaska Highway and 30 m away from the RTS 1 headwall. ERT 3 was completed on August 23, 2019. The 500 m survey ran west-east along the south side of the road embankment, going down a slight hill slope. The vegetation cover was open and colonized predominantly by small trembling aspen, willows, and some spruce saplings. ERT 4 was completed on September 12, 2019. The 500 m survey ran west-east along the north side of the road embankment, going down a slight hill slope. The vegetation cover was very similar to that encountered at ERT 3.

3.2 Above surface investigations

The thaw slump has been regularly surveyed with drones for aerial image collection since August 2019 during thaw seasons. A DJI Phantom 4 Pro V2 was used from August 2019 to July 2020 and DJI Matrice RTK 210 from August 2020 until present. Targets were placed on the ground with their position geolocated using a differential global positioning system (DGPS). The targets' locations were used as ground control points to produce centimeter-scale positional accuracy for the image processing outcome products.

Images were processed using Agisoft Metashape Professional software. Image processing produced a point cloud, a 3D model including mesh mapping and texture, a digital surface model (DSM), and an orthomosaic. All final products are projected using UTM zone 8. Orthomosaics and DSMs were used to digitize the headwall of the thaw slump with ArcGIS to measure the progression of the slump through a suite of morphometric parameters.

The groundwater seeping from the headwall of the slump was investigated and mapped flying a DJI Mavic 2 Enterprise Advanced Thermal November 21, 2021.

4 RESULTS

4.1 Borehole data

The cores of BH1 (Figure 3) shows a stratigraphy composed predominantly by clayey silt. The borehole ends at 10 m in silty sediment (99.9% silt). Lenticular, micro lenticular, reticulate and thick suspended cryostructures were identified along the profile. The volumetric excess ice content ranged from 13 to 41%. The horizon from 4.5 to 10 m contained the highest excess ice content. Overall, the borehole has a mean volumetric excess ice content of 32.5%.

The borehole BH3 shows layers of ice-rich gray clayey silt alternating with some very ice rich layers. While drilling was initiated in frozen ground, at approximately two meters depth a thin unfrozen section of soil with the presence of ground water depth was encountered. The borehole extends to six meters with clayey-silt sediment. Lenticular and micro lenticular cryostructures were identified along the profile.

Ground temperature records suggest that the top of permafrost is between two and three meters. The ground temperatures are just below 0 °C. The ground appears to be unfrozen below eight meters of depth in BH2 but cores were recovered frozen down to 10 m depth in BH1. This suggests that destructive drilling altered the thermal regime in BH2 and depth of permafrost cannot be inferred from the BH2 temperature record. The permafrost at this site can be considered as warm and susceptible to degradation. The significant amount of ice present in the ground is preventing permafrost from thawing because of the latent heat (the amount of heat required to melt all the ice in a unit of soil or rock) absorption required to change ice to liquid water.

4.2 ERT survey results

The ERT 1 survey (Figure 4) suggests that permafrost could be as deep as 30 m towards the eastern part of the survey, and at its shallowest towards the western end. Several high resistivity pockets, or clusters (darker blue shades), are present along the survey. Some lower resistivity cores (red shades) are present (~40 m). This could indicate the presence of underground water flow within the permafrost, due to the discontinuous distribution of permafrost in the Takhini Valley.

The ERT 2 (Figure 4) suggests that the permafrost is more discontinuous as we get closer to the highway. Similar high resistivity clusters (blue shades) to those observed in ERT 1 survey likely represent ice-rich permafrost. Permafrost distribution seems more localized and does not tend to go

deeper than 20 m at its deepest point (77.5 m along the profile). Low resistivity areas (red/orange shades) may indicate ice-poor and/or unfrozen material, or the presence of liquid ground water circulating within permafrost.

Figure 2. Ice-rich permafrost showing thick layered (top) and suspended (base) cryostructures in a core from BH1 at a depth of 657 cm.

The ERT 3 survey data (Figure 4) suggests a localized high resistivity area (dark blue) up to 7 m deep. Some deep, low resistivity pockets (red shades), visible at various locations, could be associated with groundwater flow.

The ERT 4 survey (Figure 4) also shows high resistivity area down to 7 m deep, along most of the profile. One large, highly resistive cluster, towards the east end of the profile shows potential ice-rich material from 17 to 35 m depth. Some shallow low resistivity pockets, between 5 and 10 m depth along the profile, could be associated with water flowing within permafrost.

Overall, the very high-resistivity areas (dark blue) are attributable to ice-rich fine-grained sediment (clayey-silts); they increase closer to the headwall and become more sporadic closer to the highway. The low resistivity values could be attributable to ice-poor and/or unfrozen material, with the lowest values possibly indicating the presence of liquid ground water. Permafrost may also be present in areas with resistivity as low as 100 ohm.m, due to higher liquid water content in fine-grained material near 0 °C.

4.3 UAV surveys

Monthly surveys include high resolution UAV surveys as well as benchmark surveys using differential GPS. With these tools, combined with satellite imagery and LiDAR data from as early as September 2016, it has been possible to monitor the retreat of the RTS headwall since 2016. The retreat of the RTS headwalls from September 2016 to September 2023 is presented in Figure 5. The shortest distance from the headwalls to the road (DTR) and the surface areas (A) of the RTS were measured from each survey. The annual area growth percentage (AAG%) between two UAV survey years was calculated as well as the elongation (length/width) of the two RTSs. The results are presented in Table 1.

The RTS 1 headwall approached the highway at an average rate of 13 m/yr from 2016 to 2018, then experienced an ablation of 16 m in summer 2019, 13 m in summer 2020, 17 m in summer 2021, 3 m in summer 2022, and 1 m in summer 2023. The retreat of the headwall decreases in proximity of the right-of-way at the location of its central axis, while the headwall continues to widen along the east side, by 14 m in summer 2022 and 13 m in summer 2023. The headwall has shown minimal progression along at the west side during summer 2023. It must be noted that the central axis area has been disturbed by heavy machinery compacting the ground during an unsuccessful attempt by contractors to drill the waste area during winter 2022. This disturbance may have impacted the advance of the headwall at this location.

The RTS 2 started to be noticeable in October 2021. Its headwall was then 95 m from the road. It then advanced by 15 m in summer 2022 and 11 m in summer 2023, having a similar average of 13 m/yr to RTS 1 from 2016 to 2018.

The evolution of the elongation at RTS 1 show the slump is progressively rounding off, becoming as wide as it is long. Interestingly, after their first two years, RTS 1 and RTS 2, share the same elongation values in 2016 and 2023, respectively.

Since 2016, the RTS 1 AAG% decreases from a year to another, except for 2021. The AAG% of RTS 2 has increased over the first two years, with the surface area increasing more than twofold.

The thermal imagery survey performed in November 2021 was used to identify and locate more that a dozen groundwater springs flowing from the headwall at RTS 1 (red spots along headwall in Figure 6). No groundwater springs were visible along RTS 2 headwalls.

To investigate how air temperature and precipitation may impact the growth of RTS 1, the surface area growth percentages between two UAV surveys were compared to the thaw degree day value and the cumulative precipitation for the same duration.

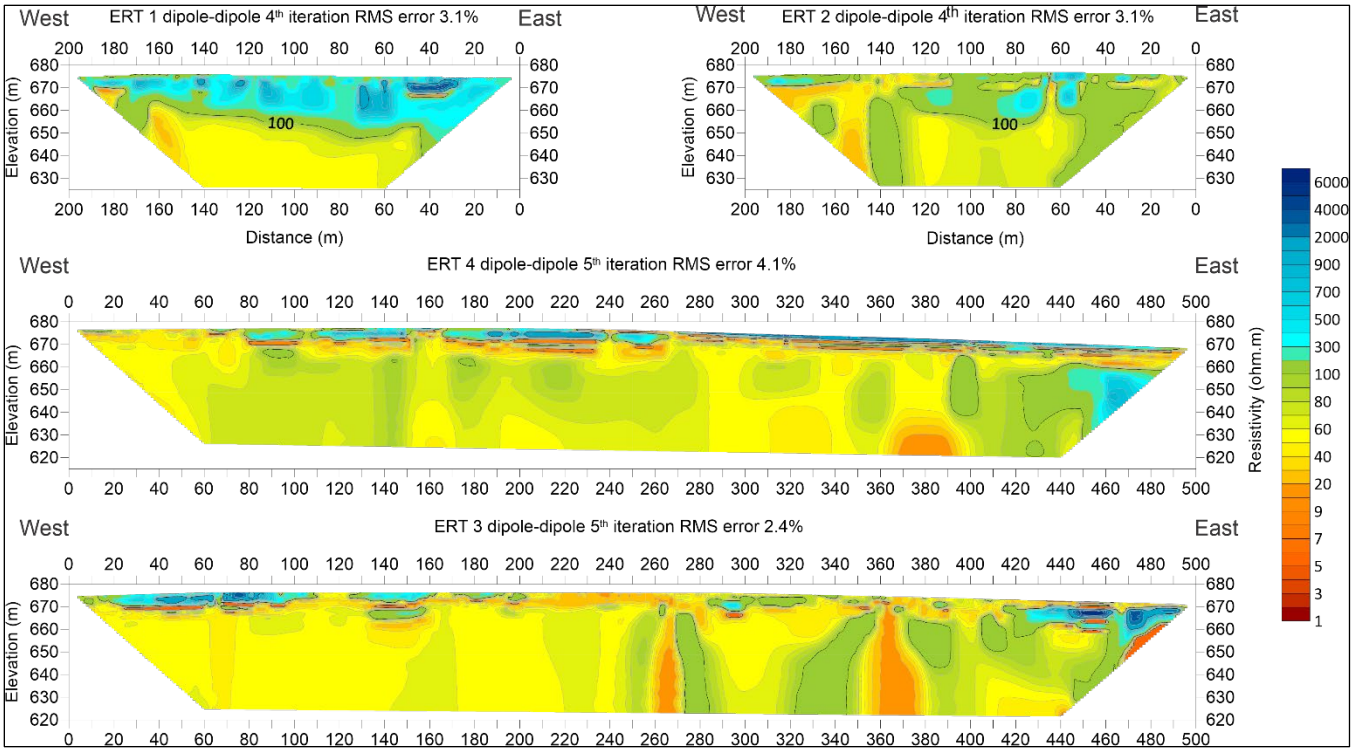

Figure 3. Four ERT profiles surveyed at the Takhini RTS site.

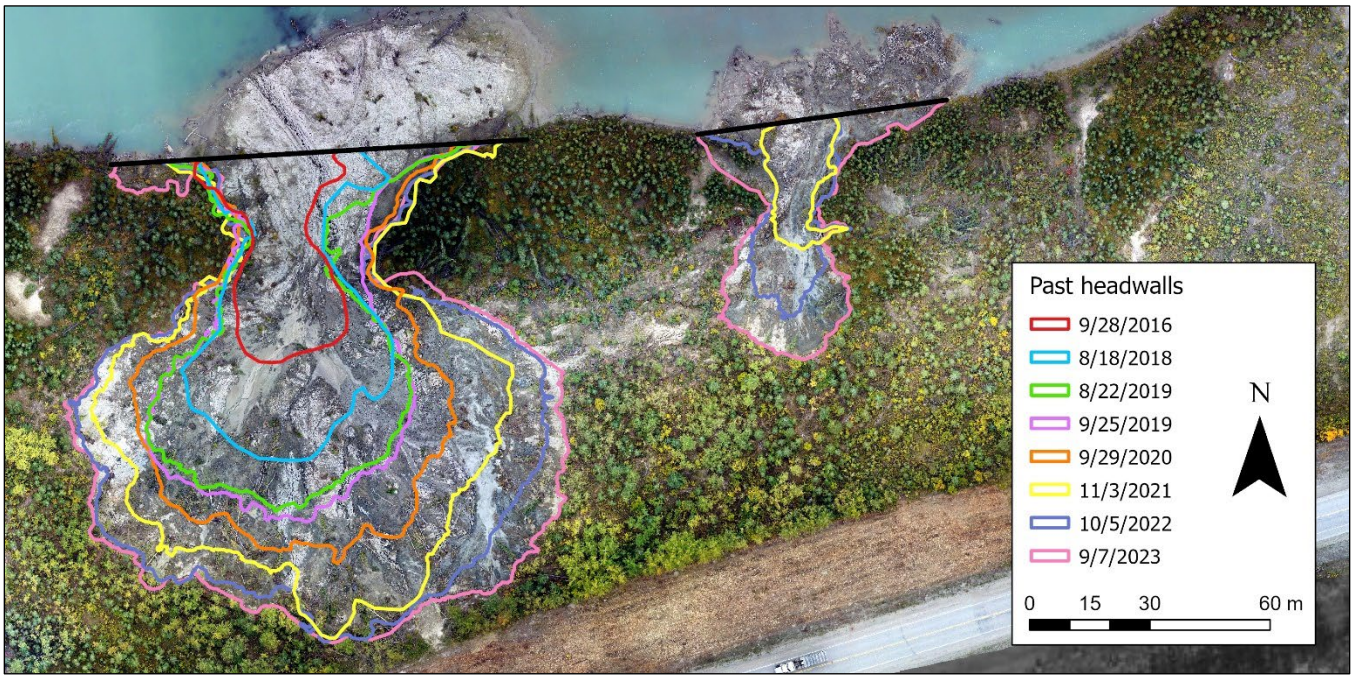

Figure 4. Retreat of the RTS headwalls from September 2016 to September 2023

Air temperature seems to have an influence on the area growth in 2020 (R^2 = 0.9685, p = 0.0118), 2021 (R^2 = 0.6665, p = 0.0034) and 2023 (R^2 = 0.6403, p = 0.0014), but not in 2022 (R^2 = 0.1269, p = 0.0404). Precipitation does not seem to have had an influence on the area growth except for 2022 (R^2 = 0.8084, p = 0.0038). The 2022 precipitation correlation likely is an anomaly as the slope of the regression line implies that higher precipitation slows down the RTS growth for this specific year, which contradicts basic permafrost thermodynamics.

Table 1. Morphometrics from UAV surveys

Main Slump

Date	A (m^2)	AAG%	Elongation	DTR (m)
2016-09-28	1201		1.82	106
2018-08-18	2608		1.43	80
2019-05-19	3760	60	1.35	80
2019-09-25	4184		1.37	66
2020-05-20	4228	32	1.37	66
2020-09-29	5519		1.28	53
2021-05-06	5680	39	1.30	52
2021-11-03	7661		1.14	36
2022-05-20	7783	19	1.14	36
2022-10-05	9091		1.05	33
2023-05-18	9135	10	1.04	33
2023-09-07	10030		1.00	32

Second Slump

Date	A (m^2)	AAG%	Elongation	DTR (m)
2021-10-07	394		3.20	95
2021-11-03	414		3.00	95
2022-05-20	424	88	3.00	95
2022-10-05	777		2.53	80
2023-05-18	932	105	2.33	80
2023-09-07	1589		1.82	69

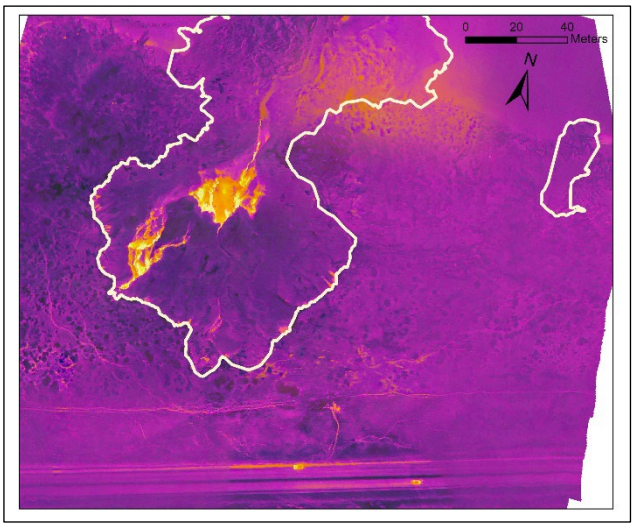

Figure 5. Aerial thermal imagery showing groundwater spring seeping from RTS 1 headwall.

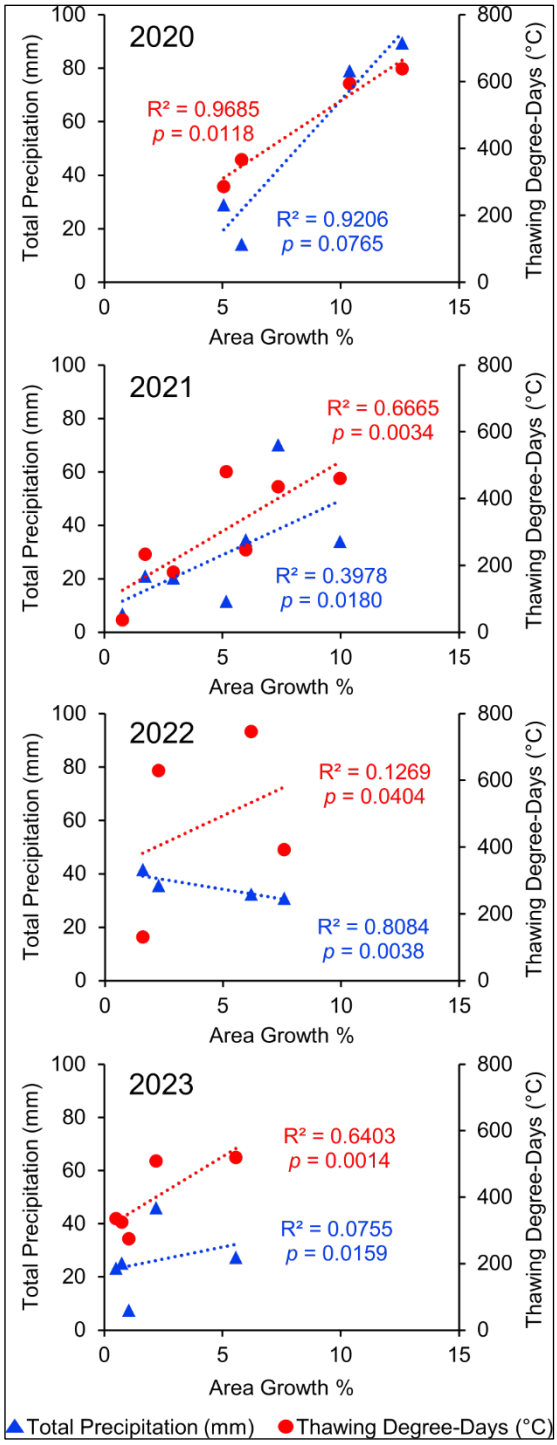

Figure 6. Surface area growth percentages vs. thaw degree-day value and the cumulative precipitation for the period between two summer UAV surveys.

5 DISCUSSION

5.1 Permafrost nature and origin

The geotechnical boreholes and ERT data show that permafrost at the RTS site formed in clayey silts which are frost susceptible. Permafrost temperature is warm, close to 0 °C. This area is consequently vulnerable to thaw. The ERT surveys showed thick, ice-rich permafrost in the forested area and more sporadic clusters of ice-rich permafrost closer to the road. This could be a result of decades of permafrost degradation under the right-of-way of the Alaska Highway since its construction in 1942.

The cryostratigraphical observations with the occurrence of suspended and thick layered cryostructure are consistent with syngenetic permafrost. The formation of this type of segregated ground ice generally occurs in fine-grained material, with abundant water supply, a slow thermal gradient, and usually an organic cover. Indeed, the abundant presence of deciduous trees and the absence of thick organic cover is atypical compared to other similar ice-rich epigenetic permafrost in discontinuous areas. Consequently, the permafrost on site may have originally formed under different environmental conditions, associated to a colder and more humid climate and different vegetation. The present-day warm permafrost temperature suggests that the relic permafrost is now in unstable equilibrium with the present climate.

This type of permafrost is generally associated with permafrost plateaus and frost heave mound environments (Calmels et al. 2008). Such conditions may have existed in the Takhini Valley when the permafrost developed. Although the vegetation and the topography have changed, the original cryostratigraphical imprint, shown by the ERT survey in the shape of ice-rich ground clusters, has remained unchanged. The shading provided by the newer deciduous forest may have contributed to the preservation of this relic permafrost.

5.2 RTS evolution

The progression of headwall and growth of the RTS 1 seem to decrease from one year to another, except for 2021. The rapid erosion of the headwall in 2021 could be related to extraordinary weather events that occurred during the summers of 2020 and 2021. Whitehorse had its ninth-rainiest summer in the weather records in 2020, with 157.8 mm over the course of the summer (Oakes 2020). Because of inertia in the system, the impact of this significant input of heat may have only been felt during summer 2021. In summer 2021 the “heat dome”, a mass of hot air sitting over the Pacific Northwest, occurred in June and July which resulted in warmer than average temperatures in the Yukon (Desmarais 2021), and could also have contributed to rapid erosion.

The decrease advance of the headwall at location of its central axis can be explained either by the lack of ground ice at this location to feed the process, or the compaction at that location by heavy machinery. The fact that the headwall section located only 10 m east of this disturbed area progressed by 14 m in summer 2022 and 13 m in summer 2023 suggests that the disturbance had an impact. The minimal progression at the west side during summer 2023 likely is attributable to the lack of ground ice in this undisturbed area. Ground ice content is variable at the study site, as shown by the ERT, and the slumping process is stalling at location where permafrost is ice-poor.

Analyses indicate that air temperature influences RTS thaw processes, while such influence was not proven for precipitation. These sites are impacted by rapidly occurring events such as heavy rain, heat waves, and unusually warm summer temperatures. Slump processes are preceded by pre-conditioning processes such as localized heat flow, ground water flow, thaw settlements, and deformation. A study by Ward et al. (2019) about RTSs in the Canadian High Arctic suggest that a decoupling of RTS dynamics from climate appears to occur over time for individual RTS as terrain factors take on a greater role controlling headwall retreat. This conclusion could also apply to the Ibex Valley RTSs. The complex interactions between those influencing factors require further analyses to better comprehend the development of RTSs. The on-going monitoring of RTS 2, that has been studied since its inception, might provide new insights in the future.

5.3 The role of groundwater

Geophysical and borehole data have emphasized the ice-rich nature of the ground at this site, as well as the presence of flowing ground water. While the thaw processes may have been initiated by bank erosion on the Takhini River, they have been exacerbated by the high ground ice content and the thermal effect of ground water flow. The UAV survey of the site using a thermal camera conducted in November 2021 has shown numerous ground water springs flowing in the slump and even generating icing events during winter. While it has not been quantified yet, ground water likely is contributing to permafrost degradation at this site.

6 CONCLUSIONS

The easy accessibility of the Takhini River site has enabled detailed and comprehensive investigation of retrogressive thaw slump processes in discontinuous permafrost. The multi-technical investigative approach highlighted permafrost features such as ground ice distribution, ground thermal regime, and groundwater flow. Frequent UAV surveys provided accurate morphometric measurements and a time-lapse evolution of two RTSs. They also provided the opportunity to investigate the relationship between the progression of the RTSs and climate at yearly and seasonal scales. Further research will allow for refinement of these studies and examination of the origin and impact of the groundwater flow on the RTSs.

Responding to the risk, the Yukon Department of Highways and Public Works has decided to relocate the road. The construction of a new section, about 80 m south of the current embankment, began in August 2023 and is scheduled to be completed during summer 2024. Because the current road and right-of-way has been degrading permafrost beneath it for decades, it is expected that, once abandoned, the old embankment will act as a barrier to the

headwall progression. Monitoring and investigations of the site will continue in the upcoming years.

7 ACKNOWLEDGEMENTS

The authors would like to acknowledge that the field sites are situated on the traditional territories of Kwanlin Dün First Nation and Ta'an Kwäch'än Council. We value the support of the Transportation Engineering Branch of Yukon Department of Highways and Public Works. We would also like to thank the numerous field and research assistants who made this work possible. Brian Horton and Stephie Saal from Climate Change Research at the YukonU Research Centre for the thermal imagery, Guy Doré and Chris Burn for their input. Thank you to the BMO Climate Institute for supporting and sharing our research.

Funding for this project was provided by Transport Canada's Northern Transportation Adaptation Initiative (NTAI) and National Trade Corridors Fund (NTCF). Additional funding was provided by ArcticNet, as well as by Crown-Indigenous Relations and Northern Affairs Canada's (CIRNAC) Climate Change Preparedness in the North (CCPN) program through the Government of Yukon's Department of Environment Climate Change Secretariat. In-kind contributions were also made by the Yukon Geological Survey, YukonU Research Centre, and Yukon government.

8 REFERENCES

Armstrong, L., Lacelle, D., Fraser, R., Kokelj, S., and Knudby, A. 2018. 'Thaw Slump Activity Measured Using Stationary Cameras in Time-Lapse and Structure From-Motion Photogrammetry', *Arctic Science* 4(4), pp. 827–845. doi:10.1139/as-2018-0016.

Ballantyne, C.K. 2018. *Periglacial Geomorphology*. New Jersey, United States: John, Wiley & Sons Ltd., ISBN 978-1-4051-0006-9.

Bernhard, P., Zwieback, S., and Hajnsek, I. 2021. 'Area and Volume Quantification of Arctic Thaw Slumps Using Time-Series of Digital Elevation Models', in *2021 IEEE International Geoscience and Remote Sensing Symposium IGARSS*. Brussels, Belgium: July 11–16, 2021, pp. 800–803. doi:10.1109/IGARSS47720.2021.9554503.

Burn, C.R. 1987. 'Thermokarst Ponds and Ground Temperatures In Takhini Valley', in S.R. Morison and C.A.S. Smith (eds.), *XII INQUA Congress, field excursions A20 and A20b Research in Yukon*. Ottawa, Ontario, Canada: July 31–August 9, 1987, p. 34.

Burn, C.R. 1998. 'The Response (1958–1997) of Permafrost and Near-Surface Ground Temperatures to Forest Fire, Takhini River Valley, Southern Yukon Territory', *Canadian Journal of Earth Sciences* 35, pp. 184–199. doi.org/10.1139/e97-10.

Calmels, F. Allard, M., and Delisle, G. 2008. 'Development and Decay of a Lithalsa in Northern Québec: A Geomorphological History', *Geomorphology* 97, pp. 287–299. doi.org/10.1016/j.geomorph.2007.08.013

Desmarais, A. 2021. 'N.W.T., Yukon break summer temperature records as heat dome lingers', *CBC News*, June 30, 2021. Available at: https://www.cbc.ca/news/canada/north/temperature-highs-nwt-yukon-1.6085005.

French, H.M. 2017. *The periglacial Environment*. 4th edition. Chichester, United Kingdom and Hoboken, New Jersey, United States: John Wiley & Sons. ISBN: 978-1-119-13278-3.

Hegginbottom, J.A., Dubreuil, M.A. and Harker, P.T. 1995. 'Canada, permafrost', in *National Atlas of Canada, 5th edition*. Natural Resources Canada, MCR 4177.

Kokelj, S.V. and Jorgenson, M.T. 2013. 'Advances in Thermokarst Research', *Permafrost and Periglacial Processes* 24(2), pp. 108–119. doi:10.1002/ppp.1779; ISSN 1099-1530. S2CID 140683397.

Kokelj, S.V., Kokoszka, J., van der Sluijs, J., Rudy, A.C.A., Tunnicliffe, J., Shakil, S., Tank, S., and Zolkos, S. 2021. 'Permafrost Thaw Couples Slopes with Downstream Systems and Effects Propagate Through Arctic Drainage Networks', *The Cryosphere* 15, pp. 3059–3081. Available at: https://doi.org/10.5194/tc-15-3059-2021.

Lewkowicz, A.G. and Way, R.G. 2019. 'Extremes of Summer Climate Trigger Thousands of Thermokarst Landslides In A High Arctic Environment', *Nature Communications* 10, 1329. Available at: https://doi.org/10.1038/s41467-019-09314-7

Oakes, B. 2020. 'The stats are in: It was a rainy summer in the North', *CBC News*, September 8, 2020. Available at: https://www.cbc.ca/news/canada/north/rainy-summer-nwt-1.5713631.

Ramage, J.L., Irrgang, A.M., Herzschuh, U., Morgenstern, A., Couture, N., and Lantuit, H. 2017. 'Terrain Controls On The Occurrence of Coastal Retrogressive Thaw Slumps Along The Yukon Coast, Canada', *Journal of Geophysical Research: Earth Surface* 122(9), pp. 1619–1634. doi:10.1002/2017JF004231.

Turner, K.W., Pearce, M.D., and Hughes, D.D. 2021. 'Detailed Characterization and Monitoring of a Retrogressive Thaw Slump from Remotely Piloted Aircraft Systems and Identifying Associated Influence on Carbon and Nitrogen Export', *Remote Sensing* 13(2), 171. doi:10.3390/rs13020171.

van der Sluijs, J., Kokelj, S.V., Fraser, R.H., Tunnicliffe, J., and Lacelle, D. 2018. 'Permafrost Terrain Dynamics and Infrastructure Impacts Revealed by UAV Photogrammetry and Thermal Imaging', *Remote Sensing*, 10(11), 1734. doi.org/10.3390/rs10111734.

Ward Jones, M.K., Pollard, W.H., and Jones, B.M. 2019. 'Rapid Initialization of Retrogressive Thaw Slumps In The Canadian High Arctic And Their Response To Climate And Terrain Factors', *Environmental Research Letters* 14(5), 055006. doi:10.1088/1748-9326/ab12fd

Yukon Ecoregions Working Group 2004. *Ecoregions of the Yukon Territory: Biophysical Properties of Yukon Landscapes*, C.A.S. Smith, J.C. Meikle and C.F. Roots (eds.). Summerland, British Columbia, Canada: Agriculture and Agri-Food Canada, PARC Technical Bulletin No. 04-01.

Machine learning for predicting permafrost and active layer temperatures at Toolik Lake, Alaska

Robert Chance[1], Aymane Ahajjam[2], Jaakko Putkonen[1] & Timothy Pasch[3]

[1]*Harold Hamm School of Geology and Geologic Engineering, University of North Dakota, Grand Forks, North Dakota, United States*

[2]*School of Electrical Engineering and Computer Science, University of North Dakota, Grand Forks, North Dakota, United States*

[3]*Department of Communication, University of North Dakota, Grand Forks, North Dakota, United States*

ABSTRACT

Climate change in Arctic regions threatens to significantly degrade permafrost leading to terrain instability, infrastructure damage, altered ecosystems, and the release of greenhouse gasses. Therefore, monitoring permafrost and active layer temperatures is key to understanding where possible permafrost degradation may occur. In areas with high data fidelity, machine learning (ML) algorithms can be utilized for the prediction of subsurface soil temperatures. Here, we present a site-specific model that uses ML in permafrost regions to predict soil temperatures. First, preliminary statistical analyses of the relationships between soil temperatures at several depths and corresponding lag periods of thermal wave propagation are conducted to select the most useful inputs. These inputs are then fed into the prediction model to estimate the corresponding active layer and permafrost temperatures. Various machine learning models, including K-Nearest Neighbors, Random Forest, Gradient Boosting, and Neural Networks, are investigated along with baseline models such as the persistence model. All models were developed using open datasets from Toolik Lake, Alaska. Results highlight the effectiveness of Gradient Boosting (RMSE = 0.13 °C for permafrost) and Random Forest (RMSE = 1.10 °C for active layer) models in predicting soil temperatures. However, these results required data from in situ ground temperature observations.

1 INTRODUCTION

Changing environmental conditions, including increasing air temperatures resulting from climate change, are expected to significantly impact permafrost (defined as any in situ geologic materials existing at a temperature of 0 °C or less for two or more years) and active layer (defined as the permafrost soil thermal layer that seasonally breaches 0 °C) temperatures in the 21st century (Melvin et al. 2016; Lawrence et al. 2005; Nitze et al. 2018).The thawing of permafrost (here defined as the annually freezing and thawing surface layer located above the permafrost table) and active layer temperatures will lead to the melting of ground ice. As such, changes in active layer thickness are the best proxy for identifying areas at risk for permafrost degradation-related hazards such as retrogressive thermokarst slumps, thermokarst lakes, and building foundation settlement (Hong et al. 2014; Nelson et al. 2001). The first step towards predicting where these degradational landforms and hazards will occur is the development of ground temperature models accounting for the environmental variability in a changing Arctic landscape.

In all soils, cyclic temperature fluctuations occur as a result of annual variations in incoming solar radiation, among other factors. Together, these factors create a complex interwoven natural system, known as the surface energy budget (Putkonen 1998). Difficulties in measuring the surface energy budget have led researchers to use alternative means to determine ground temperatures since, in most cases, individual energy and mass fluxes at the ground surface at any given location are poorly understood (Douglas et al. 2021; Euskirchen et al. 2016; Ling et al. 2003; Grünberg et al. 2020; Pomeroy et al. 2006; Anisimov et al. 2002; Walker et al. 2003; Loranty and Goetz 2012). Therefore, physics-based models have been developed to estimate and model subsurface temperatures that subvert around complications that arise while modeling ground temperatures using the surface energy budget.

The physics-based one-dimensional heat conduction equation is ubiquitous in periglacial research (Nakano and Brown 1972; Kane et al. 1991; Ling and Zhang 2004) and resolves general ground temperatures with depth well. Despite the success of the heat conduction equation, the reductionist approach given by the model prevents analysis of complex scenarios containing temperature changes, such as those that involve the melting of ground ice (Putkonen 1998). Additionally, physics-based numerical models may fail in situations where the model intends to calculate a value in which the numerical inputs are not directly or precisely known (Chen et al. 2022a). In research where physics-based numerical models fail because of improper inputs, Machine Learning (ML) may provide an alternative as these models have the advantage in that they are not based on the physical processes but rather rely on statistical relationships between various features of the input and output data.

In the realm of non-permafrost soil research, ML has been successfully used to predict soil temperatures at one meter below the ground surface (Bilgili 2010; Zounemat-Kermani 2013; Feng et al. 2019; Alizamir et al. 2020). However, using ML to determine soil temperatures has continued to be challenging due to the physical complexity and non-linearity of the soil-water system that is experiencing freeze-thaw cycles. Hybrid models in which decomposition techniques are used in conjunction with deep learning have

https://doi.org/10.52381/ICOP2024.135.1

shown promise in the prediction of ground temperatures within the active layer on the Tibetan Plateau (Chen et al. 2022b; Liu et al. 2022). However, to date, there is a dearth of published research on ML-modeled prediction of temperatures of the active layer or permafrost and Alaska specifically or the Arctic in general.

For the reasons listed above, there is significant motivation to create an ML-based prediction of soil temperatures leveraging observed temperature data in permafrost regions. Here we present initial steps towards this goal by determining soil temperature with ML algorithms at a site-specific resolution. To achieve this, we investigate in this paper ML-based techniques utilizing more than 17 years of thermal data to predict subsurface soil temperatures at Toolik Lake, Alaska. Accordingly, a preliminary analysis of temperatures at different depths is first conducted to better understand their relationship and identify the best correlated ones. Following this, different supervised conventional ML models are trained to predict the active layer and permafrost temperatures using the selected inputs. Furthermore, model performance is assessed using various metrics and benchmarked with baseline models to provide a clear understanding of their respective capabilities.

2 Study Sites

In this study, we develop site-specific soil temperature prediction models for Toolik Lake, Alaska utilizing data collected by the Natural Resources Conservation Service (NRCS; Staff 2023). This selection is motivated by the availability of long temporal coverage and high-quality data, particularly, time series of air and ground temperatures spanning 18 years at Toolik Lake.

The Toolik Lake borehole is in Northern Alaska, 115 miles south of Prudhoe Bay and north of the Brooks Range at 68.62°N, -149.61°W and at 759 m elevation. This borehole is part of the University of Alaska/National Science Foundation's Toolik Lake soil climate research station. The mean annual air temperature during the data collection period was -7.6 °C. This region experiences annual periods of zero solar insolation due to the high latitude. The monitoring station at Toolik Lake recorded air temperatures at 1.5 m above the ground surface (T_{air}) with soil temperature probes at 0.6 cm (T_0), 8.7 cm (T_8), 16.0 cm (T_{16}), 23.6 cm (T_{23}), 31.2 cm (T_{31}), 38.7 cm (T_{38}), 46.3 cm (T_{46}), 61.6 cm (T_{61}), 76.8 cm (T_{76}), and 97.8 cm (T_{97}) below the ground surface. The vegetation surrounding the borehole is low shrubs.

In March, the active layer temperatures at 76 cm (T_{76}) beneath the ground surface reach their minimum, with a mean temperature of -9.5 °C, while the maximum temperatures occur in August, with a mean temperature of -0.1 °C. Although the mean maximum ground temperature at 76 cm remains < 0 °C during the data collection period, there are instances in July, August, and September where the temperature exceeds the freezing threshold thus signifying that this depth is a transient permafrost depth. There is a noticeable time lag between air temperatures and T_{42}, with the highest air temperatures observed in July, averaging 8.6 °C. This time lag is attributed to the thermal properties of the soil. Similarly, permafrost temperatures at 97 cm (T_{97}) experience their minimum in March, with a mean temperature of -8.9 °C, and their maximum in September, with a mean temperature of -0.6 °C (Figure 1).

We note that the base of the active layer was chosen by finding the nearest ground temperature level measured at a shallower depth than the permafrost table and that contained complete and continuous data. At the considered location (i.e., Toolik lake), this was at 76 cm below the ground surface.

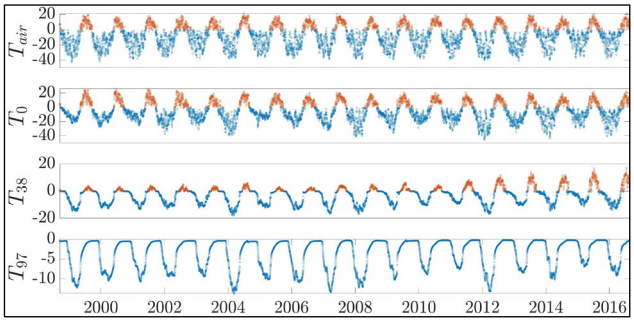

Figure 1. Time series of daily average temperatures at different elevations/depths plotted over 18 years for Toolik lake. Blue dots indicate temperatures < 0 °C and red ones indicate temperatures > 0 °C.

3 Methods

3.1 Soil Temperature Prediction

Let $\{T_d(t)\}_{t=1}^{N}$ denote the daily average soil temperature sequence (of N samples) measured at depth d over N days. Predicting the active layer (or permafrost) temperature T_d^t, at a depth d, and a time index t, can be written as:

$$\hat{T}_d^t = \mathrm{f}\left(T_d^{t-N|t-1}, \epsilon\right) \quad [1]$$

where $\hat{T}_d^t$ is the predicted active layer (or permafrost) temperature at depth d, $T_d^{t-N|t-1} = \{T_d(t-N), \ldots, T_d(t-1)\}$ is the sequence of past daily values of the active layer (or permafrost) temperatures at the same depth, f is the prediction model, N is the number of previous days considered as inputs (i.e., lag), and ϵ is the error.

However, we intend in this work to estimate the temperature of the active layer and permafrost without relying on their past values but rather on other predictors, such as ground surface or air temperature values that are more accessible. Hence, Eq. 1 becomes:

$$\hat{T}_d^t = f\left(T_{d_1}^{t-L_1|t}, T_{d_2}^{t-L_2|t}, \ldots, \epsilon\right), \quad d < d_1 < d_2 \quad [2]$$

where $T_{d_1}^{t-L_1|t} = \{T_{d_1}(t-L_1), \ldots, T_{d_1}(t)\}$ is the sequence of daily temperatures at depth d_1 over L_1 days, $T_{d_2}^{t-L_2|t} = \{T_{d_2}(t-L_2), \ldots, T_{d_2}(t)\}$ is the sequence of daily temperatures at depth d_2 over L_2 days.

Accordingly, three main types of features are employed in this work:

- Air temperature T_{air}^{t}: to provide the average daily air temperature at time index t and acquired at a height of 1.5 m.
- Soil temperatures T_{d}^{t}: to provide average daily soil temperatures at depth d and time index t.
- Time-related features: to provide temporal information reflecting the day of the month D_t ranging from 1 to 31 and month of year M_t ranging from 0 to 12, and year number Y_t. Cyclical changes in the surface energy balance impact the surface energy budget unequally throughout the year. Therefore, using the Julian calendar date for the day on which soil temperatures are to be predicted can bring useful information to the prediction model.

The raw temperature data from Toolik Lake were compiled into a single continuous time series for each location. Once the data were compiled, any temperature data anomalously higher or lower than temperatures within one week before or after the current day were removed from the dataset. Missing data values occurred for no more than one week at their greatest temporal extent, and these values were not estimated from adjacent days to prevent any potential data bias. The time series data are then analyzed to find the first measured depth of the permafrost at each location as well as the approximate active layer thickness. The latter was found by finding the highest mean ground temperature at each depth over the data collection periods. Depths with maximum yearly ground temperatures < 0 °C for a minimum of two years were considered to be permafrost, and active layer thickness was not observed to have increased during the study period, given the vertical resolution of the dataset. Next, time-related features (i.e., day of month, month of year, and year) are read from the corresponding time stamp.

The resulting data are chronologically split into training and testing sets based on an 80/20 ratio and then standardized to have a zero mean and a unit standard deviation. Standardizing the data helps simplify the calculations and improves the model's convergence. Finally, a combination of the preprocessed temperatures (i.e., air temperature or soil temperature at a certain depth), and their corresponding time features, are used as inputs to develop prediction models of the active layer and permafrost temperatures. Different temperature lags are also investigated as inputs to provide direct historical information to the prediction models.

We note that the depth of the active layer was chosen by finding the nearest ground temperature level measured at a shallower depth than the permafrost table and that contained complete and continuous data. At the considered location (i.e., Toolik lake), this was at 76 cm below the ground surface.

3.2 Predictive Models

Two main benchmarks are conducted in this paper to identify the inputs (and corresponding time lags) and models that can produce accurate active layer and permafrost temperature predictions. To accomplish this, the following conventional ML models are considered: Linear regression (LR), K-nearest neighbors (KNN), Support vector regression (SVR), Decision Tree (DT), Random Forest (RF), Gradient Boosting (GB), and Neural Networks (NN). In addition, ARIMA and historical mean persistence models were considered as two baselines for comparison purposes. Accordingly, a conventional ML model is required to outperform both baselines to be considered useful. Numerical modeling of ground temperatures is not used as a benchmark since only ground temperatures are available for Toolik Lake, and more information, such as the thermal conductivity of the soils, is necessary for an educated guess similar to the historical mean and ARIMA models. The mathematical definitions for each of these models are described in detail in (James et al 2022).

3.3 Model Tuning

We conduct a hyperparameter tuning optimization for each of the considered ML models. This optimization aims to find the optimal values for the hyperparameters of each model, which can significantly impact their predictive capabilities and reduce their computational costs. We employ grid search optimization to accomplish this, systematically exploring a predefined set of hyperparameter combinations. A 10-fold cross-validation scheme is used to combat model overfitting and improve performance.

3.4 Performance Evaluation

The prediction performance of all considered models is assessed using four metrics: Root Mean Square Error (RMSE), symmetrical Mean Absolute Percentage Error (sMAPE), R^2, and mean Directional accuracy (DA). Each of these metrics captures and assesses a certain aspect of the prediction models. For instance, RMSE and R^2 are standard regression metrics used extensively in the literature to quantify the performance of a model. More specifically, RMSE quantifies the magnitude of residuals and overall accuracy of the model, while R^2 quantifies how well the model explains the data. Lower RMSE values indicate higher performance, while the opposite is true for R^2. A third metric is sMAPE, which is a variation of MAPE that can bypass its sensitivity to extreme or outlier values and provide a more balanced measure of accuracy. Finally, DA assesses the direction of predictions (upward or downward), rather than their corresponding value.

$$RMSE = \sqrt{\frac{1}{N}\sum_{i=1}^{N}(y_i - f_i)^2} \quad [3]$$

$$sMAPE = \frac{1}{N}\sum_{i=1}^{N}\frac{|y_i - f_i|}{|y_i| + |f_i|} \times 100$$

$$R^2 = 1 - \frac{\sum_{i=1}^{N}(y_i - f_i)^2}{\sum_{i=1}^{N} {y_i}^2} \quad [4]$$

$$DA = \frac{1}{N}\sum_{i=1}^{N} P_i \, , \quad [5]$$

$$P_i = \begin{cases} 1, if \ (y_{i+1} - y_i) \times (f_{i+1} - y_i) \geq 0 \\ 0, otherwise \end{cases} \quad [6]$$

where y_i is the actual value of a test set instance, i, f_i is the predicted value of the same test set instance, and N is the number of test set instances. Accordingly, the unit of RMSE is °C while sMAPE, R^2 and DA are %.

Now that the main steps to developing the prediction models are described, we proceed to present and discuss the results of our study.

4 RESULTS

4.1 Time Series Analysis

The average Spearman's correlation coefficient computed between different inputs and outputs is shown in Figure 2.

It is clear that current values of soil temperatures are highly correlated with past values of other temperatures from shallower depths (or other heights). More specifically, past values of T_0 seem to be the most correlated with T_{76}, closely followed by those of T_{air}. The correlation coefficients keep increasing for both features until plateauing at around the considered time range limit (i.e., past 60 days) and the value 0.8. The same pattern can be seen for T_{97} with the same features as well as with T_{76}. However, only the recent values of T_{76} are most correlated with the current values of T_{97}.

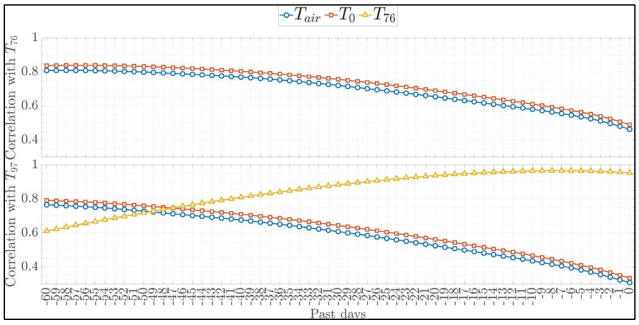

Figure 2. Average Spearman's correlation between different temperature features monitored in Toolik lake, AK. Past values ranging back to 60 days were considered for each feature to compute the average correlation coefficient.

We note that the temporal lags between input features and the soil temperatures chosen for model analysis in the subsequent subsections were guided using Spearman's correlation coefficient values.

4.2 Soil Temperature Prediction

The average prediction performances of all considered models at each soil depth are reported in Tables 1–3. Specifically, Table 1 provides the performance of the baseline models, while Tables 2 and 3 provide the performance of the ML models predicting T_{76} and T_{97}, respectively.

4.2.1 Prediction Using Baseline Models

As can be seen in Table 1, the baseline models had varying prediction performances. In particular, ARIMA consistently achieves the best performances in terms of RMSE, sMAPE, and R^2 across both depths. In addition, it requires only the current temperature of shallower depths (or elevation) to produce such performances. For instance, ARIMA only needed the contemporaneous T_0 to achieve its highest performance of $RMSE = 3.06$°C when predicting T_{76}. In comparison, the historical mean model in the same case achieved its highest performance of $RMSE = 4.01$°C using T_0^{456}, which reflects a lag of more than a year. Nonetheless, the historical mean model can provide predictions that better follow the direction of the targets in all cases.

4.2.2 Prediction Using ML Models

The best-performing baseline models consistently outperform all ML predictors at both soil depths when using only the time-related features (i.e., no information about temperature). This can also be seen when using only the temperature of a much shallower depth to predict the active layer temperature or permafrost temperatures. In both cases, the achieved performances make sense as the employed inputs provide little to no direct information about the target prediction to the prediction models, and hence, can be considered as additional baselines.

Table 1. Baseline models' overall performance (best values are bold). Only the best performing combination of inputs are reported.

Target	Model (inputs)	RMSE	sMAPE (%)	R^2 (%)	DA (%)
T_{76}	Persistence (T_0^{456})	4.01	56.03	25.80	**56.99**
	ARIMA (T_0)	**3.06**	**51.50**	**56.70**	38.37
T_{97}	Persistence (T_{76}^{4})	0.44	20.05	99.00	**39.80**
	ARIMA (T_{76})	**0.38**	**17.80**	**99.30**	31.34

Table 2. Average performance of ML models predicting the active layer temperatures at a depth of 76 cm in Toolik lake (best testing performances are bold).

Input	Model	Training		Testing	
		RMSE	R^2(%)	RMSE	R^2(%)
Time	LR	2.80	53.92	2.32	45.25
	KNN	0	100	1.42	79.36
	DT	1.02	93.89	1.71	70.35
	RF	0.97	94.49	1.62	73.10
	GB	0.64	97.55	1.52	76.39
	SVR	2.84	55.59	2.27	57.35
	NN	1.90	80.08	2.10	63.57
T_{air}	LR	3.56	25.87	2.96	10.85
	KNN	3.44	30.55	3.09	2.84
	DT	3.52	27.49	2.99	9.10
	RF	3.51	27.76	2.99	9.40
	GB	3.51	27.88	2.99	9.32
	SVR	3.67	25.90	3.04	23.22
	NN	3.64	27.10	3.08	21.24
T_0	LR	3.45	30.28	2.42	40.51
	KNN	3.33	34.79	2.30	46.18
	DT	3.40	32.21	2.11	54.67
	RF	3.40	32.36	2.13	54.01
	GB	3.40	32.19	2.19	51.13
	SVR	3.52	31.68	3.12	19.52
	NN	3.49	33.05	3.05	22.99
Time+T_0	LR	2.18	72.08	2.23	49.60
	KNN	0	100	1.43	79.18
	DT	1.06	93.42	1.61	73.49
	RF	0.98	94.38	1.55	75.54
	GB	0.64	97.56	1.47	78.11
	SVR	1.96	78.90	1.92	69.55
	NN	3.49	33.05	3.05	22.99
Time+T_0^{15}	LR	1.85	81.07	1.69	76.20
	KNN	0	100	2.14	62.14
	DT	0.46	98.81	1.94	68.84
	RF	0.25	99.66	**1.10**	**89.87**
	GB	0.47	98.78	1.30	85.88
	SVR	1.95	79.14	1.83	72.19
	NN	1.43	88.66	1.80	73.01

Table 3. Average performance of ML models predicting the permafrost layer temperatures at a depth of 97cm in Toolik lake (best testing performances are bold).

Input	Model	Training		Testing	
		RMSE	R^2(%)	RMSE	R^2(%)
Time	LR	2.54	56.36	2.15	52.71
	KNN	0	100	1.57	74.52
	DT	1.36	87.43	1.68	71.08
	RF	1.34	87.74	1.66	71.49
	GB	0.67	96.93	1.54	75.71
	SVR	2.04	71.95	1.89	63.48
	NN	1.61	82.43	1.64	72.37
T_0	LR	3.34	24.30	2.93	11.80
	KNN	3.23	29.11	3.02	6.13
	DT	3.30	26.18	2.96	10.12
	RF	3.30	26.22	2.94	11.53
	GB	3.30	26.38	2.93	11.87
	SVR	3.35	24.15	2.91	13.60
	NN	3.37	23.38	2.82	18.41
T_{76}	LR	0.42	98.79	0.38	98.49
	KNN	0.37	99.03	0.35	98.72
	DT	0.37	99.06	0.36	98.64
	RF	0.36	99.09	0.35	98.70
	GB	0.38	99.00	0.34	98.77
	SVR	0.42	98.78	0.38	98.51
	NN	0.39	98.97	0.34	98.84
Time+T_{76}	LR	0.40	98.88	0.37	98.55
	KNN	0	100	0.41	98.28
	DT	0.11	99.91	0.31	99.00
	RF	0.1	99.93	0.23	99.45
	GB	0.08	99.95	0.30	99.08
	SVR	0.24	99.62	0.32	98.98
	NN	0.24	99.61	0.30	99.07
Time+T_{76}^{30}	LR	0.16	99.81	0.18	99.67
	KNN	0	100	0.37	98.55
	DT	0.04	99.99	0.18	99.66
	RF	0.03	99.99	**0.13**	99.80
	GB	0.01	100	**0.13**	**99.82**
	SVR	0.18	99.78	0.21	99.57
	NN	0.13	99.88	0.20	99.61

However, once the current temperatures of a closer depth (to the target depth) are employed, ML models can perform better than the baselines for both soil depths. Indeed, average test RMSE improvements of 19.03% were achieved across the models when predicting the active layer temperature using the T_0 as input, compared with 5.12% when predicting the permafrost temperature using the active layer temperature as input.

Nonetheless, current temperatures of a closer depth are not enough to accurately predict the active layer or permafrost temperatures. Indeed, even higher improvements are achieved by all considered ML models when provided with a combination of current and past values of the temperatures. When comparing the models, the top prediction performances were consistently achieved using ensemble models in both locations. For instance, the best performance when predicting the active layer temperature is $RMSE = 1.10$°C and $R^2 = 89.87\%$ using the input combination $Time + T_0^{15}$ by RF. The best performance when predicting the permafrost temperature is $RMSE = 0.13$°C and $R^2 = 99.82\%$ using the input combination $Time + T_{76}^{30}$ with gradient boosting.

5 DISCUSSION

Our results show that there is a higher prediction accuracy when using data features residing closer in physical space to the predicted variable. Under thermally diffusive regimes, it would be expected that ground temperatures at adjacent and shallower depths experience temperature fluctuations before lower depths. This is further evidenced by the temporal lag in shallower ground temperatures that proved to be the best choice of data features when predicting deeper ground temperatures.

While all ML models performed well in predicting soil temperatures when given Julian date and ground temperature time series data in the summer, predictions of ground temperatures in the winter months have reduced accuracy (Figures 3 and 4). One possible cause for this is the presence of snow in the study area that was not captured in the data used in this study. In the winter heat transfer and loss occurs through the emission of radiation from the ground surface, through snow, and then into the air. Since the radiation must pass through snow before the air, and because thermal conductivity of snow differs from that of air, there is a different thermal regime in place during the fall and winter months. As such, future soil temperature prediction using ML models will likely need to account for snow depth along with air temperatures.

Beyond the reduced performance of prediction models during the winter months, a limitation of this study includes the need for ground surface temperature measurements to effectively predict deeper soil temperatures. While air temperatures are routinely measured at airports in the Arctic, very few locations monitor ground surface temperatures. Since the best models presented in this study must use either ground surface or active layer temperatures as inputs rather than air temperatures, the inability to predict ground temperatures solely with the use of air temperatures represents one limiting factor of this study. One method around this would be to predict

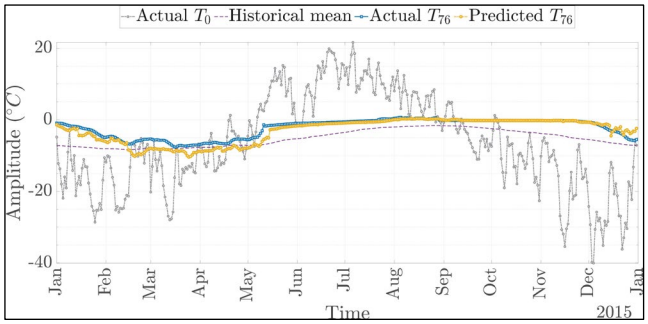

Figure 3. Prediction results of the active layer temperature T_{76} using Random Forest model and Time+T_0^{15}. The historical mean predictions and the actual temperatures over a whole year are plotted for reference.

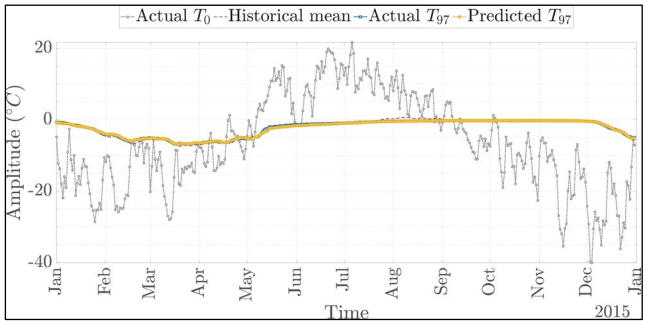

Figure 4. Prediction results of the permafrost temperature T_{97} using Gradient Boosting model and Time+T_{76}^{30}. The historical mean predictions and the actual temperatures over a whole year are plotted for reference.

increasingly deeper ground temperatures based on air temperatures. However, this was not completed for this study, and it is surmised that more than air temperatures and calendar dates would be needed to do this successfully (e.g., snow depth). Another potential method around this limitation may be to utilize an n-factors approach for our input data series (Lunardini, 1978). A second limiting factor to this study is the inability to apply ML models trained at Toolik lake to other locations since the ML models are location-dependent. Future research on the use of ML for location-independent subsurface soil temperature prediction should include additional soil property information such as soil moisture, soil grain size distribution, and surface organic layer depth, amongst other things.

6 CONCLUSIONS

Increasing air temperatures due to ongoing anthropogenic climate change are expected to cause the degradation of permafrost in the 21st century. This impending loss of permafrost will lead to the melting of ground ice in regions where it exists today and lead to many associated hazards. To predict where these outcomes may occur, physics-based numerical modeling has been the traditional approach; however, numerical modeling may be insufficient in areas of sparse data, such as the Arctic, where much of

the permafrost terrain exists. By making use of existing data series and machine learning methods, we explored the ability of machine learning to estimate the soil temperatures. The predicted temperatures were compared to actual observed soil temperatures to determine which ML methods were best and which variables were needed for optimal performance.

Our research shows that ensemble ML models can successfully predict active layer and permafrost temperatures, capturing the relationships between the air temperature and ground temperatures with the exception for the winter season. For the active layer, soil surface temperatures with a 15 days lag period provided prediction within 1.1 °C of the measured soil temperatures. For permafrost, active layer soil temperatures with lag periods with a 30 days lag period are needed to produce predictions within 0.13°C of the measured soil temperatures. Lastly, these results indicate that if in situ or remote soil temperature observations can be obtained for a given field site, then an AI-based approach may be used to generate active layer and permafrost temperature prediction for those field sites. However, it should be noted that historical soil and air temperatures are required for the training of ML models, and thus these ML models are unable to predict ground temperatures where no historical data is available. Future research should be undertaken to investigate the effectiveness of additional model inputs, such as snow depth and soil properties, for predicting Arctic soil temperatures. Advancing ML models such as those described in this study may further elucidate how Arctic landscapes will evolve with time in a changing Arctic environment.

7 ACKNOWLEDGEMENTS

DISTRIBUTION A: Approved for Public Release. Distribution is Unlimited. This material is based upon work supported by the Broad Agency Announcement Program and the Cold Regions Research and Engineering Laboratory (ERDC-CRREL) under Contract No. W913E522C0001. This work used advanced cyberinfrastructure resources provided by the University of North Dakota Computational Research Center.

8 REFERENCES

Alizamir, M., Kisi, O., Ahmed, A.N., Mert, C., Fai, C.M., Kim, N., and El-Shafie, A. 2020. 'Advanced machine learning model for better prediction accuracy of soil temperature at different depths', *PLOS ONE* 15(4). doi:10.1371/journal.pone.0231055.

Anisimov, O.A., Shiklomanov, N.I., and Nelson, F.E. 2002. 'Variability of seasonal thaw depth in permafrost regions: A stochastic modeling approach', *Ecological Modelling* 153(3), pp. 217–227. doi:10.1016/s0304-3800(02)00016-9.

Bilgili, M. 2010. 'Prediction of soil temperature using regression and artificial neural network models', *Meteorology and Atmospheric Physics* 110(1–2), pp. 59–70. doi:10.1007/s00703-010-0104-x.

Chen, T.-C., Penny, S.G., Whitaker, J.S., and Frolov, S.R. 2022a. 'Correcting systematic and state-dependent errors in the NOAA FV3-GFS using neural networks', *Journal of Advances in Modeling Earth Systems* [Preprint]. doi:10.1002/essoar.10511972.1.

Chen, L., Liu, X., Zeng, C., He, X., Chen, F., and Zhu, B. 2022b. 'Temperature prediction of seasonal frozen subgrades based on CEEMDAN-LSTM hybrid model', *Sensors* 22(15), p. 5742. doi:10.3390/s22155742.

Douglas, T.A., Hiemstra, C.A., Anderson, J.E., Barbato, R.A., Bjella, K.L., Deeb, E.J., Gelvin, A.B., Nelsen, P.E., Newman, S.D., Saari, S.P., et al. 2021. 'Recent degradation of interior Alaska permafrost mapped with ground surveys, geophysics, deep drilling, and Repeat Airborne Lidar', *The Cryosphere* 15(8), pp. 3555–3575. doi:10.5194/tc-15-3555-2021.

Euskirchen, E.S., Bennet, A., Bren, A.L, Genet, H., Lindgren, M.A., Kurkowski, T.A., McGuire, A.D., and Rupp, T.S. 2016. 'Consequences of changes in vegetation and snow cover for climate feedbacks in Alaska and Northwest Canada', *Environmental Research Letters* 11(10), p. 105003. doi:10.1088/1748-9326/11/10/105003.

Feng, Y., Cui, N., Hao, W., Gao, L., and Gong, D. 2019. 'Estimation of soil temperature from meteorological data using different machine learning models', *Geoderma* 338, pp. 67–77. doi:10.1016/j.geoderma.2018.11.044.

Grünberg, I., Wilcox, E.J., Zweiback, S., Marsh, P., and Boike, J. 2020. 'Linking tundra vegetation, snow, soil temperature, and Permafrost', *Biogeosciences* 17(16), pp. 4261–4279. doi:10.5194/bg-17-4261-2020.

Hong, E., Perkins, R., and Trainor, S. 2014. 'Thaw settlement hazard of permafrost related to climate warming in Alaska', *ARCTIC* 67(1), p. 93. doi:10.14430/arctic4368.

James, G., Witten, D., Hastie, T. and Tibshirani, R.2022. *An introduction to statistical learning: With applications in R*. Springer, Boston, Massachusetts, United States.

Kane, D.L., Hinzman, L.D., and Zarling, J.P. 1991. 'Thermal response of the active layer to climatic warming in a permafrost environment', *Cold Regions Science and Technology* 19(2), pp. 111–122. doi:10.1016/0165-232x(91)90002-x.

Lawrence, D.M. and Slater, A.G. 2005. 'A projection of severe near-surface permafrost degradation during the 21st Century', *Geophysical Research Letters* 32(24). doi:10.1029/2005gl025080.

Ling, F. and Zhang, T. 2003. 'Impact of the timing and duration of seasonal snow cover on the active layer and permafrost in the Alaskan Arctic', *Permafrost and Periglacial Processes* 14(2), pp. 141–150. doi:10.1002/ppp.445.

Ling, F. and Zhang, T. 2004. 'A numerical model for surface energy balance and thermal regime of the active layer and permafrost containing Unfrozen Water', *Cold Regions Science and Technology* 38(1), pp. 1–15. doi:10.1016/s0165-232x(03)00057-0.

Liu, Q., Niu, J., Lu, P., Dong, F., Zhou, F., Meng, X., Xu, W., Li, S., and Hu, B.X. 2022. 'Interannual and seasonal variations of permafrost thaw depth on the Qinghai-Tibetan Plateau: A comparative study using long short-term memory, convolutional neural networks, and Random Forest', *Science of The Total Environment* 838, p. 155886. doi:10.1016/j.scitotenv.2022.155886.

Loranty, M.M. and Goetz, S.J. 2012. 'Shrub expansion and climate feedbacks in Arctic Tundra', *Environmental Research Letters* 7(1), p. 011005. doi:10.1088/1748-9326/7/1/011005.

Lunardini, V.J. 1978. 'Theory of n-factors and correlations of data' in *Proceedings of Third International Conference on Permafrost*. National Research Council of Canada, Vol.1, pp. 40–46.

Melvin, A.M., Larsen, P., Boehlert, B., Neumann, J.E., Chinowsky, P., Espinet, X., Martinich, J., Baumann, M.S., Rennels, L., Bothner, A., Nicolsky, D.J., and Marchenko, S.S. 2016. 'Climate change damages to Alaska Public Infrastructure and the economics of proactive adaptation', *Proceedings of the National Academy of Sciences* 114(2). doi:10.1073/pnas.1611056113.

Nakano, Y. and Brown, J. 1972. 'Mathematical modeling and validation of the thermal regimes in tundra soils, Barrow, Alaska', *Arctic and Alpine Research* 4(1), p. 19. doi:10.2307/1550211.

Nelson, F.E., Anisimov, O.A., and Shiklomanov, N.I. 2001. 'Subsidence risk from thawing permafrost', *Nature* 410(6831), pp. 889–890. doi:10.1038/35073746.

Nitze, I., Grosse, G., Jones, B.M., Romanovsky, V.E., and Boike, J. 2018. 'Remote sensing quantifies widespread abundance of permafrost region disturbances across the Arctic and Subarctic', *Nature Communications* 9(1). doi:10.1038/s41467-018-07663-3.

Pomeroy, J.W., Bewley, D., Essery, R.L., Hedstrom, N., Link, T., Granger, R.J., Sicart, J.E., Ellis, C., and Janowicz, J. 2006. 'Shrub tundra snowmelt', *Hydrological Processes* 20(4), pp. 923–941. doi:10.1002/hyp.6124.

Putkonen, J. 1998. 'Soil thermal properties and heat transfer processes near Ny-Alesund, northwestern Spitsbergen, Svalbard', *Polar Research* 17(2), pp. 165–179. doi:10.1111/j.1751-8369.1998.tb00270.x.

Staff, S.S. 2023. *Soil climate research station data for Toolik Lake, Box*. Available at: https://nrcs.app.box.com/s/1vov5vk4mhw3msjtwcsegg9if87rhafu (Accessed: 14 September 2023).

Walker, D.A., Jia, G.J., Epstein, H.E., Raynolds, M.K., Chapin III, F.S., Copass, C., Hinzman, L.D., Knudson, J.A., Maier, H.A., Michaelson, G.J., Nelson, F., Ping, C.L., Romanovsky, V.E., and Shiklomanov, N. 2003. 'Vegetation-soil-thaw-depth relationships along a low-arctic bioclimate gradient, Alaska: Synthesis of information from the atlas studies', *Permafrost and Periglacial Processes* 14(2), pp. 103–123. doi:10.1002/ppp.452.

Zounemat-Kermani, M. 2013. 'Hydrometeorological parameters in prediction of soil temperature by means of artificial neural network: Case study in Wyoming', *Journal of Hydrologic Engineering* 18(6), pp. 707–718. doi:10.1061/(asce)he.1943-5584.0000666.

Safe blasting near rock glaciers

Alonso Cubillos[1], Eric Krumm[1], Juan Umerez[1], Lukas U. Arenson[2] & Pablo A. Wainstein[3]

[1]*BGC Engineering, Santiago, Chile*

[2]*BGC Engineering, Vancouver, British Columbia, Canada*

[3]*BGC Engineering, Calgary, Alberta, Canada*

ABSTRACT

Large mining projects have been developed and operated in glacial and periglacial environments around the world for decades. This leads to the inevitable fact that certain mining operations are located in close proximity to glacial and/or periglacial cryoforms such as glaciers or rock glaciers, respectively. In response to an increase in public awareness of these projects and climate change, regulatory bodies in various jurisdictions have heightened their focus on potential anthropogenic impacts to these cryoforms. Mining-induced blasting in close proximity to these cryoforms is considered to potentially impact these landforms. It therefore becomes of operational, regulatory and environmental importance to be able to design blasting patterns that do not cause any impact on these geological features for mining operations near such cryoforms. A critical component when designing production blasts in such settings is to determine the so-called Charge Weight per Delay Interval (CWPDI) of an acceptable blast. This paper outlines a simplified method for determining the maximum acceptable CWPDI for blasting as a function of the distance to the selected cryoform. The procedure requires knowledge of the type and weight of explosive per blast hole, the time delay pattern, in situ Peak Particle Velocity (PPV) and frequency measurements at varying distances from the blast, and a basic understanding of the cryoform's geometry and strength properties. Recognizing that not all projects will have access to such extensive data, some parameters and simplified equations are suggested to guide the assessment in those situations. This work serves to highlight the significance of responsible, informed mining practices within a vulnerable environment.

1 INTRODUCTION

Large mining projects have been developed and operated in glacial and periglacial environments around the world for decades. This leads to the inevitable fact that certain mining operations are located in close proximity to glacial and/or periglacial cryoforms such as glaciers or rock glaciers, respectively. Some mining operation activities, such as mining-induced blasting, are considered to potentially impact these landforms. It therefore becomes of operational, regulatory and environmental importance to be able to design blasting patterns that do not cause any impact on these cryological landforms.

Assessing the stability of glacial or periglacial cryoforms is complex due to the complex mechanical properties of the ice present within them (Paterson 1994; Arenson et al. 2014). In the case of a glacier, the instabilities typically evolve with time or in response to changes in temperature (air and ice) or subglacial water pressure. A creep failure (accelerated deformation under constant loading) is another mechanism of instability, and it occurs when the ice goes from a secondary to a tertiary creep stage, associated with an acceleration in cryoform deformation (Glen 1955; Duval et al. 2010). The instability and potential failure of a glacier or a rock glacier, as a whole body, is atypical unless one of the boundary conditions changes dramatically.

Regarding the morphological characteristics of rock glaciers, which are the main focus of this work, the most abrupt possible instabilities are in the form of debris flows or landslides, which are very rare because these cryoforms would simply lose their volume in response to permafrost degrades.

The most critical natural dynamic loading conditions for rock glaciers near tectonic active zones come from earthquakes. However, no evidence was reported on earthquake-induced failures of rock glaciers. Independent on this observation, dynamic loads from other sources, such as production blasting in the vicinity of rock glaciers due to exploitation of natural resources, could potentially generate rock glacier instabilities.

This work outlines a simplified method for assessing the potential impact on global slope stability to rock glaciers as a result of the mining blasting-induced vibrations. The maximum blast Charge Weight per Delay Interval (CWPDI) at different distances from the rock glacier are calculated.

2 APPROACH

The analysis of a potential impact on a glacial and/or periglacial cryoform in response to production blasting induced vibrations in an open mining context is composed of determining the cryoform's resistance to seismic induced displacements (k_y). The overall strategy is outlined in Figure 1.

https://doi.org/10.52381/ICOP2024.168.1

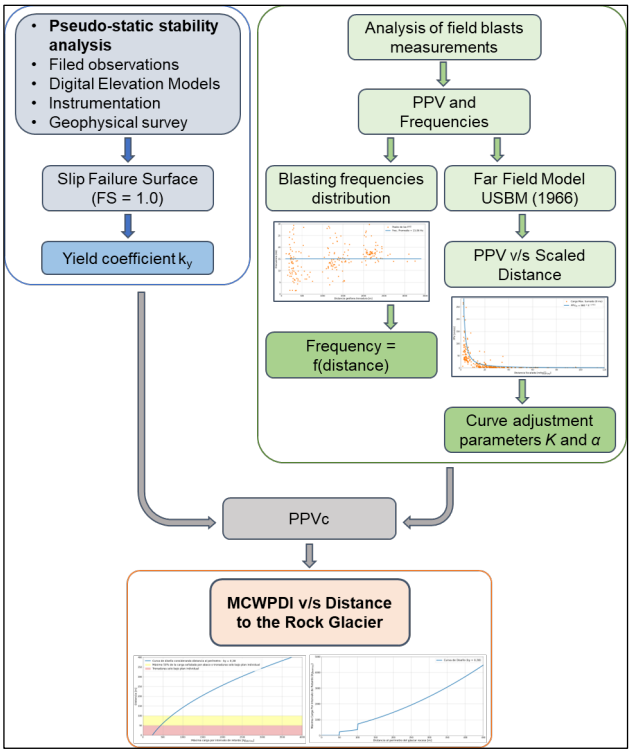

Figure 1. Analysis general strategy.

2.1 Rock Glaciers Stability

The first step is to assess which conditions are critical for a rock glacier to be stable – in traditional slope stability terms.

As previously mentioned, the instability and potential failure of a glacial or a rock glacier, as a whole body, is unusual unless one of the boundary conditions changes dramatically. Dynamic loading originating from earthquakes or, for the purpose of this work, blasting activities may have the potential to affect the overall stability of the entire cryoform.

In this work, the dynamic stability of a rock glacier is assessed using the so-called pseudo-static approach, typically used for simplified seismic stability analyses (Jibson 2011). This approach considers modeling the dynamic loading as a horizontal force acting on the gravitational center of the sliding mass (cryoform), equal to the mass of the frozen soil multiplied by the acceleration of gravity and a horizontal seismic coefficient, k_h.

The minimum value of k_h for which the disruptive forces magnitude is larger than the resisting forces is called *seismic yield coefficient* and is denoted as k_y. The yield coefficient k_y can be estimated from considering a *Factor of Safety* (FS) to sliding equal to 1.0. Hence, the k_y coefficient characterizes the maximum horizontal acceleration that the cryoform can theoretically sustain before the entire mass is failing as a rigid body.

2.1.1 *Yield coefficient k_y estimation*

The k_y coefficient can be estimated from typically used engineering stability software such as Slope/W (Geoslope International, Calgary AB, Canada) or can be estimated in more simple ways (Figure 2) for simple geometries analytically, as follows:

$$k_y = \frac{\cos(\alpha)\tan(\varphi) - \sin(\alpha)}{\sin(\alpha)\tan(\varphi) + \cos(\alpha)} \quad [1]$$

Where φ is the friction angle acting on the slipping surface. Equation 1 assumes zero cohesion.

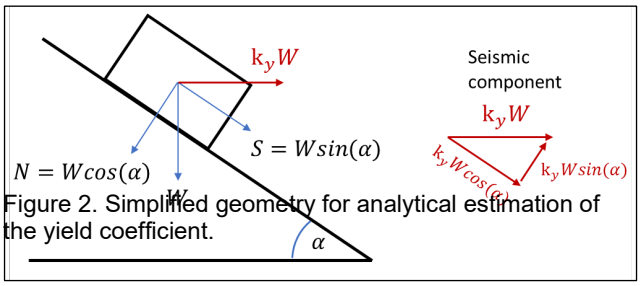

Figure 2. Simplified geometry for analytical estimation of the yield coefficient.

2.1.2 *Critical Peak Particle Velocity (PPVc) and yield coefficient (k_y)*

Once the blast is detonated, the explosive energy is released in the form of seismic waves thorough the soil and rock media. Historically, the US Bureau of Mines (USBM) has characterized the impacts of vibrations produced by blasting based on the pulse (or seismic wave) that generate the largest particle velocity. This is known as the peak particle velocity or PPV. As the wave travels away from the seismic source, it propagates as an elastic wave through the media. This wave can be modeled as a sine pulse of uniform amplitude and certain frequency. According to USBM (1980), for the wave associated with the pulse having the largest PPV, it is possible to obtain its acceleration from its velocity magnitude and wave frequency as follows:

$$a_{max} = 2\pi f \cdot PPVc \quad [2]$$

Where a_{max} and f are the acceleration and pulse frequency generated by the wave with the largest PPV.

As introduced earlier, the stability of the cryoform can be characterized by its yield coefficient k_y. The acceleration equivalent to that k_y can be calculated via multiplying k_y with the acceleration of gravity:

$$(a_{k_y} = k_y g) \quad [3]$$

Using Equation 2, the value of the PPV that would result in an acceleration that can produce a cryoform instability, which is called PPV critical (PPVc), can then be obtained as:

$$PPV_c = \frac{g}{2\pi f} k_y \quad [4]$$

Where f is the frequency of the wave that generated the PPV, g is the acceleration of gravity and k_y is the yield coefficient of the sliding mass. Equation 4 provides a limiting PPV such that if a PPV exceeds that threshold an instability of the cryoform could be triggered.

2.2 Analysis of Field Blasts

Once the stability conditions of the cryoform have been defined, the second stage is to determine the loading conditions (defined in terms of velocities and accelerations) generated by the blasting activity near the rock glacier of interest.

The intended outcome of this stage is to measure several Peak Particle Velocities (PPV) generated by the production blasting activity and then establish a relationship between the generated frequency (which is also measured in the field) and the distance between the location of blasting and the measurement point.

For this work, a series of geophones and a vibrations sensor were available to monitor the blasting activity at a mine site for several weeks (see Section 3 for more details). These instruments record velocity histories in three orthogonal directions: longitudinal, transversal, and vertical. From each of these records, the maximum value of the PPV per channel and its associated frequency is obtained. The *PPVsum* is subsequently determined as the maximum value of the norm of the velocity time vector during the entire recording:

$$PPVsum = max\left(\sqrt{V_{lon}^2 + V_{tra}^2 + V_{ver}^2}\right) \quad [5]$$

Since the PPVsum is always greater than or equal to each of the PPVs per channel, this work conservatively uses the PPVsum as an input for the USBM (1966) model. Therefore, from now on the PPVsum will be referred to as PPV only.

2.2.1 PPV and Frequency

The first objective of the analysis of field measurements is to obtain the distribution of blast wave frequencies versus the distance to the rock glacier of interest. This can be done just by plotting the frequency associated to the maximum PPV and the distance of the blast to the perimeter of the cryoform.

As described above, the PPVsum corresponds to the maximum value of norm of the velocity vector, and as such it does not have an associated frequency. In order to assign a frequency, we considered the frequency value associated with the channel of the maximum individual PPV, which is considered a conservative approach.

2.2.2 PPV and Scaled Distance

The far field vibrations model commonly used for the determination of PPV levels was initially developed by USBM (1966). The model was derived from a statistical analysis of multiple blasts in their three particle velocity components: radial, vertical, and transversal. Blasting registered by the USBM (1966) methodology allowed for establishing a relationship between the so-called *Scaled Distance* and the PPV:

$$PPV = K\left(\frac{D}{\sqrt{W}}\right)^{\alpha} \quad [6]$$

Where *PPV* is the peak particle velocity (in mm/s), *K* and α are local regression constants, *D* is the distance between the blast and the point of interest (in meters), and *W* is the Maximum Charge Weight Per Delay Interval (MCWPDI, in kilograms ammonium nitrate/fuel oil equivalent - kg ANFOeq). The Scaled Distance is defined as the product between the distance and the square root of the MCWPDI, $D/\sqrt{W}$.

The objective is to determine parameters *K* and α from a curve fit of the blasting measurements obtained during a field campaign. We recommend adjusting the data to a 90% confidence level, as will be shown in the applied case described in Section 3.

2.3 Maximum Charge Weight Per Delay Interval

ANFO is a high explosive, consisting of a mixture of ammonium nitrate and fuel oil. The relative power by weight mass refers to the energy yield of an explosive expressed as a percentage of the energy yield of an equivalent weight in ANFO. For example, a widely used explosive is Blendex 950, which has a power by weight equivalent to 88% of the ANFO (1 kg of Blendex 950 has 88% of the power of 1 kg of ANFO). The sum of the amount of ANFO explosive and the ANFO equivalent of any other explosive used during the blasting is called ANFO equivalent.

Regular production blasting activity consists of a grid composed of dozens (and even hundreds) of blast boreholes, which detonate at different times in sequences that depend on the specific objective of the blasting in question. Each of the blast holes contain bottom charges and column charges, which may use different type of explosives. For this method, it is necessary to determine the ANFOeq charge (in kg) for each borehole. The maximum charge per blasting hole is known as the Maximum Charge Weight Per Delay Interval (MCWPDI) and is an input parameter for the regression of Equation 6 (parameter *W* in the equation).

It is possible that for boreholes that detonate at similar delays their shockwaves will couple (Persson et al. 1994). If this is the case, the MCWPDI is estimated as the sum of the induvial charges of those blast. The current practice considers the superposition of ANFOeq charges for a detonation interval of 8 ms (Hoshino 2000; Singh 2006; Kuzu 2008).

2.4 Blasting Design Chart

Three key inputs have been obtained from this methodology: (1) Yield coefficient k_y; (2) Frequency distribution as a function of the distance to the rock glacier; and (3) Peak Particle Velocity (PPV) as a function of the Scaled Distance ($D/\sqrt{W}$). From these three inputs it is possible to develop a relationship between the distance and MCWPDI, for a given k_y.

For a blast to generate a PPVc in the rock glacier of interest for this study, the PPV must satisfy Equation 4 and Equation 6 at the same time. Then, by eliminating W from both equations, the following relationship is obtained:

$$W = \sqrt[\alpha/2]{\frac{KD^{\alpha} \cdot 2\pi f(D)}{g \cdot k_y}} \quad [7]$$

Where:

- W: Maximum Charge Weight Per Delay Interval.
- K and α: calibrated parameters for the PPVc and the Scaled Distance.
- D: Distance to the centroid of the rock glacier under study.
- f(D): Blast wave frequency as a function of the Distance to the cryoform.
- g: acceleration of gravity.
- k_y: yield coefficient.

From Equation 7, it is now possible to determine the maximum charge of the blast (W, in kg ANFOeq) that will generate the PPVc at a distance D (in meters) to the centroid of the rock glacier of interest. For practical operational use, it is recommended to define the maximum allowed charge of the blast (W) as function of the distance to the perimeter of the rock glacier. To do so, it is necessary to move the abscissa axis (distance) by the distance between the centroid of the slip surface with a yield coefficient k_y, and the perimeter of the rock glacier. Then, a Blasting Design Chart can be defined for the MCWPDI as a function of the distance D (from now on defined as the distance to the perimeter of the rock glacier).

Also, for practical operational use, and based on the limitations described in Section 4, the methodology presented in this paper proposes the use of two buffers for the Blasting Design Chart:

- Buffer 1 – For distances less than 50 m: No blasting unless individual blasting plans are developed.
- Buffer 2 – For distances between 50 m and 100 m: Use a maximum of 50% of the MCWPDI estimated from Equation 7 unless individual blasting plans are developed as necessary.
- Buffer 3 – For distances greater than 100 m: Use the MCWPDI obtained from Equation 7.

Based on these considerations, Figure 3 presents a general schematic of a Blasting Design Chart that would have to be developed for individual geological and topographic settings.

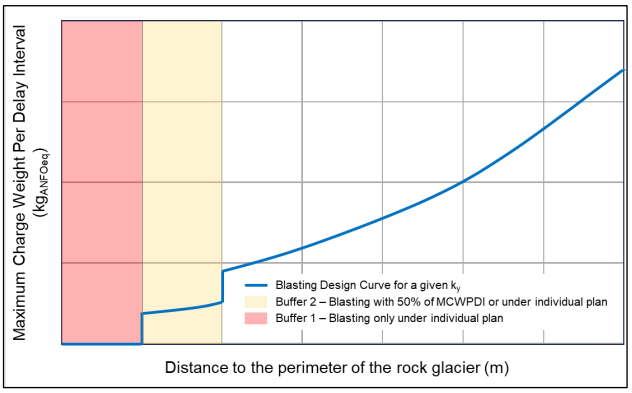

Figure 3. General schematic of the final Blasting Design Chart for a rock glacier with a yield coefficient k_y.

3 Applied Case

A case study has been assessed using the methodology described in this paper. The case is a rock glacier located in the nearby areas of an active mine pit. For confidentiality reasons, no location nor operation details will be shared, and the cryoform will be referred to as “Rock Glacier”.

The Rock Glacier of interest is located approximately 600 m from the eastern edge of the active mine pit. Figure 4 shows a schematic of the open pit and the Rock Glacier location.

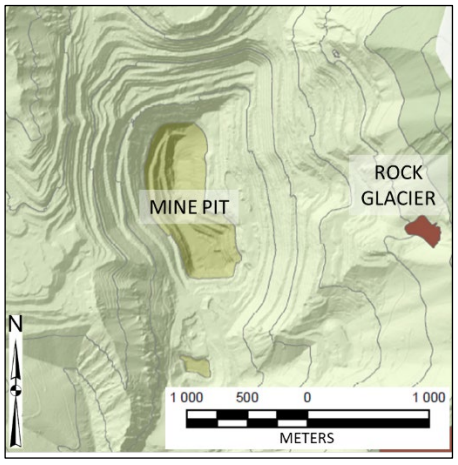

Figure 4. Mine Pit and Rock Glacier locations of the study case.

3.1 Stability and yield coefficient k_y

The first step is to assess the Rock Glacier stability and to determine the yield coefficient k_y at which the cryoform shows a global instability. A series of pseudo-static limit equilibrium slope stability analyses were carried out for a 2D section of the Rock Glacier, using Slope/W 2018 software (Geoslope International, Calgary AB, Canada).

The 2D critical profile analyzed was defined based on the maximum slope of the Rock Glacier. The geotechnical characterization of the cryoform (friction angle and cohesion of ice-rich material) was chosen based on Arenson and Springman (2005) and was based on the estimated ground ice content of the Rock Glacier. The base of the Rock Glacier was modeled as impenetrable rock.

The yield coefficient was determined for different slip surfaces at different distances from the toe of the Rock Glacier. The minimum k_y value of 0.38 was obtained for a global failure surface. Figure 5 shows the resulting slip surface for that global failure.

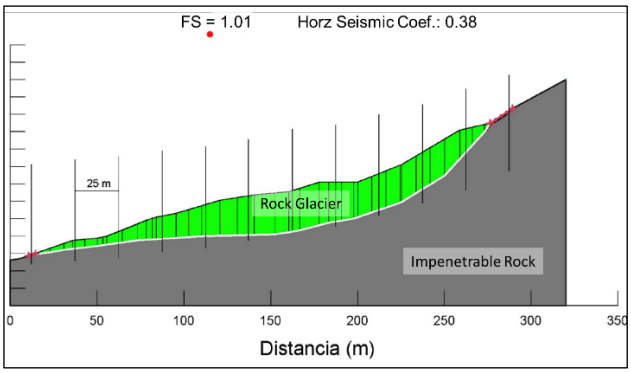

Figure 5. Resulting global slip surface with a yield coefficient k_y of 0.38 (source: Slope/W software).

3.2 Field Blasting Data

Three different sources of PPV and associated frequency measurements coming from the production blasting at the mine site were considered:

- A field monitoring campaign with two seismic monitoring systems consisting of an eight-channel datalogger and two triaxial geophones.
- A vibration sensor installed close to the Rock Glacier, that automatically measures the PPV and frequencies of the blasting activity.
- Internal recordings measured by the blasting contractor.

Figure 6 shows the location of all blast holes and sensors considered in the dataset.

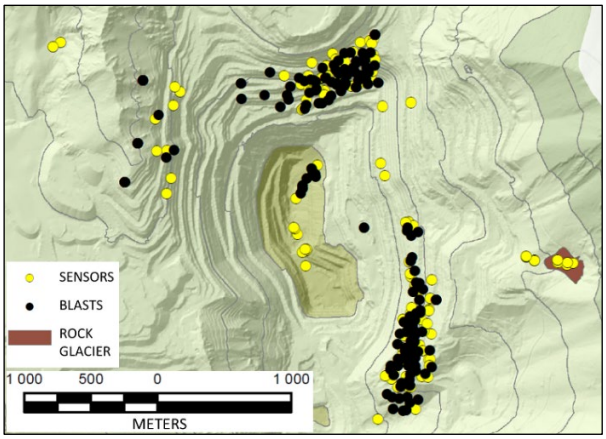

Figure 6. Location of dataset blast holes and sensors. The complete dataset used in this study consists of 272 vibration records from 141 blasts. The distances to the measurement sensors range from approximately 100 m to ~3500 m. Figure 7 shows the histogram of the detonation distances to the measurement points for the total number of records used.

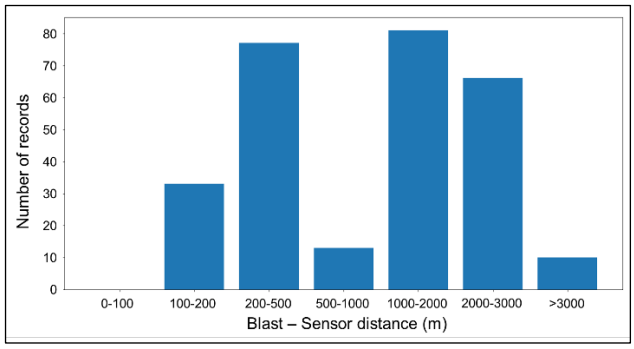

Figure 7. Histogram of distances from the blasts to their corresponding measurement sensor.

3.2.1 PPV Frequency Distribution

For several of the recorded blasts, the PPV was less than 1 mm/s. Such low PPV values are generally considered to produce no damage even in case of sensitive structures (FTA 2006; DIN 4150-3 (1999)). Therefore, frequencies associated with the highest PPV channel for PPV greater than 1 mm/s were used for the estimation of the PPV frequency as a function of distance from the blast. This eliminates records with a high noise component and improves the estimation of the frequency generated by the blast itself.

Figure 8 shows the frequencies obtained as a function of the distance to the measurement point, and their fitting curve. No trend between frequency and distance can be identified. Therefore, we considered a constant average frequency equal to ~15 Hz for the development of our Blasting Design Chart. It is important to note that this step of the methodology needs to be adjusted for each particular site.

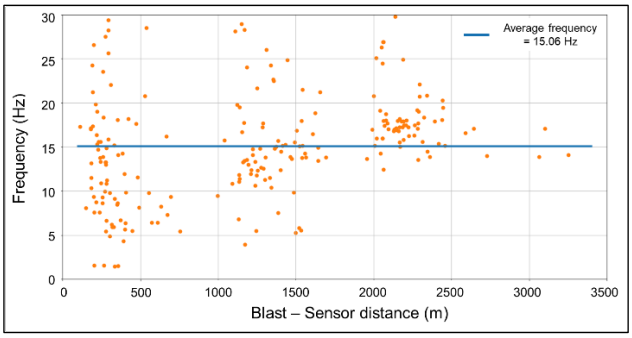

Figure 8. PPV associated frequency distribution as a function of the blast-sensor distance.

3.2.2 *PPV and Scaled Distance*

Figure 9 shows the PPV decay curve as a function of the Scaled Distance. As described in Section 2.3, the MCWPDI is considered as a superposition of individual charges for an 8 ms time interval. The regression of the data is in the form indicated in Equation 6. Conservatively, a 90% confidence level was used to determine the curve fit to the PPV. This means that there is a 90% probability that the recorded PPV would be less than the predicted PPV. From these, we derived the resulting, site-specific adjustment equation of:

$$PPV_{90\%} = 860\left(\frac{D}{\sqrt{W}}\right)^{-1.421} \quad [8]$$

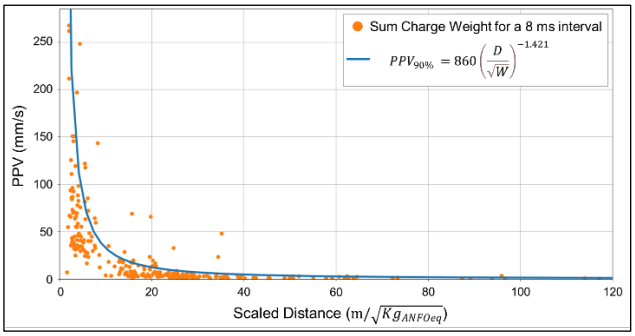

Figure 9. PPV decay curve as a function of the Scaled Distance. The fitting curve is selected such that at least 90% of the data fall under the curve.

3.3 Final Blasting Design Chart

Using the results developed in Sections 3.2.1 and 3.2.2 it is now possible to replace the values in Equation 7 and obtaining the following relationship:

$$W = \sqrt[-0.711]{\frac{8{,}295 \cdot D^{-1{,}421}}{k_y}} \quad [9]$$

By replacing the critical yield coefficient value estimated for a global stability of the Rock Glacier (see Section 3.1), it is possible to determine the final relationship between the MCWPDI (W) and the distance between the location of the blast and the centroid of the Rock Glacier slip surface (D). As described in Section 2.4, it is recommended to present these results in terms of the distance to the perimeter of the Rock Glacier and not the centroid of the failing mass. The distance between the centroid of the global slip surface (see Figure 4) and the perimeter of the Rock Glacier is ~150 m for this case. Hence, the final curve can be obtained via shifting the origin of the distance axis by 150 m to the right.

Figure 10 shows the resulting design chart for this case study, considering the shift of the x-axis and the inclusion of buffers as recommended in Section 2.4. As an example, the results show that at a distance of 350 m to the perimeter of the Rock Glacier the maximum blast charge (MCWPDI) that can be used is 3000 kg ANFOeq.

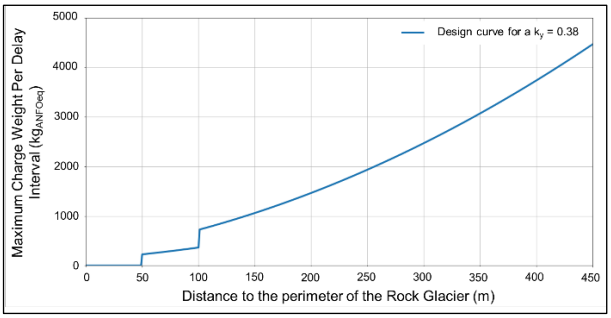

Figure 10. Final Design Chart for the MCWPDI as a function of the distance to the perimeter of the Rock Glacier.

4 Study Limitations

It is important to note that there are several limitations to the methodology and analysis described in this paper. Some specific limitations are:

- The base case from which the methodology was defined has 272 PPV and 224 frequency measurements from 141 blasts. From the frequency associated with the PPV, records are only starting from ~100 m, which results in some uncertainty in the extrapolation of the data at smaller distances. This is why a 50% decrease in the charge is recommended for distances between 50 and 100 m to the perimeter of the rock glacier.
- The analysis assumes that the motion recorded at the surface is the same as the motion that would be recorded at the center of slipping mass of the cryoform. The conservative simplification that the center of mass corresponds to the centroid determined from a plan view was also used for this analysis.
- Each blast generated a wide spectrum of vibration frequencies. Nonetheless, for each of these, the motion generated by blasting is assumed to be a simple harmonic motion with a single frequency corresponding to the predominant frequency at the instant the PPV occurs. In this way, the analysis determined the acceleration generated by the PPV at the instant when the PPV occurs.

5 Final Comments and Conclusions

A simplified method for assessing the potential impact to the stability of rock glaciers in response to production blasting induced vibrations for open pit mine sites has been outlined. The proposed method seeks to determine the Maximum acceptable Charge Weight Per Delay Interval (MCWPDI) for blasting as a function of the distance between the blast and the cryoform, avoiding the generation of an instability/slope failure. We developed a Design Chart that correlates the MCWPDI with the distance to the perimeter of a rock glacier.

Three important inputs are needed in our method for developing such a design chart: (1) A yield coefficient, k_y, which represents the maximum horizontal acceleration that ensures the cryoform stability; (2) the distribution of Peak Particle Velocities generated by the blasting-induced waves as a function of the Scaled Distance; and (3) the distribution of blasting waves predominant frequencies as a function of the distance between the blast and the point of interest.

The intent of the proposed methodology is to serve as an additional guideline to enable the safe designing of blasting near glacial and periglacial cryoforms as part of a mine operations in mountainous terrain. In response to local geological and topographic settings, and the characteristics of the glacial/periglacial cryoform(s) in question, site specific design charts must be developed using local measurements of PPVs and associated frequencies.

It is also important to note that blasting activities and procedures are subject to local and/or mine operation regulations. The proposed method should be considered as one of the factors in the decision-making process, but not the sole determining factor.

Finally, more research is required to better understand the impact of dynamic load from nearby blasting on glaciers and rock glaciers (frozen soil), specifically the absorption such cryoforms may exhibit.

6 References

Arenson, L.U. and Springman, S.M. 2005. 'Mathematical descriptions for the behaviour of ice-rich frozen soils at temperatures close to 0°C', *Canadian Geotechnical Journal* 42(2). https://doi.org/10.1139/t04-109.

Duval, P., Montagnat, M., Grennerat, F., Weiss, J., Meyssonnier, J., and Philip, A. 2010. 'Creep and plasticity of glacier ice: a material science perspective', *Journal of Glaciology* 56(200), pp. 1059–1068.

Glen, J.W. 1955. 'The creep of polycrystalline ice', *Proceedings of the Royal Society of London. Series A. Mathematical and Physical Sciences* 228(1175), pp. 519–538.

Hoshino, T., Mogi, G., and Shaoquan, K. 2000. 'Optimum delay interval design in delay blasting', *Fragblast* 4(2), pp. 139–148.

Jibson, R.W. 2011. 'Methods for assessing the stability of slopes during earthquakes-A retrospective', *Engineering Geology* 122(1–2), pp. 43–50. https://doi.org/10.1016/j.enggeo.2010.09.017

Kuzu, C. 2008. 'The importance of site-specific characters in prediction models for blast-induced ground vibrations', *Soil Dynamics and Earthquake Engineering* 28(5), pp. 405–414.

Paterson, W.S.B. 1994. *The physics of glaciers*, 3rd edition. Oxford, New York and Tokyo: Pergamon Press.

Singh, P.K., Sirveiya, A.K., Babu, K.N., Roy, M.P., and Singh, C.V. 2006. 'Evolution of effective charge weight per delay for prediction of ground vibrations generated from blasting in a limestone mine', *International Journal of Surface Mining, Reclamation and Environment* 20(01), pp. 4–19.

U.S. Bureau of Mines 1966. Effect of charge weight on vibration levels from quarry blasting. Report of investigation 6774.

Influence of storm trajectory on the stable isotope composition of precipitation at Inuvik, NT

Loucas Diamant-Boustead & Christopher R. Burn
Carleton University, Ottawa, Ontario, Canada

ABSTRACT

Stable-isotope ratios in ice-wedge ice have been used to reconstruct winter conditions in Siberia and eastern Beringia. Such reconstructions assume that temperature is the principal influence on the isotopic composition of precipitation and, hence, wedge ice. Archived data for over 100 precipitation samples, collected between August 2015 and August 2018 at Inuvik, NT, indicate two distinct populations of $\delta^{18}O$ values for summer and winter. The regression equation for $\delta^{18}O$ (‰) on mean temperature (T, °C) for the day of precipitation is $\delta^{18}O = 0.3T - 19.3$ ($R^2 = 0.59$, $p < 0.01$). For summer, the equation is $\delta^{18}O = 0.19T - 18.2$ ($R^2 = 0.01$, $p = 0.007$), and for winter $\delta^{18}O = 0.16T - 22.2$ ($R^2 = 0.15$, $p = 0.02$). The difference between the seasons dominates the regression when all data are pooled, but seasonal data indicate low to no relation between the variables. NOAA's HYSPLIT model was used to trace storms back to where the synoptic system formed as well as the trajectory taken to reach Inuvik. Systems that travel over mountains to reach Inuvik experience considerable fractionation whereas systems from the proximal Beaufort Sea do not. The $\delta^{18}O$ values for systems originating from the north, south, and west were statistically indistinguishable in both seasons, but southerly systems arrived with the warmest conditions in winter. Separate bulk samples of monthly precipitation collected from 1985–1995 provided a stronger relation between $\delta^{18}O$ values and monthly mean temperature, but R^2 (0.28) was still low.

1 INTRODUCTION

Significant climate changes have occurred recently in the Arctic with greater warming than in other regions of the Earth (Chylek et al. 2022). Arctic amplification is partly a result of reduced terrestrial snow and ice cover, diminishing sea-ice coverage, and changes in atmospheric and oceanic circulation patterns (Serreze and Barry 2011). Considerable effort is underway to understand the extent of past changes in temperature as analogues for potential future climates. The stable isotope composition of ground ice can be used to reconstruct former climate conditions, especially through examination of ice-wedge ice. Wedge ice samples collected from Russia and the western Canadian Arctic have indicated warming during winter since the mid-Holocene (Opel et al. 2017; Holland et al. 2020).

The stable isotope composition in meteoric waters is defined by the ratios of ^{18}O:^{16}O and ^{2}H:^{1}H, relative to Vienna Standard Mean Ocean Water (VSMOW; Gonfiantini 1978) via δ notation, where for ^{18}O:

$$\delta^{18}O = \frac{\frac{^{18}O}{^{16}O_{sample}} - \frac{^{18}O}{^{16}O_{VSMOW}}}{\frac{^{18}O}{^{16}O_{VSMOW}}} \times 1000 \quad [1]$$

and for hydrogen, δD, with D = ^{2}H. Characteristically, the concentration in ground ice is less than in VSMOW, due to depletion of heavy isotopes by fractionation during precipitation while the air mass is in transit from the source of vapour (Dansgaard 1964). Fractionation is the preferential incorporation of heavy isotopes into the lower energy phase (Dansgaard 1964). There is a strong linear relationship between $\delta^{18}O$ and δD in air masses. Craig (1961) presented the Global Meteoric Water Line (GMWL, eq. 2), representative of the general relation between these isotope compositions in precipitation.

$$\delta D = 8\,\delta^{18}O + 10 \quad [2]$$

The GMWL is a result of proportionate fractionation of oxygen and hydrogen isotopes during phase change. As an airmass travels from its origin, it becomes depleted in these heavy isotopes, which are preferentially precipitated. The extent of depletion depends on the origin of the air mass, its trajectory, and the temperature during condensation (Dansgaard 1964).

Temperature (T) has been regarded as the most important variable associated with the isotopic composition of precipitation. Porter et al. (2016) and Kostrova et al. (2020) reported $\delta^{18}O$:T ratios of 0.41‰ °C^{-1} from continental polar North America and 0.50‰ °C^{-1} from Siberia. Dansgaard (1964) determined the initial relation between these variables for Greenland and North Atlantic stations as:

$$\delta^{18}O = 0.69T - 13.6 \quad [3]$$

Equation 3 indicates that lower values of $\delta^{18}O$ are characteristically associated with cooler conditions.

Variations in isotopic concentrations have been used to distinguish massive and pore ice bodies in permafrost in stratigraphic terms and with respect to the climate when the ice formed (Mackay 1983a; Burn et al. 1986; Kotler and Burn 2000). Recently, the stable isotope composition of wedge ice has been presented as a winter climate proxy that is interpreted along the chronological sequence of veins in an ice wedge (Meyer et al. 2015; Opel et al. 2017).

https://doi.org/10.52381/ICOP2024.77.1

In this paper, the influences on the isotopic composition in precipitation of air-mass origin and trajectory are assessed for storms at Inuvik in the western Canadian Arctic. Samples of rain or snowfall were collected storm-by-storm at Inuvik for determination of $\delta^{18}O$ and δD in precipitation by Fritz et al. (2021). We used the NOAA HYSPLIT model to estimate the origin and back-trajectories of storm systems for which Inuvik temperature and precipitation isotope data are available between August 2015 and August 2018.

We also examined the $\delta^{18}O$:T relation for integrated samples of monthly precipitation collected between December 1985 and May 1995 at Inuvik Airport. The purpose was to determine whether $\delta^{18}O$:T relations derived on an event-by-event basis were replicated at a monthly time scale.

2 Study Area

Inuvik (68.36˚ N, 133.72˚ W; Figure 1) is located on the east side of the Mackenzie Delta, Northwest Territories. The town is in the broad plains east of the Western Cordillera, at an elevation of 15 m a.s.l. Air masses travelling from moisture sources to the south or west must cross these mountains, which reach over 4000 m a.s.l. close to the Pacific coast. The Beaufort Sea is about 100 km north of Inuvik. The land to the east is the flat and rolling terrain of the Interior Plains and Canadian Shield.

From 1991–2020, the mean annual temperature at Inuvik was -6.7 °C, an increase of 3.2 °C relative to the 1951–1980 mean (Schetselaar et al. 2023). The town has a monthly mean temperature below 0 °C between October and April. The coldest month is January, with a mean monthly temperature of -24.4 °C. In June through August, the mean temperature remains above 10 °C. Annual mean air temperatures have been rising within the region since 1971 (Thienpont et al. 2013). The rate of increase has been 0.77 °C/decade at Inuvik (Schetselaar et al. 2023).

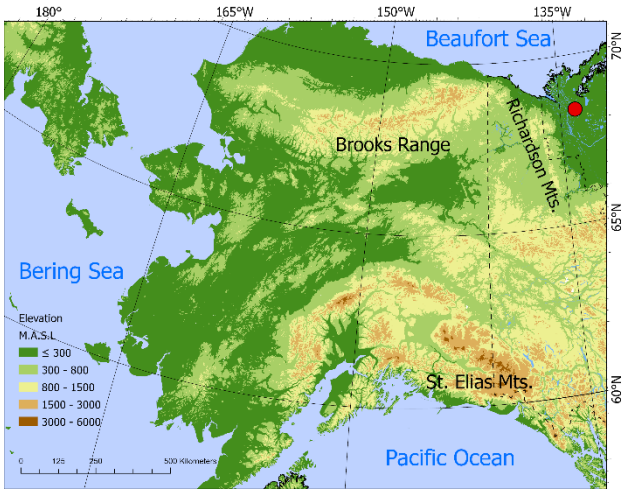

Figure 1. The western Canadian Arctic mainland and Alaska. Inuvik is indicated by the red circle in the northeastern corner of the map.

3 Methods

3.1 Precipitation 2015–2018

Fritz et al. (2021, 2022) collected 134 precipitation samples between August 2015 and August 2018 at the Aurora Research Institute in Inuvik. Samples were analyzed for δD and $\delta^{18}O$ at the Alfred Wegener Institute in Potsdam, Germany, and the results posted on the PANGEA database (Fritz et al. 2021). We combined these stable isotope values with amount of precipitation and the mean daily temperature on days with rain or snow at the Inuvik Airport (Environment Canada 2023).

3.2 HYSPLIT Model

The NOAA Hybrid Single-Particle Lagrangian Integrated Trajectory (HYSPLIT) model is a tool that simulates diffusion and movement within the atmosphere (Stein et al. 2015). The model was run for the dates of samples that could be confidently assigned to a specific precipitation event. Simulations were run using the READY web-interface. Single back-trajectories from Inuvik were generated with the 'normal' trajectory option. This allows for back-trajectories to be calculated for 315 hours (13 days), often leading to the source of the airmass, with the purpose of identifying the origin of precipitation. The National Weather Service's National Centers for Environmental Prediction Global Data Assimilation System (0.5˚ lat/long resolution) was the chosen meteorological grid model. Back-trajectories were calculated at three different levels in the atmosphere (250, 500, and 1000 m a.s.l). Commonly, these trajectories originated from the same location, but if they did not, the location with the majority was chosen.

3.3 Data Considerations

Of the 134 samples collected by Fritz et al. (2021), only 111 were used in the analysis. One sample was excluded by Fritz et al. (2022) due to an exceedingly low d-excess value of -17.8 ($\delta D - 8\delta^{18}O$); two samples were omitted due to labelling errors; nineteen were excluded due to inconclusive results from the HYSPLIT model (3), or an inability to confidently identify the storm responsible for the precipitation (16). One sample originated from the east and was not considered further due to lack of corroborating data. The 111 samples collected represented 47% of the total precipitation during the sampling period (Table 1).

Table 1. Annual total precipitation (tPrecip, mm) and in the events sampled by Fritz et al. (2021; rPrecip, mm). Percent indicates the proportion of precipitation represented in the samples collected by Fritz et al. (2021).

	n	rPrecip	tPrecip	Percent
Aug – Dec 2015	21	71.7	168.9	43%
Jan – Dec 2016	34	100.2	203.5	49%
Jan – Dec 2017	26	113.4	278.3	41%
Jan – Aug 2018	30	113.8	200.8	57%
Total	111	399.3	851.5	47%

3.4 Precipitation 1985–1995

Precipitation at Inuvik Airport, 12 km southeast of Inuvik, was collected monthly from December 1985 to March 1986 and December 1987 to May 1995, by the Atmospheric Environment Service, Environment Canada.

The precipitation received at the rain or snow gauge was stored daily in a sealed Nalgene bottle, with all precipitation collected in a calendar month blended. At the end of each month, samples were decanted into vials, sealed and sent for stable isotope analysis at the University of Waterloo Isotope Laboratory (December 1985 to February 1989) or the University of Western Ontario Department of Geology (March 1989 to May 1995).

The data processed by the University of Waterloo were released by the laboratory to the Global Network of Isotopes in Precipitation (GNIP) and were available to Fritz et al. (2022) for comparative analysis of co-isotope ratios in precipitation at Inuvik in 1985–1989. The data generated at the University of Western Ontario are presented in the Appendix at the end of this paper.

4 RESULTS

Table 2 presents the distribution of precipitation events by origin. The distribution of samples collected by Fritz et al. (2022) is representative of the broader population at Inuvik during the sampling period. The proportions of sampled events were 66, 21, and 12% from the north, west, and south, respectively, and for all events with ≥ 0.1 mm of precipitation the proportions were 60, 26, and 13%. The remaining 1% came from the east.

Table 2. Mean values of $\delta^{18}O$ (‰) and temperature (T, °C) for sampled storms, stratified by season and direction of origin. Data for $\delta^{18}O$ from Fritz et al. (2021). Total n represents the total number of storms during the sampling period in 2015–2018. Also included is the standard error of the mean (SE) for both $\delta^{18}O$ and T.

	Sample n	Total n	$\delta^{18}O$	T	$\delta^{18}O$ (SE)	T (SE)
North	74	264	-19	-1.1	0.6	1.5
Winter	20	137	-24.3	-17.6	0.7	1.0
Summer	54	127	-16.7	5.8	0.5	0.9
South	14	115	-21	0.9	1.3	2.5
Winter	6	84	-25.2	-7.1	1.0	2.2
Summer	8	31	-17.8	6.8	1.2	2.6
West	23	59	-20.5	-1.4	0.8	3.0
Winter	11	36	-23.3	-14.4	1.0	2.5
Summer	12	23	-18	10.4	0.8	1.5
Total	111	438	-19.6	-1	0.5	1.2
Winter	37	257	-25.1	-15.9	0.6	1.4
Summer	74	181	-17.5	6.7	0.3	0.6

4.1 Storm Origin and Stable Isotope Concentration

The data presented by Fritz et al. (2021) were sorted by their origin from the north, south, east, or west depending on the HYSPLIT analyses for each event. Precipitation from the north originated in the Arctic Ocean, from the south in the Pacific Ocean, and from the west in the Bering Sea, Sea of Okhotsk, or Chukchi Sea. The data were further classified as winter (October–April) or summer (May–September) events.

Overall, the $\delta^{18}O$ values in precipitation show only small differences in mean $\delta^{18}O$ when the samples are separated by direction of origin and grouped for both or either season (Table 2). Figure 2a presents box-and-whisker plots of the $\delta^{18}O$ values grouped by direction of origin that show similarity in distribution between the three groups in each season. Student's t-tests for differences between these various groups (north, south, west) by season (all year, summer, winter) did not show any statistically significant ($\alpha = 0.05$) differences between the mean values of the seasonal groups.

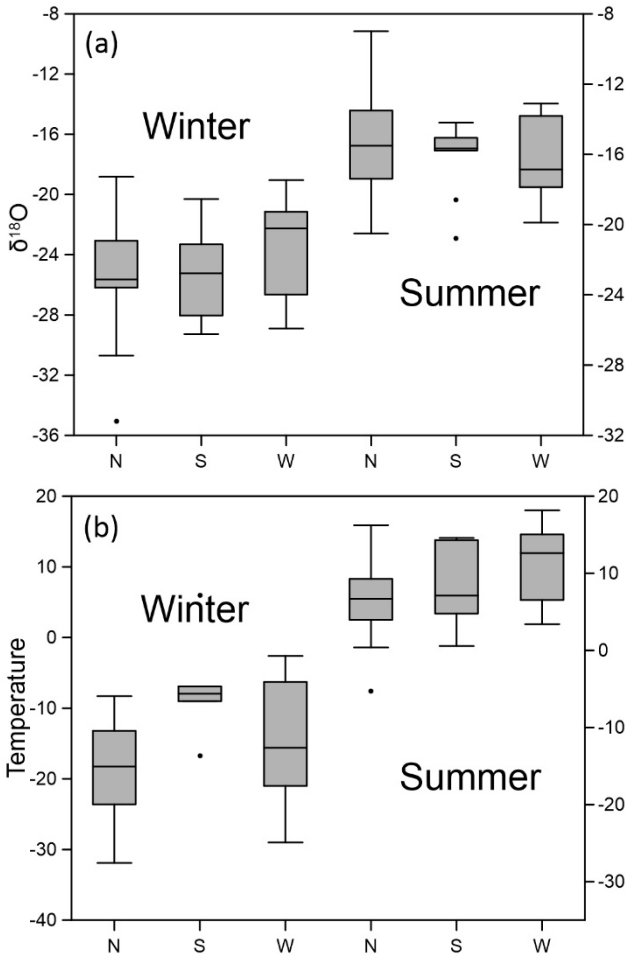

Figure 2. (a) Box-and-whisker plots of $\delta^{18}O$ (‰) grouped by direction of origin and season. (b) Mean temperature (°C) on day of precipitation grouped by origin and season.

4.2 Atmospheric Temperature and Stable Isotopic Concentration

4.2.1 Event by Event

Most precipitation events (66%) originated from the north and were associated with the lowest mean daily temperatures in summer and winter but not the lowest $\delta^{18}O$ values. In fact, during the summer months, storms from the north had the highest $\delta^{18}O$ values.

Precipitation originating in the south represented 12% of the sampled events and had relatively low $\delta^{18}O$ values. In the winter, storms from the south had $\delta^{18}O$ values 1‰ lower than northern storms but, on average, were associated with mean daily temperatures about 10 °C higher.

Western storms had the highest $\delta^{18}O$ values in winter, but the lowest in summer, despite coinciding with the warmest mean summer conditions. Overall, the results do not conform to equation 3, because the highest temperatures in summer and winter are associated with the lowest values of precipitation $\delta^{18}O$ in these seasons.

Box-and-whisker plots for mean temperature during precipitation events show considerable overlap in the distribution associated with the three directions of origin in summer but not in winter (Figure 2b). A series of t-tests indicated a statistically significant ($\alpha = 0.05$) difference in mean temperature between winter events from the north and south, and from the south and west. Similarly, in the summer there was a statistically significant difference in mean temperature between storms from the north and west, and from the south and west. The significant difference in temperature between groups without significant difference in $\delta^{18}O$ suggests that the $\delta^{18}O$:T relations for each group may not be the same.

The least-squares linear regression line fitted to the whole data set has a statistically significant slope and a coefficient of determination (R^2) of 0.59; the regression lines for the events from the north, south, and west over the year have similar R^2 (Table 3). The regression coefficients vary for the different origins but are not statistically different at $\alpha = 0.05$. The intercepts are all close to the mean values for $\delta^{18}O$ because mean T is close to 0 °C (Table 2). Figure 3 is a plot of $\delta^{18}O$ values and temperature for all sampled precipitation events. Visually, it is evident that the data plot into two groups representing summer and winter precipitation events.

Table 3. Least-squares linear regression lines for $\delta^{18}O$ on temperature from all samples collected in 2015–2018 and sorted by direction and season. Data for $\delta^{18}O$ from Fritz et al. (2021).

Origin	n	equation	R^2	p
North	74	0.33T – 18.7	0.64	<0.001
South	14	0.40T – 21.3	0.62	<0.001
West	23	0.22T – 20.2	0.60	<0.001
All Directions	111	0.30T – 19.3	0.59	<0.001
Summer	74	0.19T – 18.2	0.01	0.007
Winter	37	0.16T – 22.2	0.15	0.02

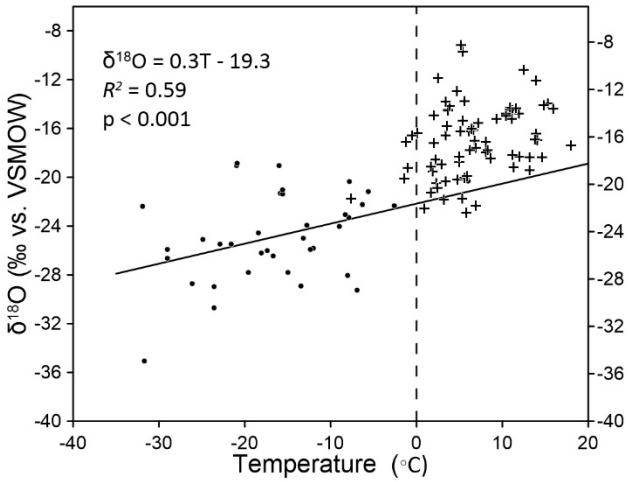

Figure 3. Scatterplot of temperature and $\delta^{18}O$ for summer (+) and winter storms (•) at Inuvik in 2015–2018 with least-squares linear regression line fitted to all data.

4.2.2 Seasonal Precipitation

In summer, the isotopic composition of rain from northern and western storms had significant relations with temperature at $\alpha = 0.05$ (Table 4). None of the relations from winter data for specific directions were statistically significant (Table 4). Figure 4 plots data from the summer and winter seasons collected from 2015–2018. The regression coefficients for both seasons are statistically significant at $\alpha = 0.05$, but both present low R^2 (Table 3), indicating little of the variation in $\delta^{18}O$ is explained by variation in T.

4.2.3 Monthly Aggregate Sampling

The least-squares linear regression lines for $\delta^{18}O$:T using all data from 1985–1995 present regression coefficients similar to the relation for 2015–2018 (Tables 3 and 5). The similarity of slope and intercept suggest that the relations between $\delta^{18}O$ and temperature are consistent at the time scales of individuals events and on a monthly basis (Tables 3 and 5). The higher coefficients of determination for the seasonal relations between $\delta^{18}O$ and temperature (Table 5) may be associated with signal smoothing for the differing

Table 4. Least-squares linear regression lines for $\delta^{18}O$ on temperature from summer and winter samples taken in 2015–2018 separated by direction. Data for $\delta^{18}O$ from Fritz et al. (2021).

Origin	n	equation	R^2	p
Summer				
North	54	0.24T – 18.1	0.13	0.01
South	8	0.11T – 18.5	0.05	0.58
West	12	0.35T – 21.6	0.47	0.01
Winter				
North	20	0.22T – 21.2	0.15	0.09
South	6	0.28T – 23.3	0.37	0.2
West	11	0.16T – 21.0	0.16	0.22

time unites of sample collection. The $\delta^{18}O$ and temperature values for 1985–1995 are monthly means. In summer, precipitation generally occurs on cool days but in winter relatively cold days are characteristically dry.

4.3 Physiographic Influences on Stable Isotopic Concentration

Table 6 presents data on the characteristics of precipitation arriving at Inuvik directly from the Beaufort Sea and in atmospheric systems that have crossed mountain ranges. Year-round, systems that passed over mountains resulted in $\delta^{18}O$ values 1‰ lower than those that did not (Table 6). However, t-tests for these data sorted by season indicated no statistically significant ($\alpha = 0.05$) difference between mean $\delta^{18}O$ for storms that travelled over mountains and those that did not. In contrast, t-tests for mean temperature on the day of the storm show a statistically significant difference during the summer between storms that passed over mountains and those that arrived directly from the Arctic Ocean.

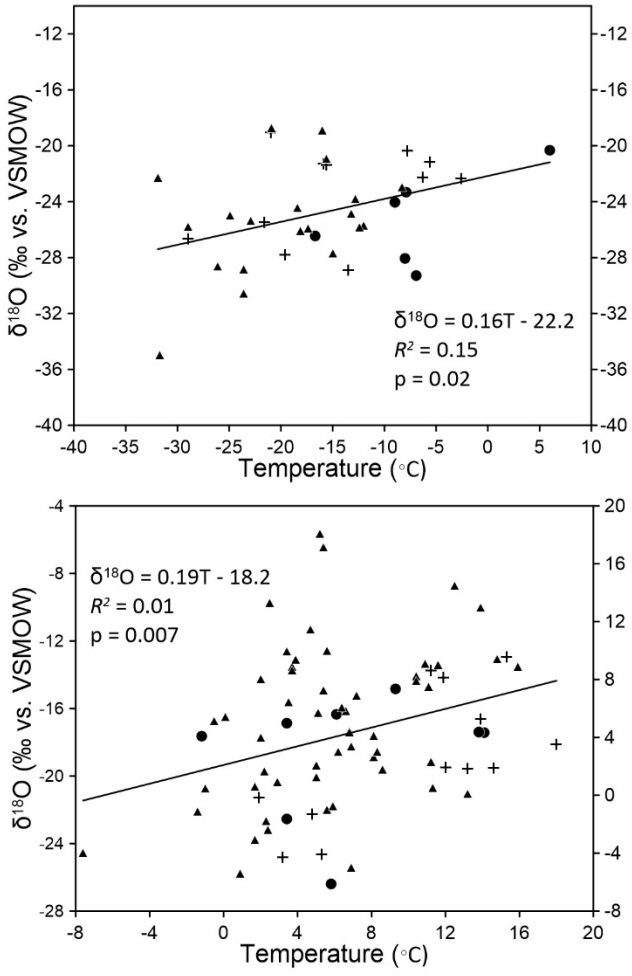

Figure 4. Scatterplots of temperature and $\delta^{18}O$ for (a) summer and (b) winter events from 2015–2018, with northern (▲), southern (•), and western (+) origins. The line has been fitted by least-squares linear regression.

Table 5. Least-squares linear regression for $\delta^{18}O$ on temperature from all monthly aggregate samples collected from 1985–95 and separated by season. Data for $\delta^{18}O$ and temperature are in the Appendix.

	n	equation	R^2	p
All data	91	0.31T – 21.9	0.71	<0.001
Summer	34	0.46T – 23.0	0.55	<0.001
Winter	57	0.26T – 23.0	0.28	<0.001

Table 6. Mean values of $\delta^{18}O$ (‰) and temperature (T, °C) of storms that passed over mountains (Yes) and those that did not (No). Also included is the standard error of the mean (SE) for both $\delta^{18}O$ and T.

Mountain Transit	n	$\delta^{18}O$	T	$\delta^{18}O$ (SE)	T (SE)
Winter					
Yes	16	-25.4	-14.1	0.7	1.5
No	21	-24.1	-17.4	1.1	2.5
Summer					
Yes	19	-17.5	9.3	0.4	0.7
No	55	-16.5	5.7	0.6	0.9

The orographic influence on isotope composition in precipitation is illustrated in Figure 5. Figure 5a displays the tracks of two storms with precipitation that fell at -32 °C. One, on 23 January 2017, had an $\delta^{18}O$ value of -35.1‰. It originated over the Arctic Ocean but travelled over the Brooks Range and Yukon mountains before arriving at Inuvik. The other, arriving directly from the Arctic Ocean 17 days later on 10 February 2017, brought precipitation with an $\delta^{18}O$ value of -22.4‰. The contrast in $\delta^{18}O$ between the storms is likely due to fractionation during condensation within the first air mass as it passed over several mountain ranges.

A similar example is presented from autumn 2015 in Figure 5b, which illustrates the path of a southerly storm and a northerly storm. The storm from the south passed over several mountain ranges and had precipitation at Inuvik with a lower $\delta^{18}O$ value than the northern storm, even though it arrived under warmer conditions. These examples represent the overall statistics presented in Table 2 regarding storms from the North and South.

5 Discussion

5.1 Physiographic Effects

Figure 5 and Table 6 show that orographic features influence the isotopic composition of air masses delivering precipitation to Inuvik. The absolute difference in $\delta^{18}O$ value between precipitation from air masses derived from the Arctic Ocean directly and those that travelled over mountains is not statistically significant at $\alpha = 0.05$, but there is a statistically significant difference in summer mean temperatures between these precipitation events (Table 6). In North America, $\delta^{18}O$ in precipitation decreases by 0.28‰ for every increase of 100 m in elevation (Poage and Chamberlain 2001), a relation that is constant throughout

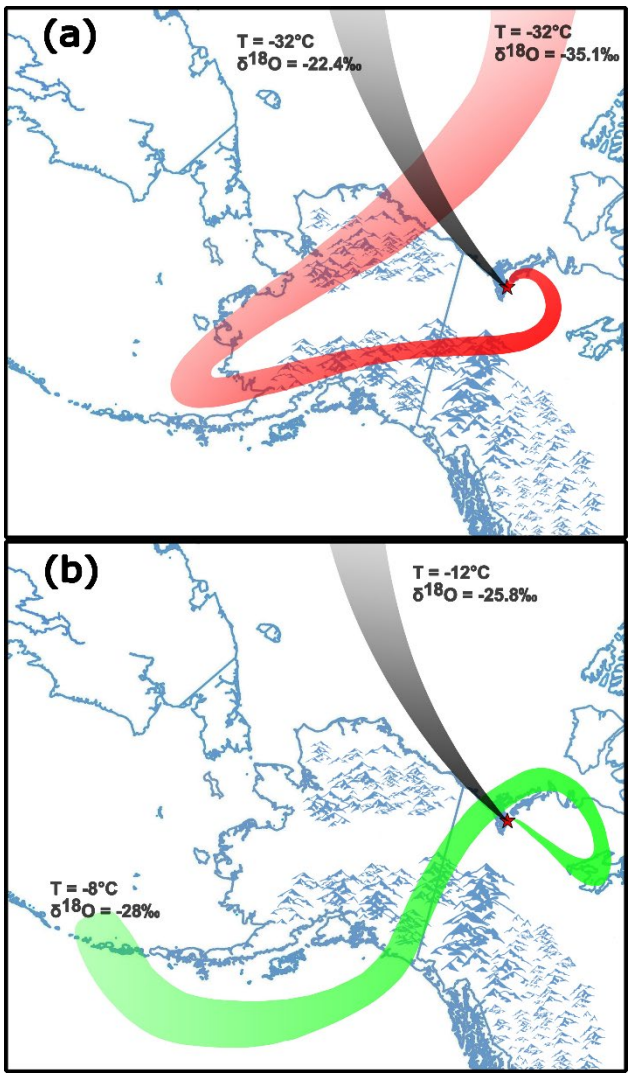

Figure 5. Illustration of storm trajectories derived from the HYSPLIT model. All trajectories show 13 days of travel. Red trajectory in (a) represents the path taken by the air mass responsible for an event on 23 January 2017; the black trajectory represents a path up to 10 February 2017. The black trajectory in (b) represents the path taken by the air mass responsible for an event on 29 October 2015; the green trajectory represents a path up to 2 November 2015.

the world, except at very high altitude (> 5000 m a.s.l) and in the Himalayas. When applied to the Canadian western Arctic, the influence of fractionation during southerly passage over mountains lowers $\delta^{18}O$ to values similar to those derived from the cold source in the Arctic Ocean nearby.

Westerly and southerly storms have $\delta^{18}O$ values similar to northern storms despite being associated with warmer air temperatures. Air masses from the south and west pass over the Coast and St. Elias mountains upon landfall, and Mackenzie Mountains once farther inland (Figure 1). Western storms typically pass over the Brooks Range in Alaska and Richardson Mountains before reaching Inuvik (Figure 1). Occasionally, air masses from the west made landfall over eastern Siberia, travelling over the Chukotka Mountains.

5.2 $\delta^{18}O$:T Relations

The regression coefficients reported here are lower than for precipitation in Antarctica (0.57‰ °C^{-1}) and Siberia (0.50‰ °C$^{-1;}$ Schlosser et al. 2004; Kostrova et al. 2020). The coefficients for all storms (e.g., 0.3‰ °C^{-1}; Tables 3 and 4) are lower than the slope determined by Porter et al. (2016) for mid-high-latitude North America (0.41‰ °C^{-1}). Porter et al. (2016) demonstrate that the western Canadian Arctic has a relatively low slope for $\delta^{18}O$:T. The even lower slopes derived when storms from 2015–2018 were separated by season and direction illustrates the complexity of these relations in the specific physiographic location of Inuvik (Table 4).

At a monthly timescale, as summarized in Table 5, the coefficients are similarly lower than data from Antarctica and Siberia, but in winter, especially, the coefficient of determination indicates a weak relation.

5.3 Influence on Ground Ice

Mackay (1983a) indicated characteristic values for $\delta^{18}O$ in various types of ground ice in western Arctic Canada. He gave a range of -18 to -20‰ for the $\delta^{18}O$ value in active layer ice. Summer precipitation from 1985–1995 had $\delta^{18}O$ values consistent with this range (see Appendix). More recently, higher $\delta^{18}O$ values have been observed (Table 2). He associated aggradational ice, i.e., the transient layer, with active layer ice now incorporated in permafrost (Mackay 1983b). He associated wedge ice (-22 to -26‰) with winter precipitation (Mackay, 1990). The $\delta^{18}O$ values for precipitation collected from 1985–1995 are below this range (see Appendix). However, they are consistent with the recent winter precipitation (Table 2). The origin of wedge ice from snow melt implies that its $\delta^{18}O$ values should be consistent with winter precipitation. In this case, the precipitation at the time of Mackay's sampling probably had lower $\delta^{18}O$ values than recently, as suggested by the 1985–95 data. Michel (1990) also noted inconsistencies between $\delta^{18}O$ in ice wedges and regional winter precipitation. Such uncertainty reduces confidence in granular interpretation of paleoclimate from wedge ice sequences over and above the weakness of the isotope-climate relations from analysis of individual storms presented here.

6 Conclusions

We draw four principal conclusions:

(1) In the western Canadian Arctic, the isotopic composition of precipitation from different source areas is relatively consistent during the summer and winter seasons because fractionation during transport over mountains to the south or west induces a similar stable isotopic composition as in precipitation coming from the Arctic Ocean.

(2) $\delta^{18}O$:T relations in precipitation at Inuvik vary with the origin of air masses and by season. The regression coefficients for $\delta^{18}O$ on T of data collected from individual

storms in summer 2015–2018 ranged from 0.11 to 0.35‰ °C^{-1} and from 0.16 to 0.28‰ °C^{-1} in winter.

(3) R^2 for $\delta^{18}O$ on T for individual events by season in 2015–2018 were ≤ 0.47 in summer and ≤ 0.37 in winter. None of the winter relations between $\delta^{18}O$ and T were statistically significant at α = 0.05. The relations derived from aggregate samples had R^2 ≤ 0.55 in summer and winter and were statistically significant.

(4) Aggregate $\delta^{18}O$:T relations for precipitation and temperature at Inuvik, derived from all precipitation and using monthly mean temperature, deliver regression coefficients of 0.46 and 0.26‰ °C^{-1} in summer and winter, respectively.

Overall, these results indicate the relations between $\delta^{18}O$ and T at a near-coastal location in western Arctic Canada are weak when derived on an event-by-event basis but are statistically stronger from smoothed aggregate samples.

7 Acknowledgements

We thank Trevor Andersen for assistance with the HYSPLIT model and with the climate record for Inuvik. Ian McKendry drew our attention to HYSPLIT. Isotopic data generated at the University of Western Ontario were kindly provided by Professor Fred Longstaffe. The research was supported by an NSERC Discovery Grant. Our field research in the western Arctic was also supported by the Aurora Research Institute and the Polar Continental Shelf Project of Natural Resources Canada. We would also like to thank Alberto Reyes and an anonymous reviewer for their valuable comments on this paper.

8 References

Burn, C.R., Michel, F.A., and Smith, M.W. 1986. 'Stratigraphic, Isotopic and Mineralogical Evidence for an Early Holocene Thaw Unconformity at Mayo, Yukon Territory', *Canadian Journal of Earth Sciences* 23(6), pp. 794–803. doi:10.1139/e86-081.

Chylek, P., Folland, C., Klett, J.D., Wang, M., Hengartner, N., Lesins, G., and Dubey, M.K. 2022. 'Annual Mean Arctic Amplification 1970–2020: Observed and Simulated by CMIP6 Climate Models', *Geophysical Research Letters* 49(13). doi:10.1029/2022gl099371.

Craig, H. 1961. 'Isotopic Variations in Meteoric Waters', *Science* 133(3465), pp. 1702–1703.

Dansgaard, W. 1964. 'Stable Isotopes in Precipitation', *Tellus* 16(4), pp. 436–468. doi:10.1111/j.2153-3490.1964.tb00181.x.

Environment Canada 2023. *Historical Climate Data, Inuvik Airport (2015–2018)*. Available at: https://climate.weather.gc.ca/index_e.html.

Fritz, M., Wetterich, S., McAlister, J., and Meyer, H. 2021. 'Stable Oxygen ($\delta^{18}O$) and Hydrogen (δD) Isotopes in Precipitation from Inuvik in the Western Canadian Arctic (2015–2018)', *PANGAEA* [dataset], https://doi.org/10.1594/PANGAEA.935027.

Fritz, M., Wetterich, S., McAlister, J., and Meyer, H. 2022. 'A New Local Meteoric Water Line for Inuvik (NT, Canada)', *Earth System Science Data* 14(1), pp. 57–63. doi:10.5194/essd-14-57-2022.

Gonfiantini, R. 1978. 'Standards for Stable Isotope Measurements in Natural Compounds', *Nature* 271(5645), pp. 534–536. doi:10.1038/271534a0.

Holland, K.M., Porter, T.J., Froese, D.G., Kokelj, S.V. and Buchanan, C.A. 2020. 'Ice-Wedge Evidence of Holocene Winter Warming in the Canadian Arctic', *Geophysical Research Letters* 47(12). doi:10.1029/2020GL087942.

Kostrova, S.S., Meyer, H., Fernandoy, F., Werner, M., and Tarasov, P.E. 2020. 'Moisture Origin and Stable Isotope Characteristics of Precipitation in Southeast Siberia', *Hydrological Processes* 34(1), pp. 51–67. doi:10.1002/hyp.13571.

Kotler, E. and Burn, C.R. 2000. 'Cryostratigraphy of the Klondike "Muck" Deposits, West-Central Yukon Territory', *Canadian Journal of Earth Sciences* 37(6), pp. 849–861. doi:10.1139/e00-013.

Mackay, J.R. 1983a. 'Oxygen Isotope Variations in Permafrost, Tuktoyaktuk Peninsula Area, Northwest Territories', *Geological Survey of Canada* Paper 83-1B, pp. 67–74. doi:10.4095/132539.

Mackay, J.R. 1983b. 'Downward Water Movement into Frozen Ground, Western Arctic Coast', *Canadian Journal of Earth Sciences* 20(1), pp. 120–134. doi:10.1139/e83-012.

Mackay, J.R. 1990. 'Some Observations on the Growth and Deformation of Epigenetic, Syngenetic and Anti-Syngenetic Ice Wedges', *Permafrost and Periglacial Processes* 1(1), pp. 15–29. doi:10.1002/ppp.3430010104.

Michel, F.A. 1990. 'Isotopic Composition of Ice-Wedge Ice in Northwestern Canada', in *5th Canadian Permafrost Conference*. Québec City, Québec, Canada: June 6–8, 1990, pp. 5–9.

Meyer, H., Opel, T., Laepple, T., Dereviagin, A.Y., Hoffmann, K., and Werner, M. 2015. 'Long-Term Winter Warming Trend in the Siberian Arctic During the Mid- to Late Holocene', *Nature Geoscience* 8(2), pp. 122–125. doi:10.1038/ngeo2349.

Opel, T., Laepple, T., Meyer, H., Dereviagin, A.Y., and Wetterich, S. 2017. 'Northeast Siberian Ice Wedges Confirm Arctic Winter Warming Over the Past Two Millennia', *The Holocene* 27(11), pp. 1789–1796. doi:10.1177/0959683617702229.

Poage, M.A. and Chamberlain, C.P. 2001. 'Empirical Relationships Between Elevation and the Stable Isotope Composition of Precipitation and Surface Waters: Consideration for Studies of Paleoelevation Change', *American Journal of Science* 301(1), pp. 1–15. doi:10.2475/ajs.301.1.1.

Porter, T.J., Froese, D.G., Feakins, S.J., Bindeman, I.N., Mahony, M.E., Pautler, B.G., Reichart, G.J., Sanborn, P.T., Simpson, M.J., and Weijers, J.W.H. 2016. 'Multiple Water Isotope Proxy Reconstruction of Extremely Low Last Glacial Temperatures in Eastern Beringia (Western Arctic)', *Quaternary Science Reviews*, pp. 113–125. doi:10.1016/j.quascirev.2016.02.006.

Schetselaar, A., Andersen, T., and Burn, C.R. 2023. 'Performance of Climate Projections for Yukon and Adjacent Northwest Territories, 1991–2020', *Arctic* 76(3), pp. 244–264. doi:10.14430/arctic77263.

Schlosser, E., Reijmer, C., Oerter, H., and Graf, W. 2004. 'The Influence of Precipitation Origin on the $\delta^{18}O$:T Relationship at Neumayer Station, Ekstrmisen, Antarctica', *Annals of Glaciology*, pp. 41–48. doi:10.3189/172756404781814276.

Serreze, M.C. and Barry, R.G. 2011. 'Processes and Impacts of Arctic Amplification: A Research Synthesis', *Global and Planetary Change* 77(1), pp. 85–96. doi:10.1016/j.gloplacha.2011.03.004.

Stein, A.F., Draxler, R.R., Rolph, G.D., Stunder, B.J.B., Cohen, M.D., and Ngan, F. 2015. 'NOAA's HYSPLIT Atmospheric Transport and Dispersion Modeling System', *Bulletin of the American Meteorological Society* 96(12), pp. 2059–2077. doi:10.1175/BAMS-D-14-00110.1.

Thienpont, J.R., Rühland, K.M., Pisaric, M.F.J., Kokelj, S.V., Kimpe, L.E., Blais, J.M., and Smol, J.P. 2013. 'Biological Responses to Permafrost Thaw Slumping in Canadian Arctic Lakes', *Freshwater Biology* 58(2), pp. 337–353. doi: 10.1111/fwb.12061.

Appendix. Mean monthly temperature (T, °C), total monthly precipitation (P, mm), and $\delta^{18}O$ (‰) for aggregate samples of monthly precipitation collected at Inuvik Airport between March 1989 and May 1995.

Date	T	P	$\delta^{18}O$	Date	T	P	$\delta^{18}O$	Date	T	P	$\delta^{18}O$
03/1989	-23.5	4.4	-25.0	**04/1991**	-8.2	6.0	-23.1	**06/1993**	12.6	3.7	-11.4
04/1989	-9.4	1.6	-28.7	**05/1991**	5.9	20.6	-18.3	**07/1993**	15.2	29.2	n/a
05/1989	0.5	18.7	-23.7	**06/1991**	10.5	33.4	-18.2	**08/1993**	11.0	41.6	-20.8
06/1989	12.3	20.2	-14.8	**07/1991**	12.4	16.7	-16.6	**09/1993**	4.2	30.6	-18.2
07/1989	16.5	63.2	-16.8	**08/1991**	9.1	73.2	-20.2	**10/1993**	-4.3	27.3	-24.4
08/1989	15.5	32.8	-16.9	**09/1991**	4.2	41.5	-19.3	**11/1993**	-17.8	13.9	-26.8
09/1989	5.3	53.9	-19.0	**10/1991**	-7.5	29.6	-23.4	**12/1993**	-23.1	19.6	-27.4
10/1989	-8.2	36.8	-28.3	**11/1991**	-24.1	13.1	-32.5	**01/1994**	-31.1	4.0	n/a
11/1989	-27.9	11.0	-34.4	**12/1991**	-29.2	9.3	-25.6	**02/1994**	-27.3	21.2	-28.9
12/1989	-26.1	11.4	-27.6	**01/1992**	-28.7	24.0	-29.8	**03/1994**	-21.9	26.1	-30.6
01/1990	-32.7	18.4	-30.5	**02/1992**	-28.2	14.8	-23.3	**04/1994**	-12.3	14.8	-16.9
02/1990	-34.3	9.0	-31.2	**03/1992**	-16.2	11.4	-24.5	**05/1994**	3.0	20.0	-20.8
03/1990	-16.3	19.6	-30.8	**04/1992**	-15.3	28.1	-27.5	**06/1994**	10.3	31.9	-18.2
04/1990	-7.7	13.1	-24.6	**06/1992**	11.8	17.1	-19.2	**07/1994**	18.3	26.0	-14.4
05/1990	1.6	0.2	n/a	**07/1992**	14.2	26.6	-17.8	**08/1994**	14.9	44.5	-15.5
06/1990	11.3	16.0	-21.9	**08/1992**	11.7	29.0	-18.3	**09/1994**	1.2	31.7	-21.4
07/1990	15.5	58.0	-18.8	**09/1992**	-1.4	48.2	-24.9	**10/1994**	-5.3	21.4	-23.9
08/1990	9.7	10.2	-15.1	**10/1992**	-10.6	26.8	-21.5	**11/1994**	-22.8	34.7	-32.5
09/1990	3.2	31.7	-21.9	**11/1992**	-19.0	14.8	-28.2	**12/1994**	-25.2	19.7	-34.1
10/1990	-7.4	25.8	-29.3	**12/1992**	-24.7	19.1	-28.7	**01/1995**	-23.6	8.0	-29.4
11/1990	-26.9	20.8	-26.7	**01/1993**	-22.8	27.5	-29.5	**02/1995**	-26.0	23.2	-29.1
12/1990	-28.7	12.4	-28.4	**02/1993**	-21.3	23.2	-27.5	**03/1995**	-25.0	23.2	-28.4
01/1991	-25.0	20.0	-28.3	**03/1993**	-18.8	6.6	-26.0	**04/1995**	-7.5	3.3	-17.1
02/1991	-28.5	13.4	-33.4	**04/1993**	-1.5	5.6	-22.5	**05/1995**	5.3	25.6	-22.9
03/1991	-23.6	19.2	-29.2	**05/1993**	0.9	8.6	-28.1				
Winter (October–April) Mean $\delta^{18}O$ 1985–1995:						**-28.2**					
Summer (May–September) Mean $\delta^{18}O$ 1985–1995:						**-19.2**					
Annual Mean $\delta^{18}O$ 1985–1995:						**-24.8**					
Winter (October–April) Mean $\delta^{18}O$ 1989–1995:						**-27.5**					
Summer (May–September) Mean $\delta^{18}O$ 1989–1995:						**-19.5**					
Annual Mean $\delta^{18}O$ 1989–1995:						**-24.3**					

Permafrost monitoring and assessment in Nunavut, Canada

Caroline Duchesne, Sharon L. Smith, Marcus R. Phillips & Jason Chartrand

Geological Survey of Canada, Natural Resources Canada, Ottawa, Ontario, Canada

ABSTRACT

Long-term permafrost thermal conditions can be indicators of a changing climate and provide essential baseline information to support land-management activities and northern infrastructure planning. Permafrost temperatures in Nunavut, Canada have been measured by the Geological Survey of Canada since 1978 at Alert. In 2008 and 2009, permafrost monitoring sites were established near several communities in collaboration with the Nunavut Government and community members. Analysis of these time-series allows an assessment of long-term changes in the ground thermal regime. In the high Arctic, ground temperatures at 24 m depth at Alert have increased at a rate of 0.4ºC per decade since 1978, but the rate has increased to 0.6 °C per decade since 2000, reflecting the greater warming observed in air temperature records. At Resolute Bay, at 15 m depth, permafrost has warmed by 1.1 °C per decade since 2008. Annual mean ground temperatures in 2022 were less than -10 °C for Alert boreholes and -10.2 °C for Resolute Bay. Farther south on Baffin Island, annual mean ground temperatures at 15 m depth in 2020–21 ranged from -4.8 to -9.4 °C and since 2008 have increased by 0.4 to 0.7 °C per decade. The monitoring sites are sparsely vegetated, generally with a thin layer of surficial deposits; hence ground temperatures are not as affected by buffering effects and closely reflect the temporal variation in air temperature observed in the Eastern Canadian Arctic.

1 INTRODUCTION

Most of Nunavut's landmass is within the continuous permafrost zone. Knowledge of current permafrost thermal conditions and their temporal variability in response to a changing climate is essential for informed infrastructure design and community adaptation planning. This is important given that climate warming is greater at higher latitudes, with increases in air temperature in Northern Canada of more than 2 °C since 1948 (Cohen et al. 2019). Changes in permafrost conditions can also have impacts on landscape stability and ecosystems, affecting the way of life of northerners.

In 2008 and 2009, permafrost monitoring sites were established in ten communities in Nunavut by the Geological Survey of Canada (GSC) in collaboration with the Nunavut Government and community members (Figure 1). These sites complement the long-term monitoring sites at Canadian Forces Station (CFS) Alert that were established in 1978 (Taylor et al. 1982) and one site maintained by Environment Canada in Iqaluit (Environment Canada 2005). In addition, two sites in the Kivalliq region at Baker Lake and Rankin Inlet provide information for central Nunavut (Figure 1).

This paper provides a summary of permafrost temperatures collected since 2008-09 at the community monitoring sites. The changes in temperature between 2008 and 2021 are also described for selected sites and are placed in the context of the longer record available for Alert.

2 NUNAVUT PERMAFROST MONITORING

Monitoring sites are located in the central and eastern Arctic within the Northern and Southern Arctic ecozones characterized by sparse and stunted vegetation. Mean annual air temperature, based on 1980–2010 climate normals (Environment and Climate Change Canada 2023) ranges from -9.3 to -17.7 °C in Iqaluit and Alert respectively,

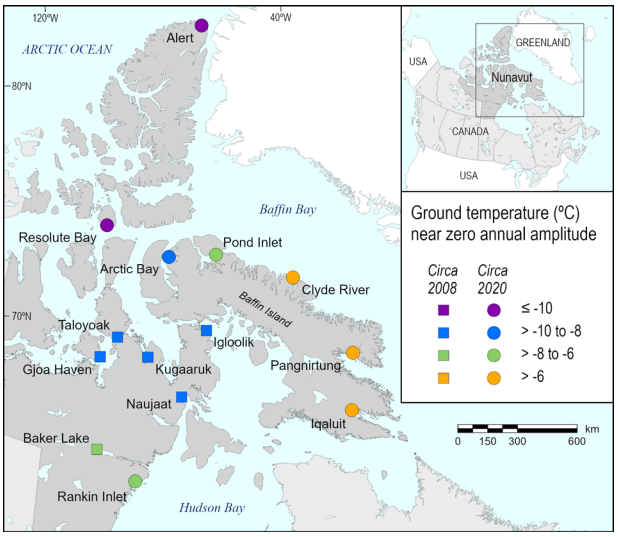

Figure 1. Location of Nunavut permafrost monitoring sites. Annual mean ground temperatures (AMGT) at the deepest sensor are shown.

With January and June temperatures ranging from -26.9 to -32.2 °C and -0.4 to 3.6 °C respectively. Total normal precipitation ranges from 158 to 404 mm for Alert and Iqaluit with about 89 to 51% falling as snow, mostly between October and May.

GSC maintains 14 permafrost monitoring sites in Nunavut (Table 1; Figure 1). In the high Arctic at CFS Alert, three 60 m and two 15 m deep boreholes were instrumented with multi-thermistor (YSI 44033) temperature cables in 1978 (Taylor et al. 1982). Ground temperature measurements

https://doi.org/10.52381/ICOP2024.156.1

were made with a multimeter at one to three-month intervals. In 2000, three boreholes were instrumented with dataloggers (RBR Ltd.) recording temperatures at eight-hour intervals (Smith et al. 2003). The measurement system allows for an overall resolution and accuracy of 0.1 °C or better.

For sites established in 2008–09 in ten Nunavut communities (Table 1), 15 m deep boreholes were instrumented with a multi-thermistor (YSI 44033) temperature cable connected to an RBR data logger collecting data at eight-hour intervals. Most boreholes were drilled in relatively undisturbed terrain with sparse vegetation. A more detailed description of borehole establishment and surficial materials is provided in Ednie and Smith (2010, 2011, 2015).

Table 1. Location and characteristics of permafrost monitoring boreholes in Nunavut. The asterisk denotes sites no longer in operation.

Community	Lat (ºN)	Long (ºW)	Year Est.	Bore-hole Depth (m)	Surficial material at borehole location
Arctic Bay	73.04	85.18	2008	15	Till, gravel surface
Baker Lake	64.33	96.04	1997	3	Coarse till
Alert BH1	82.51	62.28	1978	60	Shattered rock
Alert BH5	82.48	62.44	1978	15	Shattered rock
Clyde River	70.48	68.51	2008	15	Glaciomarine material
Gjoa Haven	68.63	95.85	2009	15	Exposed beach ridges
Igloolik*	69.38	81.80	2008	15	Marine littoral deposit
Iqaluit	63.74	68.47	1988	5	Exposed bedrock
Kugaaruk	68.54	89.79	2009	15	Exposed bedrock
Pangnirtung	66.14	65.71	2008	15	Colluvial blanket
Pond Inlet	72.69	77.95	2008	15	Till, hummocky plain
Rankin Inlet	62.83	92.13	2017	7	Till, marine sediments
Naujaat*	66.53	86.23	2009	15	Stratified sand and silt
Resolute Bay	74.72	94.97	2008	15	Frost shattered bedrock
Taloyoak	69.54	93.56	2009	15	Till veneer

Two of the boreholes installed in 2008–09 are no longer active. The cable at Naujaat was damaged in 2013. The Igloolik site was damaged between 2011 and 2021. These sites were abandoned and there has been no further data collected beyond that reported in Ednie and Smith (2015). Instrument malfunctions and infrequent site visits have also led to gaps in the data records at Taloyoak, Gjoa Haven and Kugaaruk. Data from these sites are not discussed in detail in this paper.

GSC has established other instrumented boreholes in Nunavut. A 3 m deep borehole was instrumented at Baker Lake in 1997 but was abandoned in 2009. However, it was re-established in 2021. In Rankin Inlet, a 7 m borehole was established in 2017 (Leblanc and Oldenborger 2021). Environment Canada instrumented a 5 m borehole in Iqaluit in 1988 (Environment Canada 2005) at which GSC installed an RBR data logger in 2016. There are however limited recent data available for these sites.

3 Results and Discussion

3.1 Ground temperature

Current annual mean ground temperatures (AMGT) at a depth of 15 m range from > -5 °C in the southern Baffin region at Pangnirtung to < -13 °C at Alert (Figure 1) reflecting the general decrease in air temperature with latitude. At a depth of 15 m, annual temperature variations are greater than 0.1 °C for most sites (Figure 2).

Seasonal fluctuations in air temperature are not completely filtered out at these depths. The depth of zero annual amplitude (DZAA) is therefore greater than 15 m at these sites.

The annual range in temperature at 15 m depth varies from 1.36 to 0.07 °C for Resolute Bay and Pangnirtung respectively (Table 2; Figure 2). Data from the deeper boreholes at Alert indicate that DZAA is about 20 m (Throop et al. 2012). For other sites seasonal variation generally becomes negligible at depths greater than 18 m except for Pangnirtung and Rankin Inlet where the DZAA is close to 14 m (Table 2).

Analysis of time-series of temperature data collected at the sensor nearest the DZAA, allows an assessment of long-term changes in the ground thermal regime. Current AMGT at all sites are greater than what they were in 2008 (Figures 2 and 3). For example, in 2022, AMGT at 15 m depth was -10.2 ºC for Resolute Bay, almost 2 °C higher than in 2008. Farther south on Baffin Island, AMGT at 15 m depth in 2020–21 ranged from -4.8 to -9.4 °C, up to 1 °C higher than in 2008.

Since 2008, AMGT at the community monitoring sites have increased between 0.4 to 0.7 °C per decade on Baffin Island and 1.1ºC per decade at Resolute (Figure 4). It should be noted that for some sites there is substantial interannual variation in temperature at 15 m depth, as the record for Resolute shows. Although the records for the community sites are only 10 to 12 years long, the rate of warming is similar to that observed at Alert since 2000, which is 0.6 and 0.9 °C per decade at 24 and 15 m depth respectively. These rates are considerably higher than those observed at forested sites in the Mackenzie Valley for example (Duchesne et al. 2020). This is due to the sparse vegetation and limited buffer layer such as organic layer at the Nunavut sites. The cold permafrost conditions also mean that latent heat effects are negligible, making ground temperatures more responsive to changes in air temperature (Romanovsky et al. 2010).

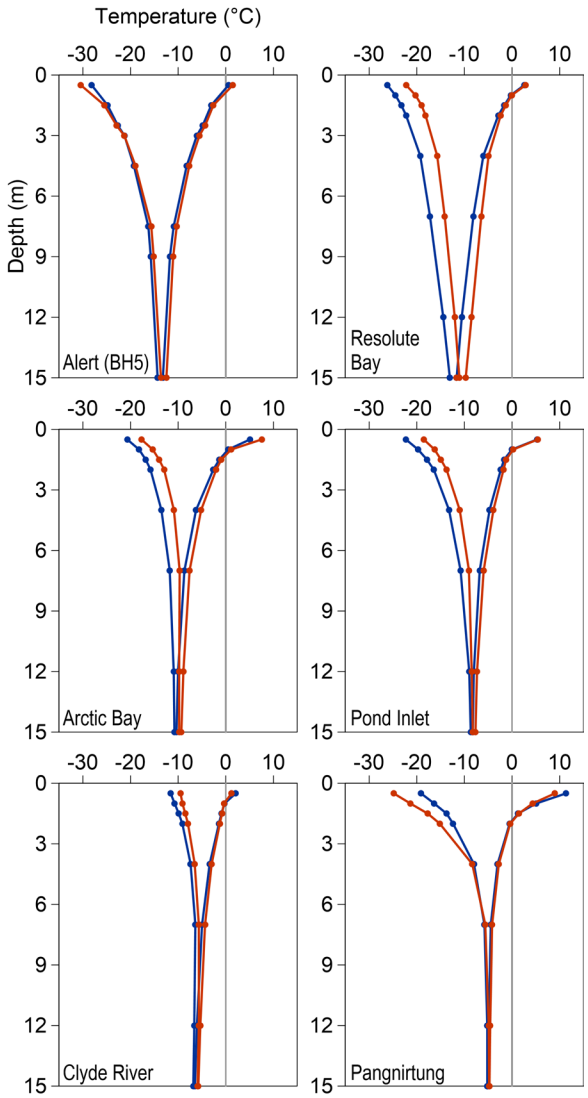

Figure 2. Ground temperature envelopes for selected sites in Nunavut. Maximum and minimum temperatures are presented for the beginning of the record (blue line), in 2008–09 (Alert 2007–08; Clyde River 2011–12), and for the most recent data available (red line), in 2019–20 (Resolute Bay 2021–22; Clyde River 2020–21).

Table 2. Estimated DZAA for specified time period and range in ground temperature (GT) at deepest sensor.

Community	Range in GT (ºC)	Depth (m)	DZAA (m)	Period (Sep. 1 to Aug. 31)
Arctic Bay	0.42	15	19.4	2009-10
Alert (BH5)	1.09	15	25.9	2007-08
Clyde River	0.33	15	18.7	2011-12
Gjoa Haven	1.22	15	28.8	2018-19
Igloolik	0.42	15	21.1	2009-10
Iqaluit	8.48	5	19.3	2001-02
Kugaaruk	0.42	15	20.4	2011-12
Pangnirtung	0.07	15	14.1	2008-09
Pond Inlet	0.42	15	20.2	2008-09
Rankin Inlet	2.24	7	14.0	2021-22
Naujaat	0.68	15	24.4	2011-12
Resolute Bay	1.36	15	29.4	2009-10

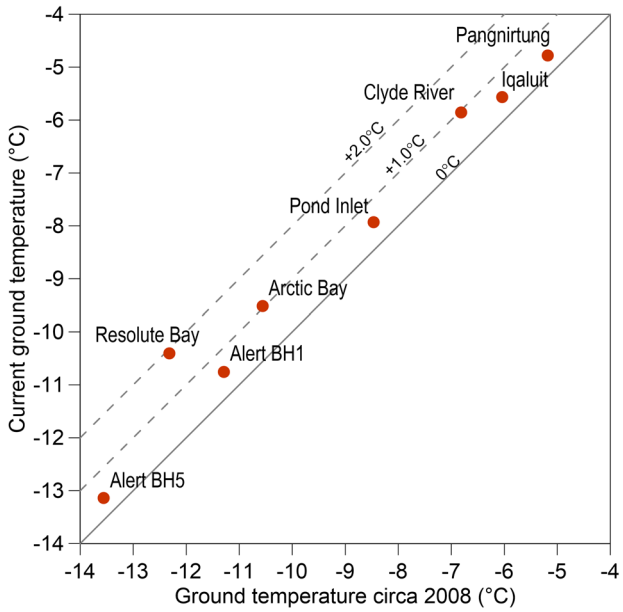

Figure 3. Comparison of AMGT at 15 m at most sites (24.4 m and 5 m for Alert BH1 and Iqaluit respectively) between the early record and the most recent data. The dashed lines represent an increase in temperature of 1 ºC and 2 ºC.

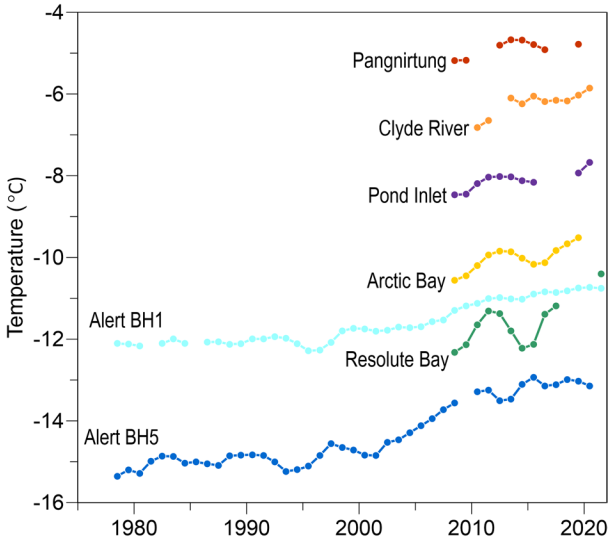

Figure 4. AMGT at 15 m depth (except for Alert BH1 at 24.5 m) for sites in Nunavut, Canada.

Changes in ground temperature generally reflect the temporal variation in air temperature (Figure 5). Increases in air temperature since the 1950s range from 0.14 to 0.28 °C per decade for Baffin Island and up to 0.39 °C per decade in the high Arctic. However, most of this warming has occurred since the late 1980s with a greater rate in the 21st century, especially in the high Arctic (Figure 5). Greater permafrost warming after 2000 is also observed in the longer records from Alert (Figure 4). For some sites (e.g., Resolute), the 15 m ground temperature record reflects the interannual variability in air temperature, with short periods of warming and cooling.

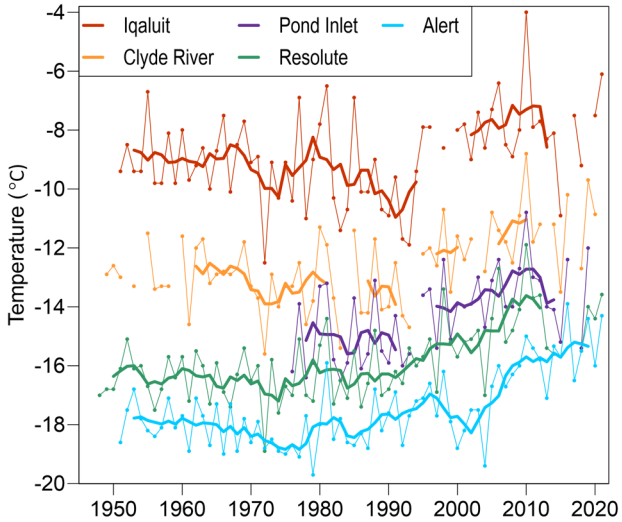

Figure 5. Annual mean air temperature for the eastern and high Arctic from weather stations where data is of sufficient quality (Environment and Climate Change Canada 2023). Thick lines present five-year running average at each station.

3.2 Active Layer Thickness

Active layer thickness (ALT) is extrapolated (when data are available) or interpolated from the shallow maximum annual ground temperature (Riseborough 2008). Shallow sensors are located at 50 and 100 cm deep at all sites except for Alert BH5, where the first and second sensors are at 76 and 152 cm respectively. At Alert, the maximum thaw depth did not reach the first sensor until 2003. Active layers are generally less than 150 cm thick at the community sites (Table 3; Figure 6). Average ALT ranges from 90 cm at Clyde River to 147 cm at Pangnirtung (Table 3). However, there is high amount of interannual variation.

Table 3. Average active layer thickness, interannual variation (range) and rates of change for selected sites. Rate of change is determined from a fitted linear regression. See figure 6 for record period.

Community	Average ALT (cm)	Range (cm)	Rate of change (cm / decade)
Arctic Bay	107	13	1.22
Alert BH5	96	29	2.53
Clyde River	90	9	0.17
Pangnirtung	147	19	-1.97
Pond Inlet	101	6	-0.89
Resolute Bay	93	51	-7.51

The level of confidence in the assessment of trends in ALT is generally low due to the relatively short records and large interannual variability (Figure 6). At most community sites, the change in ALT since 2008 is negligible and in some cases the trend is negative (Table 3). However, trends are not statistically significant for any of the sites. Similar regional ranges in trends are also found at sites elsewhere in northern permafrost zones (e.g., Smith et al. 2022).

Most of these sites are characterized by thin vegetation, low moisture content and thin snow cover, and so have little to provide a buffer between air and ground temperatures. ALT variations will therefore reflect the interannual variation in air temperature. For example, lower values of ALT in 2013 at some sites, such as Resolute Bay, Arctic Bay, Pond Inlet and Clyde River, coincide with lower mean annual air temperature (Figures 5 and 6). Higher air temperature is reflected in greater ALT values in 2010. Similar variations in ALT in response to warm or cold years have been reported elsewhere in the Arctic (e.g., Isaksen et al. 2022; O'Neill et al. 2023).

4 Summaries

An increased number of active permafrost monitoring sites in Nunavut has enhanced our knowledge of baseline ground thermal conditions. The ongoing operation of these sites and the extension of ground temperature records allows us to reduce uncertainty in assessing the changes in permafrost thermal state.

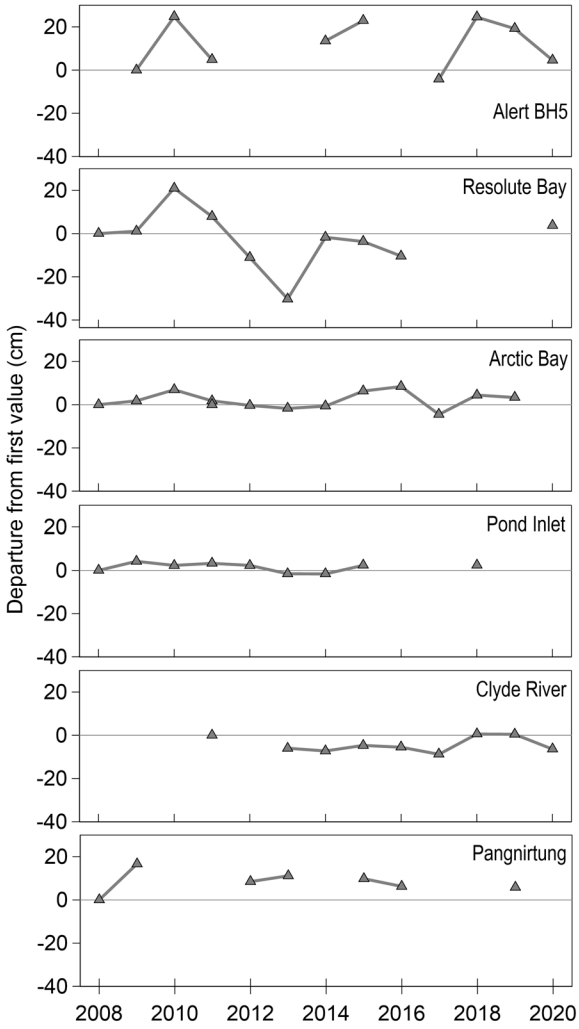

Figure 6. Departures of ALT from initial values based on interpolation from shallow maximum annual ground temperatures, for selected sites with the longest records.

Analysis of ground temperature records indicates that there has been a general warming of permafrost in Nunavut. The monitoring sites are sparsely vegetated, generally with a thin layer of surficial deposits; hence, ground temperatures are not as affected by buffering effects and closely reflect the increase in air temperature observed in the Eastern Canadian Arctic. Permafrost warming has therefore been greater than that observed at forested sites in other regions of northern Canada. Trends in active layer thickness are less clear due to the large amount of interannual variability.

Although the addition of monitoring sites since 2008 has helped to fill spatial gaps in the Nunavut portion of the Canadian permafrost monitoring network, there are significant regional gaps, especially in western Nunavut. We hope that ongoing efforts to collaborate with Nunavut partners will help to enhance the network and increase our ability to maintain existing sites and limit data loss. This ongoing data collection is essential for improved assessments of climate change impacts and to ensure that adequate baseline information is available to inform adaptation planning.

5 Acknowledgements

This research is supported by Natural Resources Canada. Establishment of monitoring sites, their maintenance and data collection would not have been possible without the contributions of several partners and colleagues including the Nunavut Government, members of the various communities, Parks Canada, Environment and Climate Change Canada, Department of National Defence and Polar Continental Shelf Program. We also thank Anne-Marie Leblanc for providing data from Rankin Inlet. Helpful comments from H. Brendan O'Neill and two anonymous reviewers were much appreciated. This paper is Natural Resources Canada contribution #20230338.

6 References

Cohen, S., Bush, E., Zhang, X., Gillett, N., Bonsal, B., Derksen, C., Flato, G., Greenan, B., and Watson, E. 2019. 'Synthesis of Findings for Canada's Regions', in E. Bush and D.S. Lemmen (eds.) *Canada's Changing Climate Report*, Chapter 8, Government of Canada, Ottawa, Ontario, pp. 424–443.

Duchesne, C., Chartrand, J., and Smith, S.L. 2020. 'Report on 2018 field activities and collection of ground-thermal and active-layer data in the Mackenzie corridor, Northwest Territories', *Geological Survey of Canada* Open File 8707. doi:10.4095/321921.

Environment and Climate Change Canada 2023. 'Historical Climate Data', *Environment and Climate Change Canada Historical Climate Data*. Available at: https://climate.weather.gc.ca/index_e.html.

Ednie, M. and Smith, S.L. 2010. 'Establishment of community-based permafrost monitoring sites, Baffin region, Nunavut', in *GEO2010, 63rd Canadian Geotechnical Conference & 6th Canadian Permafrost Conference*. Calgary, Alberta, Canada, pp. 1205–1211.

Ednie, M. and Smith, S.L. 2011. 'Establishment of Community-based Permafrost Monitoring Sites and Initial Ground Thermal Data Baffin Region, Nunavut', *Geological Survey of Canada* Open File 6727. doi:10.4095/287873.

Ednie, M. and Smith, S.L. 2015. 'Permafrost temperature data 2008-2014 from community-based monitoring sites in Nunavut', *Geological Survey of Canada* Open File 7784. doi:10.4095/296705.

Environment Canada 2005. *Climate-Permafrost Data 1985-2004.* Climate Research Branch, Downsview Ontario.

Isaksen, K., Lutz, J., Sorensen, A.M., Godoy, O., Ferrighi, L., Eastwood, S., and Aaboe, S. 2022. 'Advances in operational permafrost monitoring on Svalbard and in Norway', *Environmental Research Letters* 17: 095012. doi:10.1088/1748-9326/ac8e1c.

LeBlanc, A.-M. and Oldenborger, G.A. 2021. 'Ground temperature, active-layer thickness and ground-ice conditions in the vicinity of Rankin Inlet, Nunavut', in *Summary of Activities 2020*, Canada-Nunavut Geoscience Office, pp. 63–72.

O'Neill, H.B., Smith, S.L., Burn, C.R., Duchesne, C., and Zhang, Y. 2023. 'Widespread permafrost degradation and thaw subsidence in northwest Canada', *Journal of Geophysical Research (Earth Surface)* 128(8): e2023JF007262. doi:10.1029/2023JF007262.

Riseborough, D.W. 2008. 'Estimating Active Layer and Talik Thickness from Temperature Data: Implications from Modeling Results', in *Proceeding of the Ninth International Conference on Permafrost*. Fairbanks, Alaska, United States: vol. 2 pp. 1487–1492.

Romanovsky, V.E., Smith, S.L., and Christiansen, H.H. 2010. 'Permafrost thermal state in the polar Northern Hemisphere during the International Polar Year 2007-2009: a synthesis', *Permafrost and Periglacial Processes* 21, pp. 106–116. doi:10.1002/ppp.689.

Smith, S.L., Burgess, and M.M., and Taylor, A.E. 2003. 'High Arctic permafrost observatory at Alert, Nunavut - analysis of a 23 year data set', in *Proceedings of 8th International Conference on Permafrost*. Zurich, Switzerland: vol. 2, pp. 1073–1078.

Smith, S.L., O'Neill, H.B., Isaksen, K., Noetzli, J., and Romanovsky, V.E. 2022. 'The changing thermal state of permafrost', *Nature Reviews Earth & Environment* 3, pp. 10–23. doi:10.1038/s43017-021-00240-1.

Taylor, A., Brown, R.J.E., Pilon, J., and Judge, A.S. 1982. 'Permafrost and the shallow thermal regime at Alert, N.W.T.', in *Proceedings of 4th Canadian Permafrost Conference*, National Research Council of Canada, Calgary, Alberta, Canada, pp. 12–22.

Throop, J., Lewkowicz, A.G., and Smith, S.L. 2012. 'Climate and ground temperature relations at sites across the continuous and discontinuous permafrost zones, northern Canada', *Canadian Journal of Earth Sciences* 49, pp. 865–876. doi:10.1139/E11-075.

Ground ice content of the frozen active layer and near-surface permafrost in the Rankin Inlet area, Nunavut, Canada

Benoit Faucher[1], Anne-Marie LeBlanc[1], Greg A. Oldenborger[1], Emmanuel Carrière[2], Denis Lacelle[2] & Philippe Letellier[3]

[1]*Geological Survey of Canada, Natural Resources Canada, Ottawa, Ontario, Canada*

[2]*Department of Geography, Environment and Geomatics, University of Ottawa, Ottawa, Ontario, Canada*

[3]*Institut National de Recherche Scientifique, Québec City, Québec, Canada*

Abstract

In the context of climate change, the distribution and amount of ground ice in permafrost is critical to evaluate surface disturbances and geohazard risks. Ground ice conditions are poorly defined in northwestern Hudson Bay in the central Canadian Arctic, an area with renewed development interest. Here, we report on the near-surface (< 2 m) ground ice content of the frozen active layer and permafrost from three sites with different surface materials near Rankin Inlet, Nunavut. Cores were retrieved from nearshore, till, and alluvial deposits (all intermixed with marine sediments). Ground ice content derived from CT scan images and laboratory measurements suggested a relatively high abundance of ground ice in the nearshore marine sediments and alluvial/marine sediment cores with a lower overall content in the till/marine sediment core. Computed tomography scan analyses commonly underestimated volumetric ice content compared to laboratory measurements. This may have been caused by the coarse pixel resolution of our CT scan images (0.6 mm), making the pore space diameters of our sampled fine sediments partially unresolvable. Further, in situ seasonal thaw settlement measurements taken at each site from heave sleeves corroborated our laboratory-derived excess ice content measurements reasonably well. Excess ice content measurements were also used to predict active layer thickness increases and ground subsidence under future air temperature increases. Overall, our study provides new information on ground ice conditions in the Rankin Inlet area of Nunavut.

1 Introduction

Accurate knowledge of the distribution and amount of ground ice in permafrost is critical to evaluating ground surface (GS) disturbances and geohazard risks in Arctic regions destined for development. It is generally accepted that permafrost-bearing soils' total annual GS subsidence (GSS) should depend on 1) thaw settlement, controlled by ground ice content; and 2) volume-compressibility caused by surcharge load and self-weight (Watson et al. 1973). The latter is often disregarded because consolidation comprises only a fraction of the surface settlement (Taber 1930). In addition, the thaw settlement potential of heterogeneous soils can often be assessed by determining the edaphic properties (e.g., dry densities of soils in frozen and thawed states) of individual soil horizons with depth. This permits the calculation of their thaw strain (Pullman et al. 2007; Crory 1973). However, thaw strain can also be derived from excess ice content (EIC) measurements (i.e., van Everdingen 2005) converted into a volumetric ratio of cumulative EIC to the total thickness of the thawed soil column (Castagner et al. 2022). These data are often indispensable to predicting local GSS and possible infrastructure damage (Doré et al. 2016).

Information on ground ice content, particularly EIC, is available from northwest Canada and a few sites in the eastern Arctic but is otherwise limited. There is little information on ground ice from the northwestern Hudson Bay area around Rankin Inlet, where the air temperature is increasing, and significant infrastructure development is occurring (LeBlanc and Oldenborger 2021).

Recent research has documented the thermal state of permafrost (Oldenborger et al. 2017; LeBlanc and Oldenborger 2021) and approximated seasonal GSS (Leblanc et al. 2019; Oldenborger et al. 2020) in the vicinity of Rankin Inlet. However, due to the scarcity of sampled and investigated permafrost cores, empirical volumetric ice content (VIC) and EIC measurements remain almost nonexistent (McCuaig et al. 2022).

This study investigates the VIC and EIC of the near-surface (< 2 m) permafrost (which includes the frozen active layer) at study sites near Rankin Inlet. The goals of this study are to 1) document and describe ground ice content in sampled soil units using laboratory measurements and to compare those with computed tomography (CT) scan measurements; and 2) assess site-specific GSS potential of our investigated frozen active layer/permafrost sampling sites under climate warming-induced thaw penetration (TP) increases. Overall, our study provides new information for understanding ground ice content and spatial distribution within the Rankin Inlet area of Nunavut.

2 Study Area

The hamlet of Rankin Inlet is in the Kivalliq region of Nunavut (Canada) on the western coast of Hudson Bay (Figure 1). The hamlet's territory is within the western Churchill Province of the Canadian Shield. Its complex geology consists of Archaean Rankin Inlet Greenstone Belt felsic volcanic rocks intercalated with mafic volcanic and sedimentary rocks and granodioritic to tonalitic intrusions (Lawley et al. 2016). The surficial geology consists of

https://doi.org/10.52381/ICOP2024.80.1

glacial, marine, and glaciofluvial deposits, including eskers, with numerous bedrock outcrops (McMartin 2002) that shape the topography with elevation ranging from sea level to 300 m. The Laurentide Ice Sheet covered the region during the Wisconsin glaciation and receded by ~6 kyr BP (Dyke 2004). The postglacial Tyrrell Sea extended up to 150 km inland from the current coastline over the isostatically depressed land surface, reaching a maximum elevation of approximately 170 m above the present sea level; (Dyke 2004; Randour et al. 2016; McMartin et al. 2023).

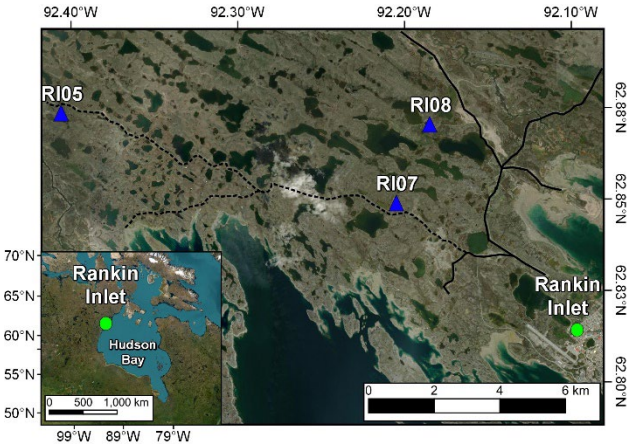

Figure 1. Location map of the frozen active layer/permafrost coring sites near Rankin Inlet (Nunavut). Coring sites and Rankin Inlet hamlet are indicated with blue triangles and green circles, respectively. Continuous and dotted lines show main roads and access trails. The background is a 0.46 m MAXAR Vivid image (September 3rd, 2022) of the area of interest.

The mean annual air temperature (MAAT) for Rankin Inlet was -10.3 °C from 1981–2020 (Environment and Climate Change Canada 2022), with an average increase of 0.05 ± 0.02 °C/year. Over the same period, the average total precipitation was 315 mm, with rainfall accounting for 184 mm and snow precipitations contributing 131 cm. There was no significant trend in total precipitation from 1981 to 2020.

Rankin Inlet is within the continuous permafrost zone, and the base of permafrost was estimated between 285 m and 430 m, with thinner permafrost being near lakes (Golder 2021). The geothermal gradient varies between 0.01 and 0.02 °C/m (Golder 2014), while the mean annual ground temperature at the top of permafrost ranges between -9.5 and -5.5 °C (LeBlanc and Oldenborger 2021). Active-layer thickness ranges from ~0.5 m in organic-rich alluvial/marine sediments to ~1.6 m in marine and organic-poor till deposits (LeBlanc and Oldenborger 2021).

3 METHODOLOGY

3.1 Field sampling

Study sites for ground temperature boreholes and permafrost coring in the Rankin Inlet region were planned to represent various terrain conditions, including developed and undeveloped land and different geological settings. Site locations were established after considering surficial geology, land access, community consultation, and field observations. Data from three shallow borehole sites with different surficial geology are analyzed herein: nearshore marine sediments (RI05); till and marine sediments (RI07); and alluvial and marine sediments (RI08; Figure 1). Site details and field observations concerning the retrieved cores and their sediments/apparent cryostructures are given by LeBlanc and Oldenborger (2021).

Boreholes at sites RI05 and RI07 were drilled in June 2018 and 2019 at site RI08 using a portable earth drill using barrels with diamond core bits modified from Calmels et al. (2005). Any unfrozen organic mat and unfrozen sediments to a depth of 2 to 15 cm were removed, set aside, and replaced as best as possible to reduce thermal disturbances as much as possible. However, some thermal disturbance to the sites occurred. Cores were measured and visually logged during drilling, bagged in plastic, and frozen for further analysis.

The shallow boreholes were cased with either sealed 1 ½" PVC pipe with an internal multi-core thermistor cable in silicone bath oil (RI05 and RI07) or with open ¾" PVC pipe with individual external thermistors (RI08). Thermistors were routed to the surface and logged continuously with 4-hour recording intervals. Ground temperatures were recorded with RBR data loggers (0.01 °C resolution; RI05 and RI07) and an Onset HOBO U12 data logger (± 0.25 °C accuracy; RI08). Ground surface temperatures (2–5 cm depth) were recorded with 4-hour recording intervals with Onset HOBO Water Temp Pro v2 loggers (± 0.21 °C accuracy; all sites).

3.2 Computed tomography scanning and image processing

For the last two decades, computed tomography (CT) scans have routinely been used to rapidly quantify volumetric ground ice contents and produce high-resolution cryostratigraphic profiles of permafrost-bearing soils (e.g., Calmels and Allard 2004, 2008; Gadylyaev et al. 2021; Fan et al. 2021).

For our study, the samples were scanned at the Institut national de la recherche scientifique (INRS) using a SOMATOM Definition AS+ 128 CT scanner by SIEMENS at 140 kV and with an exposure of 200 mAs. We then segmented the CT scan images of our permafrost cores to obtain a quick first-order estimate of their VIC and/or EIC. This was done by applying a non-local means filter to the volume to help with thresholding. The volume was then segmented (based on the visual inspection of the cores' CT scan images) using four different thresholds: air (-1024 to -500 HU), ice (-500 to 700 HU), sediment (700 to 1500 HU) and rock (1500 HU or more). For some volumes, morphological operations like opening and hole filling were applied. The segmented volumes are then recombined into a single volume, with each material having a different value. A statistical analysis was finally run on the combined volume to determine on each CT slice the percentage of the sample's area covered by each material.

3.3 Laboratory ground ice content measurements

The three frozen active layer/permafrost cores were sliced at ~2 cm intervals using a diamond blade-equipped tile saw. The frozen slices were left to thaw in sealed plastic bags and then transferred into 250 ml High-Density Polyethylene (HDPE) tubes.

EIC for each ~2 cm segment was derived from supernatant water measurements and was derived (based on Kokelj and Burn 2003) using:

$$\mathrm{EIC}(\%) = \frac{\mathrm{Ws}*1.0917}{(\mathrm{Ws}*1.0917+\mathrm{Vs})} * 100 \quad [1]$$

where *Ws* is the volume of supernatant water (cm^3), *Vs* is the volume of sediments (cm^3), and the number 1.0917 is used to convert the measured volume of supernatant water to the equivalent ice volume (Lapalme et al. 2017).

VIC was calculated (from French 2017) using:

$$\mathrm{VIC}(\%) = \frac{\mathrm{Wv}*1.0917}{\mathrm{Vt}} * 100 \quad [2]$$

where Wv is the volume of the water in the sample (cm^3), and Vt is the total volume of the sample (cm^3) established from the core dimensional data. The total mass of water in the sample (g) is used to derive Wv, assuming a water density of 1.0 g cm^3.

The measurement precision was within 1 ml; this translates to ± 1% errors in reported values. Missing data points (e.g., instances where a core segment was missing for a particular depth) were filled by deriving the mean of surrounding values. The same data-infilling approach was used to estimate the ground ice content at each site at a 1 cm resolution to approximate current and future GSS at our three sites.

A linear regression analysis (including derivations of adjusted R2 values) in the R software (R core team 2023) was used to compare CT scan-derived vs. laboratory-derived VIC and EIC measurements.

3.4 Ground surface subsidence and thaw penetration measurements

The thaw penetration depth at each of our three field sites during the 2018 (RI05 and RI07) and 2019 (RI08) summers was estimated by linear interpolation of the temperature profile close to 0 °C and/or by linear extrapolation from sensors located on the unfrozen side of the 0 °C isotherm (Riseborough 2008). The accuracy of interpolation and extrapolation is approximately 0.05 and 0.1 m for thermistor spacings of 0.25 and 0.5 m, respectively (Riseborough 2008). Summer site-specific observed GSS was measured using timelapse cameras pointing towards graduated heave sleeves described in LeBlanc and Oldenborger (2021).

The laboratory-derived measurements of EIC in our three frozen active layer/permafrost cores were employed to simulate GSS and active layer thickness (ALT) variations under current and future seasonal TP increases. ALT increases related to TP augmentations were subsequently determined by subtracting predicted GSS from TP increases (e.g., for a 50 cm TP increase and a 20 cm GSS, the ALT increase is 30 cm).

4 RESULTS

4.1 Ground ice content

4.1.1 Nearshore marine sediment core (RI05)

Laboratory analyses of the RI05 core revealed two ice-rich sections with depth (Figure 2A). The first was at the top of the core (i.e., within a ~12 cm organic-rich section), with VIC reaching a maximum of 80% and EIC being nil. Below, between 12 and 100 cm (permafrost table), a layer of silty sand sediments comprising localized gravel/pebble clasts and seashell fragments was encountered. VIC remained relatively stable within this core section, and EIC remained at or near 0% to a depth of ~92 cm, where field observations suggested a transition to finer sediments (i.e., fine sands and silts, with the latter being more abundant), until progressively increasing to 72% at the permafrost table. The second ice-rich section was found below the permafrost table. From this depth to our maximum core retrieval depth of 144 cm, VIC and EIC ranged from 48 to 92% and 20 to 85%, respectively. We estimate that the average EIC in the upper 50 cm of the permafrost at the RI05 site was ~60%.

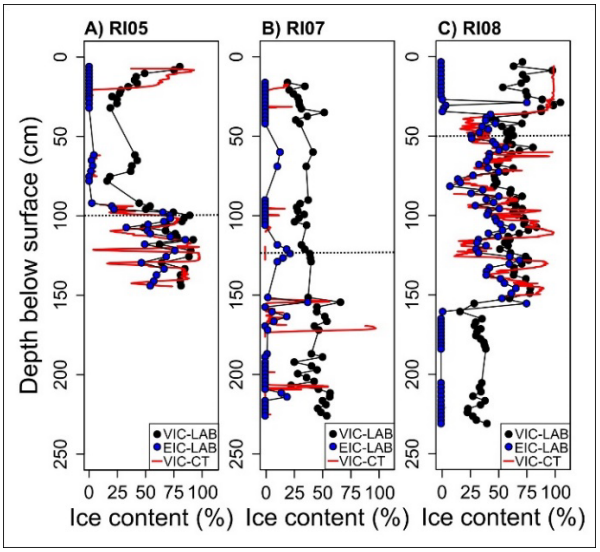

Figure 2. Laboratory (Lab) and computed tomography (CT) volumetric and excess ice contents (VIC; EIC) in the three frozen active layer/permafrost cores of the RI05 (panel A), RI07 (panel B) and RI08 (panel C) sites. The permafrost table depth relative to frozen conditions at each site is indicated with dashed lines.

4.1.2 *Till and marine sediment core (RI07)*

The RI07 core exhibited the most homogeneous ground ice content with depth out of all three sampled surficial deposit units (Figure 2B). The core was characterized by a ~4 cm thick layer of organics under which sandy sediments were observed to a depth of ~30 cm. The 30–175 cm core section is occupied by sandy sediments with pebbles (with the occasional presence of finer grains) and seashells. Gray fine sediments (likely a mix of clays and silts) were observed from this depth until the bottom of the core (225 cm). No clear trend was noted with depth for VIC: it varied from 20 to 67%, and the most notable fluctuations were observed near the core bottom (~230 cm). The core contained EIC at three depth ranges. The first was encountered between 60 and 69 cm (our only two measurements in this depth range due to no core recovery or core discarded (too small) for analyses), where EIC averaged ~12%. In the second EIC-rich section, between depths of 121 and 187 cm, EIC ranged from 2 to 38%. The third EIC-rich section was at a depth of ~210 cm (average EIC% of ~17%), where ~0.5–1 cm ice lenses were encountered. We approximate the EIC in the upper 50 and 100 cm of the permafrost at the RI07 site to average ~13 and ~7%, respectively.

4.1.3 *Alluvial and marine sediment core (RI08)*

The RI08 site had the thickest (~40 cm) layer of organic matter (peat) out of all three sites. Below that, a layer of fine sediments and sand was present to a depth of ~165 cm. Sand intermixed with finer sediments were also present from this depth until the bottom of the core (230 cm), but unlike the overlying sediments, those were highly abundant in seashells. Two distinct VIC zones characterize the RI08 core (Figure 2C). The first VIC zone includes the upper ~150 cm of the core, where VIC averaged 67%. The most ice-rich sample retrieved from this core (a frost blister horizon of ~5–7 cm) was situated within this unit at ~28 cm depth within the organic layer: it had a VIC of 100%. VIC then became much lower and stable below 150 cm, averaging 23% to a depth of 230 cm. The EIC in the upper organic-rich section of the core (upper ~38 cm) was (or very close to) nil except for the frost-blister horizon, where EIC was measured at 76%. Below that, the remaining 8 cm peat horizon had an average EIC of ~13%. A slight progressive increase in EIC was then noted from 38 to 155 cm, below which (to our maximum sampling depth of 230 cm) EIC was zero. We approximate the EIC in the upper 50 and 100 cm of the permafrost at the RI08 site to average ~38 and ~44%, respectively.

4.2 Ground surface subsidence during the 2018 and 2019 summers

GSS measurements from heave sleeve photographs at the RI05, RI07 (2018 summer) and RI08 (2019 summer) sites reached a maximum of 6.8, 4.5, and 12 cm, respectively (Figure 3). Those observations agreed reasonably well with the total predicted EIC-based GSS under interpolated TP at each site in 2018 or 2019 (RI05 = 5.8 cm; RI07 = 4.7 cm; RI08 = 15.1 cm). Additionally, the temporal evolution of observed GSS matched the EIC-based GSS predictions over the 2018 summer for the RI05 and RI07 sites. Still, by comparison, predicted GSS lags observations during the 2018 summer. Conversely, at the alluvial and marine sediment (RI08) site, the observed GSS lagged considerably behind predicted GSS during the 2019 summer TP.

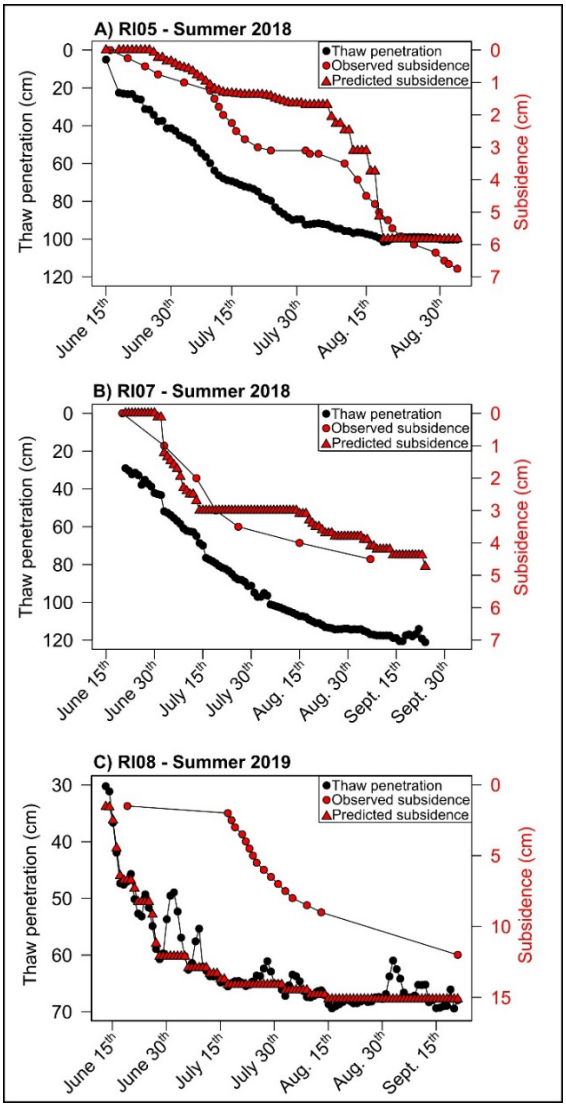

Figure 3. Time series of interpolated TP (black dots; for initial frozen conditions before GSS), observed (red dots) and predicted (red triangles) GSS during the 2018 (RI05 and RI07) and 2019 (RI08) summers. TP interpolations begin at 40 cm and 30 cm for the RI07 and RI08, respectively, since thermistor cables were only installed at those sites in mid-June. TP had already begun, and an initial ~1.5 cm of GSS had been observed (on the existing heave sleeve) beforehand at the RI08 site.

4.3 Predicted active layer dynamics and ground surface subsidence under climate warming

Our upper permafrost degradation simulations (i.e., seasonal TP increase of 50 cm at each site compared to TP interpolated for 2018 and 2019 summers) predicted that the RI05 site should have ALT and GSS increases of 20.7 and 29.3 cm, respectively (Figure 4). Further, for a 50 cm TP increase, ALT at the RI08 site is expected to increase slightly more (maximum ALT increase of 31.2 cm) than at the RI05 site. In addition, the GS at the RI08 site should subside an additional 18.8 cm if the upper 50 cm of permafrost thaws. Field and laboratory observations showed that both cores hosted an ice-rich zone (Figure 2). Yet, EIC is slightly higher with depth in the RI05 core, translating to a higher predicted GSS and lower ALT increase. Conversely, the ALT increase at the RI07 site followed by thaw penetration increases since almost no excess ice was measured in the upper permafrost section: ALT increased by 44.1 cm, and GS subsided by only 5.9 cm.

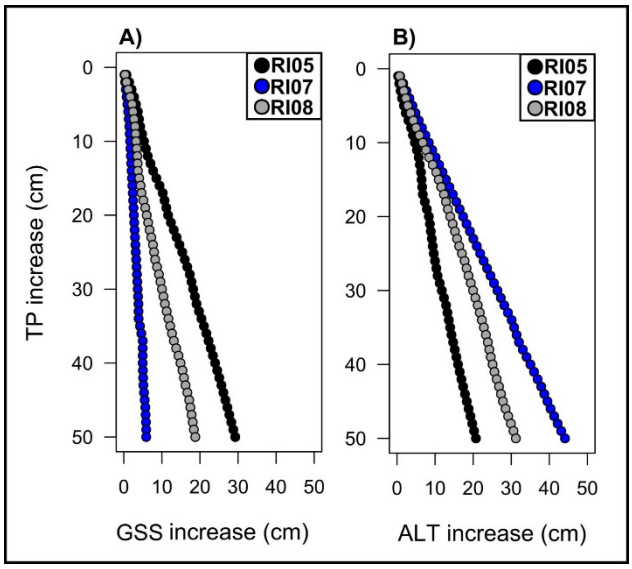

Figure 4. EIC-based GSS and ALT increase predictions in response to TP increases (1 cm increments; maximum of 50 cm) at the three surficial geology sites.

5 Discussion

5.1 Comparing CT and laboratory-derived ground ice content measurements

CT scan-derived VIC estimates (VIC-CT) mostly underapproximated laboratory-derived VIC (VIC-Lab) measurements (Figure 5). Linear regression analyses (with and without including organic-rich sections) revealed moderate correlations between VIC-CT and VIC-Lab for the RI05 and RI08 cores. Conversely, VIC-CT and VIC-Lab were poorly correlated for the RI07 core and sediments in the deeper portion of our RI08 core; VIC-CT in the latter unit was ~0% when measured VIC ranged between ~20 and 40%. Although we do not yet have reliable granulometric data (besides in situ qualitative observations), we suggest that this may have been caused by the coarse pixel resolution of our CT scan images (0.6 mm), making them partially (or completely) spatially unresolvable. This assumption is supported by studies conducted by Calmels et al. (2010) and Lapalme et al. (2017), which demonstrated that CT scans might not spatially resolve pore ice content in sediments if the pixel size is larger than the average pore space. In fact, Lapalme et al. (2017) demonstrated that for permafrost sand-rich sediments, the segmentation of CT scan images may be better suited to estimate EIC, with porosities of ~30–50% and pore-space diameters within the pixel resolution range of CT scan images. Further, for the RI05 core, VIC-CT overestimated VIC-Lab measurements made in its organic-rich section (i.e., the top of the active layer). We hypothesize this is due to the presence of organics having densities similar to water/ice (e.g., Calmels et al., 2010) and, therefore, having been classified as (almost) pure ice during our image segmentation. We suspect this material density issue might also have affected the peat-rich active layer section of the RI08 core but to a lesser extent than the organics in the RI05 core since laboratory measurements confirmed that the former contained larger amounts of VIC.

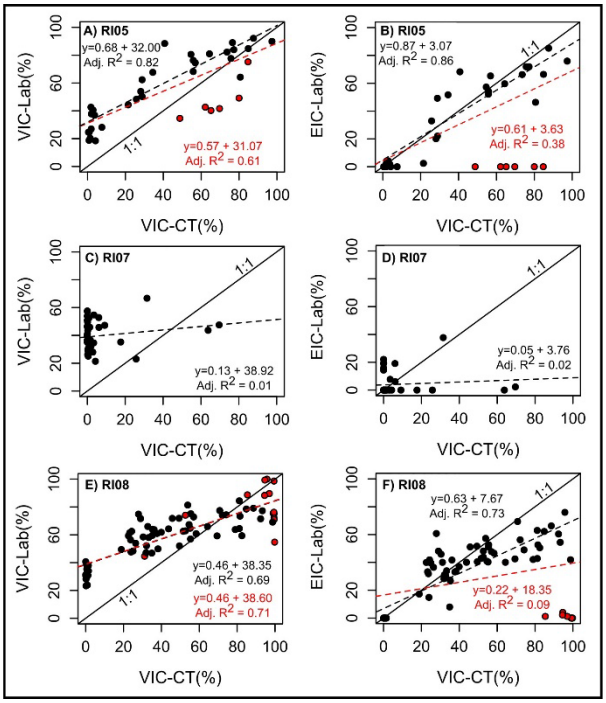

Figure 5. Computed tomography-derived VIC (VIC-CT) averaged over our sampling depth interval (2 cm) compared with laboratory-derived volumetric and EIC (VIC-LAB; EIC-Lab). Red dots indicate measurements made within organic-rich sections of the RI05 and RI08 cores. Measurements made within organic-rich sections were either included (red dotted line and text) or removed (black dotted line and text) from our linear regression analyses.

The comparison of VIC-CT vs. EIC-Lab for our three cores yielded contrasting results. For instance, laboratory analyses of the RI07 core suggest it contained very little or no EIC, yet simultaneously, VIC-CT sometimes overestimated EIC-Lab (Figure 5D). We believe that laboratory manipulation errors may have caused this. This is because the highest VIC-CT values for this core (~64–70% range) were at depths where ice lenses were present (i.e., 170–172 cm), yet our laboratory measurements did not point to high EIC at those depths, suggesting a partial (or complete) omission of those ice-rich segments in our laboratory measurements. Further, when organic-rich core sections were omitted, VIC-CT and EIC-Lab for the RI05 and RI08 cores were moderately linearly correlated. However, including organic-rich sections of those cores for VIC-CT vs. EIC linear regressions led to severe declines in adjusted R^2 values. This is because laboratory measurements indicated that their EIC was nil, while VIC-CT suggested moderate to high (50 to 100%) VIC in the upper organic-rich sections. Still, EIC in the organic-rich sections of the frozen active layer at those two sites may have been higher than we measured in the lab. This is because EIC-Lab measures highly depend on the volume of supernatant waters in respective HDPE tubes once core sections are left to thaw. Accordingly, it is plausible that organics may have absorbed supernatant waters while thawing those frozen active layer core slices.

Overall, our inability to adequately predict VIC or EIC in our cores using CT scan images was likely mostly imputable to the sediments having pore diameters above and below the CT pixel resolution. It is further unclear if this could be attributed to human-induced errors (e.g., difficulties correlating actual depths between CT scan images and laboratory). Nonetheless, what is clear is that our CT scan yields poorly reliable ground ice content estimations when organics are present (i.e., materials having similar densities to water/ice). This supports our decision to rely on laboratory-derived measurements to properly quantify ground ice in our samples to assess the thaw settlement potential of investigated surficial geology units discussed in the following section. Additionally, we plan on alleviating the likely pixel resolution issue by employing a high-resolution X-ray Computed Tomography (HRXCT) approach in the future if we do repeat CT scan analyses on frozen active layer/permafrost samples from this area (e.g., Nitzbon et al. 2022).

5.2 Observed and predicted ground subsidence during the 2018 and 2019 summers

The temporal evolution of observed GSS matched the EIC-based GSS predictions for the RI05 and RI07 sites over the 2018 summer. However, they also show that predicted GSS at the RI08 site lagged what we observed in the 2019 summer (Figure 4). We suggest that the offset between observed and predicted thaw-induced GSS at the RI08 site may have been caused by the behaviour of the 40 cm thick organic-rich (i.e., peat) top layer during the thawing season. Unlike unconsolidated sediments in permafrost, peat may retain its structure upon thawing (especially in poorly drained sites such as RI08; e.g., MacFarlane and Williams 1974). Hence, the collapse of this peat unit may only have been initiated in mid to late-July 2019, once the thaw front reached the underlying unconsolidated mineral soils (and started melting their EIC), as suggested by the observed GSS.

5.3 Active layer thickness deepening and ground surface subsidence under climate warming

Our permafrost degradation simulations enabled us to make site-specific predictions about ALT and GSS dynamics under climate warming. Notably, we showed that soils at our site hosting the least amount of excess ice (RI07) in the near-surface permafrost should not subside that much (~6 cm) under a 50 cm TP increase (i.e., ALT should instead roughly follow TP increases). Accordingly, future ALT measurements at site RI07 could serve as reliable proxies in assessing the magnitude of upper-permafrost thaw. However, this finding does not apply to our two other sites because their near-surface permafrost hosts substantial amounts of excess ice: a 50 cm TP increase and accompanying melting of excess ice at sites RI05 and RI08 should only lead to ALT increases of ~21 and ~32 cm. Ergo, this rudimentary EIC-based modelling demonstrates that ALT and GSS measurements should simultaneously be used to monitor the state of the ground ice in the upper permafrost units of the RI05 and RI08 sites, where EIC is low. This supports findings from previous studies, showing that ALT measurements alone at ice-rich sites may serve as poor permafrost degradation metrics (e.g., Shiklomanov et al. 2013; O'Neil et al. 2023) and that GSS and TP trends are more accurate at characterizing this phenomenon. Hence, care should be taken to pursue the area's ALT and GSS monitoring efforts to properly assess the permafrost's stability under climate change.

In addition, considering that those simulations are based on punctual measurements and site-specific conditions strongly influence ground ice content and distribution, our derived results should be used with prudence for extrapolations to other areas near the hamlet of Rankin Inlet with similar surficial deposits. Upscaling those findings to other areas near Rankin Inlet in hopes of providing first-order estimates on their vulnerability to climate change (e.g., destabilization potential) will most certainly require additional ground ice content measurements (especially concerning EIC) to be repeated within other areas near the hamlet hosting the same surficial units. Then, we will be able to confidently establish the vulnerability of the permafrost in the various surficial geology units occupying this area of Nunavut's Kivalliq region.

6 CONCLUSIONS

Results from the following ground ice content investigation of frozen active layer/permafrost cores taken within the vicinity of Rankin Inlet have led us to the following conclusions:

1) Our field sampling and laboratory results suggest significant excess ice occurs in surficial geology units around Rankin Inlet (NU).

2) Laboratory-derived measurements and CT scan-based estimations of VIC and EIC in our three cores produced conflicting results. We suspect this to be due to a) the low pixel resolution of our CT scan image; b) the presence of materials with similar densities as water/ice (e.g., organics); or c) human-induced errors (e.g., difficulties correlating actual depths between CT scan images and laboratory).

3) Our permafrost degradation scenario demonstrates that subsidence of 5.9 to 29.3 cm can be expected upon thawing of the upper 50 cm of permafrost at the three sites. This quantification of potential thaw effects is helpful for infrastructure development planning.

4) Further efforts will aim to investigate ground ice content (including distribution) and sediment grain size within the various surficial geology units of the Rankin Inlet area/Kivalliq region. This will allow us to make broader predictions concerning the fate of the permafrost in the area under future climate warming.

7 ACKNOWLEDGEMENTS

This work was undertaken via the Climate Change Geoscience and GEM-GeoNorth programs (Natural Resources Canada, contribution number 20210439). Andrew Branson and Kevin Brewer provided field assistance during the 2018 and 2019 field seasons. An internal review by H.B. O'Neil helped improve the paper. We thank the reviewers for their constructive comments.

8 REFERENCES

Calmels, F. and Allard, M. 2004. 'Ice segregation and gas distribution in permafrost using tomodensitometric analysis', *Permafrost and Periglacial Processes* 15, pp. 367–378. Available at: https://doi.org/10.1002/ppp.508.

Calmels, F., Gagnon, O., and Allard, M. 2005. 'A portable earth-drill system for permafrost studies', *Permafrost and Periglacial Processes*, 16, pp. 311–315. Available at: https://doi.org/10.1002/ppp.529.

Calmels, F. and Allard, M. 2008. 'Segregated ice structures in various heaved permafrost landforms through CT Scan', *Earth Surface Processes and Landforms* 33, pp. 209–225. Available at: https://doi.org/10.1002/esp.1538.

Calmels, F., Clavano, W.R., and Froese, D.G. 2010. 'Progress on X-ray computed tomography (CT) scanning in permafrost studies', in *Geo2010: 63rd Canadian Geotechnical Conference*. Calgary, Alberta, Canada.

Castagner, A., Brenning, A., Gruber, S., and Kokelj, S.V. 2022. 'Vertical distribution of excess ice in icy sediments and its statistical estimation from geotechnical data (Tuktoyaktuk Coastlands and Anderson Plain, Northwest Territories)', *Arctic Science* 9(2), pp. 483–496. Available at: https://doi.org/10.1139/as-2021-0041.

Crory, F.E. 1973. 'Settlement associated with the thawing of permafrost', in *2nd International Conference on Permafrost*. Yakutsk, U.S.S.R.: North American Contribution, pp. 599–607.

Doré, G., Niu, F., and Brooks, H. 2016. 'Adaptation methods for transportation infrastructure built on degrading permafrost', *Permafrost and Periglacial Processes* 27(4), pp. 352–364. Available at: https://doi.org/10.1002/ppp.1919.

Dyke, A.S. 2004. 'An outline of North American deglaciation with emphasis on central and northern Canada', *Developments in Quaternary Sciences* 2, pp. 373–424. Available at: https://doi.org/10.1016/S1571-0866(04)80209-4.

Environment and Climate Change Canada (2022). 'Historical climate data', *Environment and Climate Change Canada*. Available at: climate.weather.gc.ca (Accessed: January 2022).

Fan, X.W., Lin, Z.J., Gao, Z.Y., et al. 2021. 'Cryostructures and ground ice content in ice-rich permafrost area of the Qinghai-Tibet Plateau with Computed Tomography Scanning', *Journal of Mountain Science* 18(5). Available at: https://doi.org/10.1007/s11629-020-6197-x.

French, H.M. 2017. *The Periglacial Environment*. United Kingdom: Wiley.

Gadylyaev, D., Nitzbon, J., Schlüter, S., Köhne, J.M., Grosse, G., and Boike, J. 2021. 'Applying Computed Tomography (CT) scanning for segmentation of permafrost constituents in drill cores', *EGU General Assembly 2021*, online, 19–30 Apr 2021, EGU21-11395. Available at: https://doi.org/10.5194/egusphere-egu21-11395.

Golder Associates Ltd. 2014. 'SD 6-1 permafrost thermal regime baseline studies – Meliadine Gold Project', unpublished report for *Agnico-Eagle Mines Limited*. Golder Doc 225-1314280007 Ver. 0. Available at: https://www.nirb.ca/application?strP=r.

Golder Associates Ltd. 2021. 'Meliadine Extension – 2020 Thermal Assessment – Meliadine Gold Project', unpublished report prepared for *Agnico-Eagle Mines Limited*, Golder Doc 20136436-815-R-Rev2-2200. Available at: https://www.nirb.ca/application?strP=r.

Kokelj, S.V. and Burn, C.R. 2003. 'Ground ice and soluble cations in near-surface permafrost, Inuvik, Northwest Territories Canada', *Permafrost and Periglacial Processes* 14, pp. 275–289. Available at: https://doi.org/10.1002/ppp.458.

Lapalme, C.M., Lacelle, D., Pollard, W., Fortier, D., Davila, A., McKay, C.P. 2017. 'Cryostratigraphy and the sublimation unconformity in permafrost from an ultraxerous environment, University Valley, McMurdo Dry Valleys of Antarctica', *Permafrost and Periglacial Processes* 28(4), pp. 649–662. doi:10.1002/ppp.1948.

Lawley, C.J M., McNicoll, V., Sandeman, H., Pehrsson, S., Simard, M., Castonguay, S., Mercier- Langevin, P., and Dubé, B. 2016. 'Age and geological setting of the Rankin Inlet greenstone belt and its relationship to the gold endowment of the Meliadine gold district, Nunavut, Canada', *Precambrian Research* 275, pp. 471–495. Available at: https://doi.org/10.1016/j.precamres.2016.01.008.

LeBlanc A.-M., Oldenborger G.A., and Short, N. 2019. 'Mapping permafrost and terrain conditions by combining corrected DInSAR seasonal and inter-annual ground displacements', *Cold Regions Engineering 2019*, pp. 616–624.

LeBlanc, A.-M. and Oldenborger, G.A. 2021. 'Ground temperature, active-layer thickness and ground-ice conditions in the vicinity of Rankin Inlet, Nunavut', in *Canada-Nunavut Geoscience Office* Summary of Activities 2020, pp. 63–72.

McCuaig, S., McKillop, R., McGregor, C., Roy-Leveillée, P., and St-Amour, A. 2022. 'Mapping and Investigating Permafrost along the Proposed Kivalliq Hydro-Fibre Link, Manitoba to Nunavut', *GeoCalgary 2022*. Calgary, Alberta, Canada: October 2–5, 2022.

MacFarlane, I.C. and Williams, G.P. 1974. 'Some Engineering Aspects of Peat Soils', in *A.R. Aandahl (ed.) Histosols: Their Characteristics, Classification, and Use*, volume 6. Available at: https://doi.org/10.2136/sssaspecpub6.c7.

McMartin, I. 2002. 'Surficial geology, Rankin Inlet, Nunavut', *Geological Survey of Canada* Open File 4116, scale 1:50 000.

McMartin, I., Gauthier, M., and Page, A. 2023. 'Updating the limits of the postglacial marine transgression along western Hudson Bay in mainland Nunavut and northern Manitoba, Canada', in *INQUA 2023 Congress*. Rome, Italy: July 14–20, 2023.

Oldenborger, G.A., Bellehumeur-Génier, O., Short, N., Tremblay, T., and LeBlanc, A.-M. 2017. 'Ground temperatures and permafrost conditions, Rankin Inlet, southern Nunavut', in *Canada-Nunavut Geoscience Office* Summary of Activities 2017, pp. 117–128.

Oldenborger, G.A., Short, N., and LeBlanc, A.-M. 2020. 'Electrical conductivity and ground displacement in permafrost terrain', *Journal of Applied Geophysics* 181, 104148. Available at: https://doi.org/10.1016/j.jappgeo.2020.104148.

O'Neil, H.B., Smith, S.L., Burn, C.R., Duchesne, C., and Zhang, Y. 2023. 'Widespread Permafrost Degradation and Thaw Subsidence in Northwest Canada', *Journal of Geophysical Research: Earth Surface* 128(8), e2023JF007262. Available at: https://doi.org/10.1029/2023JF007262.

Nitzbon, J., Gadylyaev, D., Schlüter, S., Köhne, J.M., Grosse, G., and Boike, J. 2022. 'Brief communication: Unravelling the composition and microstructure of a permafrost core using X-ray computed tomography', *The Cryosphere* 16, pp. 3507–3515. Available at: https://doi.org/10.5194/tc-16-3507-2022.

Pullman, E.R., Jorgenson, M.T., and Shur, Y. 2007. 'Thaw Settlement in Soils of the Arctic Coastal Plain, Alaska', *Arctic, Antarctic, and Alpine Research* 39(3), pp. 468–476. Available at: https://doi.org/10.1657/1523-0430(05-045)[PULLMAN]2.0.CO;2.

Randour, I., McMartin, I., and Roy, M. 2016. 'Study of the postglacial marine limit between Wager Bay and Chesterfield Inlet, western Hudson Bay, Nunavut', in *Canada-Nunavut Geoscience Office* Summary of Activities 2016, pp. 51–60.

R Core Team 2023. 'R: A language and environment for statistical computing', *R Foundation for Statistical Computing*. Vienna, Austria. Available at: https://www.R-project.org/.

Riseborough, D. 2008. 'Estimating active layer and talik thickness from temperature data: implication for modeling results', in D.L. Kane and K.M. Hinkel (eds.), *Proceedings of the Ninth International Conference on Permafrost*. Fairbanks, Alaska, United States: June 29–July 3, 2008, v. 2, pp. 1487–1492.

Shiklomanov, N.I., Streletskiy, D.A., Little, J.D., and Nelson, F.E. 2013. 'Isotropic thaw subsidence in undisturbed permafrost landscapes', *Geophysical Research Letters* 40, pp. 6356–6361, doi:10.1002/2013GL058295.

Watson, G., Slusarchuk, W., and Rowley, R. 1973. 'Determination of Some Frozen and Thawed Properties of Permafrost Soils', *Canadian Geotechnical Journal* 10, pp. 592–606. Available at: https://doi.org/10.1139/t73-055.

Taber, S. 1930. 'The Mechanics of Frost Heaving', *The Journal of Geology* 38, pp. 303–317. Available at: https://doi.org/10.1086/623720.

van Everdingen, R.O. 2005. 'Multi-language glossary of permafrost and related ground-ice terms', *International Permafrost Association*. Available at: http://globalcryospherewatch.org/reference/glossary_docs/Glossary_of_Permafrost_and_Ground-Ice_IPA_2005.pdf (Accessed: 13 Aug 2020).

Utilizing spectral induced polarization to identify the ice core of a pingo: A case study in Haines Junction, Yukon, Canada

Hosein Fereydooni[1], Stephan Gruber[2], Derek Cronmiller[3] & David Stillman[4]

[1]*Department of Earth Sciences, Carleton University, Ottawa, Ontario, Canada*

[2]*Department of Geography and Environmental Studies, Carleton University, Ottawa, Ontario, Canada*

[3]*Permafrost Geologist, Energy, Mines and Resources, Yukon Geological Survey, Yukon, Canada*

[4]*Southwest Research Institute, Boulder, Colorado, United States*

ABSTRACT

This paper presents a field study conducted in Haines Junction, Yukon, utilizing Spectral Induced Polarization (SIP) to investigate the subsurface properties of a pingo site and specifically identify its ice core. The effectiveness of SIP analysis was demonstrated using a FUCHS frequency domain instrument, which measured electrical impedance magnitude and phase shift angle at multiple frequencies (1.46 Hz–40 kHz). The main focus of the analysis centered on the results obtained from electrical impedance magnitude and phase shift angle inversion at 40 kHz and 1.46 Hz. The inversion results revealed the presence of high resistivity layers within the subsurface, similar to results that would be expected with electrical resistivity tomography (ERT). Additionally, the SIP data revealed that some areas with high resistivity also had negative phase shift angle values, suggesting the presence of materials with polarizing properties. The analysis of the imaginary part of electrical impedance at 40 kHz for these areas highlighted the contribution of polarization, indicating the presence of ice. Furthermore, the electrical impedance magnitude at 1.46 Hz exhibited similarities to the 40 kHz analysis, but with higher resistivity. This pattern is another indicator of the presence of ice within the subsurface of the study area and was expressed using the Resistivity Frequency Effect (RFE) equation. The RFE analysis and the patterns of polarization confirmed the presence of the pingo ice core and identified its distinctive signature compared to other layers. Subsequent drilling confirmed the presence of interbedded ice and clay from 2.4–3.6 m depth and massive ice from 3.6–8.3 m depth.

1 INTRODUCTION

Permafrost is an integral component of Earth's subsurface in cold regions and encompasses a substantial volume of ground ice. Especially under climate change, melting of ground ice can give rise to various hazards, making the detection and understanding of ice within permafrost important for prevention and mitigation of associated problems. In this context, geophysical methods provide tools for detecting and characterizing ground ice.

Among the methods commonly used, ERT has been widely employed to investigate permafrost (e.g., You et al. 2013; Oldenborger 2021; Li et al. 2021; Park et al. 2023; Kasprzak et al. 2017). However, distinguishing ice from other materials via ERT alone can be challenging when resistivity values overlap between frozen ground and, for example, unfrozen bedrock. As a result, investigating alternative techniques that can detect ice with less ambiguity is important.

Spectral Induced Polarization (SIP) is a promising method for characterizing ground ice. Under Alternating Current (AC), ice and frozen soil exhibit polarization, that can be detected with SIP. The spectral signature of this polarization is linked to ice content, temperature, and salinity. While field application of SIP for detecting ground ice is only beginning, several studies have demonstrated success.

Running SIP field measurements above conductive layers such as an unfrozen and wet active layer presents significant challenges (Stillman et al. 2018). In areas with highly conductive subsurface materials, especially saline or clay-rich soils, the electrical currents tend to concentrate within these layers, leading to signal attenuation and limited penetration depth. This can result in reduced resolution and difficulties in distinguishing responses from specific target zones at depth. Additionally, clay minerals in the subsurface introduce capacitive and conductive responses (Bittelli et al. 2004). That can mask or interfere with the signature of ice or other target materials. Measurements in late winter can minimize these effects as the active layer will be maximally frozen.

Numerous processing techniques can be applied to SIP data. Initial steps involve the separation of real and imaginary parts. The imaginary part and phase shift angle reflect polarization, which can provide a signature diagnostic of ice. Data can be processed across multiple frequencies, employing equations such as the Resistivity Frequency Effect (RFE), which can enhance the clarity of ice detection.

The objective of this research is to improve and demonstrate the potential of SIP in detecting ground ice using late-winter measurements over a pingo as a case study.

First, we give a brief background and explain the methods employed to analyze our data. Subsequently, inversion was employed to compare the results with evidence obtained from logged borehole cores, considering various perspectives.

https://doi.org/10.52381/ICOP2024.211.1

2 BACKGROUND

2.1 The Dielectric Behaviour of Ice

When materials are exposed to an electric field, individual molecules are polarized by electron or proton displacements and slight molecular distortions. In ice, polarization arises from the reorientation of molecules or bonds. Certain proton configurations experience reduced energies compared to others, resulting in a net polarization of the ice at thermal equilibrium. This polarization at low frequencies is an almost perfect example of Debye relaxation (Grimnes and Martinsen 2015). While a consistent flow of current in accordance with Ohm's law can be induced in ice, it is driven by the movement of protons (Petrenko and Whitworth 1999) rather than the common electronic conduction.

Generally, electronic and atomic polarization are characterized by a resonance frequency, causing a peak in the imaginary part and a peak followed by a trough in the real part of permittivity. Conversely, ionic, interfacial, and dipolar polarizations are characterized by a relaxation frequency, which manifests as a decrease in the real part of permittivity and a peak in the imaginary part.

To extract the relaxation frequency of frozen soil and ice we can consider an equivalent circuit to simulate their electrical manner (Hobbs 2010). In this respect, we can apply the Debye equation to the result of dielectric spectra and extract the relaxation frequency for ice and frozen soil [Equations 1 and 2].

$$\varepsilon'(\omega) = \varepsilon_\infty + \frac{\Delta\varepsilon}{1+\omega^2\tau^2} \quad [1]$$

$$\varepsilon''(\omega) = \varepsilon_\infty + \frac{\Delta\varepsilon\omega\tau}{1+\omega^2\tau^2} \quad [2]$$

Where ε' is real permittivity (or dielectric constant), and ε'' imaginary permittivity (or loss factor). ε_{LF}, ε_∞ is low, and high frequency permittivity, and $\Delta\varepsilon = \varepsilon_{LF} - \varepsilon_\infty$.

At a temperature of +10 °C, water demonstrates an approximate relaxation time of $\tau = 1.2 \times 10^{-11}$ s, while ice at -10 °C exhibits a relaxation time of approximately $\tau = 5 \times 10^{-5}$ s (Petrenko and Whitworth 1999).

2.2 The Dielectric Behaviour of Frozen Soil

Frozen soil has significant variations in dielectric permittivity across frequency. At lower frequencies, there can be a pronounced increase in permittivity, potentially attributable to surface mineral polarization. At frequencies below 1 kHz, the polarization effect primarily stems from electrochemical (ionic) polarization occurring at the interface between the pore water and the solid matrix, known as the electrical double layer (EDL; Kemna et al. 2012). Particle size plays a pivotal role, with lower frequencies (< 1 kHz) witnessing considerable permittivity increases as particle size decreases, owing to factors like Maxwell-Wagner effects, surface conduction, ion exchange, and interface polarization, particularly prominent in clay-rich soils. Relaxation frequency increases with rising temperature. Water's proximity to solid surfaces also affects relaxation frequencies, with closer water molecules displaying lower-frequency relaxations. These observations suggest that the dielectric behavior of frozen soil arises from several relaxations, including those related to ice and adsorbed unfrozen water, as supported by Debye parameterization results (Bittelli et al. 2004; Grimm et al. 2015). Figure 1 shows the dielectric spectra for water and ice. The relaxation frequency (the peaks in the imaginary part) for ice (and frozen soil) occurs at a lower frequency than water.

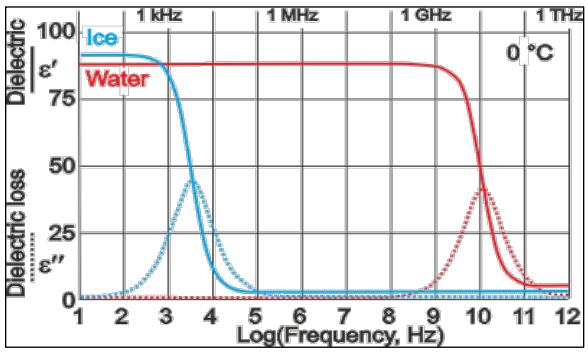

Figure 1. Relaxation frequency for ice (blue line) and water (red line) at 0 °C (Artemov and Volkov 2014).

2.3 Spectral Induced Polarization

Induced polarization (IP) is a geophysical electrical technique for measuring the electrical impedance of the subsurface. In the frequency domain, two electrodes inject a sinusoidal current into the ground, while another pair of electrodes measures the resulting phase-shifted voltage. The electrical impedance is determined by the amplitude ratio and phase-shift between the voltage and current. By conducting measurements at different frequencies, known as spectral IP (SIP), information about the frequency-dependent electrical properties of the subsurface can be obtained.

Electrical impedance Z can be expressed in terms of the magnitude and phase shift angle or as real (R, resistance) and imaginary (X, reactance) components (Equation 3; Lvovich 2012):

$$Z(\omega) = R - iX = |Z(w)|e^{i\varphi(w)} \quad [3]$$

where φ(ω) (Equation 4) represents the phase shift angle in radians:

$$\varphi(\omega) = \arctan(\frac{-X}{R}) \quad [4]$$

The angular frequency is represented by ω, which is calculated as $2\pi f$, where f is the excitation frequency.

The real component of electrical impedance accounts for energy loss associated with conduction, whereas the imaginary part (or phase-shift angle) represents the polarization effect, which can help to identify the unique

relaxation feature of ice, as demonstrated by previous studies. This paper will focus on the imaginary part, the phase shift angle, and the RFE as additional means to distinguish ice from other materials.

Bittelli et al. (2004) investigated the application of dielectric spectroscopy for estimating the presence and content of ice in frozen porous materials. They employed a dielectric mixing model to calculate the proportions of liquid water, ice, air, soil solids based on their dielectric permittivities and that of the bulk material. Measurements of dielectric permittivities were taken across a temperature range of -30 °C to +5 °C at two frequencies using an electrical impedance analyzer. One (25 kHz) close to the relaxation frequency of ice, and another (158 kHz) significantly above were used to detect ice. The approach was tested on three soil samples with varying clay concentrations. The determination of ice content was successful for the loamy sand, but challenges arose for samples with high clay content, due to surface-related effects at low frequencies such as double-layer polarization, surface conduction, and Maxwell-Wagner effects.

Grimm et al. (2015) analyzed dielectric spectra (0.1 Hz to 1 MHz) for 49 firn and ice samples obtained from ice sheets and glaciers. Results revealed two distinct dielectric relaxations, indicating the presence of different crystal populations or zonation in meteoric ice. However, high temperatures, long residence times, or elevated impurity concentrations favoured the development of a single relaxation, suggesting the merging of distinct populations due to annealing. Furthermore, frozen samples from subglacial environments displayed a single relaxation reflecting the composition of the source water. The findings emphasize the importance of multi-frequency methods for distinguishing different types of ice based on their dielectric properties.

Grimm and Stillman (2015) explored the utility of low-frequency electrical resistivity in discerning frozen ground from unfrozen soil in periglacial environments. The research established temperature-dependent relationships between ice volume and RFE through laboratory experiments using samples collected from the US Army Permafrost Tunnel in Fox, Alaska. By comparing data from laboratory and field measurements, they determined an optimal ice temperature of approximately -3 °C. Subsequently, they employed the laboratory derived RFE at this selected temperature to create a detailed ice content map within the tunnel, ranging from 45 to 95% ice volume. The field data exhibited a strong agreement with SIP results.

Stillman et al. (2018) used SIP to infer patterns of relative subsurface ice content in warm permafrost. They utilized tomographic SIP profiles, which revealed distinct ice signatures at depth based on RFE, which is the difference between the low and high-frequency resistivities normalized by the low-frequency value. Measurement in November presented a challenge because a high-conductivity unfrozen layer near the surface persisted.

Mudler et al. (2022) conducted research on detecting ice in permafrost using the high-frequency induced polarization method (HFIP). Their approach relies on Zorin and Ageev (2017) theory, which characterizes subsurface material as a combination of two components: ice and a ice-free part of the soil. The underlying assumption in this theory is that polarization is exclusively attributed to the ice fraction.

3 Field Observations

3.1 SIP measurements

SIP measurements were made on a pingo site (60.7835°N 137.5321°W) in Haines Junction, Yukon, Canada from 20–22 March, 2023. Throughout this time, the local air temperature varied between -2 °C in the morning to +4 °C in the evening.

A FUCHS III+ device was utilized, operating in the frequency domain and having a maximum current and voltage of 1.5 A and 400 V. It employs sinusoidal current for electrical impedance measurement and records, analyzes, and processes current and voltage signals in real-time, recording and displaying electrical impedance and phase shift angle spectra. It consists of a single current unit and three potential units, with one potential unit designated as the reference for suppressing local noise. Calibration was performed prior to the measurements following a manual procedure. We recorded 582 electrode configurations at 20 frequencies from 1.46 Hz to 40 kHz, resulting in 11,640 data points total at the pingo site.

We measured a survey line that spanned 30 m with electrodes one metre apart. The line was selected to be straight and wide enough for movement of persons and equipment. A geofabric ground cover was used to enable smooth movement of fibreoptic cables. We measured in dipole-dipole configuration with electrode spacings of 1–5 m and using ground electrodes placed in the center of these electrodes.

3.2 Drilling

A borehole was drilled at the 23-m mark within the SIP profile (60.783670º N, 137.53188º W) on April 5, 2023. The borehole reached a depth of approximately 11 m and the recovered core was logged and photographed in the field.

4 Data Processing

This paper focuses solely on the observations at the lowest (1.46 Hz) and highest (40 kHz) measured frequency. We excluded data points displaying negative electrical impedance magnitude and/or positive phase shift angle. Subsequently, we removed observations that were more than three standard deviations away from the mean of all measurements in each frequency, in either electrical impedance magnitude or phase shift angle.

Table 1 presents descriptive statistics for electrical impedance magnitude (IM) and phase shift angle (PA) at 40 kHz and 1.46 Hz, respectively. At 40 kHz, we excluded 16 and 28 data points for electrical impedance magnitude and phase shift angle, respectively. Similarly, at 1.46 Hz, we excluded 11 and 232 data points for electrical impedance magnitude and phase shift angle, respectively. No outlier was found for PA at 40 kHz.

Table 1. Summary of raw and filtered data (after excluding negative electrical impedance magnitude and positive phase angle) for electrical impedance magnitude (Ω) and phase shift angle (degree).

Variable	Count	Mean	StDev	Min	Max
IM (40 kHz)	582	2.55	13.36	0.02	192
IM (40 kHz Filtered)	566	0.94	1.34	0.03	8
IM (1.46 Hz)	582	3.06	18.59	0.03	336
IM (1.46Hz Filtered)	571	1.20	1.84	0.03	15
PA (1.46 Hz)	384	-2.04	5.45	-48.00	0
PA (1.46Hz Filtered)	350	-0.63	0.97	-5.20	0
PA (40 kHz filtered and unfiltered)	554	-10.99	5.82	-40.96	0

After data cleaning, ResIPy was used for inverting the SIP data. This software package has been developed for the inversion of geoelectrical data obtained from ERT and induced polarization (IP) surveys (Blanchy et al. 2020).

Considering the real part of electrical impedance and change it to apparent resistivity (Ωm) values (by using geometric factor) at the lowest (1.46 Hz) and highest (40 kHz) frequencies, we can use Equation 5 for RFE, where a value close to 1 indicates higher ice content (Grimm and Stillman 2015).

$$RFE = (\rho_{1.46Hz} - \rho_{40kHz}) / \rho_{1.46Hz} \quad [5]$$

Where ρ shows the apparent resistivity.

Additionally, we employed the loss tangent to track the relative variation in the imaginary component of electrical impedance. Termed as tan delta, the loss tangent is defined as the ratio of the imaginary part to the real part (Equation 6).

$$Loss\ tangent = \frac{Imaginary\ part\ (X)}{Real\ part\ (R)} \quad [6]$$

5 SIP Results and Interpretation

Figure 2 shows inverted electrical impedance magnitude (RMS 6%) and phase shift angle at 40 kHz (RMS 19 mrad). The electrical impedance magnitude plot uncovers the existence of a high resistivity layer situated approximately 2 m below the surface, spanning a horizontal distance of 22 to 24 m. Additionally, a distinct high resistive layer is observed within a horizontal range of 12 to 20 m.

The area with high resistivity can indicate the presence of various materials, such as ice and bedrock, that possess high resistivity properties. However, it is not possible to draw a definitive conclusion about the presence of ice solely based on resistivity measurements. To enhance the interpretation process, the study examined the results of phase shift angle inversion.

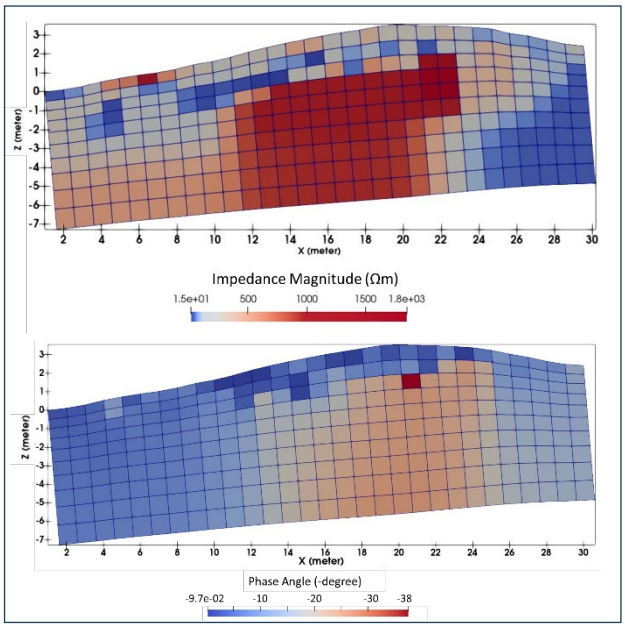

Figure 2. Electrical impedance magnitude (Ωm) and phase angle (degree) at 40 kHz.

The phase shift angle plot revealed higher negative phase values between 14 and 26 m, suggesting a positive correlation with the high resistivity area. Still, it's essential to recognize that this correlation is a sign of the existence of ice, not a definitive proof.

Using Equation 3 we can translate electrical impedance into real and imaginary components. Figure 3 illustrates both the real and imaginary components of the electrical impedance within the study area, at 40 kHz. Directing our attention to the imaginary part of the electrical impedance, it becomes evident that a clearly discernible high resistivity region is located at a depth of ~1.5 m, spanning a horizontal distance between 22 and 27 m. The imaginary part of the electrical impedance, also known as capacitive reactance (X), provides valuable insights into the presence of inductive or capacitive materials. Notably, the negative values of the phase shift angle indicate the presence of capacitive materials. Furthermore, the polarization observed in the imaginary plot (Figure 3) directly correlates with the existence of ice. Therefore, the elevated values observed in the imaginary plot (indicated by the arrows) suggest the possible presence of ice within the study area. Furthermore, the higher values observed at the surface can be attributed to the presence of snow cover.

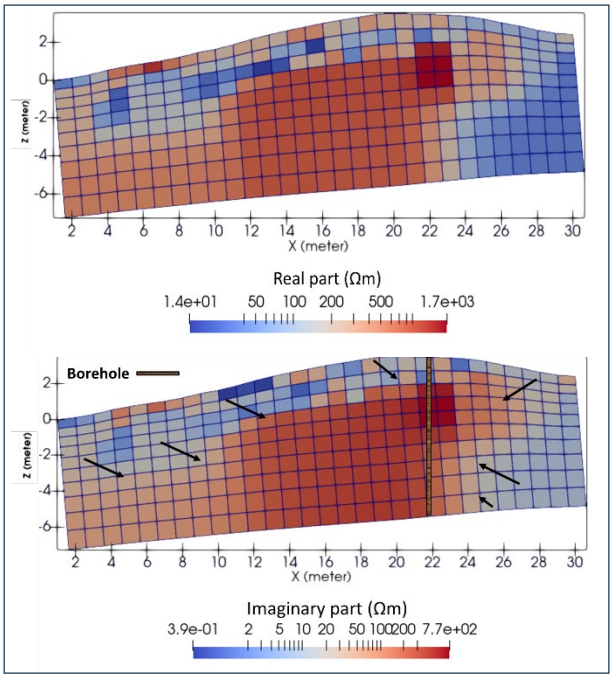

Figure 3. Real and Imaginary part (Capacitance Reactance) of electrical impedance at 40 kHz (the arrows show the elevated values observed in the imaginary plot).

The electrical impedance amplitude (RMS 2%) and phase shift angle (RMS 29 mrad) inversion results at 1.46 Hz are presented in Figure 4. The electrical impedance magnitude plot exhibits similarities with the one at 40 kHz; however, the magnitudes of these two plots differ significantly.

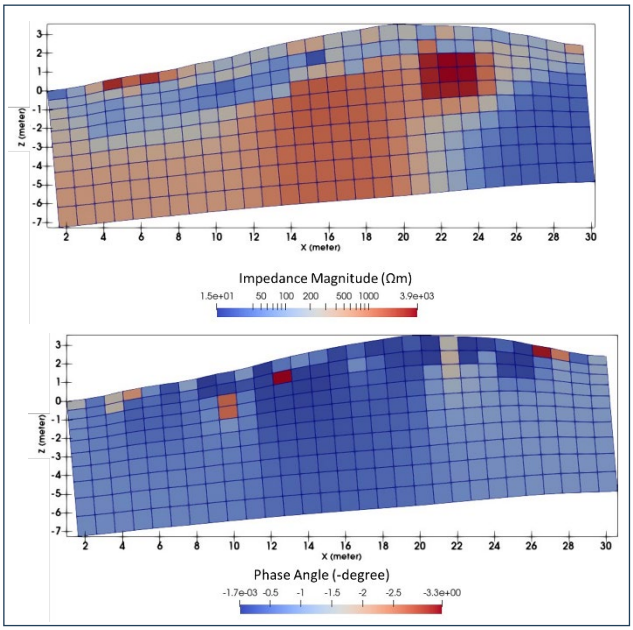

Figure 4. Electrical impedance magnitude, and phase shift angles at 1.46 Hz.

Notably, the resistivity at 1.46 Hz is higher compared to 40 kHz. It's noteworthy that ice polarization is expected within the kHz range. This anticipation is evident in the 40kHz plot, where the phase shift angle exhibits higher values, in contrast to the 1.46Hz plot where it remains below -4°. This contrast serves as a robust indicator of ice polarization.

Figure 5 shows RFE (Equation 5) image for the study area. The higher values correspond to a higher ice content. The red pixels in RFE plot shows higher ice content that is almost compatible with the electrical impedance inversion results at 40 kHz (Figure 3); there are some unanticipated differences among them that can be explained by the presence of clay in the study area especially when the presence of clay affects the real part resistivity values in the highest and the lowest frequencies.

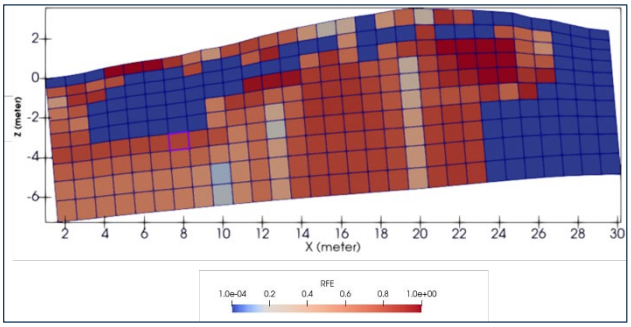

Figure 5. RFE result for the study area.

6 Comparison with Drill Logs

The borehole log (Table 2; 60.7837°N 137.53188°W; Figure 3) reveals fibric organics, including mosses and wood fragments near the surface (0–0.1 m) and subsequent layers (0.1–0.3 m) are composed of notably dry and dense silt. An air-filled void (0.3–0.6 m) is associated with cracking at the pingo's apex. Clayey silt (1.25–2.4 m) displays 5% visible ice volume and the silty clay below features increasingly prominent ice lenses. The most significant ice body (3.6–8.3 m; Figure 6) has a visible ice content of 98%. Notably, sporadic lenses of silty clay transition into diamict lenses as depth increases, with thicknesses ranging from 5 to 20 cm. Below 8.3 m, there is a water-filled section with an uncertain composition of either gravel or diamict.

Figure 7 displays variations in the phase shift angle at the borehole location. It reveals a low phase shift angle value of -2.83° in the ice-free zone at a depth of 0–0.6 m. With the presence of ice, there is a slight change from -2.83 to -2.87° at 0.6 m, aligning with the boundary between the clayey silt (lower ice content) and air layer (ice-free layer). In the middle of this layer (1.5 m), the phase shift angle experiences a significant shift, reaching -24.2° likely due to ice polarization. At 2.2 m depth, another change occurs, marking the boundary between silty clay and clayey silt with higher ice content. From a depth of 3.6 to 8.3 m, the increasing ice volume results in gradual shifts toward more negative phase shift angle values, reaching -25.2° at 8.3 m depth. The initial phase shift angle change for the last layer occurs at 4.7 m depth, approximately one meter away from

the boundary between the ice layer and silty clay, possibly due to the lower resolution of 40 kHz at greater depths.

Table 2. Log details for borehole on pingo. Ice content is given in estimated volume percent of visible ice.

Depth (m)	Material	Frozen	Ice (%)	Ice
0–0.1	Fibric organics	Y	Nil	Nf
0.1–0.3	Silt	Y	Nil	Nf
0.3–0.6	Air		Nil	-
0.6–2.4	Clayey silt	Y	5	Vx
2.4–2.9	Silty clay	Y	20	Vr
2.9–3.6	Silty clay	Y	30	Vr
3.6–8.3	Ice	Y	98	ICE+clay +diamict
8.3–10.8	Gravel	N	0	-

Figure 6. Core recovered from 6.0 to 6.6 meters depth.

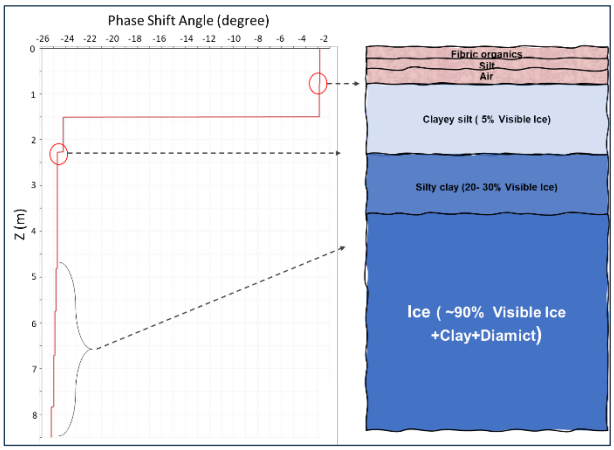

Figure 7. Phase Shift Angle at 40 kHz (extracted for the borehole location).

Figure 8 illustrates changes in electrical impedance magnitude, real and imaginary part (on the left side), as well as the loss tangent (on the right side). In the ice-free layers, the imaginary part remains stable at around 1.6 Ωm. However, at a depth of 1.5 m, these values significantly increase to 500 Ωm due to the presence of icy clayey silt layers. In the upper depth (ice-free layer), the real part is nearly equal to the electrical impedance magnitude, with a ratio close to 1. Conversely, within the ice layer, the real part contributes less to the electrical impedance magnitude, while the imaginary part takes on a more significant role (loss tangent reaching up to 0.47 at a depth of 8.3 m). Despite decreasing resistivity values at greater depths (due to clay present), the increasing ice content results in a higher loss tangent, as the contribution of the real part decreases.

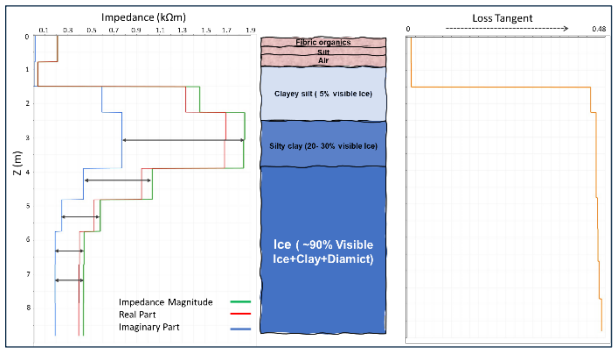

Figure 8. Electrical impedance magnitude, real, imaginary part, and loss tangent at 40 kHz (extracted for the borehole location).

7 CONCLUSIONS

This study effectively utilized Spectral Induced Polarization (SIP) to identify the ice core at the pingo site located in Haines Junction, Yukon province. The data acquisition process involved utilizing the FUCHS frequency domain instrument across a frequency spectrum ranging from 1.46 Hz to 40 kHz. At 1.46 Hz (Figure 4), the phase angle exhibited low values, indicating that the capacitance had dissipated, allowing electrical energy to flow entirely through the resistive pathway. Conversely, the phase shift angle (and imaginary part of electrical impedance) at 40 kHz (Figures 2 and 3) showed high values due to the presence of ice, aligning with the high ice volume observed in the borehole. Additionally, the RFE equation was applied to detect the core ice. While higher RFE values reliably indicated the presence of ice, the existence of clay (free ions) complicated the relationship between RFE and ice content. For the next study, the focus will be on extracting dielectric spectra across all 20 frequencies and comprehensively analyzing the relationship between ice content, water content, and temperature within the SIP data.

8 ACKNOWLEDGEMENTS

This work would not have been possible without the help of Moya Painter, and Patrick Sack.

Funding for this field campaign came from the Yukon Geological Survey, and Natural Science and Engineering Research Council of Canada (NSERC). This is Yukon Geological Survey contribution 065.

9 REFERENCES

Artemov, V.G. and Volkov, A.A. 2014. 'Water and ice dielectric spectra scaling at 0°C', *Ferroelectrics* 466(1), pp. 158–165. doi:10.1080/00150193.2014.895216.

Bittelli, M., Flury, M., and Roth, K. 2004. 'Use of dielectric spectroscopy to estimate ice content in frozen porous media', *Water Resources Research* 40(4). doi:10.1029/2003WR002343.

Blanchy, G., Saneiyan, S., Boyd, J., McLachlan, P., and Binley, A. 2020. 'ResIPy, an intuitive open source software for complex geoelectrical inversion/modeling', *Computers and Geosciences* 137. doi:10.1016/j.cageo.2020.104423.

Grimm, R.E. and Stillman, D.E. 2015. 'Field test of detection and characterisation of subsurface ice using broadband spectral-induced polarisation', *Permafrost and Periglacial Processes* 26(1), pp. 28–38. doi:10.1002/ppp.1833.

Grimm, R.E., Stillman, D.E., and MacGregor, J.A. 2015. 'Dielectric signatures and evolution of glacier ice', *Journal of Glaciology* 61(230), pp. 1159–1170. doi:10.3189/2015JoG15J113.

Grimnes, S. and Martinsen, Ø.G. 2015. 'Electrolytics', *Bioimpedance and Bioelectricity Basics*, pp. 9–36. doi:10.1016/B978-0-12-411470-8.00002-7.

Hobbs, P.V. 2010. *Ice physics*. Oxford, England: Oxford University Press.

Kasprzak, M., Strzelecki, M.C., Traczyk, A., Kondracka, M., Lim, M., and Migała, K. 2017. 'On the potential for a bottom active layer below coastal permafrost: the impact of seawater on permafrost degradation imaged by electrical resistivity tomography (Hornsund, SW Spitsbergen)', *Geomorphology* 293, pp. 347–359. doi:10.1016/j.geomorph.2016.06.013.

Kemna, A., Binley, A., Cassiani, G., Niederleithinger, E., Revil, A., Slater, L., Williams, K.H., Orozco, A.F., Haegel, F.H., Hördt, A., Kruschwitz, S., Leroux, V., Titov, K., and Zimmermann, E. 2012. 'An overview of the spectral induced polarization method for near-surface applications', *Near Surface Geophysics* 10(6), pp. 453–468.

Li, X., Jin, X., Wang, X., Jin, H., Tang, L., Li, X., He, R., Li, Y., Huang, C., and Zhang, S. 2021. 'Investigation of permafrost engineering geological environment with electrical resistivity tomography: A case study along the China-Russia crude oil pipelines', *Engineering Geology* 291. doi:10.1016/j.enggeo.2021.106237.

Lvovich, V.F. 2012. *Impedance spectroscopy: applications to electrochemical and dielectric phenomena*. Hoboken, New Jersey, United States: John Wiley & Sons.

Mudler, J., Hördt, A., Kreith, D., Sugand, M., Bazhin, K., Lebedeva, L., and Radić, T. 2022. 'Broadband spectral induced polarization for the detection of Permafrost and an approach to ice content estimation - a case study from Yakutia, Russia', *Cryosphere* 16(11), pp. 4727–4744. doi:10.5194/tc-16-4727-2022.

Oldenborger, G.A. 2021. 'Subzero temperature dependence of electrical conductivity for permafrost geophysics', *Cold Regions Science and Technology* 182. doi:10.1016/j.coldregions.2020.103214.

Park, K., Kim, K., Kim, K., and Hong, W.T. 2023. 'Characterization of active layer at different degrees of patterned ground development using electrical resistivity tomography survey', *Cold Regions Science and Technology* 208. doi:10.1016/j.coldregions.2022.103734.

Petrenko, V.F. and Whitworth, R.W. 1999. *Physics of ice*. Oxford, England: Clarendon Press.

Stillman, D.E., Grimm, R.E., and Gruber, S. 2018. 'Spectral induced polarization surveys to infer ground ice in a peatland and a lithalsa in warm permafrost near Yellowknife, Canada', in *5th European Conference on Permafrost: Extended abstracts*. Chamonix-Mont Blanc, France: pp. 1–2.

You, Y., Yu, Q., Pan, X., Wang, X., and Guo, L. 2013. 'Application of electrical resistivity tomography in investigating depth of permafrost base and permafrost structure in Tibetan Plateau', *Cold Regions Science and Technology* 87, pp. 19–26. doi:10.1016/j.coldregions.2012.11.004.

Zorin, N. and Ageev, D. 2017. 'Electrical properties of two-component mixtures and their application to high-frequency IP exploration of permafrost', *Near Surface Geophysics* 15(6), pp. 603–613.

Evaluating local drivers of ground surface temperature variability in coastal Labrador

Anika Forget[1], Robert Way[1], Yifeng Wang[1], Jordan Beer[1], Victoria Colyn[1], Rosamond Tutton[2], Andrew Trant[3] & Luise Hermanutz[4]

[1]*Northern Environmental Geoscience Laboratory, Queen's University, Kingston, Ontario, Canada*

[2]*Global Water Futures, Yellowknife, Northwest Territories, Canada*

[3]*Ecological Legacies Lab, University of Waterloo, Waterloo, Ontario, Canada*

[4]*Memorial University of Newfoundland and Labrador, St John's, Newfoundland, Canada*

ABSTRACT

Disentangling the contrasting influences of local ecosystem properties on soil temperatures is critical to understanding drivers of spatial variability in ground thermal conditions and permafrost distribution. In this study, we investigate the influence of vegetation, snow, and soil conditions on ground surface temperatures at two subarctic research basins in coastal Labrador. Eighteen ground surface temperature loggers were deployed at each basin using a stratified random deployment protocol based on land cover and snow thickness strata obtained from summer and winter uncrewed aerial vehicle surveys. Site-specific field information was also collected at each logger location in both summer and winter to contextualize ground surface temperature variability. At the southern field site (Pinware River Hills), derived microclimate indices had statistically significant associations with ground temperatures, whereas at the northern site (Nain Bay Hills), ecosystem properties including snow thickness, were important predictors of temperature variability. Ensemble model simulations of permafrost probability indicate that only 10% of loggers had more than 50% probability of having permafrost, but all of these loggers were found at Nain Bay Hills in low-snow tundra and wetland ecotypes. This research will inform regional permafrost distribution modelling and our understanding of the microclimate drivers or ground temperature variability in northern regions.

1 INTRODUCTION

Permafrost is an important component of the terrestrial cryosphere, storing carbon (Schuur et al. 2015), supporting habitat for keystone species (Joly et al. 2021), and sustaining traditional activities for Indigenous Peoples (Anderson et al. 2018). Permafrost thaw due to ongoing changes in climate and land use (Biskaborn et al. 2019; Suter et al. 2019) increases the potential for ecosystem modifications (Jin et al. 2021; Olefeldt et al. 2021). Most studies predict that permafrost in the discontinuous zone will be the first to thaw because it is usually in disequilibrium with current climate (Biskaborn et al. 2019; Holloway and Lewkowicz 2019; Hrbáček et al. 2019). However, regional permafrost changes are expected to be heterogenous because variability in snow, vegetation, and soil characteristics alter the susceptibility of landscapes to permafrost thaw (Grünberg et al. 2020; Myers-Smith and Hik 2013; Zhang et al. 2021). As these factors can vary over sub-meter scales, it is challenging to evaluate permafrost characteristics at high spatial resolution via remote sensing, especially with large gaps in permafrost observation networks (Philipp et al. 2021; Smith et al. 2005).

Previous research has shown that permafrost distribution in upland areas can be particularly heterogeneous (von Oppen et al. 2022; Zhang et al. 2021). Microclimatic conditions such as vegetation height, snow cover, and soil characteristics all influence the local thermal exchanges, resulting in highly variable ground thermal regimes (Mott et al. 2018; Myers-Smith and Hik 2018; Strum et al. 2001). This variability can be amplified in coastal mountainous areas (Davesne et al. 2017) where ground surface temperatures often vary by 2–4 °C across short distances (< 1 m) due to differing snow thicknesses; thicker snow insulates the ground surface from seasonal and daily air temperature fluctuations, resulting in warmer ground temperatures (Gisnås et al. 2016).

Recent technological advances have facilitated extensive data logger deployments across large study areas, opening new opportunities to quantify the drivers of local scale variability in ground temperatures (Garibaldi et al. 2021; Șerban et al. 2023). However, many of these studies have focused on field sites with low regional snowfall totals. As such, there are fewer observed ground surface temperatures (GST) in coastal discontinuous permafrost environments where high snow conditions can enhance variability (Bense et al. 2016; Lembrechts et al. 2020).

In this study, we investigate local-scale variability in GST at two low-relief coastal mountain research basins (Pinware River Hills and Nain Bay Hills) located at the extreme ends of the discontinuous permafrost zone in coastal Labrador. GST variability was analyzed together with in situ vegetation, snow, and soil characteristics to elucidate the effect of microclimate conditions on the ground thermal regime. These results will contribute to a better understanding of local microclimate impacts on ground temperatures.

2 METHODOLOGY

Data were collected from two hilltop plateau research basins (Pinware River Hills [PRH] and Nain Bay Hills [NBH]) located in low-relief coastal mountains in Labrador, Canada (Figure 1). Both sites were chosen following consultation with regional partners and aim to maximize variability in snow redistribution (0–5 m), ecotype (forest-tundra

https://doi.org/10.52381/ICOP2024.209.1

transition), and surficial deposits (till, bedrock, peat; Tutton et al. 2021). PRH (51.7°N, 56.6°W) is at the southern limit of the isolated patches of permafrost zone on lands claimed by the NunatuKavut Community Council. NBH (56.6°N, 62.0°W) is in the Labrador Inuit Settlement Area (Nunatsiavut) and is at the northern limit of the sporadic discontinuous permafrost (Way and Lewkowicz 2018). Eighteen locations (1 by 1 m) at both PRH and NBH were selected for logger deployment covering three ecotypes (upright vegetation, wetland, or tundra) and six snow thickness ranges.

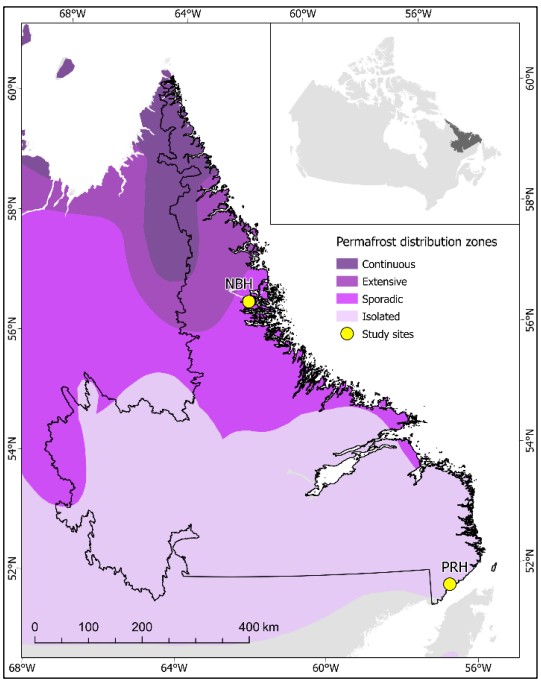

Figure 1. Location of Nain Bay Hills (NBH) and Pinware River Hills (PRH) research basins superimposed on permafrost distribution zones (Heginbottom et al. 1995).

2.1 Uncrewed Aerial Vehicles (UAV) surveys

UAV surveys were used to evaluate site characteristics (Cryderman et al. 2014; Harder et al. 2016) and to inform site selection and sampling strategies. Summer UAV surveys were collected in 2019 (PRH) and 2021 (NBH), while winter UAV surveys were collected in 2020 (PRH and NBH). Image acquisitions (450 m by 450 m double grids) used a DJI Mavic 2 Pro equipped with a 4K Hasselblad camera flown at 90 m above ground level (ground sampling distance: ~2.3 cm). Summer UAV image acquisitions used High Latitude Drone Ecology Network (HiLDEN) data collection protocols (Assmann et al. 2017), while winter UAV image acquisitions followed Walker et al. (2020). Ground control points (n = 10) were collected for each UAV flight using an Eos Arrow Gold GNSS with real-time Atlas corrections differential GPS (DGPS; VRMS < ± 8 cm). Point clouds and orthomosaics were generated using Pix4D, and digital surface models (DSM) and digital terrain models (DTM) were generated using Esri ArcMap 10.7.

UAV orthomosaics were classified according to major land cover strata (tundra, wetland, upright vegetation, bare rock, and water) with a support vector machine object-based supervised classification in ArcMap 10.7. A 1 m resolution late-winter snow depth map was obtained for each site by differencing winter DSMs from summer DTMs with small edits to remove protruding branches (Walker et al. 2020). UAV-derived snow depths for both PRH and NBH were reclassified into six strata (0–0.3 m, 0.3–0.6 m, 0.6–0.9 m, 0.9–1.2 m, 1.2–1.8 m, > 1.8 m) and were combined with three ecotypes (tundra, wetland, upright vegetation) to obtain 18 unique classes.

2.2 GST logger deployment

Thirty-six GST loggers were deployed in summer 2020 (PRH, n = 18) and summer 2021 (NBH, n = 18) at random locations within the UAV-informed 18 unique strata for each site (Figure 2). Navigation to the generated positions (± 40 cm) used a DGPS (Eos Arrow Gold RTK GNSS Receiver). At each point, HOBO MX2203 temperature data loggers (± 0.25 °C) collecting bi-hourly temperature readings were buried 5 cm beneath the ground surface, and locations were marked with metal stakes and flagging tape (Figure 3). Loggers were re-downloaded (35/36; 97% success rate) in summer 2022 enabling a full year of data collection (September 2021 – August 2022) to be analyzed.

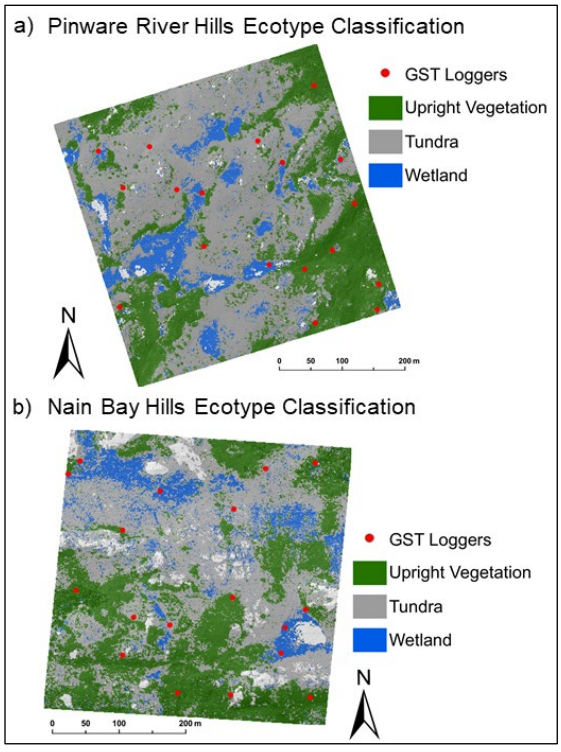

Figure 2. Ground surface temperature logger locations in a) Pinware River Hills and b) Nain Bay Hills field sites by ecotype. Water and bare rock are shown in white.

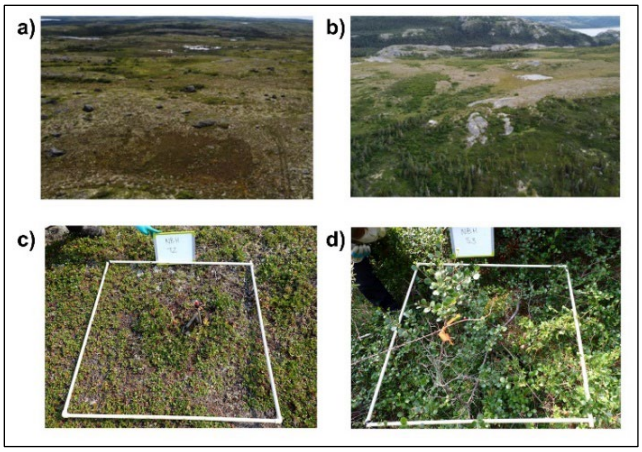

Figure 3. Oblique UAV view of field sites for a) Pinware River Hills (PRH) and b) Nain Bay Hills (NBH) with a c) tundra and d) upright vegetation logger deployment site from NBH.

2.3 Site characterization

At each logger deployment site, vegetation and soil characteristics were collected in summer 2021 and summer 2022. Vegetation plots (1 m by 1 m quadrat) and visual estimates were used to determine percent cover for key functional plant groups (lichen, moss, short shrub, tall shrub, tree, and herbaceous plants) and dominant plot species. Soil conditions were described using small (30 by 30 cm) soil pits dug to the base of the organic layer which enabled the description and thickness of the organic layer and mineral soil texture. Three instantaneous soil moisture measurements were also taken at a 20 cm depth using an Extech MO750 soil moisture meter (± 0.1%).

Late-winter snowpack conditions in mid-March 2022 at PRH and NBH were characterized at each logger position by relocating each logger (± 30 cm of true position) using a DGPS (Broxton et al. 2019; Dong 2018). Snow water equivalents (SWE) and snow densities were calculated for each point using mass measurements of snow cores (Geo Scientific Ltd.) taken within 30 cm of logger location.

Microclimate indices were calculated for each of the 35 logger locations in combinations with the air temperature data recorded at each station within 400 m of each logger (Table 1). The freezing n-factor (nf) is a unitless ratio between the freezing degree days of the soil (FDD_s) and the freezing degree days of the air (FDD_a), while the thawing
n-factor (nt) is the ratio between the thawing degree days of the soil (TDD_s) and the thawing degree days of the air (TDD_a; Burn et al. 2004; Klene et al. 2001; Liu et al. 2021). Nival offset (NVO) and thawing surface offset (TSO) were calculated using the difference between the FDD_a and FDD_s or TDD_a and TDD_s, respectively, divided by the number of days (i.e., 365 days; Way and Lewkowicz 2018). These microclimate indices summarize air-surface temperature differences and vary depending on snow and vegetation characteristics. Higher (lower) nf (NVO) values suggest thinner snow cover and lower (higher) nt (TSO) values suggest taller and/or denser vegetation cover (Hasler et al. 2015; Throop et al. 2012). Surface offset (SO) was also calculated using the difference between the mean annual ground surface temperature (MAGST) and mean annual air temperature (MAAT) to summarize the net effect of nival and thawing offsets over the year (Smith and Riseborough 2002). A correlogram between collected and derived variables was used to examine the general statistical associations between variables and MAGST.

Table 1. Derived microclimate indices.

Indices	Equation	Units
Freezing n-factor (nf)	FDDs÷FDDa	Unitless
Thawing n-factor (nt)	TDDs÷TDDa	Unitless
Nival Offset (NVO)	(FDDa-FDDs)÷365	°C
Thawing Surface Offset (TSO)	(TDDs-TDDa)÷365	°C
Surface Offset (SO)	GST-MAAT	°C
Thermal Offset (TO)	MAGT-GST	°C

2.4 Analysis of permafrost probability

The temperature at the top of permafrost (TTOP) model is a process-based equilibrium permafrost model (Smith and Riseborough 2002) that has been previously used with GST loggers to characterize permafrost distribution (Garibaldi et al. 2021). The mean annual ground temperature at the top of permafrost or the base of seasonal freezing (e.g., MAGT at TTOP) for a given logger location can be estimated by adding a thermal offset (TO; Burn et al. 2004) to MAGST following Davis et al. (2021):

$$TTOP = TO + MAGST \quad [1]$$

The MAGT at the top of permafrost was estimated for each logger location using the measured MAGST and an ensemble of TO estimates for each logger, where the ensemble of TOs were generated using observed TOs from field monitoring locations at PRH (n = 3) and NBH (n = 3) established by Tutton et al. (2021). Following Davis et al. (2021), we generated 1,000 simulated TOs (R(4.1.1)) using the mean (PRH: -0.48 °C; NBH: -0.55 °C) and standard deviation (PRH: 0.25 °C; NBH: 0.48 °C) of TOs measured at the research basins assuming a normal distribution. The ensemble was then applied (Eq.1) to the MAGST of each logger (n = 35) to generate estimates (n = 1,000) of MAGT at TTOP for each logger.

3 Results

3.1 Variability in ground temperatures

MAGSTs averaged 3 °C (range: 2.4–3.9 °C) at PRH and 1.8 °C (range: -0.9 to +3.7 °C) at NBH. Basin-wide differences in MAGST between PRH and NBH were statistically significant (t-test, $p < 0.05$), but when stratified by ecotype, only tundra ($p < 0.05$) and upright vegetation ($p < 0.05$) showed significant differences between the basins. Partitioned by field site, ecotype showed no statistically significant differences at PRH, while at NBH, only differences between tundra and upright vegetation ecotypes were near statistical significance ($p < 0.10$). Greater MAGST was observed at PRH for all ecotypes

compared to NBH (Figure 4). At NBH, variability was higher for tundra (sd: 1.5 °C) and wetland (sd: 1.5 °C) ecotypes than upright vegetation (sd: 0.6 °C), whereas at PRH, variability was greatest in the upright vegetation class (sd:

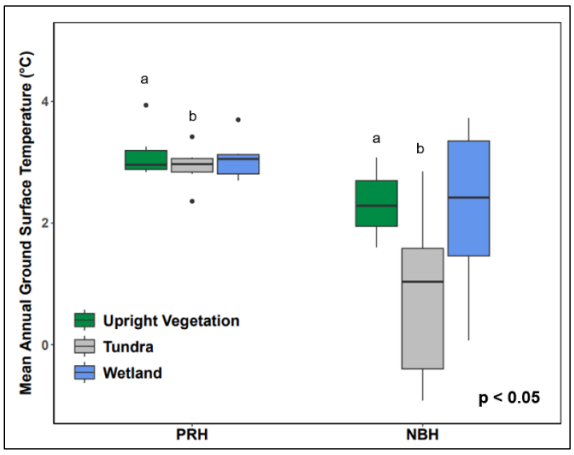

0.4 °C) and lowest in tundra (sd: 0.3 °C).

Figure 4. Mean annual ground surface temperatures (MAGST) recorded by data loggers (n = 35) stratified by research basin (Pinware Rive Hills [PRH] and Nain Bay Hills [NBH]) and ecotype. Statistical differences ($p < 0.05$) between tundra and shrub ecotypes between sites.

Derived freezing metrics (nf and NVO) showed contrasting results between PRH and NBH. The nf and NVO were significantly lower at PRH (mean: nf = 0.13, NVO = 3.3 °C) compared to NBH (mean: nf = 0.25, NVO = 4.5 °C). Stratified by ecotype, nf was the lowest for the upright vegetation ecotypes (PRH: 0.09; NBH: 0.11), indicating limited ground freezing in upright vegetation areas in winter. Similarly, at both sites, mean NVO was the highest at the upright vegetation ecotype (PRH: 3.4 °C; NBH: 5.3 °C) and lowest for tundra (PRH: 3.1 °C; NBH: 3.4 °C).

Air-surface temperature differences in the warm season (nt and TSO) showed smaller differences between the field sites. Nt was slightly lower at NBH (mean: nt = 0.98) compared to PRH (mean: nt = 1.02), whereas TSO was significantly lower at PRH (mean: -1.0 °C) compared to NBH (mean: -0.5 °C; t-test: $p < 0.05$). These data suggest that air-surface temperature differences in the warm season impact PRH more than NBH, but the magnitude of these effects is generally small (usually less than 1 °C). For both field sites, mean TSO was highest at the wetland ecotype (PRH: -0.4 °C; NBH: -0.7 °C) and lowest at the upright vegetation ecotype (PRH: -0.6 °C; NBH: -1.4 °C), indicative of shading and moisture effects on microclimate.

3.2 Correlations between local site properties

Correlograms were used to evaluate and visualize the statistical associations of MAGST and local site properties (Figure 5). Pooling PRH and NBH together, statistically significant Pearson correlations ($p < 0.05$) were observed between MAGST and most variables, except for number of snow days, nt and NVO. The highest correlation was observed between MAGST and nf (r = -0.89). For PRH, MAGST was significantly correlated with nf, SO, NVO, and TSO, with the strongest correlation found with SO (r = 0.99) and nf (r = -0.70). At NBH, MAGST had statistically significant correlations with SWE, snow depth, snow density, nf, SO, and NVO, with the strongest associations with SO (r = 0.99) and nf (r = -0.93).

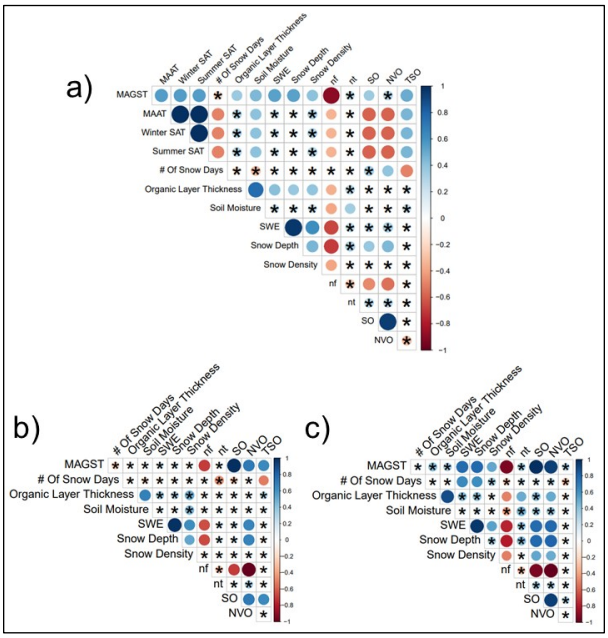

Figure 5. Correlogram of the variables obtained at each logger location for a) both field sites (n = 35), b) PRH (n = 18), and c) NBH (n = 17). Areas without an asterisk show significant correlations ($p < 0.05$), circle size indicates the magnitude of the correlation, and the colour indicates the direction. Note: winter and summer SAT are seasonal averages of air temperature at the two basins.

The derived indices show uneven positive and negative correlations among the pooled sites. nf was significantly negatively correlated with every variable except the number of snow days whereas NVO was both negatively and positively correlated with measured and derived variables. Divided by basins, freezing indices were more correlated at NBH compared to PRH, showing that snow is more important for understanding ground thermal variability at this more northern site.

The pooled data showed that nt was not significantly associated to any factors whereas TSO showed a positive correlation with air temperature (r = 0.46) and a negative correlation with the number of snow days (r = -0.49). Thawing indices showed no significant correlation at NBH, while at PRH correlations were only present for MAGST (r = 0.64) and the number of snow days (r = -0.51). Together these data suggest a lack of consistency in the statistical associations between derived microclimate indices, local site characteristics, and MAGSTs, highlighting the need for additional analyses using other statistical techniques, like structural equation modelling.

3.3 Permafrost distribution

The ensemble-based permafrost simulations showed that there was only a 9.7% probability of permafrost averaged across all 35 loggers at PRH and NBH. Only eight loggers had simulation results indicating permafrost was plausible (> 0% probability), with just three considered likely (> 50% probability). All possible and likely permafrost sites were located at NBH (Figure 6). This was interpreted to be partly because of lower overall MAGSTs at NBH but also because of greater MAGST variability and a larger range of thermal offsets used at NBH compared to PRH (PRH: -1.2 °C to 0.4 °C; NBH: -2.1 °C to 0.9 °C). Two of the three loggers where permafrost was considered likely were in tundra ecotypes and the other was in a wetland ecotype. All three likely permafrost sites had shallower snow depths (≤ 45 cm) compared to non-permafrost logger sites (> 45 cm).

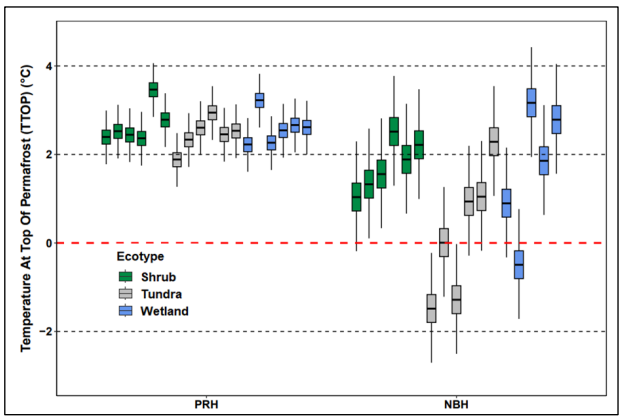

Figure 6. Ensembles of simulated temperatures at top of permafrost (TTOP) (n = 1,000) for the 35 GST loggers simulated using thermal offsets and observed MAGSTs for Pinware River Hills (PRH) and Nain Bay Hills (NBH).

4 Discussion

4.1 Variability in ground temperatures

GSTs in coastal Labrador varied considerably between the two research basins and between ecotypes. Greater within-ecotype variability was observed at the northern field site (NBH) than at the southern field site (PRH). These results are similar to those reported by Tyystjärvi et al. (2023) who found that MAGST variability increased with latitude at field sites in Finland, although Odland et al. (2017) did not find a similar latitudinal association in the Norwegian mountains. In the latter study, the authors reported greater MAGST variability than reported here but this is likely due to the comparatively smaller range in mean annual air temperature for the two basins investigated in the current study. The absence of permafrost at PRH and the low probability of permafrost at NBH may be an important contributor to muted MAGST variability, as deeper ground temperatures can exert a significant influence on near-surface soil temperatures (Riseborough et al. 2008; Smith and Riseborough 2002).

Our study did not find statistically significant differences in MAGST between ecotypes at either PRH or NBH, although the p-values at the latter basin approached significance ($p < 0.10$). This result may be explained by the logger deployment approach which ensured similar strata for snow depth between the ecotypes. Larger sample sizes, particularly at NBH, could have increased our ability to statistically detect smaller effect sizes. Aalto et al. (2018) concluded that local scale vegetation influences on ground temperatures in Finland were non-uniform with vegetation-snow interactions, leading to warmer ground temperatures due to air-surface decoupling. Conversely, Evans et al. (2022) found that at their study sites on Baffin Island, the associations between vegetation type and variability in GSTs was indirect. Instead, their findings emphasized that snow duration and microtopography exerted a more significant influence on the ground thermal regime compared to vegetation characteristics. These contrasting findings highlight the importance of study design and stratified logger deployment to ensure that GST data include a wide range of ecotypes and snow covers.

4.2 Drivers of ground temperature variability

This analysis demonstrated statistically significant associations between multiple measured and derived variables, though the strength of these associations varied when stratified by study sites. Specifically, MAGST at NBH was most correlated with snow indices (SWE, nf, NVO), whereas MAGST at PRH was significantly correlated with derived indices (SO, NVO, TSO). Stronger overall associations found at NBH compared to PRH highlight the role of regional climate differences in altering linkages between ground temperatures and local ecosystem properties, as shown previously in model scenarios by Way and Lapalme (2021). Strong correlations between winter season indices (nf, NVO) and MAGST at NBH agree with a large-scale analysis of 106 subarctic and Arctic sites by Kropp et al. (2020) who found that MAGSTs are more sensitive to variability in winter season conditions. Like Way and Lewkowicz (2018), we observed that air-surface temperature differences in the summer were correlated with the number of snow days which is suggestive of a link between late-lying snow and delayed soil temperature warming (Grünberg et al. 2020). While these associations can provide important context to the ground thermal regime, effect size cannot be determined using correlations alone and differences between basins underscores the necessity of synthesizing data from multiple sites for drawing broader conclusions.

4.3 Permafrost probability

Permafrost is likely present for low snow tundra ecotypes across NBH. This result highlights the importance of considering the effects of snow and vegetation in regional permafrost assessment. Little to no snow accumulation allows colder temperatures to be reached at the surface for longer preserving permafrost at deeper depths (Biskaborn et al. 2019). The wetland ecotype site at NBH where a high permafrost probability was estimated is near a small palsa where the permafrost is insulated by a thick layer of peat. Research by Wang et al. (2023) concluded that peatland permafrost was significantly underestimated for the

Labrador coast and that contemporary models may not be adequately representing permafrost distribution in coastal wetlands. Our results show that even at upland sites peatland permafrost can be found in localized environments with thick peat deposits and minimal snow cover.

4.4 Limitations

Although this study explores many factors influencing local-scale variability in the ground thermal regime, caution is needed to avoid over-extrapolating the results given some key limitations. The single largest limitation is the short period of analysis (one hydrological year) which could lead to differences in basin-wide MAGST compared to longer-term averages (Hargrove and Pickering 1992; Nakagawa and Cuthill 2007). This analysis intended to use two hydrological years, but owing to COVID-19 travel restrictions, NBH was not able to be visited for logger deployment until 2021. For PRH, logger deployment occurred in 2020, but we restricted our analysis to 2021–2022 to ensure comparability with NBH. The short duration of records could also impact the correlation analysis because interannual variability may affect associations between variables but overall zones of high (low) snow accumulation tended to be similar across years and changes in vegetation are generally subtle over short time periods (Myer-Smith and Hik 2013). Future work could build on these results using additional years of data from these study sites and more advanced statistical techniques to better represent spatio-temporal drivers of variability.

5 Conclusions

This study provides new insights into variability of near-surface ground temperatures in northern coastal environments using observations spanning two ends of the discontinuous permafrost zone in subarctic Labrador, northeast Canada. Using a stratified random logger deployment scheme, we were able to explore local scale variations in MAGST across a range of ecotypes and snow conditions. Our results showed that soil temperature variability was greatest at our northern site (NBH) where soil temperatures were lower. We also found that statistical associations with local site properties were also greater at NBH than PRH. These results suggests that macroclimate conditions, like regional permafrost distribution, can dictate or mediate the associations between local ecosystem properties and ground temperatures in subarctic regions. An analysis of permafrost distribution using ensembles of model simulations showed that permafrost is absent from PRH but can be found in certain environments at NBH including low snow tundra and wetland ecotypes.

Ongoing and future changes in temperature, precipitation, and land cover, coupled with expanded development in the Canadian north will necessitate an improved understanding of changes to local microclimate in highly heterogeneous environments like those presented in this study. Our study also highlights the utility of UAVs for supporting stratified sampling designs which can improve the extrapolatability of analyses of the ground thermal regime. This study will contribute to the development and evaluation of next-generation permafrost distribution models in Labrador, and will support the development of climate adaptation strategies for permafrost thaw and ecosystem shifts.

6 References

Aalto, J., Scherrer, D., Lenoir, J., Guisan, A., and Luoto, M. 2018. 'Biogeophysical controls on soil-atmosphere thermal differences: Implications on warming Arctic ecosystems', *Environmental Research Letters* 13, 074003. Available at: https://doi.org/10.1088/1748-9326/aac83e.

Anderson, D., Ford, J.D., and Way, R.G. 2018. 'The Impacts of Climate and Social Changes on Cloudberry (Bakeapple) Picking: A Case Study from Southeastern Labrador., *Human Ecology: An Interdisciplinary Journal* 46(6), pp. 849–863. Available at: https://doi.org/10.1007/s10745-018-0038-3.

Assmann, J., Kerby, J., and Myers-Smith, I. 2017. 'HiLDEN: Spectral Calibration and Guidance', *Drone Ecology Network*. Available at: https://arcticdrones.org/2017/05/12/high-latitude-drone-ecology-network-multispectral-flight-protocol-and-guidance-document/.

Bense, V.F., Read, T., and Verhoef, A. 2016. 'Using distributed temperature sensing to monitor field scale dynamics of ground surface temperature and related substrate heat flux', *Agricultural and Forest Meteorology* 220, pp. 207–215. Available at: https://doi.org/10.1016/j.agrformet.2016.01.138.

Biskaborn, B.K., Smith, S.L., Noetzli, J., Matthes, H., Vieira, G., et al. 2019. 'Permafrost is warming at a global scale', *Nature Communications* 10, 264. Available at: https://doi.org/10.1038/s41467-018-08240-4.

Broxton, P.D., van Leeuwen, W.J.D., and Biederman, J.A. 2019. 'Improving Snow Water Equivalent Maps With Machine Learning of Snow Survey and Lidar Measurements', *Water Resources Research* 55(5), pp. 3739–3757. Available at: https://doi.org/10.1029/2018WR024146.

Burn, C.R. 2004. 'The Thermal Regime of Cryosols', in J. M. Kimble (ed.), *Cryosols: Permafrost-Affected Soils*. Berlin, Germany: Springer, Berlin, Heidelberg. Available at: https://doi.org/10.1007/978-3-662-06429-0_19.

Cryderman, C., Mah, S.B., and Shufletoski, A. 2014. 'Evaluation of UAV Photogrammetric Accuracy for Mapping and Earthworks Computations', *GEOMATICA* 68(4), pp. 309–317. Available at: https://doi.org/10.5623/cig2014-405.

Davesne, G., Fortier, D., Domine, F., and Gray, J.T. 2017. 'Wind-driven snow conditions control the occurrence of contemporary marginal mountain permafrost in the Chic-Choc Mountains, south-eastern Canada: A case study from Mont Jacques-Cartier', *The Cryosphere* 11(3), pp. 1351–1370. Available at: https://doi.org/10.5194/tc-11-1351-2017.

Davis, E., Trant, A., Hermanutz, L., Way, R.G., Lewkowicz, A.G., Siegwart Collier, L., Cuerrier, A. and Whitaker, D. 2021. 'Plant–Environment Interactions in the Low Arctic Torngat Mountains of Labrador', *Ecosystems* 24, pp. 1038–1058. Available at: https://doi.org/10.1007/s10021-020-00577-6.

Dong, C. 2018. 'Remote sensing, hydrological modeling and in situ observations in snow cover research: A review', *Journal of Hydrology* 561, pp. 573–583. Available at: https://doi.org/10.1016/j.jhydrol.2018.04.027.

Evans, S.G., Raberg, J.H., Crump, S.E., Raynolds, M.K., Sugg, M.M., Brodie, A.R., and Miller, G.H. 2022. 'Control of Short-Stature Vegetation Type on Shallow Ground Temperatures in Permafrost Across the Eastern Canadian Arctic', *Journal of Geophysical Research: Biogeosciences* 127(7), e2022JG006941. Available at: https://doi.org/10.1029/2022JG006941.

Garibaldi, M.C., Bonnaventure, P.P., and Lamoureux, S.F. 2021. 'Utilizing the TTOP model to understand spatial permafrost temperature variability in a High Arctic landscape, Cape Bounty, Nunavut, Canada', *Permafrost and Periglacial Processes* 32(1), pp. 19–34. Available at: https://doi.org/10.1002/ppp.2086.

Gisnås, K., Westermann, S., Schuler, T.V., Melvold, K., and Etzelmüller, B. 2016. 'Small-scale variation of snow in a regional permafrost model', *The Cryosphere* 10(3), pp. 1201–1215. Available at: https://doi.org/10.5194/tc-10-1201-2016.

Grünberg, I., Wilcox, E.J., Zwieback, S., Marsh, P., and Boike, J. 2020. 'Linking tundra vegetation, snow, soil temperature, and permafrost', *Biogeosciences* 17(16), pp. 4261–4279. Available at: https://doi.org/10.5194/bg-17-4261-2020.

Harder, P., Schirmer, M., Pomeroy, J., and Helgason, W. 2016. 'Accuracy of snow depth estimation in mountain and prairie environments by an unmanned aerial vehicle', *The Cryosphere* 10(6), pp. 2559–2571. Available at: https://doi.org/10.5194/tc-10-2559-2016.

Hargrove, W. and Pickering, J. 1992. 'Pseudoreplication: A sine qua non for regional ecology', *Landscape Ecology* 6, pp. 251–258. Available at: https://doi.org/10.1007/BF00129703.

Hasler, A., Geertsema, M., Foord, V., Gruber, S., and Noetzli, J. 2015. 'The influence of surface characteristics, topography and continentality on mountain permafrost in British Columbia', *The Cryosphere* 9(3), pp. 1025–1038. Available at: https://doi.org/10.5194/tc-9-1025-2015.

Heginbottom, J.A., Dubreuil, M.A., and Harker, P.T. 1995. 'Canada, Permafrost', in *National Atlas of Canada, 5th edition*. Natural Resources Canada, MCR 4177. Available at: https://doi.org/10.4095/294672.

Holloway, J.E. and Lewkowicz, A.G. 2019. 'Half a century of discontinuous permafrost persistence and degradation in western Canada', *Permafrost and Periglacial Processes* 31(1), pp. 85–96. Available at: https://doi.org/10.1002/ppp.2017.

Hrbáček, F., Oliva, M., Fernández, J.-R., Kňažková, M., and de Pablo, M.A. 2019. 'Modelling ground thermal regime in bordering (dis)continuous permafrost environments', *Environmental Research* 181, 108901. Available at: https://doi.org/10.1016/j.envres.2019.108901.

Jin, X.-Y., Jin, H.-J., Iwahana, G., Marchenko, S.S., Luo, D.-L., Li, X.-Y., and Liang, S.-H. 2021. "Impacts of climate-induced permafrost degradation on vegetation: A review', *Advances in Climate Change Research* 12(1), pp. 29–47. Available at: https://doi.org/10.1016/j.accre.2020.07.002.

Joly, K., Gunn, A., Côté, S.D., Panzacchi, M., Adamczewski, J., Suitor, M.J., and Gurarie, E. 2021. 'Caribou and reindeer migrations in the changing Arctic', *Animal Migration* 8(1), pp. 156–167. Available at: https://doi.org/10.1515/ami-2020-0110.

Klene, A.E., Nelson, F.E., Shiklomanov, N.I., and Hinkel, K.M. 2001. 'The N-factor in Natural Landscapes: Variability of Air and Soil-Surface Temperatures, Kuparuk River Basin, Alaska, U.S.A', *Arctic, Antarctic, and Alpine Research* 33(2), pp. 140–148. Available at: https://doi.org/10.1080/15230430.2001.12003416.

Kropp, H., Loranty, M.M., Natali, S.M., Kholodov, A.L., Rocha, A.V., et al. 2020. 'Shallow soils are warmer under trees and tall shrubs across Arctic and Boreal ecosystems', *Environmental Research Letters* 16, 015001. Available at: https://doi.org/10.1088/1748-9326/abc994.

Lembrechts, J.J., Aalto, J., Ashcroft, M.B., De Frenne, P., Kopecký, M., et al. 2020. 'SoilTemp: A global database of near-surface temperature', *Global Change Biology* 26(11), pp. 6616–6629. Available at: https://doi.org/10.1111/gcb.15123.

Liu, L., Luo, D.-L., Wang, L., Huang, Y.-D., and Chen, F.-F. 2021. 'Dynamics of freezing/thawing indices and frozen ground from 1900 to 2017 in the upper Brahmaputra River Basin, Tibetan Plateau', *Advances in Climate Change Research* 12(1), pp. 6–17. Available at: https://doi.org/10.1016/j.accre.2020.10.003.

Mott, R., Vionnet, V., and Grünewald, T. 2018. 'The Seasonal Snow Cover Dynamics: Review on Wind-Driven Coupling Processes', *Frontiers in Earth Science* 6(197). Available at: https://doi.org/10.3389/feart.2018.00197.

Myers-Smith, I.H. and Hik, D.S. 2013. 'Shrub canopies influence soil temperatures but not nutrient dynamics: An experimental test of tundra snow–shrub interactions', *Ecology and Evolution* 3(11), pp. 3683–3700. Available at: https://doi.org/10.1002/ece3.710.

Myers-Smith, I.H. and Hik, D.S. 2018. 'Climate warming as a driver of tundra shrubline advance', *Journal of Ecology* 106(2), pp. 547–560. Available at: https://doi.org/10.1111/1365-2745.12817.

Nakagawa, S. and Cuthill, I.C. 2007. 'Effect size, confidence interval and statistical significance: A practical guide for biologists', *Biological Reviews* 82(4), pp. 591–605. Available at: https://doi.org/10.1111/j.1469-185X.2007.00027.x.

Odland, A., Bandekar, G., Hanssen-Bauer, I., and Sandvik, S.M. 2017. 'Relationships between vegetation, air and soil temperatures on Norwegian mountain summits', *Geografiska Annaler: Series A, Physical Geography* 99(4), pp. 313–326. Available at: https://doi.org/10.1080/04353676.2017.1333324.

Olefeldt, D., Heffernan, L., Jones, M.C., Sannel, A.B.K., Treat, C.C., and Turetsky, M.R. 2021. 'Permafrost Thaw in Northern Peatlands: Rapid Changes in Ecosystem and Landscape Functions', in J.G. Canadell and R.B. Jackson (eds.), *Ecosystem Collapse and Climate Change*. Switzerland: Springer, Cham, pp. 27–67. Available at: https://doi.org/10.1007/978-3-030-71330-0_3.

Philipp, M., Andreas, D., Buchelt, S., and Kuenzer, C. 2021. 'Trends in Satellite Earth Observation for Permafrost Related Analyses—A Review', *Remote Sensing* 13, 1217. Available at: https://doi.org/10.3390/rs13061217.

Riseborough, D., Shiklomanov, N., Etzelmüller, B., Gruber, S., and Marchenko, S. 2008. 'Recent advances in permafrost modelling', *Permafrost and Periglacial Processes* 19(2), pp. 137–156. Available at: https://doi.org/10.1002/ppp.615.

Schuur, E.A.G., McGuire, A.D., Schädel, C., Grosse, G., Harden, J.W., Hayes, D.J., et al. 2015. 'Climate change and the permafrost carbon feedback', *Nature* 520, pp. 171–179. Available at: https://doi.org/10.1038/nature14338.

Șerban, R.-D., Bertoldi, G., Jin, H., Serban, M., Luo, D., and Li, X. 2023. 'Spatial variations in ground surface temperature at various scales on the northeastern Qinghai-Tibet Plateau, China', *CATENA* 222, 106811. Available at: https://doi.org/10.1016/j.catena.2022.106811.

Smith, M.W. and Riseborough, D.W. 2002. 'Climate and the limits of permafrost: A zonal analysis', *Permafrost and Periglacial Processes* 13(1), pp. 1–15. Available at: https://doi.org/10.1002/ppp.410.

Smith, S.L., Burgess, M.M., Riseborough, D., and Nixon, M.F. 2005. 'Recent trends from Canadian permafrost thermal monitoring network sites', *Permafrost and Periglacial Processes* 16(1), pp. 19–30. Available at: https://doi.org/10.1002/ppp.511.

Sturm, M., Holmgren, J., McFadden, J.P., Liston, G.E., Chapin, F.S., and Racine, C.H. 2001. 'Snow–Shrub Interactions in Arctic Tundra: A Hypothesis with Climatic Implications', *Journal of Climate* 14(3), pp. 336–344. Available at: https://doi.org/10.1175/1520-0442(2001)014<0336:SSIIAT>2.0.CO;2.

Suter, L., Streletskiy, D., and Shiklomanov, N. 2019. 'Assessment of the cost of climate change impacts on critical infrastructure in the circumpolar Arctic', *Polar Geography* 42(4), pp. 267–286. Available at: https://doi.org/10.1080/1088937X.2019.1686082.

Throop, J., Lewkowicz, A., and Smith, S. 2012. 'Climate and ground temperature relations at sites across the continuous and discontinuous permafrost zones, northern Canada', *Canadian Journal of Earth Sciences* 49(8), pp. 865–876. Available at: https://doi.org/10.1139/e11-075.

Tutton, R., Way, R.G., Beddoe, R., Zhang, Y. and Trant, A. 2021. 'Modelled Soil Temperature Sensitivity to Variable Snow and Vegetation Conditions in Low-Relief Coastal Mountains, Nunatsiavut and NunatuKavut, Labrador', in J. Zufelt (ed.), *Permafrost 2021: Merging Permafrost Science and Cold Regions Engineering*. Reston, Virginia, United States: pp. 71–81. Available at: https://doi.org/10.1061/9780784483589.007.

Tyystjärvi, V.A., Niittynen, P., Kemppinen, J., Luoto, M., Rissanen, T., and Aalto, J. 2023. 'Variability and drivers of winter near-surface temperatures over boreal and tundra landscapes', *EGUsphere* [preprint]. Available at: https://doi.org/10.5194/egusphere-2023-576.

von Oppen, J,. Assmann, J.J., Bjorkman, A.D., Treier, U.A., Elberling, B., Nabe-Nielsen, J., and Normand, S. 2022. 'Cross-scale regulation of seasonal microclimate by vegetation and snow in the Arctic tundra', *Global Change Biology* 28(24), pp. 7296–7312. Available at: https://doi.org/10.1111/gcb.16426.

Walker, B., Wilcox, E.J., and Marsh, P. 2020. 'Accuracy assessment of late winter snow depth mapping for tundra environments using Structure-from-Motion photogrammetry', *Arctic Science* 7(3), pp. 588–604. Available at: https://doi.org/10.1139/as-2020-0006.

Wang, Y., Way, R.G., Beer, J., Forget, A., Tutton, R., and Purcell, M.C. 2023. 'Significant underestimation of peatland permafrost along the Labrador Sea coastline in northern Canada', *The Cryosphere* 17, pp. 63–78. Available at: https://doi.org/10.5194/tc-17-63-2023.

Way, R. and Lapalme, C. 2021. 'Does tall vegetation warm or cool the ground surface? Constraining the ground thermal impacts of upright vegetation in northern environments', *Environmental Research Letters* 16, 054077. Available at: https://doi.org/10.1088/1748-9326/abef31.

Way, R., Lewkowicz, A., and Zhang, Y. 2018. 'Characteristics and fate of isolated permafrost patches in coastal Labrador, Canada', *The Cryosphere* 12, pp. 2667–2688. Available at: https://doi.org/10.5194/tc-12-2667-2018.

Zhang, Y., Touzi, R., Feng, W., Hong, G., Lantz, T.C., and Kokelj, S.V. 2021. 'Landscape-scale variations in near-surface soil temperature and active-layer thickness: Implications for high-resolution permafrost mapping', *Permafrost and Periglacial Processes* 32(4), pp. 627–640. Available at: https://doi.org/10.1002/ppp.2104.

Detection of ice wedges in Yedoma along the Dalton Highway, Alaska, USA, using capacitive-coupled electrical resistivity tomography

Richard Fortier[1], William Schnabel[2], Kevin Bjella[3], Mikhail Kanevskiy[2] & Yuri Shur[2]

[1]*Centre d'études nordiques (CEN), Université Laval, Québec City, Québec, Canada*

[2]*University of Alaska Fairbanks (UAF), Fairbanks, Alaska, United States*

[3]*U.S. Army Engineer Research and Development Center (ERDC), Fort Wainwright, Alaska, United States*

ABSTRACT

In the 2000s, the Alaska Department of Transportation investigated the possibility of realigning about 5 km of the Dalton Highway in Alaska, USA, between the Mile Posts 8 and 12, to meet current design standards and provide safer alignments and grades than the current ones. The project area is in the continuous permafrost zone where ice-rich syngenetic permafrost with large ice wedges, known as Yedoma, formed during the late Pleistocene. To achieve a geotechnical investigation for assessing the permafrost conditions along the proposed realignment, a total of 136 boreholes were drilled.

The ground truth coming from these boreholes offers a unique opportunity to assess the capabilities of engineering geophysical investigation in delineating potentially problematic ice-rich permafrost. Therefore, in addition to this geotechnical investigation, ground penetrating radar (GPR) profiling, direct-current and capacitive-coupled electrical resistivity tomographies (DC-ERT and CC-ERT, respectively) were carried out along the proposed realignment. The permafrost table and top of ice-rich syngenetic permafrost were identified in the GPR profile. Both the higher sensitivity and spatial sampling of CC-ERT than DC-ERT allowed the individual detection of resistive ice wedges embedded in more conductive frozen silts in the model of electrical resistivity from the CC-ERT inversion. This is made possible by the high electrical resistivity contrast between ice wedges and frozen silts near 0 °C. In the DC-ERT model, only large zones of resistive ice-rich permafrost were delineated without individually detecting the ice wedges. This case study shows the capabilities of CC-ERT to delineate ice wedges in a warm permafrost environment. Geophysical investigations prior to geotechnical investigations can help in designing cost-effective drilling campaigns with fewer expensive boreholes for ground truth along planned linear infrastructures in permafrost environments.

1 INTRODUCTION

Very long linear infrastructures such as roads and airfields in permafrost environments are vulnerable to permafrost degradation due to not only their impacts on permafrost dynamics but also climate warming. To reduce their vulnerability to permafrost degradation and mitigate the impacts of permafrost degradation on their life span, performance, and maintenance cost, geotechnical investigations including drilling, permafrost sampling, and laboratory testing are carried out along their extent before construction for location planning and design purpose. However, blind geotechnical investigations without gathering a priori information from digital elevation models, aerial photographs, mapping of surficial geology and permafrost conditions, and geophysical investigation are doomed to fail in identifying the zones most vulnerable to permafrost degradation. Moreover, geotechnical investigations with high density and systematic drilling and sampling are very expensive. A way to optimize the investment in a geotechnical investigation and lower cost is to perform an engineering geophysical investigation to assess permafrost conditions and locate ice-rich permafrost zones vulnerable to degradation as targets for geotechnical investigation. But, currently, this approach of performing engineering geophysical investigations prior to geotechnical investigations along planned linear infrastructures in permafrost environments is not the norm in cold regions engineering practice, likely because there is no well-documented case study as a proof of concept showing the advantages by doing so.

The Dalton Highway, or Alaska Route 11, is a 666-km long road in Alaska, USA, which links interior Alaska to Deadhorse near the Arctic Ocean (Figure 1). This highway was built in 1974 as a supply road to support the Trans-Alaska Pipeline System. In the 2000s, the Alaska Department of Transportation (AKDOT) investigated a possible realignment of the Dalton Highway between the Mile Posts (MP) 8 and 12 near Livengood, about 130 km northwest of Fairbanks (Figures 1 and 2), to meet current design standards and provide safer alignments and grades than the current ones. However, this area is in the continuous permafrost zone (Figure 1). The proposed realignment crosses extremely complex permafrost conditions including ice-rich permafrost with large ice wedges (Figure 3), known as Yedoma, which formed syngenetically by simultaneous accumulation of silt and upward permafrost aggradation during the late Pleistocene (Kanevskiy et al. 2012). Evidence of ice-wedge degradation that results in differential thaw subsidence is visible at many places along the Dalton Highway (Figure 4).

https://doi.org/10.52381/ICOP2024.163.1

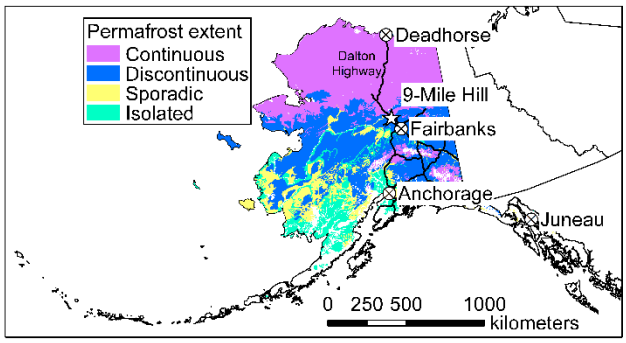

Figure 1. Permafrost map of Alaska, USA (modified from Jorgenson et al., 2008). The star identifies the location of the study site at 9-Mile Hill along the Dalton Highway about 130 km northwest of Fairbanks.

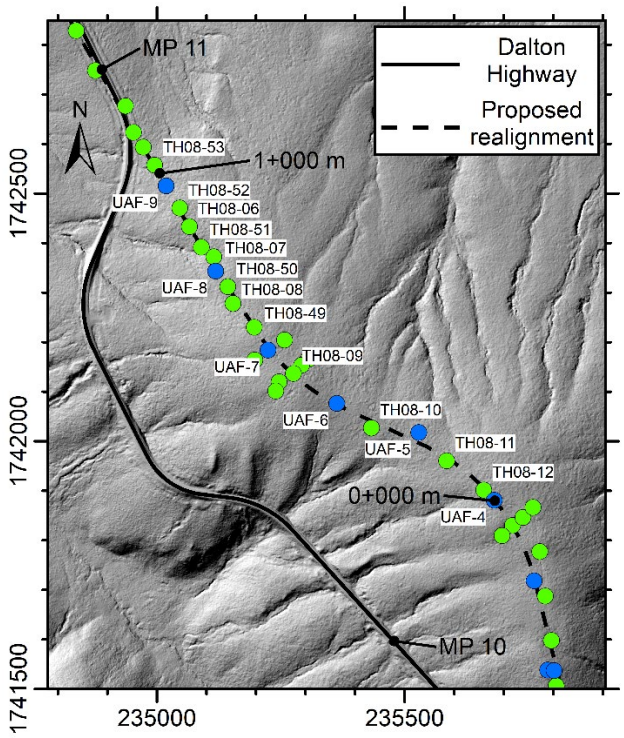

Figure 2. Hillshade map of 9-Mile Hill, Alaska, USA (modified from Hubbard et al. 2011). Location of boreholes drilled for AKDOT (green circles, TH08-XX) and AUTC (blue circles, UAF-X) along the proposed realignment of the Dalton Highway. The Meter Posts 0+000 m and 1+000 m of the geophysical survey line are identified. Projected coordinate system: NAD83 (CORS96) Alaska Albers.

In collaboration with the Alaska University Transportation Center (AUTC) of the University of Alaska Fairbanks (UAF), AKDOT carried out several geotechnical investigations to assess the permafrost conditions along the proposed realignment including 136 boreholes in total (Kanevskiy et al. 2012; Rowland, J. 2010; Schlichting and Darrow 2006; Shur et al. 2010). In Kanevskiy et al. (2012), the main results of these geotechnical investigations are provided such as soils characteristics, local stratigraphy, ice content, and a cryostratigraphic cross-section. The ground truth coming from these geotechnical investigations offers a unique opportunity to assess the capabilities of an engineering geophysical investigation in delineating potentially problematic ice-rich permafrost. The AUTC in collaboration with the Center for Northern Studies (Centre d'études nordiques – CEN) at Université Laval, Québec, Canada, and the U.S. Army Engineer Research and Development Center (ERDC) performed in May 2010 a geophysical investigation including ground penetrating radar (GPR) profiling, direct-current electrical resistivity tomography (DC-ERT), and capacitive-coupled electrical resistivity tomography (CC-ERT) along the proposed realignment of the Dalton Highway (Schnabel et al. 2014). GPR profiling and ERT used along the same survey line are complementary geophysical methods (De Pascale et al. 2008; Fortier and Savard 2010) since ERT is effective to assess the permafrost conditions such as ice-rich zones vs ice-poor or unfrozen zones and GPR can identify the subsurface stratigraphic contacts. The results of this engineering geophysical investigation relative to the borehole logs are presented herein as a proof of concept to show the advantages of performing geophysical surveys prior to geotechnical investigations of permafrost environments. Problematic zones of ice-rich permafrost can be effectively delineated with geophysical investigations, demonstrating that this approach can successfully identify targets for drilling to optimize a cost-effective drilling campaign with fewer boreholes for ground truth.

Figure 3. Ice wedge exposed in a road cut along the Dalton Highway, Alaska, USA. The baseball cap on the right provides the scale. All copyrights reserved to AKDOT.

Figure 4. Localized thaw subsidence zones along the Dalton Highway, Alaska, USA, due to the degradation of ice wedges.

2 METHODOLOGY

A Sensors & Software pulseEKKO Pro with antennas of 100 MHz was used along the realignment of the Dalton Highway on May 20th 2010 to perform two types of surveys: 1) fixed-offset reflection profiling to map the subsurface stratigraphic contacts and 2) common mid-point (CMP) sounding to assess the velocity of the radar signal in the ground. The GPR depth profile corrected for topography is given in Figure 5A. The two CMP soundings 1 and 2 carried out near the boreholes UAF-9 at 0+960 m and UAF-7 at 0+556 m, respectively, along with their analysis are given in Figure 6. The analysis of a GPR-CMP sounding involves stacking the radar traces corrected in time for several velocities to produce a travel time-velocity graph. When the time-corrected traces are stacked at an incorrect velocity, they tend to interfere destructively and to produce low amplitudes of energy on the graph. When they are stacked at a correct velocity, they add together constructively and produce high amplitudes of energy. The highest amplitudes of energy on the travel-time-velocity graph identify the radar-signal velocity.

Measurements of apparent electrical resistivity to achieve the DC-ERT were performed along the survey line from May 7 to 9th 2010 using an Earth Resistivity/IP Meter SUPER STING R1 IP from Advanced Geosciences Inc. This system is made of 4 cables of 21 connectors 2 m apart from each other for a total of 84 metal electrodes, which are driven in the ground for galvanic contact. A Wenner array was used to perform the DC-ERT with a maximum theoretical depth of investigation of about 25 m. The electrodes selection for direct injection of electrical current into the ground and measurement of induced electrical potential was made automatically by the resistivity meter according to an array program previously downloaded in its memory. Once measurements of apparent electrical resistivity were completed after scanning these 84 electrodes, one cable of 21 connectors at the beginning of the survey line was then moved at the end to perform a “roll along” and increase the DC-ERT length. In total, 11 “roll alongs” were performed for an overall DC-ERT length of 628 m and, in total, 5490 measurements of apparent electrical resistivity. The beginning and end of the DC-ERT are at 0+380 m and 1+008 m near the boreholes UAF-6 and TH08-53, respectively (Figure 2).

The apparent electrical resistivities along the survey line were also measured on May 10th 2010 using an OhmMapper TR5 system from Geometrics Ltd. to perform the CC-ERT. This system is made of one transmitter and five receivers as a dipole-dipole configuration. The transmitter and receivers are coaxial cables called line antennas lying on the ground to couple an AC signal at a frequency of about 16.5 kHz into the ground and measure the induced AC signal, respectively. The conductor in the coaxial cable acts as one plate of a capacitor and the ground acts as the other plate while the insulating sheath of the coaxial cable is the capacitor’s insulator. The AC current in the transmitter cable can pass into the ground similarly to an AC signal through a capacitor. The capacitance of the receiver cable is similarly charged, allowing the measurement of an induced AC voltage in the receiver proportional to the electrical resistivity of the ground. This provides an AC equivalent of a standard DC resistivity measurement without the galvanic contacts needed for the standard method (for more details on the theory behind the capacitively-coupled resistivity method, see Timofeev et al. 1994, and Kuras et al. 2006). Since this system does not depend on galvanic contact with electrodes driven in the ground, it can be towed on the ground surface while collecting data for fast engineering geophysical investigation. According to Kuras et al. (2006), the electrical resistivity measurement is emulated through the capacitive coupling when the ground resistivity is high such as permafrost. CC-ERT was successfully used for engineering and environmental geophysical investigations (Douma et al. 1994) of permafrost environments (Calvert 2002; De Pascale et al. 2008; Fortier and Savard 2010) and mountain permafrost (Hauck and Kneisel 2006).

The extremities of the CC-ERT are near the boreholes UAF-4 and TH08-53 (Figure 2) from 0-088 to 1+096 m for 20,973 measurements of apparent electrical resistivity in total. The CC-ERT survey line is longer than the one for the DC-ERT since the production rate in terms of meter per day is much higher for the CC-ERT than the DC-ERT. Only one day was needed to achieve the CC-ERT in comparison to three days for the DC-ERT. Markers at regular 25-m intervals put along the survey line relative to the reference position at borehole UAF-4 (0+000 m) allowed the location of the measurements of apparent electrical resistivity of the CC-ERT. Four runs with the transmitter and five receivers, different dipole lengths and spacings between the dipoles were performed along the survey line (Table 1). The variation in spacing between the current and potential dipoles changes the depth of investigation of the CC-ERT.

Before inversion, during the filtering of the DC-ERT and CC-ERT datasets, 43 and 270 values of apparent electrical resistivity, respectively, were identified as outliers and removed. The filtered datasets were then inverted using a quasi-Newton method (Loke and Barker 1996) and the software package RES2DINV (Geotomo Software 2010) to produce two models of electrical resistivity corrected for topography (Figure 5B, C, respectively).

The line antennas of CC-ERT do not exactly reproduce the dipole-dipole array of galvanic contacts with metal electrodes. The dipole length of CC-ERT is always shorter than the one of DC-ERT (Kuras et al. 2006). The difference in dipole length is the order of 80% (Oldenborger and LeBlanc 2013). Therefore, the values of apparent electrical resistivity measured with CC-ERT are lower than the ones of DC-ERT. No attempt was made to correct the dipole lengths of CC-ERT and ultimately the values of apparent electrical resistivity as proposed by Oldenborger and LeBlanc (2013) before doing the inversion of CC-ERT.

An interpretative cross-section including the borehole logs from the previous drilling campaigns (Kanevskiy et al. 2012; Rowland, J. 2010; Schlichting and Darrow 2006; Shur et al. 2010) modified from Kanevskiy et al. (2012) and the results from the geophysical investigation presented herein is given in Figure 5E.

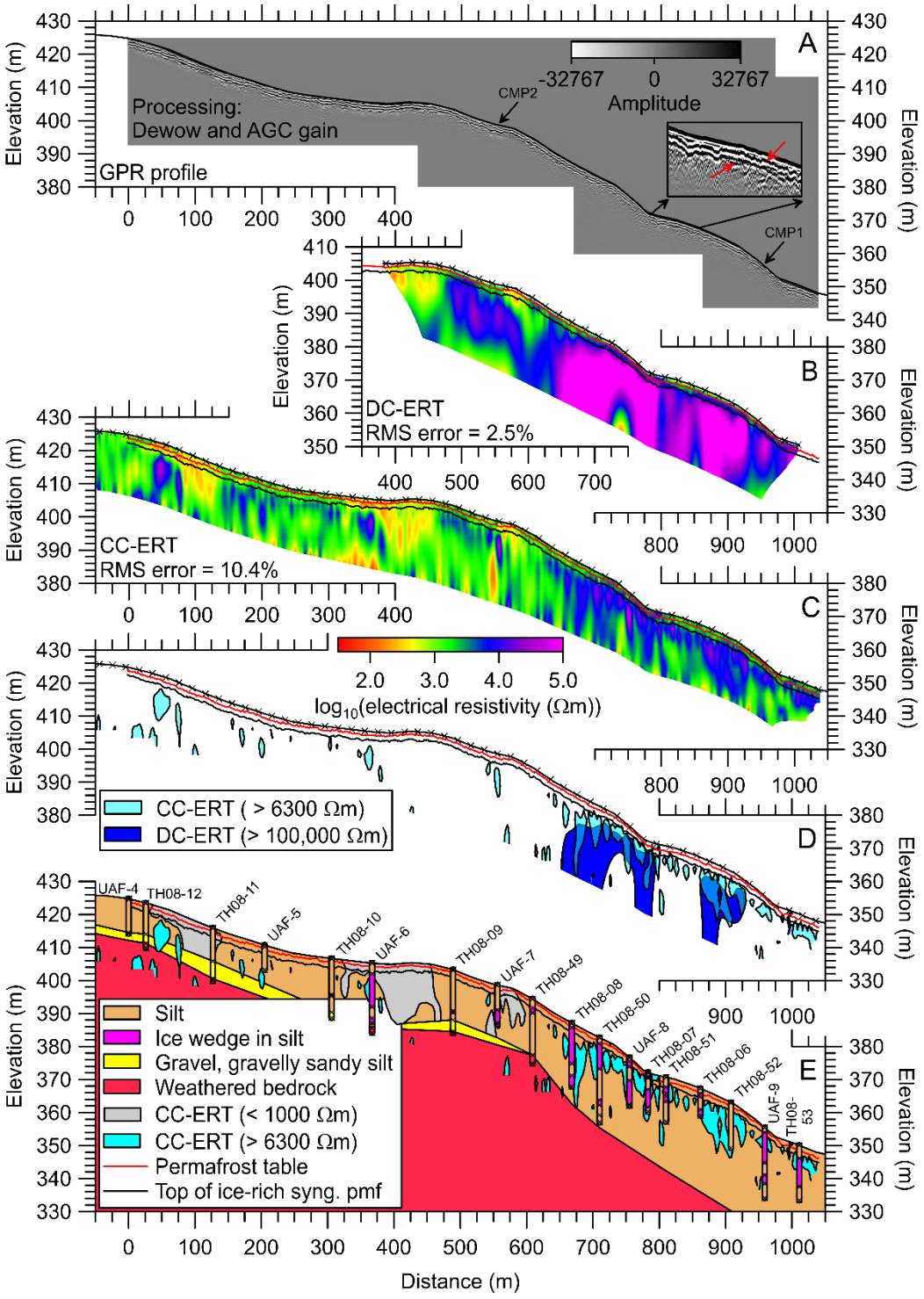

Figure 5. GPR depth profile (A) along the realignment of the Dalton Highway at 9-Mile Hill near Livengood, Alaska, USA (see Figures 1 and 2 for location). Models of electrical resistivity from the inversion of DC-ERT (B) and CC-ERT (C) carried out along the same survey line. (D) Zones of electrical resistivity more than 100,000 Ωm from DC-ERT and 6300 Ωm from CC-ERT. (E) Interpretative cross-section from boreholes (modified from Kanevskiy et al. 2012) along with the results of geophysical investigation. The permafrost table and top of ice-rich syngenetic permafrost as delineated in the GPR profile but not shown are highlighted by red and black full lines, respectively, in the models of electrical resistivity and the interpretative cross-section. Note the vertical exaggeration of 5×.

A thermistor cable driven in the borehole TH08-053 (see Figures 2 and 5 for location) allowed the measurements of ground temperature profiles on August 11th 2008 and May 5th 2010 (Figure 7).

3 RESULTS

From the analysis of the GPR-CMP soundings (Figure 6), the velocity of the radar signal varies between 0.07 (CMP2, Figure 6D) and 0.11 m/ns (CMP1, Figure 6B). A value of 0.1 m/ns was used to transform the GPR travel time profile into a GPR depth profile (Figure 5A).

The scale used in Figure 5 does not allow the identification of reflectors in the GPR profile without zooming in (Figure 5A). Therefore, an inset is provided in Figure 5A to enlarge a small section of the GPR profile and ease the analysis of the GPR profile for that section. Two reflectors as coherent radar signal phases are identified by red arrows in this inset. They are trackable all along the GPR profile, but they are not identified in Figure 5A to avoid any concealing. However, they are highlighted by red and black full lines, respectively, in Figure 5B, C, D, E for comparison purpose.

In the temperature profiles (Figure 7) measured on May 5th 2010, 15 days before performing the GPR surveys, and August 11th 2008, almost at the end of the thawing period, there are unfortunately not enough thermistors to accurately assess the depths of thawing front. A linear interpolation between the ground temperature measurements at depths of 0.8 and 3.8 m as shown by the dashed lines in Figure 7 is not adequate to do so. However, based on the borehole logs, the local stratigraphy is (Kanevskiy et al. 2012): 1) active layer (0–0.7 m), 2) ice-rich silt (0.7–1.5 m), 3) ice-poor thawed and refrozen silt (1.5–3.0 m) and 4) ice-rich syngenetic permafrost (3.0–10.0 m). The two reflectors in the GPR profile are likely due to the stratigraphic contacts between the layers 1 and 2 (permafrost table) and the layers 3 and 4 (top of ice-rich syngenetic permafrost) at respective depths of 0.7 and 3 m. The red and black full lines of these two reflectors are also plotted in the models of electrical resistivity (Figure 5B, C, D) and in the interpretative cross-section for increasing the details (Figure 5E). No other reflector in permafrost was identified at depth in the GPR profile. The depth of investigation of the GPR surveys along the survey line is shallow and limited down to 3 to 4 m deep.

As previously stated, since the CC line antennas are not an equivalent to DC dipoles, the values of electrical resistivity in the CC-ERT model (Figure 5B) are much lower that the ones in the DC-ERT model (Figure 5C). Notwithstanding these differences in electrical resistivity values, the electrical resistivity patterns in both models present striking similitudes and differences while the same permafrost environment was investigated with the two ERT methods. The downhill section of both models of electrical resistivity is more resistive than the uphill section (Figure 5B, C). The change in electrical resistivity behaviour between these two sections is located at about 0+630 m. Since the electrical resistivity is directly proportional to the ice content, one can expect that the ice content of the downhill section is higher than the one of the uphill section. From the analysis of the drilling campaigns (Kanevskiy et al. 2012; Rowland, J. 2010; Schlichting and Darrow 2006; Shur et al. 2010), the downhill and uphill

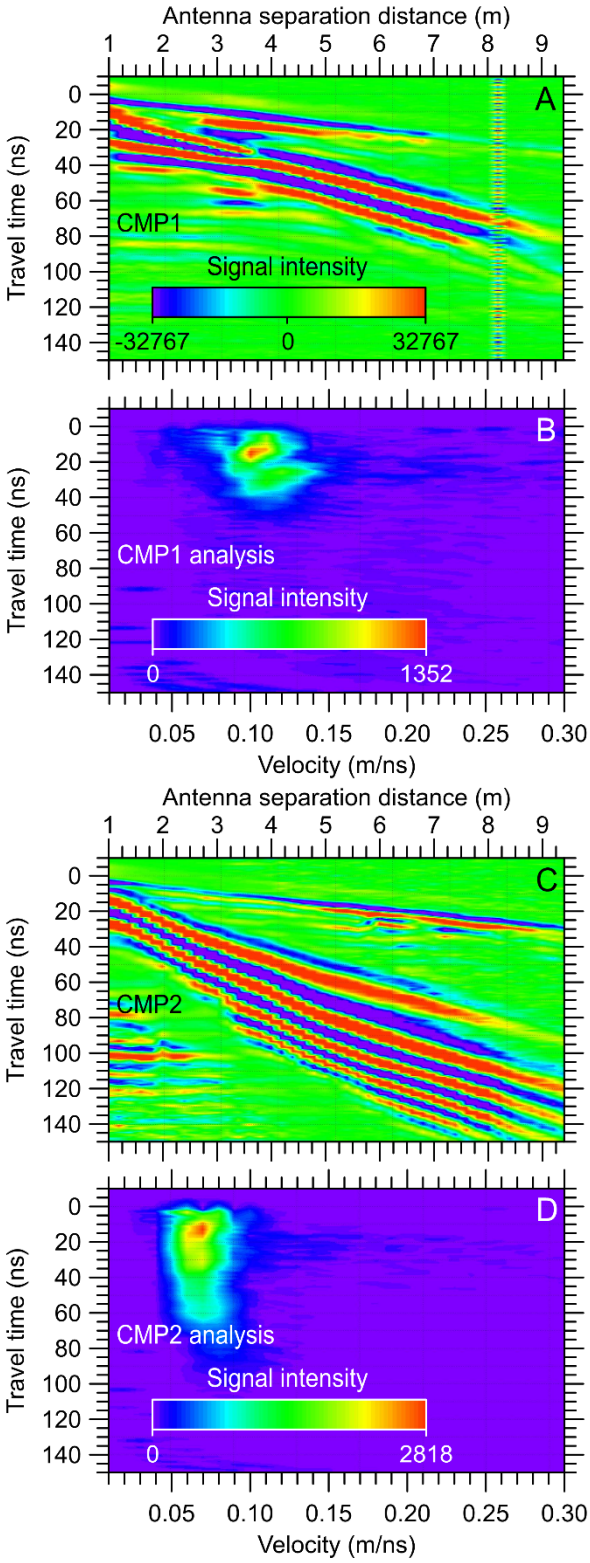

Figure 6. GPR-CMP soundings 1 (A) and 2 (C) carried out near the boreholes UAF-9 at 0+960 m and UAF-7 at 0+556 m, respectively, along the realignment of the Dalton Highway (see Figures 2 and 5 for location). Analysis of GPR-CMP soundings 1 (B) and 2 (D).

Table 1. Parameters used for the CC-ERT.

Run	Electrode cable length, dipole length, and distance between the transmitter dipole and the first receiver dipole (m)	Spacing between the transmitter dipole and the five receiver dipoles (m) (receiver number)	n factor between the dipoles	Theoretical depth of investigation (m) (Loke, 2000)
#1	2.5, 5, and 5	5 (#1)	1	2.1
		7.5 (#2)	1.5	2.8
		10 (#3)	2	3.5
		12.5 (#4)	2.5	4.2
		15 (#5)	3	4.9
#2	5, 10, and 5	5 (#1)	0.5	3.5
		10 (#2)	1	4.9
		15 (#3)	1.5	6.3
		20 (#4)	2	7.7
		25 (#5)	2.5	9.1
#3	5, 10, and 25	25 (#1)	2.5	9.0
		30 (#2)	3	11.0
		35 (#3)	3.5	13.0
		40 (#4)	4	15.0
		45 (#5)	4.5	17.0
#4	5, 10, and 50	50 (#1)	5	14.0
		55 (#2)	5.5	16.0
		60 (#3)	6	18.0
		65 (#4)	6.5	20.0
		70 (#5)	7	22.0

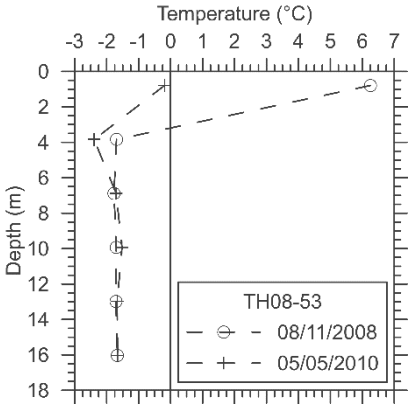

Figure 7. Ground temperature profiles measured along a thermistor cable in the borehole TH08-053 on August 11th 2008 and May 5th 2010 (see Figures 2 and 5 for location).

sections were identified as ice-rich and ice-poor permafrost sections, respectively, in the cross-section developed by Kanevskiy et al. (2012) where the downhill section has a high occurrence of ice wedges (Figure 5E). There is also a superficial layer of low electrical resistivity of about 3 m thick which is due to the units 1, 2, and 3 previously described. The high electrical resistivity contrast in both models at the depth of about 3 m is due to the stratigraphic contact between the units 3 and 4 and corresponds roughly to the second reflector in the GPR profile (see the black full line in both models of electrical resistivity in Figure 5B, C). And, finally, the CC-ERT model looks noisier than the DC-ERT one which is consistent with other studies (Hauck and Kneisel 2006).

4 DISCUSSION

The dipole-dipole array used in the CC-ERT is more sensitive to lateral variations in electrical resistivity than the Wenner array used in the DC-ERT (Dahlin and Zhou 2004). Such lateral variations in electrical resistivity are expected for ice wedges embedded in frozen silts in Yedoma. Moreover, in this study, the spatial sampling of CC-ERT and DC-ERT models is 1748 measurements per 100 m ((20,973 data points – 270 outliers)/survey length of 1184 m) and 867 measurements per 100 m ((5490 data points – 43 outliers)/survey length of 628 m), respectively, for a similar depth of investigation of about 20 m. Both of these higher sensitivity and spatial samplings of CC-ERT than DC-ERT allow the individual detection of resistive ice wedges embedded in more conductive frozen silts in the downhill section of the model of electrical resistivity from the inversion of CC-ERT dataset (Figure 5C). In the DC-ERT, only the bulk electrical resistivity of ice-rich permafrost is visible in the downhill section without individually detecting the ice wedges (Figure 5B).

The delineation of ice-rich permafrost and ice wedges in the downhill section of the DC-ERT and CC-ERT models (Figure 5B, C), respectively, can be done by identifying electrical resistivity limits between ice-poor and ice-rich permafrost and between frozen silt and ice wedges (Figure 5D). To achieve this delineation, electrical resistivity limits of 100,000 Ωm for ice-rich permafrost in the DC-ERT model and 6300 Ωm for ice wedges in the CC-ERT model were empirically assessed. Using these limits, two zones of ice-rich permafrost are delineated, and several ice wedges are individually identified in the downhill section in Figure 5D. As previously stated, the values of electrical

resistivity in the CC-ERT model are much lower than the ones in the DC-ERT model. This explains the difference in the two electrical resistivity limits. Instead of using empirical electrical resistivity thresholds, the calculation of electrical resistivity gradients in both models of electrical resistivity would have been another quantitative interpretation criterion not used herein to delineate permafrost conditions based on the identification of the highest gradients (Banville et al. 2016).

The electrical resistivity zonation in the CC-ERT model to delineate ice wedges from frozen silt (Figure 5D) is made possible through the thermal conditions of permafrost at 9-Mile Hill. The permafrost temperature is close to -2 °C (Figure 7). On one hand, at that temperature, the unfrozen water content in frozen silt can be as high as 4% (mass of unfrozen water/mass of dry soil × 100) for a total moisture content of about 55% (Tice et al. 1989) and electrical resistivity is lower than 1000 Ωm (Hoekstra and McNeill 1973). On the other hand, the electrical resistivity of pure ice can be as high as 10 MΩm close to -2 °C (Stillman et al. 2010). Although impurities in ice which are typical for ice wedges can significantly lower the electrical resistivity, there is still a strong electrical resistivity contrast between frozen silt and ice wedges at that temperature. At higher latitudes in the continuous permafrost zone with lower permafrost temperature than 9-Mile Hill, this electrical resistivity contrast with more resistive frozen ground can be lower than the one at 9-Mile Hill. In such cold permafrost environment, CC-ERT may not be as efficient to individually detect ice wedges due to weak electrical resistivity contrast (De Pascale et al. 2008).

The limits of ice wedges in the CC-ERT model (Figure 5D) are also plotted in the cross-section (Figure 5E). Moreover, uphill in both DC-ERT and CC-ERT models, there are zones of very low electrical resistivity below 1000 Ωm. This electrical resistivity limit of 1000 Ωm in the CC-ERT model (Figure 5C) is used to delineate ice-poor permafrost zones and even completely thawed silt which are plotted in the cross-section (Figure 5E). The borehole logs including the units of silt, ice wedge in silt, gravel and gravelly sandy silt, and weathered bedrock, are also superimposed to the previously delineated ice wedges and ice-poor permafrost zones in the cross-section (Figure 5E). This overlay allows the visual correlation of drilled ice wedges and zones of electrical resistivity higher than 6300 Ωm in the CC-ERT model. The agreement between the borehole logs and the CC-ERT model is judged good, such as along the UAF-06 borehole log for instance and with some discrepancies such as for the UAF-09 and TH08-53 borehole logs where the ice wedges are deeper than expected from the interpretation of the CC-ERT model.

There are zones of electrical resistivity higher than 6300 Ωm at depth in the CC-ERT model (Figures 5C, 5D, and 5E). These zones are artefacts from the inversion of ERT dataset as they are located at depth in the bedrock where the CC-ERT model is not well constrained. The depth of investigation of both DC-ERT and CC-ERT is too shallow to detect the weathered bedrock, while the unit of gravel and gravelly sandy silt is probably too thin to be detected.

Based solely on the results from the engineering geophysical investigation along the proposed realignment of the Dalton Highway (Figure 5A, B, C, D), one can design and optimize a drilling campaign to assess the permafrost conditions by identifying targets to drill and sample. For instance, instead of drilling eighteen boreholes along the 1100-m long geophysical survey line (Figure 5E), only the five boreholes TH08-12, TH08-11, UAF-6, UAF-8, and UAF-9 would have been enough to confirm the interpretation of the CC-ERT model for the identification of ice-rich and ice-poor permafrost, and ice wedges. Reduced drilling costs more than offset the costs of an engineering geophysical investigation including GPR profiling and CC-ERT. And, finally, the CC-ERT model can be reinterpreted at the light of borehole logs and constrained inversion can be achieved with these logs (Fortier et al. 2008) instead of free inversion without a priori information as for the present study. From the synthesis of the CC-ERT model and borehole logs, an interpretative cross-section of permafrost conditions can be developed (Figure 5E).

5 CONCLUSIONS

A geotechnical investigation including drilling, soil sampling, and soil testing was carried out in the 2000s along a proposed realignment of the Dalton Highway at 9-Mile Hill near Livengood about 130 km northwest of Fairbanks, Alaska, USA, to assess the permafrost conditions for designing safer alignments and grades than the current ones. The ground truth coming from this geotechnical investigation offers a unique opportunity to assess the capabilities of an engineering geophysical investigation to delineate problematic ice-rich permafrost conditions whose results are presented herein.

Ground penetrating radar profiling identified two stratigraphic contacts (permafrost table and top of ice-rich syngenetic permafrost) all along the survey line. Additionally, two methods of electrical resistivity, using metal electrodes driven in the ground (direct-current electrical resistivity tomography – DC-ERT) and line antennas capacitively coupled with the ground (capacitive-coupled electrical resistivity tomography – CC-ERT), were used to assess the spatial distribution of electrical resistivity. Due to its high production and sampling rate and high sensitivity to lateral variations in electrical resistivity, the CC-ERT has proven to be more efficient to achieve longer survey line in shorter time than the DC-ERT and to individually identify ice wedges.

The results of the geophysical investigation presented herein is a proof of concept of the advantages of performing geophysical surveys prior to geotechnical investigations of permafrost environments. The costs of a drilling campaign can be significatively reduced through its design and optimization by identifying targets in the interpretative geophysical cross-section such as different types of soil, thawed and frozen ground, permafrost table, ice-poor and ice-rich permafrost, and ice wedges.

6 ACKNOWLEDGEMENTS

This work was funded by the Alaska University Transportation Center (Project no. 410018: Geophysical Applications for Arctic/Subarctic Transportation Planning). Thanks are due to William Lee and Erin Trochim, students

at the University of Alaska Fairbanks at the time of the geophysical investigation, for their help in the field and initial processing of DC-ERT survey. The first author acknowledges the welcome of Water and Environment Research Center, University of Alaska Fairbanks, during his sabbatical leave in 2009-2010 when he participated in the geophysical investigation presented herein. Thanks are due to two anonymous reviewers for improving the paper. This paper was written without using artificial intelligence.

7 REFERENCES

Banville, D., Fortier, R. and Dupuis, C. 2016. 'Objective interpretation of induced polarization tomography using a quantitative approach for the investigation of periglacial environments', *Journal of Applied Geophysics* 130, pp. 218–233.

Calvert, H.T. 2002. 'Capacitive-coupled resistivity survey of ice-bearing sediments, Mackenzie Delta', in *72nd Annual Meeting, Society of Exploration Geophysicists*. Salt Lake City, Utah, United States.

Dahlin. T. and Zhou, B. 2004. 'A numerical comparison of 2D resistivity imaging with 10 electrode arrays', *Geophysical Prospecting* 52(5), pp. 379–398.

De Pascale, G.P., Pollard, W.H. and Williams, K.K. 2008. 'Geophysical mapping of ground ice using a combination of capacitive coupled resistivity and ground-penetrating radar, Northwest Territories, Canada', *Journal of Geophysical Research* 113, F02S90. doi:10.1029/2006JF000585.

Douma, M., Timofeev, V.M., Rogozinski, A.W. and Hunter, J.A. 1994. 'A capacitive-coupled ground resistivity system for engineering and environmental applications; results of two Canadian field tests', in *64th Annual International Meeting, Society of Exploration Geophysicists*. Los Angeles, California, United States: pp. 559–561.

Fortier, R., LeBlanc, A.-M., Buteau, S., Allard, M. and Calmels, F. 2008. 'Internal structure and conditions of permafrost mounds at Umiujaq in Nunavik, Canada, inferred from field investigation and electrical resistivity tomography', *Canadian Journal of Earth Sciences* 45, pp. 367–387.

Fortier, R. and Savard, C. 2010. 'Engineering geophysical investigation of permafrost conditions underneath airfield embankments in Northern Quebec (Canada)', in *6th Canadian Conference on Permafrost (GEOCalgary 2010)*. Calgary, Alberta, Canada: pp. 1307–1314.

Geotomo Software 2010. *RES2DINV: Rapid 2-D Resistivity & IP inversion using the least-squares method.* 151 p.

Hauck, C. and Kneisel, C. 2006. 'Application of capacitively-coupled and DC electrical resistivity imaging for mountain permafrost studies', *Permafrost and Periglacial Processes* 17, pp. 169–177.

Hoekstra, P. and McNeill, D. 1973. 'Electromagnetic probing of permafrost', in *Second International Conference on Permafrost*. Yakutsk, Russia: North American Contribution Volume, pp. 517–526.

Hubbard, T.D., Braun, M.L., Westbrook, R.E. and Gallagher, P.E. 2011. *High-resolution lidar data for infrastructure corridors, Livengood Quadrangle, Alaska* Available at: https://doi.org/10.14509/23023.

Jorgenson, T., Yoshikawa, K., Kanevskiy, M., Shur, Y., Romanovsky, V., Marchenko, S., Grosse, G., Brown, J. and Jones, B. 2008. 'Permafrost characteristics of Alaska', in *Ninth International Conference on Permafrost*. Fairbanks, Alaska, United States: pp. 121–124.

Kanevskiy, M., Shur, Y., Connor, B., Dillon, M., Stephani, E. and O'Donnell, J. 2012. 'Study of Ice-Rich Syngenetic Permafrost for Road Design (Interior Alaska)', in *Tenth International Conference on Permafrost*. Salekhard, Russia: Volume 1, International contributions, pp. 191–196.

Kuras, O., Beamish, D., Meldrum, P.I. and Ogilvy, R.D. 2006. 'Fundamentals of the capacitive resistivity technique', *Geophysics* 71, pp. 135–152.

Loke, M.H., 2000. *Electrical imaging surveys for environmental and engineering studies: A practical guide to 2-D and 3-D surveys*.

Loke, M.H. and Barker R. 1996. 'Rapid least-squares inversion of apparent resistivity pseudo-sections using a quasi-Newton method', *Geophysical Prospecting* 44, pp. 131–152.

Oldenborger, G.A. and LeBlanc, A.-M. 2013. 'Capacitive resistivity inversion using effective dipole lengths for line antennas', *Journal of Applied Geophysics* 98, pp. 229–236.

Rowland, J. 2010. 'Geotechnical report – supplemental, Dalton Highway 9 mile North', *Alaska Department of Transportation and Public Facilities, Northern Region Material Section*, Federal Project No. NHF-06502(3) / State Project No. 64899.

Schlichting, S.J. and Darrow, M.M. 2006. 'Geotechnical report, Dalton Highway 9 mile Hill North', *Alaska Department of Transportation and Public Facilities, Northern Region*, Federal Project No. NH-F-065-2(3) / State Project No. 64899.

Schnabel, W., Fortier, R., Kanevskiy, M., Munk, J., Shur, Y. and Trochim, E. 2014. 'Geophysical applications for arctic/subarctic transportation planning, Final Report', *Alaska University Transportation Center* Project # 410018, INE/AUTC 13.01.

Stillman, D.E., Grimm, R.E. and Dec, S.F. 2010. 'Low-frequency electrical properties of ice-silicate mixtures', *Journal of Physical Chemistry B* 114, pp. 6065–6073.

Shur, Y, Kanevskiy, M, Dillon, M, Stephani, E. and O'Donnell, J. 2010. 'Geotechnical investigations for the Dalton Highway innovation project as a case study of the ice-rich syngenetic permafrost', *Institute of Northern Engineering, University of Alaska Fairbanks* Report # FHWA-AK-RD-10-06, prepared for AK DOT & PF, AUTC assigned project # 207122.

Tice, A.R., Black, P.B. and Berg, R.L. 1989. 'Unfrozen water contents of undisturbed and remolded Alaskan silt', *Cold Regions Science and Technology* 17, pp. 103–111.

Timofeev, V.M., Rogozinski, A.W., Hunter, J.A. and Douma, M. 1994. 'A new ground resistivity method for engineering and environmental geophysics', in *Proceedings of the Symposium on the Application of Geophysics to Engineering and Environmental Problems*, EEGS, pp. 701–15.

Large-scale assessment of permafrost conditions using the Canadian Permafrost Electrical Resistivity Survey (CPERS) database

Teddi Herring[1], Antoni G. Lewkowicz[2], Robert G. Way[3], Yifeng Wang[3], Alexandre Chiasson[4] & Duane Froese[4]

[1]*Department of Civil Engineering, University of Calgary, Calgary, Alberta, Canada*

[2]*Department of Geography, Environment and Geomatics, University of Ottawa, Ottawa, Ontario, Canada*

[3]*Department of Geography and Planning, Queen's University, Kingston, Ontario, Canada*

[4]*Department of Earth and Atmospheric Sciences, University of Alberta, Edmonton, Alberta, Canada*

ABSTRACT

Electrical resistivity tomography (ERT) is a geophysical technique that is commonly used to investigate permafrost conditions because the resistivity of earth materials tends to increase greatly when they are frozen, particularly if they are ice-rich. Despite the increasingly widespread use of ERT for permafrost applications over the last 20 years, data sharing in Canada and most other countries has been limited. We created the Canadian Permafrost Electrical Resistivity Survey (CPERS) database as a platform for standardized and accessible sharing of historical and current ERT datasets collected in permafrost environments. Individual researchers from several Canadian institutions have already contributed 280 ERT datasets and associated descriptive, standardized metadata. These datasets were collected between 2008 and 2022 from sites in British Columbia, Labrador, Northwest Territories, Québec, and Yukon, as well as Alaska. Here, we used the published datasets to examine relationships between permafrost resistivity, climate data, and site conditions, including landform type, disturbance, and near-surface substrate. The findings show an inverse relationship between mean annual air temperature and permafrost resistivity, with variability controlled by site conditions. These analyses demonstrate the utility of the CPERS database for examining large-scale trends in permafrost conditions across northern North America, a usefulness that will increase in the future as additional datasets are incorporated.

1 INTRODUCTION

Electrical resistivity tomography (ERT) is a geophysical method that images subsurface electrical resistivity in 2D or 3D. The resistivity of unfrozen earth materials depends on factors such as porosity, saturation, pore fluid salinity, and clay content (Archie 1942; Waxman and Smits 1968). ERT has become a common technique for studying permafrost because resistivity increases sharply at the freezing point for most earth materials and is especially high in ice-rich material (Scott et al. 1990). The technique has been used for a diverse range of permafrost applications including assessing permafrost extent and ice content (Lewkowicz et al. 2011; Scapozza et al. 2011; Hilbich et al. 2022), examining the impacts of climate change on permafrost (Mollaret et al. 2019; Etzelmüller et al. 2020; Buckel et al. 2022), evaluating how permafrost thaw affects infrastructure (Lautala et al. 2016; Rossi et al. 2022), and in many other ways. Over the last two decades, the number of academic publications using ERT to study permafrost has increased from 2–3 papers per year to more than 30 per year (Herring et al. 2023). The number of unpublished ERT surveys in permafrost environments is likely much higher.

Despite the widespread use of ERT for characterizing and monitoring in permafrost environments, data sharing has been limited. Consequently, it has been impossible to easily integrate the many existing datasets to make interpretations over large spatial or temporal scales. As part of PermafrostNet, a Canadian research network supported by the Natural Sciences and Engineering Research Council of Canada, we developed the Canadian Permafrost Electrical Resistivity Survey (CPERS) database with the goals of (1) archiving data in a standardized way, (2) establishing and implementing best practices for data processing, and (3) creating a platform for accessible data sharing. Here, we describe the CPERS database and use the first data contributions to examine large-scale trends in permafrost conditions across northern North America.

2 METHODOLOGY

2.1 The CPERS Database

2.1.1 Data contributions

Researchers from the University of Ottawa, Queen's University, and the University of Alberta responded to the initial call for data. These individuals provided data for 280 ERT surveys collected along 209 different profiles (i.e., 71 surveys were repeat surveys taken at the same location). The ERT surveys were collected between 2008 and 2022 in British Columbia, Labrador, Northwest Territories, Québec, and Yukon, as well as Alaska (Figures 1 and 2). Although Alaska is not part of Canada, we chose to include these data due to their proximity and relevance to the Canadian database.

https://doi.org/10.52381/ICOP2024.160.1

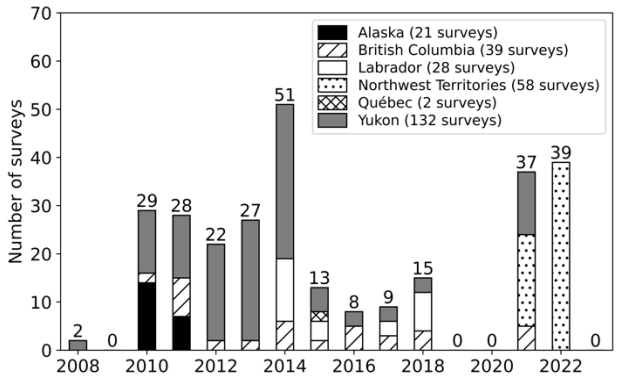

Figure 1. Survey regions and dates for the initial CPERS data publication.

For each survey, data contributors submitted several pieces of information. The first was a mandatory metadata form describing the site (e.g., location, project, related publications, borehole information if applicable), principal investigator information, profile characteristics (e.g., coordinates, landform, vegetation class, near-surface soil/sediment type), and survey characteristics (e.g., date of measurement, array type, topography). Some metadata fields were mandatory and some optional. The metadata form and database structure were developed in collaboration with the International Permafrost Association Action Group "Towards an International Database of Geoelectrical Surveys on Permafrost (IDGSP)" (Mollaret et al. 2022). Data contributors were encouraged to submit their raw ERT data. If submitted, the data contributor was given the option to publish the data immediately or after an embargo period of up to two years.

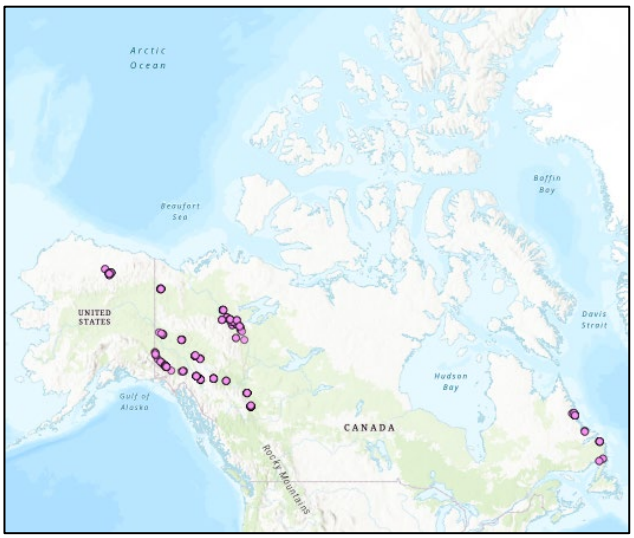

Figure 2. Map of ERT survey locations for the initial CPERS data publication.

2.1.2 *Database access*

The CPERS database currently consists of: (1) a relational PostgreSQL database hosted by NSERC PermafrostNet and supported by the Digital Research Alliance of Canada, (2) a web interface to enable easy access to data and quick visualization tools (https://data.permafrostnet.ca/cpers/; Figure 3), and (3) a data publication with the repository Nordicana D, hosted by the Centre d'études nordiques (CPERS Collective 2023) so that data are permanently archived in an established repository.

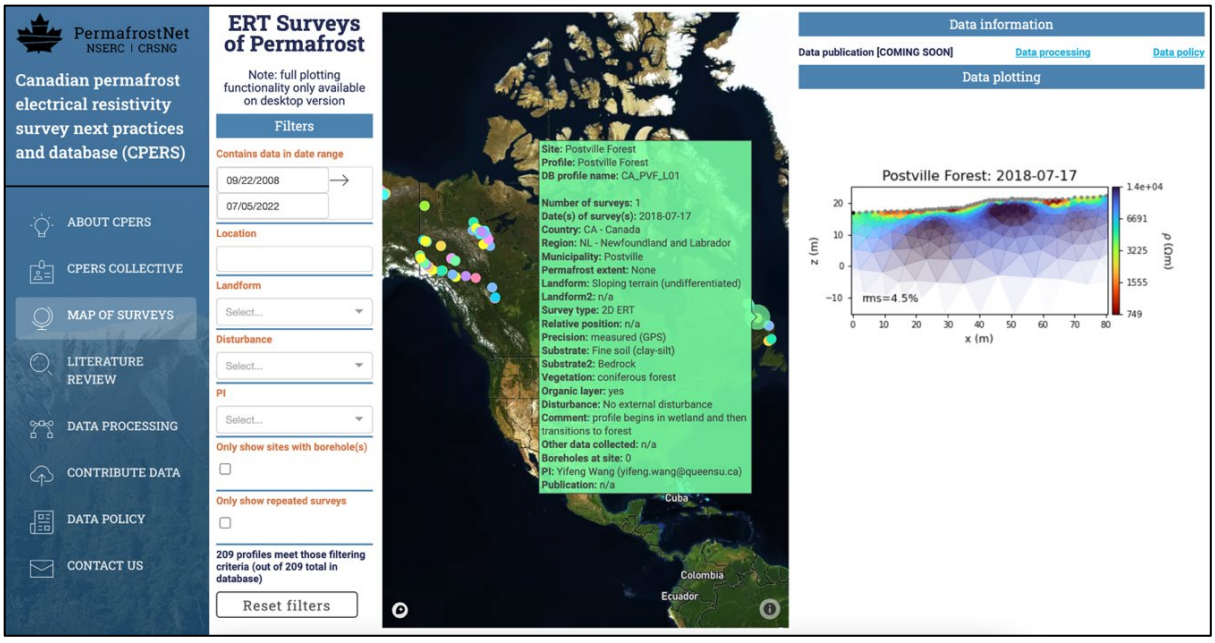

Figure 3. CPERS web interface showing (from left to right): additional resources, querying parameters, profile locations on an interactive map, and standardized data processing output for the selected survey.

The first data release was completed in 2023, and additional datasets will be added in annual database updates.

2.2 Data Analysis

2.2.1 Standardized data processing

Since data contributors provided raw, unprocessed ERT measurements, we were able to develop and apply a standardized data filtering and inversion routine to all datasets. The standardized routine for data processing was informed by a literature review (Herring et al. 2023) and iteratively tested and modified to produce reasonable results for all datasets. Data were inverted using PyGIMLi, an open-source geophysical inversion and modelling library (Rücker et al. 2017). The data processing steps are described by Herring et al. (2023) and the open-source data processing code is linked on the CPERS website (https://data.permafrostnet.ca/cpers/processing.html). The outputs of this data processing workflow are shown on the map of surveys on the CPERS website.

2.2.2 Data visualization

To better understand large-scale trends in permafrost resistivity, we plotted average resistivity as a function of mean annual air temperature (MAAT). MAAT was chosen because these data are easily available and closely related at a continental scale to the ground thermal regime (Smith and Riseborough 2002). A single average resistivity value was calculated for each ERT survey by averaging the resistivity of all model cells where the coverage value (calculated by PyGIMLi during inversion based on the normalized model sensitivity) was above 0.3. Defining this zone of sensitivity ensured that model cells with low sensitivity were not included in the calculation. The MAAT was calculated for each site by averaging Daymet air temperatures over the 10 years preceding the survey date (Thornton et al. 2022). For this analysis, only publicly available (i.e., non-embargoed) ERT datasets are used. Additionally, only data collected between June and October are presented in order to reduce the influence of seasonal variation on the results. Consequently, this analysis includes a total of 231 data points collected between 2008-2022 in British Columbia, Labrador, Northwest Territories, Québec, and Yukon, and Alaska.

3 Results

The plots of average resistivity vs. MAAT showed a trend of increasing resistivity with colder air temperatures, with significant scatter (about two orders of magnitude) around the line of best fit (Figure 4). Previous work has observed scatter in the relationship between MAAT and mean annual ground temperature at sites across Canada, with local variability attributed to lithology, snow conditions, vegetation, and water/ice content (Throop et al. 2012). Although resistivities were lower at higher MAATs, there was no sharp discontinuity in the distribution at 0 °C. This is likely because sites included in the database are biased to include sites where permafrost has been able to persist at MAATs that exceed 0 °C.

As electrical resistivity is also expected to vary with local parameters, we used the information contained in the submitted metadata to examine how different site conditions affected subsurface resistivity.

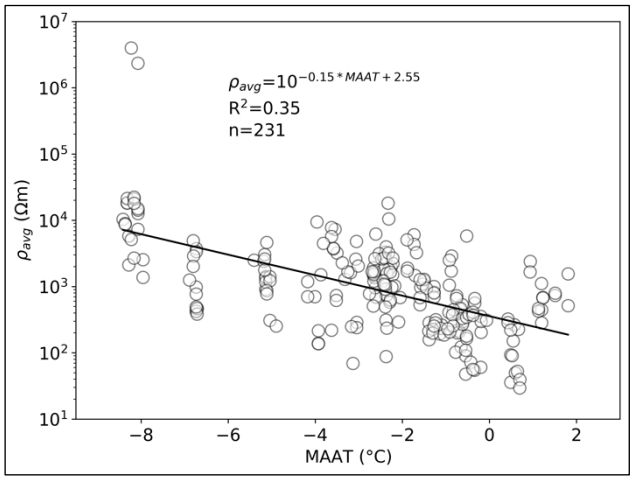

Figure 4. Average inverted resistivity in the zone of sensitivity (see text for further description) as a function of MAAT averaged over the 10 years preceding the survey date, including the line of best fit. Note the logarithmic y-axis.

We found that some of the variability in average resistivity could be attributed to landform type. Many landforms had only a few data points, making it difficult to make reliable interpretations. However, data points associated with some landforms showed clear deviation from the trendline (Figure 5a). Higher resistivities were observed in permafrost landforms that are likely to be ice-rich, like lithalsas and palsas. In contrast, thermokarst mounds tended to exhibit lower resistivities, likely due to warmer, wetter conditions (Kokelj and Jorgenson 2013).

Some variability in resistivity appeared to be correlated with near-surface conditions. We found that profiles with no organic layer tended to have lower resistivity than those where an organic layer was present (Figure 5b), potentially indicating lower ground temperatures, higher ice content, or both. Previous works have noted an organic layer of moss and/or peat serves to protect permafrost from warming climates (Yi et al. 2007; Shur and Jorgenson 2008). The observed large-scale resistivity trends suggest a link between organic layer cover and permafrost preservation.

Additionally, there was a pronounced relationship between anthropogenic surface disturbance and average subsurface resistivity, where sites with no anthropogenic disturbance had much higher average subsurface resistivities than sites where surface disturbance covered more than 50% of the profile (Figure 5c). This is likely due to local ground warming, and consequently lower resistivities at disturbed sites. Sites classified as having surface disturbance include revegetating agricultural land, school fields, cleared areas, gravel pads, a golf course, a

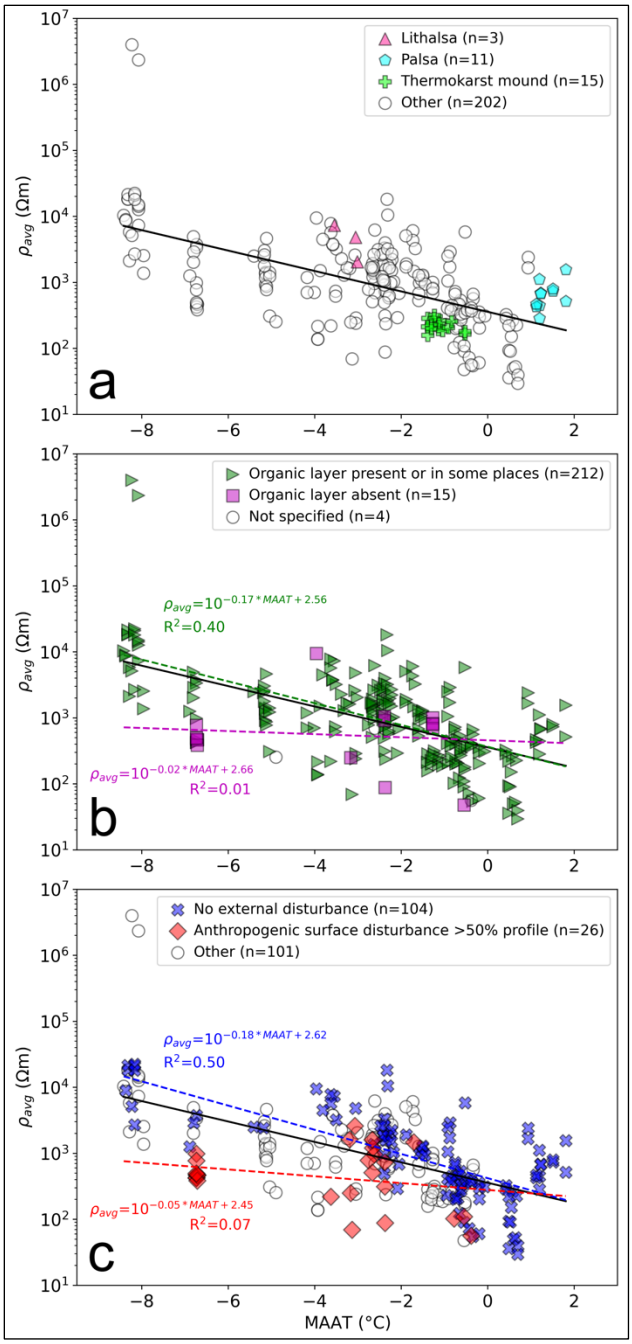

Figure 5. Average inverted resistivity in the zone of sensitivity as a function of MAAT, where the trend line for the entire dataset is shown in black and trend lines and statistics for subsets are shown in their respective colours. Some site characteristics were associated with deviations from the overall trend, including a) landform type, b) the presence or absence of a near-surface organic layer, and c) anthropogenic surface disturbance.

sewage lagoon, a firebreak, airports, roads, and trails. In several other studies, anthropogenic surface disturbances have been shown to cause permafrost thaw, subsidence, slumping, erosion, and ponding in permafrost environments (Brown and Grave 1979; Slaughter et al. 1990; Smith and Riseborough 2010; Williams et al. 2013). It is therefore not surprising that sites with surface disturbance show lower average resistivity values, representing degraded permafrost conditions.

4 Discussion

The results presented here do not represent an exhaustive analysis of every parameter that could affect permafrost resistivity, but these findings confirm the expected trend of increasing resistivity in colder regions and indicate that some of the variability is likely attributable to the landform type, near-surface conditions, and disturbance. This represents an important step towards large-scale interpretations of permafrost landscapes across Canada.

The analyses to date are limited by the number of data points in the CPERS database. The total of 231 ERT surveys included in this analysis represents an enormous collective effort of several different researchers, northern communities, and institutions. Even so, it is difficult to make conclusive interpretations of some trends. For example, sixteen different landform types are represented in the database, but there are fewer than five ERT surveys for ten of these landforms. Furthermore, the CPERS database has data gaps in the northern parts of central and eastern Canada. Some permafrost landforms and regions are therefore underrepresented in this analysis. With the contribution of additional ERT surveys to the database, we should be able to examine a larger number of relationships and identify trends and variability with greater certainty.

In this work, we used average resistivity within the zone of sensitivity as a first-pass analysis tool. This does not account for differences in survey length or depth of investigation. In other studies, researchers have averaged modelled resistivities in a manually-defined zone of interest to better represent permafrost conditions (Kneisel et al. 2014; Etzelmüller et al. 2020; Hilbich et al. 2022). Future work could involve defining a site-specific zone of interest for each ERT profile or examining resistivity as a function of depth to differentiate resistivity trends for near-surface and deeper permafrost.

Furthermore, there is some uncertainty in the resistivity and temperature values used here. Uncertainty in modelled resistivities exists due to the limited data coverage and smoothness constraints applied during the inversion. Consequently, ERT inversion does not exactly recover true subsurface resistivities, especially in permafrost environments where large resistivity contrasts and sharp boundaries are common (Supper et al. 2014; Herring and Lewkowicz 2022). There is also uncertainty in the MAAT data. The values presented were interpolated from ground-based observations, but climate stations in Canada's North tend to be sparse (Vincent et al. 2009). The MAAT values presented here therefore represent an initial estimate.

5 CONCLUSIONS

Our analysis of 231 ERT surveys collected across Canada showed a distinct overall trend of increasing average subsurface resistivity at colder sites, with a large spread about the line of best fit. This spread can be attributed to several different factors. Here, we showed that landform type and near-surface conditions, including the presence of an organic layer and degree of anthropogenic surface disturbance, correlated with deviations from the overall trend. Additional datasets and analysis techniques are expected to enable more robust interpretations of Canada-wide permafrost conditions and relationships to climatic and environmental factors. To this end, we invite researchers and practitioners to contribute their ERT datasets to the CPERS database during planned annual updates.

6 ACKNOWLEDGEMENTS

Funding for the development of CPERS was provided by NSERC PermafrostNet. We gratefully acknowledge the Indigenous Peoples on whose lands these data were collected. We thank the Inuit of Nunatsiavut, Labrador, Sahtu Dene and Métis of the Central Mackenzie Valley, Teslin Tlingit Council, Kluane First Nation, White River First Nation, Nacho Nyak Dun First Nation, Kaska Dena First Nation, Tr'ondek Hwëch'in First Nation, Vuntut Gwitchin First Nation, Nunatsiavut Government, Nunatsiavut Research Centre, NunatuKavut Community Council, and communities of Fort Good Hope, Norman Wells, and Tulita. We thank the members of the International Permafrost Association Action Group "Towards an International Database of Geoelectrical Surveys on Permafrost (IDGSP)" who collectively developed the metadata form and database structure used for this project. We gratefully acknowledge the contributions to the CPERS database (as a collaborator, data collector, or field assistant) of Brielle Andersen, Olivier Bellehumeur-Génier, Alexandre Bevington, Philip Bonnaventure, Maxime Duguay, Bernd Etzelmüller, Michael Gooseff, Sarah Godsey, Christina Miceli, Sharon Smith, Joseph Young, Alejandro Alvarez, Casey Buchanan, Alain Cuerrier, Frédéric Dwyer-Samuel, Benoit Faucher, Luise Hermanutz, Zoé Kuntz, Caitlin Lapalme, and Allison Rubin. We thank Nick Brown for the IT support, Etienne Godin for helping with the Nordicana D publication, and the Digital Research Alliance of Canada for the digital resources. We thank Greg Oldenborger, Fabrice Calmels, and Anne-Marie Leblanc for their guidance throughout this project. We thank the two reviewers for their helpful comments on an earlier version of the manuscript.

7 REFERENCES

Archie, G.E. 1942. 'The electrical resistivity log as an aid in determining some reservoir characteristics', *Transactions of the American Institute of Mining, Metallurgical and Petroleum Engineers* 146(01), pp. 54–62. doi:10.2118/942054-g.

Brown, J. and Grave, N.A. 1979. 'Physical and thermal disturbance and protection of permafrost', *United States Army Corps of Engineers*, Cold Regions Research and Engineering Laboratory. Hanover, New Hampshire, United States.

Buckel, J., Mudler, J., Gardeweg, R., Hauck, C., Hilbich, C., Kneisel, C., Buchelt, S., Blöthe, J.H., and Hördt, A. 2022. 'Identifying mountain permafrost degradation by repeating historical ERT measurements', *The Cryosphere* preprint, pp. 1–36. doi:10.5194/tc-2022-207.

CPERS Collective 2023. *The Canadian permafrost electrical resistivity survey database (CPERS) Version 1.0*. Available at: https://nordicana.cen.ulaval.ca/dpage.aspx?doi=45855XD-DC9883ABD609428B.

Etzelmüller, B., Guglielmin, M., Hauck, C., Hilbich, C., Hoelzle, M., Isaksen, K., Noetzli, J., Oliva, M., and Ramos, M. 2020. 'Twenty years of European mountain permafrost dynamics-the PACE legacy', *Environmental Research Letters* 15(10). doi:10.1088/1748-9326/abae9d.

Herring, T., Lewkowicz, A., Hauck, C., Hilbich, C., Mollaret, C., Oldenborger, G.A., Uhlemann, S., Calmels, F., and Farzamian, M. 2023. 'Best practices for using electrical resistivity tomography to investigate permafrost', *Permafrost and Periglacial Processes* 34(4). doi:10.1002/ppp.2207.

Herring, T. and Lewkowicz, A.G. 2022. 'A systematic evaluation of electrical resistivity tomography for permafrost interface detection using forward modeling', *Permafrost and Periglacial Processes* 33(2), pp. 1–13. doi:10.1002/ppp.2141.

Hilbich, C., Hauck, C., Mollaret, C., Wainstein, P., and Arenson, L.U. 2022. 'Towards accurate quantification of ice content in permafrost of the Central Andes - Part 1: Geophysics-based estimates from three different regions', *Cryosphere* 16(5), pp. 1845–1872. doi:10.5194/tc-16-1845-2022.

Kneisel, C., Rödder, T., and Schwindt, D. 2014. 'Frozen ground dynamics resolved by multi-year and yearround electrical resistivity monitoring at three alpine sites in the Swiss Alps', *Near Surface Geophysics* 12(1), pp. 117–132. doi:10.3997/1873-0604.2013067.

Kokelj, S.V. and Jorgenson, M.T. 2013. 'Advances in thermokarst research', *Permafrost and Periglacial Processes* 24(2), pp. 108–119. doi:10.1002/ppp.1779.

Lautala, P., Oommen, T., and Addison, P. 2016. 'Utilizing vegetation indices as a proxy to characterize the stability of a railway embankment in a permafrost region', *AIMS Geosciences* 2(4), pp, 329–344. doi:10.3934/geosci.2016.4.329.

Lewkowicz, A.G., Etzelmüller, B., and Smith, S.L. 2011. 'Characteristics of discontinuous permafrost based on ground temperature measurements and electrical resistivity tomography, Southern Yukon, Canada', *Permafrost and Periglacial Processes* 22(4), pp. 320–342. doi:10.1002/ppp.703.

Mollaret, C., Hilbich, C., Herring, T., Farzamian, M., Buckel, J., Dafflon, B., et al. 2022. 'Initiation of an international database of geoelectrical surveys on permafrost to promote data sharing, survey repetition and standardized data reprocessing', in *EGU General Assembly 2022*. Vienna, Austria.

Mollaret, C., Hilbich, C., Pellet, C., Flores-Orozco, A., Delaloye, R., and Hauck, C. 2019. 'Mountain permafrost degradation documented through a network of permanent electrical resistivity tomography sites', *Cryosphere* 13(10), pp. 2557–2578. doi:10.5194/tc-13-2557-2019.

Rossi, M., Dal Cin, M., Picotti, S., Gei, D., Isaev, V.S., Pogorelov, A. V., Gorshkov, E.I., Sergeev, D.O., Kotov, P.I., Giorgi, M., and Rainone, M.L. 2022. 'Active layer and permafrost investigations using geophysical and geocryological methods—A case study of the Khanovey Area, near Vorkuta, in the NE European Russian Arctic', *Frontiers in Earth Science* 10(July), pp. 1–22. doi:10.3389/feart.2022.910078.

Rücker, C., Günther, T., and Wagner, F.M. 2017. 'pyGIMLi: An open-source library for modelling and inversion in geophysics', *Computers and Geosciences*, 109(July), pp. 106–123. doi:10.1016/j.cageo.2017.07.011.

Scapozza, C., Lambiel, C., Baron, L., Marescot, L., and Reynard, E. 2011. 'Internal structure and permafrost distribution in two alpine periglacial talus slopes, Valais, Swiss Alps', *Geomorphology* 132(3–4), pp. 208–221. doi:10.1016/j.geomorph.2011.05.010.

Scott, W.J., Sellman, P.V., and Hunter, J.A. 1990. 'Geophysics in the study of permafrost', in S.H. Ward (ed.) *Geotechnical and environmental geophysics*, pp. 355–376.

Shur, Y.L. and Jorgenson, M.T. 2008. 'Patterns of permafrost formation and degradation in relation to climate and ecosystems', *Permafrost and Periglacial Processes* 18, pp. 7–19. doi:10.1002/ppp.582.

Slaughter, C.W., Racine, C.H., Walker, D.A., Johnson, L.A., and Abele, G. 1990. 'Use of off-road vehicles and mitigation of effects in Alaska permafrost environments: A review', *Environmental Management* 14(1), pp. 63–72. doi:10.1007/BF02394020.

Smith, M.W. and Riseborough, D.W. 2002. 'Climate and the limits of permafrost: A zonal analysis', *Permafrost and Periglacial Processes* 13, pp. 1–15. doi:10.1002/ppp.410.

Smith, S.L. and Riseborough, D.W. 2010. 'Modelling the thermal response of permafrost terrain to right-of-way disturbance and climate warming', *Cold Regions Science and Technology* 60(1), pp. 92–103. doi:10.1016/j.coldregions.2009.08.009.

Supper, R., Ottowitz, D., Jochum, B., Römer, A., Pfeiler, S., Kauer, S., Keuschnig, M., and Ita, A. 2014. 'Geoelectrical monitoring of frozen ground and permafrost in alpine areas: Field studies and considerations towards an improved measuring technology', *Near Surface Geophysics* 12(1), pp. 93–115. doi:10.3997/1873-0604.2013057.

Thornton, M.M., Shrestha, R., Wei, Y., Thornton, P.E., Kao, S.-C., and Wilson, B.E. 2022. *Daymet: Daily Surface Weather Data on a 1-km Grid for North America, Version 4 R1*. Oak Ridge, Tennessee, United States.

Throop, J., Lewkowicz, A.G., and Smith, S.L. 2012. 'Climate and ground temperature relations at sites across the continuous and discontinuous permafrost zones, northern Canada', *Canadian Journal of Earth Sciences* 49(8), pp. 865–876. doi:10.1139/E11-075.

Vincent, L.A., Milewska, E.J., Hopkinson, R., and Malone, L. 2009. 'Bias in minimum temperature introduced by a redefinition of the climatological day at the canadian synoptic stations', *Journal of Applied Meteorology and Climatology* 48(10), pp. 2160–2168. doi:10.1175/2009JAMC2191.1.

Waxman, M.H. and Smits, L.J.M. 1968. 'Electrical conductivities in oil-bearing shaly sands', *Society of Petroleum Engineers Journal* 8(02), pp. 107–122. doi:10.2118/1863-a.

Williams, T.J., Quinton, W.L., and Baltzer, J.L. 2013. 'Linear disturbances on discontinuous permafrost: Implications for thaw-induced changes to land cover and drainage patterns', *Environmental Research Letters* 8(2). doi:10.1088/1748-9326/8/2/025006.

Yi, S., Woo, M.K., and Arain, M.A. 2007. 'Impacts of peat and vegetation on permafrost degradation under climate warming', *Geophysical Research Letters* 34(16), pp. 1–5. doi:10.1029/2007GL030550.

Multi-year and Seasonal Trends in the Water Quality of the Niaqunguk River, Nunavut (2013–2018)

Erika Hille, Melissa Lafrenière & Scott Lamoureux

Department of Geography and Planning, Queens University, Kingston, Ontario, Canada

ABSTRACT

Anthropogenic climate change is modifying the hydrological processes that control fluvial chemistry in Arctic regions. Climatic variability and permafrost thaw have contributed to changes in the timing and intensity of spring snowmelt, the frequency of extreme rainfall events, and lateral flow pathways. Permafrost thaw can increase the connectivity of deeper, subsurface flow pathways with tributary streams and rivers. In combination with increases in snowmelt and rainfall runoff, this can increase the flux of solutes to Arctic rivers.

The Niaqunguk River is located on Baffin Island, NU. With no evidence of physical disturbances to the permafrost, the top-down thawing of permafrost is the primary type of permafrost disturbance influencing river chemistry. For the years 2013 to 2018, water samples were collected from the Niaqunguk River up to three times weekly over the course of the flow period and analyzed for major ions, dissolved organic carbon, and total dissolved nitrogen. Water sampling was co-located with a hydrometric station operated by the Water Survey of Canada. Solute fluxes to the Niaqunguk River were driven by the weathering of carbonate minerals by lateral flow pathways. For most years, solute fluxes peaked during spring snowmelt, when flows were the highest. In 2016, however, solute fluxes were highest in mid-summer, following several consecutive days of rainfall. If rainfall is increasing, as is projected for many regions of the Arctic, our data suggest that this could lead to an increase in solute fluxes to and through the Niaqunguk River. In the absence of recent precipitation data, however, it is challenging to determine whether this is the case.

1 INTRODUCTION

Contemporary climate change and permafrost thaw continue to modify the hydrological processes that control Arctic river runoff. This has profound implications for fluvial chemistry. Specifically, rising surface air and ground temperatures have contributed to the widespread degradation of permafrost across the Canadian Arctic (Smith et al. 2005; Throop et al. 2012). The top-down thawing of permafrost directly affects lateral flow pathways to Arctic rivers by increasing the thickness of the active layer (frost table depth) and in turn, the vertical infiltration of water into the soil profile (Chiasson-Poirier et al. 2020). This can lead to an increase in the connectivity of deeper, subsurface flow pathways with tributary streams and rivers (Chiasson-Poirier et al. 2020; Schwab et al. 2020).

Groundwater flow, particularly through zones of recently thawed permafrost, can be a significant a source of solutes to tributary streams and rivers (Kokelj et al. 2003; Lafrenière and Lamoureux 2013). Permafrost, in Arctic and boreal regions, contains large amounts of organic material and mineral sediment (Fouché et al. 2020; Kokelj et al. 2003). As permafrost thaws, this organic material and mineral sediment is exposed to biological and chemical reactions, which can lead to solute enrichment within thaw zones and the mobilization of solutes via lateral flow pathways (Kokelj et al. 2003; Lafrenière and Lamoureux 2013). Consequently, the response of water quality to permafrost thaw is strongly influenced by the nature and magnitude of permafrost thaw and the composition of the contributing landscape (i.e., organic material, surficial geology; Brown et al. 2020; Tank et al. 2020).

The chemistry of Arctic rivers is also driven by temporal variability in precipitation and flow pathways (Quinton et al. 2006; Beel et al. 2021). For most Arctic rivers, the spring snowmelt period, also referred to as the spring freshet, is the most significant hydrologic event of the year. At the onset of spring snowmelt, the active layer remains frozen, facilitating the rapid delivery of snowmelt water to tributary streams and rivers. Surface flow is the dominant lateral flow pathway at this time of year and is typically a source of particulate matter (Quinton et al. 1999; Quinton et al. 2006).

As the thaw period progresses, the contributing snowpack diminishes and summer rainfall becomes the primary driver of water runoff (Beel et al. 2021). As the thickness of the active layer increases, so does the relative importance of groundwater flow (Quinton et al. 2006). Groundwater flow is slowed by the active layer, which is typically a porous matrix of soil. The slower flow along groundwater flow pathways inhibits the transport of particulate matter, as compared with the rapid-flowing runoff at the ground surface (Frampton and Destouni 2015). Although groundwater flow does not easily transport particulate material, it can be an important source of dissolved material, due to the longer residence time of subsurface flow and enhanced interaction with the active layer (Quinton et al. 2006; Lafrenière and Lamoureux 2013).

Recent climate change is affecting the primary factors controlling the dominant water sources to Arctic rivers. In particular, Arctic freshwater systems are experiencing increasingly intense spring snowmelt periods and a higher frequency of extreme rainfall events (Bintanja 2018; Bush et al. 2019). As mentioned above, spring snowmelt and summer rainfall are the two most significant sources of freshwater, particulate matter, and solutes to Arctic rivers. Therefore, it is likely that these changes in precipitation regimes have and will continue to affect the hydrology and chemistry of Arctic rivers, potentially amplifying the effects of permafrost thaw on water quality.

https://doi.org/10.52381/ICOP2024.127.1

The vast majority of water quality studies in the Arctic have focused on aquatic systems impacted by physical disturbances to the permafrost (e.g., mass wasting, active layer detachments). Few studies have examined the long-term effects of permafrost thaw on aquatic networks not impacted by physical disturbances to the permafrost. Furthermore, little is known about how the water quality impacts of permafrost thaw are influenced by recent changes in precipitation, lateral runoff pathways, and stream discharge.

The availability of the Niaqunguk River dataset provides us with the opportunity to address this gap in understanding. Over a six-year period (2013–2018), water quality samples were collected from the Niaqunguk River 2–3 times a week over the course of the flow period (June to August). A temporally detailed, multi-year river chemistry dataset, such as this, is unique for this region of the Canadian Arctic.

1.1 Objectives

The overall goal of this study was to examine how the water quality of the Niaqunguk River responds to seasonal and inter-annual variability in climate and how this varied over the period of record. This was achieved via the following key objectives: i. use water quality data to examine seasonal and inter-annual variability in the chemistry of the Niaqunguk River (2013–2018); ii. examine recent meteorological data (precipitation, snowfall, rainfall) and stream discharge data, in order to ascertain how water quality responds to spring snowmelt and summer rainfall events; and iii. examine historical climate (precipitation, snowfall, rainfall) and river discharge data, in order to establish long-term trends in the primary factors controlling solute fluxes.

1.2 Study Site

The Niaqunguk River catchment is located at 63° 44' 09" N, 68° 27' 05" W on Baffin Island, Nunavut (NU), Canada (Figure 1). The Niaqunguk River has a drainage area of 58.5 km^2 and discharges into Koojesse Inlet (Environment Canada, 2017). Although the catchment is situated within a region of continuous permafrost, it does not contain substantial amounts of massive ice and thus, is not impacted by obvious physical disturbances to the permafrost. Consequently, thermal perturbation of the permafrost and subsequently, increases in maximum active layer thickness is the primary type of permafrost disturbance influencing stream and river chemistry at this site.

The Niaqunguk River is located near the community of Iqaluit, NU. The mean annual air temperature for Iqaluit is -8.9 °C (1946–2022) and the average total annual precipitation is 524.6 mm (1950–2006). For most months (typically October to May), the dominant form of precipitation is snow. On average, snowfall makes up ~59% of total annual precipitation. This was determined from the third generation Adjusted Surface Air Temperature Data for Canada (Vincent et al. 2020) and the second generation Adjusted Precipitation for Canada (Mekis and Vincent 2011).

The vegetation in the Niaqunguk River catchment is relatively sparse, as compared with other regions of the Canadian Arctic. The landscape is covered by predominantly low-lying tundra vegetation and exposed bedrock (Tremblay 2017). The active layer contains only thin, isolated units of organic material and is primarily comprised of glacial till, a carbonate matrix deposited during the early-Holocene and Wisconsinan period (Tremblay 2017; Hodgson 2003). The glacial sediments present as till (T), till veneer (Tv), till blanket (Tb), and ridged till (Tr). In the region of Tv, ~40% of the area is covered by a < 1 m thick layer of glacial till (Tremblay 2017). The remaining ~60% of the area is rock ledges, knobs, and exposed bedrock (Tremblay 2017). The Tb region contains a continuous cover of predominantly boulder diamicton, which can be up to 10 m thick (Tremblay 2017; Hodgson 2003). Notably, there are also smaller, isolated regions with glaciofluvial and glaciolacustrine deposits, whereby the sediment layer can also be quite thick (up to 40 m; Tremblay 2017; Hodgson 2003).

The bedrock comprises predominantly silicate minerals, including biotite, orthopyroxene, garnet, and K-feldspar (St-Onge et al. 2006). In particular, the bedrock is classified as biotite ± orthopyroxene ± garnet monzogranite, K-feldspar megacrystic monzogranite, and granodiorite (St-Onge et al. 2006).

2 METHODOLOGY

Water quality samples were collected up to 2–3 times weekly over the flow period in the years 2013 to 2018. This was done with support from the Nunavut Research Institute. Sampling increased to three times weekly during snowmelt and rainfall runoff events.

A portion of sample was filtered through a 0.22 µm PVDF membrane filter and stored in the refrigerator for analysis. This filtered sample was analyzed for mineral ions (Ca^{2+}, Cl^-, SO_4^{2-}, Na^+, K^+, Mg^{2+}) by ion chromatography (Thermo-Dionex ICS 3000).

The precision of the analyses was evaluated using the covariance (CV) of sample repeats (Eq. 1; n > 10).

$$\mathrm{CV}\ (\%) = (\ \overline{\mathrm{SD}}_{\mathrm{Repeats}} / \overline{\mathrm{Avg}}_{\mathrm{Repeats}}) \times 100 \qquad [1]$$

$\overline{\mathrm{SD}}_{\mathrm{Repeats}}$ is the mean standard deviation of the sample repeats and $\overline{\mathrm{Avg}}_{\mathrm{Repeats}}$ is the mean average of the sample repeats. With the exception of K^+, CV was less than 1.6% for all of the mineral ions. K^+ was higher than the other mineral ions (< 5%), due to K^+ concentrations being much lower (Standard Deviation < 0.017 ppm).

The method detection limit (MDL) of each parameter was determined using Equation 2.

$$\mathrm{MDL} = [\mathrm{Blank}] \times (3 \times \mathrm{SD}_{\mathrm{Std}}) \qquad [2]$$

[Blank] is the concentration measured in Milli-Q water and $\mathrm{SD}_{\mathrm{Std}}$ is the standard deviation of the concentration measured in the lowest calibration standard.

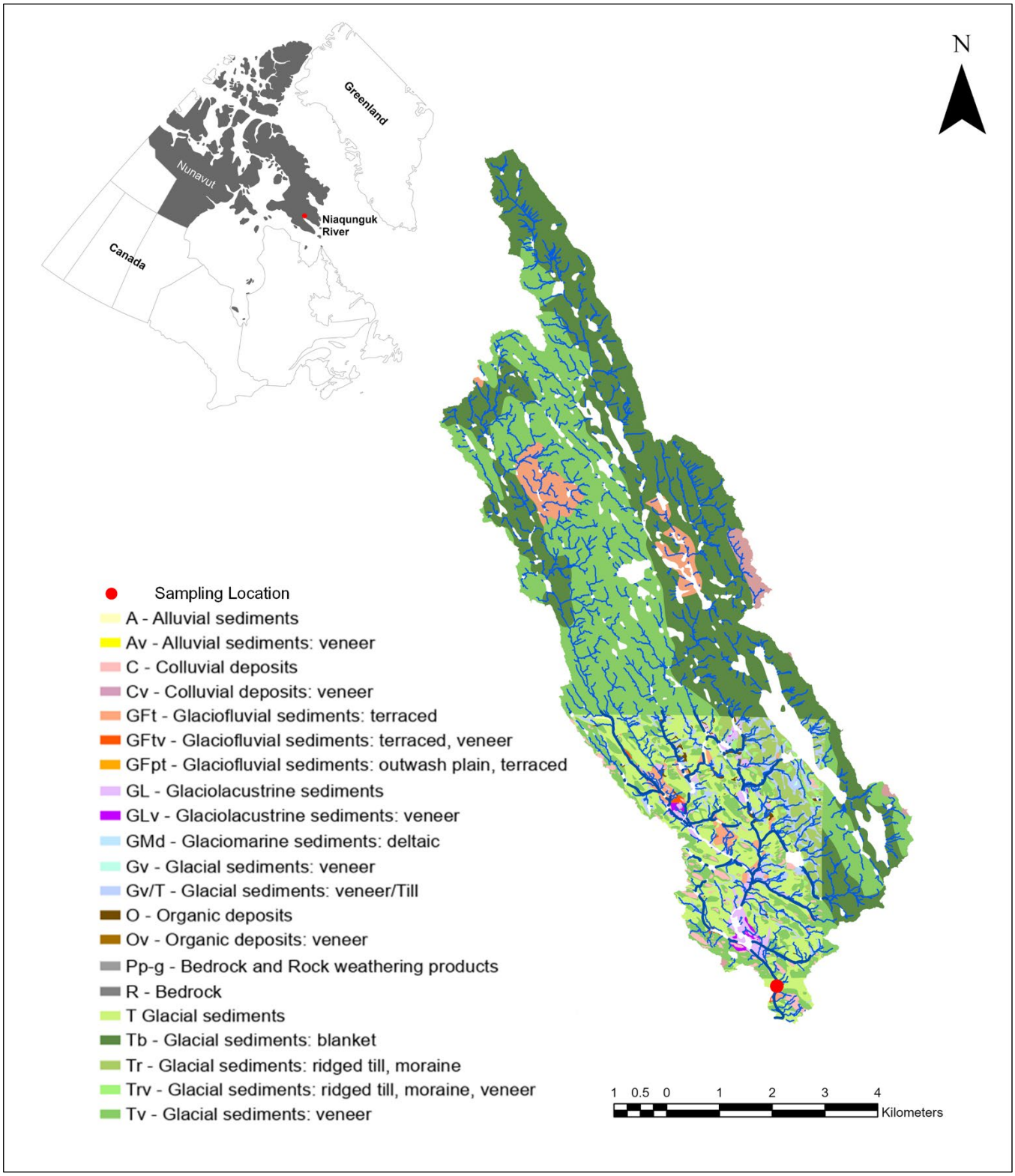

Figure 1. The surficial geology of the Niaqunguk River catchment. This is a compilation of data derived from Hodgson (2003) and Tremblay (2017). The red dot indicates the location of the sampling site and the Water Survey of Canada gauging station. The blue lines represent water flow, which was mapped in ArcGIS using a Digital Elevation Model.

Concentrations below the MDL were deemed unreliable. DL was less than 0.051 ppm for all mineral ions, except for K^+. The MDL for K^+ was less than 0.03 ppm.

HCO_3^- was determined empirically using a charge-balance approach. This approach is justified because the pH of the Niaqunguk River is within the range where HCO_3^- is the dominant contributor to DIC (Drever 1997). Table 1 demonstrates that the pH range of the Niaqunguk River falls between 6.5 and 8.3.

Table 1. The minimum, maximum, and average pH of the Niaqunguk River over each of the study years.

Study Year	pH		
	Average	Minimum	Maximum
2013	7.3	7.1	7.5
2014	7.4	6.5	8.0
2015	7.6	6.9	8.3
2016	7.2	6.8	7.5
2017	7.2	6.8	7.5
2018	7.0	6.7	7.3

Another portion of sample was filtered using a 0.7 µm glass fiber filter. Glass fiber filters were pre-combusted at 500 °C to remove organic carbon. These samples were analyzed for total dissolved nitrogen (TDN) and dissolved organic carbon (DOC) using chemiluminescence and high temperature combustion (Shimadzu TOC -V with TN-M).

Similar to above, the precision of these analyses was evaluated using the covariance (CV) of sample repeats (Eq. 1; n > 10). CV was less than 2% for TDN and DOC. The MDL was less than 0.05 ppm for TDN and less than 0.26 ppm for DOC.

All of the above analyses took place at the Facility for Biochemical Research on Environmental Change and the Cryosphere at Queens University.

Mineral ion, TDN, and DOC concentrations were reported in units of $mg.L^{-1}$). This was converted to units of $mg.m^{-3}$, whereby 1 m^3 = 1000 L. Concentration (in $mg.m^{-3}$) was then converted to flux values by multiplying concentration by mean daily discharge (in $m^3.d^{-1}$). Total daily flux (in $mg.d^{-1}$) was then divided by the catchment area (5.85 x 10^7 m^2), in order to yield flux values in units of $mg.m^{-2}.\ d^{-1}$.

A time-series plot was used to examine seasonal and inter-annual variability in solute fluxes, relative to discharge (in $mm.d^{-1}$), positive degree days (°C), and unadjusted total daily precipitation (mm).

Mean daily discharge (in $m^3.s^{-1}$) was extracted from the Environment and Climate Change Canada Historical Hydrometric Data site (https://wateroffice.ec.gc.ca/mainmenu/historical_data_index_e.html) on July 17, 2023 and July 18, 2023. This was converted to units of $m^3.d^{-1}$, whereby 1 $m^3.s^{-1}$ = 86,400 $m^3.d^{-1}$. Total daily discharge (in $m^3.d^{-1}$) was then divided by the catchment area (5.85 x 10^7 m^2), in order to yield units of $m.d^{-1}$. This was then converted to $mm.d^{-1}$.

Positive degree days are the sum total of the mean annual air temperatures that are above 0 °C. This was calculated for each day between April 20 and January 10 of the six study years using unadjusted mean daily air temperature data. Unadjusted mean daily air temperature and unadjusted total daily precipitation data were extracted from the Environment and Climate Change Canada Historical Climate Data site (https://climate.weather.gc.ca/index_e.html) on July 17, 2023 and July 18, 2023.

The composition of mineral ions was examined using a Piper Plot, which plots the proportions of ion equivalent concentrations.

Long term trends in precipitation, snowfall, rainfall, and discharge were examined using a Mann-Kendall non-parametric test for trend using XLSTAT software. Historical trends in total annual precipitation, snowfall, and rainfall data were developed using adjusted monthly data obtained from the second generation Adjusted Precipitation for Canada (Mekis and Vincent 2011). Missing data were infilled using unadjusted daily data obtained from the Environment and Climate Change Canada Historical Climate Data site (https://climate.weather.gc.ca/index_e.html) on July 17, 2023 and July 18, 2023.

Historical trends in total annual discharge were developed using total annual discharge values (in $mm.y^{-1}$) derived from discharge data extracted from the Environment and Climate Change Canada Historical Hydrometric Data site: (https://wateroffice.ec.gc.ca/mainmenu/historical_data_index_e.html) on July 17, 2023 and July 18, 2023.

3 RESULTS

3.1 River Discharge

Flow was initiated when positive degree days increased to above 0 °C. This was the onset of spring snowmelt and was marked by a steep increase in total daily discharge, followed by several defined peaks (Figure 2). The dip in river discharge between peaks is closely associated with positive degree days, which is close to 0 °C at this time of year.

For most years, total daily discharge (in $mm.d^{-1}$) was highest during spring snowmelt, which was initiated in early-June for all of the study years with available data. Over the six-year study period, the highest annual maximum total daily discharge was 17.7 $mm.d^{-1}$ and was observed on June 20, 2018. It is worth noting that this value may be higher, as total daily discharge is unavailable for the days preceding this. The lowest annual maximum total daily discharge was 11.87 $mm.d^{-1}$ and was observed on June 15, 2017.

Total daily discharge decreased over the summer months, except for temporary increases corresponding to summer rainfall events. Notably, in 2016, the annual maximum total daily discharge did not occur during spring snowmelt. Rather, the annual maximum total daily discharge (17.53 $mm.d^{-1}$) occurred in late-July, following several days of heavy rainfall. Although not as high as during spring snowmelt, several days of heavy rainfall also led to markedly higher flows in September 2013 and September 2017.

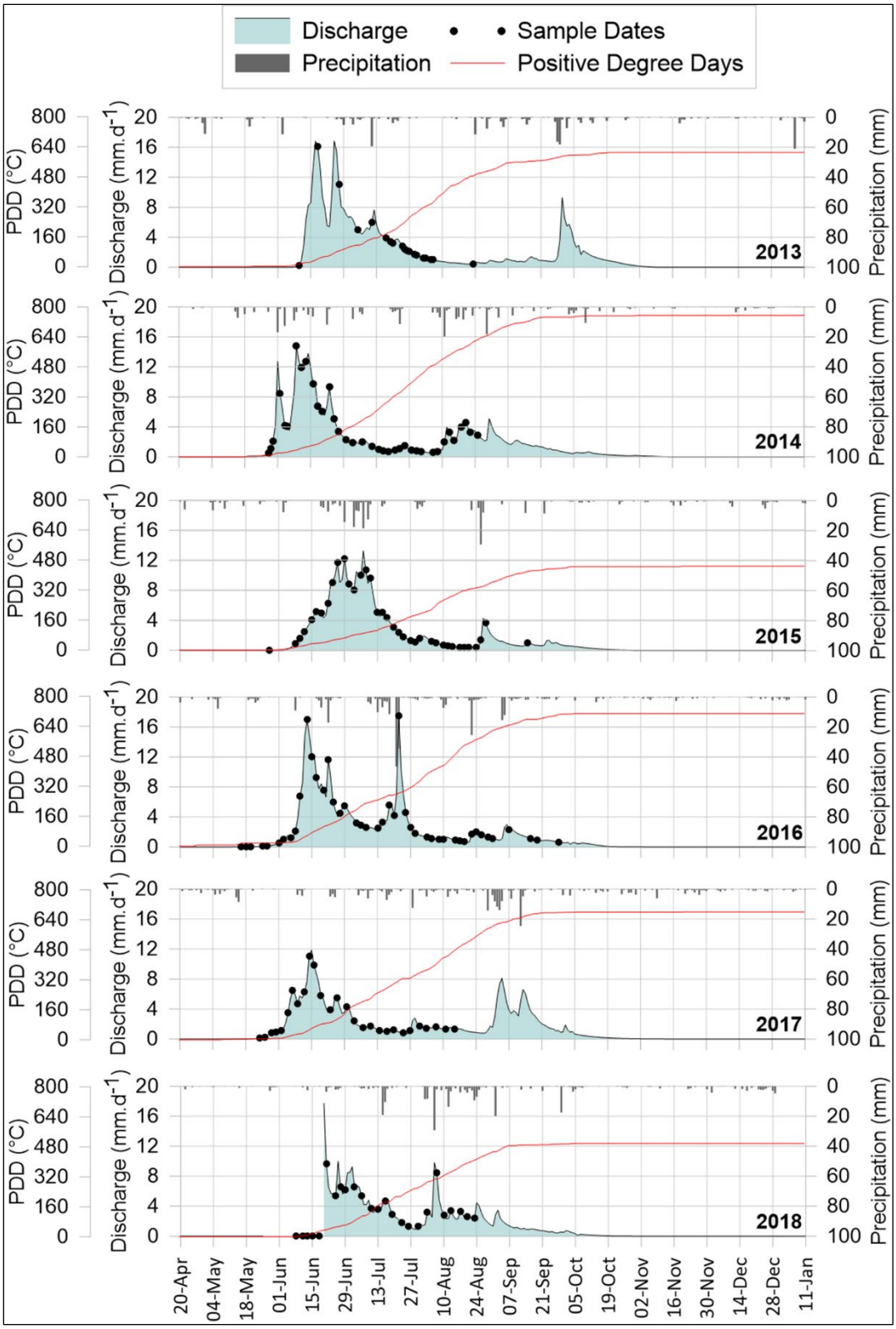

Figure 2. The total daily discharge (in $mm.d^{-1}$) measured at the Niaqunguk River for period of April 20 to January 10 is plotted for each study year (2013–2018). Flow is plotted against the positive degree days (in °C; PDD) and unadjusted total daily precipitation (in mm) for Iqaluit, NU for the same period. The sampling dates are represented by black dots.

In each study year, the water sampling successfully captured spring snowmelt, including the rising and falling limb of the hydrograph, as well as the summer period. The fall period, however, is less represented. With the exception of 2016, sampling often stopped at the end of August.

3.2 Water Chemistry

3.2.1 Mineral Ions

The flux of Ca^{2+}, Mg^{2+}, Na^{+}, K^{+}, SO_4^{2-}, and Cl^{-} (in $mg.m^{-2}.d^{-1}$) over the flow period is plotted in Figure 3. Seasonal variability in the fluxes of mineral ions (Ca^{2+}, Mg^{2+}, Na^{+}, K^{+}, SO_4^{2-}, and Cl^{-}) through the Niaqunguk River follows a similar seasonal trend as total daily discharge (Figure 3). High fluxes were associated with periods of high flow. Mineral ion fluxes rapidly increased at the onset of the flow period and for most study years, reached a maximum during spring snowmelt. Notably, this was often when the concentration of mineral ions is lowest.

Mineral ion fluxes generally decreased over the summer period, despite the higher concentrations observed at this time. This was, however, with the exception of summer rainfall events. In 2016, solute fluxes peaked on July 22, following a period of heavy rainfall. Notably, this represented the highest Ca^{2+}, Mg^{2+}, and Cl^{-} fluxes measured over the 6-year study period. The highest SO_4^{2-}, Na^{+}, and K^{+} fluxes occurred on August 20, 2014, also following a period of heavy rainfall.

Despite strong seasonal variability in fluxes, the composition of mineral ions is consistent across all seasons and all study years (Figure 4). Water samples contained high proportions of Ca^{2+}, Mg^{2+}, and HCO_3^{-} and low proportions of SO_4^{2-}, Cl^{-}, Na^{+}, and K^{+}. This is consistent with carbonate weathering.

3.2.2 Carbon

The flux of Dissolved Organic Carbon (DOC) and Total Dissolved Nitrogen (TDN) over the flow period of each study year (2013–2018) is plotted in Figure 5. DOC and TDN fluxes (in $mg.m^{-2}.d^{-1}$) also followed total daily discharge (Figure 5), in that they were typically highest during spring snowmelt and decreased over the summer period. In 2016, however, DOC and TDN fluxes were highest on July 22nd, following a period of heavy rainfall. Preceding this event, DOC was highest on June 22nd and July 18th, also following rainfall periods.

3.3 Multi-Year Trends

3.3.1 Precipitation

Adjusted total monthly snowfall and total monthly rainfall data were available for most years from 1950 to 2006. For months where adjusted data were unavailable, unadjusted total daily snowfall and rainfall data were used. This provided more years with complete data (n = 55).

A Mann-Kendall non-parametric test for trend indicated that there was a significant decrease in total annual snowfall over this period (Sen's slope = -0.272 mm per year; $p < 0.05$; Figure 6). There was a small increasing trend in total annual rainfall over the same time period. However, this was not significant ($p > 0.05$). At the time of these analyses, no complete adjusted or unadjusted snowfall or rainfall data were available after 2006.

Complete total daily precipitation data were available for 1950 to 2006 for most years. Similar to above, unadjusted total daily precipitation data were used to infill months where adjusted data were unavailable. This yielded more years with complete data (n = 54). Some data were available for the years between 2007 and 2023. However, it was not complete. For the years 1950–2006, total annual precipitation decreased at a rate of -0.23 mm per year. The percentage of total annual precipitation comprising snowfall also decreased over the period of record, at a rate of 0.223 % per year.

3.3.2 Discharge

Complete discharge data were available for the years 1989–1995 and 2007-2017. Although there are some data preceding 1989, there are not enough to calculate total annual fluxes. Additionally, there were no data available between the years 1995 and 2007 or between 2017 and 2023. The total annual discharge (in $mm.y^{-1}$) measured in the years 1989–1995 is visibly lower than the discharge measured in the years 2007–2017 (Figure 7). Consequently, there is a positive trend in total annual discharge over the period of record (Sen's slope = 5.404 $mm.y^{-1}$; $p < 0.05$). Despite this, it's important to highlight that there may be two separate trends in this figure. Total annual discharge appears to be decreasing over the 1989–2005 period, which is in line with the decrease in total annual snowfall and total annual precipitation discussed above. Conversely, total annual discharge appears to be increasing over the 2007–2017 period.

4 Discussion

Seasonal variability in river discharge was typified by spring snowmelt and summer rainfall. At the onset of spring snowmelt, there is a steep increase in river discharge. Given that the active layer is typically frozen at this stage, this can be attributed to the rapid delivery of snowmelt water via surface runoff (Quinton et al. 2006; Chiasson-Poirier et al. 2020). For most years, river discharge was highest in spring, often peaking several times over the course of the spring snowmelt period. The presence of multiple discharge peaks appears to be associated with variability in surface air temperature and in turn, the rate of snowmelt.

Following river discharge, solute fluxes were driven by seasonal changes in snowmelt and rainfall. For most study years, solute fluxes were the highest during spring snowmelt. In surface and near-surface runoff, mineral ions are typically present in low concentrations relative to subsurface flow. This is often attributed to the limited contact surface runoff has with the deeper, mineral layers of the active layer (Quinton et al. 2006; Chiasson-Porier et al. 2020). Consequently, downstream aquatic systems are normally diluted by snowmelt water (Quinton et al. 2006).

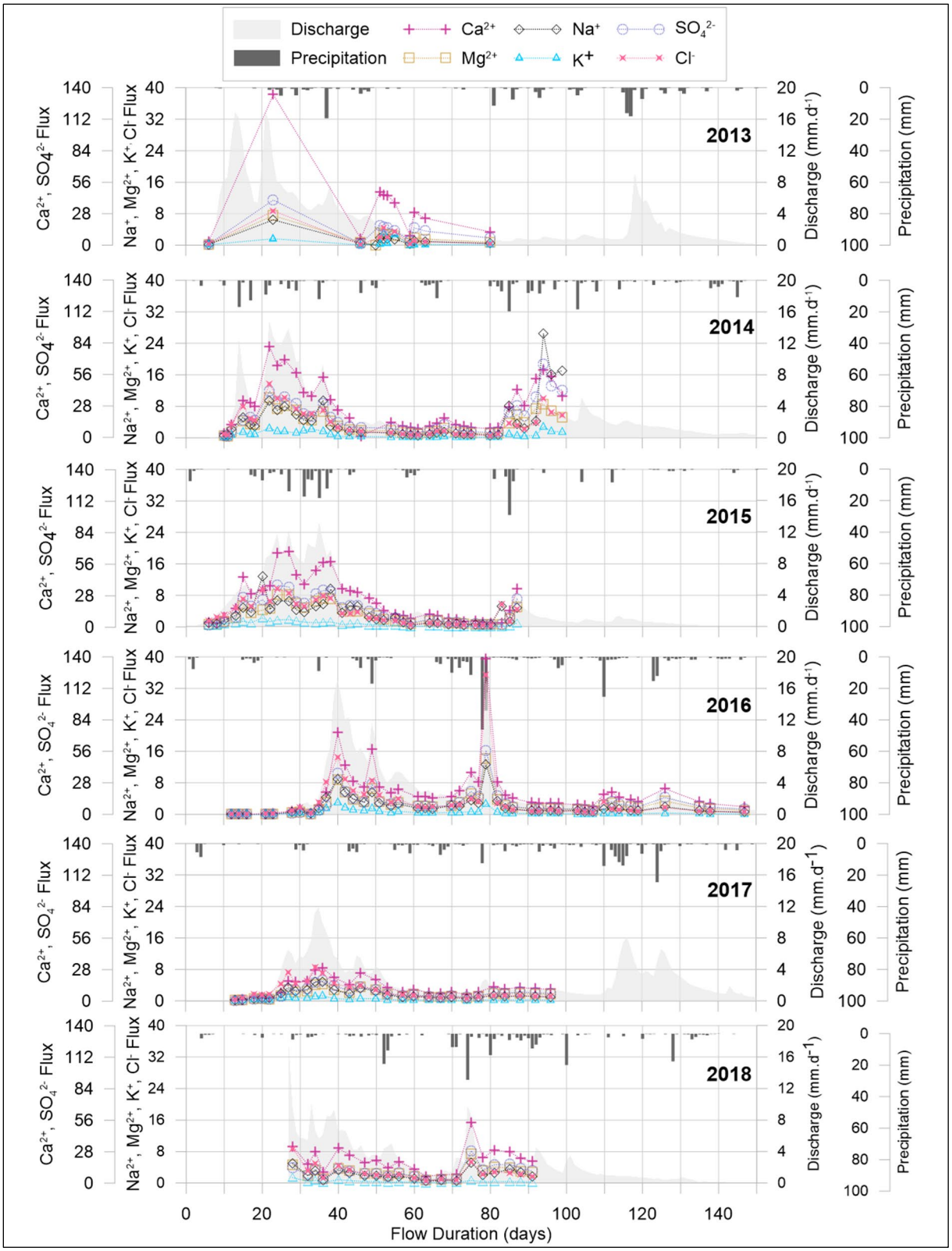

Figure 3. The flux of Ca^{2+}, Mg^{2+}, Na^{+}, K^{+}, SO_4^{2-}, and Cl^{-} (in $mg.m^2.d^{-1}$) over the flow period is plotted with the total daily discharge (in $mm.d^{-1}$) for the Niaqunguk River and the unadjusted total daily precipitation (in mm) for Iqaluit.

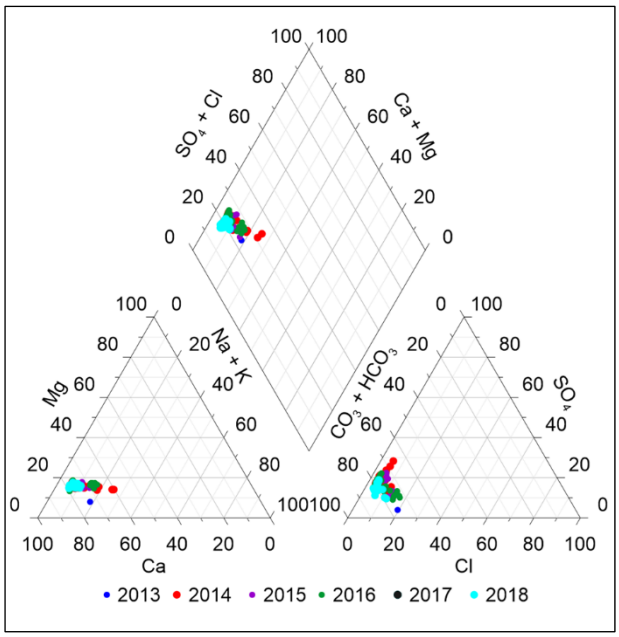

Figure 4. A piper plot of the proportions of ion equivalents of mineral ions in each of the samples across all study years.

In this study, however, mineral solute fluxes were typically highest during spring snowmelt. This indicates that snowmelt is mobilizing solute-rich pore water from near the surface. These solutes could be weathering products derived from surface runoff during spring melt, weathering products that were immobilized during freeze-up of the previous year, or dusts deposited onto the snowpack over the winter and spring.

In contrast with mineral ions, DOC and nutrient concentrations are often elevated in near-surface flow pathways, as organic material is normally the most concentrated close to the surface (Quinton et al. 2006). For the Niaqunguk River, DOC and TDN fluxes were typically the highest during spring snowmelt and decreased over the summer thaw period. This can be attributed to active layer thaw. The thawing of the active layer increases the vertical infiltration of runoff into the soil profile. Consequently, subsurface flow is routed through deeper regions of the active layer that are comprised of predominantly mineral sediment (Quinton et al. 1999, 2006; Chiasson-Porier et al. 2020). Consequently, the concentration of DOC and nutrients typically decreases over the summer (Quinton et al. 2006).

In addition to spring snowmelt, summer rainfall events also led to noticeable peaks in discharge and solute fluxes. In particular, multiple consecutive days of rainfall in 2014 and 2016 led to mineral ion fluxes that were higher than those observed during spring snowmelt. In 2016, the DOC fluxes following periods of heavy rainfall exceeded the fluxes observed during spring snowmelt. This suggests that, potentially, heavy rainfall can lead to the saturation of the active layer, allowing for soluble organic material at the surface to be mobilized.

The data presented here suggest that summer rainfall events lead to enhanced solute fluxes through the Niaqunguk River basin. As the active layer thaws, the potential for the mobilization of solutes via landscape runoff increases, intensifying the water quality response of the river to rainfall. Thus, rainfall events in fall, when the active layer reaches a maximum thickness, are likely an important source of solutes to the Niaqunguk River. Unfortunately, the sampling period did not capture the chemical composition of these runoff events.

Arctic rivers are more challenging to sample in the fall and winter, largely due inclement weather and ice conditions. This can make it difficult to travel safely to and across field sites. Additionally, the fall and winter months overlap with the two main academic terms, which often restricts university-based researchers' ability to travel to remote field locations. Consequently, the shoulder seasons are not represented in many research programs (Shogren et al. 2020). In contrast with university-based researchers, northern-based research institutions and Indigenous organizations are less constricted by the academic schedule and have greater capacity to sample during the colder months. The meaningful engagement of community-based monitors and researchers could help address this gap in understanding.

Recent climate change has contributed to more intense spring snowmelt periods and a higher frequency of extreme rainfall events for many Arctic regions (Bintanja 2017; Bush et al. 2019). The data presented here, however, indicate that there was overall, statistically significant decrease in total annual precipitation over the period of record (1950–2006; $p < 0.05$). This is likely driven by declining total annual snowfall, which showed a significant decrease over the same period ($p < 0.05$). Although there was not a significant trend in total annual rainfall, the decrease in total annual snowfall has contributed to an increase in the proportion of precipitation that falls as rain. Consequently, the relative importance of rainfall in driving discharge and solute fluxes is increasing.

There was an overall increase in total annual discharge over the period of record (1989–2017). It's important to note, however, that there may be two separate trends. Total annual discharge appears to decrease from 1989–2005. This period directly overlaps with our precipitation record, which suggests that the observed decrease in total annual discharge could be driven by declining total annual precipitation. By contrast, flow appears to have increased over the more recent period with data (2007–2017). Since there are no precipitation data for this period, the reason for this is unclear. It's possible that long term trends in precipitation have changed since 2006, which would have significant implications for solute fluxes.

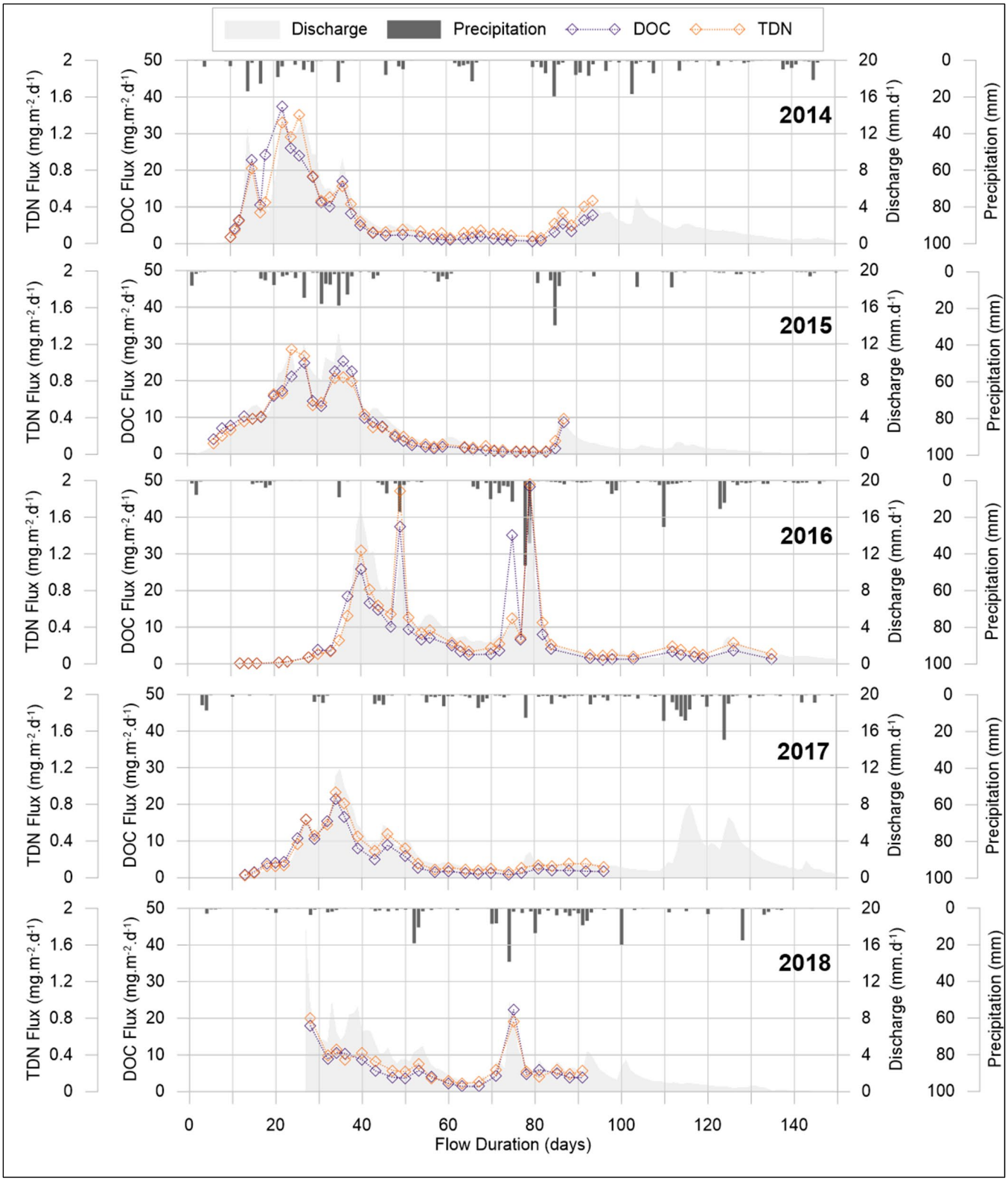

Figure 5. The flux of Dissolved Organic Carbon (DOC) and Total Dissolved Nitrogen (TDN) in units of $mg.m^{-2}.d^{-1}$ over the flow period of each study year (2013–2018). This is plotted with the total daily discharge (in $mm.d^{-1}$) for the Niaqunguk River and the unadjusted total daily precipitation (mm) for Iqaluit.

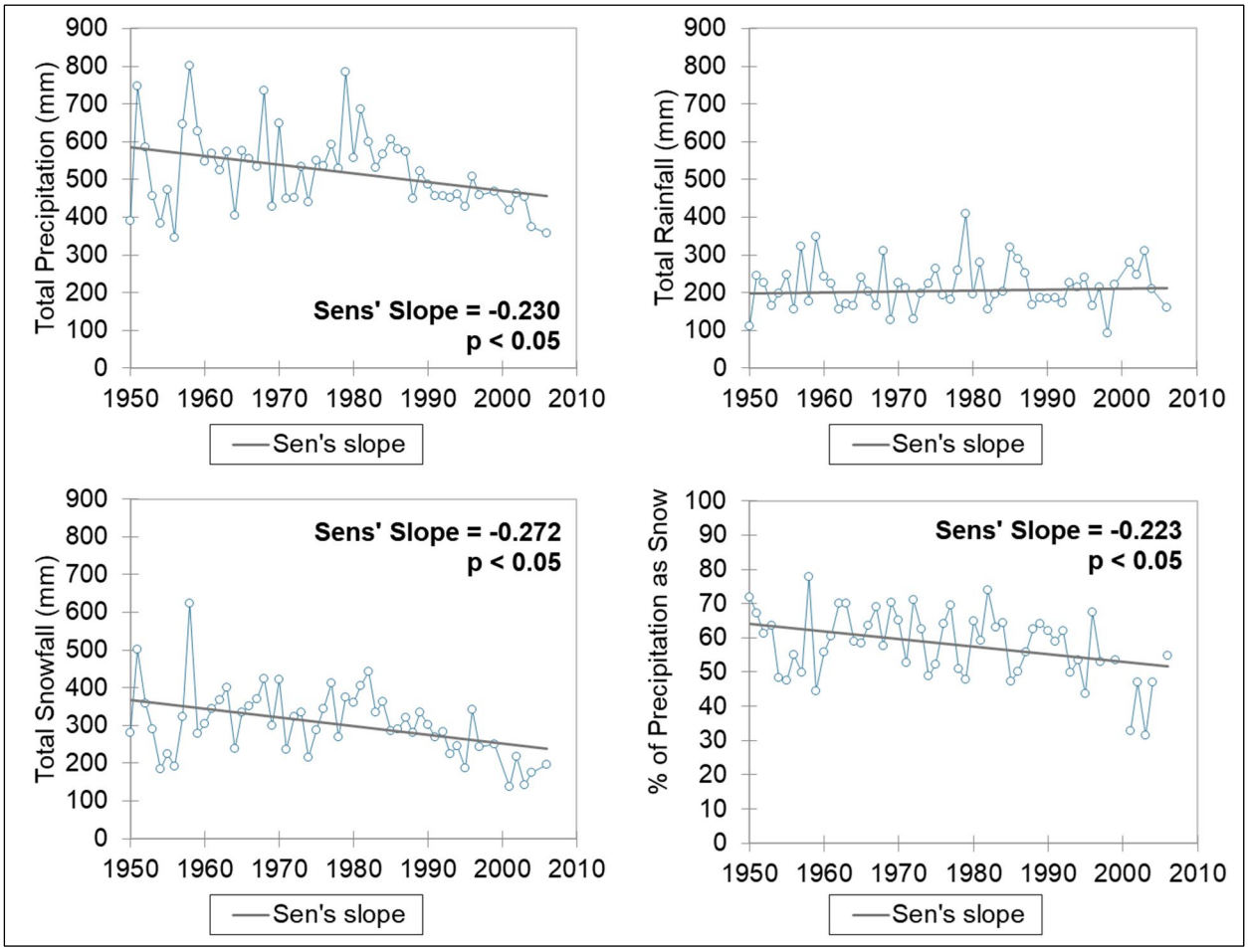

Figure 6. Mann-Kendall Trend and Sen's Slope for the Total Annual Precipitation, Total Annual Snowfall and Total Annual Rainfall in Iqaluit over the period of record.

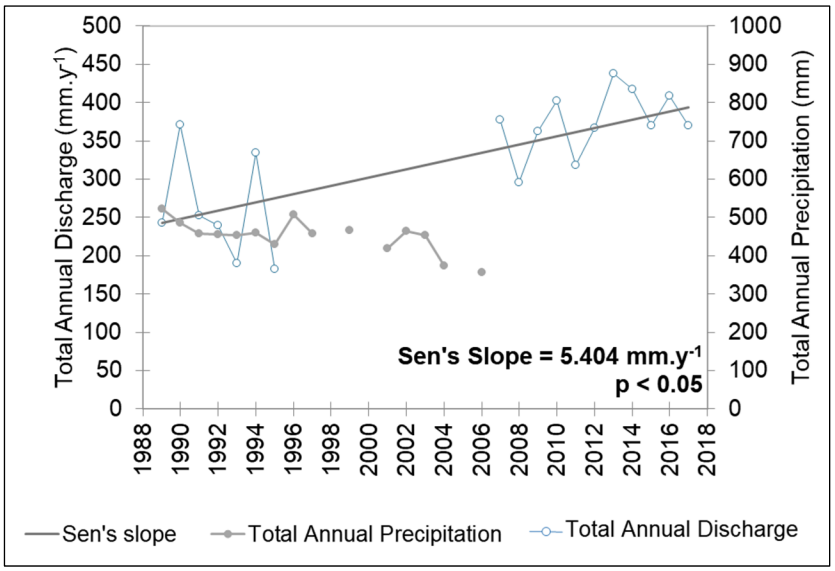

Figure 7. Mann Kendall Trend and Son's Slope for the Total Annual Discharge of the Niaqunguk River over the period of record.

The contributing landscape has limited organic deposits and as a result, DOC and total dissolved nitrogen are only present in low concentrations. The chemical composition of the Niaqunguk River indicates that water chemistry is mainly driven by the weathering of organic material and carbonate minerals, likely by carbonic acid (H_2CO_3) and organic acids. This is associated with subsurface flow through the organic material and glacial till that makes up the active layer. Note that the glacial till is rich in carbonate minerals (Tremblay 2017).

In addition to glacial till, there is extensive bedrock. However, bedrock does not weather appreciably in this environment and likely, does not contribute substantially to solute loads. If subsurface runoff was contained to the glacial till, it's reasonable to expect that increases in total annual precipitation and discharge would lead to increases in the mineral ions associated with carbonate weathering. In regions where the glacial till is thick, this would be amplified by permafrost thaw. For example, the glacial till can be up to 20 m thick in regions occupied by till blanket.

For many Arctic regions, permafrost thaw has contributed to thicker active layers and in turn, the potentiality for deeper flow pathways. If the subsurface flow pathways extended to below the carbonate-rich glacial till, we would likely see a change in water chemistry. For example, bedrock is present near the surface (less than 1 m) in many areas of the Niaqunguk River catchment. Deeper flow pathways could lead to longer rock-water contact times, which could lead to enhanced chemical weathering. In this case, we might see the emergence of solutes associated with silicate minerals, such as aluminum and iron. In future research, it would be interesting to explore techniques for deciphering the relative contribution of glacial till vs. bedrock weathering products to river chemistry.

5 Conclusions

The water chemistry of the Niaqunguk River is predominantly driven by the weathering of organic material and carbonate-rich glacial till. This is facilitated by landscape runoff during spring snowmelt and following summer rainfall events. Although spring snowmelt often leads to the highest solute fluxes, rainfall is an important factor in the mobilization of solutes from the contributing catchment. Therefore, projected increases in summer rainfall have important implications for water chemistry. Increases in summer rainfall, particularly in combination with permafrost thaw, could lead to enhanced interaction between lateral flow pathways and organic deposits, carbonate-rich glacial till, and bedrock.

The water quality of Arctic rivers is intrinsically linked to seasonal and inter-annual patterns in rainfall, snowfall, and discharge. However, the availability of these data in Arctic regions is limited. In the absence of climatic and hydrologic data, it's challenging to predict how climate change will influence Arctic freshwater systems. This is a critical gap to address, as the sustainability and health of Arctic communities is invariably linked to freshwater systems.

6 Acknowledgements

We would like to thank the Inuit peoples of Baffin Island for welcoming us and giving us permission to conduct this research. We would also like to acknowledge the students at the Facility for Biogeochemical Research on Environmental Change and the Cryosphere at Queen's University, as well as the Nunavut Research Institute. In particular, we would like to thank Jamal Shirley and the many summer interns at NRI who contributed to this work. Finally, we would like to thank ArcticNet and NSERC for supporting this work.

7 References

Beel, C.R., Heslop, J.K., Orwin, J.F., Pope, M.A., Shevers, A.J., Hung, J.K.Y, Lafrenière, M.J., and Lamoureux, S.F. 2021. 'Emerging dominance of summer rainfall driving High Arctic terrestrial-aquatic connectivity', *Nature communications* 12 (1), pp. 1448–1449. doi:10.1038/s41467-021-21759-3.

Bintanja, R. and Olivier, A. 2017. 'Towards a rain-dominated Arctic', *Nature climate change* 7 (4), pp. 263–267. doi:10.1038/nclimate3240.

Brown, K.A., Williams, W.J., Carmack, E.C., Fiske, G., François, R., McLennan, D., and Peucker- Ehrenbrink, B. 2020. 'Geochemistry of Small Canadian Arctic Rivers with Diverse Geological and Hydrological Settings', *Journal of Geophysical Research: Biogeosciences* 125(1), e2019JG005414. doi:10.1029/2019JG005414.

Bush, E. and Lemmen, D.S. (eds.) 2019. *Canada's Changing Climate Report*. Ottawa, Ontario, Canada: Government of Canada, 444 p.

Chiasson-Poirier, G., Franssen, J., Lafrenière, M.J., Fortier, D., and Lamoureux, S.F. 2020. 'Seasonal evolution of active layer thaw depth and hillslope-stream connectivity in a permafrost watershed', *Water Resources Research* 56, e2019WR025828. doi:10.1029/2019WR025828

Drever, J.I. 1997. *The Geochemistry of Natural Waters: Surface and Groundwater Environments*. Third edition. Upper Saddle River, New Jersey, United States: Prentice Hall, 436 p.

Fouche, J., Christiansen, C.T., Lafrenière, M.J., Grogan, P., and Lamoureux, S.F. 2020. 'Canadian permafrost stores large pools of ammonium and optically distinct dissolved organic matter', *Nature Communications* 11, pp. 4500–4500. doi:10.1038/s41467-020-18331-w.

Frampton, A. and Destouni, G. 2015. 'Impact of degrading permafrost on subsurface solute transport pathways and travel times', *Water Resources Research* 51, pp. 7680–7701. doi:10.1002/2014WR016689.

Hodgson, D.A. 2003. 'Surficial geology, Frobisher Bay, Baffin Island, Nunavut', *Geological Survey of Canada* Map 2042A, scale 1:100 000.

Kokelj, S.V. and Burn, C.R. 2003. 'Ground ice and soluble cations in near-surface permafrost, Inuvik, Northwest Territories, Canada', *Permafrost and Periglacial Processes* 14(3), pp. 275–289. doi:10.1002/ppp.458.

Lafrenière, M.J. and Lamoureux, S.F. 2013. 'Thermal perturbation and rainfall runoff have greater impact on solute loads than physical disturbance of the active layer', *Permafrost and Periglacial Processes* 24, pp. 241–251. doi:10.1002/ppp.1784.

Mekis, É. and Vincent, L.A. 2011. 'An overview of the second generation adjusted daily precipitation dataset for trend analysis in Canada', *Atmosphere-Ocean* 49(2), pp. 163–177. doi:10.1080/07055900.2011.583910.

Quinton, W.L., Marsh, P., Anderson, M.G., Peters, N.E., and Walling, D. 1999. 'A conceptual framework for runoff generation in a permafrost environment', *Hydrological Processes* 13(16), pp. 2563–2581. doi:10.1002/(SICI)1099-1085(199911)13:16<2563::AID-HYP942>3.0.CO;2-D.

Quinton W. and Pomeroy J. 2006. 'Transformations of runoff chemistry in the Arctic tundra, Northwest Territories, Canada', *Hydrological Processes* 20, pp. 2901–2919. doi:10.1002/hyp.6083.

Schwab, M.S., Hilton, R.G., Raymond, P.A., Haghipour, N., Amos, E., Tank, S.E., Holmes, R.M., Tipper, E. T., and Eglinton, T.I. 2020. 'An Abrupt Aging of Dissolved Organic Carbon in Large Arctic Rivers', *Geophysical Research Letters* 47(23), e2020GL088823–n/a. Available at: https://doi.org/10.1029/2020GL088823.

Shogren, A.J., Zarnetske, J.P., Abbott, B.W., Iannucci, F. and Bowden, W.B. 2020. 'We cannot shrug off the shoulder seasons: Addressing knowledge and data gaps in an Arctic Headwater', *Environmental Research Letters* 15(10), 104027. doi:10.1088/1748-9326/ab9d3c.

Smith, S.L., Burgess, M., Riseborough, D., and Nixon, F.M. 2005. 'Recent trends from Canadian Permafrost Thermal Monitoring Network Sites', *Permafrost and periglacial processes* 16, pp.19–30. doi:10.1002/ppp.511.

St-Onge, M.R., Ford, A., and Henderson, I. 2006. 'Geology, Baffin Island (south of 70°N and east of 80°W), Nunavut', *Geological Survey of Canada* Open File 4931, scale 1:500,000. Available at: \\W5-OTT-H000947\Projects\of5116\digital_release\data\bedrock_geology\bas4931_1_arc.shp.

Tank, S.E., Vonk, J. E., Walvoord, M.A, McClelland, J.W., Laurion, I., and Abbott, B.W. 2020. 'Landscape matters: Predicting the biogeochemical effects of permafrost thaw on aquatic networks with a state factor approach', *Permafrost and Periglacial Processes* 2020, pp. 1–13. doi:10.1002/ppp.2057.

Throop, J., Lewkowicz, A.G., and Smith, S.L. 2012. 'Climate and ground temperature relations at sites across the continuous and discontinuous permafrost zones, northern Canada', *Canadian Journal of Earth Sciences* 49(8), pp. 865–876. doi:10.1139/e11-075.

Tremblay, T. 2017 'Surficial Geology, Beekman Peninsula, Baffin Island, Nunavut, NTS 25P and NTS 15M (part)', *Canada-Nunavut Geoscience Office* Open File Map 2017-03, scale 1:125,000.

Vincent, L.A., Hartwell, M.M., and Wang, X.L. 2020. 'A third generation of homogenized temperature for trend analysis and monitoring changes in Canada's climate', *Atmosphere-Ocean* 58(3), pp. 173–191. doi:10.1080/07055900.2020.1765728.

Zolkos, S., Tank, S.E., Kokelj, S.V., Striegl, R.G., Shakil, S., Voigt, C., et al. 2022. 'Permafrost Landscape History Shapes Fluvial Chemistry, Ecosystem Carbon Balance, and Potential Trajectories of Future Change', *Global biogeochemical cycles* 36, e2022GB007403. doi:10.1029/2022GB007403.

Thermosyphon foundation design and performance at Iqaluit ATB and CSB

Ed Hoeve[1], Brent Wall[2] & Justin Panagapko[3]

[1]*HoevEng Consulting Ltd., Yellowknife, Northwest Territories, Canada*

[2]*Achieve Engineering Inc., Winnipeg, Manitoba, Canada*

[3]*Arctic Foundations of Canada Inc., Elie, Manitoba, Canada*

ABSTRACT

The Air Terminal Building and Combined Services Building at Iqaluit Airport are supported on thermosyphon stabilized foundations. The design incorporated the use of a "warm fill" layer above the thermosyphon system to facilitate the installation of below-grade utilities and services. This foundation design concept was an innovative variation and has since become a typical configuration for large-scale flat loop thermosyphon systems. This design concept is described. The design review analyses considered three short-term severe climatic conditions as well as projected climate warming over an assumed 50-year service life. The climate assumptions are reviewed, and the short-term conditions are found to remain conservative, but the climate change assumption may not be. The foundations were constructed in 2014 and 2015. Instrumentation was installed at the time of construction to permit the thermal performance of the foundation to be monitored. Performance monitoring data are reviewed. The available data indicate that thermal performance to-date has exceeded design expectations. The implications of the performance to-date with respect to the climatic assumptions are reviewed. Satisfactory long-term performance is still anticipated.

1 INTRODUCTION

The Iqaluit International Airport is key component of Nunavut's transportation infrastructure and Canada's sovereignty in the Arctic. It is a hub for air travel in the eastern territory, and a Forward Operating Location, operated by Defence Canada, is located there. About 10 years ago the Iqaluit International Airport Improvement project was implemented by the Government of Nunavut to improve the airside surfaces and replace two major buildings. The project was procured as a Public-Private Partnership, which was awarded to Arctic Infrastructure Limited Partners.

The new Air Terminal Building (ATB) and Combined Services Building (CSB) were constructed between 2014 and 2017 as part of the airport improvement project. Design of the buildings was coordinated by Stantec Architecture Ltd. Best (2017) provides an overview of the design features of the ATB.

Each building is founded on concrete spread footings and has a concrete slab-on-grade floor. The permafrost under the building is protected with thermosyphons and insulation. The thermosyphon system was delivered as a design-build by Arctic Foundations of Canada Inc. Thermal design of the foundation system was developed by Achieve Engineering Inc. Tetra Tech EBA Inc. was retained to provide geotechnical services to the project, including independent review of the thermosyphon system design.

The objective of this paper is to review the thermal performance of the foundation since construction, specifically with respect to the expectations at the time of design, but also to consider the implications of evolving climate warming projections since design.

2 DESIGN AND CONSTRUCTION SUMMARY

Space does not permit a thorough description of the foundation design, nor is that the purpose of this review. However, since the design has not been previously documented in an accessible publication, key elements of the design are summarized in the following sections.

2.1 Site Characterization

The community of Iqaluit is located at the northeast end of Frobisher Bay, on Baffin Island. The airport is situated at the northwest edge of the community. Figure 1 shows the location of the buildings at the airport.

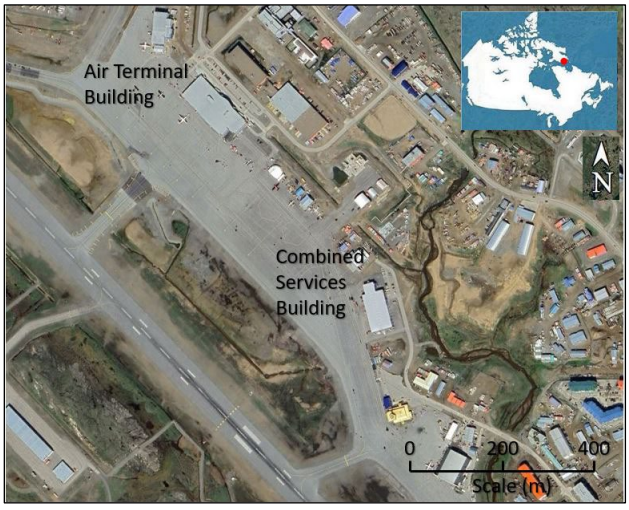

Figure 1. Site location plan.

https://doi.org/10.52381/ICOP2024.192.1

Broadly, the town is located in an area composed of predominantly quaternary sand sediments, with some granite bedrock outcrops (St-Onge et. al. 1999). The surficial geology of the area of the airport where the buildings were constructed was mapped in more detail as a glaciomarine delta (Allard et.al. 2012), though a glaciofluvial channel passes along the southeast edge of the ATB. Numerous frost cracks and ice wedges were mapped in the delta unit.

The airport site was generally investigated for the purpose of improvement project procurement (Peto MacCallum 2012a, b). The building areas were specifically investigated to support foundation design (EBA 2013).

The ATB is situated on and adjacent to a pre-existing airport apron. Where fill thickness was discernable, it was interpreted to range from about 1.0 m to 1.2 m in thickness. The CSB site was vacant prior to building construction, and while the surficial soils may have been reworked, fill was not detected. The prevalent native soil is sand. The sand was determined to generally be gravelly near the ground surface and the fines content (silt and clay-sized particles) increased with depth, such that silty sand was logged in about half the holes below about 8 m. Natural moisture contents in the sand were measured to range from 3% to 18%, and average 10% by volume, so were not high. Bedrock was not encountered within the maximum 33 m depth drilled in any of the investigations.

The community is in the continuous permafrost zone, and the ground ice is broadly characterized as low (i.e., less than 10% by volume; Heginbottom et. al. 1995). This generalization was confirmed during the site investigations. Active layer thickness was interpreted to range from about 2.5 m to 3.5 m. Ground ice was generally non-visible, with occasional traces of visible ice, which is consistent with the moisture content data. Mean annual ground temperatures, below a depth of zero annual amplitude, were found to be about -4 °C at the ATB site and -3 °C at the CSB site. The difference in ground temperature was attributed to snow being cleared from the apron area in the winter. Porewater salinity was found to be negligible at the site.

2.2 Annual Air Temperatures

At the time of design, the available Environment Canada climate normals were for the interval 1981–2010. Climate change was considered during design in accordance with the guidance of CSA (2010); specifically, a moderate emissions scenario was assumed (AR4-A1b). The possibility of anomalous years was considered through a probabilistic analysis of annual air temperature data to arrive at a 1:10 warm year and a 1:100 warm year. 2010 was warmer than the 1:100 warm year, so was considered an “extreme” warm year (Tetra Tech EBA 2014). The properties of each of these cases is summarized in Table 1.

Table 1. Summary of climatic conditions considered in thermal review.

Climatic Case	Annual Air Temperature (°C)	Freezing Index (C°-days)	Thawing Index (C°-days)
Mean (1981-2010)	-9.0	3938	673
1 in 10 Warm Year	-7.1	3350	790
1 in 100 Warm Year	-5.4	2850	900
Extreme Warm Year (2010)	-4.3	2437	904
Estimated in 2065 with Projected Climate Change (AR4-A1b)	-6.5	3192	837

Note: table derived from Table 5.3.4-1 (Tetra Tech EBA 2014).

To assess the anticipated thermal performance of the foundation system, the following cases were modeled (Tetra Tech EBA 2014):

- Long-term mean air temperatures (1981 to 2010);
- 10 years of mean air temperatures followed by 5 consecutive 1 in 10 return event warm years;
- 10 years of mean air temperatures followed by 2 consecutive 1 in 10 return event warm years plus one 1 in 100 return event warm year;
- 10 years of mean air temperatures followed by 2 consecutive 1 in 10 return event warm years plus one extreme warm year (2010); and
- 50 years of estimated air temperatures with the projected long-term climate change, assuming AR4-A1b (moderate) emissions scenario (CSA 2010).

Two-dimensional geothermal analyses were carried out using Tetra Tech EBA’s proprietary finite element computer model, GEOTHERM. The model simulates transient heat conditions with change of phase for a variety of boundary conditions, including heat flux, temperature, and ground-air boundaries using an energy balance equation (Tetra Tech EBA 2014). The theoretical formulation of the model is discussed in Hwang (1976).

2.3 Thermosyphon Design Configuration

While the use of adfreeze steel pipe piles for building foundations was considered, the desire for slab-on-grade floors resulted in a horizontal thermosyphon stabilized foundation system being selected. The generalized foundation configuration is summarized in Figure 2.

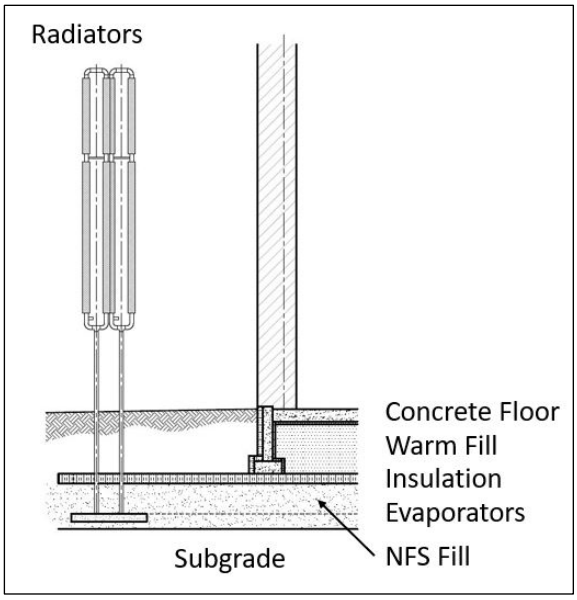

Figure 2. Thermosyphon system section.

The provision of a warm fill layer above the insulation was a relatively new, innovative variation of the foundation system at the time. The warm fill facilitates mechanical installations below the floor without compromising the continuity of the insulation layer. Incorporation of a warm fill layer has become the norm in design of buildings with at-grade floors. Concrete spread and strip footings were cast on the insulation layer. A summary of the design configuration of each building is presented in Table 2.

Table 2. Thermosyphon Stabilized System Configuration.

Item	ATB	CSB
Building Size	8112 m^2	4589 m^2
Assumed Average Floor Temperature	20°C	20°C
Concrete Floor Thickness	125 mm	150 mm
Warm Fill Thickness	875 mm / 2450 mm (airside edge)	850 mm / 2850 mm (airside edge)
Insulation Thickness	200 mm	200 mm
Perimeter Insulation Width	3000 m	3000 mm
Non-Frost-Susceptible Fill Thickness	1000 mm	1000 mm
Radiators	63 – 39 m^2; 4 – 19.5 m^2	34 – 39 m^2
19 mm dia. Evaporator Spacing	1100 mm – 1670 mm	1500 mm
Evaporator Loop Length	85 m – 165 m; avg. 129 m	87 m – 148 m; avg. 126 m

Extensive use was made of 39 m^2 radiators to accommodate the long loop lengths, i.e., more than 100 m, dictated partially by the sizes of the buildings but also by constraints on the permissible locations of radiators. At the time, this was unprecedented in Canada.

There were two deviations from the foregoing generalized profiles:

- The requirement for an elevator in the ATB necessitated the construction of a pit, which deviated from the above generalized configuration. The elevator pit was accommodated by increasing the insulation thickness to 300 mm below and around the base, increasing the non-frost-susceptible fill (NFS) thickness to 1.3 m below, and supplying a dedicated evaporator loop to the bottom of the elevator pit; and
- The floor of the CSB had a sump with an oil interceptor at the transition between the “thin” and “thick” warm fill sections. The sump had a 200 mm thickness of insulation installed on all sides, and the lower level of horizontal insulation below the sump was kept continuous, such that there were two layers of insulation below the sump.

2.4 Construction

The thermosyphons, insulation and footings were constructed in 2014. Figure 3 shows a typical evaporator layout. Thermosyphons were active during the winter of 2014/15.

Figure 3. Evaporator installation at the ATB. Rigid insulation is stockpiled in the background.

Freeze-back of the subgrade was confirmed by March 2015. The balance of fill placement and superstructure erection occurred in the summer of 2015. Temporary construction heat began in the winter of 2015/16. The buildings were turned over for operation in the summer of 2017. Figure 4 shows several radiator banks in front of the completed building.

Figure 4. Front of the ATB showing three radiator banks.

While the possible presence of ice wedges was mapped in the area, none were detected during the site investigation for the project, nor during excavation for foundation construction.

Thermistor cables were installed to permit ground temperatures to be monitored. The thermistor cables, dataloggers and associated telemetry equipment were supplied by BeadedStream of Anchorage, Alaska. The dataloggers became operational in late 2014. The installed instrumentation is summarized as:

- 4 horizontal thermistor cables at the ATB, with a total of 67 sensors, intended to record ground temperatures adjacent to each evaporator loop;
- 4 vertical thermistor cables at the ATB, one inside the building in the area of “thin” warm fill, one in the area of “thick” warm fill, and two about 6 m away from the building, with 12 sensors on each cable, installed to a nominal depth of 12 m;
- 2 horizontal thermistor cables at the CSB, with a total of 34 sensors, intended to record ground temperatures adjacent to each evaporator loop; and
- 4 vertical thermistor cables at the CSB, one inside the building in the area of “thin” warm fill, one at the transition between “thin” and “thick” warm fill, and two about 6 m away from the building, with 12 sensors on each cable, installed to a nominal depth of 12 m.

3 Evaluation of Performance Since Construction

3.1 Review of Annual Air Temperatures

Actual annual air temperature characteristics since 2015 are summarized in Table 3.

Table 3. Summary of Climatic Conditions Since Construction.

Year	Annual Air Temperature (°C)	Seasonal Freezing Index (C°-days)	Thawing Index (C°-days)
2015	-11.1	4309	445
2016	-8.3	3795	705
2017	-7.8	3825	690
2018	-9.4	3648	545
2019	-6.8	3643	787
2020	-7.8	3450	788
2021	-6.1	2996	664
2022	-8.0	3517	807
2015-2022 Average	-8.2	3648	679

Note: seasonal freezing index refers to the freezing index from the fall of the previous year to the spring of the current year.

Comparing the actual annual air temperature conditions in Table 3 with the assumed conditions presented in Table 1, two years were colder than modeled (2015 and 2018), one year was warmer than the 1:10 warm year (2019) and one year was warmer than the projected 2065 mean year (2021, though mainly because of the warm winter; the thawing index was relatively low that year).

The average annual air temperature since construction has been about -8.2 °C. The special cases modeled by Tetra Tech EBA (2014) gave annual averages of -8.4 to -8.5 °C over the 13 to 15-year intervals modeled. Therefore, the average climate since construction compares reasonably with any of the modeled special cases. While one might assume that potential thaw penetration in a particular year would be governed by the thawing index in that year, the heat load from the building is the dominant factor under most of the building and is somewhat independent of the climate.

3.2 Projected Climate

The projected climate change warrants review. The scenario assumed at the time of design is now known to be unconservative Current practice is to assume an AR5-RCP8.5 emissions scenario (CSA 2019). The projections from these scenarios are compared to the 30-year moving average air temperature for Iqaluit in Figure 5. Figure 5 suggests that even the current guidance for climate change may be unconservative.

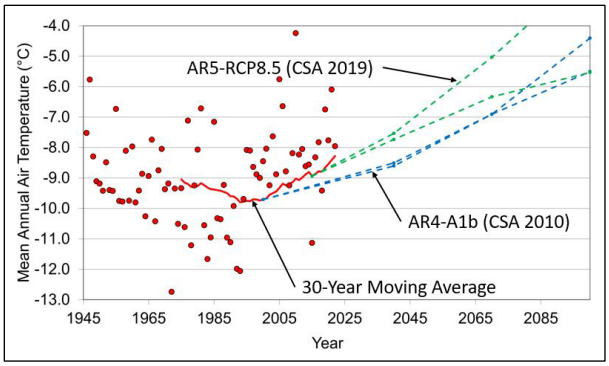

Figure 5. Comparison of climate change projections at Iqaluit with 30-year moving average of mean annual air temperature.

3.3 Review of Selected Ground Temperatures

3.3.1 Ground Temperature Profiles

Ground temperature data have been collected since the end of 2014, though there are some gaps. CSA (2010 and 2019) contains the statement "monitoring is pointless unless the data collected are evaluated". That is the primary motivation for the review described herein.

The ground temperatures recorded along the vertical thermistor cables at each building can be compared to the predictions presented in the review by Tetra Tech EBA (2014). Specifically, the ground temperature along cables V1 in each building (in the area of "thin" warm fill) can be compared to the predictions from the finite element model for Sections 1-1 for each building, and for the climatic case of 10 mean years, followed by two 1:10 warm years, followed by one extreme warm year (2010). The average annual air temperature for this assumed 13-year case would be -8.4°C, which is slightly cooler, but close to the -8.2°C average actually experienced since construction (Table 3). The comparison for each building is shown in Figure 6.

It is evident that the ground below the buildings is significantly colder than was predicted by the modeling during the design review. The design would be expected to have been conservative. The convective heat transfer characteristics of the thermosyphons were based on empirical expressions presented in Haynes and Zarling (1988). One conservative assumption is that wind speed was assumed to be half that reported from the available climate data.

The plots of actual temperature in Figure 6 show that the ground in locally cooler at about evaporator level. This indicates that the evaporators had recently become active, prior to November 15, 2022.

Vertical cables V2 in each building are in or adjacent to areas of "thick" warm fill, and deeper evaporators, so are in less sensitive areas of the buildings and are not specifically reviewed here.

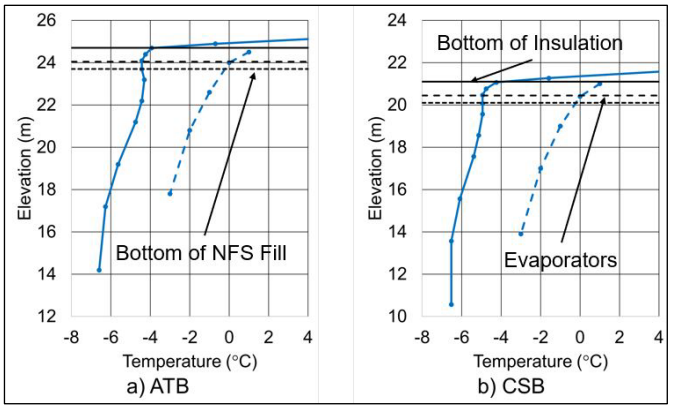

Figure 6. Comparison of measured ground temperature November 15, 2022 (solid line) to predicted (dashed line) after 10 mean, 2 1:10, and 1 extreme year (predicted profiles were extracted from Figures 2 and 6 in Appendix C of Tetra Tech EBA 2014).

3.3.2 Thaw Penetration

A specific design criterion was that thaw should not reach the base of the non-frost-susceptible fill. The ground temperature history within the non-frost-susceptible fill is shown in Figure 7.

The almost isothermal maximum end of the ground temperature envelope for the non-frost-susceptible fill in the ATB (Figure 7a) reflects an anomaly in the data. Apparent warm temperatures were recorded from about October 17 to December 8, 2019, reaching the indicated maximum on November 1, 2019. The ground temperatures of the nearest horizontal sensors (Loops 5 and 6), at evaporator level, were recording about -2.9°C at the same time. The reason for the anomaly is not known.

Removing the apparently anomalous data from the plot results in the dashed red line in Figure 7a, which compares well with what was observed in the horizontal sensors and the similar plot for the CSB (Figure 7b).

The data indicate that thaw did not penetrate below evaporator level since the later stages of building construction. Considering the relatively small temperature gradients through the non-frost-susceptible fill, the interpretation is that there has been no significant thaw below the insulation layer since the buildings have been constructed.

Further insight into the thermal conditions within the non-frost-susceptible layer can be gained by review the temperature records from the horizontal thermistor cables, which were at evaporator level (about 350 mm above the base of the non-frost-susceptible fill). A summary of the data from 2016 to 2022 is presented in Table 4. The data from 2015 are not included because initial freeze-back was still occurring in the first part of the year.

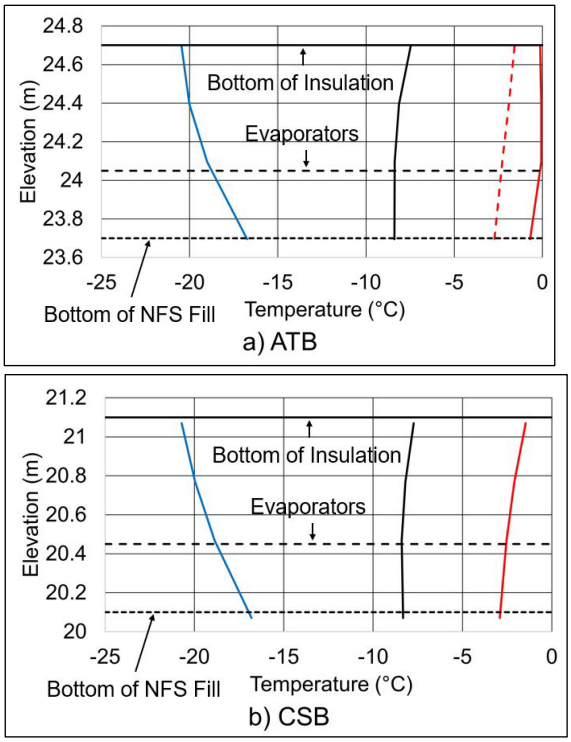

Figure 7. Observed ground temperature profiles through non-frost-susceptible fill layer (blue denotes minimum; black denotes average; red denotes maximum).

Table 4. Summary of Horizontal Thermistor Cable Temperature Readings (2016–2022).

Cable	Maximum (°C)	Minimum (°C)	Average (°C)
ATB H1 (Loops1-2; 64-66)	-1.9	-24.1	-8.9
ATB H2 (Loops 3-19; 54-56)	-2.3	-19.7	-8.6
ATB H3 (Loops 20-53)	-1.2	-20.1	-8.9
ATB H4 (Loops 59-63)[1]	-7.2	-20.8	-12.1
CSB H1 (Loops 1-14)	-2.0	-24.1	-9.1
CSB H2 (Loops 15-28)	-0.8	-16.8	-7.7
Elevator Pit	-2.5	-14.3	-6.5

Note 1: Cable ATB H4 only reflects a portion of 2016 data, as the cable was destroyed at the end of June 2016.

3.3.3 *Climate Change Revisited*

While thermal performance to-date has exceeded expectations, it is prudent to consider the implications of updated guidance with respect to potential climate warming. The modeling has been updated, this time using commercially available software, TEMP-W, considering prevailing ground temperature conditions and climate warming under an AR5-RCP8.5 (high) emissions scenario (CSA 2019). The findings are shown in Figure 8, together with the original predictions to October 15, 2065.

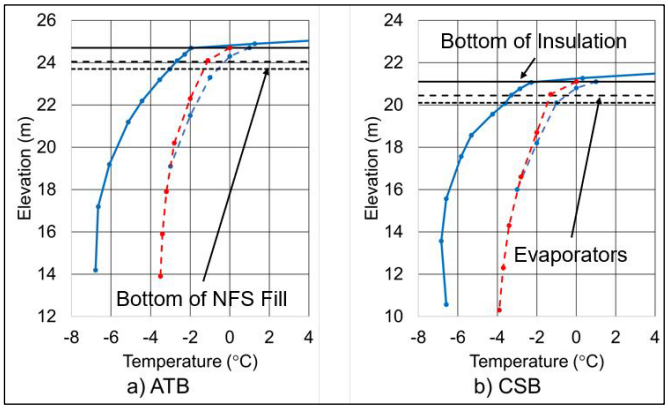

Figure 8. Actual ground temperature profiles October 15, 2022 (solid line) compared with original (dashed blue line) and updated (dashed red line) predictions for October 15, 2065 (original predicted profiles were extracted from Figures 1 and 5 in Appendix C of Tetra Tech EBA 2014).

The updated predictions, based on current guidance, suggest that ground thermal performance of the foundation system should still be satisfactory at the end of the desired service life. However, as current observations suggest that the ambient temperature predictions may be unconservative, the overall system performance should continue to be monitored and evaluated.

There are two deviations from the intended ground temperature monitoring system that should be considered:

- At the CSB, the portions of the horizontal thermistor cable that were intended to monitor the evaporators below the “thick” warm fill were installed at the same, higher elevation as the remainder of the sensors. Consequently, these sensors were installed in warm fill, and do not reflect ground temperatures at the deeper evaporators (Loops 29 to 34); and
- Data from Cables ATB-H4, ATB-V3 and ATB-V4 are not available following June 2016. It is understood that these cables were damaged during construction. Cable ATB-H4 records temperature at evaporator level for Loops 57 to 63. Cables ATB-3 and ATB-4 are outside the building.

As the affected horizontal cables are not able to confirm functionality of their associated evaporator loops, the functionality of those thermosyphons should be regularly checked by recording temperatures at the radiators, early in the freezing season.

4 CONCLUSIONS

Annual air temperatures since construction have averaged within the ranges contemplated at the time of design. However, it is now recognized that climate warming is likely to be greater than assumed at the time of design.

The thermal performance of the thermosyphon system at each building has exceeded design expectations to-date. Specifically, the ground below the buildings has been cooled more than predicted and thaw penetration has not extended significantly below the insulation, which is 1 m above the bottom of the non-frost-susceptible fill layer.

The thermal performance is expected to remain satisfactory under the current understanding of climate warming. However, this should continue to be monitored and evaluated as climate change projections continue to evolve.

The ground temperature data being collected permits most facets of thermosyphon system performance to be evaluated. But there is also merit in regularly monitoring radiator temperatures to gain a more complete understanding of system performance.

5 ACKNOWLEDGEMENTS

The authors would like to thank Arctic Infrastructure Limited Partners for permission to publish this paper and for support of continued monitoring. The willingness of Tetra Tech Canada Inc. to provide the information referenced throughout is gratefully acknowledged.

6 REFERENCES

Allard, M., Doyon, J., Mathon-Dufour, V., LeBlanc, A.-M, L'Hérault, E., Mate, D., Oldenborger, G.A., and Sladen, W.E. 2012. 'Surficial geology, Iqaluit, Nunavut', *Geological Survey of Canada* Canadian Geoscience Map 64 (preliminary version), scale 1:15,000. Available at: https://doi.org/10.4095/289503.

Best, N. 2017. 'The New Iqaluit International Airport', *Canadian Consulting Engineer* August 29, 2017. Available at: https://www.canadianconsultingengineer.com/features/new-iqaluit-international-airport/.

Canadian Standards Association (CSA) 2010. *Technical Guide: Infrastructure in Permafrost: A guideline for climate change adaptation*. CSA Reference Number: PLUS 4011-10. Available at: https://www.csagroup.org/store/product/PLUS%204011/.

Canadian Standards Association (CSA) 2019. *Technical Guide: Infrastructure in Permafrost: A guideline for climate change adaptation*. CSA Reference Number: CSA PLUS 4011:19. Available at: https://climatechange.toolkitnwtac.com/wp-content/uploads/sites/21/2019/08/Technical-Guide-Infrastructure-CSA.pdf.

EBA, A Tetra Tech Company 2013. *Geotechnical Investigation for International Airport Improvement, Iqaluit, NU*. Report submitted to Bouygues Building Canada Inc., September 2013. EBA File: Y14103133-01.

Haynes, F.D. and Zarling, J.P. 1988. 'Thermosyphons and foundation design in cold regions', *Cold Regions Science and Technology* 15, pp. 251–259.

Heginbottom, J.A., Dubreuil, M.A., and Harker, P.T. 1995. 'Canada, Permafrost', in *National Atlas of Canada*, *5th edition*. Natural Resources Canada, MCR 4177, scale 1:7,500,000. Available at: https://ftp.maps.canada.ca/pub/nrcan_rncan/raster/atlas_5_ed/eng/environment/land/mcr4177.pdf.

Hwang, C.T. 1976. 'Predictions and observations on the behaviour of a warm gas pipeline on permafrost', *Canadian Geotechnical Journal* 13(4), pp. 452–480.

Peto MacCallum Ltd. 2012a. *Draft – Geotechnical Investigation Iqaluit International Airport Improvement Project, Iqaluit, Nunavut*. Report submitted to Genivar Inc., January 2012. PML File: 11KF086.

Peto MacCallum Ltd. 2012b. *Additional Geotechnical Investigation – Iqaluit International Airport Improvement Project, Iqaluit, Nunavut*. Report submitted to Genivar Inc., December 18, 2012. PML File: 11KF086(C).

St-Onge, M.R., Scott, D.J. and Wodicka, N. 1999. 'Geology, Frobisher Bay, Nunavut', *Geological Survey of Canada* "A" Series Map 1979A, scale 1:100,000. Available at: https://doi.org/10.4095/210833.

Tetra Tech Canada Inc. 2014. *Geotechnical Design Report for Air Terminal and Combined Services Buildings, Iqaluit International Airport, NU – Revision 2*. Report submitted to Bouygues Sintra JV, July 2014. Tetra Tech File: Y14103133-01.

Characteristics and geomorphological implications of the periglacial environment of Craig Cŵts, Patagonides, Chubut, Argentina

Evan Hughes[1] & Dario Trombotto Liaudat[2]

[1]*Universidad de La Plata, Argentina*

[2]*Geocryology, IANIGLA, CCT CONICET Mendoza, Argentina*

ABSTRACT

Glaciations and cold episodes, which shaped the current Humid Andes (regional name Andes Ap Iwan) as well as the Patagonian steppe, developed mainly during the Quaternary. In this work, a geomorphological and paleoclimatic study of the region called Craig Cŵts in the Patagonides mountain range in Patagonia, is carried out. Through parameters obtained from active, inactive and fossil landforms, it was possible to develop a preliminary climatic reconstruction from the present to the Last Glacial Maximum, given that records of the most important Pleistocene glaciations were also detected. Identified Holocene events (cryogenic and glacial) were assigned to the Andean Neoglacials. These cryogenic scenarios are well represented everywhere in the Craig Cŵts range. Numerous different cryoforms that interact with the lithology, structures and hydrology of the region were found. Regional isotherms were calculated and mountain permafrost or permanently frozen ground was discovered in the highest part of the area, from 1970 m ASL upward to 2019 m ASL (the summit of Mount Edwin). The data were applied to a preliminary isotherm model to calculate possible and probable permafrost distribution scenarios. The model was also successfully compared to other models as the "Continental Permafrost Distribution Model for the South American Andes" of Arenson et al. (2021). For the first time, the Craig Cŵts region is analyzed in detail for its periglacial environment and permafrost in the present day and in the past to transform it into a key area for the Patagonides. The identified cryogenic geoforms have been shaping the current periglacial landscape until the present.

1.0 INTRODUCTION

Glaciations and cold episodes, which shaped the current Humid Andes (regional name Andes Ap Iwan) as well as the Patagonian steppe, developed mainly during the Quaternary. In this work, a geomorphological and paleoclimatic study of the region called Craig Cŵts is carried out (Figure 1). Through parameters obtained from active, inactive and fossil landforms, it was possible to develop a preliminary climatic reconstruction from the present to the Last Glacial Maximum. There, records of the most important Pleistocene glaciations have also been found. Identified Holocene events (cryogenic and glacial) were assigned to the Andean Neoglacials (see Mercer 1985). These cryogenic scenarios are well represented everywhere in the Craig Cŵts range. Numerous different cryoforms that interact with the lithology, structures and hydrology of the region were found. For the first time, the Craig Cŵts region is analyzed for its periglacial environment and permafrost in the present day and in the past to transform it into a key area for the Patagonides. The identified cryogenic geoforms have been shaping the current periglacial landscape until the present, but they also have been conditioning the regional hydrology.

2 STUDY AREA

The study area Craig Cŵts (Figure 1) is located in the Patagonides, Precordillera of the province Chubut, Argentina, an extra Andean mountain massif between parallels 43° and 43°40'S in Patagonia (also called Celtic Patagonia, because of Welsh colonization). The area is quite unexplored and unknown from a geological and geomorphological point of view. A first regional map with original names by Ap Iwan (1888) is used. Peaceful coexistence between Welsh people and Aóni Kenk and Gününa Küne ethnic groups from southern and northern Patagonia respectively, is shown on this type of map, that included many of indigenous names and help us to understand the landscapes, as well as relatively unknown zones. The calculated mean annual air temperature (MAAT) of the study area at the temporary measurement station Craig Cŵts (43°27'48''S, 70°55'17''W, 1670 m ASL) on a moraine between the glacial lakes Ogwen and Hughes, for the period between 2017 and 2022, was 2.7 °C. The precipitation regime was taken from the nearby locality Gwyndy (43°16'35''S,71°09'22''W, 710 m ASL) between 1988 and 2018, for which a mean of 315.5 mm is recorded per annum.

https://doi.org/10.52381/ICOP2024.225.1

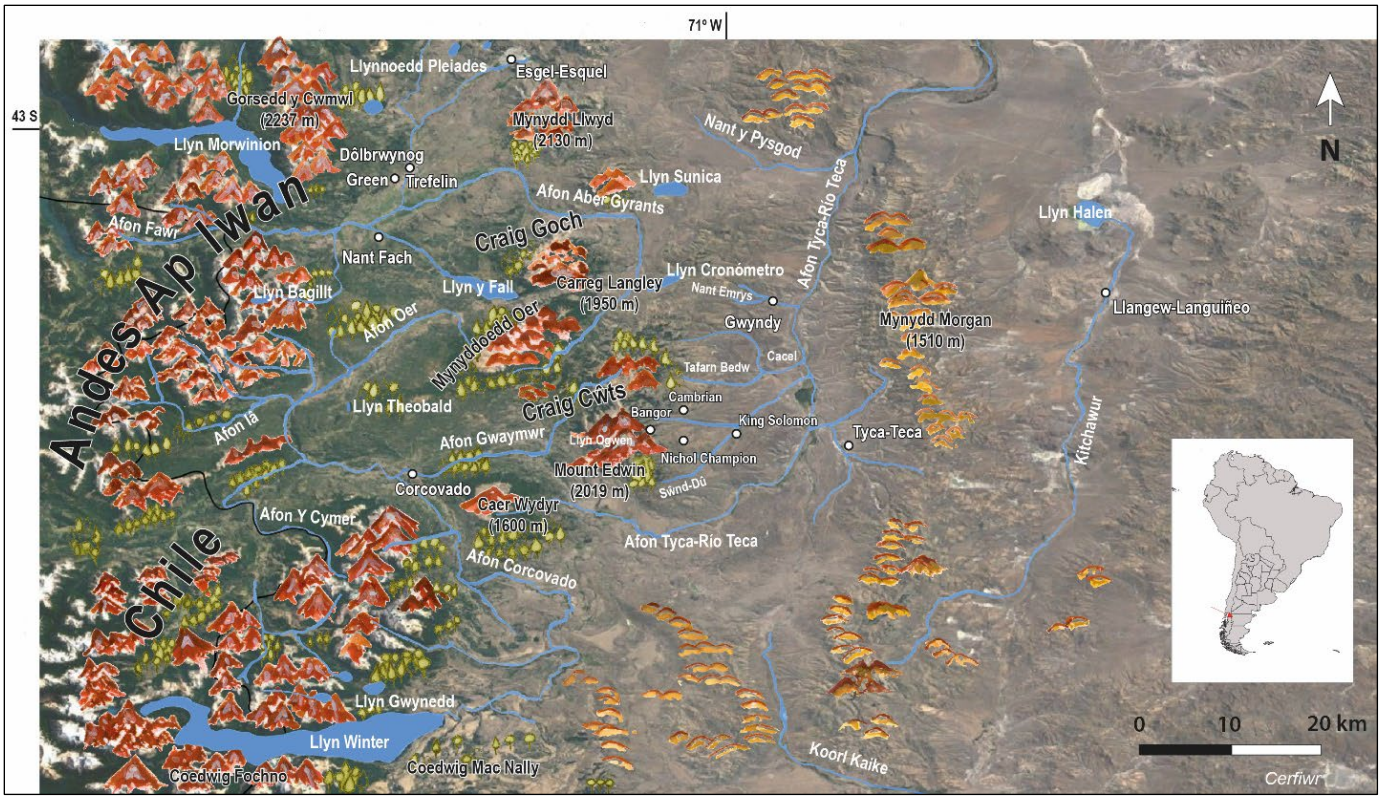

Figure 1. Study area and cryogenic landforms (Trombotto Liaudat, 2021).

The climograph (Figure 2) indicates in black the months (between May and September) when the average daily minimum and they average daily temperatures are below 0 °C. The remaining months are with absolute minimum below 0 °C. While the absolute minimum was -15.42 °C (July 2020), the daily average minimum of the coldest month was -6.4°C (July 2022). The upper limit of the forest with intense seasonal freezing cycles, cryoweathering and solifluction without permafrost reaches up to 1500 m.

The weather station at Esquel Airport (see Esgel, Figure 1) shows no long-term trend in MAAT in the period of record between 1931 and 2022. However, there is decadal variability and particularly the period between approximately 1950 and 1975 shows on average a MAAT that is about 1 °C colder than in the period from 2017 to 2022.

This implies a c. 150 m lowering of the zero isotherm at that time. The upper elevation of the tree line at Craig Cŵts is located at approximately 1510 m ASL, and descends to the east and north to approximately 1200 m. To the west and south, the forest may descend farther down, for instance to elevations of 900 and 1000 m ASL respectively. Then, the forest descends in “gallery” accompanying the creeks. Above the tree line, the landscape is largely shaped by current cryogenic processes.

The lithology of the study area is composed mainly of Early Mesozoic (Jurassic) andesitic and dacitic rocks (Massaferro 1998; Haller et al. 2010). However, from the same age, pyroclastic rocks such as tuffs, lapilli and breccias as well as clastic and carbonate rocks appear (Table 1).

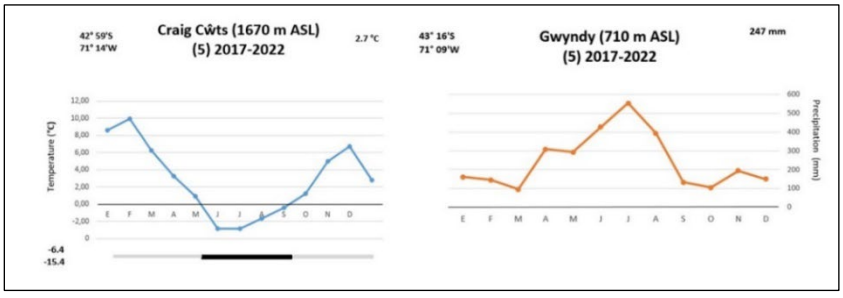

Figure 2. Walter Lieth climograph of the study area.

Given the effects of cryoweathering at Mount Edwin (2019 m ASL), unconsolidated Pleistocene to Holocene age periglacial sediments cover slopes as colluvium on surrounding slopes. Former creeping permafrost forms, such as fossil rock glaciers, carried volcanic cryoclasts (i.e., andesites, Jurassic, Lago La Plata Formation; Haller et al. 2010) below 1500 m ASL. Other clastic periglacial sediments are transported through contemporary processes including rock falls and active nivodetritic channels are also involved. Till, in the form of Pleistocene and Holocene moraines, is present around lakes Ogwen and Hughes. These are clearly seen given the absence of vegetation up to 1500 m ASL (Figure 1). Holocene fluvial and alluvial sediments are deposited in the creeks.

Table 1. Geology of the region based on Turner (1982), Massaferro (1998) and Haller et al. (2010)

Age		Geological Units	Litology
Cenozoic	Holocene		Unconsolidated periglacial, fluvial, alluvial and colluvial deposits
	Ptc. L M E		Unconsolidated glacial, periglacial, fluvial, alluvial and colluvial deposits
		Huaiqui Formation	Polymictic conglomerates
	Miocene	La Mimosa Formation	Tuffaceous siltstones, limestones
	Eocene	Huitrera Formation	Dacitic dykes, tuffs, breccias, sandstones and siltsones
Mesozoic	K	Río Hielo Granitoid	Granitoid
		Divisadero Group	Andesitic dykes and rhyodacites
	J	Lago La Plata Formation	Andesites, rhyodacites, limestones; pyroclastic, epiclastic and bioclastic rocks
		Lepá Formation	Conglomerates, sandstones and siltstones

3 METHODOLOGY

Mapping of landforms was carried out in two steps. First, from the processing and visualization of satellite images and digital elevation models (DEMs), with which it was also possible to obtain the contour lines and streams. The results were drawn into a Geographic Information System (ArcGIS). Such mapping was controlled and corrected through field surveys. Periglacial landforms (Hughes 2023) were classified according to their present state of activity, namely:

1. Paleo-permafrost landforms;
2. Landforms/Cryoforms with current permafrost; and
3. Macro and microforms related to seasonal freezing and thawing cycles.

Each landform was visited during different fieldtrips (2016–2023). Pits were made in order to find cryogenic phenomena in the stratigraphy, or specific cryogenic indicators of the active layer.

The region has no recorded instrumental weather information given the absence of weather stations. To know the in situ current climatic conditions and isotherm positions, the area has been equipped with UTL data loggers since 2017. In this way, the data were used to calculate the regional isotherms. A value of 2.7 °C (MAAT) from the lake Ogwen moraine meteorological station was established, from which the 0 °C isotherm (cf. Ruiz and Trombotto 2012a) and other isotherms at higher elevations. For this aim, two different methodologies were used.

The first method consists of using an algorithm, relating both the MAAT with altitude, and a variation gradient of the MAAT with altitude. We considered a standard adiabatic gradient for a relatively dry atmosphere of -0.65 °C/ 100 m:

$$Iso0ºC(m) = MAAT / c + h0 \quad [1]$$

where MAAT is the mean annual air temperature, h0 is the height of the station and c the thermal gradient.

To locate the position of isotherms other than 0 °C, the following linear regression was used:

$$Z1\ (m) = \frac{(T1 - T0) - (c \times Z0)}{-c} \quad [2]$$

where Z1 is the height of the 2 °C/4 °C isotherm; Z0 is the height of the Cŵts station, T1 is 2°C or 4 °C, T0 is the average annual temperature at the weather station and c is the thermal gradient.

The second method involved generating isotherms from a model consisting of a continuous field of MAAT values (Raster) interpolated from a GIS software using data from the nearest meteorological stations. As the weather stations are located at different altitudes, it was necessary to calculate a homogeneous surface using an H-reference, as well as a MAAT-reference.

ΔH= H-reference - H-weather station

For the H-reference, the H of the Craig Cŵts weather station at 1670 m ASL was used. The calculation of the MAAT-reference was made as follows:

MAAT-reference = MAAT- weather station + (c x ΔH)

The TMAA-reference was used as the Z coordinate corresponding to a station marked in the GIS software. The reference surface obtained was projected onto a DEM (Fries et al., 2012; Tapia and Trombotto, 2015). The work used the Natural Neighbor interpolation method to calculate a desired isotherm. This is calculated in a GIS software with a Raster calculator under the expression:

MAAT-isotherm = MAAT-interpolation + (c (DEM (xyz) – H-reference))

Where the expression (DEM (xyz) – H-reference) represents the altitude value of all the other points of the

DEM that are not contained on the reference surface, it is possible to obtain a new Raster whose Z coordinate represents the average annual air temperature estimated all over the DEM.

Once the height of the isotherms was known through the two methods used, three cryogenic zones with different probabilities of permafrost occurrence were defined according to the following MAAT thresholds (Ruiz and Trombotto 2012b; Tapia and Trombotto 2015):

- < 0 °C = Periglacial zone, likely permafrost (LP)
- 0 °C to < 2 °C = Periglacial zone, possible permafrost (PP)
- 2 °C to < 4 °C = Periglacial zone, no permafrost (NP), with periglacial phenomena due to strong seasonal freezing
- > 4 °C = No periglacial, seasonal freezing

The model was also successfully compared with other models such as the "Continental Permafrost Distribution Model of Arenson et al. (2021). Permafrost, perennial snow patches and regional glacierettes were mapped following geocryological classical methodologies (Washburn 1979; Karte and Liedtke 1981; Garleff and Stingl 1986; Trombotto et al. 1999; Bolch and Schroeder 2000).

4 RESULTS

4.1 Periglacial Geomorphology

The Craig Cŵts region (Figure 3) shows typical erosive and depositional glacial landforms, such as nearby U-glacial valleys, cirques, sheepback rocks, moraines and outwash plains. Today there are glacierettes in the region, but from the glacial point of view they are of little importance. However, they permanently occupy 10 highly visible nivation niches in the remaining Little Ice Age cirques (Figures 4 and 5; Table 2). Furthermore, in order to corroborate the existence of permafrost in Craig Cŵts, pits to 2.5 m depth were made in the area of perennial snow patches, and permafrost was found underneath. However, the most numerous periglacial landforms are those left by Holocene paleo-permafrost, such as stone runs, blockfields, kurums, solifluction lobes and terraces, as well as fossil rock glaciers (Figures 6 and 7). Some of these landforms are interrupted or hidden under Nothofagus forests. The most important fossil rock glacier is 800 m long in its visible part.

Above 1850 m ASL the landforms are associated with present permafrost. They include patterned ground, cryoplanation surfaces, cryogenic sedimentary slopes, nivation hollows, soli and gelifluction lobes and terraces (e.g., terracettes and garlands), protalus lobes and both active (up to approx. 80 m long) and inactive rock glaciers (Figures 3, 7 and 8).

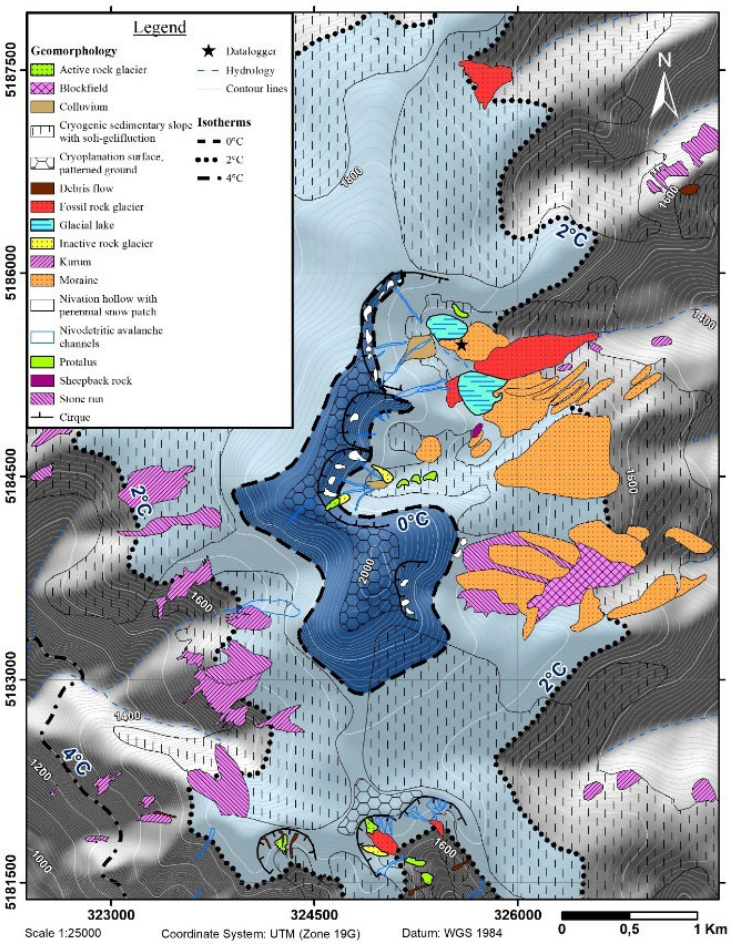

Figure 3. Cryogenic Geomorphology at Craig Cŵts.

Table 2. Comparison of present glacierette areas in the region with those indicated in the National Inventory of Glaciers for the year 2015 (software QGIS 3.28.8).

2015		2021	
Number	Area (m2)	Number	Area (m2)
1	21770.92	1	4250.92
		2	5029.9
2	26584.64	3	5776.26
		4	2882.03
3	33276.24	5	3984.44
		6	4370.96
	0	7	1734.94
4	14774.39	8	1621.95
5	27319.76	9	9790.58
6	15969.69	10	8929.98

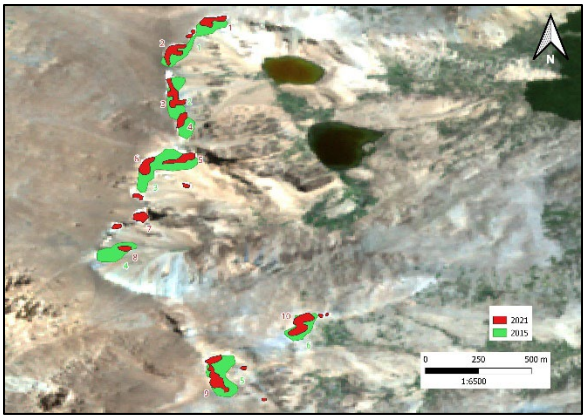

Figure 4. Image Sentinel 2A from January 30, 2021. Snow patches without number are < 1000 m^2.

Figure 5. Pits made in glacierette: a) general view of the glacierette number 2, 2021; b) section in snow patch showing structure and uppermost permafrost layer (tip of red shovel) c) firn/névé found in the section, sample at 1.6 m depth.

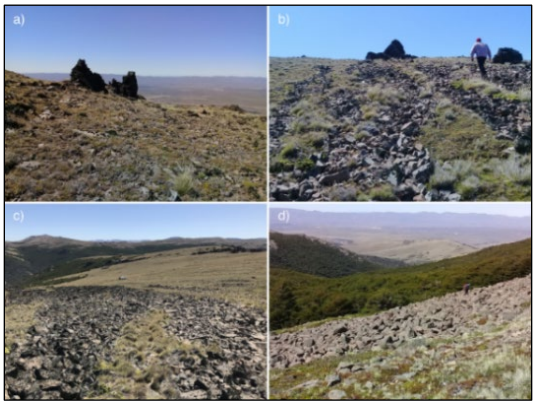

Figure 6. a) tor; b) and c) former stone runs; d) kurum.

Figure 7. Fossil rock glaciers: a) active embryonic rock glacier and protalus lobes (green), inactive (yellow) and fossil (red) rock glaciers; b) and c) fossil rock glaciers.

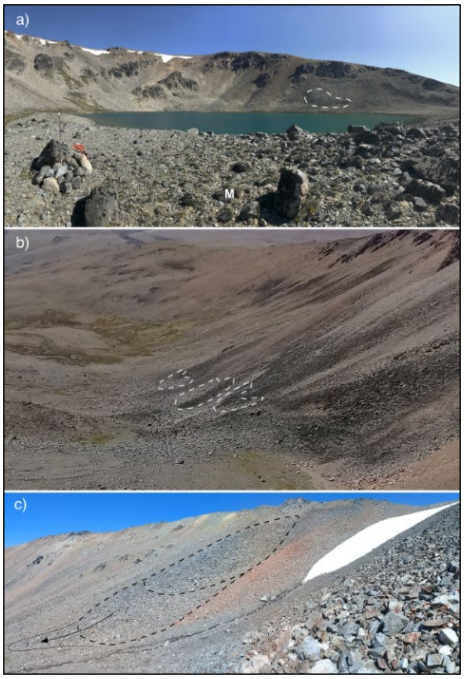

Figure 8. a) Data logger at Lake Ogwen, glacierettes, M = moraine, protalus lobe; b) Protalus; c) Active (upper) and inactive (bottom) rock glacier.

Due to the topographic shadow of Mount Edwin to the S and SW, cryogenic processes produce these landforms approximately 100 m below. Inactive rock glaciers are up to 150 m long. They are made of vulcanites from regional lithology (Lago La Plata Formation, Haller et al. 2010). The environment is exposed to many cycles of freezing and thawing that promote strong cryoweathering (formation of tors, Figure 6). The cryogenic sedimentary slopes show natural ruggedness due to the soli and gelifluction lobes (Figures 3 and 9).

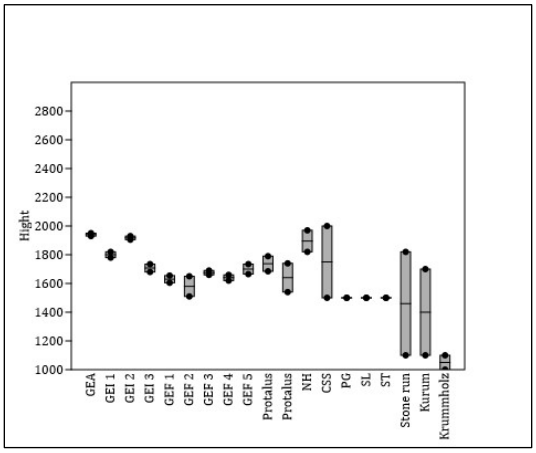

Figure 9. Lowest and highest altitudes of the most important cryogenic landforms. GEA = active rock glacier, GEI= inactive rock glacier, GEF = fossil rock glacier, NH = nivation hollow, CSS = cryogenic sedimentary slopes, PG = patterned ground, SL= solifluction lobes, ST = solifluction terraces.

Figure 9 with “boxes” shows the lowest and highest altitudes of the main cryogenic landforms. The elevations of the landforms allow the identification of fossil and currently active cryoforms.

4.2 Looking for the 0 °C isotherm through indirect ways

The position of the 0 °C isotherm following the thermal gradient and a linear regression today lies between approximately 2000 and 2100 m ASL.

However, if we use isotherms from the model consisting of a Raster of MAAT, values interpolated from a GIS software, using other data from nearby weather stations, the 0 °C isotherm somewhat lies lower, as follows:

- iso0 °C Raster = 1970 m ASL
- iso2 °C Raster = 1640 – 1650 m ASL
- iso4 °C Raster = 1300 – 1400 m ASL

4.3 Comparison with another permafrost model

Figure 10 shows the Continental Permafrost Distribution Model by Arenson et al. (2021). In this model, the 1800 m ASL contour line was drawn. It is observed that the curve covers most of the area interpreted with permafrost in our model and supports our earlier mentioned interpretation.

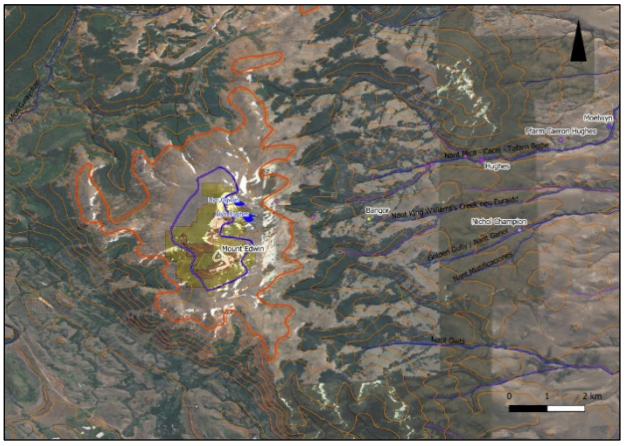

Figure 10. Permafrost distribution model according to Arenson et al. 2021. Orange = likely permafrost; yellow = possible permafrost; circle around Mount Edwin (2019 m) = contour of 2000 m ASL; violet line = contour of 1800 m ASL; and orange line = 1600 m ASL, representing lowest altitude of intense cryoweathering.

5 Discussion

5.1 Permafrost altitude

Regionally, Reato et al. (2023) analyze the meteorology that favors the periglacial environment with permafrost in the touristic region of La Hoya, Esquel (with clear indicators of anthropization in the cryogenic landscape). However, we observe from our presented data (cf. Hughes 2023), that the results and climatic regime differ when we move to the S. We believe that the mentioned climate seems to have differentially influenced cryogenic processes and landform genesis.

Looking for the 0 °C isotherm, according to the thermal gradient, two results are notable. The first is for the period until 2019, which places the isotherm of 0 °C at the summit of Mount Edwin (approximately 2000 m ASL). However, the second result places the 0 °C isotherm above it. If we add the warmest temperatures obtained between 2020 and 2023, we obtain an annual average of 2.7 °C at Lake Ogwen, which would not support permafrost.

The warm mountain permafrost found from an altitude of 1850 m ASL upwards, is associated with permanent snow patches. Active cryogenic landforms such as cryogenic lobes and active cryogenic sedimentary slopes are in patchy or island mountain permafrost areas which extent to the summit of the Craig Cŵts (2019 m ASL). On southern slopes, the permafrost altitude is approximately 1850 m ASL, but would be at 1950 m on northern slopes, as found through models. The models agree fairly closely with the most important cryogenic landform indicators (Figures 3 and 9).

The calculated area for the likely permafrost zone is 1.92 km^2 and 16.21 km^2 for the possible permafrost zone.

It may be assumed that current permafrost is in an unstable state and may soon disappear. However, island

permafrost can persist in the biggest and most elevated cryoforms for many more decades.

5.2 Age of old periglaciation in the Patagonides

After and during the last ice age, strong periglaciation and rock glacier formation was likely in the region. The glacial geomorphology consists of notable cirques and moraines. These landforms are 'fresh' in appearance and easily distinguishable. They suggest that during the Greenlandian Age (11.7–8.3 ka), Craig Cŵts would have been glaciated and that the paleo-periglacial landforms essentially appeared later, starting probably from the Meghalayan Age (4.2–0 ka). Important glaciers occupied the region until the end of the Little Ice Age and left the freshest moraines close to the cirques (Figure 8a). The rocks present clean surfaces, without oxidation patina; and so there is no organic soil or vegetation development. Regional investigations on glacial advances, that also indirectly involve Craig Cŵts, are mentioned by several authors (i.e., Caldenius 1932: Glasser and Jansson 2008).

The number, diversity, and large fossil periglacial landforms would indicate that there was a significant mountainous periglacial environment with intense cryoweathering activity, creeping permafrost, and in situ permafrost.

Through a recent work in Craig Goch, Patagonides (Fröjd et al. 2022), with similar geological and climatic characteristics and proximity, it is possible to transfer identified Neoglacials and cryogenic processes to Craig Cŵts. On this basis we identify two ages associated with soli and gelifluction lobes and terraces and an outwash plain delimited by a moraine. They are cryomeres belonging to the Little Ice Age and the previous Neoglacial known as the "*Pessimum der Völkerwanderung"* in Germanic literature (see Table 3).

Table 3. Dating old cryogenic processes at Craig Goch,

Profile	Altitude (m)	Age cal 14C yr BP	Environment and Processes	Neoglacials, other connotations	Horizont Depth (cm)
CG T1-1	1625	614	solifluction	Little Ice Age	30-36
CG T1-2	1633	1550	Stabilized solifluction	PV = Pessimum der Völkerwanderung, Dark Ages	22-28
CG T2-3	1731	1559	Outwash plain	PV = Pessimum der Völkerwanderung, Dark Ages	38-39

Patagonia (Fröjd et al. 2022).

6 Conclusions

Island permafrost appears until present in mountain ranges beyond the Andes at altitudes below 1900 m ASL and 42°S due to special topo-climatic conditions (sufficient altitude, narrow and shady valleys), southern aspect and sedimentary/volcanic lithology. However, clear indicators of rapid warming (size of glacierettes, rise of the isotherm of 0°C) are detected and coincide with the increase in MAAT since 2017.

A good example of the Patagonian cryogenic environment is the previously unknown area Craig Cŵts located in the Patagonides, Precordillera of the province Chubut, Argentina, an extra Andean mountain massif between parallels 43° and 43°40' in Patagonia, which is being studied for the first time in detail.

A rich periglacial geomorphology is present in Craig Cŵts, with active and inactive rock glaciers, nivation hollows, cryogenic sedimentary slopes, patterned ground, soli- and gelifluction lobes and terraces.

7 Acknowledgements

We thank Ivanna Pecker Marcosig and Nati Mónaco for the technical cooperation and the Hughes family for their constant support.

8 References

Ap Iwan, Llwyd. 1888. *Tiriogaeth Camwy*. Eileb o Barthlen. Museo Regional de Gaiman, Patagonia, Argentina.

Arenson, L.U., Pino, C., Schimowsky, M., Wainstein. P.A. and Cecioni, A. 2021. 'A Continental Permafrost Distribution Model for the South American Andes', *Regional Conference on Permafrost (RCOP) and 19th International Conference on Cold Regions Engineering (ICCRE)*, abstracts. Virtual conference, October 24–29, 2021.

Barsch, D. and King, L. 1975. 'An attempt to date fossil rock glaciers in Orison, Swiss Alps'. *Quaestiones Geographicae* 2, pp. 5–14.

Bolch, T. and Schröder, H. 2000. *Geomorphologische Kartierung und Diversitätsbestimmung der Perglazialenformen am Cerro Sillajhuay (Chile/Bolivien)*. Erlanger Geographishe Arbeiten, Sonderband 28, 141 pp.

Caldenius, C. 1932. 'Las glaciaciones cuaternarias en Patagonia y Tierra del Fuego'. *Geografiska Annaler* 14, pp. 1–164. Also published in Dirección General de Geología y Minería, Anales 95, pp. 1–150. Buenos Aires.

Fries, A., Rollenbeck R., Nauss Peters T. and Bendix J. 2012. 'Near surface air humidity in a megadiverse Andean mountain ecosystem of southern Ecuador and its regionalization', *Agricultural and Forest Meteorology* 152, pp. 17–30.

Fröjd, C., Trombotto Liaudat, D., Scheer, C., Pecker Marcosig, I. and Kuhry, P. 2022. 'Soil organic carbon stocks in mountain periglacial areas of northern Patagonia (Argentina)'. *Arctic, Antarctic and Alpine Research* 54(1), pp. 176–199. Available at: https://doi.org/10.1080/15230430.2022.2062102.

Garleff, K. and Stingl, H. 1986. 'Geomorphologische Aspekte aktuellen und vorzeitlichen Permafrostes in Argentinien', *Zentralblatt fuer Geologie und Palaeontologie* 1(9/10), pp. 1367–1374.

Glasser, N.F. and Jansson, K., 2008. 'The glacial map of southern South America', *Journal of Maps* 2008, pp. 175–196.

Haller, M.J., Lech, R.R., Martínez, O., Meister, C.M., Poma, S. and Viera, R. 2010. 'Hoja Geológica 4372-III/IV, Trevelin, provincia del Chubut', *Instituto de Geología y Recursos Minerales, Servicio Geológico Minero Argentino* Boletín 322, 86 pp.

Hughes, E. 2023. *Estudios geomorfológicos y paleoclimáticos del Cuaternario del Craig Cŵts, Patagonides, Chubut*. Tesina de grado, Universidad Nacional de La Plata, Argentina.

Inventario Nacional de Glaciares. 2018. *Informe de la Cuenca del río Chubut*. IANIGLA-CONICET, Ministerio de Ambiente y Desarrollo Sustentable de la Nación, Buenos Aires, 51 pp.

Karte, J. and Liedtke, H. 1981. 'The theoretical and practical definition of the term Periglacial in the geographical and geological meaning' *Biuletyn Periglacjalny* 28, pp. 123–135.

Massaferro, G. 1998. *Estratigrafía, petrología y alteración hidrotermal en el cerro Cuche*. Departamento Futaleufú. Chubut. Tesis Doctoral Facultad de Ciencias Exactas y Naturales. Universidad de Buenos Aires. 147 pp.

Mercer, J.H. 1985. 'Las variaciones glaciares del antiguo Cenozoico en Sudamérica, al sud del Ecuador'. *Acta Geocriogénica* 3, pp. 86–105.

Reato, A., Carol E. and Borzi, G. 2023. 'Hydrochemical and isotopic composition of periglacial watersheds in Northern Patagonian Andes'. *Journal of South American Earth Sciences* 123(5). Available at: https://doi.org/10.1016/j.jsames.2023.104204.

Ruiz, L. and Trombotto Liaudat, D. 2012a. 'Glaciares de escombros fósiles en el Cordón Leleque, Noroeste del Chubut: significado paleoclimático y paleogeográfico'. *Revista de la Asociación Geológica Argentina* 69(3), pp. 418–443.

Ruiz, L. and Trombotto Liaudat, D., 2012b. 'Mountain permafrost distribution in the Andes of Chubut (Argentina) based on a statistical model'. *10th International Permafrost Conference*. Salekhard, Yamal-Nenets Russia.

Tapia Baldis, C. and Trombotto Liaudat, D. 2015. 'Cinturones altitudinales criogénicos en la cuenca del río Bramadero, San Juan, Argentina', *Acta Geológica Lilloana* 27(2), pp. 146–158.

Trombotto, D., Buk, E. and Hernández, J. 1999. 'Rock glaciers in the Southern Central Andes (appr. 33° S.L.), Mendoza, Argentina: a review'. *Bamberger Geographische Schriften* 19, pp.145–173.

Trombotto Liaudat, D. 2021. *Adluniad o'r ddaearyddiaeth gyda thoponymy gwreiddiol o'r gogledd orllewin Chubut, Patagonia yn ôl gwahanol wladychwyr ac ysgrifenwyr Cymraeg eu hiaith yn 19eg a'r 20fed ganrif (anghyhoeddedyg)*. (Reconstruction of the geography with original toponymy of the northwest of Chubut, Patagonia according to different settlers and Welsh-speaking writers of the 19th and 20th centuries (unpublished)).

Turner, J.C. 1982. 'Descripción geológica de la Hoja 44c, Tecka'. *Servicio Geológico Nacional*, Boletín N 180, Buenos Aires.

Washburn, A.L., 1979. *Geocryology. A Survey of Periglacial Processes and Environments*. Norwich, UK: Edward Arnold Ltd., 406 pp.

Embankment evolution of a gravel road on permafrost terrain five years after construction: The Inuvik-Tuktoyaktuk Highway

Jennifer Kayley Humphries[1], Jurjen van der Sluijs[2], Peter D. Morse[3], & Steven V. Kokelj[4]

[1]*Aurora Research Institute, Aurora College, Inuvik, Northwest Territories, Canada*

[2]*NWT Centre for Geomatics, Government of Northwest Territories, Yellowknife, Northwest Territories, Canada*

[3]*Geological Survey of Canada, Natural Resources Canada, Ottawa, Ontario, Canada*

[4]*Northwest Territories Geological Survey, Government of Northwest Territories, Yellowknife, Northwest Territories, Canada*

ABSTRACT

The Inuvik-Tuktoyaktuk Highway (ITH) is a 137-km gravel road constructed during winters 2014–17 using frozen materials from seven borrow sources for a fill-only embankment designed to protect underlying permafrost. Road-surface settlement has occurred with active layer development and consolidation, compounded by right-of-way edge effects. To explore the evolution of a gravel road embankment on permafrost five years after construction we: 1) examine active layer development in the road and undisturbed terrain; 2) assess embankment thicknesses by differencing 2021 Lidar elevations with the 2011 pre-construction terrain; and 3) summarize field observations of underlying ice-wedge thaw and remotely-sensed rates of road-surface subsidence. In 2021, embankment centerline thaw depths approximated using ground temperature data were estimated to range from 2.3 to 3.7 m, which exceeded seasonal thaw depths in the adjacent tundra by 5-fold. The Lidar-derived embankment thicknesses in 2021 were less than 1.5 m for about 58% of the road length, suggesting that the embankment may be thawed by the end of summer for approximately half of the road length. Ice-wedge subsidence recorded at 57 locations, was associated with thin embankments and more frequent in the northern half of the corridor, excluding the last 25 km where the ITH was constructed on a pre-existing borrow pit access road that likely thawed near-surface permafrost before ITH construction. Estimated road surface subsidence from the period August 2019 to August 2021 supports these patterns. The findings demonstrate the value of systematic collection and analyses of monitoring data on road-permafrost interactions to inform design and maintenance that maximizes safety and performance.

1 INTRODUCTION

The Inuvik-Tuktoyaktuk Highway (ITH) connects Tuktoyaktuk, NWT on the Arctic Coast with Inuvik, NWT, and the rest of the National Highway System (Figure 1). Construction of the 137 km-long highway began in 2014 and it was officially opened on November 15, 2017. The road traverses complex, ice-rich permafrost terrain (Rampton 1988). To minimize ground disturbance and preserve underlying permafrost the highway was designed as a fill-only embankment constructed with frozen granular materials in winter. Construction of the highway sourced materials from seven borrow pits along the route. Materials were of variable quality, composed of unconsolidated silt, sand, and gravel sediment with significant ice content (Castagner et al. 2022). It was expected that the roadbed would settle (consolidate) in the first several years following construction, requiring maintenance efforts during this time.

Road design accounted for variations in the terrain and ground ice conditions and established a minimum thickness necessary for various terrain types to protect the underlying permafrost (Grozic and Zhang 2018). Degradation of permafrost occurs when seasonal thaw is greater than the combined thickness of the embankment and pre-construction active layer. Under thick embankments and with favorable climate conditions, permafrost may aggrade into the embankment. Informed by geotechnical investigations and ground-thermal data collected along the proposed alignment, thermal analyses were undertaken to estimate the maximum thaw depth into the road embankment under various ground and climate conditions. 2-D analyses were performed to assess temperature distributions for selected road and embankment geometries (Grozic and Zhang 2018). Minimum road height was determined to be 1.7 to 2.0 m of embankment material depending on the terrain, plus 200 mm of surface gravel (EGT Northwind 2013). Construction of the road began from the communities of Inuvik and Tuktoyaktuk and progressed towards the middle. Due to budgetary constraints, the decision was made to reduce the quantity of material for the project and reduce the embankment height for the 56 km of the road (km 20 to 76) that had not yet been constructed by the final year (CBC News 2016). The minimum embankment height was reduced to 1.2 m for the portions of the road between km 20 to 76 that were considered favorable low-risk terrain. Grozic and Zhang (2018) provided an overview of ITH construction and thaw depth development one season after road opening and described some reasons why thaw depths in 2017 were greater than those from the pre-design geothermal analysis, including thaw-consolidation of the road embankment and uncharacteristically warm summer temperatures. In conjunction with continued climate warming, variable snow accumulation, and challenges with drainage and ponding

https://doi.org/10.52381/ICOP2024.173.1

Figure 1. ITH right of way and road surface disturbances. (a) km 100: A linear depression and sinkhole caused by ice wedge thaw and surface subsidence. (b) km 46: An aerial view of ice wedge subsidence beneath the highway embankment, with the thin arrows indicating degraded troughs and thick arrows indicating degraded troughs with ponds at the embankment edge. (c) km 106: Ponding, embankment sloughing, degrading ice wedges, and a heaved mat of organic materials from a large icing and frost blister that developed in the winter 2020/21. (d) km 94: Ice wedges beneath the road expressed as subtle linear depressions, indicated by grey dashed lines, and associated degradation and ponding of ice wedges adjacent to the road. Photos by GNWT – Jurjen van der Sluijs, August 2022 (a), Aurora College – Celtie Ferguson, September 2023 (b), and June 2021 (c), and Aurora College – Jen Humphries, September 2023 (d).

along the embankment edge, the thermal and physical conditions characterizing the ITH embankment can be expected to continue evolving with implications for road performance and maintenance (Figure 1).

Collaboration of government and community partners, and investment in local monitoring capacity have enabled the establishment of an ITH thermistor network, the completion of post-construction airborne Lidar and drone topographic surveys (van der Sluijs et al. 2018, 2023; Ensom et al. 2020), and the development of a basic field survey to track road conditions and permafrost interactions.

This paper investigates the thermal and physical characteristics of the ITH embankment five years after construction and summarizes some indicators of permafrost thaw beneath the embankment. Specifically, we: 1) present thermal data to examine the range of thaw depths

measured in the road and undisturbed terrain; 2) assess 2021 embankment thicknesses by differencing 2021 Lidar elevations with the 2011 pre-construction terrain; 3) summarize settlement from 2019 to 2021 for embankments of different thicknesses; and 4) present a survey of road-surface subsidence correlating to ice-wedge thaw. These data and results support a discussion of the thermal and physical evolution of a gravel road over permafrost terrain 5 years after construction, and the value of sustained thermal and observational monitoring to inform future design and to support asset management and maintenance planning.

1.1 Study Area

The ITH forms a 137 km corridor across the forest-tundra transition zone and is underlain by ice-rich permafrost (Figure 2; Burn and Kokelj 2009). Cooler and drier conditions near the coast and warmer and wetter conditions inland are accompanied by the transition from shrub tundra to taiga forest (Lantz et al. 2013). A northward decrease in ground temperatures is associated with lower thaw season temperatures and thinner snow cover towards the coast (Kokelj et al. 2017).

Figure 2. The ITH corridor and locations of the 23 ground temperature monitoring sites. This includes 10 “Sentinel” sites in natural environments, and 13 “Embankment” sites distributed across treeline (dashed green line) from 14 to 81 km north on the ITH. NTGS 10 is a tundra hilltop at km 120.

The ITH corridor passes through two primary physiographic regions; the Anderson Plain in the south and the Tuktoyaktuk Coastlands in the north (Rampton 1988). The region was glaciated during the late Wisconsinan and surficial materials are predominantly fine-grained tills making up the rolling hills, and glaciolacustrine deposits overlain by peatlands in lower-lying areas. The southern part of the corridor is characterized by gently rolling terrain comprising moraine and colluvial deposits. The Tuktoyaktuk Coastlands to the north are a low-elevation till plain with many ice-cored hills composed of glaciofluvial sands (outwash plains and ice contact deposits) and broad lacustrine plains (Rampton 1988). The permafrost throughout the region is ice-rich, with near-surface aggradational ice common in the upper 2–3 m of ground (Kokelj and Burn 2003). Segregated intrusive ice is more common in the northern part of the corridor in association with ice contact and outwash deposits (Rampton 1988). Ice wedges occur in organic deposits throughout the region, but they become larger and more widespread north of the tall shrub transition zone, where lacustrine basins and polygonal peatlands become a dominant landscape element (Figure 1; Mackay 2000; Kokelj et al. 2014). This undulating and poorly-drained environment is also lake-rich, with a greater abundance of waterbodies in the northern half. A high density of lakes and ponds in conjunction with ice-rich and often undulating terrain produce complex landscapes for road design, with large volumes of fill required to avoid cutting slopes. This water-rich environment required the construction of 8 bridges and over 300 culverts to convey creeks, ephemeral streams, and slope runoff past the embankment. Materials were excavated in a frozen state and it was expected that the roadbed would consolidate as the active layer developed in the embankment through the first several years following construction.

Mean annual air temperature (MAAT) for the 1981–2010 period was -8.2°C and -10.1°C in Inuvik and Tuktoyaktuk, respectively (Environment Canada 2023). Over the same period, the mean total precipitation in Inuvik was 241 mm, of which 159 mm fell as snow, and 161 mm, with 103 mm as snow, in Tuktoyaktuk (Environment Canada 2023). Mean annual ground temperature (MAGT) near Inuvik ranges from 0°C to -4°C, and decreases to minimum temperatures of about -7°C near Tuktoyaktuk (Kokelj et al. 2017). Climate change is driving rapid increases in air and ground temperatures, with Burn and Kokelj (2009) reporting MAGT rising by about 2°C from to 1970s to 2010s in the Mackenzie Delta region. A wide range of permafrost temperatures and high ground ice content, particularly in the form of ice wedges and relict ice, along the ITH indicate permafrost is susceptible to thawing or degradation from climate warming, alterations to surface conditions such as snow or vegetation, and by way of disturbances such as ponding, thermal erosion, and construction (Kokelj et al. 2017; Burn et al. 2009). In the case of the ITH, rapid regional warming is occurring in concert with alterations to snow and vegetation conditions and disturbances introduced by the development of the highway.

2 METHODOLOGY

2.1 Permafrost

Ground temperature data were collected as part of two collaborative monitoring programs – the “Sentinel sites”, and the “ITH Embankment sites” (Ensom et al. 2020). The

Sentinel network comprises undisturbed hilltop, peatland, and riparian environments as well as borrow pits along the ITH corridor, while the ITH Embankment sites include boreholes through a range of embankment thicknesses from km 23 to 120 (Figure 2). The Sentinel sites analyzed in this paper (Table 1) are in undisturbed tundra ranging from 40 to 360 m away from the ITH. The 14 ITH Embankment sites were instrumented in 2017, each with a single ground temperature cable (GTC). One site, ITH 3, was destroyed early on so only 13 sites were used for the analysis (Table 1). Boreholes were drilled through the embankment and a minimum of 2 m into the native soil. GTCs were installed vertically through the embankment, and horizontally along a shallow trench to the shoulder of the road. Only the centreline data was used for this study. The total borehole depths of the GTCs ranged from 3.0 to 6.7 m. Each Embankment GTC consisted of 13 YSI #44007 thermistor beads and a Lakewood RX16 data logger. Full details on the installation of ITH Embankment sites and ground temperature data are available in Rudy et al. (2020a,b).

Table 1. Site IDs, associated project, generalized site type and occurrence of disturbance for each site.

Site IDs	Project	Site type	Disturbance
ITH 1,2, 4-14	ITH Embankment	Embankment	Disturbed
NTGS 1-10	Sentinel	Tundra	Undisturbed

* ITH 2 and 3 were destroyed, but ITH 2 had a record of <2 years
* NTGS 6 only has a shallow instrument (1.5 m), and NTGS 10 was installed to a depth of 13.5 m

As part of the Sentinel project in 2017, 16 sites were originally instrumented (NTGS 1–13, 15–17), each with a deep and shallow GTC. Only data from NTGS 1–10 were used in this study as they represent conditions in undisturbed terrain; NTGS 11–13 and 15–17 represent disturbed terrain in borrow pits, and adjacent to a thaw slump. The deep boreholes were drilled to a depth of either 10 or 20 m and were instrumented with five or six GeoPrecision PT1000 sensors and an M-Log5W data logger. The shallow GTCs were installed within 5 m of the deep GTC to a depth of 1.5 m, and were instrumented with four thermistors (Onset TMC6-HD) at 0.2, 0.5, 1.0 and 1.5 m below the surface and a four-channel HOBO U12-008 data logger. Full details of the installation and the first year of data collection at the Sentinel sites are available in Rudy et al. (2020c,d).

In total, data from 23 sites were analyzed; 13 Embankment sites with one GTC, and 10 Sentinel sites with paired deep and shallow GTCs. Daily average ground temperatures were used for examining the ground thermal regime at the 23 sites. To use the available data record, years were defined as 365-day periods beginning on October 16, 2017 and ending on October 15, 2022 (e.g., 2017–18 year covers from October 16, 2017 to October 15, 2018, and the 2021–22 year includes October 16, 2021 to October 15, 2022). The daily maximum, minimum, and average ground temperatures were calculated for each year. If there were less than 365 daily temperature values, the values were manually added or discarded. Maximum thaw depth is the depth of maximum penetration of the 0°C isotherm (Burn 1998). In a ground temperature envelope, it is the maximum depth at which the maximum daily temperature rises above 0°C. At each site, the maximum thaw depth was approximated for each year by determining where the linearly interpolated line between two thermistor depths crossed the 0°C isotherm. Thermistor depths in the embankments are reported relative to the road surface at the time of installation in 2017. It is not known how much the embankment has settled in the 5 years from construction at thermistor locations, or how operation and maintenance activities have changed the thickness of the material cover, both of which may have impacted the relative position of the GTCs.

2.2 Road Elevation and Hazards

Airborne Light Detection and Ranging (Lidar) and photogrammetry data provided baseline elevation datasets. Lidar-derived DEMs (1-m spatial resolution) for August 2011 and August 2021 were used to generate a differencing product (DEM of Difference; DOD) after accounting for vertical datum differences. More details on the Lidar data and DOD methodology are available in van der Sluijs et al. (2018). The DOD, characterizing embankment thickness, was sampled every 100 m for the entire length of the road for graphing and analysis. Photogrammetry-derived DEMs collected in August 2019 by long-endurance drone for most of the highway (km 0 to km 127; van der Sluijs et al. 2023), and by Lidar in 2021 were used to determine road-surface subsidence between 2019 and 2021 at the same 100-m sampling interval. Here elevations were differenced to obtain 2-year subsidence estimates summarized by embankment thickness class (< 0.5 m, 0.5–1.5 m, > 1.5 m), after corrections were made for any systematic DEM offsets between the two DEMs at locations away from the road surface.

To gather systematic spatial information on permafrost-related road hazards, a digital field form hosted on ESRI Survey123 was developed. The ITH was surveyed in September 2022. The survey form collected three main pieces of information for each hazard: location (coordinates), position relative to the road (on the road or right of way), and type of hazard. The main hazards were: cracking, potholes, culvert issues, washboard, subsidence, ponding, and ice wedge degradation. The form was intended to gather information on the prevalence and location of permafrost-related road hazards, and not as a comprehensive inventory of road hazards and performance issues.

3 RESULTS

3.1 Permafrost temperatures

Ground temperature envelopes show that embankment sites have a much greater near-surface seasonal temperature variation than undisturbed tundra (Figure 3), due to the contrasting material properties and ground surface conditions (vegetation and snow) between the road embankment and natural tundra environment. In undisturbed tundra, minimum winter temperatures at 1.0 m depth ranged from -9.0°C to -16.6°C in 2021–22. At comparable depths below the centreline of the snow-free

granular embankment surface (0.9 to 1.1 m), minimum temperatures were much lower, ranging from -24.4 °C to -30.5 °C over the same period. The embankment also experienced much higher maximum summer temperatures, ranging from 11.4 °C to 22.1 °C between 0.9 and 1.1 m depth, whereas maximum temperatures at 1.0 m in natural terrain ranged from -0.9 °C to 0.1 °C. The strong connection between air and road surface temperatures is reflected in high freezing and thawing n-factors (Stockton et al. 2024). As a result of these distinct ground thermal conditions, active layer thicknesses in the roadbed were more than 4 times greater than in the adjacent tundra, with medians of 2.9 m and 0.7 m, respectively (Figure 3; Table 2). In the top 5 m of ground, winter minimum temperatures in tundra and the embankment were lower in 2021–22 than in 2017–18. Maximum temperatures were similar between the two years of record at tundra sites, but at embankment sites indicate the maximum depth of thaw was greater in 2021–2022. The most significant implication of the large embankment thaw depths is the potential degradation of permafrost underlying the road.

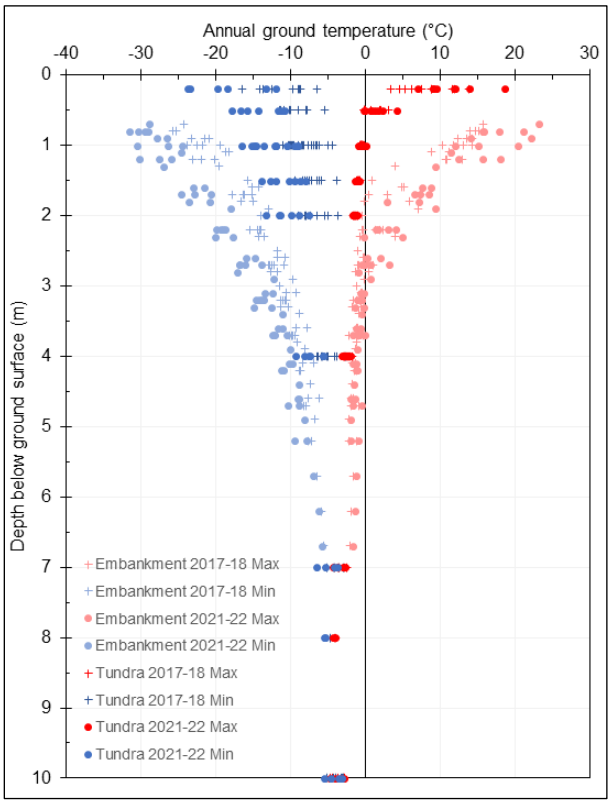

Figure 3. Ground temperature envelopes for 2017–18 and 2021–22, showing maximum and minimum daily temperatures with depth. Shaded colours are the embankment sites (ITH 1–2, 4–14), and solid colours are the tundra sites (NTGS 1–10). Depths for embankment sites are relative to the road surface at the time of installation in March 2017.

There is an inverse relationship between embankment thickness and thawing of the underlying native ground inferred from the temperature data at the 10 ITH boreholes (Figure 4). Assuming (1) the maximum active layer thickness in the original terrain that the highway was built over was between 0.5 and 1.0 m (Table 2), and (2) considering the thermistor depths relative to the original ground surface, we can estimate whether permafrost has aggraded or degraded under different embankment thicknesses (Figure 4). Maximum thaw depths relative to the 2017 embankment thicknesses at the 13 sites suggests that in all but one deep-fill embankment site, thaw depths in 2022 reach below the original ground surface. This is confirmed by the shallowest thermistor in native soils beneath the embankment which rise above 0 by end of summer 2022 for 10 out of 12 sites with available data (Table 2). The thickest embankment (4.6 m), and the greatest thaw depth (3.7 m; Table 2) were found at ITH 10; it was also the only site where thaw depth was maintained within the embankment materials above the original ground surface (Figure 4). At 7 sites with embankments between 1.5 and 2.7 m maximum thaw depths were estimated to be within the active layer of the preconstruction terrain (Figure 4). At 4 sites with embankment thicknesses of less than 1.5 m, the thaw depths exceed the thickness of the road embankment and the original active layer resulting in some permafrost degradation.

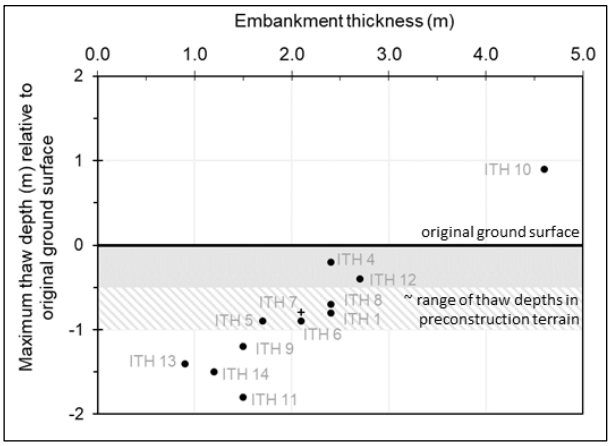

Figure 4. Estimated thaw depths at embankment sites relative to the original ground surface (i.e., native ground) against constructed embankment fill thickness in 2017. The grey box represents the preconstruction active layer zone and the hatched area approximates the position of the permafrost table in preconstruction terrain. Black dots indicate thaw depths from 2021–22; + indicate data from 2020–21.

3.2 Road Condition

Consolidated centerline embankment thickness estimated by differencing preconstruction and August 2021 Lidar, sampled at 100 m intervals, suggests that about 42% of the ITH embankment is > 1.5 m thick (Figure 5a). Although numerous deep fills occur along the highway length, the greatest abundance of thick embankments are between km 0 and km 20, and between km 105 and about km 120—the ends of the highway that were constructed early on in the project using the original design heights (see section 1), and where deep fills were required to negotiate complex

topography (Figure 5b). The DOD product suggests that in August 2021, 58% of the highway had a thickness of less than 1.5 m, and 16% had a thickness of less than 0.5 m. Based on maximum thaw depths inferred from embankment thermistor data (Table 2), it can be conservatively estimated ground beneath embankments less than 1.5 m thick thaws annually, and that the original permafrost has begun to thaw beneath embankments less than 0.5 m thick.

Table 2. Mean annual ground temperature (MAGT) near 1 m depth, estimated active layer thickness, and an indication of whether the uppermost thermistor below the embankment (native ground) thawed at sites along the ITH 2021-22.

Site	Thickness (m)	km	MAGT (°C)	MAGT Depth (m)	Active layer (m)	Embankment thawed (Y/N)
ITH 1	2.4	23	−5.1	0.9	3.1	Y
ITH 2	0.9	28	—	0.9	—	—
ITH 4	2.4	32	−6.4	0.8	2.6	Y
ITH 5	1.7	35	−6.0	1.0	2.6	Y
ITH 6	2.1	43	−6.1	0.9	3.0	Y
ITH 7	2.1	44	−5.8*	1.1	2.9*	Y*
ITH 8	2.4	47	−6.0	1.1	3.1	Y
ITH 9	1.5	51	−5.9	1.0	2.7	Y
ITH 10	4.6	57	−5.7	1.0	3.7	N
ITH 11	1.5	60	−5.6	1.0	3.3	Y
ITH 12	2.7	65	−6.2	0.8	3.1	N**
ITH 13	0.9	69	−6.0	0.8	2.3	Y
ITH 14	1.2	72	−6.3	0.8	2.7	Y
Embankment					**2.9**	
NTGS 1		14	−4.4*	1.0	0.8	
NTGS 2		14	−3.7	1.0	0.9	
NTGS 3		14	−3.9	1.0	0.5	
NTGS 4		42	−5.3*	1.0	0.5	
NTGS 5		42	−5.6	1.0	0.9	
NTGS 6		43	−4.3*	1.0	0.5	
NTGS 7		82	−4.0	1.0	1.0	
NTGS 8		81	−6.0	1.0	0.8	
NTGS 9		80	−4.5	1.0	0.7	
NTGS 10		120	−4.6*	1.0	0.8	
Tundra					**0.7**	

* data from 2020-21

** Thermistors in native soils range from 0.1 to 0.6 m depth. At ITH 12 thermistor is at 0.5 m depth.

An observational survey of thaw-induced hazards on and adjacent to the ITH was conducted in September 2022. The survey identified 57 locations where roadbed subsidence indicated the degradation of an underlying ice wedge (Figures 2a,b,d, and 5). Most of these occurrences were north of km 40, and were clustered on tundra uplands between Trail Valley and Hans Creeks (km 40 to km 55)—where the embankment was constructed to a reduced height—and in low-lying lacustrine plains with extensive polygonal peatlands between about km 80 and km 115. Although ice wedges are large and abundant near Tuktoyaktuk, there was only one observation of ice-wedge thaw directly affecting the northernmost portion of the ITH, constructed overtop of the pit 177 access road established in 2013. Within the context of these regional patterns, the highest density of ice-wedge subsidence expressed at the road surface (0.7 km^{-1}) was associated with embankments < 0.5 m thickness, and the lowest density (0.14 km^{-1}) was associated with embankments greater than 1.5 m thick.

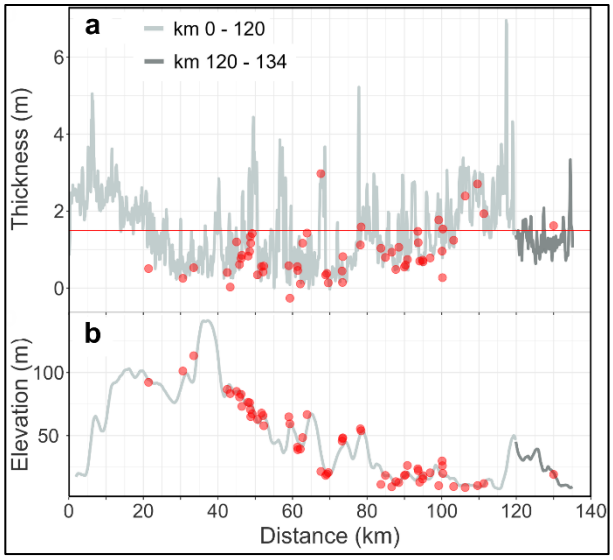

Figure 5. Longitudinal profiles along the ITH. (a) Profile of estimated embankment thickness in August 2021, and locations with evidence of ice-wedge thaw (red circles) in September 2022. The red horizontal line indicates an embankment thickness of 1.5 m. (b) Profile of terrain elevation along the road corridor, and evidence of ice-wedge thaw (red circles). Estimated embankment thicknesses were reported at 100 m intervals. The dark grey profile is the section of ITH constructed overtop of the source 177 access road.

Estimated road surface subsidence from the period August 2019 to August 2021 corroborates these patterns. Figure 6a shows that the thinnest embankments (< 0.5 m) experienced the greatest amounts of subsidence between 2019 and 2021, and those greater than 1.5 m thickness experienced little to no net elevation change (Figure 6). This pattern, in conjunction with evidence of ice-wedge thaw subsidence that was often associated with < 0.5 m embankments, supports the idea that ice-rich permafrost is thawing beneath the thinnest embankments (Figure 5), and that permafrost has either not thawed, or aggraded, beneath embankments that remain greater than 1.5 m thick. In stark contrast, net surface subsidence was not detected by this analysis for the northernmost section of the ITH, constructed over the pit 177 access road, regardless of embankment thickness.

4 Discussion

The estimated maximum thaw depths beneath the road surface (13 sites) 5 years following the completion of construction (Table 2) were on average 2.2 m greater than in undisturbed tundra (10 sites). The inferred active layer thicknesses in the road embankment estimated relative to the 2017 road surface ranged from 2.3 to 3.7 m. However, thaw consolidation and road maintenance activities such as grading, could decrease the road surface elevation, reducing the thickness of overburden between the surface and thermistors at depth resulting in an overestimation of true active layer thickness. Regardless, thermistors within

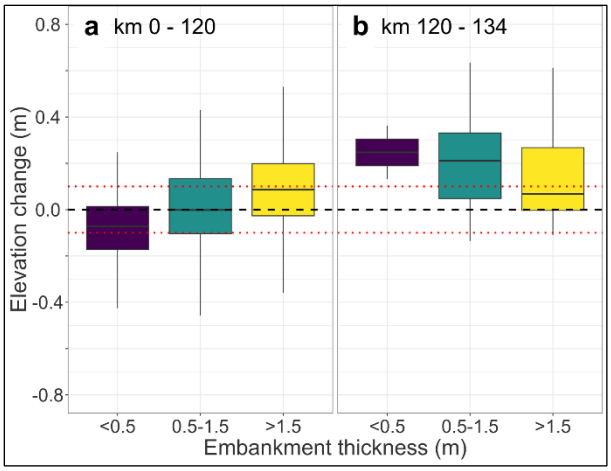

Figure 6. Box and whisker plots showing the net change in elevation of the road surface edge between August 2019 and August 2021, sampled at 100 m intervals along the ITH. Relative change stratified by embankment thickness is shown for (a) km 0 to km 120, and (b) km 120 to km 134. Red dashed line represents estimated level of uncertainty (10 cm) inferred from averaged standard deviation of elevations between the two DEMs at locations away from the road surface.

native soils below the embankment confirm that the embankment thaws at all sites with an original embankment thickness of less than 2.4 m (Table 2).

This preliminary examination of the embankment thermal data highlights the importance of monitoring thermistor cables and analyzing the data following construction because they can inform the revision of monitoring methods, and following more robust thermal analysis, enable engineers, designers, and planners to refine the assumptions and parameterization of thermal models to enhance the design of future roads. In particular, opportunities to examine thermal data and road performance may reinforce the value of conservative modeling estimates and design parameters in the context of warming air temperatures, and changing precipitation patterns. Furthermore, systematic collection of infrastructure conditions and geohazards, both on the road and within the right-of-way can guide maintenance plans.

Embankment thickness from 2021 Lidar showed 58% of the highway embankment is less than 1.5 m thick. Thin embankments are especially common between km 20 and km 100, in part due to the reduction of minimum embankment heights below design specifications during the later stages of construction. Patterns of change in road surface elevations and observations of ice-wedge subsidence suggest that permafrost beneath the thinnest embankments has begun to thaw.

Road settlement is the combined product of material quality, its ice content, level of compaction, surface grading, and the interactions of snow and water accumulation along the edge of the embankments. Once thaw exceeds embankment thickness and reaches the underlying permafrost, degradation of ice-rich ground can further increase settlement. The observations reported in this study reinforce the need for a conservative design with thick embankments, and the potential permafros implications of deviating from design. Construction of the most northerly portion of the ITH was staged by building over the pit 177 access road, which appears to have benefited the performance of the road. The pit 177 access road likely pre-thawed underlying ice-rich ground resulting in lower rates of settlement and little evidence of underlying ice-wedge thaw. Given the observations in this study that indicate the likely thawing of ice-rich permafrost underlying the ITH embankment, the complex interactions between changing right-of-way conditions, and a rapidly warming climate, systematic thermal and observational monitoring, and resources for data analysis to inform maintenance and mitigation measures are more important than ever.

5 Conclusions

Examining the thermal and physical characteristics of the embankment, five years following the construction of the Inuvik-Tuktoyaktuk Highway (ITH) several conclusions can be drawn:

(1) Estimated thaw depths in the embankment are 2.3 to 3.7 m at 13 monitoring sites and exceed embankment thicknesses at 12 of the 13 sites. Temperatures in native ground beneath the embankment confirm that the embankment thawed by end of summer at all but the two thickest fill sites;

(2) Based on a conservative approximation of embankment thaw depths and embankment thicknesses in 2021 it is estimated that the ITH embankment thaws by the end of summer along about 58% of its length;

(3) The pattern of road surface settlement between 2019 and 2021, and observations of road surface subsidence caused by ice wedge thaw indicate that permafrost beneath the thinnest embankments has begun to thaw; and

(4) The results indicate the value of systematically collecting and analyzing monitoring data along infrastructure corridors. The monitoring results can be used to assess road performance and inform future design of roads constructed over ice-rich permafrost.

6 Acknowledgements

This research has been supported by: Transport Canada's National Trade Corridors Fund (NTCF); Aurora Research Institute (ARI), Aurora College; Northwest Territories Geological Survey (NTGS), Government of Northwest Territories; NWT Centre for Geomatics, Government of Northwest Territories; Geological Survey of Canada (GSC); Inuvialuit Land Administration and Department of Infrastructure, Government of Northwest Territories. The authors are grateful to Kelly Kamo-McHugh and Richard Blake for collecting and providing ground temperature data, as well as staff from the NTGS, GSC, ARI, and Wilfrid Laurier University who have assisted with data collection

over the years. Helpful discussion with Ed Grozic and comments from two anonymous reviewers greatly improved the quality of this manuscript.

7 REFERENCES

Burn, C.R. and Kokelj, S.V. 2009. 'The environment and permafrost of the Mackenzie Delta area', *Permafrost and Periglacial Processes* 20(2), pp. 83–105. doi:10.1002/ppp.655.

Burn, C.R., Mackay, J.R., and Kokelj, S.V. 2009. 'The thermal regime of permafrost and its susceptibility to degradation in upland terrain near Inuvik, NWT', *Permafrost and Periglacial Processes* 20, pp. 221–227. doi: 10.1002/ppp.649.

Castagner, A., Kokelj, S.V., and Gruber, S. 2022. 'A Cryostratigraphic Synthesis of Inuvik to Tuktoyaktuk Highway Corridor Geotechnical Boreholes (2012–2017)', NWT Open Report 2022-002, 12 pp. + appendix.

CBC News 2016. 'Remaining Inuvik-Tuk highway to use less gravel to save money'. *CBC News* January 19, 2016. Available at: https://www.cbc.ca/news/canada/north/inuvik-tuktoyaktuk-highway-gravel-1.3411200.

EGT Northwind Ltd., Kavik-Stantec Inc., and Kiggiak-EBA Consulting Ltd. [EGT Northwind] 2013. *Design Report–Inuvik to Tuktoyaktuk Highway: 100% Geometric and Structures Design*. Prepared for Department of Transportation, Government of Northwest Territories, 299 pp.

Ensom, T.E., Kokelj, S.V., Morse, P.D., and Kamo McHugh K. 2020. 'Permafrost Ground Temperature Data Synthesis: 2013-2019 Inuvik-Tuktoyaktuk Highway region, Northwest Territories', *Northwest Territories Geological Survey* NWT Open Report 2019-020, 13 pp. + appendix.

Environment Canada 2023. *Canadian Climate Normal 1981–2010 station data*. Available at: https://climate.weather.gc.ca/climate_normals/index_e.html [Accessed: 1 August 2023].

Grozic, E. and Zhang, G. 2018. 'Inuvik to Tuktoyaktuk Highway Road Embankment Constructed on Ice-Rich Permafrost Terrain', in *Proceedings of GeoEdmonton 2018*, Edmonton, Alberta, Canada. Available at: https://members.cgs.ca/conferences/GeoEdmonton/index.html.

Kokelj, S.V. and Burn, C.R. 2003. 'Ground ice and soluble cations in near-surface permafrost, Inuvik, Northwest Territories', Canada', *Permafrost and Periglacial Processes* 14, pp. 275–289. doi:10.1002/ppp.458.

Kokelj, S.V., Lantz, T.C., Wolfe, S.A., Kanigan, J.C., Morse, P.D., Coutts, R., Molina-Giraldo, N., and Burn, C.R. 2014. 'Distribution and activity of ice wedges across the forest-tundra transition, western Arctic Canada', *Journal of Geophysical Research Earth Surface* 119, pp. 2032–2047. doi:10.1002/2014JF003085.

Kokelj, S.V., Palmer, M.J., Lantz, T.C., and Burn, C.R. 2017. 'Ground Temperatures and Permafrost Warming from Forest to Tundra, Tuktoyaktuk Coastlands and Anderson Plain, NWT, Canada', *Permafrost and Periglacial Processes* 28, pp. 543–551. doi:10.1002/ppp.1934.

Lantz T.C., Marsh, P., and Kokelj S.V. 2013. 'Recent shrub proliferation in the Mackenzie Delta Uplands and microclimatic implications', *Ecosystems* 16, pp. 47–59. doi:10.1007/s10021-012-9595-2.

Mackay, J.R. 2000. 'Thermally induced movements in ice-wedge polygons, western arctic coast: a long-term study', *Géographie physique et Quaternaire* 54, pp. 41–68. doi: 10.7202/004846ar.

Rampton, V.N. 1988. 'Quaternary Geology of the Tuktoyaktuk Coastlands, Northwest Territories', *Geological Survey of Canada* Memoir 423, 98 pp. doi:10.4095/126937.

Rudy, A.C.A., Kokelj, S.V., and Ensom, T. 2020a. 'Permafrost Geotechnical Report: Inuvik to Tuktoyaktuk Highway Embankment Boreholes', *Northwest Territories Geological Survey* NWT Open Report 2019-011, 7 pp. + geotechnical data + appendix.

Rudy, A.C.A., Kokelj, S.V., and Ensom, T. 2020b. 'Permafrost Ground Temperature Report: Inuvik to Tuktoyaktuk Highway Embankment Sites', *Northwest Territories Geological Survey* NWT Open Report 2019-016, 8 pp. + ground temperature data + appendix.

Rudy, A.C.A., Kokelj, S.V., Morse, P.D., and Ensom, T. 2020c. 'Permafrost Geotechnical Report: Inuvik to Tuktoyaktuk Highway Sentinel Program Boreholes, Northwest Territories', *Northwest Territories Geological Survey* NWT Open Report 2019-008, 7 pp. + geotechnical data + appendix.

Rudy, A.C.A., Kokelj, S.V., Morse, P.D., and Ensom, T. 2020d. 'Permafrost Ground Temperature Report: Inuvik to Tuktoyaktuk Highway Sentinel sites', *Northwest Territories Geological Survey* NWT Open Report 2019-017, 8 pp. + ground temperature data + appendix.

van der Sluijs, J., Kokelj, S.V., Fraser, R.H., Tunnicliffe, J., Lacelle, D. 2018. 'Permafrost Terrain Dynamics and Infrastructure Impacts Revealed by UAV Photogrammetry and Thermal Imaging', *Remote Sensing* 10(11), 1734. doi:10.3390/rs10111734

van der Sluijs, J., Saiet, E., Bakelaar, C.N., Wentworth, A., Fraser, R.H. and Kokelj, S.V. 2023. 'Beyond visual-line-of-sight (BVLOS) drone operations for environmental and infrastructure monitoring: a case study in northwestern Canada', *Drone Systems and Applications* 11, pp. 1–15. doi:10.1139/dsa-2023-0012.

Modeling the implications of post-fire alternative successional trajectory for boreal carbon and permafrost dynamics in Interior Alaska

Elchin E. Jafarov[1], Valeria Briones[1], Aiza Kabeer[1], Brendan M. Rogers[1], Susan Natali[1], Hélène Genet[2], Ruth M. Rutter[2] & Tobey B. Carman[2]

[1]*Woodwell Climate Research Center, Falmouth, Massachusetts, United States*

[2]*Institute of Arctic Biology, University of Alaska Fairbanks, Fairbanks, Alaska, United States*

ABSTRACT

Spruce forests have dominated Interior Alaska for millennia, generally self-replacing after wildfires. However, contemporary climate change has been linked to an increase in fire severity and frequency, promoting alternative successional trajectories and conversion to permanent deciduous forests. Because wildfire is the primary recent disturbance in interior Alaska, intensifying fire regimes have the potential to convert evergreen to deciduous-dominated landscapes. Compared to evergreen forests, deciduous forests exhibit large differences in carbon and nitrogen storage and turnover. The absence of moss cover in deciduous forests is also associated with an increase in soil temperature and deepening of the active layer compared to evergreen forests, which provide a microclimate and biochemical setting conducive to thick moss development. It is therefore critical for biosphere models to represent the biochemical and structural differences associated with boreal evergreen and deciduous forests to represent the long-term implications of climate warming and increasing fires on successional trajectories, regional carbon balance, and permafrost dynamics. In this study, we use a biosphere model developed for high latitude ecosystems to conduct a sensitivity analysis to (1) investigate the capacity of biosphere models to represent the differences in ecosystem structure and functions characterizing spruce and birch forests, (2) evaluate the differences in responses of ecosystem carbon balance and permafrost dynamics to projected climate change between these two ecosystems, and (3) evaluate the important ecological processes driving carbon and permafrost dynamics at two neighboring experimental sites representing typical black spruce dominated and birch dominated mid-successional stands. Findings will further our understanding of the impact of Arctic warming on long-term permafrost dynamics, over the next several decades.

1 INTRODUCTION

Across much of Alaska and Canada, boreal forests are dominated primarily by a mix of deciduous and spruce forests (Calef et al. 2005). For Interior Alaska, spruce forests dominated the landscape for millennia and would self-replace following wildfires (Chapin et al. 2006). However, contemporary climate change is linked to an increase in fire severity (Turetsky et al. 2011), promoting alternative successional trajectories, and the establishment of deciduous forests (Johnstone et al. 2011). With wildfire being the primary disturbance in Interior Alaska, an increase in fire severity has the potential to shift evergreen to deciduous-dominated landscapes (Pastick et al. 2016). Field investigations revealed differences in carbon and nitrogen distribution and turnover between deciduous forests and evergreen forests (Melvin et al. 2015). The absence of moss cover in many deciduous forests leads to increased soil temperature and a deeper active layer compared to evergreen forests, where a thick moss layer thrives (Jean et al. 2018). The northern boreal region contains large carbon reserves and fire disturbances dominate the distribution of plant and soil carbon (Harden et al. 2000). Predicted increases in the area burned in the boreal forest and its interactions with vegetation distribution suggest significant feedback to the climate system and potentially substantial impacts on the carbon budget, with the potential to convert vast regions of forests from sinks to carbon sources (Dieleman et al. 2020; Kasischke et al. 1999; Van Wagner 1988; Flannigan and Van Wagner 1991). Although boreal forests act as a net carbon sink over long time periods, severe fire activity can disrupt the net carbon balance thus resulting in forests turning into net carbon sources (Harden et al., 2000, Mack *et al* 2021, Walker *et al* 2019).

Understanding how terrestrial ecosystems will respond to future climate change is challenging due to complex interactions among ecosystem structure and function, soil and permafrost processes, disturbance dynamics, and regional climate (Rupp et al. 2002). Additional research is needed to simulate realistic ecosystem responses to climate change accurately, especially to evaluate the sensitivity of boreal vegetation communities to these changes (Miquelajauregui et al. 2019).

Here, we investigate how interactions among forest soils, fire characteristics, and stand characteristics influence biogeochemical dynamics under varying fire return intervals. We use a biosphere model developed for high latitude ecosystems to (1) investigate the capacity of this biosphere model to represent the differences in ecosystem structure and functions characterizing spruce and birch forests and (2) evaluate the differences in responses of ecosystem carbon balance and permafrost dynamics to varying fire return intervals. Our study aims to highlight the key processes at stand and landscape scales that require further investigation to improve our ability to predict the future dynamics of Alaskan boreal forests under future change in climate.

https://doi.org/10.52381/ICOP2024.145.1

2 MATERIALS AND METHODS

2.1 Site Description

We use two sites at Murphy Dome, near Fairbanks, Alaska, that have measured vegetation and stock carbon and nitrogen data. The sites represent evergreen (black spruce) and deciduous plant functional types. The evergreen and deciduous plant functional types are members of the boreal forest community types MD1 and MD3 correspondingly, where MD stands for Murphy Dome. Throughout the paper MD1 will be referred to as the evergreen stand, while MD3 will be referred to as the deciduous stand. The community type in the DMV-DOS-TEM includes multiple plant functional types, where each plant functional type stores carbon and nitrogen in stems, leaves, and roots.

The study site of Murphy Dome is located within the Tanana Valley State Forest located outside of Fairbanks, Alaska (64°53′N, 148°23′W). In 1958, the Murphy Dome fire destroyed the sites, which covered an area of 8,930 hectares. As a result, the area has regrown with a uniformly aged upper layer consisting of paper birch trees and a patchy lower layer of white spruce trees (Sullivan et al. 2021). The two most common forest types, across interior Alaska, are made up of evergreen stands of black spruce and deciduous broadleaf forests. Within this region, roughly 39% of the area is made up of evergreen forest and 24% deciduous forest stands (Calef et al. 2005; Jean et al. 2020). The average organic layer thickness is roughly 16.4 cm at the black spruce site, and 7.6 cm at the birch site, which subsequently results in larger carbon (C) stocks of the organic layer within the black spruce site (4.8 kg C m^{-2}) compared to the birch (2.4 kg C m^{-2}) as reported by Melvin et al. (2015).

2.2 Model Description

The Terrestrial Ecosystem Model with Dynamic Vegetation and Dynamic Organic Soil Layers (DVM-DOS-TEM) is a process-based biosphere model designed to simulate biophysical and biogeochemical processes between the soil, the vegetation and the atmosphere. DVM-DOS-TEM v0.6.1 is the latest version of the Terrestrial Ecosystem Model (McGuire et al. 1992; Raich et al. 1991) that focuses on representing carbon and nitrogen cycles in high latitude ecosystems and how they are affected at monthly-to-centennial scales by climate, disturbances and biophysical processes such as soil thermal and hydrological dynamics (Yi et al. 2009; Zhuang et al. 2002), snow cover (Euskirchen et al. 2006) and vegetation (Euskirchen et al. 2016). DVM-DOS-TEM has been used extensively in arctic and boreal permafrost regions with applications to the soil environment (Yi et al. 2009; Zhuang et al. 2002; Zhuang et al. 2001), tundra vegetation dynamics (Euskirchen et al. 2016; Euskirchen et al. 2009), carbon storage (Genet et al. 2018; Lyu et al. 2018), ecological impacts of wildfire (Balshi et al. 2007; Genet et al. 2013; Yi et al. 2010) and feedback to climate (Euskirchen et al. 2016). The ecological processes represented in DVM-DOS-TEM include carbon and nitrogen dynamics for every plant functional type of the vegetation community and every layer of the soil column. Carbon and nitrogen dynamics are driven by climate, atmospheric chemistry, soil and canopy environment, and wildfire occurrence and severity. Carbon and nitrogen from the litterfall are divided into aboveground and belowground. Aboveground litterfall is assigned only to the top layer of the soil column, while belowground litterfall is assigned to different layers of the three soil horizons based on the fractional distribution of fine roots with depth.

Before conducting the historical simulations, a typical spin-up procedure was conducted for each site in which the model was driven by averaged modern forcings for that location and this process was repeated continuously until a dynamic equilibrium was achieved (i.e., constant pools and fluxes). The resulting modeled ecosystem state for each site then served as the starting point for the historical simulation. The DVM-DOS-TEM model inputs include annual time series of atmospheric CO^2 concentration, monthly mean air temperature, total precipitation, net incoming shortwave radiation, and vapor pressure (McGuire et al. 2016).

2.3 Model Simulations

We ran experimental site simulations at a single pixel, 1 km x 1 km resolution for both the black spruce and deciduous community types at Murphy Dome with soil drainage conditions set to well-drained to simulate upland soils at the site. Historical climate data (1901–2015) for use in DVM-DOS-TEM were extracted from the Climatic Research Unit time series version 4.0 (CRU TS4.0; Harris et al. 2014) downscaled at 1 km × 1 km spatial resolution on a monthly time step, prepared by the Scenario Network for Alaska Planning (https://uaf-snap.org/; Pastick et al. 2017).

To compare baseline site characteristics, we ran simulations at each site without the occurrence of fire, by turning the fire module (DSBM) off. This allows us to first assess stand characteristics at two semi-mature forest stands without the presence of fire as well as a baseline to compare our fire disturbance simulations. We used site data from Melvin et al. (2015), which took measurements from both aboveground stand characteristics and soil characterization at the black spruce and paper birch dominated stands throughout the period between 2012–13. We compared our baseline model outputs to those of Melvin et al. (2015) to validate our results as well as ensure the model was representing the key differences between the two successional stands. To compare the effects of increased fire frequency we ran simulations forced with a fire (DSB) module turned on, to compare the effects of varying fire return intervals (FRI) on stand components such as carbon stocks. We ran a total of 5 fire simulations with FRI ranging from 50–250 at 50-year increments under a moderate severity which equates to approximately 69% of the organic soil depth combusted (Yi et al 2010). The occurrence and severity of the fire during simulations was set up to simulate the Murphy Dome fire which occurred in 1958. A lower FRI corresponds to shorter time period between fires, while a larger FRI corresponds to a longer period of time between fire disturbance. Each simulation was run at the evergreen site to simulate the effects of fire on spruce dominants forest stands to assess how increased FRI effects stand characteristics especially if we are able to observe changes in plant composition. Each FRI was

simulated during the month of July and ran at a fire severity of 3 (moderate severity), and the entire pixel (1x1 km) was burned. We ran simulations consisting of a spin-up for 250 years, equilibrium for 6,000 years, and transient for 115 years, which represented the historical period of (1901–2015).

We focused on assessing a subset of model variables for both aboveground and belowground variables, e.g., soil carbon and nitrogen stocks grouped by layer (fibric, humic, mineral), vegetation carbon for the dominant tree species (spruce, birch) also grouped by plant compartment (leaf, stem), as well as emission from vegetation and soil which are only output when a fire has occurred. In addition, we looked at fire specific model outputs to assess the impacts of each FRI. Such variables are only produced after a fire has been simulated and includes emissions outputs including burned carbon from both the vegetation and soil to the atmosphere.

3 RESULTS

3.1 Baseline Comparisons

Baseline model outputs run without the occurrence of fire showed generally good agreement to site observations from (Melvin et al. 2015) and were able to capture major stand characteristic differences. The birch stand had aboveground carbon stocks (leaf, stem) at a total aboveground 13,033.26 g C-m2-yr compared to evergreen site at 2,271 g C m2 yr (Figure 1) compared to observed total aboveground C at 5308.92 and 2281.70 2,271 g C m2 yr at the deciduous and evergreen sites respectively. Similarly, the deciduous site exhibited higher stem nitrogen (N) stocks compared to the evergreen site, at 228.92 and 38.33 g N m2 yr respectively.

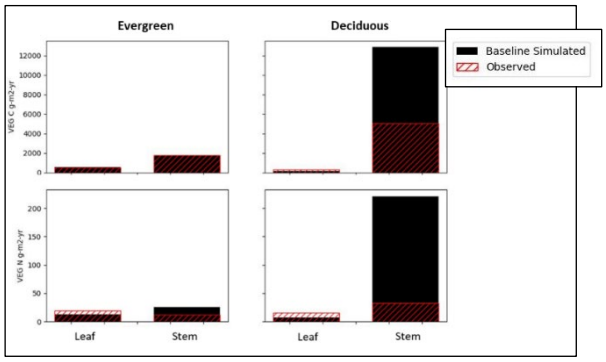

Figure 1. Comparison of simulated aboveground carbon and nitrogen stocks g m2yr at the spruce dominated (MD1) and deciduous birch dominated site (MD3) grouped by leaf and stem measured during 2012 to observations derived from Melvin et al. 2015.

Similarly, DVM-DOS-TEM was able to capture stand differences belowground. Model estimates of organic layer thickness (OLT) accurately simulated differences between evergreen and deciduous site. Our model estimated OLT at the evergreen site to be 18.3 cm while OLT at the deciduous site was 11.6 cm compared to observed OLT of 16.4 and 7.6 respectively, thus slightly overestimating for MD3. Deeper organic soils at the evergreen site also results in greater soil carbon stocks in the organic layer compared to that of soil carbon at the deciduous site as shown in Figure 2. While observed data show larger soil carbon stocks within the top 10 cm at the evergreen site than the deciduous, our baseline data show an opposite trend where we are overestimating soil carbon in the mineral layer at the deciduous site than the evergreen.

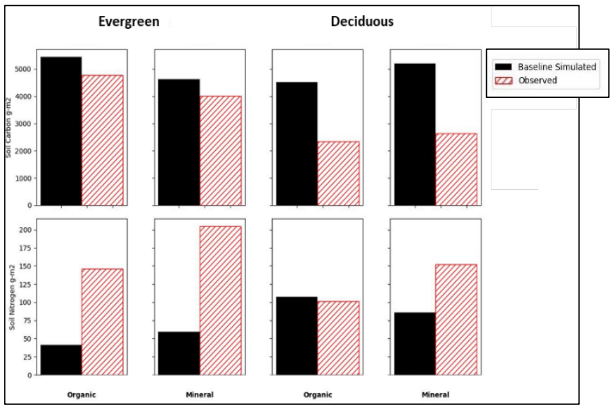

Figure 2. Soil carbon and nitrogen stocks for the Murphy Dome evergreen (MD1) and deciduous (MD3) sites. Soil carbon and nitrogen stocks are depicted for both the organic and mineral layers. Soil carbon and nitrogen were measured at the top 10 cm of the mineral layer for both sites and observations derived from Melvin et al. 2015.

A deeper OLT at the evergreen site results in slightly cooler soil temperatures at 10 cm depth particularly during the Fall and Spring shoulder months as shown in Figure 3, which the model was better able to capture at the evergreen site than at the deciduous. The baseline model run at MD3 shows an average soil temperature of -0.95 °C while observed average soil temperature is 0.95 °C during the study period at the 10 cm depth.

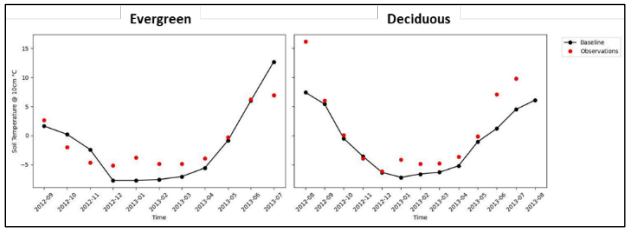

Figure 3. Soil temperature (°C) measured at 10 cm depth below soil surface for both sites at Murphy Dome: Spruce (MD1) and Deciduous (MD3) for baseline simulations and observations derived from Melvin et al. 2015. Average soil temperature at MD1 was -1.3 °C for the baseline run, and -1.25 °C for observations.

3.2 Fire Simulations

Simulated aboveground carbon stocks for simulations across varying FRI at the deciduous site shows a general increase in total aboveground biomass as FRI increases (Figure 4e). Looking at the change in carbon stocks per dominant plant functional type (PFT), we see a decrease in total aboveground biomass of evergreen trees at the shorten FRI of 50 years from baseline of 2171.12 to 1598.12 g C m2, with a switch to an increase in biomass from the baseline on FRI 100 to 2444.19 g C m2 (Figure 4a). A minimal decrease in the carbon stocks of deciduous trees (Figure 4c) also is apparent at FRIs 50 from baseline 346.47 to 284.65 g C m2 with a net increase on FRI 150–250 to 446.59 g C m2, showing more pronounced decrease in PFT evergreen trees with more frequent FRI compared to deciduous trees.

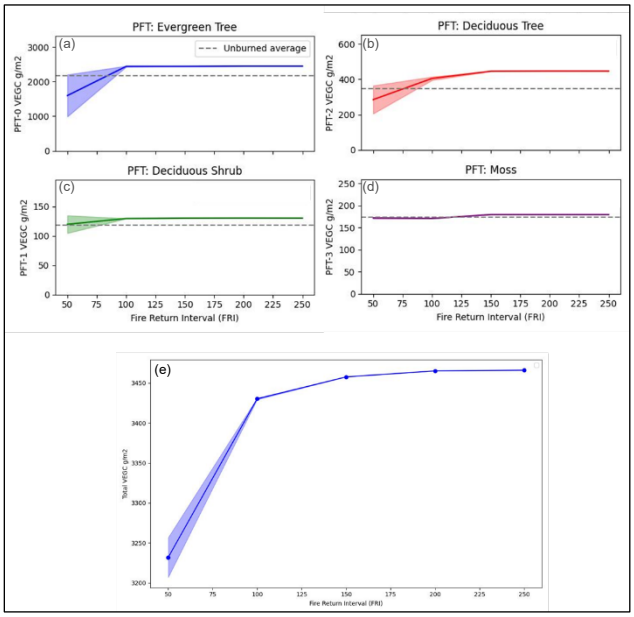

Figure 4. Comparison of the main plant function types found at spruce dominated evergreen site (MD1): (a) evergreen trees, (b) deciduous shrubs, (c) deciduous trees, and (d) moss and their respective aboveground vegetation stocks (g/m2) in relation to their baseline values (unburned, dotted lines) and varying fire return intervals (FRI) (e).

Similar to aboveground vegetation stocks, less frequent FRI results in an increase in total organic carbon (g m2 yr) for both organic layer and mineral soil carbon (Figure 5). Simulations with more frequent fire greatly reduce total organic carbon (TOC), with a decrease in TOC with shortening FRI to an average of 13,807.33 for FRI-50 with an increase in TOC starting at FRI-100 for both organic and mineral soil layers resulting in a TOC of 16261.21 g/m2 and a peak in TOC at FRI-150 before TOC begins to gradually plateau (Figure 5).

Simulations show that as the FRI becomes more frequent, fire emissions released from the soil matter increases until a threshold is reached where emissions begin to gradually decrease at FRI-150 (Figure 6). At FRI-50 carbon emissions from the soil averaged 327.89 g/m2 and carbon emissions from vegetation to the atmosphere averaged 856.78 g/m2. Both carbon emissions peaked at FRI-150 averaging 416.05 and 892.84 g/m2 for soil and vegetation to the atmosphere, respectively.

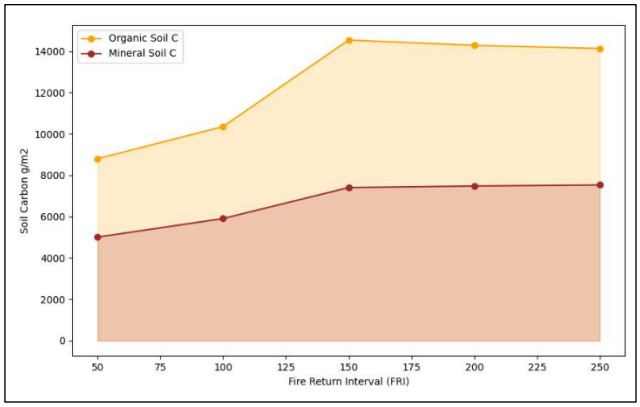

Figure 5: Relationship between soil carbon stocks (g/m2) broken up by organic and mineral layers for the spruce dominated evergreen site to variance in fire return interval (FRI).

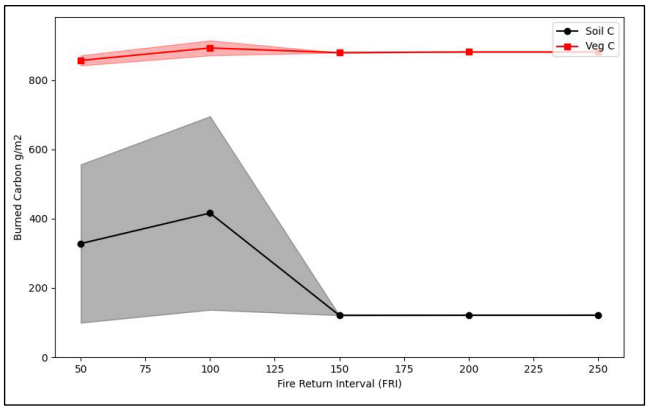

Figure 6 Change in carbon emissions from soil and vegetation burned compared across varying fire return intervals (FRI). The mean (solid lines) and standard deviation (shadow) are shown for each variable.

4 Discussion

Representing large-scale fire events in ecosystem models is critical because wildfires significantly impact ecosystem processes and carbon dynamics at landscape and regional scales (McKenzie et al. 1996; Kasischke et al. 1995; Alvarado et al. 1998). Based on our findings, the occurrence of fire disturbances play an important role in determining the abundance of different ecosystem types at a plant functional level, leading to distinct patterns and changes in carbon cycling across our sites (Rupp et al. 2000, 2002). Our results show that vegetation carbon of all dominant plant functional types in the black spruce dominant site decreased post-fire. In addition, we observe

a gradual increase in the total amount of vegetation carbon as the time between each fire occurrence increases, thus allowing more time for the vegetation community to recover post disturbance.

Our simulations suggest that changes to the frequency of fire occurrence can cause distinct changes to vegetation and soil carbon stocks, thus causing additional changes to stand characteristics of a semi-mature black spruce forest stand. Under the longer FRI of 250 years, our simulations showed an increase in total aboveground C for PFT evergreen trees at the evergreen site, deciduous trees, and an increase of moss. In comparison under the shorter FRI of 50 years, simulations showed an increase in total aboveground C for PFT evergreen trees at the evergreen site, and an increase in total aboveground C for PFT deciduous trees signifying a shift to greater biomass of deciduous trees under more frequent fire disturbance. The observed gradual increase in spruce evergreen plant functional types may be due to moderate burns which are allowing for a rapid regeneration of spruce (Kurkowski et al. 2008). These connections enable us to predict the potential shifts in landscape forest cover that could occur in response to increased severity or frequency of fires under future climate change scenarios (Gillett et al. 2004; Flannigan et al. 2005; Balshi et al. 2009).

The absence of moss can lead to warmer and drier soils, thus exposing areas underlain by permafrost to accelerated loss, contributing to a feedback of permafrost carbon loss to the atmosphere (Kasischke et al. 1995). By quantifying carbon and nutrient pools and examining potential shifts in their distribution, this research can contribute to improved predictions regarding the impact of changes in the wildfire regime on boreal ecosystems. However, it's important to acknowledge that uncertainties in model formulation and parameterization can significantly influence the results (Euskirchen et al. 2016; Genet et al. 2018). While our model validation suggests that DVM-DOS-TEM can generally simulate carbon stocks of boreal forest vegetation and soil dynamics, there remains substantial uncertainty in representing critical ecosystem processes in response to wildfires, such as changes in forest successions such as shifts in forest type from spruce dominated to deciduous, which is currently unrepresented in our model (Klupar et al. 2021; Parker et al. 2016).

Another finding is that the possibility of fire influencing changes in successional trajectories depends on landscape variables like site moisture. As a result, we should anticipate that the resilience of black spruce forests to climate and fire regime changes will vary across the landscape, and drier spruce forests might have the highest potential to transition into deciduous-dominated forests under future environmental changes.

5 Conclusions

Our study highlights the critical role of fire disturbances in shaping the composition and carbon dynamics of these ecosystems. Notably, it reveals that the frequency of fire occurrences can significantly impact vegetation and soil carbon stocks, influencing the recovery and composition of forest stands. The findings suggest that under certain conditions, prolonged fire return intervals may lead to an increase in evergreen tree abundance and a transition to deciduous-dominated forests. Moreover, the absence of moss in deciduous forests can have implications for soil temperature, permafrost dynamics, and carbon feedback to the atmosphere.

While our study enhances our understanding of boreal forest dynamics, it also underscores the complexities and uncertainties inherent in modeling such ecosystems. The need for further research to improve the accuracy of ecosystem models in predicting responses to climate change and fire disturbances is needed such as the ability for models to simulate shifts in vegetation community types and the dynamic feedbacks to soil thermal and hydrological properties. Overall, this research contributes valuable insights into the potential impacts of climate change on Alaskan boreal forests, emphasizing the importance of considering landscape variations and moisture levels in assessing forest resilience and future trajectories.

6 Acknowledgements

This project was made possible with funding through the Audacious Project and Quadrature Climate Foundation Prime Grant Number 01-21-000094 (to SMN and BR).

7 References

Alvarado, E., Sandberg, D., and Pickford, S.G. 1998. ‘Modeling large forest fires as extreme events’, *Northwest Science* 72, pp. 66–75.

Balshi, M., McGuire, A., Zhuang, Q., Melillo, J., Kicklighter, D., Kasischke, E., et al. 2007. ‘The role of historical fire disturbance in the carbon dynamics of the pan-boreal region: A process-based analysis’, *Journal of Geophysical Research* 112. doi:10.1029/2006JG000380.

Balshi, M.S., Mcguire, A.D., Duffy, P., Flannigan, M., Kicklighter, D.W., and Melillo, J. 2009. ‘Vulnerability of carbon storage in North American boreal forests to wildfires during the 21st century’, *Global Change Biology* 15(6), pp. 1491–1510. doi:10.1111/j.1365-2486.2009.01877.x.

Calef, M.P., David McGuire, A., Epstein, H.E., Scott Rupp, T., and Shugart, H.H. 2005. ‘Analysis of vegetation distribution in Interior Alaska and sensitivity to climate change using a logistic regression approach’, *Journal of Biogeography* 32(5), pp. 863–878. doi:10.1111/j.1365-2699.2004.01185.x.

Chapin, F.S., Trainor, S.F., Huntington, O., Lovecraft, A.L., Zavaleta, E., Natcher, D.C., et al. 2008. 'Increasing Wildfire in Alaska's Boreal Forest: Pathways to Potential Solutions of a Wicked Problem', *BioScience* 58(6), pp. 531–540. doi:10.1641/B580609.

Dieleman, C.M., Rogers, B.M., Potter, S., Veraverbeke, S., Johnstone, J.F., Laflamme, J., Solvik, K., Walker, X.J., Mack, M.C., and Turetsky, M.R. 2020. 'Wildfire combustion and carbon stocks in the southern Canadian boreal forest: Implications for a warming world', *Global Change Biology* 26(11), pp. 6062–6079. doi:10.1111/gcb.15158.

Euskirchen, E.S., Edgar, C.W., Turetsky, M.R., Waldrop, M.P., and Harden, J.W. 2016. Differential response of carbon fluxes to climate in three peatland ecosystems that vary in the presence and stability of permafrost, *Journal of Geophysical Research: Biogeosciences* 119(8), pp. 1576–1595. Available at: https://doi.org/10.1002/2014JG002683.

Euskirchen, E.S., McGuire, A.D., Chapin III, F.S., Yi, S., and Thompson, C.C. 2009. 'Changes in vegetation in northern Alaska under scenarios of climate change, 2003–2100: implications for climate feedbacks'. *Ecological Applications* 19(4), pp. 1022–1043. doi:10.1890/08-0806.1.

Euskirchen, E.S., McGUIRE, A.D., Kicklighter, D.W., Zhuang, Q., Clein, J.S., Dargaville, R.J., et al. 2006. 'Importance of recent shifts in soil thermal dynamics on growing season length, productivity, and carbon sequestration in terrestrial high-latitude ecosystems', *Global Change Biology*, 12(4), pp. 731–750. doi:10.1111/j.1365-2486.2006.01113.x.

Flannigan, M. and Wagner, C.E. 1991. 'Climate change and wildfire in Canada', *Canadian Journal of Forest Research* 21, pp. 66–72. doi:10.1139/x91-010.

Flannigan, M.D., Logan, K.A., Amiro, B.D., Skinner, W.R., and Stocks, B.J. 2005. 'Future Area Burned in Canada', *Climatic Change* 72(1), pp. 1–16. doi:10.1007/s10584-005-5935-y.

Genet, H., He, Y., Lyu, Z., McGuire, A.D., Zhuang, Q., Clein, J., et al. 2018. 'The role of driving factors in historical and projected carbon dynamics of upland ecosystems in Alaska', *Ecological Applications* 28(1), pp. 5–27. doi:10.1002/eap.1641.

Genet, H., McGuire, A.D., Barrett, K., Breen, A., Euskirchen, E.S., Johnstone, J.F., et al. 2013. 'Modeling the effects of fire severity and climate warming on active layer thickness and soil carbon storage of black spruce forests across the landscape in interior Alaska', *Environmental Research Letters* 8(4), 045016. doi:10.1088/1748-9326/8/4/045016.

Gillett, N.P., Weaver, A.J., Zwiers, F.W., and Flannigan, M.D. 2004. 'Detecting the effect of climate change on Canadian forest fires', *Geophysical Research Letters* 31(18). doi:10.1029/2004GL020876.

Harden, J., Trumbore, S., Stocks, B., Hirsch, A., Gower, S., O'neill, K., and Kasischke, E. 2000. 'The role of fire in the boreal carbon budget', *Global Change Biology* 6(S1), pp. 174–184. doi:10.1046/j.1365-2486.2000.06019.x.

Harris, I., Jones, P., Osborn, T., and Lister, D. 2014. 'Updated high-resolution grids of monthly climatic observations—The CRU TS3.10 Dataset', *International Journal of Climatology* 34. doi:10.1002/joc.3711.

Jean, M., Mack, M.C., and Johnstone, J.F. 2018. 'Spatial and temporal variation in moss-associated dinitrogen fixation in coniferous- and deciduous-dominated Alaskan boreal forests', *Plant Ecology* 219(7), pp. 837–851. doi:10.1007/s11258-018-0838-y.

Johnstone, J.F., Rupp, T.S., Olson, M., and Verbyla, D. 2011. 'Modeling impacts of fire severity on successional trajectories and future fire behavior in Alaskan boreal forests', *Landscape Ecology* 26(4), pp. 487–500. doi:10.1007/s10980-011-9574-6.

Kasischke, E.S., Bergen, K., Fennimore, R., Sotelo, F., Stephens, G., Janetos, A., and Shugart, H.H. 1999. 'Satellite imagery gives clear picture of Russia's boreal forest fires', *Eos, Transactions American Geophysical Union* 80(13), pp. 141–147. doi:10.1029/99EO00094.

Kasischke, E.S., Christensen Jr, N.L., and Stocks, B.J. 1995. 'Fire, Global Warming, and the Carbon Balance of Boreal Forests', *Ecological Applications* 5(2), pp. 437–451. doi:10.2307/1942034.

Klupar, I., Rocha, A.V., and Rastetter, E.B. 2021. 'Alleviation of nutrient co-limitation induces regime shifts in post-fire community composition and productivity in Arctic tundra', *Global Change Biology* 27(14), pp. 3324–3335. doi:10.1111/gcb.15646.

Kurkowski, T.A., Mann, D.H., Rupp, T.S., and Verbyla, D.L. 2008. 'Relative importance of different secondary successional pathways in an Alaskan boreal forest', *Canadian Journal of Forest Research* 38(7), pp. 1911–1923. NRC Research Press. doi:10.1139/X08-039.

Lyu, Z., Genet, H., He, Y., Zhuang, Q., McGuire, A.D., Bennett, A., et al. 2018. 'The role of environmental driving factors in historical and projected carbon dynamics of wetland ecosystems in Alaska', *Ecological Applications: A Publication of the Ecological Society of America* 28(6), pp. 1377–1395. doi:10.1002/eap.1755.

Mack, M.C., Walker, X.J., Johnstone, J.F., Alexander, H.D., Melvin, A.M., Jean, M., and Miller, S.N. 2021 'Carbon loss from boreal forest wildfires offset by increased dominance of deciduous trees', *Science* 372, pp. 280–3.

McGuire, A.D., Koven, C., Lawrence, D.M., Clein, J.S., Xia, J., Beer, C., et al. 2016. 'Variability in the sensitivity among model simulations of permafrost and carbon dynamics in the permafrost region between 1960 and 2009', *Global Biogeochemical Cycles* 30(7), pp. 1015–1037. doi:10.1002/2016GB005405.

McGuire, A.D., Melillo, J.M., Joyce, L.A., Kicklighter, D.W., Grace, A.L., Moore III, B., and Vorosmarty, C.J. 1992. 'Interactions between carbon and nitrogen dynamics in estimating net primary productivity for potential vegetation in North America', *Global Biogeochemical Cycles* 6(2), pp. 101–124. doi:10.1029/92GB00219.

Mckenzie, D., Peterson, D.L., and Alvarado, E. 1996. 'Extrapolation Problems in Modeling Fire Effects at Large Spatial Scales: a Review', *International Journal of Wildland Fire* 6(4), pp. 165–176. doi:10.1071/wf9960165.

Melvin, A.M., Mack, M.C., Johnstone, J.F., David McGuire, A., Genet, H., and Schuur, E.A.G. 2015. 'Differences in Ecosystem Carbon Distribution and Nutrient Cycling Linked to Forest Tree Species Composition in a Mid-Successional Boreal Forest', *Ecosystems* 18(8), pp. 1472–1488. doi:10.1007/s10021-015-9912-7.

Miquelajauregui, Y., Cumming, S.G., and Gauthier, S. 2019. 'Short-term responses of boreal carbon stocks to climate change: A simulation study of black spruce forests', *Ecological Modelling* 409, 108754. doi:10.1016/j.ecolmodel.2019.108754.

Moss, R.H., Edmonds, J.A., Hibbard, K.A., Manning, M.R., Rose, S.K., van Vuuren, D.P., et al. 2010. 'The next generation of scenarios for climate change research and assessment', *Nature* 463(7282), pp. 747–756. doi:10.1038/nature08823.

Parker, R.J., Boesch, H., Wooster, M.J., Moore, D.P., Webb, A.J., Gaveau, D., and Murdiyarso, D. 2016. 'Atmospheric CH_4 and CO_2 enhancements and biomass burning emission ratios derived from satellite observations of the 2015 Indonesian fire plumes', *Atmospheric Chemistry and Physics* 16(15), pp. 10111–10131. doi:10.5194/acp-16-10111-2016.

Pastick, N.J., Duffy, P., Genet, H., Rupp, T.S., Wylie, B.K., Johnson, K.D., Jorgenson, M.T., Bliss, N., McGuire, A.D., Jafarov, E.E., and Knight, J.F. 2017. 'Historical and projected trends in landscape drivers affecting carbon dynamics in Alaska', *Ecological Applications: A Publication of the Ecological Society of America* 27(5), pp. 1383–1402. doi:10.1002/eap.1538.

Raich, J.W., Rastetter, E.B., Melillo, J.M., Kicklighter, D.W., Steudler, P.A., Peterson, B.J., Grace, A.L., Moore, B., and Vorosmarty, C.J. 1991. 'Potential Net Primary Productivity in South America: Application of a Global Model', *Ecological Applications: A Publication of the Ecological Society of America* 1(4), pp. 399–429. doi:10.2307/1941899.

Rupp, T.S., Chapin, F.S., and Starfield, A.M. 2000. 'Response of subarctic vegetation to transient climatic change on the Seward Peninsula in north-west Alaska', *Global Change Biology* 6(5), pp. 541–555. doi:10.1046/j.1365-2486.2000.00337.x.

Rupp, T.S., Starfield, A.M., Chapin, F.S., and Duffy, P. 2002. 'Modeling the Impact of Black Spruce on the Fire Regime of Alaskan Boreal Forest', *Climatic Change* 55(1), pp. 213–233. doi:10.1023/A:1020247405652.

Sullivan, P.F., Brownlee, A.H., Ellison, S.B.Z., and Cahoon, S.M.P. 2021. 'Comparative drought sensitivity of co-occurring white spruce and paper birch in interior Alaska', *Journal of Ecology* 109(6), pp. 2448–2460. doi:10.1111/1365-2745.13654.

Turetsky, M.R., Bond-Lamberty, B., Euskirchen, E., Talbot, J., Frolking, S., McGuire, A.D., and Tuittila, E.-S. 2012. 'The resilience and functional role of moss in boreal and arctic ecosystems', *New Phytologist* 196(1), pp. 49–67. doi:10.1111/j.1469-8137.2012.04254.x.

Walker, X.J., Baltzer, J.L., Cumming, S.G., Day, N.J., Ebert, C., Goetz, S., et al. 2019. 'Increasing wildfires threaten historic carbon sink of boreal forest soils', *Nature* 572, pp. 520–523

Yi, S., McGuire, A.D., Harden, J., Kasischke, E., Manies, K., Hinzman, L., et al. 2009. 'Interactions between soil thermal and hydrological dynamics in the response of Alaska ecosystems to fire disturbance', *Journal of Geophysical Research: Biogeosciences* 114(G2). doi:10.1029/2008JG000841.

Yi, S., McGuire, A.D., Kasischke, E., Harden, J., Manies, K., Mack, M., and Turetsky, M. 2010. 'A dynamic organic soil biogeochemical model for simulating the effects of wildfire on soil environmental conditions and carbon dynamics of black spruce forests', *Journal of Geophysical Research: Biogeosciences* 115(G4). doi:10.1029/2010JG001302.

Zhuang, Q., McGuire, A.D., O'Neill, K.P., Harden, J.W., Romanovsky, V.E., and Yarie, J. 2002. 'Modeling soil thermal and carbon dynamics of a fire chronosequence in interior Alaska', *Journal of Geophysical Research: Atmospheres* 107(D1), pp. FFR 3-1–FFR 3-26. doi:10.1029/2001JD001244.

Zhuang, Q., Romanovsky, V.E., and McGuire, A.D. 2001. 'Incorporation of a permafrost model into a large-scale ecosystem model: Evaluation of temporal and spatial scaling issues in simulating soil thermal dynamics', *Journal of Geophysical Research: Atmospheres* 106(D24), pp. 33649–33670. doi:10.1029/2001JD900151.

Snow management to reduce ground temperatures beside a road in the boreal forest near Mayo, Yukon

Patrick A. Jardine[1], Christopher R. Burn[1], Jennifer K. Humphries[1], Blaine Peter[2], Gary Hope[2], Jamie Phillips[2] & Lawrence D. McLaren[2]

[1]*Department of Geography and Environmental Studies, Carleton University, Ottawa, Ontario, Canada*

[2]*Lands Branch, First Nation of Na-Cho Nyäk Dun, Mayo, Yukon, Canada*

ABSTRACT

A field experiment was conducted in winter 2020–21 adjacent to the South McQuesten Road, central Yukon, to determine the effect of snow compaction on ground surface temperatures. At two sites, snow machines were used to compact the snow beside the road from late November to March. Data loggers were placed at the base of the snowpack to record the temperature at compacted and untreated plots at each site. The thickness of snow layers, and their density, hardness, and grain shape and size were recorded in snow pits after each compaction. By March, the snowpack was 35–40 cm thicker at the untreated plots and on average 156 kg m^{-3} denser at the compacted plots. The depth hoar layer, 10–15 cm thick at the untreated plots, was almost entirely crushed during compaction. Over the winter, daily ground surface temperatures at the compacted plots were 2–3 °C lower on average than at the undisturbed plots. A reduction in annual mean surface temperature of 0.9–1.3 °C may be expected due to snowpack compaction. Seasonally, the *n*-factors at the compacted plots were 0.25 and 0.15 higher than at the undisturbed plots (0.37 and 0.41, respectively). These data indicate the efficacy of a local approach to mitigating ground warming beside highways.

1 INTRODUCTION

The design and construction of roads in regions of permafrost requires the use of design standards tailored to protecting the underlying frozen ground from thawing (Zubeck and Doré 2009). In regions of discontinuous permafrost, such as south and central Yukon, road design can be especially challenging, as routes cross terrain with variable permafrost conditions and ground ice contents. Snow cover is one of the dominant controls on ground temperature (Goodrich 1982). The accumulation of snowbanks on the sides of a road can lead to significant changes in the ground thermal regime of the road (Darrow 2011).

Various techniques have been examined at the Beaver Creek test section in SW Yukon to lower embankment temperatures (Malenfant-Lepage et al. 2012), but none so far have been implemented over extensive lengths of highway, partly due to expense. Thermosyphons have been installed at km 1842 on the Alaska Highway near Dry Creek at a cost of $4M over 0.5 km as a solution to embankment thaw (M. Idrees, pers. comm., 2022).

This paper discusses the results of a field experiment conducted on South McQuesten Road, north of Mayo, YT (Figure 1), to test whether ground surface temperatures beside a highway embankment may be lowered by compacting snow. This may be a relatively cost-effective technique to achieve thermal stability in the embankment.

Deep snow accumulates alongside highway embankments from plowing of the driving lanes and deposition by wind (Auerbach 1997). The high thermal resistance of snow impedes release of heat from the embankment shoulder and raises ground temperatures (Nicholson and Granberg 1973). For example, at km 124 of the Dempster Highway temperatures at the embankment toe were about 4 °C higher than at the highway centreline, where snow is cleared (Stockton et al. 2019). If ice-rich permafrost underneath the embankment shoulder degrades then it can undercut support for the side of the road. This may cause longitudinal cracking to develop on the driving surface, and, if left unmitigated, may result in shoulder rotation and separation from the sides of the road (Doré et al. 2016).

Compaction of the snowpack is intended to reduce its thermal resistance by lowering its thickness and increasing its density (Goodrich 1982; Zhang 2005). O'Neill and Burn (2017), modelled conditions on Peel Plateau, Northwest

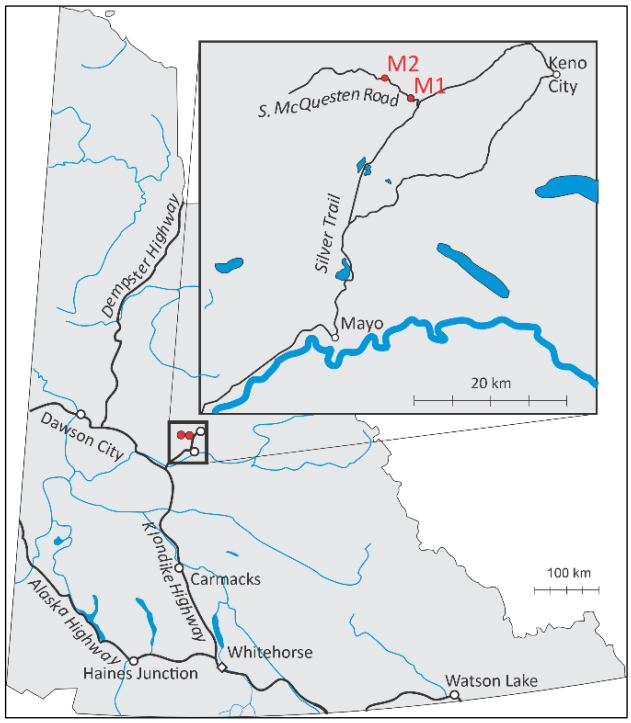

Figure 1. Location map for study sites in central Yukon.

https://doi.org/10.52381/ICOP2024.75.1

Territories, and indicated that compaction of the snowpack may reduce ground temperatures, and, in some cases, prevent permafrost degradation. The objectives of this research are to investigate: (1) whether compaction with snow machines can cause a significant reduction in snow depth and increase in density; (2) how compaction alters the structure of the snowpack and shape of snow grains; and (3), if, as a result, there is a significant reduction in ground surface temperatures.

2 Study Area

Mayo and its surroundings are in Stewart Plateau, where uplands are separated by broad river valleys (Wahl et al. 1987). Vegetation is dominated by closed canopy boreal forest, commonly interspersed with wetlands (O'Donoghue 2006). The area has widespread discontinuous permafrost with thickness up to 40 m in valleys and up to 130 m at higher elevations (Burn 1991). Typical active layer depths are 0.65–1 m (Burn 2006). Permafrost in the area is commonly found beneath organic soils, which provide insulation during the summer (Williams and Burn 1996).

The continental climate of central Yukon has short, warm summers and long, cold winters. The mean annual temperature for 1991–2020 at Mayo Airport was -2.2 °C and the mean for December to February was -18.9 °C (ECCC 2023). Throughout winter, inversions may cause temperatures to drop below -50ºC in valleys (Wahl et al. 1987). Mean snowfall from December to February was 52 cm. The mean hourly wind speed at Mayo Airport during the study was 3 km h^{-1}, with a maximum of 21 km h^{-1}. Wind speeds were commonly too low for much snow redistribution.

3 Field Methods

3.1 Site Selection

Two sites were selected in relatively flat, uniform terrain within a clear-cut right-of-way beside South McQuesten Road, an infrequently plowed road 35 km north of Mayo. One site, M1, was in an undisturbed forest 3 km from the Silver Trail, that leads north from Mayo, while M2 was in forest that had burned in 2019, 3 km farther down the road (Figure 2). The soil at the field sites was dry and without peat, so we assume they were permafrost free (Williams and Burn 1996). Snow depths were less than 1 m throughout the winter and the snow was loosely packed due to the low wind speeds. Arrival at the field sites was delayed until 26 November 2020, due to travel restrictions associated with the COVID-19 pandemic, by which time deep snow covered the ground.

3.2 Study Design

At each field site, two 50 m by 5 m plots were marked using wooden stakes, parallel to the road and beginning from the shoulder. A 5 m width was chosen to remain within the right-of-way of the road, while the 50 m length was selected to facilitate compaction. One plot at each site was compacted four times at approximately monthly intervals between late-November and mid-March, 2020–21.

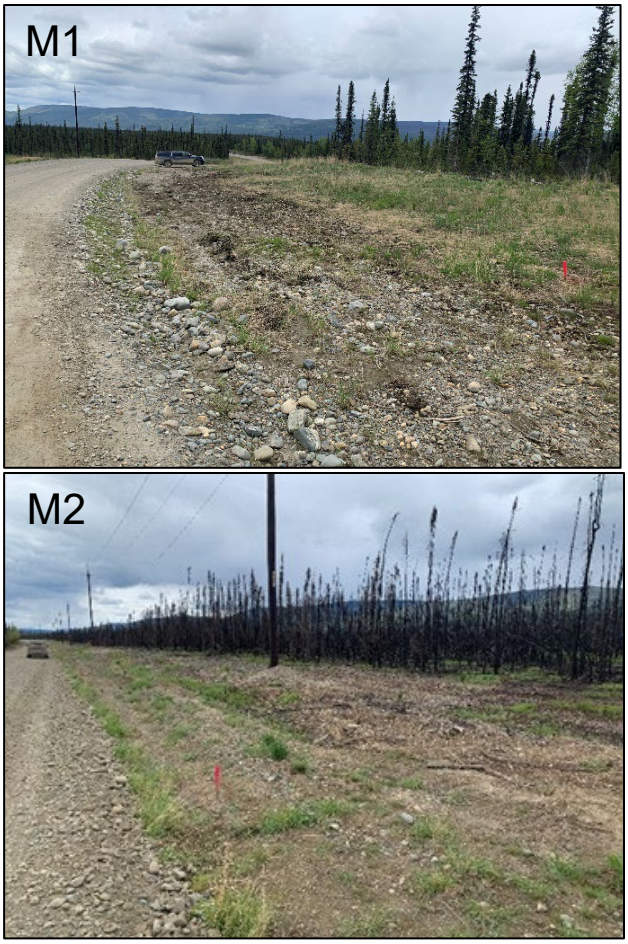

Figure 2. M1 and M2 field sites during site inspections on 4 June 2021. The coloured stakes indicate the boundary between the plots that were left undisturbed and plots that were compacted.

Onset HOBO H08-004-02 temperature loggers were used to measure temperatures at the centre of the plots. The resolution of each temperature measurement was ±0.25 °C, and the factory-specified accuracy is between ±0.5 °C and ±1 °C. The ground surface was frozen upon arrival at the field sites so burying the loggers in the ground was impractical. Instead, they were encased in PVC pipe cut to size, with plastic caps covering each end of the pipe and sealed by a layer of electrical tape. The loggers were placed at the base of the snowpack at the edge of the plot, and then pushed into place in the centre of the plot using a snow probe, with disturbed snow being replaced. Freezing *n*-factors were calculated by dividing temperatures at the base of the snowpack by air temperatures from Mayo Airport.

Figure 3. Land Guardians from the First Nation of Na-Cho Nyäk Dun compacting the snowpack at the M2 field site on 29 November, 2020.

Land Guardians from the First Nation of Na-Cho Nyäk Dun compacted one plot at each site using snow machines (Figure 3). They drove over the snowpack repeatedly until repetitions did not cause further reductions in snow depth. The snow compressed easily, and the process only took about 5 minutes. The other plot was left undisturbed.

Following compaction, snow depths were measured at the centre of the plots every 10 m along the length, to provide four measurements per plot. A snow pit was dug at each of the plots after compaction 2–3 m away from the previous visit's pit. Snow pits from undisturbed and compacted plots are shown in Figure 4. Density, hardness, and grain size and shape were measured within each layer of snow observed in the pits. Snow density was measured by weighing samples collected using a 100 ml volumetric scoop. The hardness of the layers was assessed using a semi-quantitative five-point scale including penetration with a closed fist, four fingers, one finger, a pencil, and a knife, following Fierz et al. (2009).

Grain size and shape were estimated by placing the snow grains on fine-scale graph paper and observing them with a hand lens. Snow grain shapes were categorized based on the amount of faceting they had undergone through temperature-gradient metamorphism. Temperature-gradient metamorphism can lead to development of depth hoar, i.e., loosely packed faceted crystals commonly found at the base of the snowpack (Perla and Martinelli 1978).

4 RESULTS

4.1 Snow Depth

Mean snow depths from the four depth probe measurements collected after compaction each month are shown in Figure 5. Mean snow depths over the winter at M1 were 66 cm at the undisturbed plot and 37 cm at the compacted plot; at M2 the mean snow depths were 69 cm and 39 cm, respectively. Snow depths at the undisturbed plots rose gradually throughout the winter to a peak of about 75 cm in April. At the compacted plots, snow depths peaked

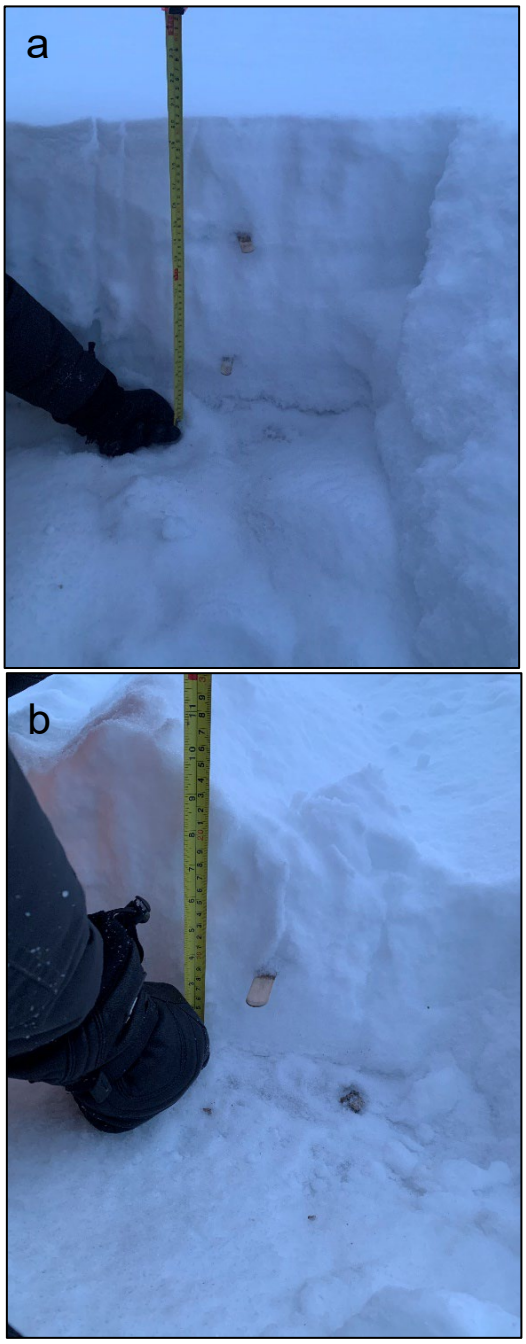

Figure 4. Snow pits dug at the M2 (a) undisturbed plot, with a depth of 53 cm and (b) compacted plot, with a depth of 23 cm, on 5 January 2021, after the second compaction.

in January at 48 and 59 cm before declining to about 40 cm for the remainder of the winter.

4.2 Snow Density and Hardness

Weighted mean density and hardness were calculated by multiplying the values for each snow layer by the thickness of the layer as a proportion of the total snowpack, then

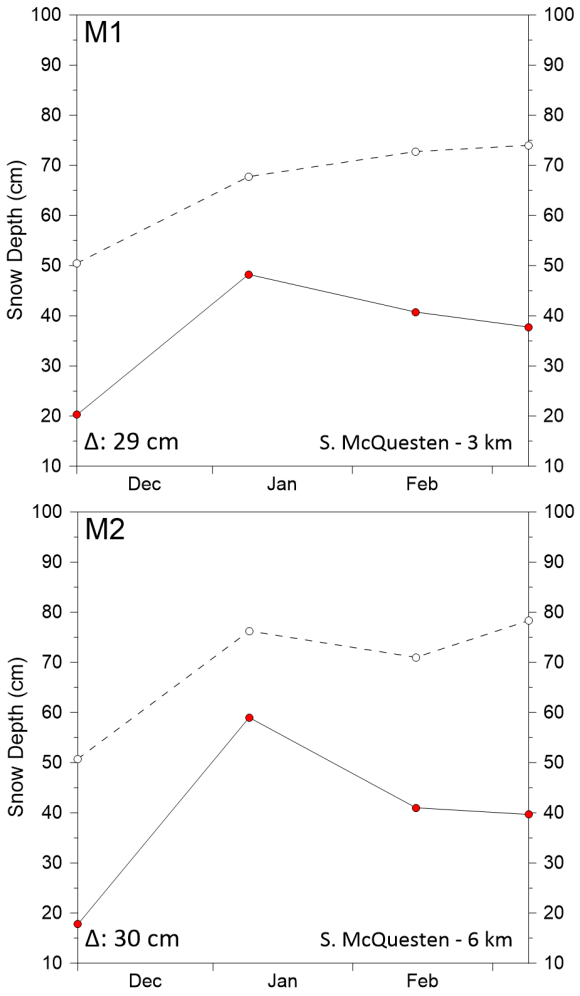

Figure 5. Snow depths (cm) at the undisturbed (white) and compacted (red) sites beside South McQuesten Road, central Yukon. Δ Indicates the mean difference between the treatments over the winter.

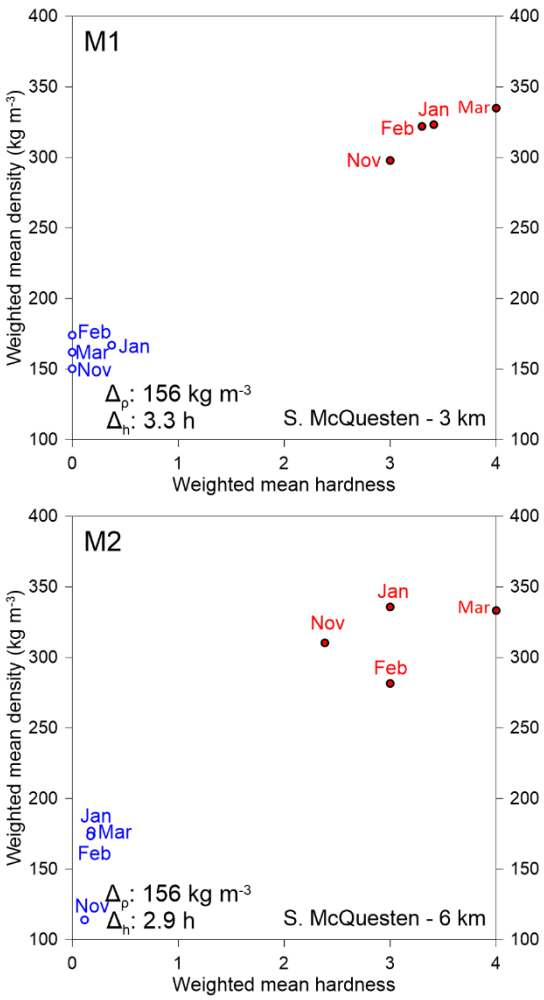

Figure 6. Weighted mean snow pack hardness and density of undisturbed (blue) and compacted (red) sites each month during winter 2020–21. The mean density and hardness were weighted by the thickness of each layer within the snowpack.

adding all layers together. Figure 6 displays the weighted average density and hardness of the snowpack from the four pits that were dug each month after compaction. Over the entire winter, the plots that were left undisturbed had mean densities of 163 and 160 kg m^{-3} at M1 and M2, respectively. At the compacted plots, mean snow densities at M1 and M2 were 319 and 315 kg m^{-3}, respectively. The mean hardness of the snowpack was near 0 at the undisturbed plots, while at the compacted plots it was 3.4 and 3.1 at M1 and M2, respectively, indicating that the snow could be penetrated by a single finger or a pencil.

The density of the snow at the undisturbed plots (Figure 6) was low compared to typical densities for settled snow (200–300 kg m^{-3}; Paterson 1994), likely due to low wind speeds and infrequent plowing at the field sites, which allowed loosely packed snow to accumulate. Compaction increased snow density to slightly greater than this range on average, and maximum densities were 335 kg m^{-3} at both plots.

4.3 Changes in Snow Structure

Figure 7 presents the mean snow-layer thickness and structure at the four plots over winter 2020–21. Dendritic snow, found at the top of the snowpack, had fresh, loosely packed grains that had retained their crystalline shape. Snow with some angular facets had undergone limited temperature-gradient metamorphism but had not fully metamorphized into depth hoar. Moderately rounded snow often had a mix of faceted and rounded snow grains.

The greatest reductions in snow depth at the compacted plots compared to the undisturbed plots were in dendritic snow and depth hoar, both of which were absent at the compacted plots after January. Dendritic snow had a mean density of 140 kg m^{-3}, which was lower than the other snow types, which all had mean densities of about 180 kg m^{-3}. At the compacted plots, dendritic snow near the surface became rounded and well-packed, depth hoar became an icy mass of partially broken faceted crystals, and the bulk of

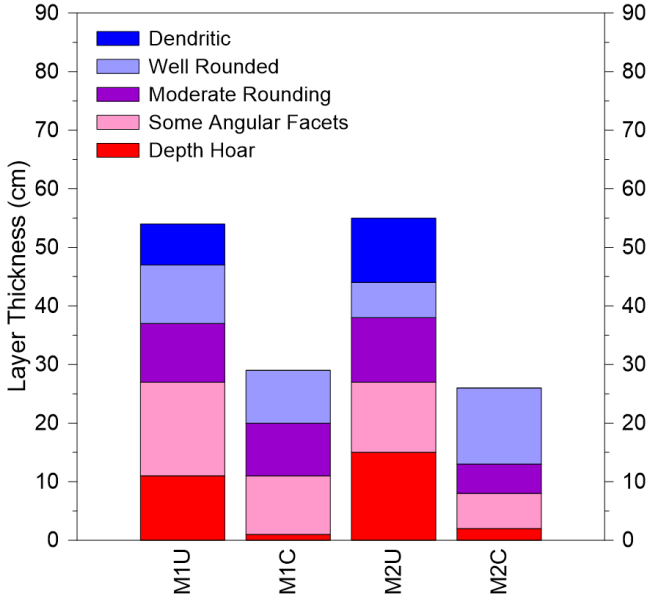

Figure 7. Mean snow structure within the snowpack at each site. The thickness of each layer is the mean value of four months of measurements.

the snowpack became a mix of closely packed rounded and faceted snow crystals. The density of the compacted snowpacks varied little between layers, ranging from 290–330 kg m^{-3}.

4.4 Daily Mean Temperatures at the Base of the Snowpack

Mean daily temperatures at the base of the snowpacks are displayed in Figure 8, along with air temperatures at Mayo Airport, 35 km south of the field sites. Over the winter, mean temperatures at the undisturbed plots were -5.2 and -5.5 °C at M1 and M2, respectively. At the compacted plots, mean temperatures were -8.4 and -7.7 °C.

Temperatures at the compacted and undisturbed plots were closely coupled in December, remaining within 1 °C at both sites, even as mean daily air temperatures fell to as low as -32 °C on December 21st. On January 5th, after several weeks of cold weather, the temperatures at the compacted plots dropped to about 2–5 °C lower than at the undisturbed plots. The sudden divergence may indicate a reduction in the latent heat flux from the freezing front towards the surface, that did not occur at the undisturbed sites. This was likely associated with the depth of frost penetration.

From January 26 to February 16 mean daily air temperatures averaged -30 °C, with a low of -38 °C on February 9. During this time divergence between the compacted and undisturbed plots reached its maximum of 12.1 °C at M1 on February 16, and 9.4 °C at M2 on February 15. The difference in temperature between the plots diminished for the remainder of the winter as air temperatures rose to -15 °C.

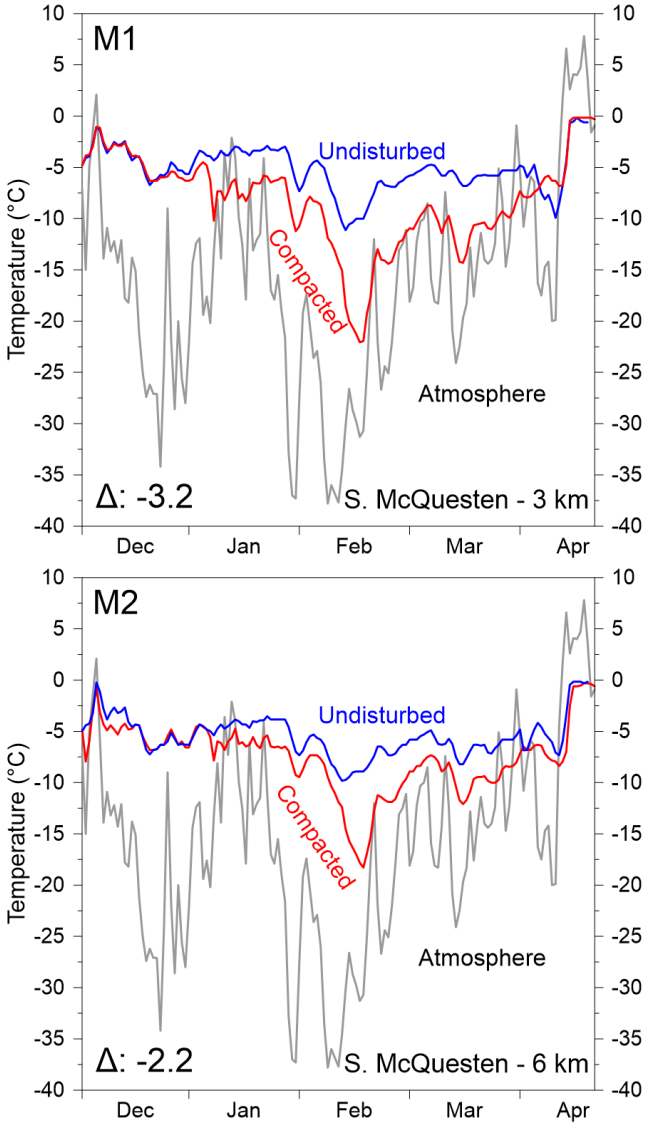

Figure 8. Daily mean temperatures measured at the base of the snowpack beneath undisturbed (blue) and compacted (red) snow. The daily mean air temperature recorded at Mayo A is also given. Data from 29 November to 22 April, 2020–21.

4.5 Weekly *n*-Factors

The weekly *n*-factors for the monitoring period at the undisturbed plots ranged from 0.19 to 0.72, and were on average 0.37 and 0.41 at M1 and M2, respectively (Figure 9). At the compacted plots, *n*-factors ranged from 0.22 to 1.18, and averaged 0.62 and 0.56.

In northwestern Canada, taiga typically has seasonal freezing *n*-factors of 0.1–0.3, while tundra has *n*-factors between 0.7–1, due to shallower and denser snow cover caused by higher wind speeds (Smith et al. 2010). At the undisturbed sites, n_f was slightly higher than published values for taiga, perhaps due to the late start of observations in the season, thereby missing freeze back of

the near surface. At the compacted plots n_f was 0.14 and 0.24 higher than the undisturbed plots, and heat flow through the snowpack more closely resembled that of tundra than taiga.

The *n*-factors for the period after January 10th, excluding the time when the near surface was freezing, were on average 0.41 and 0.44 at the undisturbed plots of M1 and M2, and 0.73 and 0.64 at the compacted plots. The high weekly *n*-factors on January 10 were due to rapidly increasing air temperatures, causing the air to be briefly warmer than the base of the snowpack.

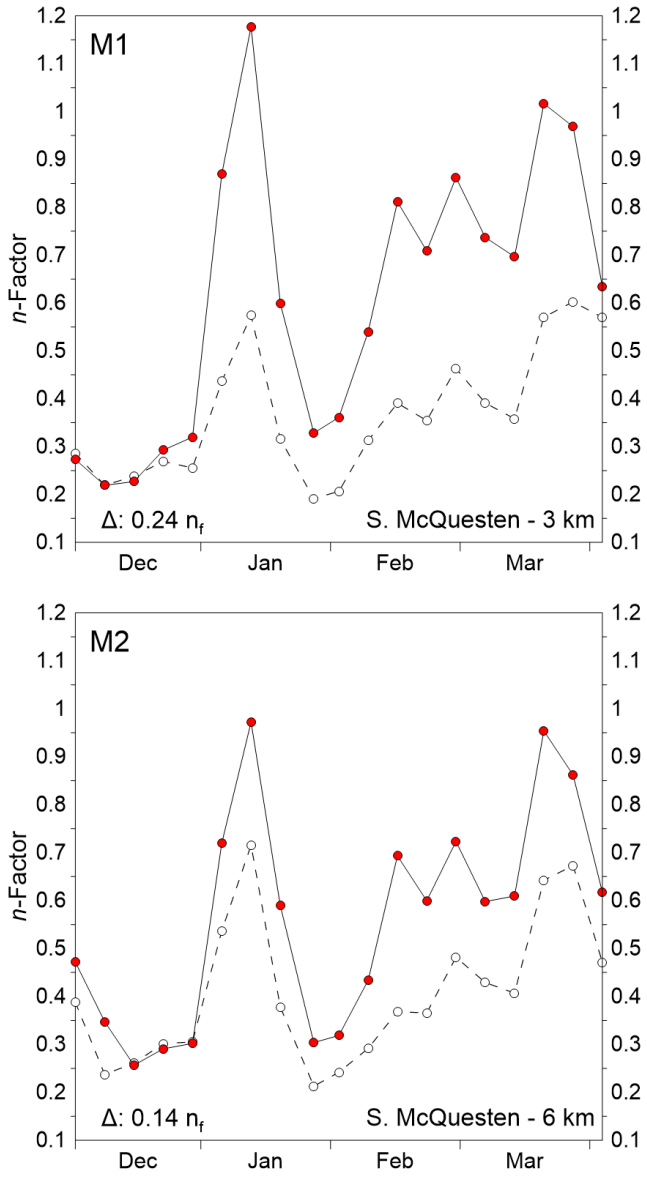

Figure 9. Weekly *n*-factors for undisturbed (white) and compacted (red) plots.

4.6 Summary of Results

The field results are summarized in Table 1. On average, the snowpack at the compacted plots was 30 cm thinner, had density that was slightly higher than is typically found in well-settled snow, and was hard enough that it could only be penetrated using a finger or pencil. Temperatures at the base of the snowpack were 2.7 °C lower, since the *n*-factor increased to values characteristic of thin, dense snow found in tundra. These seasonal adjustments and *n*-factors may underestimate the effectiveness of compaction when conducted throughout the winter including during freeze-back.

Table 1. Snow properties with and without compaction.

	Undisturbed average	Compacted average
Depth (cm)	68	38
Density (kg m^{-3})	161	317
Hardness	0.1	3.3
Mean basal temp. (ºC)	-5.3	-8.0
Seasonal *n*-factor	0.39	0.59

5. Discussion

5. 1 Influence of Site Conditions

The effect on mean annual ground temperatures caused by thermal insulation from snow cover is greatest in regions with a large annual amplitude in air temperature (Goodrich 1982). The continental climate of central Yukon therefore creates more favourable conditions for reducing the thermal resistance of the snowpack and releasing a large amount of energy from the ground than a temperate climate.

A large temperature gradient through the snowpack also causes the development of depth hoar through temperature-gradient metamorphism. The undisturbed plots had about 10–15 cm of depth hoar on average, and about half of the snowpack had faceted snow grains. The proportion of depth hoar in the snowpack is relevant for heat flow since its low density results in a lower thermal conductivity than other snow types (Zhang et al 1996; Sturm and Johnson 1992). The increased thermal insulation provided by depth hoar may raise ground temperatures by several degrees where it is present (Zhang 2005).

Low wind speeds at the study site and infrequent plowing of the road meant that snow was only slowly replenished by snowfall after being compacted. Tread marks from the previous month's compaction were generally visible at the sites during each field visit. On a road with a higher rate of snow replenishment the treatment may be less effective or may require more frequent compaction to cause the same change in n_f.

The difference in density between M1 and M2 may be due to the burned forest providing a less effective wind break, increasing snow transport, and hardening the snowpack. However, no wind measurements were taken at the plots,

and the differences in hardness and density between the plots were small (Figure 5), so the difference may also be a result of other local conditions.

5. 2 Snow Response to Compaction

The compressive strength of snow is highly correlated with its density and structure. Deformation of a snowpack under compressive force occurs partially through shifting of snow grains into air pockets, and partially through elastic bending of the skeletal ice structure (Mellor 1975). At the field sites, the low density of the snowpack (Figure 6) caused them to compress easily as snow grains could shift freely. This caused the undisturbed snowpack to be highly susceptible to compaction at the beginning of the experiment. Snow depths were reduced from approximately 50 cm to 20 cm in November (Figure 5), and density increased to approximately 300 kg m^{-3}, an upper value for settled snow (Paterson 1994).

The increased density of the snow following initial compaction caused it to be more resistant to the effects of subsequent compactions, with limited increases in density and reductions in depth compared to the undisturbed plots for the remainder of the winter.

Dry snow with a density of 200 kg m^{-3} may collapse under pressure of 4–15 kPa, while snow with a density of 400 kg m^{-3} may require 150–400 kPa (Mellor 1974). An average snow machine with rider weighs approximately 350 kg and carries the weight on skis and track of 0.65 m^2, thereby applying a pressure of approximately 5.4 kPa to the snow surface. These data explain the compaction of low-density snow at the field sites.

In addition to density, the strength of a snowpack is also governed by the texture of its snow grains. When snow grains are large in comparison with the snow necks connecting them, the increased leverage when force is applied causes them to break apart more easily (Perla and Martinelli 1978). Depth hoar had the largest snow grains of any snow type at the field site, averaging 3.8 mm, which is likely why it experienced the second largest reduction in snow depth, behind only dendritic snow (Figure 7).

5. 3 Temperature Reduction at the Base of the Snowpack

Compaction was effective at lowering basal snow temperatures at both test plots. The reductions in mean daily temperatures of 2.2 and 3.2 °C over 145 days suggests that mean annual temperatures at the base of the snowpack may be reduced by about 0.9–1.3ºC. The sudden drop in temperature at the compacted plots on January 5 suggests that compaction expedited freeze up of the near surface, since the undisturbed plots did not experience a similar drop in temperature until near the end of January. Had compaction begun shortly after the first snow fall then it may have caused the ground to freeze still earlier, increasing the effectiveness of the technique in reducing ground surface temperatures.

Due to the possibility of reduced frost penetration from the delay in beginning the compaction until late-November, 2020, 1 °C is a reasonable estimate of the immediate potential reduction in mean annual ground surface temperatures beside the road beneath a compacted snowpack. The numerical study of Goodrich (1982) suggests that a reduction in snow depth from 50 cm to 25 cm may cause a reduction in mean annual ground surface temperatures of 3–4 °C. Simulation results from O'Neill and Burn (2017) suggest that by compacting snow to a density of 400 kg m^{-3}, a 3–4 °C reduction in ground surface temperatures could be achieved in as little as two years at tundra sites. This study indicates that, in forest, compaction using light, accessible equipment, such as snow machines, may be effective at reducing ground surface temperatures.

6 Conclusions

Compaction was effective at reducing snow depths by over 50% after a single treatment, and the difference in snow depth persisted throughout the winter. The snow types that experienced the greatest reduction due to compaction were dendritic snow and depth hoar. These snow types have a low thermal conductivity due to their low density, so their susceptibility to compaction increases the efficiency of the technique in reducing snowpack thermal resistance.

By modifying the physical properties of the snowpack to more closely resemble a thin, dense snow cover, similar to a tundra snowpack, compaction caused a significant reduction in ground surface temperatures, and the effect would likely have been greater had the treatment begun at the beginning of the winter. Due to the effectiveness of the technique, along with its simplicity and low-cost, further research is warranted towards its large-scale use in northern road maintenance to mitigate the risk of damage from thawing ice-rich permafrost. In the first case, research should be conducted to determine the efficacy of compaction throughout the winter, including freeze-back. Subsequently it may be appropriate to determine the practicality of implementation of the technique along specific highways.

7 Acknowledgements

Financial support for this research was provided by the Transportation Engineering Branch, Yukon Highways and Public Works, the First Nation of Na-Cho Nyak Dun (NND), the Natural Sciences and Engineering Research Council of Canada (NSERC), the NSERC Permafrost Partnership Network for Canada, the Northern Scientific Training Program of Polar Knowledge Canada, and the Northern Transportation Adaptation Initiative of Transport Canada. Emilie-Stewart Jones assisted with fieldwork. Licensing was provided by Yukon Highways and Public Works. We thank Adrienne Hill for facilitating participation of NND staff, Toni Lewkowicz, Fabrice Calmels, and two anonymous reviewers for helpful comments that improved the paper and Robert Way, Peter Morse, and Pascale Roy-Léveillée for careful examination of the thesis from which this paper has been drawn. Jennifer Humphries is currently at the Aurora Research Institute, Aurora College, Inuvik, NT.

8 REFERENCES

Auerbach, N.A., Walker, M.D., and Walker, D.A. 1997. 'Effects of Roadside Disturbance on Substrate and Vegetation Properties, Arctic Tundra', *Ecological Applications* 7(1), pp. 218–235. doi:10.1890/1051-0761(1997)007[0218:EORDOS]2.0.CO;2.

Burn, C.R. 1991. 'Permafrost and Ground Ice Conditions Reported During Recent Geotechnical Investigations in the Mayo District, Yukon Territory', *Permafrost and Periglacial Processes* 2(3), pp. 259–268. doi:10.1002/ppp.3430020310.

Burn, C.R. 2006. 'Permafrost', in L. Bleiler, C. Burn and M. O'Donoghue (eds.), *Heart of the Yukon: a Natural and Cultural History of the Mayo Area*. Village of Mayo, Mayo, Yukon, Canada: 138 p.

Darrow, M.M. 2011. 'Thermal Modelling of Roadway Embankments over Permafrost', *Cold Regions Science and Technology* 65(3), pp. 474–487. doi:10.1016/j.coldregions.2010.11.001.

Doré, G., Niu, F., and Brooks, H. 2016. 'Adaptation Methods for Transportation Infrastructure Built on Degrading Permafrost', *Permafrost and Periglacial Processes* 27(4), pp. 352–364. doi:10.1002/ppp.1919.

Environment and Climate Change Canada (ECCC) 2023. *Homogenized Historical Climate Data*. Available at: http://canada.ca/en/environment-climate-change/services/climate-change/science-research-data/climate-trends-variability/adjusted-homogenized-canadian-data/surface-air-temperature-access.html.

Fierz, C., Armstrong R.L, Durand Y., Etchevers P., Ethan, G. D. McClung, K. Nishimura, P.S., and Sokratov, S. 2009. *International Classification for Seasonal Snow on the Ground*. Paris, France: International Hydrological Programme (IHP), IHP-VII Technical Documents in Hydrology No. 83, IACS Contribution N1, UNESCO Working Series SC-2009/WS/15.

Goodrich, L.E. 1982. 'The Influence of Snow Cover on the Ground Thermal Regime', *Canadian Geotechnical Journal* 19(4), pp. 421–432. doi:10.1139/t82-047.

Malenfant-Lepage, J., Doré, G., and Fortier, D. 2012. 'Thermal Effectiveness of the Mitigation Techniques Tested at Beaver Creek Experimental Road Site based on a heat balance analysis: Yukon, Canada', in *15th International Conference on Cold Regions Engineering.* Reston, Virginia, United States: pp. 42–51. doi: 10.1061/9780784412473.005

Mellor, M. 1975. 'A Review of Basic Snow Mechanics', in *Proceedings, Grindelwald Snow Mechanics Symposium*. Grindelwald, Switzerland: April 1–5,1974, IAHS-AISH 114, pp. 251–291.

Nicholson, F.H. and Granberg, H.B. 1973. 'Permafrost and Snow-cover Relationships near Schefferville', in *Permafrost, North American Contribution, Second International Conference.,* Washington, D.C., United States: July 13–28, 1973, pp. 151–158.

O'Donoghue, M. 2006. 'Vegetation', in L. Bleiler, C. Burn and M. O'Donoghue (eds.), *Heart of the Yukon: a Natural and Cultural History of the Mayo Area*. Village of Mayo, Mayo, Yukon, Canada: 138 p.

O'Neill, H.B. and Burn, C.R. 2017. 'Impacts of Variations in Snow Cover on Permafrost Stability, Including Simulated Snow Management, Dempster Highway, Peel Plateau, Northwest Territories', *Arctic Science* 3(2), pp. 150–178. doi:10.1139/as-2016-0036.

Paterson, W.S.B. 1994. *The Physics of Glaciers.* Tarrytown, New York, United States: Elsevier Science Inc.

Perla, R.I. and Martinelli, M. 1978. *Avalanche Handbook*. Washington, D.C., United States: US Department of Agriculture, Forest Service.

Stockton, E.J., Burn, C.R., Idrees, M., Calmels, F., and Elmer, K. 2019. 'Monitoring Ground Temperatures in Permafrost Along the Dempster Highway, Yukon and NWT', in *18th International Conference on Cold Regions Engineering and the 8th Canadian Permafrost Conference*. Reston, Virginia, United States: American Society of Civil Engineers pp. 92–101. doi:10.1061/9780784482599.011.

Sturm, M. and Johnson, J.B. 1992. 'Thermal Conductivity Measurements of Depth Hoar', *Journal of Geophysical Research* 97(B2), pp. 2129–2139. doi:10.1029/91JB02685.

Wahl, H.E., Fraser, D.B., Harvey, R.C., and Maxwell, J.B. 1987. 'Climate of Yukon', *Environment and Climate Change Canada* Climatological Studies no. 40.

Williams, D.J. and Burn, C.R. 1996. 'Surficial Characteristics Associated with the Occurrence of Permafrost near Mayo, Central Yukon Territory, Canada', *Permafrost and Periglacial Processes* 7(2), pp. 193–206. doi:10.1002/(SICI)1099-1530(199604)7:2<193:AID-PPP216>3.0.CO;2-0.

Zhang, T. 2005. 'Influence of the Seasonal Snow Cover on the Ground Thermal Regime: An overview', *Reviews of Geophysics* 43(4). doi:10.1029/2004RG000157

Zhang, T., Osterkamp, T. E., and Stamnes, K. 1996. 'Influence of the Depth Hoar Layer of the Seasonal Snow Cover on the Ground Thermal Regime', *Water Resources Research* 32(7), pp. 2075–2086. doi:10.1029/96WR00996.

Zubeck, H.K. and Doré, G. 2009. 'Introduction to Cold Regions Pavement Engineering', in *14th International Conference on Cold Regions Engineering*. Reston, Virginia, United States: American Society of Civil Engineers, pp. 337-345. doi:10.1061/41072(359)33

Climate warming and the progression of winter road degradation in northern Canada

Rob Kenyon, Ryan Dobson & Suzanne Schultz
KGS Group, Winnipeg, Manitoba, Canada

ABSTRACT

Winter roads have been the lifeline for remote northern communities in Canada for decades. The historical method of winter road building on flat terrain such as muskeg (peat) and lakes has become less effective as the climate warms and winter road seasons become shorter. The immediate concern is the reduction in serviceability of historically constructed winter roads, due to the drastically diminishing winter road seasons. This paper details the progression of climate change and subsequent consequences for our winter road networks in Canada's central provinces of Ontario and Manitoba. Nearly 6000 km of winter roads exist in Manitoba and Ontario, servicing a total of 54 separate communities, to supply food, fuel, school, medical, and construction supplies each year. Regional climate data, research, and first-hand accounts suggest that new solutions and strategies are required to maintain seasonal access for northern remote communities.

This paper presents the case study of the Fort Severn First Nation Winter Road, part the longest winter road in the world, where the continued degradation and reduced operating seasons have resulted in significant socio-economic repercussions for the community. A helicopter reconnaissance of the existing Fort Severn Winter Road alignment versus potential alternative routes revealed widespread permafrost degradation and significant ground warming. Options for relocating the existing winter road to higher and more favourable ground is detailed, while some level of permanent embankment construction is suggested through muskeg terrain. This strategy also offers the potential for future all season road development, reducing our overall environmental footprint. Adopting climate resilient winter road principles is required to maintain access to northern communities while protecting the environment and promoting sustainable and reliable infrastructure.

1 INTRODUCTION

Climate change has evolved into a climate crisis in northern Canada. Increasingly warmer mean annual temperatures have resulted in extreme changes to the environment and subsequently, the socio-economic normality of the North. The engineering profession has been challenged in recent decades to maintain or upgrade established infrastructure as the environment adjusts to a rapidly changing climate.

An immediate concern for remote communities in northern Canada is the sustainability of winter road infrastructure. Winter roads in Canada have provided essential seasonal access to fly-in only locations, typically remote northern communities and mining infrastructure, since the early 20th century (Kuryk, 2003; Sigfusson, 1992). Accounting for over 50% of Canada's winter roads, Manitoba and Ontario have a combined winter road network of approximately 5660 km, servicing 54 First Nation communities.

Conventionally constructed through low-lying terrain, winter roads have historically been routed across lakes, rivers, muskeg, and permafrost terrain. The routing process was undertaken without consideration for the characteristics of the underlying soils, leading to poor winter road performance as warmer winter season temperatures are recorded.

As the operating window of winter roads continues to shorten, First Nation communities in Canada are searching for a more reliable and permanent solution. In conjunction with the engineering profession, many First Nation communities have been able to improve accessibility by re-routing their winter road alignments to more stable higher ground. However, there are northern communities where an all-season road is not considered to be a feasible solution from a costing perspective. Construction costs for northern all-season roads can range from $2 million to $5 million per kilometer depending on terrain, topographic conditions, water crossings, borrow sourcing, and the design level of service. By using a transitional approach that improves our winter roads in the interim, engineers can plan for future all-season road development by applying a staged construction strategy. This paper presents the case study of the Fort Severn First Nation Winter Road, which is located in one of Canada's most sensitive and challenging areas, the Hudson Bay Lowlands.

1.1 Regional Climate Data

The progression of climate change has resulted in observed and projected mean annual average temperatures (MAAT) across northern Canada increasing at twice the rate of the global mean annual temperatures. The greatest increases in MAAT have been observed in the winter season, a trend projected to continue as fewer Freezing Degree Days (FDD) are observed each year (Bush et al. 2019). As shown on Figure 1, historical temperature data from four northern communities located in the Hudson Bay Lowlands region show that MAAT have increased by approximately 1.98 °C since 1935, 2.5 times the global average.

https://doi.org/10.52381/ICOP2024.217.1

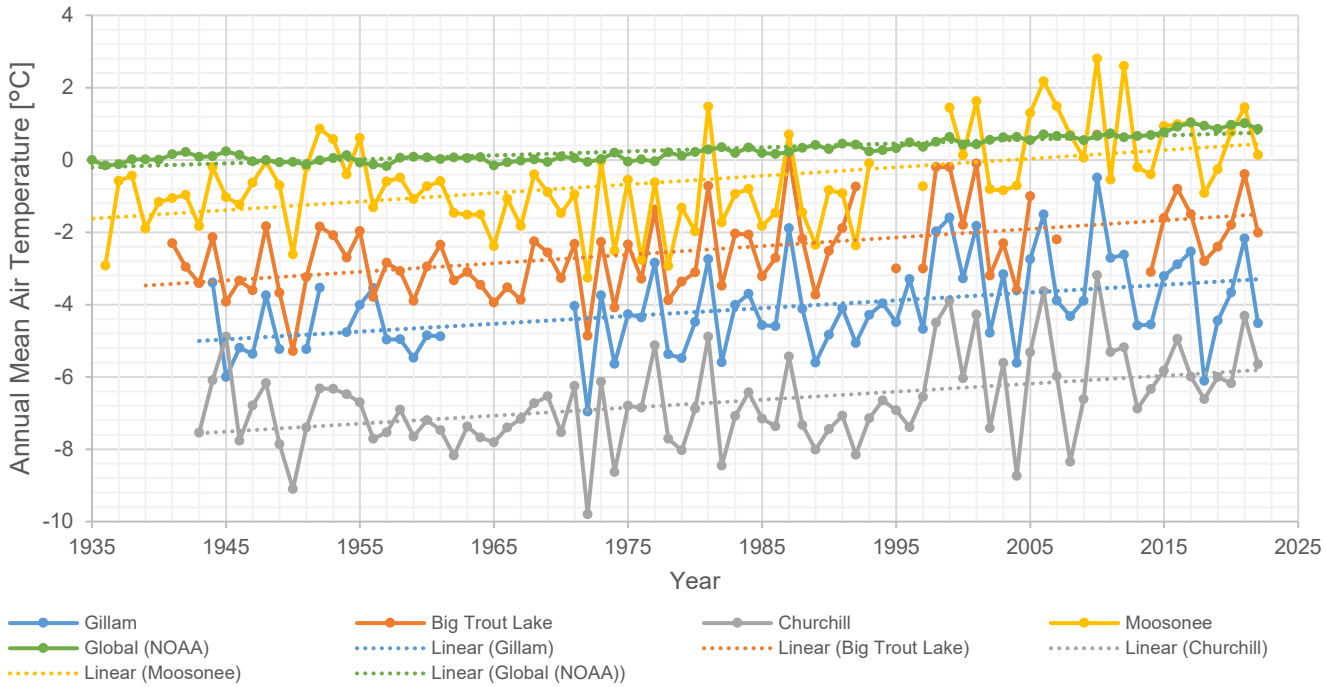

Figure 1. Annual mean air temperatures of four communities in the Hudson Bay Lowlands compared to global mean temperatures since 1935 (Government of Canada 2023; NOAA 2023).

Regional temperature forecasting based on 24 climate models in the area of the case study predict that the MAAT in the region of Fort Severn First Nation will increase by as much as 2.6 °C by 2050, as shown in Figure 2. The predicted warming trends will result in the reduction of observed annual FDD and require more effort on the winter road pre-conditioning period as more energy is required to freeze the warmer subsurface and water bodies. (Hori et al. 2017, 2018).

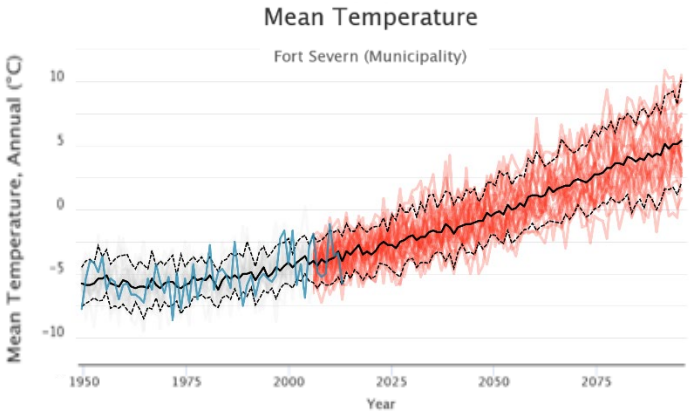

Figure 2. Mean annual temperature forecasting based on 24 climate models for Fort Severn, Ontario (Prairie Climate Center 2019).

1.2 Muskeg Terrain, Water Crossings, and Permafrost

Muskeg has become increasingly difficult to construct winter roads through despite historically being considered an economically viable winter subgrade. Insulative properties, heat generation, and high moisture contents associated with the chemical and thermal properties of muskeg contribute to its progressive inability to freeze through natural climatic processes, as more heat is transferred into the peat in the summer months (Phukan 1982).

In the northern regions of Canada, muskeg terrain is also associated with underlying permafrost as the high void ratio in peat deposits naturally insulates the perennially frozen ground against surface air temperatures. However, the insulative properties of peat are now not enough to prevent active permafrost warming and thaw in most regions of Canada, posing a greater risk to winter roads.

Water crossings have also become increasingly problematic due to late ice freezing in the fall and early thawing in the spring. Relying on ice formation to naturally bridge water bodies requires significant maintenance efforts to build ice in early winter and maintain access during warmer weather conditions. As winter road networks generally do not have built in redundancies, system functionality can rely entirely on the water crossing maintenance. In cases where a water crossing fails or becomes increasingly problematic, the entire system fails.

The increase in MAAT has resulted in long term changes to the ground temperature regime and a gradual expansion of the active zone of influence. In northern regions of Canada, the thawing of permafrost is irrevocably changing the environment through ground subsidence, slope and erosional failures, thermal regime of the subsurface, and increased saturation of soils. Terrain and landform changes (such as bog turning into fen as the groundwater table rises)

are directly connected to the increased challenges of our winter road systems.

1.3 Climate Sensitive Winter Road Strategy

Incremental re-routing solutions along shorter sections of existing alignments are no longer sufficient to maintain access along winter roads. In response, a climate sensitive winter road routing and ground improvement strategy has been developed that suggests re-routing the entire winter road system and applying fundamental all-season road routing and construction principles. The basis of the strategy is to minimize traversing organic deposits and poorly draining terrain, avoid ice rich ground, reduce or eliminate water crossings, and re-route along geological features of higher local relief (such as beach ridges, eskers, moraines, and outwash deposits) with stable subsurface characteristics that promote hard freezing.

Not only will the re-routing and ground improvement strategy aid in extending the winter road season, but this strategy provides the first step for potential future all-season road (ASR) alignments. Soon, ASR development will become a requirement to keep these remote communities connected by ground.

1.3.1 Muskeg Ground Improvement Technique

Segments of most winter roads in Canada will inevitably cross areas of muskeg terrain. The construction of a permanent shallow embankment floated on organic deposits (muskeg) offers a solution for hard freezing and potential year-round access. The synthetic embankment can be constructed by placing a thick granular layer over a swamp rated geogrid/geotextile composite to float the road on the peat, as shown in Figure 3. Alternatively, a classic corduroy road could be constructed by placing the granular fill over a mattress of tightly spaced logs.

The success of the floating road strategy relies on ability of peat to act as a foundation material, whose characteristics are highly variable based on formation, humification, and moisture content. Shear strength, which is a critical parameter to this methodology, is a function of the structure and moisture content of the peat. Peat of higher fibrosity, lower moisture contents, and lower degree of decay has greater shear strengths than less fibrous peat with a higher moisture content and level of decay (Forestry Civil Engineering 2010; Hobbs 1986; Munro 2004). The shear strength profile will typically decrease with depth as the peat loses fibrosity and becomes more amorphous. Therefore, the depth of the synthetic embankment will vary based on the shear strength of the peat. When considering constructability, the establishment of a floating embankment is more suited to winter construction to maintain the natural tensile forces in peat fibers and to reduce the risk of excessive tearing/shearing. Winter construction will also allow for gradual compression of the peat layer as it naturally thaws during the spring.

The muskeg ground improvement technique of constructing a floating embankment through muskeg terrain is typical practice for all-season road development. However, the same principle should also be applied to winter road construction to maintain serviceability along alignments where there is a risk for non-freezing muskeg or melting permafrost.

1.3.1 Water Crossing Upgrades

A crucial factor to winter road functionality is the water crossings. Winter road seasons can be extended when winter road alignments are more strategically routed to avoid or limit the number of water bodies crossed. The location of a winter water crossing should be routed in areas that promote ice generation (e.g., straight sections, low water velocities), which is quite often in conflict with the preferred crossing location for a permanent bridge structure. In areas where water crossings cannot be avoided, risk can be minimized by installing culverts, or temporary or permanent bridge structures. As a preventative measure, several provincial and territorial government bodies are currently installing permanent bridge structures.

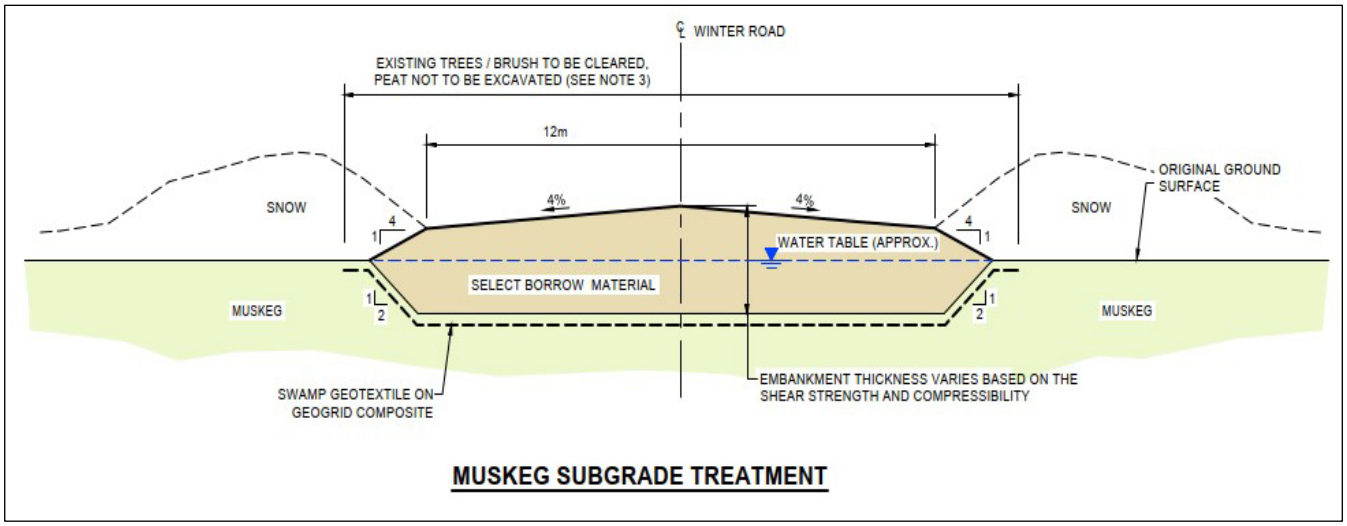

Figure 3. Example of a synthetic floating embankment as a ground improvement technique for winter roads over muskeg.

2 FORT SEVERN FIRST NATION WINTER ROAD

The existing winter road for Fort Severn, ON is part of the longest winter road in the world, the Wapusk Trail, at 752 km in length, beginning in Gillam, MB and ending in Peawanuck, ON, as shown in Figure 4. Fort Severn First Nation (FSFN) is responsible for the construction and maintenance of a 305 km section that runs east–west between FSFN and Shamattawa First Nation, MB. The winter road continues beyond Shamattawa First Nation for approximately 200 km to Gillam, MB until it connects to the Manitoba provincial all-season road network.

Figure 4. The Wapusk Trail, approximately 752 km in length, between Gillam, Manitoba and Peawanuck, Ontario.

The entire length of the winter road is located within a unique and complex region known as the Hudson Bay Lowlands, the largest wetland in Canada. The surficial geology is dominated by poorly draining organic deposits of muskeg (peat) that are typically underlain by fine-grained glacio-lacustrine clays and silts (Ontario Geological Survey 2016). Terrain within the Hudson Bay Lowlands is also heavily influenced by areas of discontinuous and continuous permafrost. The frozen soils are currently melting at an accelerated rate, posing considerable risk for winter road infrastructure.

Originally routed using the historic conventional method of winter road routing, over 90% of the current FSFN winter road route traverses flat organic terrain and lakes with limited high ground options. In recent years, the winter road season has shortened to as little as two weeks, and it was open for light traffic only, having significant socio-economic repercussions for the community. Reduced weight capacities and short winter road seasons that limit the delivery of essential supplies have major negative impacts on the community in the form of fuel shortages, inflation, and decreased economic development and growth. It has become critical for FSFN to find an adaptative and sustainable solution to maintain roadway access while preserving their culture and way of life.

2.1 Regional Surficial Geology

The Hudson Bay Lowlands is one of the most difficult settings for road building (winter road and all-season) as the low-lying terrain is poorly draining, consists of variable depths of peat deposits, and has limited high ground options and conventional borrow sourcing. Surficial geology was reviewed to assess the terrain, topography, and geological features to assess potential new routing options.

Along the Hudson Bay coastline there exists a series of historical beach ridges as long linear features with shallow relief above the neighbouring muskeg terrain, as shown in Figure 5. The beach ridges are historical marine shorelines, deposited by the Tyrell Sea as the Laurentide ice sheet retreated. Within the limits of the Hudson Bay Lowlands, glacial fluvial and alluvial deposits along the Severn River also provide some low-lying relief through the muskeg, including potential borrow sources (Ontario Geological Survey 2016). Beyond the limits of the Hudson Bay Lowlands, the surficial geology maps indicate some high ground options and aggregate resource potential that exists in the form of moraines and eskers.

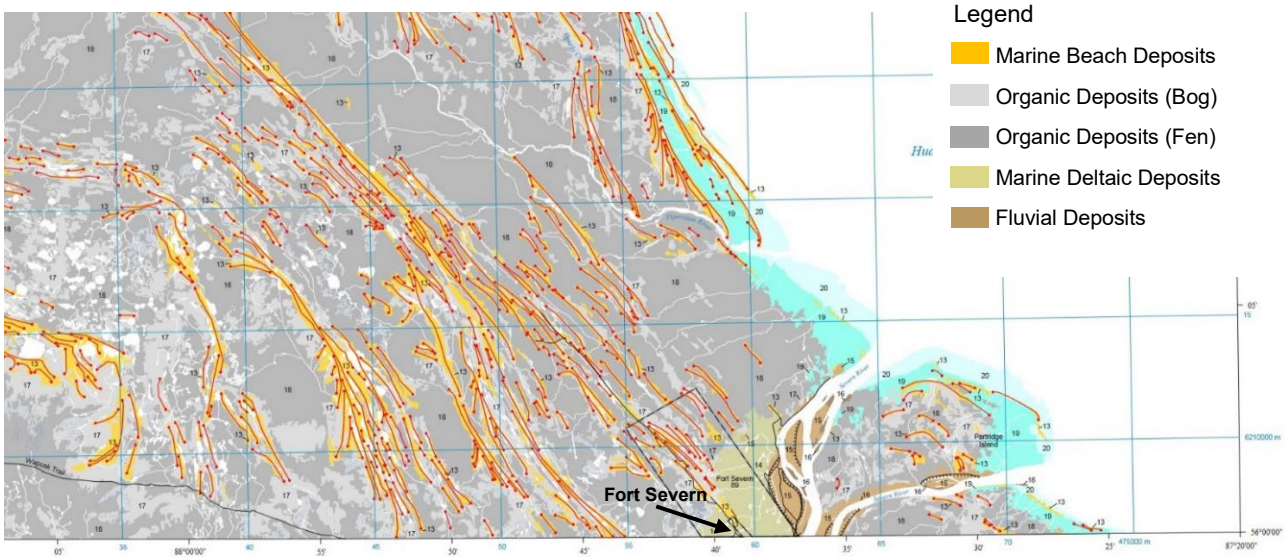

Figure 5. Surficial geology map of Fort Severn, Ontario at a scale of 1:100,000 (Ontario Geological Survey 2016).

2.2 Alternative Route Development

There are significant construction challenges and costing implications linked to the design and construction of a route through the Hudson Bay Lowlands. The length of any route examined spans a large region and the terrain characteristics change drastically along the alignment in terms of vegetation, material composition, and variable permafrost conditions. The region also has numerous environmentally sensitive areas and species at risk that further complicates the routing process. A climate sensitive routing strategy was used to focus on high ground options, minimize areas of high risk, and limit the traversing of environmentally and culturally sensitive areas.

Figure 6. Existing FSFN winter road route through muskeg terrain and across lakes.

Development of several alternative route options along the existing alignment were considered in the initial stages of the project. However, it was found that no re-alignment option had measurable improvement over the existing alignment. The beach ridges that exist become less prominent farther away from the coastline and the existing route mainly runs perpendicular to the ridges and does not provide the opportunity to route long sections directly on the ridges (Figure 6). Furthermore, the cost and construction of ground improvements would be expensive and challenging due to long sections of muskeg terrain that could not be avoided and the limited borrow sources that exist near the alignment.

Therefore, three new alternative routes were developed. The route alternatives are depicted in Figure 7 and include the following:

- Alternative Route 1 – Southern Coastal Route to Gillam, MB
- Alternative Route 2 – Northern Coastal Route to Gillam, MB
- Alternative Route 3 – Ontario Route to Bearskin Lake FN, ON

Alternative Route 1 and 2 follow along the coastline of Hudson Bay to utilize the beach ridges that can provide a favorable running surface and tree cover. The beach ridges provide numerous options for potential alignments along the coast; however, two main alternative routes were identified along the more prominent and continuous beach ridge features.

Alternative Route 3 was developed along the Severn River to take advantage of potential fluvial deposits and tree cover along the river system. Where the alignment was routed along the Severn River, it was important to remain close to the top of the bank to capture potential fluvial deposits and tree cover but offset far enough to reduce the risk of slope instabilities and natural riverbank erosional processes.

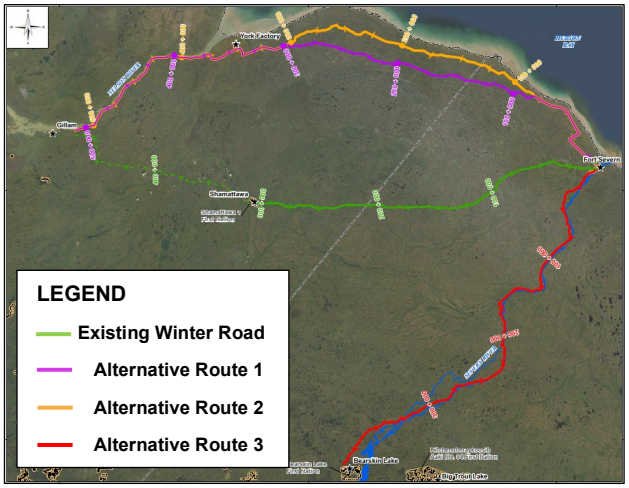

Figure 7. Alternative route options and the existing FSFN winter road alignment.

2.3 Desktop Assessment of Route Options

The alternative route options were evaluated based on the following general criteria:

- Design and Construction Challenges
- Operation and Maintenance
- Safety
- Cost
- Community Preference

The general criteria outlined above can be further defined by specific characteristics along each route alternative. A summary of key routing characteristics for each alternative route are shown in Tables 1, 2, and 3. These characteristics were used as part of the evaluation of each alternative.

Table 1. Percentage of terrain type crossed by each alternative route.

Terrain Type [%]	Route 1	Route 2	Route 3
Beach Ridges[1]	53	56	0
Forested Area[2]	32	31	71
Muskeg[3]	16	13	29

[1]Has light grading and light brushing clearing requirements.
[2]Has medium grading and tree clearing requirements.
[3]Requires the muskeg subgrade treatment (Figure 3)

Table 2. Water crossings along each alternative route.

Characteristic	Route 1	Route 2	Route 3
Creeks	221	216	172
Minor Water Crossing[1]	35	45	9
Major Water Crossing[2]	9	11	3
Ponds and Lakes	0	0	3

[1]defined as 5 to 40 m wide from shoreline to shoreline
[2]defined as greater than 40 m wide from shoreline to shoreline

Table 3. Constructable length of each alternative route

Characteristic	Route 1	Route 2	Route 3
Total Length[1]	509 km	515 km	392 km
Est.Travel Time[2]	18.5 hr	18.5 hr	23 hr

[1]Total length of a newly constructed winter road
[2]Estimated travel time to FSFN's preferred destination of Winnipeg, MB

2.4 Field Assessment of Terrain Suitability and Risk Along Alternative Routes

Following a review of aerial imagery based surficial mapping, a helicopter reconnaissance, with limited ground truthing, was conducted to assess the suitability of the terrain from a field perspective and outline potential risks of constructing a winter road along each alternative route.

The reconnaissance confirmed that the beach ridges were abundant throughout the initial 330 km of Alternative Routes 1 and 2 and offer an effective option for a new winter road alignment. It was confirmed through ground truthing that the beach ridges were composed of dry sand and gravel deposits with minimal fines content. These soils will freeze more readily than the neighboring organic terrain which was saturated at or near the ground surface.

The beach ridges also had sufficient tree cover to act as a windbreak against snow drifting when offset a minimum of 20 km from the coastline (Figure 8). The risk of putting a new winter road alignment on the existing ridges is low given that their material composition is ideal for hard freezing conditions and the community has demonstrated that all-season roads on the ridges are functional and require minimal operation maintenance (Figure 9 and 10). The beach ridge material is also suitable as borrow for the muskeg ground improvement. Using these ridges sets up the project for a future all season road which will be required at some point as climate change progresses.

It was determined during the helicopter reconnaissance that Alternative Route 2 would not be considered a feasible route in comparison to Alternative Route 1 due to the lack of tree coverage near the coastline (Figure 11) and because the ridges were smaller in width and height. Tree cover was an important safety consideration for the community as it will provide improved driving visibility and some protection from the coastal winds.

Figure 8. Beach ridges near the Hudson Bay coastline with tree cover along Alternative Route 1.

Figure 9. Existing FSFN community road located on a beach ridge north of the airport.

Figure 10. Aerial view of existing FSFN community road north of airport located on a beach ridge.

Figure 11. Beach ridges without tree cover near the Hudson Bay coastline on Alternative Route 2.

Areas routed along major river systems, such as the Nelson River and Severn River, were targeted for the moderate tree cover present and borrow potential. However, the helicopter reconnaissance proved that these areas are complex in terms of major permafrost thaw, riverbank instability, the presence of organic terrain near the top of the riverbank, and steep grades at water crossings. The helicopter reconnaissance also determined that a greater offset from riverbanks will be required to avoid slope instability and permafrost thaw slumps. However, this will require the alignment to traverse longer, and most likely deeper, sections of organic terrain as shown in Figure 12, where the organic terrain is immediately adjacent to the top of bank.

Figure 12. Muskeg terrain along Alternative Route 3 directly adjacent to the Severn River, Ontario.

One challenge to constructing a permanent embankment in the organic terrain will be navigating the widespread permafrost thaw that was observed across the entire project area, as shown in Figure 13. It became clear over the course of the helicopter reconnaissance that, although engineers have historically built our infrastructure to preserve and maintain permafrost soils, it has now become clear that the design and construction of infrastructure should consider the inevitable thawing of permafrost.

Figure 13. Widespread permafrost thaw (thermokarst) along the Nelson River in Manitoba.

2.5 Evaluation of Route Options

Alternative Route 1 was determined to be the most economical route option while carrying the least amount of long-term risk for a winter road, despite the route having one of the longer constructable lengths in the study. The route will still traverse some difficult areas. Although comparatively feasible from an engineering perspective, Alternative Route 2 was not considered to be a suitable alternative with the increased safety hazard of coastal proximity and limited tree cover. Alternative Route 3 was deemed to be high risk and did not result in a measurable improvement over the existing winter road route, as a majority of the route would require extensive construction of ground improvement techniques while avoiding riverbank instability and permafrost thaw slumps. Based on the feasibility study results, it was concluded that Alternative Route 1 poses the least risk for a potential winter road relocation, a conclusion that was supported by the FSFN community from their personal experience.

The helicopter reconnaissance confirmed that permafrost degradation poses the highest long-term risk to the region as the ever-changing subgrade conditions will affect the way northern infrastructure is designed and maintained. Therefore, the current extent of permafrost, temperature profiles, percentages of ice content and related anticipated ground subsidence must all be taken into consideration in the muskeg ground improvement design. All these factors contribute to the complexity of the terrain as the region is constantly changing due to climate warming. The next project stages will be to conduct additional geotechnical investigations and temperature instrumentation, ground ice mapping and monitoring, thermal modelling, and the construction of a ground improvement test section to assess the short- and long-term performance of the muskeg subgrade treatment.

3 CONCLUSIONS

Inaccessible by permanent or all-season road networks, remote First Nation communities rely on winter roads as a cost-effective means of ground transportation for goods and services such as the delivery of fuel, food, construction materials and equipment. The case study examined in this

paper is characteristic of the ongoing problems facing the entirety of the Canadian winter road network; diminishing serviceability, reduced operating windows, and increasing maintenance efforts. Historically routed through flat terrain such as muskeg and lakes, these conventional routes are no longer considered to be sustainable with a warming climate. Areas of permafrost are continuing to warm and melt, creating additional engineering challenges that change our traditional permafrost engineering methodology, which was once to preserve perennially frozen ground.

The case study applied climate sensitive routing strategies to determine the feasibility of the relocation and redesign of the Fort Severn First Nation Winter Road. Alternative alignment options that were adaptive to climate warming and minimize overall environmental impact were selected to provide a sustainable and cost-effective route option. In areas of muskeg, it is recommended that ground improvement techniques be implemented along winter road alignments in anticipation of a warming climate, recognizing that areas of muskeg within the Hudson Bay Lowlands cannot be avoided. Permanent crossing structures should be considered where water crossings are unavoidable to increase the longevity of a winter road season. It was determined that Alternative Route 1 along the beach ridges was the most economical option while providing the least engineering and climate-based risk.

It is now becoming crucial to relocate existing winter road systems to areas where alignments will be more resilient to climate change. Innovative and adaptive solutions will be required to maintain access to remote communities as climate change will eventually eliminate these seasonal roads on their present alignments.

4 REFERENCES

Bush, E. and Lemmen, D.S. (eds.) 2019. 'Canada's Changing Climate Report', *Government of Canada*, 444 p.

Forestry Civil Engineering 2010. *Floating Roads on Peat*. Inverness, Scotland: Scottish Natural Heritage, 82 p.

Government of Canada 2023. *Environment Canada Historical Climate Data*. Available at: https://climate.weather.gc.ca/historical_data/search_historic_data_e.html (Accessed: September 7, 2023).

Hobbs, N. 1986. 'Mire Morphology and the Properties and Behaviour of some British and Foreign Peats', *Quaternary Journal of Engineering Geology and Hydrogeology* 19(1), pp. 7–80. ISSN: 0481-2085

Hori, Y., Gough, W.A., Butler, K., and Tsuji, L.J. 2017. 'Trends in the seasonal length and opening dates of a winter road in the western James Bay region, Ontario, Canada', *Theoretical and Applied Climatology*129(3–4), pp. 1309–1320. doi:10.1007/s00704-016-1855-1.

Hori, Y., Cheng, V.Y., Gough, W.A., Jien, J.Y., and Tsuji, L.J. 2018. 'Implications of projected climate change on winter road systems in Ontario's Far North, Canada', *Climatic Change* 148(1), pp. 1–14. doi:10.1007/s10584-018-2178-2.

Kuryuk, D. 2003. 'Winter Roads in Manitoba', in *Proceedings of the 12th Workshop on the Hydraulics of Ice-Covered Rivers*, Edmonton, Alberta, Canada.

Munro, R. 2004. *Dealing with Bearing Capacity Problems on Low Volume Roads Constructed on Peat*. Inverness, Scotland: The ROADEX Project. Available at: www.roadex.org (Accessed: September 8, 2023).

NOAA 2023. 'Climate at a Glance: Global Time Series', *National Centers for Environmental Information*. Available at: https://www.ncei.noaa.gov/access/monitoring/climate-at-a-glance/global/time-series (Accessed: September 7, 2023).

Ontario Geological Survey 2016. 'Surficial Geology of Black Duck River Area Southeast', *Ontario Geological Survey* P3627, scale 1:100,000.

Phukan, A. 1982. 'Design Methods for Muskeg Area Roads', *Alaska Department of Transportation and Public Facilities*, Fairbanks, Alaska, United States.

Prairie Climate Centre 2019. *Climate Atlas of Canada*. Version 2, July 10, 2019. Available at https://climateatlas.ca.

Sigfusson, S. 1992. *Sigfusson's Roads*. Winnipeg, Manitoba, Canada: Watson and Dwyer Publishing Ltd.

Underestimated permafrost landforms – Block and talus slope distribution in the Dry Andes of Argentina

Tamara Köhler[1], Anna Schoch-Baumann[1], Rainer Bell[1], Diana Agostina Ortiz[1], Philipp Reichartz[1], Lothar Schrott[1] & Dario Trombotto Liaudat[2]

[1]*Department of Geography, University of Bonn, Meckenheimer Allee 166, 53115 Bonn, Germany*

[2]*Geocryology, IANIGLA, CCT CONICET Mendoza, Argentina*

ABSTRACT

There is a lack of explanatory approaches and analytical data on distribution patterns, landform characteristics and formative controls of block and talus slopes in the Dry Andes of Argentina, despite these being widespread and characteristic elements of the extensive periglacial belt. Their spatial distribution, internal structure and ice content have received far less attention than rock glaciers, which are included in regional and national inventories and have been studied systematically in the last decades (e.g., IANIGLA-CONICET, 2018). We extend these inventories by block and talus slopes based on a remote-sensing and field-based geomorphological mapping approach in the Agua Negra catchment (30°S, 69°W). Three sub-catchments were chosen for the manual mapping approach, reflecting the overall heterogeneity of the study area and ensuring transferability. Analysis of the uppermost sub-catchment alone reveals that only 1.6% of the surface are covered by rock glaciers, while block and talus slopes cover almost 80%. These landforms are by far the most dominant geomorphic features in the basin, typical in this part of the Andes and probably—in terms of surface area, vertical extension and permafrost distribution—unique in mountain systems worldwide. By using geomorphological mapping and statistical evaluation, spatial distribution patterns are captured and analyzed, thus providing the foundation for further analyses such as geophysical prospection and upscaling. Especially in light of global climate change, understanding the spatial distribution of potentially ice-rich permafrost landforms is imperative to assess available water resources, water quality and their evolution.

1 INTRODUCTION

The Andean cryosphere is an important hydrological reservoir that controls runoff and groundwater recharge through glacier melt, precipitation, snowmelt, and water releases from the active layer in permafrost areas (Masiokas et al. 2020; Halla et al. 2021). Especially in drought-prone areas with limited glaciation, periglacial landforms are hydrologically significant (Schaffer et al. 2019; Masiokas et al. 2020). Their delayed response to global warming will even increase their importance in the future (Schaffer et al. 2019; Arenson et al. 2022). The observed rapid glacier retreat, the significant decrease in snowfall and snow persistence as well as the increased permafrost degradation in the Argentinian Andes due to global climate change were addressed in 2010 with a national statute to protect glaciers and the periglacial environment (Masiokas et al. 2020; Blöthe et al. 2021). One of the most important outcomes was the creation of a national glacier inventory, mapping cryospheric landforms under protection (IANIGLA-CONICET 2018).

Within the Dry Andean periglacial belt, the most visible expression of mountain permafrost are rock glaciers, whose distribution and internal structure have been studied systematically (Villarroel et al. 2018; Blöthe et al. 2021; Halla et al. 2021). They are recorded in the Argentinian national inventory, while more widespread permafrost-affected block and talus slopes have received less attention. Talus slopes are sheeted and cone-shaped debris accumulations below free rock faces mainly fed by rockfall (Lambiel and Pieracci 2008; Kenner et al. 2017). They are characteristic features of periglacial mountain regions and have been subject to frequent research (e.g., Sass 2006; Lambiel and Pieracci 2008; Scapozza et al. 2015; Kenner et al. 2017). Studies on periglacial talus slopes in the Swiss Alps found possible ice contents of about 20–60% (Scapozza et al. 2015). However, there is a significant data gap in the Andes, where they were mainly examined as debris sources of talus-derived rock glaciers (e.g., Halla et al. 2021), or in terms of debris movement (Pérez 1993) and hydrological characteristics (Caballero et al. 2002). Even less research on a global scale has been devoted to blockslopes, which is not least due to varying terminology and definitions. Blockslopes, often also termed rectilinear debris-mantled slopes (Kamp et al. 2005; Trombotto Liaudat et al. 2014; French 2017) or Richter (denudation) slopes (Augustinus and Selby 1990; Fort and van Vliet-Lanoe 2007) are straight slopes of in situ weathered material. They were mainly described in the ice-free areas of Antarctica (e.g., Augustinus and Selby 1990; French 2017). Earlier studies mention their vast distribution in the semiarid to arid Andes (Garleff and Stingl 1983; Trombotto 2000; Kamp et al. 2005). If these landforms contain a not yet quantified amount of ice, they gain hydrological significance due to their large distribution in the Andes. Thus, our study investigates the spatial distribution of taluses and blockslopes in a semiarid high Andean catchment by combining geomorphological mapping and statistical terrain analysis. Our results are an extension of the existing national inventory on cryospheric landforms (IANIGLA-CONICET 2018), to quantify these underestimated permafrost landforms in the Dry Andes of Argentina.

https://doi.org/10.52381/ICOP2024.151.1

2 STUDY AREA

The Agua Negra catchment (ANC) is located in the Cordillera Frontal of the San Juan province in the Dry Andes of Argentina. It is part of the Desert Andes near the southern transition to the Central Andes (Esper Angillieri 2009), where we can see a distinct increase in cryospheric landform cover reaching down to about 3000 m asl (Figure 1). The Desert Andes are characterized by extremely low mean annual precipitation (< 250 mm) mainly falling during winter months as snow or sleet above 4000 m asl (Minetti et al. 1986; Lliboutry 1998). Snow cover is comparatively thin and of short duration (~3 months) due to the effect of high incoming solar radiation throughout the year, controlling surface temperatures and upper ground thermal regimes (Schrott 1994; Lliboutry 1998). The drier conditions in this part of the Dry Andes are also reflected by the distribution of cryogenic landforms in terms of areal coverage and altitude (Figure 1c). The median 0 °C isotherm rises by almost 1000 m compared to the Central Andes, as does the lower limit of glaciers. Rock glacier distribution is mainly concentrated in an altitudinal band between 4500 and 5000 m asl. While the areal extent of glaciers clearly dominates over periglacial forms in the Central Andes, the importance of the latter increases significantly in the Desert Andes (Sattler et al. 2016). Information on the geology is only available in coarse resolution and indicates that the ANC comprises different geological units. The Paleozoic basement of marine sedimentary rocks and local granite intrusions is covered mainly by Permian to Triassic volcanic and volcanoclastic rocks of the Choiyoi Group, accounting for almost 64% of the upland area (SEGEMAR 2019).

Within an area of 1315 km^2 the ANC covers an altitudinal range of 4735 m, with the highest peak reaching 6280 m asl. The mean precipitation dataset of the Climate Hazards Group InfraRed Precipitation with Station data (CHIRPS) from 1981 to 2020 (Funk et al. 2014) shows a mean precipitation sum of about 53 mm/yr in the lowland parts of the catchment and up to 131 mm/yr in the upland. A meteorological station in front of the Agua Negra glacier reports high global radiation values of ~430 W/m^{2}d^{-1} and low mean relative humidity of ~30% (Pitte et al. 2022). Scattered morainic remnants detectable in the whole ANC as well as the U-shaped main valley prove the more extensive glacial imprint in the catchment in the past. However, no mapping of moraines or stratigraphical studies indicating Pleistocene glaciations are available for this part of the Andes. At present, the basin shows regionally representative cryospheric conditions (Gruber 2012; IANIGLA-CONICET 2018), enabling the transferability of the results within the semiarid Argentinean Andes. It has a low glacial coverage of 1.44% and a large vertical extent of mountain permafrost of almost 2600 m with respect to the regional lower permafrost limit at ~3700 m asl (Trombotto 2000; Gruber 2012). In the entire catchment, 59 rock glaciers are mapped (IANIGLA-CONICET 2018), comprising an area of 5 km^2 or 0.38%. With 667.78 km^2 identified as areas with potential permafrost (Gruber 2012; Figure 1b) there is a clear spatial deviation between the mapped rock glaciers and the potential permafrost distribution.

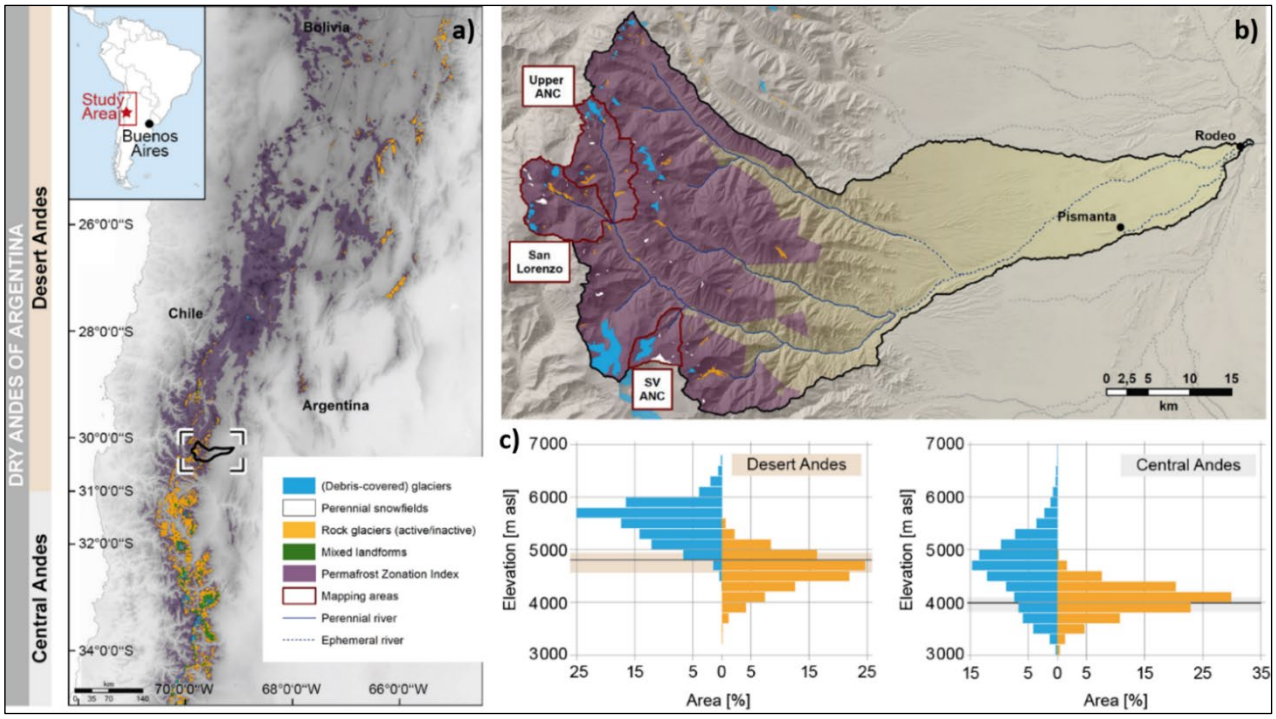

Figure 1. a) Overview of the location and cryospheric composition of the Dry Andes of Argentina, with c) the regional area-elevation distribution of glacial and periglacial landforms including the median elevation of the 0 °C isotherm surrounded by 25–75 % quantiles, calculated from ERA-5 monthly re-analysis data averaged from 1940 to present (Hersbach et al. 2023). b) Detailed overview of the study area of the Agua Negra catchment with the manual mapping areas. Permafrost Zonation Index (very low to high possibilities) based on Gruber (2012), cryospheric landforms taken from IANIGLA-CONICET (2018). Landforms in a) were optically enlarged by a 1-pt frame to enable visibility.

The basin is drained by the Agua Negra River and its tributaries, mainly fed by the meltwaters of surrounding glaciers and seasonal to perennial snowfields, precipitation, as well as contributions from active layer thawing and permafrost degradation (Halla et al. 2021, Schrott 1996). Discharge measurements confirmed that water released from the active layer and seasonally frozen ground may constitute ~30% of total discharge during the summer months in the upper ANC (Schrott 1996).

3 METHODS

We conduct a remote sensing and field-based geomorphological mapping approach of block and talus slopes in three sub-catchments of the ANC, building on the existing national inventory of cryospheric landforms (IANIGLA-CONICET 2018; Figure 1). Our mapping results are statistically evaluated to analyze the spatial distribution, characteristics and formative controls of the target landforms.

3.1 Geomorphological mapping

A geomorphological map of blockslopes, taluses and bedrock was created based on satellite imagery (Esri, Google Earth Pro) and a TanDEM-X DEM (12 m resolution). We used satellite imagery from austral summer months with minimum snow cover and shading to improve mapping accuracy. The upper ANC, San Lorenzo catchment (SLC) and a side valley in the ANC (SV ANC) were selected for manual mapping to reflect the overall heterogeneity of the basin. All three sub-catchments lie within the Permafrost Zonation Index (Gruber 2012, Figure 1a, b). Furthermore, their altitudinal range, valley orientation, size and ratio of glacial and periglacial landforms is representative. Rock glaciers, (debris-covered) glaciers and perennial snowfields (IANIGLA-CONICET 2018) as well as bedrock (manually mapped) were used to support mapping accuracy and to allow for a comparative spatial quantification of all cryospheric landforms in the sub-catchments. The inventory-based, restricted rock glacier delineation was extended to include front and marginal parts (RGIK 2022). The final output is an extended geomorphological map of cryospheric landforms (Figure 2), accurately delineating blockslopes and taluses that serve as input for the statistical analysis.

3.2 Statistical Analysis

A pixel-based analysis of block and talus slope distribution based on 15 individual variables reflecting topography, surface morphology and climatic conditions on different spatial scales was conducted to determine their spatial distribution, landform characteristics and formative controls (Table 1). In addition, the statistical analysis provides valuable insights into the suitability of the applied variables for future geostatistical modeling and semi-automatic mapping of block and talus slopes on a larger spatial scale. Since there is little information on suitable variables characterizing the distribution of blockslopes and taluses, we selected and adopted variables from comparable landform distribution studies in (periglacial) mountain landscapes (see references in Table 1). The original and

Table 1. Input variables for the statistical analysis calculated on different resolutions (12 m original TanDEM-X; *60 m resampled TanDEM-X using bilinear interpolation). ([1]Blöthe et al. 2021; [2]Brenning 2009; [3]Deluigi et al. 2017; [4]Groh and Blöthe 2019; [5]Heckmann et al. 2014; [6]IANIGLA-CONICET 2018; [7]Janke 2013; [8]Cavalli et al. 2013; [9]Otto et al. 2018; [10]Riley et al. 1999; [11]Sattler et al. 2016; [12]Schoch et al. 2018; [13]Weiss 2001).

Variable	Description	References (sel.)
Elevation	Altitude [m asl]	[3] [4]
Slope	Slope gradient [°]	[5] [11] [12]
Topographic position index (TPI_{33})	Topographic slope position based on elevation comparison of one cell to its surrounding neighborhood in a rectangular 33x33 cell moving window $TPI = z_0 - z_{mean}$ [1]	[13]
Curvature* (overall, planform, profile)	*Overall, planform (vertical) and profile (horizontal)* slope concavity and convexity	[3] [4] [5] [7]
Aspect	*North-exposedness*, cosine of the aspect	[1] [3] [12]
	East-exposedness, sine of the aspect	[1] [12]
Potential incoming solar radiation (PISR)	For the entire year 2022 based on topographic position and relief (DEM) [MWh/m^2]	[3] [11]
Topographic wetness index (TWI)	Areas with topography-controlled water accumulation defined by slope (ß) and upstream contributing area based on the D8-flow algorithm (A) $TWI = \ln(A / \tan(ß))$ [2]	[9]
Topographic roughness index (TRI, TRI_{60}*)	Elevation difference from a center cell and its surrounding neighborhood in a 3x3 cell moving window	[5] [9] [10]
Size of the contributing area (SCA)	Size of the contributing area [m^2], calculated using the D8-flow algorithm, log-transformed	[2] [4] [12]
Mean roughness of the contributing area (MRCA)	TRI-weighted flow accumulation divided by unweighted flow accumulation (D8-flow algorithm)	[5] [8]
Mean slope of the contributing area (MSCA)	Slope-weighted flow accumulation divided by unweighted flow accumulation (D8-flow algorithm)	[2] [4] [12]

the resampled (60 m) TanDEM-X DEM were used to analyze differences in the distribution and landform characteristics on several spatial scales.

We applied parameters representing topographic conditions and surface morphology (e.g., curvature, topographic roughness) as well as landform characteristics (e.g., slope inclination, different characteristics of the contributing area). To represent climatic and moisture conditions, the elevation as well as the potential incoming solar radiation (PISR) and topographic wetness (TWI) were used, since there is no meteorological network to interpolate climatic variables from measured data. The coarse resolution of satellite-derived meteorological data is insufficient for the study purpose and highly uncertain in high mountains.

Boxplots are used to summarize, examine and compare the distribution of the target landforms visually for each variable. Differences in the distribution of explanatory variables for block and talus slopes were tested for significant statistical differences ($p < 0.05$) using the Kruskal-Wallis and the Wilcoxon rank sum test for non-parametric data. Here, we present a summary of the combined analysis, detailed results of the single sub-catchments can be accessed online (http://dx.doi.org/10.13140/RG.2.2.24348.67200/1).

4 RESULTS

Block and talus slopes are widely distributed in all three sub-catchments (Figure 2). Blockslopes are by far the most dominant landform accounting for more than 60% of the areal surface. In the Upper ANC and SLC, talus slopes are the secondary landform with ~12% areal coverage, while in the more glacier and snow influenced SV ANC they account for only 2.4%. In the upper ANC, a distinct difference between the main valley slopes bordering the Agua Negra River can be observed. West of the small mountain stream with dominant slope exposures to N and E, blockslopes have a vast and uniform distribution. On the eastern valley slopes, the proportion of extensive talus sheets and coalescing talus cones below (channelized) steep cliffs increases. More than 60% of the talus coverage in the Upper ANC is located east of the Agua Negra River. The dominance of blockslopes on N and E exposed slopes is also very evident in the SV ANC, as well as southwest of the San Lorenzo stream in the SLC, though less distinct. Both landforms exhibit statistically significant ($p < 0.05$) differences for all analyzed variables, enabling statements about the distribution and formation conditions (Figure 3). As represented by the topographic position index (TPI), blockslopes mainly cover low relief plateaus and upper to middle slopes, sparsely dissected by alluvial channels or bedrock outcrops. Talus slopes primarily occur in lower slope positions bordering channels and river floodplains. The elevation differences of the landforms are particularly notable (Figure 3). Even though blockslopes were mapped at nearly all considered elevations, they are dominating between 4900 m and 5500 m asl, with an elevation mean at 5194 m asl. Talus slopes, however, are distributed in a narrower interquartile range of 4300 m and 4700 m asl with a mean elevation of 4540 m asl and an upper limit of ~5300 m asl. Upslope they are limited by bedrock outcrops feeding the talus that are incorporated in the statistical analysis due to their higher roughness values. Hence, the mean roughness values of the contributing area (MRCA) are higher. Large bedrock outcrops on the middle and upper slopes are also associated with thick talus formation. Where the material is additionally channelized, cone-

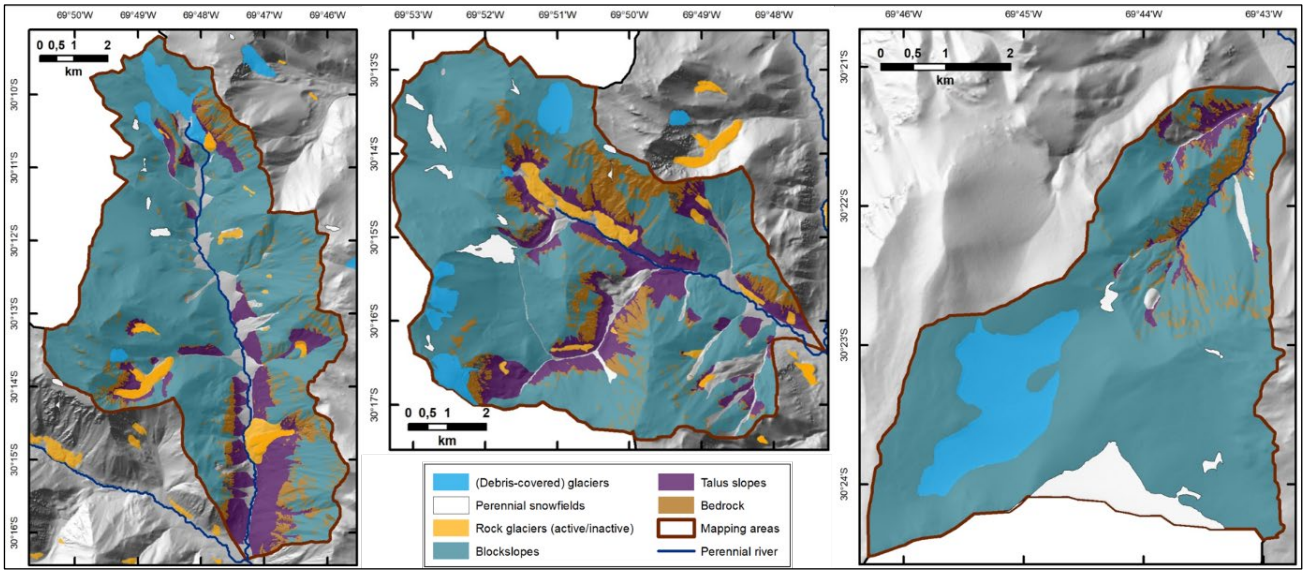

Figure 2. Geomorphological maps of blockslope, talus and bedrock distribution in the three sub-catchments of the Agua Negra catchment, with (from left to right) the Upper Agua Negra catchment (Upper ANC), San Lorenzo catchment (SLC) and the side valley farther downstream the Agua Nera catchment (SV ANC); see Figure 1 for locations. (Debris-covered) glaciers, perennial snowfields and rock glaciers from IANIGLA-CONICET (2018). The map shows the extended rock glacier outline including frontal and marginal parts (based on RGIK 2022). Note the different scales of the catchments.

shaped taluses, protalus ramparts and talus-derived rock glaciers can be found.

Talus slopes are characterized by greater mean slope inclination around 25–28° of the landform itself, but also of the contributing area (MSCA). Blockslopes mainly range from 17–22°. Despite their different slope angles, both slope types mainly occur horizontally and vertically elongate, although this pattern is much more distinct for blockslopes. For blockslopes, all three curvature layers show mean values of ±0.0, indicating a remarkable slope linearity in horizontal and vertical direction. Talus slopes, however, display a tendency towards horizontal and vertical concavity, indicated by slightly positive profile and slightly negative planform curvature (Figure 3).

While talus slopes show no clear tie to aspect except for a certain dominance in southern exposures in the three sub-catchments, blockslopes occur more frequently on N and E-facing hillsides, resulting in higher insolation (+ 0.34 MWh m^{-2}). The topographic roughness indices TRI and TRI_{60} indicate higher roughness for taluses with the latter one showing more pronounced differences between the two landforms. Although the distributional differences between blockslopes and taluses are statistically significant for all examined variables, the TWI shows the smallest effect on their distribution patterns. Both landforms show the same tendency towards low potential topographic water accumulation, and differences in contributing area sizes (SCA) are rather small. Taluses have slightly larger catchments on average, corresponding to their topographic positions in the catchments.

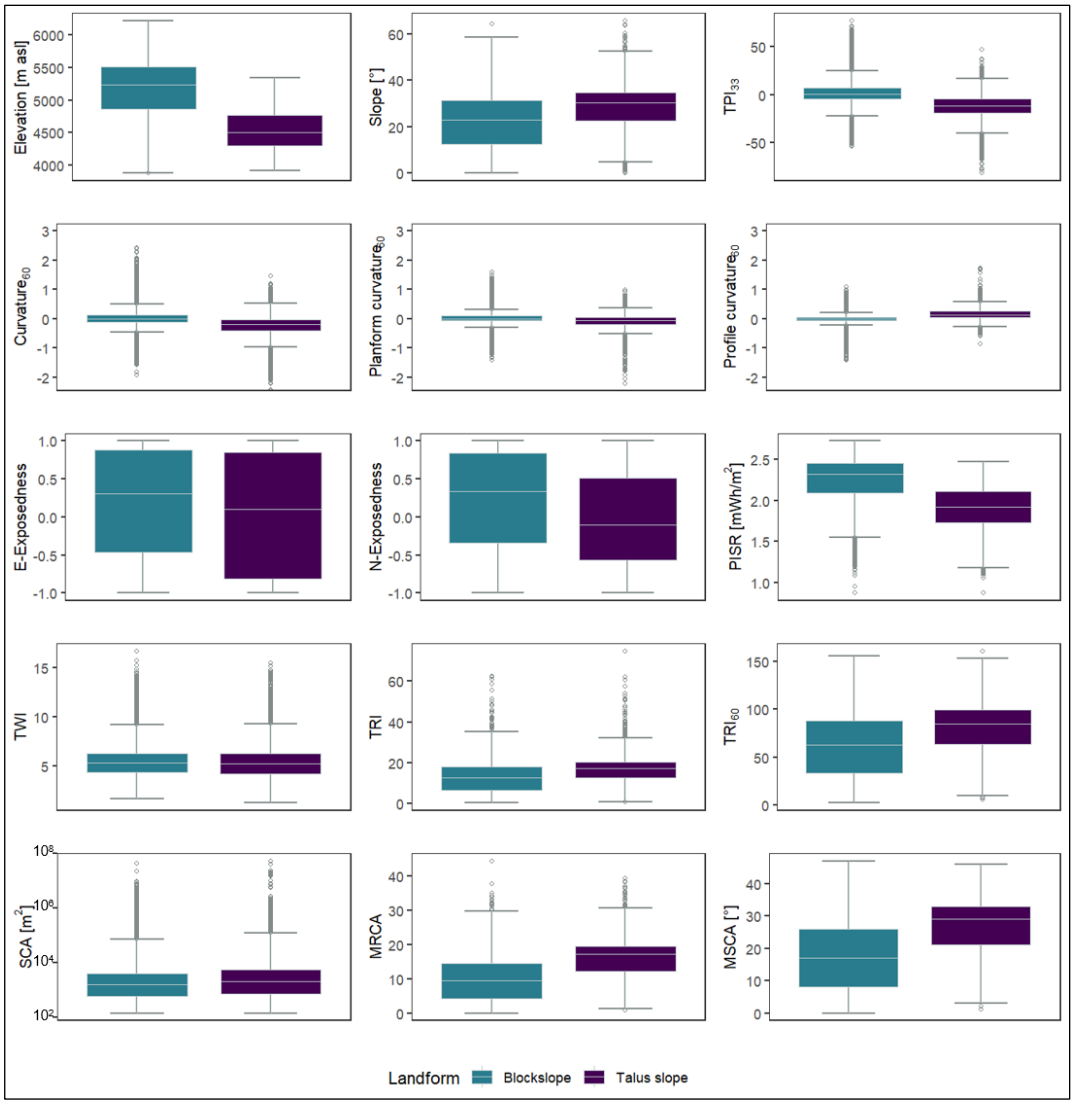

Figure 3. Boxplots showing the median and interquartile range for the analyzed environmental variables for both target landforms in all three manual mapping areas (further details and abbreviations in Table 1). Block and talus slopes show statistically significant differences ($p < 0.05$) for all examined variables.

4 DISCUSSION

The statistical analysis of the environmental characteristics of block and talus slopes point out important factors for their formation. The distribution of variables allows inferences about the characteristics and distribution of the landforms. The exceptionally high insolation associated with the semiarid, leeward climatic conditions in the Dry Andes of Argentina seem to greatly favor blockslope formation. Their apparent distribution on high elevation, low-relief plateaus and sparsely dissected, preferentially N and E-exposed upper slopes imply suitable conditions there. Thus, the development of blockslopes seems to be linked to these cold and (semi)arid conditions (e.g., Trombotto Liaudat et al. 2014; French 2017). Their wide distribution at high altitudes, mainly above 5000 m asl, in combination with high exposure to incoming solar radiation benefits strong temperature gradients, effective frost action as well as evaporation and sublimation. This is confirmed by Höllermann (1983), who describes their most common distribution in the upper part of the periglacial or subnival belt at 30–50°N and 29–35°S, with their greatest vertical extent at 30°N and 30°S in sunny exposures. Further variables like a wind shelter index (Veitinger et al. 2016) or geomorphic protection index (Kofler et al. 2020) might be useful for interpretation, as strong wind action in topographically open areas is supposed to contribute to blockslope formation via debris-removal, wind-drift, enhancing dryness and in situ weathering (Garleff and Stingl 1983; Höllermann 1983). The connection of blockslope formation to dry conditions is further supported by very low TWI values. However, talus slopes feature nearly the same TWI values. This is inconsistent with other variables, e.g., curvature, PISR, TPI and N-exposedness that indicate talus occurrence on lower slope positions with higher water-converging planform and profile curvature, and lower insolation (cf. Etzelmüller et al. 2006). The slight upward concavity and intersecting channels observed for talus slopes favor the concentration of water flow and snow accumulation through wind sheltering, thus suggesting higher water availability. A stronger topographic shading matching the smaller PISR can be derived from their higher occurrence on south-facing, lower slope positions in rugged, intersected terrain. Associated protalus rampart and talus-derived rock glacier formation is a clear indication for a certain water availability and moisture content.

We assume that debris supply from the bedrock cliffs exceeds the material removal mainly occurring at the lower talus, since the investigated taluses have a straight to slightly concave profile curvature and a decreasing slope inclination between rock wall and talus (cf. Sass 2006). Thus, sediment storages of considerable size can build up (Otto 2006). The higher slope inclinations of taluses and associated contributing areas indicate a higher angle of repose for talus accumulations beneath steep feeder rock walls compared to blockslopes. This is in accordance with our field observations of coarse-grained talus material compared to finer-grained blockslopes (cf. Otto, 2006). A higher resolution DEM is necessary to visualize grain size differences between blockslopes and taluses with the TRI. The overall higher TRI and TRI_{60} on taluses result from the smaller landform extent in combination with their topographic position bordering large bedrock outcrops, floodplains, incised channels, protalus ramparts and rock glaciers. Due to the coarse resolution of the roughness indices, these are included in the analyses and produce higher values that are not necessarily linked to landform characteristics or formation controls, but distributional patterns. The high range of roughness indices for blockslopes is largely driven by isolated bedrock outcrops below the lower mapping limit of bedrock (30 m^2), which are thus included in the blockslope analysis. Apart from these, blockslopes feature neither evident source areas, nor indications for dominant erosion and deposition with respect to curvature, roughness and slope inclination. Therefore, the presence of a rather thin layer of debris above in situ weathered bedrock is plausible and supported by Trombotto (1991), reporting only thin cryoregolith deposits. The thin debris layer migrates downslope by gravitational processes like (perma)frost creep (Fort and van Vliet-Lanoe 2007; Trombotto Liaudat et al. 2014). Debris supply and debris removal seem to be largely in equilibrium, resulting in the characteristic slope shape at repose angles of the underlying bedrock (French 2017). Their characteristic straight shape without significant channelization or de-/acceleration of debris is reflected in the name "rectilinear" slopes (Trombotto Liaudat et al. 2014; French 2017).

Based on the insulating effect of the thick debris layer and the above-mentioned topographically favorable conditions, we expect higher permafrost probabilities and ice contents in talus slopes than in blockslopes (Lambiel and Pieracci 2008). Trombotto (1991) found not only seasonal ice but permafrost in the taluses of Lagunita del Plata in the Central Andes (33°S, 69°W). In the Swiss Alps, the presence of ice-rich permafrost was mainly reported in the lower parts of the talus slopes with the greatest sediment thickness (Lambiel and Pieracci 2008; Scapozza et al. 2015). Ground ice volumes are presumably lower in blockslopes due to the extremely low TWI, high exposure to insolation and wind as well as a rather thin insulating debris layer with minor impact on ground ice protection. In addition, the low sediment thickness offers smaller storage capacities compared to thick talus accumulations. Nevertheless, the blockslope occurrence in cold and (semi)arid environments provides suitable conditions for permafrost formation (see also Permafrost Zonation Index, Figure 1) and they have been reported in areas with continuous permafrost around this latitude (e.g., Trombotto 2000; Kamp et al. 2005). The potentially low ice contents must be considered in context with their large distribution to make accurate quantifications on different spatial scales.

5 CONCLUSIONS AND OUTLOOK

Block and talus slopes are dominant in the periglacial belt of the Dry Argentinian Andes, accounting for 77.5% (67% blockslopes, 10.5% talus slopes) of the mapped sub-catchments in the ANC. Rock glaciers, by contrast, cover only 1.5% (IANIGLA-CONICET 2018). We demonstrate that both landforms provide suitable permafrost conditions for the presence of ground ice and may gain hydrological significance due to their large extent compared to other periglacial landforms. Talus slopes feature more favourable

conditions for permafrost formation and conservation due to higher insulation capacity of thick debris accumulations in sheltered, water converging lower slope positions. Blockslopes are exposed to higher insolation and frost action at high altitudes in topographically open upper slope positions and plateaus, forming a small layer of in situ weathered debris with potentially lower ice contents. To further assess their role as runoff contributors in the Dry Andes of Argentina, we need distribution analyzes at larger spatial scales and the investigation of their internal structure and potential ice content. These studies gain additional importance in the context of global warming and the depletion of glacial water resources.

6. REFERENCES

Arenson, L.U., Harrington, J.S., Koenig, C.E.M., and Wainstein, P.A. 2022. 'Mountain Permafrost Hydrology—A Practical Review Following Studies from the Andes', *Geosciences* 12(2), p. 48.

Augustinus, P.C. and Selby, M.J. 1990. 'Rock Slope Development in Mcmurdo Oasis, Antarctica, and Implications for Interpretations of Glacial History', *Geografiska Annaler: Series A, Physical Geography* 72(1), pp. 55–62.

Blöthe, J.H., Halla, C., Schwalbe, E., Bottegal, E., Trombotto Liaudat, D., and Schrott, L. 2021. 'Surface velocity fields of active rock glaciers and ice-debris complexes in the Central Andes of Argentina', *Earth Surface Processes and Landforms* 46(2), pp. 504–522.

Brenning, A. 2009. 'Benchmarking classifiers to optimally integrate terrain analysis and multispectral remote sensing in automatic rock glacier detection', *Remote Sensing of Environment* 113(1), pp. 239–247.

Caballero, Y., Jomelli, V., Chevallier, P., and Ribstein, P. 2002. 'Hydrological characteristics of slope deposits in high tropical mountains (Cordillera Real, Bolivia)', *CATENA* 47(2), pp. 101–116.

Cavalli, M., Trevisani, S., Comiti, F., and Marchi, L. 2013. 'Geomorphometric assessment of spatial sediment connectivity in small Alpine catchments', *Geomorphology*, pp. 31–41.

Deluigi, N., Lambiel, C., and Kanevski, M. 2017. 'Data-driven mapping of the potential mountain permafrost distribution', *The Science of the total environment* 590–591, pp. 370–380.

Esper Angillieri, M.Y. 2009. 'A preliminary inventory of rock glaciers at 30°S latitude, Cordillera Frontal of San Juan, Argentina', *Quaternary International* 195(1–2), pp. 151–157.

Etzelmüller, B., Heggem, E.S.F., Sharkhuu, N., Frauenfelder, R., Kääb, A., and Goulden, C. 2006. 'Mountain permafrost distribution modelling using a multi-criteria approach in the Hövsgöl area, northern Mongolia', *Permafrost and Periglacial Processes* 17(2), pp. 91–104.

Fort, M. and van Vliet-Lanoe, B. 2007. 'Permafrost and periglacial environment of Western Tibet', *Landform Analysis* 5, pp. 25–29.

French, H.M. 2017. *The periglacial environment*. Hoboken, NJ, USA: John Wiley & Sons.

Funk, C.C., Peterson, P.J., Landsfeld, M.F., Pedreros, D.H., Verdin, J.P., Rowland, J.D., Romero, B.E., Husak, G.J., Michaelsen, J.C., and Verdin, A.P. 2014. 'A quasi-global precipitation time series for drought monitoring', *US Geological Survey Data Series* 832. doi: https://doi.org/10.3133/ds832.

Garleff, K. and Stingl, H. 1983. 'Hangformen und Hangformung in der periglazialen Höhenstufe der argentinischen Anden zwischen 27° und 55° südliche Breite' in Poser and Schunke (eds.) *Mesoformen des Reliefs im heutigen Periglazialraum. Abhandlungen der Akademie der Wissenschaften Göttingen* 3(35), pp. 425–434.

Groh, T. and Blöthe, J.H. 2019. 'Rock Glacier Kinematics in the Kaunertal, Ötztal Alps, Austria', *Geosciences* 9(9), p. 373.

Gruber, S. 2012. 'Derivation and analysis of a high-resolution estimate of global permafrost zonation', *The Cryosphere* 6(1), pp. 221–233.

Halla, C., Blöthe, J.H., Tapia Baldis, C., Trombotto Liaudat, D., Hilbich, C., Hauck, C., and Schrott, L. 2021. 'Ice content and interannual water storage changes of an active rock glacier in the dry Andes of Argentina', *The Cryosphere* 15(2), pp. 1187–1213.

Heckmann, T., Gegg, K., Gegg, A., and Becht, M. 2014. 'Sample size matters: investigating the effect of sample size on a logistic regression susceptibility model for debris flows', *Natural Hazards and Earth System Sciences* 14(2), pp. 259–278.

Hersbach, H., Bell, B., Berrisford, P., Biavati, G., Horányi, A., Muñoz Sabater, J., Nicolas, J., Peubey, C., Radu, R., Rozum, I., Schepers, D., Simmons, A., Soci, C., Dee, D., and Thépaut, J.-N. (2023). 'ERA5 monthly averaged data on pressure levels from 1940 to present', *Copernicus Climate Change Service (C3S) Climate Data Store (CDS)*. Available at: https://cds.climate.copernicus.eu/cdsapp#!/dataset/reanalysis-era5-pressure-levels-monthly-means?tab=overview.

Höllermann, P. 1983. 'Verbreitung und Typisierung von Glatthängen', in Poser and Schunke (eds.) *Mesoformen des Reliefs im heutigen Periglazialraum. Abhandlungen der Akademie der Wissenschaften Göttingen* 3(35), pp. 241–260.

IANIGLA-CONICET, Ministerio de Ambiente y Desarrollo Sustentable de la Nación 2018. 'IANIGLA-Inventario Nacional de Glaciares', *Informe de la subcuenca del río Blanco*. Cuenca del río San Juan, p. 62.

Janke, J.R. 2013. 'Using airborne LiDAR and USGS DEM data for assessing rock glaciers and glaciers', *Geomorphology* 195, pp. 118–130.

Kamp, U., Bolch, T., and Olsenholler, J. 2005. 'Geomorphometry of Cerro Sillajhuay (Andes, Chile/Bolivia): Comparison of Digital Elevation Models (DEMs) from ASTER Remote Sensing Data and Contour Maps', *Geocarto International* 20(1), pp. 23–33.

Kenner, R., Phillips, M., Hauck, C. Hilbich, C., Mulsow, C., Bühler, Y., Stoffel, A., and Buchroithner, M. 2017. 'New insights on permafrost genesis and conservation in talus slopes based on observations at Flüelapass, Eastern Switzerland', *Geomorphology* 290, pp. 101–113.

Kofler, C., Steger, S., Mair, V., Zebisch, M., Comiti, F., and Schneiderbauer, S. 2020. 'An inventory-driven rock glacier status model (intact vs. relict) for South Tyrol, Eastern Italian Alps', *Geomorphology* 350, 106887.

Lambiel, C. and Pieracci, K. 2008. 'Permafrost distribution in talus slopes located within the alpine periglacial belt, Swiss Alps', *Permafrost and Periglacial Processes* 19(3), pp. 293–304.

Lliboutry, L. 1998. 'Glaciers of the Dry Andes (Glaciers of Chile and Argentina' in R.S. Williams Jr. and J.G. Ferrigno (eds.) *Satellite image atlas of glaciers of the world South America* U.S. Geological Survey Professional Paper 1386-I, pp. 1109–1147.

Masiokas, M.H., Rabatel, A., Rivera, A., Ruiz, L., Pitte, P., Ceballos, J.L., Barcaza, G., Soruco, A., Bown, F., Berthier, E., Dussaillant, I., and MacDonell, S. 2020. 'A Review of the Current State and Recent Changes of the Andean Cryosphere', *Frontiers in Earth Science* 8, p. 99.

Minetti, J.L., Barbieri, P.M., Carletto, M.C., Poblete, A.G., and Sierra, E.M. 1986. 'El régimen de precipitatiòn de la provincia de San Juan', *Informe técnico 8*. CIRSAJ-CONICET, San Juan.

Otto, J.-C. 2006. *Paraglacial sediment storage quantification in the Turtmann Valley, Swiss Alps*. Doctoral dissertation at the University of Bonn, Germany.

Otto, J.-C., Prasicek, G., Blöthe, J., and Schrott, L. 2018. 'GIS applications in geomorphology' in B. Huang (ed.) *Comprehensive Geographic Information Systems*. Bonn, GER: Elsevier Inc., pp. 81–111.

Pérez, F.L. 1993. 'Talus movement in the high equatorial Andes: A synthesis of ten years of data', *Permafrost and Periglacial Processes* 4(3), pp. 199–215.

Pitte, P., Masiokas, M., Gargantini, H., Ruiz, L., Berthier, E., Ferri Hidalgo, L., Zalazar, L, Dussaillant, I., Viale, M., Zorzut, V., Corvalán, E., Scarpa, J.P., Costa, G., and Villalba, R. 2022. 'Recent mass-balance changes of Agua Negra glacier (30°S) in the Desert Andes of Argentina', *Journal of Glaciology* 68(272), pp. 1197–1209.

RGIK 2022. *Towards standard guidelines for inventorying rock glaciers: baseline concepts (version 4.2.2)*. Fribourg, Switzerland: IPA Action Group Rock glacier inventories and kinematics, 13 p.

Riley, S.J., DeGloria, S.D., and Elliot, R. 1999. 'A terrain ruggedness Index that quantifies topographic heterogeneity', *Intermountain Journal of Sciences* 5, pp. 23–27.

Sass, O. 2006. 'Determination of the internal structure of alpine talus deposits using different geophysical methods (Lechtaler Alps, Austria)', *Geomorphology* 80(1–2), pp. 45–58.

Sattler, K., Anderson, B., Mackintosh, A., Norton, K., and de Róiste, M. 2016. 'Estimating Permafrost Distribution in the Maritime Southern Alps, New Zealand, Based on Climatic Conditions at Rock Glacier Sites', *Frontiers in Earth Science* 4, pp. 166–178.

Scapozza, C., Baron, L., and Lambiel, C. 2015. 'Borehole Logging in Alpine Periglacial Talus Slopes (Valais, Swiss Alps)', *Permafrost and Periglacial Processes* 26(1), pp. 67–83.

Schaffer, N., MacDonell, S., Réveillet, M., Yáñez, E., and Valois, R. 2019. 'Rock glaciers as a water resource in a changing climate in the semiarid Chilean Andes', *Regional Environmental Change* 19(5), pp. 1263–1279.

Schoch, A., Blöthe, J.H., Hoffmann, T., and Schrott, L. 2018. 'Multivariate geostatistical modeling of the spatial sediment distribution in a large scale drainage basin, Upper Rhone, Switzerland', *Geomorphology* 303, pp. 375–392.

Schrott, L. 1994. *Die Solarstrahlung als steuernder Faktor im Geosystem der subtropischen semiariden Hochanden (Agua Negra, San Juan, Argentinien)*. Heidelberg, GER: Selbstverlag des Geographischen Institutes der Universität Heidelberg, 199 p.

Schrott, L. 1996. 'Some geomorphological-hydrological aspects of rock glaciers in the Andes (San Juan, Argentina)', *Zeitschrift für Geomorphologie. Supplementband* 104, pp. 161–173.

Servicio Geológico Minero Argentino (SEGEMAR) 2019. *Cartas Geológicas a escala 1:250.000*. https://sigam.segemar.gov.ar/visor/index.html?mapa=12 (Accessed: 14 June 2023).

Trombotto, D. 1991. 'Untersuchungen zum periglazialen Formenschatz und zu periglazialen Sedimenten in der" Lagunita del Plata", Mendoza, Argentinien', *Heidelberger Geographische Arbeiten* 90, p. 171.

Trombotto, D. 2000. 'Survey of cryogenic processes, periglacial forms and permafrost conditions in South America', *Instituto Geológico; Revista Do Instituto Geologico* 21(1–2), pp. 33–55.

Trombotto Liaudat, D., Wainstein, P.A., and Arenson, L.U. 2014. *Guía Terminológica de la Geocriología Sudamericana. Terminological Guide of the South American Geocryology*. Buenos Aires, ARG: Vazquez Mazzini Editores.

Veitinger, J., Purves, R.S., and Sovilla, B. 2016. 'Potential slab avalanche release area identification from estimated winter terrain: a multi-scale, fuzzy logic approach', *Natural Hazards and Earth System Sciences* 16(10), pp. 2211–2225.

Villarroel, C., Tamburini Beliveau, G., Forte, A., Monserrat, O., and Morvillo, M. 2018. 'DInSAR for a Regional Inventory of Active Rock Glaciers in the Dry Andes Mountains of Argentina and Chile with Sentinel-1 Data', *Remote Sensing* 10(10), p. 1588.

Weiss, A. 2001. *Topographic position and landforms analysis*. San Diego, California, United States: ESRI user conference, Poster Presentation.

Thermal condition of Kangirsuk airstrip near Ungava Bay Coast, northern Québec, Canada

Xiangbing Kong[1] & Guy Doré[2]

[1]*Department of Mathematics, Computer Science and Engineering, Université du Québec à Rimouski, Rimouski, Québec, Canada*

[2]*Department of Civil and Water Engineering, Université Laval, Québec City, Québec, Canada*

Abstract

Kangirsuk Airport (Nunavik), completed in 1987, is located in the continuous permafrost zone. The runway is 1190 m long and 60 m wide. Thermistor cables were installed in the runway and the natural ground to monitor soil temperatures. Numerical modeling of the thermal regime of the embankment and subgrade has also been performed to reproduce the conditions and trends in the subsurface thermal regime beneath the embankment. Site-specific parameters, such as soil properties, near-surface air temperature, and embankment dimension, were measured and used as input parameters. Particular interest was paid to the foundation soil under the side slope where relatively rapid permafrost degradation was occurring due to snow accumulation. These results help government agencies evaluate the thermal conditions of underlying permafrost and deploy potential adaptation solutions at Kangirsuk, northern Québec.

1 Introduction

Nunavik, located in permafrost regions, constitutes the northern third of the province of Québec, Canada. There are 14 communities in Nunavik; they widely spaced from one another, between 80 and 240 km from the nearest neighbor (Ficheur 2011). Air transportation is essential to ensure communication between local communities and the rest of the province. Ministère des transports du Québec (MTQ) and the Centre d'études nordiques have carried out a research study related to the monitoring of permafrost conditions, during and after the construction of 14 airstrips in Nunavik. Thirteen of 14 airstrips are owned by the MTQ while one is owned by Transport Canada. The majority of the MTQ airstrips are 1090 m long and 44 m wide, covered by gravel material. Of these airports, two are built on sporadic discontinuous permafrost (Kuujjuarapik and Umiujaq).

Access roads between the airport infrastructure and local communities were gravel-surfaced during the construction and were paved in the 2000s to improve performance (L'Hérault et al. 2012). During the construction of the MTQ infrastructure in Nunavik between 1984 and 1991, the climate was relatively stable, and permafrost was considered a solid, permanent foundation. However, since the early 1990s, significant climate warming has been observed in Nunavik (Allard et al. 2018).

After the construction of the airport infrastructures, many permafrost studies were carried out by MTQ and researchers from Centre d'études nordiques to provide the information needed for developing adaptation strategies to counter the thawing of permafrost and for future construction and maintenance of runways and access roads in Nunavik.

The specific objectives of this research activity were to quantify the thermal condition of permafrost underneath the airstrip embankment, using numerical modeling techniques. One potential cost-effective adaptation solution was also proposed at Kangirsuk airstrip, in Nunavik.

2 Study Site and Field Measurement

Kangirsuk is located on the coast of Hudson Strait, 420 km northwest of Kuujjuaq (61.59N; 71.93W); it is a community of 566 inhabitants (Allard et al. 2007a; Figure 1). The village of Kangirsuk is located 10 km from the Hudson Strait, on the southeastern shore of Wakeham Bay. At Kangirsuk, the averaged air freezing index from 2005 to 2016 was 3151 days -°C, while the averaged thawing index for the same period was 895 days -°C. The warmest year was 2009–2010 with an average of -1.8 °C; 2014–2015 was the coldest, with an average of -5.7 °C.

The Kangirsuk airstrip, located in the continuous permafrost zone, is 1190 m long and 60 m wide (Allard et al. 2009). It is oriented along a northeast-southwest axis, with an altitude of over 113 m. A section of the airstrip runway was built over ice-rich till that caused settlement when thawed (L'Hérault et al. 2012). This was one of the main geotechnical problems at the airport. By 2004, an accumulated settlement of approximately 0.5 m was observed (Beaulac 2005). Signs of runway degradation were observed during the fieldwork in the summer of 2009.

To monitor the thermal regime, a thermistor string was installed in 2.9 m deep boreholes under the center of the runway in 2005. It comprised 9 thermistors, with the separation space ranging between 0.1 m and 0.4 m. This string was extended to 6.5 m depth below the embankment-soil interface to monitor the deeper ground thermal regime, in 2016. Data were recorded using a CR10 acquisition system.

In the natural ground, a thermistor string was installed in a 6.5 m deep borehole in 2010. It was located 2 m from the toe of the embankment. There were 10 thermistors, which were spaced by 0.5 m. Data were also recorded using a CR10 acquisition system, which was shared with the thermistor string under the embankment centerline. The thermistor string does not operate well, and limited data were available to analyze the ground thermal regime.

https://doi.org/10.52381/ICOP2024.88.1

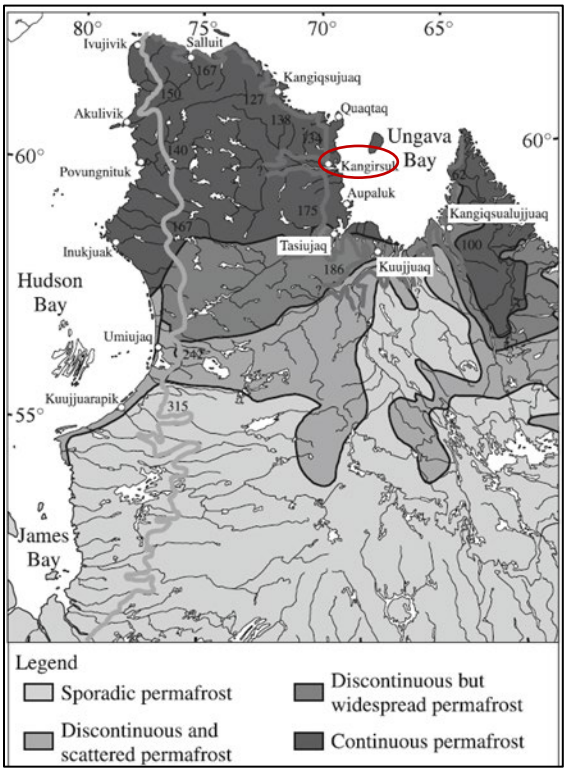

Figure 1. The location of Kangirsuk in Nunivak, Québec (Fortier et al. 2011).

Figure 2. Engineering problem observed at Nunavik, Québec.

Figure 3 illustrates temperature variations under the centerline of the airstrip embankment for 3 years, from November 2016 to August 2018. The embankment thickness was 1.4 m. The interface between the embankment and the natural ground is used as the reference level (0 m), meaning all positive values along the y-axis refer to a position inside the embankment fill. The thawfront penetrated into the natural ground in the summertime from 2016 to 2018. The permafrost table was -0.8 m below the embankment-soil interface in 2016. In the ground, the warming process generally started in June and lasted until November. During winter, there was limited change in the ground temperature from 2016 to 2018. For instance, -1 °C isotherm was located at -2.3 m in 2016 and in 2018.

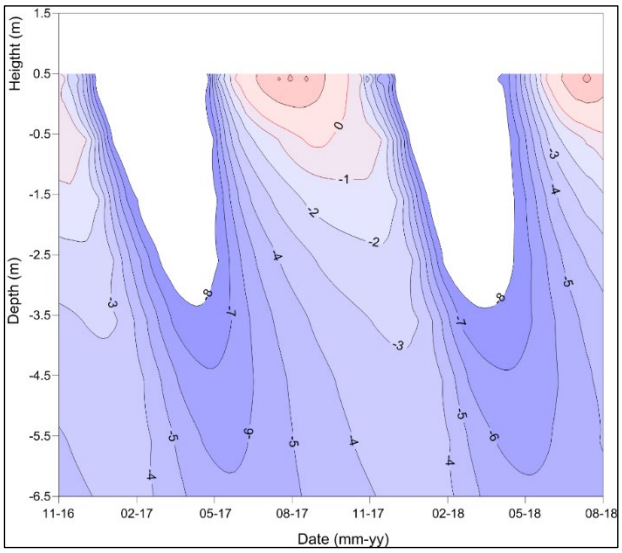

Figure 3. Evolution of embankment and ground temperature with time under the centerline of Kangirsuk airstrip, Nunavik, Canada.

The ground temperature varies with time due to many factors, including solar radiation, snow thinness, and soil depth. Figure 4 shows the temperature profiles with depth for selected mid-months under the centerline of the airstrip embankment, in 2017. The temperature profiles demonstrate a temperature range of 15.5 °C at 0.25 m below the embankment surface, with the minimum, and maximum temperatures reaching -22.5 °C and 6.2 °C, respectively. The active layer depth was approximately 0.5 m, in August. The soil temperature was still affected by the seasonal ambient air temperature at -6.6 m below the interface, with the maximum temperature and minimum temperature reaching -3.8 °C and -5.8 °C, respectively.

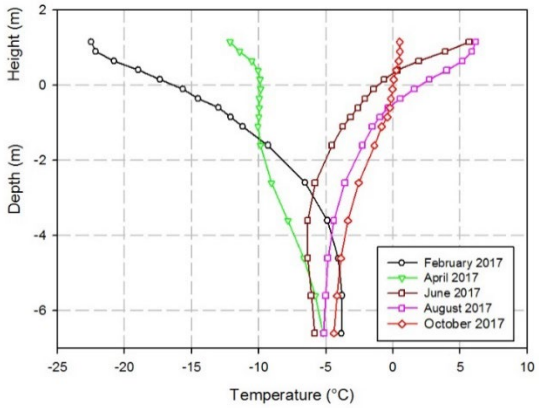

Figure 4. Measured temperature profiles with depth, under the centerline of KIanguirk airstrip, Nunivak, Québec.

3 MODEL DEVELOPMENT

A model was developed to reproduce the temperature distribution in the embankment and in the subgrade soil. Site-specific characteristics, such as air temperature and embankment dimensions, were measured and used as input parameters to improve the accuracy of the model.

The physical domain consists of a roadway embankment and an underlying foundation, as shown in Figure 5. The right half of the physical domain was chosen to carry out the simulation, due to the symmetry of the embankment. The physical domain is 65.8 m wide from the centerline of the embankment and extends to a depth of 30.0 m below the original natural ground surface. The embankment thickness is 1.4 m. The computational domain was extended for 30 m from the toe of the embankment, and the lower boundary was located 15 m beneath the ground surface. In the computational domain, part ① is the embankment fill; part ② is the till, with a thickness of 2.7 m; part ③ is the rock, with an ignorable water content of 0.01 m^3/m^3. The thermal properties of embankment fill were estimated through Kersten's equations (1949), with an assumed uniformly water content of 0.1 m^3/m^3. The thermal properties of till and rock were obtained from L'Hérault et al (2012). Table 1 lists the thermal properties of the different materials used in the model.

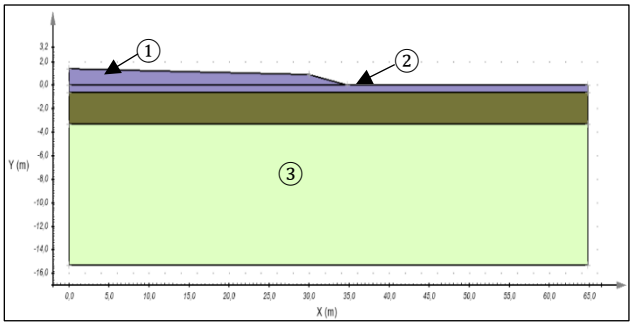

Figure 5. The physical domain of the embankment and foundation.

Table 1. Thermal properties used in the model.

Physical variable	K_f (W/m-°C)	K_u (W/m-°C)	C_f (MJ/m3-°C)	C_u (MJ/m3-°C)
Embankment fill[a]	2,65	2,00	1,67	1,92
Till[b]	2,34	2,32	2,23	3,21
Rock[b]	1,70	1,70	2,49	2,49

Note: k_f = frozen thermal conductivity; k_u = unfrozen thermal conductivity; C_f = frozen volumetric heat capacity; C_u = unfrozen volumetric heat capacity. [a] Values obtained from Kersten's equations; [b] Values obtained from L'Hérault et al. 2012.

The thermal boundary conditions consisted of temperature functions applied to the embankment and natural ground. A constant heat flux boundary was applied to the bottom, right, and left boundaries. At the left-hand and right-hand boundaries, a zero-heat flux was applied, considering the negligible temperature variation. A geothermal heat flux of 0.03 W/m2 was applied at the bottom, considering its limited effect on the permafrost temperature. The near-surface temperature is applied on the top boundaries of the physical domain. The thermal regime of permafrost is strongly affected by the snow thickness and density (e.g., Jorgenson et al. 2001), due to its insulation effect. A field investigation was done to assess the snow accumulation at Kangirsuk airstrip. Based on field measurements, the snow cover thickness was 60 cm to 75 cm (Allard et al. 2007b). The n-factor is the ratio of air temperature to surface temperature. Lanouette et al. (2015) developed the logarithmic relationship between the n-factor value and the snowpack thickness, based on the measured snow thickness and air temperature, near-surface soil temperature in Nunavik. To simplify the mode, an even snow depth of 65 cm was assumed to estimate the n-factor on the side slope of Kangirsuk airstrip. The thawing n-factor for the embankment surface and side slope was 1.86. Table 2 summarizes all the n-factors used in the model.

Table 2. Summary of n-factor used in the model.

Surface type	Thawing n-factor	Freezing n-factor
Natural ground surface	0.25	0.36
Embankment surface	1.86	1.0
Embankment side slope	1.86	0.28

4 NUMERICAL CALIBRATION AND DISCUSSION

The meshing element size ranged from less than 1.0 m in the embankment fill to approximately 1.5 m in the subgrade, covering the domain shown in Figure 5. To obtain a better solution of the active layer and the top part of permafrost, a density meshing was assigned at the natural ground surface layer.

The measured data from 2016 to 2018 were available and used for model calibration. The model was run with an automatic step of less than 1.0 days. Figure 6 shows the 2-year average measured and simulated maximum, averaged, and minimum soil temperature profiles with the depth under the centerline of the airstrip embankment at Kangirsuk, Nunivak.

The results indicate that the modeled average temperature was larger than the measured temperature with a maximum temperature difference of 0.2 °C at the depth of -1.1 m below the embankment-soil interface. Below -1.1 m, the modeled average temperature fitted well with the measured average temperature. For the maximum temperature, the modeled temperature was higher than the measured temperature in the subgrade until the depth of -4.6 m, with a maximum temperature difference of 0.9 °C occurring at -1.1 m above the interface. At the depth of -6.6 m, the modeled temperature was lower than the measured

temperature, with a difference of 0.1 °C. Comparison between the modeled minimum temperature and measured minimum temperature indicates that the measured temperature was higher than the modemed temperature in the embankment and subgrade, with the difference becoming smaller with depth. The maximum and minimum difference was 3.3 °C and 0.4 °C, respectively.

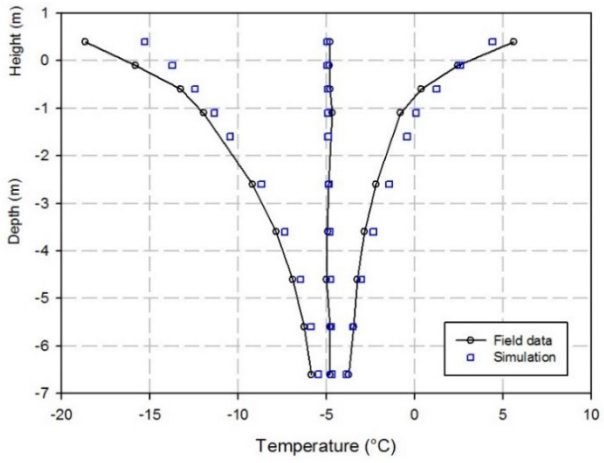

Figure 6. Comparison between the averaged field data (2016–2018) and numerical simulation of the maximum, minimum, and average temperature profiles with depth, under the centerline of Tasiuajq airstrip, Nunavik.

For the natural ground, the temperature measurement was not continuous, and the averaged temperature was unable to be obtained. Figure 7 shows the 2-year averaged measured and simulated maximum and minimum soil temperature profiles with the depth in the natural ground. Comparison between the modeled maximum temperature and measured maximum temperature indicates that the simulated soil temperature generally fitted the measured soil temperatures well, with the maximum difference less than 0.5 °C. For the minimum temperature, the measured temperature was colder than the measured temperature in below the depth of -1.0 m below the interface. The maximum difference of 1.3 °C occurred at -2.5 m. As a whole, the developed model was judged reasonable and satisfactory to reproduce the thermal regime at Kangirsuk, Nunavik.

Climate change can lead to negative impacts on the underlying permafrost, causing degradation of the infrastructure in Nunavik. In this paper, our specific interest was paid to the thermal stability of permafrost under the airstrip shoulder using the model developed at Kangirsuk, Nunivak. Batenipour et al. (2010) indicate that the thermal stability of permafrost can be assessed based on the thermal gradient of mean annual ground temperature between the embankment-soil interface and the soil depth with zero soil variation. A positive mean annual thermal gradient is an indication of warming and degrading permafrost. The modeled mean annual soil temperature at the interface under the side slope was 1.8 °C, indicating a positive thermal gradient and unstable permafrost condition. The current work is in the early stage of designing

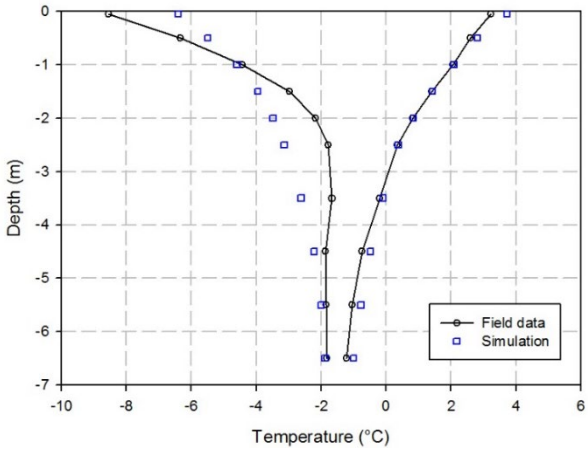

Figure 7. Comparison between the field data and numerical simulation of the maximum, and minimum temperature profiles with depth, in the natural ground.

adaptation techniques to preserve the degrading permafrost under the airstrip shoulder at Kangirsuk, Nunivak.

Poorly graded rocks with a high porosity are used to facilitate convection in an air convection embankment (ACE). Shoulder air convection embankments (ACEs) are proven to be an effective technique to counter the effect of snow accumulation on the side slope of northern infrastructure embankments (e.g., Goering 1998; Coulombe et al. 2012; Darrow and Jensen 2016). This technique has also been successfully employed to preserve underlying permafrost at Puvirnituq airstrip, Nunavik (Figure 8).

The design chart of shoulder ACE to stabilize permafrost was proposed in the previous research, and it should be used with the heat balance analysis charts for unprotected embankment (Figure 9; Kong and Doré 2021). L is the embankment thickness (Figure 9a). ΔT is the temperature difference between the mean annual winter air temperature and permafrost temperature (Figure 9b).

Figure 8. Application of ACE at Puvirnituq airstrip, Nunavik, Québec.

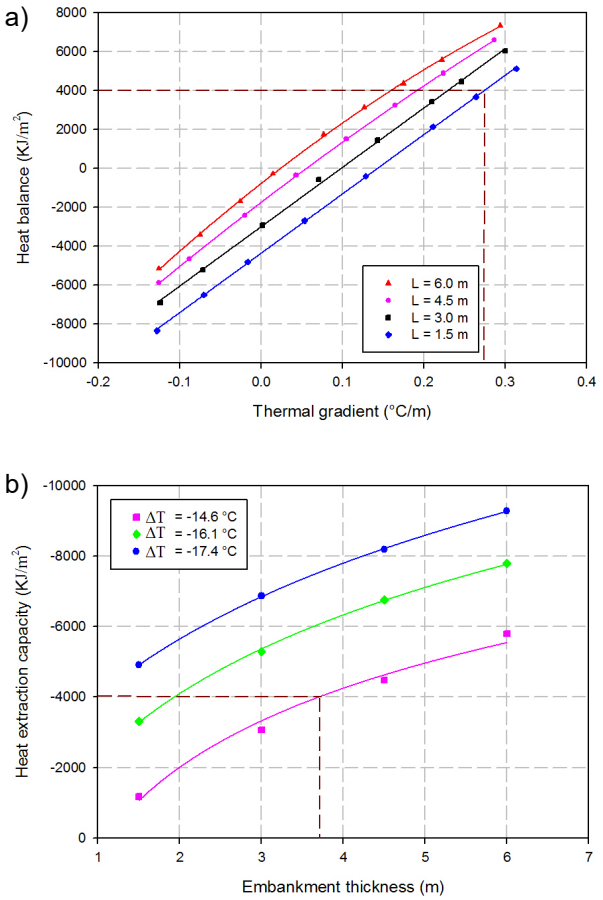

Figure 9. Thermal analysis of permafrost stability under the side slope of embankment: a) heat balance assessment chart for conventional embankments; b) heat extraction capacity chart for shoulder ACE.

5 CONCLUSIONS

A geothermal model was developed to reproduce the thermal regime of underlying permafrost beneath an embankment at Kangirsuk airstrip, Nunavik. Field measurements of ground temperature from 2016 to 2018 were available and used to calibrate the model developed. The modeled average temperature fitted with the measured average temperature closely, with the maximum temperature difference of 0.2 °C, supporting the reasonable accuracy of the developed model. After a satisfying calibration, the model was used to calculate the soil temperature at the embankment-soil interface under the side slope, to determine the thermal stability of underlying permafrost. The analysis of the thermal gradient indicates that the side slope of the airstrip embankment was thermally unstable. Considering the ongoing climate warming in Nunavik, the thermal degradation appears to continue, and effective adaptation techniques are required to preserve the Kangirsuk airstrip. Air convection embankment (ACE) provides a good option to mitigate the degrading permafrost, based on measured thermal performance in Nunavik. Future work will focus on 1) investigating the future thermal regions under different climate change scenarios using the model developed, and 2) developing of adaptation solutions to adapt to the projected thermal degradation of permafrost underneath Kangirsuk airstrip, in Nunavik, Canada.

6 ACKNOWLEDGMENTS

The authors would like to acknowledge the financial support of the Industrial Research Chair in Coastal Engineering, UQAR - Transports Québec, and the 2013–2020 Climate Change Action Plan.

7 REFERENCE

Allard, M., Fortier, R., Sarrazin, D., Calmels, F., Fortier, D., Chaumont, D., Savard, J.P., and Tarussov, A. 2007a. 'L'impact du réchauffement climatique sur les aéroports du Nunavik: caractéristiques du pergélisol et caractérisation des processus de dégradation des pistes', *Ouranos*. Available at: https://www.ouranos.ca/fr/projets-publications/pergelisol-aeroports-nunavik.

Allard, M., Calmels, F., Fortier, D., Laurent, C., L'Hérault, E., and Vinet, F. 2007b. 'Cartographie des conditions de pergélisol dans les communautés du Nunavik en vue de l'adaptation au réchauffement climatique', *Ouranos.* Available at: https://www.ouranos.ca/sites/default/files/2023-05/proj-ant-thant-allard-carto-pergelisol.pdf.

Allard, M., Doré, G., L'Hérault, E., Sarrazin, D., and Verreault, J. 2009. 'Investigations géotechniques, caractérisation du pergélisol et stratégie d'adaptation pour les aéroports du MTQ au Nunavik', *Ministère des Transports du Québec*, Rapport d'étape 2. Université Laval, Québec City, Québec, Canada, pp. 1–83.

Allard, M., Mathon-Dufour, V., L'Hérault, E., and Sarrazin, D. 2018. 'Suivi de l'évolution des conditions de pergélisol et des risques pour les infrastructures de transport du MTMDET au Nunavik dans le contexte des changements climatiques', *Ministère des transports, de la mobilité durable et de l'électrification des transports du Québec*, Rapport d'étape 2 (No. CC02.2). Université Laval, Québec City, Québec, Canada.

Beaulac, I. and Doré, G. 2005. 'Bilan de la condition des pistes et des chemins d'accès menant aux aéroports du Nunavik', *Université Laval, Département de génie civil*, rapport GCT-2005-09, 123 p.

Coulombe, S., Fortier, D., and Stephani, E. 2012. 'Using air convection ducts to control permafrost degradation under road infrastructure: Beaver Creek experimental site, Yukon, Canada', in *Proceedings, Cold Regions Engineering 2012: Sustainable Infrastructure Development in a Changing Cold Environment*, pp. 21–31.

Darrow, M.M. and Jensen, D.D. 2016. 'Modeling the performance of an air convection embankment (ACE) with thermal berm over ice-rich permafrost, Lost Chicken Creek, Alaska', *Cold Regions Science and Technology* 130, pp. 43–58.

Ficheur, A. 2011. *Experimentation de techniques de mitigation des effets de la fonte du pergelisol sur les infrastructures de transport du Nunavik: Aeroport de Tasiujaq*. MSc Thesis, Université Laval, Québec City, Québec, Canada.

Fortier, R., LeBlanc, A.M., and Yu, W. 2011. 'Impacts of permafrost degradation on a road embankment at Umiujaq in Nunavik (Quebec), Canada', *Canadian Geotechnical Journal* 48(5), pp. 720–740.

Goering, D.J. 1998. 'Experimental investigation of air convection embankments for permafrost-resistant roadway design' in *Proceedings of 7th International Conference on Permafrost*. Yellowknife, Northwest Territories, Canada: pp. 319–326.

Jorgenson, M.T., Racine, C.H., Walters, J.C., and Osterkamp, T.E. 2001. 'Permafrost degradation and ecological changes associated with a warming climate in Central Alaska', *Climatic Change* 48(4), pp. 551–579.

Kong, X. and Doré, G. 2021. 'Thermal stabilization of embankments built on thaw-sensitive permafrost', *Journal of Cold Regions Engineering* 35(3), 04021010.

Lanouette, F., Doré, G., and Fortier, D. 2015. 'Influence of snow cover on the ground thermal regime along an embankment built on permafrost: In-situ measurements', in *Proceedings of the 68th Canadian Geotechnical Conference and the 7th Canadian Permafrost Conference*. Quebec, Canada: p. 7.

L'Hérault, E., Allard, M., Barrette, C., oré, G., and Sarrazin, D. 2012. 'Investigations géotechniques, caractérisation du pergélisol et stratégie d'adaptation dans un contexte de changements climatiques pour les aéroports d'Umiujaq, Inukjuak, Puvirnituq, Akulivik, Salluit, Quaqtaq, Kangirsuk et Tasiujaq, Nunavik', *Ministère des Transports du Québec* Rapport final. Université Laval, Québec City, Québec, Canada.

Groundwater flow under permafrost conditions and talik formation

Klaus-Peter Kröhn
GRS gGmbh, Braunschweig, Niedersachsen, Germany

ABSTRACT

In Germany, the safety of a nuclear waste repository legally needs to be investigated for a period of one million years. During the past million years the whole geographic area of present-day Germany has repeatedly experienced permafrost conditions. This will therefore presumably also happen within the time frame that is relevant for the safety assessment. An integral part of such a safety assessment is the transport of radionuclides with the groundwater in case of a canister failure. This assessment requires knowledge of groundwater flow systems. These, however, undergo fundamental alterations in the event of permafrost formation as the freezing of near surface layers may shield the biosphere from possibly contaminated water in deeper aquifers.

However, taliks connecting surface waters with deeper aquifers are known to exist in permafrost regions and can potentially lead to a concentrated flux of contaminated groundwater to the surface. Unfortunately, the circumstances of their formation and their stability — highly important for the safety assessment — are largely unknown. Insight can be gained through numerical modelling which is why a mathematical model for groundwater flow under permafrost conditions including equations of state and constitutive equations has previously been stringently derived. This model is shortly revisited as a basis for a first thermo-hydraulically coupled numerical model that addresses the beginning of a cold age. This work is intended to create trust in the modelling framework as a starting point for further investigations in the future.

1 INTRODUCTION

The safety of the biosphere against undesirable release of radionuclides from a deep geological repository (DGR) is principally at risk where groundwater can corrode the metallic waste canisters. For a performance assessment of a DGR, it is therefore imperative to know the groundwater flow system over the projected lifetime of the repository. According to the current legislation in Germany, this will be over a period of a million years (Deutscher Bundestag 2017).

Over the past million years, several ice ages have occurred and have brought permafrost conditions all over present-day Germany (see Figure 1). It can therefore be expected that any conceivable DGR in Germany will sooner or later also be subject to these conditions during the coming million years. This is significant because permafrost will have a considerable impact on groundwater flow as ground freezing tends to separate deeper aquifers hydraulically from the surface.

However, it is also known that even under permafrost conditions there are local volumes of unfrozen ground, called taliks. According to van Everdingen (2005), a talik can be defined as “A layer or body of unfrozen ground occurring in a permafrost area due to a local anomaly in thermal, hydrological, hydrogeological, or hydrochemical conditions.”

Large taliks have been documented to hydraulically connecting the surface with deeper unfrozen aquifers (e.g., Burn 2020; cf. right sketch in Figure 2). Van Everdingen (2005) recommends the expression “open talik” for this phenomenon but also other terms can be found in the literature. Note that from this point on the expression “talik” is used synonymously to “open talik”.

Figure 1. Permafrost conditions during the latest ice age (after Vandenberghe and Pissart 1993; Renssen and Vandenberghe 2003).

Open taliks are known to exist below large surface water bodies such as lakes and rivers (Delisle 1998; Keller 1998; SKB 2006). Flow of contaminated waters from a possible leakage in a waste repository could be directed towards such taliks and thus lead to a strongly localized outflow into surface waters (e.g., Johansson 2016; Figure 2). Providing means of radionuclide transport to the biosphere through the permafrost and thereby concentrating the flow from the DGR towards the outlet at the surface makes taliks a key feature in the assessment of a possible exposure of the biosphere to harmful radioactive substances. The mechanisms leading to talik formation must therefore be understood to an adequate level of detail in order to allow for meaningful predictions of groundwater flow and possible subsequent contaminant transport under permafrost conditions.

https://doi.org/10.52381/ICOP2024.228.1

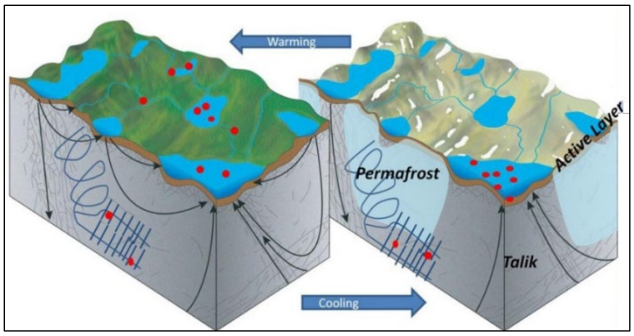

Figure 2. Impact of permafrost on radionuclide migration paths (from Johansson 2016).

Taliks cannot be observed directly, but require laborious field work to document (e.g., Harper et al. 2011). Furthermore, they provide only a snapshot of a long-lasting evolution which makes it hard to identify the relevant circumstances of its occurrence. Numerical modelling is therefore a welcome tool that can be used to understand talik formation without relying on sparse and challenging field data collections. A surprisingly large variety of mathematical formulations can be found in the literature that describe groundwater flow under freezing conditions including ice formation. Some of them have been compiled and discussed by Kröhn (2022) where some formal inconsistencies have been found between assumptions/simplifications during derivation of the balance equations and the ultimately used formulation. Also, no commonly agreed upon set of equations of state (EOS) could be identified as many of the EOS are neither realistic nor appropriate. It was thus concluded that a sound set of formulations should be derived anew to ensure that all relevant processes are properly addressed. Consequently, balance equations, constitutive equations (CE) and EOS were rigorously developed or chosen with care in Kröhn (2022).

The present paper represents the final preparatory step in providing a trustworthy numerical model for groundwater flow under permafrost conditions. This includes formulations for realistic initial and boundary conditions as well as a definition of a model domain including the related hydrogeologic parameters. As granitic rock is presently considered to be a potential host rock for a nuclear waste repository in Germany, the setting at Two Boat Lake in Greenland (e.g., Johansson et al. 2015) where a talik has actually been found (e.g., Harper et al. 2011), is used here as a template. Confidence in the modelling framework is built by having a first model run covering the latest climate cooling period leading to the last glacial maximum. Results are checked for being sensible and consistent. At this stage of development, this first model forms a starting point for future investigations.

2 METHODOLOGY

2.1 Problem definition

2.1.1 Climatic framework

Talik formation may occur either during a change from warmer to colder climates by leaving out an unfrozen “hole” in an otherwise freezing ground, or during a change from cooler to warmer climates by thawing a hole in initially frozen ground.

Presently, talik formation is quite intensively investigated in the framework of a warming cryosphere and is most commonly discussed in the context of thawing (e.g., Parazoo et al. 2018). As Germany is currently ice-free, this appears to be not as relevant in the context of geological storage as the question, where will open taliks remain in an otherwise increasingly freezing ground? It is expected that the freezing dynamics are different from the thawing dynamics since the initial temperature for freezing and thawing scenarios and thus all state variables are different. This difference in dynamics may be enhanced by groundwater flow because heat transport by convection depends on the highly non-linear Soil Freezing Characteristic Curve (SFCC) which in turn entails further non-linearities from the relative permeability. The focus of this article is therefore on a freezing scenario.

2.1.2 Domain

It is assumed that cooling and freezing of water is less complex in lakes than in rivers as rivers show considerably more turbulent water flow than lakes. To keep things as simple as possible, the model presented in this work includes a lake in the domain. This lake is located on top of a granitic formation to have some relation to talik investigations on Greenland (e.g., Johansson et. al. 2015). Porosity and permeability, however, are chosen to coincide with the conditions at the Grimsel Test Site in Switzerland (e.g., Gens et al. 2002) which is also located in crystalline rock.

Axial symmetry is assumed for the hypothetical lake as by (Mackey 1962) to reduce the computational cost. The lake has a maximum depth of 25 m at the centre and a radial extent of 50 m.

2.1.3 Physical framework

Groundwater flow is bounded by lateral no-flow boundaries in the domain. The system is initially hydrostatic. The thermal temperature boundary at the surface is allowed to evolve in time, while a heat flux according to the geothermal gradient is assigned to the base of the profile. The initial thermal conditions depend on the preceding climate which would be a warm period in this case. Within the domain, the temperature distribution is assumed to be in equilibrium with the initial boundary conditions. Modelling begins at the onset of a cold climate.

The lake is approximated in the model as a porous medium with very high values for permeability and porosity, namely 10^{-11} m² and 99 %, respectively, to avoid modelling free water.

2.2 Shaping a model

2.2.1 Mathematical framework

The formulations derived by Kröhn (2022) include the balance equations, the CE as well as their parameters and the EOS considered. They are shortly described and compiled along with a list of processes taken into account and a list of the model assumptions in Appendix A.

Two balance equations are considered. The first one describes mass conservation of water and ice and the second one conservation of heat energy in the three-phase system water, ice, and rock mass allowing for thermo-hydraulically coupled simulations.

Of all the required mathematical formulations, the constitutive equations introduce by far the highest uncertainties in the mathematical framework as they provide a parameterized description of micro-scale properties of the porous medium of interest. Furthermore, they are difficult to measure so that often enough the gut feeling of the modeller decides about the relation and the accompanying parameters to be used. The SFCC and the relative permeability for the present model, for example, are chosen from a comparison of eight related approaches compiled in Kröhn (2022), suggesting the following choice: the water fraction in the pore space S_w is represented by a point symmetric transition curve over the temperature interval -2 °C < T < 0 °C. Relative permeability of the water k_{rw} is taken to be a cubic function of S_w but leaving a residual value of 10^{-6} for $S_w(T)^3 < 10^{-6}$.

Simplified equations of state valid in the temperature range between -20 °C and +20 °C and hydraulic pressures up to 10 MPa had also been developed by Kröhn (2022). Tentative modelling of a changing surface temperature showed, though, that the induced temperature signal went considerably lower than a depth of 1000 m and thereby beyond the limit of 10 MPa (cp. section 2.3). Thus, a new set of EOS expected to be valid up to +60 °C and down to a depth of about 2 km have been derived (Kröhn 2023) and applied here. Evaluation of the modelling results included a check against transgressing the ranges of validity for the EOS (cp. section 2.3).

All these mathematical formulations are realized in the framework of the Code COMSOL Multiphysics.

2.2.4 Thermal setup

Generally, the temperature distribution in the subsurface is influenced by the temperature at the top, by the geothermal heat flux and by the thermal properties of the subsurface. Basically, two mechanisms determine the geothermal heat flux, namely radiogenic and primordial heat, (e.g., Dye, 2012). The former relates to radioactive decay of naturally occurring radioactive elements and the latter to residual heat from planetary accretion. This leads to a complex evolution over geological times. However, over the past million years, the change in heat flux from inner earth amounts only to 0.18% (Loyd et al. 2007) allowing from a rational point of view for the simplification of a constant flux over the period of interest.

According to a recent data survey, heat flux over the area of present-day Germany ranges between 20 and 192 mW/m² (Fuchs et al. 2022b). For the present model, the average of 78 mW/m² (Fuchs et al. 2022a) is adopted for the bottom boundary of the model.

A time-dependent temperature boundary condition is applied at the surface. Climate change as a driver for the evolution of permafrost and thereby of taliks is considered over ten thousand to a hundred thousand years. Data on surface temperature evolution determined from ice cores from Antarctica (Jouzel and Masson-Delmotte 2007) are of great interest when reconstructing climate data. These data are given as differences to a reference value, that dates back to pre-industrial conditions. The data from the last cooling climate are taken as an approximation for the cooling dynamics over present-day Germany which in turn may be a template for future climate changes. Only a reference temperature for pre-industrial Germany thus remains to be determined to construct absolute temperatures for the model top.

Systematic climate measurements in Germany go back to the year 1881 (e.g., Deutscher Wetterdienst (DWD), 2021). At this time, industrial revolution was underway (ERIH 2023). Twelve reconstructions of the temperature evolution of earth's northern hemisphere using "multiple climate proxy records" for the past 1300 years (Solomon et al. 2007) indicate that the temperature was not affected by industrialization until about 1900 (see Figure 3). The wanted reference temperature can thus be established on the basis of the first 20 years of temperature recorded by the DWD. According to data of the Climate Data Center of the DWD (Deutscher Wetterdienst 2023), this value amounts to about +7.6 °C. Note that these measurements refer to a surface air temperature (SAT) at 2 m height above ground.

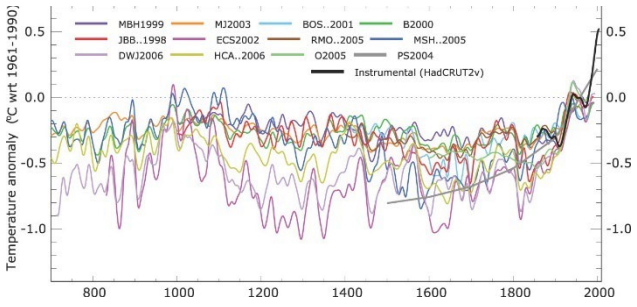

Figure 3. Reconstructions of the temperature anomaly of earth's northern hemisphere (from Solomon et al. 2007).

Daily and seasonal variations of the air temperature may reach down up to about 12 m into the ground (e.g., Deutscher Wetterdienst 2012). However, these few topmost meters can be seen as a temporary storage volume for heat energy that is filled during a warm period and drained again during a cold period. Any net effect of the heat flow fluctuations on the temperature field is attenuated

over space and time. It is therefore assumed that temperature variations between the SAT and the ground temperature at about 12 m depth can be neglected leaving annual average temperatures to be considered in this work. In other words, the SAT can directly be applied as the thermal surface boundary condition for the model. The temperature evolution for the past 250,000 years is adopted accordingly and shown in Figure 4.

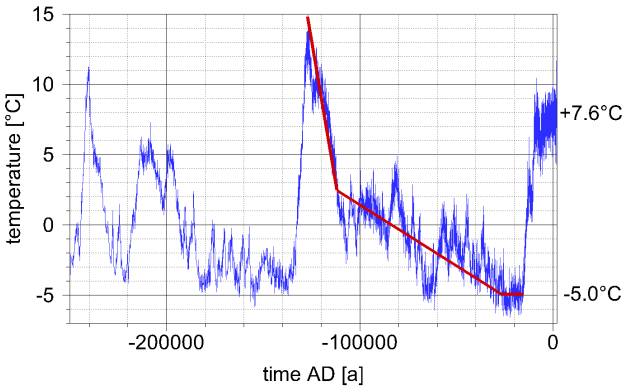

Figure 4. Adopted history of SAT over Germany; adopted data in blue, simplified curve in red.

The cooling/cold period of choice has been selected to be the interval between 127,000 and 15,500-years BC. For modelling purposes, the temperature evolution is smoothened to a polygon as indicated by the red line in Figure 4. It is also shifted in time for convenience according to Table 1.

Table 1. Simplified temperature evolution.

Real time [a BC]	Model time [a]	Temperature [°C]
127,000	0	14.80
111,600	15,400	2.45
26,600	100,400	-5.00
15,500	111,500	-5.00

The initial temperature field is calculated according to a geothermal gradient of 0.0232 °C/m where the initial temperature of 14.8 °C is assigned to the top of the model. Model calculations proved this to be consistent with the heat flux of 78 mW/m² over the bottom boundary.

It has to be noted that the effect of cyclic surface temperature variations discussed above with respect to daily and seasonal changes, applies in principle also to climate-caused fluctuations. Amplitude and frequency of these changes control the depth to which the thermal impact can be observed. The bottom of the model should thus extend beyond the zero amplitude. This is further discussed in section 2.3.2.

2.3 Modelling

2.3.1 Initial and boundary conditions

The whole set of hydraulic and thermal initial and boundary conditions is depicted in Figure 5 and subsequently discussed.

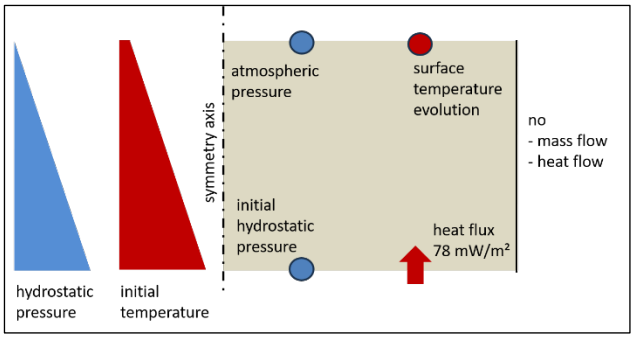

Figure 5. Hydraulic and thermal initial and boundary conditions.

As an initial condition, no groundwater flow is assumed in the model which implies a hydrostatic pressure distribution over the domain. The initial pressure distribution is generated using a hydraulic head of 0 m at the top of the model.

The lateral boundary of the axial symmetric domain is a no-flow boundary. It is expected that any influence of the lake on the freezing process can be neglected if this boundary is located sufficiently far from the lake. In this case the flow at the lateral boundary is strictly vertical and no mass exchange occurs across this boundary. The resulting model width is determined in section 2.3.2.

The pressure at the bottom boundary is fixed to the initial hydrostatic value of 19.54 MPa assuming a mean water density of 996 kg/m³. This introduces an error over time when phase change of water to ice occurs. The displacement of water due to volumetric expansion during ice formation results in lateral water migration across open model boundaries, thereby changing the weight of the water column and thus the hydraulic pressure at the bottom. Under these circumstances, a lateral no-flow boundary forces excess water out of the model through the top boundary where, in reality, the ice should impede water flow. The error from a fixed pressure at the bottom can only be limited maximizing the depth for the model domain. This is determined in section 2.3.2.

The lateral thermal boundary is assumed to be sufficiently far from the model axis that no temperature signal caused by the lake reaches the lateral boundary. In other words, the heat flux along this boundary is assumed to be strictly vertical so that no heat exchange across the boundary occurs.

2.3.2 Preparatory modelling

To prepare the final model, some preparatory modelling work was required. This included a) determining an appropriate model width and depth and b) checking for the

compliance of model temperatures and admissible temperature ranges for the EOS.

Tentative model runs indicate that lateral boundary should be arranged at a radial distance of 1000 m from the model axis to ensure a sound approximation of no flow and no heat flux across this boundary.

As discussed in subsection 2.3.1, the hydraulics require a maximized model depth. In order to ensure validity of the new EOS with respect to temperature and pressure, this depth is set to 2000 m. However, modelling by way of trial indicates that a temperature signal from the top reaches a depth of 2000 m in less than 10,000 years in this model. This is very little compared to the more than 111,500 years assessed in this study.

While further extensions of the formulations for the EOS for water would be rather hard to derive, the EOS for the rock are well-known up to a temperature of 200 °C (cf., Kröhn 2010). It is thus assumed here that exclusion of water in the pore space below a depth of 2000 m constitutes a reasonable approximation for heat transport at great depths. Different domains are consequently considered for hydraulic and for thermal processes. The domain for the hydraulic simulations remains as discussed above but the thermal model is extended downwards by an additional piece of solid rock material with zero porosity. Calculations with this enlarged model indicate that the temperature signal from the top does not reach a depth of 6000 m within 110,000 years. The undisturbed temperature at that depth is 157 °C attesting validity of the thermal EOS for rock in this model.

2.3.3 The final model

Based on the problem definition in section 2.1, the model shape described in section 2.2, and the remaining specifications from the previous subsection 2.3.2, a single model run has been performed to inspire confidence in the mathematical model and to assess the possible thermo-hydraulic conditions in the subsurface.

3 RESULTS

3.1 Simulation times of interest

Three points in time in this simulation appear to be of particular interest: (1) an early time to represent effects at the beginning of cooling, chosen to be 1000 years, (2) 60,000 years which is some time after the onset of freezing, and (3) the end of the cooling climate at 111,500 years. Results with respect to these times are presented in the following subsections.

3.1.1 1000 years: Effect of cooling

After 1000 years model time, the surface temperature has decreased from 14.8 to 14.0 °C. This relatively small difference increases the vertical temperature gradient to the extent that the heat flux over the granitic surface increases by a factor of about 2.5. The water in the lake, however, has a much lower thermal conductivity and thus shields the bottom of the lake from cooling. Heat flux from below is diverted around the lake as visualized in Figure 6 where heat flux is plotted as a vector field, as the related distribution of absolute velocity values highlighted in colour, and as a couple of pathlines. The resulting temperature field, given as isolines and a coloured scalar field in Figure 7 shows the resulting temperature anomaly of a few tenths °C around the lake.

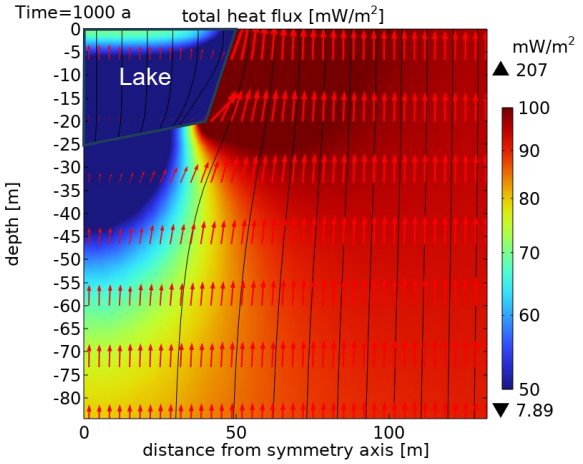

Figure 6. Total heat flux in the vicinity of the lake after 1000 years.

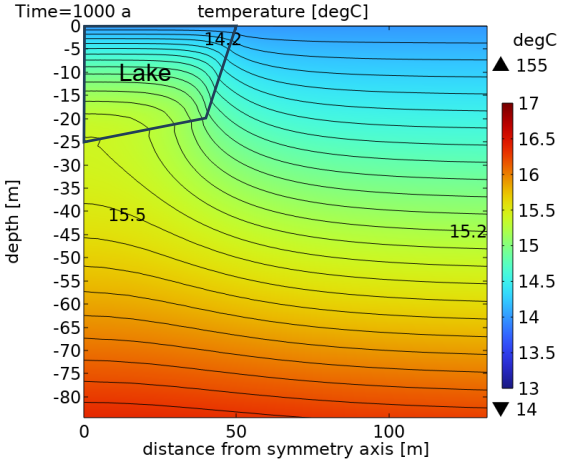

Figure 7. Temperature around the lake after 1000 years.

3.1.2 60,000 years: Effect of freezing

In the model, the surface temperature falls below 0 °C after about 43,400 years. After 60,000 years simulation time, ice can be found down to about 20 m depth. Since the model accounts for the volumetric increase of water due to freezing but does not allow for ice on the lake to heave, the remaining water in the lake gets squeezed out into the rock as illustrated in Figure 8 showing the scalar saturation field and qualitatively the velocity vectors for the water flow.

The absolute flow velocity depicted for a large part of the model in Figure 9 is quite small, less than 10^{-12} m². It is consistent, though, with the slow downward progress of the ice front because forming of ice results in volumetric expansion and leads to a downwards directed displacement of water.

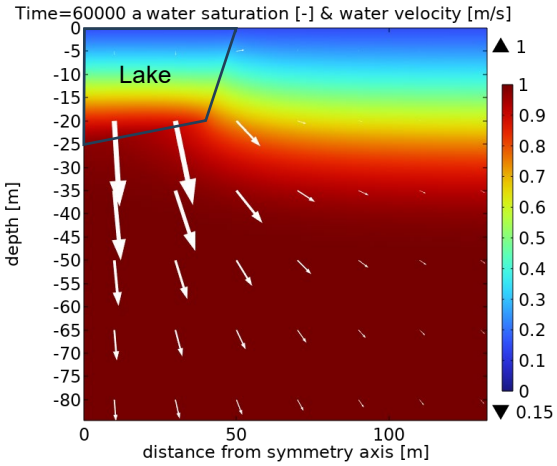

Figure 8. Liquid water saturation and water velocity in the vicinity of the lake after 60,000 years.

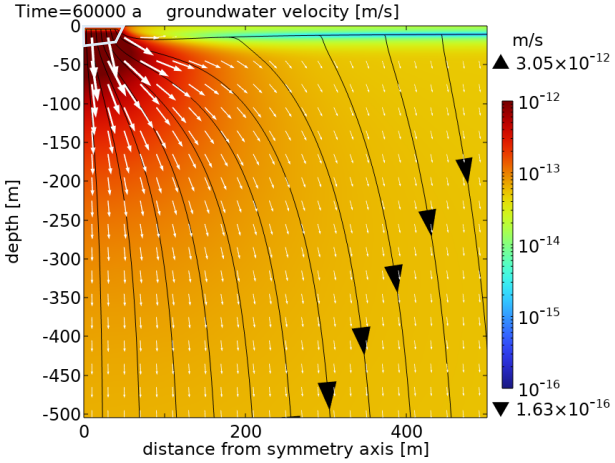

Figure 9. Water flow after 60,000 years.

3.1.3 111,500 years: End of cold age

The end of the cold age considered here is reached after 111,500 a. The model calculates a thickness of the frozen ground of about 150 m (see Figure 10). The freezing front becomes horizontal as the effect of the lake is no longer felt.

As the thermal conductivity for ice is lower than for the rock (but higher than for water), the frozen lake still forms an impediment for heat flow even if not as effective as the water at the beginning of the simulated cold age. The temperature anomaly around the lake at the end of the simulation (see Figure 11) is thus a permanent feature.

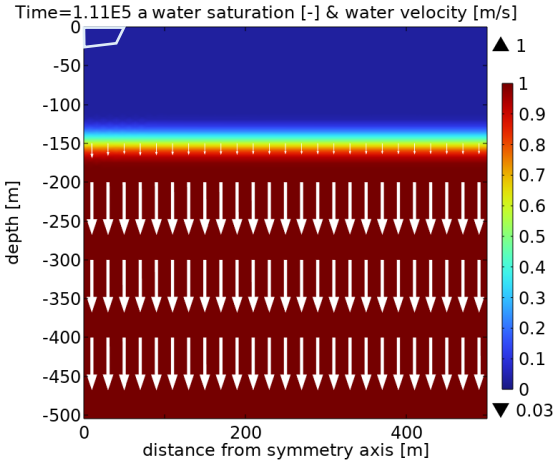

Figure 10. Water saturation and water velocity after 111,500 years.

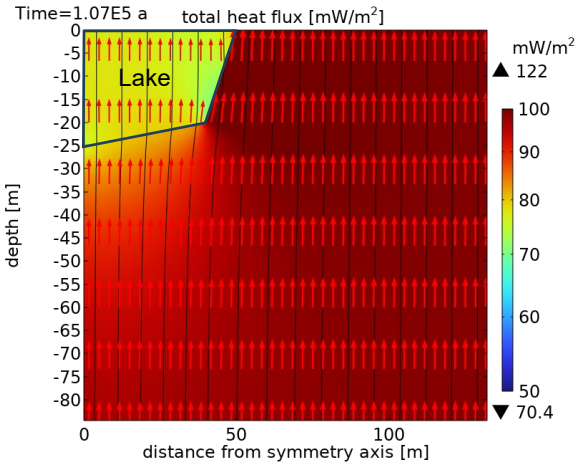

Figure 11. Total heat flux in the vicinity of the lake after 111,500 years.

3.2 Evolution of water density

The interplay of increasing temperature and hydraulic pressure with depth results in a peculiar evolution of the vertical water density distribution. While the density at the top varies only by about 1 kg/m³, it differs by 5 kg/m³ at 2000 m depth. Furthermore, the maximum water density of 999.1 kg/m³ is initially located at a depth of about 100 m but increases to 1002.3 kg/m³ and moves down to 700 m depth after 111,500 years model time (see Figure 12).

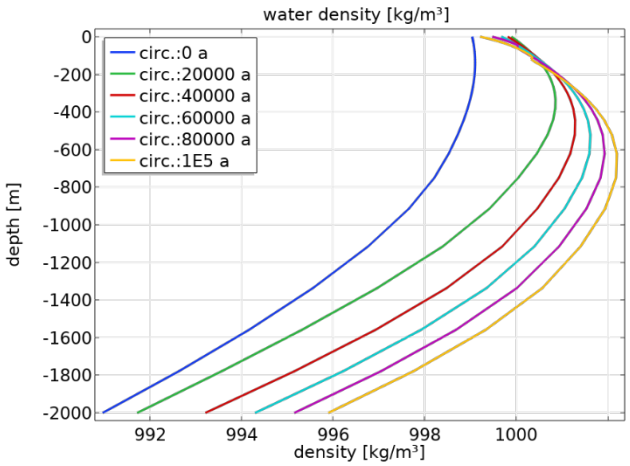

Figure 12. Evolution of the water density with depth.

4 Discussion

The first attempt to reproduce talik formation during a change to colder climates has failed. However, modelling has led to reasonable results. There is a temperature anomaly in the vicinity of the lake because the lake is shielding the ground below to a certain extent from heat loss due to its comparatively low thermal conductivity. This feature is visible over the whole simulated time and should still be visible when equilibrium of heat flow according to the thermal boundary conditions is reached.

Groundwater flow is basically driven by the freezing of water as the less dense ice displaces the remaining water due to expansion during phase change. The resulting flow velocity is very low, lying in the range of µm/a and therefore far too low to provoke heat convection. Under these circumstances, even the temperature- and pressure-dependent water density and viscosity are not sufficient to start any sort of heat convection. Thus, by and large, heat flow is restricted to conduction in this model.

Squeezing water from the lake due to the volumetric expansion during freezing is the result of having a geometrically fixed top boundary that forces the newly formed ice downwards. This is of course unrealistic as the ice would be floating on top of the lake water — at least for quite some time — and thus exerting less pressure on the lake water. In a more realistic treatment of the lake, the effect of squeezing water out under the lake ice would therefore be much less pronounced. As a result, the progress of the ice front with time would be even less disturbed by the lake and the ice front would be even less deviating from a horizontal course. However, it would also put up less resistance against a hypothetical rising of warmer water from under the lake.

5 Conclusions and Outlook

A realistic numerical model for groundwater flow under permafrost conditions has been presented. While the main goal to track talik forming numerically has been missed, the otherwise reasonable modelling results encourage further systematic investigations. A large number of model cases remain to be considered, checking for the impact of additional features such as:

- a non-horizontal groundwater table,
- higher permeability and porosity of the rock,
- varying the heat flux from the inner earth,
- seasonal temperature variations,
- a better representation of the lake in the model,
- heterogeneities in the rock, or
- the influence of a deep aquifer.

6 Acknowledgements

Funding by the Federal Ministry for Economic Affairs and Energy (BMWi) and the Federal Ministry for the Environment, Nature Conservation, Nuclear Safety and Consumer Protection BMUV under contract numbers 02 E 11809A (project HYMNE) and 02 E 11941 (project WiGru-9) are gratefully acknowledged.

7 References

Burn, C.R. 2020. 'Permafrost Landscape Features', in *Encyclopedia of the World's Biome,* Vol. 2, pp. 303–320. Available at: https://doi.org/10.1016/B978-0-12-409548-9.12423-6.

Delisle, G. 1998. 'Numerical simulation of permafrost growth and decay', *Journal of Quaternary Science* 13(4), pp. 325–333.

Deutscher Bundestag 2017. *Gesetz zur Suche und Auswahl eines Standortes für ein Endlager für hochradioaktive Abfälle (Standortauswahlgesetz - StandAG)*, decision of the Deutscher Bundestag.

Deutscher Wetterdienst (DWD) 2012. *Klimastatusbericht Deutschland, Jahr 2011*, Deutscher Wetterdienst, Selbstverlag.

Deutscher Wetterdienst (DWD) 2021. *Klimastatusbericht Deutschland, Jahr 2020*, Deutscher Wetterdienst, Selbstverlag.

Deutscher Wetterdienst (DWD) 2023. *CDC – Climate Data Center, annual air temperature over Germany*. Available at: https://opendata.dwd.de/climate_environment/CDC/regional_averages_DE/annual/air_temperature_mean/regional_averages_tm_year.txt.

Dye, S.T. 2012. 'Geoneutrinos and the radioactive power of the Earth', *Reviews of Geophysics* 50(3). Available at: https://doi.org/10.1029/2012RG000400.

Gens, A., Guimaraes, L. do N., Garcia-Molina, A., and Alonso, E.E. 2002. 'Factors controlling rock–clay buffer interaction in a radioactive waste repository', *Engineering Geology* 64, pp. 297–308.

ERIH (European Route of Industrial Heritage) 2023. *Industrial history of European countries*. Available at: https://www.erih.net/how-it-started/industrial-history-of-european-countries.

Fuchs, S., Förster, A., and Norden, B. 2022a. 'Evaluation of the terrestrial heat flow in Germany: A case study for the reassessment of global continental heat-flow data', *Earth-Science Reviews* 235(2022), 104231. Available at: https://doi.org/10.1016/j.earscirev.2022.104231.

Fuchs, S., Norden, B., and Förster, A., 2022b. 'The German Heat Flow Database 2022', *GFZ Data Services*. Available at: https://doi.org/10.5880/GFZ.4.8.2022.015.

Harper, J., Hubbard A., Ruskeeniemi, T., Claesson Liljedahl, L., Lehtinen, A., Booth, A., et al. 2011. 'The Greenland Analogue Project, Yearly Report 2010', *Svensk Kärnbränslehantering AB* Report R-11-23, Stockholm.

IAPWS (International Association for the Properties of Water and Steam) 2003. *Revised Release on the IAPS Formulation 1985 for the Viscosity of Ordinary Water Substance*. Available at: http://www.iapws.org.

IAPWS (International Association for the Properties of Water and Steam) 2008. *Revised Release on the IAPWS Formulation 2008 for the Viscosity of Ordinary Water Substance*. Available at: http://www.iapws.org.

IAPWS (International Association for the Properties of Water and Steam) 2011. *Revised Release on the IAPWS Formulation 2011 for the Thermal Conductivity of Ordinary Water Substance*. Available at: http://www.iapws.org.

IAPWS (International Association for the Properties of Water and Steam) 2015. *Revised Guideline on Thermodynamic Properties of Supercooled Water*. Available at: http://www.iapws.org.

Johansson, E. 2016. *The influence of climate and permafrost on catchment hydrology*. Doctoral Thesis, Department of Physical Geography, Stockholm University.

Johansson, E., Gustafsson, L.-G., Berglund, S., Lindborg, T., Selroos, J.-O., Claesson Liljedahl, L., and Destouni, G. 2015. 'Data evaluation and numerical modeling of hydrological interactions between active layer, lake and talik in a permafrost catchment, Western Greenland', *Journal of Hydrology* 36. doi:10.1016/j.jhydrol.2015.05.026.

Jouzel, J. and Masson-Delmotte, V. 2007. 'EPICA Dome C Ice Core 800KYr deuterium data and temperature estimates', *PANGAEA*. Available at: https://doi.org/10.1594/PANGAEA.683655.

Keller, S. 1998. 'Permafrost in der Weichsel-Kaltzeit und Langzeitprognose der hydrogeologischen Entwicklung der Umgebung von Gorleben/NW Deutschland', Zeitschrift für Angewandte Geologie 44(2), pp. 111–119.

Kröhn, K.-P. 2010. 'State Variables for Modelling Thermohaline Flow in Rocks', *Gesellschaft für Anlagen- und Reaktorsicherheit (GRS) mbH* report GRS-268. Köln.

Kröhn, K.-P. 2022. Basics for groundwater flow under permafrost conditions in the context of radioactive storage', *Gesellschaft für Anlagen- und Reaktor-sicherheit (GRS) gGmbH* report GRS-707. Braunschweig.

Kröhn, K.-P. 2023. 'Investigations On Talik Formation During Changes To Cold Climates', in *COMSOL Conference 2023*. Munich, Germany.

Leshchinsky, D. and Perry, E.B. 1987. 'A Design Procedure for Geotextile Reinforced Walls', in *Geosynthetics '87*. New Orleans, Louisiana, United States: pp. 95–107.

Loyd, S., Becker, T., Conrad, C., Lithgow-Bertelloni, C., and Corsetti, F. 2007. 'Time variability in Cenozoic reconstructions of mantle heat flow: Plate tectonic cycles and implications for Earth's thermal evolution', *Earth, Atomospheric, and Planetary Sciences* 104(36), pp. 14266–14271. doi:10.1073/pnas.0706667104.

Mackay, J.R. 1962. 'Pingos of the Pleistocene Mackenzie Delta area', *Geographical Bulletin*, pp. 21–63.

Parazoo, N.C., Koven, C.D., Lawrence, D.M., Romanovsky, V., and Miller, C.E. 2018. 'Detecting the permafrost carbon feedback: talik formation and increased cold-season respiration as precursors to sink-to-source transitions', *The Cryosphere* 12, pp. 123–144. Available at: https://doi.org/10.5194/tc-12-123-2018.

Renssen, H. and Vandenberghe, J. 2003. 'Investigation of the relationship between permafrost distribution in NW Europe and extensive winter sea-ice cover in the North Atlantic Ocean during the cold phases of the Last Glaciation', *Quaternary Science Reviews* 22, pp, 209–223.

Solomon, S., Qin, D., Manning, M., Marquis, M., Averyt, K., Tignor, M.M.B., Miller, H.L. jr., and Chen, Z. (eds.) 2007. *Climate Change 2007 - The Physical Science Basis*. Contribution of Working Group I to the Fourth Assessment Report of the Intergovernmental Panel on Climate Change. New York, New York, United States: Cambridge University Press,

Svensk Kärnbränslehantering AB (SKB) 2006. *Climate and climate-related issues for the safety assessment SR-Can.* SKB, Technical report TR-06-23, Stockholm.

van Everdingen, R.O. 2005. 'Multi-language glossary of permafrost and related ground-ice terms', *International Permafrost Association*. Available at: Glossary_of_Permafrost_and_Ground-Ice_IPA_2005.pdf.

Vandenberghe, J. and Pissart, A. 1993. 'Permafrost changes in Europe during the Last Glacial', *Permafrost and Periglacial Processes* 4, pp. 121–135.

APPENDIX A: DESCRIPTION OF MODEL BASICS

The indices w, I, and m stand for water, ice and matrix.
(for more details see Kröhn (2022) and Kröhn (2023))

A.1 Processes

- Advective water flow
- Sinks/sources for water (not used here)
- Sinks/sources of mass of water and ice due to phase changes; concurrent volumetric changes
- Heat convection and conduction
- Hydromechanical heat dispersion (not used here)
- Sinks/sources for heat (not used here)
- Release/consumption of latent heat

A.2 Assumptions

- Three phases considered: water, ice, and rock
- No movement of ice or rock
- Constant porosity
- Generalized Darcy flow including
  - Soil Freezing Characteristic Curve (SFCC)
  - Relative permeability dependent on the SFCC
- Local thermal equilibrium
- Fourier's law
- Isotropic thermal conductivity
- All EOS depend on temperature; EOS for water also on pressure
- No boiling

A.3 Balance equations

A.3.1 Mass balance

$$-\nabla\cdot\left(\rho_w\frac{k_{rw}}{\eta_w}\boldsymbol{k}\cdot(\boldsymbol{\nabla}p_w-\rho_w\boldsymbol{g})\right)=$$

$$\rho_w\,q_w-\left[\Phi\left(\rho_w-\rho_i\right)\frac{\partial S_w}{\partial T}+S_w\Phi\frac{\partial\rho_w}{\partial T}\right]\frac{\partial T}{\partial t} \qquad [A.1]$$

ρ	-	density
η	-	viscosity
k	-	permeability
k_r	-	relative permeability
p	-	pressure
g	-	gravitational acceleration
q	-	volumetric source
Φ	-	porosity
S	-	saturation
T	-	temperature
t	-	time

A.3.2 Energy balance

$$\left(\begin{array}{c}S_w\Phi\rho_w\left[T\frac{\partial c_{s\,w}}{\partial T}+c_{s\,w}\right]+S_i\Phi\rho_i\left[T\frac{\partial c_{s\,i}}{\partial T}+c_{s\,i}\right]\\+(1-\Phi)\rho_m\left[T\frac{\partial c_{s\,m}}{\partial T}+c_{s\,m}\right]-L\rho_i\Phi\frac{\partial S_i}{\partial T}\end{array}\right)\frac{\partial T}{\partial t}$$

$$+(\boldsymbol{v_{a\,w}}S_w\rho_w\Phi)\cdot\boldsymbol{\nabla}(c_{s\,w}T)$$

$$-\nabla\cdot[(S_w\Phi\,\boldsymbol{\lambda_w}+S_i\Phi\,\boldsymbol{\lambda_i}+(1-\Phi)\,\boldsymbol{\lambda_m}+S_w\Phi c_{s\,w}\rho_w\boldsymbol{D_w})\cdot\boldsymbol{\nabla}T]$$

$$=r_{hQ}+c_{s\,w}\;\rho_w\,q_w(T_w-\hat{T})+S_w\Phi\rho_wT\frac{\partial c_{sw}}{\partial p}\frac{\partial p}{\partial t} \qquad [A.2]$$

c_s	-	specific heat
L	-	latent heat
v_a	-	interstitial velocity
λ	-	thermal conductivity
D	-	hydrodynamic dispersion
r_{hQ}	-	source term for directly applied heat
$\hat{T}$	-	temperature of inflowing water

A.4 Constitutive equations

A.4.1 Equations

$\boldsymbol{v_{a\,w}}=\boldsymbol{v_{a\,w}}\left(\boldsymbol{v_{f\,w}}\left(k_{rw}(S_w(T))\right),S_w(T),\Phi,g,\rho_w,\eta_w,p_w\right)$

$S_w=S_w(T)$

$k_{rw}=k_{rw}(S_w(T))$

$\boldsymbol{J_{cond\,j}}=\boldsymbol{J_{cond\,j}}(S_j(T),\Phi,\lambda_j,T)$, j = w, i, m

$\boldsymbol{J_{disp\,w}}=\boldsymbol{J_{disp\,w}}(S_w(T),\Phi,\boldsymbol{D_w}(\boldsymbol{v_{a\,w}},\alpha_l,\alpha_t),c_{s\,w},\rho_w,T)$

A.4.2 Parameters

$\Phi, g = const.$

$\eta_w=\eta_w(p_w,T)$

$\lambda_w=\lambda_w(p_w,T)\quad\lambda_i=\lambda_i(T)\quad\lambda_m=\lambda_m(T)$

A.5 Equations of state

$\rho_w=\rho_w(p_w,T)\quad\rho_i=const.\quad\rho_m=const.$

$c_{sw}=c_{sw}(p_w,T)\quad c_{si}=c_{si}(T)\quad c_{sm}=c_{sm}(T)$

Performance of five drilling waste sumps, Mackenzie Delta, western Arctic Canada

Rae Landriau[1], Christopher R. Burn[1], Timothy Ensom[2] & Charles Klengenberg[3]

[1]*Carleton University, Ottawa, Ontario, Canada*

[2]*Government of Northwest Territories, Yellowknife, Northwest Territories, Canada*

[3]*Inuvialuit Regional Corporation, Inuvik, Northwest Territories, Canada*

ABSTRACT

Petroleum resource exploration and development has occurred in the Northwest Territories since the 1920s. Freezing-point depressants, mainly potassium chloride, were added to drilling fluids in many wells to maintain circulation and the thermal integrity of permafrost penetrated during drilling. Disposal of these fluids was generally in large pits, or sumps, excavated in permafrost, with the intention that frozen ground would contain the fluids indefinitely. Climatic warming in northwest Canada has raised the temperature of near-surface permafrost, increasing the potential for failure of over 220 sumps constructed in the region. Electro-magnetic surveys were conducted with an EM-31 to determine the ground conductivity fields on and off sumps at three locations in the outer Mackenzie Delta. The surveys were complemented by investigations of water conductivity in ponds also on and off the sump caps. Two of the sumps (C-42 and B-19) were low-lying and occasionally flooded, while the third (L-38) was at the coast and regularly inundated. Ground conductivities at these three sumps built in the 1970s were similar to undisturbed terrain. The most recent sump, 3/4/5 L-38 (2002), had high conductivity below its cap. An intermediate state was measured at 2 L-38, built in 1998, where the spatial concentration of ground conductivity has diminished since a survey in 2012. Both observations suggest the contents of the sumps are being lost. Enhanced conductivities in some ponds on sump caps imply the possible emergence of the sump fluids via these water bodies.

1 INTRODUCTION

The Mackenzie Delta is a region of significant discovered and predicted hydrocarbon (oil and gas) resources (French 1980). In the 1970s and 1980s, 16 companies drilled 230 onshore wells to prospect and delineate these reserves (Simpson and van Gulck 2020). The projects required drilling fluids with freezing points below the temperature of permafrost, as the wells would typically extend to depths around 2500 m, thereby penetrating perennially frozen ground (Shell Canada Ltd 2005).

Drilling fluids were necessary to clean the drill bits, reduce friction, and provide borehole stability (French 1980). Freezing point depressants, primarily potassium chloride (KCl), were added with other substances, such as bentonite, cellulose polymers, lignosulphonates, and sodium hydroxide, to influence the chemical and physical properties of the fluids so that they might perform well at temperatures below 0 °C (Hrudey 1979). The fluids were recycled and reused several times during each project before being discarded (Hrudey 1979). KCl in these fluids allows them to be traced in the environment, as background concentrations of KCl are low in comparison with drilling fluids (Dyke 2001).

The fluids, or drilling muds, were disposed of in pits, or sumps, blasted and dug in permafrost (French 1980). The sumps were large enough to accommodate between 0.78 and 1.3 m^3 of drilling mud for every meter of hole drilled (Hardy and Stanley 1988). The muds were sometimes frozen in the sumps before being covered with excavated ground materials to create a domed cap (Hardy and Stanley 1988). The sump caps were approximately 5 m thick and sufficient to contain the active layer (Figure 1). Permafrost then aggraded into the sumps, freezing the fluids in place for permanent disposal.

The basis for development of sumps as disposal sites was the expectation that ice-bonded permafrost would be an effective, impermeable, and permanent containment medium. This position must now be reassessed. First, snow accumulation on the sides of sumps and in vegetation that developed on sump caps has led to increases in mean annual ground temperature and warming of sump materials (Kokelj et al. 2010). Second, salinities of disposed materials were elevated in part of the sump by solute expulsion during freeze back, lowering the freezing points of the solutions. Such volumes of elevated salt concentrations have been inferred by electromagnetic surveys (Dyke 2001). Third, rising permafrost temperatures due to climatic warming no longer ensure that the ground surrounding sumps will remain at a lower temperature than the freezing point of the drilling muds (Burn and Kokelj 2009). As a result, the ability of the sumps to contain these fluids is not assured.

The purpose of this paper is to investigate the stability of five sumps of similar characteristics in a low-lying, occasionally flooded deltaic environment (Figure 2). At each sump, data were collected on ground conductivity, active-layer depth, soil grain size, and ponding. These data were compared with surveys from 15–20 years ago to determine changes in conditions at the sumps, and to assess sump performance in containing the drilling wastes.

https://doi.org/10.52381/ICOP2024.146.1

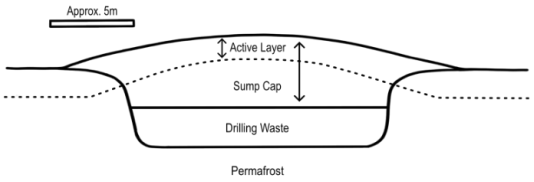

Figure 1. Cross-section of a sump with representative dimensions.

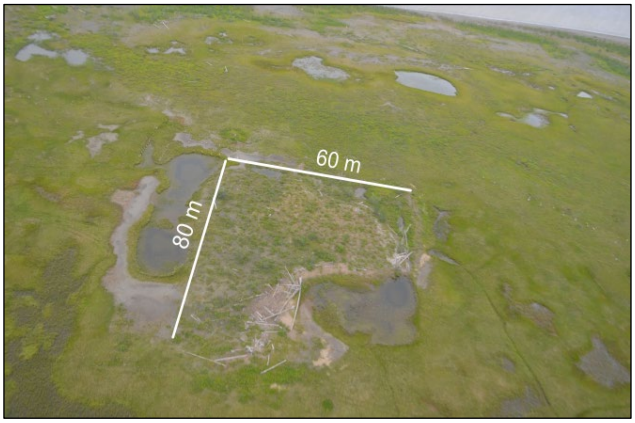

Figure 2. Aerial image of sump B-19 with dimensions indicated in meters.

2 STUDY AREA

The Mackenzie Delta is an alluvial plain 210 km in length and on average 62 km wide (Burn and Kokelj 2009). This dynamic environment has shifting channels and thousands of lakes at various stages of expansion, drainage, and infilling (Mackay 1963). The Mackenzie Delta receives about 128 Mt of sediment each year, with the vast majority supplied by Mackenzie River (Burn and Kokelj 2009). These sediments are dominantly fine sand and silts (Kokelj and Burn 2005). The five sumps studied are in the outer delta near the Beaufort Sea (Figure 3).

Vegetation distribution in the outer delta varies with gradients in soil moisture, topography, and nutrient conditions (Mackay 1963). In the alluvial plain, vegetation ranges from bare ground near the channel, through tall (1–3 m), medium (0.6–1 m), and low (0.4–0.6 m) willows, to a distil sedge wetland (Morse et al. 2012). On alluvial flats, sedges grow where it is muddy, but horsetails predominate at the outermost Delta (Mackay 1963). Snow cover in the region varies spatially. Tall vegetation traps up to 2 m of snow in some areas but vegetation-free terrain is windswept and has very shallow snow cover, typically less than 0.3 m (Kokelj et al. 2010).

Tuktoyaktuk, the closest weather station received a mean annual precipitation of 160 mm in 1981–2010 and an average annual snow depth of 103.1 cm (ECCC 2020). For the same period, the mean annual air temperature was -10.1 °C. Warming of the western Arctic has been faster than the global average; annual mean air temperatures have increased by up to 0.77 °C per decade since 1971; the magnitude of the warming in the Delta area has been up to 2.3 °C for 30-year mean temperatures and 3.7 °C in 10-year

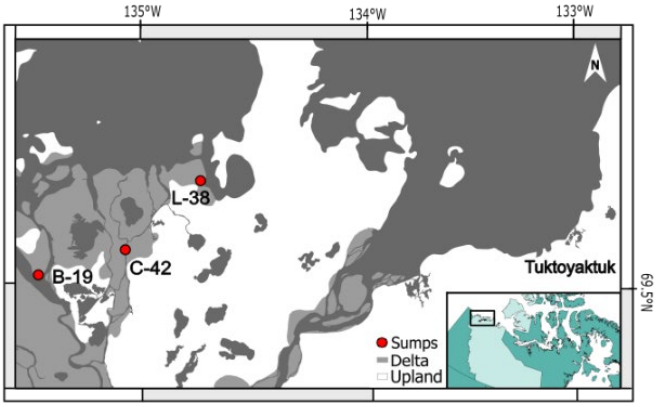

Figure 3. Study area including locations of sumps B-19, C-42, and L-38.

means for 1961–70 and 2011–20 (Burn and Kokelj 2009; Thienpont et al. 2013; Schetselaar et al. 2023).

The outer Delta area is underlain by continuous permafrost. The area was subaerially exposed for much of Wisconsinan glaciation, allowing permafrost to develop up to 600 m (Taylor et al. 1996). Sea level rise since glaciation led to submergence of most of the area, but recently progradation of the Delta has caused the ground surface to emerge (Morse et al. 2012). Mean annual ground temperatures in undisturbed ground range from -3 to -5 °C at the top of permafrost (Burn and Kokelj 2009).

The active layer in alluvial terrain is deeper than in the adjacent well-drained uplands due to early removal of snow in the spring flood and the prevalence of wet soils. At alluvial locations with low-shrub tundra, active layers are 0.4–1.2 m thick (Morse et al. 2012; Duchesne et al. 2015). Snow drifts up to 2.5 m thick may accumulate on sump caps with tall shrubs, whereas caps vegetated with only sedges and grasses have a thin snow cover similar to undisturbed tundra (Kokelj et al. 2010).

3 MACKENZIE DELTA SUMPS

Guidelines for best practices of construction were established during the development of sumps in 1960–2005 (Spencer Environmental 1987). The ideal terrain for construction is flat or gently sloping with topographic highs that promote surface drainage. Sumps should be a minimum of 100 m from the ordinary high-water mark of any permanent water body or stream. These guidelines imply that proper site selection requires inspection of the proposed site for a comprehensive assessment of terrain, hydrologic, permafrost conditions, and land use prior to the development of the sump (Kokelj and GeoNorth 2002). Used drilling fluids should be stored below the permafrost table in the sump for disposal. Since active-layer depths in the Mackenzie Delta may exceed 1.2 m, the surface of the waste fluids should be at a depth of least 2 m (Kokelj and GeoNorth 2002).

4 FIELD LOCATIONS

4.1 Mallik L-38, 2 L-38 and 3/4/5 L-38 sumps

The Mallik site is in low-lying coastal terrain of the outer Mackenzie Delta and is the farthest north of the locations discussed in this paper (Figures 3, 4A). There were three distinct projects at the site (Table 1). The first well, L-38, was drilled by Imperial Oil in 1972. The second and third projects were joint undertakings of Japex and the Geological Survey of Canada in 1998 and 2002. Saline drilling fluids were used in each case (Piraux et al. 2016). The sumps built for these wells are near sea level and are inundated from time to time. The patchy vegetation consists mainly of graminoid species, such as sedges and cotton grasses, with a few sporadic low shrubs and mosses. Sump 3/4/5 L-38 was not seeded after construction and much of the deltaic silt cap remains unvegetated (Piraux et al. 2016). Temperature measurements at 1.5 m below the sump cap have indicated that the material had an annual mean temperature of -7.8 °C in 2007–2013 (Piraux et al. 2016).

4.2 Taglu C-42

C-42 (dimensions in Table 1) is near Harry Channel of the Mackenzie Delta, approximately 140 m from the riverbank (Figure 3). This sump was also constructed in 1972 by Imperial Oil. A combination of non-aqueous drilling fluids and aqueous muds with freezing-point depressants was used for the well (Imperial Oil Resources Ltd 2004). Vegetation has colonized the cap of the sump and surrounding edges of the structure. Willows, 1–2.5 m tall, sedges and alder bushes are present throughout the disturbed area. The sump is surrounded by undisturbed, low-lying, saturated tundra. There are large ponds on and directly adjacent to the sump cap (Figure 4B).

4.2 Niglintgak B-19

B-19 (dimensions in Table 1) is 180 m from Middle Channel of the Mackenzie Delta (Figures 2 and 3). The sump was constructed in 1976 by Shell Canada and is surrounded by wooden pilings that were used to support infrastructure during drilling (Figure 4C). Aqueous KCl polymer drilling fluids were used in well development (Shell Canada Ltd 2005). Vegetation adjacent to the sump is dominated by sedges and cotton grasses in the annually flooded terrain. Stranded driftwood is scattered throughout the site. The sump cap supports a few willows, 1–2 m tall, in addition to patches of unvegetated ground.

5 FIELD METHODS

KCl and other salt solutions are electrically conductive and can be traced in the ground with electromagnetic (EM) induction techniques. Surveys of the sumps were conducted in August and September 2022 with a Geonics EM-31 instrument. The EM-31 induces an electromagnetic field in the ground and, with vertical dipole orientation, has penetration of approximately 5 m (McNeill 1980; Figure 5).

Table 1. Dimensions in meters of Mallik sumps as indicated in Piraux et al. (2016). C-42 and B-19 were measured (in meters) using Google Earth.

Sump	Width	Length	Depth
L-38	46	55	3.5
2L-38	35	45	3.5
3/4/5 L-38	85	100	2
C-42	50	60	N/A
B-19	60	80	N/A

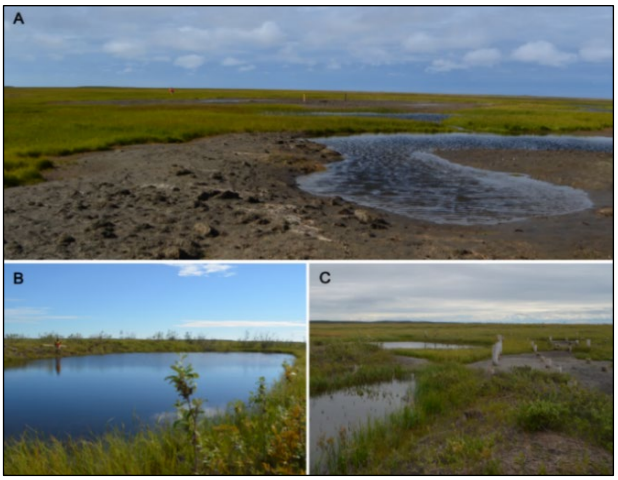

Figure 4. Ground level view of: (A) 3/4/5 L-38 looking northeast; (B) C-42 west sump cap pond; (C) B-19 sump cap facing southwest towards the abandoned pilings.

The EM-31 survey began at the centre of the sump cap and extended 100 m in all cardinal directions into undisturbed terrain (Figure 6). Concentric circles were surveyed at 10 m intervals to fill out the area. The survey was carried out around the perimeters of large ponds.

Grain size analysis was conducted by the pipette method on samples from each sump cap and undisturbed terrain 100 m from the sump. The samples were collected from 40–60 cm depth with a probe sampler. A cylindrical sample 2 cm in diameter and 20 cm long was extracted from 24 locations at each site. Four samples were collected from the sump cap and the others were collected at 20 m intervals from the sump centre along 100 m lines extending outwards in each cardinal direction. Thaw depths were obtained by probing.

Photographs were taken from the air in 2022 at each site. General characteristics of the site including the percentage of sump cap that was covered by ponds were calculated in ArcGIS Pro from these images. The conductivity of pond water was obtained with a YSI Pro 1030 conductivity meter in the lab.

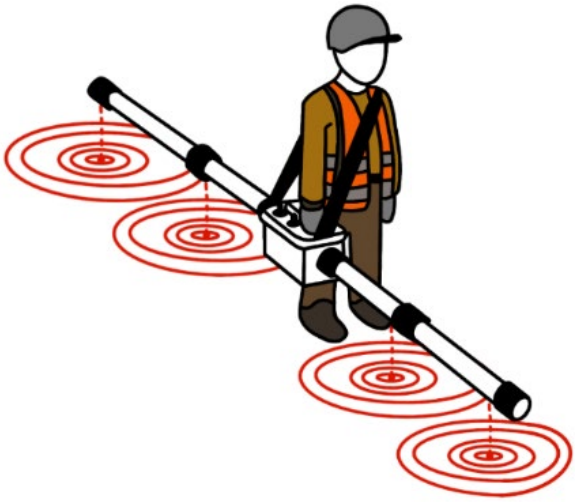

Figure 5. Diagrammatic sketch of EM-31 instrument assembled to conduct a field survey.

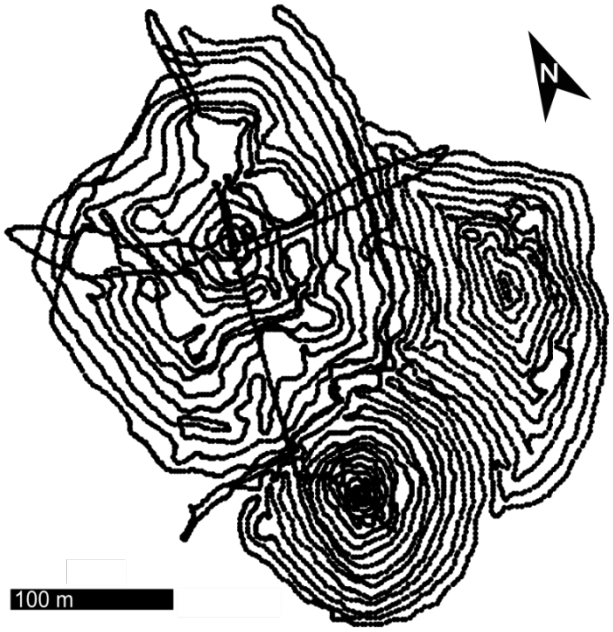

Figure 6. Path of EM-31 survey at the Mallik site.

6 RESULTS

6.1 Grain-size composition

Grain-size composition at all three locations was similar on the sump cap and in undisturbed terrain (Table 2). The dominant grain size was silt, comprising 60–70%. This is expected as the deltaic sediments of the Mackenzie River are composed primarily of fine-grained sediments. 3/4/5 L-38 had the highest sand-sized fraction at ~30%, whereas this was less than 20% for both C-42 and B-19.

Table 2. Grain-size composition on sump cap and in undisturbed terrain.

Sump	Location	% Sand	% Silt	% Clay
3/4/5 L-38	Cap	29	60	11
	Undisturbed	28	69	3
C-42	Cap	18	67	15
	Undisturbed	16	71	13
B-19	Cap	17	68	16
	Undisturbed	17	70	13

6.2 Thaw depths on and near sumps

Thaw depths at 3/4/5 L-38 and C-42 were deepest on the sump cap (Table 3). The thawed ground at B-19 was thickest on the sides of the sump. Relatively little difference was measured between thaw depths on and off the sump caps. Piraux et al. (2016) reported thaw depths in early September 2012 for 2 L-38 and 3/4/5 L-38. Depth on sump caps was recorded at 140 cm and 132 cm respectively, and 136 cm and 131 cm in the perimeter (Piraux et al. 2016).

Table 3. Average thaw depths ($\bar{X}$, cm) on and adjacent to sumps, mid-August 2022, and sample size (n).

	Cap		Sides		Undisturbed	
Sump	$\bar{X}$	n	$\bar{X}$	n	$\bar{X}$	n
3/4/5 L-38	111	2	98	8	100	8
C-42	90	2	81	2	61	9
B-19	80	1	96	8	82	3

6.3 Sump ponding

In 2022, ponds were estimated to cover 8% of the L-38 sump cap, 16% of the 2 L-38 cap, 12% at 3/4/5 L-38, 35% at C-42, and 13% at B-19. Figure 7 presents three images of sump 3/4/5 L-38 taken at 10-year intervals. Development of ponds between 2002 and 2012 is evident, but little change is observed from 2012–2022.

The thermal influence of ponds promotes thickening of the active layer and degradation of the subjacent permafrost. In the outer Mackenzie Delta area, pond water more than 1.5–2 m deep is unlikely to freeze in winter (Burn 2002). Ponds of sufficient depth are likely a route for diffusion of saline pore fluids from within the sump to the surface. No pond depths were measured in this study.

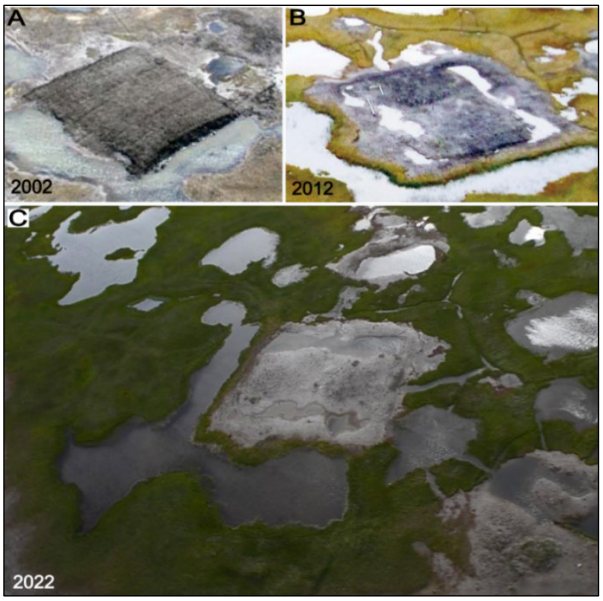

Figure 7. Development of ponds on the sump cap and surrounding terrain at 3/4/5 L-38, as recorded by aerial photographs from (A) 2002; (B) 2012; (C) 2022.

6.4 Pond Water Conductivity

Table 4 presents electrical conductivity of water from ponds on sump caps and in undisturbed ground nearby. Conductivities were highest at Mallik because of proximity to the ocean and inundation at high tide or during storm surges. Nevertheless, ponds on the two oldest sump caps at the site, L-38 and 2 L-38, had higher conductivity water than in undisturbed ground, or on the youngest sump.

At C-42, water collected from the sump cap had lower conductivity than from undisturbed ground nearby. The conductivity in these ponds declined as distance between the pond and the sump increased (Table 4). Ponds on B-19 had a conductivity higher than water from undisturbed ground at C-42, the nearest site to B-19 with samples from off the cap.

6.5 Ground conductivity surveys

EM-31 surveys were conducted in 2022 at all sumps, including the three sumps at the Mallik site (Figures 6 and 8). Records from a survey in 1998 are available for Niglintgak B-19 (Dyke 2001) and for 2012 at Mallik (Figures 8 and 9). Figure 8 presents maps of conductivity at the Mallik site. All three sumps were included in the 2022 survey (Figure 8B).

The conductivity peak evident in Figure 8A east of sump 3/4/5 also diminished in 2022, so sump 2 L-38 is not now as easily distinguished. Conductivity measurements from all three Mallik sumps and from undisturbed ground at the site are presented as box-and-whisker plots in Figure 10A. The Mallik site has relatively high values of ground conductivity because of its coastal location and susceptibility to inundation by sea water, as shown by the pond water conductivity measurements (Table 4). Figure 10A indicates the mean conductivity measured at the

Table 4. Conductivity of pond water on and adjacent to sumps (mS/m). For comparison with ground conductivity.

Sump	Location	Conductivity (mS/m)
L-38	10 m South West	127.6
	West side sump cap	151.4
2L-38	West side sump cap	147.2
3/4/5 L-38	South East sump cap	128.3
	60 m South	126.8
C-42	West sump cap	30.2
	20 m East	65.9
	40 m South	47.4
	60 m North	29.4
B-19	North side of sump cap	88.3
	South side of sump cap	75.0
Mackenzie Delta Water		30
Ocean Water		5500
Deionized Water		17.3

sumps systematically declines with time, so that in 2022, the conductivities measured at the oldest sump, L-38, are comparable to values from undisturbed terrain in the survey area. The highest measurements made at the site were within the boundaries of sump 3/4/5 L-38, but data collected from 2 L-38 were of lower conductivity than in some parts of the undisturbed coastal terrain. The presence of many outliers in undisturbed terrain at the Mallik site (Figure 10A) is due to the zone of elevated ground conductivity, where the site is flooded by Beaufort Sea water.

Figure 9 presents surveys at B-19 in 1998 and 2022. In 1998 the focus of the conductivity distribution coincides with the location of a sump-cap pond in 2022, even though the 1998 survey was conducted in April, under late winter conditions. There is a small anomaly in the northeast corner, also the location of a pond in 2022. Figure 10B presents box-and-whisker plots of ground conductivity at the site on and off the sump cap. The distributions of measurements are comparable between these two areas (cap and undisturbed).

Figure 10B also presents data collected at Taglu C-42. The distribution of conductivities shows higher values over the sump cap than in undisturbed terrain, but the population is of lower conductivity overall than at B-19.

These data are reflected in the pond-water conductivities presented in Table 4, which were also higher at B-19 than C-42.

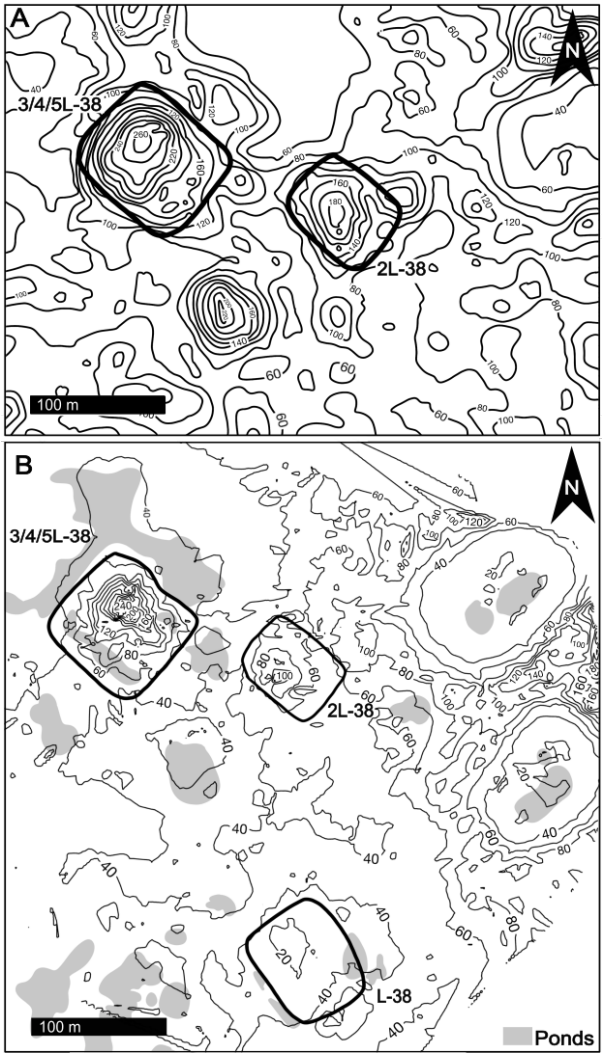

Figure 8. Maps of ground conductivity; (A) 2012 (modified from Piraux et al. 2016) and (B) 2022 surveys. Sumps are outlined in a thick black line on each diagram. The contour interval is 20 mS/m.

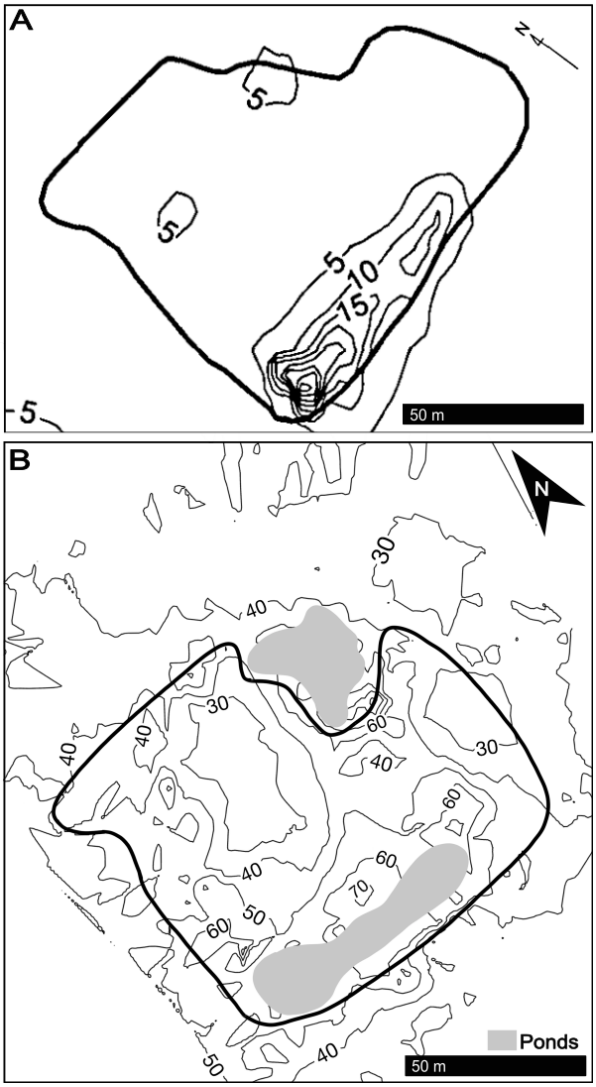

Figure 9. B-19; (A) in 1998 (modified from Dyke 2001) and (B) in 2022 surveys. The sump is outlined with a thick black line on each map. Contour lines are at intervals of (A) 5 mS/m and (B) 10 mS/m.

7 DISCUSSION

7.1 Grain-size composition and thaw depth

Soil physical properties on and off the sumps appear to be similar. The grain-size determinations indicate the similarity of sediment characteristics both on and off the sump caps and within the region (Table 1). The samples collected from the sump caps indicate that the material was locally sourced. The sumps are not covered by a sand or gravel cap, and therefore these materials will have considerable unfrozen water content at temperatures below 0 °C (Williams and Smith 1989).

No systematic differences in thaw depths were observed in these data between undisturbed terrain, sump sides, and sump cap (Table 3). The greatest thaw depths at each site were measured on the sump cap or sides, not in undisturbed terrain, but the differences were small in absolute terms.

7.2 Ground conductivity

Figure 10 indicates the distribution of conductivity measurements made on the sumps and in undisturbed ground nearby. The measurements on the caps of B-19, C-42, and L-38 were of similar value and consistent with data from undisturbed ground. These sumps were built in the 1970s. Data from the cap of 2 L-38 were elevated above the values from the older sumps, and data from 3/4/5 L-38 were the highest recorded from sump caps. The conductivities measured at 2 L-38 appeared spatially less pronounced in the survey of 2022 than in 2012.

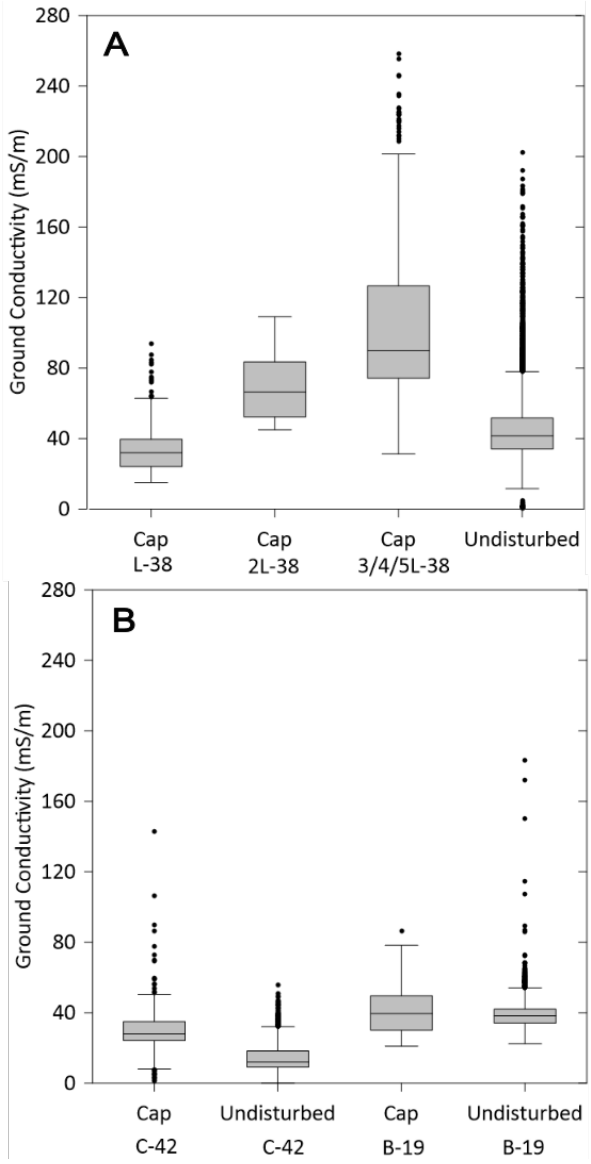

Figure 10. Distribution of ground electrical conductivity measurements between sump caps and undisturbed terrain (in mS/m) at (A) Mallik site, at sumps L-38, 2L-38 and 3/4/5L-38 and (B) C-42 and B-19. Data collected in August 2022.

All sumps were originally filled with saline drilling muds, so it is unlikely that the differences observed in 2022 (Figure 10A) derive from the original state of the materials deposited in the sump.

The conductivities of pond water samples are 3–4 orders of magnitude higher than the ground conductivities. This is due to the higher conductivity of water in comparison with ice and the presence of salts in the ponds. However, the ground conductivities are comparable to the conductivity of Mackenzie Delta water collected near Inuvik (0.3 mS/cm = 30 mS/m; Burn 1995). Water in the channels of the outer Delta is likely of higher conductivity due to the influence of the proximal Beaufort Sea. The conductivities of pond-water samples, presented in Table 4, show elevated salt concentrations from pools on sumps at Mallik and Niglintgak in comparison with undisturbed terrain. The values from Taglu are comparable between ponds on and off the sump. At Mallik, the conductivity in pond water was highest at L-38 and lowest at 3/4/5 L-38. Given that the ground conductivity values were in opposite rank order, it is possible that there is leakage of saline fluids from the containment chamber into the pools. This is a plausible hypothesis with the data available but requires further investigation, specifically at ponds.

However, unless the 5-m penetration of the EM-31 is insufficient to reach the waste materials, the data presented in Figure 10 suggest that the saline fluids have dispersed from the oldest sumps over the past 40–50 years. The conductivities are now indistinguishable between the sump caps and undisturbed terrain near L-38, C-42, and B-19. The differences between surveys in 2012 and 2022 and the values from 2 L-38 in 2022 indicate that the materials are dispersing from 2 L-38. The high ground conductivity measured at 3/4/5 L-38 and the similarity in conductivity of pond water on this sump to pond water in undisturbed ground, suggest that drilling fluids are relatively well contained in this structure.

It may be a coincidence that the ground conductivities of the Mallik sumps site decline with age, but information from pond water and the comparison of conductivities over time support the hypothesis that the oldest sumps have not performed as intended over the last 50 years. Since the ground conductivity at the three oldest sumps is similar to values measured in undisturbed terrain, these structures may have failed. Further investigation with different tools is required to verify this hypothesis, by direct ground sampling of sump contents or deeper EM penetration (e.g., EM-34 instrument).

8 CONCLUSION

On the basis of the results presented above, we conclude:

1) The electrical conductivity of the ground and pond waters at three sumps in low-lying areas of the outer Mackenzie Delta suggest that sumps built in the 1970s have failed to contain saline waste because the ground conductivity at these sumps is similar to undisturbed ground.
2) The most recent sump, Mallik 3/4/5 L-38, built in 2002, remains clearly distinguishable by its elevated ground conductivity. The conductivity of pond water on the sump is similar to the conductivity of samples from undisturbed ground nearby. This sump appears to be performing relatively well.
3) A sump built in 1998, 2 L-38, has lower conductivity than 3/4/5 L-38. A reduction in the spatial concentration of conductivity at 2 L-38 and elevated concentrations in ponds at this sump suggest that some of this sump's contents may have dispersed between 2012, the date of a previous EM survey, and 2022.

9 ACKNOWLEDGMENTS

The activities reported in this paper have been supported by the Aurora Research Institute of Aurora College, the Polar Continental Shelf Project of Natural Resources Canada, and the NSERC PermafrostNet Strategic Network. Cassandra Kuptana of the Inuvialuit Land Administration provided valuable field assistance. Helpful comments from L.D. Dyke and two anonymous referees are gratefully acknowledged.

10 REFERENCES

Burn, C.R. 1995. 'The Hydrologic Regime of Mackenzie River and Connection of "no-closure" Lakes to Distributary Channels in the Mackenzie Delta, Northwest Territories', *Canadian Journal of Earth Sciences* 32(7), pp. 926–937. doi:10.1139/e95-078.

Burn, C.R. 2002. 'Tundra Lakes and Permafrost, Richards Island, Western Arctic Coast, Canada', *Canadian Journal of Earth Sciences* 39(8), pp. 1281–1298. doi:10.1139/e02-035.

Burn, C.R. and Kokelj, S.V. 2009. 'The Environment and Permafrost of the Mackenzie Delta Area', *Permafrost and Periglacial Processes* 20(2), pp. 83–105. doi:10.1002/ppp.655.

Duchesne, C., Smith, S.L., Ednie, M., and Bonnaventure, P.P. 2015. 'Active Layer Variability and Change in the Mackenzie Valley, Northwest Territories', in *68th Canadian Geotechnical Conference and 7th Canadian Conference on Permafrost*. Québec City, Québec, Canada: Canadian Geotechnical Society, Paper 117.

Dyke, L. 2001. 'Contaminant Migration Through the Permafrost Active Layer, Mackenzie Delta area, Northwest Territories, Canada', *Polar Record* 37(202), pp. 215–228. doi:10.1017/S0032247400027248.

Environment Canada 2023. *Canadian Climate Normals 1981-2010 Station Data*. Available at: https://climate.weather.gc.ca/climate_normals/index_e.html (Accessed: September 1 2023).

French, H.M. 1980. 'Terrain, Land Use and Waste Drilling Fluid Disposal Problems, Arctic Canada', *Arctic* 33(4), pp. 794–806. doi:10.14430/arctic2596.

Hardy BBT Ltd. and Stanley Associates Engineering Ltd. 1988. 'Handling and Disposal of Waste Drilling Fluids from on-land Sumps in the Northwest Territories and Yukon', *Environmental Studies Research Funds* Report No. 093. Ottawa, Ontario, Canada: 58 p.

Hrudey, S.E. 1979. 'Sources and Characteristics of Liquid Process Wastes from Arctic Offshore Hydrocarbon Exploration', *Arctic* 32(1), pp. 3–21. doi:10.14430/arctic2601.

Imperial Oil Resources Ltd. 2004. *Application for the Approval of the Development Plan for Taglu Field: Project Description*. Calgary, Alberta, Canada: submitted to National Energy Board. Available at: https://docs2.cer-rec.gc.ca/ll-eng/llisapi.dll/fetch/2000/90464/90550/338535/338661/343073/343030/3891457/C03233%2D1_Development_Plan_for_the_Taglu_Field_%2D_A7A3C2.pdf?nodeid=3891458&vernum=-2.

Kokelj, S.V. and Burn, C.R. 2005. 'Near-surface Ground Ice in Sediments of the Mackenzie Delta, N.W.T., Canada', *Permafrost and Periglacial Processes* 16(3), pp. 291–303. doi:10.1002/ppp.537.

Kokelj, S.V. and GeoNorth Ltd. 2002. 'Drilling Mud Sumps in the Mackenzie Delta Region: Construction, Abandonment and Past Performance', *Department of Indian Affairs and Northern Development, Northwest Territories Region*. Available at: https://www.gov.nt.ca/sites/ecc/files/drilling_mud_sumps_in_the_mackenzie_delta_region_construction_abandonment_and_past_performance_2002.pdf.

Kokelj, S.V., Riseborough, D., Coutts, R. and Kanigan, J.C.N. 2010. 'Permafrost and Terrain Conditions at Northern Drilling-mud Sumps: Impacts of Vegetation and Climate Change and the Management Implications', *Cold Regions Science and Technology* 64(1), pp. 46–56. doi:10.1016/j.coldregions.2010.04.009.

Mackay J.R. 1963. 'The Mackenzie Delta Area, N.W.T', *Canada Department of Mines and Technical Surveys*, Geographical Branch, Geographical Memoir 8. doi:10.4095/329313.

McNeill, J.D. 1980. 'Electromagnetic Terrain Conductivity Measurement at Low Induction Numbers', *Geonics Limited* Technical Note TN-6. Available at: https://geonics.com/pdfs/technicalnotes/tn6.pdf.

Morse, P.D., Burn, C.R. and Kokelj, S.V. 2012. 'Influence of Snow on Near-surface Ground Temperatures in Upland and Alluvial Environments of the Outer Mackenzie Delta, Northwest Territories', *Canadian Journal of Earth Sciences* 49(8), pp. 895–913. doi:10.1139/e2012-012.

Piraux, O., Côté, M.M., Akagawa, S., Kawamoto, T., Seccombe-Hett, P., and Dallimore, S.R. 2016. 'Mallik 7-Year Drilling Waste Sump Monitoring Program: Summary Report', *Geological Survey of Canada* Open File 8015. doi:10.4095/297895.

Schetselaar, A., Andersen, T., and Burn, C.R. 2023. 'Performance of Climate Projections for Yukon and Adjacent Northwest Territories, 1991–2020', *Arctic* 76(3), pp. 244–264 doi:10.14430/arctic77263.

Shell Canada Ltd. 2005. *Niglintgak Field Development. Drill Cuttings Management Disposal Options* and *Selected Disposal Method*. Available at: https://docs2.cer-rec.gc.ca/ll-eng/llisapi.dll/fetch/2000/90464/90550/338535/338661/343073/343080/347038/SCL%2D006B_%2D_Drill_Cuttings_Management_Disposal_Options_and_Selected_Disposal_Method_Report_%28A0L8C7%29_SCL%2D6B.pdf?nodeid=347039&vernum=-2.

Simpson, B. and Van Gulck, J. 2020. *Inuvialuit Settlement Region: Drilling Sumps Failure and Climate Change report*. Available at: https://irc.inuvialuit.com/research/documents-and-resources (Accessed: July 27 2023).

Spencer Environmental 1987. *Environmental Operating Guidelines: Hydrocarbon Well-sites in Northern Canada*. Indian and Northern Affairs Canada, Land Resources, Northern Affairs Program, Ottawa, Ontario, Canada.

Taylor, A.E., Dallimore, S.R., and Judge, A.S. 1996. 'Late Quaternary History of the Mackenzie–Beaufort Region, Arctic Canada, from Modelling of Permafrost Temperatures. 2. The Mackenzie Delta–Tuktoyaktuk Coastlands', *Canadian Journal of Earth Sciences* 33(1), pp. 62–71. doi:10.1139/e96-00.

Thienpont, J.R., Rühland, K.M., Pisaric, M.F.J., Kokelj, S.V., Kimpe, L.E., Blais, J.M., and Smol, J.P. 2013. 'Biological Responses to Permafrost Thaw Slumping in Canadian Arctic lakes', *Freshwater Biology* 58(2), pp. 337–353. doi:10.1111/fwb.12061.

Williams, P.J. and Smith, M.W. 1989. *The Frozen Earth: Fundamentals of Geocryology*. Cambridge University Press. doi:10.1017/CBO9780511564437.

Antarctic water track hydrology and geochemistry from drone and ground sensors: Active layer wetland processes in a cold desert

Joseph Levy[1], Ian Andrews[1], Aidan Guller[1], Jessica Johnson[1], Izzy King[1], Emily Pfaff[1], Lily Kuentz[2] & Anna Talucci[3]

[1]*Department of Earth and Environmental Geosciences, Colgate University, Hamilton, New York, United States*
[2]*Department of Geography, University of Oregon, Eugene, Oregon, United States*
[3]*Arctic Program Woodwell Climate Research Center, Falmouth, Massachusetts, United States*

Abstract

We report on drone-borne remote sensing and ground-based geochemical results from water track soils collected in 2022–2023 in the McMurdo Dry Valleys of Antarctica that aim to address how much water is flowing through Antarctic water tracks, what remote sensing reveals about water track melt sources, and what impacts water track flow has on soil biogeochemical processes that may be leading to soil development in the water tracks. Water tracks were measured using drone-borne remote sensing: a Headwall Extended VNIR imaging spectrometer (900–1700 nm spectral range). Soil moisture content was measured during UAV flights using co-located soil moisture probes and was extrapolated beyond probe locations across the water track and adjacent dry soil using a linear fit between in situ measured water content and the depth of the 1.4 µm reflectance spectrum absorption feature associated with water. We report on ground-truth measurements of sediment characteristics, organic matter content, and dissolved silica and clay properties (abundance, soil texture, and exchange chemistry) to evaluate whether Antarctic water tracks are in a positive feedback loop, in which wetting of previously dry ground results in enhancement of soil organic matter, enhanced chemical weathering, and leading to longer wetted periods. This work expands on previous studies by presenting multiple wavelengths of remote sensing data, further refining the water budget for the Antarctic active layer, and by integrating deeper soil sensor and ground-truth measurements to explore the range of biogeochemical processes at work in these Antarctic wetland features.

1 Introduction

Recent observations of accelerating erosion and ground ice thaw in Antarctica's coastal McMurdo Dry Valleys (MDV) suggest that shrinking permafrost extents, thickening active layers, and widespread thermokarst subsidence may be early indicators of imminent, continental-scale change in the state of the Antarctic terrestrial cryosphere (Fountain et al. 2014). Groundwater-mediated thawing of permafrost has been a defining characteristic of Arctic landscapes over the past decade, where changes in drainage, thermokarst pond geometry, and active layer thermal properties have rapidly altered the distribution of soils, ice, and soil carbon (Kanevskiy et al. 2008; Gooseff et al. 2011; Jorgenson 2013; Arp et al. 2015; Strauss et al. 2016). As Antarctic ice-free area grows (Lee et al. 2017) and previously dry soils transition into wetted active layers (Levy and Schmidt 2017), it is not yet clear how Antarctica will participate in global biogeochemical and hydrological processes in a world with dramatically less ice.

"Water tracks" (Figure 1) are the basic unit of the subsurface hydrological system that feeds polar and permafrost wetlands. Water tracks are narrow bands of high soil moisture that route water downslope through soils, in the absence of overland flow (Hastings et al. 1989; McNamara et al. 1999; Levy et al. 2011). In water tracks, moisture moves as shallow groundwater, flowing through the active layer (the seasonally-thawed portion of soil column) along linear depressions in the ice table (the top of the permafrost that remains ice-cemented during summer). Because they are soil landforms, water tracks are notoriously difficult to measure because they cannot be easily gauged like a stream (Gooseff et al. 2016) or bathymetrically surveyed like a lake.

Our working model is that groundwater distribution and duration in MDV soils controls thaw depth, sedimentological composition, and solution chemistry. If groundwater hydropattern controls these near-surface hydrogeological and geomorphic systems, we can predict how changing hydropatterns will alter soil and ground ice in a warmer future (Arblaster and Meehl 2006) by determining how different spatial extents of soil wetting shape soils and ground ice now. We predict that expansion of the extent and duration of wetting, and the enrichment of saline solutions should increase thermokarst subsidence and increase chemical weathering rates. In short, wetting of previously dry active layers will drive the topographic and geological reorganization of the landscape. In particular, we hypothesize that water tracks may be in a positive feedback loop, where enhanced soil moisture for extended periods of the Antarctic summer melt season leads to enhanced chemical weathering of soils to generate clays alongside enhanced growth of soil carbon (through organic and inorganic carbon emplacement). Enrichments in soil organic matter and fine-grained sediments, accompanied by greater soil porewater solute concentrations from weathering reactions and dissolution of soil salts, may lead to increased resistance to active layer freezing, extending the water track thaw period.

To test this hypothesis, we measured water track soil and groundwater properties ("on track") as well as the properties of adjacent, "off track," soils in Taylor, Wright, and Beacon valleys (Figure 1). Here, we focus on active layer soil and

https://doi.org/10.52381/ICOP2024.68.1

groundwater conditions at the Howard Glacier (HG) water track in central Taylor Valley.

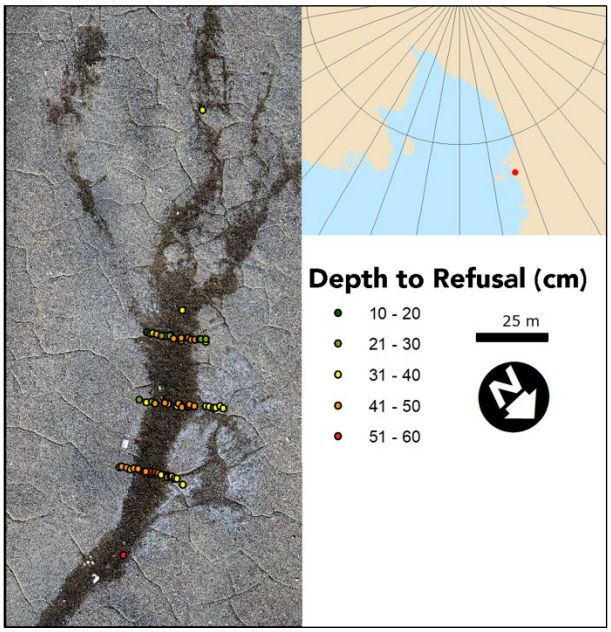

Figure 1. Context map showing the Howard Glacier water track field site, depth to refusal transects and the local of the MDV (red dot) in the Ross Sea region of Antarctica. Downslope to image bottom.

2 METHODS

Field measurements were conducted in Taylor Valley, MDV. The MDV are the largest ice-sheet-free region in Antarctica (Levy 2012) and are located at ~77–78˚S, 160–164˚E. The MDV are a cold desert that experience mean annual temperatures of ~-18˚C (Doran et al. 2002) and little snowfall, typically 3–50 mm water equivalent (Fountain et al. 2009). Field data reported here are primarily from a water track in the Howard Glacier (HG) basin watershed, supported by geochemical measurements from samples collected from across the MDV (including Wright, Beacon, and Garwood valleys).

2.1 Field Methods

In order to determine the spatial distribution of active layer thickness, depth to refusal measurements were collected in transects crossing the water track and along the water track centerline. “On track” sampling sites were selected on the basis of visible darkening of the soil due to the presence of soil moisture. “Off track” samples were dry and bright at the surface and were typically 3–5 m from the light/dark boundary of the water track. Measurements were collected in triplicate and averaged. Where buried rocks, rather than frozen sediment were encountered, measurements were recorded, but were not included in subsequent analyses.

Soil samples were collected from both water track-crossing transects and from vertical soil profiles. Sediments were air-dried to determine water content by mass, and soluble salts were extracted from 1:10 soil extracts made with 18-MΩ deionized water. Soil inorganic carbon content was determined via pressure calcimeter and soil organic carbon content was measured using a Primacs SNC-100 Carbon and Nitrogen Analyzer at the Cornell Soil Health Laboratory.

Pore waters from the water tracks were sampled directly using sterile syringes. Dissolved silica in water tracks was measured using the Heteropoly Blue Method on a Hach DR3900 spectrophotometer. Soil extract and direct water sample major ion concentrations were measured via ion chromatography.

Drone-borne remote sensing was conducted in the field in order to measure the spatial extent and concentration of surface soil moisture. We flew a Headwall Extended VNIR imaging spectrometer (900–1700 nm spectral range) on a Matrice 600 Pro aircraft to generate hyperspectral image cubes with ~4 nm spectral resolution. To support calibration of remote-sensing derived soil moisture estimates, ground-based spectra along soil sampling transects was conducted using a FLAME-NIR spectrometer with a spectral range of 950–1650 nm with 128 spectral channels (~10 nm resolution per channel).

2.2 Remote Sensing and GIS Methods

Ground-based reflectance spectra were used to generate a site-specific continuum-removed water index (CRWI) calibration for the HG water track using the methods of Levy and Johnson (2021). CRWI is calculated by determining the slope of the reflectance spectra continuum between 1.335 µm and 1.63 µm, which brackets the 1.4 µm absorption feature for water. CRWI is the difference between the continuum slope value at 1.5 µm and the measured reflectance at 1.5 µm. Here, we report a normalized CRWI value, which normalizes the measured band depth by the reflectance value of the continuum slope at 1.5 µm in order to scale CRWI to surface brightness. A linear model was then fit between the ground-measured CRWI values and the soil moisture content measured in the lab. This model,

$$\text{Soil Moisture Mass Fraction} = 0.1 \bullet \text{CRWI} + 0.007 \quad [1]$$

was then applied to the airborne hyperspectral data in order to estimate surface soil moisture across the water track surface at the spatial resolution (~5 cm/pixel) of the image cube.

In order to determine the drainage properties of the water tracks, a topographic wetness index (TWI) model was computed for the HG water track, where TWI is defined as:

$$TWI = \ln(a / \tan(b)) \quad [2]$$

where b is local surface slope and a is the upslope accumulating area for each pixel. Slope was determined from the Fountain et al. (2017) airborne lidar DEM for the MDV. Upslope accumulating area was determined using the lidar DEM to generate downslope routing from source pixels that were identified from a thresholded Worldview-2

image of the study site collected during field operations (WV02_20221202193905, panchromatic DN > 700 to identify snow and ice pixels).

3 RESULTS

Depth to refusal increases towards the center of the water track and downslope along the water track flow direction (Figures 2 and 3). Increased active layer thickness is associated with increased soil moisture at the water track surface, as well as with observations of water-saturated or muddy (unsaturated) conditions in the subsurface, based on observations of the DTR tile probe (Figure 2). Together, this indicates that the deepest parts of the water track are also the wettest, and that surface soil moisture values correlate with soil moisture conditions deeper in the water track.

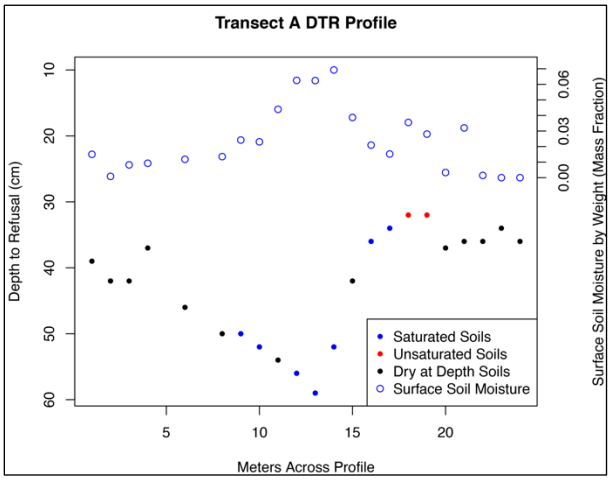

Figure 2. Depth to refusal and surface soil moisture measurements for transect A (downslope-most transect). Surface soil moisture is associated with deep active layers and saturated conditions at the bed.

Soil moisture is higher in water tracks than in adjacent off-track soils (Figure 4) and increases with depth in both on and off-track soils. Soil moisture is typically < 5% by mass for off-track soils, but reaches saturation (20–25% by mass) for water track soils.

Water track location is strongly predicted by the snowbank-initialized topographic wetness index model, and depth to refusal is correlated with TWI (Figure 5). Portions of the water track with low surface slopes lead to ponding of meltwater-derived flow and thaw of the active layer.

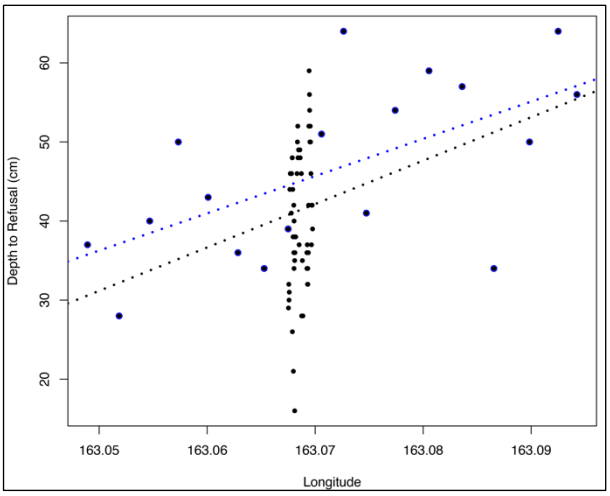

Figure 3. Depth to refusal along the water track. DTR increases along the water track flow path from west to east (left to right). Single, blue points are centerline measurements; grouped black points are transects across (transverse to) the water track. $P < 0.001$ for both linear fits. $R^2 = 0.37$ and 0.15 for centerline points and all points, respectively. DTR increases downstream, as well as towards the center of the water track. At the transect locations, there is a wide spread in DTR, but that that spread brackets the downstream tend in increasing DTR.

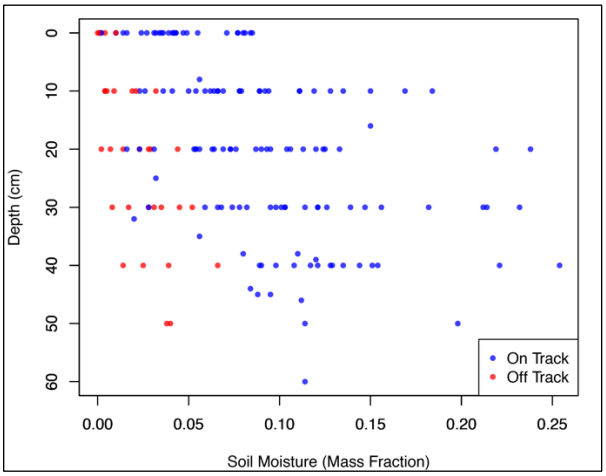

Figure 4. Soil moisture with depth for on-track and off-track soils. Soil moisture increases with depth for both on-and off-track soils, but only exceeds ~10 wt.% soil moisture for on-track soils.

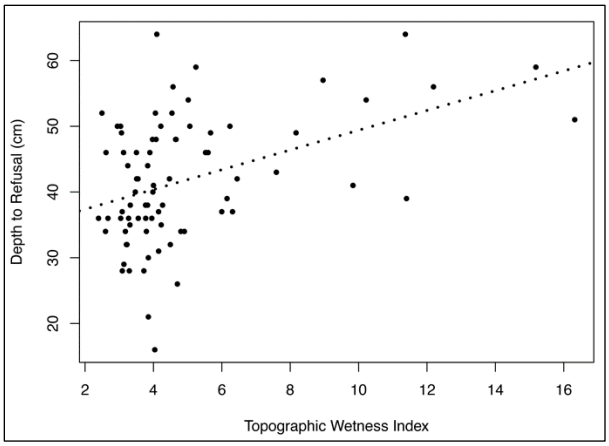

Figure 5. Depth to refusal versus topographic wetness index. Wetter soils show increased depth to refusal in comparison to drier soils. For linear model, $R^2 = 0.18$ and $P < 0.001$.

At the HG water track study site, surface soil moisture content and normalized CRWI are strongly correlated (Figure 6). On the basis of the local CRWI calibration, surface soil moisture along the HG water track spans ~0–3 wt.% (Figure 7), broadly consistent with on and off-track surface soil moisture contents measured in vertical soil profiles in and around the water track (Figure 4). CRWI-derived soil moisture increased towards the water track center and also shows variability associated with water track microtopography (gravel ripples and dunes). Wetted soils outside the water track that are associated with efflorescent salt patches are also detected in the CRWI soil moisture product.

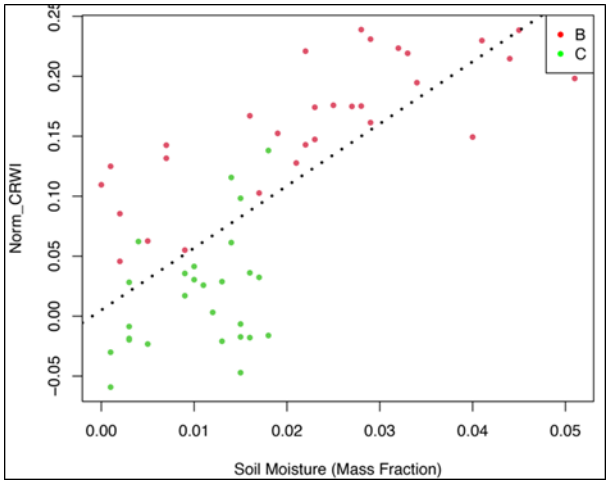

Figure 6. Calibration curve for CRWI soil moisture parameter derived from water track sampling transects sections B and C (left and right green dots in Figure 7). Wetter surface soils show higher normalized CRWI spectroscopic indices. Normalized CRWI is linearly dependent on soil moisture.

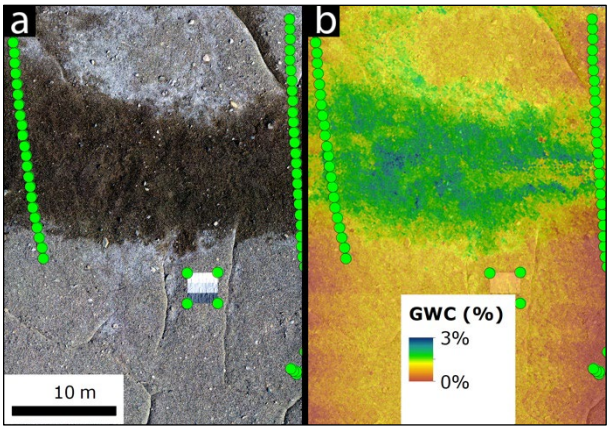

Figure 7. Surface soil moisture estimates across the HG water track using the local normalized CRWI calibration. Soil moisture is variable across water tracks and broadly agrees with surface measurements at transect points. GWC is gravimetric water content, equivalent to soil moisture weight percent.

Soil carbon at the HG sites is in-homogenously distributed. Water tracks typically have higher total carbon than off-track soils (Figure 8), although nearly all HG study site soils have < 1 wt.% total carbon. Neither on-track nor off-track soils have high organic carbon contents, with values almost always < 1 wt.%, and most < 0.2 wt.%, however, the highest organic carbon measurements in the study site are all on-track soils. Water track soil organic carbon increases towards the soil surface (Figure 9).

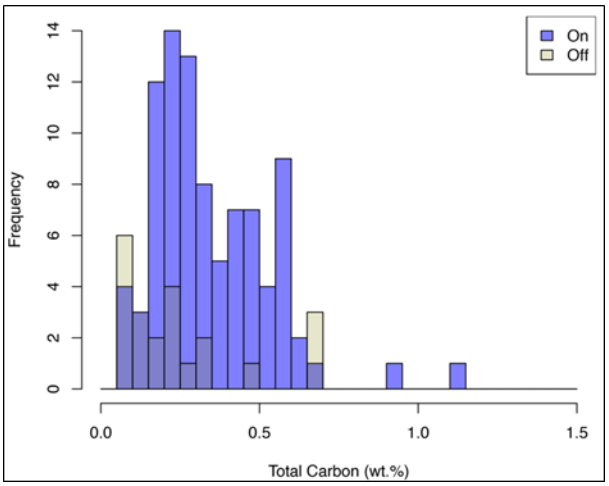

Figure 8. Total carbon on and off water tracks. Water tracks have notably higher soil carbon that off-track soils ($P < 0.02$). Water track carbon is dominated by inorganic carbon, however, the highest organic carbon contents (> 0.2%) are only from on-track samples.

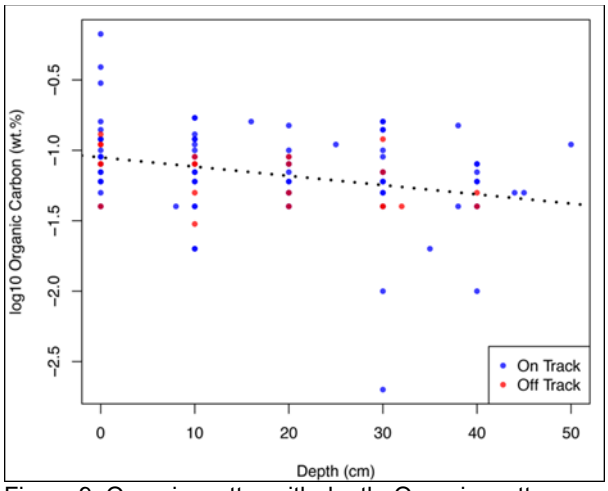

Figure 9. Organic matter with depth. Organic matter increases towards the surface in water tracks, suggesting organic matter is not just advected into water tracks in groundwater flow.

Finally, dissolved silica content is higher in nearly all water track pore waters than in snow or surface streams in the MDV (Figure 10). Silica concentrations in water tracks reach ~1 mM, which greatly exceeds typical fresh snow (< 10 µM) and surface stream water (< 100 µM). Dissolved silica concentration in water tracks increases with increasing total dissolved solids and total chloride (a conservative ion tracer), before reaching saturation between ~10^2 and 10^3 µM.

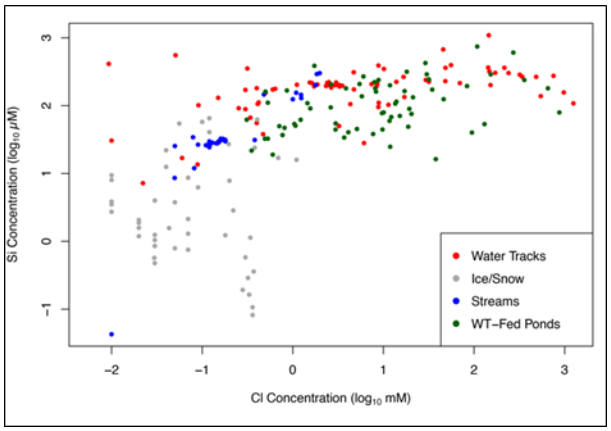

Figure 10. Dissolved silica versus chloride for water tracks and surface water in the MDV. Water tracks have ~10x greater dissolved silica contents than streams and approach silica saturation.

4 Discussion

What do ground-based observations suggest about the spatial distribution of soil moisture in water tracks and the surface energy balance/heat transfer processes that generate active layer flow? Active layer thicknesses on the HG water track increase from the bright, dry, off-track soils to the dark, wetted, on track soils. This is broadly consistent with presence of low albedo wetted soils leading to enhanced shortwave energy flux into the wetted soils, as measured on other water tracks (Linhardt et al. 2019). Thicker active layers on water tracks are also consistent with higher thermal diffusivity for wetted soils than for dry soils, leading to enhanced penetration of the seasonal thermal wave into water tracks (e.g., Levy and Schmidt 2016). Higher thermal diffusivity leads to deepening the ice table below the wettest soils. Together, these changes to surface energy balance and soil thermal regime suggest that water tracks may be self-deepening and self-channelizing systems; wet soils thaw deeply, steepening the subsurface ice table slope, and channelizing any available meltwater into water track drainage pathways. This implies that water tracks are not just persistent features of the MDV hillslope drainage environment, but could expand if additional meltwater became available, either through increases in snow melt or regional ice table thaw.

What do these findings suggest about the range of possible sources of meltwater for water tracks? Can they be used to discriminate between snow melt, ground ice melt, and soil salt deliquescence endmembers? The airborne hyperspectral observations, coupled with the strong dependence of water track darkening on high topographic wetness index, suggest that soil moisture in water tracks is largely sourced from snowmelt, rather than ground ice melt or other meltwater sources. The depth to refusal probing (Figure 2) and the hyperspectral observations both show that water track saturation conditions are heterogenous in the water tracks, and that saturated soils may be present both in the water track thalweg and perched in other channels or pools generated by ice table topography. Water track moisture wicking up from these saturated regions near the base of the water track is spatially heterogenous at the surface owing to both variability in subsurface saturation as well as variability in response to soil surface microtopography, roughness, and likely grain size. That is, moisture may rise higher in wetted in sands and fines, while the surface may be less wet at the surface over gravels and granules.

Finally, to what extent do these observations suggest that water tracks are simply advecting in soil carbon or weathering products versus generating these materials in situ? Organic carbon measured in the water tracks increases towards the surface, suggesting primary production and burial of organic carbon is the main source of water track carbon. Notably, there is no increase in organic carbon at depth in the water tracks where the majority of saturated soil groundwater flow takes place. This suggests that organic matter is not flowing into the water tracks along the ice table. In addition, carbon is enriched in the water track (both inorganic and organic), suggesting that water tracks may be important, and hitherto overlooked components in the carbon dynamics of MDV soils. Water track physical (dissolution/precipitation) and biogeochemical processes (primary production and limited consumption due to high salt contents) may build up carbon in water tracks to concentrations several times those present in adjacent off-track soils. Finally, dissolved silica is reaching saturation in water tracks (Figure 10) but is clearly entering water tracks from dissolution of primary minerals in soils, e.g., feldspar (Lyons et al. 2021). This indicates that even if clays are being advected in groundwater flow through sand pores, those clays are forming in situ in water

tracks through hydrolysis reactions that release silica into the groundwater. Together, these measurements of carbon build-up and silicate weathering in the HG water track are consistent with a positive feedback model in which water track biogeochemical reactions, driven by meltwater flow through the water tracks, lead to stronger or more persistent pedogenic processes. Groundwater flow leads to organic carbon build up; organic acids coupled with meltwater interactions with fresh sediment grains lead to enhanced chemical weathering and fines production; decreases in porosity due to the presence of organic matter, precipitated carbonates, and silt/clay particles lead to enhanced capillary rise in water tracks; and enhanced capillary rise leads to greater evaporation from water tracks, concentrating the pore water solutions into freeze-resistant soil brines, which can remain wet late into the spring and fall shoulder seasons (Kuentz et al. 2022).

5 Conclusions

Preliminary analyses of water track ground-measured soil properties and drone-borne remote sensing measurements suggests that water tracks are hydrologically and thermally re-enforcing components of the cold desert hydrological system. Deep seasonal thaw occurs in the wettest soils, and spatial heterogeneity in surface soil moisture content is correlated with differences in active layer thickness and column-integrated active layer soil moisture content. Water tracks are sites where soil biogeochemical processes concentrate soil carbon (both organic and inorganic), raising soil carbon content to levels several times that of adjacent, off-track soils. Chemical weathering of silicate grains in water track soils enriches the water track pore fluids in solutes and also concentrates fine grains in water tracks, decreasing porosity and increasing capillary rise and matric potential. Together, these two mechanisms enhance evaporation and solute concentration in the water tracks. These results suggest water tracks are likely locations where positive feedback mechanisms are generating soil from regolith on Antarctic cold desert hillslopes, which could expand or become more active under warming conditions, additional snowfall, or more widespread thaw.

6 Acknowledgements

This work was supported by NSF award OPP-1847067 to JSL. Worldview data provided by the Polar Geospatial Center

7 References

Arblaster, J.M. and Meehl, G.A. 2006. 'Contributions of external forcings to southern annular mode trends', *Journal of Climate* 19(12), pp. 2896–2905.

Arp, C.D., Whitman, M.S., Jones, B.M., Grosse, G., Gaglioti, B.V. and Heim, K. 2015. 'Distribution and biophysical processes of beaded streams in Arctic permafrost landscapes', *Biogeosciences* 12(1), pp. 29–47. Available at: https://doi.org/10.5194/bg-12-29-2015.

Doran, P.T., McKay, C.P., Clow, G.D., Dana, G.L., Fountain, A.G., Nylen, T. and Lyons W.B. 2002. 'Valley floor climate observations from the McMurdo dry valleys, Antarctica, 1986–2000', *Journal of Geophysical Research: Atomospheres* 107(D24), pp. ACL 13-1–ACL 13-12. Available at: https://doi.org/10.1029/2001JD002045.

Fountain, A.G., Nylen, T.H., Monaghan, A., Basagic, H.J. and Bromwich, D. 2009. 'Snow in the McMurdo Dry Valleys, Antarctica', *International Journal of Climatology* 30(5), pp. 633–642. Available at: https://doi.org/10.1002/joc.1933.

Fountain, A.G., Levy, J.S., Gooseff, M.N. and Van Horn, D. 2014. 'The McMurdo Dry Valleys: A landscape on the threshold of change', *Geomorphology* 225, pp. 25–35. Available at: https://doi.org/10.1016/j.geomorph.2014.03.044.

Fountain, A.G., Fernandez-Diaz, J.C., Obryk, M., Levy, J., Gooseff, M., Van Horn, D.J., Morin, P. and Shrestha, R. 2017. 'High-Resolution Elevation Mapping of the McMurdo Dry Valleys, Antarctica, and Surrounding Regions', *Earth System Science Data* 9(2), pp. 435–443.

Gooseff, M.N., Balser, A., Bowden, W.B. and Jones, J.B. 2011. 'Effects of Hillslope Thermokarst in Northern Alaska', *Eos, Transactions American Geophysical Union*, 90(4), pp. 29–30. Available at: https://doi.org/10.1029/2009EO040001.

Gooseff, M.N., Wlostowski, A., McKnight, D.M. and Jaros, C. 2016. 'Hydrologic connectivity and implications for ecosystem processes - Lessons from naked watersheds', *Geomorphology* pp. 1–9. Available at: https://doi.org/10.1016/j.geomorph.2016.04.024.

Hastings, S.J., Luchessa, S.A., Oechel, W.C. and Tenhunen, J.D. 1989. 'Standing biomass and production in water drainages of the foothills of the Philip Smith Mountains, Alaska', *Holarctic Ecology* 12(3), pp. 304–311.

Jorgenson, M.T. (2013) 'Thermokarst terrains', in R. Giardino and J. Harbor (eds.), *Treatise of Geomorphology* 8, pp. 313–324. Available at: https://doi.org/10.1016/B978-0-12-374739-6.00215-3.

Kanevskiy, M., Jorgenson, M.T., Shur, Y. and Dillon, M.R. 2008. 'Buried Glacial Basal Ice Along the Beaufort Sea Coast, Northern Alaska', in *American Geophysical Union Fall Meeting 2008.* San Francisco, California, United States: December 15–19, 2008, abstract # C11D-0531.

Kuentz, L., Levy, J. and Salvatore, M. 2022. 'Timing and duration of ephemeral Antarctic water tracks and wetlands using high temporal–resolution satellite imagery, high spatial–resolution satellite imagery, and ground-based sensors in the McMurdo Dry Valleys', *Arctic, Antarctic, and Alpine Research* 54(1), pp. 538–561. Available at: https://doi.org/10.1080/15230430.2022.2123858.

Lee, J.R., Raymond, B., Bracegirdle, T.J., Chadès, J., Fuller, R.A., Shaw, J.D. and Terauds, A. 2017. 'Climate change drives expansion of Antarctic ice-free habitat', *Nature* 547, pp. 49–54. Available at: https://doi.org/10.1038/nature22996.

Levy, J. (2012) 'How big are the McMurdo Dry Valleys? Estimating ice-free area using Landsat image data', *Antarctic Science* 25(01), pp. 119–120. Available at: https://doi.org/10.1017/S0954102012000727.

Levy, J.S., Fountain, A.G., Gooseff, M.N., Welch, K.A. and Lyons, W.B. 2011. 'Water tracks and permafrost in Taylor Valley, Antarctica: Extensive and shallow groundwater connectivity in a cold desert ecosystem', *Geological Society of America Bulletin* 123(11–12), pp. 2295–2311. Available at: https://doi.org/10.1130/B30436.1.

Levy, J.S. and Johnson, J.T.E. 2021. 'Remote Soil Moisture Measurement from Drone-Borne Reflectance Spectroscopy: Applications to Hydroperiod Measurement in Desert Playas', *Remote Sensing* 13(5), p. 1035. Available at: https://doi.org/10.3390/rs13051035.

Levy, J.S. and Schmidt, L. 2016. 'Thermal Properties of Antarctic Soils: Wetting Controls Subsurface Thermal State', *Antarctic Science* 28(5), pp. 361–370.

Linhardt, T., Levy, J.S. and Thomas, C.K. 2019. 'Water tracks intensify surface energy and mass exchange in the Antarctic McMurdo Dry Valleys', *The Cryosphere* 13(8), pp. 2203–2219. Available at: https://doi.org/10.5194/tc-13-2203-2019.

Lyons, W.B., Leslie, D.L. and Gooseff, M.N. 2021. 'Chemical Weathering in the McMurdo Dry Valleys, Antarctica', in A. Hunt, M. Egli, and B. Faybishenko (eds), *Geophysical Monograph Series*. 1st edition. Wiley, pp. 205–216. Available at: https://doi.org/10.1002/9781119563952.ch11.

McNamara, J.P., Kane, D.L. and Hinzman, L.D. 1999. 'An analysis of an arctic channel network using a digital elevation model', *Geomorphology* 29(3), pp. 339–353.

Strauss, J., Fedorov, A.N., Fortier, D., *et al.* 2016. 'Ice-Rich Yedoma Permafrost: Circum-Arctic Distribution and Thickness Synthesis', in *Annual Meeting of the 'Working Group Permafrost',* German Society for Polar Research, Hamburg, Germany, January 22–24, 2016. Available at: http://epic.awi.de/39678/.

Retrogressive thaw slump activity in the western Canadian Arctic (1984–2016)

Antoni G. Lewkowicz

Department of Geography, Environment and Geomatics, University of Ottawa, Ottawa, Ontario, Canada

ABSTRACT

The spatial distribution and links to climate of retrogressive thaw slump (RTS) activity over 32 years were examined using Google Earth Engine Timelapse videos for five areas in the western Canadian Arctic totalling 150 000 km^2, each previously identified as having a high spatial concentration of these thermokarst landforms. Four spatial datasets run from 1984 to 2016 (Banks Island, northwest Victoria Island, Bluenose moraine, Paulatuk region), while the fifth starts in 2001 (Richardson Mountains/Peel Plateau). The total number of RTSs active in the first four areas increased more than 50-fold, from 115 in 1984 to nearly 6000 in 2013. A further 573 RTSs were active in this peak year in the Richardson Mountains/Peel Plateau. RTSs developed most frequently adjacent to rivers (45%), with fewer on slopes (27%) or next to lakes (23%), and the smallest group at the coast (5%). However, there was considerable variation among the areas, and more than half in the Bluenose moraine and the Paulatuk region were initiated on lakeshores. High RTS initiations were linked to particularly warm summers, but once initiated, more than half of those RTSs with long records remained active for more than 25 years. The impacts of this geomorphic activity included changes of colour in more than 500 lakes due to direct or indirect sediment inputs from RTSs, a 30-fold increase compared to 1984. The results show that the non-linear orders of magnitude increase from the 1980s to the 2010s previously reported for Banks Island extended across other ice-rich parts of the western Canadian Arctic.

1 INTRODUCTION

Retrogressive thaw slumps (RTSs; Figure 1) are progressively expanding thermokarst landforms that develop from the subaerial exposure of near-surface ground ice and its subsequent melt over years to decades (Burn and Lewkowicz 1990). RTSs have typical dimensions of tens to hundreds of metres and areas of a few hectares, but some grow sufficiently large that they have been termed megaslumps (e.g., Kokelj et al. 2015, 2023; Kizyakov et al. 2023). RTS formation requires high ice content sediments or massive ice near the top of permafrost, a triggering mechanism to expose the ice-rich substrate, and a slope sufficient to permit thawed soils to slide or flow away from the icy headscarp, maintaining its exposure. Once initiated, energy to melt the ice is mainly supplied in summer by solar radiation and sensible heat transfer from the air (Lewkowicz 1986, 1988). RTSs stabilize in autumn as positive melt fluxes cease and the ground freezes. They restart the following summer providing the high ice-content layer and ground slope are not exhausted. Polycyclic RTSs are common because a single transgression of an RTS headwall may not melt all the ground ice available (Mackay 1966; Lewkowicz 1987). Rainfall events, while not representing large heat fluxes, can re-mobilize debris in the floor of an RTS and expose this ice, resulting in renewed or enhanced activity (e.g., Kokelj et al. 2015).

RTSs are highly concentrated spatially, being relatively uncommon across much of the Arctic (Nitze et al. 2018), while numbering in the hundreds or thousands in particularly ice-rich parts of the permafrost region (e.g., Jones et al. 2019; Lewkowicz and Way 2019; Kokelj et al. 2023; Yang et al. 2023). The latter include locations near the last glacial limit (Lacelle et al. 2015), areas that experienced still-stands during ice sheet recession (e.g., Kokelj et al. 2017; Nitze et al. 2021), and locations with thick ice-rich syngenetic permafrost (e.g., Zwieback et al. 2018). Within hillslope thermokarst landscapes (Olefeldt et al. 2016), RTSs are initiated (1) at coasts, (2) on lakeshores, (3) on riverbanks, and (4) on slopes, disconnected from coasts, lakes or rivers, including in the floors of stabilized RTSs. Until recently, it was generally assumed that RTS initiation related to waves and currents undercutting banks in the first three cases, and to thaw consolidation associated with active layer detachment formation in the fourth case. However, the strong temporal signal in initiation rates evident on Banks Island suggests that the thaw consolidation mechanism may apply to all four loci (Lewkowicz and Way 2019).

Figure 1. Example of an active RTS, Aulavik National Park, northern Banks Island, July 2019.

https://doi.org/10.52381/ICOP2024.213.1

In this paper, datasets and analyses of RTS activity in four parts of the western Canadian Arctic are compared to those previously developed for Banks Island (Lewkowicz and Way 2019). The goals are to examine which of the latter's results pertain more widely. These include the increase in numbers of active RTSs and their initiation relative to climate indices, the relative importance of the four loci of initiation, RTS longevity, and the number of lakes impacted. The research complements recent work that visually interpreted satellite images to map spatial concentrations of RTSs and other thermokarst features in the NWT (Kokelj et al. 2023) and studies that employed machine-learning techniques to identify and delimit RTS extent in this and other parts of the permafrost region (e.g., Huang et al. 2020; Nitze et al. 2021; Lin and Knudby 2023; Yang et al. 2023).

2 Study Areas

The four new study areas (Table 1: northwest Victoria Island (VI), Bluenose moraine (BM), Paulatuk region (PR), and the Richardson Mountains/Peel Plateau (RM/PP)) are characterized by high or very high ice-content permafrost (O'Neill et al. 2019, 2022) and significant concentrations of RTSs (Lacelle et al. 2015; Kokelj et al. 2017, 2023). Together with Banks Island (BI), they extend from 67.0°N to 74.6°N (Figure 2) and all are underlain by continuous permafrost, except for the easternmost portion of RMR/PP which falls into the extensive discontinuous permafrost zone due to the abundance of surface water bodies (Heginbottom et al. 1995).

Mean annual air temperatures at proximal government weather stations range from -7 °C to -13 °C and average July temperatures from 15 °C to 7 °C (1981–2010; Table 1). Mean annual precipitation follows a south to north gradient, ranging from 298 mm to 152 mm with more than half falling as snow. The BI, VI, and BM study areas have vegetation covers dominated by graminoid and prostrate-shrub tundras (CAVM Team 2003). The PR and RM/PP study areas extend across treeline with the latter's vegetation pattern being affected by elevation as well as latitude.

Table 1. Study areas in the western Canadian Arctic.

Study area[a]	Area (10^3 km^2)	Latitude (°N) and longitude (°W) ranges	Mean annual / mean July air temp. (°C)[b]	Period of analysis
BI	70	71.07–74.56; E. coast to W. coast	-12.8 / 6.6	1984-2016
VI	31	71.00–73.38; 113.90 to W. coast	-11.6 / 9.0	1984-2016
BM	21	67.75–69.77; 118.45–121.40	-10.3 / 10.9	1984-2016
PR	18	68.50–70.20; 122.70–125.43	-10.1 / 11.0	1984-2016
RM/PP	14	66.95–68.55; 134.85–136.75	-7.3 / 15.2	2001-2016

[a]BI: Banks Island; VI: NW Victoria Island; BM: Bluenose moraine; PR: Paulatuk region; RM/PP: Richardson Mountains/Peel Plateau. [b]At nearest station with 30-year climate normal (1981–2010): BI: Sachs Harbour; VI: Ulukhaktok; BM: Kugluktuk; PR: Tuktoyaktuk; RM/PP: Fort McPherson. Data from ECCC (2023a).

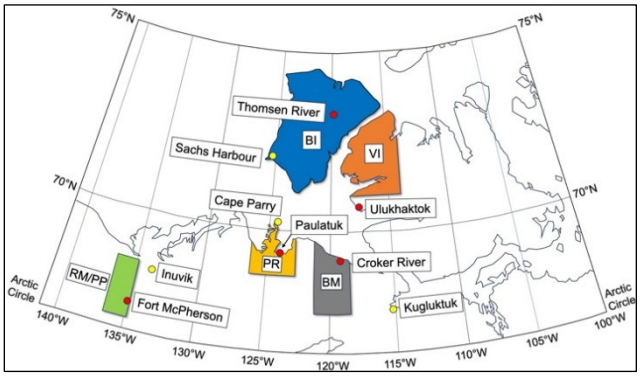

Figure 2. Study areas (see Table 1) and climate stations in the western Canadian Arctic. Study area colours correspond to those used in the line graphs (below). Red markers: representative climate stations for the study areas for the period of analysis. Yellow markers: stations used to infill missing data. Note: Sachs Harbour data were used to infill both Thomsen River and Ulukhaktok records.

3 Methods

RTS numbers, activity and locus of initiation, were analyzed using Google Earth Engine Timelapse, an internet-accessible resource that shows earth surface changes from satellite images assembled as a time-lapse video (Google Earth Engine 2023). Each frame of the video is cloud-free and shows a single year from 1984 onwards. The videos are mainly developed from Landsat data and have comparable resolutions (typically 30 m x 30 m) throughout the study period (see Lewkowicz and Way 2019). An active RTS can be detected visually (i.e., manually) because its headwall and adjacent saturated slump floor appear to move in the video as retrogression takes place. Its location can then be recorded on a Google Earth image as a point, representing the approximate centroid of the slump (Lewkowicz and Way 2019). The year of initiation, the location of initiation in the landscape and the year of stability (if an RTS becomes inactive) can also be assessed by undertaking a frame-by-frame analysis. While this provides an annually resolved dataset, the first frame in which an RTS is visible is typically from the year following initiation because most RTS are either too small to be resolved in the satellite imagery in the year that they start or because the imagery from that year pre-dates RTS formation (Lewkowicz and Way 2019). Consequently, the initiation year recorded is often (but not always) lagged relative to the true date. It can also be challenging to precisely determine the year in which an RTS ceases to be active as stabilization typically manifests as a progressive reduction in the width of the active headwall and a gradual slowing of headwall retreat, rather than a sudden and definitive cessation of retrogression.

A small number of RTSs which had been missed in the previously published analyses for BI (Lewkowicz and Way 2019) were added to that area's dataset for the time periods of 1984–2016 for total numbers and 1985–2015 for initiations. Data for the other study areas are analysed for the same periods, except for RM/PP where the record is shorter because images prior to 2001 are not included in

the Google Earth Engine Timelapse imagery for this area (Table 1).

The previous inventory of RTSs on BI was assessed as having errors of omission of 8% and of commission (incorrect identification of features as RTSs) of 1% (Lewkowicz and Way 2019). More recently, mapping undertaken with high-resolution satellite images gave an overall agreement of 84% with the BI inventory (Kokelj et al. 2023). Errors in the current work should be comparable to those in Lewkowicz and Way (2019) except perhaps in some parts of the region where the imagery was of lower quality. The complete dataset is available in Lewkowicz (2024). An example of the results is shown in Figure 3.

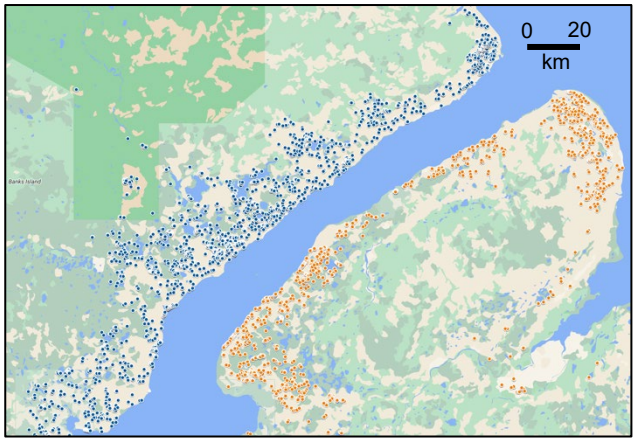

Figure 3. Locations of individual RTSs active between 1984–2016 in the NE part of BI (blue markers, left) and the NW part of VI (orange markers, right). Base map source: Google Maps.

The duration of individual RTS activity was calculated from the dates assigned to the features during the inventorying process. This analysis took into account that the potential years of activity diminished through the record so that the longevity of some RTSs could not be determined beyond a minimum number of years (Lewkowicz and Way 2019). Longevity rates were not calculated once the available sample size fell below 1% of the total number of RTSs active in each study area.

Many lakes affected by sediment inputs from RTSs changed colour in the Timelapse videos from dark blue to turquoise, or to beige. This reaction differs from some lakes in the Mackenzie Delta region which become clearer due to RTS activity on their shorelines (Kokelj et al. 2009). The timing and duration of this qualitative change was recorded. Only lakes with a direct connection to active RTSs (i.e., RTSs present on the lakeshore) or an obvious indirect connection (RTSs active upstream around a lake or on a valley floor) were included in the dataset (Lewkowicz 2024). Some lakes exhibited up to three periods of changed colour, alternating with colour reversals. As with RTS activity, the potential duration of lake colour change diminished through the record and calculations took this into account. Given the much smaller number of lake colour changes compared to active RTSs, a minimum sample size of 20% of the total number of lake colour changes in an area was required for the calculation to be undertaken.

Average summer (June to August) air temperatures for the study areas were compared to RTS initiation. The focus was on air temperature because precipitation was not revealed to be independently important in previous analyses for Banks Island (Lewkowicz and Way 2019). The air temperatures were extracted from the homogenized surface air temperature dataset (Vincent et al. 2020; Environment and Climate Change Canada 2023b) for the closest station (Figure 2). Gaps in the temporal records were infilled by regression based on highly correlated data (minimum correlation coefficient (r) of 0.9) from nearby stations, where these were available for the missing years (Figure 2).

4 RESULTS

Most results presented are for the four areas with datasets in common starting in 1984 and ending in 2016. Those from RM/PP are included where possible.

4.1 Number of active RTSs

More than 7400 individual RTSs were active in the five study areas at some point during the record. The number of active RTSs was consistently greatest on BI, with 50% or more of the total in every year, followed by VI, BM and PR (Figure 4). Numbers in RM/PP exceeded those in BM and PR after its record began in 2001.

The total number of active RTSs for all four areas increased more than 50 times, from 115 active in 1984 to nearly 6000 in 2013. In VI, BM and PR, the number of active RTSs increased by 71, 13 and 21 times, respectively, demonstrating that the orders of magnitude increase (64 times) previously reported for BI (Lewkowicz and Way 2019) was not confined to that island. A further 573 RTSs were active in the RM/PP area in 2013 bringing the total in this peak activity year, to more than 6500. A slight decline then occurred as some RTSs stabilized and only a small number of RTSs were newly initiated.

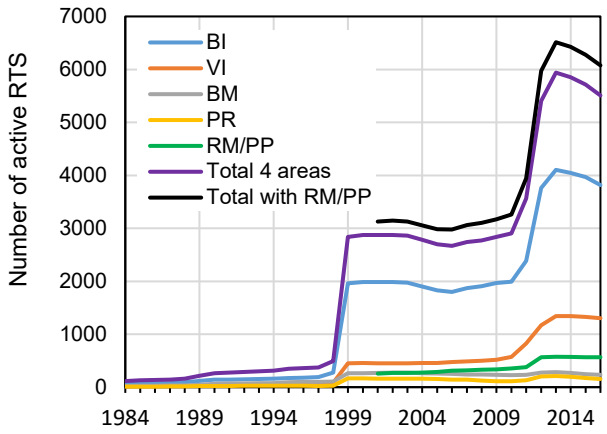

Figure 4. Number of active RTSs in the study areas (1984–2016). BI: Banks Island; VI: Victoria Island; BM: Bluenose moraine; PR: Paulatuk region; RM/PP: Richardson Mountains/Peel Plateau (from 2001 onwards).

4.2 Location of RTS initiation

RTSs within the study areas were highly concentrated spatially (e.g., see Figure 3). At the site level, the location of RTS initiation for the study areas combined was most frequently adjacent to rivers (45%), followed by slopes (27%), lakeshores (23%) and coasts (5%; Table 2). BI and VI exhibit distributions in the landscape that are quite similar to the averages and to each other. In contrast, more than half of the RTSs in BM and PR started along lake shorelines, there were fewer RTSs on riverbanks and slopes, and virtually none on the coast. In RM/PP, two-thirds of the RTSs initiated along rivers with almost all the remainder on slopes.

Table 2. Number and location of RTS initiations (1985–2015).

Study area	No. of RTSs	Coast (%)	Lakeshore (%)	Riverbank (%)	Slope (%)
BI	4604	6.4	21.0	46.2	26.4
VI	1403	6.6	15.0	44.9	33.6
BM	440	0.0	55.3	35.8	8.9
PR	327	0.3	75.2	8.9	15.6
RM/PP[a]	632	-[b]	4.1	66.4	29.4
All areas	7406	5.2	22.8	45.4	26.5

[a] 2001–2015; [b] Study area does not include coastline.

4.3 Temporal variation in RTS initiation

RTS initiation was highly concentrated in the same small number of years in three of the four regions with a full record (Figure 5). More than 82% of all newly initiated RTSs on VI and almost 79% in PR were first observed in just four of the 31 years: 1999, 2011, 2012 and 2013. These percentages are very similar to the 85% reported previously for BI for the same years (Lewkowicz and Way 2019). In BM, however, the percentage of the total initiated in the same years was only 56% and 2011 was not one of the top four initiation years. The truncated record for RM/PP means that fully comparable figures cannot be generated. However, visual observation of the size and rate of expansion of each RTS active at the start of the area's record in 2001 allowed an appraisal of whether it might have been first observable in 1999. Of the 256 RTS active in 2001, 45% were estimated to have started two years earlier. When this figure is included in the newly initiated RTS number, the dominance of 1999 and 2012 also emerges for RM/PP (Figure 5).

4.4 Duration of RTS activity

Almost all the RTSs identified were active for at least three years (Figure 6). This may partly reflect the study's methodology which might not have detected features active for shorter periods. The average probability of an RTS remaining active, based on all the data, gradually declined, reaching 55% after 25 years. The rate of decline, however, varied considerably: VI had the lowest rate, followed by BI, BM and PR. The probability of an RTS remaining active in last two areas reached 0% after 30 years, while in VI, more than 80% were still active after 25 years. The truncated

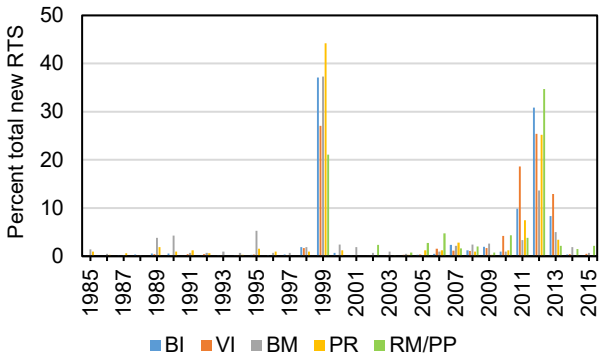

Figure 5. Temporal record of RTS initiation in the study areas (1985-2015). Note: for RM/PP, the record begins in 2002 but percentages include the 116 RTSs active in 2001 that probably would have been observable in 1999 (see text); the column for 1999 is therefore an estimate.

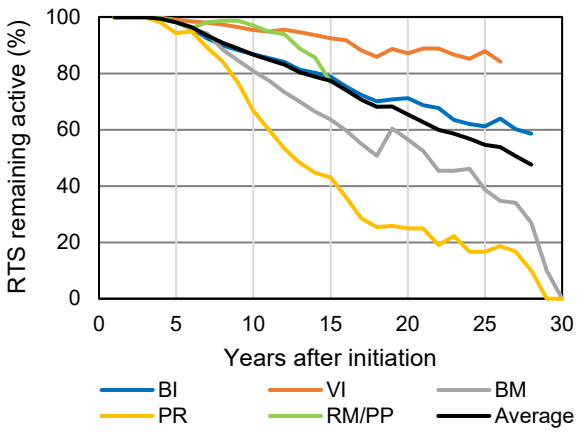

Figure 6. Duration of RTS activity. Note: lines are shown only for years when the sample size available exceeded 1% of the total number of RTS initiated in an area.

record for RM/PP lies between VI and BI but its slope was steeper for the last few points indicating that a greater percentage of RTSs were beginning to stabilize (Figure 6).

4.5 Impact of RTS activity on lake colour

Colour change due to RTS activity was observed in 574 individual lakes in the first four regions between 1984 and 2016. This number is substantial but it represents only a small fraction of the thousands of ponds and lakes in the study regions. Half of the lakes affected (288) were on BI with most of the rest divided equally between VI (124) and BM (123; Figure 7). PR had 39 lakes with changed colour. Only 11 were observed as being impacted in RM/PP after 2001, and given this small number and shorter record, these data were not analysed further.

At the start of the record in 1984, 13 lakes in the first four regions were being affected by sediment inputs from RTSs and almost all of these were in BM (Figure 8). Numbers

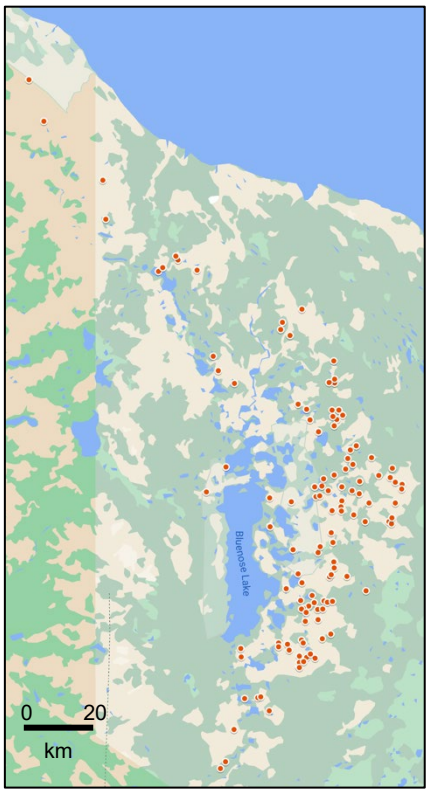

Figure 7. Spatial distribution of 124 lakes in BM that experienced colour change (red markers) due to RTS activity (1984–2016). Base map source: Google Maps.

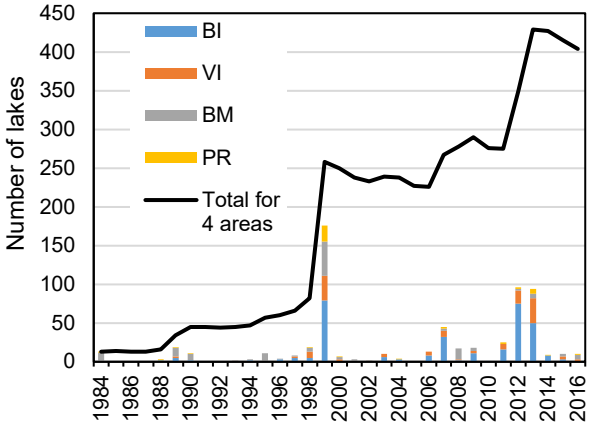

Figure 8. Number of lakes changing colour due to RTS activity (1984–2016). Stacked bars show new colour changes in the four areas with a complete record. Black line shows total number of lakes with changed colour in the same areas.

grew during the 1990s but as with RTS initiation, the first major increase was observed in 1999 when 176 lakes changed colour and the total rose to 258. Other years when substantial numbers of lakes changed colour were 2007, 2012 and 2013. In between these years, some lakes experienced colour reversals resulting in slight declines in the total of those visibly affected (Figure 8). These reversals occurred mainly where RTSs had stabilized, but at some sites, they took place even though RTS headscarps continued to retreat. The latter observation is likely due to decreases in exports of ground ice meltwater and its associated sediment load into the lake as the headwall retreated progressively from the lakeshore.

The average trend for the duration of lake colour change showed that about half of the lakes returned to their original colour within 15 years (Figure 9). The ordering among the study areas was similar to RTS longevity, with altered lake colour continuing longest for lakes in VI, while the shortest duration was in PR. However, BI and BM were similar which was not the case for RTS longevity (see Figure 6). The combination of relatively lengthy persistence for colour change and the number of newly affected lakes meant that the peak number of 429 was reached in 2013 (Figure 8), representing a 33-fold increase compared to 1984.

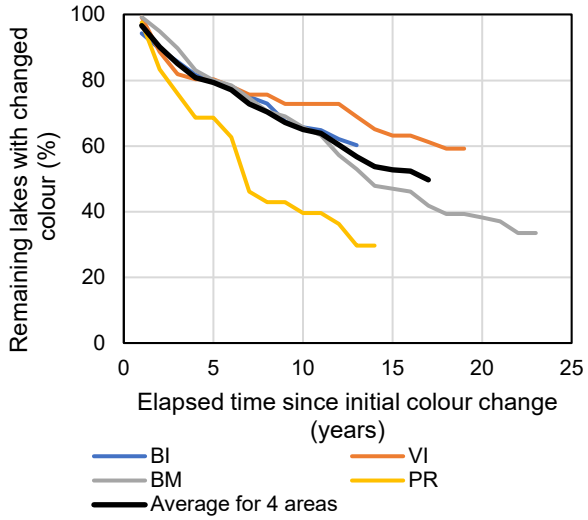

Figure 9. Duration of lake colour change due to RTS activity for four study areas. Note: lines are shown only for the period when the remaining number of lakes exceeded 20% of the total initial number.

Rapid shoreline retreat forming a new bay was observed in a small number of lakes that also experienced colour change due to RTS activity. Nine were affected in BM, five on BI, one on VI and one in PR, with shoreline retreat of up to 300 m over one to two decades. At these sites, the terrain slope is low enough and lakeside sediments are sufficiently ice-rich that their thaw results in land subsidence to below the elevation of the lake water. In each case, an RTS developed at the head of the new bay immediately following stabilization of the shoreline.

4.6 RTS initiation and summer climate

The relationship between RTS initiation and mean summer (June to August) air temperatures was examined for all five study areas. The air temperature used as the independent variable was that of the previous summer because of the expected lag in observation of initiation. Strong positive log-linear relationships were present for BI and BM (r^2 = 0.61 and 0.56, respectively), weaker relationships for

VI and PR (r^2 = 0.36 and 0.30, respectively), and no relationship for the shorter record at RM/PP (r^2 = 0.03; Figure 10). However, even though log-linear relationships were used, the best-fit lines substantially underestimated numbers of new RTSs in the peak initiation years.

Summer air temperatures linked to high levels of RTS initiation were area-specific. The lowest values were at BI and the highest at RM/PP. This underlines that it is the climatic extremes of a given distribution, not absolute values, that trigger major initiation events.

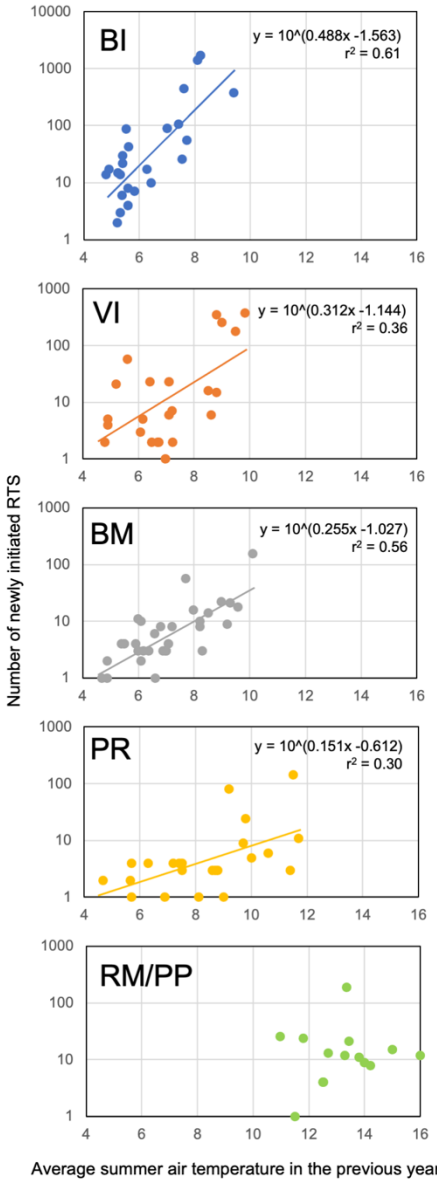

Figure 10. Relationship between average summer (June, July, August) air temperature in the previous year and the number of newly observed RTSs in the five study areas. Note the logarithmic y-axis. Statistically significant log-linear relationships are shown. Years without newly observed RTSs were excluded from the regression analyses.

Satellite image videos available on Google Earth Engine Timelapse now (in early 2024) run until 2022. However, the period of systematic analyses was not extended beyond that used for BI in Lewkowicz and Way (2019) due to the large amount of observer time that would have been required. Instead, a reconnaissance-level investigation of high concentration areas of RTSs in each of the study areas was undertaken. This showed that many of the RTSs initiated in 1998 or later remained active and continued to expand rapidly after 2016, but few newly-initiated RTSs were observed. This tentative result fits with the record of mean summer air temperatures across the region for 2017–2022, none of which exceeded those of 1998 and 2012.

5 Discussion and Conclusions

The simple counts of RTSs reported here are useful primarily to indicate the spatial distribution of these thermokarst features and to evaluate the links between temporal change and climate. The datasets (Lewkowicz 2024) can also be used to validate machine-learning methods related to RTSs (e.g., Huang et al. 2023; Lin and Knudby 2023). They cannot be used to provide details on RTS area, ice volume loss, rate of headwall retreat or many other geomorphological characteristics. Development of such data requires different methodologies, such as UAV imaging (e.g., Armstrong et al. 2018; Van der Sluijs et al. 2018; Hayes et al. 2022), AI techniques (e.g., Huang et al. 2020, 2022; Nitze et al. 2021), or RTS demarcation using high resolution satellite images (e.g., Rudy et al. 2017).

Despite the information limits imposed by the methodology, some significant results emerge from this comparative study. They support conclusions previously reached for Banks Island (Lewkowicz and Way 2019) while enlarging the geographical context.

First, active RTSs demonstrably proliferated in areas of ice-rich permafrost in the western Canadian Arctic, starting in the warm summer of 1998. Numbers rose 13 to 71 times from 1984 to 2016 in the four study areas with complete records (Banks Island, NW Victoria Island, Bluenose moraine, Paulatuk region). With the addition of the truncated record for the Richardson Mountains/Peel Plateau, more than 6500 RTSs were active in the peak summer of 2013. Once started, more than half of the all the RTSs remained active for more than two decades, although longevity varied among the study areas.

Second, the distribution of RTSs across the landscape varied by study area, with lakeshore RTSs being the most important numerically in BM and PR, and riverbank RTSs being the most important in the other areas. These differences likely relate to physiography and the distribution of ground ice, but additional investigation is required to identify the critical variables.

Third, more than 500 lakes were impacted sufficiently by RTS activity to exhibit a change in colour that in turn relates to turbidity, with a peak of 429 affected lakes in 2013. Lake colour reversal took longest on Victoria Island, which was also the area where RTSs were the longest-lasting.

Fourth, the relationships between summer climate and RTS initiation show that it is exceedance of thaw probability for a particular area that matters, not the absolute value.

Predictions of RTS initiation rates can be made using summer air temperature series, but even these log-linear relationships underestimate the number of newly initiated slumps in exceptional summers. This result underlines the threshold nature of initiation, likely linked to the thaw depths necessary to reach high ice content layers (such as buried ice). As a result, RTS activity can be expected to accelerate as the climate warms in future decades and extreme thaw events penetrate to still greater depths.

Finally, a cursory review of Timelapse videos for the study areas suggested that no major initiation events occurred from 2017–2022 and this aligns with an absence of high recurrence interval warm summers during this period. Until 2023, therefore, the summers of 2012/2013 appeared to be the latest episodes in which more than a thousand new RTSs were initiated across the region. However, the impacts of those years and the earlier warm summer of 1998 continued to affect the landscape of the western Canadian Arctic as many RTSs initiated then remained active. Furthermore, average summer air temperatures in the study areas in 2023 (data from ECCC 2023c) equalled or exceeded the values from 1998 and 2012. Time will tell whether this led to extensive RTS initiation but it seems likely given past relationships (Figure 10).

6 ACKNOWLEDGEMENTS

Students in the GEG 4101 Permafrost Environments class at the University of Ottawa in the 2019 winter semester are thanked for their initial review of RTS activity within the NW Victoria Island study area. Dr. Robert Way is thanked for his contribution to a previous publication that focused exclusively on Banks Island. The author is grateful to the two reviewers for helpful comments on an earlier version of the manuscript.

7 REFERENCES

Armstrong, L., Lacelle, D., Fraser, R.H., Kokelj, S. and Knudby, A. 2018. 'Thaw slump activity measured using stationary cameras in time-lapse and Structure-from-Motion photogrammetry', *Arctic Science* 4(4), pp. 827–845.

Burn, C.R. and Lewkowicz, A.G. 1990. 'Canadian Landform Examples - 17: Retrogressive thaw slumps', *The Canadian Geographer* 34(3), pp. 273–276.

CAVM Team 2003. 'Circumpolar Arctic Vegetation Map. Scale 1:7,500,000. Conservation of Arctic Flora and Fauna (CAFF) Map No. 1'. *US Fish and Wildlife Service*, Anchorage, Alaska.

Environment and Climate Change Canada 2023a. *Canadian Climate normals*. Available at: https://climate.weather.gc.ca/climate_normals/ (Accessed: August 31, 2023).

Environment and Climate Change Canada 2023b. *Climate data: homogenized surface air temperature data*. Available at: https://www.canada.ca/en/environment-climate-change/services/climate-change/science-research-data/climate-trends-variability/adjusted-homogenized-canadian-data/surface-air-temperature.html (Accessed: August 31, 2023).

Environment and Climate Change Canada 2023c. *Daily data report: Cape Parry, Croker River, Fort McPherson, Inuvik, Kugluktuk, Paulatuk, Sachs Harbour, Thomsen River, Ulukhaktok*. Available at: https://climate.weather.gc.ca/historical_data/search_historic_data_stations_e.html (Accessed: November 15, 2023).

Google Earth Engine 2023. *Timelapse*. Available at: https://earthengine.google.com/timelapse/ (Accessed August 1, 2023).

Hayes, S., Lim, M., Whalen, D., Mann, P.J., Fraser, P., Penlington, R. and Martin, J. 2022. 'The role of massive ice and exposed headwall properties on retrogressive thaw slump activity', *Journal of Geophysical Research: Earth Surface* 127(11), e2022JF006602.

Heginbottom, J.A., Dubreuil, M.-A., and Harker, P. 1995. 'Canada, Permafrost', in *National Atlas of Canada, 5th edition*. Natural Resources Canada, MCR 4177, scale 1:7,500,000.

Huang, L., Lantz, T.C., Fraser, R.H., Tiampo, K.F., Willis, M.J. and Schaefer, K. 2022. 'Accuracy, efficiency, and transferability of a deep learning model for mapping retrogressive thaw slumps across the Canadian Arctic', *Remote Sensing* 14(12), 2747.

Huang, L., Luo, J., Lin, Z., Niu, F. and Liu, L. 2020. 'Using deep learning to map retrogressive thaw slumps in the Beiluhe region (Tibetan Plateau) from CubeSat images', *Remote Sensing of Environment* 237. Available at: https://doi.org/10.1016/j.rse.2019.111534.

Huang, L., Willis, M.J., Li, G., Lantz, T.C., Schaefer, K., Wig, E., Cao, G. and Tiampo, K.F. 2023. 'Identifying active retrogressive thaw slumps from ArcticDEM', *ISPRS Journal of Photogrammetry and Remote Sensing* 205, pp. 301–316.

Jones, M.K.W., Pollard, W.H. and Jones, B.M. 2019. 'Rapid initialization of retrogressive thaw slumps in the Canadian high Arctic and their response to climate and terrain factors', *Environmental Research Letters* 14(5), 055006.

Kizyakov, A.I., Wetterich, S., Günther, F., Opel, T., Jongejans, L.L., Courtin, J., Meyer, H., Shepelev, A.G., Syromyatnikov, I.I., Fedorov, A.N. and Zimin, M.V. 2023. 'Landforms and degradation pattern of the Batagay thaw slump, Northeastern Siberia', *Geomorphology* 420, 108501.

Kokelj, S.V., Gingras-Hill, T., Daly, S.V., Morse, P., Wolfe, S., Rudy, A.C., van der Sluijs, J., Weiss, N., O'Neill, B., Baltzer, J. and Lantz, T.C. 2023. 'The Northwest Territories Thermokarst Mapping Collective: A northern-driven mapping collaborative toward understanding the effects of permafrost thaw', *Arctic Science* 9(4), pp. 886–918.

Kokelj, S. V., Lantz, T. C., Tunnicliffe, J., Segal, R. and Lacelle, D. 2017. 'Climate-driven thaw of permafrost preserved glacial landscapes, northwestern Canada', *Geology* 45, pp. 371–374.

Kokelj, S.V., Tunnicliffe, J., Lacelle, D., Lantz, T.C., Chin, K.S. and Fraser, R. 2015. 'Increased precipitation drives mega slump development and destabilization of ice-rich permafrost terrain, northwestern Canada', *Global and Planetary Change* 129, pp. 56–68.

Kokelj, S.V., Zajdlik, B. and Thompson, M.S. 2009. 'The impacts of thawing permafrost on the chemistry of lakes across the subarctic boreal-tundra transition, Mackenzie Delta region, Canada', *Permafrost and Periglacial Processes* 20(2), pp. 185–199.

Lacelle, D., Brooker, A., Fraser, R.H. and Kokelj, S.V. 2015. 'Distribution and growth of thaw slumps in the Richardson Mountains–Peel Plateau region, northwestern Canada' *Geomorphology* 235, pp. 40–51.

Lewkowicz, A.G. 1986. 'Rate of short-term ablation of exposed ground ice, Banks Island, Northwest Territories, Canada', *Journal of Glaciology* 32(112), pp. 511–519.

Lewkowicz, A.G. 1987. 'Nature and importance of thermokarst processes, Banks Island, Canada', *Geografiska Annaler* 69A, pp. 321–327.

Lewkowicz, A.G. 1988. 'Ablation of massive ground ice, Mackenzie Delta', in *Proceedings, Fifth International Conference on Permafrost*, Trondheim, August 1988, Trondheim, Tapir: pp. 605–610.

Lewkowicz, A.G. 2024. 'Retrogressive thaw slump activity and related lake colour change in five areas of the western Canadian Arctic', *Nordicana* D128. doi:10.5885/45888XD-C644C19F4F414D58.

Lewkowicz, A.G. and Way, R.G. 2019. 'Extremes of summer climate trigger thousands of thermokarst landslides in a High Arctic environment', *Nature Communications* 10(1), 1329.

Lin, Y. and Knudby, A.J. 2023. 'A transfer learning approach for automatic mapping of retrogressive thaw slumps (RTS) in the western Canadian Arctic', *International Journal of Remote Sensing* 44(6), pp. 2039–2063.

Mackay, J.R. 1966. 'Segregated epigenetic ice and slumps in permafrost, Mackenzie Delta area', *N.W.T. Geographical Bulletin* 8, pp. 59–80.

Nitze, I., Grosse, G., Jones, B.M., Romanovsky, V.E., and Boike, J. 2018. 'Remote sensing quantifies widespread abundance of permafrost region disturbances across the Arctic and Subarctic', *Nature Communications* 9, 5423.

Nitze, I., Heidler, K., Barth, S. and Grosse, G. 2021. 'Developing and testing a deep learning approach for mapping retrogressive thaw slumps', *Remote Sensing* 13(21), 4294.

Olefeldt, D., Goswami, S., Grosse, G., Hayes, D., Hugelius, G., Kuhry, P., Mcguire, A.D., Romanovsky, V.E., Sannel, A.B.K., Schuur, E.A.G., and Turetsky, M.R. 2016. 'Circumpolar distribution and carbon storage of thermokarst landscapes', *Nature Communications* 7, 13043.

O'Neill, H.B., Wolfe, S.A. and Duchesne, C. 2019. 'New ground ice maps for Canada using a paleogeographic modelling approach', *The Cryosphere* 13(3), pp. 753–773.

O'Neill, H.B., Wolfe, S.A., Duchesne, C. 2022. 'Ground ice map of Canada v.1.1', *Geological Survey of Canada* Open File 8713.

Rudy, A.C.A., Lamoureux, S.F., Kokelj, S.V., Smith, I.R. and England, J.H. 2017. 'Accelerating thermokarst transforms ice-cored terrain triggering a downstream cascade to the ocean', *Geophysical Research Letters* 44(21), pp. 11,080–11,087.

Van der Sluijs, J., Kokelj, S.V., Fraser, R.H., Tunnicliffe, J. and Lacelle, D. 2018. 'Permafrost terrain dynamics and infrastructure impacts revealed by UAV photogrammetry and thermal imaging', *Remote Sensing* 10(11), 1734.

Vincent, L. A., Hartwell, M.M. and Wang, X.L. 2020. 'A third generation of homogenized temperature for trend analysis and monitoring changes in Canada's climate', *Atmosphere-Ocean* 58(3), pp. 173–191.

Yang, D., Qiu, H., Ye, B., Liu, Y., Zhang, J. and Zhu, Y. 2023. 'Distribution and recurrence of warming-induced retrogressive thaw slumps on the Central Qinghai-Tibet Plateau', *Journal of Geophysical Research: Earth Surface* e2022JF007047.

Zwieback, S., Kokelj, S.V., Günther, F., Boike, J., Grosse, G. and Hajnsek, I. 2018. 'Sub-seasonal thaw slump mass wasting is not consistently energy limited at the landscape scale', *The Cryosphere* 12(2), pp. 549–564.

PermaRail: A transdisciplinary approach to increase railway resilience to degrading permafrost terrain under a warming climate

Emmanuel L'Hérault[1], Pascale Roy-Léveillée[1], Teddi Herring[2], Jocelyn Hayley[2], Ryley Beddoe[3], Shawn Kenny[4], Andy Take[5], Brett Young[6] & Kevin Jones[7]

[1]*Department of Geography, Laval University, Québec City, Québec, Canada*

[2]*Department of Civil Engineering, University of Calgary, Calgary, Alberta, Canada*

[3]*Department of Civil Engineering, Royal Military College of Canada, Kingston, Ontario, Canada*

[4]*Department of Civil and Environmental Engineering, Carleton University, Ottawa, Ontario, Canada*

[5]*Department of Civil Engineering, Queen's University, Kingston, Ontario, Canada*

[6]*Arctic Gateway Group LP, The Pas, Manitoba, Canada*

[7]*Tetra Tech Canada (retired), Edmonton, Alberta, Canada*

ABSTRACT

Across the Canadian permafrost zones, access to stable linear infrastructure networks is critical for the well-being of Northern Communities and the Canadian economy. The Hudson Bay Railway (HBR), the first major transportation infrastructure built over permafrost in Canada, is now facing significant climate-driven stability and drainage issues that have been exacerbated by climate change. These issues increase maintenance costs and threaten user safety. The focus of this transdisciplinary project is to identify and characterize permafrost-related hazards along the railway corridor and investigate potential mitigation measures for improving rail stability and minimizing risk. A multi-year comprehensive field program is currently underway to map, characterize, assess, and monitor ground and rail conditions, including permafrost, ice, soil, and surface water conditions. This field program, supplemented with experimental and numerical analyses at targeted pilot sites, will provide the basis to identify high-risk locations and support a quantitative assessment of mitigation and adaptation options under different climate scenarios. By developing a risk-based framework to assess degrading permafrost-related hazards, as well as design and mitigation best practices for railways, the long-term goal of this project is to improve the resilience, sustainability, performance, and safety of the Hudson Bay Railway. This project aims to address the unique transportation needs and priorities of specific communities in Northern Manitoba and contribute to Canadian expertise and leadership in the management of current and future linear infrastructure in permafrost regions around the world.

1 INTRODUCTION

Climate change affects our physical environment, ecology, health, socio-cultural fabric, and infrastructure performance. The effects of climate change are felt acutely in Canada's North, which is warming two to four times faster than the global average due to polar amplification (Rantanen et al. 2022). Permafrost underlies over a third of Canada's landmass, but climate change is causing permafrost to warm and thaw. As permafrost thaws, positive feedbacks can further accelerate its degradation (Schuur et al. 2022). For life in Canada's North, permafrost thaw is a significant issue that results in large scale ground disturbances, such as subsidence and landslides, damage to infrastructure, changes in surface and groundwater flow, and ecological transformations.

There are many unique engineering challenges in permafrost regions, as the ground thermal regime is often changed by infrastructures, which can affect stability and safety of the built environment. Furthermore, crucial transportation infrastructures such as the Hudson Bay Railway (HBR) were designed for stable, equilibrium permafrost conditions and are now facing significant climate-driven stability and drainage issues, requiring significant funds to maintain. These include challenges such as surface subsidence and settlement, flooding and washouts, and infrastructure damage. The PermaRail research program was developed to better understand the vulnerability of the HBR to climate change and extreme weather events and to establish reliable engineered solutions to increase resilience.

1.1 The Hudson Bay Railway

Much of Canada's early development was shaped by the Hudson Bay region, where exploration voyages sought the Northwest Passage and the establishment of a fur trade post at York Factory. In the early 1800s, it became evident that a railway linking Winnipeg to Hudson Bay to export grain and beef to foreign markets was needed. Surveys for the HBR began in 1908, with clearing of the right-of-way starting in 1912. Although the track would have to cross extensive regions of muskeg, the port of Churchill was selected as the railway terminus. The HBR officially opened on September 10, 1929.

The HBR is a 1,012 km (632 mi) railway located in northern Manitoba that connects with southern Canadian National Railway (CNR) routes in The Pas. The HBR traverses in a north easterly direction to Gillam (kilometer post (KP) 524.8), and then northward to the port of Churchill (KP 820.4). Between Gillam and Churchill, there is a gradual

https://doi.org/10.52381/ICOP2024.96.1

northward transition from a discontinuous to continuous permafrost distribution (Figure 1).

In 2018, the Arctic Gateway Group, which is entirely owned by Indigenous groups and Northern communities through OneNorth, took ownership of the HBR and port facilities of Churchill. The HBR provides trackage rights to VIA Rail Canada for passenger services to remote and isolated communities, and is a critical transportation corridor in Northern Manitoba, supporting both economic and social activities in the region.

1.2 50 years of Permafrost-Related Hazards and Mitigation Along the Hudson Bay Railway

The previous railway owners, CNR (1929–1997) and Omintrax (1997–2018), experienced operational constraints and increased maintenance costs due to permafrost thaw. During and after the construction of the rail, several locations experienced severe subsidence, commonly referred to as sinkholes, due to surface disturbance associated with construction and water ponding along the right of way (EBA Engineering Consultants Ltd. 1979). Thaw subsidence caused short sections of track to experience as much as 100 mm to 150 mm of settlement during a single summer season which required significant amounts of additional granular fill to restore the roadbed to a usable condition.

Under CNR ownership, thaw subsidence was characterized in a study of 696 active sinkholes (EBA Engineering Consultants Ltd. 1991). Comparison of sinkhole distribution over the four-year period from 1986 to 1990 demonstrated fundamental changes: the total number of sinkholes has increased, and the frequency distribution shifted northward as previously stable peat plateaus, which underly a significant portion of the rail bed, began to thaw (Figure 2).

Between 1977 and 1991, EBA Engineering undertook several studies to characterize the subgrade soils and geothermal regime to better understand sinkhole formation and assess long-term stabilization measures to mitigate permafrost degradation along the rail. Borehole logs from those studies confirmed the presence of ice-rich (30% to 70% by volume), warm permafrost (-0.4 °C to 0 °C) in the degrading areas. Mitigation techniques were designed and tested at five locations along the Herchmer Subdivision between Gillam and Weir River (KP 600.9) from 1976 to 1979 (Figure 3). Among the tested techniques, heat pipes (Cryo-Anchor Model 800) appeared to be the most efficient in stabilizing permafrost. However, the long-term stabilization measures outlined in the EBA studies were not fully implemented, and the HBR continues to experience deterioration and increased maintenance needs due to permafrost degradation.

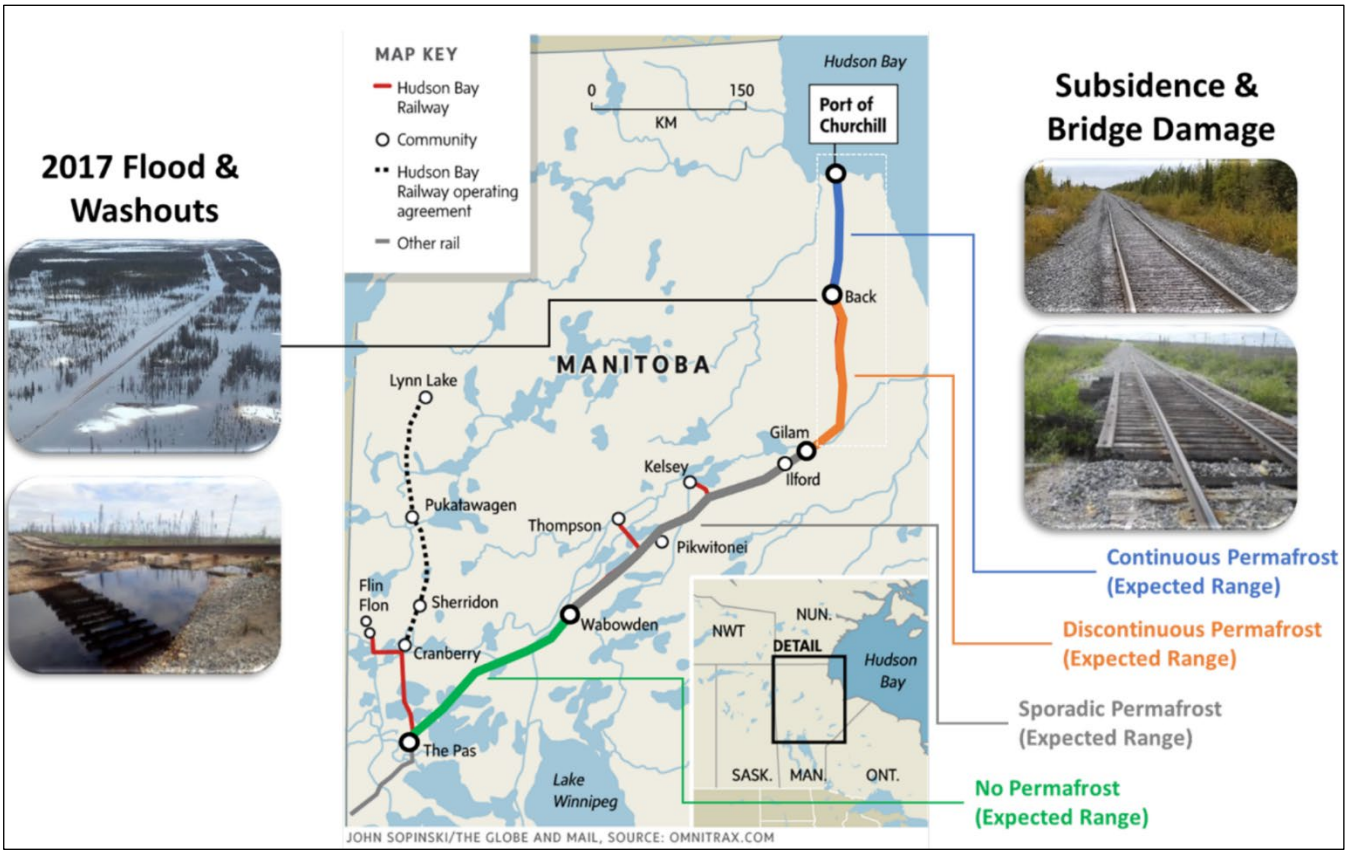

Figure 1. Map of the Hudson Bay Railway, highlighting the expected permafrost zones and observed permafrost hazards along the rail.

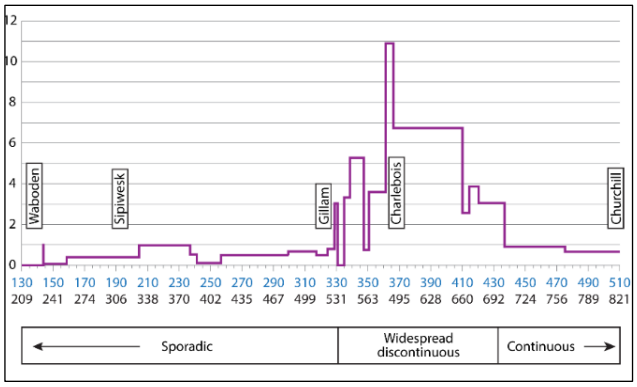

Figure 2. Frequency of sinkholes along the HBR (modified from EBA Engineering Consultants Ltd. 1991).

Flooding has also caused widespread damage to the HBR. In May 2017, along the Herchmer Subdivision between Gillam (KP 524.8) and Churchill (KP 820.4), a 200-year flooding event resulted in 31 locations with washouts and damage to culverts and bridges. The railway was temporarily shut down between May 2017 and November 2018, which severely affected Churchill and all of the communities dependent on the HBR. This event precipitated the sale of the assets from Omnitrax to Arctic Gateway Group on September 1, 2018. The Arctic Gateway Group immediately began repairs and repaired heavy washout locations using Geocell Technology. The flooding along the HBR emphasized the need to improve mitigation measures for risks related to permafrost hydrology along this linear infrastructure.

As the climate continues to warm, hazards related to permafrost thaw and extreme weather events are expected to increase. Using the high emissions scenario (RCP 8.5), the Climate Atlas of Canada projects an annual mean temperature of -1.4 and 2620 Freezing Degree Days (FDD) for Gillam by 2050. Relative to the period 1976–2005, the projections represent an increase of 2.4 °C and a decrease of 527.3 FDD. Continued warming in this area is expected to result in permafrost thaw and subsidence, degradation of peat plateaus, and thermokarst processes (Dyke and Sladen 2010). The impacts of fire, such as the burn between Cromarty and Belcher (Figure 4), will likely accelerate permafrost degradation. Understanding the influence of climate change on geotechnical and hydrological hazards along the HBR is a focus of the PermaRail research program.

Figure 3. Mitigation techniques designed and tested along the Herchmer Subdivision between Gillam and Weir River from 1976 to 1991. Top images: 800 Cryo-Anchor heat pipes and 6H:1V gentle slope with wood chips insulation. Bottom image: Thermo-probes.

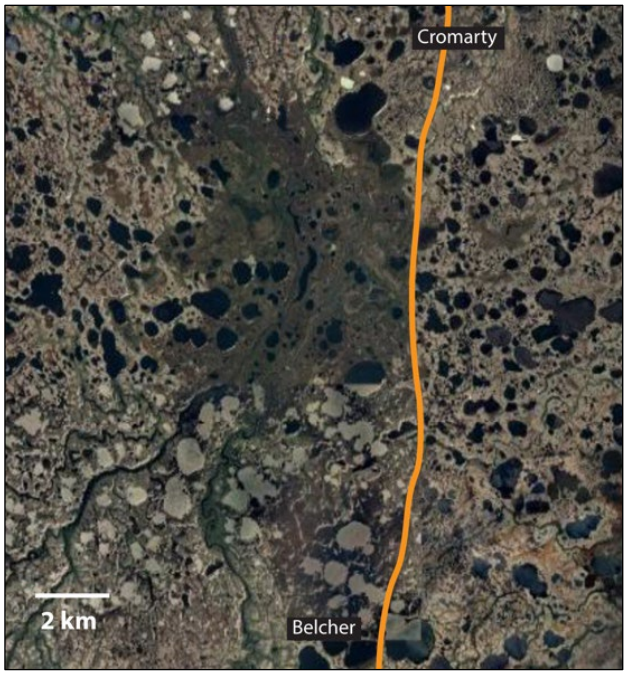

Figure 4. Fires, such as the one shown here between Cromarty and Belcher, are expected to accelerate permafrost degradation along the HBR.

1.3 The PermaRail Research Program

The PermaRail research initiative, funded by the National Trade Corridors Fund (NTCF), is a collaborative seven-year research program (2022–2028) involving the Arctic Gateway Group, who own the HBR, as well as the University of Calgary, Carleton University, Royal Military College of Canada, Queen's University, and Université Laval. Understanding vulnerability of railways, and other linear infrastructure located on permafrost, requires a transdisciplinary approach. Therefore, the team includes HBR operators, civil and geotechnical engineers, geophysicists, geotechnicians, and permafrost geomorphologists.

The PermaRail project aims to address the following key issues surrounding this unique and important northern transportation asset: 1) lack of permafrost data and characterization, 2) water management, 3) surface stabilization, and 4) infrastructure management. In addressing these four specific challenges, the overall goal of the PermaRail project is to identify, characterize, and mitigate permafrost-related and hydrological hazards along the HBR.

We plan to improve understanding of geophysical and geotechnical conditions along HBR, assess the effects of climate change on geohazards along the rail, improve understanding of the influence of permafrost thaw on hydrology, and identify strategies to bolster the resilience of HBR infrastructure. Initial research activities include permafrost characterization and an assessment of infrastructure and geohazards along the rail. Next, monitoring will provide real-time data at instrumented locations. Finally, mitigation techniques and materials will be tested to assess adaptation options, enhance rail performance and resilience, and inform engineering best practices for future infrastructure development.

The findings are intended to guide creation and testing of innovative strategies for monitoring, mitigating, and remediating permafrost-related hazards, ultimately ensuring the safety, reliability, and resilience of the railway. Based on insights from the HBR study, we plan to formulate recommendations and guidelines for future rail and linear infrastructure development in permafrost regions to increase Canadian expertise and leadership in the management of permafrost railways globally.

2 METHODOLOGY

The project combines field investigations, in-situ monitoring, laboratory experiments, physical and numerical modelling, and field tests to comprehensively study permafrost-related hazards and mitigative strategies. An overview of the methodologies and related timeline for the PermaRail project are outlined in Figure 5.

The comprehensive field investigation program will involve utilizing geophysical, geotechnical, and remote sensing techniques to characterize the ground and rail conditions, including permafrost, ice, soil and surface water conditions, properties, and behaviours. Experimental and numerical analyses will supplement the field program and provide the basis to explore future climate scenarios, identify high risk locations, and evaluate the impact of mitigation and adaptation techniques. Selected mitigation techniques will be installed and tested in the field for full-scale evaluation of performance.

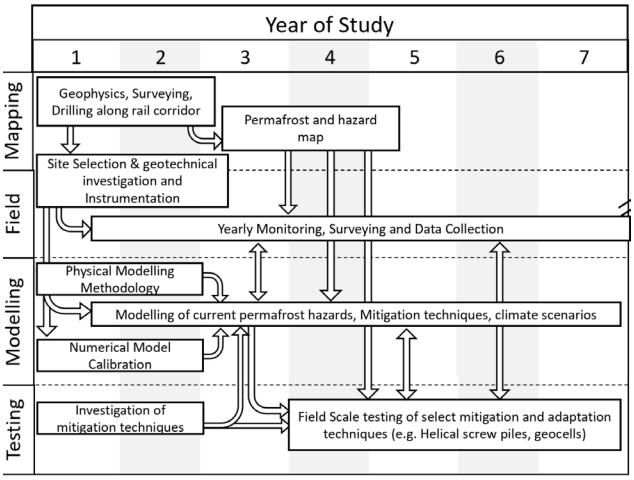

Figure 5. Flow chart of PermaRail methodologies and their timeline.

2.1 Mapping Permafrost Conditions

The first stage of PermaRail activities, which is the assessment of permafrost conditions along the rail, entails the development of a regional map of permafrost distribution and characteristics with an inventory of potential permafrost-related hazards and where they are most likely encountered. The corridor will be divided into terrain units based on a set of biophysical factors including latitude,

surficial geology, geomorphic features, hydrology, surface conditions, vegetation, topography, and climate.

Extensive field campaigns are being carried out to characterize each terrain unit. Drilling and core extractions using portable drills (Calmels and Allard 2005) are informing assessments of permafrost, including extent, temperature, thickness, and vertical ice distribution (Figure 6). Geophysical methods include ground penetrating radar (GPR) and electrical resistivity tomography (ERT), which are well-suited to permafrost and hydrology applications (e.g., Hinkel et al. 2001; Kneisel et al. 2008; Walvoord and Kurylyk 2016). GPR will provide high-resolution stratigraphic information in the near-surface to map boundaries between frozen and unfrozen ground (i.e., permafrost table, taliks, etc.) near or beneath the railway. ERT surveys will provide insights into the distribution and characteristics of frozen and unfrozen ground. High-resolution drone mapping was also carried out along specific sections of the rail to characterize surface conditions and to produce high resolution digital elevation models at a representative subset of sites.

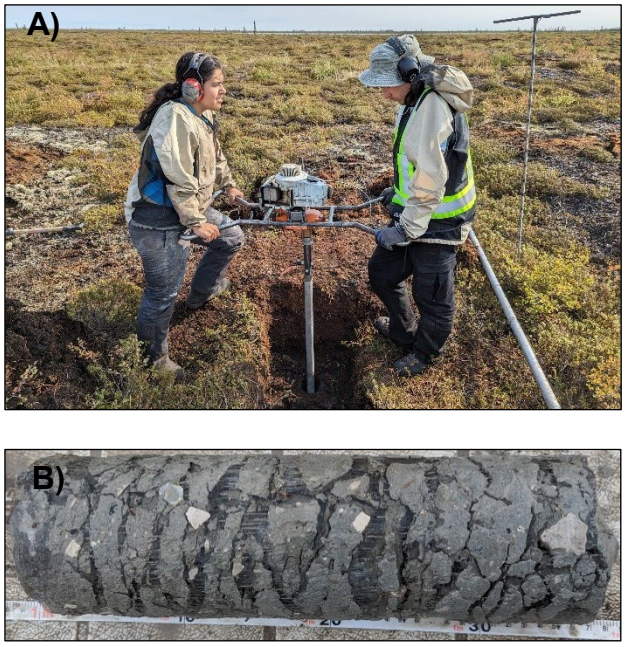

Figure 6. A) Drilling and core extractions using a portable drill at Lamprey (KP 769). B) From this site, ice-rich permafrost cores were recovered between 1.0 and 1.37 m.

This work is enabling the development of high-resolution maps of permafrost ice content, which is a key parameter that influences whether thawing ground is vulnerable to subsidence and erosion. Permafrost distribution and ground ice maps along the rail corridor will be cross-validated using existing and new borehole data, field observations, and existing maps. These enhanced maps will be a valuable tool for identifying permafrost hazards, predicting thaw settlement, and reliability mapping along the railway under changing climatic conditions.

Ground temperature monitoring stations are being initiated in strategic locations. For instance, previously instrumented sites from older studies (EBA, 1977, 1979, 1988) are being gradually re-equipped for temperature monitoring, and new instrumentation added in strategic locations (Figure 7). To monitor the temperature at the surface and at the top of the permafrost (≈ 1 m depth), 16 two-channel external data logger (interchangeability tolerance of ±0.21 °C from 0 °C to 50 °C, and 0.02 °C resolution at 25 °C) were installed for different environmental setting and surface conditions. The dataloggers were placed in a sealed 2-inch ABS casing connected to a 0.5-inch diameter, and one-meter-long PVC casing.

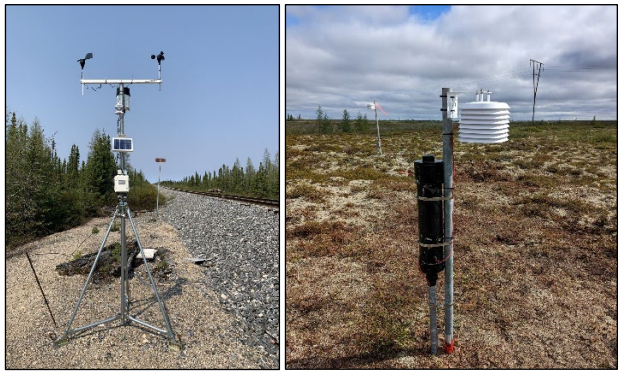

Figure 7. Weather station installed near Herchmer subdivision (left) and air and ground temperature instrumentation installed at Chesnaye subdivision (right) during summer 2022.

The selected monitoring sites reflect distinctive terrain units where a more detailed understanding is needed. Surface, ground, and air temperatures measured at those sites will be used to adjust and validate the regional scale temperature at the top of the permafrost map currently under production. Those data will also support physical model calibration.

The resulting maps and geodatabase will be the first project deliverables and will be used to identify priority areas for further instrumentation, modelling, and study in collaboration with Arctic Gateway Group. Throughout the research program, maps and associated databases will be updated as new findings improve our understanding of permafrost conditions and related hazards.

2.2 Assessing Geohazards

In parallel with the field investigation and monitoring, comprehensive physical modelling and numerical modelling studies of key geohazards identified are being performed. Some of the major geohazards include thaw subsidence, thermo-erosion, frost heave, culvert icing and flooding.

Physical models will provide conceptual understanding of the field data with highly instrumented benchtop, full-scale experiments in a cold room, and with a geotechnical centrifuge. This will allow the control of boundary conditions and materials in a 1:1 model while accelerating time for

environmentally driven processes with the geotechnical centrifuge.

Numerical and physical modelling of field site geohazards will help to bridge the gaps between discrete measurement points in the field. For each key geohazard, calibrated numerical models will use climate model outputs (i.e., CMIP6 climate scenarios) to predict the impact of the future climate on hazard frequency and magnitude.

2.3 Testing Mitigation Techniques

The earlier phases of the project will characterize permafrost distribution, material properties, the seasonal variability of selected sites along the rail (i.e., multi-year monitoring of track geometry changes and thermal and groundwater changes in the subgrade under the track structure, etc.), and track performance. In the final phase of the project, we will choose new field monitoring sites exhibiting poor track behaviour as well as sites already mitigated and equipped by EBA in the 1970s to quantitatively assess the success of different mitigation options. Candidate mitigation strategies will be examined first using physical and numerical modelling techniques to identify strategies with the highest possibility of success. Subsequently, a select number of full-scale field tests will be conducted, whereby mitigation techniques are tested in real-time on the rail. Potential mitigation techniques may include, but are not limited to, gentle slope, thermosyphon, culvert management, geogrid cells, and helical screwpiles. However, the final selection of mitigation techniques will be based on the findings and information gained from the mapping, field investigation, and modelling activities.

3 Preliminary Results

The project officially began in June 2022. During this first year, the primary focus has been on characterizing and mapping permafrost conditions along the rail in the Barrens region (≈ KP 690 to KP 790). A field characterization program, including drone mapping, geophysical surveying, and drilling, was carried out in August–September 2023 at five different sites: Umiskwuska Lake (KP 717), Belcher (KP 728), Burn (KP 737), Chesnaye (KP 751), Lamprey (KP 769).

To characterize surface conditions at each site and to produce high resolution digital elevation models (DEM), drone mapping images were obtained. An example of a high-resolution image obtained by the drone is depicted in Figure 8. The drone's aerial perspective illustrates the extensive network of ice-wedge polygons that characterize the Barrens region. Drone imagery and DEMs will be used to pinpoint sections where the railway intersects ice wedges.

Figure 8. Drone image illustrating the extensive network of ice-wedge polygons that characterize the Barrens region and that intersect the railway embankment (Belcher site).

ERT data were collected at 5 sites along the northern portion of the rail in summer 2023. In these ERT surveys, surface conditions were shown to play a critical role in permafrost conditions; surface water, vegetation, and the railway embankment all influenced subsurface resistivity distributions. For example, a survey near Belcher indicated that active layer thickness increases significantly near the embankment (Figure 9), likely due to a more pronounced snow insulation effect and surface water ponding. Thaw depths were measured in the natural terrain by frost probing along ERT profiles and were observed to be an average of 52 cm deep away from the embankment where detectable with an 80 cm probe.

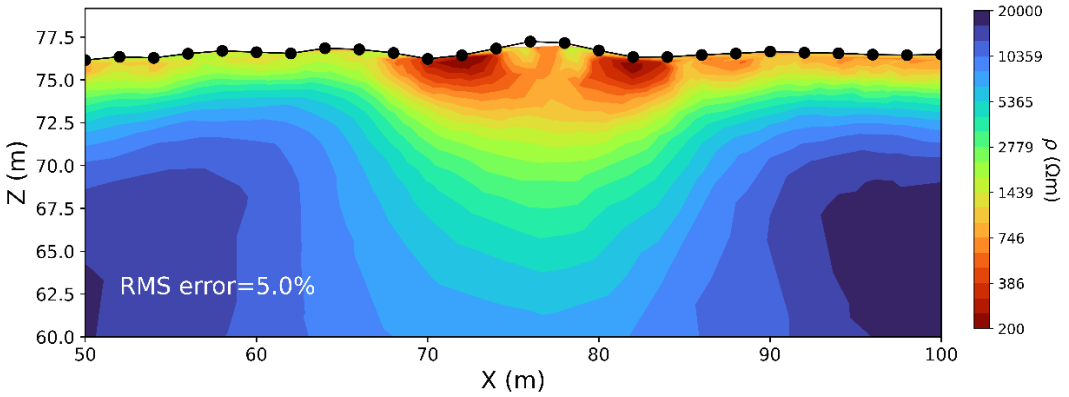

Figure 9. Electrical Resistivity Tomography (ERT) profile across the railway embankment (Belcher site).

A selection of newly drilled boreholes was instrumented during summer 2022 and 2023 to monitor ground temperatures along the rail. To date, four boreholes were instrumented with 15-thermistor strings and dataloggers. At each thermistor string location, one thermistor was placed inside a radiation shield placed 1.5 m above the ground level to monitor air temperature. Ground and air temperatures are recorded every hour and are stored in the datalogger internal flash memory. Figure 10 shows the minimum, mean, and maximum ground temperature profiles measured in the natural terrain beside the railway at Chesnaye and Belcher stations between 2022 and 2023.

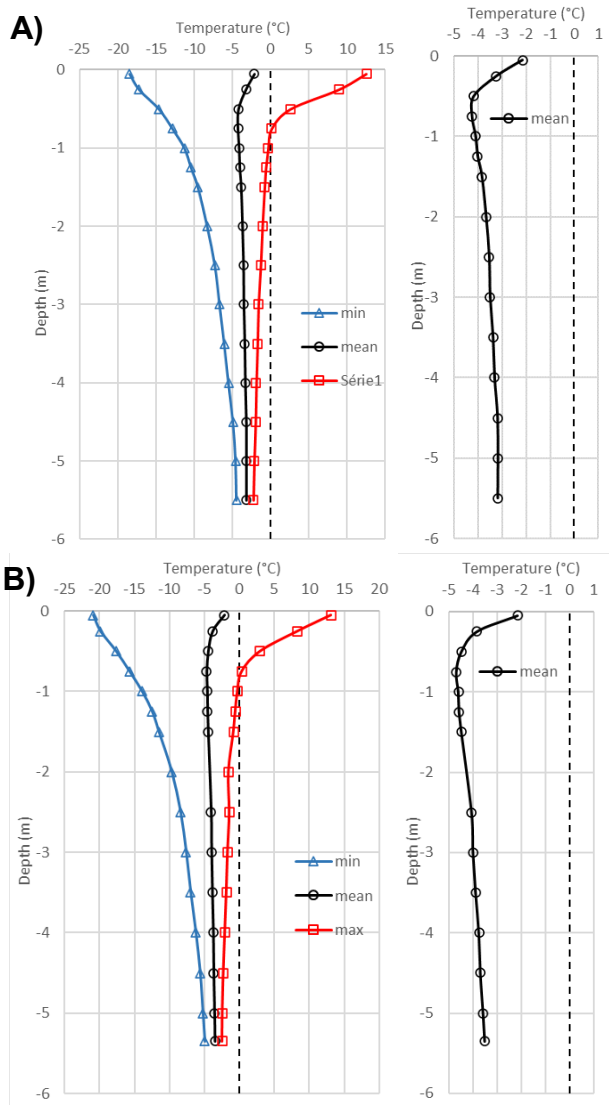

Figure 10. Minimum, mean, and maximum ground temperature profiles measured in polygon centers from 2022-09-01 to 2023-08-31 near A) Chesnaye and B) Belcher stations, Manitoba. Graphs on the right display the mean temperature profile to emphasize the thermal offset.

According to the monitoring results at Chesnaye site during the period 2022–2023, the calculated mean annual ground surface temperatures (0.05 m depth) and at the top of the permafrost (0.75 m depth) were respectively −2.14 °C and -4.25 °C (Figure 10A). These findings indicate a notable thermal offset exceeding 2 °C, primarily attributed to the substantial peat thickness (> 2 m) acting as an effective insulating layer in summer and a thermally conductive layer in winter. At 5 m depth, the mean annual ground temperature calculated was -3.17 °C. At the Belcher site, ground temperatures were slightly lower on average by about -0.4 °C. For 2022–2023, mean annual temperature at the surface and at 5 m depth were -2.14 °C and -3.57 °C respectively. As shown in Figure 10B, the thick peat cover at this site also contributes to the occurrence of a significant thermal offset.

4 Upcoming Work

As a result of the initial characterization and monitoring work done in summer 2023, a large-scale geophysical and geotechnical drilling program is being planned in coordination with HBR. The large-scale drilling is most likely to occur in 2024. Using a more powerful drill will enable thermistor strings to be installed throughout the embankment, as well as at greater depths to complete the ground temperature monitoring network along the rail.

Creep tests on frozen organic and mineral cores are currently being conducted under constant load at different temperature steps (-4 °C, -2 °C, and -1 °C) along with thaw strain consolidation tests. These tests will provide insight into long-term deformation behavior of frozen soil, and their potential settlement upon thawing. These geotechnical properties will also serve as input parameters for further thermomechanical simulations in order to assess long-term soil behavior under varying climate conditions.

More site-specific field work continues on the impact of drained lakes, understanding the frost jacking of bridges, and analysis of the track geometry data. These programs will continue to collect new field data in addition to analyzing data from monitoring sites. Over the next year, further numerical modelling work will improve our understanding of the thermal regime, how it has changed, and how it will continue to change in the future. Additionally, multi-hazard identification and vulnerability mapping will ramp up. These programs are supported by field data, which is essential for establishing appropriate model inputs, boundary conditions, and calibrations.

As the project team continues to gather data, we are also developing methodologies to share data and develop a useable database with associated map layers that includes both historical and predicted data. This will be ongoing throughout the project, and the structure of the overarching database and maps will be determined over the next 6–12 months. Establishing good data collection, documentation, and structure is a key project component.

5 CONCLUSIONS

This study will provide all stakeholders — the HBR communities and trades that use the rail corridor, Arctic Gateway Group, and the NTCF — with a proactive and forward-looking assessment of the current and future conditions of permafrost along the rail corridor. We aim to provide recommendations on effective mitigation strategies and tools for common permafrost hazards (e.g., flooding, thaw settlement, embankment stability, etc.). The results of this study will be used to develop monitoring, mitigation and remediation strategies and designs to ensure the safety, reliability, and resilience of both the HBR rail corridor and all other northern linear infrastructure networks against similar permafrost hazards.

6 ACKNOWLEDGEMENTS

Funding for this project is provided by the National Trade Corridors Fund. We thank Arctic Gateway Group for their ongoing partnership and support of the project. Thanks to the many graduate students, field assistants, and support staff who have already contributed greatly to this project.

7 REFERENCES

Calmels, F., Gagnon, O. and Allard, M. 2005. 'A portable earth-drill system for permafrost studies', *Permafrost Periglacial Processes* 16, pp. 311–315. Available at: https://doi.org/10.1002/ppp.529.

Dyke, L.D. and Sladen, W.E. 2010. 'Permafrost and Peatland Evolution in the Northern Hudson Bay Lowland, Manitoba', *Arctic* 63, pp. 429–441.

EBA Engineering Consultants Ltd. 1987. *Requirements for Subgrade Stabilization, Hudson Bay Railway*. Engineering report prepared for Canadian National Railways.

EBA Engineering Consultants Ltd., 1979. *Embankment Stablization Research Program, Grain Line Rehabilitation, Hudson Bay Division*. Engineering Report Prepared for Canadian National Railways.

EBA Engineering Consultants Ltd., 1991. *Prototype Stability Program, Hudson Bay Railway, 1990/91 Heat Pipe Effectiveness Evaluation and Geotechnical Investigation*. Engineering Report Prepared for Canadian National Railways.

Hinkel, K.M., Doolittle, J.A., Bockheim, J.G., Nelson, F.E., Paetzold, R., Kimble, J.M., and Travis, R., 2001. 'Detection of subsurface permafrost features with ground-penetrating radar, Barrow, Alaska'. *Permafrost and Periglacial Processes* 12, pp. 179–190. Available at: https://doi.org/10.1002/ppp.369.

Kneisel, C., Hauck, C., Fortier, R., and Moorman, B. 2008. 'Advances in geophysical methods for permafrost investigations', *Permafrost and Periglacial Processes* 19, pp. 157–178. Available at: https://doi.org/10.1002/ppp.

Rantanen, M., Karpechko, A.Y., Lipponen, A., Nordling, K., Hyvärinen, O., Ruosteenoja, K., Vihma, T., and Laaksonen, A. 2022. 'The Arctic has warmed nearly four times faster than the globe since 1979', *Communications Earth and Environment* 3, pp. 1–10. Available at: https://doi.org/10.1038/s43247-022-00498-3.

Schuur, E.A.G., Abbott, B., Commane, R., Ernakovich, J., Euskirchen, E., Hugelius, G., Grosse, G., Jones, M., Koven, C., Leyshk, V., Lawrence, D., Loranty, M., Mauritz, M., Olefeldt, D., Natali, S., Rodenhizer, H., Salmon, V., Schädel, C., Strauss, J., Treat, C., and Turetsky, M. 2022. 'Permafrost and climate change: Carbon cycle feedbacks from the warming Arctic', *Annual Review of Environment and Resources* 16, pp. 1–29. Available at: https://doi.org/10.1146/annurev-environ-012220-011847.

Walvoord, M.A. and Kurylyk, B.L. 2016. 'Hydrologic Impacts of Thawing Permafrost-A Review', *Vadose Zone Journal* 15, vzj2016.01.0010. Available at: https://doi.org/10.2136/vzj2016.01.0010.

Permafrost thermal stabilization using renewable energy sources

Egor Loktionov[1], Alexander Klokov[1], Alexander Tutunin[1], Abdula Bakhmadov[1], Elizaveta Sharaborova[2], Taisia Sepitko[3], Sergey Churkin[4] & Aleksei Korshunov[4]

[1]*State Lab for Photon Energetics, Bauman Moscow State Technical University, Moscow, Russia*

[2]*Lab CRYOS, Ecole Polytechnique Federale de Lausanne, Sion, Switzerland*

[3]*Institute of Track, Building and Constructions, Russian University of Transport, Moscow, Russia*

[4]*Department of Geotechnics, Northern (Arctic) Federal University, Arkhangelsk, Russia*

ABSTRACT

Increasing air temperatures are leading to thermosyphons being undercooled in winter and unable to prevent thaw in summer. Fossil fuel-powered refrigerators have to be used to maintain soil frozen in critical cases. We suggest dual use of solar panels as a sun shield and a power source alongside horizontal shallow ground probes rather than vertical in-depth ones to prevent heat penetration in soil at all. We performed a number of numerical experiments to evaluate the performance of this approach for different objects (railroad embankment, ice cellar, coastal cliff, winter road, buildings) and conditions; estimated its geographical application according to weather data and optimized heat pumps for intermittent power supply. We have also built 3 experimental setups – railroad embankment with heat diverted to residential facilities (made artificial permafrost in moderate climate); foundation thermal stabilization with heat diverted to a greenhouse (tomatoes and cucumbers yield increase in sub-Arctic); prolonged operation of a winter road with a heat pump directly connection to horizontal thermosyphons (shared refrigerant loop) and vertical bifacial east-west oriented solar panels. These experiments, both numerical and physical, have shown high potential technical, environmental, and economic benefits of the suggested approaches.

1 INTRODUCTION

Building on permafrost has always been full of challenges (Muller et al. 2008). Most of those were resolved during the construction boom in the Arctic in 1970s to large extent using underfloor ventilation and thermosyphons for enhanced soil cooling during winter time (Li et al. 2018). Now, with global warming, the cost of sufficient solutions is increasing as is the need for constant monitoring of infrastructure and the underlying ground thermal regime. This problem becomes particularly pronounced for linear infrastructural objects such as motorways (Yinfei et al. 2016), railroads (Luo et al. 2018), pipe (Li et al. 2018) and power (Wang et al. 2018) lines connecting remote settlements. To prevent disasters like the Norilsk 2020 oil spill, chilling units accompanied by power plants, fuel tanks, and staff have to be used in the most critical cases.

Permafrost thaw occurs as winters become milder and shorter while summers become hotter and longer. Particularly for this reason, widely used thermosyphons are currently operated out of designed conditions, so are not capable of keeping soil frozen. Industrial users have reported that thermosyphon performance is half of that used in calculations. Moreover, there are operational data showing about 30% of thermosyphons can be damaged at mounting and up to 50% more breakdown within a decade. Thermosyphon replacement is not always possible following construction. The problem is not easily addressed by increasing the density of thermosyphons as this can lead to soil heaving due to overcooling in winter.

Noteworthy, major research trends in this area are related to precise soil thermal state simulation rather than development of new or optimized methods of thermal stabilization (Kong 2019; Kong et al. 2019). The need for innovation is characterized by the following situation. Thermosyphons are typically proposed for soil freezing under the foundation piles, which are well below the seasonally thawed layer. This approach is widely used as it works well but does not work well for thermal stabilization of the road embankments where soil of the upper layers is moving laterally. The effect of deep freezing using vertical thermosyphons is rather poor for roads. Some reconsideration has started recently, and a combination of sloped, or flat looped thermosyphons (Holubec 2008) and insulation of the surface is used to prevent upper soil layers thawing (Mu et al. 2016). However, this combination of two methods, the complexity of assembly, and delivery costs for high volumes of insulation nearly double the cost of the solution compared to traditional vertical thermosyphons.

Heat is supplied to soil via convection at natural air motion, solar radiation absorption and can also be introduced with infiltrating rain. There are solutions to minimize this heat flow: solar reflectors and shields (Gagnon et al. 2022; Qin et al. 2020), heat insulation (Luo et al. 2018) and waterproof layers (Yinfei et al. 2016). But obviously neither of these passive methods is capable of completely eliminating ground warming. Active cooling methods are well developed in general, but demand power supply, so are very expensive and non-sustainable when using fossil fuel, unless waste heat is available on-site for absorption heat pumps (Lavrik et al. 2023).

Recently, suggestions to use solar power for active thermal stabilization of permafrost have appeared (Hu et al. 2020; Sun et al. 2024). However, these researchers did not use a significant effect of shielding solar radiation and precipitation by solar panels. Hu et al. (2020) still rely on

https://doi.org/10.52381/ICOP2024.152.1

vertical, in-depth cooling by isolated devices. Sun et al. (2024) have switched horizontal barrier cooling and using the benefits of centralized power and chill supply: electric and cooling energy redistribution.

We suggested an approach that combines minimizing heat flow into the soil by shielding solar radiation and liquid precipitation, and making a near-surface solar-powered heat diversion layer to stop heat penetration in soil depth (Loktionov et al. 2022). This concept has been patented (Sharaborova et al. 2020) and proven experimentally (Loktionov et al. 2023; Loktionov et al. 2024; Sharaborova et al. 2022). An example of such a heat diversion layer in the form of ground probe loops to be covered with 25 cm embankment is presented in Figure 1. However, this is not the only way of implementation, it can also be artificial snow or cooled thermal insulation layer, cold gas injection or inflatable mats, all of those with their own pros and cons. Our approach can provide not only improved soil thermal stabilization at competitive price only (200 $/m^2 compared to 180 $/m^2 for thermosyphons), but can also recover these costs (75 $/m^2 year) by selling energy for monitoring systems and heating. Long-term negative trends in PV panels (–15% CAGR) and heat pumps (–10% CAGR) are going to make this approach more favourable.

A cheaper but less efficient way is to use solar power to move surface heat insulation up for winter (so turning it into ventilated blinds) and back down for summer (Sharaborova and Loktionov 2022).

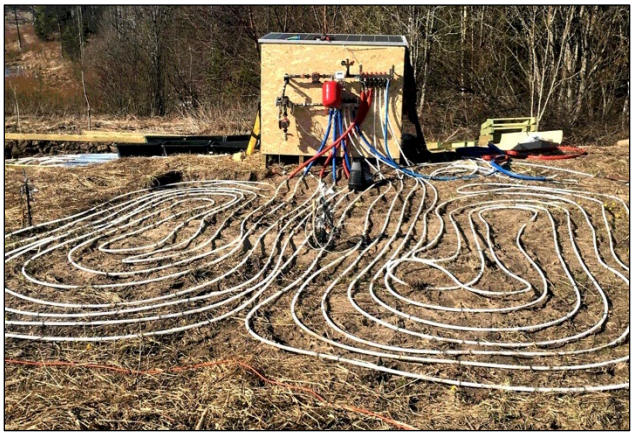

Figure 1. Ground probes of the thermal shielding layer under solar panels at the greenhouse site.

In this paper we are reporting the current progress in application of this concept to different types of objects, both in numerical simulations and experiments.

2 METHODOLOGY

Our approach to thermal stabilization has been described in details elsewhere (Loktionov et al. 2022). Solar panels are used as blinds to shield radiation and rain in summer and to keep a ventilated gap for natural cooling in winter. PV also provides power for a heat pump. We are cooling soil within an active layer (Figure 1) reducing its thickness and preventing heat penetration in permafrost, Figure 2 illustrates this effect. The coolant average temperature is -7.5 °C. Note, the brighter the sun is, more chill is available, and soil thermal inertia provides free energy storage to eliminate the main solar energy shortcoming — intermittency, particularly, once variable power output is used (Klokov et al. 2023a).

For thermal calculations, we have used Frost-3D Multi-Core GPU software (https://frost3d.ru/eng/) which has been specially developed for permafrost soil calculations, its results validity has been verified by analytical solutions (Dauzhenka and Gishkeluk 2013) and practical applications, compared to the most popular FEM packages (Alekseev et al. 2018), and conformity to relevant national and corporate (Gazprom) construction regulations certified. The details of calculation methods and data are presented in (Loktionov et al. 2022).

To date, three sites have been built to test the suggested solutions: 1) road embankment (Figure 3; Sharaborova et al. 2022); 2) greenhouse and seasonal insulation (Figure 4; Loktionov et al. 2024); 3) winter road (Figure 6; Loktionov et al. 2023). All of those were equiped with temperature (0, 10, 20, 40, 80, 160, 320, 500 cm depth) and heat flux (at heat exchage surfaces) sensors, at reference plots as well.

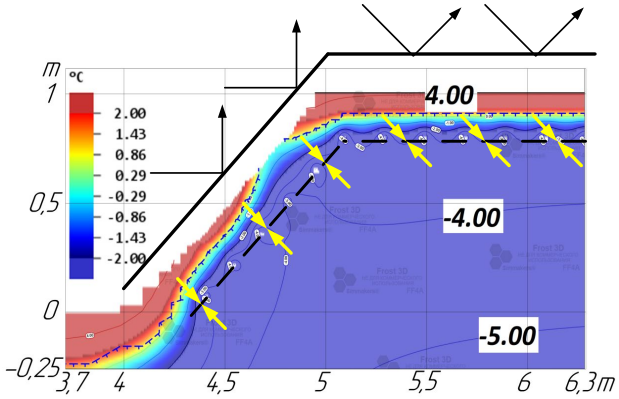

Figure 2. The effect of solar panels shielding (solid line) and heat diversion layer on road embankment in Norilsk by September, 15.

2.1 First tests in moderate climate

A detailed description of site 1 is given in (Sharaborova et al. 2022). It is a scaled model of the railroad embankment consisting of sand, and the upper surface was covered with solar panels. However, Loktionov et al. (2022) showed that solar panels could be moved from the upper surface to the embankment foot with some increase in nameplate capacity to compensate for thermal load increase. This experiment was conducted 100 km SW of Moscow, far from the permafrost extent to have better access to the equipment. In such conditions, thermal load is higher and solar panels output is lower than in the Arctic, so energy balance was accounted for. The heat was diverted to the house.

Figure 3. Road embankment site.

2.2 The greenhouse and seasonal insulation site

The greenhouse experiment site was near near Arkhangelsk, about 150 km SW of the sporadic permafrost region. The objective was to test the area's thermal stabilization with heat utilisation leading to some multiplicative effect. The heat was diverted to a greenhouse (6 x 3 m) here to test the possible effect on the yield compared to the reference. Vegetables are delivered to remote communities by air that makes those expensive and rarely available (Loktionov et al. 2024). We estimated this approach could return investment in thermal stabilization just in one year for the most remote settlements by selling these vegetables. This approach is an extension of the agrivoltaics that gains popularity recently (Klokov et al. 2023b).

Figure 4. Aerial view of the greenhouse site and seasonal insulation-shield plot (bottom right).

The ground probes in the greenhouse were 30 cm deep that ensured heat wave reaching the surface with about 12 h delay to its extraction due to heat conduction in the ground, so warming the space at night which is cooler than day even if the sun is sill above the horizon. Rain water was collected from the solar panels surface (2° inclined) to the barrel equiped with an automatic valve and drop irrigation tubing. The greenhouses were equiped with automatic ventilation frames. We also performed additional phyto-lighting using the energy harvested by solar panels and stored in small batteries (Figure 5). The heat source area (5.5 × 5.5 m) was bigger than the heat sink, resulting in soil warming up to 36 °C and low performance of the heat pump due to high temperature in the sink loop, so the latter had to be improved.

Site 1 had a straight layout with battery storage for solar power output intermittency compensation and a start-stop heat pump. High battery cost and its fast degradation due to intense cycling had led us to using invertor heat pumps as a variable load that follows actual power ouput (Klokov et al. 2023a; Tutunin and Loktionov 2023) for sites 2 and 3. To implement that we have used a solar pump invertor (by Veichi) that has an input from PV panels directly and adjusts the output frequency automatically to match the available power.

We also have tested a seasonal thermal resistance change here. Extruded polystirol of 50 mm thick was placed in wooden frames covered with metal sheets (with a ventilated air gap between those and insulation). These frames were lying on the ground in summer to reduce heating and elevated about 1 m above the ground in winter to ensure reduced snow cover for better cooling (Gagnon et al. 2022).

Figure 5. Illumination of the experimental greenhouse at dull weather when energy is insufficient for heat pump operation.

2.3 The winter road site

Winter roads are the only terrestrial way to reach many remote communities in the Arctic. These roads are impacted by climate change not only in terms of operation duration but performance predictability as well. Very often problems along short sections of the road control the availability of the whole road. These problematic areas need to have some backup cooling systems to resolve the issue (Loktionov et al. 2023). At sites 1 and 2 LDPE and PE-X ground probes were filled with ethylene glycol anti-freeze solution (isopropanol could be also used as a less hazardous medium that does not need refill every 5 years). In case of pipes damage, the anti-freeze penetrates into the soil, after that, it is extremely hard to freeze it. To avoid that, the pipes should be metal rather than plastic and filled with gas rather than liquid. This brings us close to the traditional horizontal thermosyphons in the road embankments.

Site 3 was also built in Arkhangelsk, close to site 2. We have connected 10 thermosyphons with collectors just under condensation parts and at the tips of the evaporation side, so that refrigerant (R32) outlet and inlet are as far as possible (5.5 m). Via those collectors a joint refrigerant loop with the heat pump was formed. In that case, the heat was

Figure 6. Construction of the winter road site.

diverted to a stream via a submerged corrugated stainless steel hose, that ensured high COP of the heat pump. In winter, these thermosyphons work in their usual way with natural cold.

To power the system, we used vertical east-west bifacial solar panels, 6.6 kW in total specified for one side, elevated higher than normal snow depth. Before that, we made a calculation to estimate power output and shadowing of thermally stabilized area. That gave us a positive effect compared to horizontal panels not in terms of overall energy balance only, but also in power supply uniformity over days and year. In this way, the heat pump is getting enough power from sunrise till sunset.

3 RESULTS

The results for site 1 are presented in details in (Sharaborova et al. 2022). The most remarkable one is presented in Figure 7. The soil remained frozen even at continuous +30 °C daytime air temperature, so artificial permafrost was made. It matched our numerical estimations (-2.5 °C in mid-August) well.

We have used the experimental data on heat fluxes, coolant temperatures and solar output for calculations for different cases. One is the coastal cliff (Irrgang et al. 2022; Ogorodov et al. 2020). We considered a hard case of south facing at the edge of the permafrost extent in Mezen (Figure 8). We realise there is a sliding surface so freezing a core should not be the only stabilization measure, but it could prevent catastrophic wash outs during storms. The catastrophic wave erosion takes place in autumn and in dull weather, so we considered a hybrid solar-wind power system for that case. Moreover, snow accumulation at the cliff edge would improve the slope protection unlike in natural conditions, but it was not modelled here.

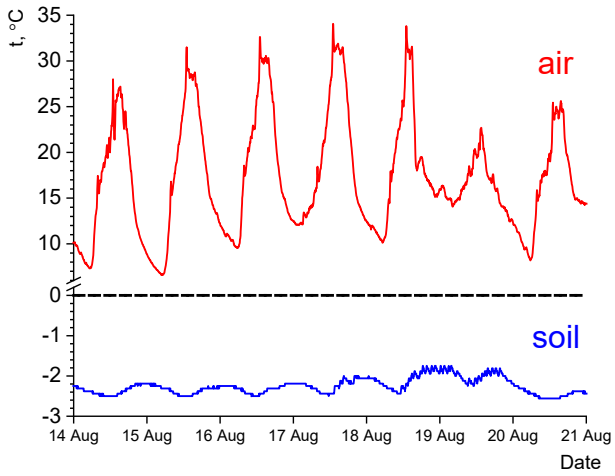

Figure 7. Near-surface air and soil (–26 cm) temperatures at road embankment site (Sharaborova et al. 2022).

Now back to our experimental results. The EER of the greenhouse site heat pump is 3.3 on average due to working most time at compressor's upper pressure limit of 22 bar and supply temperature of 60 °C. The specific yield in experimental greenhouse was twice higher for tomatoes and cucumbers than reference (for quite warm summer), and the harvest season was one month (1.5 times) longer. That resulted in 3-fold yield increase for Arkhangelsk. For the next summer that was about long term-average, the yield was 4-fold. We expect, farther north and in colder than average seasons the difference would be greater, and the weather hazards risks are reduced. This greenhouse could be coupled with the ice cellar to improve remote communities' food security (Loktionov et al. 2024).

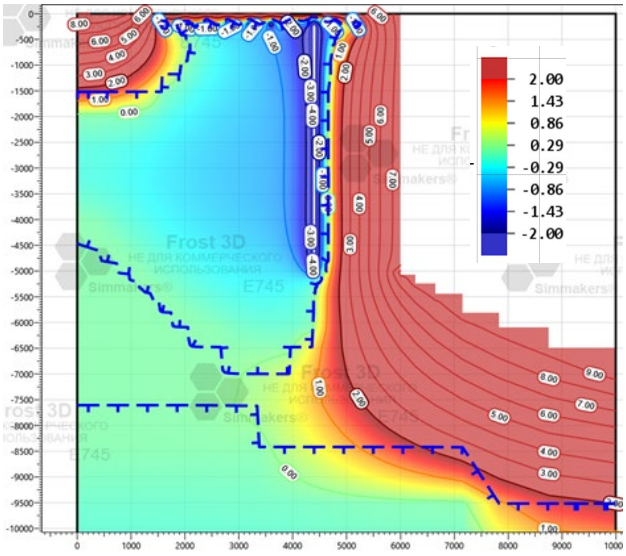

Figure 8. South-faced coastal cliff thermal stabilization in Mezen, September, 15. Permafrost border is shown by blue dashed line.

Our activities led to a significant temperature decrease in both experiments (active cooling and seasonal heat insulation) at site 2 (Figure 9). Since the soil was better cooled in summer by the heat pump, it had lower temperatures than under seasonal insulation. Since there is no underlying permafrost at the site, there is a significant heating from deeper ground layers.

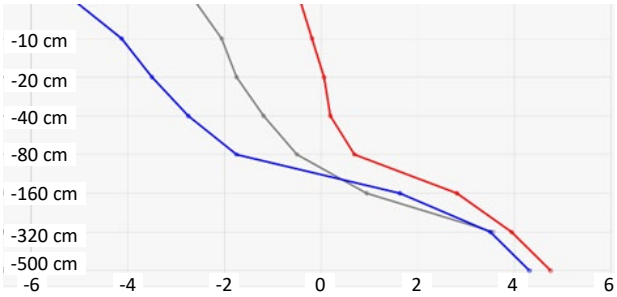

Figure 9. Temperatures (°C) at site 2 by March, 25: blue – heat pump, grey – seasonal insulation, red – reference.

The ice road site (#3) has been operational for just few months by the moment. We can also say that refrigerant temperature reaches -18.8 °C and heat flux on thermosyphons evaporators reaches 900 W/m^2 (Loktionov et al. 2024). The facility works with EER of 5.3 thanks to the cold and fast water in the stream. As observed, bifacial panels were supplying 1.5 kW sufficient for the heat pump operation even at sunrise and sunset, and in midday when direct solar radiation is parallel to their surface.

We have also considered application of our approach of heat diverting layers for the prevention of heat areas merging around oil and gas wells that imposes a serious threat on their stability (Figure 10; Loktionov 2022).

The warm halos did not merge even without using expensive heat insulated lift pipes. This approach also allows to decrease the cost of gas and oil production sites construction by multifold reducing the distance between wells, and so the site size and ground works to build it.

4 Discussion

We should note an extreme importance to measure heat fluxes in permafrost research (Sharaborova et al. 2022). So the permafrost is thawed by the amount of heat (thermal energy) absorbed, not the temperature difference exactly. In calculations, heat flow and heat flux are estimated for border conditions in rather complicated and indirect ways leading to significant inaccuracy. This refers particularly to solar irradiance. Measuring the heat flux at soil surface one can get a warning signal much earlier than observing temperatures in depth, so, seeing the reason not the reaction. These measurements are comparatively more complicated and expensive than temperature ones, but still are quite affordable. The heat flux can be also estimated form near-surface soil temperature measurements with logarithmic increment (like in Figure 9). The heat flux is not a substitution to temperature measurements, but could be a very valuable addition.

It has been shown that at permafrost thawing highest emission rates for CO_2 occur from 0–40 cm depths, for CH_4, from 40–80 cm (Jiang et al. 2020). High abundances of carbon-cycling bacteria, fungi, and archaea corresponded to 0–40 cm depths. Release of hazardous chemicals, e.g., mercury (Ci et al. 2020), has been reported too. So significant reduction of the active layer and its temperature leads not only to better structure stability, but also prevents chemical and biological hazards in the area of human activities (Miner et al. 2021). Our approach can reduce the active layer to the ground probes depth or make it even thinner. Potentially, our approach could prevent methane bubbling (Walter et al. 2006), development of thermokarst and gas emission craters (Dvornikov et al. 2019).

5 Conclusions

Once solar energy is reversed from heating the permafrost to cooling, it overpowers the rest of heat sources. Our experiments, both numerical and physical, have shown high potential technical, environmental, and economic benefits of this approach. Its implementation is based on the existing technologies. And it is the only permafrost thermal stabilization technology that can pay itself back. We have shown the suggested approach applicability to different cases when permafrost thermal stabilization is needed: area and linear infrastructure, coastal cliffs, ice cellars, oil and gas wells.

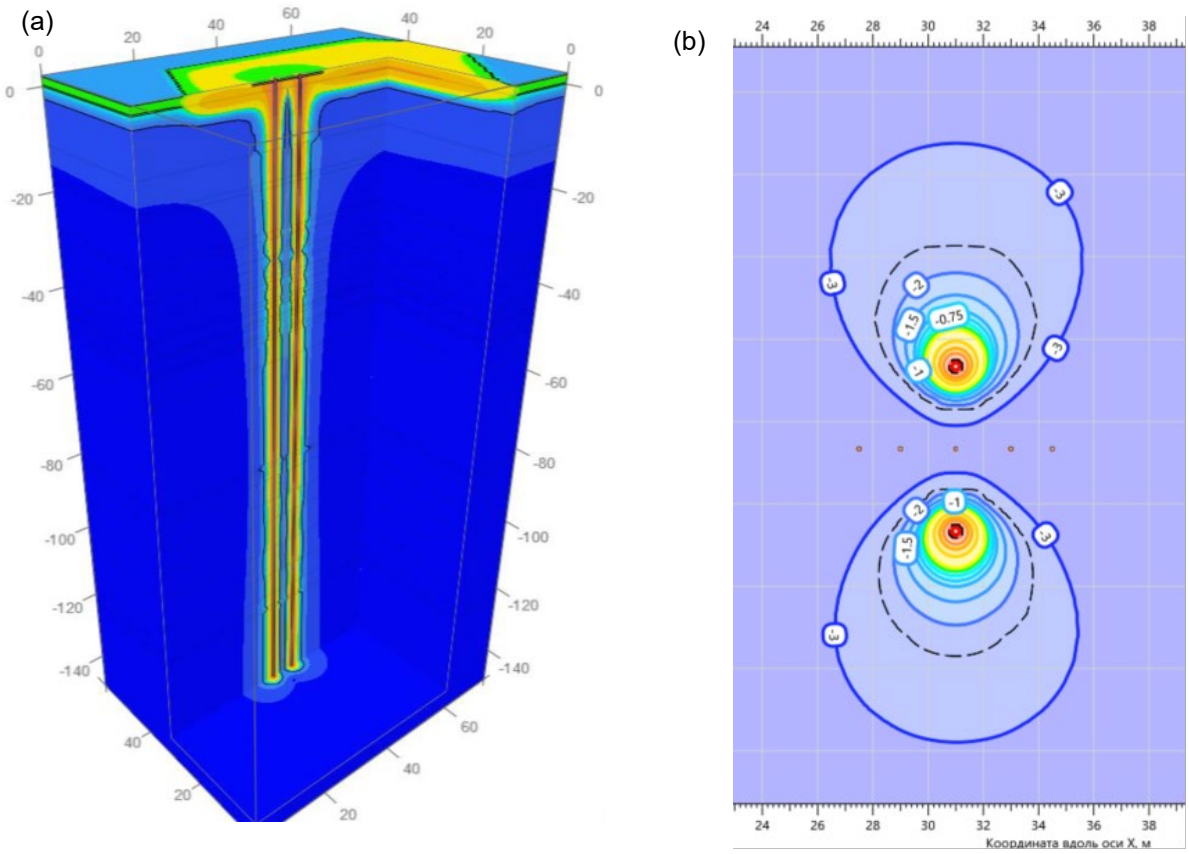

Figure 10. Temperature field in front (a) and critical cross-section (b) of two nearby gas wells with solar-powered heat sink ground probes in between.

We suggest east-west oriented bifacial solar panels are used to power invertor-mode heat pump that is able to adjust its power consumption to actual output (adaptive load). In easier cases, we suggest using solar power to lift surface thermal insulation units up in autumn to make those sun (and actually snow) screens in winter.

Considering opportunities for synergy, it could be a seasonal load for remote communities' renewable energy systems which are under loaded in summer. And it could provide electricity and heat to other activities, including agriculture to make fresh vegetables more affordable by increasing the yield and reducing weather hazards significantly compared to usual greenhouses.

6 ACKNOWLEDGEMENTS

This work was supported financially by the Russian Science Foundation and Arkhangelsk Region (grant No. 22-19-20026). We are grateful to Simmakers Ltd. for providing a free license for its Frost 3D package.

7 REFERENCES

Alekseev, A., Gribovskii, G., and Vinogradova, S. 2018. 'Comparison of analytical solution of the semi-infinite problem of soil freezing with numerical solutions in various simulation software', *IOP Conference Series: Materials Science and Engineering* 365, 042059. doi:10.1088/1757-899x/365/4/042059.

Ci, Z., Peng, F., Xue, X., and Zhang, X. 2020. 'Permafrost Thaw Dominates Mercury Emission in Tibetan Thermokarst Ponds', *Environmental Science & Technology* 54(9), pp. 5456–5466. doi:10.1021/acs.est.9b06712.

Dauzhenka, T.A. and Gishkeluk, I.A. 2013. 'Consistency of the Douglas – Rachford splitting algorithm for the sum of three nonlinear operators: application to the Stefan problem in permafrost soils', *Applied and Computational Mathematics* 2(4), pp. 100–108. doi:10.11648/j.acm.20130204.11.

Dvornikov, Y.A., Leibman, M.O., Khomutov, A.V., Kizyakov, A.I., Semenov, P., Bussmann, I., Babkin, E.M., Heim, B., Portnov, A., Babkina, E.A., Streletskaya, I.D., Chetverova, A.A., Kozachek, A., and Meyer, H. 2019. 'Gas-emission craters of the Yamal and Gydan peninsulas: A proposed mechanism for lake genesis and development of permafrost landscapes', *Permafrost and Periglacial Processes* 30(3), pp. 146–162. doi:10.1002/ppp.2014.

Gagnon, S., Fortier, D., Sliger, M., and Rioux, K. 2022. 'Air-convection-reflective sheds: A mitigation technique that stopped degradation and promoted permafrost recovery under the Alaska Highway, south-western Yukon, Canada', *Cold Regions Science and Technology* 197, 103524. doi:10.1016/j.coldregions.2022.103524.

Holubec, I. 2008. *Flat Loop Thermosyphon Foundations in Warm Permafrost I*. Holubec Consulting Inc.

Hu, T.-f., Liu, J.-k., Hao, Z.-h., and Chang, J. 2020. 'Design and experimental study of a solar compression refrigeration apparatus (SCRA) for embankment engineering in permafrost regions', *Transportation Geotechnics* 22, 100311. doi:10.1016/j.trgeo.2019.100311.

Irrgang, A.M., Bendixen, M., Farquharson, L.M., Baranskaya, A.V., Erikson, L.H., Gibbs, A.E., Ogorodov, S.A., Overduin, P.P., Lantuit, H., Grigoriev, M.N., and Jones, B.M. 2022. 'Drivers, dynamics and impacts of changing Arctic coasts', *Nature Reviews Earth & Environment* 3(1), pp. 39–54. doi:10.1038/s43017-021-00232-1.

Jiang, L., Song, Y., Sun, L., Song, C., Wang, X., Ma, X., Liu, C., and Gao, J. 2020. 'Effects of warming on carbon emission and microbial abundances across different soil depths of a peatland in the permafrost region under anaerobic condition', *Applied Soil Ecology* 156, 103712. doi:10.1016/j.apsoil.2020.103712.

Klokov, A.V., Tutunin, A.S., Sharaborova, E.S., Korshunov, A.A., and Loktionov, E.Y. 2023a. 'Inverter Heat Pumps as a Variable Load for Off-Grid Solar-Powered Systems', *Energies* 16(16), 5987. doi:10.3390/en16165987.

Klokov, A.V., Loktionov, E.Y., Loktionov, Y.V., Panchenko, V.A., and Sharaborova, E.S. 2023b. 'A Mini-Review of Current Activities and Future Trends in Agrivoltaics', *Energies* 16(7), 3009. doi:10.3390/en16073009.

Kong, X. 2019. *Development of design tools for convection mitigation techniques to preserve permafrost under northern transportation infrastructure*. Québec City, Québec, Canada: PhD thesis, Universite Laval.

Kong, X., Doré, G., and Calmels, F. 2019. 'Thermal modeling of heat balance through embankments in permafrost regions', *Cold Regions Science and Technology* 158, pp. 117–127. doi:10.1016/j.coldregions.2018.11.013.

Lavrik, A., Buslaev, G., and Dvoinikov, M. 2023. 'Thermal Stabilization of Permafrost Using Thermal Coils Inside Foundation Piles', *Civil Engineering Journal* 9(4), pp. 927–938. doi:10.28991/CEJ-2023-09-04-013.

Li, G., Wang, F., Ma, W., Fortier, R., Mu, Y., Zhou, Z., Mao, Y., and Cai, Y. 2018. 'Field observations of cooling performance of thermosyphons on permafrost under the China-Russia Crude Oil Pipeline', *Applied Thermal Engineering* 141, pp. 688–696. doi:10.1016/j.applthermaleng.2018.06.005.

Loktionov, E. 2022. *Method for preventing coalescence of thaw halos around wells in permafrost formations*. Patent RU2789556C1. Priority date 28.07.2022.

Loktionov, E.Y., Sharaborova, E.S., and Shepitko, T.V. 2022. 'A Sustainable Concept for Permafrost Thermal Stabilization', *Sustainable Energy Technologies and Assessments* 52(12), 102003. doi:10.1016/j.seta.2022.102003.

Loktionov, E.Y., Sharaborova, E.S., Klokov, A.V., Bakmadov, A.V., and A., K.A. 2023. 'On the possibility of extending the service life of winter roads using renewable energy sources', *Arktika: Ekologia i Ekonomika* 13(4), pp. 570–578. doi:10.25283/2223-4594-2023-4-447-455.

Loktionov, E.Y., Sharaborova, E.S., Klokov, A.V., Maslakov, A.A., Sotnikova, K.S., and A., K.A. 2024. 'Ice cellars preservation technologies to ensure sustainable development of northern settlements', *Arktika: Ekologia i Ekonomika* 14(1), pp. 116–126. doi:10.25283/2223-4594-2024-1-116-126.

Luo, J., Niu, F., Liu, M., Lin, Z., and Yin, G. 2018. 'Field experimental study on long-term cooling and deformation characteristics of crushed-rock revetment embankment at the Qinghai–Tibet Railway', *Applied Thermal Engineering* 139, pp. 256–263. doi:10.1016/j.applthermaleng.2018.04.138.

Miner, K.R., D'Andrilli, J., Mackelprang, R., Edwards, A., Malaska, M.J., Waldrop, M.P., and Miller, C.E. 2021. 'Emergent biogeochemical risks from Arctic permafrost degradation', *Nature Climate Change* 11(10), pp. 809–819. doi:10.1038/s41558-021-01162-y.

Mu, Y., Wang, G., Yu, Q., Li, G., Ma, W., and Zhao, S. 2016. 'Thermal performance of a combined cooling method of thermosyphons and insulation boards for tower foundation soils along the Qinghai–Tibet Power Transmission Line', *Cold Regions Science and Technology* 121, pp. 226–236. doi:10.1016/j.coldregions.2015.06.006.

Muller, S.W., French, H.M., and Nelson, F.E. 2008. *Frozen in time: Permafrost and engineering problems*. American Society of Civil Engineers.

Ogorodov, S., Aleksyutina, D., Baranskaya, A., Shabanova, N., and Shilova, O. 2020. 'Coastal Erosion of the Russian Arctic: An Overview', *Journal of Coastal Research* 95(sp1), pp. 599–604. doi:10.2112/SI95-117.1.

Qin, Y., Li, Y., and Bao, T. 2020. 'An experimental study of reflective shading devices for cooling roadbeds in permafrost regions', *Solar Energy* 205, pp. 135–141. doi:10.1016/j.solener.2020.05.054.

Sharaborova, E.S. and Loktionov, E.Y. 2022. *Soil thermal stabiliation method due to year round regulation of heat transfer*. Patent RU2779706C1. Priority date 14.03.2022.

Sharaborova, E.S., Loktionov, E.Y., and Shepitko, T.V. 2020. *Method for thermally stabilizing permafrost soils*. Patent Priority date 07.10.2020.

Sharaborova, E.S., Shepitko, T.V., and Loktionov, E.Y. 2022. 'Experimental proof of a solar-powered heat pump system for permafrost thermal stabilization', *Energies* 15(6), 2118. doi:10.3390/en15062118.

Sun, Z., Liu, J., You, T., Ren, Z., Chang, D., Fang, J., and Vladislav, I. 2024. 'Field test study on thermal performance of a novel embankment using solar refrigeration technology', *Renewable Energy* 226, 120392. doi:10.1016/j.renene.2024.120392.

Tutunin, A. and Loktionov, E. 2023. 'A Coordination of the Capacities of the Hybrid Renewable Energy System and the Seasonal Variable Load Following the Intermittent Generation', in *5th International Youth Conference on Radio Electronics, Electrical and Power Engineering (REEPE)*. 16-18 March 2023, pp. 1–8.

Walter, K.M., Zimov, S.A., Chanton, J.P., Verbyla, D., and Chapin, F.S. 2006. 'Methane bubbling from Siberian thaw lakes as a positive feedback to climate warming', *Nature* 443(7107), pp. 71–75. doi:10.1038/nature05040.

Wang, T., Zhou, G., Chao, D., and Yin, L. 2018. 'Influence of hydration heat on stochastic thermal regime of frozen soil foundation considering spatial variability of thermal parameters', *Applied Thermal Engineering* 142, pp. 1–9. doi:10.1016/j.applthermaleng.2018.06.069.

Yinfei, D., Shengyue, W., Shuangjie, W., and Jianbing, C. 2016. 'Cooling permafrost embankment by enhancing oriented heat conduction in asphalt pavement', *Applied Thermal Engineering* 103, pp. 305–313. doi:10.1016/j.applthermaleng.2016.04.115.

Long-term evaluation of mitigation techniques used for permafrost thermal stabilization at the Beaver Creek (YT) experimental road site

Ximena López, Jean-Pascal Bilodeau, Guy Doré & Chantal Lemieux
Université Laval and Centre for Northern Studies, Québec City, Québec, Canada

ABSTRACT

In northern environments, the construction of transportation infrastructures on permafrost, in combination with climate change, can have a significant impact on the thermal equilibrium of the ground. To ensure the safety of remote communities and maintain serviceability of roads, adapted embankment design methods may be needed to avoid thawing of permafrost during construction and throughout the service life. The conventional design and construction methods used in non-permafrost areas have not been adequate to prevent thermal degradation in northern Canada, resulting in considerable losses in the functional and structural capacity of some sections of roads. In order to optimize and assess the effectiveness of mitigation solutions, 12 instrumented test sections were implemented on the Alaska Highway near Beaver Creek, Yukon, Canada, in 2008. These test sections were designed to evaluate different thermal stabilization methods, such as heat drain, air convection embankments, snow and sun sheds, grass-covered embankments, and longitudinal culverts, to name a few. The main objective of this research is to evaluate the long-term effectiveness of the mitigation methods used to maintain the thermal stability of permafrost in the context of transportation infrastructures using an approach based on the temperature differential in the soil.

1 INTRODUCTION

In recent decades, increasing global warming has triggered drastic changes in Canada's northern ecosystems and geosystems. The effects of climate change in these areas have created several significant challenges, particularly with respect to soil and infrastructure stability. Over the last decades, Yukon authorities have witnessed an alarming phenomenon: previously stable structures are now showing signs of distress, posing a serious threat to the safety and sustainability of local communities, as well as a high maintenance cost of existing infrastructure (Malenfant-Lepage, 2016).

The consequences of permafrost degradation are of particular concern for transportation infrastructure in northern environments. Thawing of the underlying thaw sensitive permafrost is causing significant structural damage, such as differential settlement and embankment shoulder degradation which makes driving more difficult and increases the risk of accidents. Degradation could as well result from slope instability, creep of frozen soil under thick embankment, thermokarst and thermal erosion causing drainage issues. The temperature of the backfill and natural soil layers is influenced by various climatic and heat transfer factors, adding complexity to the challenge of thermal stabilization (Dumais and Doré 2016; Hall 2017). Landslides are also becoming more common as permafrost thaws, blocking roads, and causing significant damage to linear infrastructure. This results in significant maintenance costs and a drastic reduction in the service life of roads and embankments (Hjort et al. 2022; Cheng 2005; Reimchen et al. 2009).

To address this issue, a large-scale research initiative has been undertaken to study various techniques to mitigate permafrost warming underneath an in-service road. A test section has been constructed on the Alaska Highway near Beaver Creek in 2008, including several 50-meter-long embankment thermal stabilization experiments using innovative approaches to limit heat intake or maximize heat extraction. The techniques considered include heat drains, air convection embankment (ACE), light-colored aggregates, and snow/sun shed to limit the insulating effects of snow in the winter and to reduce heat intake from solar radiation in the summer. In addition, an extensive network of thermistors has been installed in deep boreholes, at the center and in the slope of the embankment as well as in natural ground near the toe of the slope, in each section to monitor dynamic thermal changes in the permafrost over time.

A short-term evaluation of the effectiveness of the mitigation techniques was previously done (Malenfant-Lepage et al. 2012). The study concluded that mitigation techniques showing the best short-term performance were the ACE uncovered, ACE full embankment, longitudinal culverts, snow/sun shed, and light-colored aggregates. These options provide effective solutions for reducing ground warming for infrastructure projects in permafrost areas. The assessment of their long-term effectiveness is still required to assess their economic viability. Therefore, this paper is focused on evaluating the long-term effectiveness of mitigation methods for maintaining permafrost thermal stability. To achieve this goal, temperature records of the Beaver Creek Experimental Road Site, for a 10-year period (2009–2019) were analyzed and the long-term permafrost thermal regime, and its evolution were evaluated. In addition, a comprehensive analysis of the long-term effectiveness of thermal equilibrium-based methods (Doré et al., 2016) was conducted by comparing temperature data over time. An adaptation of the thermal equilibrium principle is proposed to improve its applicability and effectiveness.

This research is intended to contribute to scientific knowledge of permafrost engineering, and to provide information for the design and implementation of effective mitigation measures based on large-scale and long-term reliable data from an experimental test site. The results will

https://doi.org/10.52381/ICOP2024.198.1

not only benefit the local communities that depend on transportation infrastructure but will also contribute to the development of more resilient and sustainable construction strategies in the context of climate change and permafrost degradation.

2 DESCRIPTION OF THE TEST SITE

The Alaska Highway, a major transportation route connecting Alaska with the rest of North America, has experienced recurring problems related to thaw settlement and longitudinal cracking, particularly in the section from Destruction Bay to the Canada-USA border. Although some sections of this highway were reconstructed about a decade ago, the degrading permafrost foundation and resulting differential settlement problems are affecting the quality and safety of travel to this day.

To address these challenges and improve road quality, Yukon Highways and Public Works partnered with the US Federal Highways Administration, Transport Canada, University of Alaska Transportation Center, Université Laval and Université de Montréal. A world class experimental site was then built to study the effectiveness of mitigation techniques used to prevent permafrost degradation underneath transportation infrastructures. The site is located near Beaver Creek, Yukon, 30 km south of the Canada-USA border at 62°22′59″N and 140°52′29″W.

This section of the Alaska Highway is in a transition zone between sporadic discontinuous permafrost and extensive discontinuous permafrost (Malenfant-Lepage, 2016). The stratigraphy of the region is characterized by a diamicton covered by a silty soil.

The test site was constructed in summer 2008. The 600-m-long road section is divided into 12 test segments (Figure 1c), each one being 50-m-long and 40-m-wide. Eleven different mitigation methods were applied to mitigate permafrost thaw and its negative impact on road infrastructure stability. One section was constructed using normal construction practice to be used as a reference section.

It is important to note that, although there is a total of 11 mitigation techniques available, only six of them are discussed in this document (Table 1). Since the original reference section is in bad condition, it was decided to use the grass-covered slope embankment as the reference section for this analysis. Some techniques were rejected due to design or construction issues noticed after construction (e.g., heat drains). The description of the techniques studied are in Table 2.

Each of the sections is equipped with thermistors strings installed in boreholes on the west-side of the road, allowing continuous monitoring of the thermal regime throughout the project under the center of the slope (Figure 1a). For some sections, thermistor strings are also positioned at the center of the road. The positioning of thermistor strings was carefully chosen to assess the thermal behavior in the zone of influence of the mitigation techniques (center and/or slope).

Table 1. Mitigation techniques considered in this study.

Mitigation technique		Section number
Air convection embankment (ACE)	ACE full embankment	1
	ACE slopes covered with vegetation	3
	ACE slopes uncovered (Fig. 1b)	9
Snow/sun shed (installed in 2009)		6
Grass-covered slope		11
Light-colored aggregates bituminous surface treatment (BST)		12

Table 2. Description of the techniques studied.

Section	Design description and cooling system
1 3 9 ACE	Constructed with porous granular material with particles size ranging between 15 and 30 cm, allowing for natural air convection to occur inside the embankment. During winter, the air cooling in the upper part of the convective material is moving downward into the embankment, causing the warm air to rise and exit from the embankment. No convection is occurring during summer and the ACE is acting as a thermal shield by keeping warm air near the surface and cool air at the base of the embankment. Also, the small contact areas between the crushed rocks and the low thermal conductivity of the air hinder heat transfer to the permafrost.
6 Shed	These structures were designed to provide permafrost protection year-round. In the summer, they reduce heat transfer to the ground by shading the surface. In the winter, they allow cold air to circulate under the structure and counteract the insulating effect of the snow cover to facilitate the evacuation of heat from the ground to the atmosphere.
11 Grass-covered	The embankment slope was seeded with a native grass seeds mix creating a suitable grass cover. Organic soils have low thermal conductivity in summer, which minimizes heat absorption on slopes. In winter, thermal conductivity increases, which accelerates the soil cooling process. This section will be used as the reference section.
12 BST	A standard bituminous surface treatment (BST) using clear aggregates was used on this section. Light-colored aggregates reflect more solar radiation, thus reducing surface temperature and heat absorption into the embankment.

a)

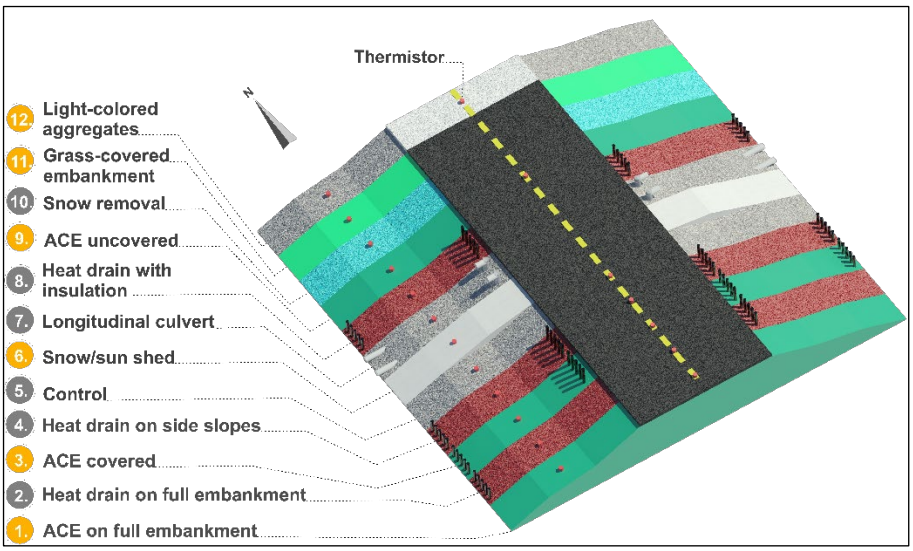

b)

c)

Figure 1. a) Schematic illustration (not to scale) of the mitigation techniques tested at the Beaver Creek Experimental Road Site, the yellow numbers indicate the sections analyzed in this paper; b) construction of the ACE uncovered section, 2008; c) view of the site (looking south), 2009 (before the installation of the snow/sun shed).

The different configurations of ACE designed and used at the Beaver Creek Experimental Road Site are shown in Figure 2.

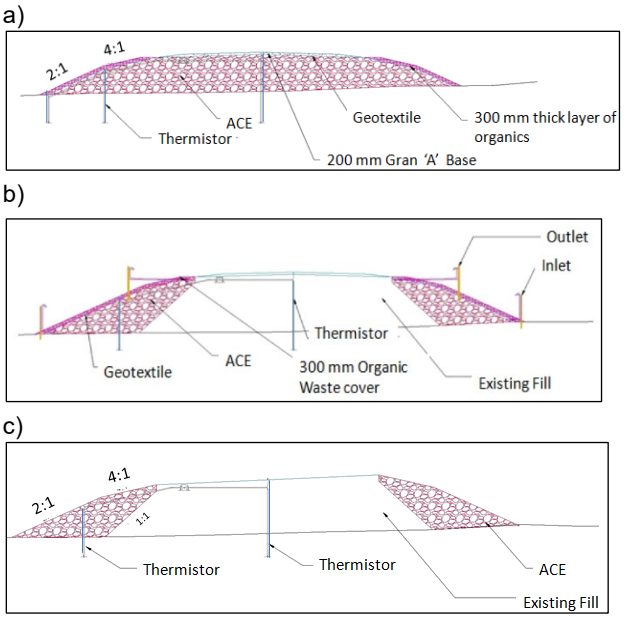

Figure 2. Schematic of a) ACE full (section 1), b) ACE on slope covered with vegetation, with ventilation pipes to improve heat evacuation (section 3); and c) ACE on slopes uncovered (section 9; Malenfant-Lepage 2012).

2.1 Instrumentation

Two or three thermistor strings were installed in each borehole to ensure that monitoring would continue even if one of the strings was damaged. These thermistor strings play a critical role in the thermal data collection approach.

Specifically, the thermistor configuration in each borehole, located on the slope and under the centerline of the embankment, was structured as follows: the first string, located just below the road surface, consists of a single thermistor. The second string is particularly important because it contains a total of 13 thermistors, spaced between 0.3 m and 1 m apart. This arrangement allows the string to reach a total depth of 15 m below the surface. The third string has 2 thermistors spaced 0.2 m apart on both sides of the interface between the embankment and the natural ground.

A total of 300 thermistors have been carefully distributed throughout the site. Each of these thermistors is strategically placed at specific depths, allowing for thorough and detailed monitoring of thermal changes throughout the project site. This extensive deployment of temperature measurement sensors ensures that comprehensive and accurate data on the ground thermal regime is available for the analysis.

Thermal data logging began in October 2008 and since then, temperatures have been recorded six times a day. These data are transmitted via satellite every four hours to the Government of Yukon SCADA (Supervisory Control and Data Acquisition) server in Whitehorse, YT. Campbell Scientific CR1000 loggers have been used for data logging in conjunction with thermistors cables supplied by EBA Engineering Consultants Ltd. These thermistors operate over a range of -50 °C to +30 °C, with an accuracy of 0.1 °C over the -10 °C to +10 °C range and 0.2 °C over the rest of the operating range. The quality of thermal data was verified by checking the consistency of the data point in time series and in space series. Afterwards, the collected thermal data have been thoroughly analyzed to extract valuable information. Temperature evolution with depth and time are studied using computer tools such as Microsoft Excel and Golden Software Grapher.

3 METHODOLOGY

The results presented in this paper are based on the analysis of the thermal data from the six sections selected, as discussed in section 2 of this paper. These raw data were provided by Yukon Highways and Public Works (YHPW) and have been subjected to an analysis process to extract relevant information, focusing on the evolution of temperature as a function of depth and time.

To characterize the effectiveness of the sections studied, temperature data from 2009 to 2019 have been used. The choice of this analysis period allows to minimize the effect thermal disturbance by construction activities during the first year and to minimize problems related to aging test sections and monitoring equipment after 2019. It is important to note that only a five-year analysis has been done for section 12 (Light-colored aggregates) due to the rehabilitation of the section with a dark BST surface at that period.

Since the sensors in the control section have shown a change in thermal behavior starting in 2014, Rioux (2017) performed an analysis of the air-ground temperature relationship in the three sections where no mitigation techniques were applied (sections 5, 11, and 12), to select the most suitable section to use as a benchmark to compare the thermal regime of another section. The results indicated that section 12 showed a more natural behavior. However, in this paper, sections 5 (control) and 12 (light-colored BST) were discarded because of an abnormal thermal behavior during the period analyzed. Therefore, section 11 (grass-covered embankment) was chosen as the new reference section in the following analysis, as its thermal behavior was considered the most representative of natural conditions for a conventional design of embankment built on permafrost.

In each of the test sections, several thermistor strings have been installed and positioned specifically to monitor the thermal performance of the different techniques used. To assess the thermal behavior in the zone of influence of the mitigation techniques, the appropriate thermistor strings were selected for the analysis depending on where in the embankment the technique is expected to influence the thermal regime (center and/or slope). For example, the ground temperatures recorded under the center of the embankment were used to analyze the light-colored BST and the ACE full embankment, while the temperature under the slope were used for the techniques installed in the slope

(snow/sun shed, grass-covered slope, ACE slopes covered with vegetation, ACE slopes uncovered). The temperatures under the slope were also used for the ACE full section considering that this technique has an effect on the entire embankment.

The annual period chosen begins in October and ends in September of the following year to include both entire winter and summer in each year analyzed. The first year, referred to as 2010, begins in October 2009 and continues through September 2010, and so on for each subsequent year. This approach provided a clearer and more relevant picture of the impact and effectiveness of the mitigation technique in each of the years studied.

To carry out a rigorous analysis, a thermal gradient analysis has been ruled out, since many movements have been observed on the road and it is not possible to confirm if the thermistor depths from the interface, have changed over the analysis period. The analysis was made using two reference depths in the systems. First, the temperatures closest to the interface of the natural ground with the embankment, in each of the sections, is considered (Tinterface, T_I), as shown in Figure 3. This measurement point is located at different depths depending on the thickness of the embankment analyzed, as shown in Table 3. An interpolation of the temperature recorded by the thermistance above and below the interface depth, has been made. The second reference depth in the system is the deepest measurement points (Tpermafrost, T_P) assumed to be close to the depth of null annual temperature variation and therefore used to quantify permafrost temperature. The difference between annual average Tinterface and annual average Tpermafrost referred to as the "temperature difference", or ΔT, was used as an indicator of thermal performance and was therefore calculated for each year of the analysis period.

Table 3. Depth of the embankment/soil interface and of the deepest measurement point.

	SLOPE		CENTER	
	Interface (m)	**Deep (m)**	**Interface (m)**	**Deep (m)**
ACE full	4.3	15.3	5.2	15.8
ACE slope covered	4.1	15.4	5.5	15.5
ACE slope uncovered	4.0	15.7	6.0	15.4
Snow/sun shed	4.6	15.3	-	-
Grass covered	3.9	15.9	-	-
Light-colored BST	-	-	4.3	15.1

It is believed that this approach will allow to effectively evaluate the relative thermal performance of each of the mitigation methods studied. Average annual thermal gradient has been used by many authors (e.g., Malenfant-Lepage 2012, 2016; Kong 2019) to assess permafrost stability. Null or negative gradients are considered to be representative of stable thermal conditions in permafrost, while positive thermal gradients are representative of unstable conditions. In this study, the difference in temperature is used without considering the difference in depth. Therefore, a null or negative ΔT indicates thermal stability of permafrost over time, providing valuable information on the effectiveness of the techniques implemented. In addition, as it is expected that T_P will have evolved very slightly in comparison with T_I, a decrease in ΔT should indicate cooling over time and increase effectiveness of the mitigation technique with time, while an increase in ΔT should be an indication of warming of the soil and reduced effectiveness with time.

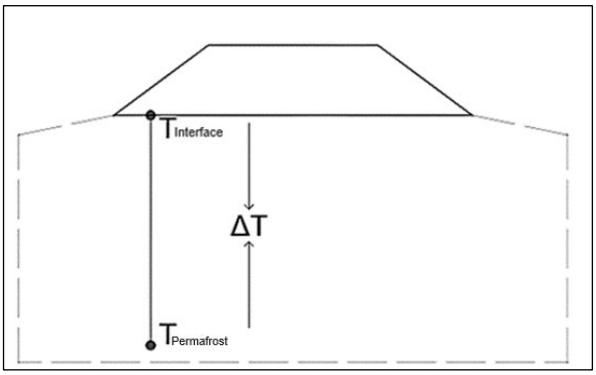

Figure 3. Schematic illustration of temperature difference ΔT, between the temperature at the embankment/soil interface (T_I) and the temperature of permafrost (T_P).

To calculate the temperature difference, the following equation will be used:

$$\Delta T = T_I - T_P \quad (1)$$

Where:

ΔT: Represents the difference in temperatures (°C)

T_I: Interface temperature (°C)

T_P: Permafrost temperature (°C)

This equation was used to analyze the effectiveness of the techniques installed for permafrost conservation at the study site. To perform the analysis, annual averages for the thermistors considered, and depth were calculated. Afterwards, Equation1 was used to assess the ΔT values and compare the evolution over time of each of the test sections considered.

4 RESULTS AND DISCUSSION

Using the mean annual soil temperature at the selected depth, located under the slope or under the centerline of the road, allows us to obtain representative values covering a wider range of thermal conditions throughout the year. These mean annual temperatures (T_I and T_P) were used in Equation 1 to calculate the temperature differences in each of the cases analyzed.

Figure 4 and Figure 5 show the mean annual temperatures of the soil at the interface of the embankment with the natural ground (T_I), at the depth of permafrost temperature (T_P), and the difference of those two temperatures, between October 2009 and September 2019 for each

technique studied, except for section 12 (light-colored aggregates BST) whose analyses stops in 2014 as previously explained. To visualize the results more easily, the analyzed mitigation methods are presented according to their zone of influence: under the slope (Figure 4) and under the center of the road (Figure 5).

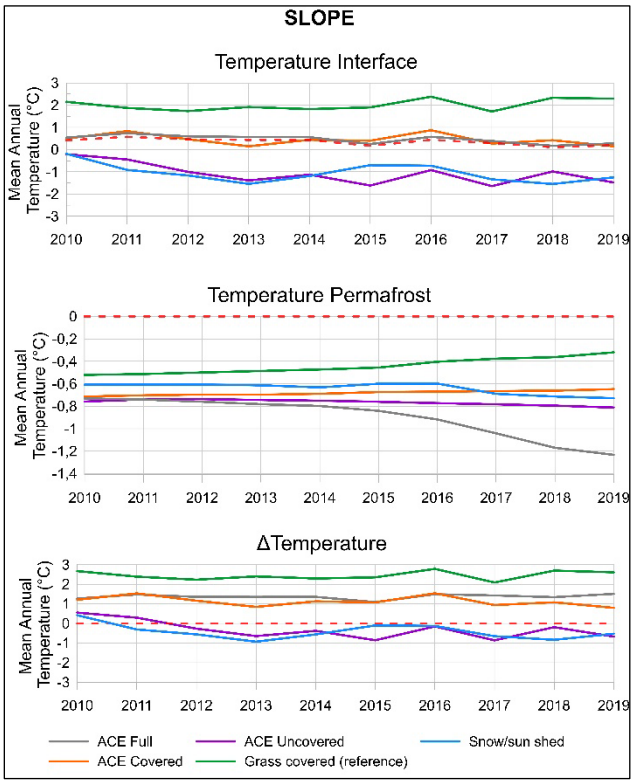

Figure 4. Soil temperatures (T_I, T_P, ΔT) under the slope of the embankment for the reference section grass covered, the snow/sun shed and three configurations of the ACE technique: ACE slope uncovered, ACE slope covered and ACE full. The red dashed line indicates 0 °C.

In Figure 4, the interface temperature under the slope reveals that the grass covered technique stands out as the warmest compared to the other four during the period analyzed. The ACE full and ACE covered methods show fluctuations between 0 and 1 °C over time, stabilizing in 2018 close to 0 °C. In contrast, the snow/sun shed and ACE uncovered techniques have the coldest temperatures, ranging between 0 and -2 °C throughout the analysis period. Both techniques show a decrease of temperature in the first few years, followed by some variations and a tendency to decrease again at the end of the period analyzed.

The permafrost temperature (T_P) is stable in the early years for all techniques. Then, from 2015, T_P of the grass covered area (reference section) begins to warm consistently from -0.5 °C to -0.3 °C in 2020 indicating a slow warming of the permafrost, thus a deepening of the permafrost table. On the other hand, T_P of the ACE full shows a decrease through time, reaching around 0.5 °C of cooling in six years from 2014 to 2020.

The difference of temperature shows that the ACE full, ACE covered and grass covered techniques are above 0 °C during the entire period analyzed showing limited capacity to induce a decrease of interface temperatures and maintaining thermal stability underneath the slope over time, although the difference does not exceed 3 °C. In contrast, the ACE uncovered and snow/sun shed techniques maintain their temperature differences below 0 °C, as soon as two years after the installation (shed), demonstrating effectiveness in maintaining thermal stability and cooling the soil under the slope.

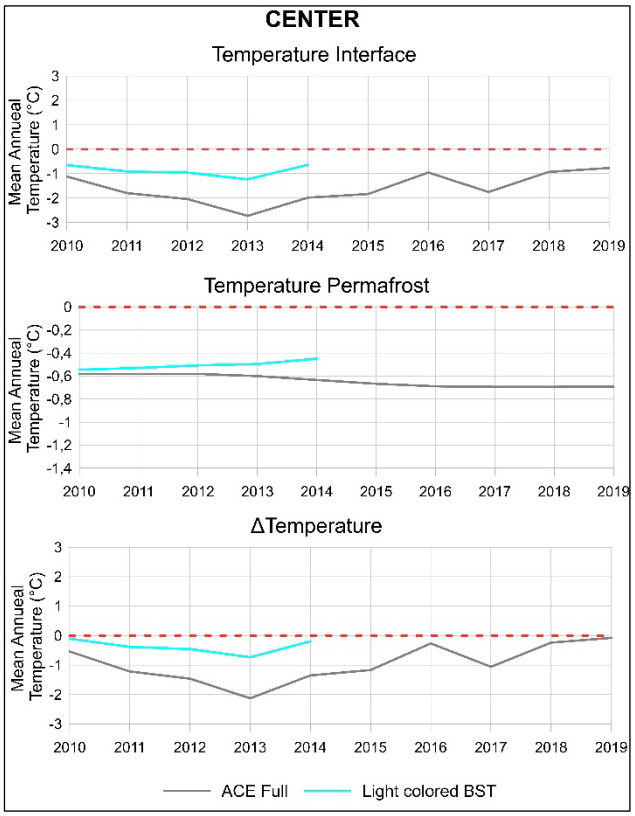

Figure 5. Soil temperatures (T_I, T_P, ΔT) under the centerline of the embankment for the BST with light-colored aggregates and the ACE full embankment. The red dashed line indicates 0 °C.

In Figure 5, the two techniques analyzed in the centre of the embankment, ACE full and BST with light-colored aggregates, are shown. Both methods show similar trend in temperature at the interface, being always colder than 0 °C, with BST section being up to approximately 1.5 °C warmer than the ACE full section. For the ACE full, it can be observed that after an initial decrease of the temperatures from 2010 to 2013 (-1.2 °C to -2.8 °C), a general increasing trend is noticed up to 2019. Other factors will be analyzed to understand this behavior, like contamination of the ACE material by fines particles, or groundwater flow.

No significant variation of the permafrost temperature over time is observed, indicating a stability in the permafrost thermal conditions maintained just under 0 °C and

supporting the effectiveness of the mitigation techniques applied.

Finally, when evaluating the difference in temperatures, both techniques remain below zero during the entire period showing thermal stability of the ground, as in general the interface temperatures are slightly colder than the permafrost temperatures. For both techniques, the ΔT follow the interface temperature tendency which decreased rapidly after construction, indicating a cooling of the system, and then starting to increase in 2013 with a stabilization just under 0 °C in 2018 for the ACE full.

Moreover, the air temperature will be analyzed throughout the studied period to better understand the ground temperatures differences, especially considering that T_P does not vary significantly over the monitoring period. This means that the interface temperature, located at a depth varying from 3.9 to 4.6 m from the surface of the embankment (slope) and 4.3 to 6 m from the surface of the road (center), would have a greater effect on the ΔT variations. Also, field observations over the period might indicates other factors influencing temperature difference, like vegetation growing on the embankment surface and water flow under the embankment.

5 CONCLUSIONS

The analysis of temperature data at the Beaver Creek Experimental Road Site provides valuable insights into the long-term performance of permafrost mitigation techniques. Over a decade of observation, promising performance in some slope protection techniques is observed, such as the ACE uncovered (section 9) and the snow/sun shed (section 6). Indeed, these two sections have shown the best embankment conditions after 15 years, during a site visit in 2023 (Figure 6).

The light-colored embankment was effective in maintaining thermal stability of the permafrost under the center of the embankment, as well as the ACE full which stands out for its ability to maintain lower temperatures in the center than in the slope of the embankment, although this technique is applied to the entire width of the embankment. However, work remains to be completed to understand some performance issues that could explain trends and observations in some sections where the permafrost continued to warm following the construction in 2008. This emphasizes the need to continue thermal analysis using different thermistor depths and calculation approach to better quantify the performance of the test sections while evaluating the durability and economics of long-term maintenance of these techniques. Ultimately, these findings will provide scientists and stakeholders with a solid basis for making informed decisions and developing effective permafrost mitigation strategies in this vulnerable environment, especially in a context where climate change is adding stress on the systems.

a)

b)

Figure 6. The snow/sun shed (a) and ACE uncovered (b) sections in 2023.

6 ACKNOWLEDGEMENTS

This research was supported by the Sentinel North program of Université Laval, made possible, in part, thanks to funding from the Canada First Research Excellence Fund. The authors also wish to thank the organizations and entities that made this research possible: Sentinel North Research Chair on Northern Infrastructures, Ministère des Transports et de la Mobilité Durable (MTMD), Hydro-Québec (HQ), Ville de Québec and the Natural Sciences and Engineering Research Council of Canada (NSERC).

7 REFERENCES

Beaulac, I. 2006. *Impacts de la fonte du pergélisol et adaptations des infrastructures de transport routier et aérien au Nunavik*. MSc, Université Laval Département de Génie Civil, Faculté des Sciences et Génies, Québec City, Québec, Canada.

Cheng, G. 2005. 'Permafrost studies in the Qinghai–Tibet plateau for road construction', *Journal of Cold Regions Engineering* 19(1), pp. 19–29. Available at: https://doi.org/10.1061/(ASCE)0887-381X(2005)19:1(19).

Dumais, S. and Doré, G. 2016. 'An albedo based model for the calculation of pavement surface temperatures in permafrost regions', *Cold Regions Science and Technology* 123, pp. 44–52. Available at: https://doi.org/10.1016/j.coldregions.2015.11.013.

Doré, G. and Zubeck, H.K. 2009. *Cold regions pavement engineering*. New York, New York, United States: McGraw-Hill.

Doré, G., Niu, F., and Brooks, H., 2016. 'Adaptation methods for transportation infrastructure built on degrading permafrost', *Permafrost and Periglacial Processes* 27(4), pp. 352–364. Available at: https://doi.org/10.1002/ppp.1919.

Ficheur, A. and Doré, G. 2011. *Experimentation of techniques to mitigate the effects of permafrost thaw on transport infrastructure in Nunavik: Tasiujaq Airport*. MSc thesis. Université Laval, Département de Génie Civil, Faculté des Sciences et Génies. Québec City, Québec, Canada.

Fortier D., Sliger M., and Rioux K. 2018. 'Performance assessment of the thermo-reflective snow-sun sheds at the Beaver Creek Road experimental site', *Transport Canada* Final Technical Report, 46 p.

Hall, M.R., Dehdezi, P.K., Dawson, A.R., Grenfell, J., and Isola, R. 2011. 'Influence of the thermophysical properties of pavement materials on the evolution of temperature depth profiles in different climatic regions', *Journal of Materials in Civil Engineering* 24(1), pp. 32–47. Available at: https://doi.org/10.1061/(ASCE)MT.1943-5533.0000357.

Hjort, J., Karjalainen, O., Aalto, J., Westermann, S., Romanovsky, V.E., Nelson, F.E., and Luoto, M. 2018. 'Degrading permafrost puts Arctic infrastructure at risk by mid-century', *Nature Communications* 9(1), 5147. Available at: https://doi.org/10.1038/s41467-018-07557-4.

Kong, X., Doré, G., and Calmels, F. 2019. 'Thermal modeling of heat balance through embankments in permafrost regions', *Cold Regions Science and Technology* 158, pp. 117–127. Available at: https://doi.org/10.1016/j.coldregions.2018.11.013.

Malenfant-Lepage, J., Doré, G., and Fortier, D. 2012. 'Thermal effectiveness of the mitigation techniques tested at Beaver Creek experimental road site based on a heat balance analysis (Yukon, Canada)', in B. Morse and G. Doré (eds.), *Cold regions engineering 2012: Sustainable infrastructure development in a changing cold environment*. Québec City, Québec, Canada: pp. 42–51. Available at: https://doi.org/10.1061/9780784412473.005.

Malenfant-Lepage, J., Doré, G., Fortier, D., and Murchison, P. 2012. 'Thermal performance of the permafrost protection techniques at Beaver Creek experimental road site, Yukon, Canada', in *Proceedings of the 10th International Conference on Permafrost*. Salekhard, Russia; June 25–29, vol. 1, pp. 261–266.

Malenfant-Lepage, J. 2016. *Experimentation of mitigation techniques to reduce the effects of permafrost degradation on transportation infrastructures a Beaver Creek Experimental Road Site (Alaska Highway, Yukon)*. MSc thesis, Université Laval, Département de Génie Civil, Faculté des Sciences et Génies. Québec City, Québec, Canada.

Reimchen, D., Doré, G., Fortier, D., and Walsh, R. 2009. 'Cost and constructability of permafrost test sections along the Alaska highway, Yukon', in *Canadian Association of Transportation annual conference*. Vancouver, British Columbia, Canada: October 18–21, 2009.

Rioux, K. 2017. *Analyse thermique d'une technique de mitigation visant à prévenir la dégradation du pergélisol sous les infrastructures de transport: Abris thermo-réflectifs, Alaska Highway, Beaver Creek, Yukon*. Mémoire honor, Université de Montréal, Montréal, Canada.

Stephani, E., Fortier, D., Shur, Y., Fortier, R., Doré, G., and Walsh, R. 2014. 'A geosystems approach to permafrost investigations for engineering applications, an example from a road stabilization experiment, Beaver Creek, Yukon, Canada', *Cold Region Science and Technology* 100, pp. 20–35. Available at: https://doi.org/10.1016/j.coldregions.2013.12.006.

Thermal and hydrological limitations on modeling carbon dynamics at wetland sites of discontinuous and continuous permafrost extent

Benjamin C. Maglio[1], Ruth Rutter[1], Tobey Carman[1], Colin Edgar[1], Eugénie Euskirchen[1], Hélène Genet[1], Andrew Mullen[2], Valeria Briones[2], Elchin Jafarov[2] & Kristen Manies[3]

[1]*Institute of Arctic Biology, University of Alaska Fairbanks, Fairbanks, Alaska, United States*

[2]*Woodwell Climate Research Center, Falmouth, Massachusetts, United States*

[3]*US Geological Survey, Menlo Park, California, United States*

Abstract

Accurate representation of cryohydrological processes is fundamental for biosphere models, particularly at high-latitudes, given their influence on carbon and permafrost dynamics in carbon-rich peatlands and wetlands. This study analyzes site-level simulations in moist and wet drainage conditions in continuous or discontinuous permafrost regions, using a terrestrial ecosystem model DVM-DOS-TEM. Functional benchmarking was conducted against eddy covariance flux alongside soil temperature, moisture, and thaw depth observations. Thermal and hydrological analysis reveals parameter sensitivity and uncertainty concerning carbon cycling and permafrost dynamics. Flux representation is markedly consistent at sites characterized by continuous permafrost with less seasonal variation, owing to longer soil freezing duration. Sites in discontinuous permafrost, exhibiting active permafrost degradation and talik formation, pose considerable challenges in accurately depicting thaw depth. Underprediction of soil moisture across all sites has more pronounced effects on boreal wetlands characterized by thick organic layers up to 1 m. These results illustrate the limitations of terrestrial ecosystem models to represent environmental and ecological dynamics in wetlands. Attempts to adjust model hydrology have yielded marginal improvements in thaw depth prediction, but revealed large effects of abrupt phase changes for poorly drained sites on discontinuous permafrost. Our analysis suggests the importance of gradual phase change representation, particularly in ice-rich wetlands with thick organic layers, which will be crucial when evaluating the permafrost carbon-climate feedback in model projections.

1 Introduction

Boreal and arctic biomes are climate-sensitive systems whose response to climate warming is dependent on local characteristics, such as drainage conditions and permafrost status (Schuur et al. 2009). Rising soil temperature increases soil carbon loss directly through the response of soil respiration to temperature (Wang et al. 2014) and indirectly through the thawing of permafrost, providing a larger pool of soil organic matter for decomposition (Trucco et al. 2012). However, hydrological regimes can slow respiration rates with increasing saturation levels, particularly in ice-rich permafrost regions, where thaw can increase thermokarst-induced wetland features on the landscape.

The northern permafrost zone may be susceptible to substantial increases in active layer through abrupt thaw of ice-rich permafrost (Hayes et al. 2014). Yet, decomposition temperature dependencies in the boreal region, occurring predominantly over discontinuous permafrost in Alaska, have been shown to be among the most variable (Chen and Tian 2005) which can inhibit the reliability of terrestrial biosphere models. Temperature and decomposition are influenced by soil moisture, thus simultaneous representation of thermal and hydrological processes is required to assess the permafrost carbon-climate feedback, though biosphere models remain uncertain when representing this linkage (McGuire et al. 2018).

In wetlands, higher saturation levels can reduce respiration rates by creating anaerobic environments (Chivers et al. 2009). This effect might be partially offset by relatively higher soil temperatures during the growing season due to modulated surface thermal conductivity and albedo related to subsurface seasonal or permanent inundation (Chapin III et al. 2000). Boreal wetlands in particular contain thick soil organic layers (OLs)—sometimes in excess of 1 m (Jorgenson et al. 1999)—insulating the ground. OL thickness (OLT) is highly coupled to permafrost occurrence and persistence (Johnson et al. 2013). Yet, areas with thick soil OLs and poor drainage conditions (such as peatlands) may experience higher thermal conductivity in thawing permafrost.

To examine linkages between soil cyrohydrology and carbon cycling, we used DVM-DOS-TEM, a terrestrial biosphere model specifically developed for the high latitudes (Raich et al. 1991; McGuire et al. 1992; Tian et al. 1999; Yi et al. 2010; Euskirchen et al. 2009). We estimated soil and vegetation carbon fluxes in a pair of poorly and moderately drained sites in both discontinuous and continuous permafrost regions. We compared simulations of a thermokarst bog and a black spruce permafrost plateau site in boreal interior Alaska (discontinuous), to a wet sedge and an acidic tussock site in the Alaskan arctic tundra (continuous). Through functional benchmarking, this study identified thermal and hydrological processes and parameters that are sources of uncertainty and evaluated model representation of drainage conditions on the linkage

https://doi.org/10.52381/ICOP2024.190.1

between permafrost dynamics and ecosystem carbon cycling. With boreal wetland extent predicted to increase under climate warming scenarios (Zhang et al. 2017), interpretation of these processes is required to produce meaningful model predictions.

2 METHODOLOGY

2.1 Field Sites

Field sites selected for model applications were chosen to represent combinations of contrasted drainage conditions (moist versus wet), and permafrost extent (continuous versus discontinuous). To inform model-data comparisons, the sites were also characterized by long-term ecological monitoring, including eddy covariance flux measurement data, and active layer depth (ALD), across similar study periods. Sites in Alaska, fitting these criteria, were found through the ABCFlux database (Virkkala et al. 2021) shown in Figure 1. The pair of moist and wet sites in discontinuous permafrost belong to the Alaskan Peatland EXperiment (Turetsky et al. 2023; Euskirchen et al. 2024) within the Bonanza Creek Long Term Ecological Research (LTER) Experimental Forest in boreal Alaska. The pair of sites included an intermediate to old aged thermokarst collapse-scar bog (BZB) wetland site, and a nearby mature black spruce stand on a permafrost peat plateau (BZS). Detailed descriptions of the boreal sites are provided by (Manies et al. 2017). The pair of sites located in continuous permafrost belong to the Imnavait Creek watershed in Arctic Alaska. The pair is composed of a fen on permanently wet sedge tundra (ICs), and a moist acidic tussock tundra (ICt). BZB and BZS had thick OLs up to 1 m (Manies et al. 2017). ICs and ICt had OLs in the range of 15–35 cm, as described by the Circumpolar Active Layer Monitoring (CALM; Brown et al. 2003) program. Detailed descriptions of the arctic sites are provided by Euskirchen et al. (2012).

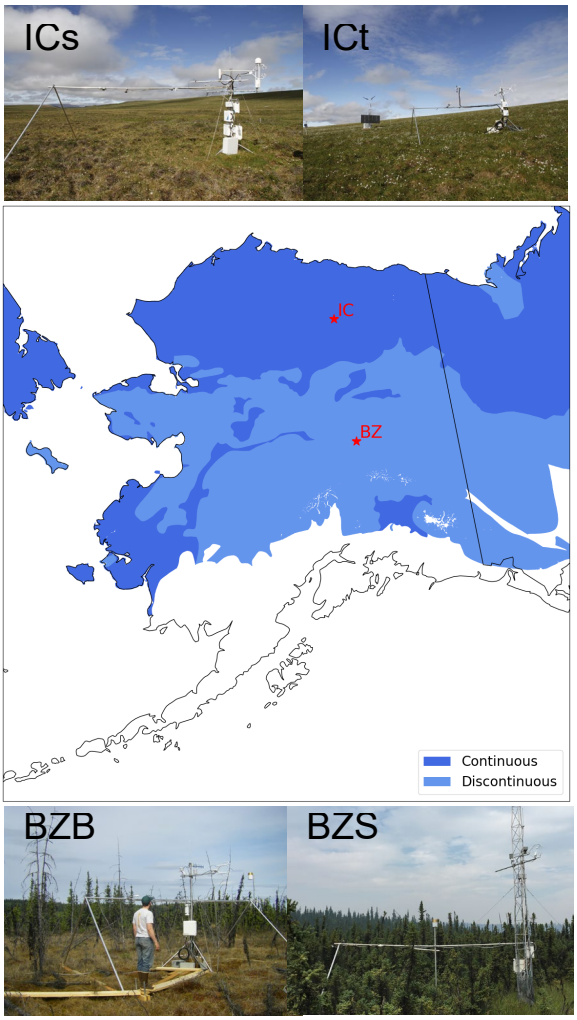

Figure 1. Continuous and discontinuous permafrost extent map (Brown and Melnikov 2002) with Imnavait Creek (IC) and Bonanza Creek (BZ) locations. Photo credits: Sebastien Biraud, Eugenie Euskirchen, Benjamin Maglio.

2.2 Data sources

Monthly flux tower data from 2011–2015 were used at all sites, though some years had missing data at BZS. ALD measurements for ICs and ICt were available through CALM. Observations of ALD at BZB and BZS were synthesized from soil temperature measurements (Turetsky et al. 2014; Manies et al. 2017; Pastick et al. 2018; Neumann et al. 2019; James et al. 2021). Subsequently, ancillary data including soil temperature and moisture at 2 cm depth, was synthesized from the AmeriFlux network (Euskirchen 2022a, b; Euskirchen et al. 2022a, b).

2.3 Model description

We used the Terrestrial Ecosystem Model with Dynamic Vegetation and Dynamic Organic Soil, DVM-DOS-TEM, (Raich et al. 1991; Tian et al. 1999; Yi et al. 2010; Euskirchen et al. 2009) to explore soil physical and biogeochemical dynamics and interactions. DVM-DOS-TEM is a process-based terrestrial biosphere model, specifically developed for high latitude ecosystems. It couples a dynamic organic soil (DOS) module, which relates moss and OL (fibric, humic) carbon stocks and thickness (Yi et al. 2010), with a dynamic vegetation model (DVM) simulating various plant functional types (PFTs) dynamics and competition for light, water and nutrients (Euskirchen et al. 2009). Soil thermal processes are resolved through numerical integration of the 1D heat equation with thaw depth derived from the Stefan algorithm (Yi et al. 2009). Hydrological dynamics are derived using the Richards equation (Zhuang et al. 2002, 2003). Biogeochemical cycling is represented by a monthly nitrogen-constrained carbon-balance representing seasonal and interannual variation, capable of simulating disturbance (e.g., wildfire, logging) and climate warming scenarios (Genet et al. 2013, 2018). Climatic Research Unit (CRU) V4.0 high resolution gridded input forcing data (University Of East Anglia CRU et al. 2019) was used to drive the model at Bonanza and Imnavait creeks respectively.

2.4 Model parameterization

Site-level parameterizations are represented by community types (CMTs)—grouped soil and vegetation-related parameters characteristic of that CMT. Parameter values were determined from observational data, literature review or model calibration. Here, we used existing parameterizations for boreal bog and black spruce peatland for BZB and BZS respectively, and for arctic wet-sedge and tussock tundra for ICs and ICt respectively. Drainage conditions for the boreal bog and arctic wet sedge sites were set to poorly drained conditions. Drainage conditions for the boreal peatland black spruce forest and the arctic tussock tundra were set to moderately-drained conditions. Although appropriate fibric and amorphous OLTs were represented across all simulations, there were distinct differences between the thermal and hydraulic conductivity ranges which could be present between sites due to different saturation levels and peat composition. Both boreal sites were composed of thick sphagnum peat, whereas the Arctic sites were primarily composed of *Carex*-dominated peat soils, both with differing combinations of live and dead, sphagnum and feather moss, providing different thermal and hydraulic conductivity (Letts et al. 2000; O'Donnell et al. 2009). *Carex* dominated peat soils have shown higher bulk density and lower porosity compared to sphagnum dominated soils (Szajdak et al. 2016; Liu and Lennartz 2019). Thus, we defined different thermal and hydraulic conductivity values at Bonanza and Imnavait creek sites respectively, as shown in Table 1, which fell within the large observed ranges.

Table 1. Solid thermal conductivity (λ_{soild}), hydraulic conductivity at saturation (k_{sat}), and OLT for modeled Bonanza Creek (BZB, BZS) and Imnavait Creek (ICs, ICt) sites.

Organic horizon	λ_{soild} [W/m/K]	k_{sat} [mm/s]	OLT (cm)	
Bonanza Creek			BZB	BZS
Moss	0.35	0.0010	2.6	2.3
Fibric	0.37	0.0020	47.1	17.7
Humic	1.90	0.0001	81.4	33.3
Imnavait Creek			ICs	ICt
Moss	0.25	0.0100	~1.0	~1.0
Fibric	0.26	0.0200	11.2	10.3
Humic	0.31	0.0010	14.7	5.4

(Manies et al. 2001) suggested that the thickness of the insulating OL is then an important control on the thermal exchange across sites of different drainage conditions in interior Alaska.

Uncertainty was greater in the hydraulic conductivity (Yi et al. 2009), which was originally parameterized using the saturated hydraulic conductivity based on (Berkowitz and Balberg 1992; Stauffer and Aharony 2017). New values were determined by considering variation in observed von Post humification index from soil cores at BZB and BZS reported by (Manies et al. 2017) compared to synthesized hydraulic conductivity values in sphagnum peat reported by (Letts et al. 2000). From these data a hydraulic conductivity depth profile was constructed in Figure 2. Not only was uncertainty high for these parameters, but due to cryoturbation processes and varying annual soil saturation levels, organic matter was not distributed linearly (increasing decomposition with increasing depth). By comparing these data, we formulated approximate hydraulic conductivity depth profiles at Bonanza Creek and used this to inform the parameters in Table 1. Data were not available at Imnavait Creek, and was estimated from *Carex*-peat literature ranges (Szajdak et al. 2016; Liu and Lennartz 2019).

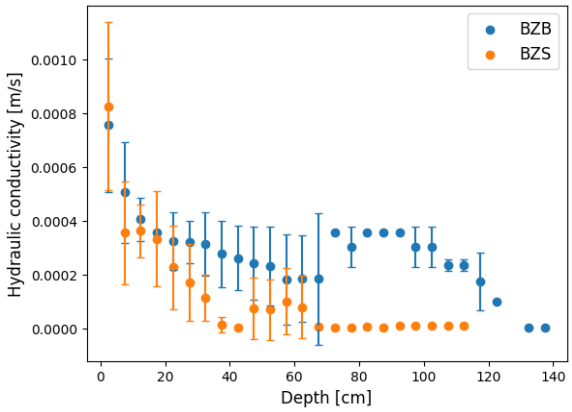

Figure 2. Conversion of observed von Post humification index at BZB and BZS (Manies et al. 2017) with synthesized hydraulic conductivity values from (Letts et al. 2000).

2.5 Model development

Adjustments to the DVM-DOS-TEM hydrology model were also considered at wetland sites (ICt and BZB), as site-level simulations have been shown to demonstrate high variability (Ekici et al. 2015) requiring more precise information on spatially explicit processes local to particular sites. BZB, the collapse-scar bog site, is hydrologically isolated and sits lower than surrounding black spruce permafrost plateaus (BZS; Wickland et al. 2006). Runoff losses were thus removed and additional input, representing surface drainage from raised forested plateau, was added. Runoff input for the bog was set to equal to the runoff simulated for the permafrost plateau black spruce forest site. Although ICs has poor drainage, it is not hydrologically isolated, instead fed by gradual subsurface flow (Connon et al. 2014), hence only surface runoff losses were removed.

2.6 Model simulation and benchmarking

To study model representation of thermal and hydrological regimes, we conducted simulations of a 100-year pre-run using constant climate based on computed monthly averages between 1901–1930 to determine biophysical state variables. Secondly, a 1000-year equilibrium stage initiated with the results of the pre-run, and using the same average climate forcing as the pre-run was conducted to

determine biogeochemical state variables. This was followed by a 250-year spinup using a cyclical but varying climate forcing from the 1901–1930 period. Finally, a transient simulation initiated with information from the spinup run, of historical data up to the end of our study period (2015).

At monthly intervals gross primary production (GPP), autotrophic respiration (RA; i.e., summed maintenance respiration (RM) and growth respiration (RG)), and heterotrophic respiration (RH) were computed (Tian et al. 1999; Euskirchen et al. 2009). GPP was computed based on air temperature from climate forcing, though can be indirectly related to soil temperature through sensible heat exchange. It is indirectly affected by soil moisture through evapotranspiration functions. RM is directly related to soil temperature based on an empirical exponential relationship scaled by a calibrated per-gram-biomass respiration rate at 0ºC, and indirectly to soil moisture based on modulation of thermal conductivities. RG equated to a 20% difference between GPP and RM. RH is affected by soil temperature through an empirical exponential relationship and proportional to a nonlinear function of soil moisture based on observed minimum, maximum, and optimum values. Ecosystem respiration (RECO = RH + RA) was calculated and used to find net ecosystem exchange (NEE = RECO - GPP). Thus, functional relationships (Luo et al. 2012) were created between GPP, RECO and soil temperature and moisture to assess model representation of carbon dynamics. Both modeled and measured data were analyzed to benchmark these behaviors. At wetland sites, simulations were run a second time with altered hydrology previously described.

3 RESULTS

GPP, RECO, and NEE more closely matched observations, particularly in shoulder seasons, for continuous permafrost sites in Figure 3 with consistently lower root mean squared error (RMSE). The moist site (ICt) outperformed the wet site (ICs) in each instance.

GPP and RECO were underestimated at BZS and overestimated at BZB. The underestimation of fluxes at BZS offset one another and provided reasonable prediction of NEE at BZS with RMSE against observations closely following ICt for years with data. Variations to model runoff showed little effect for GPP at ICs and BZB (Figure 3). There were small increases for ICs and small decreases for BZB in RECO with decreased runoff respectively. This led to only minor variation in the magnitude and seasonal patterns of NEE at BZB and ICs. There was good representation of soil temperature in Figure 4, particularly during the winter at continuous permafrost sites, though maximum summer temperatures were overpredicted at all sites.

BZS demonstrated fairly good consistency with observed thermal regimes. BZB represented summer maximum temperatures well, but significantly underpredicted winter temperatures. Model hydrology changes increased winter temperatures at ICs, more closely matching observations for some years, but had little effect on summer temperatures. At BZB the increased hydrological input modulated both summer and winter temperatures with better representation to observations, though winter temperatures were still underpredicted.

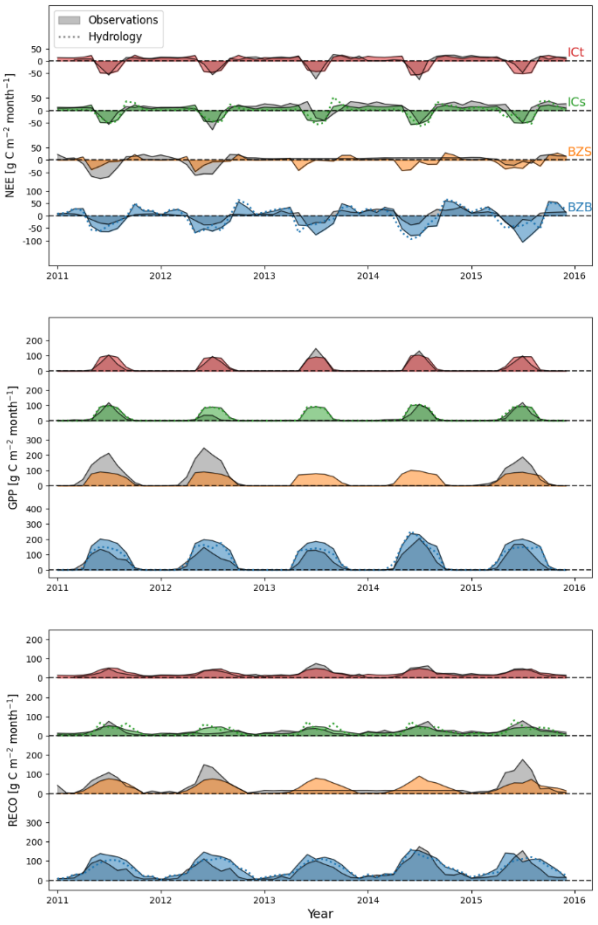

Figure 3. Observed and simulated monthly NEE, GPP and RECO.

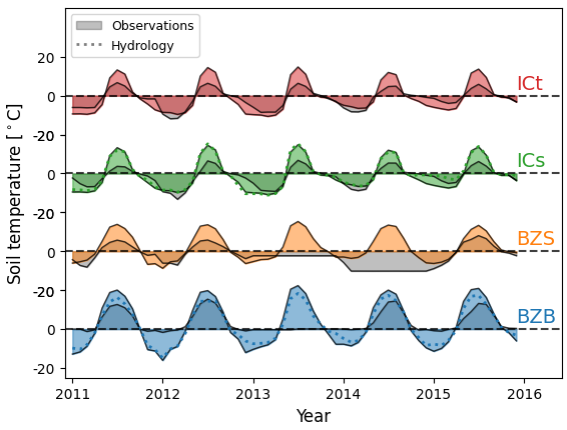

Figure 4. Observed and simulated monthly soil temperature at 2 cm depth.

Figure 5 showed soil moisture at 2 cm depth. Soil moisture was underpredicted compared to observations at every site, though BZB showed the closest representation to observations prior to variations in the hydrological model. Nevertheless, the higher soil moisture recorded at the end of 2015 was only matched when these changes were made. There was also a zeroing of soil moisture at all sites during the winter with and without hydrological changes. The effects described in Figures 4 and 5 were further conveyed by the ALD in Figure 6. Observations at BZB were not shown as this site was thermokarst and ALD was > 1.5 m showing the greatest underprediction. Observations from 2011–2015 showed BZS undergoing active permafrost degradation. The amount of permafrost was overpredicted at each site with the exception of ICt and ICs for the first two years, with ICs showing a slight increase of mean ALD compared to ICt. Hydrological model changes showed improvements at BZB and ICs, though BZB remained significantly lower than 1.5 m.

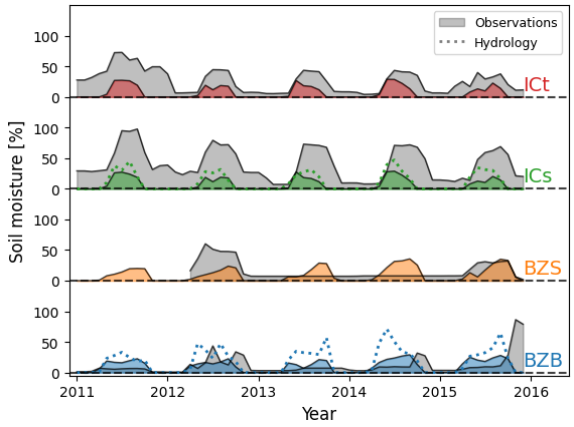

Figure 5. Observed and simulated monthly soil moisture content at 2 cm depth.

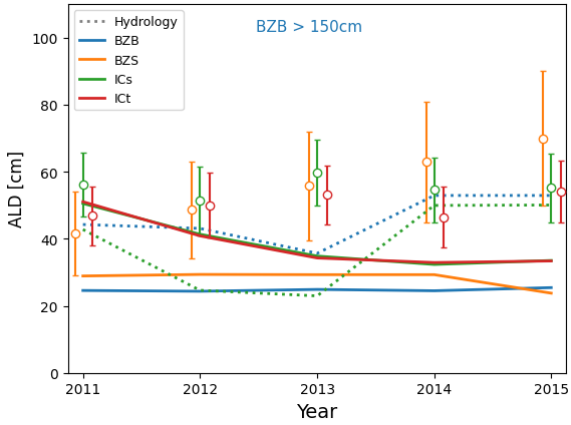

Figure 6. Observed and simulated ALD. Mean and standard deviation of ALD measurements are shown as points and error bars respectively.

Figures 7 and 8 show the functional relationship between soil temperature at 2 cm depth for GPP and RECO respectively. This relationship is best captured at continuous permafrost sites, though higher temperatures were reached in the simulation. GPP and RECO were underpredicted at BZS and overpredicted at BZB, during the summer with the highest temperatures reached at BZB. Hydrological changes had little effect at ICs, but increased maximum GPP, and RECO, while marginally reducing maximum temperatures at BZB. Figures 9 and 10 show the functional relationship between soil moisture at 2 cm depth with GPP and RECO respectively. Hydrological model changes extended simulated deeper soil moisture closer to the observed range at BZB but still underestimated all sites, with the zeroing effect shown by a clustering of points in Figures 9 and 10.

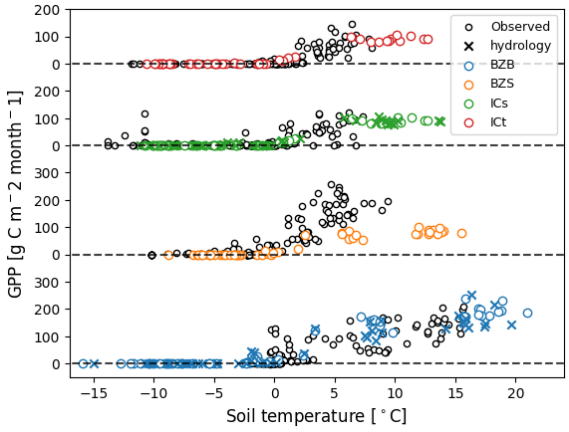

Figure 7. Observed and simulated monthly soil temperature at 2 cm depth versus GPP.

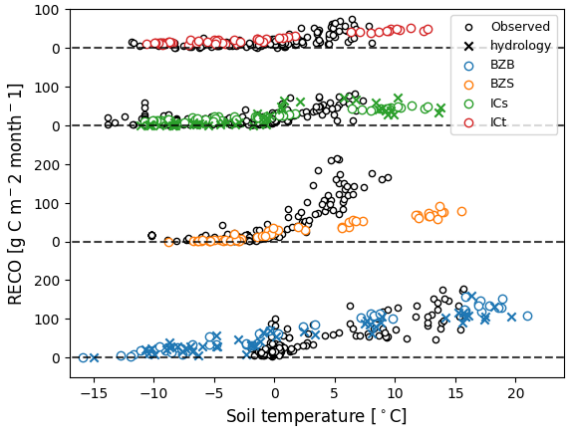

Figure 8. Observed and simulated monthly soil temperature at 2 cm depth versus RECO.

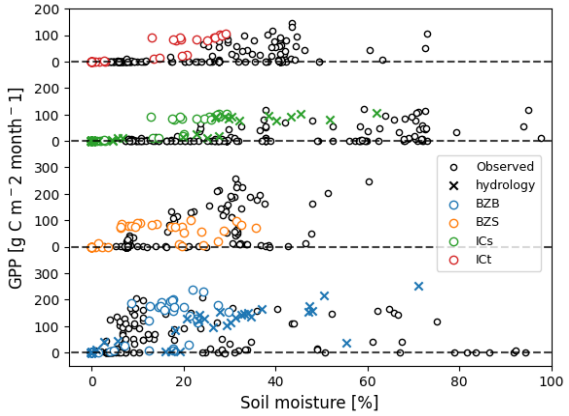

Figure 9. Observed and simulated monthly soil moisture at 2 cm depth versus GPP.

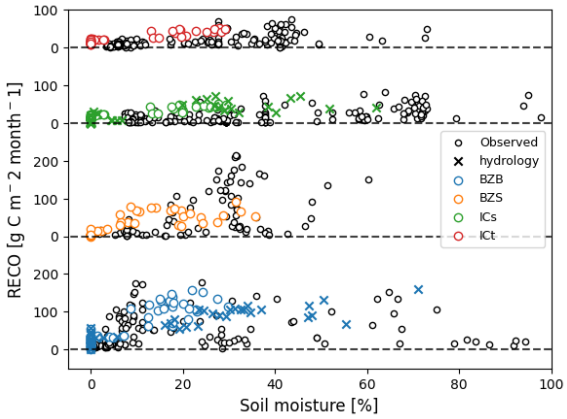

Figure 10. Observed and simulated monthly soil moisture at 2 cm depth versus RECO.

There was an increase in the range for ICs but did not surpass ~60%. The variation in predicted NEE was highest at BZB, with BZS marginally underpredicted in the summer and ICs in the winter, but with ICt showing reasonable representation across all seasons. While changes to model hydrology provided benefits in matching the observed range of soil moisture, particularly in the bog, the zeroing of winter soil moisture strongly impacted ALD prediction.

4 Discussion

We performed four site-level simulations using DVM-DOS-TEM, with paired moist and wet drainage conditions in continuous and discontinuous permafrost regions. Site-level simulations using biosphere models typically encounter large variation (Ekici et al. 2015) yet remain an integral part of benchmarking to evaluate limitations, sensitivity, and uncertainty (Mahecha et al. 2010; Ekici et al. 2014). Understanding these limitations is important when expanding simulation models to regional scales, as uncertainties may be amplified leading to misclassification of carbon sources and sinks.

Our study revealed reductions in model performance as thermal and hydrological complexity increased. Sites on continuous permafrost performed best, which was attributed to longer soil freezing duration. Soil temperatures were overpredicted at both sites of continuous permafrost for seasonal peaks with higher calculated rates of change, suggesting abrupt model phase changes. Soil moisture was significantly underpredicted for both sites, with changes to the hydrological model at ICs yielding only marginal improvements to carbon fluxes with a more variable, yet not significantly improved ALD. Depth profiles of soil moisture at continuous permafrost sites were unavailable, though may help determine hydrology influencing ALD in deeper soil layers. Modeled fluxes at sites underlain by discontinuous permafrost had greater deviation from observations, with GPP and RECO underpredicted at BZS and overpredicted at BZB. Seasonal temperature variation was captured well at BZS with soil moisture more closely matched (for years with data) than other sites. Fluxes were overpredicted at BZB, with changes to the hydrological model but showing some benefits across the study period. Summer soil temperatures were predicted well for BZB though winter temperatures were up to 18ºC colder than observed suggesting the largest impact of this abrupt phase change.

Soil moisture at BZB appeared to be significantly overpredicted at 2 cm depth, particularly after changes to the hydrological model, though this improved the mean soil moisture content at deeper layers. This suggests total hydrologic inputs may not be correctly represented without our changes. ALD was underpredicted at both discontinuous sites, while the hydrological model changes did improve outputs for BZB this came at the expense of worsening flux estimates prior to calibration of carbon cycle associated parameters. These sites present complex but important dynamics for modeling, including active permafrost degradation shown in Figure 9 at BZS and indication of a deepening talik at BZB from soil temperature profiles down to 240 cm taken during and after our study period (Turetsky et al. 2014; Manies et al. 2017; Pastick et al. 2018; Neumann et al. 2019; James et al. 2021). Additionally, both sites contained thick sphagnum peat, which can insulate permafrost, but with recent soil moisture measurements up to 80% at 30 cm depth, the thermal regime will be strongly modulated. There was zeroing of soil moisture shown in the time series in Figure 5 and clustering of points in Figure 10. This indicates that latent heat processes are occurring too fast, with abrupt transition from liquid water to ice. Hence thermal moderation from water in the soil during freeze-up is lost and significantly lower temperatures are predicted. Ultimately, this causes underprediction of the ALD and appears most prominent at BZB with larger water inputs and OLT.

The thermal and hydrological regimes, particularly at BZB, offer some insight into where model predictions can be enhanced. It is evident that thermal and hydraulic parameterization plays a role in permafrost carbon dynamics though changes to these and the underlying hydrological model may not necessarily have effects on both in the same direction nor by a high enough magnitude. Carbon fluxes are highly sensitive to parameters which are difficult to measure, so highly uncertain, therefore requiring

preliminary calibration. If soil thermal and more importantly hydrological conditions are not representative prior to or as part of this calibration it is unlikely that both permafrost and carbon dynamics will be appropriately captured simultaneously. This elucidates the importance of a stringent model calibration process alongside initial thermal and hydrological parameterization. Due to a dearth of hydraulic data, it is of utmost importance to develop parameterizations informed by soil profile measurements where available and drawing relationships between observed soil properties. However, once evaluated, additional thermal and hydrological processes may be needed to provide a more realistic representation of particular ecosystems. For example, the need to capture unfrozen water to accurately represent winter temperatures either through pore water content (Romanovsky and Osterkamp 2000) or through latent heat consideration (Hinzman et al. 1998). It may also be useful to extend the soil column depth to capture sufficient thermal inertia (Lawrence et al. 2008). Interannual variability is expected to be higher in the discontinuous permafrost with greater influence on subsurface water pathways (Walvoord and Kurylyk 2016) and advective heat transport (Neumann et al. 2019) which remain difficult to capture in biosphere models. The calibration approach present in many of these models focuses on the carbon cycle but does not effectively couple thermal and hydrological processes to provide accurate representation of the full system, which is necessary for more robust and reliable ecosystem models.

5 Conclusions

Site-level simulations were performed for areas with continuous and discontinuous permafrost extent and with differing soil saturation levels. Carbon fluxes, active layer depth, soil thermal and hydrological estimates best matched observations at areas of continuous permafrost extent due to a reduction in system complexity. Sites with higher soil moisture content performed worse, with changes to the hydrological model marginally improving active layer calculations. However, soil moisture zeroing at the beginning of winter revealed the rapidity of simulated freeze up suggesting losses in latent heat. This appears to be particularly important in boreal wetlands for capturing deeper permafrost tables and talik development.

6 Acknowledgements

This study was made possible with funding through the Permafrost Pathways project, supported by the Audacious program and the Quadrature Climate Foundation (QCL). We would also like to acknowledge great sources of data from the National Science Foundation (NSF) funded Bonanza Creek and Arctic members of the LTER Network, and the Circumpolar Active Layer Monitoring (CALM) Network. Additionally, we would like to thank the Department of Energy (DOE) Office of Biological and Environmental Research's (BER) AmeriFlux and its contributors as well as the ABCFlux database available through the Oak Ridge National Laboratory (ORNL) Distributed Active Archive Center (DAAC).

7 References

Berkowitz, B. and Balberg, I. 1992. 'Percolation approach to the problem of hydraulic conductivity in porous media', *Transport in Porous Media* 9(3), pp. 275–286. doi:10.1007/BF00611971.

Brown, J., Hinkel, K., and Nelson, F. 2003. 'Circumpolar Active Layer Monitoring (CALM) program network: description and data', *Circumpolar Active-Layer Permafrost System, Version, 2*. International Permafrost Association Standing Committee on Data Information and Communication (comp.).

Brown, J.O. Ferrians, J.A. Heginbottom, and Melnikov, E. 2002. 'Circum-Arctic Map of Permafrost and Ground-Ice Conditions, Version 2'. *National Snow and Ice Data Center*.

Chapin III, F.S., Mcguire, A.D., Randerson, J., Pielke, R., Baldocchi, D., Hobbie, S.E., Roulet, N., Eugster, W., Kasischke, E., Rastetter, E.B., Zimov, S.A., and Running, S.W. 2000. 'Arctic and boreal ecosystems of western North America as components of the climate system', *Global Change Biology* 6(S1), pp. 211–223. doi:10.1046/j.1365-2486.2000.06022.x.

Chen, H. and Tian, H.-Q. 2005. 'Does a General Temperature-Dependent Q10 Model of Soil Respiration Exist at Biome and Global Scale?', *Journal of Integrative Plant Biology* 47(11), pp. 1288–1302. doi:10.1111/j.1744-7909.2005.00211.x.

Chivers, M.R., Turetsky, M.R., Waddington, J.M., Harden, J.W., and McGuire, A.D. 2009. 'Effects of Experimental Water Table and Temperature Manipulations on Ecosystem CO2 Fluxes in an Alaskan Rich Fen', *Ecosystems* 12(8), pp. 1329–1342. doi:10.1007/s10021-009-9292-y.

Connon, R.F., Quinton, W.L., Craig, J.R., and Hayashi, M. 2014. 'Changing hydrologic connectivity due to permafrost thaw in the lower Liard River valley, NWT, Canada', *Hydrological Processes* 28(14), pp. 4163–4178. doi:10.1002/hyp.10206.

Ekici, A., Beer, C., Hagemann, S., Boike, J., Langer, M., and Hauck, C. 2014. 'Simulating high-latitude permafrost regions by the JSBACH terrestrial ecosystem model', *Geoscientific Model Development* 7(2), pp. 631–647. doi:10.5194/gmd-7-631-2014.

Ekici, A., Chadburn, S., Chaudhary, N., Hajdu, L.H., Marmy, A., Peng, S., Boike, J., Burke, E., Friend, A.D., Hauck, C., Krinner, G., Langer, M., Miller, P.A., and Beer, C. 2015. 'Site-level model intercomparison of high latitude and high altitude soil thermal dynamics in tundra and barren landscapes', *The Cryosphere* 9(4), pp. 1343–1361. doi:10.5194/tc-9-1343-2015.

Euskirchen, E. 2022a. *AmeriFlux FLUXNET-1F US-BZB Bonanza Creek Thermokarst Bog* (Dataset). US Department of Energy. Available at: https://doi.org/10.17190/AMF/1881569.

Euskirchen, E. 2022b. *AmeriFlux FLUXNET-1F US-BZS Bonanza Creek Black Spruce* (Dataset). US Department of Energy. Available at: https://doi.org/10.17190/AMF/1881572.

Euskirchen, E., Shaver, G., and Bret-Harte, S. 2022a. *AmeriFlux FLUXNET-1F US-ICs Imnavait Creek Watershed Wet Sedge Tundra* (Dataset). AmeriFlux AMP. Available at: https://doi.org/10.17190/AMF/1871138.

Euskirchen, E., Shaver, G., and Bret-Harte, S. 2022b. *AmeriFlux FLUXNET-1F US-ICt Imnavait Creek Watershed Tussock Tundra* (Dataset). AmeriFlux AMP. Available at: https://doi.org/10.17190/AMF/1881583.

Euskirchen, E.S., Bret-Harte, M.S., Scott, G.J., Edgar, C., and Shaver, G.R. 2012. 'Seasonal patterns of carbon dioxide and water fluxes in three representative tundra ecosystems in northern Alaska', *Ecosphere* 3(1), pp. 1–19. doi:10.1890/ES11-00202.1.

Euskirchen, E.S., Edgar, C.W., Kane, E.S., Waldrop, M.P., Neumann, R.B., Manies, K.L., Douglas, T.A., Dieleman, C., Jones, M.C., and Turetsky, M.R. 2024. 'Persistent net release of carbon dioxide and methane from an Alaskan lowland boreal peatland complex', *Global Change Biology* 30(1), e17139. doi:10.1111/gcb.17139.

Euskirchen, E.S., McGuire, A.D., Chapin, F.S., Yi, S., and Thompson, C.C. 2009. 'Changes in vegetation in northern Alaska under scenarios of climate change, 2003-2100: implications for climate feedbacks', *Ecological Applications: A Publication of the Ecological Society of America* 19(4), pp. 1022–1043. doi:10.1890/08-0806.1.

Hinzman, L.D., Goering, D.J., and Kane, D.L. 1998. 'A distributed thermal model for calculating soil temperature profiles and depth of thaw in permafrost regions', *Journal of Geophysical Research: Atmospheres* 103(D22), pp. 28975–28991. doi:10.1029/98JD01731.

James, S.R., Minsley, B.J., Waldrop, M.P., McFarland, J.W., Manies, K.L., and Pastick, N.J. 2021. 'Permafrost characterization at the Alaska Peatland Experiment (APEX) site: Geophysical and related field data collected from 2018-2020', *US Geological Survey*. doi:10.5066/P90M04ST.

Johnson, K.D., Harden, J.W., McGuire, A.D., Clark, M., Yuan, F., and Finley, A.O. 2013. 'Permafrost and organic layer interactions over a climate gradient in a discontinuous permafrost zone', *Environmental Research Letters* 8(3), 035028. doi:10.1088/1748-9326/8/3/035028.

Jorgenson, M.T., Roth, J.E., Raynolds, M.K., Smith, M.D., Lentz, W., Zusi-Cobb, A.L., and Racine, C.H. 1999. *An Ecological Land Survey for Fort Wainwright, Alaska*. Defense Technical Information Center, Virginia, United States.

Lawrence, D.M., Slater, A.G., Romanovsky, V.E., and Nicolsky, D.J. 2008. 'Sensitivity of a model projection of near-surface permafrost degradation to soil column depth and representation of soil organic matter', *Journal of Geophysical Research: Earth Surface* 113(F2). doi:10.1029/2007JF000883.

Letts, M.G., Roulet, N.T., Comer, N.T., Skarupa, M.R., and Verseghy, D.L. 2000. 'Parametrization of peatland hydraulic properties for the Canadian land surface scheme', *Atmosphere-Ocean* 38(1), pp. 141–160. doi:10.1080/07055900.2000.9649643.

Liu, H. and Lennartz, B. 2019. 'Hydraulic properties of peat soils along a bulk density gradient—A meta study', *Hydrological Processes* 33(1), pp. 101–114. doi:10.1002/hyp.13314.

Luo, Y.Q., Randerson, J., Abramowitz, G., Bacour, C., Blyth, E., Carvalhais, N., et al. 2012. 'A framework of benchmarking land models', *Biogeosciences* 9, pp. 3857–3874.

Mahecha, M.D., Reichstein, M., Jung, M., Seneviratne, S.I., Zaehle, S., Beer, C., Braakhekke, M.C., Carvalhais, N., Lange, H., Le Maire, G., and Moors, E. 2010. 'Comparing observations and process-based simulations of biosphere-atmosphere exchanges on multiple timescales', *Journal of Geophysical Research: Biogeosciences* 115(G2). doi:10.1029/2009JG001016.

Manies, K.L., Fuller, C.C., Jones, M.C., Waldrop, M.P., and McGeehin, J.P. 2017. 'Soil data for a thermokarst bog and the surrounding permafrost plateau forest, located at Bonanza Creek Long Term Ecological Research Site, Interior Alaska', *US Geological Survey* Open-File Report 2016-1173.doi:10.3133/ofr20161173.

Manies, K.L., Harden, J.W., Yoshikawa, K., and Randerson, J. 2003. 'The effect of soil drainage on fire and carbon cycling in central Alaska', in J.P. Galloway (ed.), *Studies by the U.S. Geological Survey in Alaska, 2001* US Geological Survey Professional Paper 1678, pp. 145–152.

McGuire, A.D., Lawrence, D.M., Koven, C., Clein, J.S., Burke, E., Chen, G., et al. 2018. 'Dependence of the evolution of carbon dynamics in the northern permafrost region on the trajectory of climate change', *Proceedings of the National Academy of Sciences* 115(15), pp. 3882–3887. doi:10.1073/pnas.1719903115.

McGuire, A.D., Melillo, J.M., Joyce, L.A., Kicklighter, D.W., Grace, A.L., Moore III, B., and Vorosmarty, C.J. 1992. 'Interactions between carbon and nitrogen dynamics in estimating net primary productivity for potential vegetation in North America', *Global Biogeochemical Cycles* 6(2), pp. 101–124. doi:10.1029/92GB00219.

Neumann, R.B., Mooreberg, C.J., Lundquist, J.D., Turner, J.C., Waldrop, M.P., McFarland, J.W., Euskirchen, E.S., Edgar, C., Turetsky, M.R., and Bonanza Creek LTER. 2019. 'Warming effects of spring rainfall increase methane emissions from thawing permafrost: Site-level data from bog complex IV - Soil Temperatures 2014-2016', *Environmental Data Initiative*. Available at: https://doi.org/10.6073/pasta/51521e888f301ae9e0c97455764daa77.

Pastick, N.J., Kass, M.A., Wylie, B.K., James, S.R., Rey, D.M., Minsley, B.J., and Ebel, B.A. 2018. 'Alaska permafrost characterization: Geophysical and related field data collected from 2016-2017', *US Geological Survey*. Available at: https://doi.org/10.5066/P99PTGP4.

Raich, J.W., Rastetter, E.B., Melillo, J.M., Kicklighter, D.W., Steudler, P.A., Peterson, B.J., Grace, A.L., Moore, B., and Vorosmarty, C.J. 1991. 'Potential Net Primary Productivity in South America: Application of a Global Model', *Ecological Applications: A Publication of the Ecological Society of America* 1(4), pp. 399–429. doi:10.2307/1941899.

Romanovsky, V.E. and Osterkamp, T.E. 2000. 'Effects of unfrozen water on heat and mass transport processes in the active layer and permafrost', *Permafrost and Periglacial Processes* 11(3), pp. 219–239. doi:10.1002/1099-1530(200007/09)11:3<219::AID-PPP352>3.0.CO;2-7.

Schuur, E.A.G., Vogel, J.G., Crummer, K.G., Lee, H., Sickman, J.O., and Osterkamp, T.E. 2009. 'The effect of permafrost thaw on old carbon release and net carbon exchange from tundra', *Nature* 459(7246), pp. 556–559. doi:10.1038/nature08031.

Stauffer, D. and Aharony, A. 2017. *Introduction To Percolation Theory*. Second Edition. London, England: Taylor & Francis.

Szajdak, L.W., Lapshina, E.D., Gaca, W., Styła, K., Meysner, T., Szczepański, M., and Zarov, E.A. 2016. 'Physical, chemical and biochemical properties of Western Siberia Sphagnum and Carex peat soils', *Environmental Dynamics and Global Climate Change* 7(2), pp. 13–25. doi:10.17816/edgcc7213-25.

Tian, H., Melillo, J.M., Kicklighter, D.W., McGuire, A.D., and Helfrich, J. 1999. 'The sensitivity of terrestrial carbon storage to historical climate variability and atmospheric CO2 in the United States', *Chemical and Physical Meteorology* 51(2), pp. 414–452. doi:10.3402/tellusb.v51i2.16318.

Trucco, C., Schuur, E.A.G., Natali, S.M., Belshe, E.F., Bracho, R., and Vogel, J. 2012. 'Seven-year trends of CO2exchange in a tundra ecosystem affected by long-term permafrost thaw', *Journal of Geophysical Research: Biogeosciences* 117(G2). doi:10.1029/2011JG001907.

Turetsky, M., Kane, E., Euskirchen, E., Dieleman, C., Rober, A., Wyatt, K., Keller, J., Cox, W., and Webb, H. 2023. 'The Alaska Peatland Experiment: two decades of hydrologic experiments show resilience in peatland CO2 respiration', in *EGU23, the 25th EGU General Assembly*. Vienna, Austria: 23–28 April, 2023. doi:10.5194/egusphere-egu23-10683

Turetsky, M.R., Harden, J.W., Waddington, J.M., and Bonanza Creek LTER. 2014. 'APEX beta SE site: hourly soil temperature, soil moisture and net radiation', *Bonanza Creek LTER* – University of Alaska Fairbanks, BNZ:449. doi:10.6073/pasta/adf68aab327f3e3365b68c4aae5f559f.

Virkkala, A.-M., Natali, S., Rogers, B.M., Watts, J.D., Savage, K., Connon, S.J., et al. 2021. *The ABCflux Database: Arctic-Boreal CO2 Flux and Site Environmental Data, 1989-2020*. ORNL DAAC, Oak Ridge, Tennessee, United States. Available at: https://doi.org/10.3334/ORNLDAAC/1934.

Walvoord, M.A. and Kurylyk, B.L. 2016. 'Hydrologic Impacts of Thawing Permafrost—A Review', *Vadose Zone Journal* 15(6), vzj2016.01.0010. doi:10.2136/vzj2016.01.0010.

Wang, X., Liu, L., Piao, S., Janssens, I.A., Tang, J., Liu, W., Chi, Y., Wang, J., and Xu, S. 2014. 'Soil respiration under climate warming: differential response of heterotrophic and autotrophic respiration', *Global Change Biology* 20(10), pp. 3229–3237. doi:10.1111/gcb.12620.

Wickland, K.P., Striegl, R.G., Neff, J.C., and Sachs, T. 2006. 'Effects of permafrost melting on CO2 and CH4 exchange of a poorly drained black spruce lowland', *Journal of Geophysical Research: Biogeosciences* 111(G2). doi:10.1029/2005JG000099.

Yi, S., McGuire, A.D., Harden, J., Kasischke, E., Manies, K., Hinzman, L., Liljedahl, A., Randerson, J., Liu, H., Romanovsky, V., Marchenko, S., and Kim, Y. 2009. 'Interactions between soil thermal and hydrological dynamics in the response of Alaska ecosystems to fire disturbance', *Journal of Geophysical Research: Biogeosciences* 114(G2). doi:10.1029/2008JG000841.

Yi, S., McGuire, A.D., Kasischke, E., Harden, J., Manies, K., Mack, M., and Turetsky, M. 2010. 'A dynamic organic soil biogeochemical model for simulating the effects of wildfire on soil environmental conditions and carbon dynamics of black spruce forests', *Journal of Geophysical Research: Biogeosciences* 115(G4). doi:10.1029/2010JG001302.

Zhang, Z., Zimmermann, N.E., Stenke, A., Li, X., Hodson, E.L., Zhu, G., Huang, C., and Poulter, B. 2017. merging role of wetland methane emissions in driving 21st century climate change', *Proceedings of the National Academy of Sciences* 114(36), pp. 9647–9652. doi:10.1073/pnas.1618765114.

Numerical modelling of permafrost-impacted groundwater flow systems in the context of a deep geological repository

Mahsa Malmir, John Molson & René Therrien

Department of Geology and Geological Engineering, Université Laval, Québec City, Québec, Canada

ABSTRACT

Numerical modelling of a hypothetical geosphere setting in the Canadian Shield is employed to assess the impact of permafrost growth and decay cycles on groundwater flow and thermal conditions relevant to the near and far-field environment of a deep geological repository (DGR). This study aims to examine how transient events linked to long-term climate change and glacial cycles may affect the evolution of a deep groundwater flow system. Simplified conceptual models on relevant spatial and time scales are developed in part from field data and insights gained from a northern research site located near Umiujaq, in Nunavik, Quebec, Canada. Future climate transitions are based on the past 1 million years of air temperature data, which are considered an analogue for future changes. Simulated processes include coupled groundwater flow, heat and mass (brine) transport, with freeze/thaw, latent heat and ice-fraction dependent relative permeability. Initial simulations have shown how permafrost cycles can affect deep groundwater pathways, leading to the formation of a transient barrier that restricts groundwater flow and brine transport between the geosphere and biosphere, potentially leading to longer flow and transport pathways and increased groundwater residence times. However, the formation of below-lake taliks lakes can also maintain hydraulic connections between the geosphere and biosphere, creating transient groundwater pathways even during glacial periods. The findings of this research will provide valuable insights into the impact of future glaciations on the long-term safety of DGRs.

1 INTRODUCTION

Numerous countries, including Canada, that use nuclear power for electricity generation, are currently exploring the possibility of storing their used nuclear fuel in deep geological repositories (DGRs) located within suitable geological formations (Taylor 2021). Over the long term, some DGRs will undergo multiple glacial and climate cycles, including permafrost formation and thaw, which will significantly affect surface water hydrology networks, groundwater recharge and discharge, and deep groundwater flow systems, all of which may have implications for DGRs (Holden et al. 2009). Comprehensive studies are necessary to understand freeze-thaw cycles including permafrost during glacial periods and its impact on the long-term safety of repositories.

A large part of northern Europe and North America has been glaciated repeatedly over the past two to three million years, and such cycles are expected to continue in the future due to variations in solar insolation caused by Earth's orbital dynamics (Fischer et al. 2021). Both the ground surface and subsurface environment, including associated hydrological systems, may be affected by climate-induced changes, such as the advance and retreat of continental-scale ice sheets and permafrost. Thus, when assessing the performance of a deep geological repository, such changes must be considered (Sheppard et al. 1995; Talbot 1999).

To predict the long-term behavior of DGRs, several numerical models have been developed that consider thermal, hydraulic, mechanical, and chemical (THMC) processes. For instance, the DECOVALEX Project (Development of Coupled THMC Models and their Validation against Experiments) examined the potential impacts of glaciation on DGRs by simulating the coupled effects of THMC processes (Chan et al. 2005). Other studies, such as Walsh and Avis (2010), investigated the effects of glaciation on a hypothetical repository in the Canadian Shield, focusing on the impact of multiple glacial cycles on the long-term transport of radionuclides from a defective container, but without investigating salinity effects. Studies have also looked at the impact of long-term climatic variability on groundwater flow and permafrost dynamics in different geological settings (Scheidegger et al. 2019) as well as the impact of glaciation on groundwater flow which has been identified in northern latitudes as one of the most intense perturbations associated with long-term climate change (Chan et al. 2005).

Though much research has been conducted on permafrost modelling and groundwater flow, significant research gaps still remain regarding the significance and impact of frozen ground on the long-term stability of a repository. Areas that require further investigation include geophysical and geochemical changes induced by freezing, including pressure and hydromechanical loading, geological variability and geometrical uncertainties (Scheidegger et al. 2019), changes in groundwater flow paths, formation of taliks, groundwater salinity at depth (Scheidegger et al. 2019; Busby et al. 2015), and groundwater flow and solute transport dynamics in cold regions (Mohammed et al. 2021; McKenzie et al. 2021). Moreover, the impact of large-scale changes in permafrost over climate-cycle time scales in the context of deep flow systems and DGRs, remains poorly understood (Busby et al. 2015). Such research gaps can be filled by numerically investigating groundwater systems which include permafrost freeze/thaw and a deep zone of natural formation brines that may become perturbed over geological time.

This study aims to investigate the impact of permafrost growth and decay cycles on groundwater flow, heat, and brine transport in the near-field and far-field environments of a DGR. The analysis of cryo-hydrogeological processes will be conducted using numerical modelling coupled with

https://doi.org/10.52381/ICOP2024.83.1

field data to develop and test hypothetical conceptual models.

2 CONCEPTUAL MODEL

2.1 Geological Setting

The conceptual simulations are conducted for a hypothetical site, based in part on data from the Umiujaq permafrost research field site in Nunavik, Quebec, Canada. The approach focuses on evaluating the sensitivity of a coupled system of groundwater flow, heat and brine transport driven by surface air temperature time-series.

2.2 Surface Temperatures

Prior studies have used marine oxygen isotope ratio ($\delta^{18}O$) records to infer past temperatures (Bintanja and van de Wal 2008). In this study, a similar approach is employed, constructing the surface air temperature (SAT) using the proxy temperature record of the Northern Hemisphere (Scheidegger et al. 2019).

To account for uncertainties in past surface temperatures across the region, four different temperature scenarios spanning the last 1 million years are used (e.g., as in Scheidegger et al. (2019), with two scenarios presented here). Each scenario is generated by linearly scaling the $\delta^{18}O$ time-series. The temperature at any given time (T_t) is described using Eq. 1:

$$T_t = \frac{\delta^{18}O_t - \delta^{18}O_0}{\max(\delta^{18}O_t - \delta^{18}O_0)}\Delta T + T_0 \qquad [1]$$

where T_0 is the present-day mean annual air temperature of 0.5 °C at Umiujaq, ΔT are the temperature offsets of -10, -14, -18, and -25 °C below the present temperature at the time of maximum $\delta^{18}O$ (Bintanja and van de Wal 2008; Scheidegger et al. 2019), $\delta^{18}O_t$ is the $\delta^{18}O$ value at the given time, and $\delta^{18}O_0$ is the present-day $\delta^{18}O$ value.

To predict future climate, we can draw insights from past events and assume they will repeat in the future (Busby et al. 2015; Fischer et al. 2021); here we will assume that the historic SAT will follow the same trend over the next 1 million years. Figures 1 and 2 show the global $\delta^{18}O$ time-series after Lisiecki and Raymo (2005) and the scaled surface temperature time-series in the Umiujaq region using ΔT ranging from -10 to -25 °C, respectively.

A 15,000-year spin-up cycle (Period 1 shown in Figure 2) was chosen based on test simulations to avoid artificial effects from the initial or boundary conditions. Such effects can originate, for example, from the initial permafrost or brine layers which are not in equilibrium with the boundary conditions or flow system. The present time in Figure 2 (at 15,000 yrs) is the end of period 1 (shown with the dashed black line), then the simulation continues for the next 65,000 yrs (shown as Period 2 in Figure 2, covering one glacial and interglacial period). Due to space limitations, the results are only shown for two different temperature scenarios, ΔT= -10 and -25 °C, referred to as S1 and S4 scenarios, respectively.

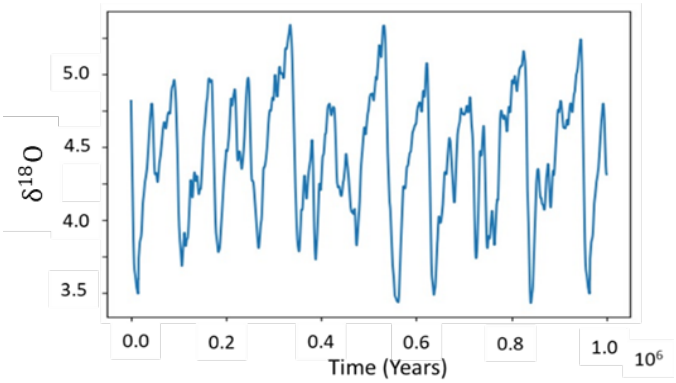

Figure 1. Global $\delta^{18}O$ time-series after Lisiecki and Raymo (2005).

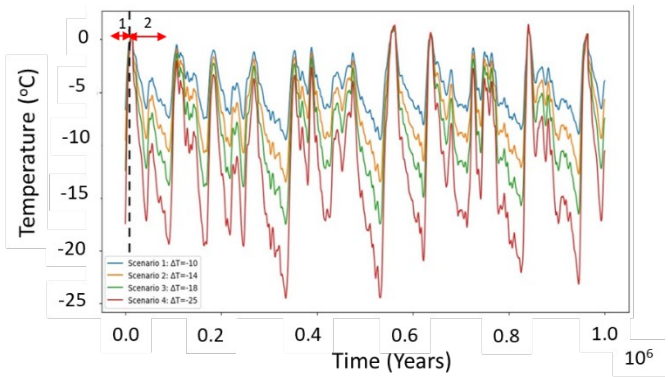

Figure 2. Scaled SAT time-series of the Umiujaq study area using ΔT ranging from -10 to -25 °C.

2.3 Numerical Model

2.3.1. Theoretical Approach

The transient groundwater flow, heat and mass transport equations were solved using the HEATFLOW-SMOKER finite element numerical model developed by Molson and Frind (2024). The model includes density-dependent groundwater flow, advective-dispersive mass transport, advective-conductive heat transport, phase change (freeze-thaw) with latent heat, and considers the influence of temperature on water density, viscosity, thermal conductivity, heat capacity, unfrozen water content, and relative permeability. Fluid density and viscosity are also concentration dependent. HEATFLOW-SMOKER has been successfully applied in many field-scale systems involving heat storage, thermal tracers, and permafrost, (e.g. Pehme et al. 2013; Shojae Ghias et al. 2018). The general advective-conductive heat transport equation, as resolved by the HEATFLOW-SMOKER code, is expressed in Eq. 2 as:

$$-\frac{\partial}{\partial x_i}\left(\theta \cdot S_w c_w \rho_w v_i T\right) + \frac{\partial}{\partial x_i}\left(\bar{\lambda} + \theta \cdot S_w c_w \rho_w D_{i,j}\right)\frac{\partial T}{\partial x_j} = \frac{\partial (C_0 T)}{\partial t} \qquad [2]$$

where θ is the porosity, S_w the (unfrozen) water saturation, C_w the specific heat of water (J/kg/K), ρ_w is the water density (kg/m^3), v_i is the mean linear groundwater flow velocity (m/s), T is the temperature (°C), $\bar{\lambda}$ is the thermal conductivity of the bulk porous medium (J/m/s/K), $D_{i,j}$ the

hydrodynamic dispersion coefficient (m^2/s), C_o the volumetric heat capacity of the porous medium ($J/m^3/K$), $x_{i,j}$ the spatial coordinates (m), and t is time (s). The mass transport equation can be expressed as:

$$\frac{\partial C}{\partial t} = \frac{\partial}{\partial x_i}\left(D_{i,j}\frac{\partial C}{\partial x_j}\right) - v_i\frac{\partial C}{\partial x_i} \quad [3]$$

where C is the concentration. Picard iteration is applied to handle all nonlinearities (Molson and Frind, 2022). Expressions for the unfrozen water saturation function (W_u) and relative permeability (k_r) are given in Eqs. 4, 5, and 6, respectively:

$$W_u(T) = p + (1-p)\cdot e^{(q\cdot T)} \quad \text{for } T < 0°C \quad [4]$$

$$W_u(T) = 1 \quad \text{for } T \geq 0°C \quad [5]$$

$$k_r = \max\left[10^{-\Omega\cdot\theta(1-w_u(T))}, 10^{-6}\right] \quad [6]$$

where p is the terminal fraction of unfrozen moisture at a very low temperature, q is a corresponding shape factor, and Ω is an empirical impedance factor. All parameters, including the thermal properties for the solids, water, and ice fractions, are presented in Table 1. For simplicity and due to the absence of site-specific data, the freezing function parameters p, q, and Ω were assumed uniform throughout the domain, consistent with the chosen geological settings. Furthermore, the relative permeability function described by Eq. 6 varies with the porosity of each unit (see Table 2). Units with higher porosity have a steeper decrease in relative permeability as the temperature decreases.

Table 1. Model parameters.

Properties and parameters	Value
Density of water (ρ_w; reference at 4 °C)	1,000 kg/m^3
Density of ice (ρ_i)	920 kg/m^3
Thermal conductivity of water (λ_w)	0.58 W/m K
Thermal conductivity of ice (λ_i)	2.14 W/m K
Specific heat of water (c_w)	4,187 J/kg K
Specific heat of ice (c_i)	2,108 J/kg K
Latent heat of water (L)	3.34 × 10^5 J/kg
Terminal unfrozen water saturation (p)*	0.01
Shape factor for unfrozen water saturation (q)*	1.0
Impedance factor (Ω) for k_r (Eq. 6)	10

* See Eqs. 4 and 5

2.4. Model Domain and Physical Properties

The 2D conceptual model is 5000 m long and 500 m deep, discretized using 500 × 50 (= 25,000) elements in the horizontal and vertical directions, respectively (Figure 3). The model consists of three hydro-stratigraphic layers, including a shallow aquifer underlain by two progressively less permeable hydrogeological units, with an initial 4.5 km long permafrost layer. The thermal and hydraulic properties of these layers are provided in Table 2. The permafrost extends between 290 m and 490 m elevation. Two lakes (Lake 1 and Lake 2) are also included within the model domain.

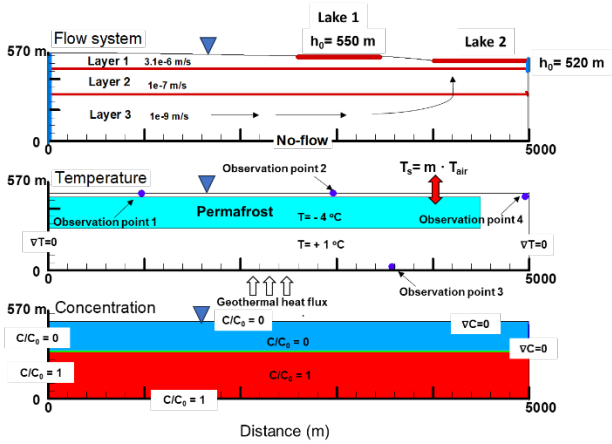

Figure 3. Boundary and initial conditions for flow, heat, and mass transport processes.

Table 2. Thermal and hydraulic properties assumed for the hydro-stratigraphic layers (Lemieux et al. 2020; Dagenais et al. 2020).

Layer	K* (ms^{-1})	θ (-)	λ_s (J/m/s/K)	c_s (J/kg/K)	ρ_s (kg/m^3)
Layer 1	3.1×10^{-6}	0.120	3.0	850	2650
Layer 2	10^{-7}	0.075	2.8	850	2650
Layer 3	10^{-9}	0.001	2.0	850	2650

*K: Hydraulic conductivity

2.5 Boundary and Initial Conditions

2.5.1 Groundwater Flow System

The flow system is driven by a fixed watertable represented by two quarter-cosine functions separated by Lake 1, which is assigned a constant head of 550 m (Figure 3). Further downgradient, Lake 2 assumes the role of the main discharge zone, situated at the far right of the top boundary with a head of 520 m. Although a fixed Type-1 watertable is usually not recommended in most flow models due to its tendency to overly restrict solutions and potentially lead to unrealistic recharge rates, it can be beneficial under freeze-thaw conditions since the recharge rate adapts automatically depending on the freeze-thaw state of the shallow groundwater. The base boundary is set as no-flow (impermeable), the left boundary is assigned a fixed head of 570 m, and the upper part of the right boundary was assigned a head of 520 m. This adherence to the maximum watertable elevation at the left boundary enables inflow (when thawed) from an upgradient area beyond the model domain, progressing toward the discharge zone. Four observation points (P1, P2, P3, and P4; Figure 3), are also included, allowing the computed heads, temperatures, and concentrations to be tracked over time.

2.5.2 Heat Transport System

The left and right thermal boundaries are characterized by zero-gradient temperature conditions, implying negligible horizontal conductive heat transport (Figure 3). Following

the approach used by Liu et al. (2022), the top boundary is assigned transient Type-1 (Dirichlet) temperatures determined from regressed linear relationships (m-factors) between surface air temperatures (SATs) and ground temperatures observed at Salluit, a research station north of Umiujaq. For each of two surface classes, being plateau and lakes, a freezing and thawing slope (m_f and m_t) is assigned. Here, the plateau (upgradient and inter-lake area) m-factors are assumed the same, defined by $m_f = m_t = 0.8$ for the freezing and thawing domains, respectively, while for the two lakes we assume $m_f = 0.04$ and $m_t = 0.8$, respectively. The model base is assigned a geothermal heat flux of 0.05 W/m² (Ling and Zhang 2004). The initial permafrost temperature is set at -4 °C, while the rest of the domain is initially set to +1 °C.

2.5.3 Mass Transport System

For mass transport, a fixed relative concentration of C/Co = 0 is applied at watertable recharge areas and along the upper part of the left boundary to represent freshwater infiltration. Zero-gradient conditions are imposed on discharge boundaries, including those along discharge zones of Lake 1 and 2, allowing advective discharge of fresh or salt water. A normalized concentration of C/Co = 1, corresponding to a brine total dissolved solids (TDS) concentration of 34,500 mg/L, is imposed along the bottom boundary and as the initial condition below the permafrost, extending from 0 to 300 m in elevation, whereas C/Co = 0 is applied as the initial condition in the rest of the system.

3 SIMULATION RESULTS

Simulation results of the two temperature scenarios are presented in Figure 4 a, b, c, and d (base Scenario S1) and in Figure 5 a, b, c, and d (colder Scenario S4) at 5k, 20k, 50k, and 80k yrs, showing simulated hydraulic heads and streamtraces (particle tracks), temperatures, TDS concentrations as well as hydraulic conductivity.

3.1 Flow System

The simulated flow systems clearly indicate the presence of distinct recharge and discharge zones, with noticeable variations in flow rates due to geological structure and permafrost (Figures 4a and 5a). Groundwater originates from upgradient regions at the left and flows towards the lake discharge areas. In these conceptual models, Lake 2 serves as a discharge zone, while Lake 1 plays a dual role, functioning as both a recharge zone and a discharge zone. Groundwater flow is slower in areas of permafrost, indicated by dense time markers, while flow is faster below the permafrost and within the warmer taliks below the two lakes (e... Figures 4a at 80k yrs and 5a at 50k and 80k yrs).

An important distinction emerges between the two scenarios S1 (warmer SAT) and S4 (colder SAT), with generally lower flow velocities in S4 due to more extensive freezing of the system where conductive heat transport dominates. As shown in Figure 4 a and b in the warmer S1 SAT scenario, while groundwater tends to follow paths of least resistance in thawed zones, it can also pass through the permafrost layers. At 80k yrs, for example (Figure 4a), although the system is frozen down to an elevation of approximately 250 m (indicated by the 0 °C isotherm), some groundwater entering from the left boundary below the permafrost still tends to flow through the permafrost towards the discharge zones. Note that because of the assumed freezing function for k_r (Eq 4), flow velocities do not abruptly decrease at the freezing front, but decrease exponentially until temperatures decrease to about -3 or -4 °C. Although velocities are much lower within the permafrost, they can still be significant on geological time scales (depending also on the intrinsic unfrozen K).

Advective particle tracks (superimposed on the hydraulic head fields in Figures 4a and 5a) are used to estimate advective travel times through the flow system. Since they are generated assuming a steady-state flow system at specific times, the particle tracks are not meant to be representative of radionuclide transport from a potential DGR. In both scenarios, travel times extend to millions of years which is much longer than the estimated lifespan of a DGR (Taylor 2021). However, as they represent only snapshots of the transient system, these travel times are likely overestimated during peak glaciation and underestimated during interglacial periods.

3.2 Heat Transport System

The temperature distributions and permafrost depths for both scenarios, represented by the 0 °C isotherm, are shown in Figures 4b and 5b. Only Scenario S4 (colder SAT) produces a permafrost depth reaching the reference depth associated with an assumed DGR 500 m deep. The thermal regime shows a generally stratified system due to strong thermal conduction, with the T = 0 °C isotherm propagating deeper over time following the 15k-yr warming spin-up period. (Note, the SATs for each scenario are provided in Figure 2 and in more detail in Figure 6a).

At 5,000 yrs in each scenario (Figures 4b and 5b), the system is still in a warming phase starting from the assumed initial condition with the extensive permafrost layer. At 20k yrs, the two systems are near their warmest, being only 5k yrs after the peak SATs (Figure 6a). Domain temperatures from 20k to 80k yrs are generally cooling, despite the short warming trend in the SAT from about 45k to 55k yrs. Because of thermal insulation of the lakes, warmer zones persist below each lake in the form of taliks.

The results also highlight the influence of the underlying thermal state on groundwater flow, including the effect on groundwater discharge to Lake 1 and Lake 2. As an example, in the warmer Scenario S1 and the colder Scenario S4, Figures 4a, b and 5a, b show that despite the freezing conditions beneath the plateau (upgradient) areas, Lakes 1 and 2 continue to serve as discharge zones.

3.3 Mass Transport System

Changes in long-term surface temperature conditions also lead to variations in the position and characteristics of the brine interface. The simulated interface is affected by the transient flow system which depends on the concentration-dependent fluid density and viscosity, as well as on the temperature-dependent relative permeability (through the variable ice content). This coupling between temperature

conditions and flow dynamics highlights the sensitivity of the brine system to climatic variations. Nevertheless, except for the below-lake talik regions, the generally lower hydraulic conductivities at depth upgradient of the lakes due to both geologic structure and lower ice-fraction dependent relative permeabilities result in limited changes to the depth and movement of the brine interface.

Despite the high density of the brine, which tends to stabilize the interface, the gravity-induced groundwater flow system depresses the brine interface between through the warmer and thus more permeable taliks, where flow is diverted deeper below the inter-lake frozen zone (Figure 4b, c and 5b, c at 50k and 80k yrs). Initial stages of the S1 simulation show a dynamic system of infiltrating fresh water, leading to brine dilution beneath Lake 1 (Figure 4c). As the system warms during the 15k yr spin-up, by 20k yrs, the initial cold front between the two taliks has significantly thawed, and brine migrates upward toward the Lake 2 discharge zone. At 50k yrs, as the system cools, the downward extension of the cold front below the inter-lake area forces infiltrating upgradient freshwater to circumvent the inter-lake frozen zone and pass through the thawed and thus higher permeability layers, pushing down the brine interface. This behavior intensifies at 80k yrs when the system becomes even colder. A similar pattern can be seen with a greater impact in the colder Scenario S4 (Figure 5c).

3.4 Hydraulic Conductivities

Effective hydraulic conductivities reflect variability in both the imposed geological structure and the transient freeze/thaw state (Figure 4d and 5d). While some geological structure is still evident at early time as horizontal stratification (at 5k and 20k yrs), by 50k and 80k yrs the impact of ice-fraction dependent relative permeability becomes significant as the system freezes and lateral changes in hydraulic conductivity due to the below-lake taliks become more apparent. Specifically, in the upgradient (left) half of the domain between 400 and 450-m elevations, the temperature-dependent hydraulic conductivity is lower compared to the areas within the warmer taliks below each lake (Figure 4b, d). Groundwater velocities are thus also significantly lower compared to other parts of the domain (Figure 4a). Similar behavior can also be observed in Figure 5b, d, for the colder Scenario S4.

3.5 Breakthrough Curves

Breakthrough (arrival) curves for temperature and concentration are provided in Figure 6a and b, respectively, at monitor points P1–P4; the input SATs are also included in Figure 6a. Note that in both scenarios, a SAT temperature peak occurs at around 15k yrs (the assumed present time) and a temperature dip occurs around 45k yrs, followed by a rapid rise and a clear peak shortly around 55k yrs. Directly beneath Lake 1 (at P2), the temperatures for both scenarios remain near 0 °C because of the imposed freezing m-factors of m_f = 0.04 (Figure 6a). At the deeper point P3, the minimum and maximum temperatures align with the SAT in both scenarios but are also influenced by the geothermal flux at the model base, contributing to warmer temperatures. In warmer Scenario S1, characterized by higher flow velocities and a more dynamic environment compared to S4, upward migration of brine to P4 at Lake 2 occurs somewhat faster compared to Scenario S4, especially after 40k yrs (Figure 6b). In both scenarios, over geological time, the flow system tends to induce continued upward migration of the brine towards Lake 2, despite the cooling temperatures. This is accentuated in the warmer scenario S1 with a more dynamic system. In both scenarios, the relatively small and short-lived SAT temperature peak at around 55k yrs has no significant impact on salt transport toward the discharge zone (Figure 6b).

4. DISCUSSION

The simulations have demonstrated the influence of geological structure and climate-induced freeze-thaw processes on deep regional groundwater flow systems. Although the presence of permafrost decreases the effective hydraulic conductivity of the host rock, under the assumed conditions of a non-zero unfrozen water content at low temperature, groundwater flow through permafrost (i.e., 80k yrs in S1 and 50k and 80k yrs in S4) can still be significant over glacial/interglacial time scales depending on the relative permeability and hydraulic gradients.

The presence of taliks beneath lakes can establish a deep link between the geosphere and biosphere, generating transient groundwater pathways even during glacial conditions. The study also highlighted the sensitivity of the system to climatic variations and the influence of subsurface permeability on brine transport dynamics. Subsurface temperatures need to decrease to at least -3 to -4 °C before the flow velocities are significantly reduced. In both scenarios, the salt concentration steadily increases in the discharge area of Lake 2 with a more pronounced effect in warmer Scenario S1 due to higher flow velocities compared to S4.

In these scenarios, because of the relatively low temperature variations, the effect of concentration-dependent fluid density is more significant than the impact of temperature-dependent density. The simulated temperature trends at the screening points follow the SAT trends, with more influence in deeper layers from the geothermal flux in deeper layers. Furthermore, comparing times of glacial maximum conditions and corresponding temperatures underscores the dynamic relationship between Surface Air Temperature (SAT) and the subsurface flow system's response time. This aspect highlights the system's complex behavior under varying thermal conditions.

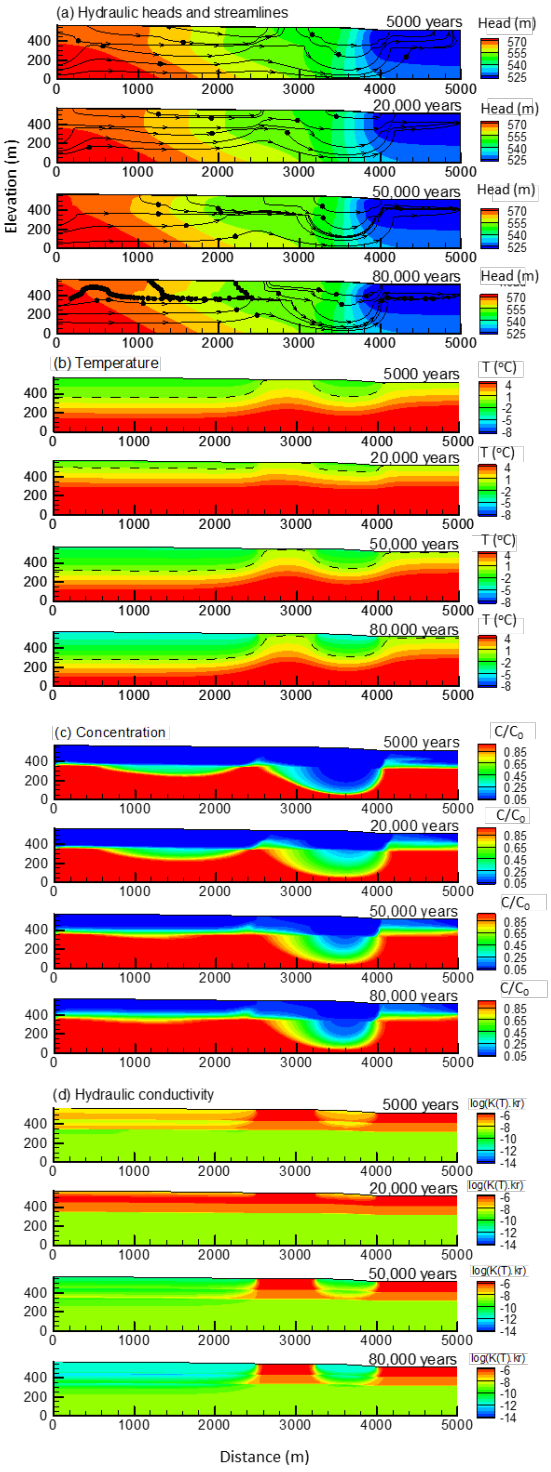

Figure 4. Simulated results over time, Scenario S1 (warmer): (a) hydraulic heads and particle tracks (time marker interval is 80k yrs.), (b) temperature, (c) concentration and (d) hydraulic conductivity. C/Co = 1 corresponds to 34,500 mg/L TDS.

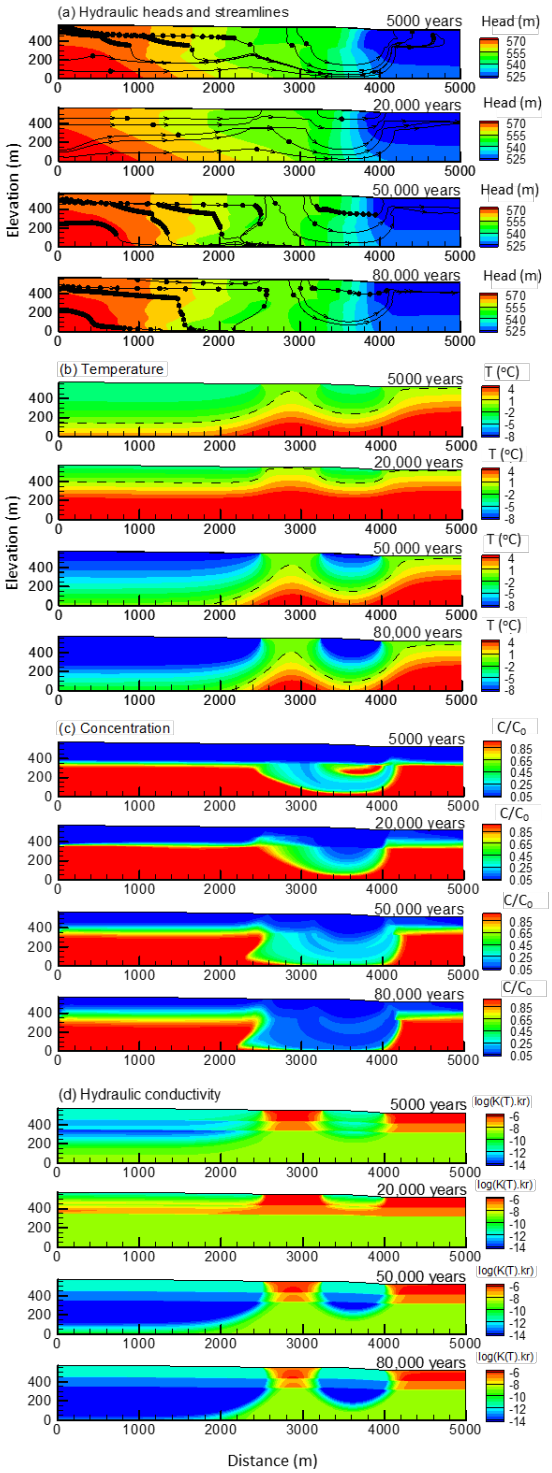

Figure 5. Simulated results over time, Scenario S4 (colder): (a) hydraulic heads and particle tracks (time marker interval is 800k yrs.), (b) temperature, (c) concentration and (d) hydraulic conductivity. C/Co = 1 corresponds to 34,500 mg/L TDS.

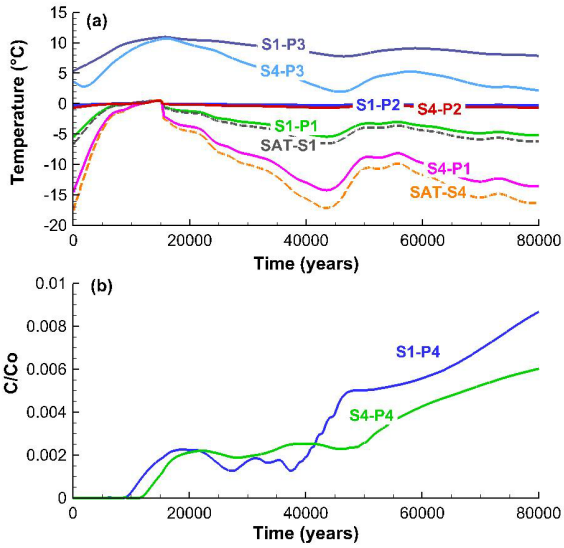

Figure 6. Simulated breakthrough curves at selected observation points for Scenarios S1 and S4, showing: (a) temperature and (b) concentrations; C/Co = 1 corresponds to 34,500 mg/L TDS. Dashed lines in (a) are surface air temperatures (SATs) for Scenarios S1 and S4.

The long travel times underscore the enduring effects of past glacial periods on subsurface hydrodynamics. This highlights the importance of considering paleoclimatic conditions in understanding present-day subsurface flow patterns.

The results emphasize the need to consider climatic conditions, geological structure, and freeze-thaw processes when evaluating the suitability of a potential DGR site. Insights have been provided into the behavior of deep cryo-hydrogeological systems and the importance of improving our understanding of groundwater flow, heat transport, and solute transport dynamics in cold regions.

5 Model Limitations and Future Work

Several limitations and assumptions must be recognized while interpreting the results. Groundwater flow was assumed fully saturated, and cryo-suction, ice segregation, and effects of glacial loading and unloading were neglected. Ice-fraction dependent unfrozen moisture content and relative permeability are only temperature dependent and neglect effects of salt concentration. Furthermore, the adopted continuum approach assumes a fully connected pore space, in particular for the terminal unfrozen moisture content. Longer simulations including warmer and colder periods over multiple glacial cycles should be carried out. Future studies should also conduct sensitivity analyses of hydraulic properties to understand performance under different geological and climatic conditions, with particular focus on the impact of the unfrozen moisture content (freezing function).

6 Summary and Conclusions

In this study we have used numerical simulations to investigate the potential impact of permafrost growth and decay cycles on groundwater flow, heat, and brine transport in the context of a DGR. The conceptual model was designed to incorporate key processes of density-dependent groundwater flow, advective-conductive heat transport, and advective-dispersive mass (brine) transport, including water-ice phase change, and latent heat effects. The findings enhance our understanding of the coupling between groundwater flow, heat transport, and brine transport in permafrost environments.

In addition, the study emphasized the system's sensitivity to climatic fluctuations and the role of subsurface permeability in brine transport dynamics, while also shedding light on how temperature variations impact groundwater flow rates and patterns, specifically in relation to groundwater discharge into surface water bodies.

The study also highlights the pivotal role of unfrozen moisture content in allowing groundwater flow through parts of the frozen ground that still contain liquid water, suggesting that unfrozen water within permafrost can control groundwater flow behavior. More investigation on defining realistic values of unfrozen moisture content and their effect on such systems seems to be necessary.

The system's behavior is complex under varying surface temperatures and density-dependent thermohaline conditions. Although only relatively low salt concentrations were assumed here (on the order of seawater), on these geological time scales changes in fluid density due to salt content still played a significant role in affecting the flow field. Effects of salt concentrations on density were clearly more significant than those of temperature.

7 Acknowledgements

The authors thank the NWMO (Nuclear Waste Management Organization Canada) for funding this research project. Additionally, we acknowledge the support of the CatchNet research group (https://skb.se/catchnet/this-is-catchnet/). Special thanks are also extended to the CEN (Centre d'études nordiques) and CentrEau (Centre de recherche sur l'eau) for their contributions and support.

8 References

Bintanja, R. and van de Wal, R. 2008. 'North American ice-sheet dynamics and the onset of 100,000-year glacial cycles', *Nature* 454, pp. 869–872.

Busby, J., Lee, J., Kender, S., Williamson, J., and Norris, S. 2015. 'Modelling the potential for permafrost development on a radioactive waste geological disposal facility in Great Britain', *Proceedings of the Geologists' Association* 126 (2015), pp. 664–674. Available at: https://doi.org/10.1016/j.pgeola.2015.06.001.

Chan, T., Christiansson, R., Boulton, G., Ericsson, L., Hartikainen, J., Jensen, M., Ivars, D.M., Stanchell, F., Vistrand, P., and Wallroth, T. 2005. 'DECOVALEX III BMT3/BENCHPAR WP4: The thermo-hydromechanical responses to a glacial cycle and their potential implications for deep geological disposal of nuclear fuel waste in a fractured crystalline rock mass', *International Journal of Rock Mechanics and Mining Sciences* 42, pp. 805–827.

Dagenais, S., Molson, J., Lemieux, J.-M., Fortier, R., and Therrien, R. 2020. 'Coupled cryo-hydrogeological modelling of permafrost dynamics near Umiujaq (Nunavik, Canada)', *Hydrogeology Journal* 28, pp. 887–904.

Fischer, U.H., Bebiolka, A., Brandefelt, J., Cohen, D., Harper, J., Hirschorn, S., Jensen, M., Kennell, L., Liakka, J., Näslund, J.-O., et al. 2021. 'Radioactive waste under conditions of future ice ages', in W. Haeberli and C. Whiteman (eds.), *Snow and Ice-Related Hazards, Risks, and Disasters (Second Edition)*. Amsterdam, Netherlands: Elsevier.

Holden, B., Stotler, R., Frape, S., Ruskeeniemi, T., Talikka, M., and Freifeld, B.M. 2009. 'High lake permafrost comparison site: permafrost phase IV', *Nuclear Waste Management Organization* NWMO TR-2009-11.

Lemieux, J-M., Fortier, R., Murray, R., Dagenais, S., Cochand, M., Delottier, H., Therrien, R., Molson, J., Pryet, A., and Parhizkar, M. 2020. 'Groundwater dynamics within a watershed in the discontinuous permafrost zone near Umiujaq (Nunavik, Canada)', *Hydrogeology Journal* 28(3), pp. 833–851.

Ling, F. and Zhang, T. 2004. 'A numerical model for surface energy balance and thermal regime of the active layer and permafrost containing unfrozen water', *Cold Regions Science and Technology* 38(1), pp. 1–15.

Lisiecki, L.E. and Raymo, M.E. 2005. 'A Pliocene-Pleistocene stack of 57 globally distributed benthic δ18O records', *Paleoceanography* 20(1).

Liu, W., Fortier, R., Molson, J., Lemieux, J.M. 2022. 'Three-dimensional numerical modeling of cryo-hydrogeological processes in a river-talik system in a continuous permafrost environment', *Water Resources Research* 58(3), 2021WR031630.

McKenzie, J.M., Kurylyk, B.L., Walvoord, M.A., Bense, V.F., Fortier, D., Spence, C., and Grenier, C. 2021. 'Invited perspective: What lies beneath a changing Arctic?', *The Cryosphere* 15, pp. 479–484.

Mohammed, A.A., Bense, V.F., Kurylyk, B.L., Jamieson, R.C., Johnston, L.H., and Jackson, A.J. 2021. 'Modeling reactive solute transport in permafrost-affected groundwater systems', *Water Resources Research* 57, e2020WR028771.

Molson, J.W. and Frind, E.O. 2024. *HEATFLOW-SMOKER USER GUIDE, Density-dependent flow and advective-dispersive transport of mass, thermal energy or residence time in 3D fractured porous media, Version 5.0*. Université Laval and University of Waterloo.

Pehme, P., Parker, BL., Cherry, J.A., Molson, J.W., and Greenhouse, J.P. 2013 'Enhanced detection of hydraulically active fractures by temperature profiling in lined heated bedrock boreholes', *Journal of Hydrology* 484, pp.1–15.

Scheidegger, J.M., Jackson, C.R., McEvoy, F.M. and Norris, S. 2019. 'Modelling permafrost thickness in Great Britain over glacial cycles', *Science of the Total Environment* 666, pp. 928–943

Sheppard, M.I., Amiro, B., Davis, P., and Zach, R. 1995. 'Continental glaciation and nuclear fuel waste disposal: Canada's approach and assessment of the impact on nuclide transport through the biosphere', *Ecological modelling* 78, pp. 249–265.

Shojae Ghias, M., Therrien, R., Molson, J., and Lemieux, J-M. 2018. 'Numerical simulations of shallow groundwater flow and heat transport in a continuous permafrost setting under the impact of climate warming', *Canadian Geotechnical Journal*, 56(3), pp. 436–448.

Talbot, C. 1999. 'Ice ages and nuclear waste isolation', *Engineering Geology* 52, pp. 177–192.

Taylor, A. 2021. 'Deep Geological Repository Transportation System Conceptual Design Report Crystalline/Sedimentary Rock, Technical Report', *Nuclear Waste Management Organization*, APMREP-00440-0209-R001.

Walsh, R. and Avis, J., 2010. 'Glaciation Scenario: Groundwater and Radionuclide Transport Studies, Technical Report', *Nuclear Waste Management Organization* (NWMO) DGR TR-2010-09.

Estimation rates of permafrost degradation and their impact on ecosystems across Alaska

Sergey Marchenko[1], Kevin Bjella[2], Dmitry Nicolsky[1] & Vladimir Romanovsky[1]

[1]*Geophysical Institute, University of Alaska Fairbanks, Fairbanks, Alaska, United States*

[2]*U.S. Army Engineer Research and Development Center (ERDC), Cold Regions Research and Engineering Laboratory (CRREL), Fairbanks, Alaska, United States*

ABSTRACT

The main goal of this research is to evaluate the vulnerability and behavior of permafrost under climate warming across the different ecosystems and surface conditions in respect of ecosystem stability, socio-economic impact, and to provide stakeholders with information for better understanding possible future environmental changes. We suggested the new version of the spatially distributed permafrost dynamics model (GIPL2-MPI), which is developed in the Geophysical Institute (GI), University of Alaska Fairbanks (UAF). This model is based on the ecosystem approach to simulate the permafrost dynamics, which we are discussing in this paper. The combined ground-based observations and numerical freeze/thaw modeling using climate-ecosystem-permafrost interactions allow us to understand the physical processes and mechanisms controlling permafrost physical state. It was attempting to predict the changes in permafrost conditions using output from two GCMs (NCAR-CCSM4 and GFDL-CM3) and Five-Model Average for the RCP-4.5 and RCP-8.5 scaled down to 1 by 1 km spatial resolution (https://uaf-snap.org) across entire Alaska. Our result shows that by the end of the current century widespread permafrost degradation could begin everywhere in Alaska southward of the Brooks Range as well as across some spots of the North Slope. The most significant changes in the upper layer (0.5–5.0 m) of ground could occur under the climate scenario provided by the GFDL-CM3 climate model, especially in areas with ice-rich permafrost.

1 INTRODUCTION

Recent observations indicate a warming of permafrost in many northern regions with a resulting degradation of ice-rich and carbon-rich permafrost. In the last 30–40 years, warming in permafrost temperatures observed in the Northern Hemisphere has resulted in the thawing of permafrost in natural, undisturbed conditions in areas both close to the southern and north boundary of the permafrost distribution. The impact of climate warming on permafrost and the potential of climate feedbacks resulting from permafrost thawing have recently received a great deal of attention. Most of the permafrost observatories in the Northern Hemisphere show substantial warming of permafrost since the 1980s (Biskarbon et al. 2019; Smith et al. 2010; Romanovsky et al. 2010). The magnitude of permafrost warming has varied with location but was typically from 0.5 to 3 °C. A more pronounced warming has been observed in cold permafrost in higher northern latitudes and a smaller increase in temperature was typical for the warmer permafrost (because latent heat). Permafrost temperatures were stable or even slightly cooling during the last several years in the lower northern latitudes.

A comprehensive system of permafrost observatories at Alaska was established in the late 1970s and early 1980s by the Geophysical Institute, University of Alaska Fairbanks along the Trans-Alaska Pipeline and at other locations in Alaska (Osterkamp 2005, 2008).

Permafrost extent and active layer depth are very important for the high-latitude temperature regimes and water cycle. Changes in the hydrologic cycle and soil temperature can have significant consequences for local people: degrading permafrost very often could lead to ecosystem changes and threatens to damage infrastructure. Understanding how the tightly coupled permafrost and hydrology will behave in a warming world is vitally important for local communities in Alaska and throughout the circumpolar North.

Alaska is warming very fast. Permafrost temperature has increased by 0.5 to 2 °C in Alaska during the last 30 to 35 years (e.g., Osterkamp 2007; Romanovsky et al. 2010; Smith et al. 2010). Therefore, there is an urgent need to develop a robust modeling tool for projecting changes associated with thawing permafrost in this region. Many important questions about present day and future ecosystems change can be answered with such tools. Even with all the uncertainty of future climate change projections this model will be useful in creating estimations of the range of future permafrost change in Alaska. Many of the proposed developments will be experimental in nature, with a final goal of providing society with robust expert assessments of changes that are important for infrastructure for several decades ahead.

In the discontinuous permafrost zone with ground temperatures near the freezing point, the presence of vegetation and organic soil layers strongly affect the ground thermal regime due to insulation effect. Shur and Jorgenson (2007) classified permafrost according to patterns of formation and degradation in relation to climate and ecosystems. They propose five main permafrost zones:

1) Climate-driven;
2) Climate-driven, ecosystem-modified;
3) Climate-driven, ecosystem protected;
4) Ecosystem-driven; and
5) Ecosystem-protected permafrost.

https://doi.org/10.52381/ICOP2024.231.1

Permafrost in each zone reacts differently to external disturbances. The permafrost types 'climate-driven, ecosystem protected', 'ecosystem-driven', and 'ecosystem-protected' are in a state of disequilibrium with the current climate; minimal disturbances have already caused widespread permafrost degradation (Jorgenson et al. 2008).

Recently, several permafrost models were developed for various regions (e.g., Gisnås et al. 2013; Westermann et al. 2013; Zhang et al. 2013; Fiddes et al. 2015). In many of the permafrost models, properties for the mineral and organic soil layers (Marchenko et al. 2008; Jafarov et al. 2012) or properties for the sediment and bedrock material (Westermann et al. 2013), or values of n factors and thermal properties of the ground material (Gisnås et al. 2013) produce a large number of distinct combinations of the input-data classes, the parameterization of which is a difficult task involving various assumptions and datasets. In some publications, the texture of mineral soils and other input parameters are used (Zhang et al. 2013) to reduce several input-data classes by considering 26 so-called ecosystem types.

In this manuscript, we consider the ecosystem types and group existing ground temperature observations across the ecosystem types. This grouping allows estimation of the soil properties using the data assimilation technique for each input-data class to Alaska. Justification of this approach is based on the analysis of spatial and temporal variability of near-surface ground temperatures measured across entire Alaska (Osterkamp and Jorgenson 2006; Osterkamp 2008; Romanovsky et al. 2008, 2010).

The modes of permafrost degradation are highly variable, and its topographic and ecological consequences depend on the interactions of slope positions, soil texture, hydrology, ice content, etc. However, it is still not clear how surface conditions could affect the hydrothermal dynamics of permafrost and active layer; how to determine these factors are most important in estimating for surface condition. Knowledge of processes affecting the vulnerability of permafrost in respect to ecosystems stability, infrastructures, and socio-economic impacts, provides stakeholders with information for better understanding the range of possible future changes, to help guide land management and decision-making.

2 PERMAFROST DYNAMICS MODEL GIPL2-MPI

To evaluate the vulnerability of permafrost under climate warming across entire Alaska in respect to ecosystems stability, infrastructure and socioeconomic we applied the physical process-based permafrost dynamics model developed in Geophysical Institute Permafrost Lab (GIPL) University of Alaska Fairbanks (Marchenko et al. 2008; Nicolsky et al. 2009; Jafarov et al. 2012).

In this research, we employ the transient permafrost dynamics model GIPL2-MPI, which simulates soil temperature dynamics and the depth of seasonal freezing and thawing by solving 1D non-linear heat equation with phase change using the finite difference method. The GIPL2-MPI model captures physical processes essential to robust and appropriate modeling of soil temperature dynamics, active layer thickness and talik development if so. Specifically, soil thermal properties are parameterized according to soil texture and organic matter. In this model, the process of soil freezing/thawing is occurring in accordance with the unfrozen water content and soil thermal properties, which are specific for each soil layer and for each geographical location. Additionally, GIPL2-MPI includes thermal insulation of the snow cover, and geothermal heating at the appropriately selected depth. The GIPL2-MPI model also incorporates an efficient algorithm to estimate soil thermal properties using in-situ temperature measurements in the active layer and in permafrost. This simplifies model calibration for specific sites. The conceptual representation of permafrost dynamics in the GIPL2-MPI Model could be expressed as:

- Numerical finite difference solution of heat diffusion,
- At least 100 m vertical computational domain (vertical depth's grid), contains 128–256 vertical grid nodes,
- Moss insulation explicitly considered,
- Organic soil insulation explicitly considered,
- Snow insulation explicitly considered,
- Effect of unfrozen water on phase change explicitly considered,
- Thermal conductivity and heat capacity are the functions of soil moisture content, soil temperature, and unfrozen water.

3 MODEL VALIDATION AND CALIBRATION

Different earth's materials have varying thermal properties. The soil thermal conductivity and heat capacity vary within the different soil layers as well as during the thawing/freezing cycles and depend on the unfrozen water content that is a certain function of temperature. The method of obtaining these properties is based on numerical solution for a coefficient inverse problem and on minimization locally the misfit between measured and modeled temperatures by changing thermal properties along the direction of the steepest descent. The method used and its limitations are described in more detail elsewhere (Alifanov 1994; Alifanov et al. 1996; Tikhonov et al. 1996; Marchenko and Gorbunov 1997; Nicolsky, 2009).

For the initial model calibration, we used measured data from more than twenty shallow boreholes (1–1.5 m in depth) from across Alaska. These high-quality ground temperature measurements (precision generally at 0.01 °C) are available from the beginning of 1990s to present. Soil water content and snow depth measurements were also available at most of these boreholes for the different landscape settings for the initial model validation (Romanovsky and Osterkamp 1997; Osterkamp 2005; Romanovsky et al. 2010). The temperature measurements in the shallow holes performed with vertical spacing of 0.08–0.15 m. At most, of these sites, soil water content and snow depth also were recorded. In addition, more than 20 relatively deep boreholes, from 29 m to 100 m in depth, along the same transect were available for the model validation in terms of permafrost temperature profiles and permafrost thickness.

The developed approach attempts to addresses the problem of computing the ground temperature projections at the regional scale that is sufficient to gain some understanding how potential changes in the permafrost might affect ecosystems and impact the infrastructure under various climate scenarios. The developed parametrization of the ground thermal properties is obtained using a data assimilation technique (e.g., Marchenko and Gorbunov 1997; Nicolsky et al. 2009). The mean values for ALT are computed over the 1996–2022 period, while the MAGT values are computed over the period when the observations are available. Generally, the modeling results very well agree with observations (Figure 1).

The example of the reconstructed soil thermal properties is shown in Table 1. Some year-to-year differences between the modeled and observed annual cycles exist. However, in general, the modeled and observed ground temperature climatology agree well with each other. The error is typically less or close to 0.25 °C, except during the snowmelt season. The subsurface thermal properties input datasets were compiled using both the GIS environments and specially developed tools as well.

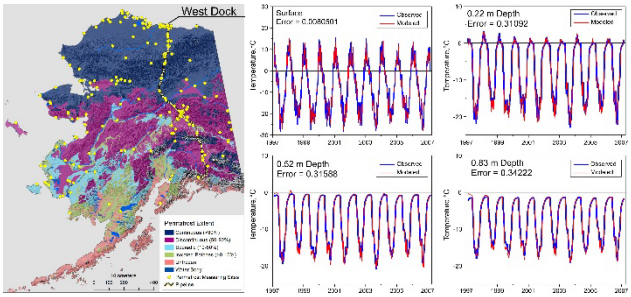

Figure 1. (Left) Map of measuring site locations (yellow dots), and (right) example of the GIPL2-MPI model calibration for the specific site west dock represents the north slope of alaska arctic tundra ecotype. The blue line is a measured data, and the red one is the GIPL2-MPI modeled.

4 Ecosystem Approach of Permafrost Dynamic Modeling

This research explores data on the ground thermal properties and surface conditions for the major ecotypes and deposits across Alaska, which were obtained using the ecosystem and vegetation maps, map of deposit types and ground ice as a source of a priory information (Figure 2) and the solution of the inverse problem as well (Alifanov 1994; Alifanov et al. 1996; Tikhonov et al. 1996; Marchenko and Gorbunov 1997; Nicolsky et al. 2009). For each ecosystem type the soil texture and thickness of the organic layer were parameterized according to field measurements and maps.

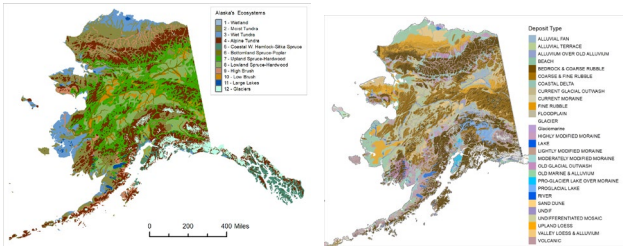

Figure 2. Ecosystem Map of Alaska (Geological Survey 1970) used for determination of properties for surface vegetation (left) and Map of Deposit Type of Alaska (Jorgenson et al. 2008) used for determination of soil thermal properties within the upper sub-surface soil layer (right).

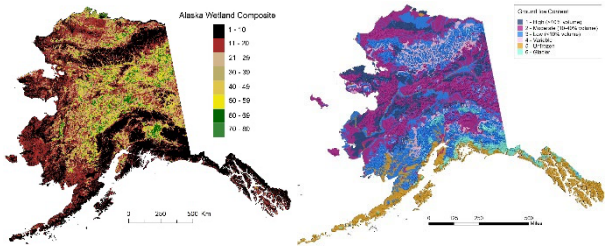

Figure 3. Alaska Wetland Composite map at 30 m spatial resolution (He et al. 2016) used for determination of soil water content (left). Excess ice volume in top 5 m based on surficial geology relationships (right). Variable ice associated with buried glacial ice (Jorgenson et al. 2008)

Table 1. The reconstructed ground thermal properties for sub-polar or polar soil type and moist and wet tundra (grassland-lichen-moss) ecosystem class at the North Slope Alaska (West Dock).

	Heat Capacity		Thermal Conductivity			
VWC (m^3/m^3)	Thawed ($J/m^3/K$)	Frozen ($J/m^3/K$)	Thawed (W/m*K)	Frozen (W/m*K)	Depth (m)	Layer matter (description)
0.694	1.72E+06	1.21E+06	0.242	0.895	0.0-0.12	moss
0.596	1.93E+06	1.51E+06	0.452	1.032	0.12-0.22	peat 1 (shallow organic, fibrous)
0.543	2.02E+06	1.65E+06	0.524	1.056	0.22-0.68	peat 2 (deep organic, amorphous)
0.456	2.54E+06	1.72E+06	1.023	1.516	0.68-5.68	mineral 1, silt
0.442	2.93E+06	2.23E+06	1.216	1.645	5.68-8.8	mineral 2, silt
0.426	3.43E+06	2.83E+06	1.424	1.849	8.8-48.5	mix of silt, gravel, sand, debris
0.384	3.63E+06	3.12E+06	1.832	2.214	48.5-52.0	gravel, coarse sand, debris
0.041	3.85E+06	3.46E+06	2.502	2.589	52.0-100	bedrock

We used the maps of surface vegetation, surficial geology, deposit types, primary soil texture, permafrost extent and ground ice volume. The map of ground ice distribution used for additional information to compile the initial soil ice/water content (Figure 3). Ground ice volumes were estimated for the upper 5 m of permafrost using terrain relationships established by Jorgenson et al. (2008) and our field data. Ground ice volume near the surface is higher in colder regions due to active ice-wedge formation and ice segregation in fine-grained deposits. Buried glacial ice in old or stagnant young moraines is included, but is irregularly distributed at this map scale.

5 Computational Domain and Climate Forcing

We defined the computational domain across Alaska with a spatial resolution of 1 by 1 km, which covered Alaska entirely except the small part of the Aleutian Islands. For computation this area consisted of 1,497,645 grid cells.

We prepared the SNAP dataset as a climate forcing to drive the GIPL2-MPI permafrost model. CMIP5/AR5 selected GCM's (https://uaf-snap.org/how-do-we-do-it) scaled down to 1 km spatial resolution were used to drive the GIPL2-MPI model. We used outputs for two operating separately GCMs GFDL-CM3 and NCAR-CCSM4 as well as for five-model average, and for two different greenhouse gas concentration trajectory RCP4.5 and RCP8.5.

The five-model average is the average model output from the top five models that best replicate historical climate in Alaska and the Arctic regions such as NCAR-CCSM4, GFDL-CM3, GISS-E2-R, IPSL-CM5A-LR, MRI-CGCM3 (Walsh et al. 2018). The five-model average is best for looking at general climate trends over time, as it smooths over the year-to-year and decade-to-decade variability. NCAR-CCSM4 and GFDL-CM3 are the best for the Alaska region for exploring climatic extremes or annual variability. Only individual models can provide that type of information.

RCP is a greenhouse gas concentration trajectory adopted by the IPCC (IPCC 2014). Four pathways were used for climate modeling and research for the IPCC fifth Assessment Report (AR5) in 2014. The pathways describe different climate futures, all of which are considered possible depending on the volume of greenhouse gases (GHG) emitted in the years to come. The RCPs—originally RCP2.6, RCP4.5, RCP6.0, and RCP8.5—are labelled after a possible range of radiative forcing values in the year 2100 2.6, 4.5, 6, and 8.5 W/m2, respectively (Moss et al. 2008; van Vuuren 2011; Weyant et al. 2009).

The RCP2.6 scenario was included in the RCP set to show what it would take to limit globally averaged warming to about 1 °C by 2100. RCP2.6 is generally not used in presenting plausible futures because it requires such extreme mitigation that it is considered by many climate experts to be unrealistic. The RCP2.6 scenario required that after 2020, CO2 emissions would decline and become negative by 2100 (i.e., we find ways to sequester more carbon than we are emitting in 2100). Given the present increase in the rate of emissions and CO2 concentrations, a near-term stabilization and decrease of emissions is not plausible.

Table 2. Two Global Climate Models (GCM) and a composite of five-model averaged GSMs scaled down to 1 by 1 km spatial resolution across Alaska used for permafrost dynamics simulation.

Project	Center	Model	Acronym
CMIP5/ AR5	National Center for Atmospheric Research	Community Earth System Model 4	NCAR-CCSM4
CMIP5/ AR5	NOAA Geophysical Fluid Dynamics Laboratory	Coupled Model 3.0	GFDL-CM3
CMIP5/ AR5	5-model averaged	Calculated as the mean of the 5 models	5-model average

6 Sensitivity Analysis

Uncertainties in the presented model lie in specifying the thermal parameters such as heat capacity of frozen and thawed soils and thermal conductivity. But mostly uncertainties are affected by thermal conductivity and the volumetric soil moisture content. The employed values for the soil properties are recovered by assimilating in situ temperature observations at a series of the Geophysical Institute, UAF and USGS sites across Alaska. The model is verified by comparing with available active layer thickness at the Circumpolar Active Layer Monitoring (CALM) sites, permafrost temperature, and snow depth records from existing permafrost observatories in Alaska. All of these datasets may contain some biases and errors. To gain some knowledge about how they act together and influence the results, we conduct a sensitivity analysis for a typical permafrost observing station at the region of discontinuous permafrost distribution. For a few other locations within continuous and sporadic permafrost regions, we obtained similar results.

For the Livengood station, a station with a typical natural condition at the interior Alaska, we analyze sensitivity of the mean annual ground temperature (MAGT) at 1 m depth and active layer thickness (ALT) with respect to the volumetric soil moisture content, thermal conductivity of thawed and frozen soils (Figure 4) and surface conditions. Our previous investigations shown that variations in the heat capacity frozen and thawed soils do not significantly affect the modeling results for ALT and MAGT (Marchenko 2008; Nicolsky et al. 2009; Wang 2012; Huang et al. 2014; Hirota et al. 2002). The obtained sensitivity results for thermal conductivity are shown in Figure 4. As the MAGT increased, the ALT increased also.

The most influence on the mean ALT and MAGT is imposed by the values of thermal conductivity of thawed soils (Figure 4). The most impact on the MAGT is imposed by the values of thermal conductivity of thawed and frozen soils for the first 0.25 m in depth and soil layers between 0.1 m and 1 m

in depth. The value of frozen conductivity affects the soil layer below 1 m, and soil water content for the layer between 0.1 and 1.0 m depth. Values of the thermal conductivity for the upper layers is a primary function of the organic matter content and soil moisture. It is probable that for the future long-term projections modeling runs it is necessary to incorporate a module of organic matter accumulation dynamics into the GIPL2-MPI model.

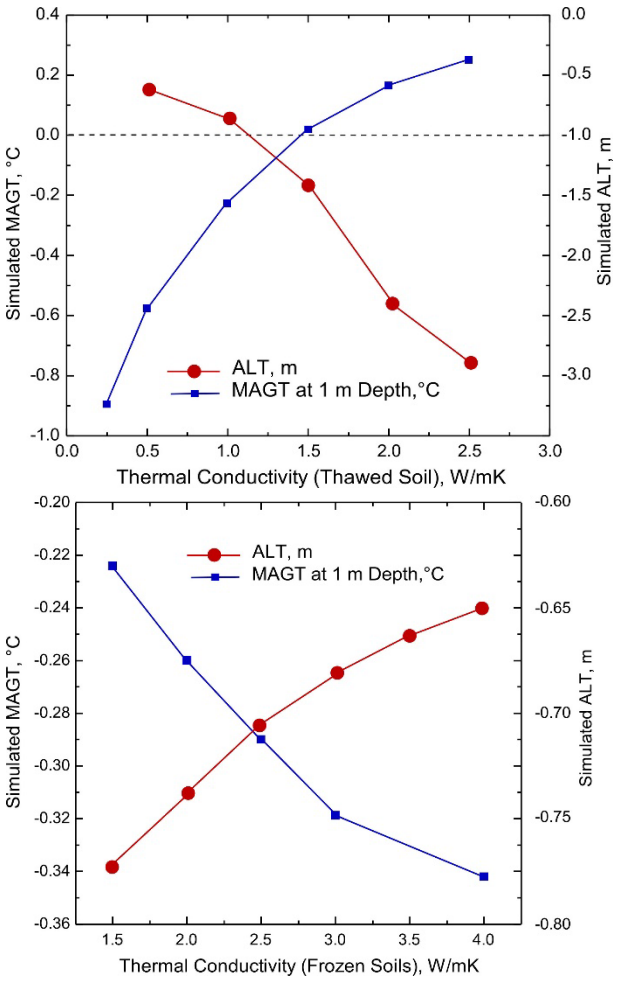

Figure 4. The sensitivity of the modeled MAGT at 1 m depth averaged for 1995–2020 (blue line with rectangles) and averaged ALT for the same period (red line with rounds) on changes in the thermal conductivity for the thawed and frozen materials for each soil layer for the Livengood Station.

7 Discussion

The developed model allows computations of the MAGT at different depths, ALT, and talik thickness projections into the future for various climate scenarios. In this research, we demonstrate the projections for two GCMs and five-model average only for RCP4.5 and RCP8.5 scenarios and illustrate a drastic difference in the future near-surface ground temperature regimes in 2070s and 2110s. For the RCP8.5 scenario, we found that ALT or top of permafrost deepening, up to 1.5 m on average in 2021, increases by a factor of 2.5 by 2070 and by a factor 3.5 from 2070 to 2120, according to the GFDL-CM3 RCP8.5 scenario. ALT continues to increase and widespread taliks starts to develop in interior Alaska and even at the North Slope region. According to NCAR-CCSM4 RCP8.5 scenario the factor of permafrost top deepening increased by 1.8 from 2021 to 2070 and by the factor of 3.2 from 2070 to 2120. Development of talik will have serious implications for ecosystems, human activities (infrastructure and subsistence lifestyle), and potential feedback to climate change. On the other hand, for the RCP4.5 scenario, the current model predicts only a modest increase in the near-surface permafrost temperatures and a limited degradation of the near-surface permafrost in the Alaska North Slope region. Finally, we mention that according to our computer experiments, to keep permafrost from the substantial thawing, the RCP4.5 scenario most likely needs to be a target for the greenhouse gas emissions.

8 Conclusions

As shown in the modeling result, the most significant changes in the upper layer (0.25–5.0 m) of ground temperature, active layer thickness as well as talik development, occurred under the climate scenario provided by the GFDL-CM3 climate model both 4.5 and 8.5 RCPs. As described by the IPCC the RCP4.5 is an intermediate scenario. Increase in soil temperature in RCP4.5 peaks around 2051–2070, then observed relative decline. RCP4.5 is more likely than not to result in global temperature rise between 2.5 °C and 3.5 °C, by 2120. In RCP8.5, ground temperature continues to rise throughout the 21st century.

The GFDL-CM3 provides more aggressive climate change scenario in comparison with NCAR-CCSM4 climate model. Under the same ecosystem conditions, the greatest changes in permafrost occur according to the GFDL-CM3, mostly under RCP-8.5 scenario.

9 Acknowledgements

This project funded under the Department of Defense (DoD), U.S. Army Engineer Research and Development Center (ERDC), the Cold Regions Research and Engineering Laboratory (CRREL) under Contract No. W913E521C0010. The GIPL2-MPI/GCM simulations were supported in part by the high-performance computing and data storage resources operated by the Research Computing Systems Group at the University of Alaska Fairbanks Geophysical Institute.

10 References

Alifanov, O. 1994. *Inverse Heat Transfer Problems*. Springer, Berlin.

Alifanov, O., Artyukhin, E., and Rumyantsev, S. 1996. *Extreme Methods for Solving Ill-Posed Problems with Application to Inverse Heat Transfer Problems*. New York, New York, United States: Begell House.

Biskaborn, B.K., Smith, S.L., Noetzli, J. et al. 2019. 'Permafrost is warming at a global scale', *Nature Communication* 10, 264(2019). Available at: https://doi.org/10.1038/s41467-018-08240-4.

Fiddes, J., Endrizzi, S., and Gruber, S. 2015. 'Large-area land surface simulations in heterogeneous terrain driven by global data sets: Application to mountain permafrost', *Cryosphere* 9, pp. 411–426.

Gisnås, K., Etzelmüller, B., Farbrot, H., Schuler, T., and Westermann, H. 2013. 'CryoGRID 1.0: Permafrost distribution in Norway estimated by a spatial numerical model', *Permafrost Periglacial Processes* 24, pp. 2–19.

He, Y., Genet, H., McGuire, A.D., Zhuang, Q., Wylie, B.K., and Zhang, Y. 2016. 'Terrestrial carbon modeling - Baseline and projections in lowland ecosystems of Alaska', in Z. Zhu and A.D. McGuire (eds.), *Baseline and projected future carbon storage and greenhouse-gas fluxes in ecosystems of Alaska*. U.S. Geological Survey Professional Paper 1826, pp. 133–158. Available at: https://doi.org/10.3133/pp1826.

Hirota, T., Pomeroy, J.W., Granger, R.J. and Maule, C.P. 2002. 'An extension of the force-restore method to estimating soil temperature at depth and evaluation for frozen soils under snow', *Journal of Geophysical Research* 107, pp. 4767.

Huang, F., Zhan, F., Ju, W., and Wang, Z. 2014. ,Improved reconstruction of soil thermal field using two-depth measurements of soil temperature', *Journal of Hydrology* 519, Part A, pp. 711–719.

IPCC 2014. 'Climate Change 2014: Synthesis Report', in R.K. Pachauri and L.A. Meyer (eds.) *Fifth Assessment Report of the Intergovernmental Panel on Climate Change*. Geneva, Switzerland: Contribution of Working Groups I, II and III, 151 pp.

Jafarov, E., Marchenko, S., and Romanovsky, V.E. 2012. 'Numerical Modeling of Permafrost Dynamics in Alaska Using a High Spatial Resolution Dataset', *The Cryosphere* 6, pp. 613–624.

Jorgenson, T., Yoshikawa, K., Kanevskiy, M., Shur, Y., Romanovsky, V., Marchenko, S., Grosse, G., Brown, J., and Jones, B. 2008. 'Permafrost Characteristics of Alaska', in D. Kane and K. Hinkel (eds.), *Ninth International Conference on Permafrost*. Fairbanks, Alaska, United States: June 29–July 3, 2008, pp. 121–122.

Marchenko, S.S. and Gorbunov, A.P. 1997. 'Permafrost Changes in the Northern Tien Shan Mountains during the Holocene', *Permafrost and Periglacial Processes* 8, pp. 427–435.

Marchenko, S., Romanovsky, V., and Tipenko, G. 2008. 'Numerical Modeling of Spatial Permafrost Dynamics in Alaska', in D. Kane and K. Hinkel (eds.), *Proceedings of the Ninth International Conference on Permafrost*. Fairbanks, Alaska, United States: June 29–July 3, 2008, pp. 1125–1130.

Moss, R.H., et al. 2008. *Towards New Scenarios for Analysis of Emissions, Climate Change, Impacts, and Response Strategies*. Geneva, Switzerland: Intergovernmental Panel on Climate Change, 132 pp.

Nicolsky, D., Romanovsky, V., and Panteleev, G.G. 2009. 'Estimation of soil thermal properties using in-situ temperature measurements in the active layer and permafrost', *Cold Regions Science and Technology* 55, pp. 120–129.

Osterkamp, T.E. and Jorgenson, J.C. 2006. 'Warming of Permafrost in the Arctic National Wildlife Refuge', Alaska', *Permafrost and Periglacial Processes* 17, pp. 65–69. doi:10.1002/ppp.538.

Osterkamp, T.E. (2007). 'Characteristics of the recent warming of permafrost in Alaska', *Journal of Geophysical Research* 112(F2): F02S02. doi:10.1029/2006JF000578.

Osterkamp, T.E. 2005. 'The recent warming of permafrost in Alaska', *Global and Planetary Change* 49, pp. 187–202.

Osterkamp, T.E. 2008. 'Thermal state of permafrost in Alaska during the fourth quarter of the twentieth century', in D. Kane and K. Hinkel (eds.) *Proceedings of the Ninth International Conference on Permafrost*. Fairbanks, Alaska, United States: June 29–July 3, 2008, pp. 1333–1338.

Romanovsky, V.E., Marchenko, S.S., Daanen, R., Sergeev, D.O., and Walker, D.A. 2008. 'Soil Climate and Frost Heave Along the Permafrost/Ecological North American Arctic Transect', in D. Kane and K. Hinkel (eds.) *Proceedings of the Ninth International Conference on Permafrost*. Fairbanks, Alaska, United States: June 29–July 3, 2008, pp. 1519–1524.

Romanovsky, V.E., Smith, S.L., and Christiansen, H.H. 2010. 'Permafrost Thermal State in the Polar Northern Hemisphere during the International Polar Year 2007–2009: a Synthesis', *Permafrost and Periglacial Processes* 21, pp. 106–116. doi:10.1002/ppp.689.

Shur Y.L. and Jorgenson M.T. 2007. 'Patterns of permafrost formation and degradation in relation to climate and ecosystems', *Permafrost and Periglacial Processes* 18, pp. 7-19.

Smith, S., Romanovsky, V., Lewkowicz, A., Burn, C., Allard, M., Clow, G., Yoshikawa, K., and Throop, J. 2010. 'Thermal state of permafrost in North America: A contribution to the International Polar Year', *Permafrost Periglacial Processes* 21, pp. 117–135.

Tikhonov, L. and Leonov, A. 1996. *Nonlinear Ill-posed Problems. Vol. 14 of Applied Mathematics and Mathematical Computation Series*. London: Chapman and Hall.

van Vuuren, D.P., Edmonds, J., Kainuma, M. et al. 2011. 'The representative concentration pathways: an overview', *Climatic Change* 109(5). Available at: https://doi.org/10.1007/s10584-011-0148-z.

Wang, Z.H. 2012. 'Reconstruction of soil thermal field from a single depth measurement', *Journal of Hydrology* 464–465, pp. 541–549.

Westermann, S., Schuler, T., Gisnås, K., and Etzelmüller, B. 2013. 'Transient thermal modeling of permafrost conditions in southern Norway', *Cryosphere* 7, pp. 719–739.

Weyant, J., Azar, C., Kainuma, M., Kejun, J., Nakicenovic, N., Shukla, P.R., La Rovere, E., and Yohe, G. 2009. *Report of 2.6 Versus 2.9 Watts/m2 RCPP Evaluation Panel (PDF)*. Geneva, Switzerland: IPCC Secretariat.

Zhang, Y., Wang, X., Fraser, R., Olthof, I., Chen, W., Mclennan, D., Ponomarenko, S., and Wu, W. 2013, 'Modelling and mapping climate change impacts on permafrost at high spatial resolution for an Arctic region with complex terrain', *Cryosphere* 7, pp. 1121–1137.

Appendix A. Result of the GIPL2-MPI Spatial and Temporal Permafrost Dynamics Modeling.

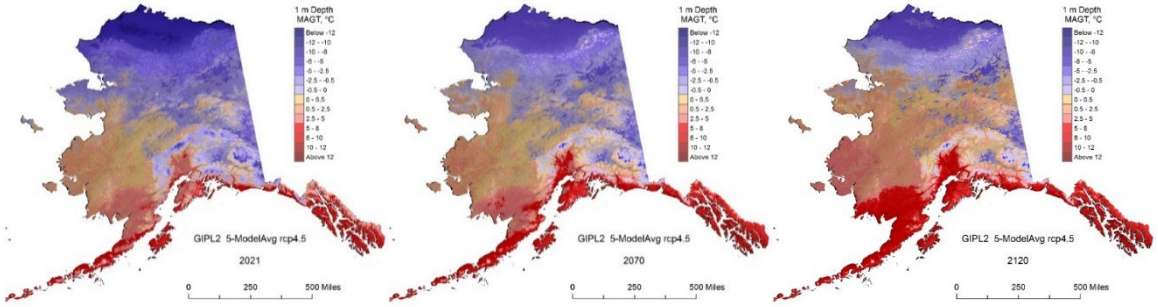

A B C

Figure 5. The GIPL2-MPI modeled mean annual ground temperature at 1 m depth for 2021 (A), 2070 (B) and 2120 (C) using five-model average RCP4.5 as a climate forcing.

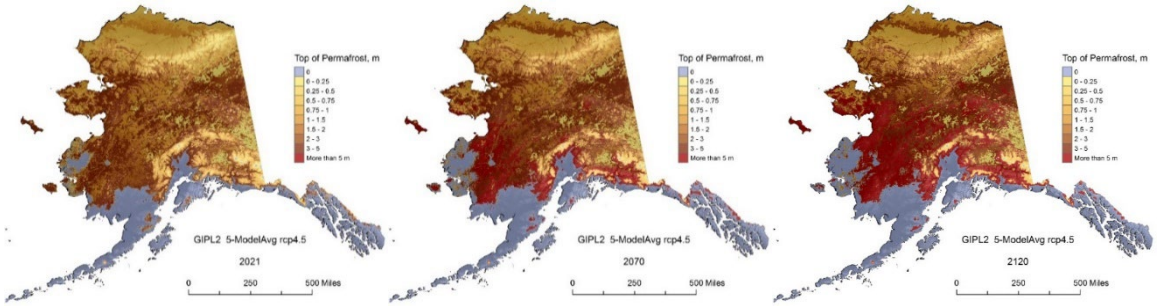

A B C

Figure 6. The GIPL2-MPI modeled top of permafrost (permafrost table) position for 2021 (A), 2070 (B) and 2120 (C) using five-model average RCP4.5 as a climate forcing.

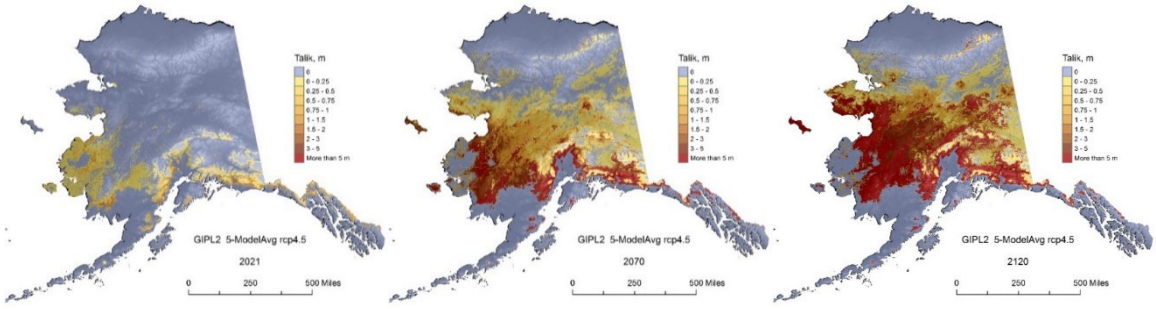

A B C

Figure 7. The GIPL2-MPI modeled Talik thickness for 2021 (A), 2070 (B) and 2120 (C) using five-model average RCP4.5 as a climate forcing.

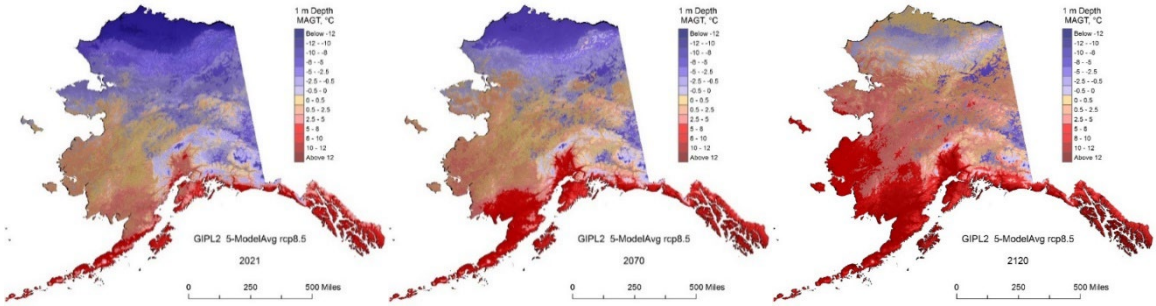

A B C

Figure 8. The GIPL2-MPI modeled mean annual ground temperature at 1 m depth for 2021 (A), 2070 (B) and 2120 (C) using five-model average RCP8.5 as a climate forcing.

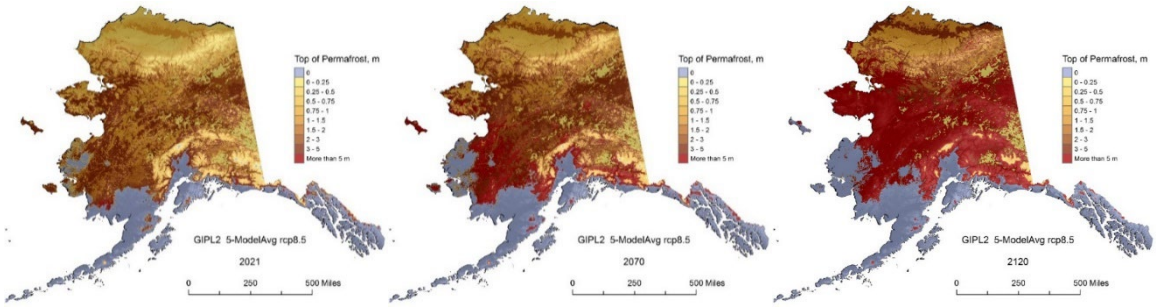

A B C

Figure 9. The GIPL2-MPI modeled top of permafrost (permafrost table) position for 2021 (A), 2070 (B) and 2120 (C) using five-model average RCP8.5 as a climate forcing.

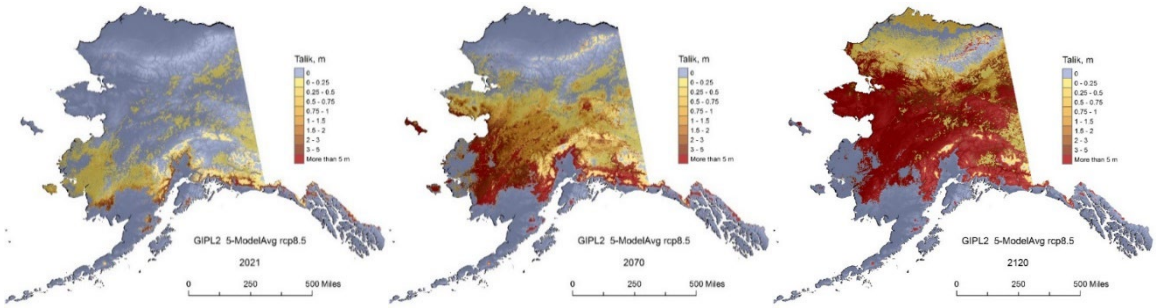

A B C

Figure 10. The GIPL2-MPI modeled Talik thickness for 2021 (A), 2070 (B) and 2120 (C) using five-model average RCP8.5 as a climate forcing.

Collaborative workflow among first nations, territorial governments and consultants for mapping geohazards in three communities in northern Canada

Robin McKillop[1], Shirley McCuaig[1] & Jim Coates[2]
[1]*Palmer, Vancouver, British Columbia, Canada*
[2]*Kryotek Arctic Innovation, Whitehorse, Yukon, Canada*

ABSTRACT

The rapidity of landscape response to climate change in Boreal to Arctic regions has spurred geohazard mapping in Canada's northern communities. Such mapping is critical to planning-level decisions regarding existing and proposed land use and infrastructure. Limited availability of geotechnical data, community remoteness, accessibility limitations, and local ground sensitivity pose special challenges for such mapping initiatives. A cost-effective, collaborative workflow for community-scale geohazard mapping involving First Nations, territorial governments and consultants, each of which has distinct roles, is outlined based on experience gained through three case studies in Yukon. In Carmacks, Little Salmon/Carmacks First Nation highlighted its mapping priorities and evaluated different approaches, then Yukon Government contributed funding and field resources to consultant-led mapping initiatives. In Whitehorse, Kwanlin Dün First Nation scoped and commissioned a consultant-led, geohazard and development constraints mapping project that leveraged new, community-scale surficial geology mapping and permafrost investigations completed by Yukon Geological Survey. In Aishihik Village, at the north end of Aishihik Lake, Champagne and Aishihik First Nations meaningfully contributed to permafrost-related geohazard mapping through assistance with field research and sharing of observations and experiences of landscape changes that predate historical (aerial photography) records. These mapping projects highlight the value of multi-party collaboration, which might also or alternatively involve academic institutions, and underscore the importance of territorial governments and consultants actively seeking opportunities to engage First Nations in northern communities in the development of mapping products on which they will be basing decisions about land use and infrastructure in the years to come.

1 INTRODUCTION

Climate is changing more rapidly in northern regions of Canada, where permafrost and remoteness increase the vulnerability of communities, than in the more densely populated southern parts of the country. The effects of climate change differ from community to community, but new challenges for land use and infrastructure planning are common. Northerners are scrambling to adapt to, or mitigate, the risks associated with geohazards, such as thermokarst activity and associated retrogressive thaw-flows (e.g., Kokelj et al. 2015; Kokelj et al. 2017), mass movements including shallow (e.g., active-layer detachments) and deep-seated landslides (e.g., Blais-Stevens et al. 2014), riverine or coastal flooding and erosion (e.g., Irrgang et al. 2019; Douglas and Lamb 2024), and wildfires (e.g., McCoy and Burn 2005; Lipovsky et al. 2006). All are exacerbated by the warming and degradation (thaw) of permafrost, which is accelerating in response to climate change.

Despite exposure to a variety of climate-related geohazards, northern communities tend to have the least and lowest quality information on which to base important decisions regarding existing and proposed land use and infrastructure. Territorial and First Nation governments in Canada have recognized this knowledge gap and have taken steps to better inform northern communities about geohazards that may affect them. Geohazard mapping initiatives spearheaded by government and commonly supported by academia have, for example, produced geohazard maps for a number of communities in Yukon (e.g., Benkert et al. 2015; Cronmiller et al. 2020), regional-scale thermokarst mapping (Kokelj et al. 2023) and community-scale surficial geology mapping in communities in Northwest Territories (various 1:10,000 to 1:30,000 maps awaiting publication as open files), landscape hazard maps for communities in Nunavut (e.g., Forbes et al. 2014), and permafrost-related risk maps for the Nunavik region of northern Quebec (e.g., Allard et al. 2020). Still, many northern communities remain with little to no geohazard-related information.

Consultants offer such communities a means of expediting the preparation of geohazard maps, by drawing on internal resources, flexible scheduling and practical experience, although this efficiency must be weighed against the potential cost-savings and opportunity for additional field rigour associated with academic involvement. Exactly which collaborators are best able to meet the needs of communities, and with what roles and timelines, should be established prior to project commencement.

Drawing on experience from case studies in Carmacks, Whitehorse, and Aishihik Village, Yukon (Figure 1), this paper outlines a collaborative workflow among representatives from First Nations, territorial governments and consultants for community-scale geohazard mapping in northern Canada. It demonstrates effective approaches, the importance of engagement of all parties, and highlights opportunities for improvement. This workflow aims to inspire and guide future collaboration in geohazard mapping projects in northern communities.

https://doi.org/10.52381/ICOP2024.230.1

1.1 Effects of Climate Change on Northern Geohazards

The rapidity of climate change in Yukon has important implications for permafrost and associated geohazards. Perrin and Jolkowski (2022) document a consistent increase in average Yukon air temperature since the mid-1900s, with an increase of 2 °C over the past 50 years, and a possible slight increase in average annual precipitation. Wildfire activity may also be increasing in frequency and severity (McCoy and Burn 2005). The resultant thickening of the active layer is altering surface hydrology and flood patterns, accelerating thermokarst activity in areas of ice-rich permafrost, increasing the vulnerability of coastal bluffs and riverbanks to erosion, and increasing the distribution, frequency and magnitude of landslides. Reductions in sea ice extent within the Beaufort Sea (Perrin and Jolkowski 2022) compound the effects of permafrost degradation by increasing exposure of Yukon's northern coastline to waves.

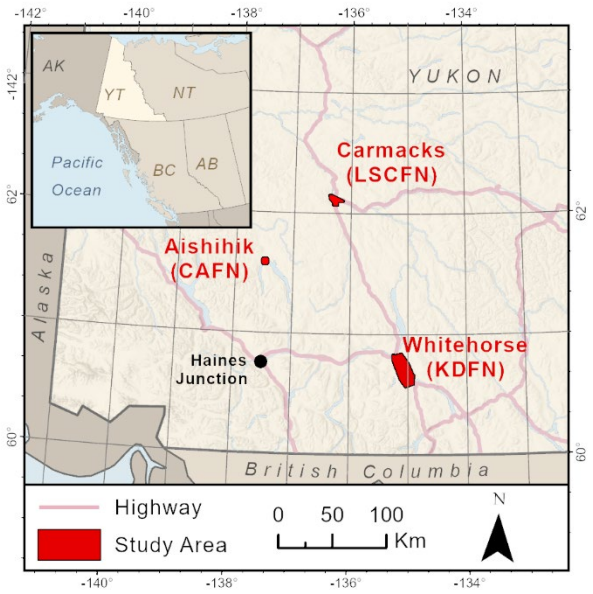

Figure 1. Study areas of community-scale geohazard mapping case studies in Carmacks (LSCFN = Little Salmon/Carmacks First Nation), Whitehorse (KDFN = Kwanlin Dün First Nation), and Aishihik (CAFN = Champagne and Aishihik First Nations) in southern Yukon, Canada.

Air temperatures and precipitation are both expected to continue increasing in Yukon, albeit at rates and with magnitudes that differ depending on the projected greenhouse gas emission scenario (Perrin and Jolkowski 2022). Extrapolation of temperature trend data, for three unique greenhouse gas emission scenarios, projects continued increases by 1.0 °C (RCP 2.6) to 6.0 °C (RCP 8.5) by 2100, while precipitation is projected to increase by 4 to 17% over the next 50 years (Perrin and Jolkowski 2022). The response of geohazards will continue to vary spatially according to differences in topography, surficial materials, vegetation cover, ground temperature and ground ice content. Overall, geohazards are expected to increase in distribution, frequency, and magnitude, which underscores the importance of better informing northern communities of the nature and distribution of these phenomena.

2 Geohazard Mapping Case Studies in Three Yukon Communities

Highlights from community-scale geohazard mapping projects within prioritized areas of the Traditional Territories of Little Salmon/Carmacks First Nation (LSCFN; Carmacks; L), Kwanlin Dün First Nation (KDFN; Whitehorse; K) and Champagne and Aishihik First Nations (CAFN; Aishihik; C) are provided below, with emphasis on the roles of each collaborator (Table 1). The maps informed the communities of the general distribution, characteristics and implications of geohazards, although they are not a substitute for site-specific geotechnical investigation. All three projects were substantially, if not fully, completed prior to release of the Risk-based Approach for Community Planning in Northern Regions – Requirements and Guidance (Bureau de normalisation due Québec 2023), but future similar projects will benefit from review and adoption of applicable elements of this pertinent resource.

Table 1. Summary of collaborator roles and responsibilities in three community-scale geohazard mapping projects in Yukon.

Task	Consultant			Territorial Government			First Nation		
1. Scoping and Kick-off	L	K	C		K		L	K	C
2. Preliminary Mapping	L	K	C		K				
3. Field Investigation	L	K	C	L	(K)			(K)	C
4. Final Mapping and Reporting	L	K	C	L	K		L	K	C

Notes:

Mapping project examples: Little Salmon/Carmacks (L), Kwanlin Dün (K) and Champagne and Aishihik (C) First Nations.

Parentheses indicate participation invited but timing failed.

For clarity, the first row indicates that consultants were involved in scoping all three mapping projects, as were First Nations for their respective mapping projects, but that the territorial government only supported scoping for the project within the Traditional Territory of KDFN (K).

2.1 Carmacks – Little Salmon/Carmacks First Nation

LSCFN was advancing efforts to update its Official Community Plan in Carmacks, Yukon (Figure 1). Carmacks is located in a formerly glaciated, level to hilly section of the Yukon River valley in central Yukon in the zone of extensive discontinuous permafrost (Heginbottom et al. 1995). LSCFN reviewed, helped refine and ultimately commissioned an initial scope of work involving desktop-based, interpretive mapping of land development

constraints in its settlement lands within Carmacks. The results of this unpublished mapping emphasized the importance of LSCFN gaining a broader understanding of geohazard susceptibility in the surrounding area, where development interests and plans for government-led upgrades to road infrastructure were being pursued. Yukon Government then spearheaded a consultant-led project to map and field-check local susceptibilities to fluvial, hillslope and permafrost processes within a broader area encompassing LSCFN's settlement lands.

Consultant-led, 1:15,000-scale surficial geology mapping was completed, in accordance with Yukon Geological Survey's adaptation of the Terrain Classification System for British Columbia (Howes and Kenk 1997), based on interpretation of stereo-aerial photography, satellite imagery and LiDAR-derived topographic data (Cronmiller et al. 2020). The surficial geology mapping, with reference to complementary spatial data (e.g., digital elevation models, riverbank erosion mapping, permafrost probability mapping (Bonnaventure et al. 2012)), was then reclassified into individual and composite hazard susceptibilities based on the approach used by Benkert et al. (2015; Figure 2).

Field reconnaissance to enable validation and refinement of the mapping was completed collaboratively by a representative from the consultant mapping team and the Yukon Geological Survey (territorial government). This partnership took advantage of the local knowledge and field resources (e.g., truck, equipment) of the territorial government and the mapping expertise and experience of the consultant. Measurements were made of riverbank position, relative to at-risk property or infrastructure, for baseline reference for any future monitoring undertaken by LSCFN or the territorial government.

A corresponding report drafted by the consulting team, reviewed by the territorial government and shared with LSCFN, was ultimately published by the Yukon Geological Survey to explain and make public the geohazard susceptibility mapping for Carmacks (Cronmiller et al. 2020).

2.2 Whitehorse – Kwanlin Dün First Nation

KDFN was interested in better positioning itself to evaluate proposals for land and infrastructure development within its settlement lands in the City of Whitehorse and more broadly in its encompassing Traditional Territory. Whitehorse is situated in a broad, formerly glaciated valley of southern Yukon (Figure 1), with diverse landform assemblages, including glaciolacustrine terraces, hummocky glaciofluvial complexes, and steep bedrock slopes. It is located in the zone of sporadic discontinuous permafrost (Heginbottom et al. 1995). Degrading permafrost slopes, riverine flooding and erosion, and landsliding, in particular, pose challenges for existing and proposed infrastructure. Based on advice received from the territorial government, KDFN retained a consultant to produce maps of land development constraints (including geohazards) within the limits of the City of Whitehorse, to help guide its land use planning.

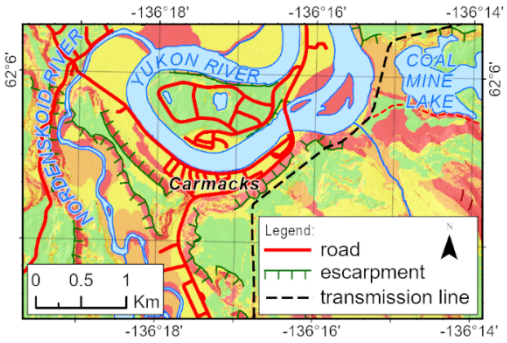

1:50 000 scale topographic base data (incl. 10 m contours) produced by CENTRE FOR TOPOGRAPHIC INFORMATION, NATURAL RESOURCES CANADA

HAZARD SUSCEPTIBILITY CLASSIFICATION

Low susceptibility: Characterized by flat to gently-sloped terrain, devoid of ice-rich permafrost, and distant from watercourses prone to flooding or erosion. This terrain typically comprises well-drained eolian, glaciofluvial, till, bedrock, or anthropogenic materials.

Moderate susceptibility: Characterized by moderately sloping materials and inactive fluvial terraces susceptible to only rare extreme flood events. Fluvial erosion is not expected. Landslide initiation and gully erosion are unlikely. Where permafrost is probable, materials are coarse and susceptibility to thermokarst is low.

Moderately high susceptibility: Characterized by moderately steep to steep slopes where landslide initiation is rare. Permafrost is common but with low to moderate susceptibility to thermokarst. Inactive fluvial plains and active fluvial fans susceptible to uncommon flood events.

High susceptibility: Characterized by steep slopes, landslide initiation, fluvial erosion or frequent flood activity, and permafrost in fine-grained or organic materials. Active fluvial plains or areas of seasonal inundation are included in this category. Includes areas that may be susceptible to fluvial erosion within a 50-year forecast period. Areas of permafrost may be susceptible to thermokarst.

Figure 2. Excerpt from community-scale geohazard mapping for Carmacks, Yukon (reproduced from digital data from Cronmiller et al. 2020). The four-level classification depicted on this map (red = high, orange = moderately high, yellow = moderate, and green = low) represents a composite susceptibility to permafrost (thermokarst), hillslope (landslides) and fluvial (flooding and erosion) hazards.

KDFN was fully involved in project scoping, including the establishment of the mapping area, scale and legend protocols, drawing on its familiarity with previous, similar mapping projects in the region. The consultant-led mapping, which so far remains unpublished, was based on a semi-automated reclassification of 1:15,000-scale surficial geology mapping recently completed by the territorial government for the Whitehorse area (Lipovsky 2023) and complementary spatial data, such as Whitehorse area permafrost thaw sensitivity mapping produced by Roy

et al. (2021). Erosion hazard zones were additionally delineated alongside riverbanks based on projection from time-averaged rates and trajectories of channel migration since 1946 (Figure 3). The resultant mapping for KDFN differentiates areas (as defined by pre-mapped surficial geology units) according to the applicability and relative severity of up to seven distinct constraints for development, including geohazards (flooding, erosion, landslides, thermokarst) and phenomena that complicate construction (shallow bedrock, steep topography, compressible/weak soils, poor surface drainage).

Preliminary, desktop-based mapping and reporting were reviewed by representatives from both KDFN and Yukon Geological Survey. Limited field reconnaissance was conducted by the consultant mapping team, when last-minute unavailability meant KDFN members or Yukon Geological Survey staff were unable to participate. Field checks were completed, and representative photographs were taken to help illustrate different geohazards and development constraints for improved understanding and use by KDFN. KDFN subsequently allowed Yukon Government to use and refine the results of the constraints mapping to inform local-scale, comparative evaluation of two areas for future urban expansion.

2.3 Aishihik – Champagne and Aishihik First Nations

CAFN maintain, and seasonally use, a small village at the north end of Aishihik Lake, in southwestern Yukon (Figure 1). Yukon Energy Corporation regulates Aishihik Lake for the production of hydroelectricity through the Aishihik Generating Station. The lake is situated in a valley that, during deglaciation of the region, was occupied by a much larger lake into which fine-grained glaciolacustrine sediments were deposited. It is located within the zone of sporadic discontinuous permafrost (Heginbottom et al. 1995). CAFN was forced to abandon and relocate Aishihik Village from the original, delta-front site to the mainland across a small bay after its citizens expressed concerns about accelerating subsidence and shoreline recession.

CAFN established a collaborative approach to support Yukon Energy Corporation in its relicensing of the Aishihik Generating Station. As part of the relicensing process for the station, a consulting team was tasked with investigating and mapping permafrost-related instabilities along the shoreline of Aishihik Lake (McKillop et al. 2019). Preliminary field reconnaissance in the vicinity of Aishihik Village revealed shoreline landforms comprising fine sands with 0.45 m to more than 1.2 m thick active layers overlying ice-rich permafrost. The ice-rich permafrost was inferred from abundant field evidence of active thermokarst (e.g., tilted trees, tension cracks, retrogressive thaw-flows), as well as relatively rapid recession of lake and inland-pond shorelines that predates hydroelectric operations based on comparative analysis of historical aerial photographs (Figure 4). The current limits of areas of active subsidence or erosion were benchmarked for later comparison to monitoring data.

Subsequent field investigations leveraged the assistance, local knowledge, and historical accounts of a CAFN member. Reporting in support of the relicensing application was thoroughly reviewed by YEC and CAFN to ensure findings provided a wholesome reflection of observations and experiences.

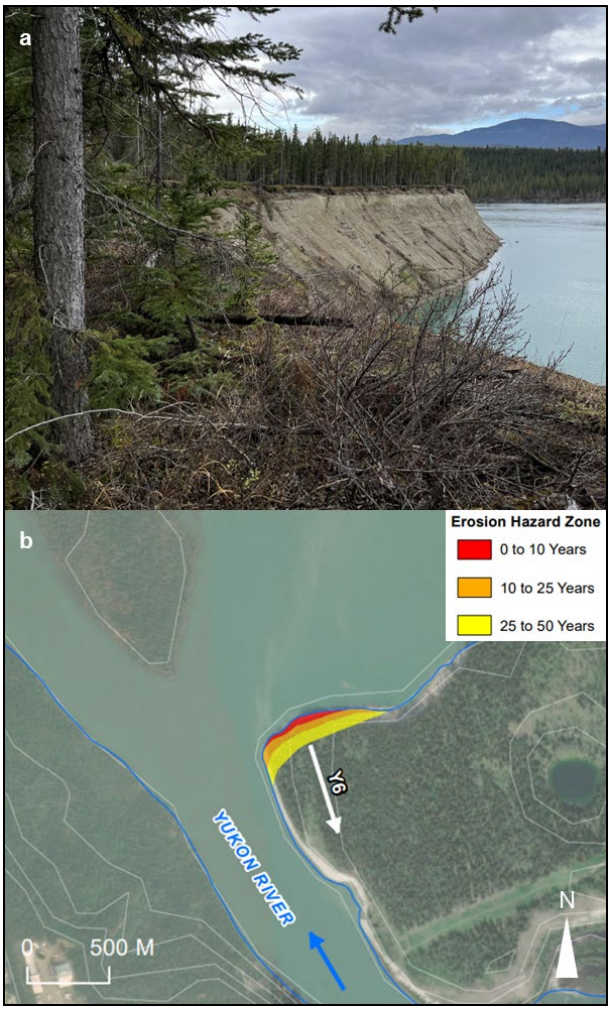

Figure 3. Erosion-prone scarp along Yukon River, within the Whitehorse city limits and Traditional Territory of KDFN (a), and corresponding excerpt of mapping of erosion hazard zones based on extrapolation of time-averaged rates and trajectories of recent bank recession (b) The rate of bank recession at Y6, for example, is 0.9 m/year.

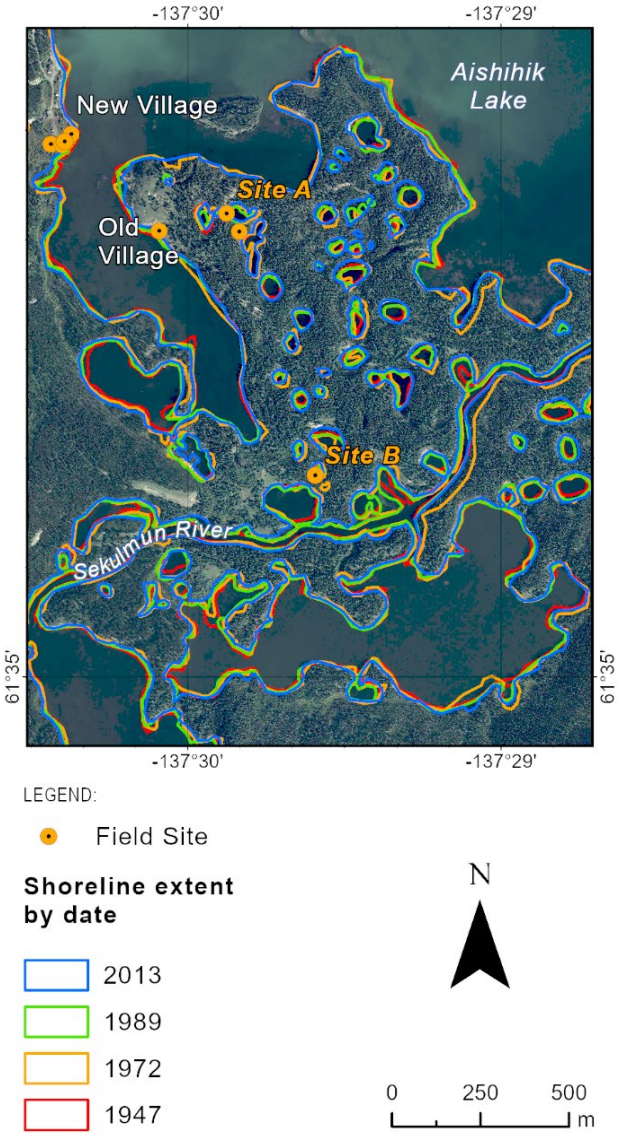

Figure 4. Thermokarst-induced recession of pond and lake shorelines, between 1947 and 2013, near the Aishihik Village sites at the north end of Aishihik Lake, Yukon. Delineations were based on field reconnaissance and comparison of shoreline positions in historical aerial photography. Investigations at sites A and B revealed variable thaw depths in deltaic fine sands, tilted trees and tension cracks along actively slumping shorelines, and pond levels that are elevated above, and isolated from, water levels in Aishihik Lake.

3 Collaborative Workflow for Geohazard Mapping

A collaborative workflow for community-scale geohazard mapping in northern communities is proposed based on the successes and limitations of each of the three case studies outlined above, professional experience in other similar mapping projects, pertinent findings from retrospective evaluations of community-scale geohazard mapping in northern Canada (Flynn et al. 2019; Northern Futures Planning 2019), and the new standard and guidance for risk-based community planning in northern regions (Bureau de normalisation due Québec 2023; Figure 5). The workflow is divided into four sequential "phases", each of which involves the completion of several main tasks. The key contributions to each task of each of the three collaborators – First Nation, Territorial Government, and Consultant – are described along with colour-coded differentiation of lead (green) and supporting (peach) responsibilities. A typical minimum turnaround time for each of the phases, allowing for inter-organizational communication and feedback, is provided for context. Highlights of each phase are summarized below:

- Scoping and Kick-off (Phase 1) is critical to the success of any mapping project. It involves the establishment of study area, objectives, data sources, deliverable format(s), timeline and associated cost. The expected rigour of field investigations is best determined at this stage. The consultant and First Nation must be involved, and territorial government involvement is optional; in some cases, the territorial government advises and assists the First Nation in scoping the project.
- Preliminary Mapping (Phase 2) begins following the completion of a comprehensive background review, consultation with knowledge-keepers within the First Nation and territorial government (especially to identify any relevant, unpublished sources of information), and finalization of mapping protocols and legends to ensure results are understandable to the target audience(s). Interpretations are made based on the best available spatial data (e.g., aerial/satellite imagery, topography, geophysics, geotechnical). Recognition of surface indicators of existing or potential instability, and corresponding landform associations, is fundamental to extrapolation of results over broad areas with limited site-specific data. The consultant leads this task, with optional input from the territorial government and/or First Nation.
- Field Investigation (Phase 3) is necessary, at least at a reconnaissance level, to ground truth desktop-based interpretations and collect additional information that cannot be interpreted remotely. It also provides a valuable opportunity to take photographs representative of the diversity of conditions within the study area, which can help illustrate the meaning of different map units to community members and other stakeholders. Field investigations could additionally involve geotechnical drilling, geophysical surveys, and/or instrumentation for long-term monitoring purposes (ideally supported by the local First Nation, especially in dynamic landscapes). The consultant typically leads this task, but is encouraged to involve representatives of the territorial government and/or First Nation to maximize opportunities for on-site information sharing.

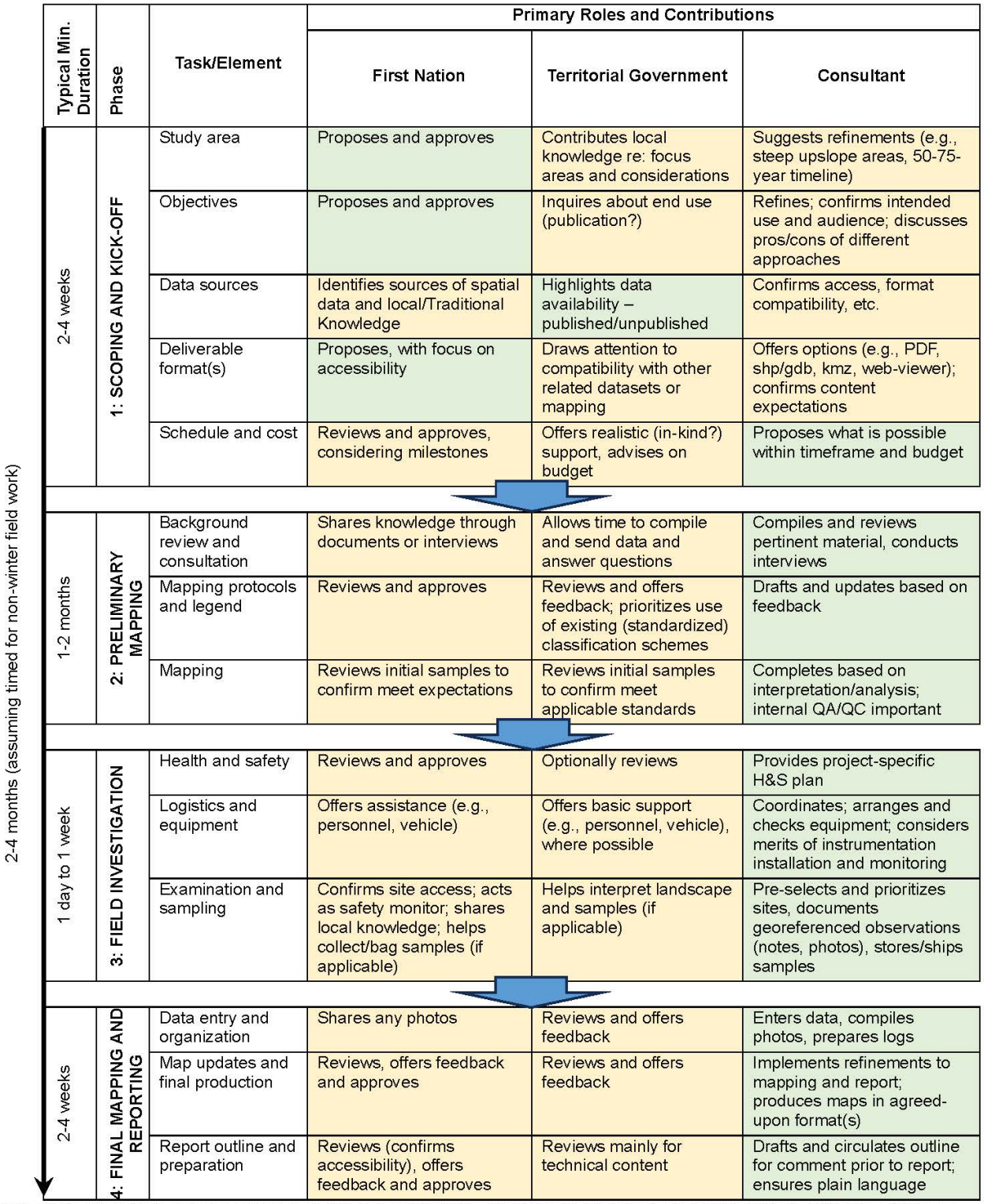

Typical Min. Duration	Phase	Task/Element	Primary Roles and Contributions		
			First Nation	Territorial Government	Consultant
2-4 weeks	1: SCOPING AND KICK-OFF	Study area	Proposes and approves	Contributes local knowledge re: focus areas and considerations	Suggests refinements (e.g., steep upslope areas, 50-75-year timeline)
		Objectives	Proposes and approves	Inquires about end use (publication?)	Refines; confirms intended use and audience; discusses pros/cons of different approaches
		Data sources	Identifies sources of spatial data and local/Traditional Knowledge	Highlights data availability – published/unpublished	Confirms access, format compatibility, etc.
		Deliverable format(s)	Proposes, with focus on accessibility	Draws attention to compatibility with other related datasets or mapping	Offers options (e.g., PDF, shp/gdb, kmz, web-viewer); confirms content expectations
		Schedule and cost	Reviews and approves, considering milestones	Offers realistic (in-kind?) support, advises on budget	Proposes what is possible within timeframe and budget
1-2 months	2: PRELIMINARY MAPPING	Background review and consultation	Shares knowledge through documents or interviews	Allows time to compile and send data and answer questions	Compiles and reviews pertinent material, conducts interviews
		Mapping protocols and legend	Reviews and approves	Reviews and offers feedback; prioritizes use of existing (standardized) classification schemes	Drafts and updates based on feedback
		Mapping	Reviews initial samples to confirm meet expectations	Reviews initial samples to confirm meet applicable standards	Completes based on interpretation/analysis; internal QA/QC important
1 day to 1 week	3: FIELD INVESTIGATION	Health and safety	Reviews and approves	Optionally reviews	Provides project-specific H&S plan
		Logistics and equipment	Offers assistance (e.g., personnel, vehicle)	Offers basic support (e.g., personnel, vehicle), where possible	Coordinates; arranges and checks equipment; considers merits of instrumentation installation and monitoring
		Examination and sampling	Confirms site access; acts as safety monitor; shares local knowledge; helps collect/bag samples (if applicable)	Helps interpret landscape and samples (if applicable)	Pre-selects and prioritizes sites, documents georeferenced observations (notes, photos), stores/ships samples
2-4 weeks	4: FINAL MAPPING AND REPORTING	Data entry and organization	Shares any photos	Reviews and offers feedback	Enters data, compiles photos, prepares logs
		Map updates and final production	Reviews, offers feedback and approves	Reviews and offers feedback	Implements refinements to mapping and report; produces maps in agreed-upon format(s)
		Report outline and preparation	Reviews (confirms accessibility), offers feedback and approves	Reviews mainly for technical content	Drafts and circulates outline for comment prior to report; ensures plain language

Note: Green and peach shading denote lead role and support role, respectively. Durations are typical minima, depending on scope, size and complexity of the study area, and collaborator availabilities.

Figure 5. Framework for collaborative geohazard mapping workflow among First Nations, territorial governments and consultants.

- Final Mapping and Reporting (Phase 4) involves updating and finalizing mapping based on observations and measurements from field investigations (Phase 3). An accompanying report explains the mapping and its implications for the First Nation, with at least a plain-language summary to ensure understanding. All mapping is provided digitally, optimally including in accessible formats such as a Google Earth KMZ file, and is accompanied by applicable metadata. Delivery of hard copy maps is also an option. Although reporting is led by the consultant, it is expected that the First Nation and, potentially, the territorial government will review and provide feedback. The territorial government may also publish the results, if acceptable to the First Nation, thereby improving broader accessibility.

4 Conclusions and Geohazard Mapping Priorities

The geohazard mapping projects that have been showcased for three Yukon First Nations demonstrate the value of, and a variety of opportunities for, collaboration among First Nations, territorial governments, and consultants. First Nations must have a role in scoping mapping projects so that deliverables best meet their current and future needs and are easily understood by a diverse audience. Preliminary mapping is typically led by a qualified consulting team, but can be coordinated with related initiatives by the territorial government for efficiencies. Field investigations are optimally coordinated among at least two of the three collaborators to provide opportunities for on-site information exchange. Where possible, key field sites should be instrumented as a comparative reference for future monitoring. Consultant-led reporting to accompany and explain the map product(s) is best reviewed by both the First Nation and the territorial government to ensure representation of different perspectives.

Post-mapping follow-up with each of the three communities is warranted to better understand how the geohazard information is being used to support prioritization of geotechnical investigations and overall risk management. Future geohazard mapping initiatives should prioritize meaningful and ongoing engagement of First Nations, from scoping and kick-off to final mapping and reporting, and clear communication with territorial governments to streamline mapping and leverage opportunities for complementary investigations or long-term monitoring. Collaborations involving participation of academic institutions offer cost-effective alternatives, when timelines allow, given the opportunity they provide for longer-term data collection and analysis by graduate students.

5 Acknowledgments

The authors appreciate the opportunity to support, and work with, Little Salmon/Carmacks, Kwanlin Dün and Champagne and Aishihik First Nations in association with geohazard-related studies. We also acknowledge the ongoing collaborative support Yukon Geological Survey offers to geohazard-related initiatives in Yukon. This paper has been improved thanks to the comments provided by R. Beddoe, K. Karunaratne and an anonymous reviewer.

6 References

Allard, M., Chiasson, A., B. St-Amour, A., Mathon-Dufour, V., Aubé-Michaud, S., L'Hérault, E., Bilodeau, S., and Deslauriers, C. 2020. *Geotechnical characterization and permafrost mapping project in the Inuit communities of Nunavik*. Executive summary and recommendations. Québec, Centre d'études nordiques, Université Laval.

Benkert, B.E., Kennedy, K., Fortier, D., Lewkowicz, A., Roy, L.-P., Grandmont, K., de Grandpré, I., Laxton, S., McKenna, K., and Moote, K. 2015. *Dawson City Landscape Hazards: Geoscience Mapping for Climate Change Adaptation Planning. Northern Climate ExChange*. Yukon Research Centre, Yukon College, 166 p. and 2 maps.

Blais-Stevens, A, Kremer, M., Bonnaventure, P.P., Smith, S.L., Lipovsky, P., and Lewkowicz, A.G. 2015. 'Active Layer Detachment Slides and Retrogressive Thaw Slumps Susceptibility Mapping for Current and Future Permafrost Distribution, Yukon Alaska Highway Corridor' in G. Lollino, A. Manconi, J. Clague, W. Shan and M. Chiarle (eds.), *Engineering Geology for Society and Territory – Volume 1*. Available at: https://doi.org/10.1007/978-3-319-09300-0_86.

Bonnaventure, P.P., Lewkowicz, A.G., Kremer, M., and Sawada, M.C. 2012. 'A permafrost probability model for the southern Yukon and northern British Columbia, Canada', *Permafrost and Periglacial Processes* 23, pp. 52–68.

Bureau de normalisation due Québec 2023. 'Risk-based Approach for Community Planning in Northern Regions – Requirements and Guidance', *CAN/BNQ 9701-500/2023, National Standard of Canada*.

Cronmiller, D.C, McParland, D.J., Goguen, K.M., and McKillop, R.J. 2020. 'Carmacks surficial geology and community hazard susceptibility mapping', *Yukon Geological Survey* Miscellaneous Report 20, 16 p. plus appendices.

Douglas, M.M. and Lamb, M.P. 2024. 'A model for thaw and erosion of permafrost riverbanks', *Journal of Geophysical Research: Earth Surface* 129, e2023JF007452. Available at: https://doi.org/10.1029/2023JF007452.

Flynn, M., Ford, J.D., Labbé, J., Schrott, L., and Tagalik, S. 2019. 'Evaluating the effectiveness of hazard mapping as climate change adaptation for community planning in degrading permafrost terrain', *Sustainability Science* 14, pp. 1041–1056. Available at: https://doi.org/10.1007/s11625-018-0614-x.

Forbes, D.L., Bell, T., James, T.S., and Simon, K.M. 2014. 'Reconnaissance assessment of landscape hazards and potential impacts of future climate change in Arviat, southern Nunavut', in *Summary of Activities 2013* Canada-Nunavut Geoscience Office, pp. 183–192.

Heginbottom, J.A., Dubreuil, M.A., and Harker, P.T. 1995. 'Canada, permafrost', in *National Atlas of Canada, 5th edition*. Natural Resources Canada, MCR 4177, 1 sheet, scale: 1:7,500,000.

Howes, D.E. and Kenk, E. 1997. 'Terrain Classification System for British Columbia (Version 2)', *Province of British Columbia*, Resource Inventory Branch, Ministry of Environment, Lands and Parks; Recreational Fisheries Branch, Ministry of Environment; and Surveys and Resources Mapping Branch, Ministry of Crown Lands, 102 p.

Irrgang, A.M., Lantuit, H., Gordon, R.R., Piskor, A., and Manson, G.K. 2019. 'Impacts of past and future coastal changes on the Yukon coast – threats for cultural sites, infrastructure, and travel routes', *Artic Science* 5(2), pp. 107–126.

Kokelj, S., Gingras-Hill, T., Daly, S., Morse, P., Wolfe, S., Rudy, A., et al. 2023. 'The Northwest Territories Thermokarst Mapping Collective: a northern-driven mapping collaborative toward understanding the effects of permafrost thaw', *Arctic Science* 9, pp. 886–918. Available at: http://dx.doi.org/10.1139/AS-2023-0009.

Kokelj, S.V., Lantz, T.C., Tunnicliffe, J., Segal, R., and Lacelle, D. 2017. 'Climate-driven thaw of permafrost preserved glacial landscapes, northwestern Canada. Geology 45(4), pp. 371–374. Available at: https://doi.org/10.1130/G38626.1.

Kokelj, S.V., Tunnicliffe, J., Lacelle, D., Lantz., T.C., Chin, K.S., and Fraser, R. 2015. 'Increased precipitation drives mega slump development and destabilization of ice-rich permafrost terrain, northwestern Canada', *Global and Planetary Change* 129, pp. 56–68.

Lipovsky, P.S. 2023. 'Surficial geology and geohazards of the greater Whitehorse area', *Yukon Geological Survey* Open File 2023-1, 67 p. plus appendices.

Lipovsky, P.S., Coates, J., Lewkowicz, A.G., and Trochim, E. 2006. 'Active-layer detachments following the summer 2004 forest fires near Dawson City, Yukon', in D.S. Emond, G.D. Bradshaw, L.L. Lewis and L.H. Weston (eds.), *Yukon Exploration and Geology 2005*, Yukon Geological Survey, pp. 175–194.

McCoy, V.M. and Burn, C.R. 2005. 'Potential alteration by climate change of the forest-fire regime in the boreal forest of central Yukon Territory', *Arctic* 58, pp. 276–285.

McKillop, R., Sacco, D., and Cronmiller, D. 2019. 'Permafrost-Related Erosional Effects of Water Level Regulation and Climate Change along the Shorelines of Aishihik and Canyon Lakes, Southwest Yukon', in *Proceedings of the 18th International Conference on Cold Regions Engineering and the 8th Canadian Permafrost Conference*. Reston, Virginia, United States: pp. 289–297.

Northern Futures Planning 2019. *Pan-Northern Meeting on Permafrost Hazard Mapping, Summary Report*. March 7-8, 2018. Report dated January 8, 2019.

Perrin, A. and Jolkowski, D. 2022. *Yukon climate change indicators and key findings 2022*. YukonU Research Centre, Yukon University, 126 p.

Roy, L.-P., Lipovsky, P.S., Calmels, F., Laurent, C., Humphries, J., and Vogt, N. 2021. 'Greater Whitehorse area permafrost characterization', *Yukon Geological Survey* Miscellaneous Report MR-22, 185 p. including appendices.

The effects of the “Mega-drought” in small periglacial mountain streamlets (Dry-Central Andes of Argentina)

Martín Mendoza[1], Carla Tapia Baldis[1], Dario Trombotto Liaudat[1] & Noelia Sileo[2]

[1]*IANIGLA: Instituto Argentino de Nivología, Glaciología y Ciencias Ambientales, CCT Conicet, Mendoza, Argentina*

[2]*CNEA: Comisión Nacional de Energía Atómica PNGRR, Regional Cuyo, Mendoza, Argentina*

ABSTRACT

In the Dry-Central Andes of Argentina (31° to 35°S), hydrological systems are cryospheric, influenced by variable snowfall, and shaped by solid-state water reservoirs. Permafrost is expected between 3400 and 4200 m asl under favorable topographic conditions. Since 2010, a strong hydrological drought, caused by reduced precipitations and rising air temperatures, impacted small mountain stream discharges. The Chasquillar basin (31°45'S and 70°15'W), displays periglacial landforms in its upper part at 3800 m asl, such as active and transitional rock glaciers. Glacial moraines cover the middle and the lower part, where the Chasquillar streamlet flows. This small mountain streamlet has a perennial flow, fed by a spring with a surrounding wetland ecosystem. Since 2018, hydrological parameters were monitored in the field, with the aim of elucidate the interplay between the meteorological variables and the flow dynamics under the drought conditions. Using a site-specific calibration equation, discharge was calculated from water level, measured with a data logger placed in a metallic cutthroat-flume gauge station. The device recorded data every 4 hours between April 2018 and April 2023. Soil moisture and temperature were monitored upstream from the spring sampling point between April 2019 to April 2023, at depths from 0 to 80 cm. Results show a peak discharge of 20-30 l/s but, between April 2019 to October 2022, it remained at 4–5 l/s (base flow), with seemingly small contributions from snow melting, due to the “Mega-drought” condition.

1 INTRODUCTION

The Central Andes of Argentina and Chile (31–35°S) comprise the largest periglacial continental belt in the southern hemisphere (Gruber 2012). The cycles of freezing and thawing that occur extensively in cold regions, as well as the distribution of permafrost, influence runoff distribution, groundwater flows, and the physical-chemical processes. In this region, water sources primarily result from the summer (dry season) melting of snow and glaciers (Corte 1983; Masiokas et al. 2010). These sources include contributions from seasonally frozen soils and permafrost, each playing distinctive hydrological roles (Schaffer et al. 2019; Hayashi 2020). A central element of the periglacial hydrological system is the active layer. Some authors refer to this unit as a temporary or seasonal aquifer (Halla et al. 2021; Liaudat et al. 2020), as it stores water during the cold months in the form of seasonal ground ice, releasing it during the summer as the thawing front penetrates the soil.

Climate trends for the Central Andes forecast drastic decreases in surface water supply, resulting from a combination of various factors. Since 2010, the region has been experiencing what is referred to as a "mega-drought (hydrological)" (Garreaud et al. 2020; Rivera et al. 2021). One of the primary contributors to this phenomenon is the reduction in the duration and extent of seasonal snow cover in mountainous regions, as the global average temperature continues to rise (Zazulie et al. 2018). According to the latest reports, the air temperature in mountainous regions at a global scale shows an increase ranging from 0.1 to 0.3 °C per decade throughout the 21st century (Biskaborn et al. 2019; Hock et al. 2019). For the Central Andes, the trend between 1991 and 2021 was +0.2 °C per decade and it is projected to continue rising to +2 °C between 2024 and 2048 under an SSP-1 scenario (Caragunis et al. 2020). There is evidence that in some regions of the world, the threshold for peak water has been exceeded, especially in areas where ice bodies are small, such as the Central and Southern Andes, western Canada, and the Alps. Consequently, it is expected that the solid water reserves in mountainous regions (snow, glaciers, and frozen soils) will continue to experience high environmental stress. As glaciers retreat and eventually disappear, the role of frozen soils and permafrost in the hydrology of mountain systems will become increasingly significant for the water balance. The trend is toward a modification of the hydrological system, shifting from snow/glacier-dominated dynamics to periglacial ones (Haeberli et al. 2019; Arenson et al. 2022). The periglacial environment response shows a dynamic behaviour, responding differently to climate variability. The hydrological significance of rock glaciers in the Central Andes has been explored by numerous authors, often in relation to discharge prediction (Schrott 1991; Trombotto et al. 1997), and this subject has been a topic of discussion at both regional and global scales (Arenson and Jakob 2010; Duguay et al. 2015; Trombotto-Liaudat and Bottegal 2020). Recent studies have contributed to quantifying the water storage capacity of rock glaciers, clarifying their role in the hydrological cycle, and interpreting various flows within the periglacial system (Arenson et al. 2022; Halla et al. 2021; Hilbich et al. 2022; Hoelzle et al. 2022; Liaudat et al. 2020; Sileo et al. 2020).

1.1 Objectives

The aim of this study is to comprehensively examine the hydrology of a periglacial mountain basin situated in the Central Dry Andes of Argentina. Our objective is to analyze the behavior of the hydrological system in years of drought and periods of increased precipitation. This will be achieved by distinguishing between yearly segments of accumulation

https://doi.org/10.52381/ICOP2024.133.1

and recession in the discharge hydrological data. For each period, regression analyses from 'wet' and 'dry' years could be explained in terms of the meteorological variables. Specifically, we seek to gain a deeper understanding of the crucial roles played by periglacial Andean processes, including snowmelt, soil freezing and thawing, and groundwater discharge across the aforementioned basin.

1.2 Study Area

The study area is situated on the western slope of the Santa Cruz Mountain range (Central Andes of Argentina), spanning coordinates 31°45'S and 70°12'W to 31°48'S and 70°15'W and an elevation range spanning from 3400 m asl to 4800 m asl. The “Chasquillar” valley conforms a north-northeast to south-southwest elongated valley, which acts as a minor tributary of the Santa Cruz River, a permanent stream with a mean module of 306 l/s (Figure 1).

The geomorphology of the study area exhibits three distinct altitudinal segments. Periglacial processes, resulting in widespread landforms such as rock glaciers, protalus ramparts, soli-gelifluction slopes, and cryoplanation terraces, dominate the upper section (Figure 2). These features collectively constitute 25% of the total basin surface. The middle section displays landforms of ancient glacial origin. The valley bottom contains till deposits and till exhibiting cryogenic characteristics, accounting for 12% of the total area. Although fluvioglacial units cover a mere 1% of the landscape, it is inferred that they play a significant role in the basin’s hydrogeology. Detrital slopes encompass 12% of the total area, while additional units of gravitational and alluvial origin make up 7%.

The lower basin section accommodates a main permanent streamlet, primarily fed by a spring surrounded by meadows colloquially referred to as the "Chasquillar" stream. In this portion, the prevailing features are mainly detrital slopes and ancient glacial deposits. Noteworthy within the basin's topography is a slope discontinuity between the second and third segments, marked by a moraine front approximately 100 m in thickness. This moraine front suggests distinct ice advances during the Quaternary period.

According to the Köppen classification, the climate is polar tundra of high-altitude (ETH), with minimum to null excess water, scarce summer precipitation, and permafrost presence. Annually, the thawing season with monthly mean air temperatures > 0 °C extends from November to April, while the freezing season starts in May and lasts to December. The precipitation patterns show a well-defined seasonal regime, with maximum precipitation during the cold season and scarce precipitation during the warm season. Precipitation is nival, with annual means ranging from 300 to 400 mm (Arenson et al. 2010), being strongly controlled by the phase of El Niño Southern Oscillation (ENSO) (Montecinos and Aceituno, 2003), with annual maximums of 1100–1200 mm during its occurrence. The mean annual air temperature (MAAT) at approximately 3600 m asl is 0.18 °C; during the thawing season MAAT ascends up to 7.2 °C, descending down to -5.43 °C during the cold season. Mean air temperature in the coldest month (July) was -11.55 °C at 3600 m asl, with a historical minimum close to -30 °C during July of 2000.

Various lithological units are exposed in the area, predominantly pyroclastic rocks of rhyolitic composition (Rancho de Lata formation), volcanic andesites (Choiyoi group), and porphyritic rocks of andesitic/dacitic composition (Farellones formation intrusive). Secondary hydrothermal alteration minerals have affected a portion of the area.

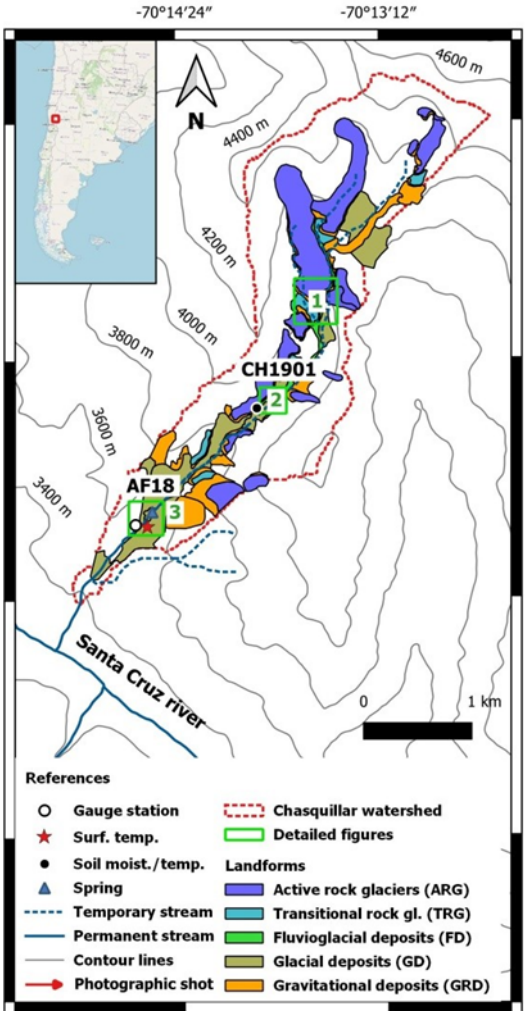

Figure 1. Geomorphology of the Chasquillar basin, displaying main landforms and drainage network. Sampling and instrumentation points are shown.

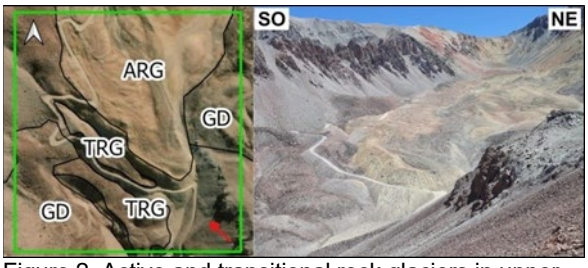

Figure 2. Active and transitional rock glaciers in upper section of the basin (see reference for detailed Figure 1).

2 METHODS

2.1 Field Instrumentation

2.1.1 Flume design

We installed a "cutthroat flume" structure at the chosen site (AF18 3480 m asl) with the following design specifications: it is a cutthroat flume measuring 10 cm in width (*W*) and 90 cm in length (*L*), constructed from 2 mm thick iron plate with reinforcements. Here, *W* represents the throat width, and *L* represents the total length of the flume (Figure 3).

Figure 3. "Cutthroat flume" in the Chasquillar streamlet, at the lower section of the homonymous basin (see reference for detailed figure 3).

The theoretical calculation of discharge in a cutthroat flume, assuming free-flow conditions, can be determined using the following formula:

$$Q = C \times {H_a}^n \quad [1]$$

In this equation, *Q* represents the discharge in cubic meters per second (m³/s), *C* is the coefficient of free flow, H_a (m) is the water level measured upstream at a distance from the throat equal to 2/9L (m), and *n* is the exponent of the equation.

For the specific geometric design mentioned, the equation can be expressed as:

$$Q = 0.35 \times {H_a}^{1.84} \quad [2]$$

After the installation of the flume, a calibration test was conducted using the salt dilution gauging method. This test yielded four discharge measurements corresponding to different values of H_a (water level). The calibration range spanned from 4.84 liters per second (l/s) to 7.10 l/s.

Based on the test results, an empirical adjustment of the coefficients *C* and *n* was performed to align the flume equation with the observed relationship between Q (discharge) and H_a. As a result, the calibrated flume equation is as follows:

$$Q = 0.13 \times {H_a}^{1.5} \quad [3]$$

2.1.2 Water discharge

In this study, we employed a HOBO U20L-04 data logger, placed inside a watertight chamber attached to the flume channel, as illustrated in Figure 3. This chamber is hydraulically connected to the flume through a slot located at the $H_a$reading site. The data logger is designed to operate within a pressure range of 0 to 4 m of water (at sea level) and can function in temperatures ranging from -20 °C to 50 °C. It provides precise measurements of absolute pressure with an accuracy of ± 0.4 cm H_20 and a resolution of 0.14 cm H_20. Additionally, it measures water temperature with an accuracy of ± 0.44 °C and a resolution of 0.10 °C. Data from this equipment were collected continuously from April 2018 to April 2023, with readings taken at intervals of 4 hours. At the measurement point H_a, we determined the hydrostatic pressure by calculating the difference between the absolute pressure recorded by the HOBO U20L-04 sensor and the atmospheric pressure. These measurements were expressed in meters of water, converting them into the corresponding discharge rates using the flume calibrated curve (equation 3).

We created a hydrograph illustrating the discharge rates observed in the Chasquillar stream (site AF18) from 2018 to 2023, accompanied by water temperature readings. To filter the discharge curve, we applied the following criteria during specific periods:

a) When the water column was completely frozen, as indicated by the bottom-of-the-flume water temperature readings, we considered a maximum depression of the freezing point equal to -0.09 °C.
b) During periods when the top of the water column was frozen, we identified intervals on which the water temperature remained steady and variability tended to be minimal, a phenomenon referred to as the "zero curtain".

After filtering, we classified the discharge rates into their respective hydrological years. Each hydrological year was further divided into two intervals:

1) The accumulation interval, starting from the beginning of the series and extending to the point of maximum discharge.
2) The recession interval, starting from the point of maximum discharge and concluding at the start of an extended freezing period in the stream.

2.1.3 *Recession curves*

The recession intervals of the hydrograph were analyzed in terms of aquifer discharge, which can be represented by an exponential equation with a negative exponent in the form of:

$$Q_t = Q_0 e^{-\propto t} \quad [4]$$

Here, Q_0 represents the initial discharge, Q_t the discharge at time t, $\propto$ the coefficient of the aquifer and e, the base of the natural logarithm.

In complex aquifers, the recession can be interpreted by a function that is the sum of several exponential segments, where the intervals represent different stages in the drainage process.

2.1.4 *Soil temperature and moisture content*

At site CH19, we deployed four Truebner SMT100 sensors to measure soil temperature and soil volumetric water content (VWC) at different depths (0.05 m, 0.2 m, 0.5 m, and 0.8 m; Figure 4). These sensors were connected to a data logger that collected data every 4 hours from April 2019 to April 2023. The sensors have an accuracy of ± 3% for VWC and ± 0.2 °C for temperature in mineral soils, with a resolution of 0.1% for VWC and 0.01 °C for temperature. After deploying the sensors at the specified depths, we filled the pit with sediments extracted during excavation.

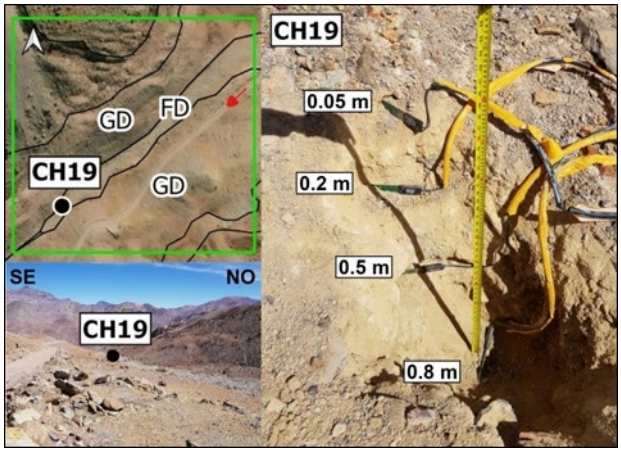

Figure 4. Site CH19, with SMT-100 sensors to measure soil temperature and soil volumetric water content at different depths (see reference for detailed Figure 2).

2.1.5 *Meteorological data sources*

For various meteorological variables, we relied on gridded data series obtained from global reanalysis models to compensate for the lack of instrumental data in the study area. Although there are meteorological stations near the study area, these stations only have historical records, and the most recent data are either sporadic or unavailable. The selected reanalysis models covered the following variables:

- Air temperature was represented using the ERA5 model.
- Rainfall data were derived from the ERA5 model.
- Snow cover thickness was obtained from the ERA5-AG model.
- Atmospheric pressure was determined using the NCEP NNRP model, specifically the flow subset R1 (2D) with a forecast every 6 hours. The grid had a resolution of 1.875° x 1.904° and covered surface-level data.

All the mentioned gridded data series were validated through correlation analysis with historical records from the nearest meteorological station, Pachón (31°45'34.60"S and 70°24'45.30"W)

2.1.6 *Correlation and multivariable regression analysis*

Using the "sample cross correlation function (CCF)" tool within R, we analyzed meteorological variables to define the degree of correlation with the discharge curve in the accumulation intervals, considering their possible delays (lag).

3 RESULTS

3.1 "Mega drought" meteorological settings

Compared to a reference period (2010–2023), the years 2018 to 2023 were warmer and dryer. The warmest years were 2019 and 2020 (mild El Niño anomaly), with MAATs of 0.89 and 0.79 °C, representing anomalies of +2.0 °C and +1. 8°C, respectively (at 3704 m asl). Moreover, no negative air temperature anomaly was recorded since the coldest year 2010 (-0.3 °C anomaly); all the remaining years showed positive temperature anomalies (Figure 5 and Table 1). The same trend was also observed at the soils, that displayed exceptionally high temperatures with MAGTs above 4.0 °C (at 20 cm depths) during the whole observation period.

Regarding the precipitation, the year 2019 was the driest of the whole period, with a precipitation anomaly of -180 mm/yr, compared to a mean value of 280 mm/yr (1981–2021). Since 2010, precipitation records have always shown a deficit, especially notorious in the winter-accumulated values (Table 1). In the soil moisture profile, seasonally, periods with a negative gradient (moisture decreases with depth) occur during snowmelt and soil thawing, while positive gradient periods occur during late summer and the onset of soil freezing.

Table 1. Summary of meteorological variables during 2018–2023 at 3704 m asl.

	18/19	19/20	20/21	21/22	22/23
MAAT (°C)	-0.20	0.89	0.79	-0.02	-0.83
MAAT Anomaly (°C)	+0.9	+2.0	+1.8	+1.2	+0.8
MAGT (°C)	-	5.13	4.51	4.62	4.01
Mean T° Warm season (°C)	10.24	9.76	8.83	10.56	8.70
Mean T° Cold season (°C)	-10.17	-8.61	-8.71	-10.57	-9.49
Annual Precip. (mm/yr)	453.73	311.93	439.86	333.57	401.65
Precip. Anomaly (mm/yr)	-105	-180	-160	-170	-100
Summer Precip. (mm/yr)	113.20	89.36	168.94	165.24	50.29
Winter Precip. (mm/yr)	329.72	257.79	159.57	155.87	334.54
Snow coberture (%)	52.43	38.29	36.81	33.20	49.52
Accumulated snow (mm)	2495	1345	1804	1143	2326

3.2 Discharge analysis

Peak streamflow occurs in mid-December to late-April and is due to snowmelt rather than summer rainfall. The dominance of seasonal snowmelt creates a hydrograph with a steep rising limb and gradual recessional limb. In terms of water discharge from the Chasquillar streamlet, two distinctive periods were observed: “wet” years (2018–2019 and 2022–2023), versus “dry” years (2019–2022).

In wet years, the average flow ranges from 7.8 to 9.2 l/s, while maximum flows range from 30.1 to 23.5 l/s. In dry years, the average flow ranges from 1.7 to 2.9 l/s, while maximum flows range from 5 to 5.3 l/s. In the first case, the peak discharge occurs in December (beginning of the austral summer), whereas in dry years, the streamflow curve is very stable, and the maximum flow occurs between March and April (austral autumn; Figure 5 and Table 2).

Regarding water temperature, the freezing period occurs at the beginning of each hydrological year, typically lasting between 80 and 89 days. In the year 2021–2022, it had a shorter duration. Moreover, in wet years, the low flow period (< 5 l/s) occurs at the end of winter (freezing period) and before snowmelt leads to an increase in flow. It represents between 25% (2018–2019) and 38% (2022–2023) of the streamflow curve. In dry years, the entire curve remains below 5 l/s (Table 2).

Table 2. Summary of meteorological hydrological variables during 2018–2023 at site AF18.

Hydrological Year	18/19	19/20	20/21	21/22	22/23
Duration (days)	353	372	382	383	-
Freezing period (days)	89	80	89	106	81
Accumulation period (days)	114	240	177	211	105
Recession period(days)	145	36	96	65	-
Min. discharge (l/s)	0.94	0.5	0.47	0.13	4.96
Max. discharge (l/s)	23.54	5.33	5.13	4.96	30.15
Avg. discharge	9.18	2.9	2.93	1.7	7.83
High flow duration (days)	192	-	-	-	147
Low flow duration (days)	67	276	273	276	91

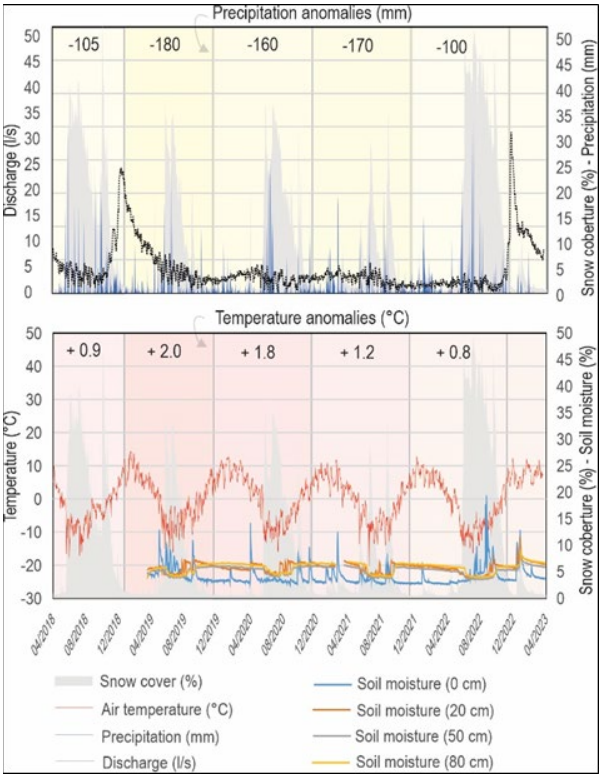

Figure 5. Daily values of water discharge (l/s), precipitation (mm/day) and snow cover (%) at AF18 site (upper figure). Down: daily air temperature records (°C) and soil moisture content (%) at site CH19.

3.3 Recession curves and regression analysis

In wet years, the accumulation (related to snowmelt) and recession (related to groundwater discharge) periods of the flow curve are well defined. For the year 2018–2019, the

accumulation period lasted 114 days. The recession of this hydrological year can be divided into two segments: the first segment comprises the first 22 days of recession, with an alpha value of -0.019, and the second recession segment spans 99 days, with an alpha value of -0.009 (Figure 6). For the year 2022–2023, the accumulation period lasted 105 days. The recession of this hydrological year, divided into two segments, results in a first segment comprising the first 24 days of recession, with an alpha value of -0.036, and the second recession segment spans 109 days, with an alpha value of -0.008 (Figure 6). It is important to emphasize the similarity in the alpha value for the second segment of recession in the two analyzed wet years. This could be considered an indicator of the properties of the basin's aquifers.

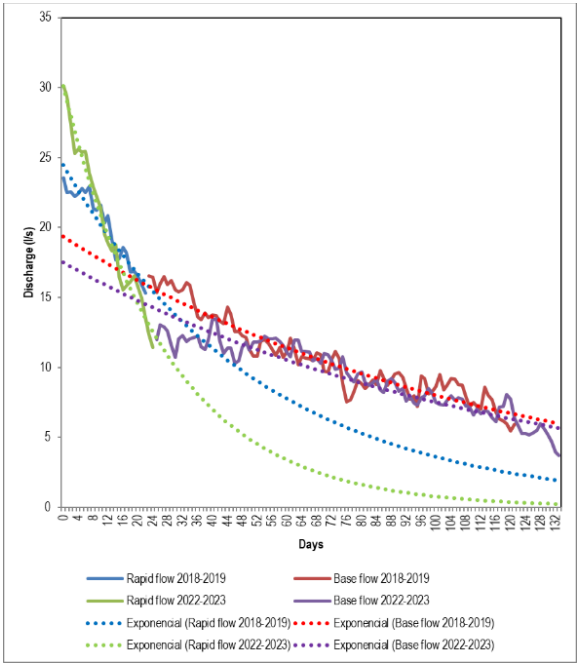

Figure 6. Recession curves during the “wet” years and best fitting model.

In wet years, the accumulation segment of the discharge curve can be explained in terms of the following meteorological variables: snow depth, precipitation, and air temperature, with R-squared values ranging from 0.86 (2018–2019; Table 3) to 0.63 (2022–2023; Table 4). In the year 2022–2023, the soil temperature at a depth of 80 cm is also a significant predictor in the regression model. Soil moisture at a depth of 20 cm shows a negative relationship with streamflow, primarily evident in dry years (R-squared equal to 0.4 in the year 2019–2020, with a lag of 15 days). In wet years, there is no significant relationship between soil moisture and the streamflow curve.

On the other hand, in dry years, the correlation between discharge and the mentioned meteorological variables is negligible (R-squared between 0.16 and 0.18), except for the year 2020–2021, in which snowfall was slightly more intense, and the correlation with meteorological variables reaches 0.58.

Table 3. Accumulation model for 2018–2019 “wet” period.

	Estimate	Std. Error	T value	Pr(>|t|)
Intercept	8.86	0.62	14.39	<2e-16
Snow depth	-0.01	0.001	-4.77	5.7e-06
Precipitation	1.78	0.21	8.38	2.1e-13
Air temperature	0.66	0.11	5.75	8.3e-08
	Residuals	Multiple R-squared		0.86
Min	-5.95	p-value		< 2,2e-16
1Q	-1.58			
Median	-0.22			
3Q	0.99			
Max	8.57			

Table 4. Accumulation model for 2022–2023 “wet” period.

	Estimate	Std. Error	T value	Pr(>|t|)
Intercept	-4.27	0.98	-4.37	3.5e-0.5
Snow depth	0.01	0.001	8.90	2.4e-14
Precipitation	0.54	0.1	4.00	1.2e-04
Air temperature	0.34	0.13	2.41	1.8e-02
Soil temp. 0.8 m	1.94	0.25	7.88	4.01e-12
	Residuals	Multiple R-squared		0.78
Min	-9.11	p-value		<2.2e-16
1Q	-1.45			
Median	0.15			
3Q	1.07			
Max	12.64			

4 DISCUSSION

During 2019–2022, the precipitations below the average were simultaneous with positive anomalies of winter temperatures, interrupting the seasonal freezing in the upper part of the basin (above 3800 m asl). Then, the scarce accumulated snow melted in the middle of winter and meltwater flowed into the uppermost part of the active layer, introducing heat into the ground, and so decreasing the freezing depth. By the beginning of the snow-melting period in November, the accumulated snow is very thin, melting quickly and percolating, but soil water does not reach the saturation point. If the snow coverture threshold is below a 30%, in terms of basin surface; and soil moisture below 10%, not enough snowmelt water is available to produce a discharge and no peak-flow is observed.

The recorded water discharges in the Chasquillar streamlet during “dry” years, were similar to the ones found at the tongue of the “Dos Lenguas” rock glacier, in the Dry Andes (Schrott 1991), of 5–6 l/s. When comparing with the Vallecitos basin, in the Central Andes of Mendoza, the average discharge flow (1991–1993) was much higher: 500 l/s during wet years (Trombotto et al. 1997; Sileo 2019). Other studies obtain discharge values from rock glacier-fed basins varies between ~5 and ~250 l/s (Harrington et al. 2018; Krainer and Mostler 2002). As in many other studies,

the seasonal variations in discharge occur with the lowest flows observed in winter, consisting mostly, if not completely, of base flow (Burger et al. 1999; Krainer et al. 2007).

Under stable permafrost conditions, the contribution from interstitial thaw to surface runoff is extremely small/negligible, for example Krainer et al. (2015), found an average annual rate of ground ice melt from thawing permafrost of 10 cm/year, which represented only 2.3% of the average discharge from the rock glacier catchment area. However, the contribution to the runoff from permafrost thaw can change in response to climate shifts. Local permafrost maps could enhance the interpretation of these findings, again, in terms of any likely spatial gradient therein.

5 CONCLUSIONS

This study lacks measurements for the soil water content at depth > 1 m. Because of the observed relationship between streamflow and meteorological variables in wet years, we can interpret the main sources of water in the Chasquillar basin: snowmelt and late-season precipitation are two significant components that together explain part of the observed variability. Furthermore, the relationship between streamflow with air temperature, and particularly with soil temperature, can be interpreted as indicators of the role played by soil thawing in the accumulation phase of the streamflow curve. The segmentation observed in recession curves can be interpreted in terms of a fast-flow component, which manifests in the first 25 days after the peak flow, and a slow-flow component corresponding to groundwater discharge.

The lack of correlation between soil moisture and streamflow suggests that the sources feeding the Chasquillar stream are primarily controlled by underground flows, which have an indirect relationship with surface infiltration in the upper and middle parts of the basin. However, in years with diminished total snow accumulation and melt, it is expected that there will be a
decrease in groundwater recharge, that in turn will decrease the peaks of groundwater discharge to the streams.

6 ACKNOWLEDGEMENTS

This study was funded by the project PIP 1222015-0100913, granted by the Consejo Nacional de Investigaciones Científicas y Técnicas (CONICET), and the project PICT-2019-03799 granted by the Agencia Nacional de Promocion de la Investigación, el Desarrollo Tecnológico y la Innovacion. The authors express their gratitude to Silvio Pastore, Jorge García, and Dino Taillant for their valuable help during field tasks.

7 REFERENCES

Arenson, L.U. and Jakob, M. 2010. 'The significance of rock glaciers in the dry Andes - A discussion of Azócar and Brenning (2010) and Brenning and Azócar (2010)', *Permafrost Periglacial Process* 21, pp. 282–285. Available at: https://doi.org/10.1002/ppp.693.

Arenson, L.U., Pastore, S., Liaudat, D.T., Bolling, S., Quiroz, M.A., and Ochoa, X.L. 2010. 'Characteristics of two Rock Glaciers in the Dry Argentinean Andes Based on Initial Surface Investigations', in *Proceedings GEO2010*, 63rd Canadian Geotechnical Conference & 6th Canadian Permafrost Conference. Calgary, Alberta, Canada: pp. 1501–1508.

Arenson, L.U., Harrington, J.S., Koenig, C.E.M., and Wainstein, P.A. 2022. 'Mountain Permafrost Hydrology—A Practical Review Following Studies from the Andes', *Geosciences* 12(2), 48. Available at: https://doi.org/10.3390/geosciences12020048.

Biskaborn, B.K., Smith, S.L., Noetzli, J., Matthes, H., Vieira, G., Streletskiy, D.A., et al. 2019. 'Permafrost is warming at a global scale', *Nature Communications*, 10(1), 264. Available at: https://doi.org/10.1038/s41467-018-08240-4.

Burger, K.C., Degenhardt, J.J., and Giardino, J.R. 1999. 'Engineering geomorphology of rock glaciers', *Geomorphology*, 31(1), pp. 93–132. Available at: https://doi.org/10.1016/S0169-555X(99)00074-4.

Caragunis, J., Rivera, J., and Penalba, O. 2020. 'Characterisation of hydrological droughts in central north Argentina and their atmospheric and oceanic drivers', *Climate Research*, 80(1), pp. 1–18. Available at: https://doi.org/10.3354/cr01593.

Corte, A. 1983. *Geocriología*. El frío en la Tierra., Ediciones Culturales de Mendoza (ed.), Mendoza, Argentina.

Duguay, M., Edmunds, A., Arenson, L., and Wainstein, P. 2015. 'Quantifying the significance of the hydrological contribution of a rock glacier – A review' in *GEOQuebec 2015,* 68th Canadian Geotechnical Conference & 7th Canadian Permafrost Conference. Québec City, Québec, Canada: 8 p.

Garreaud, R.D., Boisier, J.P., Rondanelli, R., Montercinos, A., Sepúlveda, H.H., and Veloso-Aguila, D. 2020. 'The Central Chile Mega Drought (2010–2018): A climate dynamics perspective', *International Journal of Climatology* 40, pp. 421–439.

Gruber, S. 2012. 'Derivation and analysis of a high-resolution estimate of global permafrost zonation', *The Cryosphere* 6, pp. 221–233. Available at: https://doi.org/10.5194/tc-6-221-2012.

Haeberli, W., Oerlemans, J., and Zemp, M. 2019. 'The Future of Alpine Glaciers and Beyond', *Oxford Research Encyclopedia of Climate Science*. Available at: https://doi.org/10.1093/acrefore/9780190228620.013.769.

Halla, C., Blöthe, J.H., Tapia Baldis, C., Trombotto Liaudat, D., Hilbich, C., Hauck, C., Schrott, L. 2021. 'Ice content and interannual water storage changes of an active rock glacier in the dry Andes of Argentina', *The Cryosphere* 15, pp. 1187–1213. Available at: https://doi.org/10.5194/tc-15-1187-2021.

Harrington, J.S., Mozil, A., Hayashi, M., and Bentley, L. R. 2018. 'Groundwater flow and storage processes in an inactive rock glacier', *Hydrological Processes*, *32*(20), pp. 3070–3088. Available at: https://doi.org/10.1002/hyp.13248.

Hayashi, M. 2020. 'Alpine Hydrogeology: The Critical Role of Groundwater in Sourcing the Headwaters of the World', *Groundwater* 58, pp. 498–510. Available at: https://doi.org/10.1111/gwat.12965.

Hilbich, C., Hauck, C., Mollaret, C., Wainstein, P., and Arenson, L.U. 2022. 'Towards accurate quantification of ice content in permafrost of the Central Andes – Part 1: Geophysics-based estimates from three different regions'. *The Cryosphere*, 16(5), pp. 1845–1872. Available at: https://doi.org/10.5194/tc-16-1845-2022.

Hock, R., Rasul, G., Adler, C., Cáceres, B., Gruber, S., Hirabayashi, M., et al. 2019. 'Chapter 2: High Mountain Areas' in H.-O. Pörtner, D.C. Roberts, V. Masson-Delmotte, P. Zhai, M. Tignor, E. Poloczanska, K. Mintenbeck, A. Alegría, M. Nicolai, A. Okem, J. Petzold, B. Rama, N.M. Weyer (eds.) *IPCC Special Report on the Ocean and Cryosphere in a Changing Climate*. Cambridge, UK: Cambridge University Press, pp. 181–202. Available at: https://doi.org/10.1017/9781009157964.004.

Hoelzle, M., Hauck, C., Mathys, T., Noetzli, J., Pellet, C., and Scherler, M. 2022. 'Long-term energy balance measurements at three different mountain permafrost sites in the Swiss Alps', *Earth System Science Data* 14(4), pp. 1531–1547. Available at: https://doi.org/10.5194/essd-14-1531-2022.

Krainer, K. and Mostler, W. 2002. 'Hydrology of Active Rock Glaciers: Examples from the Austrian Alps', *Arctic, Antarctic, and Alpine Research*, *34*(2), pp. 142–149. Available at: https://doi.org/10.1080/15230430.2002.12003478.

Krainer, K., Bressan, D., Dietre, B. et al. 2015. 'A 10,300-year-old permafrost core from the active rock glacier Lazaun, southern Ötztal Alps (South Tyrol, northern Italy)', *Quaternary Research* 83, pp. 324–335.

Krainer, K., Mostler, W., and Spötl, C. 2007. 'Discharge from active rock glaciers, Austrian Alps: A stable isotope approach', *Austrian Journal of Earth Sciences* 100, pp. 102–112.

Liaudat, D.T., Sileo, N., and Dapeña, C. 2020. 'Periglacial water paths within a rock glacier-dominated catchment in the Stepanek area, Central Andes, Mendoza, Argentina'. *Permafrost and Periglacial Process* 31, pp. 311–323. Available at: https://doi.org/10.1002/ppp.2044.

Masiokas, M.H., Villalba, R., Luckman, B.H., and Mauget, S. 2010. 'Intra- to Multidecadal Variations of Snowpack and Streamflow Records in the Andes of Chile and Argentina between 30° and 37°S', *Journal of Hydrometeorology* 11, pp. 822–831. Available at: https://doi.org/10.1175/2010JHM1191.1.

Montecinos, A. and Aceituno, P. 2003. 'Seasonality of the ENSO-Related Rainfall Variability in Central Chile and Associated Circulation Anomalies', *Journal of Climate*,16(2), pp. 281–296. Available at: https://doi.org/10.1175/1520-0442(2003)016<0281:SOTERR>2.0.CO;2.

Rivera, J.A., Otta, S., Lauro, C., and Zazulie, N. 2021. 'A Decade of Hydrological Drought in Central-Western Argentina', *Frontiers in Water* 3, 640544. Available at: https://doi.org/10.3389/frwa.2021.640544.

Schaffer, N., MacDonell, S., Réveillet, M., Yáñez, E., and Valois, R. 2019. 'Rock glaciers as a water resource in a changing climate in the semiarid Chilean Andes', *Regional Environmental Change* 19, pp. 1263–1279. Available at: https://doi.org/10.1007/s10113-018-01459-3.

Schrott, L., 1991. 'Global solar radiation, soil temperature and permafrost in the Central Andes, Argentina: A progress report'. *Permafrost and Periglacial Processes* 2, pp. 59–66. Available at: https://doi.org/10.1002/ppp.3430020110.

Sileo, N.R. 2019. *Estudio del comportamiento hidrogeoquímico de las aguas subterráneas y superficiales relacionadas con glaciares, glaciares cubiertos y glaciares de escombros, en la cuenca del río Vallecitos, Cordillera Frontal, Mendoza*. Universidad Nacional de Buenos Aires (UBA).

Sileo N.R., Dapeña C., and Trombotto Liaudat D. 2020. 'Isotopic composition and hydrogeochemistry of a periglacial Andean catchment and its relevance in the knowledge of water resources in mountainous areas', Isotopes in Environmental and Health Studies. Available at: https://doi.org/10.1080/10256016.2020.1814278.

Trombotto-Liaudat, D. & Bottegal, E. 2020. 'Recent evolution of the active layer in the Morenas Coloradas rock glacier, Central Andes, Mendoza, Argentina and its relation with kinematics', *Cuad. Investig. Geográfica* 46, pp. 159–185.

Trombotto, D., Buk, E., and Hernández, J. 1997. 'Monitoring of Mountain Permafrost in the Central Andes, Cordon del Plata, Mendoza, Argentina', *Permafrost and Periglacial Processes* 8(1), pp. 123–129.

Zazulie, N., Rusticucci, M., and Raga, G.B. 2018. 'Regional climate of the Subtropical Central Andes using high-resolution CMIP5 models. Part II: Future projections for the twenty-first century'. *Climate Dynamics* 51(7), pp. 2913–2925. Available at: https://doi.org/10.1007/s00382-017-4056-4.

Numerical modelling of multi-component mass transport in a permafrost-impacted groundwater flow system

John Molson[1], Aaron Mohammed[2] & Mario Schirmer[3]

[1]*Department of Geology & Geological Engineering, Université Laval, Québec City, Québec, Canada*

[2]*Department of Earth and Environmental Sciences, Syracuse University, New York, United States*

[3]*Department of Water Resources and Drinking Water, Eawag - Swiss Federal Institute of Aquatic Science and Technology*

ABSTRACT

A 3D numerical model has been developed to simulate groundwater flow, heat transport, and the transport and fate of reactive organic contaminants in a thawing permafrost environment. Insight is needed under such conditions as the climate warms and northern economic development accelerates, increasing the risk of groundwater resource contamination. The model includes coupled density-dependent groundwater flow, advective-conductive heat transport with latent heat and freeze/thaw, and advective-dispersive multi-component reactive mass transport. The reactive transport component can account for multi-component aerobic and anaerobic biodegradation with multiple electron acceptors and microbial growth/decay, with temperature-dependent reaction rates governed by Monod kinetics. Model functionality and performance are tested on a 2D vertical-plane conceptual model of a field-scale cryo-hydrogeological system including thawing discontinuous permafrost and an evolving groundwater flow system. The test case includes a surface gasoline spill containing dissolved benzene, toluene, ethylbenzene, and xylene (BTEX), and a bulk residual component, migrating within a shallow aquifer and undergoing aerobic biodegradation. The presence of thawing permafrost, with associated effects on ice-fraction dependent relative permeability, strongly modulated subsurface hydraulic properties and connectivity, with subsequent changes to groundwater flow and mass transport pathways. Results show how evolution of the dissolved BTEX component plumes is controlled not only by the permafrost-impacted flow system, but also by the interacting thermal and chemical controls on overall biodegradation kinetics as the system evolves during permafrost thaw.

1 INTRODUCTION

As the climate warms and northern development accelerates, risks of contaminant spills in thawing permafrost environments will increase, posing risks to groundwater resources (Wiebe et al. 2023). Hydrocarbon spills such as gasoline and diesel fuel are a particular threat due to their mobility and toxicity at low concentrations.

While much is known about the fate of dissolved hydrocarbons in aquifer systems within temperate climates, much less is known about their behavior and potential for degradation in cold regions. In permafrost environments, frozen ground can affect recharge and discharge zones, and can change flow rates and contaminant pathways. Colder temperatures can also affect component solubilities and can reduce microbial activity, reducing biodegradation rates. The processes are complex and highly non-linear, and are difficult to interpret or predict without advanced numerical models.

Many numerical models have been developed for simulating coupled groundwater flow and heat transport in cold regions (e.g., see reviews by Lamontagne-Hallé et al. 2020 and Grenier et al. 2018). Frampton and Destouni (2015) use numerical flow modelling to investigate travel times in degrading permafrost environments, and advanced coupled models for simulating heat and reactive mass transport in cold regions have also recently appeared (Ramezanzadeh et al. 2023; Mohammed et al. 2021; Yi et al. 2021a,b; Barkow et al. 2020; Lessels et al. 2015). Applications of cryo-hydrogeological models for simulating aerobic or anaerobic biodegradation of organic contaminants in permafrost environments have not yet been published.

In this paper, we present a newly-developed finite element numerical model, SMOKER-BIO, for simulating density-dependent groundwater flow, heat transport and multi-component reactive mass transport under aerobic or anaerobic biodegradation, including temperature-dependent reaction rates. The numerical model is applied to a 2D conceptual model of a gasoline spill in a shallow aquifer containing thawing discontinuous permafrost. The source is a 3-component gasoline spill zone composed of dissolved benzene, a lumped component of toluene, ethylbenzene and xylene (together referred to as BTEX), and a bulk residual gasoline component.

Evolution of the flow system, temperature distribution and dissolved plumes is simulated over time, until complete permafrost thaw.

2 NUMERICAL MODEL

The new 3D SMOKER-BIO model is a hybrid version of the BIONAPL/3D code for groundwater flow and multi-component reactive mass transport (Molson 2022), coupled with the HEATFLOW/SMOKER code for heat transport and permafrost thaw (Molson and Frind 2023). Field applications of the original codes include Freitas et al. (2010), Dagenais et al. (2020) and Liu et al. (2022).

https://doi.org/10.52381/ICOP2024.126.1

SMOKER-BIO couples a 3D transient groundwater flow equation with an advective-conductive heat transport equation, and with multiple advective-dispersive-reactive mass transport equations, one for each component and one for each electron acceptor, and includes microbial growth and decay. The equations are briefly reviewed below. For simplicity the groundwater flow equation is omitted.

2.1 Governing equations

The governing equation for heat transport is written as:

$$\frac{\partial (C_o T)}{\partial t} = -\frac{\partial}{\partial x_i}\left(\theta S_w c_w \rho_w v_i T\right) + \frac{\partial}{\partial x_i}\left(\left(\lambda + \theta S_w c_w \rho_w D_{ij}\right)\frac{\partial T}{\partial x_j}\right) \quad (1)$$

where T is the temperature (°C), θ is the porosity, S_w the unfrozen water saturation (-), c_w the specific heat (J/kg/K), ρ_w the fluid density (kgm^{-3}), v_i the pore velocity (ms^{-1}), λ is the bulk thermal conductivity of the porous medium (J/m/s/K), D_{ij} the hydrodynamic dispersion coefficient (m^{2}s^{-1}), t is time (s) and x_{ij} are the spatial coordinates (m). In Eq. 1, the temperature-dependent heat capacity C_o (Jm^{-3} K^{-1}), is defined as:

$$C_o = \theta S_w c_w \rho_w + \theta S_i c_i \rho_i + (1-\theta) c_s \rho_s + \theta \rho_i L \left(\frac{\partial S_w}{\partial T}\right) \quad (2)$$

where *L* is the latent heat of water (J/kg) and the subscripts *w*, *i* and *s* refer to the water, ice and solids, respectively. The unfrozen water saturation S_w in the above equations is here replaced by the temperature-dependent function *Wu*, which in turn is used to define an exponential relative permeability function $k_r(T)$ which accounts for pore blockage from ice formation. Further details are provided in Molson and Frind (2023).

The governing equation for advective-dispersive-reactive mass transport can be written as:

$$R\frac{\partial C^\alpha}{\partial t} = \frac{\partial}{\partial x_i}\left[D_{ij}\frac{\partial C^\alpha}{\partial x_j}\right] - v_i\frac{\partial C^\alpha}{\partial x_i} - \lambda^\alpha_{BIO} C^\alpha \quad (3)$$

where C^α is the concentration of component α (kgm^{-3}), R is the retardation factor to account for sorption, and λ^α_{BIO} is the effective biodegradation rate (s^{-1}), given by:

$$\lambda^\alpha_{BIO} = \sum_{n=1}^{N_A}\left[\tilde{k}^{\alpha,n} M^n \left(\frac{1}{K_C{}^{\alpha,n} + C^\alpha}\right)\bullet\left(\frac{A^n}{K_A{}^{\alpha,n} + A^n}\right)\right] \quad (4)$$

where $\tilde{k}^{\alpha,n}$ is the temperature-dependent maximum substrate utilization rate (kg$_S$kg$_M$$^{-1}$day^{-1}), A^n is the concentration of electron acceptor n (kgm^{-3}), M^n is the microbe concentration (kgm^{-3}), $K_C{}^{\alpha,n}$ is the organic half-utilization-rate concentration (kgm^{-3}), $K_A{}^{\alpha,n}$ is the electron acceptor half-utilization-rate concentration (kgm^{-3}) and N_A is the number of electron acceptors.

Following Mohammed et al. (2021), the temperature-dependency of the maximum utilization rate in Eq. 4 is expressed using a power function as:

$$\tilde{k}^{\alpha,n} = k^{\alpha,n} \cdot Q_{10}{}^{0.1\cdot(T-T*)} \quad (5)$$

where $k^{\alpha,n}$ is the intrinsic maximum degradation rate at the reference temperature T*, and Q_{10} is the rate increase factor for each 10 °C increase in temperature. While Eq. 5 was used by Mohammed et al. (2022) for DOC reactions, lacking specific temperature-dependent biodegradation rates for BTEX components, we adopt it here for simplicity. We note that in SMOKER-BIO, Eq. 5 can be easily replaced in a single line of code as more reliable rate laws become available.

Eq. 3 for each component is coupled with corresponding equations for transport and consumption of each electron acceptor:

$$R\frac{\partial A^n}{\partial t} = \frac{\partial}{\partial x_i}\left[D_{ij}\frac{\partial A^n}{\partial x_j}\right] - v_i\frac{\partial A^n}{\partial x_i} - \lambda^n_{BIO} A^n \quad (6)$$

where λ^n_{BIO} is the electron acceptor consumption rate (s^{-1}) which can be written as:

$$\lambda^n_{BIO} = \sum_{\alpha=1}^{Nc}\left[\tilde{k}^{\alpha,n} M^n X^{\alpha,n}\left(\frac{C^\alpha}{K_C{}^{\alpha,n} + C^\alpha}\right)\bullet\left(\frac{1}{K_A{}^{\alpha,n} + A^n}\right)\right] \quad (7)$$

where $X^{\alpha,n}$ is the stoichiometric ratio of the mass of electron acceptor consumed per mass of organic consumed (kg/kg) and N_c is the number of components. A single microbial population of concentration M^n is associated with each electron acceptor, and can grow or decay depending on the availability of substrates and electron acceptors. For simplicity, we neglect inhibition. See Molson (2022) for further details on the governing equations.

2.2 Solution approach

The groundwater flow, heat and mass transport equations are discretized using a Galerkin finite element scheme with Picard iteration to handle the non-linearities including temperature-dependent fluid density, viscosity, relative permeability (due to ice fraction), and the maximum substrate utilization rates $\tilde{k}^{\alpha,n}$. The bulk thermal conductivity, aquifer heat capacity, unfrozen water saturation and relative permeability are also temperature-dependent functions (see Molson and Frind, 2023).

Under Monod kinetics, the substrate and electron acceptor reaction rates (λ^α_{BIO} and λ^n_{BIO} in Eq. 4 and 7) are also non-linear and depend on the relative concentrations of the organic substrates, electron acceptors and microbial populations. Full details are provided in Molson and Frind (2023) and Molson (2022). While fully 3D, the model is here applied in a 2D vertical plane only.

3 MODEL APPLICATION

3.1 Conceptual model

The 2D vertical-plane conceptual model (Figure 1) is based on a reference scenario presented in Molson et al. (2002) in which a residual ethanol-free gasoline is dissolving into a shallow sandy aquifer under uniform temperature conditions. The changes for the current system include: 1) an increase in the aquifer thickness from 10 to 50 m to more realistically allow the addition of a permafrost layer, 2) replacement of the imposed flux condition at the left boundary by a fixed head boundary to allow a natural variation in flux depending on the freeze/thaw state, 3) replacement of the dissolving non-aqueous phase liquid (NAPL) source zone by an initial condition of dissolved-phase BTEX concentrations (avoiding the need for defining temperature-dependent NAPL dissolution rates which are not well known), 4) the addition of discontinuous permafrost within a horizontal silt layer, and 5) addition of temperature-dependent reaction rates.

The background sand aquifer is assumed isotropic with an intrinsic (unfrozen) hydraulic conductivity of 1e-5 m/s and a porosity of 0.35. Consistent with conditions at the Umiujaq field site (Nunavik, Québec, Canada; Dagenais et al. 2020), the discontinuous permafrost is set within a 20 m thick silt layer (see Figure 1 and Table 1 for all physical parameters).

The conceptual model includes a 3-component dissolved gasoline source zone, a single electron acceptor of oxygen, and a single aerobic microbial population. As applied in Molson et al. (2002), the three gasoline source components are i) benzene, ii) a lumped component representing toluene, ethylbenzene and xylene (TEX), and iii) a bulk component representing all (heavier) remaining hydrocarbons in the gasoline (Table 2; hereinafter, this source is simply referred to as BTEX).

Table 1. Flow, heat and component-independent transport parameter values assumed in the simulations.

Parameter	Value
Hydraulic conductivity K *	1e-5, 1e-6 m/s
Porosity*	0.35, 0.2
Specific storage	0.0 m^{-1}
Dry bulk density (ρ_b)	1700 kg/m^3
Thermal conductivity of water λ_w	0.58 J/m/s/K
Thermal conductivity of ice λ_i	2.14 J/m/s/K
Thermal conductivity of solids λ_s	2.0 J/m/s/K
Specific heat of water	4174 J/kg/K
Specific heat of ice	2108 J/kg/K
Specific heat of solids	800 J/kg/K
Density of solids	2630 kg/m^3
Dispersivities (α_L, α_{TV})	1.0, 0.01 m
Freezing function p,q**	0.1, 5.0
Latent heat of water	3.34e5 J/kg

* Intrinsic K (at T > 0°C): background, silt layer
** See Eq 19 and 24 in Molson and Frind (2023)

Table 2. Reaction stoichiometry and mass ratios used in the multi-component simulations (see Molson et al. 2002).

Gasoline Component	Reaction Stoichiometry	O_2:Substrate Mass Ratio $\chi^{\alpha,n}$ (kg_A/kg_S)
Benzene	$C_6H_6 + 15/2\ O_2 \rightarrow 6CO_2 + 3H_2O$	3.08
TEX	$C_7H_8 + 9O_2 \rightarrow 7CO_2 + 4H_2O$	3.13
Bulk	$C_8H_{18} + 25/2\ O_2 \rightarrow 8CO_2 + 9H_2O$	3.5

3.2 Domain, boundary and initial conditions

The 2D model domain is 400 m long by 50 m deep (Figure 1) which is discretized using a 1 m x 1 m square hexahedral mesh (the grid is 1 element wide in the transverse direction), for a total of 20,000 elements. A mean annual recharge rate of 200 mm/yr is applied across the top watertable boundary, a fixed head of 55 m is applied across the left inflow boundary, and a head of 50 m is applied at the right outflow boundary. The base is assumed impermeable.

For heat transport, the watertable is assumed to remain at a yearly average temperature of +1 °C over the 30-year simulation period, while a zero-gradient temperature condition is applied at the left and right, allowing advective energy inflow and outflow, respectively. A constant geothermal flux of 0.032 J/s/m^2 is applied at the base (Figure 1).

For mass transport, zero-gradient concentration conditions are applied for all components at the left, right and bottom, while Dirichlet (type-1) constant concentrations are applied at the top, representing background recharge water (i.e., BTEX concentrations of 0.0 mg/L and a dissolved oxygen concentration of 3.8 mg/L). Note that the initial background oxygen concentration is assumed less than its solubility due to oxidation of natural organic carbon.

The initial temperature of the discontinuous permafrost layer is assumed at -5 °C while an initial background temperature of +1 °C is applied everywhere else. For simplicity in this test example, a separate initial equilibration period is not included, and the model is run until all permafrost is thawed and the flow system has stabilized.

The aquifer is assumed initially uncontaminated with c = 0 for all components, and with background oxygen and microbe concentrations of 3.8 mg/L and 3.0 mg/L, respectively. Initial dissolved phase concentrations (C_o) for the BTEX and bulk components in the source zone (Table 3) are based on their pure phase solubilities and mole fractions of a standard gasoline (after Molson et al. 2002).

For the temperature-dependent rate expression of Eq. 5, we assume Q_{10} = 2.0 and a reference temperature T* = 10 °C. The effective biodegradation reaction rate thus decreases by a factor of 2 between 10 °C (where the reference rate applies) and 0 °C. Below 0 °C the reaction rate is assumed zero.

A uniform time step of 0.5 days was used for all simulations for which convergence was usually attained within 2–3 iterations at each time step. The model was run to

11,000 days (~30 years), by which time the permafrost had completely thawed.

Table 3. Reactive transport parameters and source concentrations assumed in the simulations for each component (from Molson et al. 2002).

Parameter	Benzene	TEX	Bulk
R (-)	1.1	2.0	2.8
D* (m^2/s) (1)	7.7e-10	6.2e-10	6.2e-10
$k^{\alpha,n}$ ($kg_S kg_M^{-1} d^{-1}$)	1.0	1.0	0.1
$K_C^{\alpha,n}$ (kg/m^3)	0.002	0.002	0.002
$K_A^{\alpha,n}$ (kg/m^3)	0.002	0.002	0.002
$X^{\alpha,n}$ (kg_A/kg_S)	3.08	3.13	3.5
C_o (g/L) (source)	0.0320	0.0455	0.0165

(1) D*: effective diffusion coefficient

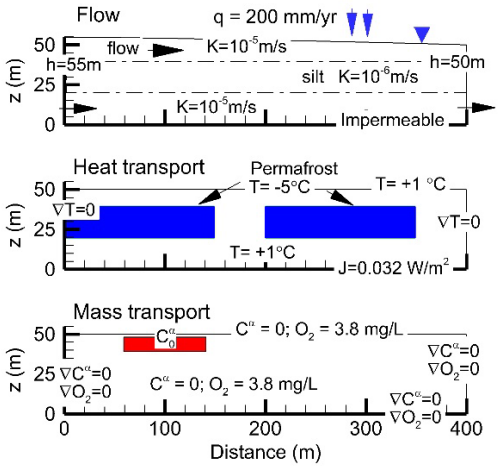

Figure 1. Simulation domain for the coupled reactive transport system showing boundary and initial conditions for flow, heat and mass transport.

3.3 Assumptions and limitations

The main assumptions in the simulations presented here include a fully saturated isotropic 2D porous medium, local thermal equilibrium, and linear equilibrium sorption. While the model can account for multiple electron acceptors, the reaction kinetics in this example assume only oxygen is present, they neglect inhibition, and assume the BTEX components degrade under complete mineralization (to CO_2 and H_2O). The microbial population is assumed immobile, and assumed inactive at T < 0 °C, and there is no effect of component concentrations on the freeze/thaw behaviour of groundwater. We note that by design, the time scale of permafrost thaw in this example (~30 years) is relatively fast, on the same order as the plume evolution, which helps identify process interaction and model functionality more rapidly. The example is not a verification of the model but a conceptual case only.

4 Simulation Results

Simulation results are provided in the vertical plane for the base case Scenario 1 with temperature-dependent reaction rates ($\tilde{k}^{\alpha,n}$), after 10 yrs and 30 yrs, respectively, in Figures 2 and 3. The flow system is illustrated as hydraulic head contours and using flow lines calculated from particle tracking with Tecplot©. Outlines of the three substrates (benzene, TEX and Bulk components), and of dissolved oxygen and the microbe population, are shown using concentration contours, with oxygen appearing as a depletion plume.

Acknowledging the simplifications of this example, model functionality with respect to coupling of the governing physical processes is nevertheless well illustrated.

Migration of the gasoline components is primarily driven by the background flow system, which at 10 yrs is still diverting around the two thawing permafrost zones (Figure 2) due to their lower relatively permeability. While several flow lines originating from the top left of the upper aquifer remain in the shallow zone above both permafrost blocks, others divert downward through the intervening talik (unfrozen zone within the silt), where they pass below the base of the right permafrost block.

While only representing a snapshot of the transient flow field, the particle tracks and time markers show advective travel times through the shallow unfrozen zone of about 20–30 yrs. Very low flow velocities through the permafrost lead to much longer travel times. Note that velocities also remain relatively low through the talik since the intrinsic (unfrozen) hydraulic conductivity of the silt layer remains 10 times less than the background aquifer. The presence of permafrost reduces the hydraulic conductivity much further.

These perturbations in the flow system due to the presence of (thawing) permafrost have subsequently affected evolution of the gasoline component plumes. Up to about 10 yrs, for example (Figure 2), the lower relative permeability of the permafrost tended to force the plumes to remain in the shallow thawed zone, rather than migrate and disperse deeper into the aquifer. At 10 yrs, the benzene plume, being the most mobile component, has reached the intervening talik, and begins to split, with one portion continuing in the shallow thawed zone while another follows the flow downward through the talik and eventually into the thawed zone below the right permafrost block.

Due to their higher retardation, the TEX and Bulk component plumes lag respectively behind the benzene plume (Figure 2). The corresponding dissolved oxygen plume, being non-retarded and depleted due to consumption during biodegradation of the hydrocarbons, migrates slightly ahead of the benzene plume, also showing a splitting effect through the talik due to the flow system. The tail of the oxygen depletion plume more closely follows the TEX and Bulk component plumes, the oxidation of which also consumes oxygen once the benzene plume has passed. Growth of the microbe population follows the BTEX plumes and oxygen depletion plumes.

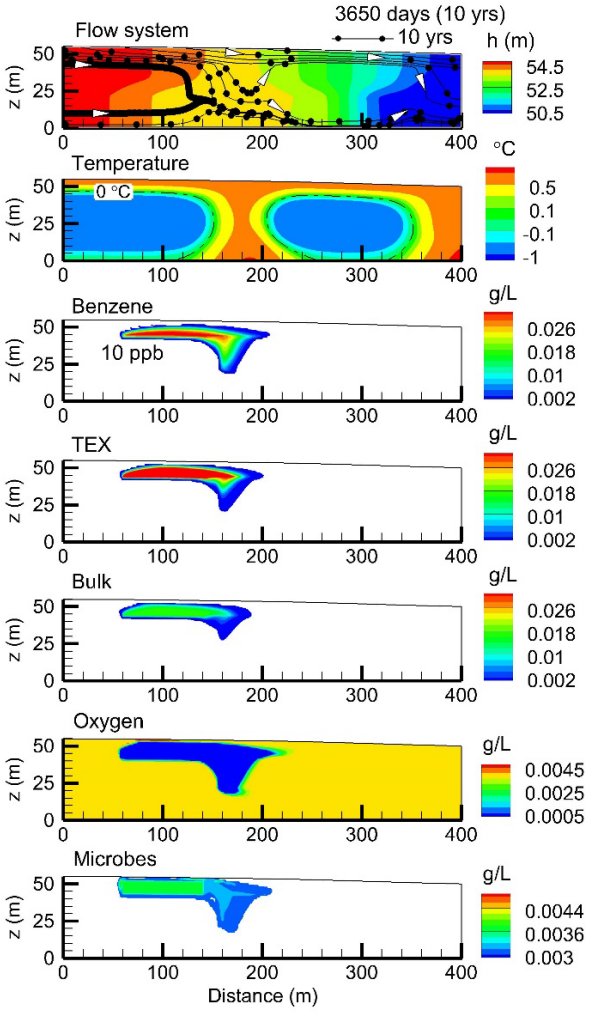

Figure 2. Base case (Scenario 1) simulation at 3650 days(10 yrs) with temperature-dependent reaction rates $\tilde{k}^{\alpha,n}$ (Eq. 5), showing the flow system, temperature, component concentrations, and dissolved oxygen and microbe concentrations. Time marker interval in the flow system is 5 yrs. Vertical exaggeration is 1.5x.

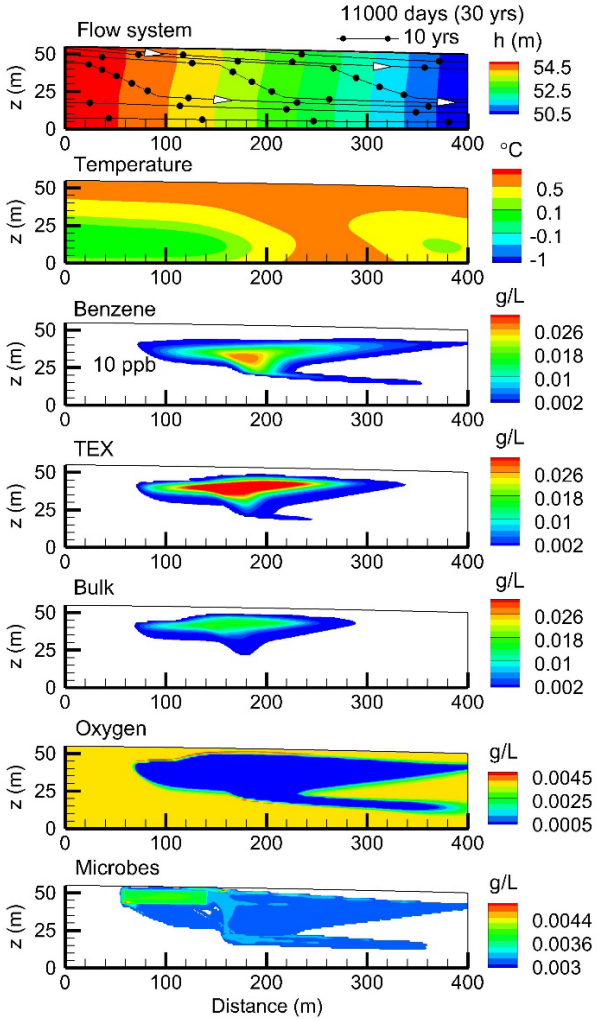

Figure 3. Base case (Scenario 1) simulation at 11,000 days (~30 yrs) with temperature-dependent reaction rates $\tilde{k}^{\alpha,n}$ (Eq 5), showing the flow system, temperature, component concentrations, and dissolved oxygen and microbe concentrations. Time marker interval in the flow system is 5 yrs. Vertical exaggeration is 1.5x.

Plume behavior with sorption, and with multi-component reactions in the presence of thawing permafrost, thus depends strongly on the transient flow system, notwithstanding the lower reaction rates due to colder temperatures. Different parts of each component plume, which are migrating at different velocities, respond differently to the local transient conditions.

By 30 yrs, the permafrost has completely thawed and the flow system has equilibrated, with flow dominantly in the upper and lower aquifers separated by the now unfrozen but still less permeable silt layer (Figure 3). Maximum travel times have decreased to about 60 yrs for flow passing through the silt. Of particular note is the asymmetrical shape of the benzene plume due to remnant effects of the talik and permafrost, with a relatively more elongated upper portion of the plume and a lower plume finger migrating in the lower aquifer. In comparison, due to their slower migration rates, the TEX and bulk component plumes show somewhat less asymmetry, having felt more of the recovered late-time flow system following permafrost thaw. In the oxygen depletion and microbial growth plumes, remnant plume 'fingers' are also evident within the lower aquifer.

To compare the effect on plume concentrations of the lower reaction rates with lower temperatures (Eq. 5), a second simulation (Scenario 2) was run with no temperature effect on the reaction rates, thus assuming the reference rates at 10 °C (while retaining the same conceptual model). These two scenarios are compared in Figures 4 and 5 as differences in concentration (Scenario 1 – Scenario 2) at 10 and 30 yrs, respectively.

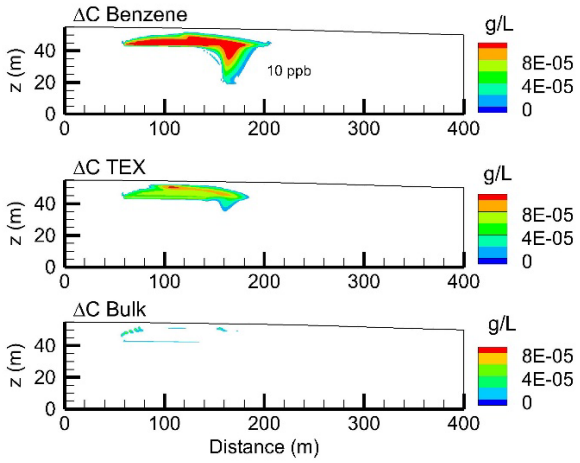

Figure 4. Concentration differences (ΔC) at 10 yrs, where ΔC = (Scenario 1 (temperature-dependent rates $\tilde{k}^{\alpha,n}$) – Scenario 2 (reference rates at 10 °C)), for B, TEX and Bulk components. Limit contour is 10 ppb for each component. Vertical exaggeration is 1.5x.

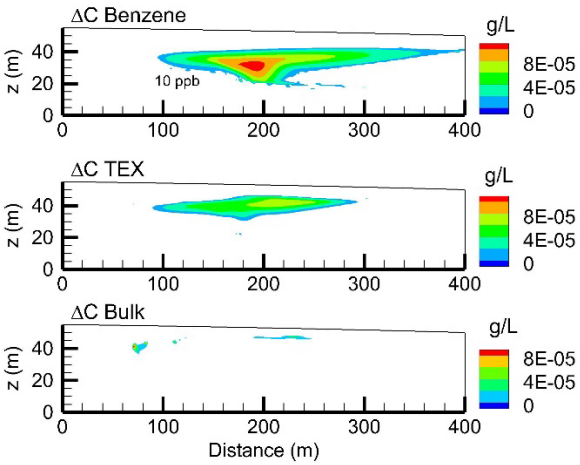

Figure 5. Concentration differences (ΔC) at 30 yrs, where ΔC = (Scenario 1 (temperature-dependent rates $\tilde{k}^{\alpha,n}$) – Scenario 2 (reference rates at 10 °C)), for B, TEX and Bulk components. Limit contour is 10 ppb for each component. Vertical exaggeration is 1.5x.

Concentrations of the gasoline components are higher with the temperature-dependent rates in Scenario 1 (hence positive differences in Figures 4 and 5) since the reaction rates are assumed up to 2x lower at temperatures near 0 °C (and reactions are assumed to cease at 0°C). However, the maximum differences for benzene are only on the order of 100 ppb (1e-4 g/L), and even less for TEX and the bulk components. The effects of temperature on reaction rates, even assuming a maximum 2x decrease from 10 °C to 0 °C, are somewhat attenuated since the effective reaction rates (Eq. 4 and 7 for the substrates and oxygen, respectively), even in the reference 10°C case, remain oxygen-limiting.

Oxygen limitations (and in general for any electron acceptor) arise from limited dispersive mixing and due to low background oxygen concentrations. Dispersive mixing is restricted by the low dispersivities (Table 1; in particular the transverse vertical dispersivity of 0.01 m), by the assumed homogeneous layers of the porous medium, and by the underlying low permeability permafrost. Although not included in this study, the higher solubility of oxygen at lower temperatures could further reduce the impact of lower reaction rates at lower temperatures.

Compared to benzene, the relative impact of temperature on plume concentrations decreases for TEX, and even further for the bulk component, because of lower intrinsic degradation since oxygen limitations increase for retarded plumes, and because the maximum utilization rate $\tilde{k}^{\alpha,n}$ is lowest for the bulk component (Table 3).

5 CONCLUSIONS

A 3D finite element numerical model has been developed for simulating coupled groundwater flow, heat transport with freeze/thaw, and multi-component advective-dispersive reactive transport. The model was applied and tested in a 2D vertical plane domain including thawing discontinuous permafrost, three dissolved gasoline components, and with dissolved oxygen as an electron acceptor.

Transport and fate of the dissolved gasoline components followed typical behavior associated with electron acceptor-limited biodegradation in more temperate climates, including plume separation due to differing retardation factors among the components, and the sequential consumption of dissolved oxygen. In this context of plume evolution in cold climates, which included discontinuous permafrost, the most significant effect on the hydrocarbon plumes was due to the perturbed flow system impacted by permafrost. In particular, flow deviation around the relatively lower permeability permafrost zones, and recovery of the flow system during permafrost thaw, was a controlling factor. While the lower-K silt layer had a persistent effect on the flow system, the presence of permafrost within the silt had an even greater influence, especially at early time when permafrost temperatures and the associated relative permeabilities of the silt, were lowest.

Effects of lower temperatures on reducing reaction rates were somewhat attenuated in this case since the system was effectively oxygen-limited, even without a temperature effect on the reaction rates. Temperature-dependent reaction rates might be expected to have greater effect under multi-electron acceptor systems (where availability of

specific electron-acceptors would be offset by the presence of others), with higher dispersive mixing, and with a seasonally-varying active layer.

Further testing of the model is underway under these more complex conditions, including under transient ground surface temperatures and benchmarking against other codes. Such models should also be tested against real field spills and using component-specific reaction rates determined under cold temperature conditions.

6 REFERENCES

Barkow, I.S., Oswald, S.E., Lensing, H-J., and Munz, M. 2020. 'Seasonal dynamics modifies fate of oxygen, nitrate, and organic micropollutants during bank filtration—temperature-dependent reactive transport modeling of field data', *Environmental Science and Pollution Research* 28, pp. 9682–9700. doi:10.1007/s11356-020-11002-9.

Dagenais, S., Molson, J., Lemieux, J.-M., Fortier, R., and Therrien, R. 2020. 'Coupled cryo-hydrogeological modelling of permafrost dynamics near Umiujaq (Nunavik, Canada)', *Hydrogeology Journal* 28, pp. 887–904. doi:10.1007/s10040-020-02111-3.

Frampton, A. and Destouni, G. 2015. 'Impact of degrading permafrost on subsurface solute transport pathways and travel times', *Water Resources Research* 51(9), pp. 7680–7701, doi:10.1002/2014WR016689.

Freitas, J., Mocanu, M., Zoby, J.L.G., Molson, J., and Barker, J. 2010. 'Migration and fate of ethanol-enhanced gasoline in groundwater: A modelling analysis of a field experiment', *Journal of Contaminant Hydrology* 119 (25–43), doi:10.1016/j.jconhyd.2010.08.007.

Grenier, C., Anbergen, H., Bense, V., Chanzy, Q., Coon, E., Collier, N., et al. 2018. 'Groundwater flow and heat transport for systems undergoing freeze-thaw: Intercomparison of numerical simulators for 2D test cases', *Advances in Water Resources* 114, pp. 196–21. Available at: https://doi.org/10.1016/j.advwatres.2018.02.001.

Lamontagne-Hallé, P. McKenzie, J.M., Kurylyk, B.L., Molson, J., and Lyon, L.N. 2020. 'Guidelines for cold-regions groundwater numerical modeling', *WIREs Water* 7, e1467. doi:10.1002/wat2.1467.

Lessels, J.S. Tetzlaff, D., Carey, S.K., Smith, P., and Soulsby, C. 2015. 'A coupled hydrology-biogeochemistry model to simulate dissolved organic carbon exports from a permafrost-influenced catchment', *Hydrological Processes* 29(26), pp. 5383–5396. doi:10.1002/hyp.10566.

Liu, W., Fortier, R., Molson, J., and Lemieux, J.-M. 2022. 'Three-dimensional numerical modeling of cryo-hydrogeological processes in a river-talik system in a continuous permafrost environment', *Water Resources Research* 58, https://doi.org/10.1029/2021WR031630.

Mohammed, A.A., Bense, V.F., Kurylyk, B.L., Jamieson, R.C., Johnston, L.H., and Jackson, A.J. 2021. 'Modeling reactive solute transport in permafrost-affected groundwater systems', *Water Resources Research* 57, doi:10.1029/2020WR028771.

Mohammed, A.A., Guimond, J.A., Bense, V.F., Jamieson, R.C., McKenzie, J.M., and Kurylyk, B.L. 2022. 'Mobilization of subsurface carbon pools driven by permafrost thaw and reactivation of groundwater flow: a virtual experiment'. *Environmental Research Letters* 17(12), 124036.

Molson, J.W., Barker, J., Frind, E.O., and Schirmer, M. 2002. 'Modelling the impact of ethanol on the persistence of benzene in gasoline-contaminated groundwater', *Water Resources Research* 38(1), pp. 4-1–4-12.

Molson, J.W. and Frind, E.O. 2023. *HEATFLOW-SMOKER User Guide, Density-dependent flow and advective-dispersive transport of mass, thermal energy or residence time in 3D porous* or discretely-fractured porous media. Version 5.0. Québec City, Québec, and Waterloo, Ontario, Canada: Université Laval and University of Waterloo.

Molson, J.W. 2022. *BIONAPL/3D User Guide, A 3D coupled flow and multi-component NAPL dissolution and reactive transport model*. Québec City, Québec, and Waterloo, Ontario, Canada: Université Laval and University of Waterloo.

Ramezanzadeh, M., Slowinski, S., Rezanezhad, F., Murr, K., Lam C., Smeaton, C., Alibert, C., Vandergriendt, M., and Cappellen, V.P. 2023. 'Effects of freeze-thaw cycles on methanogenic hydrocarbon degradation: Experiment and modeling' *Chemosphere* 325.

Yi, X., Su, D., Bussière, B., and Mayer, K.U. 2021a. 'Thermal-hydrological-chemical modeling of a covered waste rock pile in a permafrost region', *Minerals* 11(6), p. 565. doi:10.3390/min11060565.

Yi, X., Su, D., Seigneur, N., and Mayer, K.U. 2021b. 'Modeling of thermal-hydrological-chemical (THC) processes during waste rock weathering under permafrost conditions', *Frontiers in Water* 3, 645675. doi:10.3389/frwa.2021.645675.

Wiebe, A.J., McKenzie, J.M., Hamel, E., Rudolph, D., Mulligan, B., and de Grandpré, I. 2023. 'Groundwater vulnerability in the Yukon and Northwest Territories, Canada', *Hydrogeology Journal*. doi:10.1007/s10040-023-02720-8.

Controls on permafrost-related landform distributions, Dempster and Inuvik-Tuktoyaktuk Highway corridors, northwestern Canada

Peter D. Morse[1], Wendy E. Sladen[1], Ryan J.H. Parker[1], Sharon L. Smith[1] & Steven V. Kokelj[2]

[1]*Geological Survey of Canada, Natural Resources Canada, Ottawa, Ontario, Canada*

[2]*Northwest Territories Geological Survey, Government of Northwest Territories, Yellowknife, Northwest Territories, Canada*

ABSTRACT

Knowledge of the distributions of permafrost landforms are important because they serve as indicators of ground ice conditions and thaw sensitivity. Permafrost degradation at these locations changes the physiographic, hydrologic, and ecologic conditions and impacts northern landscapes, wildlife, and infrastructure. Geospatial inventories of these landforms are time-consuming to make and are often limited in extent and landform type, reducing their utility to support informed decisions regarding land management, resource development, infrastructure design and maintenance, and climate adaptation strategies. Such inventories did not exist in northwestern Canada where permafrost degradation is modifying environmental system dynamics and challenging the performance of the Dempster and Inuvik-Tuktoyaktuk Highway (DH-ITH). We analyzed a new, comprehensive geodatabase of 8746 permafrost-related landforms (periglacial, mass movement, and hydrological features) developed for an 875 km-long, 10 km-wide DH-ITH corridor. Though intuitive, our findings demonstrate how broad-scale spatial distributions of 25 different permafrost-related landforms relate to surficial geology, glacial history, and permafrost conditions, which are intrinsic to the set of physiographic regions in this area.

1 INTRODUCTION

In northwestern Canada (Figure 1), a range of physiographic settings exist as a function of variations in geology (Roots and Hart 2004), Quaternary deposits and history (Thomas and Rampton 1982a,b,c,d,e,f; Rampton 1988; Duk-Rodkin and Hughes 1992a,b; Gordey and Makepeace 2003), and permafrost conditions (Heginbottom et al. 1995). These physiographic variations have been characterized into distinct regions (Matthews 1986; Rampton 1988; Bostock 2014), and since the Second World War there has been great effort to study the processes and landforms that define them (e.g., Mackay 1963). This history of research has supported development of infrastructure for transportation, communities, and natural resource exploration and continues to this day (e.g., Kokelj et al. 2021). However, there are still great uncertainties regarding the distribution of ground ice, and consequently thaw sensitive terrains, despite recent, significant advancements on modelling regional ground ice distribution (e.g., O'Neill et al. 2019; Castagner et al. 2023).

Many permafrost-related landforms indicate ground ice presence and thaw susceptibility. Knowledge of their distributions is important, because permafrost degradation at these locations reduces ground stability, modifies terrain, and reconfigures drainage patterns, affecting terrestrial and aquatic ecosystems (e.g., Kokelj and Jorgenson 2013), and challenges the integrity of northern infrastructure (Hjort et al. 2022). Geospatial inventories of permafrost-related landforms can facilitate understanding of the broad-scale controls on their distributions and their associations with terrain settings (i.e., physiography, surficial geology, glacial history, and permafrost and ground ice conditions).

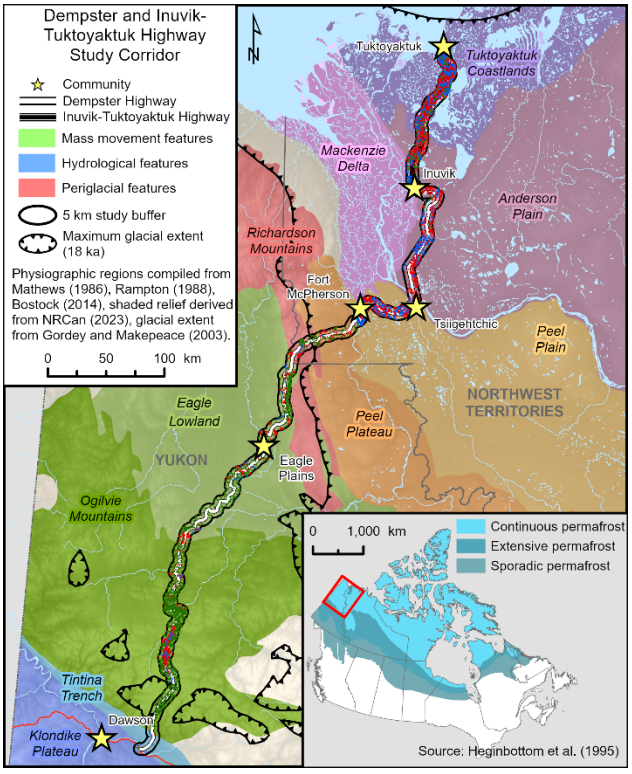

Figure 1. The DH-ITH mapping corridor, feature class distributions, physiographic regions, and maximum glacial extent. Inset shows study area location and continuous and discontinuous permafrost extents.

https://doi.org/10.52381/ICOP2024.140.1

Empirically based datasets are required to provide testing and validation data for predictive mapping activities (e.g., Rudy et al. 2019), and these data are also needed to increase the quality and quantity of information for decision-making related to land management, resource development, infrastructure design and maintenance, and climate change adaptation strategies (e.g., McKillop et al. 2016; Weiss et al. 2021).

Such inventories are typically limited to small extents, few landform types, or to broad scales using approaches that do not map individual landforms (e.g., Charbonneau et al. 2018; Gibson et al. 2021; Kokelj et al. 2021; Lou et al. 2022; Wolfe et al. 2023). Consequently, few detailed inventories are broad in spatial extent and comprehensive in the potential suite of thaw susceptible landforms, and until this study no comprehensive inventory has been developed for northwestern Canada.

The combined Dempster Highway and Inuvik-Tuktoyaktuk Highway (DH-ITH) corridor region (Figure 1) is an ideal regional north-south transect to develop a comprehensive inventory and investigate broad-scale controls on permafrost-related landform distributions, including surficial geology, glacial history, permafrost extent and ice content, and physiographic region. Changing permafrost conditions are significantly impacting transportation infrastructure at various locations along this corridor (Stockton et al. 2021), with new transmission infrastructure currently being buried adjacent to the DH. Thus, a multivariable landform inventory could be used to determine variation in the terrain sensitivity and potential vulnerabilities of the infrastructure to inform adaptation strategies and maintenance planning.

The 875 km-long, all-season, gravel DH-ITH connects southern Canada to the Arctic Ocean (Figure 1). Completed in 1978, the DH starts within unglaciated terrain of the Klondike Plateau in Yukon near Dawson (64.1°N), crosses the Tintina Trench, and runs northward through the high-relief Ogilvie Mountains of the Northern Cordillera. It continues through the rolling, unglaciated Eagle Lowland (or Plain) and then up into the higher relief of the unglaciated southern ranges of the Richardson Mountains where it crosses the Yukon – Northwest Territories border at Wright Pass (67.0°N). It then traverses the ice-rich morainal Peel Plateau and descends through the comparatively subdued relief of the Peel Plain with hummocky rolling moraine and poorly drained till plain with fens and peatlands until it meets the Mackenzie River near Tsiigehtchic. From the north shore of the river, the DH crosses gently-sloping, rolling terrain of Anderson Plain with till veneer and organic deposits, and terminates at Inuvik (68.4°N). Completed in 2017, the ITH begins at Inuvik and runs northward across the Anderson Plain where there is a range of unconsolidated deposits (the study corridor here includes Mackenzie Delta alluvium). At treeline, the route transitions to the Tuktoyaktuk Coastlands characterized by rolling and hummocky tills with dispersed lacustrine plains, reaching the Beaufort Sea coast at Tuktoyaktuk (69.4°N). Permafrost within the corridor is continuous except for the most southern ~100 km that is in extensive discontinuous permafrost (Heginbottom et al. 1995), and various forms of ground ice are present, dominated by wedge ice, segregated ice, intrusive ice, and buried glacial ice (Burn et al. 2015; O'Neill et al. 2019).

In this context, our aim is to provide an (qualitative) assessment of factors that influence the distribution of permafrost-related landforms and terrain sensitivity along the DH-ITH corridor. Our objectives are to: i) use a comprehensive approach to identify and map thermokarst and periglacial landforms, and ii) summarize the distributions of permafrost-related landforms based on permafrost and ground ice conditions, surficial geology, glacial history, and physiographic region (Figures 1, 2 and 3). To do this we analyze a geodatabase of permafrost-related landforms mapped within a 10 km-wide corridor (8560 km^2) that extends to the "height of the land" and is centred on the combined DH-ITH alignment (Sladen et al. 2022).

2 METHODOLOGY

The geodatabase of permafrost-related landforms for the DH-ITH corridor (Sladen et al. 2022) was generated using a new methodological protocol co-developed by the Geological Survey of Canada and the Northwest Territories Geological Survey to classify and digitize geomorphic features of permafrost terrain using high-resolution (0.6 m) satellite imagery (Sladen et al. 2021). Landforms were identified at 1:10,000 scale based on Canadian Digital Elevation Model (CDEM; NRCan 2023), and digitized at 1:5000 scale in a 3-D environment using Summit Evolution™ and ArcMAP™ platforms. Landforms were classified according to main formational process yielding sets of periglacial, mass movement, and hydrological features (Table 1). Landform verification was conducted in the field on a subset of mapped features during summer 2018, and other features were verified using Northwest Territories Ecological Land Classification Photos (NWTCG 2020). Landform attributes were assigned in a geographic information system according to overlay analysis with datasets for physiographic region (Mathews 1986; Rampton 1988; Bostock 2014), surficial geology (Thomas and Rampton 1982a,b,c,d,e,f; Rampton 1988; Duk-Rodkin and Hughes 1992a,b), glacial history (Gordey and Makepeace 2003), and permafrost extent and ground ice conditions (Heginbottom et al. 1995). The spatial data coordinate system used to calculate areas for this analysis is CSRS NAD 1983 datum projected to UTM Zone 8N.

Here we report the spatial density of landforms stratified by: i) continuous high ice (CH), continuous medium-to-high ice (CM-H), continuous low-to-medium ice (CL-M), continuous low ice (CL), and extensive discontinuous low-to-medium ice (EL-M) permafrost units (Heginbottom et al. 1995); ii) alluvium (A), colluvium (C), eolian (E), glaciofluvial (GF), glaciolacustrine (GL), lacustrine (L), moraine/till (M), organic (O), and bedrock (R) surficial geology units (Thomas and Rampton 1982a,b,c,d,e,f; Rampton 1988; Duk-Rodkin and Hughes 1992a,b); iii) glaciated (GLA) and unglaciated (UGLA) glaciation units (Gordey and Makepeace 2003); and iv) Klondike Plateau (KP), Tintina Trench (TT), Ogilvie Mountains (OM), Eagle Lowland (EL), Richardson Mountains (RM), Peel Plateau (PPT), Peel Plain (PPL), Anderson Plain (AP), Mackenzie Delta (MD), and Tuktoyaktuk Coastlands (TC) physiographic regions

(Mathews 1986; Rampton 1988; Bostock 2014). An alternate perspective on presenting landform densities is according to "land" area, but this does not work well for many of the hydrological features, and extensive water bodies (≥ 20% area) are limited to PPL, MD, AP, and TC (Figure 2). Thus, we report densities with respect to total area within the corridor. We do not investigate the roles of elevation or aspect as these local-scale factors of relief are not relevant to all features, and broad-scale influences of relief are captured by the different physiographies that are considered here.

Table 1. Landform classes, codes, counts and areas of based on dominant process and their associated landform types and subtypes.

Landform class	Code	Count (n)	Area (km^2)
Periglacial		5123	300.21
Ice-wedge polygon		3868	190.46
High centre	IWP-H	3204	152.30
Low centre	IWP-L	555	28.90
Undifferentiated	IWP-UN	109	9.26
Palsa	PALSA	4	0.12
Peat plateau complex	PEATP	762	78.07
Pingo	PINGO	113	0.97
String / Net fen	SNF	375	30.65
Unclassified	UN	1	30.65
Mass movement		2435	156.76
Complex	CX	3	0.24
Fall	FA	15	0.80
Flow		2218	152.76
Active-layer detachment	FL-ALD	155	1.76
Debris flow	FL-DF	925	50.96
Rock glacier	FL-RG	40	5.18
Retrogressive thaw slump	FL-RTS	389	4.52
Solifluction	FL-SO	662	87.95
Unclassified	FL-UN	47	2.40
Slide		93	1.17
Rotational slide	SL-RS	5	0.45
Shoreline slump	SL-SS	57	0.28
Unclassified	SL-UN	31	0.44
Unclassified	UN	106	1.80
Hydrological		1188	129.12
Aufeis	AUF	34	1.12
Beaded stream	BS	119	12.29
Drained-lake basin		118	19.74
Fully-drained	DLB-F	27	1.55
Partially-drained	DLB-P	91	18.19
Lake/pond affected by thermokarst	TL	917	95.97

3 RESULTS

With respect to area (Figure 2) and density (Figure 3), nearly 89% of the corridor area is continuous permafrost, with ground ice content generally increasing northward from low and medium at KP and TT to high throughout AP, MD, and TC. The most widespread surficial geology units are C (~39%), M (~32%), and A (~14%). Units C, A, and R (~2% overall), are concentrated in the five southernmost physiographic units that have comparatively high relief (KP northward to RM), with nearly 35% of RM composed of R. Over 95% of these same physiographic regions is outside the maximum limit of the Laurentide Ice Sheet (UGLA). From PPT north to TC, the terrain is entirely GLA, and surficial geology is dominated by glacial deposits M and GF (~6% overall), with the exception of MD physiographic unit with Holocene-age A deposits. In the north, L (~4% overall) is widespread in TC and comprises ~32% of deposits there.

Sladen et al. (2022) inventoried 8746 landforms (~586 km^2) within the DH-ITH corridor, including 5123 periglacial features (~300 km^2), 2435 mass movement features (~157 km^2), and 1188 hydrological features (129 km^2; Figure 1; Table 1). The density of all landforms in the corridor is 6.8%.

According to class, periglacial landforms are the most extensive with respect to area within the corridor (3.5%), followed by mass movement (1.8%), and hydrological (1.5%; Figure 4). Periglacial landforms are present in all physiographic units, with highest densities in TC (15.5%), PPL (12.0%), AP (10.8%), and OM (8.6%), but with densities ≤ 5% in the remaining units. According to permafrost unit, the highest densities of permafrost landforms are in CH (8.0%) and CL-M (4.1%) and are < 1.5% elsewhere. Most periglacial landforms are concentrated in glaciated terrain (5.2% of GLA) and are less dense (2.0%) in UGLA. With respect to surficial geology, nearly 25% of O comprises mappable permafrost landforms, compared to ~13.2%, ~9%, and ~8% for L, GF, and GL respectively, with densities < 5% in remaining units.

Unlike the periglacial class, mass movement and hydrological landforms are strongly partitioned by physiographic unit (Figure 4). Hydrological landform densities range from 0.9 to 9.7% in the four northern most physiographic units but are only 0.0 to 0.2% south of PPL. Hydrological landform densities are nearly zero beyond the maximum glacial limit UGLA, being concentrated in GLA (3.0%). Similarly, hydrological landforms are most dense in CH permafrost (4.5%) and are an order of magnitude less dense in other permafrost units. Hydrological features are most concentrated in A, GF, GL, L, and M surficial geology units with densities ranging from 1.5 to 6.2%, but are nearly absent in other units. Conversely, mass movement landforms are concentrated beyond the extent of the Laurentide ice sheet (3% in UGLA versus 0.5% in GLA), especially in OM (5.5%), EL (1.6%), and RM (1.6%) physiographic units. Mass movement densities are low (0.3%) in CM-H and CH permafrost units but range from 3.4 to 5.6% in other units.

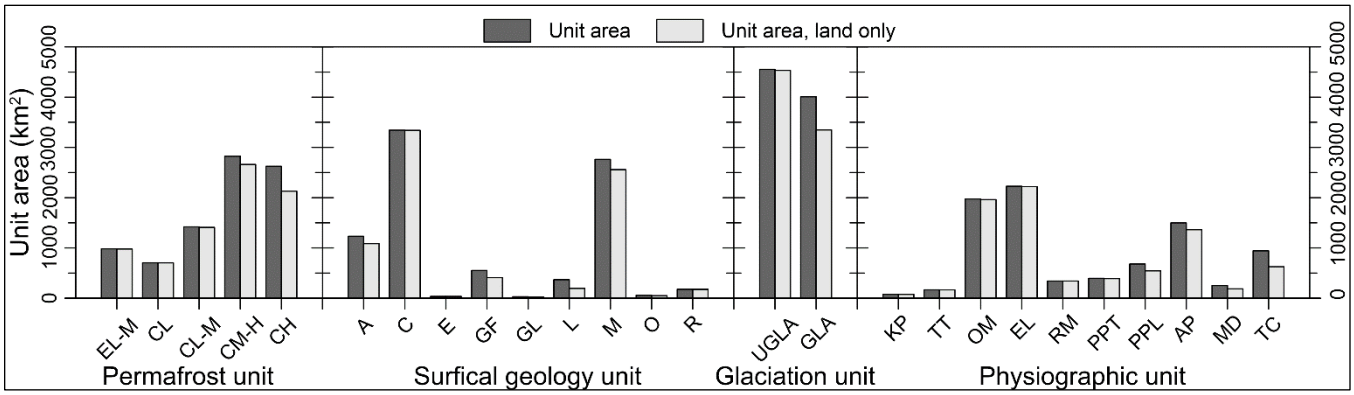

Figure 2. Total area and land-only area (water bodies excluded) with respect to permafrost, surficial geology, glaciation, and physiographic region. Unit codes are as defined in the methodology.

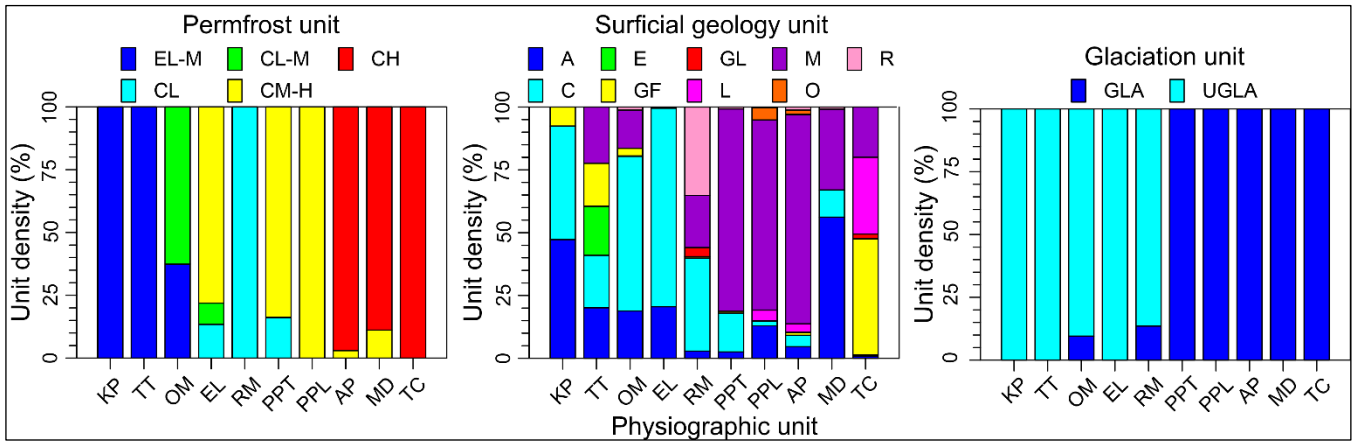

Figure 3. Distributions of permafrost, surficial geology, and glaciation with respect to physiographic region. Unit codes are as defined in the methodology. Physiographic regions are ordered from south to north.

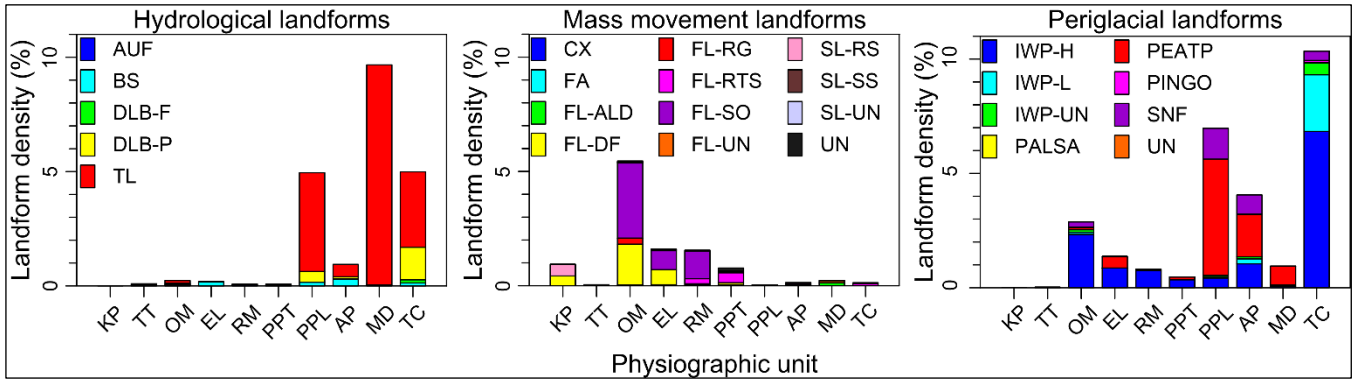

Figure 4. Densities of hydrological, mass movement, and periglacial landform classes with respect to spatial units of permafrost, surficial geology, glaciation, and physiographic region. Unit codes are as defined in the methodology.

With respect to densities of landform type and subtype for each major landform class according to physiographic region (Figure 5), almost 74% of the hydrological landform area comprises TL, and 72% is within PPL (4.3% density), AP (0.5% density), MD (9.6% density), and TC (3.3% density) physiographic units, where another ~14% of hydrological landform area comprises DLB-P in these very same physiographic units. Though densities are ≤ 0.3 everywhere, BS has the third highest contribution to total hydrological landform area (9.5%) and is most dense in AP (0.3%). Areas for AUF and DLB-F hydrological landforms are low (Table 1), with densities generally less than 0.1%.

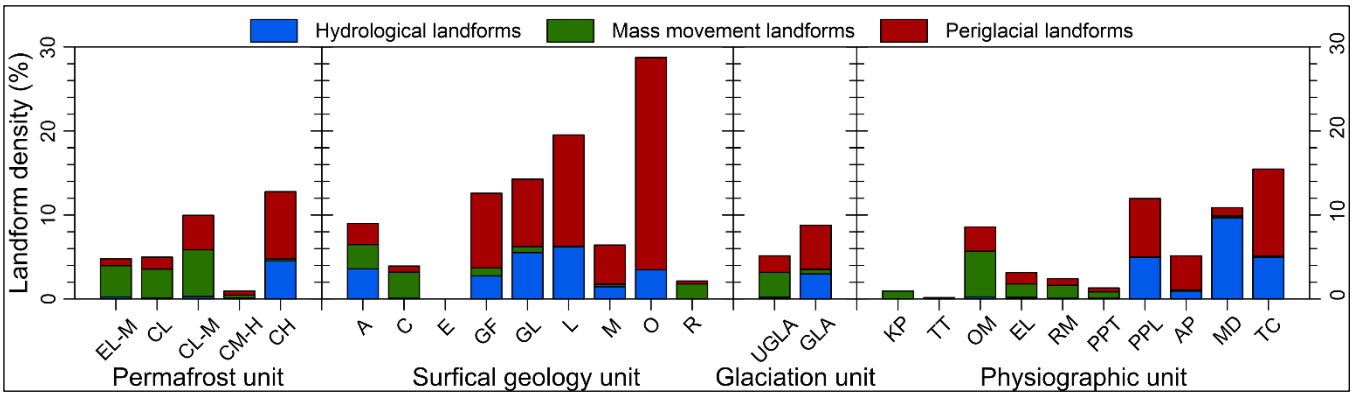

Figure 5. Densities of landforms for hydrological, mass movement, and periglacial landform classes summed with respect to physiographic region. Landform codes are as defined in Table 1. Physiographic region codes are defined in the methodology.

Of the 12 different mass movement landforms mapped, FL-SO accounts for ~56% of their combined area, with another ~33% from FL-DF. These two landforms are densest in OM physiographic unit, but FL-SO is common in EL and RM physiographic unis, and FL-DF in KP and EL. Also notable are FL-RTS that are concentrated at PPT.

Periglacial landforms are negligible at KP and TT but are otherwise common. Ice wedge polygons are the densest landforms, and ~51% of periglacial landform area is dominated by the thermokarst phase (IWP-H), but the active growth phase (IWP-L) is common at TC (23 km^2; ~10% of periglacial landform area). Nearly 26% of periglacial landform area is PEATP that is most dense in PPL (5.1%) and AP (1.8%) and with notable densities in MD (0.8%) and EL (0.5%). Finally, SNF are also commonplace, but are concentrated in PPL (1.3%), AP (0.8%), TC (0.4), and OM (0.2%).

4 DISCUSSION

Our summary of landforms mapped within the DH-ITH corridor has demonstrated that the spatial distributions of the hydrological, mass movement, and periglacial landforms in the vicinity of the DH-ITH vary according to permafrost extent and ground ice condition, surficial geology, glacial history, and physiographic region (Table 1; Figures 1 and 3 to 5). Periglacial and hydrological features are concentrated in the northern portion of the corridor and coincide with terrains that were glaciated and have continuous permafrost with medium-high and high ground ice content, whereas mass movement features dominate the southern portion of the corridor, most of which was unglaciated during the Wisconsinan.

Hydrological landforms are most densely distributed throughout GLA terrain (~93% of hydrological landform area), with continuous permafrost and high ground ice contents (CH) (~92% of hydrological landform area), and with relatively low relief terrains associated with glacial deposits (GF, GL, M), Holocene thermokarst lake basins (L), and alluvium (A) and organic (O) deposits. The combinations of these conditions promote dense distributions of hydrological landforms in PPL, AP, MD, and TC physiographic units, which are dominated by TL landforms though DLB-P are common in PPL and TC. Hydrological landforms are sparse within UGLA terrain, with BS being most dense. Together these findings emphasize the influence that ice-rich glacial deposits have had on both past and contemporary thermokarst development, and likely on future thermokarst associated with climate warming.

Mass movement landforms, in contrast to hydrological landforms, are densest and most extensive in UGLA (~86% of mass movement landform area), where there is low and low-to-medium ground ice content in permafrost (~90% of mass movement area), and especially where there is C surficial geology unit (~66% mass movement area). Consequently, this class of landforms is extensive within OM, EL, RM physiographic units (~94% mass movement area) that have high relative relief. FL-SO and FL-DF landforms dominate this landform class. Locally common, FL-RG occurs exclusively within OM (~3% of mass movement landform area), and within GLA, FL-RTS (~3% mass movement area) have densities ≥0.1% in RM, PPT, and TC physiographic units. These findings demonstrate the influence that location with respect to the Laurentide Ice Sheet margin has on the spatial variation of mass movement landforms. They further suggest and that FL-SO, FL-DF, and FL-RG likely deserve more scientific attention, which in northwestern Canada has predominantly focused on FL-RTS (e.g., Kokelj et al. 2017, 2021).

Periglacial landforms are the most numerous, extensive, and densest landform class, occurring throughout the corridor region within GLA and UGLA, all permafrost units, and nearly all surficial geology units. However, they are concentrated in continuous permafrost of GLA, where there are glacial or modified glacial surficial deposits (M, GF, GL, and L). Though nearly 25% of O comprises mappable periglacial landforms, as with GL and E it comprises <1% of the corridor area. In high-relief, UGLA terrain the most densely distributed landform is IWP-H (OM, EL, RM physiographic units) as frost cracking was likely promoted throughout the Wisconsinan in C and A surficial geology units, whereas permafrost was obliterated beneath the Laurentide Ice Sheet in many places that were glaciated (Rampton 1988). The thermokarst phase (IWP-H) is dominant everywhere ice wedges were mapped, including

TC physiographic unit, where there is a notable density of IWP-L (2.5%) and many ice wedges in TC are known to be active (e.g., Kokelj et al. 2014). Within PPL and AP physiographic units, PEATP and SNF are comparatively dense, where we have observed that the gently sloping, rolling terrain has widespread areas of poor drainage that have promoted extensive permafrost peatlands and wetlands. Pingos, although of cultural and scientific interest, have a density of only 0.1% in TC where they are among the most concentrated in the world (Mackay 1963; Wolfe et al. 2023), but contribute little to the regional density of periglacial landforms.

Primarily a desktop study, the main database limitation is the CDEM used for 3-D visualization. It was available for the entire study area, but its ~20-m resolution is not well matched to the satellite imagery. This created some difficulty identifying and/or delineating some landforms. In such cases, available high-resolution LiDAR data were consulted. Other limitations relate to using optical imagery and the ground being obscured in places by cloud cover or shadow, or temporal or spatial breaks between satellite images that may have influenced identification of some features. Finally, some digitized landforms may have offset geographic positions due to the difficulty of orthorectifying satellite imagery in some areas due to insufficient ground control points. Human errors during landform mapping likely exist but were minimized using standardized criteria and protocols to identify and digitize features, and landform digitization was evaluated in an iterative manner between two expert mappers (Sladen et al. 2021). We used the most appropriate attribute data available at the time of mapping, but these datasets are dated, and unit boundaries will likely change if they are refined in the future.

Our research sets the stage for future work including quantitative statistical analysis to improve understanding of how landforms combine and control environmental variables, and spatial analysis of specific periglacial landform types with respect to field-based observations of ground ice and with national-scale estimates of ice-wedge, segregated, and buried ground ice distributions (O'Neill et al. 2019). Our results can be used to train thaw susceptibility modelling for the entire corridor region following the machine learning approach of Rudy et al. (2019), complimenting available landform data. Further, specific landforms in the database may be compared to existing (e.g., Lantz et al. 2017) or developing (e.g., Kokelj et al. 2023) landform inventories to build a more robust understanding of controls on landform distributions and their fate in a changing climate, and to provide insights on methodological limitations and advantages of the various approaches. Finally, the mapping protocol has been modified and applied to develop an analogous landform database for a proposed transportation corridor that would link Yellowknife, NT, to Grays Bay, NU (Morse et al. 2023). Comparison of the two landscape transects (and potentially others) can facilitate improved understanding of permafrost landscape evolution in northern Canada. From a practical perspective, this analysis and data can be used to extend geohazard mapping such as that by McKillop et al. (2016) to the height of the land, which can inform decisions regarding highway realignments to address infrastructure integrity issues due to climate change (Stockton et al. (2021).

5 CONCLUSIONS

This is the first investigation to use a set of 25 permafrost-related landforms, derived from a comprehensive geodatabase, and demonstrate how their varying spatial distributions in northwestern Canada relate to differences in permafrost extent and ground ice conditions, surficial geology, and glacial history, which are characteristics inherent to regional physiographic variation. Using a multi-variate approach, the research shows the distribution of permafrost-related landforms and their combined influence on terrain sensitivity. This fine-scale mapping compliments other recent initiatives that advance a multivariate approach to understand landform combinations and drivers of variation in northwestern Canada (Kokelj at al. 2023).

Glacial history is a clear control on the distributions of hydrological and mass movement landform classes, in agreement with Kokelj et al. (2021). Hydrological landforms (predominantly TL) are most dense in northern glaciated terrains with rolling relief and relatively poor drainage, whereas mass movements (predominantly FL-SO and FL-DF) are concentrated in unglaciated terrain with high relative relief and comparatively good drainage. Periglacial landforms, dominated by IWP-H that occur throughout the corridor, have greatest densities in northern, glaciated terrains where 97% of FL-RTS area is mapped.

Permafrost exerts control on landform densities through its extent and ground ice content. Within extensive discontinuous permafrost terrain (southernmost ~100 km of the corridor), the density of permafrost-related landforms is low and comprises almost entirely mass movements FL-DF and SL-RS. Permafrost is continuous elsewhere, with higher landform densities in southern terrains where ice content is low-medium, and highest in northern terrains where ice content is high. Landform densities are low in permafrost with low to medium ice content, based on the generalized classification of Heginbottom et al. (1995).

Surficial geology units, which are influenced by landscape history and geological setting, have clear relationships to distributions of permafrost-related landforms. In mountainous, unglaciated terrains, landform densities are predominantly related to occurrences of C and A as these two units are extensive. In glaciated areas, M, A, GF, and L units are the most extensive (in descending order), but landforms are most dense in O, L, GL, GF, and M units (in descending order). Units with higher densities of permafrost-related landforms potentially have a higher climate response. Thus, based on surficial geology unit areas and landform densities, M, C, and A may represent the geological units with the most overall climate response as they account for 86% of total area and 71% of total landform area, especially M that accounts for > 30% of both land and landform areas.

Physiographic units reflect the terrain conditions they are characterized by and landform densities among them vary substantially. TC, located at the maximum extent of the Laurentide Ice Sheet, with extensive glacial deposits and ice-rich permafrost, has the highest density of landforms,

which are dominantly periglacial and hydrological. Landform densities in PPL and MD are the same magnitude as TC, but MD is characterized by extensive TL hydrological landforms in A, whereas PPL has extensive PEATP and SNF in in contrast to extensive ice-wedge polygons within TC. From an area perspective, however, OM may exhibit the greatest physical response to climate change within this corridor even though permafrost generally has low to medium ice content. This is because OM has the second greatest area and the fourth highest density of landforms, which are predominantly FL-SO, FL-DF, and IWP-H that occur in association with C, A, and M deposits.

The suite of landform densities draws attention to types like solifluction, debris flows, and rock glaciers that are common and even locally widespread but have not received as much scientific attention as ice-wedge polygons or retrogressive thaw slumps.

6 ACKNOWLEDGEMENTS

This research was supported by Natural Resources Canada, Northwest Territories Geological Survey, and Transport Canada. The authors would like to highlight the significant contributions of Erik Duncan, Samuel Jardine, and Andrew Branson for meticulous identification and digitization of features. Marcus Phillips provided valuable feedback on the manuscript. Comments by anonymous reviewers are appreciated.

7 REFERENCES

Bostock, H.S. 2014. 'Physiographic Regions of Canada', *Geological Survey of Canada* "A" Series Map 1254A, 3 sheets. doi:10.4095/293408.

Burn, C.R., Moore, J.L., O'Neill, H.B., Hayley, D.W., Trimble, J.R., Calmels, F., Orban, S.N., and Idrees, M. 2015. 'Permafrost Characterization of the Dempster Highway, Yukon and Northwest Territories', in *GeoQuébec 2015*, Proceedings of the 7th Canadian Permafrost Conference. Québec City, Québec, Canada: Paper 705.

Castagner, A. Brenning, A., Gruber, S., and Kokelj, S.V. 2023. 'Vertical Distribution of Excess Ice in Icy Sediments and its Statistical Estimation from Geotechnical Data (Tuktoyaktuk Coastlands and Anderson Plain, Northwest Territories)', *Arctic Science* 9(2), pp. 483–496. doi:10.1139/as-2021-0041.

Charbonneau, A.A. and Smith, D.J. 2018. 'An Inventory of Rock Glaciers in the Central British Columbia Coast Mountains, Canada, from High Resolution Google Earth Imagery', *Arctic, Antarctic, and Alpine Research* 50(1), e1489026. doi:10.1080/15230430.2018.14890.

Duk-Rodkin, A. and Hughes, O.L. 1992a. 'Surficial Geology, Fort McPherson-Bell River, Yukon-Northwest Territories', *Geological Survey of Canada* Map 1745A. doi:10.4095/184002.

Duk-Rodkin, A., and Hughes, O.L. 1992b. 'Surficial Geology, Arctic Red River, District Mackenzie, Northwest Territories', *Geological Survey of Canada* Map 1746A. doi:10.4095/184003.

Gibson, C., Cottenie, K., Gingras-Hill, T., Kokelj, S.V., Baltzer, J.L., Chasmer, L., and Turetsky, M.R., 2021. 'Mapping and Understanding the Vulnerability of Northern Peatlands to Permafrost Thaw at Scales Relevant to Community Adaptation Planning', *Environmental Research Letters* 16, 055022. doi:10.1088/1748-9326/abe74b.

Gordey, S.P. and Makepeace, A.J. 2003. 'Yukon Digital Geology (v.2)', *Geological Survey of Canada* Open File 1749. doi:10.4095/214639.

Heginbottom, J.A., Dubreuil, M.A., and Harker, P.T. 1995. 'Canada – Permafrost', in *National Atlas of Canada*, 5th edition. Natural Resources Canada, MCR 4177. doi:10.4095/294672.

Hjort, J., Streletskiy, D., Doré, G., Wu, Q., Bjella, K., and Luoto, M. 2022. 'Impacts of Permafrost Degradation on Infrastructure', *Nature Reviews Earth and Environment* 3, pp. 24–38. doi:10.1038/s43017-021-00247-8.

Kokelj, S.V. and Jorgenson, M.T. 2013. 'Advances in Thermokarst Research', *Permafrost and Periglacial Processes*, 24(2), pp. 108–119. doi:10.1002/ppp.1779.

Kokelj, S.V., Gingras-Hill, T., Daly, S.V., Morse, P.D., Wolfe, S.A., Rudy, A.C.A, et al. 2023. 'The Northwest Territories Thermokarst Mapping Collective: A Northern-Driven Mapping Collaborative Toward Understanding the Effects of Permafrost Thaw'. *Arctic Science* 9, pp. 886–918. doi:10.1139/AS-2023-0009.

Kokelj, S.V., Kokoszka, J., van der Sluijs, J., Rudy, A.C.A., Tunnicliffe, J., Shakil, S., Tank, S.E., and Zolkos, S. 2021. 'Thaw-driven Mass Wasting Couples Slopes with Downstream Systems, and Effects Propagate Through Arctic Drainage Networks', *The Cryosphere* 15, pp. 3059–3081. doi:10.5194/tc-15-3059-2021, 2021.

Kokelj, S.V., Tunnicliffe, J.F., and Lacelle, D. 2017. 'The Peel Plateau of Northwestern Canada: An ice-rich Hummocky Moraine Landscape in Transition', in O. Slaymaker(ed.), *Landscapes and Landforms of Western Canada*. Switzerland: Springer Cham, pp.109–122. Available at: https://doi.org/10.1007/978-3-319-44595-3_7.

Kokelj, S.V., Lantz, T.C., Wolfe, S.A., Kanigan, J.C., Morse, P.D., Coutts, R., Molina-Giraldo, N., and Burn, C.R. 2014. 'Distribution and Activity of Ice Wedges Across the Forest-tundra Transition, Western Arctic Canada', *Journal of Geophysical Research: Earth Surface* 119, pp. 2032–2047. doi:10.1002/2014JF003085.

Lantz, T., Steedman, A., Kokelj, S.V., and Segal, R. 2017. 'Inventory of Polygonal Terrain in the Tuktoyaktuk Coastlands, Northwest Territories', *Northwest Territories Geological Survey* NWT Open Report 2016-22. doi:10.46887/2016-022.

Luo, J., Niu, F., Lin, Z., Liu, M., Yin, G., and Gao, Z. 2022. 'Inventory and Frequency of Retrogressive Thaw Slumps in Permafrost Region of the Qinghai–Tibet Plateau', *Geophysical Research Letters* 49, e2022GL099829. doi:10.1029/2022GL099829.

Mackay, J.R. 1963. 'The Mackenzie Delta Area, N.W.T.', *Geographical Branch, Mines and Technical Surveys* Memoir 8.

Mathews, W.H. 1986. 'Physiographic Map of the Canadian Cordillera', *Geological Survey of Canada* "A" Series Map 1701A. doi:10.4095/122821.

McKillop, R.J., Brown, C.E., McParland, D.J., Sacco, D.A. and Coates, J. 2016. 'Inventory of Mass Movement Geohazards along the Dempster Highway, Yukon', *Yukon Geological Survey* Miscellaneous Report 17.

Morse, P.D., Parker, R.J.H., Smith, S.L., and Sladen, W.E. 2023. 'Permafrost-Related Landforms and Geotechnical Data Compilation, Yellowknife to Grays Bay Corridor Region, Slave Geological Province', *Geological Survey of Canada* Open File 8986. doi:10.4095/332017.

Natural Resources Canada (NRCan) 2023. 'Canada Digital Elevation Model, 1945-2011', *Government of Canada* Open Maps. Available at: https://open.canada.ca/data/en/dataset/7f245e4d-76c2-4caa-951a-45d1d2051333 [Accessed: 14 July 2023].

Northwest Territories Centre for Geomatics (NWTCG) 2020. 'Ecological Land Classification Photos, Spatial Data Warehouse (SDW)', *Northwest Territories Centre for Geomatics*, Government of Northwest Territories. Available at: https://www.maps.geomatics.gov.nt.ca/Html5Viewer/index.html?viewer=SDW [Accessed on 14 July, 2023].

Rampton, V.N. 1988. 'Quaternary Geology of Tuktoyaktuk Coastlands, Northwest Territories', *Geological Survey of Canada* Memoir 423. doi:10.4095/126937.

Roots, C. and Hart, C. 2004. 'Bedrock Geology', in C.A.S. Smith, J.C. Meikle and C.F. Roots (eds.), *Ecoregions of the Yukon Territory: Biophysical Properties of Yukon Landscapes*. Summerland, British Columbia, Canada: Agriculture and Agri-Food Canada, pp. 11–14.

Rudy, A.C.A., Morse, P.D., Kokelj, S.V., Sladen, W.E., and Smith, S.L. 2019. 'A New Protocol to Map Permafrost Geomorphic Features and Advance Thaw-Susceptibility Modelling', in J.-P. Bilodeau, D.F. Nadeau, D. Fortier and D. Conciatori (eds.) *Cold Regions Engineering 2019*, proceedings of the 18th International Conference on Cold Regions Engineering and the 8th Canadian Permafrost Conference. Québec City, Québec, Canada: pp. 661–669. doi:10.1061/9780784482599.

Sladen, W.E., Parker, R.J.H., Kokelj, S.V., and Morse, P.D. 2021. 'Geomorphologic Feature Mapping Methodology Developed for the Dempster Highway and Inuvik to Tuktoyaktuk Highway Corridors', *Geological Survey of Canada* Open File 8751. doi:10.4095/328181.

Sladen, W.E., Parker, R.J.H., Morse, P.D., Kokelj, S.V., and Smith, S.L. 2022. 'Geomorphic Feature Inventory Along the Dempster and Inuvik to Tuktoyaktuk Highway Corridor, Yukon and Northwest Territories', *Geological Survey of Canada* Open File 8885. doi:10.4095/329969.

Stockton, E.J., Burn, C.R., and Humphries, J. (eds.) 2021. 'Compendium of Permafrost Reports: Northern Transportation Adaptation Initiative (NTAI) 2011-2021', *Carleton University*, Ottawa, Ontario. doi:10.52381/CPR.NTAI.2021.

Thomas, R.D. and Rampton, V.N. 1982a. 'Surficial Geology and Geomorphology North Klondike River, Yukon Territory', *Geological Survey of Canada* Preliminary Map 6-1982. doi:10.4095/119397.

Thomas, R.D. and Rampton, V.N. 1982b. 'Surficial Geology and Geomorphology Upper Blackstone River, Yukon Territory', *Geological Survey of Canada* Preliminary Map 7-1982. doi:10.4095/119066.

Thomas, R.D. and Rampton, V.N. 1982c. Surficial Geology and Geomorphology Engineer Creek, Yukon Territory, Preliminary Map 8-1982, Geological Survey of Canada, Ottawa, ON, Canada. doi:10.4095/119068.

Thomas, R.D. and Rampton, V.N. 1982d. 'Surficial Geology and Geomorphology Lower Ogilvie River, Yukon Territory', *Geological Survey of Canada* Preliminary Map 9-1982. doi:10.4095/119382.

Thomas, R.D. and Rampton, V.N. 1982e. 'Surficial Geology and Geomorphology Moose Lake, Yukon Territory', *Geological Survey of Canada* Preliminary Map 10-1982. doi:10.4095/119383.

Thomas, R.D. and Rampton, V.N. 1982f. 'Surficial Geology and Geomorphology Rock River, Yukon Territory', *Geological Survey of Canada* Preliminary Map 11-1982. doi:10.4095/119386.

Weiss, N., Kokelj, S.V., Rudy, A.C.A., Baltzer, J.L., Daly, S.V., Ferguson, C., Gingras-Hill, T., Morse, P.D., Paul, J.R., Pope, M., Wilson, A., and Wolfe, S.A. 2021. 'Contrasts in NWT Community Sensitivity to Permafrost Thaw from Broad-Scale Thermokarst Mapping', *Northwest Territories Geological Survey.* Available at: https://www.nwtgeoscience.ca/gsforum/contrasts-nwt-community-sensitivity-permafrost-thaw-broad-scale-thermokarst-mapping.

Wolfe, S.A, Morse, P.D., Parker, R., and Philips, M. 2023. 'Distribution and Morphometry of Pingos, Western Canadian Arctic, Northwest Territories, Canada', *Geomorphology* 431, 108694. doi:10.1016/j.geomorph.2023.108694.

Fostering climate resilience through northern standards: Shaping a resilient future

Ulrikke Oernholt, Patricia Chartrand, Stephanie Poirier & Kala Pendakur

Standards Council of Canada, Ottawa, Ontario, Canada

ABSTRACT

Climate-resilient standards and guidelines – those that consider a future-looking climate and account for associated risks – can be powerful resources for professionals, practitioners, and governments in designing and implementing sustainable solutions. By standardizing best practices, National Standards of Canada (NSCs) can streamline and harmonize the field of climate resilience while playing an integral role in improving the overall health and safety of Canadians, and of their environment. The Standards Council of Canada (SCC) is leading the development of climate-resilient standards that can be implemented to adapt communities to climate change and extreme natural events.

Since 2011, SCC has been working with communities, standards development organizations, and experts from across northern Canada to lead the development of standards that consider climate change impacts in northern infrastructure design, planning and management. This paper will cover the development of standards and guidelines that support the design of foundations and infrastructure in permafrost regions, namely:

- CSA S500:21 Thermosyphon foundations for buildings in permafrost regions
- CSA S501:21 Moderating the effects of permafrost degradation on existing building foundations
- BNQ 9701-500 Risk-based approach for community planning in northern region
- CSA PLUS 4011:19 Technical guide: Infrastructure in permafrost: A guideline for climate change adaptation

The purpose of this study is to highlight standards that will help building owners and operators, as well as those responsible for public and community infrastructure, build and maintain infrastructure in a changing climate in permafrost regions. Further, it is meant to inform northern practitioners on the benefit of building and designing infrastructure with guidance that goes “beyond the building code” under a changing climate.

1 INTRODUCTION

1.1 Standards and climate change

Communities worldwide are facing negative impacts from climate change and extreme weather events. Canada's Northern Region is particularly vulnerable, experiencing temperatures rising three times faster than the global average (Bush and Lemmen 2019). This has led to more intense storms, higher precipitation, melting sea ice, and coastal erosion. Further, changing permafrost conditions pose a significant challenge, as most buildings were historically designed to account for frozen ground. Climate change has disrupted this norm, leaving older structures unprepared for shifting permafrost and thus more susceptible to damage like sinking and cracking. Given the high costs and challenges of building in remote regions of the North, it is important that buildings are made to be resilient. Climate-informed standards can play a crucial role in ensuring this durability and adaptability (Standards Council of Canada 2023a).

1.2 Standards as part of a toolbox

Standards outline accepted practices, guidelines, and technical criteria for diverse sectors and areas. Engineers, asset owners and planners rely on standards to ensure developed products and services meet a minimum level of performance and provide assurance to the owner and user of the product or service. Standards are voluntary by default but become mandatory when referenced in codes, acts or regulations.

Building standards, that consider a future looking climate, are an integral part of a community’s adaptation strategy and provide a concrete framework on how to address the challenges presented by climate change by assessing the risks and impacts to infrastructure.

With climate-informed infrastructure standards, communities will be able to adapt and adjust for future impacts to deliver reliable, equitable, and sustainable services to all of society by factoring in climate change adaptation into their operational practices (Environment and Natural Resources Canada 2023).

1.3 The Standards Council of Canada (SCC) and the Northern Infrastructure Standardization Initiative (NISI)

SCC is a federal crown corporation with the mandate to promote efficient and effective voluntary standardization in Canada.

A significant initiative under SCC is the Standards to Support Resilience in Infrastructure Program (SSRIP). Collaborating with Canada’s national standardization network, academia, industry, and all levels of government, SSRIP spearheads the creation and application of standardized solutions to enhance infrastructure resilience,

https://doi.org/10.52381/ICOP2024.196.1

thus fostering more resilient communities for the people of Canada. The primary goal of SSRIP is to advance technical guidance that empowers Canadian households, businesses, and communities to adapt to the challenges posed by climate change and extreme weather events. The program envisions a built environment in Canada that is not only sustainable but also capable of withstanding the impacts of climate change. Currently in its second phase (2021–2028), SSRIP has successfully developed over 41 standardization solutions geared towards strengthening the climate resilience of Canadian infrastructure and communities.

A considerable focus of these efforts lies within Canada's Northern Region, which faces heightened vulnerability due to ongoing climate change threats. This area experiences unique impacts (such as permafrost thaw), necessitating specific strategies to mitigate them. NISI, a subprogram of SSRIP, is designed to assist infrastructure owners, operators, and custodians of public and community facilities in adapting to a changing climate. This initiative is tailor-made for the North, and all standards produced under NISI are carefully curated by a Northern Advisory Committee. The Northern Advisory Committee comprises representatives from Nunavut, the Northwest Territories, Yukon, and Nunavik, ensuring that the standards cater to the unique needs of these regions. Additionally, Crown-Indigenous Relations and Northern Affairs Canada has been a steadfast supporter of NISI since its inception.

A vital aspect of this process involves collaboration with Standards Development Organizations (SDOs) to ensure that the standards are crafted by experts with Northern experience or those residing in the North. This approach guarantees that the resultant standards genuinely address the requirements of northern communities. To date, nearly a dozen standards have been formulated to assist in constructing structures on permafrost, dealing with extreme weather conditions like high winds and heavy snowfall, planning community systems including wastewater facilities, and adopting a forward-looking approach to design that considers climate change risks.

For a standard to achieve recognition as a National Standard of Canada (NSC) that has been formulated by an SCC-accredited SDO, it must adhere to the following:

- Consensus Development: The standard should be formulated through consensus among a well-balanced assembly of stakeholders;
- Transparency: The standard must undergo public scrutiny, ensuring transparency and inclusivity in its development;
- Language Accessibility: Publication of the standard in both of Canada’s official languages is essential;
- Alignment with International Standards: The standard should either be consistent with or incorporate existing relevant international and foreign standards;
- Trade Facilitation: The standard should not act as a trade barrier; and
- Ongoing Maintenance: Regular maintenance, typically through periodic reviews (usually on a five-year cycle) or as necessary due to changes, is crucial.

The distinctiveness of NSCs lies in their consensus-based and interdisciplinary approach. This sets them apart from industry or professional standards that are specific to certain sectors or industries and do not necessarily require a balanced consensus methodology. The collaborative and diverse development process ensures their robustness and relevance across a broader spectrum of applications and scenarios.

The maintenance cycle of NSCs means that every five years, the standard must either be updated, confirmed as is, or withdrawn. As a result, the standards are continuously reviewed to include the latest knowledge and technology, making them a strong tool for northern communities.

2 METHODOLOGY

In crafting this article, we've adopted a case study approach.

Our selection of the case study strategy is rooted in its appropriateness for cultivating a deep understanding of the significance, application, and worth of standards in assisting northern communities to navigate climate change and foster climate resilient infrastructure through the implementation of northern standards.

This report presents a comprehensive overview of four NSCs dedicated to facilitating the planning, creation, and maintenance of foundations and infrastructure within permafrost regions. The analysis of these standards encompasses an assessment of their impact, the extent of their practical application, and their utilization as points of reference. Their potential to aid communities in adjusting to the challenges posed by climate change and climate hazards remains a focal point throughout the assessment.

3 RESULTS; CANADIAN STANDARDS AND GUIDANCE ON PERMAFROST

What follows is an overview of four technical guidance documents that were prioritized by SCC’s Northern Advisory Committee and are now available for use. These standards go “beyond the building code” and are meant to support a climate-resilient future. Several communities across Canada’s north have begun implementation of:

- CSA S500:21 Thermosyphon foundations for buildings in permafrost regions;
- CSA S501:21 Moderating the effects of permafrost degradation on existing building foundations;
- BNQ 9701-500 Risk-based approach for community planning in northern region; and
- CSA PLUS 4011:19 Technical guide: Infrastructure in permafrost: A guideline for climate change adaptation

3.1 CSA S500:21 Thermosyphon foundations for buildings in permafrost regions

3.1.1 Project description

Shifting climate conditions across northern Canada have led to documented changes in temperature, precipitation, and typical weather patterns. These alterations hold the potential to induce significant impacts on permafrost conditions and hydrogeological attributes of specific construction sites, consequently affecting both the infrastructure in the northern regions and the local inhabitants.

In November 2012, the SCC entrusted CSA Group with the task of developing four standards as part of NISI. The inaugural standard in this series pertains to thermosyphon foundations for buildings in permafrost regions. The development of this standard emerged from the cooperative efforts of representatives from territorial and federal governments, universities, the private sector, and local community governance organizations. A second edition, published in 2021, supersedes the earlier 2014 version and fills the void that previously existed – the absence of guidelines or standards for designing, constructing, and maintaining thermosyphon-supported foundations.

CSA S500: Thermosyphon foundations for buildings in permafrost regions is designed to enable northern Canadians to adapt to the evolving environment through the utilization of thermosyphon foundations. Functioning by transferring heat from the ground to the air during appropriate temperature differences, thermosyphons effectively sustain frozen and stable ground in cold climates. Notably, structures constructed on permafrost without such mitigative systems can trigger permafrost degradation and compromise a structure's foundational integrity (SCC.2014).

The standard's scope encompasses all phases of a thermosyphon foundation's life cycle for new buildings on permafrost, covering site assessment, design, installation, commissioning, monitoring, and maintenance. It is strategically designed to ensure the enduring performance of thermosyphon-supported foundation systems under changing environmental circumstances.

Intended for designers, contractors, building proprietors, and operators, the standard offers insight into the design and construction processes required to guarantee the implementation of adequate measures during these phases. Furthermore, the standard outlines expectations for monitoring and maintenance for building operators.

Primarily targeting new buildings on permafrost sites, particularly those employing materials sensitive to thawing, the standard furnishes guidance regarding geotechnical investigations and advises on foundation conditions that either support or challenge the use of thermosyphons as a foundational system. The standard underscores the importance of preserving permafrost to uphold building support and design integrity before its implementation (CSA Group 2021a).

3.1.2 Impact

Since the first edition was published, several northern infrastructure projects have implemented the standard. Further, the standard has been referenced in the Société d'habitation du Québec's Housing Construction in Nunavik – Guide to Good Practices (Société d'habitation du Québec 2018), as well as in the Northwest Territories Good Building Practice for Northern Facilities requirements (Government of Northwest Territories 2021). As such, it is being recognized as being a best practice in these regions.

Arctic Foundations, a leading manufacturer of thermosyphons in Canada, ensures that CSA S500:14 (the first edition) is followed on every building related installation they have performed since 2014 (adherence is specific to their portion of the work, i.e., final review, modelling, design, manufacturing, and installation). Further, the first edition of this standard is referenced in CSA S6:19 Canadian Highway Bridge Design Code (CSA Group 2019b), CSA S6.1-2019 Commentary on CSA S6:19 Canadian Highway Bridge Design Code (CSA Group 2019c), and in the new Yukon Government Design Standards Manual (Government of Yukon 2023).

Moreover, the standard was used in the following projects:

- Qikiqtani Correctional Healing Centre Expansion – Iqaluit, NU;
- Arctic Bay Fire Hall – Arctic Bay, NU;
- Kugaaruk Fire Hall – Kugaaruk, NU;
- Heath centre and housing project – Old Crow, YT;
- Rankin Inlet Airport Maintenance Garage – Rankin Inlet, NU ;
- Igloolik High School – Igloolik, NU; and
- Tununuk Apartments (Thermopiles) – Inuvik, NT.

The establishment of this standard serves as a crucial stride towards safeguarding the stability of existing and forthcoming infrastructure within northern communities and showcases how standards serve to harmonize and streamline best practices across jurisdictions, regulatory frameworks, and guidelines.

Furthermore, by being referenced in territorial building and design guides, the territorial governments are endorsing the use of the standard and in many cases, they design publicly funded infrastructure in accordance with these guidelines.

3.2 CSA S501:21 Moderating the effects of permafrost degradation on existing building foundations

3.2.1 Project description

In the northern regions of Canada, the foundations of buildings are anchored deeply into the permafrost, the persistently frozen layers of soil and sediment. Building designs factor in the cyclic thawing and freezing of the active layer – the topsoil – during summers and winters. However, as the northern climate undergoes change, this active layer expands, resulting in permafrost degradation that poses a threat to the foundations of vital infrastructure.

CSA S501 Moderating the effects of permafrost degradation on existing was developed by CSA Group under NISI. Inputs from SCC's Northern Advisory Committee helped to shape the scope and need for the standard. The standard encompasses a range of strategies for preserving permafrost or mitigating its degradation concerning existing structures, including:

- Site techniques, such as site grading and drainage, snow management, and shading or albedo alteration; and
- Foundation techniques, such as encompassing ventilation, ground insulation, foundation adjustment and leveling, mechanized refrigeration, thermosyphons, and foundation replacement.

Additionally, the standard accommodates responses like site abandonment or structure demolition due to permafrost degradation. Monitoring holds a central role within this framework.

The standard's intended users encompass a diverse group:

- Building Owners and Operators: Responsible for structures susceptible to permafrost degradation;
- Community Infrastructure Managers: Overseeing infrastructure like drainage systems, necessitating permafrost maintenance or degradation remediation;
- Building Contractors: Engaging in engineering interventions;
- Design Professionals and Reviewers: Including consulting engineers, architects, and technical services staff, engaged in designing, assessing, approving, and supervising engineering interventions;
- Educators: For knowledge transfer; and
- Regulators: Such as building inspectors (CSA Group 2021b).

The standard complements existing building codes by offering guidance on conserving permafrost beneath established structures. It also provides methodologies for addressing buildings impacted by permafrost degradation, evaluates engineering approaches for preserving permafrost, and furnishes best practices to minimize the effects of permafrost deterioration on standing buildings. In essence, this standard not only addresses the pressing issue of permafrost degradation in northern communities but also provides a comprehensive guide for various stakeholders to ensure the stability and longevity of existing structures in the face of changing climatic conditions.

3.2.2 Impact

The standard has been widely referenced and used across the north. For instance, it has been referenced in the Société d'habitation du Québec's Housing Construction in Nunavik – Guide to Good Practices (Société d'habitation du Québec 2018), as well as in the Northwest Territories Good Building Practice for Northern Facilities requirements (Government of Northwest Territories 2021). Further, it has been referenced in the Yukon's 2022 Design Requirements and Technical Standards Manual which provides standards, strategies, and technical requirements for the planning, design and construction of new buildings (Government of Yukon 2023).

It's also referenced in the NWT Association of Communities' Climate Toolkit (Northwest Territories Association of Communities 2014). Further, the standard, as with many other NISI standards, has been referenced as a resilience measure in funding applications, such as funding under Infrastructure Canada (Infrastructure Canada 2021). Lastly, it was referenced in a review of climate impacts to infrastructure in Ross River, Yukon (Northern Climate Exchange 2021)

This standard's widespread application in territorial design guidelines, climate impact assessments, and federal funding applications exemplifies its significance and the way in which it harmonizes the field of climate resilience with the support of territorial and federal government.

3.3. BNQ 9701-500 Risk-based approach for community planning in northern region

3.3.1 Project description

When determining optimal locations for new community infrastructure, it's crucial to assess potential construction areas for hazards, vulnerabilities, and future climate risks. This standard serves to guide communities in understanding the advantages and disadvantages of infrastructure development across various zones (Standards Council of Canada 2023b). It outlines the minimum requisites for generating Land Development Suitability (LDS) maps, focusing on climate change within a risk management framework.

LDS maps offer invaluable insights for managing current infrastructure and pinpointing areas susceptible to climate change impacts. For instance, elevated air temperatures and increased precipitation influence ground temperatures, impacting permafrost stability. Consequently, numerous northern communities grapple with issues like land erosion and heightened flooding due to these effects. Incorporating these processes and vulnerabilities into the mapping process is essential for drafting LDS maps that ensure sustainable territorial development (Bureau de normalisation du Québec 2023).

Developed as part of NISI, the standard was shaped by inputs from the Northern Advisory Committee, alongside representatives from territorial governments, the federal government, universities, the private sector, and northern community governance bodies.

Outlined within this standard are the essential prerequisites for planning, preparing, and approving potential construction maps. These maps serve as a crucial resource for community planning decisions in the northern regions, bolstering community expansion in alignment with risk management principles. The primary audience includes land-use planning specialists and northern communities engaged in updating community plans and designing land development projects. It's also intended for use by geotechnical consultants, building designers, and contractors (Standards Council of Canada 2019).

The standard's goal is to establish a consistent and harmonized methodology for constructing potential construction maps, particularly addressing the unique considerations for building in permafrost zones and confronting climate change effects in northern regions (Standards Council of Canada 2019).

Overall, the standard facilitates informed decision-making in the face of evolving climate challenges, aiding in the sustainable growth of northern communities.

3.3.2 Impact

The standard was released in January 2023, and as such SCC does not yet have any use cases. However, discussions with northern communities suggest that funding applications are underway to support implementation of the standard across the territories. Consequently, the endorsement of governments will provide a consistent and coherent risk management approach for community planning across territories.

3.4. CSA PLUS 4011:19 Technical guide: Infrastructure in permafrost: A guideline for climate change adaptation

3.4.1 Project description

Engineering endeavors in northern areas frequently confront the challenge of permafrost within their foundation environments. The load-bearing capacity of frozen ground for supporting structures hinges primarily on local climatic conditions, ground temperatures, soil/rock properties, and ground ice conditions.

Anticipating significant climate warming in northern Canada, it becomes imperative to site community infrastructure in permafrost terrain while accounting for potential shifts in foundation conditions due to permafrost warming and thawing. The scope of analysis for addressing permafrost and climate change-related factors will vary across projects, contingent upon the nature of the infrastructure, its design, location, lifespan, and purpose.

This guideline effectively supports the incorporation of climate change-related considerations during the planning, design, and management phases of various community infrastructure projects in permafrost regions. Its key objectives are as follows:

- To elucidate permafrost as an environmental factor, focusing on its response to climate and environmental changes;
- To provide a broad assessment of trends in climatic and permafrost conditions across northern Canada;
- To outline prevalent foundation types employed in permafrost environments for community infrastructure; and
- To present a systematic approach for integrating climate change effects, as relevant, into the selection of project sites and the design of their foundations.

3.4.2 Impact

This technical guide is referenced in the Government of the Northwest Territories Good Building Practices. Moreover, it is referenced in CSA S6.1:19 Commentary to the Canadian Highway Bridge Design Code (CSA Group 2019c), and will therefore be used as guidance when needed in designing a bridge structure in permafrost conditions.

The first edition of CSA Plus 4011 was mentioned in the Development Assessment Report for the all-weather road to the Prairie CK mine in NWT (where it was used as a screening tool for climate change analysis; Canadian Zinc Corporation Vancouver 2010). It was also referenced in the Société d'habitation du Québec's Housing Construction in Nunavik – Guide to Good Practices (Société d'habitation du Québec 2018*)*. Moreover, it has also been referenced in the Yukon's 2022 Design Requirements and Technical Standards Manual (Government of Yukon 2023).

This guidance document is crafted to aid decision-makers, who might not be permafrost experts, yet play pivotal roles in planning, procuring, developing, or operating community infrastructure in permafrost regions. It ensures that these decision-makers are equipped to address the intricate challenges posed by permafrost conditions and climate change impacts in the context of infrastructure development.

Essentially, the evidence of referencing demonstrates that the technical guide plays a vital role in bringing consistency and efficiency to best practices across different areas such as jurisdictions, regulations, and frameworks through the endorsement of federal and territorial governments.

4 DISCUSSION

Canada's northern regions face the direct impact of climate change, with rising temperatures causing permafrost thaw, severe storms, increased precipitation, melting sea ice, and coastal erosion. Recognizing this reality is fundamental for informed decision-making.

The process of adapting and repairing buildings in the North is financially demanding, especially for smaller communities. Understanding the economic strain is crucial when formulating strategies to bolster infrastructure resilience.

Northern communities require effective tools to minimize infrastructure vulnerability and mitigate climate change impacts. Investing in resources that provide actionable solutions is crucial for long-term resilience.

SCC has been playing a critical role by supporting the creation and dissemination of new resources tailored to northern infrastructure needs. Its involvement signifies a commitment to proactive adaptation strategies.

The success of NISI is rooted in its approach. The success of NISI extends beyond the SCC. Collaboration among territorial governments, federal entities, universities, the private sector, and community organizations is pivotal, showcasing the power of collective efforts. Standards are crafted to cater to the unique requirements of the North, ensuring they genuinely address local challenges. A key aspect of NISI's success is the active engagement of the North. The program's structure fosters ownership,

encouraging northern stakeholders to endorse and advocate for standards adoption within codes and training.

NISI capitalizes on the distinct needs of northern regions, aligning its standards with the region's challenges. This targeted approach ensures that standards are not just relevant but also embraced by the local communities.

Developing standards that cater to northern needs signifies a long-term vision. These standards are not merely quick fixes but serve as foundational tools for resilient infrastructure in the face of ongoing climate change.

Innovative measures found in these standards and highlighted in the previous sections include progressive initiatives that demonstrate value in exceeding code when in high-risk regions. The development of these standards and application in multiple regions demonstrates value in allocating resources beyond code minimums, particularly for new construction. As climate change and extreme natural events continue to influence innovations in adaption and resilience, cost/benefit data will increasingly support federal and local governments, designers, builders and the insurance industry to corroborate what needs to be adapted in existing building practice and what will be deemed an amenity.

In summary, the Northern Infrastructure Standardization Initiative exemplifies the positive impact that tailored standards can have on enhancing the resilience of infrastructure in climate-vulnerable regions. By recognizing local challenges, promoting ownership, and fostering implementation, this initiative serves as a valuable model for proactive climate adaptation strategies.

5 CONCLUSION

In conclusion, the insights garnered and resources harnessed via NISI underscore the vital role that standards play in navigating the challenges posed by climate change and evolving permafrost conditions. The four highlighted standards within this case study exemplify how standards serve as dynamic tools for adapting and mitigating the impacts of climate change on Northern built infrastructure. Crucially, these standards are meticulously designed to genuinely address the specific needs of northern communities, ensuring the creation of sustainable and high-quality infrastructure.

The standards spotlighted within NISI's framework hold the promise of aiding building owners, operators, and custodians of public and community infrastructure. By embracing these standards, stakeholders in permafrost regions are equipped with the knowledge and methodologies to construct and sustain infrastructure amidst the fluctuations of a changing climate. These standards encapsulate a holistic approach, encompassing both adaptation and maintenance, thereby fostering resilience and longevity.

Ultimately, the success of NISI and the associated standards demonstrates how strategic collaboration, and a localized approach can lead to the development of resources that are not just responsive but proactive. The synthesis of knowledge and the creation of purpose-fit tools culminate in the promotion of adaptable, robust, and sustainable infrastructure, which stands as a testament to the capacity of standards to effectively address the challenges of a dynamically changing world.

6 ACKNOWLEDGEMENTS

This report is part of the NISI stream of the SSRIP program which is financed by Infrastructure Canada (INFC). We would like to thank INFC and National Research Council of Canada (NRC) for their ongoing commitment.

We would like to extend our thanks to the Northern Advisory Committee for overseeing the development of all NISI standards as well as Crown-Indigenous Relations and Northern Affairs Canada who have supported NISI since it's beginning.

Special thanks to CSA Group and Bureau de normalisation du Québec (BNQ) for their contributions to northern standards and for providing evidence of implementation.

7 REFERENCES

Bureau de normalisation du Québec 2023. *Community Planning in Northern Regions, Bureau de normalisation du Québec*. Available at: https://www.bnq.qc.ca/en/standardization/civil-engineering-and-urban-infrastructure/community-planning-in-northern-regions.html (Accessed: August 24, 2023).

Infrastructure Canada 2021. *Green and Inclusive Community Buildings Applicant Guide*. Available at: https://www.infrastructure.gc.ca/alt-format/pdf/gicb-bcvi/GICB-Applicant-Guide-BCVI-Guide-du-demandeur-EN.pdf.

Canadian Zinc Corporation Vancouver 2010. *Prairie Creek Mine Developer's Assessment Report*. Available at: https://reviewboard.ca/upload/project_document/EA0809-002_Developer_s_Assessment_Report__Vol_1_of_4_.PDF.

CSA Group 2019a. *CSA PLUS 4011:19 Technical Guide: Infrastructure in permafrost: A guideline for climate change adaptation*. Available at: https://www.csagroup.org/store/product/2703076/.

CSA Group 2019b. *CSA S6, Canadian Highway Bridge Design Code*. Available at: https://www.csagroup.org/canadian-highway-bridge-design-code/?gclid=Cj0KCQjw0bunBhD9ARIsAAZl0E3kz2gSCDo_rSYPuTtNvM3jkjVFmTb_AIu-luPxoR6gjSpFRhXlkFUaAo7HEALw_wcB.

CSA Group 2019c. *CSA S6.1-2019 Commentary On CSA S6:19, Canadian Highway Bridge Design Code*. Available at: https://www.csagroup.org/store/product/CSA%20S6.1:19/.

CSA Group 2021a. *CSA S500:21 Thermosyphon foundations for buildings in permafrost regions*. Available at: https://www.csagroup.org/store/product/CSA%20S500%3A21/.

CSA Group 2021b *CSA S501:21 Moderating the effects of permafrost degradation on existing building foundations*. Available at: https://www.csagroup.org/store/product/CSA%20S501%3A21/.

Bush, E. and Lemmen, D.S. 2019. *Canada's Changing Climate Report*. Available at: https://publications.gc.ca/collections/collection_2019/eccc/En4-368-2019-eng.pdf.

Environment and natural resources Canada 2023. *Canada's National Adaptation Strategy, Canada's National Adaptation Strategy*. Available at: https://www.canada.ca/en/services/environment/weather/climatechange/climate-plan/national-adaptation-strategy/full-strategy.html (Accessed: August 24, 2023).

Government of Northwest Territories 2021. *Good Building Practice for Northern Facilities*. Available at: https://www.inf.gov.nt.ca/sites/inf/files/resources/3789-gnwt_infrastructure-good_practises_manual_april07_web.pdf.

Government of Yukon 2023. *Design Requirements and Technical Standards Manual*. Available at: https://yukon.ca/en/government-yukon-design-requirements-and-technical-standards.

Northern Climate Exchange, Yukon Research Centre, Yukon College 2021. *Assessment of Risk to Infrastructure from Permafrost Degradation and a Changing Climate, Ross River*. Available at: https://www.yukonu.ca/sites/default/files/inline-files/ross%20river%20permafrost%20high-res_final.pdf.

Northwest Territories Association of Communities 2014. *Integrating Climate Change Measures into Municipal Planning and Decision-Making A Guide for Northern Communities*. Available at: https://climatechange.toolkitnwtac.com/wp-content/uploads/sites/21/2018/02/IntegratingClimateChange-book-lowres-v1-Feb2015-2.pdf.

Heale, R. and Twycross, A 2017. 'What is a case study?', *BMJ journals* 21(1). Available at: https://ebn.bmj.com/content/21/1/7.

Société d'habitation du Québec 2018. *Housing construction in Nunavik – Guide to good practices*. Available at: http://www.habitation.gouv.qc.ca/fileadmin/internet/documents/English/HousingConstructionInNunavik.pdf

Standards Council of Canada 2010. *PLUS 4011-10 TECHNICAL GUIDE - Infrastructure in permafrost: A guideline for climate change adaptation, The Standards Council of Canada*. Available at: https://www.scc.ca/en/standardsdb/standards/26121 (Accessed: August 24, 2023).

Standards Council of Canada 2019. *Risk-Based Approach for Community Planning in Northern Regions, The Standards Council of Canada*. Available at: https://www.scc.ca/en/standards/notices-of-intent/bnq/risk-based-approach-for-community-planning-northern-regions (Accessed: August 24, 2023).

Standards Council of Canada 2023a. *Future by design: standards for a climate resilient Canada*. Available at: https://www.scc.ca/en/about-scc/publications/general/future-design-standards-for-a-climate-resilient-canada.

Standards Council of Canada 2023b. *Designing with climate change and risk in mind*. Available at: https://www.scc.ca/en/nisi/designing-with-climate-change-and-risk#:~:text=BNQ%209701%2D500%20Risk%2Dbased,the%20potential%20future%20climate%20risks (Accessed: August 24, 2023).

Standards Council of Canada 2023c. *Northern Infrastructure Standardization Initiative*. Available at: https://www.scc.ca/en/nisi (Accessed: August 24, 2023).

Standards Council of Canada & CSA Group 2014. *Standards Council of Canada approves new national standard to help address the effects of climate change on Canada's North*. Available at: https://www.scc.ca/en/news-events/news/2014/standards-council-canada-approves-new-national-standard-help-address-effects-climate-change-canadas (Accessed: August 24, 2023).

University of Melbourne 2011. *CASE STUDIES: Research Methods*. Available at: https://library.unimelb.edu.au/__data/assets/pdf_file/0011/1924175/Casestudy_Research.pdf.

Modelled ground ice conditions in the Kivalliq region, Nunavut, Canada

H. Brendan O'Neill, Stephen A. Wolfe & Caroline Duchesne

Geological Survey of Canada, Natural Resources Canada, Ottawa, Ontario, Canada

ABSTRACT

Significant infrastructure development is proposed in the Kivalliq Region, Nunavut, including a 1,200 km long hydroelectric/fibre optic link to southern Canada. Knowledge of ground ice conditions is important to mitigate the effects of climate change and permafrost thaw on infrastructure. Nevertheless, only limited information exists in this region. The Geological Survey of Canada (GSC) has developed updated ground ice mapping for Canada and tested the modelling framework at regional scales using more detailed surficial geology mapping. The ground ice modelling depicts the estimated relative abundance of relict (buried glacial) ice, segregated ice, and wedge ice in the upper five metres of permafrost. Here we present modelling for the Kivalliq region based on standardized 1:125,000 scale surficial geology mapping. Such modelling is useful at a reconnaissance level and to guide more detailed ground ice investigations. Relict ice is predicted over limited areas above the postglacial marine limit. High segregated ice abundance occurs in fine-grained marine deposits within the limit of inundation. Modelled segregated ice abundance is medium or low in thicker till deposits. Wedge ice abundance is negligible or low due to the dominantly thin and coarse-grained surficial cover, and (relatively) limited time since subaerial exposure of the terrain following deglaciation near the coast. Overall, the highest ice contents are predicted above marine limit in thick, fine-grained till deposits. Areas with high relict ice abundance coincide with evidence of ice-cored terrain in satellite imagery, and modelled segregated ice is in general agreement with the limited field observations from the region.

1 INTRODUCTION

Permafrost is warming and thawing in response to climate change (Smith et al. 2022). Land use planning and adaptation requires knowledge of ground ice due to its role in the stability of permafrost terrain under warming conditions (Doré et al. 2016). The Kivalliq region in Nunavut is undergoing significant development, but fundamental information on ground ice and permafrost is lacking in the region. Preliminary investigations on permafrost temperatures and ground ice conditions (LeBlanc and Oldenborger 2021; McQuaig et al. 2022), permafrost hazards (Forbes et al. 2014), and thaw sensitivity based on remote-sensing imagery analysis (Oldenborger et al. 2022b) have begun addressing this knowledge gap. Most of these studies were focused near the communities of Rankin Inlet and Arviat. Herein, modelled regional-scale ground ice abundance is presented to contribute to foundational permafrost knowledge in the region and complement ongoing field-based investigations (e.g., Faucher et al. 2024). The specific objectives are to 1) estimate the abundance and distribution of excess ice in upper permafrost from relict (buried glacial), segregated, and wedge ice, 2) present patterns in ground ice abundance and associations with surficial geology and environmental conditions, and 3) discuss the accuracy of the predictions based on available information on ground ice, limitations of the modelling, and implications given proposed development in the region.

1.1 Study area

The study area extends from the Manitoba/Nunavut border (60°N) to beyond Baker Lake, NU (65°N) along the western coast of Hudson Bay, and inland to 98°W (Figure 1). The region was covered by the Laurentide Ice Sheet during the Wisconsin glaciation. Following deglaciation, which

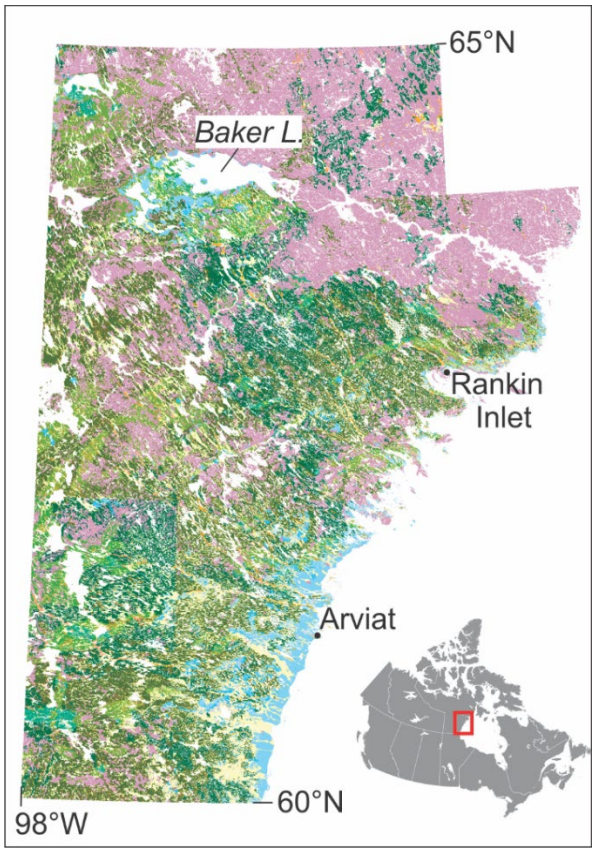

Figure 1. Study region surficial geology compilation. Pink = bedrock; all green shades = tills; blues = marine and lacustrine; yellows = alluvial; oranges = glaciofluvial; purples = glaciolacustrine deposits.

https://doi.org/10.52381/ICOP2024.85.1

occurred between 9 and 6 14C ka BP, the land was inundated up to about 170 m above the modern sea level by the postglacial Tyrell Sea, which extended up to 150 km inland (Dyke 2004). Isostatic rebound following deglaciation drove emergence and subsequent permafrost development within inundated areas.

Surficial geology includes exposed bedrock, glacial tills, marine, glaciofluvial, glaciolacustrine, lacustrine, and alluvial deposits. Organic deposits, 30 to > 100 cm thick, occur in pockets in flat areas, and predominantly overlie fine-grained materials (Arsenault et al. 1981; McMartin 2002; Forbes et al. 2014). Topography is subdued and comprises bedrock hills and eskers, moraines, and drumlins that are widespread in the region (McMartin et al. 2021).

The study area is within the continuous permafrost zone. The mean annual air temperatures (1981–2010) at Arviat, Rankin Inlet, and Baker Lake are -9.3, -10.5, and -11.3 °C, respectively (Environment Canada 2023). At Rankin Inlet, annual mean ground temperatures near the top of permafrost range from -9.5 to -5.5 °C (LeBlanc and Oldenborger 2021). Annual mean ground temperatures at Baker Lake in 1998–2003 were about -7 to -8 °C (Smith et al. 2005).

Limited information exists on ground ice conditions. Faucher et al. (2024) observed high excess ice contents in two cores from marine sediments with individual samples having up to 85% excess ice. Lower excess ice contents occurred in a dominantly till core. McQuaig et al. (2022) estimated volumetric ice content visually from cores drilled along the proposed infrastructure corridor. Samples from organic and finer-grained marine sediments had moderate to high ice contents (up to 50–60%) comprising mainly segregated ice. Fluvial sands and silts had moderate ice contents (10–20%), whereas coarser grained till and glaciomarine deposits had low ice contents (5–10%). Elevated segregated ice content is also inferable from the presence of solifluction lobes over some fine-grained deposits (e.g., Oldenborger et al. 2022a).

Polygonal ground, interpreted as ice wedge polygons, are mapped extensively along the proposed Kivalliq Hydro-Fibre Link in coarse-grained glaciofluvial, beach ridge, and nearshore marine sediments, and in fine-grained fluvial, offshore marine, and organic deposits (McQuaig et al. 2022). Well-developed polygons are observed in marine sediments overlain with organic material near Arviat (Forbes et al. 2014). Ice wedge polygons are also mapped in various deposits near Rankin Inlet (McMartin 2002; Oldenborger et al. 2022a). However, there are no known volumetric estimates of wedge ice in the region.

2 METHODOLOGY

Sixteen 1:125,000 scale Canadian Geoscience Maps formed the surficial materials compilation used for the modelling (Geological Survey of Canada 2017a–n, 2018a, b). These maps conform to the Geological Survey of Canada's Surficial Data Model, which standardises legends and digital formatting for the mapped units (Deblonde et al. 2019). Original vector polygon shapefiles were combined and converted to raster with pixel size of 250 m. The pixel size was chosen to preserve small surficial geology units and cartographic detail around waterbodies with complex shorelines. As with the surficial materials compilation for the *Ground Ice Map of Canada* (GIMC), till units were classified into fine and coarse-grained dominant textures based on underlying bedrock geology (O'Neill et al. 2019). As a result, 33 surficial units are mapped in the study area, which comprise bedrock, and multiple till, alluvial, marine, lacustrine, glaciofluvial, and glaciolacustrine units (Figure 1).

Surficial units that appear on the national-scale mapping retain their model parameter values from the GIMC. Units that are not represented are assigned parameters based on a review of surficial geology-ground ice associations informed by the surficial geology map unit legends and observations from prior investigations, including those west of the study region in the Slave Geological Province (e.g., Dredge et al. 1999).

The surficial geology information was altered on one map sheet (Geological Survey of Canada 2018a) where an inconsistency during the conversion from the paper map to the standardized digital form was noted. On this sheet, areas mapped primarily as bedrock with secondary coverage of till veneer or felsenmeer were mapped as till veneer in the digitized version, in contrast to adjacent map sheets. These areas were edited in the GIS to be mapped as bedrock for consistency.

The models use an expert-system approach implemented in a GIS, and incorporate conceptual principles gained from empirically based research of ground ice. Datasets on surficial geology, deglaciation, paleovegetation distribution, permafrost, and glacial lake and marine limits are used to model estimates of the abundance of relict (buried glacial), segregated, and wedge ice in the upper 5 m of permafrost. The modelling routines are fully described by O'Neill et al. (2019). In contrast with the GIMC modelling, we use a recent (McMartin et al. 2022), region-specific geospatial dataset of postglacial inundation to simulate the melt of relict ice in previously submerged areas, rather than the *Glacial Map of Canada* (Prest et al. 1968).

The model results for the three ice types were combined using the methodology presented for the *Ground Ice Map of Canada* (O'Neill et al. 2022).

3 RESULTS

The distribution of modelled relict ice is restricted mainly to the west of the study region, above the level of postglacial inundation (Figure 2). High relict ice abundance is predicted in fine-grained hummocky till and moraine complexes, while areas of medium abundance are modelled in fine-grained till blankets, and coarse-grained hummocky till and moraine complexes, and glaciolacustrine and glaciofluvial units. Lower abundance is modelled in other coarse-grained till units and outwash fan sediments. Since nearly all the study area has been in the herb tundra biome since deglaciation, little modelled melt of relict ice due to transitions to warmer climates and associated biomes has occurred.

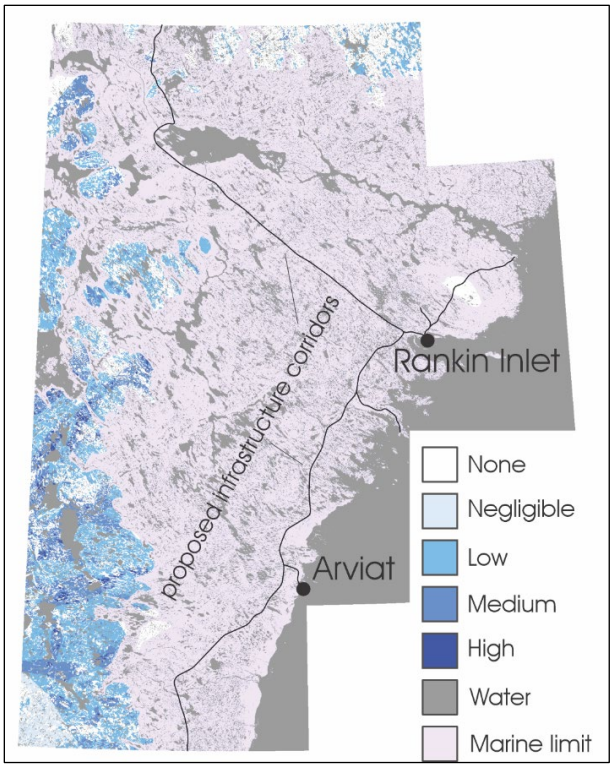

Figure 2. Modelled relict (buried glacial) ice abundance. Marine limit indicated from McMartin et al. (2022). Infrastructure routing modified from McQuaig et al. (2022).

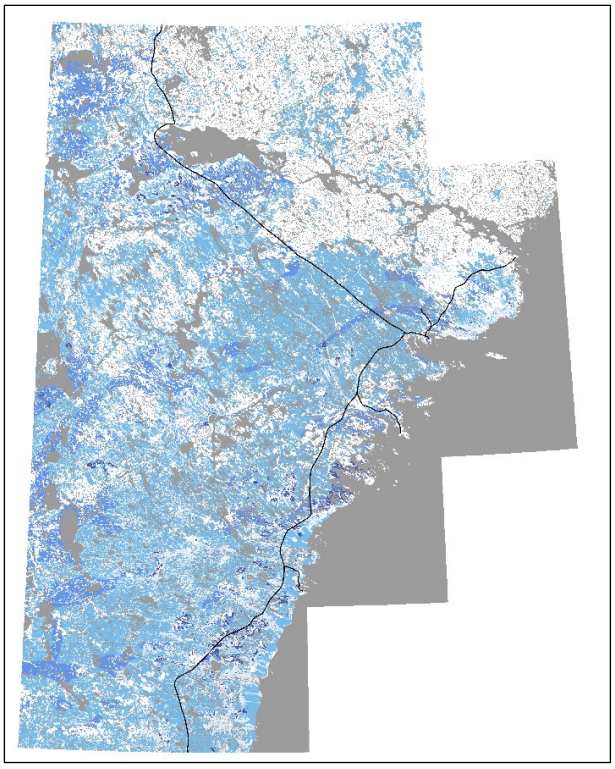

Figure 3. Modelled segregated ice abundance. See Figure 2 legend.

Modelled segregated ice abundance is highest in frost-susceptible, fine-grained marine sediments that are mainly distributed near the modern Hudson Bay coastline, but also occur in smaller pockets inland within the limit of postglacial submergence (Figure 3). Medium segregated ice abundance is modelled predominantly in areas with fine-grained till units, which are differentiated in the study region based on the presence of underlying Neoarchean sedimentary rocks (Wheeler et al. 1996). In the northeast part of the study region the distribution of modelled segregated ice is limited due to the widespread occurrence of exposed bedrock (Figures 1 and 3).

Wedge ice abundance is modelled as negligible over much of the study area (Figure 4). Inland, some areas of low abundance occur in fine-grained tills and marine sediments. As with segregated ice, there is no modelled wedge ice in the bedrock-dominated northeast.

The combined ice abundance in the study region ranges from none to high (Figure 5). There are no areas modelled with very high combined ice contents.

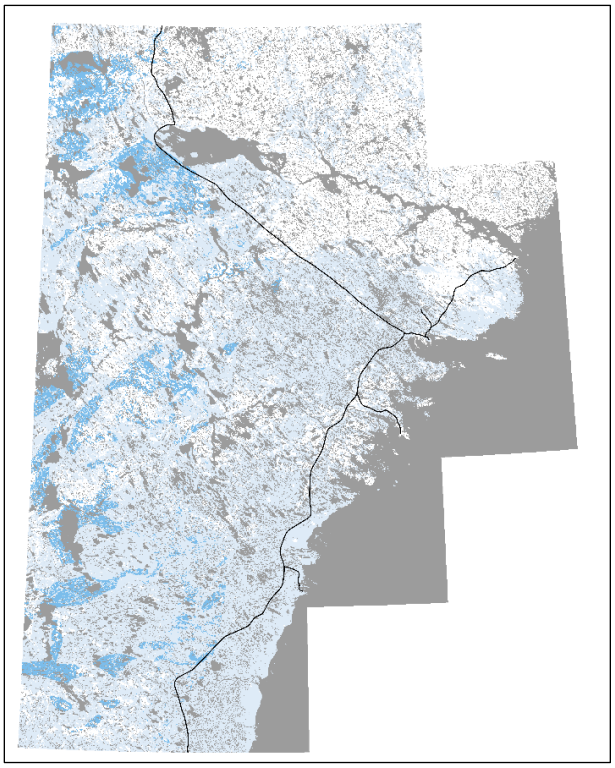

Figure 4. Modelled wedge ice abundance. See Figure 2 legend.

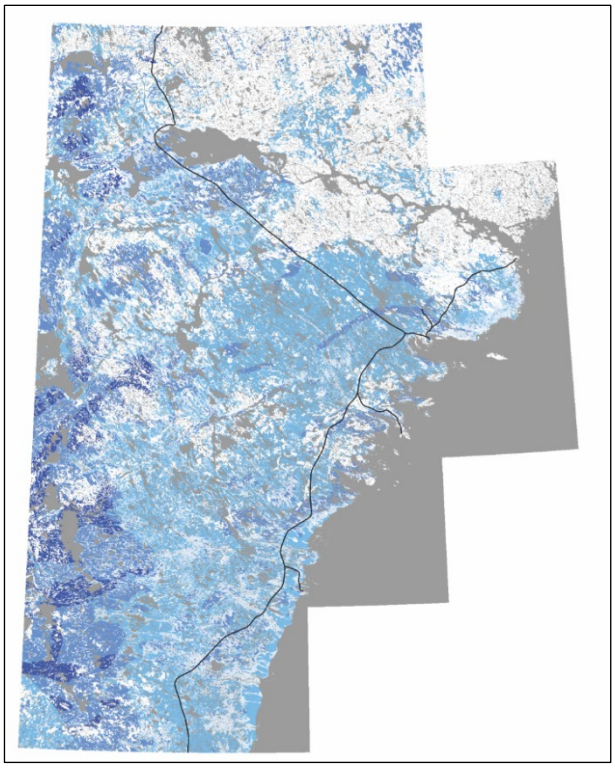

Figure 5. Modelled combined ice abundance. See Figure 2 legend.

4 Discussion

4.1 Relict ice

Direct validation of the relict ice modelling requires information from core drilling or systematic mapping of features associated with relict ground ice, such as retrogressive-thaw slumps (Kokelj et al. 2017) or other evidence of ice-cored terrain. In our knowledge, such information is not available from the study area. However, preserved glacial ice is encountered to the west in the Slave Geological Province in hummocky tills, glaciolacustrine deltas, and glaciofluvial deposits (Wolfe 1998; Subedi et al. 2020), and that area shares many similarities with the Kivalliq region in terms of ground ice-surficial geology associations (Dredge et al. 1999).

Evidence of ice-cored terrain is visible in satellite imagery in areas modelled with high relict ice (Figure 6). This includes irregular topography and the presence of lakes with steep-sided shores in the upslope direction, which may indicate past or current melt of relict glacial ice. Much of the existing and planned infrastructure in the region is below the marine limit where postglacial inundation lasted thousands of years. Therefore, relict ice likely poses no hazard to development in these settings, unless thermal conditions at the sea-bottom were sufficient to maintain frozen ground.

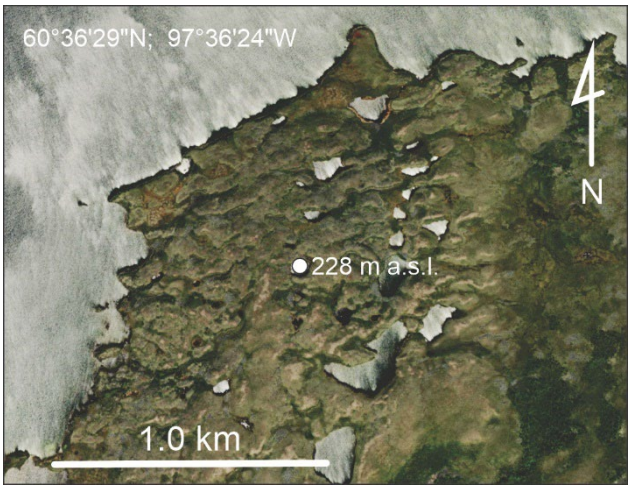

Figure 6. Interpreted ice-cored terrain in an area modelled with high relict ice abundance. Imagery from ArcGIS Earth.

4.2 Segregated ice

Modelled segregated ice is widespread except in the northern part of the study region, where bedrock dominates the surficial geology. Since the entire region is within the continuous permafrost zone and herb tundra biome, the modelled output for segregated ice is controlled by the inferred frost-susceptibility of materials based on interpretation of the dominant grain sizes (O'Neill et al. 2019). Therefore, the results largely correspond with available observations of the highest segregated ice in fine-grained marine sediments and lower contents in coarser grained till (McQuaig et al. 2022; Faucher et al. 2024). Fine-grained marine units, mainly near the coast and Baker Lake, likely pose the greatest hazards for development due to the characteristically high ice contents and potential for significant long-term settlement as permafrost thaws (e.g., O'Neill et al. 2023). Finer grained till units derived from sedimentary bedrock may also pose challenges. Otherwise, much of the region is modelled with low, negligible, or no segregated ice abundance due to the presence of coarse grained or thin unconsolidated deposits, making the consequences of permafrost thaw from segregated ice limited. Numerous lineations with no modelled segregated ice generally trend southeast and represent coarse-grained glaciofluvial deposits (eskers), which consist predominantly of sand and gravel (Phillips and LeBlanc 2024).

Some limitations exist in the modelling and uncertainties in the validity of model rules, which could be tested in this study region. For example, washing of finer grained materials to lower-lying areas occurred as the water level subsided following deglaciation (e.g., McMartin et al. 2022). Therefore, it can be expected that within an individual unit, such as a till blanket, finer material and higher segregated ice contents can be expected in lower-lying areas if the deposit has been wave-washed. The modelling does not capture this type of variation. Furthermore, in areas

mapped as bedrock or till veneer with none or negligible-low modelled segregated ice abundance, smaller pockets of thicker or finer grained unconsolidated material with higher ice contents can be expected in the field, but may not be modelled due to the scale of the surficial mapping.

4.3 Wedge ice

Wedge ice abundance is modelled as either negligible or low in the study area due to the relatively short period since emergence, which is < 5000 years near the modern Hudson Bay coastline, and because modelled wedge ice accumulation is slower in the coarse-grained sediments that cover much of the study area inland. Near the coast, polygonal ground occurs in a variety of deposits and trough networks appear most developed in marine sediments (Figure 7a), which may be overlain by Holocene peat deposits between 0.4 and 1.0 m thick (Arsenault et al. 1981; McMartin 2002; Forbes et al. 2014; McQuaig et al. 2022; Oldenborger et al. 2022a).

Enhanced thermal contraction cracking and ice-wedge growth may occur in areas with organic cover, due to the thermal properties of peat and the high thermal contraction coefficient of water, which forms most of the volume of saturated peat. The modelling does not capture these conditions because the mapped surficial geology polygons represent the underlying material (e.g., marine deposits) when the peat is thinner, though its presence is indicated in the legend text of original surficial geology maps. Similarly, well-developed ice wedge troughs up to about 2 m wide are observed near Rankin Inlet in sandy nearshore marine sediments (A.M. Leblanc, pers. communication), where the thermal properties of the substrate are conducive to rapid cooling. These factors may result in a modelled underestimation of wedge ice in some locales. However, the relatively low abundance of modelled wedge ice in the region is broadly reasonable, as areas with high wedge ice abundance on the GIMC have far wider troughs and much higher polygonal densities than the polygons visible in marine sediments of the Kivalliq region, implying a much higher volumetric wedge ice content in upper permafrost (Figure 7).

Estimates of wedge ice volume in the region derived from field measurements and imagery will allow more rigorous validation efforts and improve knowledge on the volume of wedge ice in upper permafrost (e.g., Frappier and Lacelle 2021). Though the overall ice wedge volume is likely far lower in the Kivalliq region than in these regions of the western Arctic, ice wedges nonetheless may pose challenges to development due to the appreciable differential subsidence that occurs in polygonal terrain when permafrost thaws, and potential issues associated with water impoundment as runoff pathways are modified (Kanevskiy et al. 2022).

5 Conclusions

Ground ice was modelled in the Kivalliq region using 1:125,000 scale surficial geology. Modelling routines from the *Ground Ice Map of Canada* were improved to incorporate regional postglacial inundation limits. The results indicate that the highest combined ground ice abundances occur above marine limit in thick, fine-grained till units predicted to include medium or high relict ice, medium segregated ice, and low wedge ice abundance. Below the limit of postglacial submergence, fine-grained marine sediments are predicted to have high segregated ice content and include wedge ice, and likely represent the most thaw-susceptible material near the coast. Wedge ice abundance is modelled as negligible or low over the region due to the nature of surficial materials and limited time for accumulation since deglaciation and subaerial exposure as the Tyrell Sea receded.

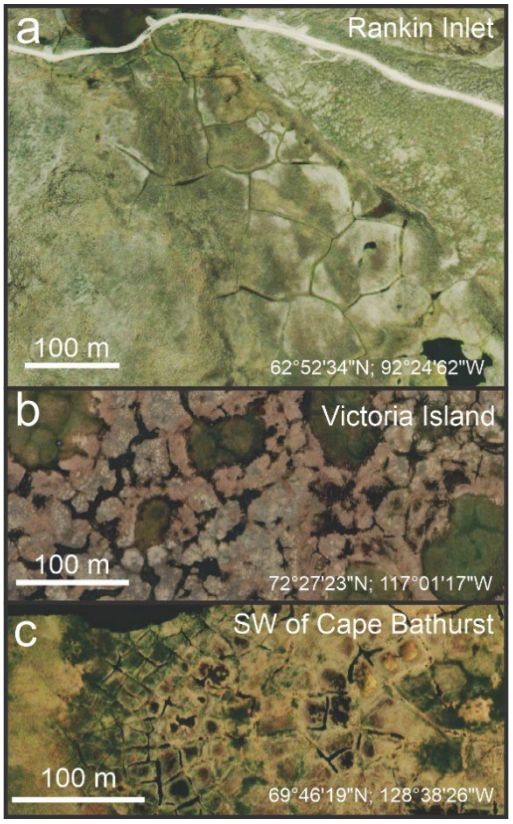

Figure 7. Polygonal ground near a) Rankin Inlet, in fine-grained marine sediments where the modelling predicts negligible abundance, and two examples where the GIMC predicts high abundance on b) northwest Victoria Island and c) SW of Cape Bathurst. Imagery from ArcGIS Earth.

6 Acknowledgements

This research was supported by NRCan's GeoMapping for Energy and Minerals Program (GEM-GeoNorth) and the Climate Change Geoscience Program. We thank Anne-Marie Leblanc for helpful discussions that contributed to the manuscript, and Sharon Smith and two anonymous reviewers for their suggestions during the review. This paper is NRCan contribution #20230258.

7 REFERENCES

Arsenault, L., Aylsworth, J.M., Cunningham, C.M., Kettles, I.M., and Shilts, W.W. 1981. 'Surficial geology, Eskimo Point, District of Keewatin', *Geological Survey of Canada* Preliminary Map, 8-1980.

Deblonde, C., Cocking, R.B., Kerr, D.E., Campbell, J.E., Eagles, S., Everett, D., Huntley, D.H., Inglis, E., Parent, M., Plouffe, A., Robertson, L., Smith, I.R., and Weatherston, A. 2019. 'Surficial Data Model: the science language of the integrated Geological Survey of Canada data model for surficial geology maps', *Geological Survey of Canada* Open File 8236, version 2.4.0.

Doré, G., Niu, F., and Brooks, H. 2016. 'Adaptation methods for transportation infrastructure built on degrading permafrost', *Permafrost and Periglacial Processes* 27(4), pp. 352–364. doi:10.1002/ppp.1919.

Dredge, L.A., Kerr, D.E., and Wolfe, S.A. 1999. 'Surficial materials and related ground ice conditions, Slave Province, N.W.T., Canada', *Canadian Journal of Earth Sciences* 36(7), pp. 1227–1238. doi:10.1139/e98-087.

Dyke, A.S. 2004. 'An outline of North American deglaciation with emphasis on central and northern Canada', in J. Ehlers and P.L. Gibbard (eds.), *Developments in Quaternary Sciences*, pp. 373–424.

Environment Canada 2023. *Canadian Climate Normals*. Available at: https://climate.weather.gc.ca/climate_normals/index_e.html (Accessed: 30 June 2023).

Faucher, B., LeBlanc, A.-M., Oldenborger, G.A., Carrière, E., Lacelle, D., and Letellier, P. 2024. 'Ground ice content of the active layer and near-surface permafrost in the Rankin Inlet area, Nunavut, Canada', in *12th International Conference on Permafrost*. Whitehorse, Yukon, Canada: June 16–20, 2024.

Forbes, D.L., Bell, T., James, T.S., and Simon, K.M. 2014. 'Reconnaissance assessment of landscape hazards and potential impacts of future climate change in Arviat, southern Nunavut', *Canada-Nunavut Geoscience Office* Summary of Activities 2013.

Frappier, R. and Lacelle, D. 2021. 'Distribution, morphometry, and ice content of ice-wedge polygons in Tombstone Territorial Park, central Yukon, Canada', *Permafrost and Periglacial Processes* 32(4), pp. 587–600. doi:10.1002/ppp.2123.

Geological Survey of Canada 2017a. 'Reconnaissance surficial geology, Dawson Inlet, Nunavut, part of NTS 55-F', *Geological Survey of Canada* Canadian Geoscience Map, 241.

Geological Survey of Canada 2017b. 'Reconnaissance surficial geology, Eskimo Point, Nunavut, NTS 55-E', *Geological Survey of Canada* Canadian Geoscience Map, 240.

Geological Survey of Canada 2017c. 'Reconnaissance surficial geology, Ferguson Lake, Nunavut, NTS 65-I', *Geological Survey of Canada* Canadian Geoscience Map, 85.

Geological Survey of Canada 2017d. 'Reconnaissance surficial geology, Gibson Lake, Nunavut, NTS 55-N', *Geological Survey of Canada* Canadian Geoscience Map 246.

Geological Survey of Canada 2017e. 'Reconnaissance surficial geology, Hyde Lake, Nunavut, NTS 55-D' *Geological Survey of Canada* Canadian Geoscience Map 239.

Geological Survey of Canada 2017f. 'Reconnaissance surficial geology, Kaminak Lake, Nunavut, NTS 55-L', preliminary, surficial data model v.2.2 conversion, *Geological Survey of Canada* Canadian Geoscience Map 245.

Geological Survey of Canada 2017g. 'Reconnaissance surficial geology, MacQuoid Lake, Nunavut, NTS 55-M', Geological Survey of Canada Canadian Geoscience Map, 225.

Geological Survey of Canada 2017h. 'Reconnaissance surficial geology, Marble Island, Nunavut, part of NTS 55-J', *Geological Survey of Canada* Canadian Geoscience Map, 242.

Geological Survey of Canada 2017i. 'Reconnaissance surficial geology, Tavani, Nunavut, NTS 55-K', preliminary, surficial data model v.2.2 conversion, *Geological Survey of Canada* Canadian Geoscience Map, 244.

Geological Survey of Canada 2017j. 'Reconnaissance surficial geology, Thirty Mile Lake, Nunavut, NTS 65-P', *Geological Survey of Canada* Canadian Geoscience Map, 326.

Geological Survey of Canada 2017k. 'Surficial geology, Chesterfield Inlet, Nunavut, NTS 55-O', *Geological Survey of Canada* Canadian Geoscience Map, 247.

Geological Survey of Canada 2017l. 'Surficial geology, Edehon Lake, Nunavut, NTS 65-A', *Geological Survey of Canada* Canadian Geoscience Map, 243.

Geological Survey of Canada 2017m. 'Surficial geology, Henik Lakes, Nunavut, NTS 65-H', preliminary, surficial data model v.2.2 conversion, *Geological Survey of Canada* Canadian Geoscience Map, 238.

Geological Survey of Canada 2017n. 'Surficial geology, Schultz Lake, Nunavut, NTS 66-A', *Geological Survey of Canada* Canadian Geoscience Map, 324.

Geological Survey of Canada 2018a. 'Reconnaissance surficial geology, Tehery Lake, Nunavut, NTS 56-C', *Geological Survey of Canada* Canadian Geoscience Map, 343.

Geological Survey of Canada 2018b. 'Surficial geology, Baker Lake, Nunavut, NTS 56-D' Geological Survey of Canada Canadian Geoscience Map, 329.

Kanevskiy, M., Shur, Y., Walker, D.A., Jorgenson, T., Raynolds, M.K., Peirce, J.L., Jones, B.M., Buchhorn, M., Matyshak, G., Bergstedt, H., Breen, A.L., Connor, B., Daanen, R., Liljedahl, A., Romanovsky, V.E., and Watson-Cook, E. 2022. 'The shifting mosaic of ice-wedge degradation and stabilization in response to infrastructure and climate change, Prudhoe Bay Oilfield, Alaska, USA', *Arctic Science*, 8(2), pp. 498–530. doi:10.1139/as-2021-0024.

Kokelj, S.V., Lantz, T.C., Tunnicliffe, J., Segal, R., and Lacelle, D. 2017. 'Climate-driven thaw of permafrost preserved glacial landscapes, northwestern Canada', *Geology* 45(4), pp. 371–374. doi:10.1130/G38626.1.

LeBlanc, A.-M. and Oldenborger, G.A. 2021. 'Ground temperature, active-layer thickness and ground-ice conditions in the vicinity of Rankin Inlet, Nunavut', *Canada-Nunavut Geoscience Office* Summary of Activities 2020.

McMartin, I. 2002. 'Surficial geology, Rankin Inlet, Nunavut', *Geological Survey of Canada* Open File 4116.

McMartin, I., Gauthier, M.S., and Page, A.V. 2022. 'Updated post-glacial marine limits along western Hudson Bay, central mainland Nunavut and northern Manitoba', *Geological Survey of Canada* Open File 8921.

McMartin, I., Godbout, P., Campbell, J.E., Tremblay, T., and Behnia, P. 2021. 'A new map of glacigenic features and glacial landsystems in central mainland Nunavut, Canada', *Boreas* 50(1), pp. 51–75. doi:10.1111/bor.12479.

McQuaig, S., McKillop, R., McGregor, C., Roy-Léveillée, P., and St-Amour, A. 2022. 'Mapping and Investigating Permafrost along the Proposed Kivalliq Hydro-Fibre Link, Manitoba to Nunavut', in *GeoCalgary 2022: Reflections on Resources*, pp. 1–8.

Oldenborger, G.A., Bellehumeur-Génier, O., LeBlanc, A.-M., and McMartin, I. 2022a. 'Landform mapping, elevation modelling, and thaw subsidence estimation for permafrost terrain using a consumer-grade remotely-piloted aircraft', *Drone Systems and Applications* 10(1), pp. 309–329. doi:10.1139/dsa-2021-0045.

Oldenborger, G.A., Short, N., and LeBlanc, A.-M. 2022b. 'Permafrost thaw sensitivity prediction using surficial geology, topography, and remote-sensing imagery: a data-driven neural network approach', *Canadian Journal of Earth Sciences* 59(11), pp. 897–913. doi:10.1139/cjes-2021-0117.

O'Neill, H.B., Smith, S.L., Burn, C.R., Duchesne, C., and Zhang, Y. 2023. 'Widespread Permafrost Degradation and Thaw Subsidence in Northwest Canada', *Journal of Geophysical Research: Earth Surface* 128(8), pp. 1–16. doi:10.1029/2023JF007262.

O'Neill, H.B., Wolfe, S.A., and Duchesne, C. 2019. 'New ground ice maps for Canada using a paleogeographic modelling approach', *The Cryosphere* 13(3), pp. 753–773. doi:10.5194/tc-13-753-2019.

O'Neill, H.B., Wolfe, S.A., and Duchesne, C. 2022. 'Ground ice map of Canada (version 1.1)', *Geological Survey of Canada* Open File 8713.

Phillips, M. and LeBlanc, A.-M. 2024. 'Visible ice content in permafrost in the Kivalliq Region, Nunavut: digitization and analysis of data from historic drilling program', in *12th International Conference on Permafrost*. Whitehorse, Yukon, Canada: June 16–20, 2024.

Prest, V.K., Grant, D.R., and Rampton, V.N. 1968. 'Glacial map of Canada', *Geological Survey of Canada* "A" Series Map 1253A, scale 1:5,000,000.

Smith, S.L., Burgess, M.M., Riseborough, D., and Mark Nixon, F. 2005. 'Recent trends from Canadian permafrost thermal monitoring network sites', *Permafrost and Periglacial Processes* 16(1), pp. 19–30.

Smith, S.L., O'Neill, H.B., Isaksen, K., Noetzli, J., and Romanovsky, V.E. 2022. 'The changing thermal state of permafrost', *Nature Reviews Earth & Environment* 3(1), pp. 10–23. doi:10.1038/s43017-021-00240-1.

Subedi, R., Kokelj, S.V., and Gruber, S. 2020. 'Ground ice, organic carbon and soluble cations in tundra permafrost soils and sediments near a Laurentide ice divide in the Slave Geological Province, Northwest Territories, Canada', *The Cryosphere* 14(12), pp. 4341–4364. doi:10.5194/tc-14-4341-2020.

Wheeler, J.O., Hoffman, P.F., Card, K.D., Davidson, A., Sanford, B.V., Okulitch, A.V., and Roest, W.R. 1996. 'Geological map of Canada', *Geological Survey of Canada* "A" Series Map, 1860A.

Wolfe, S.A. 1998. 'Massive ice associated with glaciolacustrine delta sediments, Slave Geological Province, NWT, Canada', in *Seventh International Permafrost Conference*. Yellowknife, Northwest Territories, Canada, pp. 1125–1131.

Ice content in permafrost in the Kivalliq Region, Nunavut: Digitization and analysis from historic drilling program

Marcus R. Phillips & Anne-Marie LeBlanc

Geological Survey of Canada, Natural Resources Canada, Ottawa, Ontario, Canada

ABSTRACT

The Kivalliq Region on mainland Nunavut west of Hudson Bay, Canada is an area of interest for major infrastructure projects. Proposals include a 450-km all-season road between Arviat and Chesterfield Inlet as well as the Kivalliq Hydro-Fibre Link which would connect the region to electrical power and extended high-speed internet service from Manitoba. Permafrost and ground-ice data are crucial to responsible development in the region, yet little data are available. We introduce a newly digitized database containing geotechnical, cryostratigraphic, and geospatial data created from paper reports of a field drilling campaign completed in 1975–1977 by the Polar Gas consortium of companies in support of a proposed, but never realized, pipeline running from Melville Island to Ontario via the Kivalliq Region. The section from the Nunavut-Manitoba border to Baker Lake is discussed here. We found that (1) boreholes in alluvial and glacial sediments are substantially more likely to contain ice-rich permafrost than boreholes in glaciofluvial sediments, and (2) boreholes below the maximum postglacial marine limit are more likely to be ice-rich than those above the marine limit, but (3) caution is necessary in interpretation of visible ice content data from this dataset. The newly digitized data have some weaknesses, but also contain considerable useful data on permafrost and ground ice.

1 INTRODUCTION

Ground ice content is an important property of frozen ground that affects the stability of infrastructure. Ground ice is the most critical factor of potential thaw settlement. Recent advances in modelling of ground ice (e.g., O'Neill et al. 2019, 2024) have considerably improved our ability to predict the distribution of ground ice; however, direct observations are still useful for land-use planning in permafrost and for validation of model results. Unfortunately, direct observations of ground ice are relatively difficult to obtain.

The Kivalliq Region of Nunavut is home to two active mines (MeadowBank-Amaruq and Meliadine) and is also a region of interest for development. Proposed projects include a 450 km all-season road from Arviat to Chesterfield Inlet as well as the Kivalliq Hydro-Fibre Link (KHFL) project (Nukik Corporation 2023; McCuaig et al. 2022), which proposes to connect the region to electrical power and extended high-speed internet service from Manitoba. Permafrost and ground-ice data are crucial to responsible development in the region, yet there are few relevant studies. Much of the published work about permafrost in the Kivalliq Region comes from a set of related studies working within about 20 km of Rankin Inlet. LeBlanc and Oldenborger (2021) report on ground temperatures and give descriptions of sediments and ground ice in seven boreholes, and Faucher et al. (2024) use laboratory measurements to study ground ice in a shallow (< 2.5 m) subset of three of these boreholes. Remote-sensing, geophysical, and machine learning studies of the same area investigated sensitivity to thaw subsidence (Oldenborger et al. 2020, 2022). Outside the Rankin Inlet area, McCuaig et al. (2022) have mapped surficial geology and described ground ice and permafrost in the KHFL corridor along the coast of Hudson Bay and inland from Rankin Inlet to Baker Lake. These studies provide permafrost information for the region but cover only a small fraction of the area and all are below the upper limit of post-glacial marine inundation in the region (McMartin et al. 2022).

From 1975 to 1977, the Polar Gas consortium of companies completed a drilling program in support of planning and construction for a proposed, but never realized, pipeline from the Canadian Arctic Archipelago to Ontario via the Kivalliq Region of Nunavut. The entire drilling program included logs and sample data from nearly 500 boreholes which, heretofore, have been available only in a few paper copies. The Polar Gas Project (PGP) Drilling Program included 72 boreholes in the Kivalliq Region between the Nunavut-Manitoba border and Baker Lake (Figure 1). These data represent the only available permafrost and geotechnical investigation along a north-south transect for large portions of the Kivalliq Region, yet they have not been digitized or evaluated by modern practitioners or academics.

From the paper copies of PGP drilling reports (EBA 1975, 1976, 1977), we digitized geospatial, cryostratigraphic, stratigraphic, and other geotechnical data into an internal database, greatly expanding the permafrost data in readily useable formats for this region. In this paper, we examine visible ground ice characteristics of these boreholes in the context of publicly available datasets of surficial geology (Geological Survey of Canada 2017a, b, c, d, e) and postglacial marine transgression limits (McMartin et al. 2022) to illustrate the potential of this newly digitized database.

2 KIVALLIQ REGION

The area considered in this paper is a part of the Kivalliq Region of mainland Nunavut on the western coast of

https://doi.org/10.52381/ICOP2024.174.1

Hudson Bay. During the Wisconsinan glaciation, the entire region was covered by the Laurentide Ice Sheet, which retreated from the region 6–8 ka (Dyke 2004). The ice sheet caused substantial isostatic depression, and the region was partially covered by a marine transgression that extended about 90–400 km inland of the current coast (Dyke 2004; McMartin et al. 2022). The median elevation of the marine limit is 140 m, but due to a range of deglacial ages and proximity to a former ice-load centre causing substantial glacio-isostatic rebound the elevation of the marine limit varies from 132 to 170 m asl through the study area (McMartin et al. 2022). The PGP pipeline route traverses the marine limit in multiple locations (Figure 1), and the surficial geology is a complex mixture of alluvial, glacial, glaciofluvial, and marine deposits with bedrock outcrops (Geological Survey of Canada 2017a, b, c, d, e). The region is within the continuous permafrost zone (Heginbottom et al. 1995).

3 METHODS

The PGP Field Drilling Program took place from 1975 to 1977 (EBA 1975, 1976, 1977), and covered the entire proposed pipeline corridor from northern Melville Island to Longlac, Ontario (Figure 1). While the full drilling program included nearly 500 boreholes, only the 72 located in the Kivalliq Region between the Nunavut-Manitoba border and Baker Lake, Nunavut will be discussed in this paper. The terminal depth of boreholes in this region ranges from 2.5 to 13 m, and more than 75% of boreholes reach more than 5.5 m depth. Boreholes were drilled using a rotary wireline diamond drill. Drilling techniques used in 1975 often yielded poor core recovery, as heat generated at the cutting face, especially when drilling through coarse materials, combined with unrefrigerated drilling fluid, substantially thawed samples and caused the fine matrix to be washed away. In 1976 the PGP drilling program added a refrigeration unit which maintained the circulating drilling fluid at a temperature below 0 °C. This improved core recovery such that they "effectively cut and retained core in almost every soil type encountered in [the Kivalliq region]" (EBA 1976). However, sample recovery was still poor where frozen material was not well ice bonded. For some locations that were stone-free, they also used a Cold Regions Research and Engineering Laboratory (CRREL) permafrost drilling system.

PGP technicians recorded logs of soil type, visible ground ice content, and ground ice type. They estimated visible ice content to the nearest 5%. We recognize that visible ice content has weaknesses as a measure of ground ice, and we consider that in our analysis (see discussion). In addition to estimated percent visible ice content, PGP technicians used a simple ground ice description system common in North America (Table 1) based on a hybrid of ice content (assessed visually) and basic cryostructure. This approach remains in use among practitioners, but a more cryostructure-focused description is also commonly used among academics (cf. Murton and French 1994). Technicians extracted samples at selected depths and subsets of samples were analyzed for various properties.

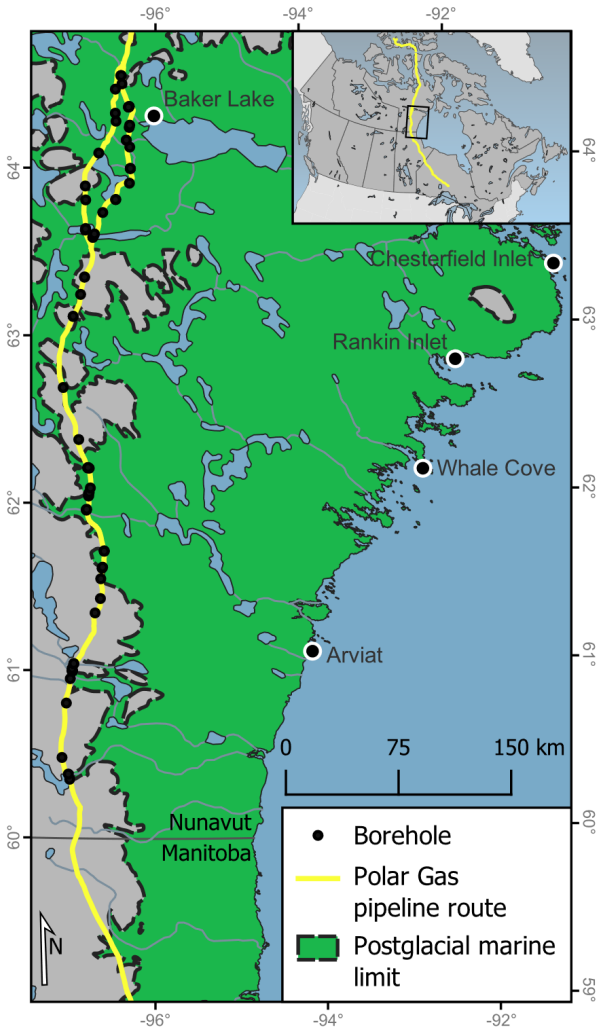

Figure 1. Map of the PGP pipeline route and borehole locations through the Kivalliq Region of Nunavut, Canada. Note that some borehole locations are too close together to be individually resolved at this scale. The full pipeline route is shown on the inset map. Postglacial marine limit at 132–170 m asl from McMartin et al. (2022).

We manually transcribed text and numeric data from PGP Drilling Program reports without using optical character recognition software. There were two broad types of information: (1) data from drilling logs, including literal soil descriptions, soil classification codes using the Unified Soil Classification System, ground ice description codes (Table 1), and visible ice content; and (2) data from laboratory analyses conducted on samples from boreholes, including gravimetric water content, field-moist density, particle size distribution, and Atterberg limits. We manually traced the PGP proposed pipeline route from index maps in the PGP drilling program reports using QGIS software (QGIS 2023). We used the index maps for initial borehole placement, then refined locations using photographs and air photos in the PGP reports. We detected some errors in the paper reports. These errors were rare (less than 1%) and appeared to be dominantly typographical errors made during the

compilation of borehole logs in reports. Where data were very likely erroneous, we used our judgement and available context (i.e., other data from the reports) to correct errors whenever possible. In circumstances where we judged that context was insufficient to make a confident correction, the offending data were removed and left blank.

Table 1. Ground ice description scheme used in PGP reports (EBA 1975, 1976, 1977). Where borderline or mixed classifications existed PGP technicians used dual symbols. A similar scale is described in French and Shur (2010).

Visible ice content category	Ground ice description code	Description
Ice not visible	Nf	Poorly bonded or friable
	Nbn	No excess ice, well bonded
	Nbe	Excess ice, well bonded
Visible ice < 50% by volume	Vx	Individual ice crystals or inclusions
	Vc	Ice coatings on particles
	Vr	Random or irregularly oriented ice formations
	Vs	Stratified or distinctly oriented ice formations
Visible ice > 50% by volume	ICE+	Ice with soil inclusions
	ICE	Ice greater than 2.5 cm thick without soil inclusions

We overlaid borehole locations on surficial geology maps of the region produced at a scale of 1:125,000 (Geological Survey of Canada 2017a, b, c, d, e). Because these maps have a high categorical resolution relative to the number of boreholes, surficial geology categories were downgraded from detailed subcategories (e.g., glaciofluvial sediments – ice-contact sediments) to broad categories (e.g., glaciofluvial sediments). Downgrading generally retained a proportionally representative sample of surficial geology subtypes, though alluvial sediments were somewhat biased towards locations with a marine sediment subtype. We assigned boreholes to surficial categories based on a spatial join using QGIS software (QGIS 2023). We classified boreholes as either above or below the maximum marine limit defined by McMartin et al. (2022), which they assessed with a moderate to high level of confidence for this region. This limit also affects the surficial materials present (e.g., no marine or wave-washed sediments are present above the limit) and, therefore, the ground ice type and content.

Ground ice type description codes used by PGP technicians include semi-quantitative information on visible ice content. Whereas they recorded detailed information on ice disposition (e.g., Vr – random or irregularly oriented ice formations – visible ice < 50% by volume), we downgraded these into broader categories that refer only to the visible ice content (e.g., visible ice < 50% by volume). This includes the visible ice content categories from Table 1, as well as additional categories for (1) unfrozen sections, (2) "frozen" material that they noted was cryotic but made no other notes about ground ice in that section, and (3) material for which they made no notes on freezing or ice characteristics. PGP reports indicate that because of the use of unrefrigerated drilling fluid in 1975 there were poor sample returns when drilling through coarse fragments, and many of these cases were assigned to these additional categories. The "frozen" category is assumed to refer to material that was identified as frozen during drilling, but for which returns were insufficient to evaluate ice richness. Thus, this category represents underestimates in the other frozen categories. With the 1976 drilling season, PGP staff introduced refrigerated drilling fluid and the "frozen" category was no longer used. We calculated wet-basis gravimetric water content (w_w; g water g^{-1} field-moist soil) from dry-basis gravimetric water content (w_d; g water g^{-1} dry soil) using the following relation from Phillips et al. (2015):

$$w_w = w_d / (1 + w_d) \quad [1]$$

4 RESULTS

PGP Drilling staff noted that in 15 boreholes in the region (about 21%) they did not encounter frozen ground. Of these 15 boreholes, 14 were drilled in the first year of the drilling program when they were still using unrefrigerated drilling fluid. It is likely that in many cases permafrost was present but the drilling technique caused thawing and technicians were not able to recognize the presence of frozen ground.

Reported visible ice contents from boreholes where frozen ground was detected ranged from 5 to 90%, with a median of 15%. Wet-basis gravimetric water content ranged from 0.02 to 0.95 g water g^{-1} field-moist soil, with a median of 0.17 g g^{-1} and a mean of 0.25 g g^{-1}. Only a subset of samples included measurements for water content. The relationship between water content and visible ice content is shown in Figure 2. There are about 40 of over 1,200 data

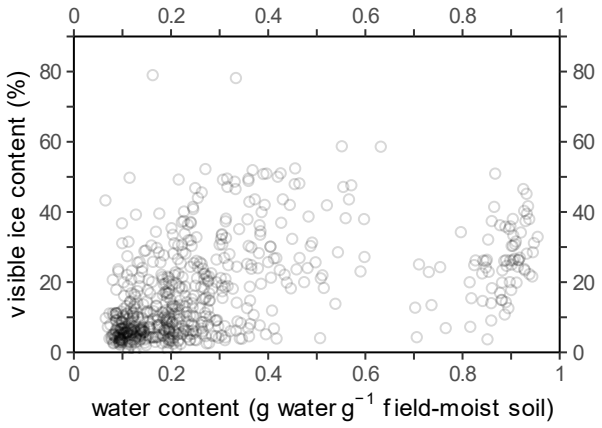

Figure 2. Scatterplot of wet-basis gravimetric water content vs visible ice content. A water content of 1 would indicate pure water or ice. To reduce overlapping of data points, water content (originally measured to the nearest 0.01 g g^{-1}) was randomized to ±0.005 g g^{-1} and visible ice content (originally estimated to the nearest 5%) was randomized to ±2.5% from the original values.

points where the ground ice description code indicates there is no visible ice, yet a visible ice content of 5, 10, or 15% is recorded.

Ground ice descriptions indicate that there is visible ice in more than 25% of all depth increments deeper than 0.9 m and shallower than 5 m (Figure 3). This increases to more than 35% if boreholes, where frozen ground was not recovered, are ignored. Most boreholes with frozen ground and shallow thaw depths (< 1 m) have some visible ice near the top of permafrost, and 40–50% of boreholes with frozen ground have some visible ice to depths of more than 4 m. In marine sediments PGP staff noted frozen ground in 4 of 6 boreholes; however, data on ice from them were scarce or depth intervals not well defined. Because of this lack of data, marine sediments are excluded from discussion here (not shown in Figure 3). The most ice-rich soils are found in the top 3.5 m of boreholes drilled in areas mapped as glacial and alluvial sediments, including all sections with visible ice content greater than 50%. A majority of the area along the pipeline route mapped as alluvial sediments, and of the PGP boreholes within alluvial sediments, fall in map units that have a secondary category of marine sediments. There is generally more visible ice in boreholes drilled in alluvial or glacial sediments than in glaciofluvial sediments, though no frozen soil was recovered in 3 of 7 boreholes in glaciofluvial sediments. Visible ice is present in more than 20% of depth increments shallower than 5 m in boreholes drilled in areas mapped as bedrock; however, closer examination of the individual borehole logs and descriptions reveals that all instances of visible ice are in pockets of another surficial material overlying bedrock, usually a silty to sandy till, but were mapped as bedrock in surficial geology maps.

Depth intervals with more than 50% visible ice were present only in boreholes located within the postglacial marine limit (Figure 4). There is a much greater proportion of depth intervals with visible ice in the top 2 m in locations below the marine limit than in locations above the marine limit, and also a greater proportion of boreholes that encounter frozen ground at any depth. At first examination of Figure 4 it may appear that there is substantially more visible ice distributed at depths below 3 m in boreholes above the marine limit. However, this is an artifact of the data visualization type. It is caused because the number of boreholes decreases with depth, and the boreholes that do not reach greater depths are disproportionately those where frozen ground was not detected, increasing the apparent proportion of ground ice in the remaining boreholes.

Mean grain size distribution (Table 2) indicates that all surficial geology types are dominantly sandy, but alluvial and glacial sediments had a substantially greater mean fines content (41 and 43%, respectively) than did glaciofluvial sediments (26%). This suggests that the lack of frost susceptibility of the sediments may be an important control in glaciofluvial sediments.

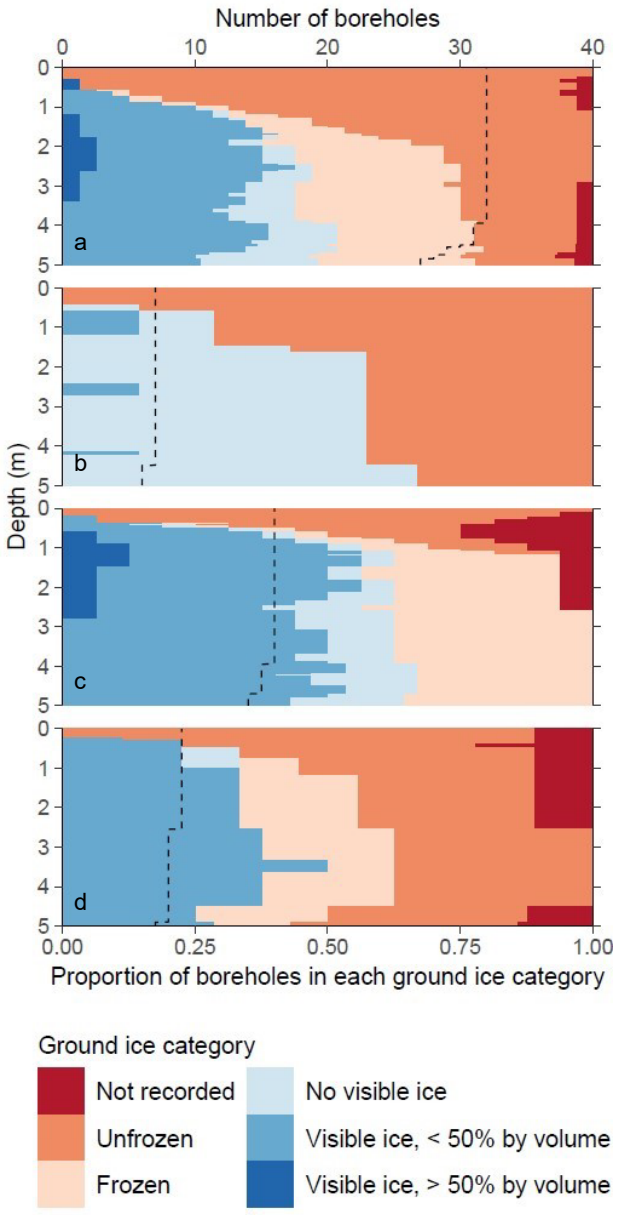

Figure 3. Proportion of boreholes falling within each ground ice category, by depth, in mapped surficial geology categories (a) glacial deposits, (b) glaciofluvial deposits, (c) alluvial deposits, and (d) thin layers of other surficial material (usually glacial deposits) overlying bedrock at locations mapped as bedrock. Using the secondary axis at the top of the figure, dashed lines indicate the number of boreholes in each category at each depth. The “frozen” category likely represents underestimates of other categories (see text). Boreholes in the marine surficial geology category are not shown because *n* was small and data on ground ice was limited. Figures are limited to 5 m depth because the number of boreholes drops sharply below this depth.

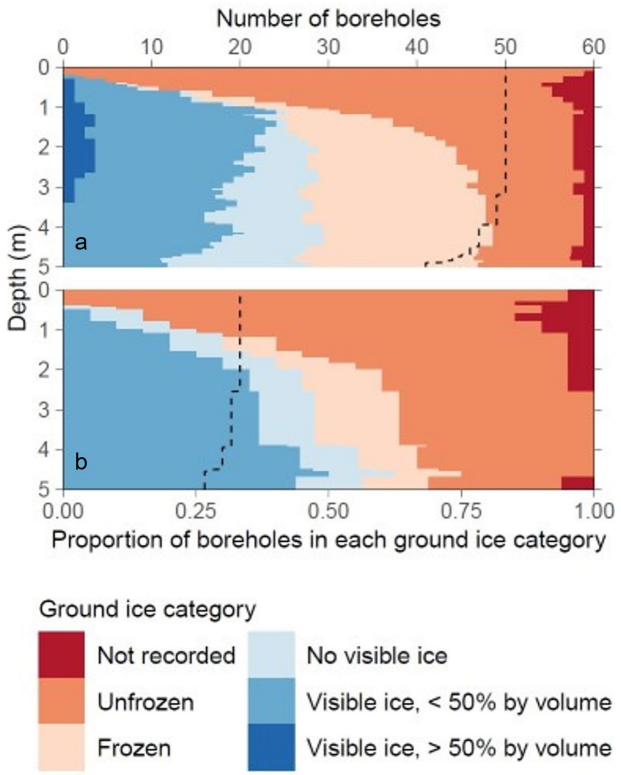

Figure 4. Proportion of boreholes falling within each ground ice category, by depth, (a) within and (b) beyond the postglacial marine limit (McMartin et al. 2022). Using the secondary axis at the top of the figure, dashed lines indicate the number of boreholes in each category at each depth. The "frozen" category likely represents underestimates of other categories (see text). Figures are limited to 5 m depth because the number of boreholes drops sharply below this depth.

Table 2. Mean grain size distribution in samples from boreholes in mapped surficial geology types.

Surficial material type	Sand	Silt	Clay	Gravel	*n*
Alluvial	49	34	7	10	43
Glaciofluvial	55	25	1	19	17
Marine	55	17	3	24	9
Glacial	45	38	5	13	55

5 DISCUSSION

Caution is necessary when interpreting data from these digitized reports. The purpose of the PGP Field Drilling Program was to gather information for pipeline construction, not to provide a representative sampling of the landscape to be upscaled for scientific investigations. This focus on pipeline planning means they concentrated on locations where they expected pipeline construction challenges (e.g., river crossings) and locations where they hoped to find aggregate resources. This sampling strategy is unlikely to produce a complete picture of regional permafrost conditions. Moreover, drilling practices in the first year and dubious percent visible ice content estimates mean that some of the data should be treated with skepticism. Nevertheless, this database contains considerable useful permafrost and geotechnical data for a region with very few other observations.

The proportion of boreholes that did not include any notation of frozen ground was relatively high (about 21%) considering that the region is within the continuous permafrost zone, where 90% or more of terrain is expected to be underlain by permafrost (Heginbottom et al. 1995). This may be explained, for some, by the focus on river crossings, as some boreholes were drilled only metres from riverbanks and may be located within a talik caused by a major river, but most are likely incorrect. Nearly all boreholes for which PGP technicians did not encounter frozen ground were drilled in 1975, when they were still using unrefrigerated drilling fluid. It is likely that this caused thawing at the cutting face and permafrost was not recognized despite being present.

The association between water content and visible ice content is weak (Figure 2), particularly for the highest water contents where the volume of ice is greater than the thawed porosity of the soil and any increase in water content should cause a corresponding increase in visible ice content. Instead, we see a large scatter in visible ice content and only a weak increase. Moreover, a considerable number of the values seem to be impossible to reconcile. For example, if we assume a particle density for soil solids of 2.65 g cm^{-3} and a relatively large (i.e., conservative) thawed porosity of 0.6, we expect volumetric ice contents in excess of pore space (i.e., approximate visible ice content) of 68% and 80% for wet-basis gravimetric water contents of 0.7 and 0.8 g water g^{-1} field-moist soil, respectively; however, data from the PGP Drilling Program show a range in visible ice content from only 5 to 35% for this water content range. It is unlikely that a simple routine analysis like gravimetric water content is substantially incorrect. The percent visible ice content by volume is subject to expert interpretation, and therefore could have been under or over-estimated and inconsistently recorded by different technicians over the 3 years. For instance, even when assessed by current experts, estimated visible ice content may show unreasonable scatter and poor correlation against measured volumetric ice content (e.g., Castagner et al. 2023). It is also possible that there is a scale mismatch between the two data types and the visible ice contents represent larger depth increments than the corresponding samples do. For these reasons, we opted to discuss the semi-quantitative scale (Figures 3 and 4) instead of visible ice content data from this dataset. However, if future ice content measurements are done for the region, it may still be possible to use regression models to produce a better result from visible ice content (cf. Castagner et al. 2023).

The ground ice distributions determined here are in general agreement with previous studies from the region, with minor differences. McCuaig et al. (2022) found moderate ice content in fluvial sands and silts along the proposed KHFL corridor near the coast, and Faucher et al. (2024) found that the upper permafrost was ice-rich in a core drilled in alluvial

and marine undifferentiated sediments near Rankin Inlet. A majority of the area along the pipeline route mapped as alluvial sediments and a majority of the boreholes located within alluvial sediment surficial geology map units, including those that most strongly contribute to the relatively high ice content in alluvial sediments, fell in areas mapped as alluvial sediments with a significant secondary category of marine sediments, suggesting that marine sediments may be an important component of the relatively high ice content in alluvial sediment surficial units. The PGP data indicate that there is more ice at depths beyond 1.5 m in alluvium than Faucher et al. (2024) found in their core, which was in the alluvium/marine surficial geology type. McCuaig et al. (2022) found that glacial sediments along the KHFL corridor had excess ice, though typically in relatively low volumes (5–10%), but they acknowledge that they had relatively few samples. Faucher et al. (2024) noted a similar result from their core in till and marine undifferentiated sediments near Rankin Inlet. Working with data from a relatively large number of boreholes in glacial sediments (Figure 3), we note that the visible ice (< 50% by volume) is common at all depths, which could include relatively low excess ice volumes similar to those found by McCuaig et al. (2022) and Faucher et al. (2024); however, there are also boreholes where there are some intervals with > 50% visible ice, by volume, far higher than noted by either previous study. These differences in ice contents of glacial sediments do not necessarily put our results and interpretation at odds with those of Faucher et al. (2024) or McCuaig et al. (2022), as they had few samples from glacial sediments. Only a few of those from the PGP dataset showed higher ice content, and these could easily be missed in a study with a lower number of observations. In a spatially distributed examination of geological, topographic, and multispectral variables Oldenborger et al. (2022) predicted the thaw sensitivity of the ground near Rankin Inlet using a reference classification based on seasonal ground subsidence and expert knowledge on ground ice content and distribution in frozen active layer and permafrost. They found that a larger proportion (> 75%) of areas mapped as glaciofluvial sediments are thaw stable than the proportions of glacial sediments (< 75%) or alluvial sediments (about 25%), and a smaller proportion of glaciofluvial sediments have a high or very high thaw sensitivity (< 3%) than the proportions of glacial sediments (> 6%) or alluvial sediments (> 25%). The general agreement of their results with ours strengthens confidence in our findings.

Both PGP reports and McCuaig et al. (2022) note that ice-wedges are common in several materials, including coarse-grained glaciofluvial deposits, yet boreholes in glaciofluvial deposits are rarely noted to have substantial visible ice in PGP reports (Figure 3). It is common that PGP site descriptions for boreholes will note abundant ice wedges, but borehole logs that explicitly penetrate wedge ice are absent. It is possible that there was a sampling bias where PGP technicians were systematically avoiding ice wedges in their drilling. Thus, there may be substantial near-surface ground ice as ice wedges that is not accounted for in this dataset.

The presence of noteworthy visible ice in boreholes from areas mapped as bedrock highlights a difficulty inherent to generalizing when comparing point-based measurements to complex surficial geology. These boreholes were all in pockets of other material (usually glacial deposits) too small to be mapped at the scale of the surficial geology maps. This highlights the need for caution in interpretation of these data when combined with regional surficial geology maps. Analysis of boreholes in spatially determined groupings as we have done here can give valuable impressions of trends and typical values, but where more precise or locally relevant results are desired the surficial geology type determined from maps should be compared against that inferred from the borehole stratigraphy, especially for categories with few boreholes.

6 SUMMARY

Though the Kivalliq Region of Nunavut is an area of interest for infrastructure development, heretofore the availability of permafrost data from the region has been poor. We have digitized and introduced a historic dataset of geotechnical, cryostratigraphic, and geospatial data from paper records of the PGP Field Drilling Program of 1975–77 completed in the Kivalliq Region between the Nunavut-Manitoba border to Baker Lake. Important results from this portion of the dataset include (1) the most ice-rich locations are in areas mapped as alluvial and glacial sediments, whereas those mapped as glaciofluvial tend to be ice-poor, (2) boreholes within the maximum limit of postglacial marine inundation are more likely to be ice-rich than those beyond the marine limit; however, (3) caution is necessary in interpretation of PGP data, particularly data on percent visible ice content. There are weaknesses of this dataset related to collection methods of the period, particularly where drilling methods caused sample degradation and in poor visible estimates of percent ice content, but there remains considerable potential to extract informative permafrost and geotechnical information.

7 DATA AVAILABILITY

At the time of writing, final data compilation is ongoing. We intend to release the data publicly along with additional analyses of publicly available datasets as a Geological Survey of Canada Open File, but it is not yet available. Once it is ready, it will be available to download at GEOSCAN (https://geoscan.nrcan.gc.ca). We intend to expand the geographic scope of the digitization project in the future.

8 ACKNOWLEDGEMENTS

This data digitization and research is supported by Natural Resources Canada, Climate Change Geoscience and GEM-GeoNorth Programs. The data digitization framework development was supported by discussions and collaboration with Tabatha Rahman, Pascale Roy-Léveillée, and Emmanuel L'Hérault. H. Brendan O'Neill provided helpful discussions during the analysis process and comments on the manuscript. Tommy Tremblay scanned the paper reports, and Louis Roberson georeferenced index maps from those scanned reports. Allessandra Kempson assisted with early data entry.

9 REFERENCES

Castagner, A., Brenning, A., Gruber, S., and Kokelj, S.V. 2023. 'Vertical distribution of excess ice in icy sediments and its statistical estimation from geotechnical data (Tuktoyaktuk Coastlands and Anderson Plain, Northwest Territories)', *Arctic Science* 9(2), pp. 483–496. doi:10.1139/as-2021-0041.

Dyke, A.S. 2004. 'An outline of North American deglaciation with emphasis on central and northern Canada', in J. Ehlers and P.L. Gibbard (eds.), *Developments in Quaternary Sciences*, pp. 373–424.

EBA Engineering Consultants 1975. *Polar Gas Field Drilling Program 1975*.

EBA Engineering Consultants 1976. *Polar Gas Compilation of Field Data Summer, 1976*, vols. 1–5.

EBA Engineering Consultants 1977. *Polar Gas Compilation of Field Data Summer, 1977*, vols. 1–3.

LeBlanc, A.-M. and Oldenborger, G.A. 2021. 'Ground temperature, active-layer thickness and ground-ice conditions in the vicinity of Rankin Inlet, Nunavut', *Canada-Nunavut Geoscience Office* Summary of Activities 2020, pp. 63–72.

Faucher, B., LeBlanc, A.-M., Oldenborger, G.A., Carrière, E., Lacelle, D., and Letellier, P. 2024. 'Ground ice content of the active layer and near-surface permafrost in the Rankin Inlet area, Nunavut, Canada', in *12th International Conference on Permafrost*. Whitehorse, Yukon, Canada: June 16–20, 2024.

French, H. and Shur, Y. 2010. 'The principles of cryostratigraphy', *Earth-Science Reviews* 101(3), pp. 190–206. doi:10.1016/j.earscirev.2010.04.002.

Geological Survey of Canada 2017a. 'Reconnaissance surficial geology, Ferguson Lake, Nunavut, NTS 65-I', preliminary, Surficial Data Model v. 2.3 conversion, *Geological Survey of Canada* Canadian Geoscience Map 85, scale 1:125,000. doi:10.4095/305361.

Geological Survey of Canada 2017b. 'Surficial geology, Henrik Lakes, Nunavut, NTS 65-H', preliminary, Surficial Data Model v. 2.3 conversion, *Geological Survey of Canada* Canadian Geoscience Map 238, scale 1:125,000. doi:10.4095/299882.

Geological Survey of Canada 2017c. 'Surficial geology, Edehon Lake, Nunavut, NTS 65-A', preliminary, Surficial Data Model v. 2.3 conversion, *Geological Survey of Canada* Canadian Geoscience Map 243, scale 1:125,000. doi:10.4095/301672.

Geological Survey of Canada 2017d. 'Surficial geology, Schultz Lake, Nunavut, NTS 66-A', preliminary, Surficial Data Model v. 2.3 conversion, *Geological Survey of Canada* Canadian Geoscience Map 324, scale 1:125,000. doi:10.4095/305328.

Geological Survey of Canada 2017e. 'Reconnaissance surficial geology, Thirty Mile Lake, Nunavut, NTS 65-P', prelim. 2, Surficial Data Model v.2.3 conversion, *Geological Survey of Canada* Canadian Geoscience Map 326, scale 1:125,000. doi:10.4095/305841.

Heginbottom, J.A., Dubreuil, M.A., and Harker, P.T. 1995. 'Canada, Permafrost', in *National Atlas of Canada, 5th edition*. Natural Resources Canada, Geomatics Canada, MCR 4177, scale: 1:750,000. doi:10.4095/294672.

LeBlanc, A.-M. and Oldenborger, G.A. 2021, 'Ground temperature, active-layer thickness and ground-ice conditions in the vicinity of Rankin Inlet, Nunavut', *Canada-Nunavut Geoscience Office* Summary of activities 2020, pp. 63–72.

McCuaig, S., McKillop, R., McGregor, C., Roy-Levéillée, P., and St-Amour, A. 2022. 'Mapping and investigating permafrost along the Proposed Kivalliq Hydro-Fibre Link, Manitoba to Nunavut', in *GeoCalgary 2022 Conference*. Calgary, Alberta, Canada: Paper 311, 8 p.

McMartin, I., Gauthier, M.S., and Page, A.V. 2022. 'Updated postglacial marine limits along western Hudson Bay, central mainland Nunavut and northern Manitoba', *Geological Survey of Canada* Open File 8921, 1 .zip file. doi:10.4095/330940.

Murton, J.B. and French, H.M., 1994. 'Cryostructures in permafrost, Tuktoyaktuk coastlands, western arctic Canada', *Canadian Journal of Earth Sciences* 31(4), pp. 737–747. doi:10.1139/e94-067.

Nukik Corporation 2023. *Kivalliq Hydro-Fibre Link*. Available from: https://www.nukik.ca/kivalliq-hydro-fibre-link (Accessed: 5 September 2023).

Oldenborger, G.A., Short, N., and LeBlanc, A.-M. 2020. 'Electrical conductivity and ground displacement in permafrost terrain', *Journal of Applied Geophysics* 181, article 104148. doi:10.1016/j.jappgeo.2020.104148.

Oldenborger, G.A., Short, N., and LeBlanc, A.-M. 2022. 'Permafrost thaw sensitivity prediction using surficial geology, topography, and remote-sensing imagery: a data-driven neural network approach', *Canadian Journal of Earth Sciences* 59(11), pp. 897–913. doi:10.1139/cjes-2021-0117.

O'Neill, H.B., Wolfe, S.A., and Duchesne, C. 2019. 'New ground ice maps for Canada using a paleogeographic approach', *The Cryosphere* 13, pp. 753–773. doi:10.5194/tc-13-753-2019.

O'Neill, H.B., Wolfe, S.A., and Duchesne, C. 2024. 'Modelled ground ice conditions in the Kivalliq region, Nunavut, Canada', in *12th International Conference on Permafrost*. Whitehorse, Yukon, Canada: June 16–20, 2024.

Phillips, M.R., Burn, C.R., Wolfe, S.A., Morse, P.D., Gaanderse, A.J.R., O'Neill, H.B., Shugar, D.H., and Gruber, S. 2015. 'Improving water content description of ice-rich permafrost soils', in *GeoQuebec 2015 Conference*. Quebec City, Quebec, Canada: 7 p. doi:10.13140/RG.2.1.4760.1126.

QGIS.org 2023. *QGIS Geographic Information System*. QGIS Association. Available at: http://www.qgis.org.

Analysis of a topographic-based InSAR SWE estimation technique for low-land permafrost terrain north of Inuvik, Northwest Territories

Allison Plourde

Department of Engineering Science, Simon Fraser University, Burnaby, British Columbia, Canada

ABSTRACT

InSAR (Interferometric Synthetic Aperture Radar) is a well-established method for measuring small-scale surface deformations over large regions; however, contaminating effects of snow cover on the InSAR phase prevents the use of (usually less noisy) winter InSAR data, limiting the accuracy of comprehensive measurement of seasonal dynamics in permafrost terrain. In this study we investigate if a previously developed topography-based approach for estimating the contribution of the Snow Water Equivalent (SWE) from repeat pass InSAR phase is accurate enough to correct the displacement phase of the winter data. We use a stack of TerraSAR-X strip map data covering several winters over a study region located in low-lying permafrost north of Inuvik, Northwest Territories. In the study region several ground truth sites have been instrumented with (1) an inclinometer to measure vertical surface deformation due to active layer dynamics of the permafrost, and (2) an ultra-sonic range finder to measure snow-depth. Our analysis found a high uncertainty in the topographic SWE estimates around our ground truth sites due to insufficient variation in terrain preventing us from evaluating the method directly against the ground truth. Estimates for other areas with higher terrain variability farther away from our ground truth sites, however, showed more promising results in terms of error estimates from the topographic SWE estimation being small enough to correct the phase of winter InSAR data to allow their use for comprehensive permafrost active layer displacement measurements.

1 INTRODUCTION

Differential Interferometric Synthetic Aperture Radar (DInSAR) is an established method for precise measurement of surface deformations across large expanses. In terrain underlain by permafrost, the seasonal freeze-thaw cycle can result in widespread surface deformations on the order of millimeters to centimeters, making it appropriate for measurement using InSAR techniques (Liu et al. 2010, 2014; Short et al. 2011). The active layer of permafrost refers to the upper portion of the ground that experiences seasonal freezing and thawing. During freeze back, moisture in the active layer freezes. When the excess water freezes, it undergoes an increase in volume; the expansion exerts pressure on the surrounding soil, causing the ground to heave. Alongside seasonal deformations, long-term subsidence trends stemming from permafrost degradation are also of concern. Distinguishing the seasonal signal from long-term trends is necessary for certain applications, such as estimating Active Layer Thickness (ALT; Liu et al. 2012; Schaefer et al. 2015). Separating these signals can be difficult due to decorrelation of the InSAR phase during spring, when snow is melting, as well as in the fall when snow begins to accumulate; hence, InSAR analyses are often limited to snow-free scenes (Liu et al. 2010, 2014; Short et al. 2011; Strozzi et al. 2018; Rouyet et al. 2019; Scheer et al. 2023).

Phase coherence in InSAR refers to the stability and consistency of the phase measurements over time. Phase decorrelation occurs due to alterations in surface characteristics, such as variations in soil moisture, vegetation, and snow cover on the scale of the microwave wavelength (in these media). In the case of cold, dry snow, the snow layer also acts as a refracting medium. While interferometric pairs with and without snow may exhibit complete decorrelation, pairs captured with short time intervals during the dry-snow season can demonstrate high coherence (Guneriussen et al. 2001). Additionally, after freeze back, the ground surface is relatively stable; thus, if the phase due to snow could be accounted for, long-term trends independent of the seasonal freeze-thaw cycle could be established using winter scenes.

Furthermore, an increase in mean annual snow cover can increase ground temperatures and deepen the active layer, causing the ground to gradually subside from thaw of ice-rich permafrost (Burn et al. 2009). Consequently, there is a need for the ability to accurately monitor snow cover over large areas for which InSAR techniques, such as the method examined in this paper, could prove to be a viable solution.

In this paper, the suitability of a topographic-based approach for estimating the Snow Water Equivalent (SWE) with InSAR (Eppler et al. 2022) to correct the phase of winter InSAR data (so that only the displacement phase component remains) is evaluated for a region of low-land, continuous permafrost in a tundra environment north of Inuvik, Northwest Territories. Section 2 provides background on the relevant InSAR techniques for snow-covered and permafrost landscapes followed by a description of the research area in Section 3. Section 4 outlines the methodology used for both in situ field measurements as well as the InSAR processing steps. In Section 5, the results are presented followed by a discussion in Section 6.

2 BACKGROUND

Repeat pass InSAR (DInSAR) is a remote sensing technique that can measure mm-scale displacements by measuring the phase difference between two synthetic aperture radar (SAR) acquisitions taken at different times. Radar satellites have the advantage of providing a cost-

https://doi.org/10.52381/ICOP2024.65.1

effective solution of monitoring large regions of land over many years.

In general, the interferometric phase, ϕ, is a result of the superposition of several components (Equation 1).

$$\phi_{total} = \phi_{topographic} + \phi_{atmospheric} + \phi_{soil\ moisture} + \phi_{snow} + \phi_{surface\ displacement} \quad [1]$$

The challenge of InSAR measurements is separating these components to isolate the desired element, such as surface displacement. Studies that have measured permafrost-related surface displacements using InSAR methods have often limited the analysis to snow-free scenes due to the complexities introduced by the presence of snow (Liu et al. 2010, 2014; Short et al. 2011; Strozzi et al. 2018; Rouyet et al. 2019; Scheer et al. 2023). However, snow cover is often present throughout a significant portion of the year in regions with continuous permafrost; thus, eliminating such scenes can significantly reduce the amount of available data.

Several approaches have emerged to measure SWE from both SAR and InSAR scenes. SAR methods use principles of backscatter — the amplitude of the SAR signal — to measure SWE (Tsang et al. 2022), whereas InSAR methods examine the phase difference between two SAR acquisitions. When considering the effect of snow on the InSAR signal, there are two mechanisms that need to be considered. Firstly, radar signals are impenetrable to liquid water, hence when snow is wet (during thaw) the signal is reflected at the snow surface. Methods that have capitalized on this mechanism compare snow-free and wet snow scenes to measure total SWE (Larsen et al. 2005). When snow is dry, the signal is reflected at the snow-ground interface resulting in a signal delay due to refraction in the snow-layer (Guneriussen et al. 2001). Methods that take advantage of this mechanism include the delta-k method (Engen et al. 2004), the method in this paper which exploits variations in topography (Eppler et al. 2022), among others (Guneriussen et al. 2001; Leinss et al. 2015; Lei et al. 2016).

3 Ground Truth Sites

The study area is situated in low-lying permafrost terrain north of Inuvik, Northwest Territories in the uplands of the Mackenzie Delta (Figure 1). Several ground truth sites have been established where in situ measurements of vertical surface displacement along with snow depth are collected year-round.

The ground truth sites are located between kilometer 20 and 35 of the Inuvik-Tuktoyaktuk Highway (ITH) within 400 m of the road. The study uses satellite images from TerraSAR-X, the footprint covers a 13 km by 30 km area extending from the west side of Noell lake up to just south of Trail Valley Creek.

The research area is part of the continuous permafrost zone and is characterized by low-shrub tundra. The surficial geology is predominantly hummocky and rolling moraine, interspaced by colluvial and lacustrine deposits (Rampton

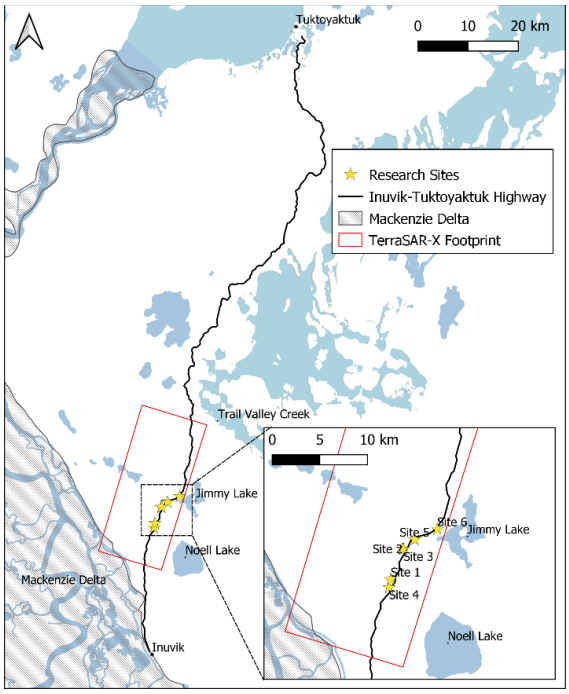

Figure 1. Overview of study Area. Depicted are the six ground truth sites with instrumentation for in situ measurements as well as the footprint for the TerraSAR-X strip map radar stack.

1987). Ground temperatures in the uplands decrease northwards across the treeline, and the thickness of snow cover also decreases in this direction (Burn and Kokelj 2009).

3.1 Detailed Site Description

Homogenous Terrain (Sites 1 and 4): Site 1 was established in 2018 and is the longest running site, covering a 4-year record of inclinometer measurements along with a 3-year record of snow depth measurements. Site 4 was established in 2022 with inclinometer measurements for that year. Regions of polygonal wedges surround these sites and permafrost related activity, such as frost boils are visible within the vicinity. Site 1 has been determined to be underlain by ice-rich permafrost, whereas site 4 was discovered not to be ice-rich.

Undulating Terrain (Sites 2 and 3): Site 2 and 3 were established in 2019 and due to instrumentation errors have sparse data. Undulating terrain was desirable to determine if the topographical approach for InSAR SWE estimation would be suitable for this area.

Sloping Lacustrine Terrain (Sites 5 and 6): Sites 5 and 6 were established in 2022 and both contain inclinometer and snow depth measurements dating from July 2022 to July 2023. They were selected for their proximity to sloping terrain as well as coherence in the InSAR imagery in both summer and winter months.

4 METHODOLOGY

Using a collection of TerraSAR-X strip map images, we evaluate the viability for DInSAR phase correction of a method developed by Eppler et al. (2022) that exploits variations in topography to quantify the effects of SWE on interferometric phase. By identifying the phase component due to SWE, an avenue is established for the measurement of surface deformation throughout the winter season.

The method exploits variations in topographic slope according to Equation 2.

$$\xi \doteq \frac{d\Phi_{SWE}}{dSWE} = \frac{4\pi}{\lambda\rho}\cos\alpha\left(\sqrt{\epsilon(\rho) - \sin^2\theta} - \cos\theta\right) \quad [2]$$

Where ξ is the sensitivity and is defined as the change in phase due to SWE, Φ_s, versus the change in SWE itself. This component is dependent on the radar wavelength, λ, the density of the snow ρ, the terrain slope angle, α, the permittivity of snow ϵ, and the local incidence angle θ. The snow density is assumed to be 0.3, a suitable assumption according to previous studies (Leinss et al. 2015; Eppler et al. 2022). Considering that the method estimates the relative change in SWE rather than total SWE, ρ is also related to changes in the snowpack rather the absolute ρ. In Eppler 2022, it was shown that misspecification of ρ for values between 0 and 0.5 would result in a positive or negative bias of less than 5% the total SWE. The permittivity is derived from ρ according to Leinss et al. (2015). The wavelength and incidence angle are known values of the satellite configuration and the slope angle can be derived from a Digital Elevation Model (DEM).

The ground truth sites are equipped with inclinometers to measure vertical deformation and ultrasonic range finders to measure snow depth (Figure 2).

Figure 2. (A) Ultrasonic snow depth sensor and (B) inclinometer. The center pole is mounted into the permafrost such that it remains stationary.

4.1 Inclinometer Measurements

The vertical surface displacement is derived from the inclination angle measured by either an RST tilt logger or GeoPrecision tilt logger attached to a lever arm. The mechanism design is based on Gruber (2020). A sample of vertical surface displacement recorded between July 2022 and July 2023 at each of the sites is provided in Figure 3.

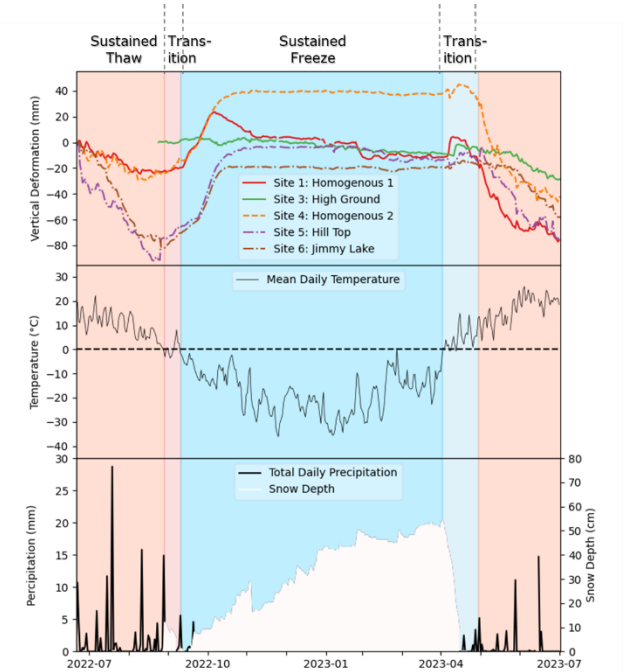

Figure 3. (Top) Vertical deformation as measured by inclinometers between July 2022 and July 2023. (Middle) Mean daily temperature and (bottom) precipitation at Inuvik (Environment Canada).

From the inclinometer data, it can be observed that there is marginal surface displacement from the beginning of November through to the end of March, with the exception of site 1, which recorded a downward trend in subsidence throughout the winter. The mechanism of this downward trend is unclear and may be due to errors related to the weight of snow accumulation or in the sensor setup itself; however, there are mechanisms that can result in negative heave (Mackay et al. 1979). For simplicity, and due to the overall similarities between sites 1 and 4, it was assumed for this analysis that this phenomenon was isolated, and that for the spatial scale of the SWE estimates in this analysis, heave between November and March could be neglected. These measurements, as described in the next section, are used in this study to correct the snow depth measurements for surface heave.

4.2 Snow Depth Measurements

The snow depth was measured at five sites using a Judd ultra sonic sensor designed for snow depth measurements. Sites 1–3 were instrumented with sensors in 2019, sites 5–6 were installed in 2022. Snow depth at each of the sites for

the 2022–2023 season is shown in Figure 4. Site 4 was instrumented with an experimental sensor that did not hold up in the harsh conditions of the tundra and so no data are available at this site.

Two corrections need to be applied to the snow depth data. Firstly, to avoid spurious measurements of vegetation height, the date of first snow at Inuvik is used to zero the data. Additionally, as can be seen in Figure 2A, the pole supporting the sensor is anchored into the permafrost, thus, the ground is free to move and the sensor would also be subject to detecting changes in the ground height due to heave and subsidence. As shown in Figure 3 these displacements can be quite significant. The tilt logger data was used to correct for these displacements; a sample of the 'heave-corrected' snow depths for the 2022–2023 season are provided in Figure 4 along with Environment Canada data collected at Inuvik and Trail Valley climate stations. Inclinometer data at site 2 was not available and was not included.

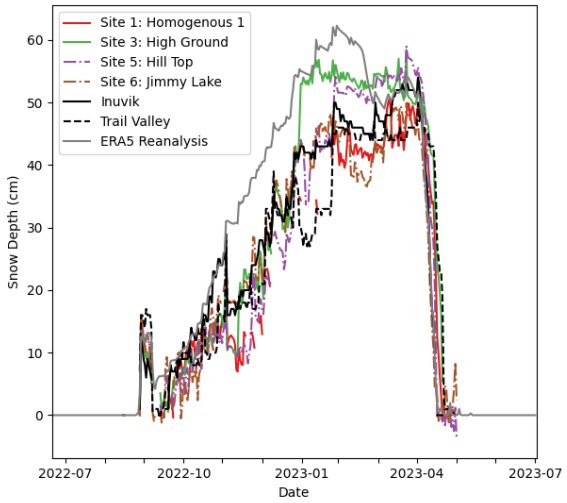

Figure 4. (Top) Heave-Corrected in situ snow depth measurements for 2022-2023 alongside measurements from the Inuvik and Trail Valley Environment Canada climate stations.

5 InSAR Processing

A stack of 106 TerraSAR-X strip map scenes were collected spanning from February 2018 until August 2023. Of those, a total of 78 pairs could be formed that had a 11-day interval between the time of acquisition, 30 of which were between the months of November through to the end of March where snowfall would be present and surface heave would be negligible. The interferograms were generated using standard processing steps using the GAMMA software package (GAMMA Remote Sensing AG, Switzerland).

Firstly, the single-look complex (SLC) scenes were registered to a common master scene and multi-looked by a factor of 2 in both range in azimuth. They were topographically corrected with a Tandem-X 12m DEM. Adaptive phase filtering was then applied using a Werner-Goldstein filter.

For this analysis, atmospheric effects on the InSAR phase are mitigated by estimating the SWE in 1 km^2 windows, such that the dynamic atmosphere is assumed to be constant. Finally, the SWE estimation method does not require phase unwrapping, in which the 2π ambiguity of the InSAR data is resolved (Eppler et al. 2022).

6 Results

The SWE was estimated for 30 interferograms and compared to in situ data collected at the sites, Environment Canada climate data for the Inuvik and Trail Valley stations, as well as ERA5 reanalysis data.

A sensitivity map for the study area based on Equation 2 is shown in Figure 5. The SWE estimation method is dependent on the local spatial variability in the phase sensitivity. The standard deviation over 1 km^2 windows was calculated for the de-meaned 2D sensitivity map to estimate the quality of SWE estimations in Figure 5. It can be observed that much of the region, which is dominated by relatively flat terrain, has a low standard deviation in ξ. The areas where there is the highest standard deviation are deep cut valleys in the terrain as shown in Figure 6.

In addition to variability in SWE, the magnitude of the local incidence angle may also be of concern in producing accurate results since steeper angles result in smaller changes in path-length of the signal through dry snow. The relationship between incidence angle and phase due to 10 mm of SWE over a constant slope is shown in Figure 7. It can be observed for steep incidence angles, there is very little change in phase; between 0 and 25°, with respect to the local terrain slope, the phase varies by 0.26 rad for 10 mm of SWE. For angles above 25° the difference in phase due to the local incidence angle becomes much more pronounced; between 25° and 50°, the phase varies by 1.71 rad. It was discovered that a sufficiently shallow incidence angle with respect to the local slope of the terrain was required to get precise estimations since shallower angles increase the modulating effect of SWE on the phase, which the algorithm is dependent on; thus, a thresholding mask was used to limit the estimation to areas where α was greater than 25°, the result of which is also shown in Figure 6.

It can be observed that the ground truth sites set up in this study are in a region of low variability in terrain slope and thus, low sensitivity to the SWE estimation method. For this reason, an additional point in the region of highest variability in sensitivity was also included in the SWE estimation results. The SWE for each point is taken to be the average over a circular region around the point with a diameter of roughly 300 m – which corresponds to an average over about 2000 pixels. This point is compared to the SWE at Inuvik in Figure 8. The color of the points in the figure represents the mean coherence of the area and the error bars represent the standard deviation of the estimated SWE in the area. Results for SWE estimations at site 1 compared with the in situ data are shown in Figure 9.

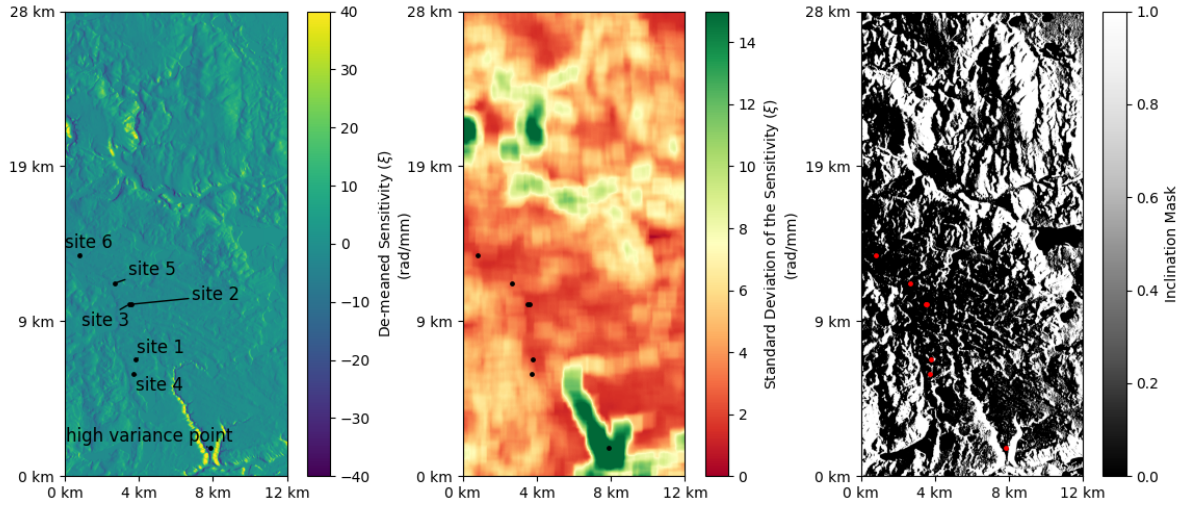

Figure 5. (Left) Derived sensitivity map with ground truth sites indicated. (Middle) A ξ quality map derived from the standard deviation of the sensitivity map. Areas in green indicate regions with high variability in ξ and thus are expected to provide quality estimations for SWE. (Right) Local incidence angle masking used to eliminate regions with a steep incidence angle (black) from the SWE estimation.

Figure 6. Example of terrain with a high variability of sensitivity to SWE north of site 6.

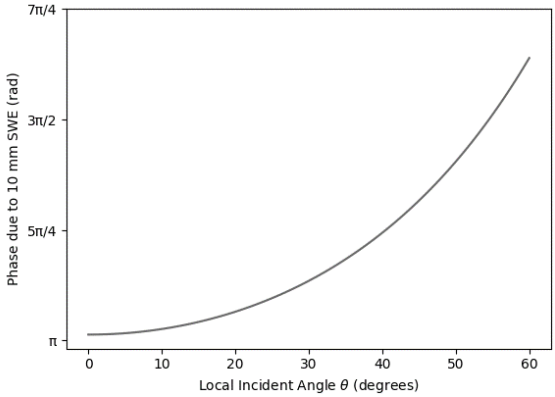

Figure 7. Resulting phase component due to 10 mm of SWE over constant sloped terrain with varying local incidence angle according to Equation 2.

The in situ data are compared to the coarser ERA5 Reanlysis data in Figure 10. Comparing the in situ data provides insight into the spatial variability of the SWE and the expected error when comparing the InSAR results to the in situ measurements. Excluding sites 5 and 6, where minimal data are available, the average Root Mean Squared Error (RMSE) between the in situ data and ERA5 data is 18.6 mm of SWE. The InSAR estimate for the region with high variability in ξ showed a similar RMSE compared to the Inuvik data, which was the closest in situ measurement, of 15.8 mm of SWE. The RMSE between the InSAR estimate for site 1 compared with the in situ measurement at site 1 was much higher, with a value of 38.8 mm of SWE.

7 Discussion

The objective of this analysis was to assess the applicability of a topographic-based InSAR method for estimating Snow Water Equivalent (SWE). The motivation behind this investigation was to assess the potential for the method to account for the phase due to snow, enabling the measurement of long-term subsidence trends using winter InSAR data. The SWE estimations were limited to the period between November and March in which the inclinometer data showed that there would be negligible surface movement.

In situ snow depth was measured at 4 of the 6 ground truth sites as well as Inuvik and Trail Valley Environment Canada stations and compared to the coarser ERA5 Reanalysis data. These measurements were converted to SWE by assuming a snow density of 0.3. The variability of the in situ data was found to be similar to the variability in the InSAR estimates at the point with high variability in ξ, suggesting that the method may be suitable for this particular region.

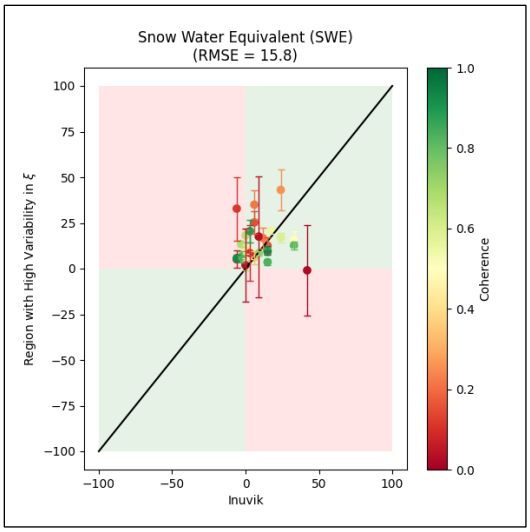

Figure 8. Estimated SWE at location with high variation in ξ compared with derived SWE from measured snow depth at Inuvik. The coherence of the window is indicated by color and the error bars represent the standard deviation of the SWE estimation.

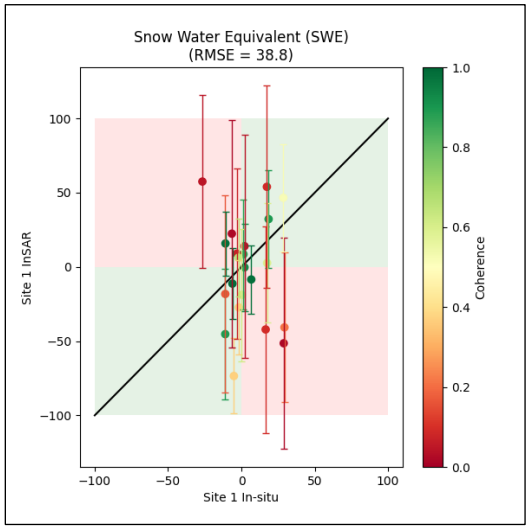

Figure 9. Estimated SWE at site 1 compared with in situ measurements. Due to the low variability in ξ in this region, there is a greater uncertainty in the results.

However, there was substantially more variability between the InSAR estimates for site 1 when compared to the site 1 in situ measurements.

In the region with high variability in ξ, the InSAR estimates tended to be higher than values reported at Inuvik and Trail Valley. However, this area is a region of deep cut valleys and so may be more prone to snow accumulation, resulting in the higher estimates.

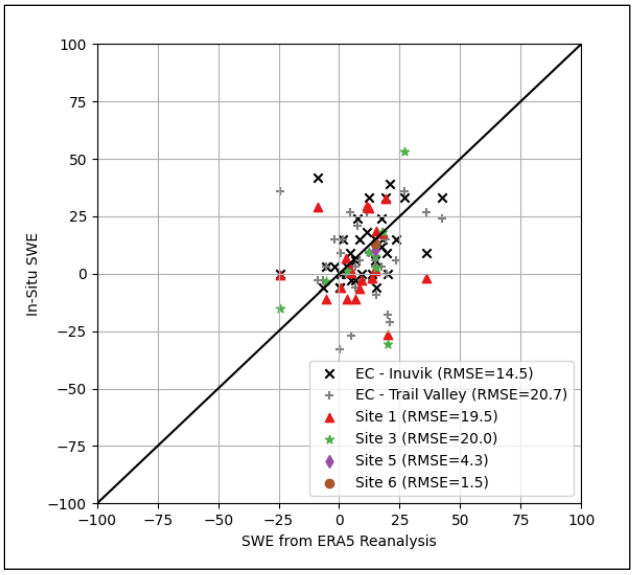

Figure 10. Relative in situ SWE compared with coarse ERA5 Reanalysis data.

The ground truth sites were located in a region with low variability in ξ. There was a high standard deviation, resulting in a greater uncertainty in the predictions at the ground truth sites when compared to the region with high variability. For this reason, along with the higher RMSE, it is believed that the SWE estimation method detailed here in this report may not be suitable for such regions. However, the estimation method showed more promising results at these sites when the area in the interferograms had a higher coherence.

Using the in situ data, it may be possible to derive a phase based on the snow depth measurements according to Equation 2. When averaged over large spatial areas, such phase screens could be used to correct the InSAR stack for the phase component due to snow. Established DInSAR techniques could then be applied to the corrected interferograms, thus, allowing for measurement of surface displacement in winter months.

The steep incidence angle of the TerraSAR-X strip map imaging mode used in this study may be a limiting factor to the applicability of this method. In the future, it would be useful to perform similar studies with a shallower incidence angle. Additionally, in situ ground truth stations setup in the regions with high variability in ξ would be beneficial to further validate the SWE estimation method. The largest limiting factor in this study was the low variability in the terrain at the in situ ground truth sites.

8 CONCLUSIONS

This paper investigated the use of a previously established method (Eppler et al. 2022) for estimating the snow water equivalent (SWE) over large areas using InSAR. The method exploits variations in topographic slope to estimate the SWE. It was discovered that this method may not be suitable for correcting winter InSAR phase for areas with low variability in topography. Additionally, it was also

presumed that the incidence angle of the radar sensor may also be important to consider, noting that the incidence angle of the TerraSAR-X strip map stack of roughly 24° is too steep to generate the variation in sensitivity required to detect changes in SWE precisely as the algorithm relies on the modulating effect SWE has on the phase; there is a greater modulating effect for shallower angles as the path of the signal travels a greater distance through the snow layer.

The data was compared to in situ snow depth data that was corrected for surface heave due to freeze back. However, due to the low variation in terrain slope and sparse availability of suitable interferometric pairs, a robust comparison between the in situ and InSAR data unfortunately could not be obtained. We discovered that the in situ data, when corrected for heave, was representative of the data obtained at nearby Environment Canada climate stations and so such datasets should be useful therefore for studying the effectiveness of the SWE retrieval algorithm in areas of higher terrain variability where SWE errors are smaller.

9 ACKNOWLEDGEMENTS

We extend our gratitude to the Permafrost Network and the Geological Survey of Canada's Climate Change Geoscience Program for their invaluable support and funding, which were instrumental in making our research endeavors possible.

Special thanks are also due to Peter Morse and H. Brendan O'Neill for their exceptional assistance and guidance in the field. Their expertise greatly enhanced the quality of our work.

10 REFERENCES

Burn, C.R. and Kokelj, S.V. 2009. 'The environment and permafrost of the Mackenzie Delta area', *Permafrost and Periglacial Processes* 20, pp. 83–105. Available at: https://doi.org/10.1002/ppp.655.

Burn, C.R., Mackay, J.R., and Kokelj, S.V. 2009. 'The thermal regime of permafrost and its susceptibility to degradation in upland terrain near Inuvik, N.W.T.', *Permafrost and Periglacial Processes* 20, pp. 221–227. Available at: https://doi.org/10.1002/ppp.649.

Engen, G., Guneriussen, T., and Overrein, Y. 2004. 'Delta-K interferometric SAR technique for snow water equivalent (SWE) retrieval', *IEEE Geoscience and Remote Sensing Letters* 1, pp. 57–61. Available at: https://doi.org/10.1109/LGRS.2003.822880.

Eppler, J., Rabus, B., and Morse, P. 2022. 'Snow water equivalent change mapping from slope-correlated synthetic aperture radar interferometry (InSAR) phase variations', *The Cryosphere* 16, pp. 1497–1521. Available at: https://doi.org/10.5194/tc-16-1497-2022.

Guneriussen, T., Hogda, K.A., Johnsen, H., and Lauknes, I. 2001. 'InSAR for estimation of changes in snow water equivalent of dry snow', *IEEE Transactions on Geoscience and Remote Sensing* 39, pp. 2101–2108. Available at: https://doi.org/10.1109/36.957273.

Gruber, S. 2020. 'Ground subsidence and heave over permafrost: hourly time series reveal interannual, seasonal and shorter-term movement caused by freezing, thawing and water movement', *The Cryosphere* 14, pp. 1437–1447. Available at: https://doi.org/10.5194/tc-14-1437-2020.

Larsen, Y., Malnes, E., and Engen, G. 2005. 'Retrieval of snow water equivalent with envisat ASAR in a norwegian hydropower catchment', in *IEEE International Geoscience and Remote Sensing Symposium*, 2005. Seoul, South Korea: pp. 5444–5447. Available at: https://doi.org/10.1109/IGARSS.2005.1525972.

Lei, Y., Siqueira, P., and Treuhaft, R. 2016. 'A dense medium electromagnetic scattering model for the InSAR correlation of snow', *Radio Science* 51, pp. 461–480. Available at: https://doi.org/10.1002/2015RS005926.

Leinss, S., Wiesmann, A., Lemmetyinen, J., and Hajnsek, I. 2015. 'Snow Water Equivalent of Dry Snow Measured by Differential Interferometry', *Journal of Selected Topics in Applied Earth Observations and Remote Sensing* 8, pp. 3773–3790. Available at: https://doi.org/10.1109/JSTARS.2015.2432031.

Liu, L., Zhang, T., and Wahr, J. 2010. 'InSAR measurements of surface deformation over permafrost on the North Slope of Alaska', *Journal of Geophysical Research: Earth Surface* 115. Available at: https://doi.org/10.1029/2009JF001547.

Liu, L., Schaefer, K., Zhang, T., and Wahr, J. 2012. 'Estimating 1992–2000 average active layer thickness on the Alaskan North Slope from remotely sensed surface subsidence', *Journal of Geophysical Research: Earth Surface* 117. Available at: https://doi.org/10.1029/2011JF002041.

Liu, L., Jafarov, E.E., Schaefer, K.M., Jones, B.M., Zebker, H.A., Williams, C.A., Rogan, J., and Zhang, T. 2014. 'InSAR detects increase in surface subsidence caused by an Arctic tundra fire', *Geophysical Research Letters* 41, pp. 3906–3913. Available at: https://doi.org/10.1002/2014GL060533.

Mackay, J.R., Ostrick, J., Lewis, C.P., and Mackay, D.K. 1979. 'Frost Heave at Ground Temperatures Below Zero Degrees Centigrade, Inuvik, Northwest Territories', *Geological Survey of Canada* Current Research Part A, pp. 403–406. doi:10.4095/104879.

Rampton, V.N. 1987. 'Surficial Geology, Tuktoyaktuk Coastlands, District of Mackenzie, Northwest Territories', *Geological Survey of Canada* "A" Series Map 1647A, 1 sheet. Available at: https://doi.org/10.4095/125160.

Rouyet, L., Lauknes, T.R., Christiansen, H.H., Strand, S.M., and Larsen, Y. 2019. 'Seasonal dynamics of a permafrost landscape, Adventdalen, Svalbard, investigated by InSAR', *Remote Sensing of Environment* 231, 111236. Available at: https://doi.org/10.1016/j.rse.2019.111236.

Schaefer, K., Liu, L., Parsekian, A., Jafarov, E., Chen, A., Zhang, T., Gusmeroli, A., Panda, S., Zebker, H.A., and Schaefer, T. 2015. 'Remotely Sensed Active Layer Thickness (ReSALT) at Barrow, Alaska Using Interferometric Synthetic Aperture Radar', *Remote Sensing* 7, pp. 3735–3759. Available at: https://doi.org/10.3390/rs70403735.

Scheer, J., Caduff, R., How, P., Marcer, M., Strozzi, T., Bartsch, A., and Ingeman-Nielsen, T. 2023. 'Thaw-Season InSAR Surface Displacements and Frost Susceptibility Mapping to Support Community-Scale Planning in Ilulissat, West Greenland', *Remote Sensing* 15, 3310. Available at: https://doi.org/10.3390/rs15133310.

Short, N., Brisco, B., Couture, N., Pollard, W., Murnaghan, K., and Budkewitsch, P. 2011. 'A comparison of TerraSAR-X, RADARSAT-2 and ALOS-PALSAR interferometry for monitoring permafrost environments, case study from Herschel Island, Canada', *Remote Sensing of Environment* 115, pp. 3491–3506. Available at: https://doi.org/10.1016/j.rse.2011.08.012.

Strozzi, T., Antonova, S., Günther, F., Mätzler, E., Vieira, G., Wegmüller, U., Westermann, S., and Bartsch, A. 2018. 'Sentinel-1 SAR Interferometry for Surface Deformation Monitoring in Low-Land Permafrost Areas', *Remote Sensing* 10, 1360. Available at: https://doi.org/10.3390/rs10091360.

Tsang, L., Durand, M., Derksen, C., Barros, A.P., Kang, D.-H., Lievens, H., et al.2022. 'Review article: Global monitoring of snow water equivalent using high-frequency radar remote sensing', *The Cryosphere* 16, pp. 3531–3573. Available at: https://doi.org/10.5194/tc-16-3531-2022.

An improved approach for thaw depth evaluation considering unfrozen water in frozen soil

Greg Qu
WSP, Oakville, Ontario, Canada

ABSTRACT

The thaw depth of permafrost is known to depend on the ice content in frozen soil. Current engineering practice of thaw depth calculation often ignores the unfrozen water in permafrost and assumes that all water in the soil completely freezes below the water freezing temperature (e.g., 0 °C). Fine-grained soil typically contains silts and clays and may have significant amounts of unfrozen water below freezing temperature. The assumption of ignoring the unfrozen water leads to a less conservative estimation of the thaw depth by typically about 10% to 20% (up to 30%) for fine-grained soils. There is a need to develop a practical and industry-friendly approach for thaw depth assessment, which takes account of the unfrozen water content in frozen soil. The studies by Tice et al. (1976), Anderson and Ladanyi (2003) and Qu and Pham (2023) suggested a correlation between unfrozen water content in frozen soil and temperature below freezing point. The correlation (Qu and Pham 2023) can be established using the liquid limit and total water content of soil, which are available for most commercial projects. This paper presents an improved approach for thaw depth evaluation to take account of the unfrozen water content in frozen soil using the correlation associated with temperature.

1 INTRODUCTION

The current engineering practice to calculate thaw depth often ignores the unfrozen water and assumes that all water in the soil completely freezes below 0 °C (see Canadian Geotechnical Society 2006 and Bianchini and Gonzalez 2012). The volumetric latent heat of fusion, as a key parameter for the thaw depth (see the modified Berggren equation in Canadian Geotechnical Society 2006) is governed by the content of the ice in soil, which can be thawed into water. This assumption leads to underestimating the thaw depth, particularly for fine-grained soils, where the water in soil freezes over a wide range of temperatures from -20 °C to 0 °C. Underestimation of thaw depth could lead to unsafe design for piles and potential thaw settlement for infrastructures in permafrost areas.

This paper presents an improved and practical approach for thaw depth evaluation by taking into account the impact of unfrozen water in frozen soil. This approach adopted the correlation of unfrozen water content with temperature based on the studies by Tice et al. (1976), Anderson and Ladanyi (2003) and Qu and Pham (2023). This approach intends to support a preliminary assessment of thaw depth in engineering practice and requires only inputs from the routine standard laboratory test data. For critical projects, design engineers may consider a field test (thermistor) or advanced laboratory tests, for example, nuclear magnetic resonance (NMR) test.

2 BACKGROUND

2.1 General

The theoretical methodology for thaw depth has been well established and the engineering practice usually adopts the modified Berggren equation, as recommended in the Canadian Foundation Engineering Manual (CFEM; Canadian Geotechnical Society 2006) and Bianchini and Gonzalez (2012). Equation [1] shows the formula.

$$X = \lambda\sqrt{2k_s I_s / L_s} \quad [1]$$

where

X = thaw depth
I_s = surface thaw index
k_s= thermal conductivity of the soil
L_s= volumetric latent heat of the soil
λ = a dimensionless coefficient

Modified Berggren equation was developed using a series of assumptions and simplifications. The key simplifications are described below:

1. The mathematical model assumes one dimensional heat flow with the soil mass.
2. In the initial state prior to thaw, the soil mass has a uniform temperature of T_g, i.e., the mean annual ground temperature. Figure 1 shows the initial state.
3. In the thawing state, the top surface of the soil mass has a temperature of T_t, i.e., the mean temperature during the thaw season. Figure 3 shows the thaw season duration (see the shaded area) state.
4. The surface temperature of the soil mass changes suddenly as a step function from T_g to T_t and remains at T_t throughout the period (t_t in days) of the thawing season. Figure 2 shows the simplified temperature change.

Figure 3 illustrates the ground temperature change, and the physical meaning of T_g, T_t, and t_t.

https://doi.org/10.52381/ICOP2024.102.1

There are two key factors of soil mass impacting the thaw depth. One is the latent heat required to thaw the ice in frozen soil mass. The other one is the volumetric heat of the frozen soil.

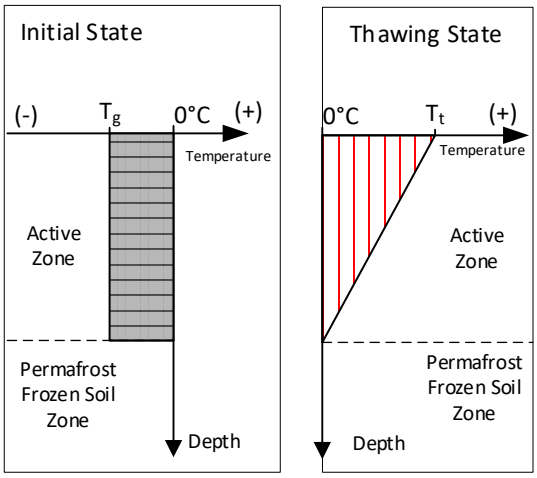

Figure 1. Initial and thawing state in mathematical model for thaw depth calculation.

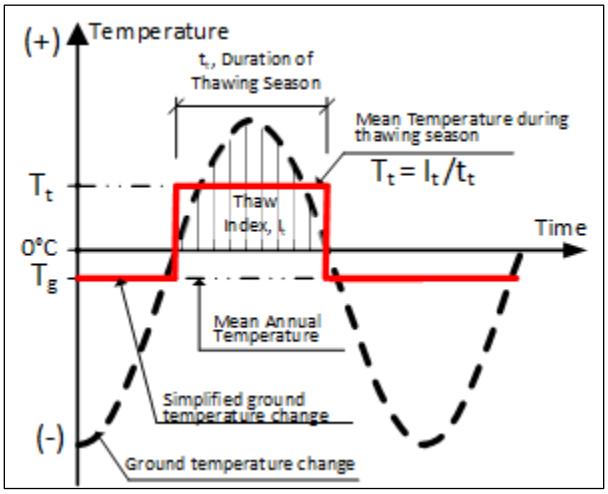

Figure 2. Simplified temperature change between initial state and thawing state (modified Andersland and Ladanyi 2003).

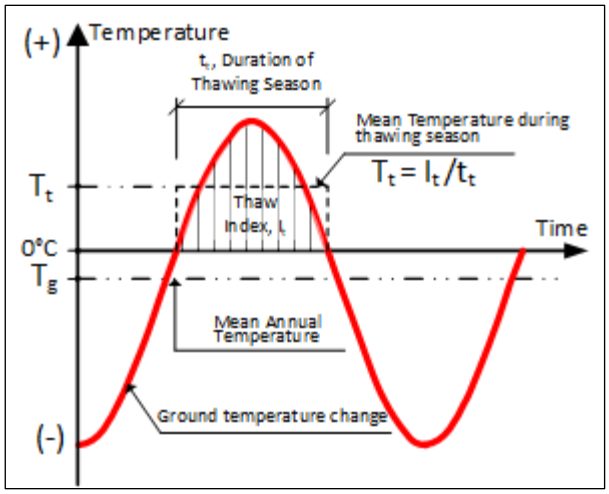

Figure 3. Typical Ground Temperature Change and Physical Meaning of T_g, T_t, and t_t (modified from Andersland and Ladanyi 2003).

One key input for the calculation is the volumetric latent heat of fusion (L_s) for soil, which is the amount of energy required to thaw the frozen water in soil to the thawed state. Therefore, the actual frozen water content in frozen soil has a significant impact to the latent heat and consequently the thaw depth. L_s can be obtained from the formula below:

$$L_s = \gamma_d w_i L \quad [2a]$$

where

L_s = volumetric latent heat of fusion

γ_d = dry unit weight of soil

w_i= frozen water (i.e., ice) content in frozen soil. $w_i = w_c$ if ignoring the unfrozen water in frozen soil, where w_c is total water content (including both frozen and unfrozen water) in soil.

L= latent heat of fusion between water and ice, 334 kJ/kg

The ice content in frozen soil within the thaw depth can be estimated using the equation below:

$$w_i = w_c - w_u(T_g) \quad [2b]$$

where T_g represents the mean annual ground temperature in ℃. It is less than 0℃ in permafrost areas. w_c is total water content (including both frozen and unfrozen water) in soil. $w_u(T_g)$ is the unfrozen water content and can be calculated using Eq. [3].

The calculation approach has been widely adopted in industry, as recommended by Canadian Geotechnical Society (2006) and Bianchini and Gonzalez (2012). As highlighted in the CFEM (Canadian Geotechnical Society 2006), the assumption of ignoring the unfrozen water in frozen soil ($w_i = w_c$) will lead to the unconservative design for both thaw depth and thaw depth evaluation.

3 UNFROZEN WATER CONTENT IN FROZEN SOIL

The studies have been carried out to quantify the unfrozen water content in frozen soil using correlation with specific area of soil (Anderson and Tice 1972; Anderson and Morgenstern 1973; Anderson et al. 1973) or liquid limit index (Tice et al. 1976; Anderson and Ladanyi 2003; Qu and Pham 2023). The specific surface area refers to the total surface area contained in a unit mass of soil. The correlation approach based on specific area was not widely adopted as the lab test to determine specific area of soil is often not available for most engineering projects.

Tice et al. (1976) first proposed the correlation with liquid limit and obtained a good match with the lab tests. This approach requires the input parameters of $LL_{N=25}$ (Liquid Limit) and $LL_{N=100}$ from non-standard lab tests (i.e., non-standard liquid limit test of N=100, N is the number of blows required to close the standard groove in the liquid-limit test). The requirement of $LL_{N=100}$ potentially limited the application of this approach in industry.

Qu and Pham (2023) proposed an improved approach based on the framework by Tice et al. (1976). For the improved approach, the input parameters can be obtained based on the routine laboratory tests (liquid limit and water content). The study by Qu and Pham (2023) shows that a reasonable agreement was obtained for the improved correlation and the laboratory measurement data of the unfrozen water content in frozen soil.

The following presents the correlation proposed by Qu and Pham (2023) to estimate the unfrozen water content in frozen soil.

$$w_u(T) = \begin{cases} w_c - (w_c - w_{u1}) \times (-T) & for\ T \in (0, -1℃) \quad [3a] \\ w_{u1} \times (-T)^{\beta} & for\ T < -1℃ \quad [3b] \end{cases} \quad [3]$$

$$w_{u1} = w_{u,T=-1℃} = 0.35 \times LL - 3\% \quad [4]$$

where

T is the temperature in Celsius degree (℃).

w_{u1} is the unfrozen water content in frozen soil at $T = -1℃$, which can be estimated using the equation [4] for preliminary evaluation or specific tests.

β is a material parameter with a default value of -0.25 Qu and Pham (2023) provide further discussion of sensitivity studies for this parameter.

Figure 4 illustrates the correlation from Eq. [3]. In general, the unfrozen water content (w_u) decreases with lower temperature. For temperature from 0 to -1 °C, w_u reduces linearly from the total water content, w_c to w_{u1}, see Eq. [3a]. Below -1 °C, the w_u reduction is in a linear log-log correlation which is governed by the slope of the log-log plot, β, see Eq. [3b].

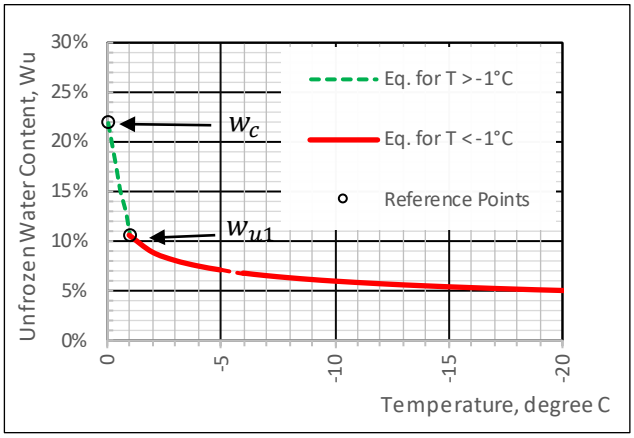

Figure 4. Illustration of correlation (Equation [3]) between unfrozen water content in frozen soil and temperature. (Notes:w_c=22%, LL=40%, α= w_{u1}=10.6%, β= -0.25).

The following describes the main features of the improved approach by Qu and Pham (2023).

1. The improved approach eliminates the requirement for non-standard liquid limit tests, see Eq. [3b]. The parameters for this approach can be obtained based on the routine laboratory tests (liquid limit and water content).
2. For the temperature range from 0 to $-1℃$, the proposed approach adopts a linear correlation of unfrozen water content from the total water content (w_c) to w_{u1}, as shown in Eq. [3a] and Figure 4. For the formula proposed by Tice et al. (1976), the w_u approaches to an infinitely high value as the temperature approaches 0℃, leading to potential numerical issues in analysis.

4 THAW DEPTH CALCULATION

This section presents the proposed procedure in the thaw depth calculation (i.e., modified Berggren approach) to consider the unfrozen soil water content.

Step 1 – Prepare site-specific climate data.

This step is to obtain the key climate parameters, T_g, T_t, and t_t (see Section 2 for details).

Step 2 - Prepare soil data.

This step is to characterize the soil at site including soil type, liquid limit, dry unit weight, and total water content (w_c).

Step 3 – Evaluate surface n-factor.

The step is to assess the site-specific ground condition and evaluate the surface n-factors. The assessment of n-factors is beyond the scope of this paper. Detailed evaluation of N-factors is summarized by Anderson and Ladanyi (2003) and Canadian Geotechnical Society (2006).

Step 4 – Estimate ice content in the initial state and other parameters.

The step is to calculate the ice content in the frozen soil at the initial state corresponding to T_g using Eq. [3] and Eq. [4]. The other parameters such as soil thermal conductivity and latent heart can be obtained using the formula recommended by Canadian Geotechnical Society (2006) or Bianchini and Gonzalez (2012).

Step 5 – Evaluate thaw depth in the thawing state.

This step is to calculate the thaw depth using the modified Berggren approach with the inputs from steps 1 to 4.

Canadian Geotechnical Society (2006) provides a series of graphs to assist engineers for manual calculation using the modified Berggren approach. Qu (2023) provides a step-by-step calculation template in both MatchCAD and Excel formats, which are available for download at the website listed in the reference.

5 Application and Discussions

This section shows the application of the proposed approach of thaw depth calculation and illustrate the impact of the unfrozen water factor to the calculated thaw depth.

Two representative sites were selected for the thaw depth calculation. One site is located at cold permafrost with the mean annual ground temperature (MAGT) of -14.6 °C and the other site is located at warm permafrost with MAGT of -2 °C. Table 1 lists the parameters for these two sites.

Table 1. Summary of site conditions in sensitivity study. Note: The soils at Site 1 and Site 2 are fine-grained soil.

Parameters	Site 1	Site 2
I_α (°C -days)	1984	425
nt	1.2	1.2
w_c (%)	22%	22%
LL(%)	40%	40%
γ_s (kN/m^3)	17	17
MAGT (°C)	-4.3	-14.6
MAGT (°C)	-2	-9.5
t (days)	160	102

Table 2 presents the calculated thaw depths. Figure 5 shows the results. The following summarizes the findings.

1. Site 1 has a much deeper thaw depth than Site 2 due to its colder MAGT.
2. The assumption of ignoring unfrozen water would lead to an *underestimation* of thaw depth, by an arrange from 21% to 11% for Site 1 and Site 2 respectively.

Table 2. Summary of calculated thaw depths. Note: See the parameters in Table 1.

Cases	Site 1	Site 2
Case accounting for unfrozen water **(base case)**	2.84 m (100%)	1.01 m (100%)
Case Ignoring w_u	2.25 m (79%)	0.90 m (89%)

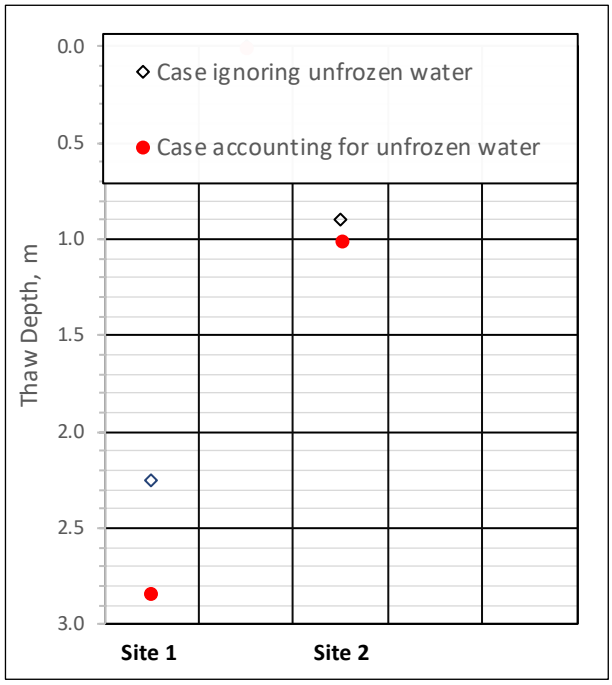

Figure 5. Sensitivity of thaw depth at three sites for four cases: (1) assuming fully frozen water (ignoring Wu), and (2) considering unfrozen water in frozen soil.

Figure 6 shows the calculated thaw depths according to different total water content. The thaw depth ratio was used to evaluate the impact of unfrozen water to the thaw depth. This represents the ratio of the thaw depth ignoring unfrozen water to that accounting for unfrozen water. The following summarizes the findings.

With a wider range of w_c from 15% to 30%, the assumption of ignoring unfrozen water would lead to an underestimation of thaw depth, by an arrange from 31% to 9%.

The impact of ignoring unfrozen water to the thaw depth increases with the higher total water content for both Site 1 and Site 2.

The impact of unfrozen water is more significant for Site 1 at warm permafrost, in comparison with the cold permafrost Site 2.

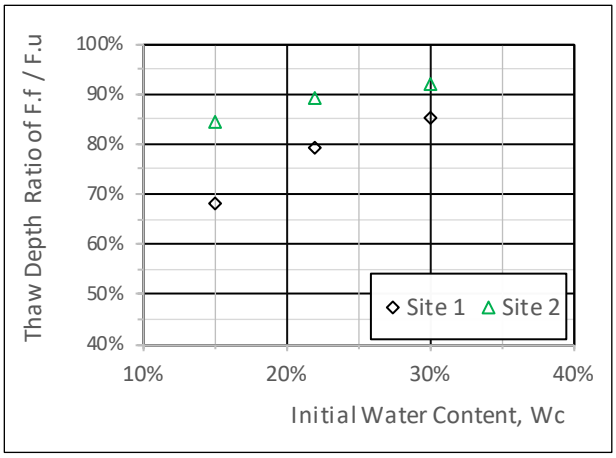

Figure 6. Sensitivity of thaw depth with initial water content (thaw depth ratio: thaw depth for the case ignoring Wu divided by that for the case considering Wu (unfrozen water in frozen soil) using Eq. [3]).

6 SUMMARY AND CONCLUSIONS

This paper presented an improved approach for engineers to calculate the thaw depth considering the unfrozen water in frozen soil. In comparison with the conventional approach which ignores the unfrozen water in frozen soil below freezing temperature, this approach provides a more conservative thaw depth (by about 10% to 20%) for the fine-grain soil. The thaw depth calculation approach was coded in Mathcad and Excel formats and is available for download at the website listed in the reference (Qu 2023). The following summarizes the main findings.

1. The proposed approach is practical as it requires only two basic input parameters, i.e., total initial water content and liquid limit, which can be obtained from routine standard tests and are usually available in most projects.
2. The proposed approach would lead to a more conservative thaw depth (typically about 10% to 20%, up to 30%) for fine-grained soil, in comparison to the conventional approach ignoring the unfrozen water in frozen soil. For soil with a lower water content, the proposed approach yields a similar thaw depth estimate with the conventional approach as the unfrozen water content is relatively low in this case.
3. If salts are present in soil, a correction should be applied to the proposed approach for thaw depth calculation, depending on the salinity measurement from the site.
4. Future studies using laboratory or field tests will be helpful to verify the findings presented in the paper regarding the impact of unfrozen water in frozen soil on thaw depth.

7 LIST OF PARAMETERS

N: the number of blows required to close the standard groove in the liquid-limit test.

w_c : total water content in frozen soil, including both unfrozen and frozen water.

w_u : unfrozen water content in frozen soil.

w_{u_avg}: average unfrozen water content in frozen soil.

w_i: ice content in frozen soil.

γ_d: dry soil unit weight.

γ_s: bulk soil unit weight.

γ_w: unit weight of water.

I_a: air freezing index

I_s: surface freezing index.

L: latent heat of fusion of water to ice, typical value of 334 kJ/kg.

L_s: volumetric latent heat of the soil.

k_f thermal conductivity of the frozen soil.

w_{u1} : unfrozen water content in frozen soil at $T = -1℃$. It can be estimated using the equation [4].

β: soil parameter for correlation between unfrozen water content in frozen soil and temperature, depending on the soil types, see Eq. [3].

LL: Liquid limit of soil.

T: Temperature in Celsius, degree.

θ: Absolute value of temperature in Celsius, degree (always a positive value).

8 REFERENCES

Andersland, O.B. and Ladanyi, B. 2003. *Frozen ground engineering*. 2nd edition. John Wiley & Sons, 384 p.

Anderson, D.M. and N.R. Morgenstern 1973. 'Physics, chemistry, and mechanics of frozen ground: A review', in *North American Contribution Second International Conference on Permafrost*. Yakutsk, USSR: July 13–28, 1973, pp. 257–88.

Anderson, D.M. Tice, A.R. and McKim, H.I. 1973. 'The unfrozen water and the apparent specific heat capacity of frozen soils', in *North American Contribution, Second International Conference on Permafrost*. Yakutsk, USSR: July 13–28, 1973, pp. 289–95.

Anderson, D.M. and Tice, A.R. 1972. 'Predicting unfrozen water contents in frozen soils from surface area measurements', *Highway Research Record* 393, pp. 12–18.

Bianchini, A. and Gonzalez, C.R. 2012. 'Pavement-transportation Computer Assisted Structural Engineering (PCASE) implementation of the Modified Berggren (ModBerg) equation for computing the frost penetration depth within pavement structures', *US Army Corps of Engineers* Technical Reports 12-15.

Canadian Geotechnical Society 2006. *Canadian Foundation Engineering Manual* (CFEM). 4th edition. Canadian Geotechnical Society.

Department of the Army and the Air Force 1983. 'Arctic and subarctic constructions for structures', *Department of the Army and the Air Force* Technical Manual TM 5-852-4/AFM 88-19, Chapter 4.

Hu, G., Zhao, L., Zhu, X., Wu, X., Wu, T., Li, R., and Hao, J. 2020. 'Review of algorithms and parameterizations to determine unfrozen water content in frozen soil', *Geoderma* 368, 114277.

Nixon, J.F. and McRoberts, E.C. 1973. 'A study of some factors affecting the thawing of frozen soils', *Canadian Geotechnical Journal* 10(3), pp. 439–452.

Patterson, D.E. and Smith, M.W. 1981. 'The measurement of unfrozen water content by time-domain reflectometry: Results from laboratory tests', *Canadian Geotechnical Journal* 18(1), pp. 131–44.

Tsytovich, N.A. 1975. *The Mechanics of Frozen Ground*..New York, New York, United States: McGraw-Hill Inc., 426 p.

Tsytovich, N.A., 1960. *Bases and Foundations on Frozen Soil*. Washington, DC, United States: National Research Council Highway Research Board, Special Report 58.

Tice, A.R., Anderson, D.M., and Banin, A. 1976. 'The Prediction of Unfrozen Water Contents in Frozen Soils from Liquid Limit Determinations', *National Technical Information Service* Report CRREL-76-8.

Qu, G. and Pham, N. 2023. 'An Improved Approach for Frost Depth Evaluation Considering Unfrozen Water in Frozen Soil', in *GeoSaskatoon2023*, Canadian Geotechnical Society Annual Conference. Saskatoon, Saskatchewan, Canada: October 1–4, 2023.

Qu, G. 2023. *MathCAD Calculation Sheet for Thaw Depth Calculation - Considering Unfrozen Water Content in Frozen Soil*. Available at: https://www.researchgate.net/publication/370604091_Thaw_Depth_Calculation_-_Considering_Unfrozen_Water_Content_in_Frozen_Soil.

Impacts of convective storms on runoff, erosion, and carbon export in a continuous permafrost landscape

Marisa Repasch[1], Josie Arcuri[2], Irina Overeem[2], Suzanne P. Anderson[2], Robert S. Anderson[2] & Joshua C. Koch[3]

[1]*Department of Earth and Planetary Sciences, University of New Mexico, Albuquerque, New Mexico, United States*

[2]*Department of Geological Sciences & Institute of Arctic and Alpine Research, University of Colorado, Boulder, Colorado, United States*

[3]*US Geological Survey, Alaska Science Center, Anchorage, Alaska, United States*

Abstract

Permafrost holds more than twice the amount of carbon currently in the atmosphere, but this large carbon reservoir is vulnerable to thaw and erosion under a rapidly changing Arctic climate. Convective storms are becoming increasingly common during Arctic summers and can amplify runoff and erosion. These extreme events, in concert with active layer deepening, may accelerate carbon loss from the Arctic landscape. However, we lack measurements of carbon fluxes during these events.

Rivers are sensitive to physical, chemical, and hydrological perturbations, and thus are excellent systems for studying landscape responses to thunderstorms. We present observations from the Canning River, Alaska, which drains the northern Brooks Range and flows across a continuous permafrost landscape to the Beaufort Sea. During summer 2022 and 2023 field campaigns, we opportunistically monitored river discharge, sediment, and organic carbon fluxes during several thunderstorms. During one notable storm, river discharge nearly doubled from ~130 m^3/s to ~240 m^3/s, suspended sediment flux increased 70-fold, and the particulate organic carbon (POC) flux increased 90-fold relative to non-storm conditions. Taken together, the river exported ~16 metric tons of POC over one hour of this sustained event, not including the additional flux of woody debris. Furthermore, the dissolved organic carbon (DOC) flux nearly doubled. Although these thunderstorm-driven fluxes are short-lived (hours to days), they play an outsized role in exporting organic carbon from Arctic rivers. Understanding how these extreme events impact river water, sediment, and carbon dynamics will help predict how Arctic climate change will modify the global carbon cycle.

1 Introduction

Permafrost soils hold more than twice the amount of carbon currently in our atmosphere (Schuur et al. 2013). The Arctic is warming four times faster than the rest of the world (Rantanen et al. 2022), causing this carbon-bearing permafrost to thaw. Along with warming air temperatures, convective storms may be occurring more frequently now than in the past and the fraction of annual precipitation from convective storms is projected to increase in the future (Bennett and Walsh 2015; Poujol et al. 2020; Bieniek et al. 2022). Increases in the amount of precipitation delivered by extreme events are predicted to be greater than increases in mean annual precipitation over the next 80 years (Bennett and Walsh 2015; Bieniek et al. 2022). Earlier sea ice retreat and a lengthening open water season increases the probability of precipitation during the Arctic summer (Galley et al. 2016; Broadman et al. 2020; Blaskey et al. 2023). Increased runoff generated by these thunderstorms may accelerate erosion of the landscape, such that the carbon stored in previously frozen soil is now being removed from the landscape and transported down rivers to the Arctic Ocean. We hypothesize that intense convective storms are causing Arctic watersheds to lose more carbon now than in the past, but we lack evidence of how these extreme events affect the amount of organic carbon exported by Arctic rivers. Here we aim to understand how the Arctic landscape is physically changing in response to thunderstorms and how much carbon is lost from the landscape as permafrost soils thaw and runoff increases.

Rivers are profoundly sensitive to changes in runoff and erosion across the landscape, as they are conduits for water, solutes, and sediment from the surrounding landscape. Catchments underlain by permafrost have limited subsurface water storage capacity, and thus generate runoff more rapidly than in non-permafrost catchments (McNamara et al. 1998; Kane et al. 2003; Koch et al. 2013). Even in spongy, organic-rich soils, water tracks on hillslopes appear to be efficient conduits for runoff, generating a rapid response in Arctic rivers (Evans et al. 2020). Early season (May–June) rain-on-snow events are effective at enhancing runoff, however intense rain storms in July and August can also generate a large and rapid runoff response. Individual rain events in the Arctic summer season can generate peak discharges that rival peaks generated by spring snowmelt runoff (Kane et al. 2003; Arp and Whitman 2022). Observations from the Upper Kuparuk River catchment in July 1999 showed that the runoff response from a single thunderstorm was three times larger than any river discharge recorded over the preceding eight years (Kane et al. 2003). The geomorphic effects of this runoff in permafrost river catchments are poorly understood, as we lack observational data of river turbidity and sediment fluxes during these events and few rivers have long-term discharge gauging stations.

In addition to potential geomorphic change associated with high intensity rainfall events, increases in river discharge may amplify the fluxes of organic carbon exported from the Artic landscape to the ocean. There are two possible mechanisms for storm runoff to enhance river organic carbon fluxes. Active river corridors store organic carbon

https://doi.org/10.52381/ICOP2024.104.1

from both allochthonous sources (i.e., transported from upstream in the catchment) and autochthonous sources (soils and biomass accumulating on fluvial sediment deposits). Increases in river stage and discharge generate bed shear stresses sufficient to entrain the POC stored within the channel belt, thereby removing this carbon from the floodplain and transferring it downstream. To a lesser extent, active layer soils, which contain ~61% of the total soil organic carbon stock of Alaska (Mishra and Riley 2012), can be mobilized by riverbank erosion and thermokarst gulley erosion across tundra hillslopes. Riverbank and gulley erosion can cut deeply into frozen soils, causing rapid thaw and potential mobilization of deep permafrost carbon during runoff events. Determining which mechanism of organic carbon export is dominant in Arctic watersheds is challenging due to the lack of long-term carbon flux monitoring data.

Several studies have investigated the temporal variability in dissolved organic carbon (DOC) export in Arctic rivers using both field-based (Finlay et al. 2006; Holmes et al. 2012; Koch et al. 2013, 2021; Shogren et al. 2021), and remote sensing methods (Griffin et al. 2018; Huang et al. 2019; El Kassar et al. 2023). These studies show that DOC concentrations increase with increasing river discharge in Arctic rivers, with the highest DOC fluxes in May–June during the spring freshet and more modest peaks throughout the summer. This suggests that storms have an important impact on export of labile organic matter from Arctic rivers but does not indicate when and how sensitive particulate organic carbon fluxes are to storm runoff.

Due to the challenge of monitoring and sampling suspended sediment in Arctic rivers, few studies have evaluated the temporal variability of particulate organic carbon (POC) export from Arctic rivers. Together, the six largest pan-Arctic rivers (Lena, Kolyma, Ob', Mackenzie, Yenisey, and Yukon) export ~$3x10^{12}$ gC/yr (McClelland et al. 2016), but this estimate does not account for the temporal variability in river suspended sediment and POC concentrations across the summer season. Furthermore, smaller watersheds may have a stronger river runoff response than these continental-scale river systems which have greater land surface area for water to infiltrate, dampening the river runoff response. Given the flashy behavior of Arctic rivers (Mcnamara et al. 1998; Stuefer et al. 2017), we hypothesize that summer thunderstorms exert an outsized impact on suspended sediment and particulate organic matter export from Arctic watersheds. However, existing discharge-POC rating curves for Arctic rivers do not capture the effects of intense rainfall events, and thus likely underestimate POC export from these catchments.

Here we report observations of an Arctic river responding to thunderstorms that occurred in July 2022 on the North Slope of the Brooks Range in northern Alaska. We opportunistically collected measurements of river discharge, suspended sediment concentration, organic carbon content, and dissolved chemistry before, during, and after thunderstorm-driven runoff events to understand how much sediment and carbon is mobilized and exported to the Arctic Ocean during these extreme events. Over the course of two thunderstorms during this field campaign, we were able to measure changes in river discharge, POC, and DOC. Although thunderstorm-driven changes in river discharge are typically short-lived (hours), our work shows that they have an outsized impact on organic carbon export from Arctic rivers.

2 Study Area and Methods

2.1 The Canning River, Alaska

We studied the effects of thunderstorms on river discharge and particulate organic carbon fluxes in the Canning River on the North Slope of Alaska (Figure 1). The Canning River drains the northern flank of the Brooks Range between -146.5° and -145° longitude and flows for ~200 km across the Coastal Plain to the Beaufort Sea. With a catchment area of 7,142 km^2, it is the largest river basin on the North Slope east of the Sagavanirktok River. The Canning is a braided, gravel-bed river with several narrow, single-thread sections. Active layer depths across the Coastal Plain and Brooks Range foothills range from ~35 to 80 cm (Wang et al. 2018), offering very limited storage capacity for rain water delivered to these hillslopes during high intensity convective storms. Combined with steep hillslope gradients > 30° in the headwaters, runoff may rapidly increase river water discharge.

The US Geological Survey (USGS) maintained a river discharge gauging station on the Canning River near the Staines airstrip (69.881523, -146.388850) from June 2008 until October 2012 (US Geological Survey, 2021). This gauging record shows that the river is frozen during the winter, and thus water flows predominantly during the summer season. From 1 May to 31 October, the average river discharge at Staines is 90.44 m^3/s. Precipitation records are not available for the Canning River catchment, making it difficult to directly link river runoff to extreme precipitation events.

We rafted down the Canning River from 28 June to 10 July 2022, from the upper Canning within the headwaters to the mouth at the Beaufort Sea coast. During this field campaign, we selected five locations along the active channel to conduct Acoustic Doppler Current Profiler (ADCP) surveys for river discharge measurement and collect river water samples for suspended sediment and POC (Repasch et al. 2024). T1 is the farthest upstream transect and T5 is the farthest downstream (Figure 1). There are nine notable tributaries between T1 and T3, which could deliver sediment to the mainstem during storms. T4 is 25 km downstream of T3, and over this distance, there are approximately eight small ephemeral streams, which were inactive at the time of our sampling campaign. Due to this lack of notable tributaries, water discharge at T3 and T4 should be similar. Just downstream of T4 is the delta apex, where the river becomes a distributary delta system and water discharge is partitioned between two main channels. Based on our summer 2023 ADCP surveys at T4 and T5 (Repasch et al. 2024), the Staines branch (west) and Canning branch (east) convey roughly 68% and 32% of the river discharge, respectively.

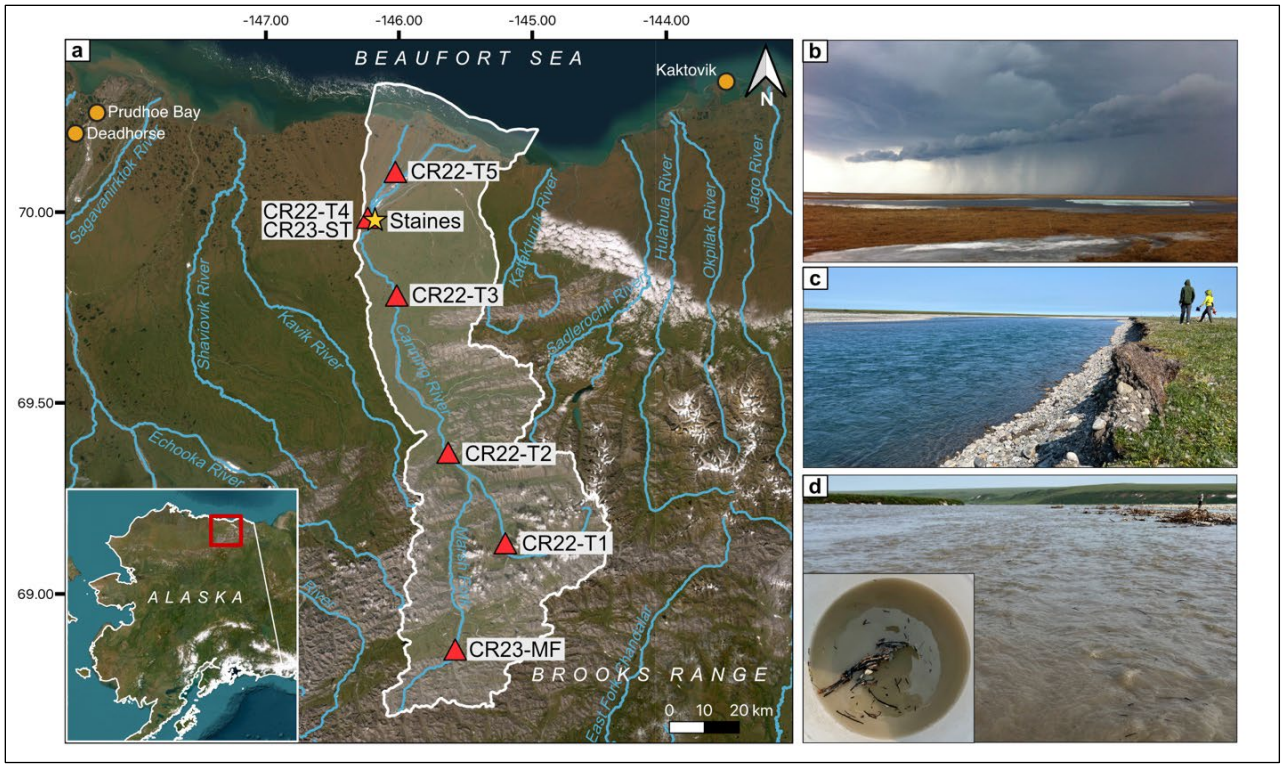

Figure 1. a) Esri satellite image of the study area in the eastern part of Alaska's North Slope (Esri 2023). The Canning River catchment (white shaded area) extends from the Brooks Range to the Beaufort Sea. Red triangles denote locations of ADCP surveys and suspended sediment sampling activities in 2022 (CR22) and 2023 (CR23). Yellow star shows the location of the historic USGS gauging station at Staines, which was operated June 2008–October 2012 (US Geological Survey 2021). Inset map is a satellite image of Alaska, with the red box showing the study area extent. b) Photo of convective storm clouds and precipitation over the north slope near the Chipp River, AK on 13 June 2013. Photo by J. Koch, USGS. c) Photo of clear water in the Canning River at Staines on 26 July 2023. Photo by M. Repasch, University of Colorado Boulder. d) Photo of turbid water in the Canning River at site CR22-T3 during a thunderstorm-triggered high flow event on 5 July 2022. Inset shows buoyant woody debris and organic matter in surface water collected during this event. Photos by M. Repasch, University of Colorado Boulder.

2.2 River discharge analysis

We measured river discharge and channel geometry during our summer 2022 and 2023 field campaigns using a Sontek RiverSurveyor ADCP (Repasch et al. 2024). These ADCP surveys were conducted where the river narrows and nearly all discharge flows within a single thread. The ADCP was towed across the channel on a SonTek HydroBoard attached to a packraft. We measured discharge across a minimum of 6 transects and calculated the discharge as the mean of the highest quality transects.

In addition to field measurements and observations, we analyzed the summer river runoff response in the historic USGS gauging record, which spanned June 2008 to September 2012 (US Geological Survey, 2021). This station was located on the Canning River at the Staines airstrip, where the river is confined to a single thread with a cross-section width up to 400 m under bank-full conditions. This is the same location as our "CR22-T4" and "CR23-ST" sample and ADCP transect location. The USGS surveyed this section of the river channel by ADCP thirty times over the period of gauging, ensuring a well-calibrated dataset.

Using this nearly 5-year discharge record, we identified peak flows and determined how often the river discharge exceeds 200 m^3/s. This threshold value was chosen based on a discharge-suspended sediment rating curve constructed with our field observations.

2.3 Sediment and carbon fluxes

At each river discharge measurement site, we collected river water samples from the channel thalweg using a 2.2-liter van Dorn style horizontal sampling bottle (Wildco Beta Plus Bottle). Sampled water was temporarily stored in clean 10-liter LDPE cubitainers and then filtered through 0.45 µm polyethersulfone (PES) filter membranes using a Geotech barrel filter. Filtered sediment was stored in a cooler until returning to the laboratory for processing. We measured the flux of coarse particulate organic matter (CPOM), or woody debris, transported at the water surface by holding a bucket (opening diameter = 0.3 m) at the water surface for a fixed time interval to collect material. We separated

the solid material from the river water using a net and returned the CPOM samples to the lab for processing.

We rinsed sediment off the filters into clean evaporating dishes using ultrapure water, and then dried at 50 °C until desiccated. We calculated suspended sediment concentrations (SSC) by weighing the dry sample mass and dividing by the volume of water filtered. Instantaneous suspended sediment fluxes were then calculated by multiplying the sediment concentration by the total water discharge at the corresponding sampling site. We calculated the CPOM/woody debris carbon flux by drying and weighing the samples, dividing the dry mass by time, then multiplying by 0.49, as woody biomass is estimated to contain ~49% organic carbon (Martin et al. 2021).

We used 0.5 g aliquots of sediment for total organic total organic carbon (TOC) measurement. Samples were ground to a fine powder and decarbonated using repeated treatments with 7% HCl in an 80 °C water bath (Galy et al. 2007). TOC was measured on an elemental analyzer. POC concentrations were determined by correcting the weight percent TOC for mass lost during carbonate removal, and then multiplying by the suspended sediment concentration.

3 RESULTS

3.1 Observed changes in river discharge, suspended load, and organic carbon fluxes

In early July 2022, we observed several thunderstorms in the Canning River headwaters, two of which had notable effects on the river discharge and turbidity. While at site T2 in the foothills (Figure 1a), we deployed a pressure transducer to monitor water level changes. Here we observed a dramatic increase in water level from 2 July to 3 July, which equates to a 30% increase in instantaneous river discharge (from ~75 m^3/s on 2 July to ~98 m^3/s on 3 July). During the rising stage, we observed a rapid increase in turbidity, with a measured suspended sediment concentration of 148 mg/L (sample T2-W1). Three hours later, we measured a suspended sediment concentration of 91 mg/L (sample T2-W2), despite no change in water level over this period. This suggests that more sediment is entrained and transported during the initial rise in water discharge and this sediment supply may become depleted over the duration of the high flow event. We measured a similar decrease in the POC concentration and flux over this three-hour period, reducing from 1.22 to 0.85 mgC/L and 119.7 to 83.5 gPOC/s, respectively. The DOC concentration and flux did not change appreciably during the event, decreasing only slightly from 0.66 to 0.62 mgC/L and 64.5 to 60.6 gDOC/s, respectively. Due to our limited time at site T2, we were not able to collect a systematic timeseries of water samples to determine how this 30% increase in discharge impacted the suspended sediment and POC fluxes.

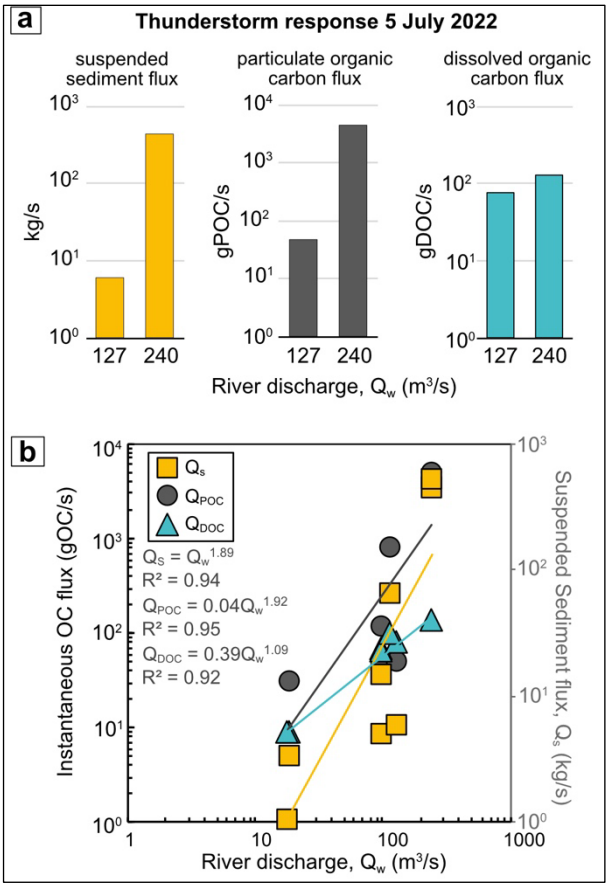

Figure 2. a) Bar chart showing the response of suspended sediment flux, POC flux, and DOC flux to the 5 July 2022 thunderstorm-triggered high flow event at site T3 (240 m^3/s) compared with non-storm flow (127 m^3/s) measured at site T4. b) River discharge (Q_W) versus instantaneous particulate organic carbon flux (Q_{POC}), dissolved organic carbon flux ($Q_{DOC;}$ y-axis left), and suspended sediment flux ($Q_{S;}$ y-axis right) at all Canning River locations in 2022. The trendlines represent the power-law relationships between Q_W and Q_S, Q_{POC}, and Q_{DOC}, expressed by the equations on the plot (Repasch et al. 2024).

Downstream at site T3, we observed a second thunderstorm during the night from 4 July to 5 July 2022. This site is ~127 km downstream from the headwaters, at the transition from the foothills to the coastal plain (Figure 1). This thunderstorm caused a significant increase in water level and turbidity (Figure 1d). ADCP measurements show that discharge increased to 240 m^3/s during this high flow event, representing a 90% increase in water discharge relative to non-storm conditions (127 m^3/s measured at Staines (site T4) on 7 July 2022; Figure 1c). The suspended sediment concentration increased from ~50 mg/L to ~1800 mg/L, resulting in an increase in suspended sediment flux from ~8 kg/s to ~440 kg/s. The POC concentration increased from ~0.5 mgC/L to ~19 mgC/L, resulting in an increase in POC flux from ~0.05 to 4.5 kgC/s (Figure 2a; Repasch

et al. 2024). Despite relatively low DOC concentrations during this high flow event (0.54 mgC/L), the DOC flux nearly doubled due to the substantial increase in discharge (Figure 2a), increasing from ~75 gDOC/s to ~130 gDOC/s (Repasch et al. 2024).

We also measured the flux of CPOM/woody debris, transported at the water surface during this high flow event, which averaged 4 kgC/s. (Repasch et al. 2024). Taken together, the river exported ~31 metric tons of POC and CPOM, and an additional ~0.5 metric tons DOC over approximately one hour of this sustained sediment flux. This thunderstorm-driven 240 m^3/s discharge event at site T3 (transition from foothills to coastal plain) had a much larger impact on the Canning River carbon fluxes than the ~100 m^3/s discharge event observed at site T2 (foothills) described above. This difference is likely due to higher carbon stocks in the tundra soils of the foothills and coastal plain compared to the bedrock hillslopes dominating the catchment area upstream of site T2 (Figure 1a).

3.2 Peak flows in the river discharge gauging record

Based on these observations, we propose that flows exceeding 200 m^3/s, or roughly double the mean summer flow of 90 m^3/s, account for the majority of POC export throughout the summer. To test this hypothesis, we analyzed the long-term discharge record at Staines from 2009 to 2012 (US Geological Survey, 2021; Figure 3).

This record shows that the highest flows occur during late May to early June, with the highest recorded discharges exceeding 800 m^3/s. Sporadic rainstorms generate high flow events from June to August, with peak flows ranging from 250 to 650 m^3/s. On average, there are 5–6 discharge peaks per year exceeding 200 m^3/s (Figure 3), and this discharge is exceeded only ~6%, or ~22 days of the year. Based on POC flux measurements from summer 2022 (Repasch e al. 2024), it is likely that most of the annual POC load is transported during these events, although, some of these high flows occur during river ice breakup when we have no data on suspended sediment or POC fluxes.

3.3 Storm contributions to annual POC fluxes

Using our ADCP measurements and suspended sediment (SS), POC, and DOC data (Repasch et al. 2024), we were able to construct a rudimentary rating curve to describe the relationship between river discharge and SS, POC, and DOC fluxes (Figure 2b). SS, POC, and DOC have strong positive correlations with river discharge, following power-law functions. SS and POC scale with discharge to the powers of 1.89 and 1.92, respectively, while DOC scales with discharge to the power of 1.09.

Because this discharge-POC scaling relationship is based on a very small dataset, we cannot confidently apply this rating curve to the long-term daily mean discharge record to calculate the average annual POC export from the Canning River. Our measurements from early July 2022 do not account for the discharge peaks that occur during spring freshet, nor do they account for the late summer runoff that may occur after the sediment and POC supplies have diminished.

4 Discussion and Conclusions

4.1 Storm-triggered organic carbon export

The goal of this study is to demonstrate that summer thunderstorms in continuous permafrost watersheds are effective generators of runoff, leading to mobilization and transport of sediment and organic carbon that were once stored in the Arctic landscape. We found strong power-law relationships between discharge and suspended

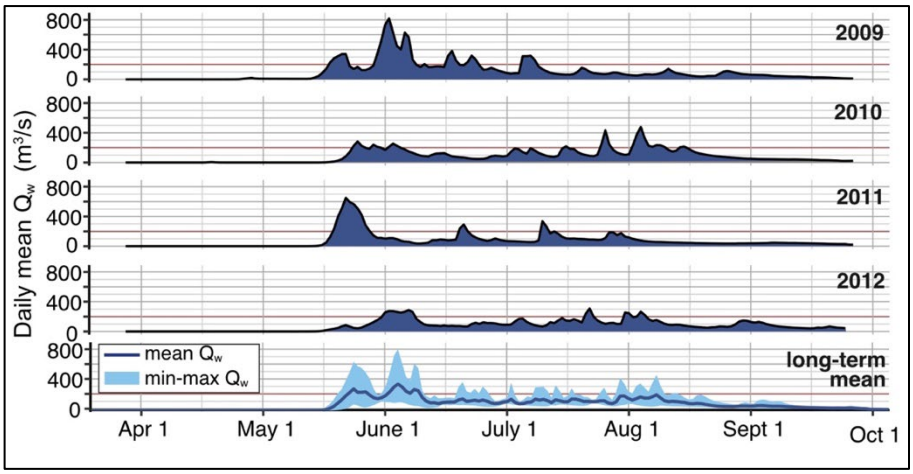

Figure 3. Continuous record of river water discharge at USGS gauging station 15955000 (Canning River at Staines near Deadhorse, AK) measured from 2009 to 2012 (US Geological Survey 2021). This gauging station was active from June 2008 until September 2012. The red lines indicate 200 m^3/s river discharge, which was exceeded during the thunderstorm-driven high flow events we observed in the field. The bottom panel shows the long-term daily mean, minimum, and maximum daily discharge over this four-year record.

sediment, POC, and DOC fluxes in the Canning River. During summer, the POC flux increases by a power of two for every unit increase in river water discharge, suggesting that POC fluxes are highly sensitive to runoff generated during thunderstorms. There are two possible mechanisms that could drive the increase in POC export during these high flow conditions: 1) new erosion of organic-rich soils via runoff and bank erosion, and 2) remobilization of organic matter stored transiently within the active channel belt.

We observed very few abrupt thaw hillslope erosion features in the Canning watershed, suggesting it is unlikely that storm-generated runoff events trigger enough hillslope soil erosion to elevate river SS and POC fluxes. More commonly observed are freshly cut stream and riverbanks, where thawed permafrost soil has collapsed upon loss of its pore ice. This soil slumps into the margins of the river channel, providing a supply of unconsolidated fine sediment and organic carbon for the river to entrain during high flows. It is possible that riverbank erosion is most active during peak flows associated with river ice breakup, generating a supply of sediment and organic matter on the banks. Each subsequent high flow event would mobilize some of this riverbank material, causing this supply to dwindle over the summer season. As such, the SS and POC fluxes associated with large runoff events would decrease throughout the summer.

Gravel braid bars in the active floodplain trap sand and silt, uprooted willows and tundra vegetation, and other forms of particulate organic matter eroded during river ice break-up and transported with early season flows. As water levels rapidly increase with storm runoff, this material becomes entrained, increasing the river suspended load. In July 2022, we observed uprooted willows and tundra vegetative mats tumbling downstream in these high flows at site T5 (downstream distributary system), where the channel was deeper and narrower due to river aufeis still occupying the left side of the channel. This observation highlights the elevated transport capacity of the river during storm-driven peak flows. It is likely that this supply of sediment and organic carbon on the active floodplain dwindles throughout the summer. However, the short duration of these high flow events may result in deposition of entrained organic matter further downstream on the floodplain, requiring multiple years for this material to be transported out of the system. Future measurements of the radiocarbon content of these samples may help to identify whether relatively young organic carbon is flushed out of the channel, or if riverbank and runoff channels are eroding into aged permafrost soil carbon stocks.

During a second field campaign in August 2023, we observed one thunderstorm-triggered runoff event at Staines (CR23-ST). This event caused river discharge to increase from 150 to 228 m^3/s over a period of ~16 hours (Repasch et al. 2024). Although samples are still being processed for POC, we measured a more than seven-fold increase in suspended sediment concentration (from 73.4 mg/L to 511 mg/L), resulting in a ten-fold increase in suspended sediment flux (from 11.0 kg/s to 116 kg/s). The DOC concentration also increased from 0.66 to 0.82 during this rise in discharge, resulting in a DOC flux increase from 96 gC/s to 187 gC/s. Compared to the early July 2022 event, this August 2023 storm generated a much smaller increase in suspended load, but comparable increase in DOC load. We observed less buoyant woody debris in transport during the August 2023 event than in the July 2022 event. One hypothesis is that the available POC in the active channel had been flushed from the river system earlier in the summer. If this is true, then the power-law relationship between discharge and POC would weaken over the duration of the summer. Alternatively, the location of the upstream thunderstorm may impact how much organic carbon is delivered to the river. More suspended sediment sampling efforts could fill in these data gaps.

This flushing of POC from within the active channel belt limits the carbon storage capacity of the floodplain and increases export of POC to the Canning River delta, and ultimately the Arctic Ocean. As summer thunderstorms continue to increase in frequency and intensity, the ability of river gravel bars to store organic carbon will diminish. Alternatively, increasing active layer depths across the Arctic may increase subsurface water storage capacity, thereby progressively dampening the runoff response to extreme precipitation events over time.

We acknowledge that our data are insufficient to develop robust discharge-SS and POC rating curves, prohibiting us from modeling future POC export with predicted increases in thunderstorm frequency. A longer-term and more systematic sampling approach could result in a robust discharge-POC flux rating curve and determine the contribution of thunderstorm runoff to carbon export from Arctic rivers. Further research efforts are needed to capture the high temporal variability in these fluxes during river ice breakup, snowmelt, permafrost thaw, and sediment and carbon supply. While some of the largest peak flows are associated with early season river ice breakup, the thawed layer is quite shallow during this time, suggesting that mobilization and transport of ancient permafrost carbon should be limited. Future efforts should aim to monitor, measure, and sample river water, sediment, and carbon fluxes in Arctic rivers, in conjunction with rain gauge data, over several years may help to understand how the rainfall-runoff response changes over time and determine the mechanisms driving organic carbon export from Arctic rivers.

4.2 Future predictions of Arctic carbon export

Increasing thunderstorm frequency and river discharge across the high Arctic (Poujol et al. 2020; Feng et al. 2021; Blaskey et al. 2023) competes with a deepening active layer. If subsurface water storage capacity increases over time, the river runoff response to high intensity rain events may be significantly dampened, thereby reducing river sediment transport capacity and the rate at which carbon is exported to the Arctic Ocean. Future predictions of dissolved and particulate nutrient fluxes in Arctic rivers will depend on this balance between enhanced convective storm activity and changing water storage capacity within the active layer. Another

consideration is Arctic shrubification, which may stabilize river banks (Ielpi et al. 2023), preventing accelerated bank erosion during these high flow events. Monitoring long-term trends in river runoff response to summer rain events and trends in active-layer water storage capacity may constrain the sign and magnitude of these feedbacks.

5 CONCLUSIONS

Climate change in the Arctic is causing profound changes in the Arctic environment. One such change is an increase in convective storm activity, which can trigger a strong rainfall-runoff response in continuous permafrost river catchments. We investigated the response of river discharge, suspended sediment, and particulate and dissolved organic carbon fluxes in the Canning River, which drains a continuous permafrost watershed in the northern Brooks Range of Alaska. We show that thunderstorm runoff can more than double river discharge and drive nearly 70-fold and 90-fold increases in suspended sediment and particulate organic carbon fluxes, respectively. While these events are short in duration, there are more than 22 days every summer when high flows have been recorded, suggesting that these events could contribute most of the annual organic carbon export from the Canning River. Given the projected increase in thunderstorms in a warmer future Arctic (Bennett and Walsh 2015; Poujol et al. 2020; Bieniek et al. 2022), these storm-triggered fluxes could flip the carbon balance of Arctic watersheds, by eroding soil and river banks containing aged permafrost soil carbon and limiting carbon storage within the floodplain. Long-term monitoring and sampling efforts could allow development of rating curves required to predict future changes in carbon export from Arctic permafrost landscapes.

6 ACKNOWLEDGEMENTS

This work was supported by National Science Foundation (NSF) award 2001225 (to IO, RSA, and SPA) and NSF award 2219107 (to MR). Field support was provided by Polar Field Services, Arctic Wild, and Kavik River Camp. Any use of trade, firm, or product names is for descriptive purposes only and does not imply endorsement by the U.S. Government.

7 REFERENCES

Arp, C.D. and Whitman, M.S. 2022. 'Lake basins drive variation in catchment-scale runoff response over a decade of increasing rainfall in Arctic Alaska', *Hydrological Processes* 36(5). doi:10.1002/hyp.14583.

Bennett, K.E. and Walsh, J.E. 2015. 'Spatial and temporal changes in indices of extreme precipitation and temperature for Alaska', *International Journal of Climatology* 35(7), pp. 1434–1452. doi:10.1002/joc.4067.

Bieniek, P.A., Walsh, J.E., Fresco, N., Tauxe, C., and Redilla, K. 2022. 'Anticipated Changes in Alaska Extreme Precipitation', *Journal of Applied Meteorology and Climatology* 61(2), pp. 97–108. doi:10.1175/JAMC-D-21-0106.1.

Blaskey, D., Koch, J.C., Gooseff, M.N., Newman, A.J., Cheng, Y., O'Donnell, J.A., and Musselman, K.N. 2023. 'Increasing Alaskan river discharge during the cold season is driven by recent warming', *Environmental Research Letters* 18(2), 024042. doi:10.1088/1748-9326/acb661.

Broadman, E., Kaufman, D.S., Henderson, A.C.G., Malmierca-Vallet, I., Leng, M.J., and Lacey, J.H. 2020. 'Coupled impacts of sea ice variability and North Pacific atmospheric circulation on Holocene hydroclimate in Arctic Alaska', *Proceedings of the National Academy of Sciences* 117(52), pp. 33034–33042. doi:10.1073/pnas.2016544117.

El Kassar, J., Juhls, B., Hieronymi, M., Preusker, R., Morgenstern, A., Fischer, J., and Overduin, P.P. 2023. 'Optical remote sensing (Sentinel-3 OLCI) used to monitor dissolved organic carbon in the Lena River, Russia'. *Frontiers in Marine Science* 10.

Esri 2023. *ESRI Satellite (ArcGIS/World Imagery)*. Available at: https://services.arcgisonline.com/ArcGIS/rest/services/World_Imagery/MapServer, scale not given (Accessed: July, 2023).

Evans, S.G., Godsey, S.E., Rushlow, C.R., and Voss, C. 2020. 'Water Tracks Enhance Water Flow Above Permafrost in Upland Arctic Alaska Hillslopes', *Journal of Geophysical Research: Earth Surface* 125(2), e2019JF005256. doi:10.1029/2019JF005256.

Feng, D., Gleason, C.J., Lin, P., Yang, X., Pan, M., and Ishitsuka, Y. 2021. 'Recent changes to Arctic river discharge', *Nature Communications* 12(1), 6917. doi:10.1038/s41467-021-27228-1.

Finlay, J., Neff, J., Zimov, S., Davydova, A., and Davydov, S. 2006. 'Snowmelt dominance of dissolved organic carbon in high-latitude watersheds: Implications for characterization and flux of river DOC'. *Geophysical Research Letters* 33(10). doi:10.1029/2006GL025754.

Galley, R.J., Babb, D., Ogi, M., Else, B.G.T., Geilfus, N.-X., Crabeck, O., Barber, D.G., and Rysgaard, S. 2016. 'Replacement of multiyear sea ice and changes in the open water season duration in the Beaufort Sea since 2004', *Journal of Geophysical Research: Oceans* 121(3), pp. 1806–1823. doi:10.1002/2015JC011583.

Galy, V., Bouchez, J., and France-Lanord, C. 2007. 'Determination of Total Organic Carbon Content and δ 13 C in Carbonate-Rich Detrital Sediments', *Geostandards and Geoanalytical Research* 31(3), pp. 199–207.

Griffin, C.G., McClelland, J.W., Frey, K.E., Fiske, G., and Holmes, R.M. 2018. 'Quantifying CDOM and DOC in major Arctic rivers during ice-free conditions using Landsat TM and ETM+ data', *Remote Sensing of Environment* 209, pp. 395–409. doi:10.1016/j.rse.2018.02.060.

Holmes, R.M., McClelland, J.W., Peterson, B.J., Tank, S.E., Bulygina, E., Eglinton, T.I., Gordeev, V.V., Gurtovaya, T.Y., Raymond, P.A., Repeta, D.J., Staples, R., Striegl, R.G., Zhulidov, A.V., and Zimov, S.A. 2012. 'Seasonal and Annual Fluxes of Nutrients and Organic Matter from Large Rivers to the Arctic Ocean and Surrounding Seas', *Estuaries and Coasts* 35(2), pp. 369–382. doi:10.1007/s12237-011-9386-6.

Huang, J., Wu, M., Cui, T., and Yang, F. 2019. 'Quantifying DOC and Its Controlling Factors in Major Arctic Rivers during Ice-Free Conditions using Sentinel-2 Data', *Remote Sensing* 11(24), 2904. doi:10.3390/rs11242904.

Ielpi, A., Lapôtre, M.G.A., Finotello, A., and Roy-Léveillée, P. 2023. 'Large sinuous rivers are slowing down in a warming Arctic', *Nature Climate Change 13, pp. 375–381*. doi:10.1038/s41558-023-01620-9.

Kane, D.L., McNamara, J.P., Yang, D., Olsson, P.Q., and Gieck, R.E. 2003. 'An Extreme Rainfall/Runoff Event in Arctic Alaska', *Journal of Hydrometeorology* 4(6), pp. 1220–1228. doi:10.1175/1525-7541(2003)004<1220:AEREIA>2.0.CO;2.

Koch, J.C., Dornblaser, M.M., and Striegl, R.G. 2021. 'Storm-Scale and Seasonal Dynamics of Carbon Export From a Nested Subarctic Watershed Underlain by Permafrost', *Journal of Geophysical Research: Biogeosciences* 126(8), e2021JG006268.doi:10.1029/2021JG006268.

Koch, J.C., Runkel, R.L., Striegl, R., and McKnight, D.M. 2013. 'Hydrologic controls on the transport and cycling of carbon and nitrogen in a boreal catchment underlain by continuous permafrost', *Journal of Geophysical Research: Biogeosciences* 118(2), pp. 698–712. doi:10.1002/jgrg.20058.

Martin, A.R., Domke, G.M., Doraisami, M., and Thomas, S.C. 2021. 'Carbon fractions in the world's dead wood', *Nature Communications* 12(1), 889. doi:10.1038/s41467-021-21149-9.

McClelland, J.W., Holmes, R.M., Peterson, B.J., Raymond, P.A., Striegl, R.G., Zhulidov, A.V., Zimov, S.A., Zimov, N., Tank, S.E., Spencer, R.G.M., Staples, R., Gurtovaya, T.Y., and Griffin, C.G. 2016. 'Particulate organic carbon and nitrogen export from major Arctic rivers', *Global Biogeochemical Cycles* 30(5), pp. 629–643. doi:10.1002/2015GB005351.

Mcnamara, J.P., Kane, D.L., and Hinzman, L.D. 1998. 'An analysis of streamflow hydrology in the Kuparuk River Basin, Arctic Alaska: a nested watershed approach', *Journal of Hydrology* 206(1–2), pp. 39–57. Available at: https://doi.org/10.1016/S0022-1694(98)00083-3.

Mishra, U., and Riley, W.J. 2012. Alaskan soil carbon stocks: spatial variability and dependence on environmental factors. Biogeosciences, 9(9): 3637–3645. doi:10.5194/bg-9-3637-2012.

Poujol, B., Prein, A.F., and Newman, A.J. 2020. 'Kilometer-scale modeling projects a tripling of Alaskan convective storms in future climate', *Climate Dynamics* 55(11–12), pp. 3543–3564. doi:10.1007/s00382-020-05466-1.

Rantanen, M., Karpechko, A.Yu., Lipponen, A., Nordling, K., Hyvärinen, O., Ruosteenoja, K., Vihma, T., and Laaksonen, A. 2022. 'The Arctic has warmed nearly four times faster than the globe since 1979', *Communications Earth & Environment* 3(1), 168. doi:10.1038/s43247-022-00498-3.

Repasch, M., Overeem, I., Arcuri, J., Anderson, S., and Anderson, R.S. 2024. *Instantaneous discharge, suspended sediment, and organic carbon fluxes in the Canning River, Alaska, June-July 2022 and July-August 2023*. Arctic Data Center. Available at: https://arcticdata.io/catalog/view/doi:10.18739/A2M61BR63.

Schuur, E.A.G., Abbott, B.W., Bowden, W.B., Brovkin, V., Camill, P., Canadell, J.G., et al. 2013. 'Expert assessment of vulnerability of permafrost carbon to climate change', *Climatic Change* 119(2), pp. 359–374. doi:10.1007/s10584-013-0730-7.

Shogren, A.J., Zarnetske, J.P., Abbott, B.W., Iannucci, F., Medvedeff, A., Cairns, S., Duda, M.J., and Bowden, W.B. 2021. 'Arctic concentration–discharge relationships for dissolved organic carbon and nitrate vary with landscape and season', *Limnology and Oceanography* 66(S1), pp. S197–S215. doi:10.1002/lno.11682.

Stuefer, S.L., Arp, C.D., Kane, D.L., and Liljedahl, A.K. 2017. 'Recent Extreme Runoff Observations From Coastal Arctic Watersheds in Alaska', *Water Resources Research* 53(11), pp. 9145–9163. doi:10.1002/2017WR020567.

US Geological Survey 2021. *USGS water data for the Nation*. US Geological Survey National Water Information System database. Available at: https://waterdata.usgs.gov/nwis (Accessed: June 2023).

Wang, K., Jafarov, E., Overeem, I., Romanovsky, V., Schaefer, K., Clow, G., Urban, F., Cable, W., Piper, M., Schwalm, C., Zhang, T., Kholodov, A., Sousanes, P., Loso, M., and Hill, K. 2018. 'A synthesis dataset of permafrost-affected soil thermal conditions for Alaska, USA', *Earth System Science Data* 10(4), pp. 2311–2328. doi:10.5194/essd-10-2311-2018.

Time series analysis of remotely sensed snow cover data: Revealing permafrost thermal state and vegetation dynamics

Sebastian Roessler, Andreas Dietz & Samuel Schilling

German Aerospace Center, German Remote Sensing Data Center, Wessling, Germany

ABSTRACT

Snow cover plays a crucial role in climate change and is considered an essential climate variable by the Global Climate Observing System (GCOS). To accurately monitor daily snow cover extent, optical medium-resolution remote sensing systems like MODIS and VIIRS are employed. DLR's Global SnowPack (GSP) product, derived from daily MODIS/VIIRS snow cover data, addresses data gaps caused by clouds or polar night, providing gap-free daily datasets since February 2000. The extended time series allows the identification of trends in snow cover duration (SCD), which has implications for the thermal state of permafrost soils and vegetation dynamics. Snow acts as an insulating barrier against colder winter air temperatures, enabling the underlying permafrost layer to retain higher temperatures. The 23-year dataset of SCD data from GSP allows both the determination of a long-term average and the derivation of trends. We compared both the mean SCD and the trend with annual changes in parameters describing horizontal and vertical permafrost extent, as well as changes in land cover classifications (both provided by ESA CCI). Regarding "Greening of the Arctic" we found changes in land cover classes, but in the observed period since 2000 there was little dynamism, and this is only slightly reflected in the SCD. Obvious developments were found in the thermal state of the permafrost – mainly degradation, but increases were also noted, similar to the positive trends in snow cover duration. Changes in Active Layer Thickness (ALT) could be best explained with SCD changes. Overall, additional data are needed to make quantitative predictions about permafrost development using SCD.

1 INTRODUCTION

The Arctic region is undergoing rapid and profound transformations driven by the escalating impacts of climate change (Lemke et al. 2007). In this context, permafrost degradation has emerged as a vital indicator of ecological shifts. These shifts involve the deepening of the active layer (Streletskiy et al. 2015), the greening of the Arctic (Myers-Smith et al. 2020, Shijin and Xiaoqing 2023), changes in precipitation (Wang et al. 2021), and increasing air temperatures (Guo and Wang 2016). These intertwined changes, along with their complex dynamics, demand innovative monitoring approaches that can unravel their connections and implications. An invaluable tool in this pursuit is the analysis of time series data on snow cover duration, as derived from Moderate Resolution Imaging Spectroradiometer (MODIS) imagery. This study explores the potential of MODIS-derived variability and trends in snow cover duration to monitor changes in the permafrost thermal regime and the associated land cover changes, shedding light on their interconnectedness and broader implications.

Permafrost, the frozen ground underlying vast Northern Hemisphere regions, is a sensitive indicator of climate change. Its degradation leads to the release of greenhouse gases, accelerating global warming and triggering cascading environmental consequences. Monitoring permafrost's spatial extent and thermal conditions, including active layer thickness, is pivotal for gauging the pace and magnitude of these changes (Xu and Zhuang 2023).

Parallel to permafrost degradation, the Arctic landscape is experiencing a visible transformation in land cover and vegetation patterns, collectively referred to as "Arctic greening". This phenomenon involves increased vegetation growth, shifts in vegetation composition, and altered ecosystem distributions (Bhatt et al. 2013). These changes have the potential to amplify permafrost degradation, as shifts in land cover can alter energy exchange processes and temperature regimes, further exacerbating thawing dynamics (Langer et al. 2013).

Effectively monitoring the complex interplay between permafrost dynamics and land cover changes in the expansive and remote Arctic region presents great challenges. Ground-based measurements are limited in their spatial coverage and are often unable to capture the full extent of changes. This underscores the importance of remote sensing technologies in addressing these challenges. Remote sensing provides comprehensive, consistent, and spatially extensive data, enabling researchers to monitor changes across vast landscapes (Jorgenson and Grosse 2016).

Among the myriad of remote sensing parameters, snow cover duration emerges as a valuable indicator of climate change effects on permafrost and land cover. Snow cover duration directly influences the ground's thermal regime, impacting permafrost thawing rates (Domine et al. 2022). Concurrently, it influences the timing and duration of vegetation growth, thus linking snow cover dynamics with land cover changes.

MODIS, with its daily global coverage, presents an ideal data source for analyzing snow cover dynamics (Dietz et al. 2012). By examining variability and trends in snow cover duration derived from MODIS imagery, researchers can gain insights into the Arctic environment's transformations (Muster et al. 2015). The consistent, long-term records provided by MODIS facilitate the identification of temporal patterns and potential relationships between snow cover duration and broader environmental changes.

https://doi.org/10.52381/ICOP2024.158.1

This study seeks to address two fundamental research questions:

1. Can MODIS-derived variability and trends in snow cover duration serve as indicators of changes in the permafrost thermal regime? By analyzing the relationships between snow cover duration and active layer thickness, we can investigate whether longer snow-free periods contribute to increased permafrost degradation. This question aims at the connection between the dynamics of the snow cover and the stability of the permafrost.
2. Can MODIS-derived snow cover duration data be used to monitor land cover changes associated with Arctic greening? Investigating correlations between snowmelt timing, snow-free periods, and vegetation growth patterns can provide insights into how shifts in snow cover influence the timing and extent of Arctic greening. This research question addresses the relationship between snowpack dynamics and changes in vegetation composition and spatial distribution.

Due to the availability of already existing high-quality datasets, this contribution uses data from the ESA Climate Change Initiative (CCI), like permafrost data mainly derived from MODIS LST and land cover classification, that contains MODIS NDVI data among others instead of the raw data products.

2 Dataset and Methods

2.1 Snow Cover

The DLR product GSP (Dietz et al. 2015) forms the database for the global daily snow cover. It is based on the daily MODIS snow products (Hall et al. 2002) from the Terra and Aqua platforms and essentially represents a method of gap filling (through clouds or the polar night). In four consecutive steps, gaps are first filled by combining the daily snow product of both platforms. In the second step, the remaining gaps are first filled with data from the previous day and then with those from the following day. A digital elevation model is then used to determine the upper snow line (elevation above which only snow occurs) and the lower snow line (elevation below which only snow-free pixels occur). All pixels above or below are determined accordingly. The last step is a gradual filling with the data from the previous days. This results in a gap-free global snow coverage daily.

From this daily binary information on snow cover extent, the time within which a pixel was snow-covered is determined: the snow cover duration (SCD). The SCD can be further used to determine long-term trends, but strong deviations in near real-time can also be used to detect natural hazards. Linking SCD to river runoff can be used to identify extreme hydrological events (floods or droughts) at an early stage. This was successfully shown for rivers in Lapland. (Rößler et al. 2021). Figure 1 shows the arithmetic mean of the annual snow cover duration for the northern hemisphere.

The annual deviation from this long-term average is further examined in the trend analysis.

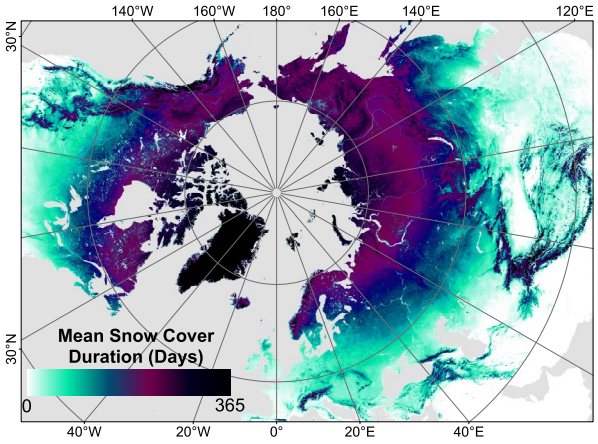

Figure 1. Mean annual snow cover duration in the northern hemisphere.

2.2 Permafrost

The permafrost data used within this study are derived from the ESA Climate Change Initiative Project "Permafrost_CCI" (Obu et al. 2021). We used the Permafrost Year 3 Climate Research Data Package available at the CEDA archive (https://archive.ceda.ac.uk/, accessed on 06/21/2023). For the years 2000–2019 (since the start of MODIS Terra) we obtained the datasets for Permafrost Fraction (PFR) and Active Layer Thickness (ALT).

The datasets have a spatial resolution of 1 km and are available as the arithmetic mean of the horizontal (PFR) and vertical (ALT) permafrost extent for each year. For the PFR dataset, the continuous coverage values (from 0 to 100%) were divided into seven evenly distributed classes. This gives the values 0 for permafrost-free areas and 14, 29, 43, 57, 71, 86, and 100, which each represent the area percentage of the permafrost cover. Since we have no continuous values, Figure 2 shows the modal value of the PFR time series from 2000 to 2019.

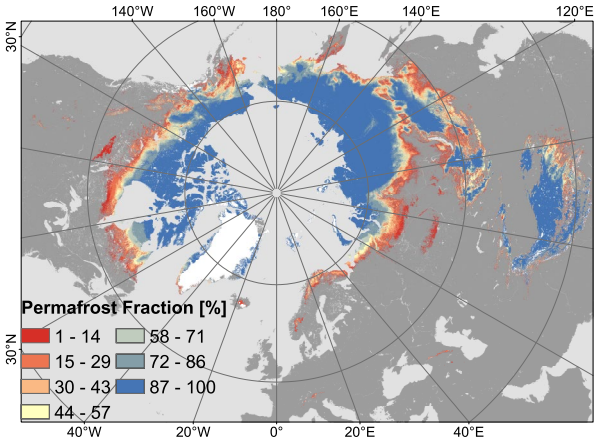

Figure 2. Permafrost Fraction (PFR) modal value for the period 2000–2019.

The ALT dataset reflects the continuous depth of the thaw layer in meters. However, since 99% of the depths do not exceed 2.55 m, we converted them to cm and also divided this range into seven classes with the same number of pixels (quantile subdivision) of the overall mean ALT value for examination. The resulting ranges are 1–40, 41–56, 57–73, 74–89, 90–108, 109–141 and 142–255 cm. Figure 3 shows the classes of mean annual ALT.

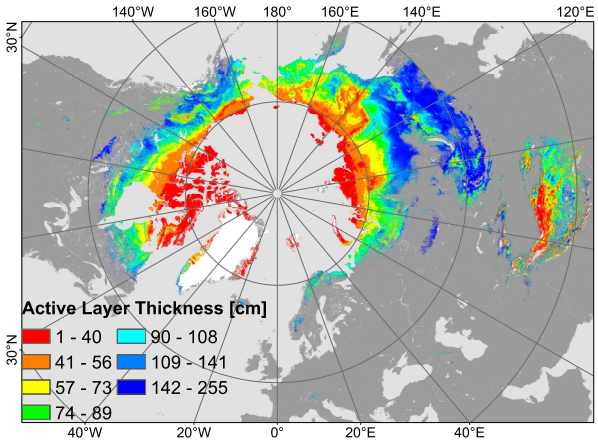

Figure 3. Map showing the quantile-based classification of the mean annual active layer thickness.

These two permafrost classifications (horizontal and vertical) form the basis for the following investigations of the 20-year time series.

2.3 Land Cover

Land cover (LC) time series data are also obtained from the ESA Climate Change Initiative (CCI). The dataset (Bontemps et al. 2013) distinguishes 37 land cover classes, although we have reduced these to 22 by merging the subclasses. Based on the overall extent of the seven PFR classes, we found that only six land cover classes make up the majority of land coverage (about 75%). Figure 4 shows their composition depending on the PFR.

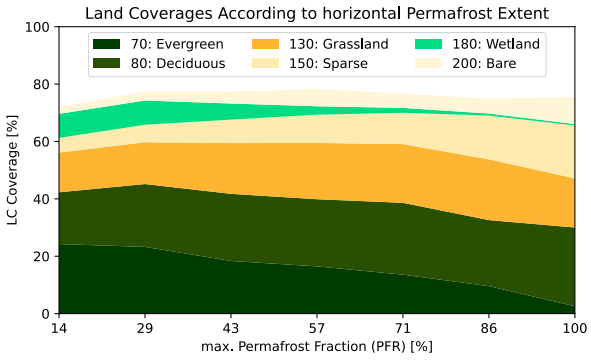

Figure 4, Change of the six permafrost land cover classes composition for the seven PFR classes (horizontal permafrost extent).

Figure 5 shows the modal distribution of these classes for the years 2000 to 2019.

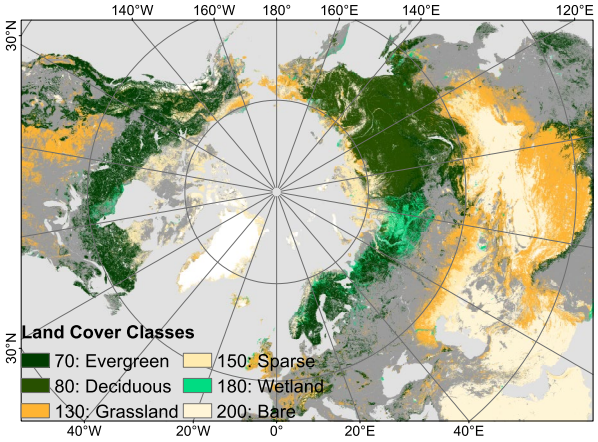

Figure 5, Modal distribution of the six selected permafrost land cover classes.

2.4 Time Series Analysis

2.4.1 Snow Cover

A Mann–Kendall test was performed to analyze the statistical significance of the trends of SCD (Hussain and Mahmud 2019). In this analysis, the null hypothesis (H0), stating the absence of a monotonic trend was tested against three alternatives: (i) a positive monotonic trend, (ii) a negative monotonic trend, or (iii) no monotonic trend. The null hypothesis is rejected if the *p*-value is below the chosen significance level of 0.1. Autocorrelation was absent in the datasets, allowing the use of the null hypothesis test. The magnitude of the trend was determined by the Theil-Sen slope, which, in contrast to linear regression, is more robust against outliers.

2.4.2 Permafrost and Land Cover

Since both the data on permafrost extent and that on land cover are either discrete or categorical, the continuous data on Active Layer Depths were also classified to enable a uniform procedure.

We are interested in the changes that occur from one year to another. It is then determined for each class how many pixels have changed to another class at this time. This gives us an array with the dimensions $[x, y, z]$, where x and y has the same dimensions and describe the number of classes. The third axis $z$describesthe time axis (i.e., 19 annual transitions). For each element of this array, mean snow cover information is then extracted (SCD and slope).

For each variable examined, we get $x * y * z$ results, which can either be displayed as an average over the zz-axisor can span a 2-dimensional point space with the axes SCD and slope to delineate transition regions. These transition zones are an ellipse surrounding an area showing the mean SCD and Theil-Sen slope (± standard deviation) for each group. The latter will be shown in this paper to identify possible separation possibilities.

3 RESULTS AND DISCUSSION

3.1 Snow Cover Dependencies

3.1.1 Development of Snow Cover

The SCD trend is calculated from the snow cover duration of each hydrological year (beginning of meteorological autumn to the end of meteorological summer) from 2000 to 2019 and the slope is given in days per year. The major part of the northern hemisphere shows a decrease in snow cover duration for the full year. The pixel-based slopes are shown in Figure 6.

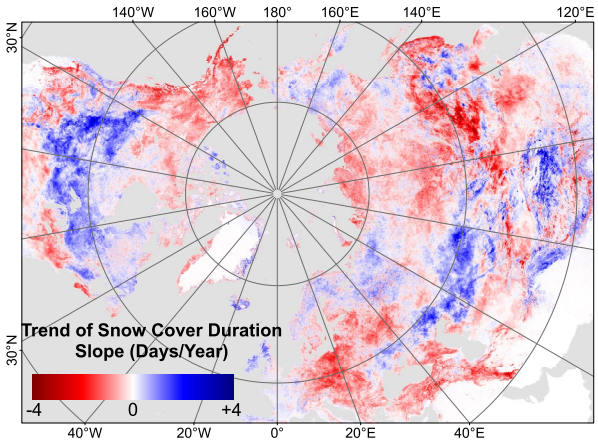

Figure 6. Theil-Sen slope of the SCD development.

However, especially in continental regions in North America and Asia, there has been an increase in the snow cover duration over large areas. For example, the Central Asian Syr Darya Lake Balkash and the Nelson River in North America had a significant increase in November.

3.1.2 Snow Cover of Classes

The next step was to analyze the snow cover variability of the permafrost and land cover classes. We start again with the horizontal permafrost extent (Figure 7).

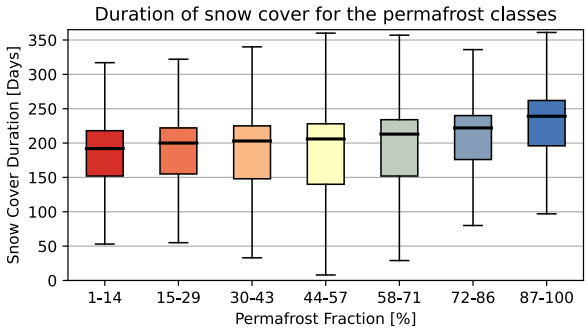

Figure 7. Snow cover duration boxplots for the Permafrost Area Fraction classes.

We see a clear decrease in the SCD with a decreasing area percentage of permafrost. The same can be observed for the vertical permafrost extent (ALT; Figure 8).

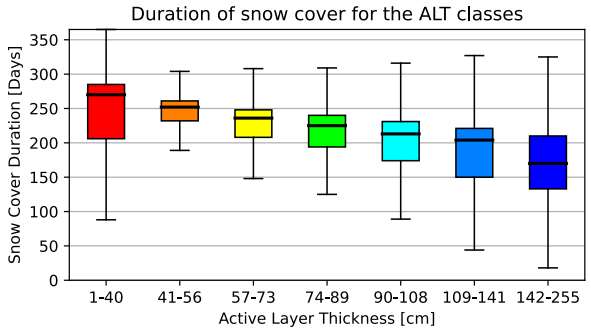

Figure 8. Snow cover duration boxplots for the Active Layer Thickness classes.

It is noteworthy here that the boxes (interquartile range) of classes 41–56, 57–73, and 74–89 are small and statistically different and should allow a good distinction between each other. A much clearer variability can be seen in the land cover classes (Figure 9).

In particular, “Grassland” (130) and “Bare” (200) show high SCD variability.

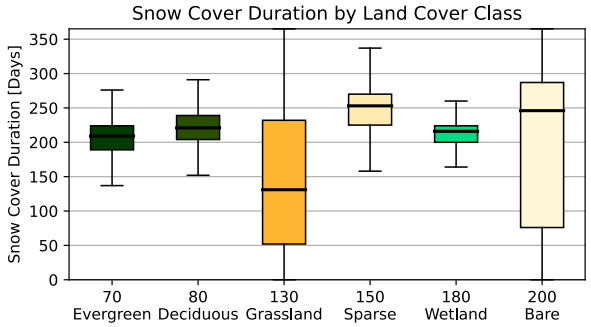

Figure 9. Snow cover duration boxplots for the land cover classes.

3.2 Findings from the Time Series

All work aims at detecting permafrost degradation using snow cover duration data. To give us an initial overview, a different map was created in which the extent of the permafrost in the year 2000 is compared with the situation 20 years later. To do this, we looked at the difference between the PFR and the ALT of both years. In this simplified approach, the pixel was then recognized as degraded permafrost if the ALT difference was above 50 cm, or if the PFR difference was more than 24%. The alarming result can be seen in Figure 10.

In the following, we will take a closer look at the changes. The changes are presented in two ways: the matrix figures show to which class classes will change (or what percentage of pixels remain the same). From this, you can already tell whether degradation is taking place. In the ellipse figures, only the changing pixels are considered and their snow cover duration and trend are shown to determine whether these parameters can already indicate future developments.

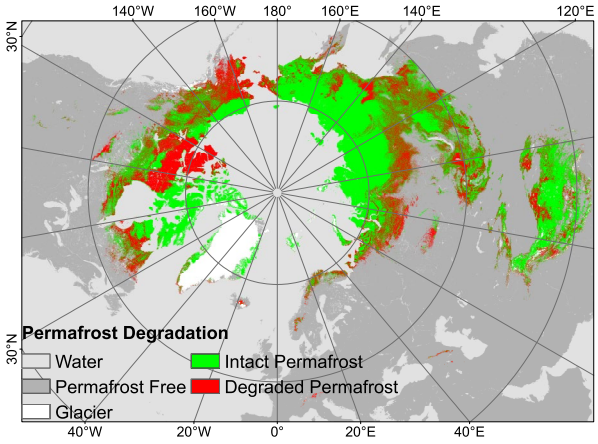

Figure 10. Maps showing permafrost degradation between 2000 and 2019 (either PFR or ALT).

3.2.1 *Permafrost Area Fraction*

Figure 11 shows the mean transitions of the 7 PFR classes (only maximum percentage is shown) over the 20 years. The matrix reads as follows: On the x-axis, you will find the class affiliation in the current year, and on the y-axis the class affiliation in the previous year. If you take the PFR value of 57 as an example, in the next year 94.03% will still belong to this class, 2.21% of the pixels have moved up to the next higher class (71) and 3.42% to the next lower class (43).

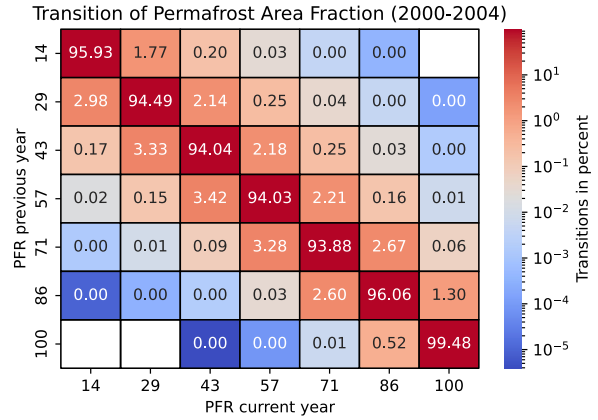

Figure 11. Transition diagram of the Permafrost Area Fraction (PFR).

In general, we see that there is a tendency towards a decrease in the permafrost fraction. Also, the transitions occur mostly in the neighboring classes. To find out how the class transition is connected to SCD and its development, the changing pixels are displayed as a 2-dimensional point cloud (where SCD is shown on the x-axis and the slope on the y-axis). The ellipses show the standard deviation around the respective mean values. The more clearly the ellipses can be distinguished, the better the separation. From Figure 12 you can see that the areas of the PFR transition largely overlap and are therefore not recognizable only by SCD and its development.

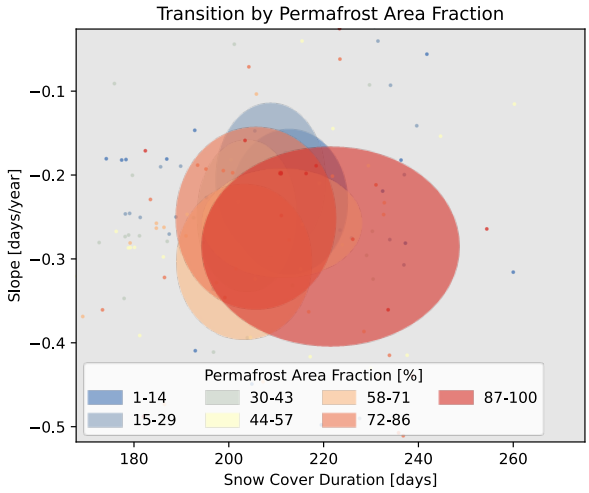

Figure 12. Snow coverage metrics for the transition regions of the PFR classes

In addition to the large overlap area of almost all classes with snow cover duration between 190 and 220 days and a slope of -0.2 to 0.3 days/year, the class "PFR = 100%" in the range of SCD > 230 and a slope > -0.2 stands out.

3.2.2 *Active Layer Thickness*

As with the horizontal permafrost classes, we also find a predominant increase in the Active Layer Thickness. This is visible in the transition diagram of ALT (Figure 13).

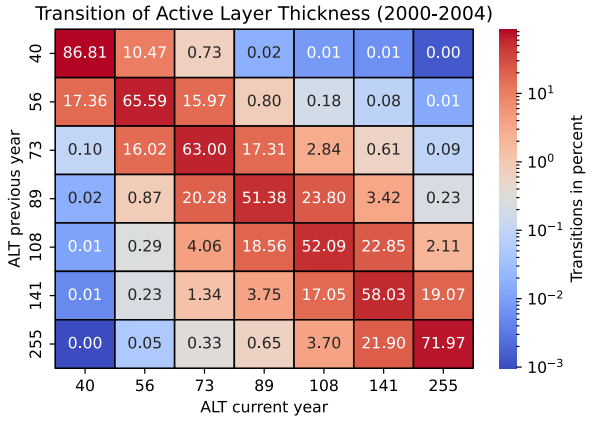

Figure 13. Transition diagram of the development of the Active Layer Thickness (ALT).

What we also see is a stronger variability in ALT. In contrast to PFR, a maximum of 80% remain in the previous class, mostly around 50%.

To see whether this development is also reflected in the snow information, Figure 14 shows the transition regions for the final class affiliation.

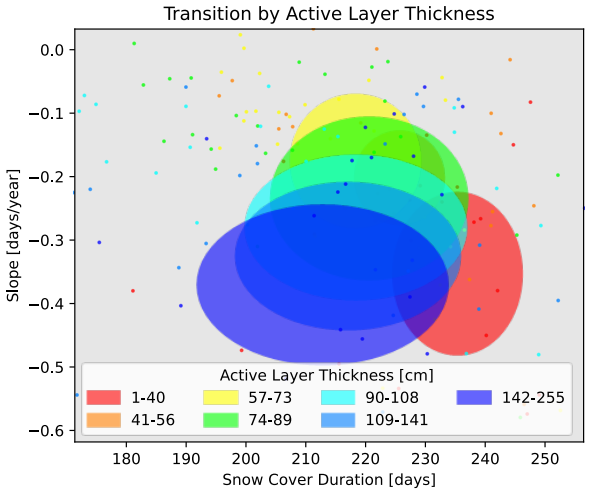

Figure 14. Snow coverage metrics for the transition regions of the ALT classes.

The smooth transitions are also reflected in the snow cover statistics. Although there is a large area of overlap between 210 and 230 days SCD and a slope between -0.2 and -0.4 days/year, there is a clear tendency for the ALT to increase more with lower initial snow cover duration and a larger slope. Only the lowest ALT (1–40 cm) occupies a distinct region between 230 and 240 days SCD and slopes ranging from 0.2 to 0.45 days/year. Studies in Alaska confirm these short-term changes, a shortening of the SCD by 10 days led to a temperature increase of several degrees, but they also speak of the fact that the effect on ALT is low (Ling and Zhang 2003).

3.2.3 Land Cover

In connection with the topic "Greening of the Arctic," we are interested in whether the information on snow cover can provide information about changing land cover. However, it is apparent from Figure 15 that these changes take longer than the observed 20 period.

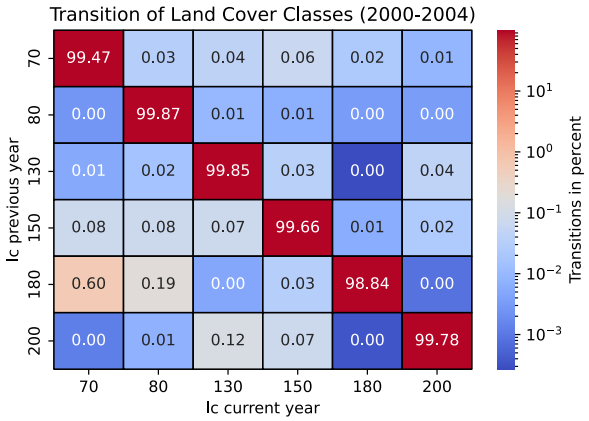

Figure 15. Transition diagram of the Land Cover (LC).

Class membership is very stable and few transitions have taken place. If we now look at the snow cover metrics in which these transitions occur (Figure 16), it becomes clear that “Bare” (200) or ”Sparse” (150) in particular overlap.

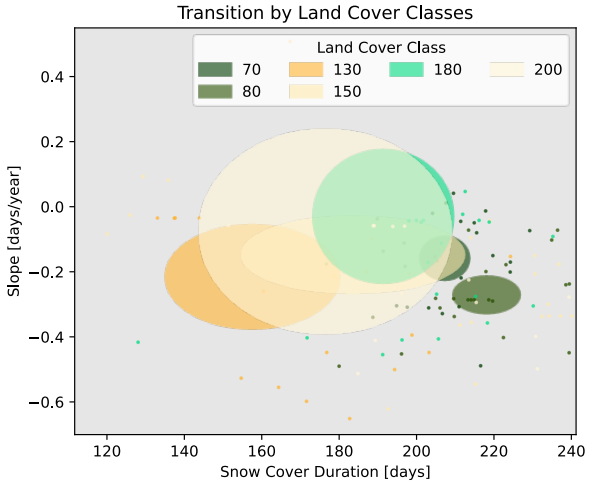

Figure 16. Snow coverage metrics for the transition regions of the Land Cover classes.

“Deciduous” (80) is best distinguished from the others because it has a relatively long average SCD of 210 to 230 days and the slope is also in a narrow range of between -0.2 and -0.3 days/year. Shorter snow cover durations (135–180 days) and a larger area slope (-0.5 to -3.5 days/year) are occupied by “Grassland” (130), which is a typical element at average PFR (~50%).

4 DISCUSSION

Regarding the limitations, the following can be summarized. The spatial resolution of MODIS can be insufficient, especially in mountainous regions, the limitations by clouds are mitigated by using an advanced gap-filling method (i.e., GSP), but this is still an assumption. Although snow depth has a large influence on thermal insulation (Domine et al. 2022), optical remote sensing can only detect two-dimensional snow coverage. However, the filled GSP daily snow coverage can help downscale this information from passive microwave (Tanniru and Ramsankaran 2023) in the future. Another issue is the period in which the data are collected. The information provided by ESA CCI Permafrost is averaged over calendar years, but snow cover duration is based on hydrological years (meteorological autumn to summer). Recent studies show that changes in snow cover usually occur at the end of autumn/beginning of winter (Roessler and Dietz 2022). This annual update of land cover classes, for example, was also the reason why the ESA product was used and not specific circumarctic products such as the CAVM (Walker et al. 2005; Raynolds 2022).

In the results, we observed various relationships between snow cover duration and permafrost parameters. On the one hand, there is a strong connection between horizontal (PFR) and vertical (ALT) permafrost extent, and this is reflected in the average snow cover duration of the classes.

There are also some clear connections between the land cover classes: with increasing PFR, the class “Evergreen” (70) almost completely disappear and “Deciduous” (80) increases. The classes “Grassland” (130), “Sparse” (150), and “Bare” (200) also increase with increasing PFR. The high SCD variability of "Grassland" (130) and "Bare" (200) in Figure 9 can be explained by their broader use: "Grassland" includes arctic tundra and steppe, "Bare" includes the polar cold desert (high SCD) and the deserts (low SCD) of lower latitudes.

The transition tables were able to clearly show the time frame within which permafrost changes occur. As expected, the slowest changes occurred in land cover. What's interesting here is the transition from "Bare" (200) to "Sparse" (150) or even "Grassland" (130) — a sign of Arctic Greening, just like the expansion of the boreal coniferous forest (Myers-Smith et al. 2020). It is also interesting that changes occur in both directions (degradation predominates), which affects both PFR and ALT. This is consistent with the observed trend of SCD. ALT also turned out to be the most variable permafrost parameter. On the one hand, this is where most of the changes took place between the years, and on the other hand, this is where we could see the clearest connection with the SCD (in terms of both the mean SCD and the trend). This can be explained by the insulating effect of the snow cover, as we can assume that a longer-lasting snow cover is associated with greater snow thickness (better insulation).

Our first research question was whether it is possible to understand permafrost developments with the average snow cover duration and their trend. This does not seem possible for PFR (yet) but is possible for vertical permafrost extent (ALT). Our future approach will involve integrating meteorological data and potentially AI techniques to enhance the comprehensiveness of outcomes. Similarly, in the context of the second research question, the gradual adaptation of land cover to evolving climatic conditions introduces a temporal lag, challenging the real-time linkage between snow cover and processes like Arctic greening. But here too we were able to identify classes that show distinctive mean SCD and trend.

5 Conclusions

In this study, we utilized time series data from ESA CCI to analyze permafrost and land cover dynamics. Our objective was to detect permafrost degradation (due to decreasing permafrost area extent, active layer deepening, and arctic greening) and correlate them with MODIS snow cover data. Results consistently revealed permafrost degradation across active layer thickness, permafrost extent, and land cover classes.

Despite considerable variability in snow cover duration, we successfully identified regions with pronounced distinctions in both snow cover duration and SCD slope values during class transitions. This outperformed the resolution capabilities of lower-resolution sensors like passive microwave sensors.

Remote sensing-derived snow coverage data are a valuable tool to affirm permafrost degradation trends and augment spatial resolution relative to coarser sensors.

Nonetheless, this tool alone falls short of independently substantiating assertions regarding permafrost degradation and Arctic greening complexities. Subsequent steps involving meteorological data integration and AI-driven methodologies are imperative for a comprehensive understanding of these intricate dynamics.

6 References

Bhatt, U., Walker, D., Raynolds, M., Bieniek, P., Epstein, H., Comiso, J., Pinzon, J., Tucker, C., and Polyakov, I. 2013. ‘Recent Declines in Warming and Vegetation Greening Trends over Pan-Arctic Tundra’, *Remote Sensing* 5(9), pp. 4229–4254. doi:10.3390/rs5094229.

Bontemps, S., Defourny, P., Radoux, J., Van Bogaert, E., Lamarche, C., Achard, F., Mayaux, P., Boettcher, M., Brockmann, C., Kirches, G., et al. 2013. ‘Consistent global land cover maps for climate modelling communities: current achievements of the ESA’s land cover CCI’, in *Proceedings of the ESA living planet symposium*. Edinburgh, United Kingdom: ESA SP-722, pp. 9–13.

Dietz, A.J., Kuenzer, C., and Dech, S. 2015. ‘Global SnowPack: a new set of snow cover parameters for studying status and dynamics of the planetary snow cover extent’, *Remote Sensing Letters* 6(11), pp. 844–853. doi:10.1080/2150704X.2015.1084551.

Dietz, A.J., Wohner, C., and Kuenzer, C. 2012. ‘European Snow Cover Characteristics between 2000 and 2011 Derived from Improved MODIS Daily Snow Cover Products’, *Remote Sensing* 4(8), pp. 2432–2454. doi:10.3390/rs4082432.

Domine, F., Fourteau, K., Picard, G., Lackner, G., Sarrazin, D., and Poirier, M. 2022. ‘Permafrost cooled in winter by thermal bridging through snow-covered shrub branches’, *Nature Geoscience* 15(7), pp. 554–560. doi:10.1038/s41561-022-00979-2.

Guo, D. and Wang, H. 2016. ‘CMIP5 permafrost degradation projection: A comparison among different regions’, *Journal of Geophysical Research: Atmospheres* 121(9), pp. 4499–4517. doi:10.1002/2015JD024108.

Hall, D.K., Riggs, G.A., Salomonson, V.V., DiGirolamo, N.E., and Bayr, K.J. 2002. ‘MODIS snow-cover products’, *Remote Sensing of Environment* 83(1–2), pp. 181–194. doi:10.1016/S0034-4257(02)00095-0.

Hussain, M. and Mahmud, I. 2019. ‘pyMannKendall: a python package for non parametric Mann Kendall family of trend tests’, *Journal of Open Source Software* 4(39), 1556. doi:10.21105/joss.01556.

Jorgenson, M.T. and Grosse, G. 2016. ‘Remote Sensing of Landscape Change in Permafrost Regions’, *Permafrost and Periglacial Processes* 27(4), pp. 324–338. doi:10.1002/ppp.1914.

Langer, M., Westermann, S., Heikenfeld, M., Dorn, W., and Boike, J. 2013. 'Satellite-based modeling of permafrost temperatures in a tundra lowland landscape', *Remote Sensing of Environment* 135, pp 12–24. doi:10.1016/j.rse.2013.03.011.

Lemke, P., Ren, J., Alley, R.B., Allison, I., Carrasco, J., Flato, G., Fujii, Y., Kaser, G., Mote, P., Thomas, R.H., and Zhang, T. 2007. 'Observations: Changes in Snow, Ice and Frozen Ground', in S. Solomon et al. (eds.), *Climate Change 2007: The Physical Science Basis. Contribution of Working Group 1 to the Fourth Assessment Report of the Intergovernmental Panel on Climate Change*. Cambridge, United Kingdom: Cambridge University Press.

Ling, F. and Zhang, T. 2003. 'Impact of the timing and duration of seasonal snow cover on the active layer and permafrost in the Alaskan Arctic', *Permafrost and Periglacial Processes*, 14(2), pp. 141–150. doi:10.1002/ppp.445.

Muster, S., Langer, M., Abnizova, A., Young, K.L., and Boike, J. 2015. 'Spatio-temporal sensitivity of MODIS land surface temperature anomalies indicates high potential for large-scale land cover change detection in Arctic permafrost landscapes', *Remote Sensing of Environment* 168, pp. 1–12. doi:10.1016/j.rse.2015.06.017.

Myers-Smith, I.H., Kerby, J.T., Phoenix, G.K., Bjerke, J.W., Epstein, H.E., Assmann, J.J., et al. 2020. 'Complexity revealed in the greening of the Arctic', *Nature Climate Change* 10(2), pp. 106–117. doi:10.1038/s41558-019-0688-1.

Obu, J., Westermann, S., Barboux, C., Bartsch, A., Delaloye, R., Grosse, G., et al. 2021. 'ESA Permafrost Climate Change Initiative (Permafrost_cci): Permafrost Ground Temperature for the Northern Hemisphere, v3.0', *NERC EDS Centre for Environmental Data Analysis*. Available at: https://data-search.nerc.ac.uk/geonetwork/srv/eng/catalog.search#/metadata/6e2091cb0c8b4106921b63cd5357c97c.

Raynolds, M. 2022. *Raster Circumpolar Arctic Vegetation Map*, Mendeley Data, version 1. doi:10.17632/c4xj5rv6kv.1.

Roessler, S. and Dietz, A.J. 2022. 'Development of Global Snow Cover—Trends from 23 Years of Global SnowPack', *Earth* 4(1), pp. 1–22. doi:10.3390/earth4010001.

Rößler, S., Witt, M.S., Ikonen, J., Brown, I.A., and Dietz, A.J. 2021. 'Remote Sensing of Snow Cover Variability and Its Influence on the Runoff of Sápmi's Rivers', *Geosciences* 11(3), 130. doi:10.3390/geosciences11030130.

Shijin, W. and Xiaoqing, P. 2023. 'Permafrost degradation services for Arctic greening', *CATENA*, 229, 107209. doi:10.1016/j.catena.2023.107209.

Streletskiy, D., Anisimov, O., and Vasiliev, A. 2015. 'Permafrost Degradation', in *Snow and Ice-Related Hazards, Risks, and Disasters*. Elsevier, pp. 303–344.

Tanniru, S. and Ramsankaran, R. 2023. 'Passive Microwave Remote Sensing of Snow Depth: Techniques, Challenges and Future Directions', *Remote Sensing* 15(4), 1052. doi:10.3390/rs15041052.

Walker, D.A., Raynolds, M.K., Daniëls, F.J.A., Einarsson, E., Elvebakk, A., Gould, W.A., Katenin, A.E., Kholod, S.S., Markon, C.J., Melnikov, E.S., Moskalenko, N.G., Talbot, S.S., Yurtsev, B.A.(†), et al. 2005. 'The Circumpolar Arctic vegetation map', *Journal of Vegetation Science* 16(3), pp. 267–282. doi:10.1111/j.1654-1103.2005.tb02365.x.

Wang, P., Huang, Q., Tang, Q., Chen, X., Yu, J., Pozdniakov, S.P., and Wang, T. 2021. 'Increasing annual and extreme precipitation in permafrost-dominated Siberia during 1959–2018', *Journal of Hydrology* 603, 126865. doi:10.1016/j.jhydrol.2021.126865.

Xu, Y. and Zhuang, Q. 2023. 'The importance of interactions between snow, permafrost and vegetation dynamics in affecting terrestrial carbon balance in circumpolar regions', *Environmental Research Letters* 18(4), 044007. doi:10.1088/1748-9326/acc1f7.

Ground temperature monitoring and permafrost distribution mapping, Coffee Mine Project, Yukon

Vladislav E. Roujanski[1], Ernest Palczewski[1], Javed Iqbal[1] & Shirley McCuaig[2]
[1]*Tetra Tech Canada Inc., Edmonton, Alberta, Canada*
[2]*Palmer, Edmonton, Alberta, Canada*

ABSTRACT

Tetra Tech completed several geotechnical investigation programs in support of the proposed development of the Coffee Mine Project (the Project) owned by Newmont. The Project is located in west-central Yukon, in the discontinuous permafrost zone. A key objective was to acquire permafrost data, including ground temperature and ground ice content information, that would allow design of the mine infrastructure. Tetra Tech's geotechnical investigations, completed between 2015 and 2019, consisted of coring overburden and bedrock with a helicopter-transportable diamond drill rig. Chilled drilling fluid was used to minimize thermal disturbance of permafrost and recover undisturbed frozen core samples. Twenty multi-bead ground temperature cables and numerous single-bead thermistor strings were installed in some of the 103 geotechnical boreholes completed to determine ground thermal conditions and monitor changes in permafrost temperatures. The data collected allowed for accurate mapping of permafrost distribution. The surface appearance of terrain units where permafrost conditions were confirmed was extrapolated, and slope aspect and geobotanical indicators of permafrost occurrence were also used to map permafrost extent in areas lacking boreholes. Calculations of permafrost distribution within the Project Area show that approximately 61% of the mapped area is underlain by warming, locally ice-rich permafrost. Geospatial machine-learning models were created based on terrain derivatives (slope, aspect, elevation, topographic position index, and landforms), available orthoimage information (vegetation indices), and were compared to the newly mapped permafrost distribution (about 8,000 ha) to predict presence/absence of permafrost in the larger Project Area (about 39,000 ha). The model accuracy was 58% for the broader area.

1 INTRODUCTION

The Coffee Mine Project (the Project) is an open pit and heap leach mining project owned by Newmont. The Project is situated on the divide between the headwaters of Latte Creek and Halfway Creek, located in the northern Dawson Range, in west-central Yukon, approximately 400 km northwest of Whitehorse, as shown on Figure 1.

The map of Canada-Permafrost (Heginbottom et al. 1995) shows the Project Area to be within the zone of extensive discontinuous permafrost (50% to 90% of land area underlain by permafrost).

Several geotechnical field investigation programs and desktop studies have been completed in the Project Area since 2011, as discussed in Section 1.3. Tetra Tech have been advising the owners of the Project on the permafrost-related aspects of the mine development since 2013.

1.1 Background

In addition to other environmental assessments to be completed as part of the permitting and approval process, the permafrost mapping component of the environmental work was undertaken by Tetra Tech. Geotechnical and permafrost data were acquired, including frozen and unfrozen overburden and bedrock conditions, to characterize ground conditions in support of mine infrastructure design. These investigations took place between 2013 and 2019.

The ongoing monitoring of permafrost conditions carried out by Newmont and Tetra Tech includes regular collection and analysis of ground temperatures across the Project Area. The ground temperatures and other subsurface permafrost data (ground ice content, etc.) gathered in 103 geotechnical boreholes have been used by Tetra Tech to map permafrost distribution within the Project Area.

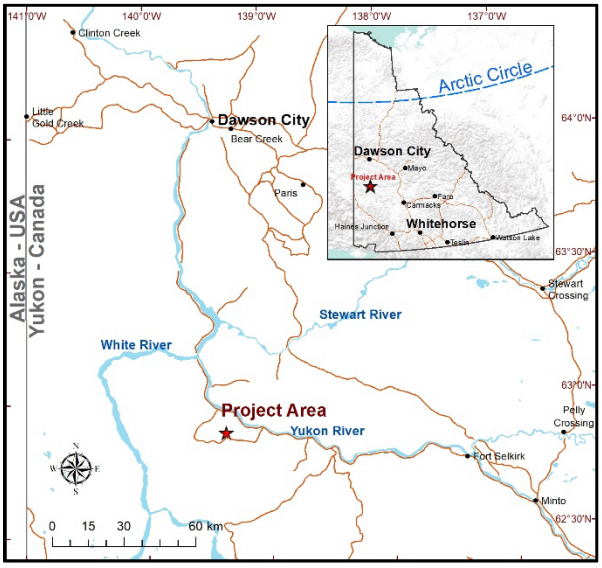

Figure 1. Project location.

https://doi.org/10.52381/ICOP2024.74.01

1.2 Rationale and Objectives

A recent increase in the intensity of mining activities in west-central Yukon generated interest in better understanding the permafrost distribution and its characteristics.

The objective of the study was to improve the assessment of the baseline permafrost conditions in the Project Area. This paper presents results of the ongoing ground temperature monitoring and permafrost distribution mapping within the Project Area. This includes an overview of the mapping methods used, as well as new methods, such as geospatial machine learning (ML) algorithms, that can be applied for more efficient permafrost distribution mapping.

1.3 Previous Studies

The most significant geotechnical investigation programs and desktop studies completed in the Project Area since 2011 include:

- Geomorphological mapping and landscape model development at the Project Area, Summer 2012 (AECOM 2012).
- Hydrogeological field investigation, Fall 2013 (Tetra Tech EBA 2014).
- Hydrogeological field investigation (Lorax 2014).
- Geotechnical field investigation, August to September 2014 (Knight Piesold 2015).
- Hydrogeological field investigation, March 2015 (Lorax 2015).
- Geotechnical field investigation with sonic drill, April 2015 (SRK 2015).
- Hydrogeological field investigation, April to June 2015 (Lorax 2015).
- Terrain stability and hazard mapping, August 2015 (PECG 2016).
- Mapping permafrost distribution along proposed Kaminak road alignment (Tetra Tech EBA 2016a).
- Environmental baseline study, the Project Area: Surficial Geology, Permafrost and Terrain Stability, 2015 to 2016 (Tetra Tech EBA 2016b).
- Mapping permafrost and related geohazards within the Project Area (Tetra Tech EBA 2016c).
- Geotechnical investigation: diamond drilling with chilled drilling fluid, Fall 2016 (Tetra Tech and SRK 2017).
- Geotechnical investigation: diamond drilling with chilled drilling fluid, Summer 2017 (Tetra Tech 2017a).
- Testpitting program, Fall 2017 (Tetra Tech 2017b).
- Geotechnical investigation: diamond drilling with chilled drilling fluid, 2018 (Tetra Tech and SRK 2019).
- Testpitting program, Fall 2018 (Tetra Tech 2019a).
- Permafrost distribution mapping update, April 2019 (Tetra Tech 2019b).
- Ground temperature monitoring update, 2022 (Tetra Tech 2023).

1.4 Physical Setting

The Project Area is located within the Klondike Plateau physiographic region. The Klondike Plateau is a Tertiary-age upland that has undergone variable uplift and stream dissection, resulting in rounded summits and ridges, and deep V-shaped valleys (Mathews 1986; Huscroft 2002). Most valley sides exhibit convex profiles, with concave profiles restricted to localized bench and gully features and valley bottoms filled with material derived from upslope erosion (PECG 2016).

The Project Area, which is situated within the Coffee Creek and Yukon River watershed, was not glaciated during the last Wisconsin glaciation (Duk-Rodkin 1999) and has since been modified by frost action and permafrost-related geomorphic processes (Tetra Tech EBA 2016b). The lack of glaciation in the Project Area means that the area has experienced a significant period of weathering. Surficial deposits consist of weathered bedrock, colluvium derived from weathered bedrock, loess, and fluvial deposits (Huscroft 2002; AECOM 2012). Colluvium is coarser grained on steeper slopes, while colluvial aprons on lower slopes commonly include ice-rich resedimented loess and peat (informally called “black muck” when intermixed; Huscroft 2002; McKenna and Lipovsky 2014). Colluvial deposits dominate high-elevation areas and upper to mid-slopes in valleys, while ice-rich “black muck” is found on lower slopes, and fluvial deposits in valley bottoms.

The climate of the Project Area is continental characterized by warm, short summers and long, cold winters. Mean annual air temperature is near -5 °C, mean January temperatures range from -23 °C to -32 °C and mean July temperatures from 10 °C to 15 °C (Yukon Ecoregions Working Group 2004). Strong thermal inversions are common from December to February in association with prolonged atmospheric stability (Williams 1995). During this period, air temperatures in valley bottoms can be tens of degrees lower than surrounding higher-elevation areas (PECG 2016). Mean annual precipitation ranges from about 300 mm to 500 mm, giving the region a semi-arid classification. The wettest period occurs in summer, when most precipitation falls as rain during rain showers and thunderstorms (Yukon Ecoregions Working Group 2004).

The Project Area comprises ecosystems ranging from boreal forests and wetlands in valleys to alpine tundra on ridge crests. Below treeline, black spruce and white spruce dominate the ecoregion in both pure stands and mixed stands that include various deciduous species, such as trembling aspen and Alaska birch (Yukon Ecoregions Working Group 2004).

2 METHODOLOGY

Tetra Tech has been studying and mapping permafrost within the Project Area since 2013. The main objective was to provide accurate characterization of the spatial variability of permafrost conditions, such as permafrost distribution,

ground temperatures, volumetric ice contents, and thickness of the permafrost interval.

2.1 Geotechnical Investigations in Permafrost

Accurate mapping of spatial variability of permafrost conditions was achieved through analyses of the high-quality data collected by coring permafrost with chilled (refrigerated) drilling fluids to minimize thermal disturbance of frozen ground containing ground ice. Drilling was performed using a helicopter-portable D-10 Duralite 500 diamond drill rig with a triple tube coring system. The drilling fluid was chilled to a temperature of approximately -6 °C to -7 °C. This chilled fluid allowed the recovery of undisturbed frozen core samples and accurate estimation of volumetric ice content (% by volume of visible ice) in ice-rich permafrost. To assist with visual assessments, field "beaker" testing (Kokelj and Burn 2005) was performed on each recovered ice-rich frozen core sample to improve the accuracy of the volumetric ice content determination.

Tetra Tech reviewed deep borehole data collected by Lorax during several hydrogeological field investigations (Lorax 2016) to analyze the thickness of the permafrost interval throughout the Project Area. Permafrost depths were also determined from three ground temperature profiles plotted with ground temperature data collected in the 2018 boreholes (SRK-AP-18-06, -07, and -08) completed in the Halfway Creek valley (Tetra Tech and SRK 2019).

In total, 103 geotechnical boreholes were drilled within the Project Area.

2.2 Ground Temperature Monitoring

Completed boreholes were instrumented with single-bead thermistor strings (SBTSs) and multi-bead ground temperature cables (GTCs) to confirm the presence (or the absence) of permafrost and monitor in situ ground temperatures. SBTSs were installed to a depth of at least 6 m below the ground surface (usually between 6 m and 10 m), such that a thermistor bead would be located below the base of the active layer.

Twenty multi-bead GTCs and numerous SBTSs were installed in selected geotechnical boreholes to determine ground thermal conditions and to monitor changes in permafrost temperatures. Subsurface conditions observed in 57 testpits from Tetra Tech's 2017 program (Tetra Tech 2017b) and in 69 testpits from Tetra Tech's 2018 program (Tetra Tech 2019a) were also used to refine the permafrost mapping of the Project Area.

2.3 Air Photo Interpretation

Digital colour air photos covering the Project Area were acquired at a nominal scale of 1:20,000. These were used to generate three-dimensional (3D) digital models. Permafrost distribution mapping was initially carried out by Tetra Tech at 1:20,000 scale, based on stereoscopic interpretation of the colour air photos. The initial mapping linework was then refined in early 2016 using the 3D visualization PurVIEW system at 1:5,000 to 1:25,000 scale, the latter being a smaller scale than the nominal 1:20,000. The refined map was presented to Kaminak, the Project's previous owner, at a scale of 1:20,000 in a Technical Memo (Tetra Tech EBA 2016c), and the map has been updated since then.

Permafrost and permafrost-free polygons were delineated according to:

Geobotanical indicators:

- Stunted black spruce stands ("drunken forest") with thick moss cover (reliable indicators of shallow ice-rich permafrost),
- Deciduous (dominantly trembling aspen and / or Alaska birch) dense stands – suggesting predominantly permafrost-free terrain, and
- Mixed stands of Alaska birch (with or without aspen) and spruce (black and white) – commonly indicating permafrost-free terrain. However, mixed stands are not reliable predictors of permafrost presence or absence (McKillop et al. 2013).

Slope aspect:

- North-facing slopes indicate permafrost terrain; whereas,
- South-facing slopes suggest predominantly permafrost-free terrain.

Ground surface appearance:

- Texture, colour, hue, etc.) of those terrain units, where permafrost presence was confirmed by ground temperature measurements), was extrapolated to areas where no ground temperature instrumentation has been installed, thus allowing delineation of permafrost polygons.

ArcGIS technology was used to calculate percentages of delineated permafrost terrain units (map polygons) within the Project Area. Map polygon areas were determined within ArcGIS, followed by an export of the data to Microsoft Excel where totals and percentages were refined. The results are presented in Section 3.2.

2.4 Machine Learning (ML) Modeling

Several studies have used ML methods for high-resolution digital mapping in permafrost terrain (e.g., Siewert (2018) for soil organic carbon), but relatively few have focused on permafrost distribution. Predictive models for permafrost distribution in the Project Area were created using the mapped permafrost polygons as training data and associating spatio-statistical relationships with other available data that include LiDAR terrain derivatives (aspect, slope, landform, etc.) and imagery. The annual permafrost mapping update was input to create algorithms incorporating other key permafrost indicators based on the terrain and vegetation parameters using ML.

The permafrost distribution modeling outputs are produced at 1 m raster resolution, corresponding to the LiDAR terrain derivatives. The borehole and ground temperature data were not used as an input in the ML model. The data required 3D interpolation and complex processes that can be included in the next phase of a more detailed model. Similarly, due to the lack of high-resolution multispectral data for the site, vegetation species composition and tree

height parameters were not incorporated into the model. As an alternative, a 10 m resolution Normalized Difference Vegetation Index (NDVI) and a Normalized Difference Water Index (NDWI) were calculated from Sentinel-2 data (Copernicus Sentinel data 2021-07-12 retrieved from Copernicus Open Access Hub, processed by European Space Agency).

Geospatial ML models were based on NDVI, NDWI, slope, aspect, landform, and elevation data. These factors and the classes represented are shown in Figure 2.

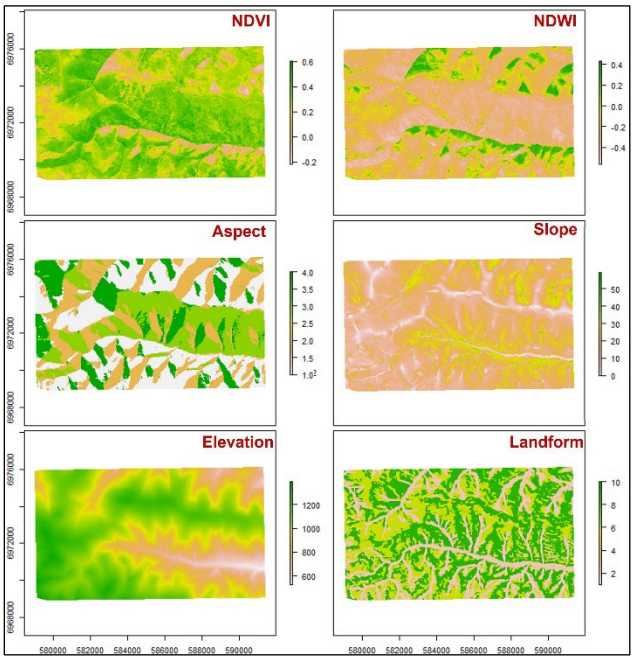

Figure 2. Factors used for ML model.

3 RESULTS

3.1 Ground Temperature Monitoring

The GTC installed in Borehole GT17-39T at the bottom of the Halfway Creek valley (Figure 3) has shown a significant increase in ground temperature of approximately 1.7 °C from 2019 to 2022 within the 12 m to 13 m depth interval; however, the same GTC later showed an approximate 0.7 °C decrease in ground temperatures from 2022 to 2023 (Figure 4). Increasing ground temperatures have resulted in an increase in the active layer thickness by approximately 0.4 m since monitoring began in the Project Area in 2017. The active layer at this location consists of a layer of peat 200 mm thick underlain by silt with some organics approximately 0.5 m thick. The silt layer is underlain by sandy gravel. The thickness of the active layer increased from approximately 0.8 m in 2018 to approximately 1.2 m in 2022 (Figure 4). The thickness of the permafrost interval at this location has slightly decreased, by approximately 0.5 m from 2017, with the permafrost base currently located at a depth of approximately 5 m below the ground surface (Figure 4).

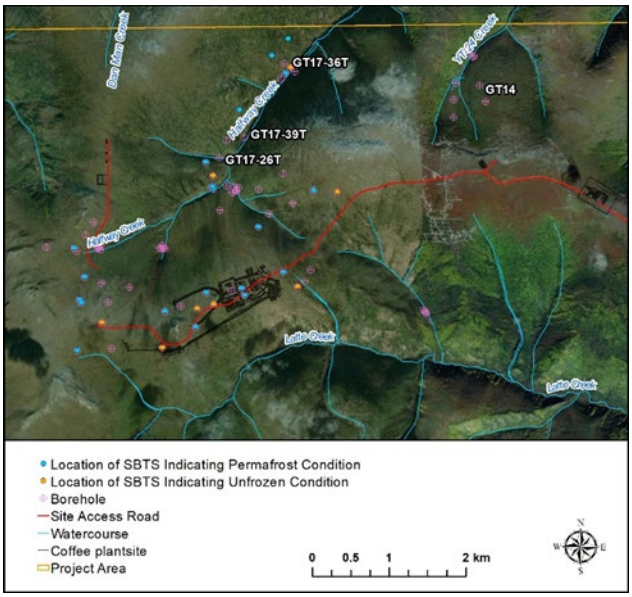

Figure 3. Coffee Mine Project Area with proposed plant site and selected borehole locations.

Temperature trends since 2016 showing ground warming were observed in 11 of the 20 instrumented boreholes in the Project Area. For Borehole GT-14, located on a northwest-facing slope covered at this borehole location by a layer of intermixed silt and organic material approximately 250 mm thick underlain by sandy gravel (Figure 3), warming of permafrost of almost 0.2 °C has occurred since 2019 (Figures 5 and 6). The active layer thickness at GT-14 has increased since measurements began in 2016, from approximately 1.5 m in 2016 to 2.5 m in 2019 and 3.75 m in 2023 (Figure 5).

The lowest permafrost temperatures (-2.1 °C) in the Project Area were measured at Borehole GT17-36T on a north-facing slope of the Halfway Creek valley (Figure 3) at a depth between 17 m and 20 m below ground surface (Figure 7). The active layer thickness (approximately 3.0 m) at this location has remained unchanged since monitoring began in 2017 (Figure 7).

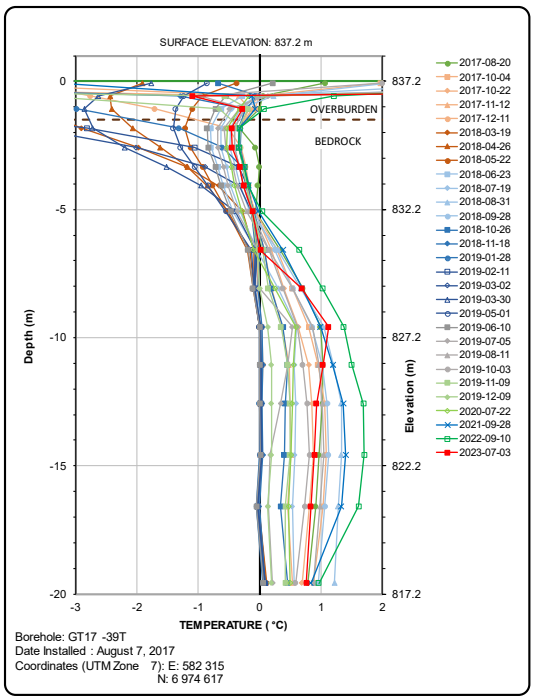

Figure 4. Ground temperature profile at Borehole GT17-39T showing a warming trend (Bottom of Halfway Creek Valley).

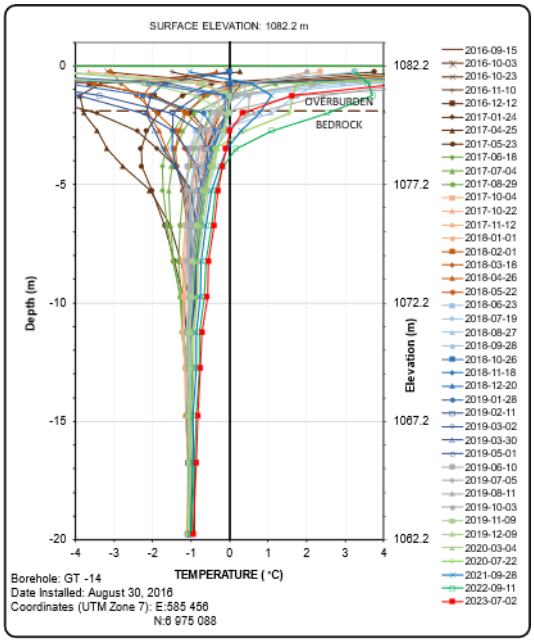

Figure 5. Ground temperature profile at Borehole GT-14 showing slight warming trend (a northwest-facing slope).

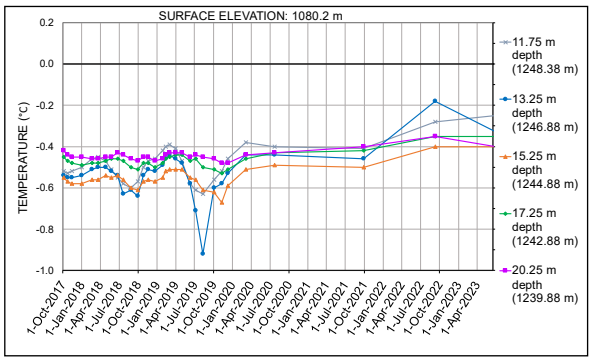

Figure 6. Ground temperature profile at Borehole GT-14 showing increase in permafrost temperatures from 11.75 m to 20.25 m depth below ground surface between 2017 and 2023 (north-facing slope of Halfway Creek).

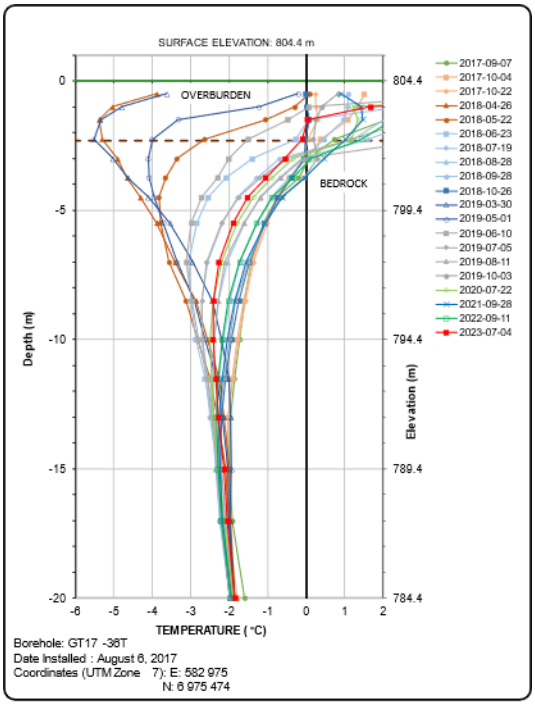

Figure 7. Ground temperature profile at Borehole GT17-36T showing lowest permafrost temperatures (a north-facing slope of Halfway Creek).

Four other GTCs have shown very slight cooling trends since 2017. The largest temperature decrease, up to approximately 0.2 °C from 2022 to 2023, occurred in an area of unstable permafrost temperatures, i.e., very warm permafrost (close to 0 °C) located at an east to northeast-facing slope of an unnamed creek tributary of Halfway Creek (Borehole GT17-26T; Figure 3). The remaining GTCs show no apparent changes in ground temperatures since 2017.

3.2 Permafrost Distribution Mapping

The initial map of the spatial distribution of permafrost in the Project Area (Tetra Tech EBA 2016c) was updated (Tetra Tech 2019b, 2023a, 2023b), as new permafrost data became available. The latest mapping update, completed in July 2023, is shown in Figure 8.

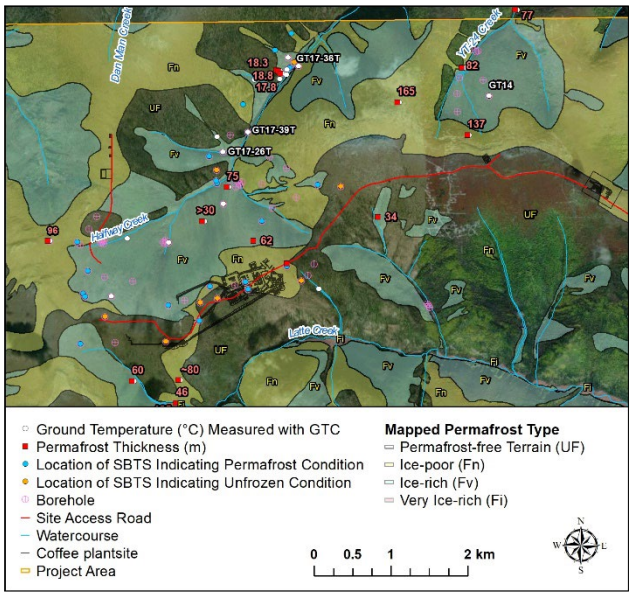

Figure 8. Permafrost distribution and thickness in the project area.

Permafrost distribution within the Project Area was divided into four terrain units (shown on Figure 8):

- Predominantly very ice-rich permafrost – ground ice content exceeding 50% by volume of visible ice (ICE and SOIL) – labeled as "**Fi**" on the map;
- Predominantly ice-rich permafrost – ground ice contents ranging between 10% and 50% by volume of visible ice – labeled as "**Fv**" on the map;
- Predominantly ice-poor permafrost – ground ice content generally less than 10% by volume of visible ice or non-visible ground ice – labeled as "**Fn**" on the map; and
- Areas confirmed by SBTSs and GTCs to be mainly permafrost-free – labelled as "**UF**" on the map and shown as transparent (not coloured) polygons. These areas may contain patches of permafrost where ground conditions are favourable, such as localized shallow low-lying areas with patches of peat or organic-enriched soil.

Tetra Tech's calculations of permafrost distribution, i.e., percentages of delineated permafrost terrain units (map polygons) show that approximately 61% of the Project Area is underlain by permafrost. This result agrees with the Canada-Permafrost map (Heginbottom et al. 1995), which shows the Project located within the zone of extensive discontinuous permafrost (50% to 90% of land area is underlain by permafrost).

The permafrost distribution within the Project Area was further broken down, as follows:

- 0.5% of the area is underlain by very ice-rich permafrost (**Fi**);
- 31% of the area is underlain by predominantly ice-rich permafrost (**Fv**);
- 29.5% of the area is underlain by predominantly ice-poor permafrost (**Fn**), and
- 39% of the Project Area is expected to be permafrost-free (**UF**).

Review of the deep borehole data collected by Lorax (Lorax 2016) shows that the thickest permafrost interval (165 m) measured to date within the Project Area underlies a north-facing slope of the divide between the Halfway Creek and the YT-24 Creek (Figure 8).

3.3 Machine Learning Modeling

The output from the ML model is presented in Figure 9. The model provided the ability to map permafrost at a 1-m resolution which can easily be overlooked by the human eye. An additional advantage of the ML model was to extend the permafrost mapping to areas that were not mapped initially. Permafrost presence-absence model output using just these two classes of permafrost distribution showed higher accuracies (58%) compared to the test data that is based on the manual permafrost distribution mapping (Section 3.2), but the accuracies of individual classes of permafrost distribution (ice-poor **Fn**, ice-rich **Fv** and very ice-rich **Fi**) were lower (42%) than the permafrost presence-absence model outputs.

4 DISCUSSION

Permafrost distribution is difficult to identify directly on a large scale. The 3D mapping used in this study, coupled with ground temperature monitoring, is the most accurate method for completing this type of work, but it is time-consuming and requires expertise in vegetation identification and knowledge of permafrost derivative parameters (slope, aspect, landform, etc.). Landscape indicators combined with terrain data, multispectral remote sensing data, and other GIS tools can be used in combination with the existing mapping done to take advantage of ML on a large scale.

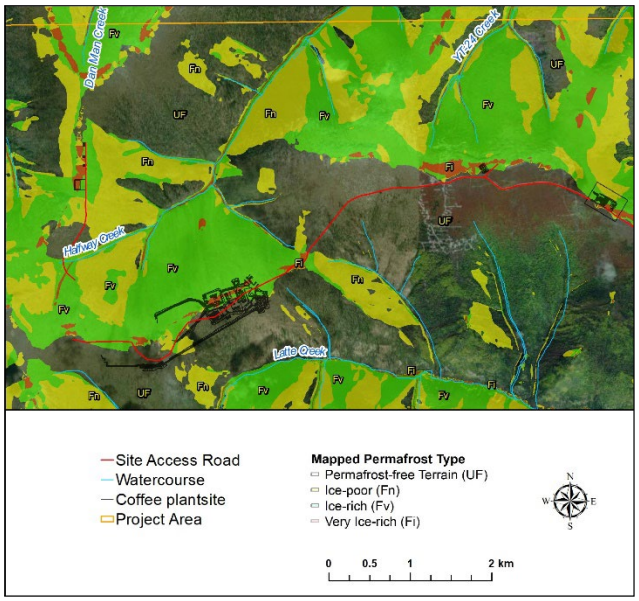

Figure 9. ML model output for same classes as that of the training data (permafrost-free, ice-poor, ice-rich, and very ice-rich).

The preliminary results achieved using the available data for the current ML model are promising. The model outputs could have been further improved with the inclusion of key landscape variables such as species composition and tree height. Both parameters could be acquired while utilizing available remote sensing techniques and models like Random Forest on multi-temporal high-resolution multi-spectral data. Further work will benefit greatly from the inclusion of these types of data.

ML models allow for efficient, high-resolution permafrost distribution mapping. Such models can be created and improved on a regional scale. Model outputs can be created for areas where data is available and checked/ corrected from local knowledge, borehole, and ground temperature data. The time required to make the checks and corrections will be significantly less than on-screen digitizing of a large area.

Permafrost distribution mapping is a specialized field with a handful of experts in the world. Permafrost distribution mapping on a fine scale is done manually based on field observations/data and experience. Capturing expert knowledge (to train data) and empirical data to produce relationships between key indicators and spatial variables can be accomplished using Bayesian networks (BN; Iqbal and MacLean 2010). BN, together with ML, is an avenue to be further explored for more efficient, high-resolution, large-scale mapping.

The use of SBTSs in completed boreholes is a simple, proven, useful, and cost-effective method to confirm the presence (or the absence) of permafrost at specific locations and depths within the discontinuous permafrost zone. The ground temperature data collected with SBTSs can be efficiently used for permafrost distribution mapping. SBTSs should be installed to a depth of at least 6 m below the ground surface (usually between 6 m and 10 m) to ensure the thermistor bead is located within permafrost, if present, i.e., below the base of the active layer. The use of SBTSs should be incorporated in every geotechnical drilling plan in the discontinuous permafrost zone, ideally with a SBTS installed in every borehole without a GTC.

5 CONCLUSIONS

Although the monitoring period of ground temperatures and permafrost extent in the Project Area is relatively short (seven years), the data collected allows improved assessment of baseline permafrost conditions, informs impact assessment, and facilitates identification of project effects.

The permafrost data collected and analyzed by Tetra Tech allowed for accurate mapping of permafrost distribution, showing that approximately 61% of the Project Area is underlain by warm, locally ice-rich, permafrost up to 165 m thick, with permafrost temperatures ranging from 0.0 °C to -2.1 °C at the depth of zero annual amplitude (between 15 m and 20 m).

The mapping process has been time-consuming, involving on-screen digitization using 3D visualisation software (PurVIEW). The ML model utilizing the terrain-derived outputs and training data from the manual permafrost mapping shows promising preliminary results. Model accuracy for the broader permafrost presence-absence map option, compared to the 8,000 ha already mapped was 58%. Further work will include additional data inputs to the model: multispectral data, vegetation species composition, and tree heights. This is expected to improve model accuracy. Regional scale ML models are also scheduled to be completed.

6 ACKNOWLEDGEMENTS

This paper is published with the approval of Newmont.

The authors are grateful for the interest and support for the permafrost studies at the Coffee Mine Project by the Project's previous owners (Kaminak and Goldcorp), the current owner (Newmont), and their colleagues at Tetra Tech, particularly Christian Roldan, James Scott, and Kevin Jones.

The authors are thankful for the thorough review of the draft paper and the comments provided by Rita Kors-Olthof and Dr. Hongwei Xia. Final review and formatting of the paper was completed by Jen Forbes.

The constructive comments received from both anonymous reviewers are gratefully acknowledged.

7 REFERENCES

AECOM Canada Ltd. 2012. *Geomorphological Mapping and Landscape Model Development for Strategic Soil Geochemical Sampling at the Coffee Gold Project, Yukon Territory*. Report prepared for Kaminak Gold Corporation, dated March 30, 2012.

Duk-Rodkin, A. 1999. 'Glacial Limits Map of Yukon Territory', *Geological Survey of Canada* Open File 3694, Indian and Northern Affairs Canada Geoscience Map 1999-2, Scale 1:1,000,000.

Heginbottom, J.A., Dubreuil, M.-A., and Harker, P.A. 1995. 'Canada, permafrost' in *National Atlas of Canada, 5th edition*. Natural Resources Canada, MCR Series 4177, scale 1:7,500,000. doi:10.4095/294672.

Huscroft, C.A. 2002. 'Surficial Geology, Coffee Creek, Yukon Territory (115J/14)', *Geological Survey of Canada* Open File 4344, Scale 1:50,000.

Iqbal, J. and MacLean, D.A. 2010. 'Prediction of balsam fir sawfly defoliation using Bayesian networks', *Canadian Journal of Forest Research* 40, pp. 2322–2332.

Kokelj, S.V. and Burn, C.R. 2005. 'Near-Surface Ground Ice in Sediments of the Mackenzie Delta, Northwest Territories, Canada', *Permafrost and Periglacial Processes* 16, pp. 291–303.

Lorax Environmental Services Ltd. 2016. 'Coffee Gold Feasibility Study: Appendix J2: Hydrogeology', *Kaminak Gold Corporation* Report prepared by Lorax Environmental Services Ltd., dated February 1, 2016.

Mathews, W.H. 1986. 'Physiography of the Canadian Cordillera', *Geological Survey of Canada* Map 1701A, scale 1:5,000,000.

McKenna, K.M. and Lipovsky, P.S. 2014. 'Surficial Geology, Dawson Region, Yukon: Parts of NTS 115014 & 15 and 116B/1, 2, 3 & 4', *Yukon Geological Survey* Open File 2014-12, Scale 1:25,000.

McKillop, R., Turner, D., Johnson, K., and Bond, J. 2013. 'Property-Scale Classification of Surficial Geology for Soil Geochemical Sampling in the Unglaciated Klondike Plateau, West-Central Yukon', *Yukon Geological Survey* Open File 2013-15, 85 p., including appendices.

Palmer Environmental Consulting Group (PECG) Inc. 2016. 'Terrain Stability and Hazard Mapping for the Coffee Gold Project'. PN 13103', *Kaminak Gold Corporation* prepared by Palmer Environmental Consulting Group, dated March 19, 2016.

Siewert, M.B. 2018. 'High-resolution digital mapping of soil organic carbon in permafrost terrain using machine learning: a case study in a sub-Arctic peatland environment', *Biogeosciences* 15, pp.1663–1682.

SRK Consulting (U.S.), Inc. 2016. '2015 Geotechnical Field Investigation, Coffee Gold Project, Yukon Territory, Canada', *Kaminak Gold Corporation* report prepared by SRK Consulting, dated January 4, 2016.

Tetra Tech EBA Inc. 2016a. 'Map of Permafrost Distribution along Proposed Kaminak Road Alignment (Issued for Use)', *Kaminak Gold Corporation*, dated April 28, 2016.

Tetra Tech EBA Inc. 2016b. 'Coffee Gold Project, Environmental Baseline Report (Issued for Use), Mine Site Study Area: Surficial Geology, Permafrost, and Terrain Stability', *Kaminak Gold Corporation*, dated May 2, 2016.

Tetra Tech EBA Inc. 2016c. 'Technical Memorandum No. 2 (Issued for Use – Revision 2): Permafrost and Related Geohazard Mapping within the Coffee Mine Site Study Area', *Kaminak Gold Corporation*, dated May 3, 2016.

Tetra Tech Canada Inc. and SRK Consulting (Canada) Inc. 2017. 'Fall 2016 Geotechnical Investigation Data Report (Issued for Use), Coffee Mine Site, Coffee Gold Project', *Goldcorp Inc.*, dated March 20, 2017.

Tetra Tech Canada Inc. 2017a. 'Summer 2017 Geotechnical Investigation Data Report, Coffee Mine Site, Coffee Gold Project', *JDS Energy & Mining Inc.*, November 2017.

Tetra Tech Canada Inc. 2017b. 'Fall 2017 Testpitting Program, Coffee Mine Site: Phase 1: Proposed Infrastructure Footprints; Phase 2: Proposed Open Pit Areas', *JDS Energy & Mining Inc.*, dated December 2017.

Tetra Tech Canada Inc. and SRK Consulting (Canada) Inc. 2019. '2018 Geotechnical Investigation Data Report (Issued for Review), Coffee Gold Project', *JDS Energy & Mining Inc.*, dated February 1, 2019.

Tetra Tech Canada Inc. 2019a. 'Fall 2018 Testpitting Program (Issued for Use), Coffee Gold Project', *JDS Energy & Mining Inc.*, dated January 9, 2019.

Tetra Tech Canada Inc. 2019b. 'Permafrost Distribution Mapping Update (Issued for Use), Coffee Mine Site Development Area, Coffee Gold Project', *JDS Energy & Mining Inc.*, dated April 9, 2019.

Tetra Tech Canada Inc. 2023. 'Ground Temperature Monitoring Update (Issued for Use), Coffee Mine Project, YT', *Newmont Canada*, dated August 16, 2023.

Williams, D.J. 1995. *Predicting the Location of Permafrost in Central Yukon Territory*. Unpublished MA Thesis, Carleton University, Ottawa, Ontario, Canada

Yukon Ecoregions Working Group. 2004. 'Klondike Plateau', in C.A.S. Smith, J.C. Meikle, and C.F. Roots (eds.) *Ecoregions of the Yukon Territory: Biophysical Properties of Yukon Landscapes*, Agriculture and Agri-Food Canada, PARC Technical Bulletin No. 04-01, Summerland, British Columbia, Canda, pp. 159–168.

A long term synthesis of permafrost ground temperature data along the Alaska Highway, Yukon, Canada

Louis-Philippe Roy, Frances Amyot, Casey Buchanan, & Fabrice Calmels

Permafrost and Geoscience Research Group, Yukon Research Centre, Yukon University, Whitehorse, Yukon, Canada

ABSTRACT

As a remote territory, the Yukon relies on the Alaska Highway as the only ground transportation route into the territory and Alaska, delivering food and other essential goods, connecting communities, and linking industries to international markets. Within the boundaries of the Yukon, the Alaska Highway is built on a wide variety of landscapes, including sporadic and extensive discontinuous permafrost, which has important impacts on the road conditions as it thaws. The North Alaska Highway, in particular, experiences ongoing permafrost thaw issues.

To assess changes in the thermal regime of permafrost along the northern stretch of the Alaska Highway, we use data from the seven longest running ground temperature monitoring sites from Burwash Landing to the Canada-US border from 2013–2022. Ground temperature increased at all sites over the study period except for the second most southern site (BH02). Ground temperature at the northern sites warmed faster than at the southern sites. This difference could be attributed to the presence of greater ice content at the southern sites relative to the northern sites, as well as warmer overall ground temperature regimes arising from more recent deglaciation at the southern sites. Warming air temperatures since the late 1960s are also likely to contribute to a general rise in ground temperature. Higher overall snow deposition in the Beaver Creek region likely contributes to the faster rate of ground temperature increase at the northern sites relative to the southern sites due to the insulating effects of snow. This study provides an important first look at permafrost conditions along the Northern Alaska Highway.

1 INTRODUCTION

The Alaska Highway serves as the primary transportation artery within the Yukon, playing a pivotal role in sustaining and fostering economic growth, enhancing the well-being of the population, and facilitating international connections. Considering current and expected climate change trends, there has been a significant increase in permafrost temperatures in northern regions (Osterkamp and Romanovsky 1999; Smith at al. 2010; Lewkowicz et al. 2012), and this warming trend is projected to continue (Osterkamp 2005; Christiansen et al. 2010). The integrity of transportation infrastructure in the North could be at risk due to permafrost changes, especially in regions where the soil contains substantial ice content. This could have adverse effects on economic development, including increasing the complexity and cost of road maintenance, as well as increasing the costs of transporting goods across these northern regions.

Since its construction, the section of the Alaska Highway between Burwash Landing and the Canada-US border has experienced ongoing permafrost thaw issues. This has become a significant challenge for residents and travellers of this area who rely on dependable access to transportation infrastructure to support their livelihoods.

Understanding the distribution and dynamics of permafrost is crucial when designing infrastructure in permafrost regions, including extensive linear projects like pipelines and highways. In the 1970s, substantial data were gathered to characterize subsurface conditions in support of a proposed gas pipeline venture along the Alaska Highway Corridor. The Geological Survey of Canada conducted ground temperature measurements in a set of boreholes between 1978 and 1981 to assess ground thermal regime (Burgess et al. 1982). Since then, there has been a lack of

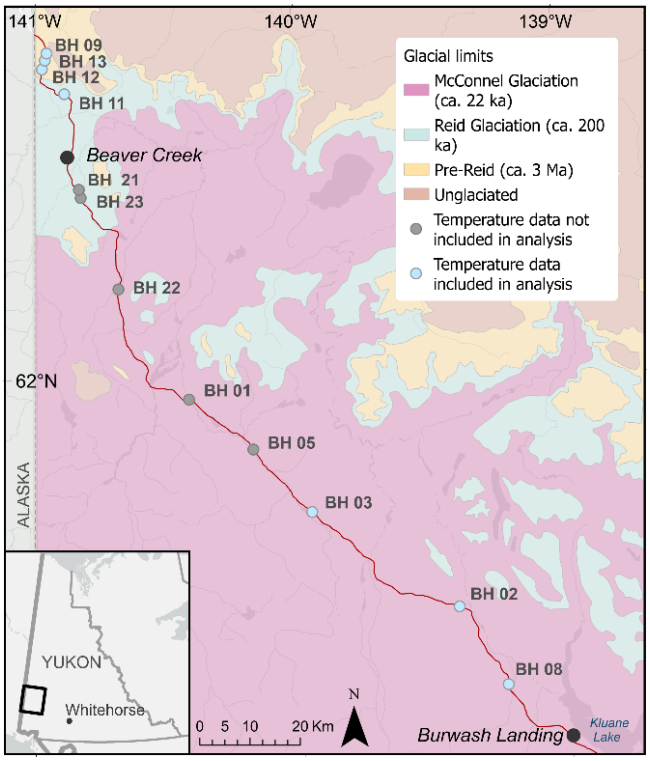

Figure 1. Ground temperature monitoring stations and glacial limits (Duk-Rodkin, 1999; Yukon Geological Survey, 2020) along the Northern Alaska Highway.

https://doi.org/10.52381/ICOP2024.139.1

data along this corridor. The need to develop strategies to adapt the current highway infrastructure has renewed the interest for updated information regarding the permafrost conditions and how they are changing over time.

In 2013, Yukon University's Permafrost and Geoscience Research Group (PGR) partnered with the Yukon Government's Highways and Public Works (HPW) to evaluate the susceptibility of the Alaska Highway to permafrost thaw along a 200-km stretch between Burwash Landing and the Canada-US border. The installation of an array of ground temperature stations dedicated to long-term data collection in areas of concern along this problematic section of the highway served to monitor its thermal stability. In total, 25 stations were installed within a 3–4-year span, with records spanning 10 years (2013–2023).

This paper presents a selection of sites that contain the most complete records since 2013 from Burwash Landing, northwest of Haines Junction and Beaver Creek at the Canada-US border. We take a first look at the most prevalent ground temperature patterns and behavior along the highway since 2013 and compare these behaviors with local environmental conditions, such as snow cover and mean annual air temperature. These key parameters are used to describe the permafrost-climate relationship (Smith and Riseborough 1996, 2002) and help to better understand the variation in ground temperatures over time.

1.2 Study Sites

The section of the Alaska Highway being studied spans from 61°45'N to 62°37'N latitude; between Burwash Landing and the Canada-US border on the traditional territories of White River First Nation and Kluane First Nation.

This region falls within the Cordilleran Orogeny, encompassing diverse mountain ranges with elevations ranging from 250 m above sea level (masl) along the Yukon River to surpassing 5000 masl in the St. Elias Mountains. The Alaska Highway traverses a heterogeneous terrain with a wide spectrum of soil surface deposits, ranging from very fine sediments to considerably coarser materials like gravel, pebbles, and cobbles. These deposits have varying origins, including glacial deposits dating from the Pliocene to the Early Pleistocene, postglacial deposits from the late Pleistocene, and more recent Holocene deposits.

This section of the Alaska Highway transects the sporadic, discontinuous, and continuous permafrost zones (Figure 1), where it is often underlain by ice-rich and thaw-sensitive permafrost (Calmels et al. 2015, 2016, 2021, 2022).This region is characterized by warm permafrost, where ground temperatures hover around 0 °C. The current thermal conditions of the permafrost are a culmination of historical climatic conditions, construction activities, and alterations in surface conditions. The prevailing climate in this area is primarily subarctic continental, with slight variations based on elevation and the orientation of mountain slopes. Winters tend to be prolonged and frigid, while summers are brief and warm. Precipitation is limited throughout the year, with an annual total of 417 mm in Beaver Creek and 274 mm in Burwash Landing (Environment Canada 2023a,b) over a thirty-year average (1981–2010).

1.2.1 Site descriptions

In total, seven sites were selected due to the consistency and quality of the ground temperature data since 2013. Three sites, referred to as the 'southern sites', were chosen closer to Burwash Landing (BH08, BH02 and BH03), and four sites, referred to as the 'northern sites', were chosen North of Beaver Creek (BH11a, BH12, BH13 and BH09). These boreholes were drilled and instrumented during the summers of 2012 and 2013 in collaboration with Highways and Public Works (HPW; Calmels et al. 2015).

1.2.1.1 BH08 – KM 1719.1

This site was drilled in organic fluvial sediments. The ground is covered by thick moss and surrounded by an open white spruce forest. The borehole was drilled to a depth of 3.48 m. The cores showed ice volume content as high as 59%, with lenticular cryostructure for the full length of the profile. The sediment was composed mostly of silty sand and the amount of coarse material increased with depth.

1.2.1.2 BH02 – KM 1738.7

BH02 is located on the bank of a thermokarst pond in organic deposits. The borehole was drilled to a depth of 4.27 m. The presence of organic cover (moss and peat) has promoted the growth of ice-rich permafrost. The samples showed excess ice content as high as 45%. Lenticular cryostructures, with thicknesses ranging from 1 cm to 1 dm, consistently occurred along the profile. The sediment was composed mainly of silty sand with gravel.

1.2.1.3 BH03 – KM 1776.1

BH03 is located in fluvial deposits. Sediments ranged from silt to gravel and overlie morainic and drift material. The borehole was drilled to a depth of 4.75 m where it reached groundwater from surrounding thermokarst lakes. Consequently, the base of this borehole remains unfrozen throughout the year. Here the organic cover is thin, and vegetation is sparse. The cores showed water content as high as 76% and excess ice content around 50%. Lenticular cryostructures, from 1 mm to 10mm thick, consistently occur along the vertical profile.

1.2.1.4 BH11a – KM 1886

Unlike the previous sites, this section of the road was not glaciated during the McConnell glaciation, but during the Reid glaciation (Figure 1). BH11a is located on a frost mound near a thermokarst lake. The borehole was drilled to 8.5 m. The soil stratigraphy alternated between layers of sandy silt and silty sand and the excess ice content remained high in both types of materials. The ice content reached a maximum of 85% in the silty sand layers.

1.2.1.5 BH12 – KM 1894.8, BH13 – KM 1896.3, BH09 – KM 1897.8

These sites were glaciated during the pre-Reid glaciation and have since remained unglaciated (Figure 1). BH12 is located in a valley bottom within fluvial deposits. BH13 and

BH09 are located in organic and colluvium deposits, respectively. BH12 was drilled to a depth of 9.5 m and showed an average excess ice content of 70%. In 2014, HPW dug an intercepting ditch along the highway at this location. This triggered thermal erosion near this site where a small stream intersected the ditch. BH13 was drilled to 13 m. The amount of coarse material decreased with depth and the excess ice content ranged from 63 to 99%. BH09 is located in a dense white spruce forest with a thick moss cover. The borehole was drilled to a depth of 5.44 m. The cores showed ice volume content as high as 73%, with lenticular ice toward the bottom of the profile. The sediment was mostly composed of sandy silts.

1.2.2 Glacial History

The Yukon boasts one of North America's most ancient and intricate glacial histories, which has been extensively detailed in Duk-Rodkin (2004) and Duk-Rodkin et al. (2004). Notably, the Alaska, Klondike, and Dempster highways traverse regions featuring both glaciated and unglaciated terrain. A significant portion of the Alaska Highway is constructed in areas that were glaciated during the McConnell glaciation, approximately 22,000 years ago, with the glacial boundary situated around kilometer 1854 (Duk-Rodkin 1999; Yukon Geological Survey 2020) which includes BH08, BH02 and BH03 (Figure 1). The area between kilometer 1854 and km 1893 (BH11a) was glaciated during the Reid Glaciation (200 ka), and the area from km 1893 to beyond the Canada-US border (BH12, BH13, BH09) was glaciated during the Pre-Reid Glaciation (3 Ma; Figure 1; Duk-Rodkin 1999; Yukon Geological Survey 2020).

This diverse glacial history offers valuable insights into permafrost conditions along the road network. In regions that underwent glaciation during the McConnell glaciation, permafrost tends to be relatively shallow (less than 20 m) and relatively warm (above -2 °C), potentially containing ice-rich layers near the surface. In contrast, unglaciated terrains harbor older, thicker, and colder permafrost, often with significant ice content of varying origins extending from the near surface to depths of tens of meters. Transition zones lying between glacial boundaries are areas where the presence of buried massive ice remains a possibility.

2 METHODS

Because of the complexity of this area, multiple sources of data were used to interpret current permafrost vulnerability and to anticipate future permafrost thermal conditions. Geophysical data, existing geotechnical reports, HPW maintenance records, surficial geology maps, and other available information were combined with field investigation and laboratory soil testing to investigate the thaw sensitivity of the permafrost that underlies the highway.

The site investigations, drilling methodologies and geotechnical data are described in Calmels et al. (2015).

2.1 Ground Temperature

2.1.1 Ground Temperature Logger Installation

Each ground temperature station consists of a down-hole PVC conduit, in which a cluster of thermistor strings is suspended. Each pipe was filled with silicone oil to allow for heat conduction from the ground to the thermistors, while preventing vertical air circulation. The depth of each thermistor was chosen based on borehole depth, prior knowledge about the depth of permafrost, and proximity to ground surface. However, to maximize consistency, thermistor depths are usually set to 0 m and 0.5 m, and then at 1.0 m intervals to 12 m base depth. The thermistor strings are connected to a HOBO UX-120 (resolution of 0.03 °C at 20 °C) or a Campbell Scientific weather station equipped with a CR1000 datalogger (YSI44033 thermistors; resolution of ± 0.05 °C) and set to record temperature at each depth every two hours. Some stations are equipped with a HOBO UA-002-64 (resolution of 0.14 °C at 25 °C) to record the temperature at ground level. The logger batteries provided approximately a year of logging, though the batteries were replaced earlier to avoid data gaps. The Campbell Scientific weather stations are fully autonomous and are set to record data with minimum maintenance for multiple years.

2.2.2 Ground Temperature Processing and Analysis

Sites presented in this paper were chosen for having the longest records and minimal time gaps. Monthly averages of ground temperature were calculated for each sensor depth at each site. Prior to calculation, erroneous values and large time gaps were removed. This was accomplished by identifying extreme outliers (e.g., > 100 °C), which result from a faulty connection or wire, and outliers that, while physically possible, were unrealistic given known behavior of ground temperature in permafrost regions. Outlier filtering was visually assisted by analyzing the residuals of a symmetrical moving average with a 60-day window size. Following outlier filtering, linear interpolations were constructed for record gaps smaller than two weeks. Months with a gap greater than two weeks, herein referred to as ‘large time gaps’, were not used in further statistical analysis.

Linear regressions of monthly average temperature over time were computed and significance was determined at a 95% confidence interval. For sites that did not display a significant change in ground temperature, an average temperature was calculated for the entire study period. For sites with significant temperature changes, the change was calculated by taking the difference between the average temperature of the first three full years and average of the last three full years.

2.3 Environmental conditions

To better understand regional climatic conditions and their relationship to permafrost conditions, environmental conditions such as air temperature and snow depth were analyzed.

2.3.1 Air Temperature Processing and Analysis

2.3.1.1 Beaver Creek and Burwash Landing

Air temperature data for Beaver Creek and Burwash Landing were downloaded from Environment Canada using the weathercan package (LaZerte and Albers 2018) in R. Air temperature measurements were available from 1966–2023 in Beaver Creek, and from 1968–2023 in Burwash Landing. However, many years needed to be removed from the dataset due to missing measurements. If more than ten days were missing in a month, the year was excluded from the dataset. If less than ten days were missing, they were estimated using a linear interpolation according to World Meteorological Organization (WMO) standards (2017).

2.3.1.2 Koidern and BH12

Air temperature data were available for Koidern and BH12 from Campbell Scientific weather stations from 2013–2022. Any erroneous data points (e.g., > 100 °C) were removed from the dataset, and no linear interpolations were required. Mean daily air temperature data were computed from hourly air temperature measurements.

2.3.1.3 Mean Annual Air Temperature

To better understand trends in regional climate, and potential impacts on permafrost, mean annual air temperature (MAAT) values were calculated from mean daily temperatures for Burwash Landing, Beaver Creek, Koidern, and BH12. Normal values were computed using 15-year periods instead of 30-year periods to account for the data gaps (WMO 2017).

2.3.2 Snow Depth Processing and Analysis

Snow depth data were downloaded from the Government of Yukon (2020) Water Data Catalogue. One snowpack depth measurement was recorded per month from January-April for each year from 1975–2023. Any years with unrealistic data (e.g., 0 cm) were removed from the dataset. To better understand trends in regional snowpack, and potential impacts on permafrost, yearly maximum snowpack depths in Beaver Creek and Burwash Landing were computed.

3 RESULTS

3.1 Ground Temperature

In general, ground temperature increased over the course of the study period for all depths, and the magnitude of these temperature increases over time decreased with depth at each site. Temperature changes at 0.5 m depth, however, were usually insignificant ($p > 0.05$). These findings are presented in greater detail in the following sections.

3.1.1 BH02

BH02 ground temperature data were recorded at depths of 0.5 m, 2.0 m, and 4.27 m. Available data range between 2013-07-20 and 2023-06-24, with large time gaps from 2017-09-10 to 2018-10-17 and from 2021-08-24 to 2021-09-28. Average ground temperatures over the study period were -1.01 °C, -1.07 °C, and -0.79 °C, respectively. No significant temperature increases or decreases were observed at any of the depths.

3.1.2 BH03

BH03 ground temperature data were recorded at 0.5 m and 3.0 m depths. Available data range from 2013-07-20 to 2023-06-24 with no major gaps. Ground temperature at 6.0 m depth was not used as the basal depth because warm temperatures (~0.5 °C) indicated permafrost never existed at this depth during the study period. Temperature at 0.5 m depth remained steady at an average of -0.55 °C, while temperature increased significantly from -0.31 to -0.19 °C (+0.12 °C) at 3.0 m depth.

3.1.3 BH08

BH08 ground temperature data were recorded at 0.5 m, 2.0 m, and 3.44 m depths. Available data range from July 27, 2013 to June 22, 2023 with no major time gaps. Ground temperature increased significantly for 0.5 and 3.44 m depths from -1.64 to -0.95 °C (+0.69 °C) and from -1.55 to -1.25 °C (+0.29 °C), respectively. Temperature increased with marginal significance ($p = 0.06$) at 2.0 m from -1.51 to -1.14 °C (+0.37 °C).

3.1.4 BH09

BH09 ground temperature data were recorded at 0.5, 3.0, and 5.44 m depths between 2013-07-21 and 2023-06-20 with no major gaps. Average temperature at 0.5 m remained steady at an average of -1.28 °C with no significant change. Temperatures increased significantly from -1.13 to -0.8 6°C (+0.28 °C) and from -1.16 to -0.96 °C (+0.20 °C) for 3 m and 5.44 m, respectively.

3.1.5 BH11a

BH11a ground temperature data were recorded at depths of 0.5, 3.0, 8.5 m between 2013-10-09 and 2023-06-20 with no major gaps. Mean monthly temperature remained steady at -1.23 °C over the study period at 0.5 m. Significant temperature increases from -1.92 to -1.63 °C (+0.29 °C) and from -1.54 to -1.34 °C (+0.2 °C) were observed for 3.0 m and 8.5 m, respectively.

3.1.6 BH12

BH12 ground temperature data were recorded at depths of 0.5, 3.0, and 9.5 m between 2013-08-04 and 2022-09-28 with no major gaps. Temperature at 0.5 m remained steady at an average of -0.11 °C over the study period.

Temperature increased significantly from -3.16 to -1.30 °C (+1.86 °C) at 3.0 m depth. Temperature change at 9.5 m depth in BH12 was divided into two periods: the first spanning between the beginning of the study period and 2017-12-05; and the second spanning between 2017-12-05 and the end of the study period. During period one, a small but significant temperature increase from -3.17 to -3.06 °C (+0.11 °C) was observed. For this calculation only two averages—one for 2014 and one for 2016—were computed to avoid overlap between the years being averaged. During period two, a larger significant increase of -2.05 to -0.54 °C (+1.51 °C) was observed. To avoid overlapping of years being averaged, only 2018 and 2019 were averaged for the start temperature, and 2020 and 2021 averaged for the end temperature. The total temperature increase over the study period at 9.5 m depth was therefore 1.62 °C. Ground temperature increase at BH12 is anomalously higher than at other sites.

3.1.7 BH13

BH13 ground temperature data were recorded at depths of 0.5, 3.0, 13.2 m between 2013-10-09 and 2023-06-20 with no major gaps. Temperature remained constant at 0.5 m depth at an average of -1.59 °C over the study period. Significant temperature increases of -2.32 to -2.00 °C (+0.31 °C) and -1.97 to -1.85 °C (+0.12 °C) were observed at 3.0 m and 13.2 m, respectively.

3.8 Environmental Conditions

3.8.1 Mean Annual Air Temperature

3.8.1.1 Burwash Landing

MAAT was computed from 1967–2022 in Burwash Landing after removing incomplete years (1966, 1987, 2001, 2002, 2005, 2008–2013, 2023), and is presented in Figure 2. Overall, MAAT shows a slight but significant increase over time (r^2 = 0.19, $p < 0.05$), from a mean of -4.5 °C in 1967–1981 to -2.9 °C in 1999–2022.1976 appeared to be an unusually cold year in Burwash Landing (MAAT -10.8 °C), that seemed to be driven by a cold winter, followed by a very mild summer, with few days reaching 19 °C (maximum daily mean temperature). Removing this value had no impact on the significance or strength of the relationship.

3.8.1.2 Beaver Creek

MAAT was computed from 1969–2022 in Beaver Creek after removing incomplete years (1978–1979, 1981–1983, 1989, 2002, 2003, 2006–2014, 2017, 2023), and is presented in Figure 2. MAAT shows a slight but significant increase in MAAT over time (r^2 = 0.34, $p < 0.05$), from a mean of -5.8 °C in 1967–1990 to -4.6 in 1996–2022.

3.8.1.3 Koidern

MAAT was computed from 2014–2021 for Koidern after removing incomplete years (2013, 2022). MAAT (3) shows an insignificant downward trend.

3.8.1.4 BH12

MAAT was computed from 2014–2021 for BH12 after removing incomplete years (2013, 2022). MAAT (Figure 3) shows an insignificant downward trend.

3.8.2 Snow Depth

3.8.2.1 Burwash Landing

Maximum annual snow depths from 1975–2023 in Burwash Landing are shown in Figure 4. There are no significant trends across the dataset, however, when the data are subset from 2014–2023, there is a strong positive correlation (r^2 = 0.88, $p < 0.05$) between snow depth and time.

3.8.2.1 Beaver Creek

Maximum annual snow depths from 1975–2023 in Beaver Creek are shown in Figure 4. Snow depths are increasing slightly across the dataset (r^2 = 0.14, $p < 0.05$), however, when the data are subset from 2014–2023, there is a positive correlation (r^2 = 0.54, $p < 0.05$) between snow depth and time.

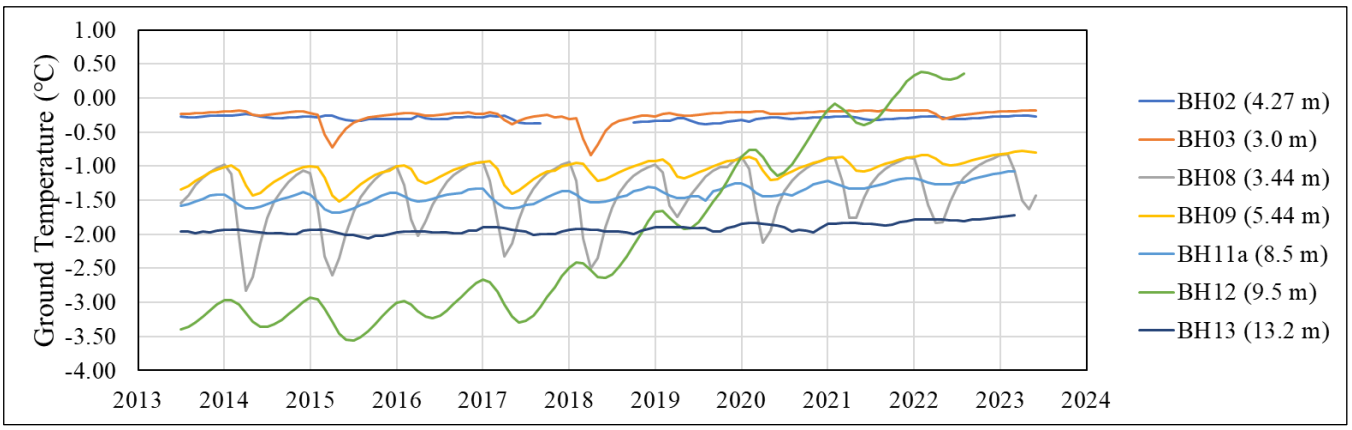

Figure 2. Time series of ground temperature at basal depths.

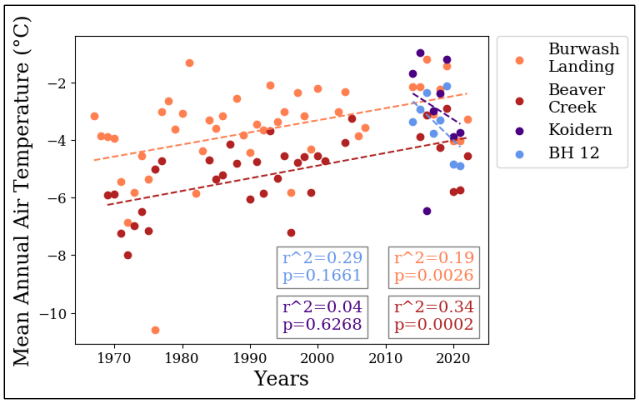

Figure 3. Mean Annual Air Temperature (°C) for Burwash Landing, Beaver Creek, Koidern and BH12.

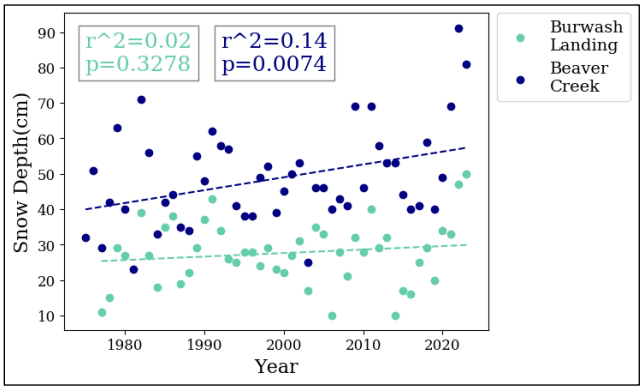

Figure 4. Maximum annual snow depth (cm) for Burwash Landing and Beaver Creek.

4 DISCUSSION

All sites except BH02 show a significant increase in permafrost temperatures since 2014. BH12 shows a much higher increase in ground temperature since 2014 (1.86 °C at 3.0 m and 1.62 °C at max depth) than any other site (0.22 °C at 3.0 m and 0.18 °C at max depth across all sites). This was likely due to the thermal erosion caused by the drainage ditch described in Section 1.2.1.5. As such, this site was considered an outlier and was omitted from overall trend analyses.

To compare temperature increases across all of the sites, values at 3.0 m are used to account for the boreholes at the southern sites being shallower than those at northern sites. When computed without BH12, temperatures at 3 m have increased by 0.3 °C for the northern sites, compared to 0.14 °C for the southern sites.

The base of the northern boreholes is deeper than the southern ones, so the base depth is more likely to be closer to the depth of zero annual amplitude (DZAA), providing a clearer picture of permafrost conditions. The mean basal temperature across all northern sites (except BH12) has increased by 0.17 °C since 2014. This is within the range reported by Smith et al. (2022) who described warm permafrost in subarctic regions warming at a rate of 0.3 °C/decade at the DZAA.

Several factors could account for the more pronounced warming observed in the northern sites compared to their southern counterparts. To begin with, the glacial histories of these regions play a role in shaping the nature and distribution of ground ice within the permafrost. In particular, the southern section experienced deglaciation more recently during the McConnell Glaciation, while the northern section went through deglaciation during the Reid and pre-Reid Glaciations (Figure 1), which occurred earlier. This temporal difference in deglaciation leads to the formation of younger, and consequently, warmer epigenetic permafrost in the southern sites.

Given this genesis, the southern sites tend to exhibit a higher prevalence of segregated ice, often associated with ice-rich permafrost. It is worth noting that increases in permafrost temperatures have generally been smaller in warmer permafrost regions that hover around the freezing point, particularly in areas with ice-rich fine-grained materials. As permafrost temperatures approach 0 °C, ground ice undergoes a phase change, melting over a range of sub-zero temperatures (Smith et al. 2022). This phase change requires the input of latent heat, which results in a lower apparent thermal diffusivity and less energy directed toward elevating ground temperatures. This could explain why the smallest temperature increase was observed at BH02, a site characterized by its extremely high ice content and the presence of thick ice lenses.

The opposite is true for the northern sites, which were glaciated during the Reid and pre-Reid glaciations, resulting in permafrost that is both older and colder than the southern sites due to longer exposure to cold climate. These areas typically have lower levels of unfrozen water content, which in turn result in a higher thermal conductivity (Williams and Smith 1989). When temperatures are colder, energy is mostly spent on warming permafrost and not on melting ground ice (Williams and Smith 1989). As temperatures approach 0 °C in these northern sites, the rate at which ground temperature increases should decelerate due to the increase in unfrozen water content.

Environmental conditions such as air temperature and precipitation are known to impact permafrost conditions and stability (Shur and Jorgenson 2007; Smith et al. 2022; Stieglitz et al. 2003). The significant increases in MAAT since the late 1960s in Beaver Creek and Burwash Landing are likely to contribute to the warming of permafrost. Air temperatures, like ground temperatures, are colder in Beaver Creek than in Burwash Landing, and are also rising more rapidly. Though recent trends in air temperature (BH12 and Koidern) suggest a decrease in MAAT, they are insignificant ($p > 0.05$), and mirror insignificant decreases in MAAT in parallel subsets (2013–2022) from Beaver Creek and Burwash Landing. Without additional data, Koidern and BH12 should be considered within the broader context of MAAT since the 1960s in Burwash Landing and Beaver Creek.

Even though total precipitation values were unavailable for Beaver Creek or Burwash Landing, maximum snow depth data provide insight into the potential role of precipitation on permafrost, since snow cover acts as a highly efficient

insulator on the ground and limits the extraction of heat from the ground in the winter (Goodrich 1982; Williams and Smith 1989; Smith and Riseborough 2002; Ishikawa 2003). Beaver Creek experiences approximately twice the amount of snow as Burwash Landing, which could partially explain why ground temperatures are increasing more, especially in recent years as snow depth is significantly increasing.

Limitations to our study exist, including incomplete datasets (e.g., precipitation), inconsistent thermistor string depths, limited borehole depths, and faulty sensors. Recent upgrades to our infrastructure will allow for more complete analyses in future studies.

5 CONCLUSIONS

This study takes a first look at ground temperature profiles collected by PGR along the Alaska Highway from kilometer 1719 to kilometer 1897 between 2013 and 2022. We found that ground temperature increased at all sites over the study period except for the second most southern site (BH02). This is consistent with previous studies in the subarctic. Furthermore, ground temperature at the northern sites warmed faster than at the southern sites. This difference could be attributed to the presence of greater ice content at the southern sites relative to the northern sites, as well as warmer overall ground temperature regimes arising from more recent deglaciation at the southern sites. Warming air temperature since the late 1960s could also have been an important driver to a general rise in ground temperature. Higher overall snow deposition in the Beaver Creek region likely contributed to the faster rate of ground temperature increase at the northern sites relative to the southern sites due to insulating effects.

Future work could include more in-depth analyses on the relationships between multiple variables such as ice content, vertical ground ice distribution, snowpack depth and timing, temperature at top of permafrost (TTOP), mean annual ground surface temperature (MAGST), active layer thickness (ALT), and DZAA, which were outside the scope of this study.

6 ACKNOWLEDGEMENTS

The authors would like to acknowledge that this work was conducted on the Traditional Territories of the White River First Nation and Kluane First Nation. We would like to thank all the participants in this project for their enthusiasm and commitment. We would like to express our appreciation to the Government of Yukon's Highways and Public Works and the Transportation and Engineering Branch, Transport Canada, White River First Nation, Kluane First Nation, Duane Froese (University of Alberta), Joel Pumple (University of Alberta), Cyrielle Laurent (Yukon University), Cathy Koot (Yukon University), Philip Sedore (Yukon University) and all the field assistants who helped support this project throughout the years.

Funding for this project was provided by Crown-Indigenous Relations and Northern Affairs Canada, Government of Canada (National Trade Corridors Funds), Bank of Montreal (BMO) and ArcticNet's North-by-North Program.

7 REFERENCES

Burgess, M.M., Judge, A.S., and Taylor, A.E. 1982. 'Yukon Ground Temperature Data Collection 1966 to August 1981', *Earth Physics Branch, Energy, Mines and Resources Canada* Open File 82-1.

Calmels, F., Allard, M., Fortier, D., Amyot, F., L'Hérault, E., Sliger, M., Roy, L.P., Laurent, C., and Gauthier, S. 2022. 'Design and implementation of early detection and warning systems for transportation infrastructure impacted by permafrost-related geohazards', YukonU Research Centre, Yukon University, p. 203. Available at: https://www.yukonu.ca/sites/default/files/inline-files/NTAI%20Alarm%20Report%20FC%2001-31%20Standard.pdf.

Calmels, F., Dore, G., Kong, X., Roy, L. P., Lemieux, C., and Horton, B. 2016. 'Vulnerability of the north Alaska Highway to permafrost thaw: Design options and climate adaptation', *Yukon Research Centre, Yukon College*. Available at: https://bpb-ca-c1.wpmucdn.com/scholar.yukonu.ca/dist/8/7/files/2022/12/Vulnerability-of-the-north-Alaska-Highway-to-permafrost-thaw-Design-options-and-climate-change-adaptation.pdf.

Calmels, F., Roy, L.P., Laurent, C., Allard, M., Kinnear, L., Benkert, B., Horton, B., and Pumple, J. 2015. 'Vulnerability of the North Alaska Highway to permafrost thaw: A field guide and data synthesis', *YukonU Research Centre, Yukon University*, p. 121. Available at: https://www.yukonu.ca/sites/default/files/inline-files/permafrost_report.pdf.

Calmels, F., Roy, L.P., Laurent, C., Amyot, F., Cubley, J., and Lipovsky, P. 2021. 'Assessment and monitoring of a new retrogressive thaw slump at km 1456 of the Alaska Highway: A rare opportunity', *YukonU Research Centre, Yukon University*, p. 72. Available at: https://www.yukonu.ca/sites/default/files/inline-files/PGR_2021_01_Tak_Slump_NTAI_0.pdf.

Christiansen, H.H., Etzelmüller, B., Isaksen, K., Juliussen, H., Farbrot, H., Humlum, O., Johansson, M., Ingeman-Nielsen, T., Kristensen, L., Hjort, J., Holmlund, P., Sannel, A.B.K., Sigsgaard, C., Åkerman, H.J., Foged, N., Blikra, L.H., Pernosky, M.A., and Ødegård R. 2010. 'The thermal state of permafrost in the Nordic area during IPY 2007–2009', *Permafrost and Periglacial Processes* 21, pp. 156–181. doi:10.1002/ppp.687.

Duk-Rodkin, A. 1999. 'Glacial Limits Map of Yukon', *Geological Survey of Canada* Open File 3694, scale 1:1,000,000.

Duk-Rodkin, A. 2004. 'Glacial history', in C.A.S. Smith, J.C. Meikle and C.F. Roots (eds.), *Ecoregions of the Yukon Territory: Biophysical properties of Yukon Landscapes*. Summerland, British Columbia, Canada: Agriculture and Agri-Food Canada, PARC Technical Bulletin 04-01, pp. 24–31.

Duk-Rodkin, A., Barendregt, R.W., Froese, D.G., Weber, F., Enkin, R., Smith, I. R., Zazula, G.D., Waters, P., and Klassen, R. 2004. 'Timing and extent of Plio-Pleistocene glaciations in north-western Canada and east-central Alaska', in J. Ehlers and P.L. Gibbard (eds.), *Developments in Quaternary Sciences, Quaternary Glaciations-Extent and Chronology Part II: North America*. Elsevier, pp. 313–345.

Environment Canada 2023a. *Canadian Climate Normals 1981-2010 Station Data: Beaver Creek, Yukon*. Available at : https://climate.weather.gc.ca/climate_normals/results_1981_2010_e.html?searchType=stnProv&lstProvince=YT&txtCentralLatMin=0&txtCentralLatSec=0&txtCentralLongMin=0&txtCentralLongSec=0&stnID=1518&dispBack=0.

Environment Canada 2023b. *Canadian Climate Normals 1981–2010 Station Data: Burwash Landing, Yukon*. Available at : https://climate.weather.gc.ca/climate_normals/results_1981_2010_e.html?searchType=stnProv&lstProvince=YT&txtCentralLatMin=0&txtCentralLatSec=0&txtCentralLongMin=0&txtCentralLongSec=0&stnID=1525&dispBack=0.

Goodrich, L.E. 1982. 'The influence of snow cover on the ground thermal regime', *Canadian Geotechnical Journal* 19(4), pp. 421–432. doi:10.1139/t82-047.

Government of Yukon 2020. *Yukon Water Data Catalogue*. Available at: https://open.yukon.ca/data/datasets/water-data-catalogue?gad_source=1&gclid=Cj0KCQjwwYSwBhDcARIsAOyL0fgqo3EZ7UoOu0RGs_-dK0CQqztFOjgj6HQTlGW-gbumm0Tuygd_628aAhE8EALw_wcB.

Ishikawa, M. 2003. 'Thermal regimes at the snow–ground interface and their implications for permafrost investigation, *Geomorphology* 52(1–2), pp. 105–120. doi:10.1016/S0169-555X(02)00251-9.

LaZerte, S.E. and Albers, S. 2018. weathercan: Download and format weather data from Environment and Climate Change Canada', J*ournal of Open Source Software* 3(22), 571. doi:10.21105/joss.00571.

Lewkowicz, A.G., Bonnaventure, P.P., Smith, S.L., and Kuntz, Z. 2012. 'Spatial and thermal characteristics of mountain permafrost, Northwest Canada', *Geografiska Annaler: Series A, Physical Geography* 94(2), pp. 195–213. doi:10.1111/j.1468-0459.2012.00462.x.

Osterkamp, T.E. and Romanovsky, V.E. 1999. 'Evidence for Warming and Thawing of Discontinuous Permafrost in Alaska', *Permafrost and Periglacial Processes* 10, pp. 17–37. doi:10.1002/(SICI)1099-1530(199901/03)10:1<17::AID-PPP303>3.0.CO;2-4.

Osterkamp, T.E. 2005. 'The recent warming of permafrost in Alaska', *Global and Planetary Change* 49, pp. 187–202. doi:10.1016/j.gloplacha.2005.09.001.

Shur, Y.L. and Jorgenson, M.T. 2007. 'Patterns of permafrost formation and degradation in relation to climate and ecosystems', *Permafrost Periglacial Processes*, 18(1), pp. 7–19. doi:10.1002/ppp.582.

Smith, M.W. and Riseborough, D.W. 1996. 'Permafrost monitoring and detection of climate change', *Permafrost and Periglacial Processes* 7(4), pp. 301–309. doi:10.1002/(SICI)1099-1530(199610)7:4<301::AID-PPP231>3.0.CO;2-R.

Smith, M.W. and Riseborough, D.W. 2002. 'Climate and the limits of permafrost: a zonal analysis', *Permafrost and Periglacial Processes* 13(1), pp. 1–15. doi:10.1002/ppp.410.

Smith, S.L., Romanovsky, V.E., Lewkowicz, A.G., Burn, C.R., Allard, M., Clow, G.D., Yoshikawa, K., and Throop, J. 2010. 'Thermal state of permafrost in North America – A contribution to the International Polar Year', *Permafrost and Periglacial Processes* 21(2), pp. 117–135. doi:10.1002/ppp.690.

Smith, S.L. and Riseborough, D.W. 2010. 'Modelling the thermal response of permafrost terrain to right-of-way disturbance and climate warming', *Cold Regions Science and Technology* 60(1), pp. 92–103. doi:10.1016/j.coldregions.2009.08.009.

Smith, S.L., O'Neill, H.B., Isaksen, K., Noetzli, J., Romanovsky, V.E. 2022. 'The changing thermal state of permafrost', *Nature Reviews Earth & Environment 3*, pp. 10–23. doi:10.1038/s43017-021-00240-1.

Stieglitz, M., Déry, S.J., Romanovsky, V.E., and Osterkamp, T.E. 2003. 'The role of snow cover in the warming of arctic permafrost', *Geophysical Research Letters*, 30(13). doi:10.1029/2003GL017337.

Williams, P.J. and Smith, M.W. 1989. 'The frozen earth: Fundamentals of geocryology', *Soil Science* 154(4), 336.

World Meteorological Organization 2017. *WMO Guidelines on the Calculation of Climate Normals.* Available at: https://library.wmo.int.

Yukon Geological Survey 2020. Yukon *Glacial Limits*. Available at: https://data.geology.gov.yk.ca/Compilation/29#InfoTab.

Increases in highway maintenance costs in a permafrost environment undergoing climate change, Yukon, Canada

Astrid B. Schetselaar & Christopher R. Burn

Department of Geography and Environmental Studies, Carleton University, Ottawa, Ontario, Canada

ABSTRACT

Assessment of infrastructure vulnerability to climate change in permafrost environments has emphasized increases in ground temperature, deepening of the active layer, and differential settlement. Hydrological factors are less emphasized. Yukon's Transportation Maintenance Database records expenses for 61 activities on the 21 maintenance sections of the territorial highway network. The costs associated with snow clearing, icing control, washout repair, and landslide removal have been examined from April 1994 to March 2022. These are directly related to climate and are primarily associated with hydrologic processes. For Yukon's entire highway network, climate-related maintenance expenditures have increased by $169,000 per year (in constant 2021 CA$) since 1994. Topography, surficial deposits, permafrost, and climate create specific sub-regional financial responses to a changing environment. For example, snow clearing expenditures are greatest for highways in the Coast Mountains region (now over $600,000 per year), icing control expenditures dominate on the Silver Trail in the discontinuous permafrost zone (over $250,000 annually), while intermittent clearing of landslides and repair of washouts are greatest for the Ogilvie section of the Dempster Highway in steeply sloping terrain and continuous permafrost ($825,000 in 2013). This paper presents expenditure profiles for seven representative maintenance camps in distinct physiographic and permafrost environments within the highway network.

1 INTRODUCTION

In Canada, Yukon and Mackenzie Valley have experienced the greatest recent increases in air temperatures (Vincent et al. 2015). Long-term trends in precipitation are not as clear, but rain is replacing snowfall in the shoulder seasons (Vincent et al. 2015). These changes will likely continue for the next several decades, at least (Bush and Lemmen 2019).

Road infrastructure may destabilize permafrost and induce its thaw. In turn, degradation of near-surface permafrost affects the road, reducing its bearing capacity and causing differential subsidence. For example, in western sections of the Alaska Highway in Yukon (Figure 1), the road is undulating, necessitating repeated rehabilitation and local reductions in operating speeds (Oldenborger et al. 2015). Such damage, treated by resurfacing sealed sections and grading of gravel roads, increases in both intensity and magnitude with climate change.

Less consideration is typically given to the hydrological aspects of climate change affecting infrastructure. Nevertheless, in permafrost environments characterized by limited infiltration, road hazards are closely associated with local precipitation and surface hydrology (Michel and van Everdingen 1994). These hazards include the development of icings (aufeis), washouts, and landslides. Such hazards may disrupt vital routes which facilitate the distribution of resources, and private and business travel connecting northern communities to the south.

Yukon's highway network encompasses both primary and secondary routes linking most communities throughout the territory (Figure 1). The network is entirely operated and maintained by Highways and Public Works, Yukon. A total of 21 maintenance camps are distributed around the network, each responsible for distinct highway sections (Figure 1).

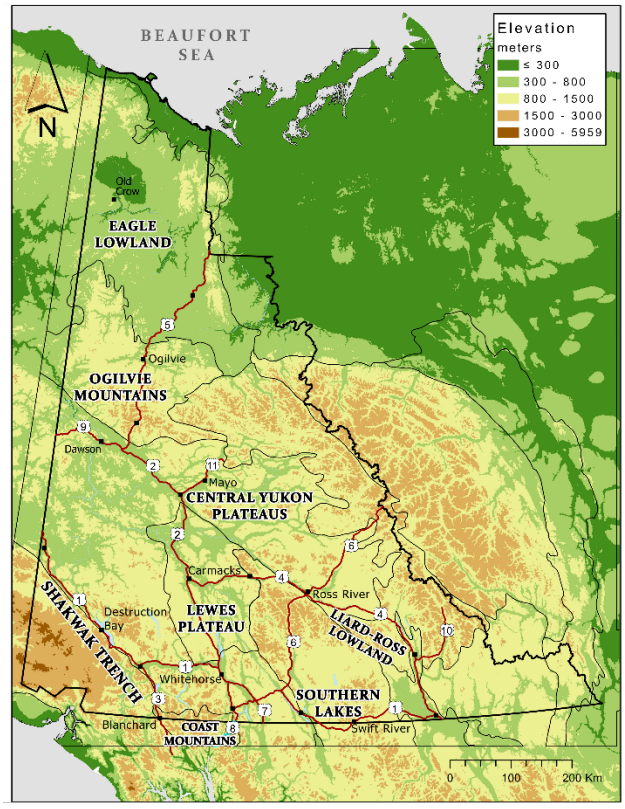

Figure 1. Highway network in Yukon, with locations of maintenance camps discussed in the paper. Physiographic regions are identified. The highway numbers are displayed in Table 1. Elevation data retrieved from ArcticDEM (Porter et al. 2018).

https://doi.org/10.52381/ICOP2024.82.1

Detailed accounts of maintenance expenditures are recorded daily at each camp and archived in a generalized database. In this paper, we present a retrospective analysis of highway maintenance expenditures associated with climate conditions from 1994 to 2022. The analysis examines variations in expenditures due to climate and physiographic conditions and underlying permafrost in seven distinct regions. Three climate-related maintenance activities were selected for examination here, and annual totals for seven highway maintenance sections in Yukon are presented. The three sets of costs are for snow removal, icing (locally called "glacier") control, and repairs after landslides and washouts. The research helps evaluate the changing magnitude of public costs associated with climate and provides insight on records of consequence for infrastructure management. The information will be valuable for planning ongoing maintenance of Yukon's highways in order to maintain functional integrity throughout their service life.

2 CLIMATE CHANGE IN YUKON

2.1 Air Temperature

Since about 1970, the climate in Canada has changed throughout the country (Bush and Lemmen 2019). The change has been particularly pronounced at higher latitudes where increases in temperature since 1979 have been recorded at rates up to four times the planetary average (Rantanen et al. 2022). In Yukon, mean annual air temperatures increased by 2.5 °C between 1948 and 2021, or more than double the global average (Perrin and Jolkowski 2022). The warming has been prominent in winter, with mean air temperatures increasing by 4.3 °C between 1972 and 2012 (Vincent et al. 2015). Temperature records in 1971–2020 for southern (Whitehorse) and central (Dawson) Yukon indicate that annual warming has been at rates of 0.43 and 0.48 °C per decade, respectively, while winter warming has been faster at 0.97 and 1.15 °C per decade (Figure 2; Schetselaar et al. 2023).

2.2 Precipitation

Although precipitation records between stations in Yukon are poorly correlated (Schetselaar et al. 2023), Perrin and Jolkowski (2022) detected an increase of 3% in total annual precipitation for 1966–2015 in the territory. Increases in the precipitation record are not statistically significant, due to high interannual variability, but the regime is expected to shift with increasing temperatures, especially to rain in autumn (Bintanja and Andry 2017). Early detection of this shift may be evident in the frequency distribution of August and September rainfall at Mayo presented for 1961–2020 as a normal probability plot (Figure 3). If events were evenly distributed, each 20-year interval would contribute six or seven events to the upper, middle, and lower thirds of the distribution. However, the most recent 20-year interval (2001–20) is overrepresented in the upper third of the distribution, indicating that rainfall has increased in this season.

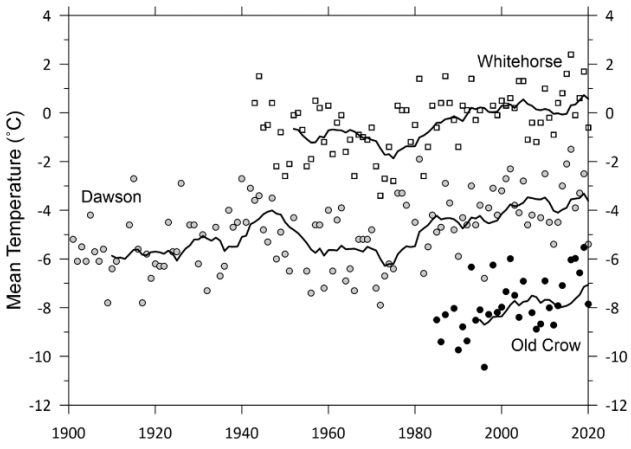

Figure 2. Annual mean temperature record for southern (Whitehorse), central (Dawson), and northern (Old Crow) Yukon. The lines show the running mean for the previous ten years of data. Data retrieved from Environment and Climate Change Canada (ECCC 2020).

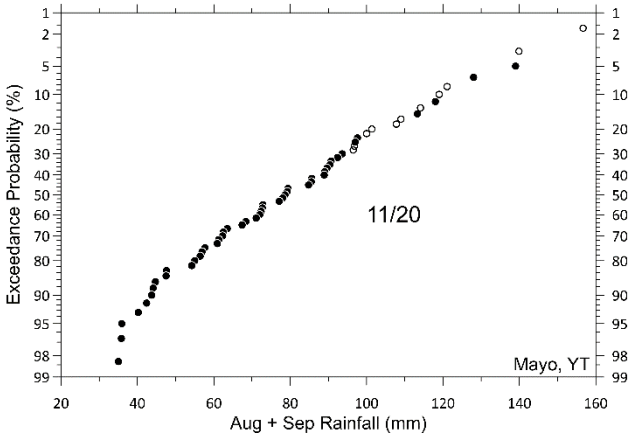

Figure 3. Exceedance probability distribution for August and September rainfall at Mayo, YT, for 1961–2020. Open circles are years from 2001–2020 in the upper third of the distribution and are listed as a fraction of the 20 upper years. Data from Environment and Climate Change Canada (ECCC 2020).

3 PHYSIOGRAPHY OF YUKON

We divided the highway network into seven distinct physiographic regions following Bostock (1948) and Matthews (1986). Here we present physiographic information for each region (Figure 1). The highway responsibility of a representative maintenance camp for each region is presented in Table 1.

Table 1. Summary of Yukon's highway network, maintenance camps investigated in this paper, and lengths of highway for each camp. Highway number is marked in Figure 1.

Physiographic Region	Camp	Highway (#)	Length (km)	Kilometer Post
Shakwak Trench	Destruction Bay	Alaska Highway (1)	133.8	Km 1636.6 -1770.4
Coast Mountains	Blanchard	Haines Road (3)	121.3	Km 71.3 - 192.6
Southern Lakes	Swift River	Alaska Highway (1)	131.2	Km 1062.8 - 1194.0
Liard-Ross Lowland	Ross River	Robert Campbell Highway (4)	184.6	Km 230.0 - 414.6
Lewes Plateau	Carmacks	Klondike Highway (2)	174.6	Km 256.2 - 430.8
Central Yukon Plateaus	Mayo	Silver Trail (11)	110.4	Km 0 - 110.4
Ogilvie Mountain-Eagle Lowland	Ogilvie	Dempster Highway (5)	146.8	Km 139.2 - 286.0

3.1 Shakwak Trench

The northwestern section of the Alaska Highway, from near Haines Junction to Beaver Creek, is mainly in the Shakwak Trench, a 4–8 km wide fault between Yukon Plateaus and St. Elias Mountains (Figure 1). The climate is influenced by St. Elias Mountains, which separate the maritime Pacific coast from drier interior conditions (Yukon Ecoregions Working Group 2004). The terrain is mainly composed of glacial and colluvial materials. Over 80% of the highway section is underlain by permafrost (Rampton et al.1983).

3.2 Coast Mountains

The Klondike Highway, south of km 146, and the Haines Road traverse units of Coast Mountains characterized by rugged terrain with glaciated peaks up to 2400 m a.s.l. (Yukon Ecoregions Working Group 2004; Figure 1). Valleys dissecting this terrain channel maritime air ascending from the Pacific coast, resulting in high levels of precipitation. Permafrost is rarely found beneath both roads.

3.3 Southern Lakes

The Alaska Highway, from km 1468 west of Whitehorse to Watson Lake, is situated within physiographic units of Teslin, Nisutlin, and Dease plateaus. The region features wide valleys, rounded peaks, and numerous lakes associated with deglaciation of the McConnell (Late Wisconsinan) ice sheet. There is sporadic discontinuous permafrost. The climate of this region is generally dry due to the rain shadow of Coast Mountains (Yukon Ecoregions Working Group 2004).

3.4 Liard-Ross Lowlands

The Robert Campbell Highway from Watson Lake to km 528 traverses broad flats and rounded hills surrounded by mountains and plateaus. In Pelly Mountains, west of Ross River, areas with steep terrain are prone to landslides, rock falls, and avalanches (Yukon Ecoregions Working Group 2004). The region has moderate precipitation, with most falling as rain (ECCC 2020).

3.5 Lewes Plateau

The Klondike Highway from Whitehorse north to Minto, and the Robert Campbell Highway from Carmacks to km 528 are in glaciated terrain characterized by rounded, rolling hills with broad valleys (Figure 1). Dry and coarse surficial materials in the region are generally free of ground ice whereas glaciolacustrine deposits in valleys are ice-rich (Yukon Ecoregions Working Group 2004). Precipitation is relatively low.

3.6 Central Yukon Plateaus

The Klondike Highway from km 432 to Dawson City and the Silver Trail traverse units of the central Yukon plateaus. These include Tintina Trench, a 450 km ancient fault trace, Klondike Plateau, displaying distinct rounded ridges dissected by deep valleys characteristic of unglaciated Beringia, and Stewart Plateau featuring tablelands interspersed with broad valleys (Figure 1). Surficial deposits include thick till deposits in glaciated areas and coarse-grained glacial outwash in unglaciated zones (Yukon Ecoregions Working Group 2004). This region experiences strong seasonal variability, with severe inversions in winter trapping cold air in valleys.

3.7 Ogilvie Mountains-Eagle Lowland

The Dempster Highway is a 736 km route, of which 465 km is in Yukon, connecting the Klondike Highway, 40 km east of Dawson City, to Inuvik, NT. The highway lies in deep valleys of southern Ogilvie Mountains and on rolling hills of Eagle Lowland (Yukon Ecoregions Working Group 2004). Valleys between km 75 and km 129 were glaciated while the remainder of the route is in unglaciated Beringia (Burn et al. 2015). Permafrost is ubiquitous. Ground and surface water in the mountains cause frequent icings at the base of hillslopes (Burn et al. 2015). The climate of this region is influenced by the topographic relief of the terrain. Valley bottoms are extremely cold in winter due to cold air pooling and topographic shading (Burn et al. 2015).

4 PERMAFROST ROAD HAZARDS

Yukon supports all categories of permafrost due to its climatic and physiographic conditions, but generally the proportion of the ground underlain by permafrost and its thickness increase northward (Figure 4).

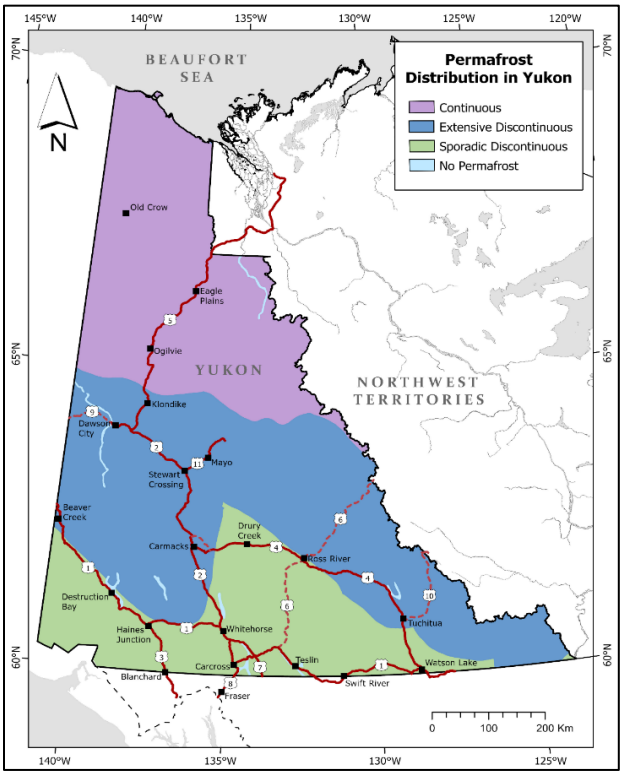

Figure 4. Distribution of permafrost relative to the highway network in Yukon. Permafrost limits from Heginbottom et al. (1995).

4.1 Hydrologic processes

Permafrost acts as an impermeable layer restricting groundwater movement to the active layer and taliks. Water flow in the active layer is closely associated with local precipitation and surface hydrology. Icings commonly develop adjacent to roads, may reach the driving surface, overflow, and create hazardous conditions (Figure 5). Icings may also block culverts leading to washouts during freshet. These hazards most commonly form in discontinuous permafrost at the foot of slopes (Turcotte et al. 2023). Low infiltration in permafrost regions, particularly in the continuous zone creates rapid hydrographic response to precipitation. Such events may erode road embankments adjacent to river channels. Washouts may be initiated by heavy rainfall or unserviceable culverts and occur during freshet or following rainstorms (Figure 6; Burn et al. 2015). Embankments in valley floors of rugged terrain and near rivers are particularly susceptible to this process.

Figure 5. Surface icing adjacent and covering the Dempster Highway at km 20, November 2022. Photo by kind permission of L.P. Roy.

Figure 6. Road washout at km 237 on the Dempster Highway, May 2023. Photo by O. Didier.

4.2 Slope processes

Mass movements in permafrost terrain include gradual phenomena like solifluction and immediate movements such as landslides, particularly, active-layer detachments and retrogressive thaw slumps (Figure 7). In Yukon, hillslopes with permafrost are susceptible to downslope mass movements (Burn et al. 2015). Active-later detachments occur in ice-rich ground on mid-to-upper slopes during late summer after heavy rain and following forest fires (Lewkowicz 1992). As infrastructure is predominantly constructed in valley floors with little room for alternate routes, mass movement events may disrupt traffic flow throughout the territory.

Figure 7. Landslides adjacent to Dempster Highway at km 244, July 2018. Photo by C.R. Burn.

5 HIGHWAY MAINTENANCE DATABASE

Financial data were retrieved from an internal database of Highways and Public Works, Yukon. Each expenditure is recorded with a 21-digit identifier code by camp, highway, activity, and program. Monthly expenditures were examined over 28 years from April 1994 to March 2022. Maintenance costs were converted to constant 2021 Canadian dollar values using the Consumer Price Index for Whitehorse as a measure of inflation (Statistics Canada 2023).

Three maintenance activities were identified as directly related to climate. First, snow removal, including drift control and sanding (Figure 8), is predominantly carried out from October to April. Second, icing control includes both physical removal of aufeis from road surfaces and maintaining flow inside culverts to prevent overflow (Figure 5). This activity is primarily carried out between freeze-up and freshet. Third, clearing of landslides and repair of embankments after washouts. Landslides may be triggered by late summer rainfall or following forest fires. Washouts are common after rapid runoff events during spring freshet and after heavy rainfall. These events occur on an intermittent basis (Figures 6 and 7).

Annual totals for snow removal, icing control, and the repair of landslides and washouts were tabulated for seven maintenance camps (Table 1). The sum of these individual activities was determined to define total climate-related expenditures. Five-year means were calculated by camp for the beginning (1994/1995–1998/1999) and end of the series (2017/2018–2021/2022) for each individual climate-related activity, and total operation and maintenance expenditures.

6 HIGHWAY MAINTENANCE EXPENDITURES

6.1 Total operation and maintenance

The operation and maintenance (O&M) for the entire highway network in Yukon covers all activities and camp overhead expenditures by fiscal year. Camp overheads are indirect expenses necessary for overall operation and management of highways and include expenses for activities such as field supervision, freight, road inspection, stockpiling, transport, and building and ground maintenance. In 1994–2022, the total O&M expenditures, adjusted for inflation, varied between $32M and $43M. Total expenditures, adjusted for inflation, have slightly decreased over time, although there has been substantial interannual variation (Figure 9). However, the proportion of the total cost devoted to camp overheads has increased from 24% to 31% (Figure 10). As a result, the resources available for maintenance operations declined from $28.4M/yr in 1994–99 to $25M/yr in 2017–22.

6.2 Climate-related maintenance

Mean annual climate-related maintenance expenditures, increased, in constant dollars, from $6.6M in 1994–1999 to $10.2M in 2017–2022. The rate of increase was $169,000/yr (Figure 11). Climate-related costs rose from 24% of total maintenance, excluding overheads, to 43% (Figure 12). The greatest increase in cost was for snow removal, with an 18% increase of the total between 1994–1999 and 2017–2022; the repair of slides and washouts increased from 1% to 3%; and icing control remained at the same percentage of the total.

Figure 8. Snow removal in Hurricane Alley, Dempster Highway, YT. December 2021. Photo by kind permission of C. Brais (2021).

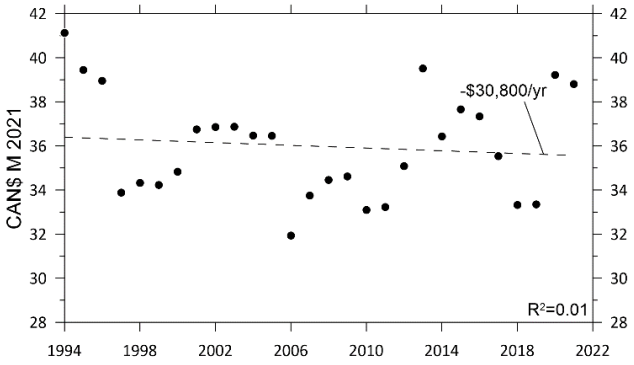

Figure 9. Total operation and maintenance costs (including camp overheads) for Yukon highways in 1994–2022.

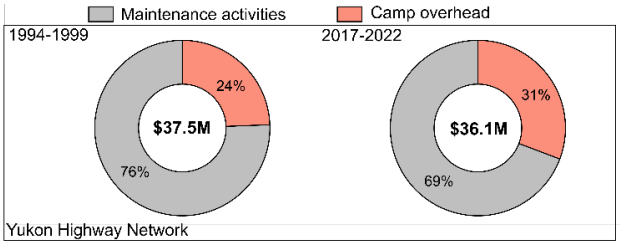

Figure 10. Proportion of annual camp overheads in 1994–1999 and 2017–2021.

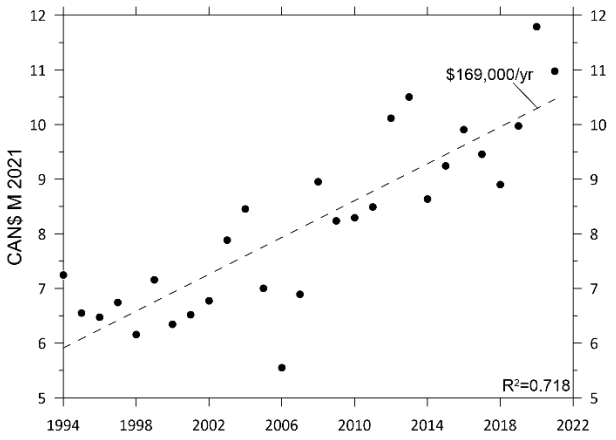

Figure 11. Annual climate-related maintenance expenditures for Yukon highways in 1994–2022.

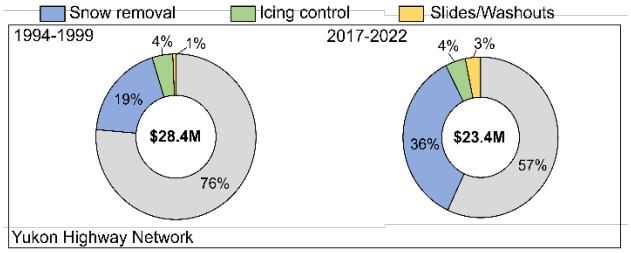

Figure 12. Break-down of annual mean climate-related maintenance costs for snow removal, icing control, and slides/washouts in 1994–1999 and 2017–2022 for Yukon's entire highway network. All other maintenance activities are indicated in gray shading. Camp overheads have been excluded from this figure.

6.3 Effects of physiography

Snow removal expenses dominate operation and maintenance costs at each camp, but they vary throughout the network (Figure 13). Blanchard, located in the Coast Mountain region, stands out with the highest proportion of these expenditures, reaching up to 71% in 2017–2022. This can be attributed to high snowfall in the region due to its elevation and proximity to the Pacific Ocean, which is a recurrent source of moisture-laden air masses. Additionally, blowing snow and accumulation of snow drifts are common occurrences above treeline in these high-altitude regions.

Mayo, in the central Yukon plateaus region, and Ross River, in Liard-Ross Lowland, have notably high expenses for icing control (Figure 13). Most recently, the proportion of such expense at Ross River rose to 14% and to 23% at Mayo. These regions are within extensive discontinuous permafrost with groundwater flow concentrated in creek taliks. Groundwater discharge and successive overflow lead to frequent icing formation. Sites vulnerable to icings are also typically found at the foot of slopes, where groundwater is forced to the surface (Turcotte et al. 2023).

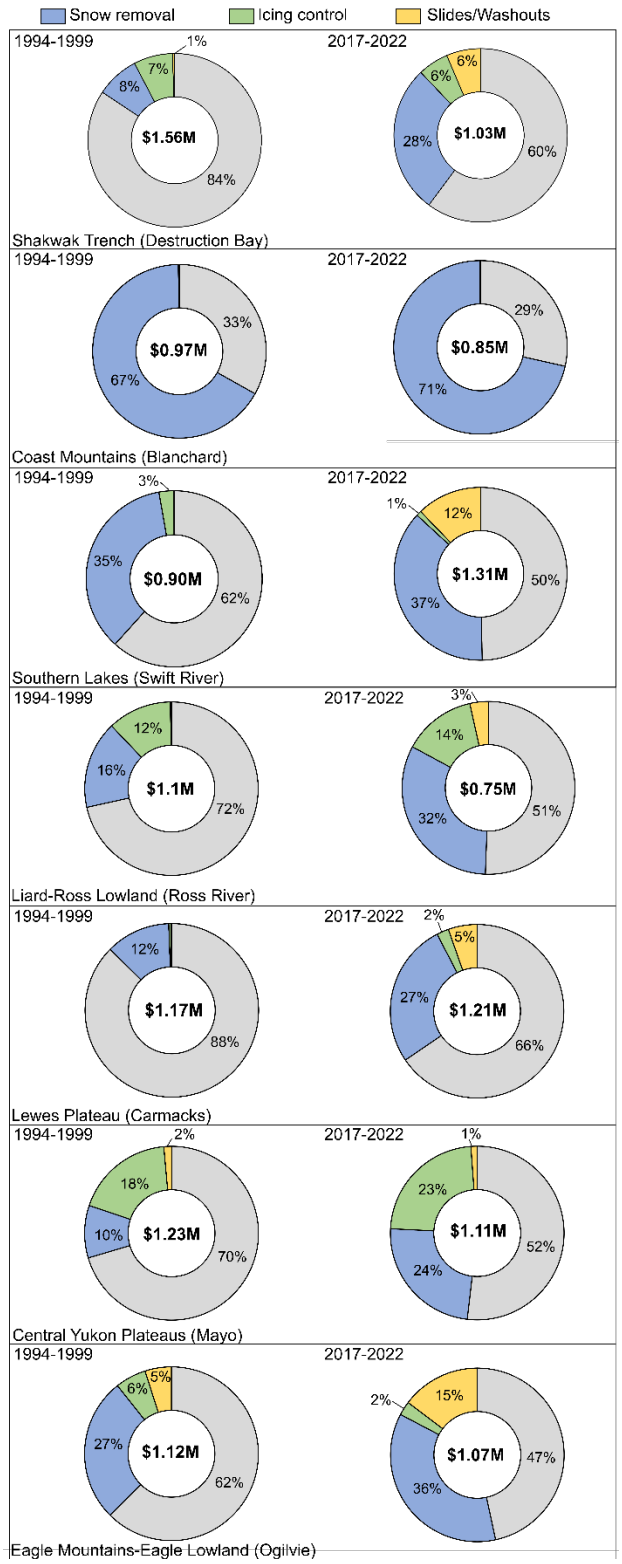

Figure 13. Break-down of annual mean climate-related maintenance costs for a representative camp in each physiographic region in 1994–1999 and 2017–2022. All other maintenance activities indicated by gray shading. Camp overheads have been excluded from this figure.

For instance, the Ross River highway section is situated near the slopes of Pelly Mountains and the Silver Trail (Mayo) traverses slopes on the edge of Stewart Plateau.

Huscroft et al. (2004) describe a close association between the occurrence of landslides and presence of unconsolidated material on steep slopes, river erosion, and degradation of ice-rich permafrost. Expenses for slides and washouts at Swift River, in the Southern Lakes region, increased to 12% in 2017–2022 (Figure 13), and are associated with proximity to waterbodies and steep slopes. In the Ogilvie Mountains-Eagle Lowland, expenses for the Ogilvie camp rose from 5% to 15% (Figure 13) due to a combination of proximity to steep slopes, degradation of permafrost, and proximity to the Ogilvie River in a narrow valley (Figure 6). Highway repairs after washouts may also incur costs allocated to capital budgets. These costs are not included in this analysis and therefore the full cost of these events is underestimated in the maintenance budgets.

6.4 Expenditures by permafrost zone

Maintenance activities discussed here are influenced by permafrost occurrence and primarily driven by hydrologic processes. However, permafrost distribution indirectly affects activities such as icing control and occurrence of slides and washouts. Washouts are primarily associated with the limited infiltration in frozen ground during rainstorms or snow melt as surface water accumulates and subsequent rapid runoff occurs. Landslides in permafrost environments are often caused by elevated pore water pressure as permafrost thaws, reducing its shear strength, and with rainfall saturating the active layer (Harris et al. 2009). Icings occur due to emergence of groundwater which subsequently freezes at the surface (van Everdingen 1982).

An overlay analysis was conducted for the highway network and a high-resolution permafrost distribution model (Bonnaventure et al. 2012). The model, with a pixel resolution of 30 x 30 m, divides the study area into four distinct zones of permafrost. It only extends to about 65°N, but farther north the Dempster Highway is assumed to lie in the zone of continuous permafrost (Heginbottom et al. 1995). Maintenance expenditures are recorded on a section basis and therefore each section was classified by permafrost zone. Highway sections situated in two zones are assumed to be in the zone where majority of the highway length is situated (i.e., > 50%). The Whitehorse section was excluded due to higher level of service required with greater traffic flows. According to this model and assumptions, roughly half of the network, excluding the Whitehorse section, lies in extensive discontinuous permafrost, 34% in sporadic discontinuous permafrost, 13% in continuous permafrost, and 9% in isolated patches (Table 2).

Maintenance costs associated with the presence of permafrost have been highest in the extensive discontinuous permafrost zone, with total costs reaching over $16,000/km in 1994–2022 (Table 2). Relatively high costs were also observed for highway sections underlain by continuous permafrost. On a per kilometer basis, maintenance costs for highways situated in zones where more than half of the terrain is underlain by permafrost (i.e., extensive discontinuous and continuous permafrost) are more than 50% higher than in sections with lower permafrost presence.

Some of the costs associated with the northern permafrost zones may be elevated because of the steep, mountainous terrain, limited availability of construction materials, and the remote locations of the maintenance sections.

Table 2. Highway length, proportion of network, and total maintenance expenditures for icing control and the repair of slides and washouts (1994–2022) in each permafrost zone. Expenditures for Whitehorse are excluded.

Permafrost Zone	Length (km)	Proportion of network (%)	Cost ($/km)
Continuous (>90%)	461	13	11,400
Extensive discontinuous (50-90%)	1553	44	16,600
Sporadic discontinuous (10-50%)	1185	34	7200
Isolated patches (0-10%)	325	9	4700

7 CONCLUSIONS

The examination of historical maintenance costs associated with climate change in Yukon leads to the following five key results:

1. Although the total operation and maintenance budget, adjusted for inflation, remained relatively stable, climate-related maintenance expenditures increased in 1994–2022.
2. Across all maintenance camps, the most substantial increases have been observed in snow removal expenditures.
3. Icing control expenditures are greatest for highway sections situated near hillslopes in extensive discontinuous permafrost.
4. Landslides and washout expenditures increased at all representative camps, except in Coast Mountains, where there is little permafrost.
5. On a per kilometer basis, maintenance expenditures influenced by the presence of permafrost (i.e., icing control and the repair of slides and washouts) are 50% greater for highways in the extensive discontinuous and continuous permafrost zones than in areas of sporadic discontinuous permafrost or isolated patches of permafrost.

8 ACKNOWLEDGEMENTS

The research presented in this paper has been supported by: Transportation Engineering Branch, Transportation Maintenance Branch, and Transportation Planning Branch of the Government of Yukon; NSERC Permafrost Partnership Network for Canada; Transport Canada's NTAI program; and Polar Knowledge Canada's NSTP program. The authors thank, in particular, Trevor Andersen, Amanda Price, Ken Jeffrey, Sandra MacDougall, Crystal Blair, Derek Parker, Michael Scarizzi, Cathy Brais, and Nathalie Gionet for data support and helpful discussions. We thank Fabrice Calmels and two anonymous reviewers for helpful comments on the paper.

9 REFERENCES

Bintanja, R. and Andry, O. 2017. 'Towards a Rain-dominated Arctic', *Nature Climate Change* 7, pp. 263–267 doi:10.1038/nclimate3240.

Bonnaventure, P., Lewkowicz, A., Kremer, M., and Sawada, M. 2012. 'A Permafrost Probability Model for the Southern Yukon and Northern British Columbia, Canada', *Permafrost and Periglacial Processes* 23, pp. 52–68. doi:10.1002/ppp.1733.

Bostock, H.S. 1948. 'Physiography of the Canadian Cordillera, with Special Reference to the Area North of the Fifty-Fifth Parallel', *Geological Survey of Canada* Memoir 247.

Burn, C.R., Moore, J.L., O'Neill, H.B., Hayley, D.W., Trimble, J.R., Calmels, F., Orban, S.N., and Idrees, M. 2015. 'Permafrost Characterization of the Dempster Highway, Yukon and Northwest Territories', in *68th Canadian Geotechnical Conference and 7th Canadian Permafrost Conference*. Québec City, Québec, Canada: Paper 705.

Bush, E. and Lemmen, D.S. 2019. 'Canada's Changing Climate Report', *Government of Canada*. Ottawa, Ontario, Canada. doi:10.4095/314614.

Environment and Climate Change Canada (ECCC) 2020. *Canadian Climate Normals 1981–2010*. Available at: https://climate.weather.gc.ca/climate_normals/index_e.html.

Harris, C., Arenson, L.U., Christiansen, H.H., Etzelmuller, B., Frauenfelder, R., Gruber, S., Haeberli, W., et al. 2009. 'Permafrost and Climate in Europe: Monitoring and Modelling Thermal, Geomorphological and Geotechnical Responses', *Earth-Science Reviews* 92(3-4), pp. 117–171. doi:10.1016/j.earscirev.2008.12.002.

Heginbottom, J.A., Dubreuil, M.A., and Harker, P.T. 1995. 'Canada, Permafrost', in *National Atlas of Canada, 5th edition*. Natural Resources Canada, MCR 4177. doi:10.4095/294672.

Huscroft, C.A., Ward, B.C., Berendregt, R.W., Jackson, L.E., and Opdyke, N.D. 2004. 'Pleistocene Volcanic Damming of Yukon River and the Maximum Age of the Reid Glaciation, West-Central Yukon', *Canadian Journal of Earth Sciences* 41(2), pp. 151–164. Doi:10.1139/e03-098.

Lewkowicz, A. 1992. 'A Solifluction Meter for Permafrost Sites', *Permafrost and Periglacial Processes* 3(1), pp. 11–18. doi:10.1002/ppp.3430030103.

Matthews, W.H. 1986. 'Physiography of the Canadian Cordillera', *Geological Survey of Canada* Map 1701A.

Michel, F.A. and van Everdingen, R.O. 1994. 'Changes in Hydrogeologic Regimes in Permafrost Regions Due to Climatic Change', *Permafrost and Periglacial Processes* 5(3), pp. 191–195 doi:10.1002/ppp.3430050308.

Oldenborger, G.A., LeBlanc, A-M., Stevens, C.W., Chartrand, J., and Loranger, B. 2015. 'Geophysical Imaging of Permafrost Conditions Along the Northern Yukon Alaska Highway', in *68th Canadian Geotechnical Conference and 7th Canadian Permafrost Conference*. Québec City, Québec, Canada: Paper 318.

Perrin, A. and Jolkowski, D. 2022. *Yukon Climate Change Indicators and Key Findings 2022*. Whitehorse, Yukon, Canada: Yukon University Research Centre.

Rampton, V.N., Ellwood, J.R. and Thomas, R.D. 1983. 'Distribution and Geology of Ground Ice Along the Yukon Portion of the Alaska Highway Gas Pipeline', in *4th International Conference on Permafrost*. Fairbanks, Alaska, United States: pp. 1030–1035.

Rantanen, M., Karpechko, A.Y., Lipponen, A., Nordling, K., Hyvarinen, O., Ruosteenoja, K., Vihma, and T., Laaksonen, A. 2022. 'The Arctic Has Warmed Nearly Four Times Faster than the Globe Since 1979', *Nature Communications Earth and Environment* 3(168). doi:10.1038/s43247-022-00498-3.

Schetselaar, A., Andersen, T., and Burn, C.R. 2023. 'Performance of Climate Projections for Yukon and Adjacent Northwest Territories, 1991–2020', *Arctic* 73(3), pp. 244–264. doi:10.14430/arctic77263.

Statistics Canada 2023. *Consumer Price Index, Annual Average, not Seasonally Adjusted*. Available at : https://www150.statcan.gc.ca/t1/tbl1/en/tv.action?pid=1810000501).

Turcotte, B., Dubnick, A., McKillop, R., and Ensom, T. 2024. 'Icing and Aufeis in Cold Regions I: The Origin of Overflow', *Canadian Journal of Civil Engineering* 51: in press. doi:10.1139/cjce-2023-0057.

van Everdingen, R.O. 1982. 'Management of Groundwater Discharge for the Solution of Icing Problems in the Yukon', in *Fourth Canadian Permafrost Conference*. Calgary, Alberta, Canada: pp. 212–226.

Vincent, L.A., Zhang, X., Brown R.D., Feng, Y., Mekis, E., Milewska, E.J., Wan, H., and Wang, X.L. 2015. 'Observed Trends in Canada's Climate and Influence of Low-Frequency Variability Modes', *Journal of Climate* 28(11). doi:10.1175/JCLI-D-14-00697.1.

Yukon Ecoregions Working Group 2004. *Ecoregions of the Yukon Territory: Biophysical Properties of Yukon Landscapes*. C.A.S. Smith, J.C. Meikle, and C.F. Roots. (eds.), PARC Technical Bulletin 04-01, Agriculture and Agri-Food Canada, Summerland, BC, Canada.

A high-resolution rock glacier inventory of South Tyrol: Evaluating lithologic, topographic, and climatic controls

Riccardo Scotti[1], Volkmar Mair[2], Daniel Costantini[2] & Francesco Brardinoni[3]

[1]*Servizio Glaciologico Lombardo, La Valletta Brianza, Lecco, Italy*

[2]*Office for Geology and Building Materials Testing, Cardano, Bolzano, Italy*

[3]*Department of Biological, Geological and Environmental Sciences, University of Bologna, Bologna, Italy*

ABSTRACT

In South Tyrol, a comprehensive and homogeneous database of rock glaciers is missing. This is a critical shortcoming for the basic understanding of creeping permafrost in the region, as well as for geohazard assessment and planning, especially in relation to contemporary climate warming. To this purpose, we have: (1) compiled a regional inventory through visual inspection of optical and LiDAR-derived imagery; and (2) analyzed the spatial distribution of rock glaciers in relation to topography, lithology, and climate. Climatic attributes were drawn from regionally interpolated data of the 3PClim project. The inventory tallies 2798 rock glaciers that occupy a surface of 146 km^2. Of these, 502 were classified as active rock glaciers, 615 as inactive, and 1681 as relict. Median front elevation of the active landforms (2695 m) is 100 m and 440 m higher than that of the inactive and relict ones. This offset can vary over 200 m as a function of slope aspect. Median MAAT on active and inactive rock glaciers is respectively -2.3 and -1.6 °C, and above the melting point (+0.2 °C) on relict landforms. Despite such differences, we find that median days of snow cover is comparable in active and inactive landforms (310 and 302 respectively) and significantly lower in relict ones (273). Most of the rock glaciers develop(ed) on paragneiss, mica schists and phyllites (83%), followed by orthogneiss (21%), and limestones and dolostones (8%). Lithologic effects, except in calc schists, which score distinctively lower than schists and orthogneiss, are largely masked by interactions between topographic and climatic conditions across physiographic zones.

1 INTRODUCTION

The spatial distribution and activity of rock glaciers contain critical information on the past and present state of permafrost (Barsch 1996). In South Tyrol, Italy, a number of active rock glaciers are known for their interference with infrastructure, or as prospective sources of hazard, however, a comprehensive appraisal of their spatial distribution is missing. This is a critical shortcoming for geohazard assessment and regional planning, especially in relation to contemporary climate warming.

From a basic, process-oriented standpoint, the variety of physiographic settings across South Tyrol, in conjunction with available high-resolution topography, geological mapping, and gridded climate data, offer the opportunity to investigate possible controls on creeping permafrost occurrence, exerted by elevation, lithology and climate (e.g., mean annual temperature (MAAT) and precipitation (MAP)).

To address the foregoing needs, in this contribution we present a new rock glacier inventory of South Tyrol, compiled at high spatial-resolution. In particular, we (1) examine and characterize the spatial distribution of active, inactive and relict rock glaciers in South Tyrol; and (2) explore the spatial variability of rock glaciers across five physiographic zones, with respect to varying topography, lithology, and climate (Figures 1 and 2).

1.1 Geological setting and physiographic zones

South Tyrol, an autonomous province in the Central-Eastern Alps, lies south of the Alpine divide and encompasses three tectonic sub-regions, which, proceeding southward, include: the Pennidic, the Austroalpine, and the Southalpine domains (Schmid et al. 2004). The Pennidic domain, which belongs to the High Tauern mountain range, is located in the northeastern corner of the province and is characterized by the large extent of calc-silicate schist (> 50%; here for brevity termed calc schist), followed by orthogneiss, and by mica schist and paragneiss. The Austroalpine domain, which occupies more than half of the province (Figure 1a), is dominated by mica schist and paragneiss (> 85%), with lesser orthogneiss, granite, and dolostone. The Southalpine domain, bounded westward and northward by the Periadriatic Line, is underlain by sedimentary rocks (about 50%)—mainly limestone and dolostone, with lesser marl and sandstone—followed by mica schist and paragneiss, and by volcanics and granitoids.

In order to account for the spatial variability in precipitation (Figure 1b) and elevation (Figure 2), the broad Austroalpine domain has been further subdivided into three physiographic zones. Consequently, in this work we will consider the spatial distribution of rock glaciers across five physiographic zones: Western (WestAu), Central (CentrAu) and Eastern Austroalpine (EastAu), Pennidic (Penn), and Southalpine (SudAlp) (Figure 1). The altitudinal, lithologic and climatic characterizations of each zone (Table 1) and the relevant terrain distributions across elevations (Figure 2) refer to topography located above 1400 m a.s.l. This altitudinal cut-off is dictated by the elevation of the lowermost rock glacier mapped in the inventory.

https://doi.org/10.52381/ICOP2024.176.1

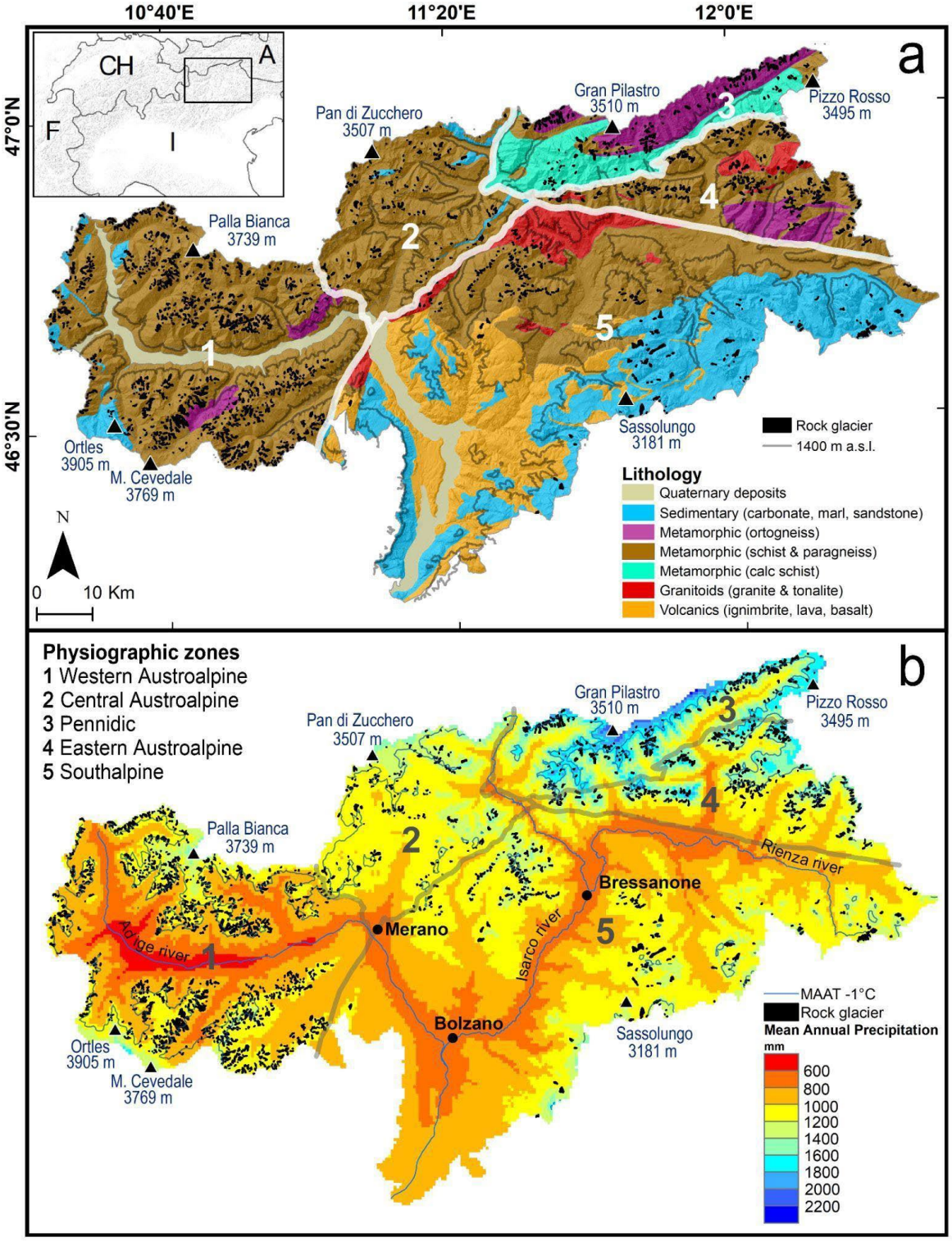

Figure 1. Rock glacier inventory map of South Tyrol superimposed on: (a) large-scale geology (after Keim et al. 2023); and (b) Mean Annual Precipitation (1981–2010; 3PClim 2023). In panel a), thick white linework separates the five physiographic zones constrained in this study (see numbering 1 through 5); dark grey linework marks the 1400 m contour line. In panel b), black linework marks the MAAT -1 °C isotherm.

Table 1. Main characteristics of the five physiographic zones. MAP refers to the mean value of precipitation, with standard deviation in brackets. MAAT refers to the mean elevation of Mean Annual Air Temperature. Lithologic categories are ranked by percent area. All values refer to terrain elevation > 1400 m a.s.l.

Physio. zone	Area	MAP	MAAT -1°C	Lithologic categories			
	(km²)	(mm/a)	(m a.s.l.)	I	II	III	IV
WestAu	1512	957 (±154)	2585	Schist 92%	Sedi 5%	Ortho 3%	-
CentrAu	629	1156 (±111)	2468	Schist 95%	Sedi 5%	-	-
Penn	545	1479 (±250)	2440	Calc-S 52%	Ortho 36%	Schist 12%	-
EastAu	602	1241 (±216)	2436	Schist 74%	Ortho 16%	Gran 10%	-
SudAlp	1855	1074 (±112)	2615	Sedi 48%	Schist 29%	Volc 16%	Gran 7%

Calc-S=calc schist; Gran=granitoids; Ortho=orthogneiss; Schist=mica schist and paragneiss; Sedi=Sedimentary, Volc=Volcanics

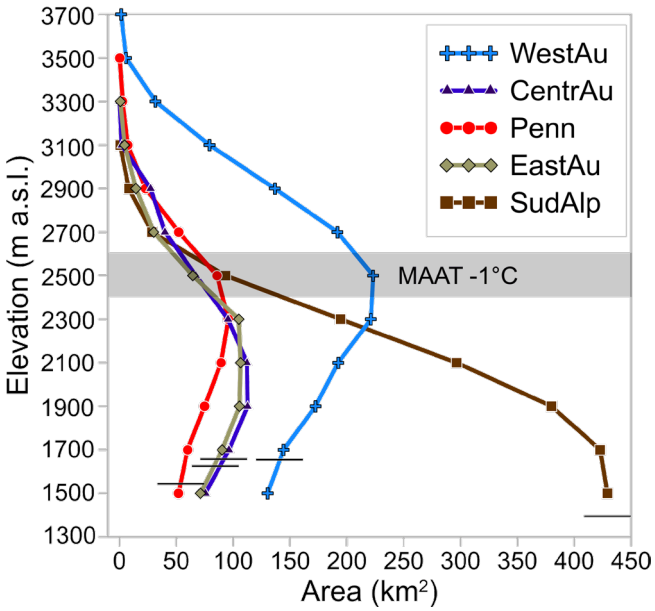

Figure 2. Terrain area as a function of elevation across the five physiographic zones. The -1 °C MAAT (1981–2010) represented as the range of variation in the five sectors, is a rough proxy for the altitudinal limit for contemporary permafrost occurrence (after Haeberli 1983 and Haeberli et al. 1989). Horizontal lines mark the elevation of the lowermost rock glacier front mapped in each zone.

The distribution of terrain area as a function of elevation shows comparable patterns across CentrAu, EastAu, and Pennidic zones, and differs greatly from that in WestAu and SudAlp. In particular, with respect to the first-order, altitudinal limit for contemporary permafrost occurrence, WestAu and SudAlp represent end members, as they contain respectively the largest and smallest extent of terrain above MAAT -1 °C (Figure 2).

Among the five zones, climate is driest in WestAu, with mean MAP = 957 mm. This figure increases progressively across SudAlp (1074 mm), CentrAu (1156 mm), EastAu (1241 mm), and the Pennidic zone (1479 mm; Table 1).

2 METHODOLOGY

Rock glacier detection, mapping and dynamic classification was conducted via visual inspection of gridded orthophotos with resolution between 0.2 and 0.5 m, acquired between 2008 and 2017, and LiDAR-derived hillshade raster of a 2.5-m Digital Terrain Model (DTM) surveyed between 2004 and 2006. Where available, information drawn from local reports on road closure or damage to infrastructure associated with the advance of rock glacier fronts was also used to complement the remotely based morphologic assessment on rock glacier activity.

Rock glacier delineation includes the extended footprint at the front and along the lateral margins, and excludes the topographic depression associated with the rooting zone (e.g., Brardinoni et al. 2019; RGIK 2023).

Following Barsch (1996), our geomorphologic inventory adopts the classification scheme that combines genetic (talus vs. debris), geometric (tongue-shaped vs. lobate), and dynamic (active, inactive and relict) attributes. Accordingly, active rock glaciers would contain an amount of permafrost sufficient to sustain downslope creep and/or shearing at depth over large parts of their surface, including front advance. Inactive (or transitional) rock glaciers, which would contain permafrost in a lesser amount, may exhibit subsidence but no frontal displacement. Relict rock glaciers, due to permafrost exhaustion, do not display any surface displacement.

Additional attributes include vegetation cover (as evaluated from optical imagery), rock glacier area, and a number of topographic variables extracted from the LiDAR DTM, such as elevation (front, mean, and maximum), mean slope gradient, and slope aspect of the main flow line.

Climatic characterization of each rock glacier is conducted through data extraction from 0.5-km climatic grids of the Austria-Italy Interreg project 3PClim, which refer to the 1981–2010 period. Attributes, extracted at the centroid of each landform, include mean annual air temperature (MAAT, °C), mean annual precipitation (MAP, mm), mean annual snowfall (SF, cm), and mean annual snow cover duration (SCD, day). In addition, mean annual incoming solar radiation (ISR, Wh/m²) is drawn from a 25-m grid (Solar Tirol 2023).

Dominant rock glacier lithology is extracted from the general geologic map of South Tyrol (Keim et al. 2023), the compilation of which relies on published and unpublished results of the 1:50,000 Geological Cartography Project of Italy and the Basiskarte project, the 1:100,000 Italian Geological Map, the 1:500,000 Structural Model of Italy 1:500,000 (Bigi et al. 1990), the 1:50,000 geological map of the Geologische Bundesanstalt (Wien) and the Geological Overview map of Tyrol (Brandner 1980).

The simplified classification of the rock units into six lithologic classes (Figure 1a) provides a first-order characterization of the conditioning that lithology would exert on mechanical weathering, and especially on frost cracking as a supplier of debris for rock glacier development. Obviously, a similar broad-scale approach cannot capture the spatial

heterogeneity in rock resistance within and across lithologies, for example, layer thickness, orientation, and dipping (e.g., sedimentary rocks and some volcanics), joint spacing and compaction.

In this work, starting from a regional lithologic ranking of resistance to fracturing (e.g., in decreasing order: granitoids, orthogneiss, volcanics, mica schist and paragneiss, calc schist, and sedimentary rocks; Grill 2014), we evaluate the actual number of rock glaciers (#) per unit lithologic area (i.e., rock glacier density, expressed as #/km^2), while considering covariation in climatic and topographic characteristics. To reduce noise, we limit our comparative analysis to the regional altitudinal belt that hosts rock glaciers, that is, above 1400 m a.s.l.

Given the uncertainty that typically characterizes the dynamic classification of rock glaciers in traditional geomorphologic inventories (Brardinoni et al. 2019), possible lithologic effects on rock glacier density will be explored on the entire inventory, without distinguishing among active, inactive and relict landforms. Uncertainty may be greatly reduced through InSAR-based kinematic classification of rock glaciers (Strozzi et al. 2004), as shown in western South Tyrol by Bertone et al. (2024).

3 RESULTS

The inventory encompasses 2798 rock glaciers, for a combined area of 146 km^2, out of 5143 km^2 of terrain that lies above 1400 m a.s.l. (2.8%). Most rock glaciers are of the talus type (2605, 93%), with only 193 qualifying as debris type (Table 2). Following the morphologically-based dynamic classification of rock glaciers, about 60% are assessed as relict (n = 1681), 615 as inactive (22%), and 502 as active (18%). Accordingly, about 40% of the mapped polygons would qualify as intact, permafrost-bearing features.

Table 2. Rock glacier count by genetic and dynamic type.

RG type count (%)	Active	Inactive	Relict	Total
Talus	444 (17)	580 (22)	1581 (61)	2605 (93)
Debris	58 (30)	35 (18)	100 (52)	193 (7)
Combined	502 (18)	615 (22)	1681 (60)	2798 (100)

Despite the above-mentioned uncertainty involved in the assessment of rock glacier activity conducted via visual interpretation of optical imagery, examination of climatic characteristics across activity classes is helpful. MAAT increases progressively from active through inactive to relict rock glaciers (Figure 3a), with interquartile separation between relict and the other two categories. Median values of the two intact categories plot below the melting point (i.e., active = -2.3 °C; inactive = -1.6 °C), whereas the relict counterpart is significantly higher (+0.2 °C). Distributions of mean annual ISR do display the same pattern of increase, but inter-categorical differences are subtle (Figure 3b), suggesting that this variable is rather insensitive to rock glacier activity and would not represent an effective predictor.

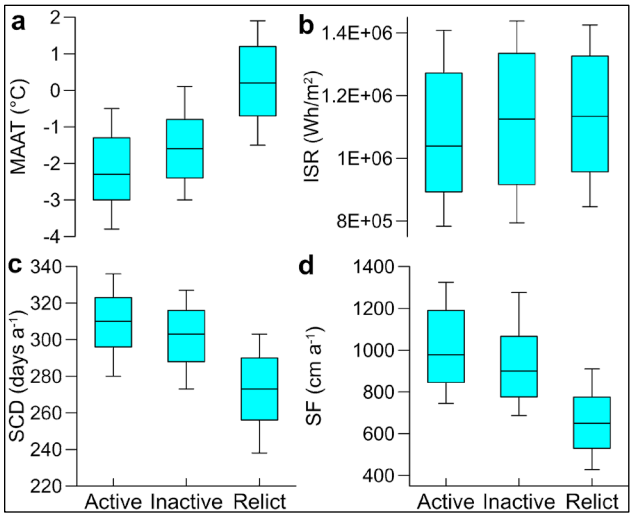

Figure 3. Climatic and topographic characterization of active, inactive, and relict rock glaciers. Variability of mean annual: (a) air temperature (MAAT), (b) incoming solar radiation (ISR), (c) snow cover duration (SCD), and (d) snowfall (SF). Climate data refer to the average from 1981–2010. Whiskers indicate respectively the 10th and the 90th percentiles; boxes enclose interquartile ranges and the horizontal lines represent median values.

By contrast, both variables related to snow, namely snow cover duration (SCD), and (d) snowfall (SF), decline systematically as one proceeds from active to relict landforms. Specifically, median SCD values decline from 310 days in active landforms, to 303 days and 273 days in inactive and relict counterparts, respectively (Figure 3c). Median SF sets at 978 cm a^{-1} and declines to 900 and 650 cm a^{-1} for inactive and relict landforms, respectively (Figure 3d).

Overall, median front elevation of active rock glaciers (2690 m) is respectively 95 m and 435 m higher than that of the inactive (2595 m) and relict ones (2255 m; i.e., Comb in Figure 4). By modulating incoming solar radiation, slope aspect appears to significantly affect the elevation of a given activity class, with values gradually increasing from north- through south-facing aspects. The maximum offset ranges from 212 m for intact to 286 m for relict landforms. Despite the general predictability of rock glacier distribution in the aspect-

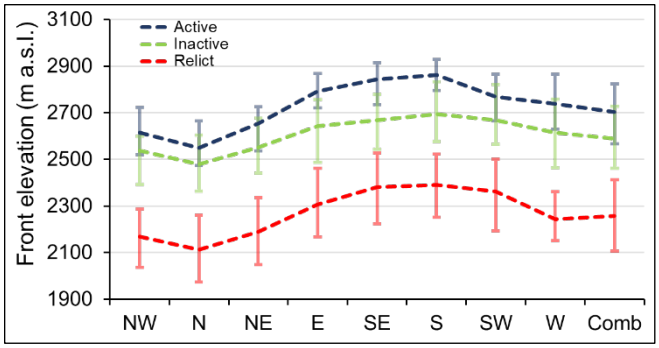

Figure 4. Rock glacier front elevation as a function of slope aspect. Dashed linework connects median values; whiskers enclose interquartile ranges. Comb = combined.

elevation space, active rock glacier fronts facing east and southeast reach elevations similar to those facing south, and plot significantly higher than the west and southwest counterparts (Figure 4). The same pattern, albeit less pronounced, is visible across relict rock glaciers.

With respect to rock glacier occurrence across lithologies (Figure 5), highest densities are observed in mica schists and paragneiss (0.76 #/km^2)—here termed *schists* for simplicity—and orthogneiss (0.63 #/km^2), followed by granitoids (0.27 #/km^2), which exhibit a 3-fold drop, calc schists (0.21 #/km^2), sedimentary rocks (mainly dolostone and limestone with lesser marl and sandstone; 0.15 #/km^2), and finally by volcanics (ignimbrite, lava, and basalts; 0.02 #/km^2).

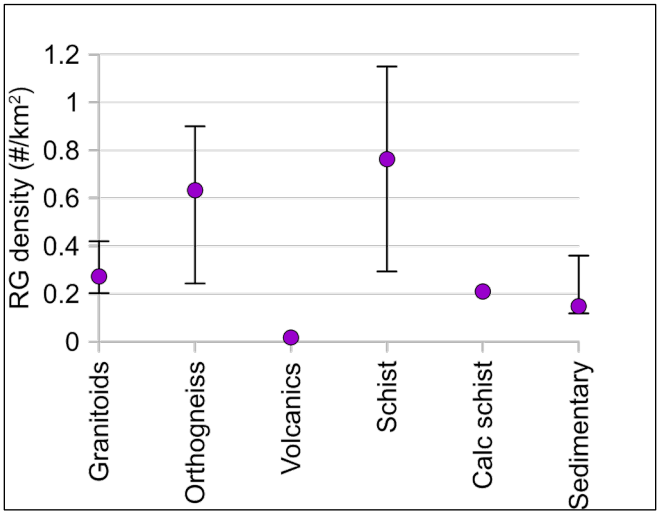

Figure 5. Overall rock glacier density by lithology in South Tyrol (filled circles). Whiskers indicate the minimum and maximum density values across the five physiographic zones. Terrain area refers to topography located at elevations > 1400 m a.s.l.

4 Discussion and Conclusions

4.1 Rock Glacier Types and Activity

Regarding rock glacier genetic classification, our inventory displays proportions of talus and debris rock glaciers that are in line with those reported in inventories compiled elsewhere in the European Alps, such as in Swiss Ticino (Scapozza and Mari 2010), the Austrian Tyrolean Alps (Krainer and Ribis 2012), and the Italian central Alps (i.e., Lombardy, Scotti et al. 2013). Albeit heavily affected by inter-operator variability, a limitation that makes direct comparison of rock glacier activity among different inventories problematic, similarities apply also to the relative abundance of intact (40%) and relict (60%) rock glaciers, considering the percentages documented in Ticino (intact 45% and relict 55%), in Lombardy (42% and 58%), and in the Tyrolean Alps (45.5% and 54.5%). By contrast, in Trentino (Italy) and in the Eastern Alps (Austria) relict rock glaciers appear to be more prevalent, accounting respectively for 75% and 79% (Kellerer-Pirklbauer et al. 2012; Seppi et al. 2012). We interpret this discrepancy as the effect of broad, low-lying, pre-alpine terrain (e.g., the Lagorai in Trentino), which today largely host relict landforms.

Mean front elevations of active, inactive and relict rock glaciers in South Tyrol mimic closely those of the neighbouring Tyrolean Alps in Austria (Krainer and Ribis 2012), for which the main discrepancy is represented by the mean elevation of the active fronts (2628 m), located just 62 m below.

As shown in Figure 3, stratification into active, inactive and relict rock glaciers aids identifying a number of useful climatic and altitudinal dependences. Considering the -1 °C to -2 °C threshold for discontinuous permafrost in the Alps (Haeberli 1983; Haeberli et al. 1989), a median MAAT around the melting point—even if partly affected by post-industrial climate warming—today could not sustain permafrost occurrence. This observation suggests that significantly cooler conditions, compared to the average of the Holocene, must have promoted the development of currently relict rock glaciers (mean MAAT +0.2 °C). Indeed, going farther back from the Holocene, summer temperature during the Younger Dryas was 3 to 5 °C lower than today (Ivy-Ochs et al. 2023), thus supporting the likely onset of rock glacier development during the latest and slightly milder phases of this stadial (e.g., Frauenfelder et al. 2001; Böhlert et al. 2011; Kellerer-Pirklbauer et al. 2012; Scotti et al. 2017).

Rock glacier stratification by activity further shows that increasing snow persistence on the ground may have an important role in the thermal insulation of blocky debris, as annual snow free conditions, on average, decline progressively from active (55 days), to inactive (62 days), and especially to permafrost devoid rock glaciers (92 days; Figure 3c). A similar altitudinal transition across active, inactive and relict landforms is also observed in terms of annual snowfall (Figure 3d) and should not surprise, since all snow-related climatic parameters depend directly on elevation. The lack of spatially-distributed climatic data in other inventories, makes it difficult to evaluate the significance of the correlations shown in Figure 3, also in relation to prospective scenarios of climate change.

4.2 Lithologic Effects and Interactions with Topo-climatic Characteristics

The question of lithologic controls on rock glacier formation and growth is a challenging one. On one hand, rock glaciers require a high supply of debris to induce and support over time creep and shearing at depth, a supply that in principle would increase with decreasing rock strength of the source walls. On the other hand, to favour thermal ventilation and permafrost persistence, a coarse blocky supply of debris is needed (as opposed to fine-grained material), a condition that would require greater rock strength, as well as outcrops characterized by thick bedding planes and high joint spacing.

Our results show that rock glacier density varies across lithologies in a complex way (Figure 5), which does not follow an intuitive ranking related to rock strength, or its opposite, thus suggesting that efficient interactions with other factors may be involved, including the variety of weathering mechanisms in cold regions (Hall et al. 2002). For example, rock glacier density in orthogneiss scores second highest—although regarded as one of the most resistant rock types—and much higher than granitoids, which one would expect to

bear at least comparable resistance. Likewise, densities in granitoids and sedimentary rocks are surprisingly very similar.

Table 3. Rock glacier count, combined area, and density across physiographic zones. RG densities are computed on mountain terrain located above 1400 m a.s.l.

Physiographic zone	RG count	RG combined area (km^2)	RG density ($\#/km^2$)
WestAu	**1642**	70.4	1.08
CentrAu	**208**	10.0	0.33
Penn	**265**	17.2	0.48
EastAu	**385**	24.9	0.64
SudAlp	**298**	23.5	0.16
Combined	**2798**	146.1	0.54

Examination of rock glacier density across physiographic zones, each characterized by different combinations of climatic, topographic and lithologic boundary conditions, helps provide better context to the integrated environmental conditions that may favour rock glacier development (Figure 1; Tables 1 and 2). WestAu stands out—both within the Austroalpine domain and among all the physiographic zones—for showing, by far, the highest rock glacier densities (Table 3). Given comparable lithologic composition among the three Austroalpine sub-zones (Table 1), this outcome suggests that more continental climatic conditions, in conjunction with a comparably greater portion of terrain located above 2300 m a.s.l., foster rock glacier formation (Figures 2 and 6). On the opposite end, in SudAlp, similar continental conditions (Figure 6b), but a topography distribution heavily skewed towards lower (< 2300 m) elevation (Figure 6a) and a dominance of sedimentary rocks (Table 1), yields an order-of-magnitude lower rock glacier density (Table 3).

In part, the scarcity of rock glaciers associated with sedimentary rocks (i.e., mainly limestone and dolostone) agrees with Johnson et al. (2007), according to whom, compared with metasedimentary rocks, water loss to subsurface in limestones could be the cause of unfavourable conditions for permafrost development and creep onset. This interpretation, although based on limited proportions of terrain within each physiographic zone (i.e., ~5%), is further supported by consistently low rock glacier densities across sedimentary rocks of WestAu and CentraAu (i.e., ~0.31 $\#/km^2$; Figure 6).

Among metamorphic lithologies, rock glacier scarcity is particularly evident in calc schist (Figure 6), especially when looking at and around the Pennidic domain. Here, high rock glacier clustering on orthogneiss (violet) and on schist and paragneiss (brown), contrasts sharply with calc schist (cyan), where very few rock glaciers were mapped (Figure 7). This finding agrees with prior studies indicating that lithologies disintegrating into fine and platy debris would not favour rock glacier development (Wahrhaftig and Cox 1959; Evin 1987; Matsuoka et al. 1997; Haeberli et al. 2006).

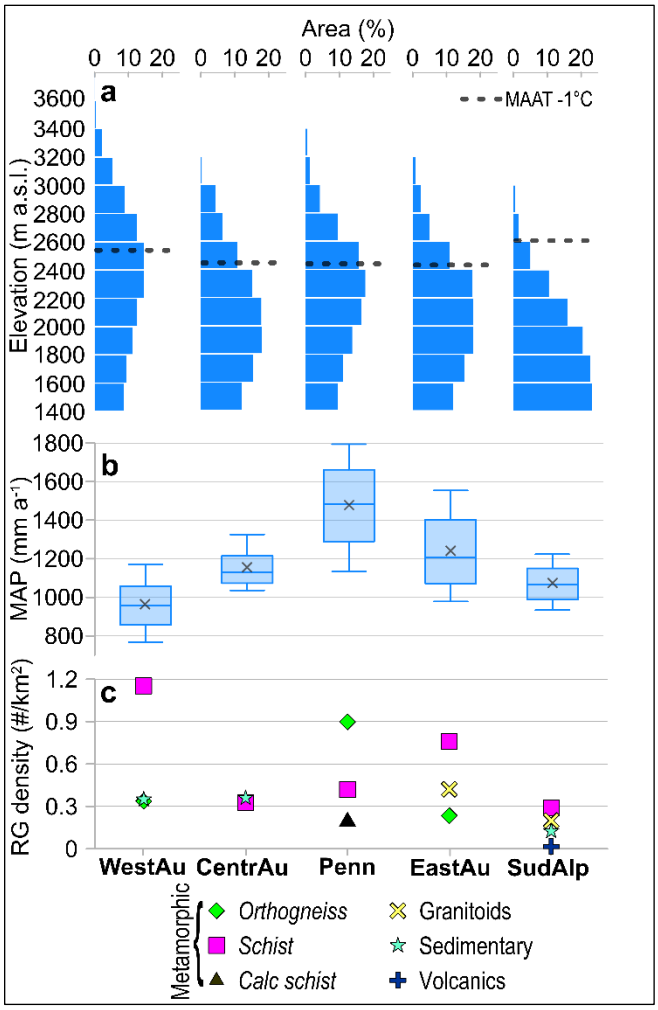

Figure 6. Rock glacier occurrence in the five physiographic zones, and relevant topographic and climatic conditions. (a) Percent terrain area as a function of elevation above 1400 m a.s.l.; (b) Frequency distribution of gridded Mean Annual Precipitation (1981–2010); and (c) rock glacier density by lithology. In panel (a), -1 °C MAAT is reported as a first-order proxy of the lower altitudinal limit for permafrost occurrence. In panel (b), horizontal lines and Xs represent median and mean values respectively. Whiskers mark the 10th and 90th percentiles; boxes bound the interquartile range.

Aside from the calc schist case, lithologic effects in the study region appear heavily masked by inter-zonal variation of climatic and topographic conditions, and possibly by additional confounding exerted by the spatial distribution of glacial till. Our interpretation is exemplified by the most common lithologies in South Tyrol, such as mica schist, paragneiss and orthogneiss. By encompassing a broad range of topo-climatic settings, these lithologies are also characterized by highest inter-zonal variability (Figure 6). While in some instances the direction and magnitude of this variability may be justified by the different positioning of a given lithology within alpine valleys (cf., spatial distribution of orthogneiss in Penn and WestAu), in other cases—at the coarse spatial scale of this work—explanation remains

elusive. For example, with respect to rock glacier density in orthogneiss, we explain the 3-fold increase observed in Penn, compared to EastAu, with the altitudinal position that this lithology occupies within the landscape. Specifically, while in Penn orthogneiss outcrops at high elevations along the main Alpine divide, in EastAu it lies on mid to lower slopes and along tributary valley bottoms (Figure 1a).

To reduce uncertainty and improve the reliability of the rock glacier inventory presented in this contribution, especially with respect to the dynamic discrimination among active, inactive, and relict landforms, a regional effort is underway to integrate geomorphologic mapping and characterization with InSAR-based kinematic information (i.e., Bertone et al. 2022).

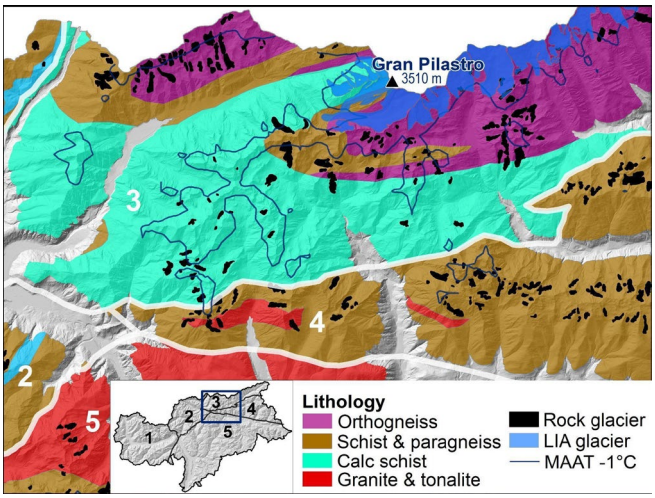

Figure 7. Map showing lithology above 1400 m a.s.l. and the rock glacier distribution in the upper Val d'Isarco area. Note rock glacier clustering in orthogneiss and in schist-paragneiss, as opposed to the sparse pattern in calc schist. 2 = Central Austroalpine; 3 = Pennidic; 4 = Eastern Austroalpine; 5 = SouthAlpine. Little Ice Age glacier extent from Knoll et al. (2009).

5 Acknowledgements

We thank Ulrich Obojes and David Tonidandel for fruitful discussions on rock strength and rock glaciers in South Tyrol. Constructive reviews by two anonymous referees are also greatly acknowledged.

6 References

3PClim, 2023. *Past, Present and Perspective Climate of Tirol, Südtirol-Alto Adige and Veneto*. Interreg IV Italia-Austria (2007-2013). Available at: http://www.3pclim.eu/ (Accessed: December 20, 2023)

Barsch, D. 1996. *Rockglaciers: Indicators for the present and former geoecology in high mountain environments*. Berlin, Germany: Springer.

Bertone, A. *et al.* 2022. 'Incorporating InSAR kinematics into rock glacier inventories: insights from eleven regions worldwide', *The Cryosphere* 16, pp. 2769–2792. Available at: https://doi.org/10.5194/tc-16-2769-2022.

Bertone, A., Jones, N., Mair, V., Scotti, R., Strozzi, T., and Brardinoni, F. 2023. 'A climate-driven, altitudinal transition in rock glacier dynamics detected through integration of geomorphologic mapping and sinthetic aperture radar interferometry (InSAR)-based kinematic information', *The Cryosphere* 18, pp. 2335–2356. Available at: https://doi.org/10.5194/tc-18-2335-2024.

Bigi, G., Castellarin, A., Coli, M., Dal Piaz, G.V., and Vai, G.B. (eds.) 1990. *Structural Model of Italy, scale 1:500.000, sheet 2*. C.N.R., Progetto Finalizzato Geodinamica, SELCA, Firenze. Available at: https://www.socgeol.it/438/structural-model-of-italy-scale-1-500-000.html (Accessed: January 9, 2023)

Böhlert, R., Egli, M., Maisch, M., Brandová, D., Ivy-Ochs, S., Kubik, P.W., and Haeberli, W. 2011. 'Application of a combination of dating techniques to reconstruct the Lateglacial and early Holocene landscape history of the Albula region (eastern Switzerland)', *Geomorphology* 127, pp. 1–13. Available at: https://doi.org/10.1016/j.geomorph.2010.10.034.

Brandner, R. 1980. *Geologische und Tektonische Übersichtskarte von Tirol, Tirol-Atlas, C1, C3*. Innsbruck, Austria: Universitätsverlag Wagner.

Brardinoni, F., Scotti, R., Sailer, R., and Mair, V. 2019. 'Evaluating sources of uncertainty and variability in rock glacier inventories', *Earth Surface Processes and Landforms* 44(12), pp. 2450–2466. Available at: https://doi.org/10.1002/esp.4674.

Evin, M., 1987. 'Lithology and fracturing control of rock glaciers in southwestern Alps of France and Italy', in J.R. Giardino, J.F. Shroder Jr., and J.D. Vitek (eds.) *Rock Glaciers*. Boston, MA: Allen and Unwin, pp. 83–106.

Frauenfelder, R., Haeberli, W., Hoelzle, M., and Maisch, M. 2001. 'Using relict rock-glaciers in GIS-based modelling to reconstruct Younger Dryas permafrost distribution patterns in the Err-Julier area, Swiss Alps'. *Norwegian Journal of Geography* 55(4), pp. 195–202.

Grill, A. 2014. 'Interreg IV–Projekt GeoResources: Naturstein Ressourcen in Nord-, Ost-und Südtirol–Vorkommen, Eigenschaften und Bedarf', *BHM Berg-und Hüttenmännische Monatshefte* 8(159), pp. 342–349.

Haeberli, W. 1983. 'Permafrost-glacier relationships in the Swiss Alps-today and in the past' *in Proceedings of the 4th International Conference on Permafrost*. Fairbanks, AK, USA: National Academic Press, pp. 415–420.

Haeberli, W. 1985. 'Creep of mountain permafrost: internal structure and flow of Alpine rock glaciers', *Mitteilungen der Versuchsanstalt fur Wasserbau, Hydrologie und Glaziologie an der ETH Zurich* 77, pp. 5–142.

Haeberli, W., Alean, J.-C., Müller, P., and Funk, M. 1989. 'Assessing risks from glacier hazards in high mountain regions: some experiences in the Swiss Alps', *Annals of Glaciology* 13, pp. 96–102. doi:10.3189/S0260305500007709.

Haeberli, W. *et al.* 2006. 'Permafrost creep and rock glacier dynamics', *Permafrost and Periglacial Processes* 17, pp. 189–214.Hall, K., Thorn, C.E., Matsuoka, N., and Prick, A. 2002. 'Weathering in cold regions: some thoughts and perspectives', *Progress in Physical Geography* 26 (4), pp. 577–603. Available at: https://doi.org/10.1191/0309133302pp353ra.

Ivy-Ochs, S., Monegato, G., and Reitner, J.M. 2023. 'Chapter 58 - The Alps: glacial landforms from the Younger Dryas Stadial', in D. Palacios, P.D. Hughes, J.M. Garcia-Ruiz, and N. de Andrés (eds.) *European Glacial Landscapes*. Amsterdam: Elsevier, pp. 525–539. Available at: https://doi.org/10.1016/B978-0-323-91899-2.00058-9.

Johnson, B.G., Thackray, G.D., and Van Kirk, R. 2007. 'The effect of topography, latitude, and lithology on rock glacier distribution in the Lemhi Range, central Idaho, USA', *Geomorphology* 91(1-2), pp. 38–50.

Keim, L., Mair. V., and Morelli. C. 2023. *Geological overview map of Trentino-South Tyrol*. Office for Geology and Building Materials Testing, Autonomous Province of Bolzano, Cardano. Available at: https://maps.civis.bz.it/#context= PROV-BZ-GEOLOGY-CARG&login=false (Accessed September 1, 2023).

Kellerer-Pirklbauer, A., Lieb, G.K., and Kleinferchner, H. 2012. 'A new rock glacier inventory of the Eastern European Alps', *Austrian Journal of Earth Sciences* 105(2), pp. 78–93.

Knoll, C., Kerschner, H., Heller, A. and Rastner, P. 2009. 'A GIS-based reconstruction of Little Ice Age glacier maximum extents for South Tyrol, Italy', *Transactions in GIS* 13(5-6), pp. 449–463. Available at: https://doi.org/10.1111/j.1467-9671.2009.01173.x.

Krainer, K. and Ribis, M. 2012. 'A rock glacier inventory of the Tyrolean Alps (Austria)', *Austrian Journal of Earth Sciences* 105(2), pp. 32–47.

Matsuoka, N., Hirakawa, K., Watanabe, T., and Moriwaki, K. 1997. 'Monitoring of periglacial slope processes in the Swiss Alps: the first two years of frost shattering, heave and creep', *Permafrost and Periglacial Processes* 8, pp. 155–177.

RGIK, 2023. *Guidelines for inventorying rock glaciers: baseline and practical concepts (version 1.0)*. IPA Action Group Rock glacier inventories and kinematics, 25 pp. doi:10.51363/unifr.srr.2023.002.

Scapozza, C. and Mari, S. 2010. 'Catasto, caratteristiche e dinamica dei rock glaciers delle Alpi Ticinesi', *Bollettino della Società Ticinese di Scienze Naturali* 98, pp. 15–29.

Schmid, S.M. *et al.* 2004. Tectonic map and overall architecture of the Alpine orogen. Eclogae Geologicae Helvetiae 97, pp. 93–117. doi:10.1007/s00015-004-1113-x.

Scotti, R., Brardinoni, F., Alberti, S., Frattini, P., and Crosta, G.B. 2013. 'A regional inventory of rock glaciers and protalus ramparts in the central Italian Alps', *Geomorphology* 186, pp. 136–149. doi:10.1016/j. geomorph.2012.12.028.

Scotti, R., Brardinoni, F., Battista Crosta, G., Cola, G., and Mair, V. 2017. 'Time constraints for post-LGM landscape response to deglaciation in Val Viola, Central Italian Alps', *Quaternary Science Reviews* 177, pp. 10–33. Available at: https://doi.org/10.1016/j.quascirev.2017.10.011.

Seppi, R., Carton, A., Zumiani, M., Dall'Amico, M., Zampedri, G., and Rigon, R. 2012. 'Inventory, distribution and topographic features of rock glaciers in the southern region of the Eastern Italian Alps (Trentino)', *Geografia Fisica e Dinamica Quaternaria* 35, pp. 185–197. doi:10.4461/ GFDQ.2012.35.17.

Strozzi, T., Kääb, A., and Frauenfelder, R. 2004. 'Detecting and quantifying mountain permafrost creep from in situ inventory, space-borne radar interferometry and airborne digital photogrammetry', *International Journal of Remote Sensing* 25, pp. 2919–2931.

Tirol Solar, 2023. *Solar potential in Tyrol and the province of Bolzano*. Interreg IV Italia-Austria (2007-2013).Available at: https://www.eurac.edu/en/institutes-centers/institute-for-earth-observation/projects/solar-tirol (Accessed: December 20, 2023).

Wahrhaftig, C. and Cox, A. 1959. 'Rock glaciers in the Alaska Range', *Geological Society of America Bulletin* 70, pp. 383–436.

Using RADARSAT constellation mission imagery to support talik mapping, Rankin Inlet, Nunavut, Canada

Wendy E. Sladen[1], Anne-Marie LeBlanc[1], Jason Chartrand[1] & Joost van der Sanden[2]

[1]*Geological Survey of Canada, Natural Resources Canada, Ottawa, Ontario, Canada*

[2]*Canada Centre for Mapping and Earth Observation, Natural Resources Canada, Ottawa, Ontario, Canada*

Abstract

In continuous permafrost regions, taliks (perennially unfrozen ground) are mainly found beneath lakes that do not freeze to their bottom. Open taliks penetrate permafrost and provide conduits between surface water and groundwater. Knowledge of these pathways is critical for mining projects to understand mine-water inflow and assess the effects of mining activities on the groundwater-surface water system. Among other factors, talik extent is a function of lake bottom temperature, lake size, and the presence of shallow terraces, where bottom-fast ice (BFI) may occur. In this paper, we use RADARSAT Constellation Mission (RCM) imagery to support the classification of lakes with potential for open taliks in the Rankin Inlet area, Nunavut. We use RCM images collected in December 2022 and March 2023 to classify pixel values as BFI or floating ice (FI) based on image differencing and a threshold of -2 dB. The classified BFI showed good agreement with available bathymetry and field measurements. Ninety-nine percent (98.9%) of BFI mapped coincided with lake depths < 2 m. Lake depths < 0.5 m were classified as having on average 28.4% BFI. The lower proportion of BFI at the shallow depths is likely related to the timing of the reference RCM image. Classified BFI was less than half as extensive as lake terraces determined from multi-spectral imagery, suggesting that this methodology would result in a greater number of lakes with potential taliks. These results could be improved by obtaining imagery earlier in the season before BFI is established.

1 Introduction

In continuous permafrost regions, taliks, also known as perennially unfrozen ground, are expected beneath lakes deeper than the maximum ice thickness and for which annual mean lake-bottom temperature is typically above 0 °C. Conversely, permafrost is usually sustained below shallow lakes and lake terraces where water freezes to the bottom (Mackay 1992, Burn 2002). The timing and duration of lake-bed ice contact (bottom-fast ice; BFI), in addition to on-ice snow cover, affect lake-bottom temperature and dictate permafrost presence or absence (Stevens et al. 2010). Taliks may penetrate permafrost (open talik) beneath large lakes or be enclosed in permafrost (closed talik) beneath smaller lakes (Sumgin 1927). Knowledge of open taliks is critical for mining projects to understand mine-water inflow and assess the effects of mining activities on the groundwater-surface water system. However, open taliks are rarely observed directly (O'Neill et al. 2020), and assessments of sublacustrine open taliks have been achieved using numerical models (e.g., Ling et al. 2012; Golder 2021), airborne geophysics (Minsley et al. 2012), and geothermal modelling (e.g., Burn 2002). In a mineral resource-rich region, it is advantageous to develop a methodology based on remote sensing to locate where open taliks may be present. LeBlanc et al. (2022) used a supervised classification of multi-spectral imagery to map shallow lakes and lake terraces (< 2 m; first order estimate of permafrost presence) and deep waters (> 2 m; permafrost absence) at the regional scale. This mapping was then combined with a steady-state thermal model for open talik assessment (e.g., Burn 2002). However, this mapping approach relies on colour, which is influenced by the lake limnology and is not necessarily representative of depth (Duguay and Lafleur 2003) and, in addition, does not indicate BFI presence and duration. Space-borne synthetic aperture radar (SAR) has been an established tool for evaluating floating ice (FI) and BFI at high latitudes since the 1990s (Murfitt and Duguay 2021) and could, therefore, be used as proxy data for classification of lakes with potential open taliks. Active microwaves readily penetrate cloud, darkness, dry snow, and freshwater ice into the underlying water or sediment. High backscatter values have been observed in Ku-, X-, C-, and L-band SAR for FI due to the high dielectric contrast between ice and water and surface scattering at the rough ice-water interface, whereas the low dielectric contrast between ice and sediment causes the incident waves to be absorbed into the ground producing low backscatter values for BFI (Murfitt and Duguay 2021). As a result, the backscatter from BFI is usually significantly less than from FI. Sellman et al. (1975) and Mellor (1982) were among the first to show that BFI and FI can be differentiated from each other using X-band (9.6 GHz) and L-band (1.25 GHz) side-looking airborne radar whereas Jeffries et al. (1994) was one of the earliest studies to examine C-band (5.3 GHz) SAR images from ERS-1 data. Airborne and satellite SAR imagery have been applied to shallow lakes to get knowledge on lake ice regime and thickness, lake depth, and indirectly to assess permafrost and thermokarst processes, methane gas emissions, overwintering fish habitat, and freshwater availability for regions in Alaska, northern Manitoba, Mackenzie Delta, and Russia, and at the circumpolar scale (Murfitt and Duguay 2021). Threshold-based methods using C-band co-polarized signals (HH and VV) are the

https://doi.org/10.52381/ICOP2024.86.1

most common approaches used to classify FI and BFI (van der Sanden et al. 2012; Engram et al. 2018; Murfitt and Duguay 2021; Shaposhnikova et al. 2023). These methods use the difference in backscatter between FI and BFI to identify threshold(s) capable of differentiating between the two types of ice cover. Approaches vary from applying a single threshold for binary classification to a variable threshold determined through interactive threshold algorithms according to the diversity of the SAR datasets involved (e.g., French et al. 2004; Engram et al. 2018). Using this difference in backscatter, van der Sanden et al. (2012) classified BFI and FI by taking the difference of two images that straddle the winter season and classed BFI based on the reduction in backscatter.

In this paper, we use HH-polarized C-band RADARSAT Constellation Mission (RCM) imagery as a first exploration of this dataset. Working with only one freezing season and SAR platform, we use a simple image differencing method to support the classification of lakes with potential for open taliks for the Rankin Inlet area, Nunavut (LeBlanc et al. 2022). Our goal is to determine the lake ice regime (FI and BFI) for lakes in our study area. We assume that permafrost is sustained below lake areas with BFI, in other words that annual lake-bottom temperature is below 0 °C. We compare our results with available bathymetry (Golder 2012a, b), lake ice thickness measurements, and shallow water (< 2 m) extent determined from multi-spectral imagery analysis for the same area (LeBlanc et al. 2022).

2 Study Area

The 1242 km^2 study area is located near the Hamlet of Rankin Inlet, Nunavut (62°48′35″N, 92°05′58″W) and encompasses the Meliadine Mine (Figure 1). The topography is relatively flat with elevation ranging from sea level to 300 m; the Mine is about 60 m above sea level in low-lying topography with numerous lakes. The area was covered by the Laurentide Ice Sheet during the Wisconsinan glaciation until approximately 6 ka (Dyke 2004).

The region is situated within the continuous permafrost zone (Heginbottom et al. 1995) and permafrost thickness is estimated between 285 m and 430 m, with the thinner permafrost being near lakes, while the depth of the basal cryopeg is estimated to be between 280 m and 290 m below ground surface (Golder 2021). Modelled segregated ice abundance ranges from low to medium, the latter concentrated across the centre of the study area, near the Meliadine Mine, where fine-grained tills overlie sedimentary rocks (O'Neill et al. 2024). Kettle lakes and lakes shaped by glaciofluvial or glacial processes are common in the area (Golder 2014), in contrast to thermokarst lakes. The glacial and glaciofluvial deposits are oriented in a northwest-southeast direction, which is also the preferential lake orientation (Figure 1). Lakes cover 30% of the study area and range in size from 221 to 1.3 x 10^8 m^2 (Meliadine Lake) with an average and median lake size of 80,090 and 4,567 m², respectively. Maximum lake depth of about 100 surveyed lakes, around the Meliadine Mine, ranges from 0.11 to 23.5 m (Golder 2012a, b). The study area is in the Maguse River Upland ecodistrict of the Southern Arctic Ecoregion (Ecological Stratification Working Group 1995). Vegetation is primarily shrub and heath tundra dominated by ericaceous shrubs up to 50 cm in height and moss in well to moderately-drained areas and wet graminoid or sedge wetlands in poorly-drained areas (Campbell et al. 2012).

The mean annual air temperature (1981–2010) for Rankin Inlet is −10.5 °C (ECCC 2023). The average annual total precipitation is 311 mm, of which 41% falls as snow. The freezing season generally starts in early October. Ice covers start to form by the end of October and are completely formed in early November and remain until June (Golder 2014). Lake-ice thicknesses in the Meliadine Mine area, measured between 1998 and 2011, ranged from 1.0 to 2.3 m with an average thickness of 1.7 m (Golder 2014).

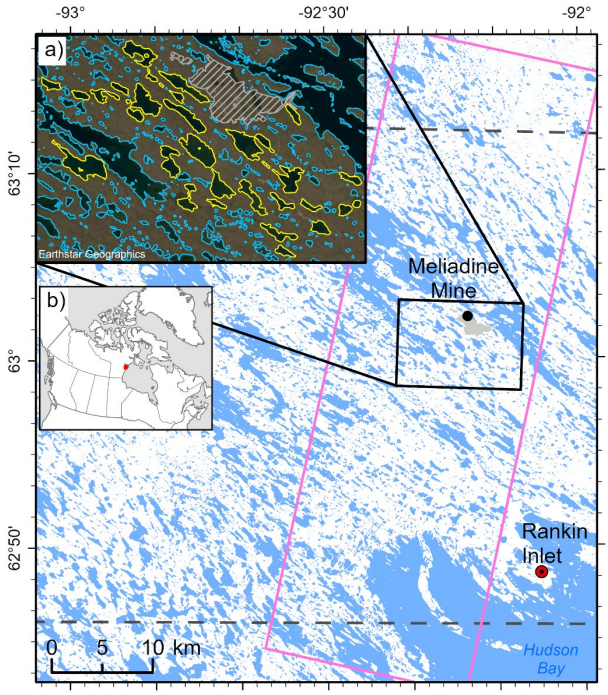

Figure 1. Map showing extent of RCM imagery (pink), bathymetry dataset (black) and north–south extent of shallow water mapping (dashed black). Rankin Inlet and Meliadine Mine are indicated. Inset a) shows lakes with bathymetry (yellow), Meliadine Mine is in grey hatching. Inset b) shows the study area location.

3 Methodology

3.1 Data

The SAR image dataset was obtained from the Canadian Space Agency's recently launched (2019) RADARSAT Constellation Mission. The RCM SAR images were collected from December 2022 to March 2023 in the Quad-Polarization (QP) mode, which has a spatial resolution of 9 m. The SAR data were accessed through the Canada Centre for Mapping and Earth Observation's Earth Observation Data Management System (EODMS). To determine the maximum extent of BFI, we selected an image pair that includes an early (reference) image acquired after freeze-up, but desirably before ice starts

freezing to the bottom, and a later (working) image acquired at maximum ice thickness but prior to any surface snow melt (van der Sanden et al. 2012). We focused on the HH polarization as this is observed to have the greatest potential in detecting FI and BFI (van der Sanden et al. 2012). In addition, to eliminate the requirement to correct for incidence angle, images were selected from the same beam mode. Following these credentials QP13 images acquired on December 14, 2022 and March 16, 2023 were selected (Figure 2). The RCM SAR imaging parameters are found in Table 1.

Table 1. RCM SAR imaging details.

Parameter	Specification
Image Dates (yyyy-mm-dd)	2022-12-14, 2023-03-16
Operational Mode	Quad-Polarization
Beam Position	QP13
Spatial Resolution	9 m
Swath Width	20 km
Nominal NESZ*	-24 dB
Incidence Angle	31.24° (near), 32.85° (far)
Polarizations	HH, HV, VH, VV

*Noise Equivalent Sigma Zero

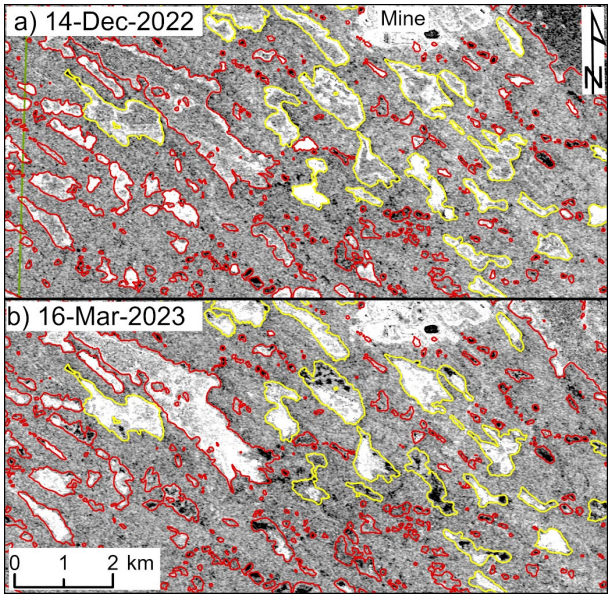

Figure 2. A close-up area of the RCM HH-polarization images in dB for a) 2022-12-14 (reference image) and b) 2023-03-16 (working image). Lakes with bathymetry are highlighted in yellow, all other lakes are outlined in red. Meliadine Mine is shown in upper right of images.

Daily mean air temperature determined from the meteorological data for Rankin Inlet (ECCC 2023), approximately 20–25 km SE of the study area, were used to determine the start and end of the 2022–2023 freezing season and select imagery dates. To evaluate the lake ice regime classification, we used the bathymetry dataset for 33 lakes near Meliadine Mine (Golder 2012a; LeBlanc et al. 2022). The bathymetric depth interval is 0.5 m (Figure 3). The CanVec 1:50,000 waterbody was used to restrict the analysis to lakes (NRCan 2017). The shallow lake and terrace (shallow waters) dataset produced from multi-spectral imagery (RapidEye) analysis and Maximum Likelihood Classification (LeBlanc et al. 2022) was used to compare the BFI extents.

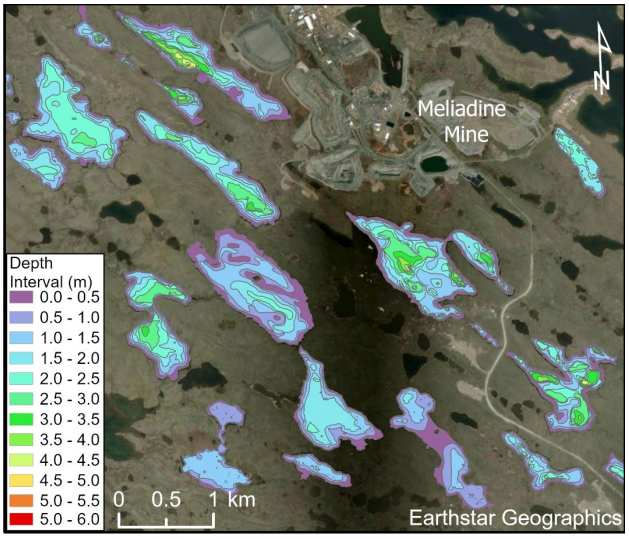

Figure 3. A subset of the lakes with bathymetry in the study area (modified from Golder 2012a, b). Depth intervals are in 0.5 m. The Meliadine Mine is visible near the top of the image.

3.2 Image Processing

Pre-processing of the SAR image data was conducted using the EODMS SAR Toolbox. The pre-processing of the Single Look Complexes included 1) radiometrically calibrating to Gamma Nought values; 2) converting complex values to detected values; 3) applying a GAMMA Map filter (Lopes et al. 1993) twice to reduce SAR speckle noise; and 4) orthorectification using rational function, nearest neighbour resampling, 5-m pixel spacing, Canada Digital Elevation Model, and projected to UTM/WGS84. The resulting TIF images were imported into PCI® Geomatica® Banff Focus and converted to a linear decibel (dB) scale using Raster Calculator and scaled for visual interpretation (Figure 2).

3.3 Lake Ice Regime Determination

Lake ice regime was determined using the image differencing method outlined in van der Sanden et al. (2012), where an earlier (reference) image is subtracted from a later (working) image. Image differencing was carried out using the Change Detection tool in PCI. The reference image (2022-12-14) is subtracted from the working image (2023-03-16) to determine the change in dB. To isolate the analysis to lakes only, the CanVec waterbody mask was applied. Based on observations in a similar Canadian Shield lake environment, a threshold of -2 dB, where values < -2 dB were classified as BFI and > -2 dB as

FI, was used for lake-ice classification (after van der Sanden et al. 2012). The raster results were imported into ArcGIS® Pro and cleaned using Majority Filter and Boundary Clean tools before converting to polygon shapefiles.

3.4 Analysis

The BFI and bathymetry datasets were overlain and the intersecting BFI area was calculated per lake depth interval in ArcGIS Pro. Percent BFI coverage per lake depth intervals was then determined in Excel®. This approach was also used to compare the BFI dataset with the shallow waters dataset determined from multi-spectral imagery.

4 RESULTS

4.1 Lake Ice Regime

There are 5387 lakes that lie completely within the 1242 km^2 study area, ranging in size from 221 m^2 to 9.5 x 10^6 m^2 (9.5 km^2). Lake size distribution is positively skewed; the median lake size is 4407 m^2, 75% of the lakes are smaller than 16,000 m^2, and 91% less than 64,000 m^2. Bottom-fast ice was detected in 2347 (43.6%) of the lakes by March 16, 2023 (Table 2). Of the lakes with BFI, the percent BFI areal coverage per lake ranged from 0.4% to 94.8% (average 25.5%, median 19.7%, standard deviation (SD) 21.2%). The 56.4% of lakes in which no BFI was detected, were generally a magnitude smaller in area than the lakes with BFI (Table 2). Isolated areas of BFI generally less than 1000 m^2 were mapped in the middle of less common larger, deeper lakes.

Table 2. Summary of lakes in the study area with and without bottom-fast ice (BFI) detected.

	Count	Area (m^2)			
		Mean	Median	Minimum	Maximum
All Lakes	5387	32,801	4407	221	9.5x10^6
Lakes with BFI	2347	71,268	18,759	368	9.5x10^6
Lakes with no BFI	3040	3104	1314	221	4.5x10^4

4.2 Bottom-fast Ice Validation

The lake ice regime results were compared against the set of bathymetric data and the 2023 field observations. Ice thickness was observed at 12 locations on five lakes in the southern portion of the study area in April 2023. Ice thickness ranged from 1.5 to 1.8 m (average 1.7 m, SD = 0.12) and was observed to be floating at all sites. The lake ice regime was classified as FI at the same locations.

Bottom-fast ice was detected in all lakes with bathymetric data (n = 33; Figure 4). Maximum lake depths ranged from 1.5 m (n = 33) to 6 m (n = 1), with 94% (n = 31) and 76% (n = 25) of the lakes reaching 2 m and 2.5 m depth, respectively. On average, 98.9% (SD = 2.1%) of the BFI determined per lake coincided with lake depths of ≤ 2.0 m and 90.8% (SD = 11.5%) corresponded to depths of ≤ 1.5 m. Less than 1% of BFI was mapped in areas deeper than 2 m and no BFI coincided with lake depths greater than 4.5 m.

Bottom-fast ice matched best with lake depth intervals 1–1.5 m and 0.5–1 m, with an areal coverage per lake averaging 67.6% (SD = 22.7%) and 59.4% (SD = 16.4%), respectively (Figure 4). At shallower (0–0.5 m) and deeper (1.5–2 m) depth intervals, the average areal extent of BFI per lake was less, averaging 28.4% (SD = 12.4) and 33.2% (SD = 34.5), respectively. Overall, BFI covered 49.3% (SD = 18.9%) of lake depths < 2 m on average.

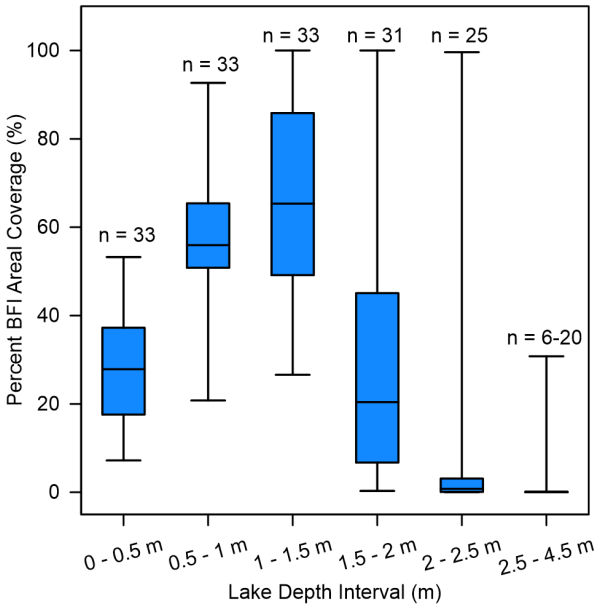

Figure 4. Box-whisker plot of the percent areal intersect of bottom-fast ice (BFI) and lake depth interval. n represents the number of lakes with the associated depth interval. The number of lakes to reach depths between 2.5 and 4.5 m ranges from 6 to 20.

4.3 BFI and Multi-spectral Classification of Shallow Waters

The BFI dataset was compared to the shallow waters dataset to evaluate the applicability of these two methods for estimating potential taliks in the Rankin Inlet area (Figure 5). Of the 3897 lakes within the overlapping BFI and shallow waters study areas, BFI was detected in 1846 (47%) of the lakes, slightly more than half of the lakes in which shallow waters were identified (3438, 88%). Bottom-fast ice was mapped in 1809 (52.6%) lakes with shallow waters and 37 lakes without shallow waters. On average, 72.8% of BFI coincided with the shallow water areas, whereas only 14.4% of shallow water areas were classed as BFI. Overall, for the lakes with BFI, the aerial extent per lake averages 25.6%, whereas shallow water extent averaged 65.1% in the lakes with shallow waters.

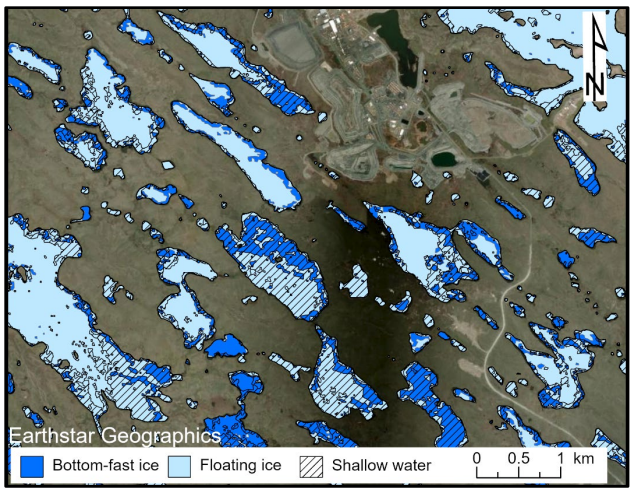

Figure 5. Example of lakes showing the extent of shallow waters (< 2 m) derived from RapidEye multi-spectral imagery (cross-hatched), bottom-fast ice (dark blue) and floating ice (light blue).

5 DISCUSSION

Validation of the bottom-fast ice mapping results requires in situ field observations. Although no BFI was observed in the field during the study period, the limited ice-thickness measurements and available bathymetry were used to assess the BFI mapping results. Bottom-fast ice extent aligned well with the bathymetry with 90.8% and 98.9% of classified BFI corresponding to depths shallower than 1.5 m and 2 m, respectively. The 12 field ice-thickness observations were all of floating ice, matching 100% with the lake ice regime mapping at the same points. Lake depth intervals 0.5–1 m and 1–1.5 m, showed the highest BFI coverage, ranging from 59.4% to 67.6%. However, the correspondence between BFI extent and the shallowest lake depth interval (0–0.5 m) was lower than expected, averaging 28.4%, with an overall average of 49.3% for lake depths < 2 m.

To explain the lower values of BFI extent detected at shallower depths, ice growth was modelled using the weather station data at Ranking Inlet for 2022–2023 (ECCC 2023). Daily mean air temperatures first dropped below 0 °C on September 30 and remained below freezing as of October 21. Ice growth was estimated using the Stefan formula and freezing degree-days for windy lakes with no snow and lakes with snow (Michel 1971; Lunardini 1981; Figure 6). Model results indicate that ice cover started to form between October 8 and 16. Modelled ice thickness ranged from 0.5 m to 0.8 m on December 14 and from 1.0 to 1.6 m on March 16, the dates of the reference and working RCM images. The upper range of the modelled ice thickness is inline with field observations made in April 2023 suggesting that this model is appropriate for the area. This agrees with thicker ice expected in tundra environments where wind dominates control of ice formation leading to thinner and denser snowpack (Roy-Léveillée et al. 2014).

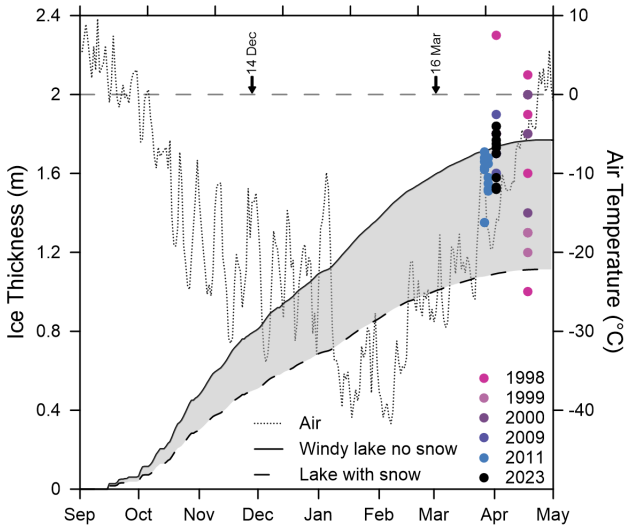

Figure 6. Daily mean air temperature for winter 2022 - 2023 for Ranking Inlet (dotted line; ECCC 2023), range of modelled ice thickness for lakes with (dashed line) and without snow (solid line) using freezing degree days (after Michel 1971). Ice thickness observations (dots) for 1998–2011 (Golder 2014) and 2023. The grey dashed line represents 0 °C air temperature and 2-m ice thickness. SAR image dates are noted.

With the March modelled ice thickness range of 1.0 to 1.6 m, we would expect the 1–1.5 m and 1.5–2 m lake depth intervals to be partially covered with BFI, which is the case. Likewise, we would expect the depth intervals 0–0.5 m and 0.5–1 m depths to be covered 100% with BFI, however, this is not observed. This is likely explained by the modelled ice thickness at the time of the reference image, where lake depths less than 0.5 to 0.8 m may already have bottom-fast ice. In this case, areas with BFI in the reference image would have low backscatter values and not produce a large negative change associated with BFI during image differencing and thus go unidentified (Figure 7). Likewise, this may be the case for the many small and thus presumably shallow lakes in the study area that had no BFI detected (Table 2). Indeed, of 78 lakes in the study area with known maximum depths (Golder 2012a, b), the 22 lakes for which no BFI was detected had a maximum depth on average of 0.65 m (SD = 0.3 m, range: 0.19–1.2 m). In addition, backscatter for some lakes has been observed to be consistently low for unknown reasons (van der Sanden et al. 2012).

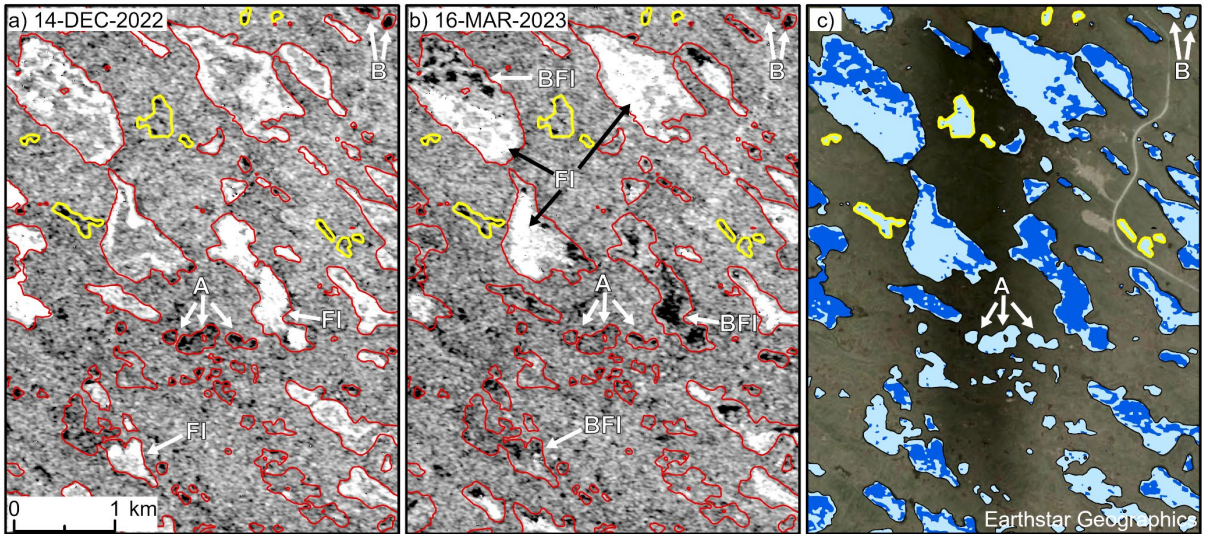

Figure 7. RCM HH images for a) 2022-12-14 and b) 2023-03-16, and c) resulting floating ice (FI, light blue) and bottom-fast ice (BFI, dark blue) classification for the same area. Lakes with a known maximum depth < 1 m are highlighted in yellow. "A" and "B" highlight lakes with low backscatter (dark) in both images resulting in ice classed as FI for these small lakes.

Acquisition of RCM imagery earlier in the season would help address the issue of missing early BFI in shallow lakes and lake terraces < 0.5 m deep. The modelled ice growth for 2022–2023, indicates that imagery acquired in early to mid-November when ice thickness is estimated to be less than 0.5 m, should improve BFI results. A study of lake-bottom temperature in the Rankin Inlet area confirms this timing of BFI in shallow waters (LeBlanc et al. 2024). In regions where there is a range of lake sizes, multiple early (reference) images may be required to detect BFI to account for the temporal window when smaller lakes are ice covered but ice is not bottom fast, and larger lakes are not yet frozen.

Other possible reasons for the lower correspondence between BFI and the shallower lake depths include change in lake levels. Lake levels in 2022 may have differed from those at the time the bathymetry was measured thus producing discrepancies in the areas classified to have BFI. In addition, the waterbody mask may not align perfectly with the current lakeshores and contribute to land being classified as FI or BFI. As for the isolated patches of BFI classed in the middle of deeper lakes, these have been observed in other studies (Duguay and Wang 2019; Shaposhnikova et al. 2023). Overestimation of BFI in these areas remains a challenge and is possibly due to ice cracking or local thinning (Pointner et al. 2019; Pointner and Barsch 2020).

Similarly to the bathymetry dataset, BFI extent matched well with the shallow waters extent (72.8%) but only 14.4% of shallow waters were mapped as BFI. The smaller number of lakes with BFI and smaller BFI extent relative to the multi-spectral classification of shallow waters may partly be explained by misinterpreting all light colors in the multi-spectral imagery as shallow areas less than 2 m. Field validation of water depth in 2023 indicated that some mapped terraces reached depths greater than 2 m. The overestimation of lake terrace extent may be related to lake limnology, one of the limitations of using multi-spectral imagery for lake depth (Duguay and Lafleur 2003). As a result, the shallow waters extent in the multi-spectral classification of lake bottom regimes may be overestimated. In addition, BFI extent may be underestimated in this study due to the timing of the reference image as previously mentioned. It is possible that agreement between the two datasets may improve if the full extent of BFI is captured. However, only the SAR classification provides information on BFI timing and duration, which remains an advantage for open talik assessment. These initial results indicate that the potential for taliks using BFI as a proxy for lake terrace width in steady-state thermal modelling governing open talik presence would result in a greater number of lakes with taliks and larger taliks with a greater potential for open taliks as compared to using the shallow waters dataset from multi-spectral imagery.

The BFI determined from the RCM SAR imagery processing shows good correspondence with the lake bathymetry and is a promising tool for use in talik mapping. Future work includes the collection and processing of multiple RCM scenes over the freezing season to determine the start of BFI establishment and growth. The timing and duration of BFI in conjunction with the monitoring of lake terrace temperature (LeBlanc et al. 2024) will be examined further to validate our talik mapping approach using BFI classification from SAR. In addition, our threshold value of -2 dB, based on past experience in a similar Canadian Shield lake environment, provided good results for this study area, however, further research will include the selection of threshold value(s) specific for the area.

6 CONCLUSIONS

Our results show that RCM SAR imagery can be successfully used to map bottom-fast ice using image differencing and is a promising tool for assessing lakes with potential open taliks in the Rankin Inlet area. Image

differencing using RCM image pairs is a simple and time-efficient method for determining BFI. Timing of the early (reference) image is critical for determining the full extent of BFI and will vary depending on the lake morphology of the area under study. In lieu of in situ ice-thickness measurements and observations of ice regime, modelling ice growth with Stefan's formula can help in determining the timing of imagery required for BFI analysis. These results suggest that mapping BFI using this methodology provides a more conservative (i.e., greater) estimate of lakes with potential open taliks compared to supervised classification of multi-spectral imagery. Bottom-fast ice is likely underestimated in this study due to the timing of the first image being after BFI was established in shallow lake areas (less than 0.5–0.8 m). To improve BFI results for this study area, future work is underway to acquire imagery during the start of freeze-up with the intent to capture and map the full extent of BFI and refine the threshold. Exploration of the different polarizations, as well as combining beam modes to determine BFI timing and growth are also planned.

7 ACKNOWLEDGEMENTS

This work was supported by Natural Resources Canada's GEM-Geonorth program (contribution number 20230334). The author's wish to thank Naomi Short, CCMEO, for putting together the RCM imagery acquisition order and providing guidance on RCM imagery access. Field validation of ice thicknesses and water depths was made possible thanks to the support of Kangiqliniq HTO (Andre Aokaut) and the assistance provided by our wildlife monitor Roger Pilakapsi. The authors thank the reviewers for their comments which improved this manuscript.

10 REFERENCES

Burn, C.R. 2002. 'Tundra lakes and permafrost, Richards Island, western Arctic coast, Canada', *Canadian Journal of Earth Science* 39(8), pp. 1281–1298. doi:10.1139/e02-035.

Campbell, M.W., Shaw, J.G., and Blyth, C.A. 2012. 'Kivalliq Ecological Land Classification Map Atlas: A Wildlife Perspective', *Government of Nunavut, Department of Environment* Technical Report Series #1-2012, 274 p. Available at: https://www.gov.nu.ca/environment/information/kivalliq-ecological-land-classification-map-atlas (Accessed: 15-sep-2023).

Duguay, C.R. and Lafleur, P. 2003. 'Determining depth and ice thickness of shallow sub-Arctic lakes using space-borne optical and SAR data', *International Journal of Remote Sensing* 24, pp. 475–489. Doi:10.1080/01431160304992.

Dyke, A.S. 2004. 'An outline of North American deglaciation with emphasis on central and northern Canada', *Developments in Quaternary Sciences* 2, pp. 373–424. Doi.org/10.1016/S1571-0866(04)80209-4.

ECCC 2023. *Environment and Climate Change Canada Canadian Climate Normals*. Available at: https://climate.weather.gc.ca/climate_normals/ (Accessed: 15-Sep-2023).

Ecological Stratification Working Group 1995. *A National Ecological Framework for Canada*. Agriculture and Agri-Food Canada, Research Branch, Centre for Land and Biological Resources Research and Environment Canada. State of the Environment Directorate, Ecozone Analysis Branch, Ottawa/Hull. Report and national map at 1: 7,500,500 scale. Available at: https://sis.agr.gc.ca/cansis/publications/maps/eco/all/districts/eco_all_districts_3m_nwtnu.jpg (Accessed: 15-sep-2023).

Engram, M., Arp, C.D., Jones, B.M., Ajadi, O.A., and Meyer, F.J. 2018. 'Analyzing floating and bedfast lake ice regimes across Arctic Alaska using 25 years of space-borne SAR imagery', *Remote Sensing of Environment* 209, pp. 660–676. doi:10.1016/j.rse.2018.02.022.

French, N., Savage, S., Shuchman, R., Edson, R., Payne, J., and Josberger, E. 2004. 'Remote Sensing of Frozen Lakes on the North Slope of Alaska', in *IEEE International Geoscience and Remote Sensing Symposium*. Anchorage, Alaska, United States: September 20–24, 2004, pp. 3008–3011. doi:10.1109/IGARSS.2004.1370330.

Golder 2012a. 'SD 7-1 Aquatics Baseline Synthesis Report, 1994 to 2009 - Meliadine Gold Project, Nunavut – Meliadine Gold Project', *Agnico-Eagle Mines Limited*, unpublished report prepared by Golder Associates Ltd., Doc 327-1013730076 Ver. 0. (report accessible at www.nirb.ca).

Golder 2012b. 'SD 7-2 2011 Aquatic Baseline Studies - Meliadine Gold Project, Nunavut – Meliadine Gold Project', *AgnicoEagle Mines Limited*, unpublished report prepared by Golder Associates Ltd., Doc 246-1013730076 Ver. 0. 77. (report accessible at www.nirb.ca).

Golder 2014. 'SD 6-1 permafrost thermal regime baseline studies – Meliadine Gold Project', *Agnico-Eagle Mines Limited*, unpublished report prepared by Golder Associates Ltd., Doc 225-1314280007 Ver. 0. (report accessible at www.nirb.ca).

Golder 2021. 'Meliadine Extension–2020 Thermal Assessment–Meliadine Gold Project', *Agnico-Eagle Mines Limited*, unpublished report prepared by Golder Associates Ltd., Doc 20136436-815-R-Rev2-2200. (report accessible at www.nirb.ca).

Heginbottom, J.A., Dubreuil, M.A., and Harker, P.A. 1995. 'Canada-permafrost', in *National Atlas of Canada, 5th edition.* Natural Resources Canada, MCR4177. doi:10.4095/294672.

Jeffries, M.O., Morris, K., Weeks, W.F., and Wakabayashi, H. 1994. 'Structural and stratigraphic features and ERS-1 synthetic aperture radar backscatter characteristics of ice growing on shallow lakes in NW Alaska, winter 1991-1992', *Journal of Geophysical Research: Oceans* 99(22), pp. 22459–22471. doi:10.1029/94JC01479.

LeBlanc, A.-M., Chartrand, J., and Smith, S.L. 2022. 'Regional assessment of the presence of taliks below Arctic lakes, Nunavut', *Geological Survey of Canada* Scientific Presentation 138, 1 poster. doi:10.4095/330205.

LeBlanc, A.-M., Sladen, W.E., and Faucher, B. 2024. 'Lake-bottom temperature on shallow and deep terraces for sublacustrine open talik assessment near Rankin Inlet, Nunavut, Canada', in *ICOP2024, 12th International Conference on Permafrost*. Whitehorse, Yukon, Canada: June 16–20, 2024.

Ling, F., Wu, Q., Zhang, T., and Niu, F. 2012. 'Modelling Open-Talik Formation and Permafrost Lateral Thaw under a Thermokarst Lake, Beiluhe Basin, Qinghai-Tibet Plateau', *Permafrost and Periglacial Processes* 23, pp. 312–321. doi: 10.1002/ppp.1754.

Lopes, A., Nezry, E., Touzi, R., and Laur, H. 1993. 'Structure detection and statistical adaptive speckle filtering in SAR images', *International Journal of Remote Sensing* 14(9), pp. 1735–1758. doi:10.1080/01431169308953999.

Lunardini, V.J. 1981. *Heat Transfer in Cold Climates*. New York, New York, United States: Van Nostrand Reinhold Company, 731 p.

O'Neill, H.B., Wolfe, S.A., and Duchesne, C. 2024. Modelled ground ice conditions in the Kivalliq region, Nunavut, Canada, in ICOP2024. Whitehorse, Yukon, Canada: June 16–20.

O'Neill, H.B., Roy-Leveillee, P., Lebedeva, L., and Ling, F. 2020. 'Recent advances (2010–2019) in the study of taliks', *Permafrost and Periglacial Processes* 31. pp. 346–357. doi:10.1002/ppp.2050.

Pointner, G. and Bartsch, A. 2020. 'Interannual variability of lake ice backscatter anomalies on Lake Neyto, Yamal, Russia', *GI Forum Journal* 8, pp 47–62. doi:10.1553/giscience2020_01_s47.

Pointner, G., Bartsch, A., Forbes, B. C., and Kumpula, T. 2019. 'The role of lake size and local phenomena for monitoring ground-fast lake ice', *International Journal of Remote Sensing* 40, pp. 832–858. doi:10.1080/01431161.2018.1519281.

Mackay, J.R. 1992. 'Lake stability in an ice-rich permafrost environment: Examples from the western Arctic coast, in R. Robarts and M. Bothwell (eds.), *Aquatic Ecosystems in Semi-arid Regions: Implications for Resource Management*. Saskatoon, Saskatchewan, Canada: August 27–30, 1990, pp. 1–25.

Mellor, J.C. 1982. *Bathymetry of Alaskan Arctic Lakes: A key to resource inventory with remote sensing methods*. PhD Thesis, Faculty of the University of Alaska. 361 p.

Michel, B., 1971. 'Winter Regime of Rivers and Lakes', *U.S. Army Cold Regions Research and Engineering Laboratory* Monograph III-B1a, 131 p.

Minsley, B.J., Abraham, J.D., Smith, B.D., Cannia, J.C., Voss, C.I., Jorgenson, M.T., Walvoord, M.A., Wylie, B.K., Anderson, L., Ball, L.B., Deszcz-Pan, M., Wellman, T.P., and Ager, T.A. 2012. 'Airborne electromagnetic imaging of discontinuous permafrost', *Geophysical Research Letters* 39(2), pp. 1–8. doi:10.1029/2011GL050079.

Murfitt, J. and Duguay, C.R. 2021. '50 years of lake ice research from active microwave remote sensing: Progress and prospects', *Remote Sensing of Environment* 264. doi:0.1016/j.rse.2021.112616.

NRCan 2017. 'Lakes, Rivers and Glaciers in Canada, CanVec Series, Hydrographic Features', 1:50,000, *Natural Resources Canada*. Available at: www.open.canada.ca.

Roy-Léveillée, P., Burn, C.R., and McDonald, I.D. 2014. 'Vegetation-permafrost relations within the forest-tundra ecotone near Old Crow, Northern Yukon, Canada', *Permafrost and Periglacial Processes* 25, pp. 127–135. doi:10.1002/ppp.1805.

Sellman, P.V., Weeks., W.F., and Campbell, W.J. 1975. 'Use of sidelooking airborne radar to determine lake depth on the Alaskan North Slope', *U.S. Army Cold Regions Research and Engineering Laboratory* Special Report 230.

Shaposhnikova, M., Duguay, C., and Roy-Léveillée., P. 2023. 'Bedfast and floating-ice dynamics of thermokarst lakes using a temporal deep-learning mapping approach: case study of the Old Crow Flats, Yukon, Canada', *The Cryosphere* 17(4), pp. 1697–1721. doi:10.5194/tc-17-1697-2023.

Stevens, C.W., Moorman, B.J., and Solomon, S.M. 2010. 'Modeling ground thermal conditions and the limit of permafrost within the nearshore zone of the Mackenzie Delta, Canada', *Journal of Geophysical Research* 115. doi:10.1029/2010JF001786.

Sumgin, M.I. 1927. *Permafrost Soil within the USSR*. 1st edition. Vladivostok, Russia: Far-Eastern Geophysical Observatory, 372 p.

van der Sanden, J.J, Geldsetzer, T., Short, N., and Brisco, B. 2012. *Advanced SAR Applications for Canada's Cryosphere (Freshwater Ice, and Permafrost)*, final technical report. Canadian Space Agency, Government Related Initiatives Program (GRIP), Natural Resources Canada, 54 pages. doi:10.4095/291867

Long-term permafrost monitoring in northern Canada – What have we learned?

Sharon L. Smith, Caroline Duchesne & H. Brendan O'Neill

Geological Survey of Canada, Natural Resources Canada, Ottawa, Ontario, Canada

ABSTRACT

The Geological Survey of Canada has monitored permafrost temperatures and active layer thicknesses across northern Canada for over three decades at some sites. The continuous observation of these two indicator variables has facilitated assessment of change and variation in permafrost thermal state. Permafrost continues to warm across northern Canada by more than 0.5 °C per decade in the colder Arctic permafrost. Temperatures of warmer permafrost of the discontinuous zone have changed very little over the past two to three decades, and isothermal temperature profiles are observed as thaw progresses. Data from the Mackenzie Valley network indicate that active layer thickness has generally increased since the 1990s but with much variability between sites. Measurements such as ground surface elevation and the base of the thawed layer acquired from thaw tubes at these sites provide additional information to better assess the loss of shallow permafrost, particularly where excess ice is present. The analysis of shallow ground temperatures also provides evidence of permafrost table lowering over time. These ground temperature and thaw tube data are helping to create a more complete picture of long-term warming and thaw of Canada's permafrost. The data collected from the monitoring network facilitates improved climate change assessments and provides essential data to inform climate change adaptation planning.

1 INTRODUCTION

Two key indicator variables for assessing changes in permafrost are permafrost thermal state and active layer thickness. These indicators also contribute to the permafrost Valued Ecosystem Component under northern Canadian monitoring programs and the Essential Climate Variable (ECV) under the Global Climate Observing System. The Geological Survey of Canada (GSC), in collaboration with partners, has monitored these indicators across northern Canada, for over three decades at some sites (e.g., Smith et al. 2019). This continuous monitoring has facilitated assessment of change and variation in permafrost thermal state. However, the interpretation of the results of the time series analysis is challenging particularly as permafrost temperatures approach 0 °C (Smith et al. 2022a). Although active layer thickness (ALT) is commonly used as an indicator of permafrost degradation and for validation of models, interpretation of trends in ALT is not straight forward. Despite the wide use of ALT, it is not always the best indicator of permafrost degradation.

The analysis of other data along with these two indicators can address some of the challenges in interpretation (Smith et al. 2022a). This includes analysis of shallow ground temperatures in addition to temperature at the depth generally used for the ECV indicator (i.e., depth of zero annual amplitude, DZAA), and measurements of ground surface elevation over time for assessment of surface subsidence. The extensive records for GSC monitoring sites provide essential data that can facilitate improved characterization of the recent changes in permafrost environments and assessments of permafrost loss.

In this paper, an update on the trends in the indicator variables is provided. The challenges and limitations associated with interpretation of these trends will be discussed along with how analysis of additional data can provide further insights into how permafrost conditions are changing in northern Canada.

2 THE MONITORING NETWORK

The GSC in collaboration with partners, measures ground temperatures at 103 sites with instrumentation in 140 different boreholes that are currently active (Figure 1). Some have been operating for more than three decades including those at Alert and some in the Mackenzie Valley. Many monitoring sites were established over the past 20 years under various programs such as International Polar Year. Boreholes are instrumented with multi-thermistor cables with most connected to RBR data loggers

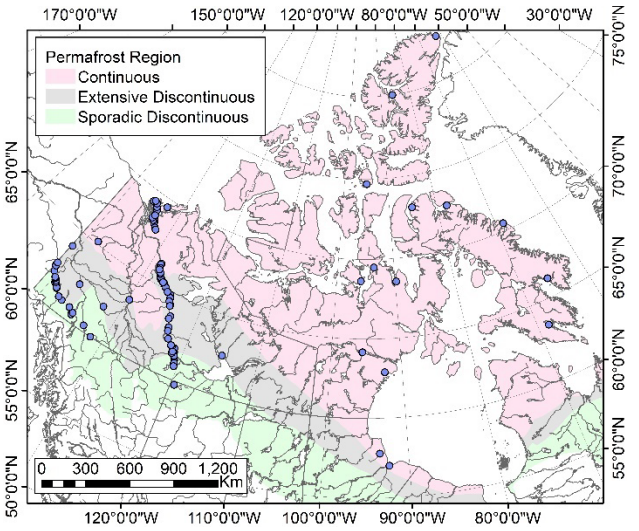

Figure 1. Location of GSC thermal monitoring sites (circles). Permafrost zones from Heginbottom et al. (1995).

https://doi.org/10.52381/ICOP2024.84.1

that record temperatures at 8-hour intervals and only manual readings during site visits at others. The precision and accuracy of the monitoring system is generally better than ± 0.1 °C. Additional details on the ground temperature monitoring network are found in Smith et al. (2009, 2010, 2015), Ednie and Smith (2011), and Duchesne et al. (2020).

A network of thaw tubes in the Mackenzie Valley has been maintained since the early 1990s (e.g., Nixon and Taylor 1994; Duchesne et al. 2015). The instrumentation facilitates measurement of seasonal thaw depth relative to a fixed reference datum, ground surface elevation and derivation of active layer thickness.

The monitoring network provides information on ground thermal and active layer conditions for a range of climate and permafrost conditions, from warmer permafrost of the discontinuous zone to the colder permafrost of the continuous zone. A range of vegetation conditions (boreal to tundra), geological and terrain conditions are also represented.

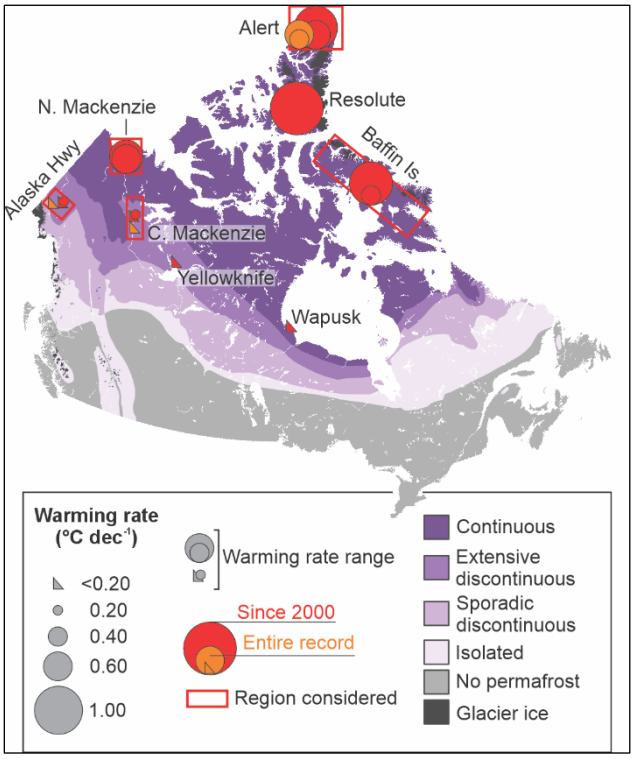

Figure 2. Regional permafrost warming rates based on ground temperature records. The trends (based on linear regression) for the entire record (for sites with longer records) and since 2000 are shown. Circle sizes are proportional to the trend.

3 TRENDS IN INDICATORS

3.1 Permafrost Temperature

For assessments of long-term changes in permafrost thermal state, the temperature measured at or close to the DZAA is generally used, where seasonal variation is < 0.1 °C. At this depth annual variations are filtered out, allowing longer term trends to be more readily examined. For many sites in the monitoring network boreholes are deeper than DZAA but for some sites this depth was not reached (due to limitations with drilling equipment), and temperatures are assessed at the greatest measurement depth. This is the case for some tundra sites such as those on Baffin Island where drilling to DZAA was not possible.

Widespread warming of permafrost is observed across northern Canada (Figure 2) with regional variability in the magnitude of change. This warming has persisted over the last three to four decades as indicated by longer records available for some sites (Figure 3). These observations agree with those from records of similar length for Alaska (Smith et al. 2022b).

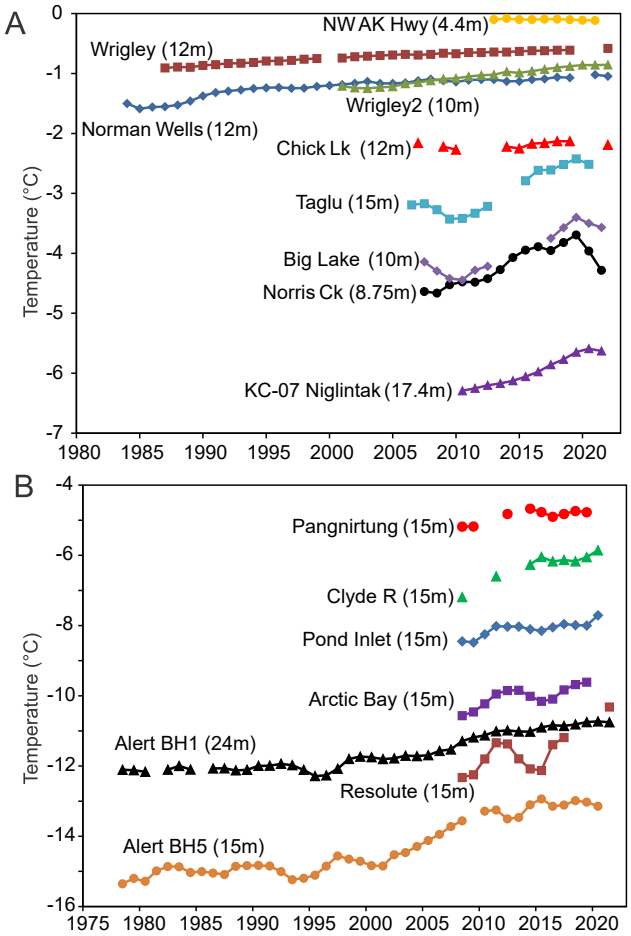

Figure 3. Mean annual ground temperatures for sites in Northern Canada. (A) Northwestern Canada in the Mackenzie Valley (forested sites in the central valley to tundra sites in the Mackenzie Delta region) and one site in the Alaska Highway Corridor, Yukon. (B) Eastern and high Arctic. The measurement depth is indicated in parentheses. Note difference in vertical and horizontal scale.

As reported in earlier assessments (e.g., Smith et al. 2019, 2022b), increases in permafrost temperature are generally lower in the warmer permafrost of the discontinuous permafrost zone, typically less than 0.2 °C per decade. This is illustrated by the time series for the central Mackenzie Valley (Figure 3a). Records in southern Yukon are fewer with most only about a decade long. However, trends are similar to those in the central Mackenzie Valley, generally being less than 0.2 °C per decade (Figure 2) with slight cooling at some sites. Assessment of trends since 1978–1979 for some re-activated sites in the Alaska Highway Corridor, through comparison to earlier data collected by GSC (Smith et al. 2015), indicates that permafrost has warmed up to 0.1 °C per decade between 1978 and 2021.

Generally, greater increases in ground temperature are observed in the colder permafrost of the continuous zone (Figures 2 and 3). Increases in ground temperature in the northern Mackenzie region and Nunavut range from about 0.4 to 1 °C per decade (Figure 2), which is similar to elsewhere in the Arctic including northern Alaska and Svalbard (Smith et al. 2022b; Isaksen et al. 2022; Box et al. 2021). The records since 1978 for Alert (Figure 3b) show that a large part of the permafrost warming has occurred in the 21st century. Some cooling of permafrost occurred beginning about 2020 in the northern Mackenzie (Figure 3a) similar to that observed for northern Alaska (Smith et al. 2022b).

Trends in permafrost temperature generally reflect those for mean annual air temperature (MAAT), with long-term MAAT increasing by 0.4 to 0.7 °C per decade in the Mackenzie Valley (Figure 4a) and 0.3 to 0.6 °C per decade in the eastern and high Arctic (Figure 4b). Since 2000 however, changes in air temperature are up to 1.7 °C per decade for the high Arctic (e.g., Alert and Resolute Bay) and the central and northern Mackenzie (e.g., Inuvik and Norman Wells). The greater increase in air temperatures is reflected in the greater rates of permafrost warming observed at Alert since 2000. The decrease in ground temperature after 2019 in the northern Mackenzie is likely due to the lower mean annual air temperature in 2020 and 2021 (Figure 4a).

Changes in ground temperature are also observed below DZAA. For sites with deeper boreholes these are observed to depths of more than 50 m (Figure 5). At Alert, temperature increased between 1979 and 2022 at depths of DZAA (about 24 m) by more than 1.3 °C and more than 0.7 °C at depths up to 50 m. Increases in permafrost temperature over periods of more than three decades at all measurement depths are observed, with greater increases for colder tundra sites compared to the warmer forested sites. The greater surface buffer layer including an organic

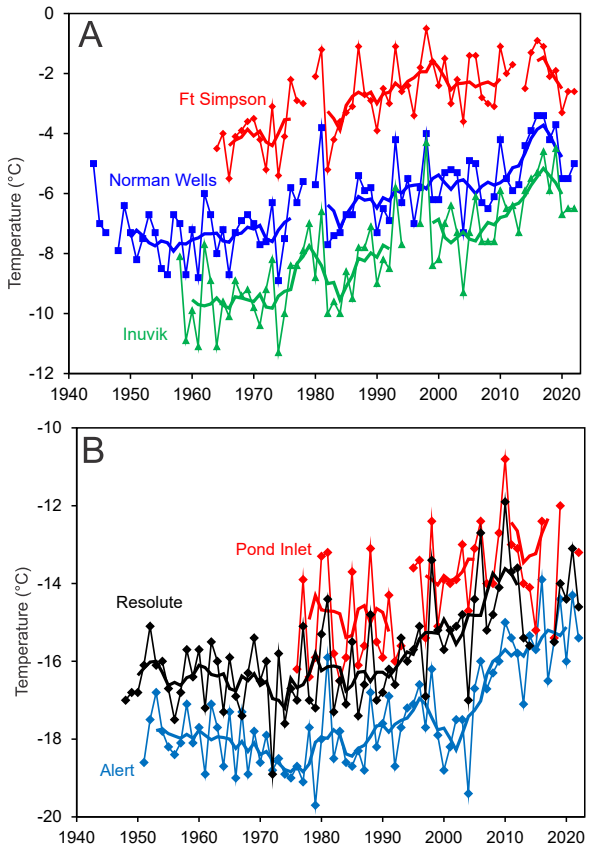

Figure 4. MAAT for Environment and Climate Change Canada (2023) stations for (A) Mackenzie Valley and (B) eastern and high Arctic. The thick line is the 5-year running mean. Note difference in vertical scale.

layer at the forested sites is partly responsible for lower increase in ground temperature for the sites in the central Mackenzie Valley (Norman Wells and Wrigley in Figures 3 and 5). Farther north, at the tundra upland site at Niglintak (KC-07) in the northern Mackenzie region, a greater increase in temperature is observed over a shorter time period (Figure 5). Snow cover can also influence the magnitude of the response of ground temperature to changes in air temperature. This is illustrated at the Alert boreholes where greater snow cover generally accumulates at BH1 (up to 80 cm) and BH3 (35–75 cm) compared to BH5 (< 20 cm), providing greater insulation from increases in winter air temperature that have occurred (Smith et al. 2012). Ground temperatures have therefore changed less at BH1 and BH3, below 10 m depth, compared to BH5 (Figure 5).

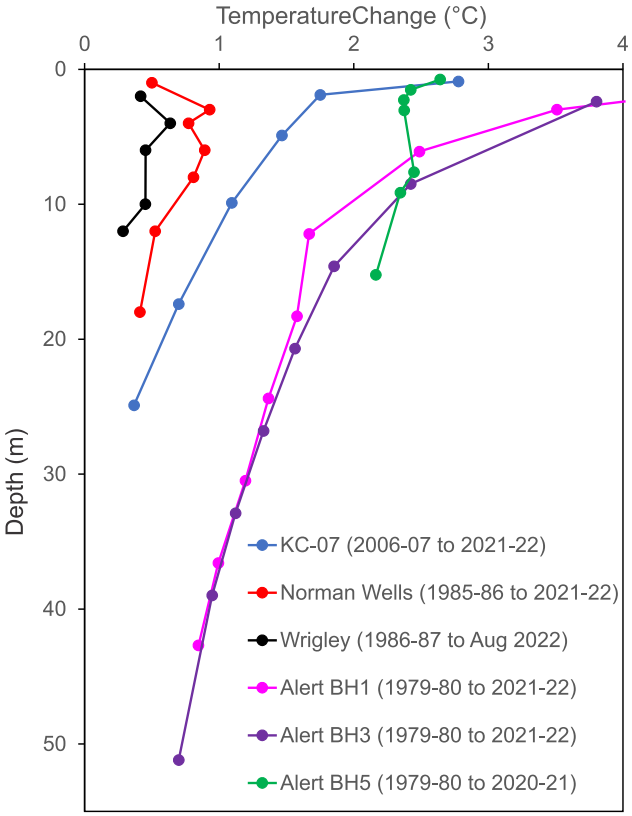

Figure 5. Total change in mean annual ground temperature over the available record for sites at Alert and in the Mackenzie Valley.

3.2 Active Layer

ALT responds more to higher frequency variations in air temperature and snow conditions compared to permafrost temperatures measured at DZAA, making it more difficult to assess long-term trends. Analysis of ALT data acquired from thaw tubes in the Mackenzie Valley indicates ALT has increased on average by about 1 cm per decade (Figure 6). However, this trend is not statistically significant and there is a large range in trends for individual sites, from > +20 to -3 cm per decade, with trends being significant at about 35% of the sites (O'Neill et al. 2023). This wide range in ALT trends is also observed across the circumpolar permafrost region (Smith et al. 2022a).

Overall, the greatest ALT occurred in 1998 (Figure 6), which was one of the warmest years during the 30-year monitoring period (Figure 4a). Although ALT decreased in subsequent years there was a general increase after 2008, consistent with a general increase in air temperature (Figure 4a). Greater rates of ALT increase were observed in the 2010s compared to the preceding two decades (O'Neill et al. 2023).

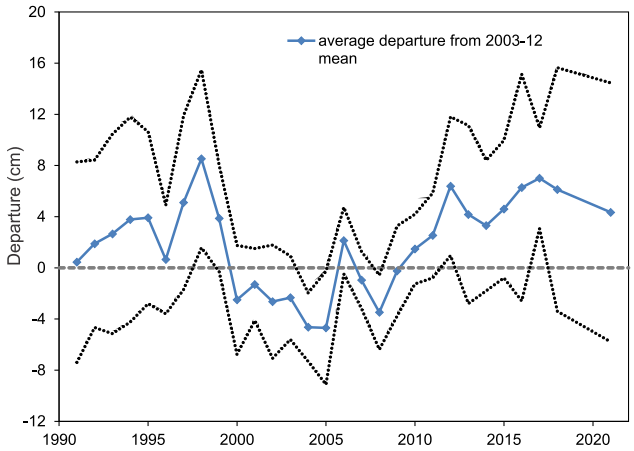

Figure 6. Average departure of ALT relative to 2003-12 mean based on data collected from thaw tubes at 25 sites in the Mackenzie valley. Note: no data were collected in 2020 and 2021 and the value shown for 2021 represents the maximum thaw depth for the 2019–2021 thaw seasons. Dotted lines delineate one standard deviation from the mean. Updated from Duchesne et al. (2020).

4 Challenges Interpreting Trends

Assessment of trends in the indicator variables provides important information on changes in permafrost conditions. However, it is important to be aware of the challenges in interpreting these trends and the limitations of using only the ECV indicators for assessments of permafrost change.

Assessing changes in permafrost conditions is challenging in warm permafrost at temperatures close to 0 °C where rates of temperature change are generally low or negligible (Figure 3a). This is particularly true in ice-rich material. As ground temperatures approach 0 °C, ground ice melts over a range in temperature and latent heat effects dominate (Romanovsky et al. 2010). This is the case at the warm ice-rich permafrost site near Wrigley where the total increase in ground temperature has generally been less than 0.5 °C over the 36-year period at all depths (Figure 5). In contrast at the colder tundra site in the Mackenzie Delta region at Niglintak (KC-07 in Figure 5), greater increases in temperature are observed at all depths over a shorter time period.

As ground ice melts, temperature profiles become isothermal and, although deeper temperatures at DZAA may show little change, near surface temperatures do increase over time and increases in thaw depth may be observed. This is shown for a site near Wrigley (DZAA about 10 m) where maximum annual ground temperatures have generally increased over the monitoring period with accompanying increases in thaw depth, although there are short-term fluctuations (Figure 7).

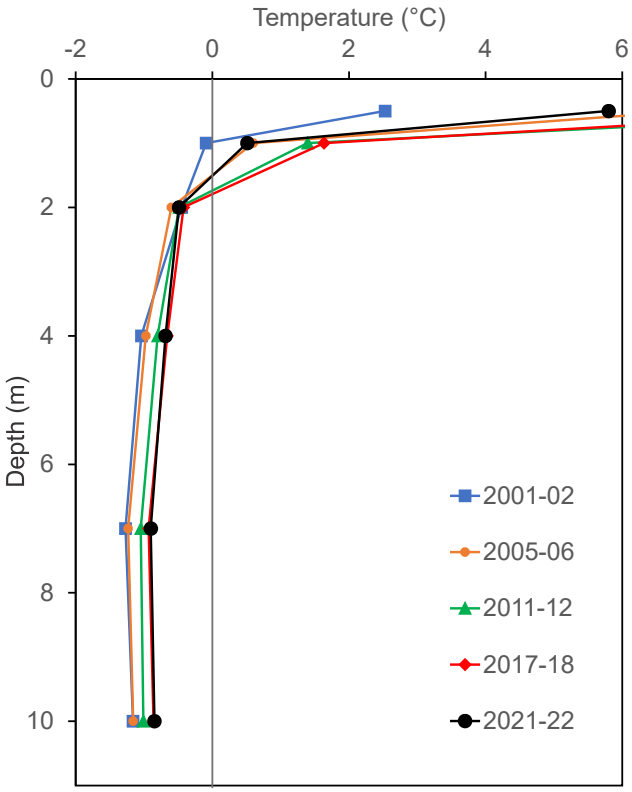

Figure 7. Maximum annual ground temperature profiles for a site near Wrigley in the central Mackenzie Valley.

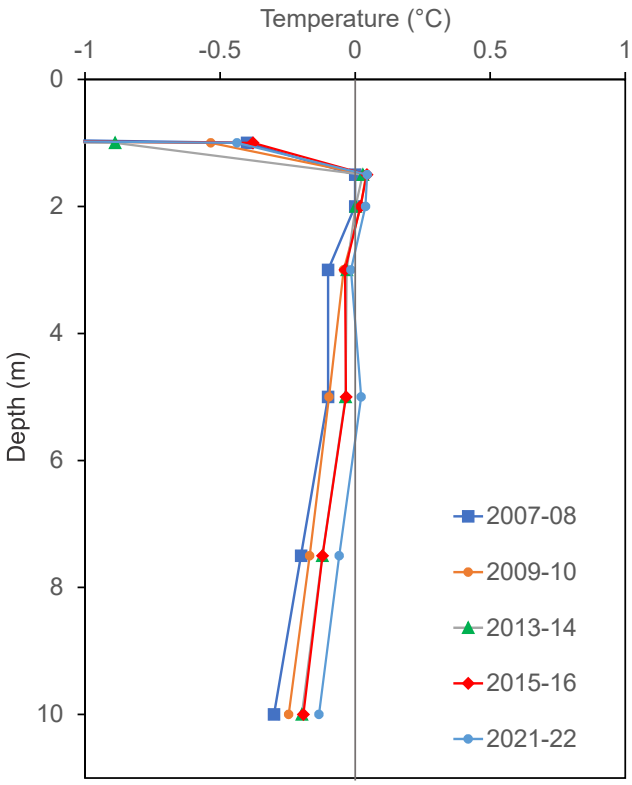

Figure 8. Minimum annual ground temperature profiles for a recovering burn site near Tulita.

Minimum annual temperatures can also increase in the upper part of the ground. For example, at a recovering burn site (burned in 2005, two years before site establishment) in the central Mackenzie Valley near Tulita, mean annual temperature at 7.5 m (DZAA) has increased by < 0.1 °C per decade. However, the minimum annual ground temperatures have generally increased since 2007–08 (Figure 8). This is likely due to a combination of increases in air temperature and the effects of the fire such as impacts on the organic layer and reduced snow interception due to damage to the tree canopy. Minimum annual temperatures at 1.5 to 2 m have been above 0 °C, since 2009–10. Temperatures are close to 0 °C, with the small increases above 0 °C being generally near the precision of the instrumentation. A talik may be forming as warming and thawing of the ground occurs.

Although lack of temporal variability in ALT for some sites implies that thawing is minimal over the monitoring period, examination of complementary data collected from the thaw tubes indicates that substantial permafrost degradation has occurred (O'Neill et al. 2023). At sites underlain by ice-rich permafrost, thawing of the ground can result in surface subsidence and soil consolidation as ground ice melts. Measurements of thaw penetration, relative to the initial ground surface, indicate that thaw progresses deeper into the ground as excess ice thaws and subsidence occurs even though the ALT changes very little over time. For the ice-rich permafrost site shown in Figure 9a, ALT increases by 20 cm between 1994 and 2016. However, the depth of the frost table increased by 44 cm accompanied by about 21 cm of surface subsidence due to the melting of excess ice. At a site underlain by ice-poor permafrost, little subsidence accompanies thawing and ALT shows a greater increase of about 51 cm between 1994 and 2016, which is only 9 cm less than the total increase in the depth of the frost table (Figure 9b). The change in the thaw depth relative to the fixed reference datum therefore provides a better indication of permafrost degradation over time. Shallow ground temperatures can also be used to determine frost table depth (e.g., Figure 7) and provide evidence of permafrost degradation.

Mechanical probing is used at most of the Arctic sites contributing to the Circumpolar Active Layer Monitoring Network. ALT measurements acquired by using only this method therefore underestimate the degradation of permafrost in ice-rich terrain. Results from the thaw tube network in the Mackenzie Valley indicate that significant increases in thaw penetration relative to a fixed datum (median rate 8 cm per decade), occurred at over 70% of the sites (O'Neill et al. 2023). Significant subsidence (median rate 4 cm per decade) also occurred at over 70% of the sites. Similar rates of subsidence, based on surface elevation surveys, are also observed at other sites in the Mackenzie Valley along the Norman Wells pipeline corridor (Smith et al. 2008; Burgess and Smith 2003) and in Alaska (e.g., Streletskiy et al. 2017; Nyland et al. 2021).

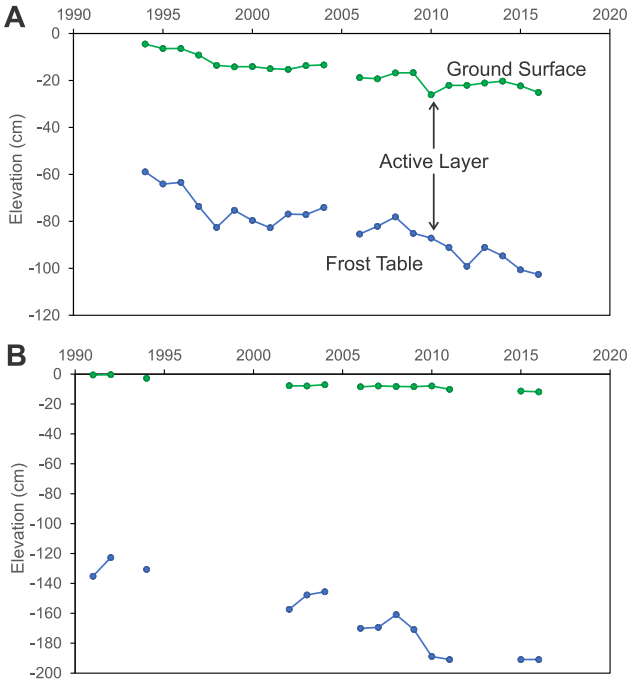

Figure 9. Elevation of ground surface and frost table, relative to original ground surface elevation, for (A) ice-rich site and (B) ice-poor site in the northern Mackenzie. The active layer is the layer between the ground surface and the frost table. Note difference in vertical scale.

5 SUMMARY

Analysis of permafrost temperatures indicates that permafrost continues to warm across the Canadian north although there are periods of short-term cooling at some sites. The rate of warming in the 21st century ranges from < 0.2 °C per decade in the warm permafrost of the discontinuous permafrost zone up to about 1.0 °C per decade in the continuous permafrost zone. Similar rates are observed elsewhere in the Arctic. Over the past four decades permafrost temperatures at the coldest site have increased by more than 1.3 °C, based on the temperature at 24 m depth at Alert. This means that the overall range in permafrost temperature at DZAA for northern Canada has decreased over the past four decades by more than 1.3 °C. Records from the active layer monitoring sites in the Mackenzie region indicate a general increase in ALT since the 1990s, but trends are highly variable.

The trends in permafrost temperature, measured at DZAA, provide a good indicator of permafrost change. However, for ice-rich permafrost at temperatures close to 0 °C, where latent heat effects are important, analysis of other data such as shallow temperatures can provide additional information on changing conditions including degradation of permafrost. Measurements of thaw depth relative to a fixed reference datum derived from thaw tubes or ground temperature measurements provide a better indication of permafrost loss than active layer thickness derived through mechanical probing especially where permafrost is ice-rich. Results from the thaw tubes in the Mackenzie Valley indicate that permafrost is degrading at many sites accompanied by substantial surface subsidence. These results provide important information for assessment of landscape change in permafrost environments.

The GSC permafrost monitoring network provides important information to assess the state and change in permafrost conditions. Analysis of the data collected has provided evidence of ongoing warming and thawing of permafrost in northern Canada over the past three to four decades. Essential information is being provided for improved climate change assessments and to inform climate change adaptation.

6 ACKNOWLEDGEMENTS

This research is supported by Natural Resources Canada and various funding sources over the last several years. The logistical support provided by Polar Continental Shelf Program is greatly appreciated. Jason Chartrand has provided ongoing support for data processing and management. Site establishment, maintenance and data collection would not have been possible without the contributions of several partners and collaborators including numerous GSC colleagues, University of Ottawa (A. Lewkowicz), Northwest Territories Geological Survey, Environment and Climate Change Canada, Nunavut Government, Yukon Geological Survey, Yukon Research Centre (Yukon University), Parks Canada, Department of National Defence, and members of various communities. Comments on the manuscript by Stephen Wolfe (GSC) are much appreciated. Comments by the reviewers are also appreciated. NRCan Contribution Number:20230251

7 REFERENCES

Box, J.E., Bhatt, U.S., Christensen, T.R., Derksen, C., Gerland, S., Granskog, M., Isaken, K., Kohler, J., Mard, J., Meier, W.N., Mudryk, L., Romanovsky, V.E., Shiklomanov, A., Smith, S., Vanha-Majamaa, I., Wouters, B., and Yang, D. 2021. 'Recent developments in Arctic climate observational indicators', in *AMAP Arctic Climate Change Update 2021: Key Trends and Impacts*. Arctic Monitoring and Assessment Programme (AMAP), Tromso, Norway. pp. 7–29. Available at: https://www.amap.no/documents/download/6890/inline

Burgess, M.M. and Smith, S.L. 2003. '17 years of thaw penetration and surface settlement observations in permafrost terrain along the Norman Wells pipeline, Northwest Territories, Canada', in M. Phillips, S.M. Springman, and L.U. Arenson (eds.), *Proceedings of 8th International Conference on Permafrost*. Zurich, Switzerland: July 2003, pp. 107–112.

Duchesne, C., Chartrand, J., and Smith, S.L. 2020. 'Report on 2018 field activities and collection of ground-thermal and active-layer data in the Mackenzie corridor, Northwest Territories', *Geological Survey of Canada* Open File 8707. Available at: https://doi.org/10.4095/321921.

Duchesne, C., Smith, S.L., Ednie, M., and Bonnaventure, P.P. 2015. 'Active layer variability and change in the Mackenzie Valley, Northwest Territories', in *GEOQuébec 2015 (68th Canadian Geotechnical Conference and 7th Canadian Conference on Permafrost)*. Québec City, Québec, Canada: Paper 117.

Ednie, M. and Smith, S.L. 2011. 'Establishment of community-based permafrost monitoring sites and initial ground thermal data Baffin Region', *Nunavut, Geological Survey of Canada* Open File 6727. Available at: https://doi.org/10.4095/287873.

Environment and Climate Change Canada 2023. *Adjusted and homogenized Canadian climate data*. Available at: https://www.canada.ca/en/environment-climate-change/services/climate-change/science-research-data/climate-trends-variability/adjusted-homogenized-canadian-data.html.

Heginbottom, J.A., Dubreuil, M.-A., and Harker, P.A. 1995. 'Canada, permafrost', in *National Atlas of Canada, 5th edition*. Natural Resources Canada, MCR 4177, scale 1:7,500,000. doi:10.4095/294672.

Isaksen, K., Lutz, J., Sorensen, A.M., Godoy, O., Ferrighi, L., Eastwood, S., and Aaboe, S. 2022. 'Advances in operational permafrost monitoring on Svalbard and in Norway', *Environmental Research Letters* 17: 095012. doi:10.1088/1748-9326/ac8e1c.

Nixon, F.M. and Taylor, A.E. 1994. 'Active layer monitoring in natural environments, Mackenzie Valley, Northwest Territories', *Geological Survey of Canada* Current Research, 1994-B, pp. 27–34. Available at: https://doi.org/10.4095/193650.

Nyland, K.E., Shiklomanov, N.I., Streletskiy, D.A., Nelson, F.E., Klene, A.E., and Kholodov, A.L. 2021. 'Long-term Circumpolar Active Layer Monitoring (CALM) program observations in Northern Alaskan tundra', *Polar Geography* 44(3), pp. 176–185. doi:10.1080/1088937X.2021.1988000.

O'Neill, H.B., Smith, S.L., Burn, C.R., and Zhang, Y. 2023. 'Widespread permafrost degradation and thaw subsidence in northwest Canada', *Journal of Geophysical Research (Earth Surface)* 128(8), e2023JF007262. doi:10.1029/2023JF007262

Romanovsky, V.E., Smith, S.L., and Christiansen, H.H. 2010. 'Permafrost thermal state in the polar Northern Hemisphere during the International Polar Year 2007-2009: a synthesis', *Permafrost and Periglacial Processes* 21, pp. 106–116. doi:10.1002/ppp.689.

Smith, S.L., Burgess, M.M., and Riseborough, D.W. 2008. 'Ground temperature and thaw settlement in frozen peatlands along the Norman Wells pipeline corridor, NWT Canada: 22 years of monitoring', in D.L. Kane and K.M. Hinkel (eds.), *Ninth International Conference on Permafrost*. Fairbanks, Alaska, United States: vol.2, pp. 1665–1670.

Smith, S.L., Chartrand, J., Nguyen, T.N., Riseborough, D.W., Ednie, M., and Ye, S. 2009. 'Geotechnical database and descriptions of permafrost monitoring sites established 2006-07 in the central and southern Mackenzie Corridor', *Geological Survey of Canada* Open File 6041. Available at: https://doi.org/10.4095/226435.

Smith, S.L., Duchesne, C., and Lewkowicz, A.G. 2019. 'Tracking changes in permafrost thermal state in Northern Canada', in J.-P. Bilodeau, D.F. Nadeau, D. Fortier, and D. Conciatori (eds.), *Cold Regions Engineering 2019, Proceedings of the 18th International Conference on Cold Regions Engineering and the 8th Canadian Permafrost Conference*. Québec City, Québec, Canada: August 18–22, 2019. pp. 670–677.

Smith, S.L., Lewkowicz, A.G., Ednie, M., Duguay, M.A., and Bevington, A. 2015. 'Characterization of permafrost thermal state in the southern Yukon', in *GEOQuébec 2015 (68th Canadian Geotechnical Conference and 7th Canadian Conference on Permafrost)*. Québec City, Québec, Canada: Paper 331.

Smith, S.L., O'Neill, H.B., Isaksen, K., Noetzli, J., and Romanovsky, V.E. 2022. 'The changing thermal state of permafrost', *Nature Reviews Earth & Environment* 3, pp. 10–23. doi:10.1038/s43017-021-00240-1.

Smith, S.L., Romanovsky, V.E., Isaksen, K., Nyland, K.E., Kholodov, A.L., Shiklomanov, N.I., Streletskiy, D.A., Drozdov, D.S., Malkova, G.V., and Christiansen, H.H. 2022. '[Arctic] Permafrost [in "State of the Climate in 2021"]', *Bulletin of the American Meteorological Society* 103(8), S286-S290. doi:10.1175/BAMS-D-22-0082.1.

Smith, S.L., Romanovsky, V.E., Lewkowicz, A.G., Burn, C.R., Allard, M., Clow, G.D., Yoshikawa, K., and Throop, J. 2010. 'Thermal state of permafrost in North America - A contribution to the International Polar Year', *Permafrost and Periglacial Processes* 21, pp. 117–135. doi:10.1002/ppp.690.

Smith, S.L., Throop, J., and Lewkowicz, A.G. 2012. 'Recent changes in climate and permafrost temperatures at forested and polar desert sites in northern Canada', *Canadian Journal of Earth Sciences* 49, pp. 914–924. doi:10.1139/E2012-019.

Streletskiy, D.A., Shiklomanov, N.I., Little, J.D., Nelson, F.E., Brown, J., Nyland, K.E., and Klene, A.E. 2017. 'Thaw subsidence in undisturbed tundra landscapes, Barrow, Alaska, 1962–2015', *Permafrost and Periglacial Processes* 28, pp. 566–572. doi:10.1002/ppp.1.

Vertical surface change signals of rock glaciers: combining UAV and Pléiades imagery (Agua Negra, Argentina)

Melanie Stammler[1], Diego Cusicanqui[2], Rainer Bell[1], Benjamin Robson[3], Xavier Bodin[4], Jan Blöthe[5] & Lothar Schrott[1]

[1]*Department of Geography, University of Bonn, Bonn, Germany*

[2]*Institut des Sciences de la Terre (ISTerre), CNRS/Université Grenoble Alpes, Grenoble, France*

[3]*Department of Earth Science, University of Bergen, Bergen, Norway*

[4]*Laboratoire EDYTEM, CNRS/Université Savoie Mont-Blanc, Le Bourget du Lac, France*

[5]*Institute of Environmental Social Sciences and Geography, University of Freiburg, Freiburg, Germany*

ABSTRACT

Detailed analyses of rock glacier change are essential in the Dry Andes, where rock glaciers store essential waters whose input to hydrological systems are forecast to gain relative importance due to climate change. The rugged terrain and high elevation present challenges when conducting high-resolution monitoring with demanding UAV flying, and steep slopes that can be occluded. Degradation processes often manifest themselves in surface changes whose investigation of local patterns assists in understanding the landforms' runoff contribution.

We investigate vertical surface change on Dos Lenguas (San Juan, Argentina) using UAV flights and tri-stereo, panchromatic Pléiades imagery (austral summers 2022/2023). We compare three photogrammetric processing strategies to assess which method can be used to resolve the subtlest vertical rock glacier changes. The processing of Pléiades imagery in Agisoft Metashape Professional leads to the most appropriate representation of ridges and furrows, whereas the DEMs produced in Catalyst Professional contain noise larger than the magnitude of annual change. We find that processing Pléiades imagery in Ames Stereo Pipeline allows for the DEMs of Difference to reproduce vertical rock glacier surface change to an extent suitable for a geomorphological interpretation in terms of magnitude and pattern, with high similarity to UAV based results and low errors. We suggest combining UAV and Pléiades imagery to bridge detailed small-scale and less detailed regional assessment. We envision that this opens up novel possibilities for interpreting previously undetected change signals. These could provide new insights in our process-response understanding of the high Andean (peri)glacial landscape and its hydrological significance.

1 INTRODUCTION

Periglacial and cryogenic meltwaters represent an essential water source to domestic, agricultural and industrial water use in the Dry Andes and their foreland (Trombotto and Borzotta 2009; Schrott 1994; Schrott and Götz 2013), as in the study area of the Agua Negra catchment (San Juan Province/Argentina, 30ºS and 69ºW). Climate change induced melting of glaciers and snow, as well as the degradation of permafrost pose risk in terms of water scarcity. While glacial and cryogenic water storages are diminishing quickly (Dussaillant et al. 2019; Masiokas et al. 2020; Ferri et al. 2020; Pitte et al. 2022), rock glaciers show a delayed water release to surface runoff. Their ice and water storage capacities are primary controls on groundwater recharge (Halla et al. 2021; Geiger et al. 2014) and discharge contribution. Already today, (peri)glacial runoff contribution is specifically important in areas characterised by scarce precipitation; with increasing hydrological significance towards the future (Arenson et al. 2022; Masiokas et al. 2020).

Rock glaciers and glaciers which exist in close proximity suggest mutual (de)coupling relations (Cusicanqui et al. 2023). Examples are acting as mechanical entity (Etzelmüller and Hagen 2005) or water becoming an agent of transient interaction (Miesen et al. 2021). Surface changes are indicators of alterations in melting/thawing processes. Surface change analysis can explain not only local patterns of surface variations but also meltwater contribution to runoff (Blöthe et al. 2021; Halla et al. 2021; Vivero and Lambiel 2019). It is hypothesized, that co-existence of glacial and periglacial systems, e.g., moraine-derived rock glaciers, showcase diverging surface processes to non-glacially impacted periglacial systems, e.g., talus-derived rock glaciers, in terms of their magnitude and pattern due to interim water storage. Thus, it is important to move from single landform-focused analyses to investigating change signals for multiple landforms, over larger areas. For an accurate and precise understanding of the surface changes and related processes (thawing and (re)freezing of ice bodies and active layer, degradation of permafrost), highly resolved elevation data is crucial (Mueting et al. 2021; Robson et al. 2022).

Stereophotogrammetry allows for a generation of high-resolution DEMs which can be intercompared to derive elevation changes (Halla et al. 2021; Robson et al. 2022). While UAV surveying offers highest resolutions, these acquisitions are dependent on favourable weather conditions and can be challenging at high altitudes. Sub-metre tri-stereo satellite sensors such as Pléiades enable DEM generation with resolutions of up to 1 m (e.g., Bagnardi et al. 2016) at spatial coverage much higher than common UAV surveys.

https://doi.org/10.52381/ICOP2024.138.1

We test combining Pléiades and UAV imagery to interpret previously undetected change signals. This might provide new insight into our process-response understanding of the high Andean (peri)glacial landscape and its hydrological significance. We (i) generate high-resolution DEMs based on tri-stereo, panchromatic Pléiades data and repeated UAV flights (austral summers 2022/2023) for Dos Lenguas rock glacier, (ii) compare results from three software, (iii) evaluate the Pléiades DEMs of Difference (DoDs) against the UAV DoD, and (iv) apply the developed Pléiades workflow for El Paso rock glacier. This research is a proof of concept to allow future large(r) scale investigation.

1.1 Study area

The Agua Negra catchment is located in the Western part of San Juan Province, Argentina (30°S and 69°W). It is part of the Cordillera Principal, extents over 435 km² (Schrott 1994) and hosts glacial and periglacial landforms (Figure 1). Today's (peri)glacial high-alpine landscape in the catchment represents a 'geomorphic palimpsest' (Hewitt 2002) of relict, transient and replacement forms. As part of the Dry Andes, the catchment is characterized by extremely low mean annual precipitation (~250 mm) and constant high solar radiation (Croce and Milana 2002; Lliboutry et al. 1998; Schrott 1994). Surface temperatures and upper ground thermal regimes are mainly controlled by incoming solar radiation (Schrott 1994). The active layer in areas underlain by permafrost generally varies between 2–3 m; reduced to a few centimetres above 5000 m where continuous permafrost is present (Halla et al. 2021).

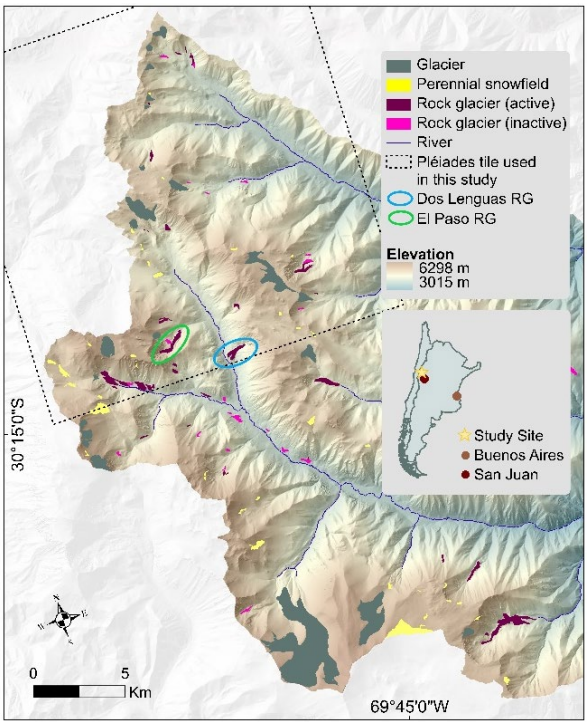

Figure 1. Upper part of the Agua Negra catchment with typical (peri)glacial landform distribution. Hillshade based on TanDEM-X DEM, elevation on Pléiades DEM. All landform polygons by IANIGLA-CONICET (2018).

2 METHODOLOGY

We use tri-stereo, panchromatic Pléiades data acquired in 2022/2023 for DEM and DoD generation on Dos Lenguas and El Paso rock glaciers. We apply three software to study their impact on the generated products. A Phantom DJI 4 RTK was used for conducting two UAV surveys on Dos Lenguas to obtain very high resolution DEMs to compare to the Pléiades DEMs (Table 1). UAV imagery was collected at constant elevation above a TanDEM-X DEM (12 m, 2011–2014). We measured 20 points with a Trimble DGNSS (R8s base/R2 rover, RTK) with vertical and horizontal precisions of < 0.02 m; for georeferencing (ground control points, GCPs) and quality check (control points, CPs).

Table 1. Acquisition parameters for UAV flights on Dos Lenguas (Figure 1) and the Pléiades data acquisition.

UAV model	Phantom 4 RTK (Terrain Awareness)	
Date (dd.mm.yy)	24.03.22	12.02.23
Number of images	1509	2160
Flight altitude, speed	40 m, 5 m/s	50 m, 5 m/s
Overlap (ver/hor.)	65/65 %	70/70 %
GCPs / CPs	15/5	15/5
Geometry	Tri-stereo (panchromatic, multi-spectral)	
Date (dd.mm.yy)	08.02. to 22.02.22	13.02. to 20.02.23

Agisoft Metashape Professional (Agisoft) utilizes structure-from-motion techniques to obtain DEMs (Smith et al. 2016) on UAV and satellite imagery. We base the sparse clouds on all imagery, independent of their date of acquisition (Cook and Dietze 2019; Haas et al. 2021), separate the aligned cameras per acquisition and georeference the UAV sparse cloud using 15 GCPs and 5 CPs (Figure 2A). For the Pléiades data, we rely on the rational polynomial coefficients (RCPs) for solving the exterior orientation and use higher key and tie point limits than for the UAV processing. We build dense clouds using the 'high' quality and 'moderate' depth filtering options before generating the DEMs.

Catalyst Professional (Catalyst) follows a traditional photogrammetric approach and is well used for glacial and periglacial change analysis. We create maximum overlapping epipolar images and generate DEMs using the semi-global matching algorithm (SGM), also making use of the RCPs.

Ames Stereo Pipeline (ASP, Beyer et al. 2018) is open source and freely available. We project the Pléiades imagery using a SRTM DEM (30 m) as seed DEM. We proceed with the projected imagery to derive DEMs applying the SGM algorithm using both tri-stereo pairs without GCPs. Given our local focus, we do not fill gaps (due to only minimal presence) and do not correct sensor undulations.

We co-register the 2023 Pléiades DEMs to the 2022 Pléiades DEMs clipped by study site and paired by software following Nuth and Kääb (2011) in DEMCOREG (Shean et al. 2016). During co-registration, we assume non-rock glacier surfaces to be stable with slopes < 40°, validated

using the GCPs/CPs. When evaluating the Pléiades DoDs against the UAV DoD, we focus on the rock glacier outlines by IANIGLA-CONICET (2018) as we use them to define stable terrain during co-registration (Figure 3BD).

3 RESULTS

3.1 Digital elevation models (DEMs)

With a maximum UAV DEM resolution for Dos Lenguas of 3.09 cm/pixel (2022) and 2.76 cm/pixel (2023), modelled GCP locations deviate approximately 1 cm from DGNSS measurements. The total error in x, y and z directions for 2022 is 0.6 cm, 1.0 cm, and 0.25 cm. The total error for 2023 is similar with 0.6 cm, 0.9 cm, and 0.3 cm. The DEM reproduces known points not included in the model (CPs) with a maximum distance of 10 cm. Deviations between the modelled CPs and DGNSS measurements are lower on stable terrain, and higher in the upper part of the rock glacier.

The Pléiades DEMs processed in Agisoft appear clearest and with furrows and ridges produced most similarly to the UAV DEMs (Figures 2B and 4). The processed Pléiades DEM in Catalyst leads to coarser surfaces and 'flattened' microtopography (Figures 2C and 4). The ASP results occur smoothest with limitations in representing boulders in the rock glaciers' upper part while portraying furrows and ridges (Figures 2D and 4). None of the DEMs has voids over the target site. All Pléiades DEMs are generated with a resolution of 1 m.

The offset between DEMs prior to co-registration is largest for Agisoft, followed by Catalyst and ASP (Table 2). ASP DEMs are most consistent in their offset compared to 20 DGNSS measurements (GCP/CPs; Figure 2A; Table 3). The spatial distribution of error (Eltner et al. 2016; James et al. 2019) is most consistent in time for the ASP DEMs, based on a comparison of the 5 highest Pléiades DEM deviations from the 20 DGNSS measurements. In 2022, errors are largest in the upper part of Dos Lenguas r (Agisoft, Catalyst; Figure 2B, C) and at the sides and front (ASP, Figure 2D). In 2023, largest errors occur at the center, front and the sides (Agisoft, Figure 2B) and only the front and sites (Catalyst, ASP; Figure 2C, D). While differences in absolute elevation exist between processing strategies, co-registration per processing strategy is efficient (Figure 4).

Table 2. Linear co-registration shifts calculated over stable terrain between respective Pléiades DEMs, relying on RCP files for DEM generation. Co-registration of 2023 Pléiades to 2022 Pléiades DEMs following Nuth and Kääb (2011) in DEMCOREG (Shean et al. 2016).

	Shift in x (m)	Shift in y (m)	Shift in z (m)
22/23: Agisoft	-35.84	15.06	15.22
22/23: Catalyst	-8.41	3.70	32.08
22/23: ASP	-0.35	-0.04	1.15

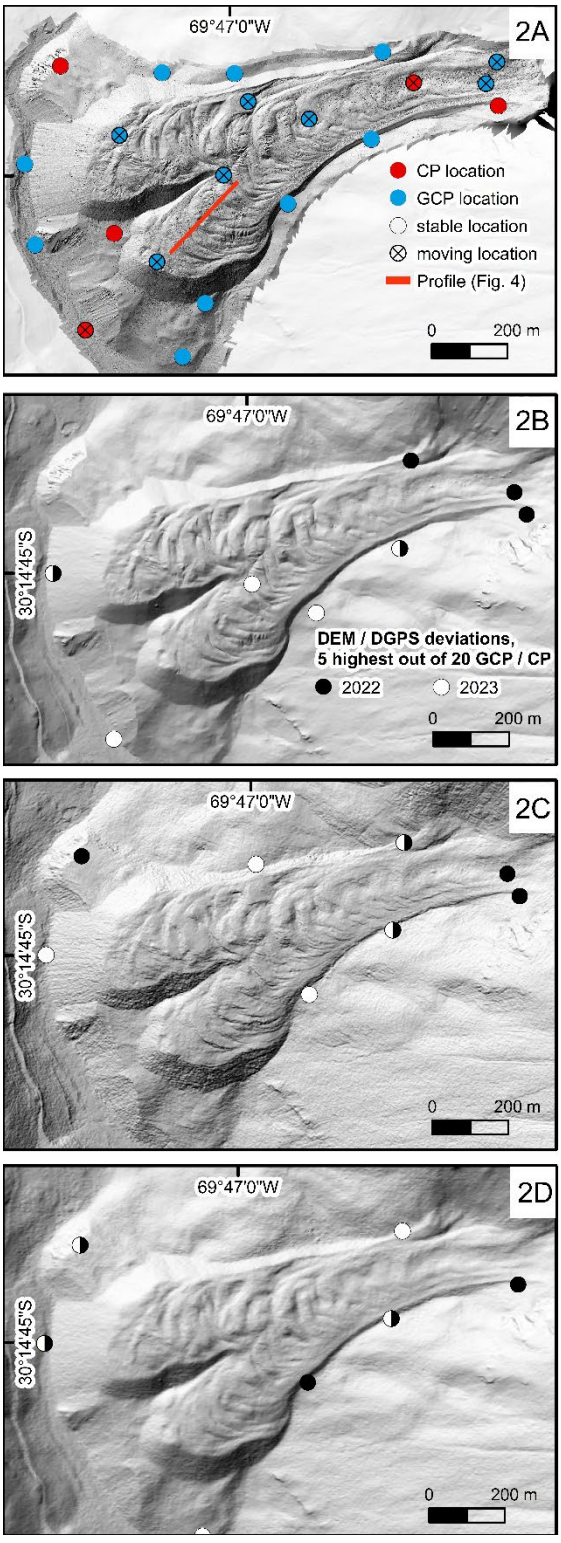

Figure 2. DEM visual appearance of Dos Lenguas rock glacier (2022) based on UAV/Agisoft (A), Pléiades/ Agisoft (B), Pléiades/Catalyst (C), and Pléiades/ASP (D). GCP/CP locations measured 2022 and 2023. Line indicates the profile location taken for Figure 4 (A). For explanation on deviations (2B-D), see chapter 3.1.

Table 3. Consistency of DEM offsets calculated as standard deviations (σ) of the differences between 20 known DGNSS points (each for 2022 and 2023) and the respective DEM, similar to Mueting et al. (2021). As we rely on the RCP files for DEM generation, none of the DGNSS measurements is included in the DEM.

	σ 2022	σ 2023
DGNSS to Agisoft DEM	6.46	2.48
DGNSS to Catalyst DEM	2.15	1.13
DGNSS to ASP DEM	0.83	1.02

3.2 DEMs of Difference (DoDs)

Given its very high resolution, the UAV DoD shows magnitude and distribution of vertical surface change on Dos Lenguas rock glacier between 2022 and 2023 in most detailed manner (Figure 3A; 5 cm resolution based on resampled UAV DEMs 2022 and 2023 for better comparison between UAV DEMs). The Pléiades DoD processed in Agisoft overestimates negative change throughout the entire surface of the rock glacier compared to the UAV DoD, yet appropriately represents ridges and furrows (Figure 3B). The Pléiades DoD processed in Catalyst overestimates negative change particularly towards the lower part of the rock glacier and does not adequately portray the microtopography, especially in comparison to the UAV DoD but despite being characterized by the same resolution also compared to the Pléiades DEM processed in Agisoft (Figure 3C). The processing of Pléiades imagery in ASP results in a DoD most similar to the UAV results in terms of magnitude as well as distribution of vertical surface change (Figure 3D).

Pixel frequencies for vertical surface change are unimodal and normally distributed independent of image source and processing strategy (Figure 5). Highest surface changes do not exceed ± 2 m with most changes occurring below zero. The UAV processing in Agisoft and the Pléiades processing in ASP show most similar distributions. The Pléiades processing in Agisoft and Catalyst leads to wider distributions with lower maxima, and with overall shifts to more negative values. The magnitude of calculated negative and positive surface changes between 2022 and 2023 (mean change below or above zero, uncertainty based on stable terrain for Pléiades DoDs) are higher for the Pléiades processing in Agisoft and Catalyst, and lower for the UAV processing in Agisoft and the Pléiades processing in ASP (Table 4).

Pléiades DoD based vertical surface change for El Paso rock glacier between 2022 and 2023 (Figure 1) is similar to vertical surface change on Dos Lenguas rock glacier during the same time period. This applies to the range of the pixel frequency distribution of vertical surface changes (below ± 2 m; Figures 5 and 6), the similarity of the magnitude of change of the Pléiades processing in ASP (Tables 4 and 5), and the lower mean negative and higher mean positive changes when processing Pléiades imagery in Agisoft and Catalyst in comparison to ASP (Figures 5 and 6; Tables 4 and 5).

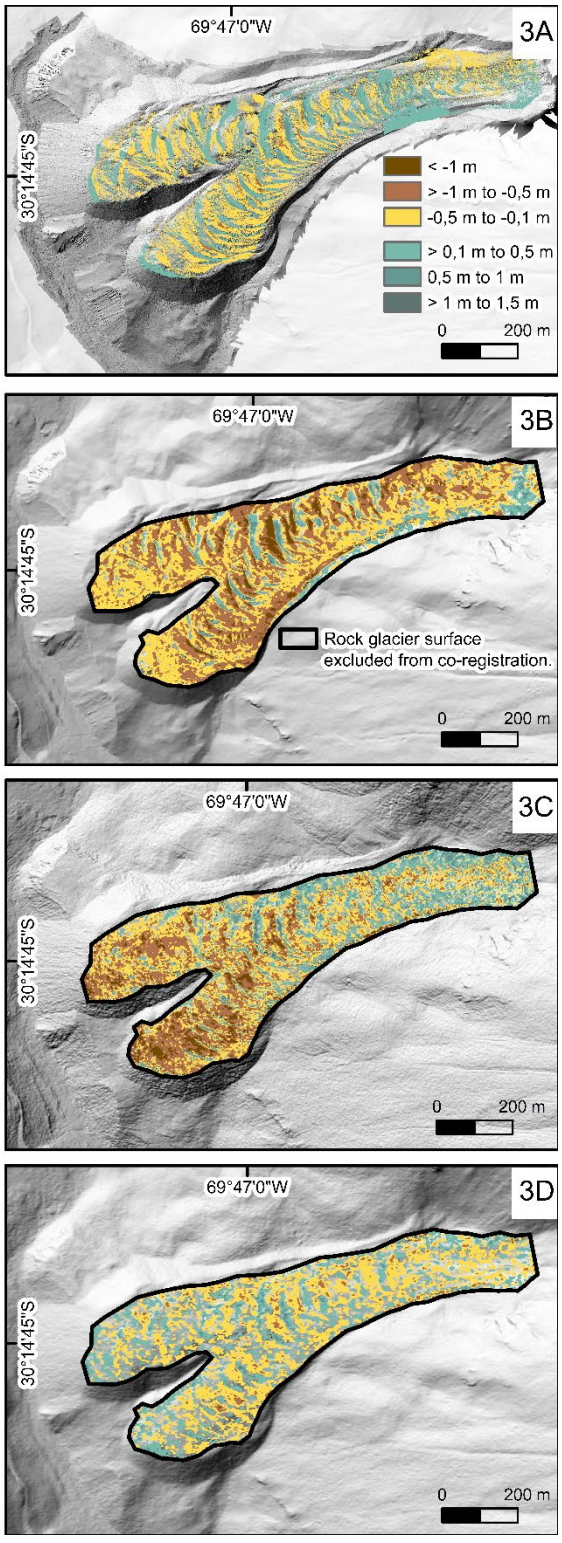

Figure 3. Vertical surface change (m) on Dos Lenguas rock glacier (2022/2023) based on UAV/Agisoft (A), Pléiades/Agisoft (B), Pléiades/Catalyst (C), and Pléiades/ASP (D). The rock glacier outline (3B–D) as mapped by IANIGLA-CONICET (2018) is used to exclude the rock glacier surface from co-registration.

Table 4. Mean negative and positive vertical surface changes (m) on Dos Lenguas rock glacier (2022–2023).

	Mean negative (m)	Mean positive (m)
UAV Agisoft	-0.16	0.16
Pléiades Agisoft	-0.49 ± 0.09	0.24 ± 0.09
Pléiades Catalyst	-0.47 ± 0.08	0.29 ± 0.08
Pléiades ASP	-0.19 ± 0.01	0.17 ± 0.01

Table 5. Mean negative and positive vertical surface changes (m) on El Paso rock glacier (2022 – 2023).

	Mean negative (m)	Mean positive (m)
Pléiades Agisoft	-0.28 ± 0.04	0.22 ± 0.04
Pléiades Catalyst	-0.26 ± 0.03	0.24 ± 0.03
Pléiades ASP	-0.19 ± 0.02	0.15 ± 0.02

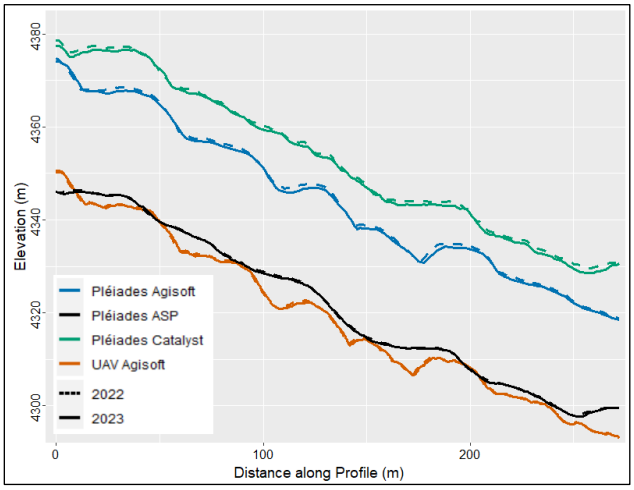

Figure 4. Surface profiles across the UAV and Pléiades DEMs on Dos Lenguas rock glacier, separated by processing strategy. For the profile location, see Figure 2A.

4 Discussion

4.1 Comparison of processing strategies for DEM and DoD generation

Despite using the same Pléiades imagery as input, the DEMs vary distinctively in visual appearance (Figure 2B–D), quality and robustness (Tables 2 and 3) and absolute elevation (Figure 4). These variations caused by the three processing strategies propagate and lead to differences in calculated vertical surface change on Dos Lenguas rock glacier between 2022/2023 visually (Figure 3B–D), in pixel frequency distribution (Figure 5), and in terms of mean change values (Table 4). The differences not only hold true for Dos Lenguas but also for El Paso rock glacier (Figure 6; Table 5).

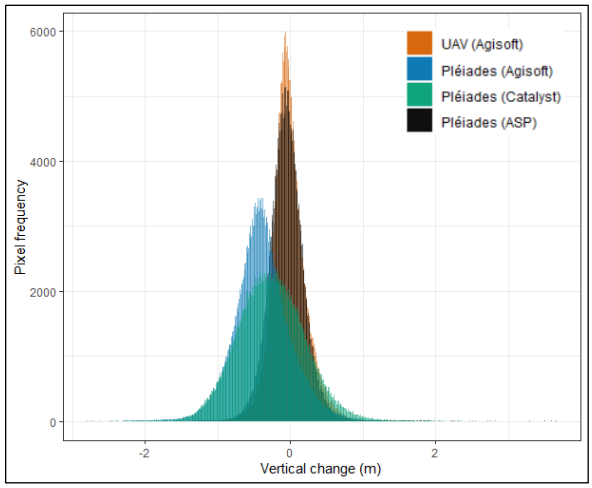

Figure 5. Vertical surface change (m) for Dos Lenguas rock glacier (2022–2023), separated by image source and processing strategy.

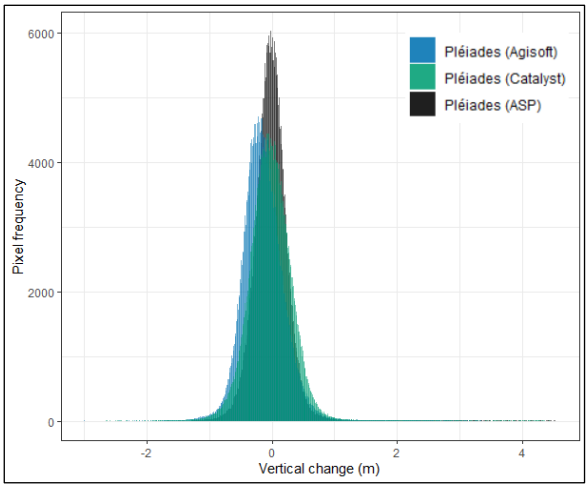

Figure 6. Vertical surface change (m) for El Paso rock glacier (2022–2023), separated by processing strategy.

Our processing strategy for Pléiades imagery in Agisoft outperforms the Catalyst and ASP results in reproducing coherent furrows and ridges as well as landform neighbouring ridges and erosional gullies (Figure 2B). We assume that for this reason the Agisoft Pléiades processing is the sole strategy that shows deposition on the rock glacier's orographic right side slope (Figure 3B). Agisoft allows a combined processing of Pléiades tiles (Figure 1; extent of tile used for this study), enabling smooth transitions between overlapping tiles and direct, unrestricted investigation of rock glaciers located close to tile edges. We hypothesize that to the disadvantage, this combined processing causes distortions resulting in the shifts between the DEMs before co-registration and the poor consistency of offsets between DEMs and DGNSS measurements (Tables 2 and 3). We interpret the

inconsistency of the spatial error distribution throughout time as additional indication of low data robustness (Figure 2B). Potentially due to these limitations, the Agisoft Pléiades DoDs overestimate negative vertical surface change for the entire rock glacier, compared to the UAV results.

Our Pléiades processing strategy in Catalyst leads to 'flattened' and smoothed ridges on the DEMs (Figures 2C and 4). This effect propagates to the DoD with the vertical surface change in the lower part of the rock glacier being similar in magnitude to the Pléiades based results in Agisoft but less coherent with and confined to the microtopography (Figure 3C). The maximum of the Pléiades Catalyst based pixel frequency distribution is more similar to the UAV based results than the Pléiades Agisoft processing (Figure 5). However, this is caused by the balancing of overestimation of negative changes in the lower and of positive changes in the upper part compared to the UAV DoD (Figure 3C; Table 4), hence, is no sign of quality of the dataset.

The ASP processing of Pléiades imagery clearly stands out in its similarity of the pixel frequency distribution of vertical surface change and its mean negative and positive change in comparison to the Agisoft UAV DoD (Figure 5; Table 4). With the ability to gauge the errors of our UAV based results, we deem the ASP based results for the Pléiades data as most correct. This corresponds well to the highest overall data quality (Tables 2 and 3) and the highest consistency of spatial error (Figure 2D) of the ASP Pléiades analysis. The example highlights that Agisoft performs better when used for processing UAV imagery, than Pléiades imagery. For processing Pléiades data, ASP can clearly be attributed the best performance in terms of data quality and robustness. In terms of visualisation it lacks, e.g., the ability of reproducing single rocks on in the rock glaciers' root zone, in comparison to the Agisoft Pléiades DEM. We hypothesise that the smoothing performed when applying the SGM is causing this difference. This might also explain the similarity of the Catalyst and ASP derived profiles (Figure 4) as in both cases SGM is used for image correlation.

Co-registration significantly reduces shifts between the 2022 and 2023 Pléiades DEMs independent of processing strategy and notably improves the quality of the DoDs. The shift that occurs for our Agisoft and Catalyst results are uncommonly high (Table 2). Rieg et al. (2018) generate Pléiades based DEMs using a SGM algorithm available in ERDAS IMAGINE along with the RPC files and, depending on study site, automatically identified and manually controlled tie points (TPs) or GCPs. They investigate glaciers in the European Alps and the Khumbu Himal and encounter maximum offsets of 4 m, -3.2 m and 4.8 m in x, y and z directions. In comparison, the detected offsets for the ASP based Pléiades DEMs for Dos Lenguas rock glacier are minimal.

We decide on co-registering the 2023 to the 2022 Pléiades DEM per processing strategy to maintain independence between the photogrammetric software. We chose to not co-register the Pléiades DEMs to the UAV DEMs for a robust co-registration (UAV flights barely cover stable terrain) and to develop an UAV independent workflow for future use in larger regions. Despite well-performed co-registration of DEMs of the same processing strategy, absolute differences in elevation between the processing strategies occur (Figure 4). It is apparent that the UAV DEMs processed in Agisoft and the Pléiades DEMs processed in ASP are relatively similar in absolute elevation despite the difference in data source, in processing software and without any co-registration. We hypothesize that this is due to an unintended similarity in z values between the SRTM DEM used as seed DEM to generate the Pléiades DEM in ASP and the GCPs and CPs used for processing the UAV imagery in Agisoft.

4.2 Rock glacier surface change

We can confirm the ridge and furrow surface pattern as described by Halla et al. (2021) both in our UAV as well as in our Pléiades based DEMs, consequently also in all DoDs. Vertical surface change patterns are a compound signal of vertical and horizontal surface change with horizontal movements imprinting the vertical differences by shifting features, e.g., ridges, downslope from one year to the other. This results in negative change at the original location and positive change at the location downslope (Figure 3). While this causes strong changes in terms of vertical surface change pattern, the horizontal movement partially equals itself in terms of net surface change balance at locations where pronounced ridges are present (Halla et al. 2021).

None of the rock glaciers investigated expresses strong net negative vertical surface changes between 2022 and 2023, based on mean positive and negative changes (Tables 4 and 5). While this holds true for all processing strategies and data sources we focus on the UAV processing in Agisoft and Pléiades processing in ASP given the quality of the data (Tables 2–5; chapter 4.1). Halla et al. (2021) calculate UAV based annual net balances of vertical surface change on Dos Lenguas rock glacier of -0.36 m a^{-1} for 2016-2017 and +0.27 m a^{-1} for 2017–2018. These findings showcase interannual variability and similarities to our results.

Monnier and Kinnard (2017) calculate vertical rock glacier surface changes within Navarro complex of up to -1 m a^{-1} based on aerial photography and spaceborne DoDs, for the period 2000 to 2014. While the Navarro complex is located approximately 200 km south of our study area, the magnitude of vertical surface change is in agreement with our Pléiades result processed in ASP (Figure 5; minimum -1.32 m). Our UAV result processed in Agisoft exceeds these values (minimum -2.83 m). We attribute this to the difference in resolution (UAV DoD 5 cm, Pléiades DoD 1 m) and highlight the scale dependency of change values.

In the neighboring valley west of Agua Negra catchment (La Laguna catchment, Chile), Robson et al. (2022) calculate vertical surface changes of > -0.1 m a^{-1} on several rock glaciers between 2012 and 2020 which corresponds to the most frequent surface changes of our UAV based Agisoft and our Pléiades based ASP processed findings (Figures 5 and 6; Tables 4 and 5). The presented microtopography is similar to Dos Lenguas and El Paso rock glacier surfaces.

5 CONCLUSIONS

We present a local analysis on Dos Lenguas rock glacier (Dry Andes/Argentina) where we compare DEMs and DoDs based on repeated UAV surveys and Pléiades acquisitions (austral summer 2022 to austral summer 2023). We derive the Pléiades based results using three software, namely Agisoft, Catalyst and ASP. Further, we apply the Pléiades based approach to El Paso rock glacier which is located in the same study area.

We find that the choice of processing strategy strongly affects the Pléiades based results. While Pléiades based Agisoft derived DEMs and DoDs appear more appealing visually (less noise, appropriate ridges and furrows), we find their quality in terms of offset and distortion to cause an overestimation of negative vertical rock glacier surface change. Pléiades based DEMs and DoDs processed in Catalyst 'flatten' the furrows and ridges on the rock glacier surface and overestimate negative surface change particularly in the lower part. The Pléiades based results generated in ASP outperform the other processing strategies with highest consistencies of offsets to 20 known DGNSS locations, lowest shifts between DEMs before co-registration and strongest consistency of the spatial distribution of error. Pixel frequency distributions of vertical change are very similar to our UAV DoD processed in Agisoft and surface change values are in agreement with published results. Our example highlights the suitability of Agisoft for processing UAV imagery and of ASP for processing Pléiades imagery.

We can provide Pléiades based change analysis at El Paso rock glacier where we did not obtain UAV imagery. The findings allow for an interpretation of a more general behaviour in the study area. Given that the choice of software propagates to very similar impact when calculating vertical surface change for both rock glaciers, we conclude that attention should not only be focused on potential differences due to variability in co-registration techniques, but also to the choice of software for DEM generation.

A detailed analysis of surface change patterns is only possible with very high resolution DoDs, which clearly attributes benefit to UAV based DoDs. Pléiades DoDs, however, provide insight to general surface patterns. They can, using an appropriate processing strategy, deliver surface changes similar to UAV based investigation. Given the limitations of UAV surveys imposed by high-alpine conditions, such as for example strong winds, changing weather conditions, and/or limited access; Pléiades based DoDs enable vertical surface change magnitude and pattern analysis at the cost of spatial resolution but at the gains of increased spatial coverage, "access" to previously unvisited sites, and insights beyond the limitations of fieldwork.

We conclude that tri-stereo Pléiades imagery provides distinguishable benefits for analysing vertical rock glacier surface changes. We highlight the need for robust co-registration and prior knowledge of the study area to carefully assess the suitability of Pléiades DoDs at a specific location. We recommend processing Pléiades data in ASP and highlight the possibility to derive visually detailed Pléiades DEMs in Agisoft. We advocate perceiving these benefits as complementation to UAV surveys, so that highest spatial coverage is achieved by the first and highest spatial resolution by the latter. In view of permafrost degradation, we are certain that an analysis on both spatial scales is relevant.

6 ACKNOWLEDGEMENTS

This research is funded by the Deutsche Forschungsgemeinschaft (DFG, 461744503). We are thankful for the support received for acquiring the Pléiades imagery by the Centre National d'Etudes Spatiales (CNES). ASP computations presented were performed using the GRICAD infrastructure (gricad.univ-grenoble-alpes.fr), supported by Grenoble research communities. The authors thank all fieldwork campaign participants F. Flöck, F. Wester, D. A. Ortiz, T. Köhler, P. Reichartz, T. Wenzel, M. Cramer. MS further thanks A. Müting for all advice shared.

MS: conceptualization, resources, investigation, formal analysis (UAV, Pléiades; Agisoft, Catalyst), visualization, writing-original draft, writing-review and editing. DC: formal analysis (Pléiades, ASP), writing-review and editing. RB: conceptualization, resources, writing-review and editing. BR: resources, writing-review and editing. XB: resources, writing-review and editing. JB: supervision, writing-review and editing. LS: supervision, funding acquisition, writing-review and editing. All authors contributed to the final version of this manuscript.

7 REFERENCES

Arenson, L.U., Harrington, J.S., Koenig, C.E.M., Wainstein, P.A. 2022. 'Mountain Permafrost Hydrology - A Practical Review Following Studies from the Andes', *Geosciences* 12(2), 48 p. doi:10.3390/geosciences12020048.

Bagnardi, M., González, P.J., and Hooper, A. 2016. 'High-resolution digital elevation model from tri-stereo Pleiades-1 satellite imagery for lava flow volume estimates at Fogo Volcano', *Geophysical Research Letters* 43(12), pp. 6267–6275. doi:10.1002/2016GL069457.

Beyer, R.A., Alexandrov, O., and McMichael, S. 2018. 'The Ames Stereo Pipeline: NASA's Open Source Software for Deriving and Processing Terrain Data', *Earth and Space Science* 5(9), pp. 537–548. doi:10.1029/2018EA000409.

Blöthe, J.H., Halla, C., Schwalbe, E., Bottegal, E., Trombotto Liaudat, D., and Schrott, L. 2021. 'Surface velocity fields of active rock glaciers and ice-debris complexes in the Central Andes of Argentina', *Earth Surface Processes and Landforms* 46(2), pp. 504–522. doi:10.1002/esp.5042.

Cook, K.L. and Dietze, M. 2019. 'Short Communication: A simple workflow for robust low-cost UAV-derived change detection without ground control points', *Earth Surface Dynamics* 7(4), pp. 1009–1017. doi:10.5194/esurf-7-1009-2019.

Croce, F.A. and Milana, J.P. 2002. 'Internal structure and behaviour of a rock glacier in the Arid Andes of Argentina', *Permafrost and Periglacial Processes* 13 (4), pp. 289–299. doi:10.1002/ppp.431.

Cusicanqui, D., Bodin, X., Duvillard, P.-A., Schoeneich, P., Revil, A., Assier, A. et al. 2023. 'Glacier, permafrost and thermokarst interactions in Alpine terrain: Insights from seven decades of reconstructed dynamics of the Chauvet glacial and periglacial system (Southern French Alps)', *Earth Surface Processes and Landforms*, pp. 1–18. doi:10.1002/esp.5650.

Dussaillant, I., Berthier, E., Brun, F., Masiokas, M., Hugonnet, R., Favier, V. et al. 2019. 'Two decades of glacier mass loss along the Andes', *Nature Geoscience* 12(10), pp. 802–808. doi:10.1038/s41561-019-0432-5.

Eltner, A., Kaiser, A., Castillo, C., Rock, G., Neugirg, F., and Abellán, A. 2016. 'Image-based surface reconstruction in geomorphometry – merits, limits and developments', *Earth Surface Dynamics* 4(2), pp. 359–389. doi:10.5194/esurf-4-359-2016.

Etzelmüller, B. and Hagen, J.O. 2005. 'Glacier-permafrost interaction in Arctic and alpine mountain environments with examples from southern Norway and Svalbard', in *Geological Society, London*, Special Publication 242, pp. 11–27. doi:10.1144/GSL.SP.2005.242.01.02.

Ferri, L., Dussaillant, I., Zalazar, L., Masiokas, M.H., Ruiz, L., Pitte, P. et al. 2020. 'Ice Mass Loss in the Central Andes of Argentina Between 2000 and 2018 Derived From a New Glacier Inventory and Satellite Stereo-Imagery', *Frontiers in Earth Science* 8, 530997. doi:10.3389/feart.2020.530997.

Geiger, S.T., Daniels, J.M., Miller, S.N., and Nicholas, J.W. 2014. 'Influence of Rock Glaciers on Stream Hydrology in the La Sal Mountains, Utah', *Arctic, Antarctic, and Alpine Research* 46(3), pp. 645–658. doi:10.1657/1938-4246-46.3.645.

Haas, T. de, Nijland, W., McArdell, B.W., and Kalthof, M.W.M.L. 2021. 'Case Report: Optimization of Topographic Change Detection With UAV Structure-From-Motion Photogrammetry Through Survey Co-Alignment'. *Frontiers in Remote Sensing* 2-2021, Article 626810. doi:10.3389/frsen.2021.626810.

Halla, C., Blöthe, J.H., Tapia Baldis, C., Trombotto, D., Hilbich, C., Hauck, C., and Schrott, L. 2021. 'Ice content and interannual water storage changes of an active rock glacier in the dry Andes of Argentina', *The Cryosphere* 15, pp. 1187–1213. doi:10.5194/tc-15-1187-2021

Hewitt, K. 2002. 'Introduction: Landscape Assemblages and Transitions in Cold Regions', in K. Hewitt, M.L. Byrne, M. English, and G. Young (eds.), *Landscapes of Transition*. The GeoJournal Library, vol 68. Springer, Dordrecht.

IANIGLA-CONICET 2018. *Inventario Nacional de Glaciares y Ambiente Periglacial*. Informe de la subcuenca del río Blanco. Cuenca del Río San Juan. With assistance of Ministerio de Ambiente y Desarrollo Sustentable de la Nación.

James, M.R.; Chandler, J.H., Eltner, A., Fraser, C., Miller, P.E., Mills, J.P. et al. 2019. 'Guidelines on the use of structure-from-motion photogrammetry in geomorphic research', *Earth Surface Processes and Landforms* 44(10), pp. 2081–2084. doi:10.1002/esp.4637.

Lliboutry, L., Williams, R., and Ferrigno, J.G. 1998. 'Glaciers of Chile and Argentina', *US Geological Survey* Professional Paper 1386-I-6.

Masiokas, M.H., Rabatel, A., Rivera, A., Ruiz, L., Pitte, P., Ceballos, J.L. et al. 2020. 'A Review of the Current State and Recent Changes of the Andean Cryosphere', Frontiers in Earth Science 8, Article 99. doi:10.3389/feart.2020.00099.

Miesen, F., Dahl, Dahl, S.O., and Schrott, L. 2021. 'Evidence of glacier-permafrost interactions associated with hydro-geomorphological processes and landforms at Snøhetta, Dovrefjell, Norway', *Geografiska Annaler: Series A, Physical Geography* 103(3), pp. 273–302. doi:10.1080/04353676.2021.1955539.

Monnier, S. and Kinnard, C. 2017. 'Pluri-decadal (1955–2014) evolution of glacier–rock glacier transitional landforms in the central Andes of Chile (30–33°S)'. *Earth Surface Dynamics* 5(3), pp. 493–509. doi:10.5194/esurf-5-493-2017.

Mueting, A., Bookhagen, B., and Strecker, M.R. 2021. 'Identification of Debris-Flow Channels Using High-Resolution Topographic Data: A Case Study in the Quebrada del Toro, NW Argentina', *JGR Earth Surface* 126(12). doi:10.1029/2021JF006330.

Nuth, C. and Kääb, A. 2011. 'Co-registration and bias corrections of satellite elevation data sets for quantifying glacier thickness change', *The Cryosphere* 5(1), pp. 271–290. doi:10.5194/tc-5-271-2011.

Pitte, P., Masiokas, M., Gargantini, H., Ruiz, L., Berthier, E., Ferri Hidalgo, L., Zalazar, L., Dussaillant, I., Viale, M., Zorzut, V., Corvalán, E., Scarpa, J.P., Costa, G., and Villalba, R. 2022. 'Recent mass-balance changes of Agua Negra glacier (30°S) in the Desert Andes of Argentina', *Journal of Glaciology* 68(272), pp. 1197–1209. doi:10.1017/jog.2022.22.

Rieg, L., Klug, C., Nicholson, L., and Sailer, R. 2018. 'Pléiades Tri-Stereo Data for Glacier Investigations—Examples from the European Alps and the Khumbu Himal', *Remote Sensing* 10(10), 1563. doi:10.3390/rs10101563.

Robson, B.A., MacDonell, S., Ayala, Á., Bolch, T., Nielsen, P.R., and Vivero, S. 2022. 'Glacier and rock glacier changes since the 1950s in the La Laguna catchment, Chile', *The Cryosphere* 16(2), pp. 647–665. doi:10.5194/tc-16-647-2022.

Schrott, L. and Götz, J. 2013. *Forschen im Gebirge. Investigating the mountains*. Christoph Stadel zum 75. Geburtstag. Verlag der Österreichischen Akademie der Wissenschaften (IGF-Forschungsberichte, Band 5). Wien.

Schrott, L. 1994. *Die Solarstrahlung als steuernder Faktor im Geosystem der subtropischen semiariden Hochanden (Agua Negra, San Juan, Argentinien)*. Heidelberger Geographische Arbeiten 94.

Shean, D.E., Alexandrov, O., Moratto, Z.M., Smith, B.E., Joughin, I.R., Porter, C., and Morin, P. 2016. 'An automated, open-source pipeline for mass production of digital elevation models (DEMs) from very-high-resolution commercial stereo satellite imagery', *ISPRS Journal of Photogrammetry and Remote Sensing* 116, pp. 101–117. doi:10.1016/j.isprsjprs.2016.03.012.

Smith, M.W., Carrivick, J.L., and Quincey, D.J. 2016. 'Structure from motion photogrammetry in physical geography', *Progress in Physical Geography: Earth and Environment* 40(2), pp. 247–275. doi:10.1177/0309133315615805.

Trombotto, D. and Borzotta, E. 2009. 'Indicators of present global warming through changes in active layer-thickness, estimation of thermal diffusivity and geomorphological observations in the Morenas Coloradas rockglacier, Central Andes of Mendoza, Argentina', *Cold Regions Science and Technology* 55(3), pp. 321–330. doi:10.1016/j.coldregions.2008.08.009.

Vivero, S. and Lambiel, C. 2019. 'Monitoring the crisis of a rock glacier with repeated UAV surveys', *Geographica Helvetjca* 74(1), pp. 59–69. doi:10.5194/gh-74-59-2019.

Thermal performance of sloped thermosyphons installed at the Dry Creek Highway section, Yukon, Canada

Christopher Stevens[1], Idrees Muhammad[2] & Justin Panagapko[3]

[1]*Northern Permafrost Consulting, Eagle River, Alaska, United States*

[2]*Government of Yukon, Whitehorse, Yukon, Canada*

[3]Arctic Foundations of Canada, Elie, Manitoba, Canada

ABSTRACT

A total of 58 sloped thermosyphons were installed to arrest permafrost thaw beneath a section of the Alaska Highway at Dry Creek, Yukon, Canada. The highway foundation consists of warm (> -0.5 °C) permafrost with massive ground ice that is locally in excess of 9 m thick. In the fall of 2019, construction commenced with minimal vegetation clearing within the right-of-way and shallow excavation along the east tow of the highway embankment. Thermosyphons were installed in cased boreholes drilled beneath the embankment at an 11° incline, approximately every 7 m on centre. Each thermosyphon unit consisted of a single 19.5 m^2 radiator attached to an approximately 35 m long, 76 mm diameter schedule 80 evaporator pipe. The thermosyphons have increased winter heat loss from the foundation since completion of installation in 2020. Permafrost temperature has decreased by several degrees and the permafrost table has vertically aggraded up to 2.5 m above its pre-construction position. The greatest ground cooling has occurred beneath the thickest section of embankment fill which acts to reduce heat gain during the thawing season. The thermosyphons are expected to continue to contribute to permafrost stabilization over the 30-year design life. This project contributes to evaluation of techniques for the adaptation of highway infrastructure to climate change in permafrost environments.

1 INTRODUCTION

The Alaska Highway in the Yukon between Burwash Landing and the international border with Alaska extents across extensive discontinuous, warm (> -1 °C), permafrost that is commonly ice-rich (Calmels et al. 2016). Permafrost degradation resulting in thaw-settlement of the highway embankment has caused the need for frequent and costly maintenance and remediation.

The Dry Creek highway section (kilometre 1841) of Alaska Highway is approximately 400 m in length (Figures 1 and 2). This section of highway was built across a glaciofluvial deposit consisting of ice-rich permafrost with massive ground bodies of ice up to 9 m thick. In 2017, Yukon Highways and Public Works (YHPW) initiated a study to stabilize the permafrost foundation at the site due to the potential risk of embankment failure.

A solution was developed based on the installation of sloped thermosyphons to increase heat extraction from the foundation and arrest permafrost thaw. Realignment of the highway was not considered a viable option due to the presence of ice-rich permafrost within the surrounding terrain.

In this paper, we describe design and initial thermal performance of the sloped thermosyphons that have been used to stabilize permafrost at the Dry Creek highway section. Thermal performance of the design is important to determine its effectiveness and the need for improvement to similar designs in permafrost environments.

Figure 1. Location of Dry Creek highway section of the Alaska Highway, Yukon, Canada.

2 DRY CREEK HIGHWAY SECTION

The Dry Creek highway section extends across a well-drained glaciofluvial deposit (Rampton 1979; Figure 2).

https://doi.org/10.52381/ICOP2024.159.1

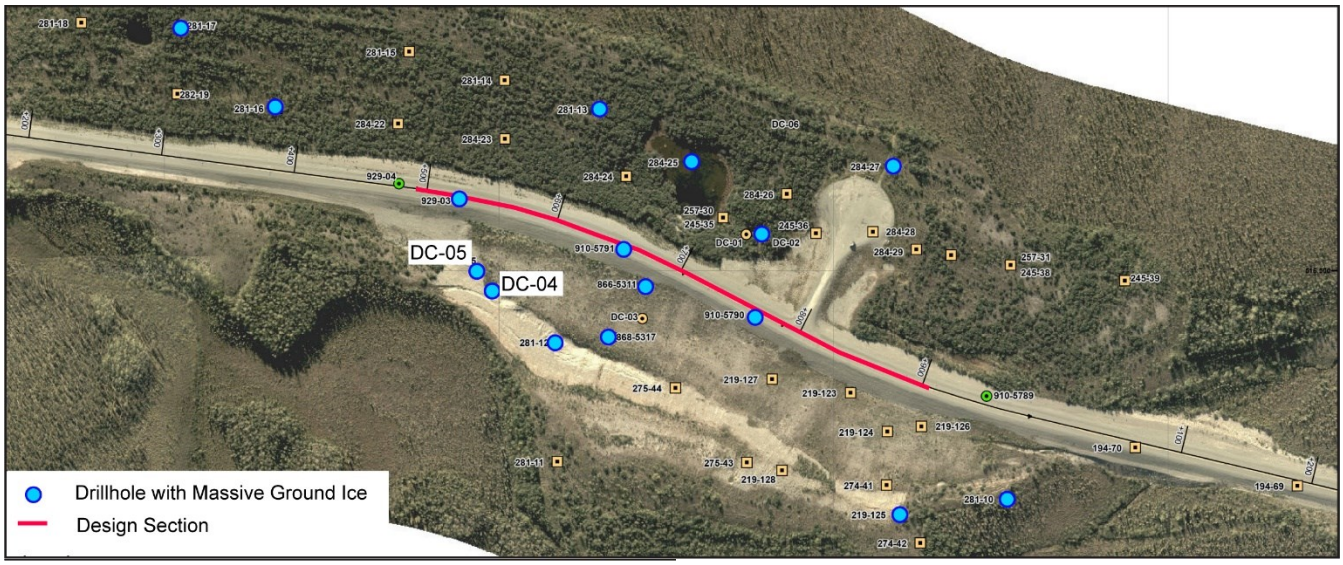

Figure 2. Aerial photograph of the Dry Creek highway section showing the design section (red line) and drillholes intercepting massive ground ice (solid blue circles).

The north-south trending deposit is surrounded by relatively low-lying terrain characterized by wetlands with organics and sparely populated stunted black spruce.

2.1 Site History

The northern portion of the Alaska Highway that includes the Dry Creek highway section was rebuilt between 1992 and 2005 (YES 1996). During this time, the glaciofluvial sand and gravel immediately surrounding the current alignment was excavated and used for construction material. Massive ground ice was exposed during development of the borrow material which subsequently required placement of backfill to arrest immediate thaw.

The Dry Creek highway section was reconstructed in 2014, which included raising, straitening, and widening of the alignment to improve traffic flow and safety (Government of Yukon 2024). In some locations, near surface ground ice was excavated and replaced with structural fill.

2.2 Climate

The site is characterized by continental climate with warm, dry summers and relatively long cold winters. Baseline climate data for the region is reported for Beaver Creek A, located approximately 26 km to the north of Dry Creek due to continuity and longevity of the station record.

The mean annual air temperature recorded at Beaver Creek is -4.9 °C for the most recent climate normals (1981–2010; ECCC 2023). Figure 3A shows the average monthly air temperature for the period of 1981 to 2010. Average annual air temperature recorded at Dry Creek from 2019 to 2022 ranged from -3.8 to -4.0 °C.

The Beaver Creek climate normals indicate mean annual precipitation is 416.3 mm, with 295.7 mm falling as rain and 123.1 cm falling as snow (ECCC 2023). On the ground snow depth has been measured to range from 54 to 84 cm in late winter for areas of natural ground located adjacent to the highway (Lepage 2016). The average annual windspeed recorded at the Beaver Creek highway test section, located approximate 20 km north of Dry Creek was 1.1 m s^{-1} from 2008 to 2016. Winter windspeed was 0.9 m s^{-1} from October to April with the dominant wind direction from the southwest. Average winter windspeed was measured at Dry Creek to be 0.7 m s from 2019 to 2022.

Historical air temperature measured at Beaver Creek indicates an increase of 0.45 °C per decade for the period of 1969 to 2022 (Figure 3B). Climate change model projections from the Sixth Assessment Report (AR6) Shared Socio-economic Pathways (SSPs) SSP1-2.6, SSP2-4.5, and SSP5-8.5 estimate an increase in air temperature of 0.41 °C per decade, 0.47 °C per decade and 0.53 °C per decade, respectively. The project mean annual air temperature is -2.6 °C for SSP5-8.5 and -3.0 °C for SSP1-2.6 at the end of the 30-year design life (Figure 3B).

2.3 Background Ground Temperature

The ground thermal regime prior to installation of the sloped thermosyphons was based on measurements from two ground temperature cables installed by the Northern Climate ExChange at Yukon College, referred to as DC-04 and DC-05 (Calmels et al. 2016). These sites are located outside of direct influence from the highway embankment (approximately 60 m from the embankment) within the area of historic surface disturbance caused by excavation of borrow material.

At DC-04 and DC-05, permafrost temperature measured at approximately 12 m below ground surface (bgs) is -0.9 °C and -0.7 °C, respectively. At DC-04, the active layer depth was 2.2 m in 2015 and 2.9 m in 2016. Additional baseline ground temperature measurements for the highway foundation are discussed in Section 6.1.

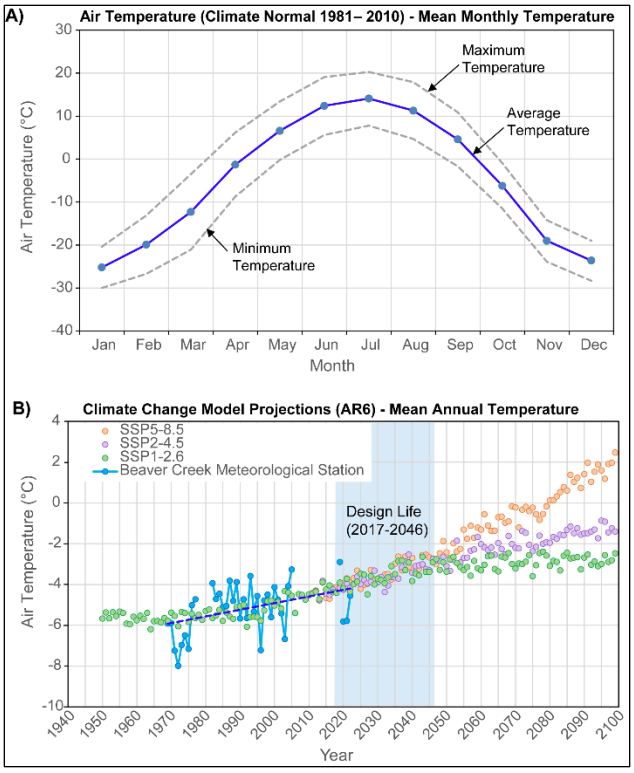

Figure 3. A) Average monthly air temperature measured at Beaver Creek, Yukon from 1981 to 2010 and B) future climate change model projections of mean annual air temperature for Dry Creek, Yukon.

2.4 Foundation Conditions

The Dry Creek highway section foundation consists of well and poorly sorted sand (SW-SP) and gravel (GW-GP) which is underlain by silt (ML). The glaciofluvial sand and gravel is variable in thickness, in part due excavation. The thickness of the lowermost glaciolacustrine silt is unknown due to drillholes terminating prior to reaching bedrock. Embankment thickness is anticipated to 2.0 to 2.5 m thick.

Ground ice was originally observed during auger drilling and excavation of borrow material in the mid-1990s (Figure 4). Additional geotechnical programs were completed between 2011 and 2018. Massive ground ice (ICE) based on the Standard Practice for Description of Frozen Soils (ASTM D4083-89) has been identified to be in excess of 9 m thick and spatially discontinuous across the site (Figure 2).

Historic auger drilling completed during development of borrow material identified massive ground ice in 8 of 33 historical boreholes, with massive ice ranging from 0.6 to 4.0 m thick. The historic depth to the top of massive ground ice prior to removal of surface material was recorded to be from 4.7 to 11.6 m bgs. In 2015, two sonic drillholes were completed and confirmed 3 to 4.6 m of poorly and well graded gravel underlain by 3 to 5 m of massive ground ice (ICE). Material below the massive ground ice is characterized by silt, silty sand, and gravel. Ground ice in intervals of silt is described as being stratified lenses (Vs) and randomly oriented ice lenses (Vr). Three

Figure 4. Massive ground ice exposed during excavation of borrow material in 1995.

additional sonic drillholes were completed in March of 2017. Two of the three drillholes indicates massive ground ice extends from 5.8 mbgs to 10.3 mbgs and from 6 m bgs to 15 m bgs. Drilling completed in 2018 confirmed the top of massive ice was approximately 7 m below the embankment which corresponded to the top of ice-bonded (frozen) permafrost.

3 DESIGN

3.1 Overview

A 30-year design life (2017-2046) for the permafrost stabilization was defined by YHPW. Thermal performance of the design was evaluated over this 30-year period with consideration of climate change.

Preliminary designs for the Dry Creek highway section considered two options: i) construction of an air convection embankment (ACE) using coarse crushed rock and ii) installation of sloped thermosyphons beneath the existing highway embankment (SRK 2017).

Ground thermal modeling completed for the site showed that both ACE and sloped thermosyphons could be used to reduce ground temperature and limit permafrost thaw beneath the highway embankment. However, the thermosyphon-based design was determined to provide more immediate and dependable heat loss to stabilize permafrost at the site and minimal earthwork activity. In comparison to the ACE design that would require full excavation of the existing embankment, relatively high cost of rock development and transport, and greater uncertainty in thermal performance immediately following construction.

3.2 Sloped Thermosyphons

The sloped thermosyphon design accepted by the YHPW specified a total of 58 thermosyphon evaporator pipes (76.2 mm diameter, schedule 80 pipe), approximately 34 m in length, installed in a cased borehole drilled 7 m on centre at an ~11° incline beneath the highway embankment (Figure 5A, B). A vertical riser pipe, with a 19.5 m^2 thermosyphon radiator was installed at a minimum height of one meter above the design grade (Figure 5B).

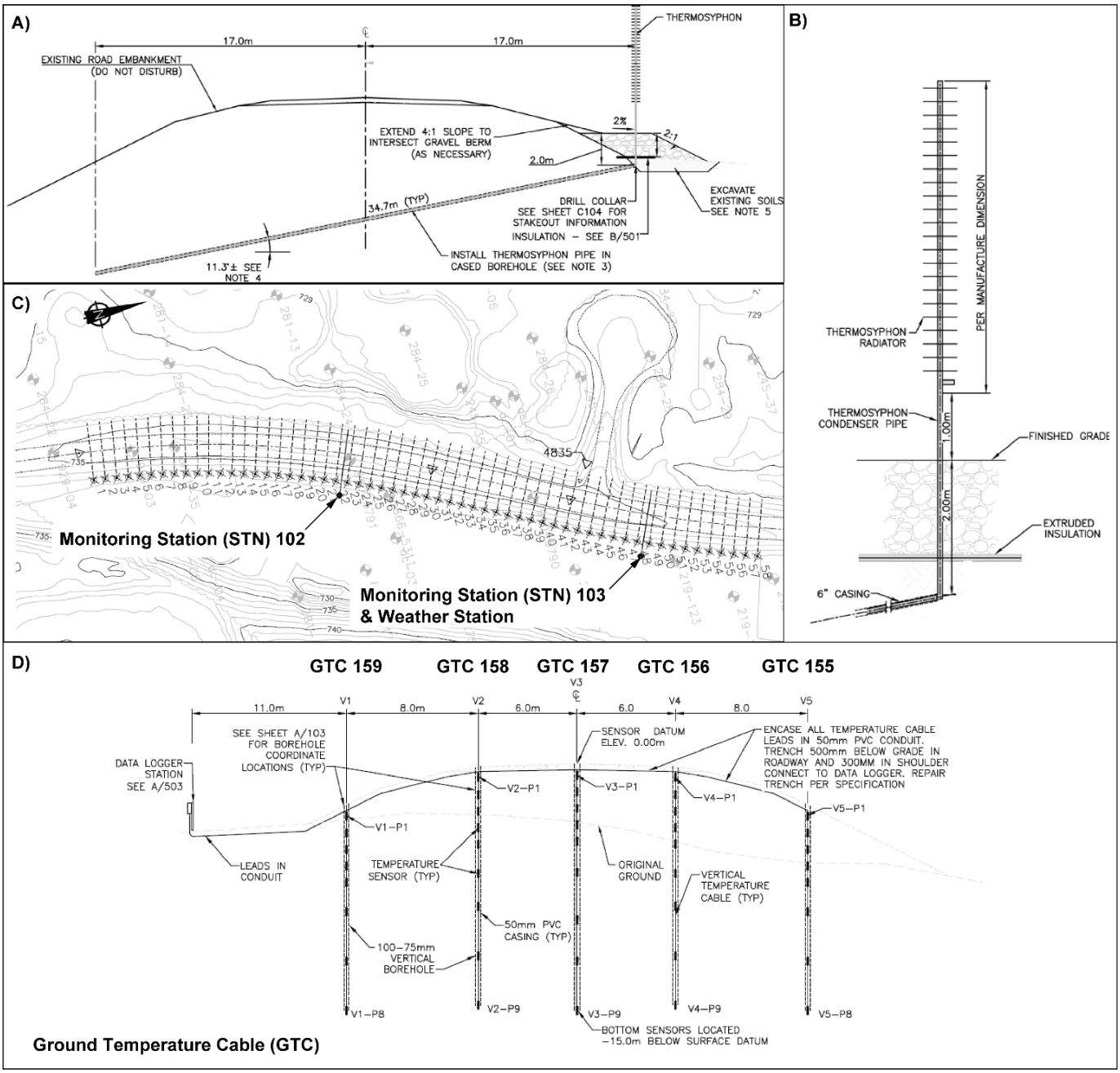

Figure 5. Design showing A) cross-sectional view with slope thermosyphon evaporator pipe beneath existing highway embankment, B) thermosyphon riser and radiator, C) plan view evaporator pipe layout, and D) cross-section of vertical ground temperature cables (GTCs) installed at monitoring stations STN 102. Ground temperature cable installed along inclined evaporator pipe not shown.

Thermosyphon units installed at Dry Creek were manufactured and installed by Arctic Foundations of Canada (AFC). Each thermosyphon unit consists of a pressurized sealed pipe, charged with a two-phase working gas that vaporizes and condenses to move heat without the need of a mechanical pump. The passive thermosyphons include an evaporator pipe buried in the ground that is connected to a vertical riser pipe and surface radiator (Figure 5A). The radiator section is manufactured with horizontal fins attached to the radiator pipe to enhance heat transfer with the atmosphere.

Thermosyphon heat transfer is a function of composition and physical properties of the working gas, radiator and evaporator design, temperature difference between the upper and lower sections of pipe, ground thermal properties, and exposure of the radiators to advective cooling from the wind, among other things.

Numerical thermal modeling was completed to predict thermal performance of the sloped thermosyphon design. Model simulations were completed for the 30-year design life. Thermal performance was evaluated with the objective of maintaining the top of the massive ice below -2 °C over the 30-year period, with consideration of climate change. The warmest location in the ground between two thermosyphon evaporator pipes were used to evaluate the predicted performance.

A thermosyphon radiator surface area (size) of 19.5 m^2 with a maximum evaporator pipe separation of 7 m was estimated to meet the thermal design criteria. Several years were predicted to have a maximum ground temperature greater than 0 °C at the uppermost surface of the massive ground ice, and therefore could be subject to seasonal thaw. A greater level of confidence in short and long-term performance of the thermal design was predicted for model cases with a decrease in evaporator pipe separation.

4 CONSTRUCTION

4.1 Construction Timeline

Construction began in the fall of 2018 and extend to the early summer of 2020 (Figure 6). The major construction events included:

- October 2018 – Installation of monitoring system; ground temperature cables and weather station to established pre-construction baseline conditions.
- Fall 2019 – Vegetation clearing, excavation along the embankment toe and start of inclined drilling for installation of casing and evaporator pipes (Figure 6A).
- Early winter 2020 – Completion of drillholes, installation of casing, and evaporator pipes.
- Early winter 2020 – Temporary installation of sloped thermosyphon radiators charged with working fluid (Figure 6B).
- Early summer 2020 – Permanent installation of thermosyphon radiators in vertical orientation, placement of backfill and final grading at riser pipes (Figure 6C).

4.2 Drilling and Installation

A hammer drill was used to advance inclined boreholes and casing (Figure 6A). The holes were cased to ensure integrity of the borehole wall prior to evaporator pipe installation. Drill site requirements limited use of drill fluids to minimize thermal disturbance of the foundation. At the time of construction, it was discovered that the casing strength (schedule 40) was not sufficient to advance during drilling. This required shipment of additional schedule 80 casing to the site before proceeding with the construction which consequently delayed completion of the project. As a result, the thermosyphon radiators were temporarily installed horizontally to allow for removal of heat induced by the drilling method used on-site (Figure 6B). The horizontally aligned radiators were removed during the next construction season to allow for vertical installation of the riser components and continuation of civil works, including installation of insulation within the toe berm and compaction of fill material (Figure 5A). The system was commissioned in the summer of 2020 (Figure 6C).

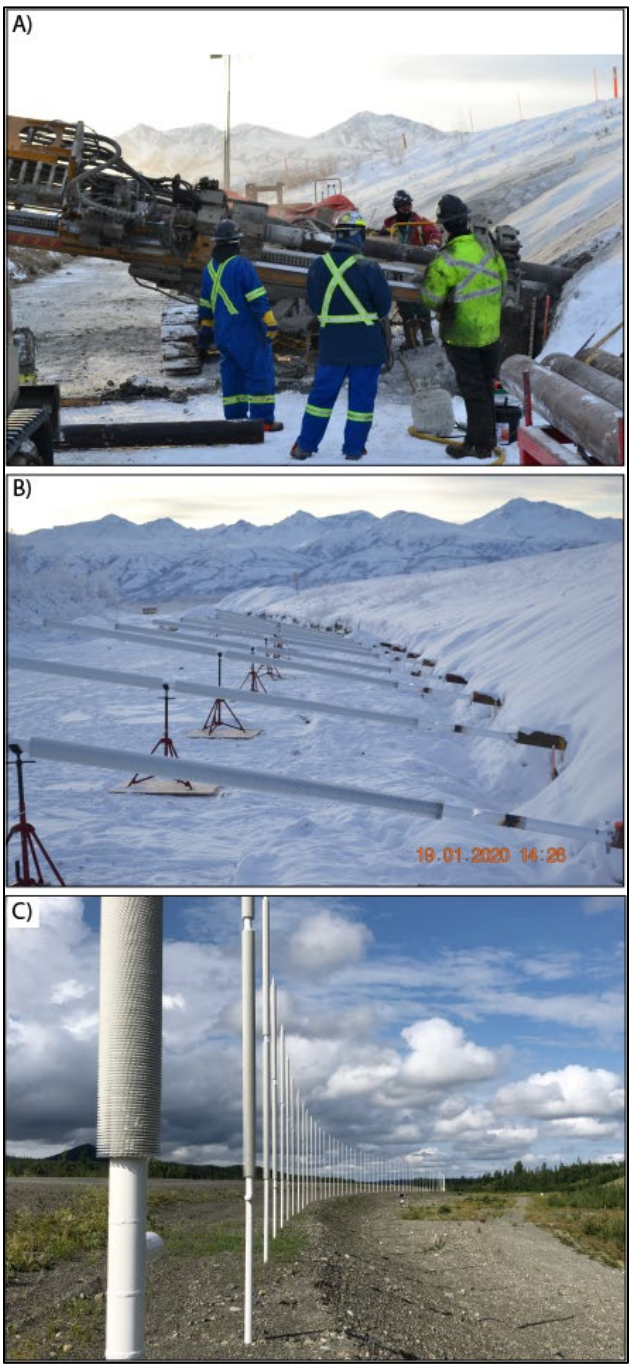

Figure 6. Construction photographs showing A) horizontal directional drilling beneath the highway embankment, B) temporary installation of surface radiators, and C) completed vertical installation of surface radiators and graded backfill along east toe of the embankment.

5 MONITORING SYSTEM

A long-term monitoring system was developed to verify the ground thermal performance and function of the thermosyphon units and to provide information that supports future sloped thermosyphon designs. The system includes two monitoring sections referred to as STN102 and STN103 (Figure 5C). This paper presents data collected at STN102 where massive ground ice was confirmed with drilling. Massive ground ice was not confirmed at STN 103 and provides contrasting ground conditions for future evaluation of thermosyphon performance.

Figure 5D shows the general arrangement of ground temperature cables and the cable naming convention for monitoring station STN102. Five thermistors of the six cables are vertically installed to measure embankment fill and permafrost foundation temperature. An additional thermistor cable was installed on the sloped thermosyphon evaporator pipe. Ground temperature cables were calibrated to ± 0.1 °C prior to installation. One meteorological station was installed at the location of STN103 to measure hourly ambient air temperature, windspeed, and humidity.

6 THERMAL PERFORMANCE

6.1 Baseline Period

Baseline ground temperature prior to construction was measured from the five vertically installed ground temperature cables at monitoring station STN102 (Figure 5D). The measurements have been summarised on the basis of a thermal year extending from October 1 to September 30. The thermal year approach was used to avoid combining values measured across two different winter seasons that are within the same calendar year.

The average annual temperature at the top of permafrost prior to construction was -0.2 °C (Figure 8A). At a depth of 12 m bgs, the permafrost temperature ranged from -0.4 °C to -0.5 °C. The active layer was measured to be 7 m bgs for STN102 GTC 157, located beneath the highway centerline (Figure 7A). Seasonal thaw at this location corresponds to the top of massive ground ice, as confirmed by drilling. Seasonal freezeback to this depth is facilitated by snow clearing from the driving surface which promotes heat loss from the ground.

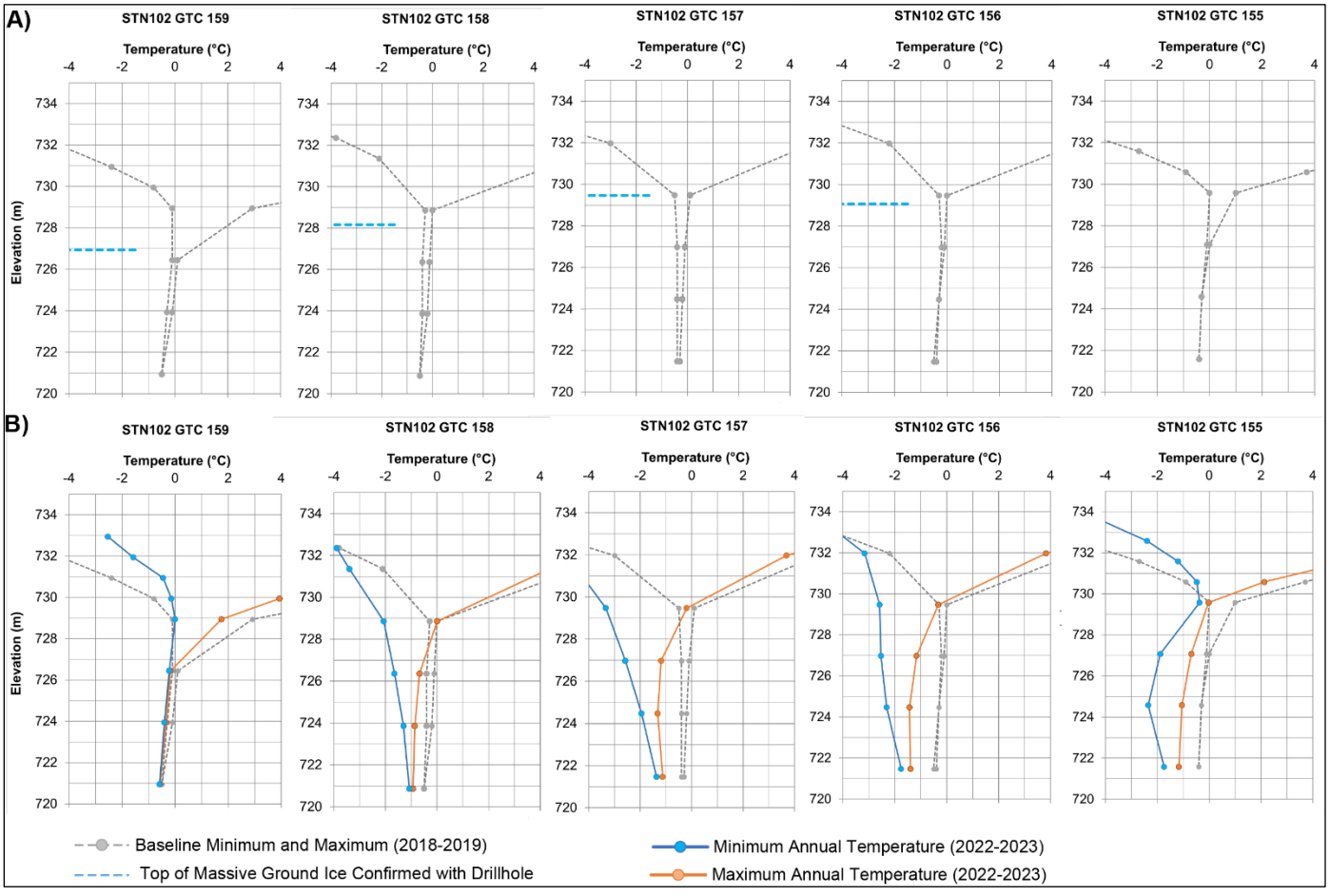

Figure 7. Minimum and maximum annual ground temperature at Monitoring Station STN 102: A) prior to construction during baseline period (2018–2019) and B) post-construction (2022–2023) compared to baseline period.

Ground temperature measured at STN102 GTCs 155 and 159 beneath the embankment toe indicate thaw exceeded seasonal freezeback during the baseline period and a suprapermafrost talik was present (Figure 7A). Minimum heat loss from foundation was measured beneath the embankment toe due in part to the suprapermafrost talik that remains perennially unfrozen. At STN GTC 159, the top of massive ground ice was confirmed with drilling to correspond to the permafrost table (Figure 7A).

The positive ground thermal gradient of permafrost (i.e., the increase in the ground temperature with depth) measured at each of the five locations and the presence of suprapermafrost talik indicates permafrost degradation has occurred beneath and adjacent to the embankment prior to construction.

6.2 Post-Construction Period

The thermosyphons installed at Dry Creek have been designed to passively extract heat from the ground without the need of a mechanical pump. Figure 8 shows the evaporator pipe temperature compared to air temperature for the first three years since installation. Activation of the thermosyphons has taken place each winter in early-to-mid October when the air temperature is less than the ground temperature. The thermosyphon units become inactive in early-to-mid April when the air temperature is warmer than the ground temperature. The current duration of thermosyphon function at the site each year is approximately 183 days. The average winter ground temperature at the evaporator pipe has been -8 °C to date, with a minimum temperature of -17.5 °C. Baseline ground temperature prior to installation of the thermosyphons was significantly warmer (winter minimum of -0.4 °C) and characterized by minimum winter heat loss from the ground.

Figure 7B shows the ground temperature at the warmest location between two evaporator pipes for the most recent thermal year and the baseline period. Both the minimum and maximum annual ground temperature has decreased (Figure 7B). The greatest ground cooling has taken place beneath the thickest embankment fill and/or the deepest installation depth of the sloped thermosyphon. These locations include the centreline of the highway embankment STN102 GTC 157 beneath the thickest section of fill and STN102 GTCs 156 and 155 where the evaporate pipe is effectively deeper in the ground.

Figure 9 shows the relative change in the permafrost table. The permafrost table immediately beneath the highway embankment has aggraded upwards by approximately 20 cm over the first three years. The greatest upward aggradation of permafrost has been at STN 102 GTC 155, representing the former location of a suprapermafrost talik observed beneath the embankment toe. The permafrost table at this location has aggraded upwards by approximately 2.5 m. The talik has completely frozen back with the uppermost ground subjected to seasonal thaw during development of the active layer. This location is represented by the deepest installation depth of the evaporator pipe. At the opposing embankment toe beneath the surface radiator, the placement of insulation in the toe berm has above STN 102 GTC 159 has maintained the permafrost table at a higher elevation (Figure 9A). While the insulation installed in the toe berm reduces heat gain to the ground, there is limited heat loss from the thermosyphon evaporator pipe at this location (Figure 9C). This location is particularly sensitive to future thaw.

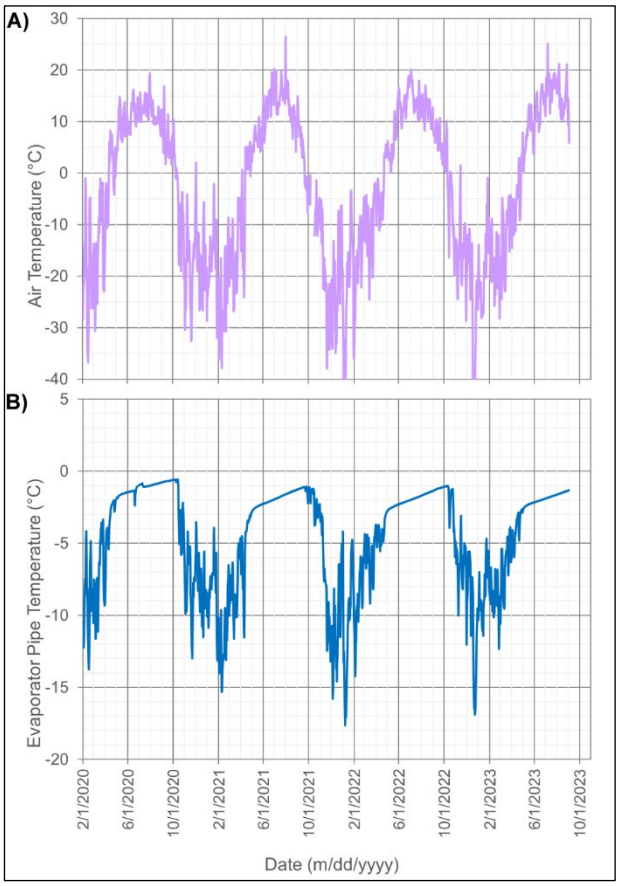

Figure 8. A) Air temperature and B) thermosyphon evaporator pipe temperature.

7 Conclusions

The Dry Creek highway section is characterized by glaciofluvial sand and gravel underlain by glaciolacustrine silt and clay. The presence of warm permafrost (> -0.5 °C) and massive ground ice in excess of 9 m thick necessitated stabilization of the site to reduce ongoing thaw settlement and risk of embankment failure.

The sloped thermosyphons design was developed to maintain integrity of the existing embankment without disruption of highway traffic. Thermosyphons have performed as expected during the initial three full years following construction, with notable decrease in the minimum and maximum annual ground temperature. The greatest ground cooling has occurred beneath the thickest section of embankment fill which acts to reduce heat gain during the thawing season. At locations of reduced embankment fill or where the evaporator pipe is installed at a shallower depth, the ground temperature is warmer due to the seasonal heat gain to the ground that is not directly

addressed by the design implemented at the site. Additional measures could be taken to reduce heat gain to the ground, such as installation of insulation within the embankment fill above the position of the evaporator pipes.

Change in the ground thermal regime has decreased permafrost temperature and aggraded the permafrost table upward beneath the highway embankment.

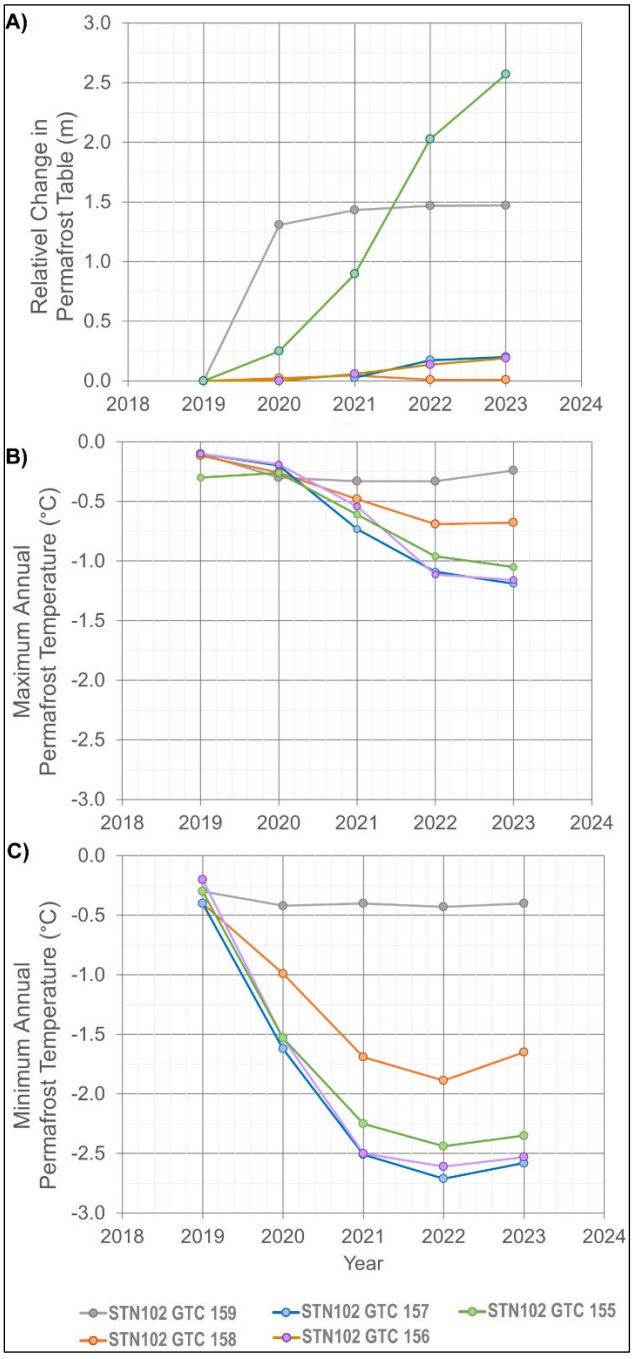

Figure 9. A) Relative change in permafrost table compared to baseline period, B) change in maximum annual and C) minimum annual permafrost temperature at 9.5 m bgs.

Suprapermafrost taliks located beneath the embankment toe have also frozen back to arrest permafrost degradation. The thermosyphons are expected to continue to contribute to permafrost stabilization over the 30-year design life.

The Dry Creek Permafrost Stabilization project contributes to evaluation of techniques for the climate change adaptation of highway infrastructure in permafrost environments. Information obtained from the site can be used to support similar designs.

8 ACKNOWLEDGEMENTS

The Dry Creek Permafrost Stabilization project was funded by the Government of Yukon and Transport Canada. Several individuals contributed to the success of this project including Bill Stanley, Kisa Elmer, Ivan Clark, Mike Watt, Harvey Kearns, and David Lorenzi. Thermal design was completed under the primary author's tenure with SRK Consulting. Civil design was completed by Ivan Clark.

9 REFERENCES

Calmels, F., Dore, G., Kong, X., Roy, L., Lemieux, C., Horton, B. 2016. *Vulnerability of the North Alaska Highway to Permafrost Thaw: Design Options and Climate Change Adaptation*. Whitehorse, Yukon, Canada: Northern Climate ExChange, Yukon Research Centre, Yukon College, 130 p.

Golder 2012. *Geotechnical Site Investigation Shakwak Highway Project – North Alaska Highway – Yukon km 1710 to km 1902*. Report submitted to Government of Yukon, Highway and Public Works, 548 p.

Government of Yukon 2014. *Highway Restoration and BST, Alaska Highway #1, KM 1856.6 to KM 1869.2, As-Built Drawings*. Government of Yukon, Highways and Public Works, Transportation Engineering Branch

Lepage, J.M. 2016. *Experimentation of mitigation techniques to reduce the effects of permafrost degradation on transportation infrastructures at Beaver Creek experimental road site Alaska Highway, Yukon*. Québec City, Québec, Canada: University of Laval, MSc Thesis, 629 p.

Rampton, V.N. 1979. 'Surficial Geology and Geomorphology, Koidern Mountain, Yukon Territory', *Geological Survey of Canada* Preliminary Map 5-1978, 1 sheet.

SRK Consulting Canada Inc. (SRK) 2017. *Dry Creek Highway Section Preliminary Design and Thermal Modeling*. Report submitted to Government of Yukon, Highways and Public Works, Transportation Engineering Branch.

Yukon Engineering Services (YES) 1996. 'Highway Construction, Alaska Highway #1, As-Built Drawings, KM 1893.7 to KM 1915.7'., in *Shakwak Highway Reconstruction KM 1893.7 to KM 1915.7*. YES Job 94-032.

Road surface *n*-factors across elevational and latitudinal treelines, Dempster–ITH corridor, western Arctic Canada

Emma J. Stockton[1], Christopher R. Burn[1], M. Alice Wilson[2] & Steven V. Kokelj[2]

[1]*Carleton University, Ottawa, Ontario, Canada*

[2]*Northwest Territories Geological Survey, Government of Northwest Territories, Yellowknife, Northwest Territories, Canada*

ABSTRACT

Relationships between air and ground surface temperatures can be summarized by *n*-factors for the freezing (n_f) and thawing (n_t) seasons. The theory of *n*-factors assumes that a homogenous surface, such as a road, has spatially consistent relationships between ground surface and air temperatures. The 400 km Dempster–ITH corridor in NWT crosses elevational and latitudinal treelines between the territorial border and the Beaufort Sea coast. Road surface *n*-factors along the corridor have been determined at nine sites to examine their variation in the range of climatic environments encountered. They have also been compared with values from four borrow pits to examine the influence of snow on the *n*-factor. During the study, air temperatures varied from -42.6 to 26.2 °C over two years beginning in October 2020. Values for n_t varied from 1.00 to 1.36, while n_f varied from 0.89 to 1.06 at the road sites and 0.10 to 0.76 at the pits. Values for n_t of 1.26 and n_f of 0.96 appear robust for a gravel road across a range of climatic environments.

1 INTRODUCTION

Design and maintenance challenges imposed by frost action affect almost all of Canada's highway network. In permafrost regions, a common approach to highway design is to contain thaw penetration within the road embankment and protect underlying permafrost from thaw. Embankment and road surface integrity may be compromised if ice-rich permafrost beneath the embankment thaws and the driving surface settles (e.g., Alfaro et al. 2009). Engineers seldom have access to ground surface temperatures when designing road geometry. Such values are a product of the surface energy balance and require monitoring of several microclimatic variables if they are to be reliably determined. Instead, *n*-factors are used to estimate surface temperatures from projected air temperatures (Lunardini 1978). The indices were developed for constructed surfaces such as roads because the surface energy balance is simplified by the removal of ecological effects. The temperature indices from which *n*-factors are derived can be determined by the summation of mean daily temperatures in degree days (°C-d) for the freezing (FDD) and thawing (TDD) seasons (Thompson 1963). The freezing (n_f) and thawing (n_t) *n*-factors may be expressed as:

$$n_f = \frac{FDD_s}{FDD_a} \quad [1]$$

$$n_t = \frac{TDD_s}{TDD_a} \quad [2]$$

where the subscripts *s* and *a* denote the surface and air, respectively. The *n*-factor is dimensionless and ranges from 0 to ∞. Values near 1.0 indicate a close relation between air and surface temperatures; high n_f and n_t represent relatively cold winter and warm summer surfaces, respectively. Reliable determination of an *n*-factor requires concurrent measurements in the air and at the surface, which is often impractical. Engineers manage this issue by selecting rational values from published literature. The theory of *n*-factors assumes a homogenous surface, such as a road, should have spatially consistent thermal relationships with the atmosphere.

The applicability of *n*-factors for identical road surfaces may differ with location. For example, Instanes and Anisimov (2008) found that a value of 1.0 simulated measured ground temperatures well in Longyearbyen, Svalbard, but not in Fairbanks, AK, or Yakutsk, Russia. Using book values to determine the *n*-factor may lead to uncertainty in the frost depth of 25–30% (Johnston 1981). Differences may be associated with changes in net radiation, turbulent heat transfer, construction materials, and surface roughness (e.g., Lunardini 1978). To the authors' knowledge, no previous studies have attempted to quantify the spatial variability of *n*-factors along a highway transect through varying climatic zones.

The Dempster and Inuvik–Tuktoyaktuk Highways (the Dempster–ITH corridor) provide an opportunity to investigate *n*-factors across elevational and latitudinal treelines along gravel roads (Palmer et al. 2012; O'Neill et al. 2015). Values were also derived for gravel surfaces with snow accumulation in borrow pits to examine the influence of snow on the *n*-factor and duration of the freezing and thawing seasons in the same region.

2 STUDY AREA

The Dempster–ITH corridor in Northwest Territories (NWT) traverses the traditional territories of the Inuvialuit, Nihtat Gwich'in, Gwichya Gwich'in, Tetlit Gwich'in, Vuntut Gwich'in, and Na-Cho Nyak Dun. This study focuses on the 400 km between the Yukon/NWT border and Tuktoyaktuk (Figure 1). The route is the only surface link from southern

https://doi.org/10.52381/ICOP2024.143.1

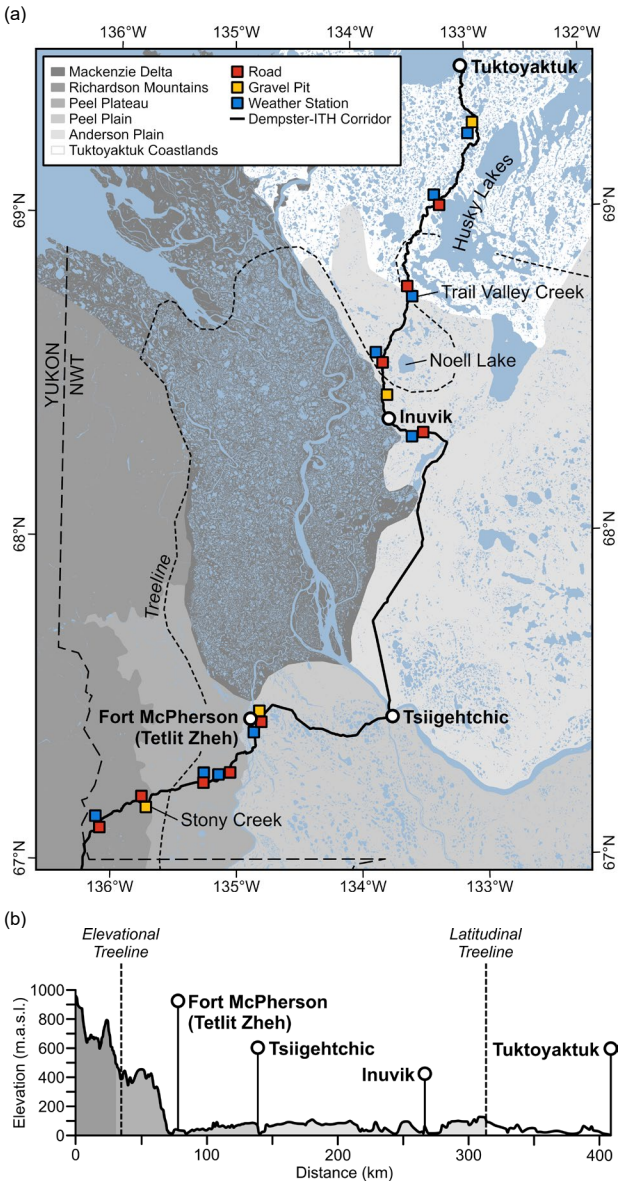

Figure 1. (a) Map with physiographic units and air and ground temperature monitoring sites across elevational treeline between the territorial border and Fort McPherson, and latitudinal treeline between Inuvik and Tuktoyaktuk (e.g., Ensom et al. 2020). (b) Elevation profile of the route with latitudinal treeline near Trail Valley Creek. Water bodies are from Canvec (Natural Resources Canada 2023).

Canada providing all-weather access for freight transport, private travel, tourism, and subsistence harvesting to Fort McPherson (Tetlit Zheh), Tsiigehtchic, Inuvik, and Tuktoyaktuk.

2.1 Highway Design and Construction

The Dempster Highway was completed in 1979 to a recommended embankment height of 1.4 m based on experience at Inuvik Airport (Johnston 1982). Post-construction surveys commended the serviceability of the highway but deemed the fill thickness insufficient in areas of flat, poorly drained terrain (Lingnau 1985). The conceptual design was a basal pad of sandstone and shale built directly on the ground and topped with a gravel driving surface. Suitable gravel sources were limited, so quarried limestone was also used as surfacing material (Huculak et al. 1978). The design of the ITH considered foreseeable changes in climate and permafrost conditions, the thermal influence of the embankment, and the sustainability of construction materials to meet the 75-year service life. Approximately 4.8 million m^3 of granular material were used to construct the ITH (Grozic and Zhang 2018). Embankment construction and borrow source extraction occurred in winter to minimize disturbance to the thaw sensitive terrain. The design incorporated an overbuild of about 0.45 m on top of the minimum thickness of 1.7–2.0 m, to account for settlement of frozen-placed materials in the summers following construction (Grozic and Zhang 2018). However, budget constraints reduced the fill in some areas and in turn the preservation of near-surface permafrost within a few years of the highway opening in 2017 (de Guzman et al. 2021).

2.2 Physiography, Climate, and Ground Temperatures

The corridor traverses several physiographic units and climatic regimes (Figure 1). At the territorial border, the climate is influenced by the elevation and topography of Richardson Mountains. Total annual precipitation is moderate (300–400 mm) and mostly falls in summer. Clear skies and low temperatures are common in January due to stabilized weather patterns from high-pressure cells (Wahl et al. 1987). Occasional disturbances in the shoulder seasons lead to higher temperatures and snowfall. The eastern flanks of the mountains mark the terminal limit of the Laurentide Ice Sheet.

Peel Plateau is a fluvially incised, glacially altered, and eastward sloping landscape. Permafrost is ice-rich and prone to thermokarst processes (Kokelj et al. 2017). FDD decreases with elevation due to strong atmospheric inversions resulting in mean winter temperatures on Peel Plateau about 4 °C higher than at Fort McPherson (O'Neill et al. 2015). Peel Plain is underlain by an ice-rich, fine grained till veneer over unexposed shale and mudstone bedrock quarried for the highway (Norris 1984). Mean annual air temperatures and total annual precipitation decrease northward from Fort McPherson (-7.3 °C, 300 mm) to Tuktoyaktuk (-10.1 °C, 160 mm; Environment Canada 2023).

North of Tsiigehtchic the corridor traverses Anderson Plain, an undulating and imperfectly drained landscape of gentle slopes, incised valleys, and uplands (Mackay 1963). Tuktoyaktuk Coastlands are characterised by thicker surficial deposits, few bedrock outcrops, and low, rolling terrain interspersed with lakes (Rampton 1988). Polygonal terrain is abundant and increases with proximity to the coast (Kokelj et al. 2014). TDD decreases northward due to onshore winds blowing across persistent sea ice and cold coastal waters, resulting in a mean monthly temperature

difference of about 4 °C between Inuvik and Tuktoyaktuk in early summer (Burn 1997; Burn and Kokelj 2009).

The corridor is underlain by continuous permafrost but mean annual ground temperatures vary due to differences in climatic and environmental conditions. Across latitudinal treeline, permafrost temperatures decrease from about -3 °C in the forest to -6 °C in the tundra due to declining air temperatures and snow depth (Burn and Kokelj 2009). However, across elevational treeline, tundra permafrost is about 1 °C warmer than permafrost at Fort McPherson (-2.5 °C), due to higher winter air temperatures and earlier snow accumulation (O'Neill et al. 2015).

2.3 Treeline

Winter temperature inversions control a steep elevational gradient and treeline on Peel Plateau (O'Neill et al. 2015). The corridor descends from low shrub tundra in the mountains (≥ 1000 m asl), to tall shrub tundra (~400 m asl), to open canopies of black spruce (*Picea mariana*) and tamarack (*Larix laricina*) at Fort McPherson (~30 m asl). Latitudinal treeline crosses Anderson Plain north of Inuvik. It is associated with declining summer air temperatures due to differences in net radiation and onshore winds (Burn 1997). Anderson Plain is characterised by a sparse overstory of tamarack, black spruce, white spruce (*Picea glauca*), and paper birch (*Betula papyrifera*; Ritchie 1977). Tall shrub tundra prevails about 30 km north of Inuvik, while low shrub tundra occupies the polygonal terrain of the Tuktoyaktuk Coastlands. Alder (*Alnus spp.*) and willow (*Salix spp.*) are common in disturbed areas.

3 Methodology

In October 2020, nine road sites were established in the corridor to capture a range of thermal conditions at the highway surface across elevational and latitudinal treeline (Figure 1). Road surface temperatures were measured hourly using Geoprecision PT 1000 thermistors and M-Log5W data loggers. The instruments, housed in sealed PVC pipe, were installed by hand drill to a depth of 0.15 m below the highway centerline and the boreholes were backfilled with drill cuttings. The thermistor depth was recommended by Government of the Northwest Territories Department of Infrastructure (GNWT-INF) to prevent damage from maintenance operations, such as grading and snow ploughing. Thermistors were downloaded wirelessly to a laptop using FG2-Shell Geoprecision software.

Similar thermistors were installed at "gravel pits" where snow accumulated in winter. These include a gravel pad at Stony Creek and three borrow sources at Fort McPherson (FM500), Noell Lake (Pit I401A), and Husky Lakes (Pit 177). Thermistor cables with sensors up to 10 m depth were also installed at the two pits along the ITH and, at some locations beneath the road embankment (e.g., Rudy et al. 2020a,b). Data from 2–4 m depth at the Noell Lake pit (I401A) and road sites are used in the analysis. These boreholes were drilled by auger in 2017 and instrumented with Geoprecision PT 1000 and Lakewood RX-16 thermistors at the pit and road, respectively (Ensom et al. 2020).

Air temperatures were collected from nine weather stations along the route managed by Environment Canada and GNWT (Kokelj et al. 2022). Air and surface temperatures were divided into two years from 16th October 2020. Daily *n*-factors were calculated using eq. 1 and 2 and averaged seasonally, i.e., when both variables were < 0 °C for n_f or > 0 °C for n_t, since daily fluctuations may not be simultaneous.

Snow depth and density were measured at the gravel pits in late March to mid April. Median snow depth was calculated from five measurements with a metal meter stick. Snow density was measured using a Metric Prairie Snow Sampler (Geo Scientific Ltd., Vancouver, BC) with Lexan graduated plastic tube and steel cutter. Samples were placed in a clear plastic bag and weighed using a Pesola Medio Spring Scale. The density was calculated from the snow mass and volume occupied in the tube.

4 Defining the Freezing and Thawing Seasons

For this paper, the onset and duration of the freezing (S_f) and thawing seasons (S_t) were defined by daily *n*-factors and varied between sites. The seasons began when the *n*-factor was calculable for three consecutive days, i.e., both air (T_a) and surface temperatures (T_s) were of the same sign. If a period of equal or greater length without a *n*-factor followed, the season would restart. The end of the seasons was delineated by the cessation of *n*-factors for three or more days. S_f and S_t were separated by spring and autumn when T_a and T_s fluctuated asynchronously. At the end of the season, T_a and T_s were close at the road sites. However, in the pits, T_s lagged T_a due to the intervening snowpack. When T_a was higher than T_s, but below 0 °C, the daily *n*-factor might be large. In this case, *n*-factors greater than three standard errors above the seasonal mean were neglected (i.e., $n_f \gtrsim 1.7$ and $n_t \gtrsim 2.7$).

At the road, S_f and S_t were long and well-defined because T_s conformed to changes in T_a. Installation of the road thermistors in mid October 2020 missed the start of S_f by one or two weeks. At the road, S_f began in late September to early October and ended in mid to late April, lasting 186–214 days. The length of S_f was similar among the sites each year, but it began earlier at higher elevations. S_t started in early June and ended in late September, lasting 104–115 days. During spring and autumn, T_a and T_s were close to 0 °C and had relatively little impact on seasonal FDD or TDD. The duration of spring was relatively consistent (45–51 days), while autumn was shorter at higher elevations (3 days) than north of Fort McPherson (14 days).

At the gravel pits, the onset and duration of the seasons were similar to the road, but T_s did not fluctuate to the same extent as at the road during S_f due to the snow cover. S_f started in early to mid October and ended in mid April to mid May, lasting 177–214 days. Each year the onset of S_f was similar among sites, but the season was extended by up to four weeks at Husky Lakes (Pit 177) due to continuously cool air temperatures near the coast. At the remaining pits, the duration of S_f was about ten days shorter than the road due to the air temperature being between 0 °C and T_s, as discussed above. S_t at the pits was comparable to the road with an onset in early June and a duration of 104–113 days. The duration of spring ranged from 19–53 days, while

autumn lasted 14–22 days. Longer S_f at Husky Lakes (Pit 177) resulted in a shorter spring and rapid transition to summer.

5 AIR AND ROAD SURFACE TEMPERATURES

Figure 2 is a scatter plot of monthly mean temperatures for T_a and T_s at each site over two years. The measurements have equal precision; thus, the relation can be summarized using the functional fit, in this case the principal axis (Mark and Church 1977). The data show a strong, linear correlation with higher T_s than T_a over the year. Data with slightly increased scatter from -10 to 10 °C are the shoulder seasons. Figure 3 shows daily mean T_a and T_s at all sites with principal axes for S_f and S_t.

The principal axis in Figure 2 and the seasonal means in Table 1 indicate T_s was higher than T_a, except for the Territorial Border in 2020–2021. The principal axes in Figure 3 yield a summary of the relation on a daily, rather than a seasonal basis. For S_t, the functional relation indicates T_s is about 2.4 °C higher than T_a, which is comparable to data in Table 1. Data from spring and autumn are not included in Figure 3. In 2020–2021, the range in annual mean T_s was 2.5 °C among all nine sites, and 1.5 °C across both gradients (Table 1). During this period, the surface offset (T_s–T_a) was 1.7–1.8 °C across latitudinal treeline (Inuvik to Husky Lakes), and 1.1–2.6 °C across elevational treeline (Territorial Border to Fort McPherson). At higher elevations, T_s during S_t was lower than Fort McPherson, while T_s during S_f was higher due to atmospheric inversions.

6 THE *N*-FACTOR

6.1 Road Surface *n*-factors

The seasonal mean *n*-factors shown in Table 1 are within the large range of values reported in the literature for cleared gravel surfaces. Published n_f vary from 0.60–1.00 and n_t from 1.00–2.01 (e.g., Johnston 1982). Over the study period, n_f and n_t varied from 0.89–1.06 and 1.08–1.36, respectively (Table 1). Mean n_f and n_t for the entire corridor are 0.96 and 1.26, respectively. During S_t, surface temperatures are a result of available radiation and advected air mass characteristics, while during S_f air and surface temperatures are primarily a function of the prevailing air masses. Hence, n_t is generally higher than n_f.

Among sites, values for n_f and n_t evolve similarly over the season as degree day totals progressively increase. Figure 4 illustrates this with daily cumulative *n*-factors and daily cumulative degree days for the Noell Lake road site. At the beginning of the season *n*-factors fluctuate because degree day totals are low and sensitive to small changes in T_s or T_a. As the seasons advance, *n*-factors become insensitive to daily temperature changes due to the large degree day totals, causing oscillations to dampen and the ratio to level off. The *n*-factor is stable when daily cumulative values differ from the seasonal mean by less than 10%. Along the corridor daily cumulative *n*-factors stabilized after one to three weeks.

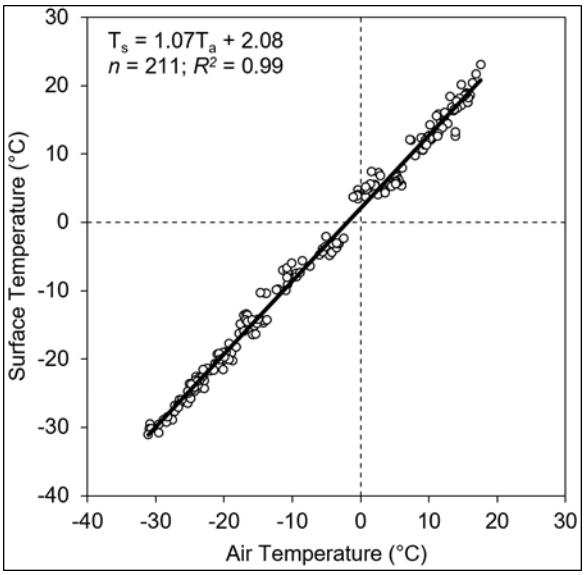

Figure 2. Monthly mean Ta and Ts for the road with the principal axis, 2020–2022.

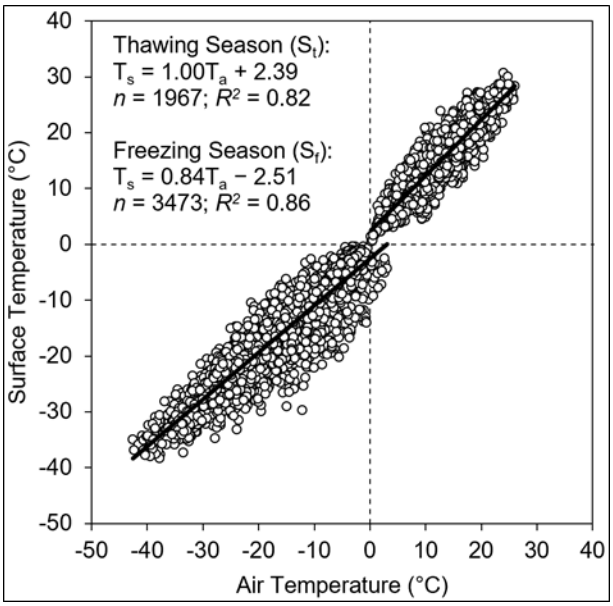

Figure 3. Daily mean Ta and Ts for the road with the principal axis for the freezing and thawing seasons, 2020–2022.

At all sites, FDD totals accumulated analogously throughout most of winter, but at the beginning of the season FDD_a was greater than FDD_s, resulting in low n_f. As the relative increase in FDD_s approached FDD_a, daily cumulative n_f rose and eventually became constant. At the end of the season, the rate of growth slowed and FDD_s departed from FDD_a. In contrast, the relative increase in TDD_s was greater than TDD_a at the beginning of the season likely due to high incident radiation in June, causing high n_t. As the relative increase in TDD_a approached TDD_s, daily cumulative n_t declined and eventually stabilized. Once stabilized the relative increases in degree-day totals for both seasons was about 2–6% per day.

The small range in *n*-factors indicate the minimal effects of latitude and elevation along the corridor (Table 1). Several studies suggest *n*-factor variability may be associated with turbulent heat transfer. For example, greater wind speed may decrease n_t and increase n_f (e.g., Sanger 1966).

However, mean annual wind speeds along the corridor were relatively uniform (2–4 m s^{-1}) and vehicle-generated wind effects are unlikely due to the low volume of traffic. Shading from adjacent vegetation could reduce n_t but this is unlikely due to stunted forest growth, brushing in the right-of-way, and high solar elevation in the Arctic. Surfacing materials are relatively uniform along the corridor, but minor differences may cause *n*-factor variability. For example, lighter surfaces may increase albedo and reduce *n*-factors. Daily *n*-factors may vary with the frequency of ploughing in winter and water infiltration from precipitation or dust suppression activities in summer.

Several studies have estimated *n*-factors for the Dempster–ITH corridor from the available literature. Piamsalee (2019) selected an n_f of 0.80 and an n_t of 1.30 and de Guzman et al. (2021) selected an n_f of 0.95 and an n_t of 1.00. Some of the published values underestimated the measured *n*-factors presented here. A more conservative embankment design favours overestimated *n*-factors that assume a thicker active layer and warmer permafrost.

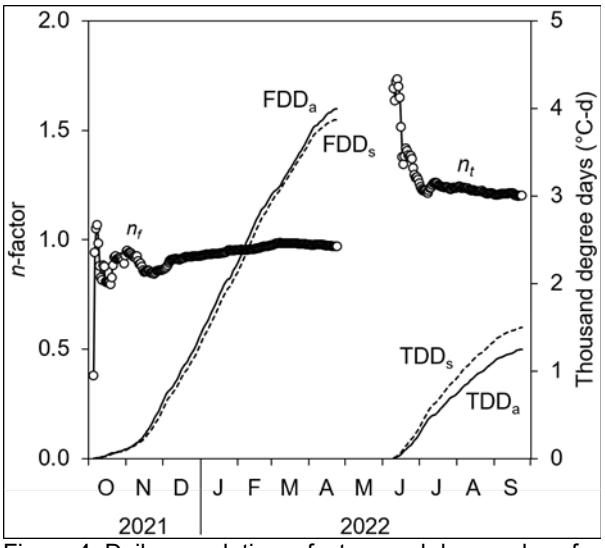

Figure 4. Daily cumulative n-factors and degree days for the air and road at Noell Lake, 2021–2022.

Table 1. Climate and road surface data for the Dempster–ITH corridor over two years beginning in October 2020. Annual mean and seasonal mean temperatures (°C) for the air (T_a) and road surface (T_s), seasonal degree days for the air (FDD_a, TDD_a) and road surface (FDD_s, TDD_s), and mean daily freezing (n_f) and thawing (n_t) *n*-factors. T_a at Midway Airstrip were used to calculate *n*-factors at Stony Creek.

	Annual		Freezing Season					Thawing Season				
2020–2021	T_a	T_s	T_a	FDD_a	T_s	FDD_s	n_f	T_a	TDD_a	T_s	TDD_s	n_t
Territorial Border	-6.8	-5.6	-19.1	3682	-19.5	3612	1.06	10.5	1212	12.8	1566	1.29
Stony Creek	-	-5.1	-	-	-19.0	3479	1.01	-	-	13.4	1626	1.23
Midway Airstrip	-6.6	-5.5	-19.6	3723	-19.5	3588	1.00	11.4	1332	13.3	1593	1.21
Peel Plateau	-5.6	-4.5	-18.8	3522	-18.8	3430	1.01	12.4	1496	14.5	1792	1.22
Fort McPherson	-6.7	-4.1	-21.9	4084	-20.6	3781	0.93	13.6	1633	17.9	2269	1.35
Inuvik	-6.8	-5.1	-21.1	4010	-21.5	3894	1.03	12.5	1536	15.6	2027	1.28
Noell Lake	-7.4	-5.7	-21.7	4143	-20.8	3861	0.96	12.1	1426	14.7	1790	1.25
Trail Valley Creek	-8.0	-6.2	-21.7	4209	-21.2	3975	0.98	11.0	1308	13.9	1708	1.33
Husky Lakes	-8.3	-6.6	-22.0	4286	-21.2	3990	0.96	10.5	1256	12.7	1594	1.26
2021–2022												
Territorial Border	-7.0	-5.4	-17.6	3792	-16.9	3571	0.94	10.8	1228	13.0	1584	1.24
Stony Creek	-	-4.6	-	-	-15.7	3288	0.89	-	-	13.6	1616	1.10
Midway Airstrip	-6.0	-5.4	-17.0	3699	-16.6	3545	0.92	13.2	1496	13.6	1583	1.08
Peel Plateau	-5.7	-4.1	-16.7	3543	-16.0	3320	0.89	12.3	1467	14.8	1811	1.29
Fort McPherson	-6.7	-4.4	-19.9	4019	-18.6	3730	0.90	13.0	1592	16.7	2144	1.34
Inuvik	-7.0	-5.6	-19.5	3992	-19.1	3781	0.97	12.0	1444	13.8	1755	1.26
Noell Lake	-7.4	-5.9	-20.0	4063	-19.4	3877	0.95	11.7	1360	14.0	1740	1.28
Trail Valley Creek	-8.0	-6.2	-20.2	4137	-19.3	3877	0.93	10.6	1223	13.3	1629	1.34
Husky Lakes	-8.2	-6.4	-20.7	4193	-19.7	3919	0.94	10.3	1202	12.6	1598	1.33

6.2 Gravel Pit *n*-factors

Values for n_f and n_t at the gravel pits ranged from 0.10–0.76 and 1.00–1.30, respectively (Table 2). At all sites *n*-factors were less than the adjacent road, indicating warmer winter and cooler summer surfaces. Figure 5 is a scatter plot of monthly mean temperatures for T_a and T_s at the pits over two years. During S_t, there is a linear correlation similar to the road between T_a and T_s, but during S_f the data are scattered due to differences in winter surface conditions

The principal axis for S_t indicates the gravel pit surfaces are warmer than the air in summer and about 1.4 °C lower than the adjacent road (Figures 2 and 5). However, at Husky Lakes (Pit 177) in 2021 and Stony Creek in 2022, n_t is at unity because T_s was higher than T_a for about half of S_t. At the other sites, n_t is higher because T_s was higher than T_a for 57–89% of S_t.

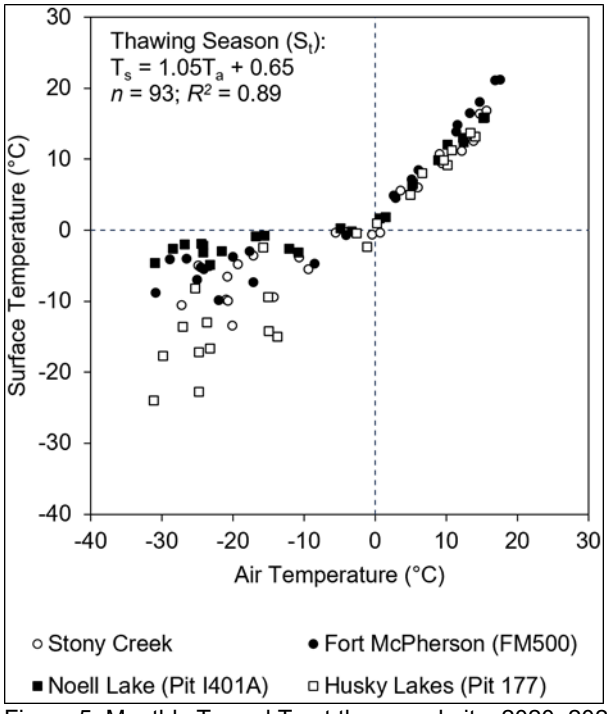

Figure 5. Monthly Ta and Ts at the gravel pits, 2020–2022. The principal axis for the thawing season (St) is given.

At all sites n_f was lower and more variable than the road. Since n_f for the road was relatively consistent, variability at the pits was likely controlled by snow and subsurface thermal conditions. The rank order of n_f was the same in both years but values at all sites were lower in 2021–2022 than in 2020–2021 because snow depth increased.

In the pits, mean n_f was highest at Husky Lakes (Pit 177) where thin snow cover promoted ground surface cooling. Stabilization of n_f occurred about 140 days after n_f at the road. Snow conditions at Stony Creek were associated with strong winds and proximity to the road. Compaction and the introduction of gravel and ice from ploughing increased snow thermal conductivity. Thus, n_f was higher than at sites with lower snow depths (Table 2). Stabilization of n_f occurred in mid winter, about 70 days after n_f at the road.

In both years, n_f were distinct at Fort McPherson (FM500) and Noell Lake (Pit I401A) even though snow depths and T_a were similar (Table 2). T_s was lower at Fort McPherson (FM500) despite having a more insulative snow cover (Figure 6a). These data indicate subsurface conditions influenced winter surface temperatures, and, in turn, n_f. At Noell Lake (Pit I401A), the top of permafrost is at 3.75 m depth with a mean annual temperature (T_p) near 0 °C. In 2021–2022, frost penetration began in early October and active layer freezeback was complete after six weeks (Figure 6b). Although, subsurface ground temperature data are not available at Fort McPherson (FM500), the rapid decline in Ts in mid November indicates a similar freezeback period (Figure 6a).

Table 2. Late winter snow depths (cm) and densities (kg m^3), and mean daily freezing (nf) and thawing (nt) n-factors at the gravel pits over two years beginning in October 2020.

2020–2021	Snow Depth	Snow Density	n_f	n_t
Stony Creek	77.0	500.7	0.54	1.10
Fort McPherson (FM500)	37.0	154.5	0.35	1.26
Noell Lake (Pit I401A)	34.5	224.6	0.13	1.13
Husky Lakes (Pit 177)	8.5	284.6	0.76	1.00
2021–2022				
Stony Creek	147.0	456.7	0.22	1.00
Fort McPherson (FM500)	58.0	115.9	0.19	1.30
Noell Lake (Pit I401A)	58.5	255.6	0.10	1.19
Husky Lakes (Pit 177)	13.5	294.0	0.52	1.15

At Noell Lake (Pit I401A), ground temperatures in the active layer were about -0.3°C throughout S_f (Figure 6b). The thick active layer underlain by permafrost with T_p steadily increasing by 0.5°C during 2017–2022 indicates permafrost at this site is degrading. Water in the active layer, some likely released from permafrost, alters the thermal properties and introduces latent heat effects which prevent rapid ground cooling (Riseborough 1990; Romanovsky and Osterkamp 2000). Thus, n_f is low at sites with thick active layers and warm permafrost because of the continuing release of latent heat during freezing, as evident in the temperatures at 2 m (Figure 6b).

At the Fort McPherson pit (FM500), divergence of TDD_a and TDD_s resulted in high n_t comparable to the road. At the other pits, n_t was closer to one because the relative increase in TDD totals were similar. Field observations showed surface conditions at Fort McPherson (FM500) were relatively dry. Therefore, we suggest lower n_t at the other pits, was associated with the availability of moisture for evaporation, hence similar T_a and T_s.

At the Noell Lake road site, active layer depth was at most 3.25 m and T_p was -4.5°C. Snow clearing as well as low soil moisture and T_p facilitated a shorter freeze back period (four weeks) than at the pit, allowing T_s to decline and n_f to stabilize (Figures 4 and 6c). During S_f, the temperature

gradient from the ground surface to the top of permafrost is positive at both sites. The steeper gradient at the road (7.6 °C m^{-1}) increased the heat flux out of the ground, while the low gradient at the pit (1.4 °C m^{-1}) reduced ground cooling (Kokelj et al. 2014).

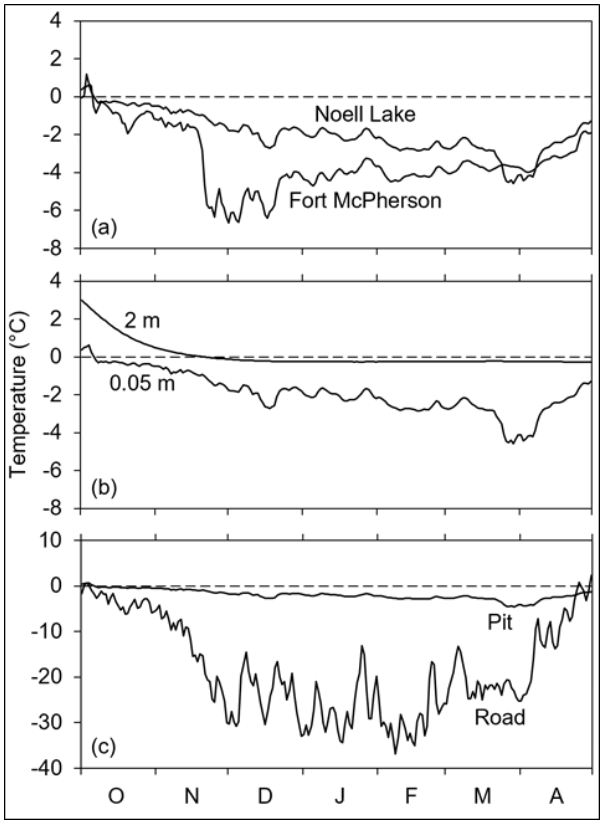

Figure 6. Daily mean ground temperatures from October 2021 to April 2022 at (a) the surface at the Noell Lake (I401A) and Fort McPherson (FM500) pits; (b) the surface and 2 m depth at the Noell Lake pit (I401A); and (c) the surface at the pit and road at Noell Lake.

In 2021–2022, both pits had a similar increase in snow depth but the change in n_f was greater at Fort McPherson (FM500; Table 2). Between years, T_a during S_f increased by about 2 °C at both pits, while T_s increased by 1.0 °C at Noell Lake (Pit I401A) and 3.7 °C at Fort McPherson (FM500). Although increased snow density at Noell Lake (Pit I401A) likely constrained the thermal effects of the deeper snow cover, T_s was less sensitive to changes at the surface because of latent heat effects at depth. These results indicate that surface conditions have less influence on n_f than subsurface conditions where the active layer is deep and permafrost is degrading. Thus, determining *n*-factors for constructed surfaces beneath a homogenous snowpack is complicated by the thermal state of permafrost.

Borrow sources account for a proportion of the thermal disturbance associated with highway construction. These data show surface boundary modifications caused by pit development can lead to permafrost degradation in subarctic settings. Reclamation procedures to preserve permafrost after excavation include natural revegetation, recontouring for drainage, and replacement of the organic layer. At sites with degrading permafrost, additional measures, such as snow compaction, could lower ground temperatures and stabilize thermal conditions. However, these interventions are often difficult to apply in practice. Gravel is a valuable commodity in the Mackenzie Delta region and gravel pits are commonly opened as part of development projects. The effects of permafrost thaw in such pits should be recognized during planning and regulatory review, particularly under a warming climate.

7 CONCLUSIONS

The principal conclusions derived from this study are:

(1) The *n*-factors used to summarize relationships between air and road surface temperatures were relatively consistent along the Dempster–ITH corridor, ranging from 0.89–1.06 for the freezing *n*-factor and 1.08–1.36 for the thawing *n*-factor, with little variation over two years. Values of 0.96 and 1.26 for the freezing and thawing *n*-factors, respectively, appear robust for a gravel road across a range of climatic environments;

(2) At the pits, *n*-factors were less than the road indicating warmer winter and cooler summer surfaces. Snow characteristics had less influence on freezing *n*-factors than ground thermal properties where the active layer is deep and permafrost is degrading; and

(3) Gravel pits experiencing permafrost degradation, such as Noell Lake, would require active mitigation to lower ground temperatures and stabilize thermal conditions. However, permafrost thaw induced by pit development is likely inevitable under a warming climate.

8 ACKNOWLEDGEMENTS

This research was supported by the Natural Sciences and Engineering Research Council of Canada, the Northwest Territories Geological Survey, Aurora Research Institute, and Carleton University. We extend particular thanks to Joel McAlister, Edwin Amos, Ryan McLeod, Greg Elias, Jennifer Humphries, Celtie Ferguson, Eli Nasogaluak, Kathryn Barr, Bill Conley, Miles Dillon, Mary Cockney, Wayne Thrasher, Andrew Koe, Ashley Rudy, and Tim Ensom. Discussions with GNWT-INF and the Imaryuk Monitoring Program improved the study. We thank Richard Blake for sharing embankment data along the corridor, and two anonymous reviewers for their helpful comments.

9 REFERENCES

Alfaro, M.C., Ciro, F.G., Thiessen, K.J., and Ng, T. 2009. 'Case Study of Degrading Permafrost Beneath a Road Embankment', *Journal of Cold Regions Engineering* 23(3), pp. 93–111. doi:10.1061/ASCE0887-381X200923:393.

Burn, C.R. 1997. 'Cryostratigraphy, Paleogeography, and Climate Change During the Early Holocene Warm Interval, Western Arctic Coast, Canada', *Canadian Journal of Earth Sciences* 34(7), pp. 912–925. doi:10.1139/e17-076.

Burn, C.R. and Kokelj, S.V. 2009. 'The Environment and Permafrost of the Mackenzie Delta Area', *Permafrost and Periglacial Processes* 20(2), pp. 83–105. doi:10.1002/ppp.655.

de Guzman, E.M.B., Alfaro, M.C., Arenson, L.U. and Doré, G. 2021. 'Thermal Regime of Highway Embankments in the Arctic: Field Observations and Numerical Simulations', *Journal of Geotechnical and Geo-environmental Engineering* 147(6), pp. 1–25. doi:10.1061/(ASCE)GT.1943-5606.0002502.

Grozic, E.M. and Zhang, G. 2018. 'Inuvik to Tuktoyaktuk Highway Road Embankment Constructed on Ice-rich Permafrost Terrain', in *GeoEdmonton 2018*, 71st Canadian Geotechnical Conference and 13th Joint CGS/IAH-CNC Groundwater Conference. Edmonton, Alberta, Canada: September 23–26, Paper 256.

Ensom, T., Kokelj, S.V., Morse, P.D., and Kamo McHugh, K. 2020. 'Permafrost Ground Temperature Data Synthesis: 2013-2019 Inuvik–Tuktoyaktuk Highway Region, Northwest Territories', *Northwest Territories Geological Survey* NWT Open Report 2019-020, 13 p.

Environment Canada 2023. *Canadian Climate Normals 1981–2010 Station Data*. Available at: https://climate.weather.gc.ca/climate_normals/index_e.html (Accessed: 7 August 2023).

Huculak, N.A., Twach, J.W., Thomson, R.S., and Cook, R.D. 1978. 'Development of the Dempster Highway North of the Arctic Circle', in *3rd International Conference on Permafrost*. Edmonton, Alberta, Canada: July 10–13, 1978, vol. 1, pp. 798–805.

Instanes, A. and Anisimov, O. 2008. 'Climate Change and Arctic Infrastructure', in *9th International Conference on Permafrost*. Fairbanks, Alaska, United States: Institute of Northern Engineering, University of Alaska Fairbanks, vol. 1, pp. 779–784.

Johnston, G.H. 1981. *Permafrost: Engineering Design and Construction*. New York, New York, United States: John Wiley & Sons.

Johnston, G.H. 1982. 'Design and Performance of the Inuvik, N.W.T., Airstrip', in *4th Canadian Permafrost Conference*. Calgary, Alberta, Canada: March 2–6, 1981, pp. 577–585.

Kokelj, S.V., Lantz, T.C., Wolfe, S.A., Kanigan, J.C., Morse, P.D., Coutts, R., Molina-Giraldo, N. and Burn, C.R. 2014. 'Distribution and Activity of Ice Wedges Across the Forest-tundra Transition, Western Arctic Canada', *Journal of Geophysical Research (Earth Surface)* 119(9), pp. 2032–2047. doi:10.1002/2014/JF003085.

Kokelj, S.V., Lantz, T.C., Tunniclifee, J., Segal, R. and Lacelle, D. 2017. 'Climate-driven Thaw of Permafrost Preserved Glacial Landscapes, Northwestern Canada', *Geology* 45(4), pp. 371–374. doi:10.1130/G38626.1.

Kokelj, S.A., Beel, C.R., Connon, R.F., Graydon, C.E.D., Kokelj, S.V., and Burn, C.R. 2022. 'Peel Plateau Climate Data, Northwest Territories', *Northwest Territories Geological Survey* NWT Open Report 2022-005, 16 p. doi:10.46887/2022-005.

Lingnau, B. 1985. *Observation of the Design and Performance of the Dempster Highway*. University of Alberta, Department of Civil Engineering, Master's thesis.

Lunardini, V.J. 1978. 'Theory of n-factors and Correlation of Data', in *3rd International Conference on Permafrost*. Edmonton, Alberta, Canada: July 10–13, 1978, vol. 1, pp. 40–46.

Mackay, J.R. 1963. 'The Mackenzie Delta Area, N.W.T.', *Geographical Branch, Mines and Technical Surveys* Memoir 8.

Mark, D.M. and Church, M. 1977. 'On the Misuse of Regression in Earth Science', *Mathematical Geology* 9(1), pp. 63–75.

Natural Resources Canada 2023. *Geospatial Data Extraction*. Available at: https://maps.canada.ca/czs/index-en.html (Accessed: 8 August 2023).

Norris, D.K. 1984. 'Geology of the Northern Yukon and Northwestern District of Mackenzie', *Geological Survey of Canada* Map 1581A, scale 1:500000.

O'Neill, H.B., Burn, C.R., Kokelj, S.V. and Lantz, T.C. 2015. ''Warm' Tundra: Atmospheric and Near-surface Ground Temperature Inversions Across an Alpine Treeline in Continuous Permafrost, Western Arctic, Canada', *Permafrost and Periglacial Processes* 26(2), pp. 103–118. doi:10.1002/ppp.1838.

Palmer, M.J., Burn, C.R., and Kokelj, S.V. 2012. 'Factors Influencing Permafrost Temperatures Across Tree Line in the Uplands East of the Mackenzie Delta, 2004–2010', *Canadian Journal of Earth Sciences* 49, pp. 877–894. doi:10.1139/e2012-002.

Piamsalee, A. 2019. *Field and Numerical Studies of an Arctic Highway Embankment Compacted with Frozen Fill over Permafrost*. University of Manitoba, Master's thesis.

Rampton, V.N. 1988. 'Quaternary Geology of the Tuktoyaktuk Coastlands, Northwest Territories', *Geological Survey of Canada* Memoir 423.

Riseborough, D.W. 1990. 'Soil Latent Heat as a Filter of the Climate Signal in Permafrost', in *5th Canadian Permafrost Conference*. Québec City, Québec, Canada: Nordicana, pp. 199–205.

Ritchie, J.C. 1977. 'The Modern and Late Quaternary Vegetation of the Campbell-Dolomite Uplands, near Inuvik, N.W.T., Canada', *Ecological Monographs* 47(4), pp. 401–423.

Romanovsky, V.E. and Osterkamp, T.E. 2000. 'Effects of Unfrozen Water on Heat and Mass Transport Processes in the Active Layer and Permafrost', *Permafrost and Periglacial Processes*, 11(3), pp. 219–239. doi:10.1002/1099-1530(200007/09)11:3<219::AID-PPP352>3.0.CO;2-7.

Rudy, A.C.A., Kokelj, S.V., Morse, P.D., and Ensom, T. 2020a. 'Permafrost Ground Temperature Report: Inuvik to Tuktoyaktuk Highway Sentinel sites, Northwest Territories', *Northwest Territories Geological Survey* NWT Open Report 2019-007, 8 p.

Rudy, A.C.A., Kokelj, S.V., and Ensom, T. 2020b. 'Permafrost Ground Temperature Report: Inuvik to Tuktoyaktuk Highway embankment sites, Northwest Territories', *Northwest Territories Geological Survey* NWT Open Report 2019-016, 8 p.

Sanger, F.J. 1966. 'Degree-days and Heat Conduction in Soils', in *1st International Conference on Permafrost*. Lafayette, Indiana, United States: pp. 253–262.

Thompson, H.A. 1963. 'Freezing and Thawing Indices in Northern Canada', in *1st Canadian Conference on Permafrost*. Ottawa, Ontario, Canada: pp. 18–36.

Wahl, H.E., Fraser, D.B., Harvey, R.C., and Maxwell, J.B. 1987. 'Climate of Yukon', *Environment Canada, Atmospheric Environment Service*, Climatological Studies No. 40.

The Verkhoyansk Range Permafrost Monitoring Network, eastern Siberia

Robert Sysolyatin, Sergei Serikov & Mikhail Zheleznyak
Melnikov Permafrost Institute, Yakutsk, Russia

ABSTRACT

Ground temperature regimes have important influences on hydrological, geomorphological, and biological processes in the East Siberian Mountains, but the area has been less studied than other regions with mountain permafrost. To help fill this knowledge gap, permafrost studies have been started in 2010 along a 62-63°N longitudinal transect that crosses the Verkhoyansk Range at elevations between 283 and 1821 m. Based on the long-term monitoring, it was established that, mean annual ground temperature at the depth of 1 m ranges between -1.1 and -10.1 °C, while maximum active layer thickness varied from 0.3 m to 2.6 m depending on the landscape. Three 30-m and one 20-m permafrost temperature-monitoring boreholes were established near weather stations in August 2022 to determine the depth of zero annual amplitude, cryostratigraphy, thermal properties and environmental factors influencing the ground temperature regime. A borehole situated in the famous Oymyakon village, the coldest place in Siberia, and another borehole in Central Yakutia are used for inter-sites comparison. In addition, a 6.7 m deep borehole drilled in August 2021 in a floodplain recorded a talik thermal regime. This showed that substrates near large rivers freeze seasonally to ~5.5 m and may warm to +6 °C by flow of water through the permeable layer. Notwithstanding severe climate conditions in eastern Siberia, the permafrost state influenced by numerous mountain environment gradients has distinctive patterns. However, without scaling comprehensive and integrated research, this area will remain on the permafrost study's periphery.

1 INTRODUCTION

East Siberia has a severe climate, one of the coldest globally. Permafrost ecosystems in the region are particularly sensitive to climate change and their evolution has already had significant impacts on river discharge (Makarieva et al. 2019), livelihoods (Lytkin et al. 2021), the sustainability of infrastructure, geomorphological processes and slope stability.

This study focuses on the Verkhoyansk Range and adjacent territory, where there is a relative paucity of permafrost studies (Figure 1). The key features of this region are extremely low air temperatures (down to -60 °C in winter), complex terrain and high geothermal heat flux (up to 0.1 W m^{-2}). Mean annual air temperatures at numerous meteorological stations have risen at rates of 0.3–0.4 °C/decade (Gorokhov and Fedorov 2018), but the temperature regime of permafrost has remained unknown until recently.

Permafrost conditions were determined in the 1960s and 1970s at a few sites, mostly using deep boreholes (Figure 1). Those investigations showed that permafrost is continuous with thicknesses from 100 to 600 m and that temperatures at the depth of zero annual amplitude (D_{zaa}) range from -9 to -2 °C (e.g., Nekrasov 1976).

The contemporary stage of permafrost study in this region was resumed by the high-mountain monitoring network, which has been established in 2010 (Sysolyatin et al. 2020) and the further extension of the ESPT boreholes network project (Sysolyatin et al. 2023), focused on permafrost temperature monitoring near the governmental meteorological stations. To date, the sites located between 132°E and 145°E are unified. Overall, the thermal state of permafrost is stable, but at some areas thermal state is close to 0 °C, and at floodplain only seasonal freezing occurs. Recent results allow to improve the permafrost features of a huge territory of Asian northeast.

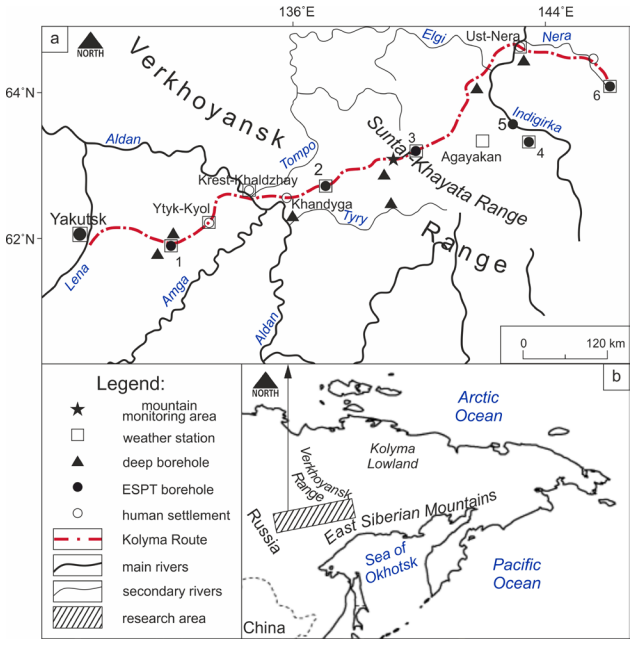

Figure 1. (a) Location of study sites within the Verkhoyansk Range and adjacent areas. ESPT boreholes: 1. Churapcha; 2. Tyoply Klyuch; 3. Vostochnaya; 4. Tomtor; 5. Oymyakon; and 6. Delyankir. (b) Location of study area in eastern Asia.

2 STUDY AREA

The Verkhoyansk Range stretches roughly 1000 km from the Lena Delta at the Laptev Sea coast in the north to the Yudoma-Maya Highlands in the south. The landscape of this region comprises smooth mountains with vast intermontane basins separated by numerous rugged ridges. The Kolyma Route, connecting Yakutsk and

https://doi.org/10.52381/ICOP2024.147.1

Magadan, crosses the middle of the range and was used to establish several weather stations during WWII. This route is favourable for permafrost temperature monitoring since it provides access to a variety of environmental gradients. Elevations along the route range from 94 to 1303 m a.s.l and adjacent peaks rise to 2300–2500 m a.s.l. Substrates are typically ice-rich Quaternary sediments of glacial origin up to 30 m thick, underlain by bedrock of Upper Paleozoic and Mesozoic age.

3 METHODOLOGY

Air, surface and shallow (up to 5 m deep) ground temperatures of the high-mountain environment have been monitored since 2010 at 15 sites at elevations of 850 to 1,821 m a.s.l in the Suntar-Khayata Range using Onset HOBO loggers (U22-001, U23-001, U12-008 with TMC50-HD sensors). Due to a variety of reasons (mainly by the wild animals invade) only a limited number of sites are suitable for presenting (Table 4).

The East Siberia permafrost transect (ESPT) project dates are from 2022. The aim is to establish the ground temperature regime at the main weather stations and to identify the factors controlling the permafrost thermal state in the Verkhoyansk Range. Five boreholes with depths of up to 30 m were drilled (with core sampling) in August 2022. Temperatures were measured using Russian-manufactured “Impedans” logger systems with calibrated ADT7410 sensors. Calibration took place under simulated winter conditions (-25 °C) in a TERMOTEST-100 chamber where temperatures can be controlled with an accuracy of 0.01 °C. The HOBO and Impedans logger systems had +0.1 and -0.15 offsets, respectively (Table 1).

Table 1. Temperature test of logger systems with ambient temperature at -25 °C.

Temperature calibration chamber, °C	HOBO, °C (TMC50-HD)	Impedans, °C
10	10.05	9.85
5	5.06	4.85
3	3.06	2.88
1	1.08	0.86
0	0.08	-0.12
-1	-0.91	-1.13
-3	-2.89	-3.13
-5	-4.90	-5.11
-10	-9.88	-10.12

4 RESULTS

4.1. Verkhoyansk Range

4.1.1. ESPT preliminary data

Conditions in the Verkhoyansk Ranges are represented by the Vostochnaya, Tomtor, Oymyakon and Delyankir permafrost monitoring sites. With the exception of the Oymyakon site, these are all located close to a weather station (Table 2). Data are available for mid-September 2022 to mid-August 2023 except for Oymyakon where loggers failed in June 2023. The results are presented as temperature profiles in Figures 2 and 3, and the main parameters are in Table 3.

Vostochnaya is the highest monitoring site and it experiences the most moderate air and ground temperature regime. The absence of vegetation leads to relatively thick active layer, even though snow cover was present at this site for more than 70% of the study period. At the end of summer, the thick of active layer exceeds even Central Yakutia’s site — Churapcha (Figure 3).

The Tomtor and Oymyakon study sites are located at similar elevations within Oymyakon valley, but the former has a surface cover of grasses and the latter is forested. These locations experience extremely low air temperatures in winter and have relatively thin snow covers. The open Tomtor site has a thinner active layer and colder permafrost than the Oymyakon site (Figure 2).

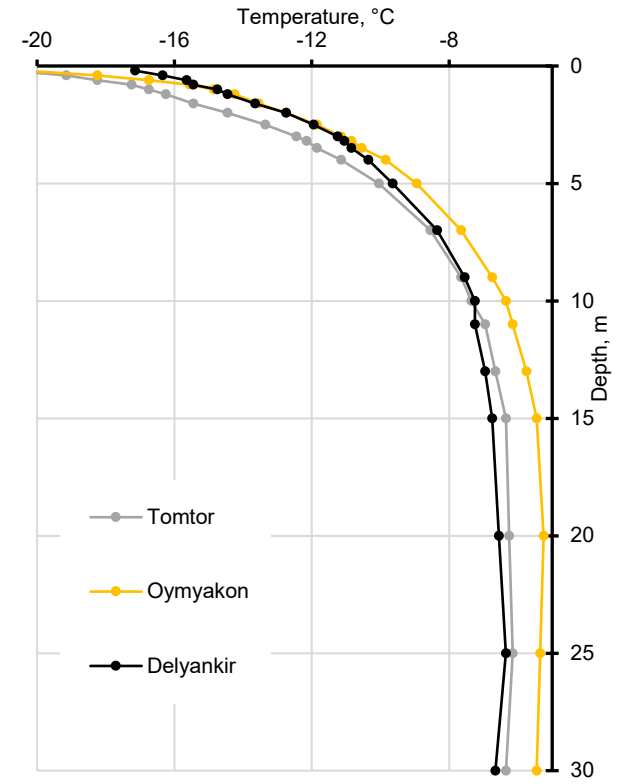

Figure 2. ESPT borehole minimum temperature in the 2022/2023 winter period.

Delyankir is the coldest ESPT monitoring borehole in the Verkhoyansk Range. The lowest air temperature, a moss vegetation cover and the shortest snow cover period result in the thinnest active layer (0.8 m) and the coldest permafrost temperature at D_{zaa} (-6.7 °C). Although Delyankir has the greatest air temperature amplitude, the D_{zaa} at this site is shallower than at the other sites.

Overall, the temperature profiles at end of thaw period below 15 m are similar despite differing environmental conditions (Figure 3). The minimum surface temperature ranges from -20.8 to -17.2 °C, while the D_{zaa} temperatures are around -6 °C. The refreezing time continues until the end of November (Table 3).

Table 2. Meteorological station site characteristics from 2005 to 2022.

Site	Elevation, m (a.s.l.)	Location (lat/long)	MAAT, °C	Air temp. amplitude, °C	Mean air temperature for January, °C	Vegetation
Churapcha	186	N 61° 58' E 132° 25'	-8.8	89.8	-40.0	Grass
Tyoply Kluch	289	N 62° 48' E 136° 54'	-9.9	93.4	-40.7	Larch forest and mosses
Vostochnaya	1288	N 63° 14' E 139° 38'	-12.1	82.5	-34.5	Sporadic mosses and grass
Tomtor	740	N 63° 15' E 143° 11'	-14.1	94.1	-45.4	Grass
Oymyakon	682	N 63° 28' E 142° 46'	~ -14.1	~ 94.1	~ -45.4	Sparce larch wood and grass
Delyankir	801	N 63° 51' E 145° 36'	-14.5	94.1	-43.1	Larch wood with thick mosses

Table 3. Main parameters at the studied meteorological stations in 2022/2023 study period.

Site	Winter air daily min, °C (date)	Sum of negative daily temperature, °C	Max snow depth, cm	Days with snow cover	Min surface temp (0.2m), °C (date)	Min temp at top of permafrost*, °C (sensor depth)	Date of complete refreezing**
Tyoply Kluch	-52.9 (17.01.2023)	-5588	82	215	-12.3 (26.02.2023)	-1.7 (7 m)	11.02.2023
Vostochnaya	-45.6 (10.12.2022)	-5778	53	256	-19.0 (15.02.2023)	-	~ 25.11.2022
Tomtor	-58.9 (12.12.2022)	-6852	34	192	-20.8 (26.02.2023)	-16.3 (1.2 m)	01.11.2022
Oymyakon	~ -58.9	~ -6852	~ 34	~ 192	-20.4 (26.02.2023)	-13.6 (1.6 m)	21.10.2022
Delyankir	-58.8 (12.12.2022)	-6882	40	176	-17.2 (26.02.2023)	-15.5 (0.8 m)	08.10.2022

* is almost comparable to the thickness of the active layer
** the date when all sensors on the temperature's string are fixed the negative values

4.1.2. High-mountain monitoring sites.

Despite the differences in the sites, the air temperatures within the high-mountain monitoring area were 3–4 °C warmer than at the Vostochnaya meteorological station. Likewise, a lapse rate is present as a result of inversion — from 800–900 to 1300–1400 m, it is positive, and as altitude increases, it slightly decreases. Nevertheless, the relation between altitude and ground temperature is less distinct. Selected sites set and ground temperature are summarized in Table 4. The stone stream temperature regime is close to the air temperature due to less snow and the chimney effect. Meanwhile, the features related to the incoming solar radiation result in relatively high temperatures at the mountain peaks, taking into consideration the cooling effect of air temperature inversion and triangle shape of peak. Snow is highly variable inter-annually at the elevation and led to the sharp shifting of 1 m depth ground temperature (e.g., the lateral moraine site). The floodplain site is influenced by groundwater heat transfer resulting in the warmest ground temperatures.

Table 4. Shallow depth monitoring sites, the Suntar-Khayta Range.

Elevation, m (a.s.l.)	Landform	MAGTs at 1 m depth, °C (min/max)	Available data*
1750	Mountain peak	-5.2/-5.2	2016-17
1586	Flat field (peneplain)	-5.9/-5.1	2016-17
1209	Saddle (mountain pass)	-6.9/-6.0	2016-17
1011	Stone stream (kurum)	-10.4/-8.4	2014-20
916	Lateral moraine	-5.0/-2.6	2013-19
896	Floodplain valley	-2.6/-0.8	2013-20

*entire calendar year

The ground temperature at a depth of 1 m in particular sites can vary with an amplitude around 40 °C. The average annual temperature ranged from -0.8 to -10.4 °C. The thickness of the active layer varied from 0.5–0.7 m to 1.8–2 m. The minimum values occurred in wet areas with a moss cover. The thickness of the active layer within the moraine deposits varied from 1.5–1.7 m, whereas on mountain peaks due to a shorter period of positive temperatures it almost exactly does not exceed about 1.2–1.4 m.

The minimum average surface temperature (exclude kurums) from July 2017 to July 2018 was -8.8 °C at a site with an elevation of 936 m. The temperature on the surface of the southern slope in the cold season can drop to -42.2 °C. Sites in the valley and on the northern slope, at an elevation of 1209 m, have an average surface temperature of -7.1 °C. The highest average surface temperature (-6.1 °C) for the selected period was for the site at an altitude of 1750 m.

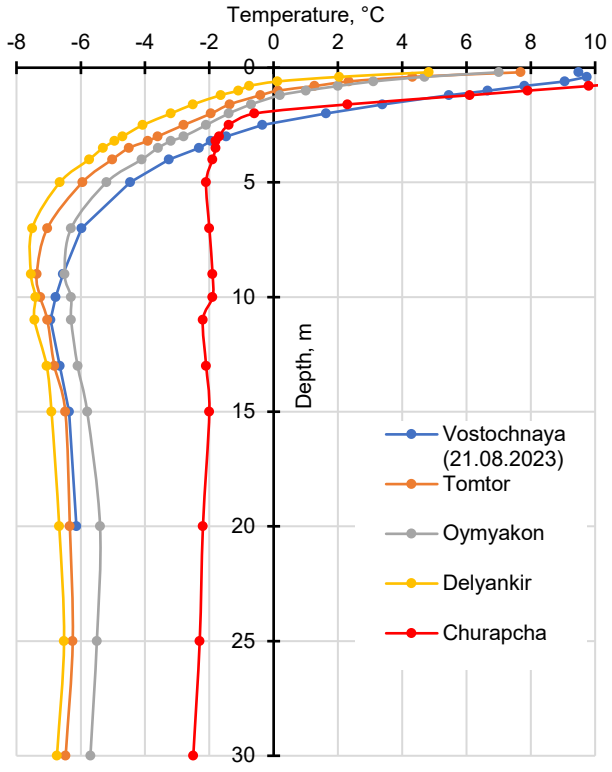

Figure 3. Ground temperature profiles in the ESPT boreholes on 15.08.2023. Note: Tyoply Klyuch shown separately due to logger failure.

4.2. Verkhoyansk Range foothills

Tyoply Klyuch has been selected for permafrost characteristics on the west slope of the Verkhoyansk Range. Unfortunately, logger failure has interrupted data collection on 24.05.2023, and we are connecting this event with spring snowmelt. Ground temperatures at the Tyoply Klyuch site in a larch forest were quite high despite low air temperatures, with a MAAT around -10 °C (Table 2). Permafrost temperatures below 11 m almost do not change and fluctuated around -1 °C during the study period (Figure 4). A huge impact on the temperature regime was made by seasonal groundwater flow and convection heat exchange in the upper layer. A month after drilling the borehole, when the heat disturbance becomes negligible, the active layer thickness was found to be 5–7 m. Furthermore, the significant thickness of the snow cover is also contributing to a relatively warm temperature regime. Thus, Tyoply Klyuch is the warmest site east of the Aldan River with permafrost persistence.

4.3. Central Yakutia

The ESPT project includes a monitoring borehole site near the Churapcha weather station that represents permafrost condition in Central Yakutia. This borehole was drilled in June 2023 and temperatures were measured on 15.08.2023 (Figure 3). Ground temperatures downwards from the base of the ~1.9 m active layer were about -2 °C, significantly warmer than at the Verkhoyansk Range sites. Permafrost temperatures slowly decreased below 20 m. A similar temperature curvature pattern was recorded in a ~600 m deep borehole in the same area (Kirillin et al. 2022). The effects of agricultural activity and a warming climate resulted in the lowest permafrost temperature being observed only at depths of 150–200 m.

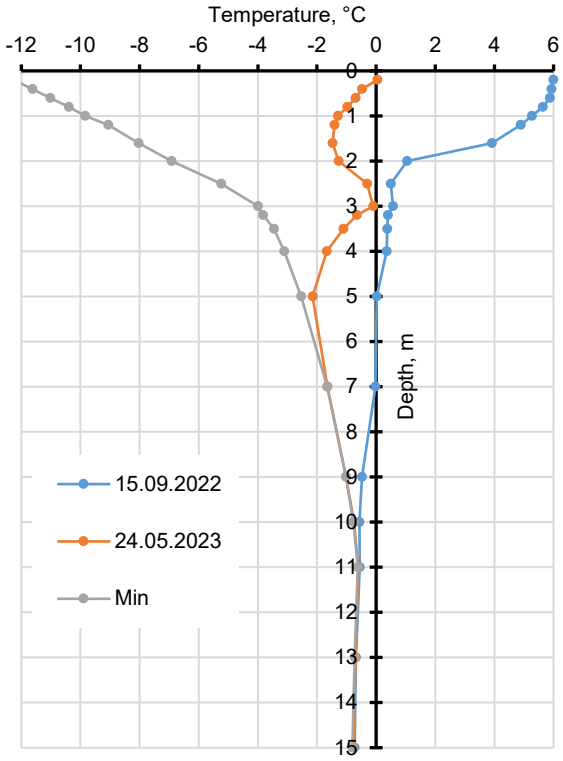

Figure 4. Tyoply Klyuch ground temperatures after the disappearance of heat disturbances from drilling and at the last moment of measurements. Minimal temperatures also provide for each depth correspond to various dates.

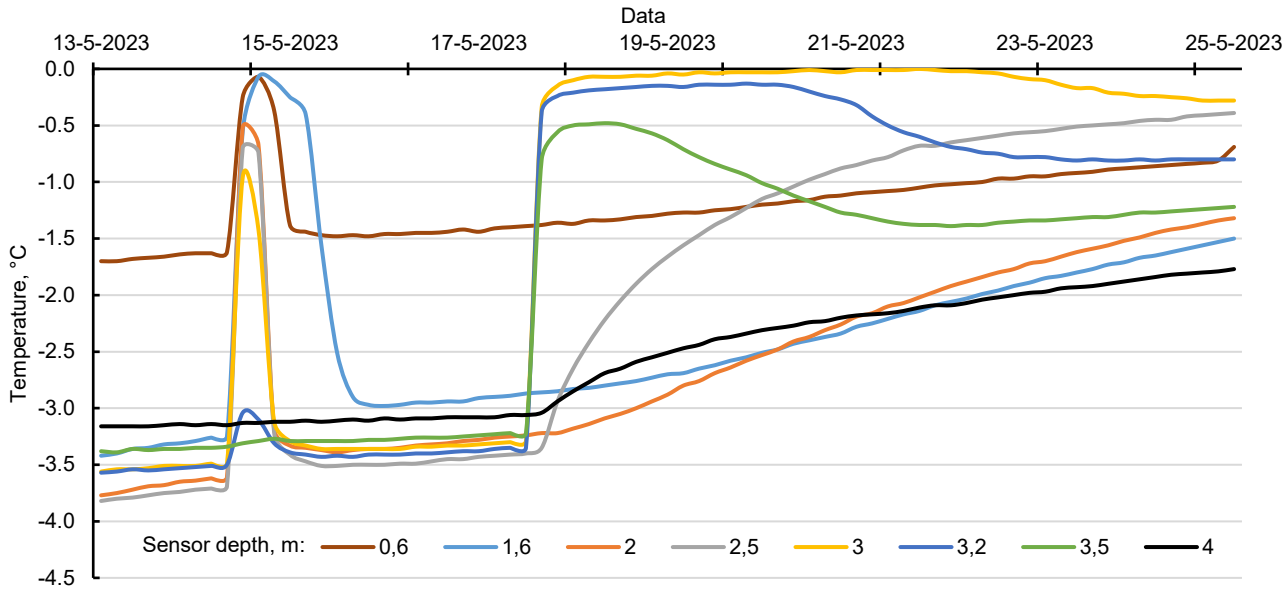

Figure 5. Groundwater infiltration event and its impact on the thermal regime on the Tyoply Klyuch site.

5 Discussion

Macroclimate, and MAAT itself to a greater extent, is a major control on the permafrost temperature regime of the Verkhoyansk Range. Generally, the latitude and longitude increasing decreases air/ground surface temperatures and reduces the summer period that creates severe climate conditions. As a fact, as the winter months' mean temperature does not rise above -35 °C, the D_{zaa} temperature around -6 °C is quite justified. However, the specific sites have active layer thickness up to 2.5 m enlarged by incoming radiation. The floodplain substrate can only be seasonally frozen, and below 5–6 m it remains unfrozen: in general, the territory covered by the thermophyte plants (e.g., poplar).

For the 2022–2023 initial monitoring period of the ESPT project, the moment of the subsurface minimum temperature within the study sites has been found. Despite the lowest air temperature being detected synchronously in the second decade of December 2022, the subsurface sensors on the remote sites have been detecting minimums at the one time but in February (Table 3). Tomtor meteorological station is the only on Oymyakon valley and characterized by lowest subsurface and top of permafrost temperatures due to extremely low snow cover depth in study period. However, low thermal diffusivity of the Delyankir site soil prevents ground thawing more than 0.8 m.

High-located sites (Vostochnaya) experienced the complex influence of air temperature inversion, incoming solar radiation, and groundwater evaporation. This led to a thick active layer, whereas ground temperatures below 10 m are similar to those at eastern ESPT sites. Similar features were reported by Throop et al. (2012) for the Sixty Mile site.

For the high-mountain environment the huge differentiation is typical. A variety of elevation, aspect, soil and rock material, vegetation etc., influence on the ground temperature regime. The landforms are more useful for assessing ground temperature regime, at least at shallower depths (Table 4). Indeed, the stone streams slopes (kurums) is colder due to the chimney effect despite of the valley location (Gorbunov et al. 2004). In turn, the floodplain is the warmest ground temperature regime caused by groundwater flow and the permeability of the sediments. The feature of seasonal thaw is crucial for slope stability and road infrastructure sustainability. For mountain areas, floodplain, and high roughness parts, there is a potential risk.

The Verkhoyansk Range foothills encompass a huge territory east of the Aldan River. At Tyoply Klyuch, the bedrock is overlain by 15–20 m of coarse-grained till sediments. At a depth of 3 m, a viable pathway for groundwater flow occurs during the snowmelt season, disturbing the thermal regime. Indeed, a slight positive temperature at D_{zaa} proves the repeating nature of this process. In Figure 5, a 3 m depth sensor immediately responds to penetrating water moving in the zero-curtain zone, while upward sensors remain at negative temperature values.

The Central Yakutia is the dramatic example of ice-rich permafrost degradation (Lytkin et al. 2021). The evolution of surface energy balance led to harmful consequences for rural dwellers. A single measurement of Churapcha borehole shown a dreary outcome of husbandry activities on the cryolithozone.

6 CONCLUSIONS

The presented monitoring network has potential for prolongate it to eastward and can be scaling next to meteorological station on crucial landforms. To date, the main results include:

1. The permafrost is stable with quite low temperatures through most of the Verkhoyansk Range, with the exception of sites affected by groundwater flow.
2. Despite the famously severe climate of the Oymyakon valley, lower permafrost temperatures were observed elsewhere at similar elevations and in similar geomorphological settings.
3. Permafrost was absent beneath alluvial gravel deposits in a floodplain and was present but with relatively high temperatures in the foothills.
4. Assessing the response of permafrost in the region to climate warming remains a major challenge. We have taken the first steps by developing a baseline monitoring network that can be used for further engineering or scientific investigations.

7 ACKNOWLEDGEMENTS

This work was carried out within the framework of state assignment of the Ministry of Science and Higher Education of the Russian Federation no. AAAA-A20-120111690010-2 “Specific features of thermal field and permafrost in the northeast of Russia”. The authors would like to thank our colleagues of the North-East Federal University and the Melnikov Permafrost Institute for their assistance and willingness to exchange knowledge during this project.

8 REFERENCES

Gorbunov, A.P., Marchenko, S.S., and Seversky, E.V. 2004. ‘The thermal environment of blocky materials in the mountains of Central Asia’, *Permafrost and Periglacial Processes* 15(1), pp. 95–98. doi:10.1002/ppp.478.

Gorokhov, A.N. and Fedorov, A.N. 2018. ‘Current Trends in Climate Change in Yakutia’, *Geography and Natural Resources* 39(2), pp. 153–161. doi:10.1134/S1875372818020087.

Kirillin, A.R., Zhelezniak, M.N., and Zhizhin, V.I. 2022. ‘New data on thickness of permafrost at the Lena-Aldan watershed’, *Earth’s Cryosphere* 26(3), pp. 3–11. doi:10.15372/KZ20220301.

Lytkin, V., Suleymanov, A., Vinokurova, L., Grigorev, S., Golomareva, V., Fedorov, S., Kuzmina, A., and Syromyatnikov, I. 2021. ‘Influence of Permafrost Landscapes Degradation on Livelihoods of Sakha Republic (Yakutia) Rural Communities’, *Land* 10(2), 101. doi:10.3390/land10020101.

Makarieva, O., Nesterova, N., Post, D.A., Sherstyukov, A., and Lebedeva, L. 2019. ‘Warming temperatures are impacting the hydrometeorological regime of Russian rivers in the zone of continuous permafrost’, *The Cryosphere* 13(6), pp. 1635–1659. doi:10.5194/tc-13-1635-2019.

Nekrasov, I.A. 1976. *Permafrost of the North-East and the South of Siberia and the Regularities of Its Development*. Yakutsk, Russia: Book Publishing House.

Sysolyatin, R., Kalinicheva, S., Fedorov, A., and Rozhina, M. 2023. ‘Eastern Siberia permafrost transect (ESPT). A first stage: The Verkhoyansk Range part’, *Journal of Mountain Science* 20(6), pp. 1499–1507. doi:10.1007/s11629-023-7965-1.

Sysolyatin, R., Serikov, S., Zheleznyak, M., Tikhonravova, Y., Skachkov, Y., Zhizhin, V., and Rojina, M. 2020. ‘Temperature monitoring from 2012 to 2019 in central part of Suntar-Khayat Ridge, Russia’, *Journal of Mountain Science* 17(10), pp. 2321–2338. doi:10.1007/s11629-020-6175-3.

Throop, J., Lewkowicz, A.G., and Smith, S.L. 2012. ‘Climate and ground temperature relations at sites across the continuous and discontinuous permafrost zones, northern Canada’, *Canadian Journal of Earth Sciences* 49(8), pp. 865–876. doi:10.1139/e11-075.

Predicting the future hydrology of western Canadian Arctic watersheds dominated by thermokarst lakes

Robin Thorne[1], Branden Walker[1], Rosy Tutton[2], Alexander Fogal[1], Jackson Seto[1], Malcolm Brocket[1], Brampton Dakin[1], Nadia Abumazan[1] & Philip Marsh[1]

[1]*Cold Regions Research Centre, Wilfrid Laurier University, Waterloo, Ontario, Canada*

[2]*Wilfrid Laurier University, Yellowknife, Northwest Territories, Canada*

ABSTRACT

Across extensive areas of the Arctic, watersheds have a myriad of lakes that cover up to 50% of the total surface area and can be linked together in complex streamflow networks. Warming of ice-rich permafrost has significant impacts on the interactions between surface water, shallow surface water, lakes, and streamflow. Most of these lakes formed from the melting of massive ground ice over the past millennia and are termed thermokarst lakes. Thermokarst lakes are susceptible to rapid, or catastrophic, drainage due to permafrost degradation, especially where ice-wedge polygons occur in low-lying areas adjacent to these lakes. These drainage events are increasing as of recent, for reasons unknown, and can create extreme floods that are a risk to people and infrastructure located downstream, and the destruction of fish habitat. To answer key questions related to this apparent crossing of a key tipping point in the viability of these lakes, this is a review of the new projects we have initiated at the Trail Valley Creek research station, north of Inuvik, NT, to investigate the controls on thermokarst lake drainage. We will use a combination of field observations, satellite data, remote sensing, and ultra high-resolution modelling focused on thermokarst lakes, ice-wedge polygons, and the impact of beaver activities, to answer key questions related to the history of lake drainage over the last 70 years and consider the future viability of these lakes. Insights gained from this study will help support climate change mitigation efforts for northern communities and ecosystems.

1 INTRODUCTION

Recent changes in the Arctic are having an impact on the interactions between surface water, supra-permafrost water, lakes and streamflow, particularly as ongoing climate warming continues to thaw ice-rich permafrost (Box et al. 2019). This recent and continuing thawing of permafrost poses a threat to ecosystems, infrastructure, and indigenous communities in the Canadian Arctic (Hjort et al. 2018; Krogh and Pomeroy 2021) and will change the water and carbon balance in the region (Burke et al. 2017; Anderson et al. 2020).

Arctic watersheds have a myriad of lakes that range from seasonally flooded wetlands to shallow or deep lakes and are important for controlling streamflow, aquatic habitat and supplying local water for northern communities (Marsh et al. 2009; Webb et al. 2022). In ice-rich permafrost, many of these lakes are formed, or enlarged, by the thawing and draining of meltwater during warm periods, which leads to land subsidence and creates topographic depressions that may be infilled by water (Marsh et al. 2009; Woo 2012). For these types of lakes, termed thermokarst lakes, the lake water surface elevation is sensitive to changes in lake water balance/lake level, increased groundwater outflow as the permafrost thaws, or by the erosion and/or melting of the shoreline by thermokarst processes, which can happen at annual or decadal periods (Kokelj et al. 2009; Marsh et al. 2009; Pohl et al. 2009).

Thermokarst lakes are susceptible to rapid, or catastrophic, drainage due to the warming of the permafrost, especially where ice-wedge polygons occur in low-lying areas adjacent to these lakes (Marsh et al. 2009; Jones et al. 2023). Thermokarst lake drainage, not coinciding with the original lake outlet, could be due to melting of ground ice currently holding in lakes. Mackay (1988, 1992) suggests at least two common scenarios for rapid lake drainage, both dependent on high lake levels (due to snowmelt or after heavy rainfall events), which leads to water flowing over or through ice-wedge networks. The first is when the lake level is high, commonly in the spring, lake water will enter through interconnecting winter ice-wedge cracks (i.e., thermal contraction cracks), allowing for tunnel flow, where the wedge ice can melt, leading to rapid drainage. A second possibility is when water from the high lake level overflows ice-wedge troughs and the sustained flow thaws the wedge ice from the top down. These drainage events can create extreme floods that are a risk to people and infrastructure located downstream, and the destruction of fish habitat (Marsh and Neumann 2001; Marsh et al. 2009).

Over the last 8,000 years, thermokarst lakes in the western Canadian Arctic have been draining at a rate of approximately one lake per year (Mackay 1988). Marsh et al. (2009) showed that between 1950 and 2000, the rate of lake drainage had decreased by one third. As the climate continues to warm and permafrost thaws, a tipping point would be reached where the rate of drainage would increase dramatically. Recent work by Kariyawasam and Marsh (2022) found that the rate of lake drainage has almost tripled between 2004 and 2019. Similar trends of lake drainage were found in the permafrost regions of Northern Alaska by Lara et al. (2021). Reasons for this recent increased rapid lake drainage are not well known, as only a few thermokarst lake drainage events have been studied (Mackay 1974; Jones et al. 2023), which raises significant concerns.

This recent increasing trend has been attributed to increases in mean annual air temperature and precipitation, lengthening of the thaw season, and increasing near-

https://doi.org/10.52381/ICOP2024.199.1

surface permafrost ground temperature that will destabilize ice-rich permafrost soils (Swanson 2019; Nitze et al. 2020; Lara et al. 2021). The presence of beaver activity in low Arctic tundra regions of Alaska and Canada has implications for surface water changes and ice-rich permafrost degradation (Jones et al. 2020) and is responsible for some rapid lake drainage events (Jones et al. 2023; Tape et al. 2018, 2022).

With recent warming and changes occurring in the Arctic, we expect these lakes will continue to change dramatically in the future, but due to our lack of knowledge of the controlling processes and the lack of data on their current state, we do not have an understanding of how these lakes are currently changing or how they will change in the future. Thermokarst lakes drainage is increasing as of recent for reasons unknown, which are a risk to people and infrastructure located downstream, and the destruction of fish habitat. To answer key questions related to this apparent crossing of a key tipping point in the viability of these thermokarst lakes, new projects, using a combination of field observations, satellite data, remote sensing, and ultra high-resolution modelling, will examine permafrost degradation and monitor changes to the surface and subsurface hydrology, and thermal regimes in ice-wedge polygons, and investigate the impact of beavers on lake levels, in order to consider the future viability of these lakes.

2 Trail Valley Creek Research Observatory

The Trail Valley Creek (TVC) research observatory, approximately 50 km north of Inuvik, NT, is located in the taiga-tundra transition zone and underlain by ice-rich continuous permafrost (Figure 1). As a long-term research facility, it provides +30 years of available climate, lake and permafrost observations supporting the studying of controlling processes and ongoing changes in the region. In and around the TVC watershed, there are two Environment Canada and Climate Change hydrometric gauges: one on TVC, where the watershed contains 16 lakes that cover <1% of the basin area; and at Hans Creek, a neighbouring watershed, which contains 293 lakes that cover 10% of the basin area. These hydrometric stations have provided streamflow measurements since 1979. The nearby Inuvik-Tuktoyaktuk highway (ITH) provides easy access in tundra region and the research site. The TVC research observatory has enhanced instrumentation such as precipitation radar, cosmic ray sensors for snow and soil moisture, and a network of eddy covariance systems in place. In addition, five lakes are currently monitored in the TVC watershed for water levels, evaporation, and discharge. This paper is a review of the new projects implemented at the TVC research observatory, that are focused on the drainage of thermokarst lakes and how these events relate to ice-wedge polygons, and the impact of beavers on lake levels.

3 Monitoring Thermokarst Lakes

With the western Canadian Arctic having many thermokarst lakes that cover a large percentage of the total land surface, there is limited monitoring of thermokarst lake size and water surface elevation, with only a few studies having mapped these lakes (Marsh et al. 2009; Cooley et al. 2019). Additionally, lake-hydrology models used in past studies for this region have a limited capacity to simulate changes in permafrost lake area, occurrence, or water surface elevation (Pohl et al. 2009, Bowling and Lettenmaier 2010).

With the focus on thermokarst lakes within the Trail Valley Creek and Hans Creek basins, we will develop, test, and apply an integrated system of ground-based observations, satellite remote sensing, and enhanced hydrological models, to monitor changes in lake area and water elevation across the sensitive permafrost terrain. An extensive lake observation network across the study region is currently in place, with observations of water surface elevation and outlet discharge, to quantify the variability in lake conditions. Processes controlling lake water balance for single lakes will be examined and applied to further develop a lake-hydrology model for simulating water balance and water surface elevation.

Five thermokarst lakes are currently being monitored in the Trail Valley Creek basin for water levels, evaporation, and discharge. Two of these five lakes, Big Bear and Little Bear lakes (BBL and LBL) are currently instrumented to monitor water temperature, surface elevation and outflow (Figure 1). This project will use the existing data for these lakes from the last 5 years, and continue the collection of current and new observations, which will include runoff from surrounding watershed into the lakes, lake level, lake evaporation using eddy covariance, and lake outflow to document all aspects of the lake water balance. This will allow us to detect changes and advance the development of predictive watershed/lake models to further understand the drivers and trajectory of changes to thermokarst lakes.

3 Ice-Wedge Polygon Site

Ice-rich permafrost regions contain ice-wedge polygon terrain that form when frozen ground cracks due to thermal contraction and fill with meltwater that freezes to form a vein of ice (Mackay 1974). Repeated cracking over hundreds or thousands of years can lead to the development of large ice-wedges spanning several meters across (French 1974). Polygonal terrain can contain high, intermediate, or low-centred polygons, where the troughs in between provide favourable locations for infiltration, water storage and flow (Woo 2012). Troughs are modified and enlarged by thermo-erosion of the wedge ice, the collapse of side walls, and by erosion due to running water. Troughs can link up to form a gully system that conveys the flow to a stream or fans out to inundate depressions downslope (Woo 2012). With Arctic warming, ice-wedge degradation increases, creating deep ponded troughs and the destruction of low-centred polygon rims, to create high-centred polygons that could develop into a well-established drainage network of troughs (Woo 2012).

With instruments recently installed at an ice-wedge polygon site, just northeast of the TVC research observatory (Figure 1), we will use a combination of field sampling, drones, and a high-resolution hydrological model to examine permafrost degradation and monitor changes to the surface and subsurface hydrology and thermal regimes. During the

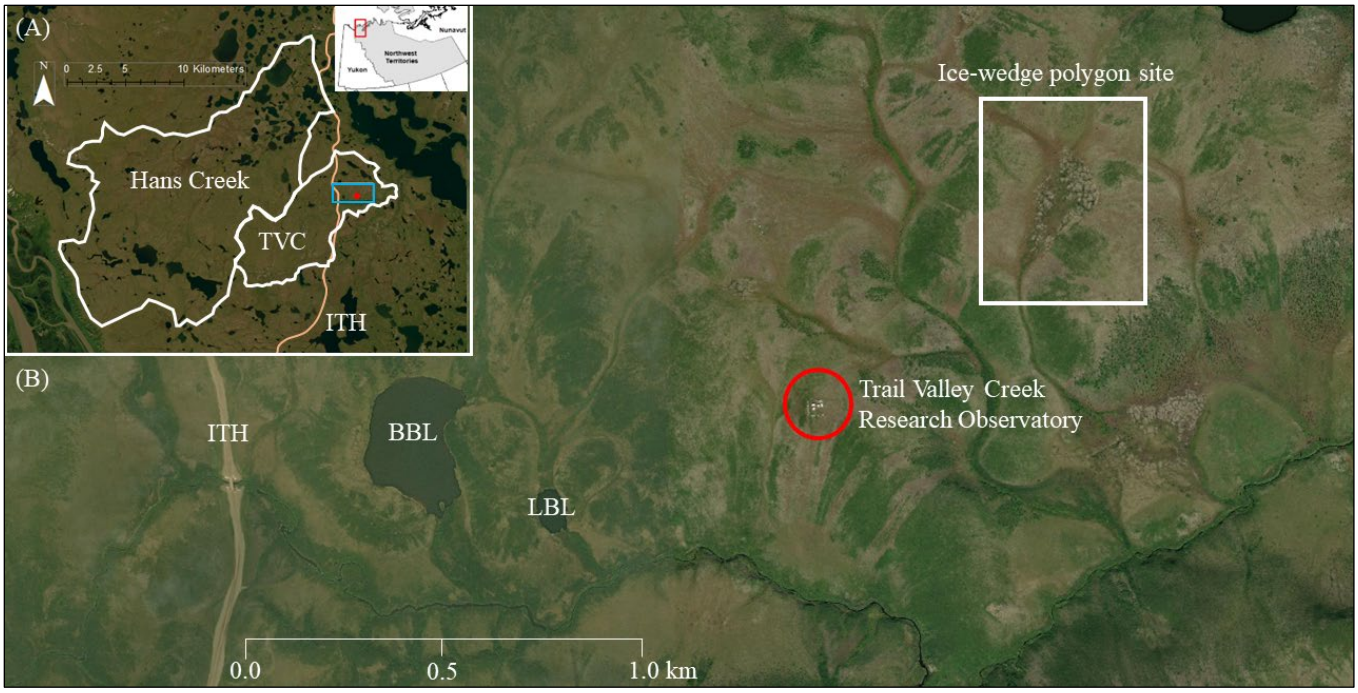

Figure 1. (A) Location of the Hans Creek and Trail Valley Creek (TVC) watersheds, and the Inuvik-Tuktoyaktuk Highway (ITH), in the Northwest Territories. Blue box is the spatial extend of the Trail Valley Creek watershed around the TVC research observatory, located by the red dot. (B) Spatial extend of the TVC watershed around the research observatory (circled in red), with the location of the ITH, Big Bear Lake (BBL), Little Bear Lake (LBL), and the ice-wedge polygon site (white box).

summer of 2022, the ice-wedge polygon site was outfitted with nine ground temperature boreholes and thirteen water level wells. Monitoring sites were installed along three transects roughly perpendicular to the calculated flow direction (Figure 2). We will conduct an analysis of the permafrost conditions along these transects with a focus on polygon centre, rim, and trough regions. The maximum ground temperature borehole depths range from 1.5 m (troughs and rims) to 3 m (centres). Groundwater wells were installed at maximum depths of 1.5 m to monitor groundwater gradients throughout the ice-wedge polygon field. Frost table depths were recorded along the transects throughout each summer.

Using this newly instrumented polygon site, we will investigate both lake and ice-wedge controls on the observed changes in thermokarst lake drainage. Specifically, we will consider two key processes: ice-wedge cracking and overtopping of ice-wedge fields. We will determine if permafrost temperatures within ice-wedge polygons increased sufficiently to minimize ice-wedge cracking over the period 1950 to present, and therefore resulted in a decrease in the rate of lake drainage due to this cracking. We will examine if there is an increase in overtopping events due to higher lake levels or deeper active layer. We will model winter ice-wedge temperatures and active layer (i.e., depth to the top of the ice-wedge) to consider the impact of climate changes on processes controlling rapid lake drainage.

Process-based models are essential tools to help understand complex hydrological processes in the Arctic. There is a need for a new generation of hydrological models that can account for spatial heterogeneity and can integrate surface and subsurface hydrology, lakes, vegetation, and permafrost. Our study will use the cryohydrogeological model GEOtop, a finite-difference numerical model, which integrates the surface/subsurface model of permafrost thermal hydrology (Endrizzi and Marsh 2010; Endrizzi et al. 2014). It has been shown to be applicable for simulating surface energy balance, hydrology, and permafrost conditions, and has been tested at a hyper-resolution scale (Endrizzi and Marsh 2010; Endrizzi et al. 2014). It uses coupled numerical solution of heat and water flow equations in soil and snow cover, which can consider frost table depth, soil moisture and runoff. We will be applying GEOtop to understand changes in permafrost temperature and therefore, ice-wedge cracking over the full study period. It will also be applied to understand increasing active layer thickness at the top of the ice-wedge polygons, therefore the increasing probability of the flow of lake water over the tops of this terrain.

Using data collected from the polygon centres, rims, and troughs, we will use GEOtop to further examine permafrost degradation and the effect of microtopography on the thermal hydrology in the system. When modelling we will consider the model initialization, dividing the subsurface into moss, peat and mineral soil layers, the trough depths (e.g., deeper troughs lead to increase snow entrapment), the lateral water fluxes (e.g., water flow from centre to trough or reversed), how the polygon rims are exposed to summer and winter climate extremes, and will compare simulated and modelled soil temperatures at different depths for each centre, rim, and trough.

Figure 2. Ice-wedge polygon site located just northeast of the Trail Valley Creek research observatory. White lines represent the three transects, which are roughly perpendicular to calculated flow direction (blue arrow), that are used as continuous monitor sites.

4 BEAVER IMPACT RESEARCH

Beaver activity in this tundra region offers an opportunity to study the interactions between beavers, permafrost, and thermokarst lake dynamics (Jones et al. 2020) and how they relate to the increased growing season length and an increase in shrub cover (Tape et al. 2006, 2018). Increased winter snowfall and increasing winter air temperature is likely increasing the over-wintering habitat potential for beavers (Arp et al. 2018). Shorter winters reduce the duration that beavers must remain in their lodges. Finally, change in native subsistence and hunting lifestyles in the region and the reduction in the desire of beaver pelts and underfur (Tape et al. 2018).

Streamflow and lake levels in low tundra regions are prone to changes due to beaver activities (Woo and Waddington 1990). Jones et al. (2020) have shown that beavers can cause lake expansion and drainage, thaw slump initiation and permafrost degradation. Stream and river channels are more stable prior to beaver activity, whereas once introduced into the basin, there is pond formation, evolution and channel modification or diversion (Tape et al. 2018). Dammed basins tend to lose more water to evaporation, with the lake outflow suppressed and an increase in basin water storage.

Beaver activities have been found to contribute to rapid lake drainage (Tape et al. 2018, 2022). Jones et al. (2020) found that beavers were the primary driver of surface water area increases in Northern Alaska, but their engineering activities had caused the drainage of some thermokarst lakes. Jones et al. (2023) found the presence of a beaver in a lake just days before the drainage of a thermokarst lake on the Baldwin Peninsula. Shrubs that were chewed on the shore indicates that the beaver may have played a role in the lake drainage event. Marsh et al. (2009) surveyed select areas in 2004 to determine if these areas were due to drained lakes. When the area was resurveyed in 2007, two small partially drained lakes were noted near Noell Lake. These lakes had beaver dams at the outlet and were breached, resulting in partial lake drainage. Kariyawasam and Marsh (2022) monitored a thermokarst lake site in August 2019 and discovered a rise and sudden collapse in lake level due to a beaver dam. Jones et al. (2023) hypothesize that beaver activity by burrowing into the banks of a thermokarst lake could promote underground tunnel flow and the erosion of ice-wedges, contributing further to the increase rate of Arctic lake drainage, thus becoming a new thermokarst lake drainage mechanism to be considered.

With a combination of digital imagery and field sampling, we will identify and locate beaver dams and beaver activity around the TVC region, using the protocol for mapping beaver lodges, and dams based on beaver dam classifications by Woo and Waddington (1990). Water level recorders were installed at selected lakes across the region to record surface water elevation, while Water Survey of Canada discharge measurements and manual discharge measurements are obtained for select sites. A variety of remote sensing methods to map changes in snow, vegetation, beaver locations, and lake properties will be used. This study will quantify beaver impacts on water storage and discharge through observations of stream and lake properties with and without active beaver populations and dams. We will assess how water storage from beaver dams will impact streamflow and address the role of beavers in limiting discharge during drought and their impacts on incised streams. We will consider impacts on lake or pond area, lake water storage volume, lake/stream flows and water temperature.

5 SUMMARY

Vast number of lakes across the western Canadian Arctic are in areas of ice-rich permafrost. As climate is rapidly changing, important controls on thermokarst lakes are also changing, making them prone to rapid drainage and being transformed into drained lake basins. Observed and expected changes include permafrost thaw, influence of beaver activities, changes to evaporation rates, lake levels, lake ice depth and duration of ice cover, changes in precipitation, snow accumulation and melt timing. These anticipated changes will have significant impacts on ecosystems and northern communities.

The Trail Valley Creek research observatory, underlain by ice-rich continuous permafrost, has various ice-wedge polygon sites located near and across the tundra-taiga ecotone. As a long-term research facility, it provides over 30 years of available climate, lake, and permafrost observations supporting the studying of controlling processes and ongoing changes in the region. These new projects at TVC will be a synthesis of monitoring snow, ground temperature, and permafrost conditions, with modelling efforts focused on the drainage of thermokarst lakes and how these events relate to ice-wedge polygons, and the impact of beavers on lake levels. We will apply high-resolution mathematical models of permafrost-lake-hydrology systems to investigate the crossing of an apparent tipping point in thermokarst lake drainage and consider the future viability of these thermokarst lakes.

6 ACKNOWLEDGEMENTS

Funding for these projects was supported by ArcticNet. The authors acknowledge that this study was conducted in the Inuvialuit Settlement Region in the western Canadian Arctic. The authors wish to acknowledge the advice and comments provided by the reviewers of this paper.

7 REFERENCES

Andresen, C.G., Lawrence, D.M., Wilson, C.J., McGuire, A.D., Koven, C., Schaefer, K., Jafarov, E., Peng, S., Chen, X., Gouttevin, I., Burke, E., Chadburn, S., Ji, D., Chen, G., Hayes, D., and Zhang, W. 2020. 'Soil moisture and hydrology projections of the permafrost region – a model intercomparison', *The Cryosphere* 14, pp. 445–459. doi:10.5194/tc-14-445-2020.

Arp, C.D., Jones, B.M., Engram, M., Alexeev, V.A., Cai, L., Parsekian, A., Hinkel, K., Bondurant, A.C. and Creighton, A. 2018. 'Contrasting lake ice responses to winter climate indicate future variability and trends on the Alaskan Arctic Coastal Plain', *Environmental Research Letters* 13(12), 125001. doi:10.1088/1748-9326/aae994.

Bowling, L.C. and Lettenmaier, D.P. 2010. 'Modeling the effects of lakes and wetlands on the water balance of arctic environments', *Journal of Hydrometeorology* 11(2), pp. 276–295. doi:10.1175/2009JHM1084.1.

Box, J.E., Colgan, W.T., Christensen, T.R., Schmidt, N.M., Lund, M., Parmentier, F.W., Brown, R., Bhatt, U.S., Euskirchen, E.S., Romanovsky, V.E., Walsh, J.E., Overland, J.E., Wang, M., Corell, R.W., Meier, W.N., Wouters, B., Mernild, S., Mård, J., Pawlak, J. and Olsen, M.S. 2019. 'Key indicators of Arctic climate change: 1971–2017', *Environmental Research Letters* 14(4). doi:10.1088/1748-9326/aafc1b.

Burke, E.J., Ekici, A., Huang, Y., Chadburn, S.E., Huntingford, C., Ciais, P., Friedlingstein, P., Peng, S. and Krinner, G. 2017. 'Quantifying uncertainties of permafrost carbon-climate feedbacks', *Biogeosciences* 14(12), pp. 3051–3066. doi:10.5194/bg-14-3051-2017.

Cooley, S.W., Smith, L.C., Ryan, J.C., Pitcher, L.H. and Pavelsky, T.M. 2019. 'Arctic-Boreal lake dynamics revealed using CubeSat imagery', *Geophysical Research Letters*, 46, pp. 2111–2120. doi:10.1029/2018GL081584.

Endrizzi, S. and Marsh, P. 2010. 'Observations and modeling of turbulent fluxes during melt at the shrub-tundra transition zone 1: Point scale variations', *Hydrology Research* 41, pp. 471–491. doi:10.2166/nh.2010.149.

Endrizzi, S., Gruber, S., Dall'Amico, M. and Rigon, R. 2014. 'GEOtop 2.0: simulating the combined energy and water balance at and below the land surface accounting for soil freezing, snow cover and terrain effects', *Geoscientific Model Development* 7, pp. 2831–2857. doi:10.5194/gmd-7-2831-2014.

Hjort, J., Karjalainen, O., Aalto, J., Westermann, S., Romanovsky, V.E., Nelson, F.E., Etzelmüller, B., and Luoto, M. 2018. 'Degrading permafrost puts Arctic infrastructure at risk by mid-century', *Nature Communications* 9, article number 5147. doi:10.1038/s41467-018-07557-4.

Jones, M.C., Grosse, G., Treat, C., Turetsky, M., Anthony, K.W. and Brosius, L. 2023. 'Past permafrost dynamics can inform future permafrost carbon-climate feedbacks', *Communications Earth & Environment* 4, 272. doi:10.1038/s43247-023-00886-3.

Jones. B.M., Tape, K.D., Clark, J.A., Nitze, I., Grosse, G. and Disbrow, J. 2020. 'Increase in beaver dams controls surface and thermokarst dynamics in an Arctic tundra region, Baldwin Peninsula, northwestern Alaska', *Environmental Research Letters* 15. doi:10.1088/1748-9326/ab80f1.

Kariyawasam, D. and Marsh, P. 2022. *Changes in lake drainage in the western Canadian Arctic*. Waterloo, Ontario, Canada: Wilfrid Laurier University, Theses and Dissertations (Comprehensive), MSc Thesis. Available at: https://scholars.wlu.ca/etd/2458.

Kokelj, S.V., Lantz, T.C., Kanigan, J., Smith, S.L. and Coutts, R. 2009. 'Origin and polycyclic behaviour of tundra thaw slumps, Mackenzie Delta region, Northwest Territories, Canada', *Permafrost and Periglacial Processes* 20(2), pp. 173–184. doi:10.1002/ppp.642.

Krogh, S.A. and Pomeroy, J.W. 2021. 'Simulating site-scale permafrost hydrology: sensitivity to modelling decisions and air temperature', *Journal of Hydrology* 602. doi:10.1016/j.jhydrol.2021.126771.

Lara, M.J., Chen, Y. and Jones, B.M. 2021. 'Recent warming reverses forty-year decline in catastrophic lake drainage and hastens gradual lake drainage across northern Alaska', *Environmental Research Letters* 16. doi:10.1088/1748-9326/ac3602.

Mackay, J.R. 1974. 'Ice-wedge cracks, Garry Island, Northwest Territories', *Canadian Journal of Earth Sciences* 11, pp. 1366–1383. doi:10.1139/e74-133.

Mackay J.R. 1988. 'Catastrophic lake drainage, Tuktoyaktuk Peninsula area, District of Mackenzie', in *Current Research, Part D*, Geological Survey of Canada, Paper 88-1D, pp. 83–90. doi:10.4095/122663.

Mackay J.R. 1992. 'Lake stability in an ice-rich permafrost environment: examples from the western Arctic coast', in R.D. Robarts and M.L. Bothwell (eds), *Aquatic Ecosystems in Semi-Arid Regions: Implications for Resource Management*. Saskatoon, Saskatchewan, Canada: National Hydrology Research Institute Symposium Volume 7, August 27–30, pp. 1–26.

Marsh, P., Russell, M., Pohl, S., Haywood, H. and Onclin, C. 2009. 'Changes in thaw lake drainage in the Western Canadian Arctic from 1950 to 2000', *Hydrological Processes* 23, pp. 145–158. doi:10.1002/hyp.7179.

Nitzbon, J., Westermann, S., Langer, M., Martin, L.C.P., Strauss, J., Laboor, S., and Boike, J. 2020. 'Fast response of cold ice-rich permafrost in northeast Siberia to a warming climate', *Nature communications* 11(1), article number 2201. doi:10.1038/s41467-020-15725-8.

Pohl, S., Marsh, P., Onclin, C. and Russell, M. 2009. 'The summer hydrology of a small upland tundra thaw lake: implications to lake drainage', *Hydrological Processes* 23, pp. 2536–2546. doi:10.1002/hyp.7238.

Swanson, D.K. 2019. 'Thermokarst and precipitation drive changes in the area of lakes and ponds in the national parks of northwestern Alaska, 1984–2018', *Arctic, Antarctic, and Alpine Research* 51, pp. 265–279. doi:10.1080/15230430.2019.1629222.

Tape, K., Sturm, M. and Racine, C. 2016. 'The evidence for shrub expansion in Northern Alaska and the Pan-Arctic', *Global Change Biology* 12, pp. 686–702. doi:10.1111/j.1365-2486.2006.01128.x.

Tape, K.D., Jones, B.M., Arp, C.D., Nitze, I. and Grosse, G. 2018. 'Tundra be dammed: beaver colonization of the Arctic', Global Change Biology, 24(10), pp. 4478–4488. doi:10.1111/gcb.14332.

Tape, K.D., Clark, J.A., Jones, B.M., Kantner, S., Gaglioti, B.V., Grosse, G. and Nitze, I. 2022. 'Expanding beaver pond distribution in Arctic Alaska, 1949 to 2019', *Nature* 12, article number 7123. doi:10.1038/s41598-022-09330-6.

Webb, E.E., Liljedahl, A.K., Corderio, J.A., Loranty, M.M., Witharana, C. and Lichstein, J.W. 2022. 'Permafrost thaw drives surface water decline across lake-rich regions of the Arctic', *Nature Climate Change* 12, pp. 841–846. doi:10.1038/s41558-022-01455-w.

Woo, M.K. 2012. *Permafrost Hydrology*. New York, New York, United States: Springer, Berlin Heidelberg. doi:10.1007/978-3-642-23462-0.

Woo, M.K. and Waddington, J.M. 1990. 'Effects of beaver dams on subarctic wetland hydrology', *Arctic* 43(3), pp. 223–230. doi:10.14430/arctic1615.

The cold desert of Atacama – Mapping previously unknown cryophenomena in the Ojos de Salado Region

Dario Trombotto Liaudat[1], Manfred Buchroithner[2], Amit Mushkin[3] & Benjamin Schröter[2]

[1]*Geocryology, IANIGLA, CCT CONICET Mendoza, Argentina*

[2]*Institute for Cartography, Technische Universität Dresden, Germany*

[3]*Geological Survey of Israel, Israel*

ABSTRACT

The volcano-surrounded endorheic basin of the Valle de Barrancas Blancas in the Chilean High Atacama belongs to the *Dry Andes*. The basin displays and preserves a unique suite of active and paleocryogenic processes. In this contribution an attempt is made to describe their physical and temporal interaction. Permafrost occurs in the Valley of Barrancas Blancas. Regarding its climatic conditions the study area represents an extremely cold desert region with particular microclimatic characteristics on the bottom of the valley which allow for an active layer of 30 to 45 cm in depth (at approximately 5000 m ASL). At some higher sites, such as the top of the Llanos de Rivera towards the south of the study area and in cryoplanated areas, however, the permafrost table was found at greater depth (e.g., at an altitude of roughly of 5400 m ASL at approximately 65 cm). The cryogenic geomorphology of the study area shows most varied micro (patterned ground) and mesoforms (rock glaciers, cryoplanation surfaces). Gelifluction strongly affects the slopes. Moreover, and for the first time in the Southern Hemisphere two new types of cryophenomena are described: a specific type of a small pingo, the Atacama pingo (*pingo atacamensis*), and the frosted dunes (*dunas heladas*). At the same time, the conducted research provides excellent clues for the comprehension extraterrestrial environments. Furthermore, it has an impact on the exploration of the urgently needed water reserves in the High Atacama.

1 INTRODUCTION

The Valle de Barrancas Blancas is an endorheic basin situated at elevations above 4850 m, west of the Ojos del Salado Massif (6893 m), east of the Nevado Tres Cruces Massif (6748 m) and south of the Cerros de Barrancas Blancas (Cordón Foerster, 6119 m), in the High Atacama Andes of Chile (68°39'W, 27°02'S; Figure 1A). The valley trends more or less in NNW–SSE direction, with its Y-branches running in ENE–WSW and SSE–NNW directions. The study area (approximately160 km^2) contains a series of well-preserved landforms resulting from a unique combination of slope (aero-gravitational), aeolian, lacustrine/littoral, fluvial, glacial and periglacial regimes. A broad spectrum of cryogenic geomorphic landforms has not yet been described in this entire region (Buchroithner et al. 2010). Following the general geomorphological interest in cryospheric landforms in the Arid Diagonal of South America, and in the Atacama Desert specifically (cf. García et al. 2017), our results reveal subrecent subsurface features, which were not documented before and may be crucial for water management within the specific area and beyond.

The geological background of the Valle de Barrancas Blancas Region is covered by the Hydro-Geological Map of the Chilean Servicio Nacional de Geología y Minería (Santibáñez et al. 2006) and also described in Baker, Gonzalez-Ferran and Rex (1987). The study area displays mountain permafrost in situ (Trombotto 2000) and also creeping permafrost. It is a periglacial macro-environment where interdependent processes, such as cryogenic processes together with erosion, eolian deposition and the action of fluvial washout mainly caused by precipitation, accumulation, retransportation/redeposition and melting of snow, play an important role (Buchroithner et al. 2010).

As defined on the basis of temperature Andean permafrost is ground (soil or rock and included ice and organic material) that remains at or below 0 °C for at least two consecutive years, which according to Trombotto Liaudat et al. (2014) shows altitudinal zonification.

Permafrost is synonymous with perennially cryotic ground. Permafrost related with temperature descending due to the altitude is called *mountain permafrost*; in the case of the Andes, it is called *Andean Permafrost*. Garleff and Stingl (1986) called this type *quasi continuous permafrost* because of the difficulty in distinguishing continuous and discontinuous permafrost in the Andes, as they are described for the lowlands of the Northern Hemisphere. It is a cold permafrost type, reinforced on south-exposed slopes and particularly restricted to the mountain topography of the Andean Cordillera and their mean annual air temperature (MAAT) and an annual precipitation of 300 mm/y involved landforms. According to Garleff and Stingl (1986) it occurs in the Argentine Puna up – 1/-2 °C MAAT.

Permafrost appears because of topographic as well as thermal conditions. The mountain summits are generally frozen if the MAAT is below -2 °C and they show tors as well as sediments from cryogenic weathering.

https://doi.org/10.52381/ICOP2024.222.1

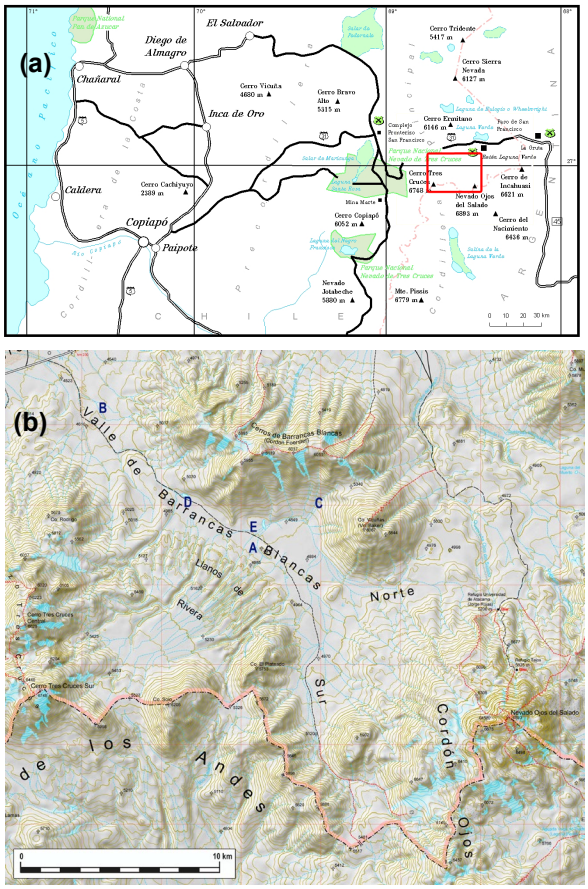

Figure 1. (a) Location of Valle de Barrancas Blancas (red rectangle), Buchroithner et al. 2004. (b) Locations mentioned in paper: A Valle de Barrancas Blancas; B patterned ground; C embryonic rock glacier; D Pingo atacamensis; E frosted dunes

Permafrost is denominated in situ if it is found below the surface without any sign of movement (Trombotto 2000). Another type of permafrost is rock glacier permafrost, which is characterized by downslope creeping movement caused by gravity and its rheological properties. Small micro landforms like gelifluction lobes are also related with the occurrence of permafrost, but with the movement of the active layer, which is the layer that covers permafrost and which thaws in summer.

The cryogenic geomorphology of the Valle de Barrancas Blancas is most varied and contains all kinds of examples known for the Andes, which were mentioned above, from microforms such as sorted and unsorted patterned ground, patterned ground with extrusion forms caused by cryoturbation (Figure 1B) to mesoforms like rock glaciers and cryoplanation surfaces (Figure 1C). Slopes are strongly affected by gelifluction. Nagy Et al. (2018; 2020) made an important contribution to ground ice and the presence of permafrost in the region. In the study area important niveo-eolian processes (van Straelen 1946, *in fide* Jahn, 1972) occur which not only participate in the erosion of pre-existing landforms in the sense of Jahn but also in the formation of subterraneous ice layers and the retransportation/redeposition of sediments as already described by Cailleux (1972) for Nouveau-Quebec and Victoria Land.

The aim of this paper is to describe landforms that have not been previously documented from the South America context and from the Southern Hemisphere as a whole.

2 METHODOLOGY

The work consisted of making a periglacial geomorphological survey. The cryogenic landforms were interpreted by taking soil temperatures at different depths with data loggers. These temperature recordings were only carried out for very short time, from 14 to 20 February 2011. Pits were dug specifically in each new landform to recognize the cryogenic sedimentology, origin of the landform and to find ground ice. Geophysical sounding (Ground Penetrating Radar) was also used to interpret the presence and depth of the ground ice. With terrestrial laser scanning at one of the Atacama pingos, work to know its evolution or growth was begun.

3 RESULTS AND DISCUSSION

3.1 Conditions of the Periglacial Environment

The mean annual air temperatures (MAAT) of the Valle de Barrancas Blancas, an endorheic basin according to the Hydro-Geological Map (Santibáñez et al. 2006), vary between -2 and -4 °C. Lower temperatures occur with increasing elevation and on south-facing slopes. The valley bottom consists of pebbles, predominantly of pumice (piedra pómez) and other volcanic and sedimentary materials. Data loggers installed close to the surface at a few sites (in the shade) indicate daily mean air temperatures of -2 to -3 °C (Figures 2 and 3).

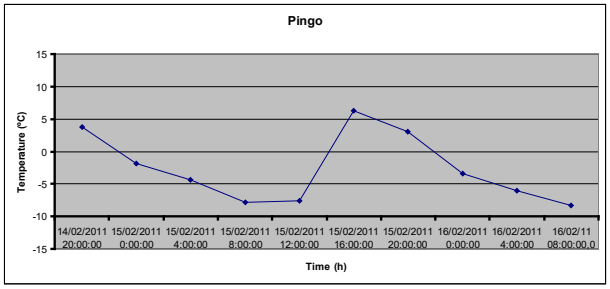

Figure 2. Representative temperature (36 hours during Austral summer) of a pingo at the valley bottom of the Valle de Barrancas Blancas at an elevation of approx. 4900 m ASL at the ground/air interphase (Figure 1b, location D). This temperature > 0 °C favours the adherence of snow to the ground and the generation of frosted dunes (Figure 1b, location E).

According to the hydrogeological map (Santibáñez et al. 2006) and according to field observations precipitation in the study area is approximately 150 mm/year. Snowfall is frequent, but the snow is quickly sublimated, redeposited and/or covered by cryosediments, i.e., mainly pumice pebbles.

The climatic conditions in the study area stand for an extremely cold desert region with particular microclimatic characteristics on the bottom of the valley, which allow for an active layer of 30 to 45 cm in thickness.

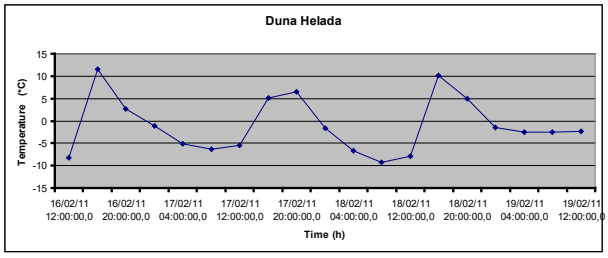

Figure 3. Temperature of a *duna helada* (Figure 1b, location E) at the valley bottom of the Valle de Barrancas Blancas at approximately 4860 m ASL at the ground/air interphase.

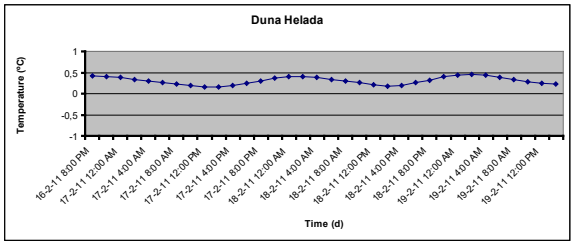

Figure 4. Temperatures at approx. 70 cm depth at a "*duna helada"*, at the valley bottom at 4860 m ASL (Figure 1b, location E)

Along some south-facing slopes the thickness of the active layer increases. In those cases, typically a dark-coloured sediment occurs and facilitates higher absorption of energy resulting in high temperatures at the interphase zone (ground/air). Wherever an excavation was made to study the subsoil (i.e., at numerous locations), the permafrost table was found close to the surface, or temperatures around 0 °C indicated its proximity.

At some higher sites, like the top of the Llanos de Rivera (6205 m; Figure 1) towards the south of the study area and in cryoplanated areas, the permafrost table was found at greater depth (e.g., at 65 cm at an altitude of approximately 5400 m ASL). It is assumed that due to its topography and location the bottom of the main valley of the Valle de Barrancas Blancas keeps pockets of very low temperatures over a long period of time.

Along the contact between the permafrost table or the detected massive, pure sediment-covered ice bodies and the sedimentary layer, thermistors showed temperatures close to 0 °C, which may be explained by the phenomenon of the 'zero curtain' documented in this region (Batbaatar et al. 2020) where the latent heat has not completely dissipated because of the summer conditions during the field campaign. This is possibly also true for the influence of snowfall and the air temperature variations (cf. Figures 4 and 5).

The bottom of the Valle de Barrancas Blancas does not only act as a reservoir of sediments with cryogenic weathering origin due to transport by melting water from higher altitudes and eolian transport. Snow fall throughout the year in this valley is one of the key agents of erosion and deposition in this landscape.

During the measurement expedition in February 2011 (La Niña year) it snowed frequently at different times of the day and sastrugis or snow-sand dunes were shaped. The sand layers of the dunes are interbedded with snow. Granule-pebble ripples like in Antarctica (Selby et al. 1974) are also present in the valley.

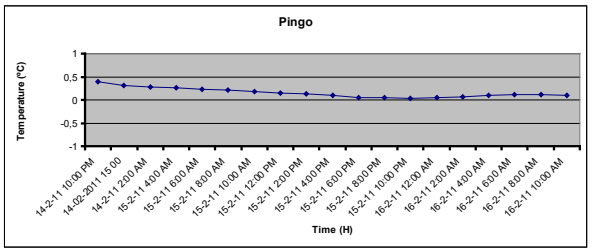

Figure 5. Temperatures at approximately 45 cm depth below the top of a pingo at the valley bottom of the Valle de Barrancas Blancas at 4900 m ASL (Figure 1b, location D).

It is worth mentioning though, that the snow is generally either quickly redeposited by wind, it sublimates, or melts and percolates through the mentioned thin active layer where possible, or otherwise helps to build puddles where proximate permafrost impedes permeability. This is often the case in many parts of the valley but particularly in its lowest parts. The pH of the puddles, ranges between 4 and 5, and the temperatures in the shallow areas, where samples were taken, were 8 to 10 °C (at midday). This process formed two lakes of remarkable size (Figure 8): one in the lower and one in the upper part of the Valle de Barrancas Blancas (Figure 1b, location B). The latter one showed a pH of > 6 and hosts a type of copepods, similar to the extremophile microfauna observed in the Lagunita del Plata in Mendoza, Argentina, at approximately 4000 m ASL (Trombotto 1991). All water bodies presented icings. In deeper ones like the larger lake in the SE part, ice is present on the rims. The bottom of the valley seems to have been the bottom of a former lake. Hence, different terraces can be distinguished and are likely associated with more humid and warmer Quaternary conditions. The prevailing pumice and its physical characteristics of low specific weight help to delimit former coastal lines as well as the perimeter of the bottom of the valley associated to a comparatively big lake that previously existed. In this context, GPS and TLS (terrestrial laser scanner) measurements are still waiting to be analyzed.

When snow is blown away by wind, the moving snow mingles with sediments which also experience eolian transport. This process allows for bodies of snow to remain in dunes in closed basins and are covered by sand and smaller pebbles (mainly of pumice). These landforms display an interstratified profile like the one Jahn (1972) presented for Sudetenland. Subsequently, part of the snow is transformed into firn and finally into ice (Schwikowski et al. 2010). This special condition facilitates the rise of the permafrost table and enhances the presence of different

types of ice, such as layers of massive pure ice, bodies altering with sediments from the transversal side valleys that end up in the valley bottom of the Valle de Barrancas Blancas, or massive ice present as cores, inside the permafrost itself on the bottom of the main valley.

On the other hand, snow increases erosion of the slopes, shapes the landscape of the volcanics, predominantly pumice and lapilli, and the formation of steep side valleys, more or less transversal to the main valley of Barrancas Blancas. These, constitute the Llanos de Rivera plains and dissect the pumice formations with a predominant SSW-NNE orientation. The erosive shaping of the valleys creates a typical landscape of subpyramidal landforms at their endings at the main valley that can mimic desert barchans.

At approx. 4000 m ASL permafrost table was found to be at varying depths in the Valle de Barrancas Blancas (Figures 6, 7 and 8).

Figure 6. Physical sounding of permafrost table (see metal avalanche probe sticking in sediment) and clearing of cryoforms from sedimentary veneer.

3.2 Cryogenic forms of the region

3.2.1 Patterned ground

In particular at the relief threshold of the “entrance pass” (Figure 1b, location B) many examples of patterned ground can be found. They are characterized by their irregular shape and a length of various meters with extrusion cryoforms or nubbins as a result of the expulsion of the sediments towards the surface caused by cryoturbation and the presence of a near-surface permafrost. The diameter of these nubbins is 20 cm and more. When they are found on soft slopes of more than 2°, the soil displays the typical shape of a comet as described by Büdel (1978). Other types of patterned ground also frequently found in this region are irregular unsorted polygons delimited by thermal contraction cracks. The latter may create extended lines of several meters with collapse structures of cryosediments as explained by Trombotto (1991). In rather peneplanated areas, desert (stone) pavements are frequently observed (Figure 8; Dietze et al. 2011).

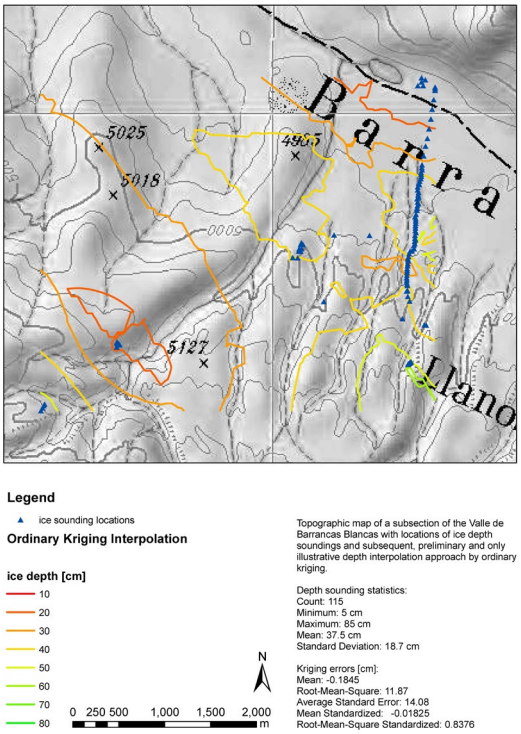

Figure 7. Location of February 2010 sounding profiles of the permafrost table in the Valle de Barrancas Blancas with areal extrapolation of its depth (extrapolation and visualization courtesy Michael Dietze (University of Göttingen).

Figure 8. View from the western slopes of Cerro Vicuñas (6007 m) towards the west onto the Tres Cruces Massif (left: Cerro Tres Cruces Sur, 6748 m). The larger of the two cryo-lakes mentioned in the text above appear in the middle ground.

3.2.2 Rock glaciers

The rock glaciers found in the area are of the cryogenic type; they originate through the contribution of cryosediments and snow from the slopes through niveo-detritic runnels or hollows, in particular at the range of the Nevados de Barrancas Blancas (Figure 1b, location C).

There are cases, however, where the niveo-detritic hollows are not well delimited, and the cryoforms seem to be related with subterranean creeping of 'ice slopes'

Trombotto et al. (1999) proposed that melted active layers of mountain permafrost, frozen in winter, snowfall and graupel mainly feed the discharge of mountain rivers. It is possible that with continuing global warming, water melting may also occur in supra-permafrost. On the other hand, important recent geophysical studies in the Central Andes have corroborated the coexistence and movement of supercooled water in the structure of the rock glacier, promoting high dynamics (Blöthe et al. 2021; Halla et al. 2021). What is quite unique though in the Valle de Barrancas Blancas, is the occurrence of a cryoform like a small rock glacier at the lower slopes of the Cerros de Barrancas Blancas created from a colluvial cone, the front of which show clear signs of creeping (Figure 1C).

3.2.3 Gelifluction lobes

The south facing slopes of the 'Cerros of Barrancas Blancas' are mainly composed of rhyolite type eruptives with gelifluction lobes and terrace landforms modified by snow patches (see Trombotto 1991).

3.2.4 Debris slopes

The slopes with gelifluction lobes are debris slopes formed by cryosediments of varied thickness correlated with the corresponding thickness of the active layers. The slopes are usually sorted with surface blocks of a diameter of 10–40 cm, although isolated blocks of a size of 1 m and more are also common. Below, coarse sand is found altering with the aforementioned blocks.

3.2.5 Cryoplanation surfaces

The southern part of the study area called "Llanos de Rivera" reaches up to an altitude of approximately 5400 m and reveals cryoplanation surfaces and cryopediments shaped by the action of cryogenesis and nivation on top of the *pumice* formations on which it is built (Figure 8). The transport of the material can be explained by gelifluction, although wind and subaquatic action may also be involved. Snow generates melting water during some part of the day, as was observed during summer expeditions. It is remarkable that between 4 and 8 pm data loggers registered positive temperatures that would explain this phenomenon of considerable transport of cryosediments.

3.3 New Cryoforms in South America

3.3.1 Atacama pingo (Pingo atacamensis)

This new type was defined by Buchroithner and Trombotto 2012).

This new geomorphological feature can be described as an oblong cryoform, mainly composed of pumice pebbles with varying sizes of tens of meters in planimetric extension. It is the first time that this kind of pingo has been discovered in South America in the Valle de Barrancas Blancas, at the foot of the south-eastern slopes of Cerro de Barrancas Blancas Central (27°01'26"S, 68°40'48"W) which are composed of rhyolithic eruptives (Figure 8).

It is a cryoform composed of different units, and due to its shape is hardly comparable to an open-system pingo like those of the northern hemisphere. However, the Atacama Pingo appears to be comparable to other known pingos in terms of its possible hydraulic genesis (Porsild 1938; Müller 1959).

In the NE sector of the discovered pingo and on the top of the cryoform, the permafrost table was detected at a depth of 65 cm with dry permafrost until 76 cm of the excavation. The temperature registered among the cryosediments was -0.1 °C.

In the SW sector of the relatively flat top of the pingo, the permafrost table was found at a depth of 46 cm and without dry permafrost. No massive ice was found. In the center of the landform a slight depression was identified which might be indicating permafrost degradation as part of its evolution.

Figure 9. Terrestrial laser scanning of one of the *Atacama Pingos.*

Small varieties of hydrolaccoliths, with a hydraulic genesis of the pingo type, were described by other authors (Porsild 1938; Müller 1959). These were denominated 'open system pingos' or East Greenland pingos, but of much smaller size with a contribution of the lateral injection of subterraneous water through the active layer of rhyolithic debris slopes, also exist. Three of these cryoforms were studied in more detail.

One of the analyzed forms had a size of 12 × 8 m and a height of approximately 0.6 m (Figure 9). With a remarkable comet-like shape that links the cryoform with the slope indicating the flow of subterranean waterways towards the endorheic basin or the main valley. A detailed geometric analysis of an Atacama Pingo (Pingo atacamensis) uncovered from sediment revealed that massive and pure ice grew in convex botryoidal shape on the permafrost table (Figure 1b, location D).

The analysis of a profile made of the Atacama Pingo (Pingo atacamensis, Figure 10) revealed that massive and pure ice grew in convex botryoidal shape on the permafrost table.

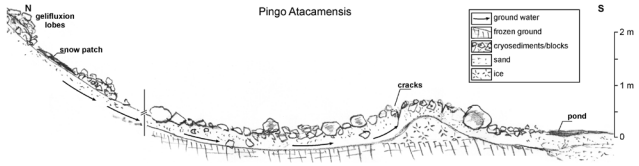

Figure 10. Proposed cross-section of the Atacama Pingo.

Its surface corresponds to the characteristics of the debris slopes at the edge of the bottom of the valley where it is located. Large blocks on the surface have a diameter of 30 to 85 cm. The cryogenic open fabric is complemented by smaller blocks of 4 or 5 and up to 8 cm in the matrix of the major ones. Below those blocks there is a sorted layer of sand similar to the 'kora' of the pingos found in the northern hemisphere (Davis 2000), with a thickness of approximately 45 cm. This layer is in contact with the massive pure ice that characterizes the cryoform. Large blocks with a length of up to 85 cm have been lifted by cryostatic pressure and are located in the upper part of the cryoform. Longitudinal, i.e., W–E trending, and lateral near-surface cracks characterize the surface.

The pingo formation is correlated with the flow of subterranean water which moves through an active layer. The active layer can have a significant thickness on the debris slope, in some cases a thickness of 70 to 80 cm was measured at this one particular feature. The debris slope 'crashes' with the pingo's perimeter at the bottom of the valley, and with a permafrost top at minor depth (30–45 cm, see above) which hinders the water to flow into the Valle de Barrancas Blancas and hence produces its accumulation and rises the piezometric level. Cryostatic pressure subsequently causes the generation of ice bodies on the permafrost table.

In another case of this type of cryogenic landform a 'kora', with an average thickness of over 30 cm was completely removed to observe different units with rounded convex forms of considerable size, indicating that the cryoform may be composed of various units of ice growth (Figure 11). This Atacama Pingo behaves like a secondary pingo next to the big one derived from the detritic slope shown in Figure 8.

The ice of the Atacama Pingos in both of the two studied cases was massive and transparent. The measured ice crystals that grow at the top layer of the permafrost reached a length of up to 12 cm and a diameter of about 3 cm, displaying growth in the typical hexagonal system (Figure 12). In one of the cases the ice allowed to distinguish different planes of growth, and it may be assumed that these correspond to different ages. The Atacama Pingos of this area developed after the emptying or drying of the ancient lake mentioned above.

Figure 11. Botryoidal ice core of a secondary Pingo atacamensis.

Figure 12. Typical hexagonal ice crystals in the top layer of the permafrost showing sizes up to 12 cm length and 3 cm in diameter.

3.3.2 Frosted Dunes ("Dunas heladas")

Frosted dunes or 'dunas heladas' are eolian-induced cryoforms (Figure 13) in the relief of the bottom of the Valle de Barrancas Blancas, rooting in the permafrost of the "*bajo sin salida"* or main valley.

A profile through a comparatively mighty '*duna helada*' shows a total height above the surrounding terrain close to 150 cm. The sediment cover (active layer) reaches from 35 to 50 cm on the western windward side.

It shows 55 cm on the crest of the ice core, and varies from 70 cm down to 55 cm on the leeward side, resulting in a depth of ±35 cm at the plain ground immediately east of the frost dune. The length is about 10 m. “Dunas heladas” facilitate the upheaval of the permafrost table. At the same time the permafrost helps to anchor the dune, preferably at

Figure 13. Digging a sediment-free profile of a ‘duna helada’ (frost dune). The grainsize gradation is clearly visible Frosted Dunes (Dunas heladas).

its base, in the periglacial landscape of the Barrancas Blancas Valley. “Dunas heladas” were also found in Victoria Land and were studied by Selby et al. (1974). It should be noted that in the present case their cryogenic origin through cryogenic weathering is affecting the pumice formations. The sand cover of the “dunas heladas” is loose and sorted. It represents the active layer and reaches a thickness of up to 70 cm. The lateral parts show an active layer thickness of up to 46 cm. Similar values have been registered at various frosted dunes in the main valley of the Valle de Barrancas Blancas. It is worth mentioning that their structure resembles that of classical desert dunes.

The layers of cryosediments at the peak of the dune are subhorizontal and the flanks preserve the angularity of the asymmetrical slopes, but due to the lee effects on the extended slope and to that of the windward side, in a rather limited and abrupt way. The frequent, nearly daily winds loaded with sediments and snow are either impeded or rasp on their way and produce an accumulation of sediments, in this case cryosediments (as they are the product of rocks from cryogenic weathering) and snow.

The permafrost table of dunas heladas shows an oblong perimeter and a relatively stepped tendency at the lee side, presumably associated to different accumulation events of snow during various episodes which have gradually been transformed into ice. In some sectors apparently more intense than in others, the presence of massive ice in form of cores or “eyes” within some parts of permafrost has been detected. The snow has delivered the percolated melting water which intruded into the upper part of the permafrost and enriched it with ice.

4 Conclusions

Studies of this periglacial environment are crucial for the understanding of past environments such as the Tundrean paleoenvironment of Patagonia (Trombotto 2002) and that of the European Doggerland. At the same time, this kind of research gives excellent clues for the comprehension of extraterrestrial environments. Furthermore, they have an impact on the exploration of the urgently needed water reserves in the High Atacama.

Note: as observed during a field check in 2017 the formerly remote and untouched area had become a subject of mineral exploration. Hence, the condition described in this paper present conditions which do not exist anymore.

5 Acknowledgements

The financial support of the 2010 field campaign by Deutsche Forschungsgemeinschaft (DFG; KL 701/10-1) is acknowledged. Logistic support by SERNATUR Atacama, Copiapó (Lelia Manterola), Prof. Ronald Sletten and Prof. Allan Gillespie (University of Washington), for all expeditions is greatly appreciated. The active assistance of Michael Dietze (TU Dresden, 2010), Fernando Millar (Univ. de Santiago de Chile, 2010) and Thomas Loriaux (CECS, Valdivia, Chile) represents an indispensable prerequisite for this paper. The authors’ thanks go to all these organisations and individuals for all expeditions is greatly appreciated.

6 References

Baker, P.E., González-Ferran, O. and Rex, D.C. 1987. ‘Geology and Geochemistry of the Ojos del Salado Volcanic Region, Chile’, *Journal of the Geological Society of London* 144, pp. 85–-96.

Batbaatar, J., Gillespie, A., Sletten, R., Mushkin, A., Rivka, R., Trombotto Liaudat, D., Liu, L. and Petrie, G. 2020. **‘**Toward the detection of permafrost using land surface temperature mapping’, *Remote Sensing 12*(4), p. 695.

Blöthe, J.H., Halla, C., Schwalbe, E., Bottegal, E., Trombotto Liaudat, D. and Schrott, L. 2021. ‘Surface velocity fields of active rock glaciers and ice-debris complexes in the Central Andes of Argentina’, *Earth Surface Processes and Landforms*. doi:10.1002/esp.5042.

Buchroithner, M., Fleischer, K. et al. 2004. *Nevado Ojos del Salado. Chile/Argentinien. Trekkingkarte 1:100000. Alpenvereinskarte 0/13*. München, Germany: Deutscher Alpenverein (German Alpine Club).

Buchroithner, M.F., Dietze, M. and Kleber, A. 2010. ‘Barrancas Blancas (Nevado Ojos del Salado Massif, Atacama Andes) driven by the entire spectrum of geomorphological processes‘, in *18th International Sedimentological Congress*. Mendoza, Argentina: Sept. 26–Oct. 1, 2010, CD-ROM.

Buchroithner, M. and Trombotto Liaudat. D. 2012. ‘Cryophenomena in the Cold Desert of Atacama’, *European Geoscience Union (EGU) General Assembly 2012*. Vienna, Austria: EGU2012-654.

Büdel, J. 1978 *Klima-Geomorphologie*. Gebrüder Borntraeger, Berlin Stuttgart, 304 pp.

Cailleux, A. 1972. 'Les formes et dépôts nivéo-éoliens actuels en Antarctique et au Nouveau-Québec'. *Cahiers de Géographie de Quebec* 16(39), pp. 377–408.

Davis, N. 2000. *Permafrost – a guide to frozen ground in transition*. Fairbanks, Alaska, United States: University of Alaska Press.

Dietze, M., Buchroithner, M.F. and Kleber, A. 2011. 'Das Valle de Barrancas Blancas: ein Werkstattbericht zur Landschaftsgeschichte in einem hyperariden Hochgebirgsraum' in *Arbeitskreis Wüstenrandforschung, German Society for Geographyciety* Annual meeting February 2011: poster. CD-ROM.

García, A., Ulloa, C., Amigo, G., Milana, J. and Medina, C. 2017. 'An inventory of cryospheric landforms in the arid diagonal of South America (high Central Andes, Atacama region, Chile)', *Quaternary International* 438, pp. 4–19.

Garleff, K. and Stingl, H. 1986. 'Geomorphologische Aspekte aktuellen und vorzeitlichen Permafrostes in Argentinien', *Zentralblatt für Geologie und Paläontologie* 1(9/10), pp. 1367–1374.

Halla, C., Blöthe, J.H., Tapia Baldis, C., Trombotto Liaudat, D., Hauck, C. and Schrott, L. 2021. ,Ice content and interannual water storage changes of an active rock glacier in the dry Andes of Argentina', *The Cryosphere* 15, pp. 1187–1213.

Jahn, A. 1972. 'Niveo-eaolian processes in the Sudetes Mountains' *Geographia Polonica* 23, pp. 93–110.

Müller F. 1959. 'Beobachtungen über Pingos', *Meddelelser om Grønland* 153(3), 130 pp.

Nagy, B., Ignéczi, A., Kovács, J., Szalai, Z. and Mari, L. 2019. 'Shallow ground temperature measurements on the highest volcano of the Earth, the Mt. Ojos del Salado, Arid Andes, Chile'. *Permafrost Periglacial Processes* 30, pp. 3–18.

Nagy,B., Kovács, J., Ignéczi, A., Beleznai, S., Mari, L., Kereszturi, A. and Szalai, Z. 2020. 'The Thermal Behavior of Ice-Bearing Ground: The Highest Cold, Dry Desert on Earth as an Analog for Conditions on Mars, at Ojos del Salado, Puna de Atacama-Altiplano Region', *ASTROBIOLOGY* 20(6), pp. 701–722.

Porsild, A. 1938. 'Earth mounds in unglaciated Arctic Northwestern America', *Geographical Review* 28(1), pp. 46–58.

Santibáñez, I., Venegas, M. and Espinoza, C. 2006. 'Hidrogeología de la Cuenca Campo de Piedra Pómez-Laguna Verde. Región de Atacama'. *Servicio Nacional de Geología y Minería, Subdirección Nacional de Geología*, Carta Geológica de Chile, Serie Hidrogeología 1:100 000, No.4. Santiago de Chile.

Schwikowski, M., Ciric, A., Kellerhals, T., Schläppi M., Kleber, A. and Buchroithner, M.F. 2010. 'Ancient Ice in the Arid Central Andes?', *Paul Scherer Institute Annual Report 2009*, p. 39.

Selby, M.J., Rains R.B. and Palmer, W.P. 1974. 'Eolian Deposits of the ice free Victoria Valley, southern Victoria Land, Antarctica', New Zealand *Journal of Geology and Geophysics* 17(3), pp. 543–562.

Trombotto, D. 1991. ,Untersuchungen zum periglazialen Formenschatz und zu periglazialen Sedimenten in der 'Lagunita del Plata', Mendoza, Argentinien', *Heidelberger Geographische Arbeiten* 90, 171 pp.

Trombotto, D. 2000. 'Survey of Cryogenic Processes, Periglacial Forms and Permafrost Conditions in South America', *Revista do Instituto Geológico* 21(1/2), pp. 33–55.

Trombotto, D. 2002. 'Inventory of fossil cryogenic forms and structures in Patagonia and the mountains of Argentina beyond the Andes', *South African Journal of Science* 98, pp. 171–180.

Trombotto, D., Buk, E. and Hernández, J. 1999. 'Rock Glaciers in the Southern Central Andes (appr. 33° S.L.), Mendoza, Argentina: a Review', *Bamberger Geographische Schriften* 19, pp. 145–173.

Trombotto Liaudat, D., Wainstein, P. and Arenson, L. 2014. *Terminological Guide of the South American Geocryology*. Buenos Aires, Argentina: Vázquez Mazzini Editors, 127 pp.

Antarctic ground ice in a changing climate

Marjolaine Verret[1], Denis Lacelle[2], Warren Dickinson[3], David Fisher[4] & Dale T. Andersen[5]

[1]*Department of Arctic Geology, The University Centre in Svalbard, Longyearbyen, Svalbard and Jan Mayen*

[2]*Department of Geography, Environment and Geomatic, University of Ottawa, Ottawa, Ontario, Canada.*

[3]*Antarctic Research Centre, Victoria University of Wellington, New Zealand*

[4]*Department of Earth Sciences, University of Ottawa, Ottawa, Ontario, Canada*

[5]*Carl Sagan Centre, SETI Institute, Mountain View, California, United States*

ABSTRACT

Ground ice is one of permafrost's most important and dynamic geologic components. Its occurrence and distribution are essential to understand landscape evolution. Early investigations of permafrost and ground ice in the McMurdo Dry Valleys of Antarctica identified ice-cemented permafrost, ice wedges, buried glacier ice, and buried remnants of the Ross Sea ice sheet in low elevations. At high elevations (> 1000 m a.s.l), it was initially thought that dry permafrost dominated the region, but recent studies discovered ubiquitous ice-cemented permafrost at shallow depths. Here, we review the current state of knowledge of permafrost and ground ice in the McMurdo Dry Valleys and other ice-free areas in Antarctica to understand the role of ground ice in a changing climate. The study presents a summary of depths to icy permafrost, vertical distribution of ground ice, and δD-$\delta^{18}O$ profiles for a range of Antarctic sites. Mechanisms of ground ice emplacement are discussed over various timescales, including the freezing of evaporated snowmelt and the condensation of vapour diffusion into the permafrost. The variability in the distribution and origin of ground ice is attributed to ground surface temperature and moisture conditions, which separate Antarctic permafrost into three distinct zones: upland, mixed and coastal zones. Ground ice of vapour-deposition origin is predominantly situated in the stable upland zone, whereas ground ice formed by the freezing of evaporated snow meltwater is predominantly found in the coastal thaw zone.

1 INTRODUCTION

Ground ice is a general term used to define all types of ice contained in frozen ground (French 2017; Harris et al. 1988). It plays a central role in landscape development of permafrost environments and geohazard risks. Unlike the Arctic, where the distribution and origin of ground ice have been extensively studied (French 2017), relatively few studies about ground ice have been conducted in cold and hyper-arid Antarctica (e.g., Bockheim et al. 2007). Campbell et al. (1998) and Bockheim et al. (2007) classified permafrost in Antarctica as either (1) dry permafrost (contains negligible moisture, < 3% wt; Campbell et al. 1998); (2) ice-cemented permafrost; and (3) massive ground ice or buried ice. In the Arctic, ice-cemented permafrost is typically sub-divided based on volumetric ice content (see full classification in French and Shur 2010). Here, the term ice-cemented permafrost (or *icy*) is used as an umbrella term to describe permafrost that harbours ice, irrespective of ice content (e.g., McKay et al. 2019). Muller (1945) introduced the concept of dry permafrost as a geotechnical application for engineering projects. Pewe (1959) later suggested its occurrence in Antarctica, but dry permafrost was first observed with the use of thermistors at Linnaeus Terrace in Upper Wright Valley (McKay et al. 1998). Dry permafrost has subsequently been observed in most regions in the Transantarctic Mountains, notably in the McMurdo Dry Valleys (MDV; Campbell et al. 1998; Marinova et al. 2013), Ellsworth Mountains (e.g., McKay et al. 2019), Queen Maud Land (e.g., Kotze and Meiklejohn 2017), Enderby Land, MacRobertson Land (e.g., Alekseev and Abakumov 2020) and Wilkes Land (e.g., Alekseev and Abakumov 2020). The occurrence of massive ground ice and buried ice in Antarctica typically relates to the presence of ice wedges (e.g., Raffi and Stenni 2011), buried glacial ice (Gardner et al. 2022; Swanger 2017; Swanger et al. 2019; Swanger et al. 2010) or buried remnants of the Ross Sea ice sheet (Levy et al. 2013).

The only attempt at classifying ground ice distribution in the uppermost meter was from the MDV (Bockheim et al. 2007). In this region, dry permafrost and ice-cemented permafrost occupied 43% and 55%, respectively of the area. However, recent studies have since observed ice-cemented permafrost (e.g., Lacelle et al. 2013; Lapalme et al. 2017; Verret et al. 2021) or massive ice (Gardner et al. 2022; Swanger 2017; Swanger et al. 2010) in locations previously classified as dry permafrost. This suggests that ground ice abundance might be underestimated in the MDV and elsewhere in Antarctica (Figure 1). Here, we present a summary of the active layer thickness and depth to the ice table and discuss the concept of a transient layer. We then present a summary of the vertical distribution of ground ice and δD-$\delta^{18}O$ profiles for a range of Antarctic sites, discuss mechanisms of ground ice emplacement and the role of Antarctic ground ice in a changing climate.

2 ACTIVE LAYER AND ICE TABLE

Permafrost is defined as ground that remains at or below 0 °C for two or more consecutive years, and the active layer corresponds to the near-surface soils that warm above 0 °C during the summer season (Harris et al. 1988). The thickness of the active layer corresponds to the maximum

https://doi.org/10.52381/ICOP2024.93.1

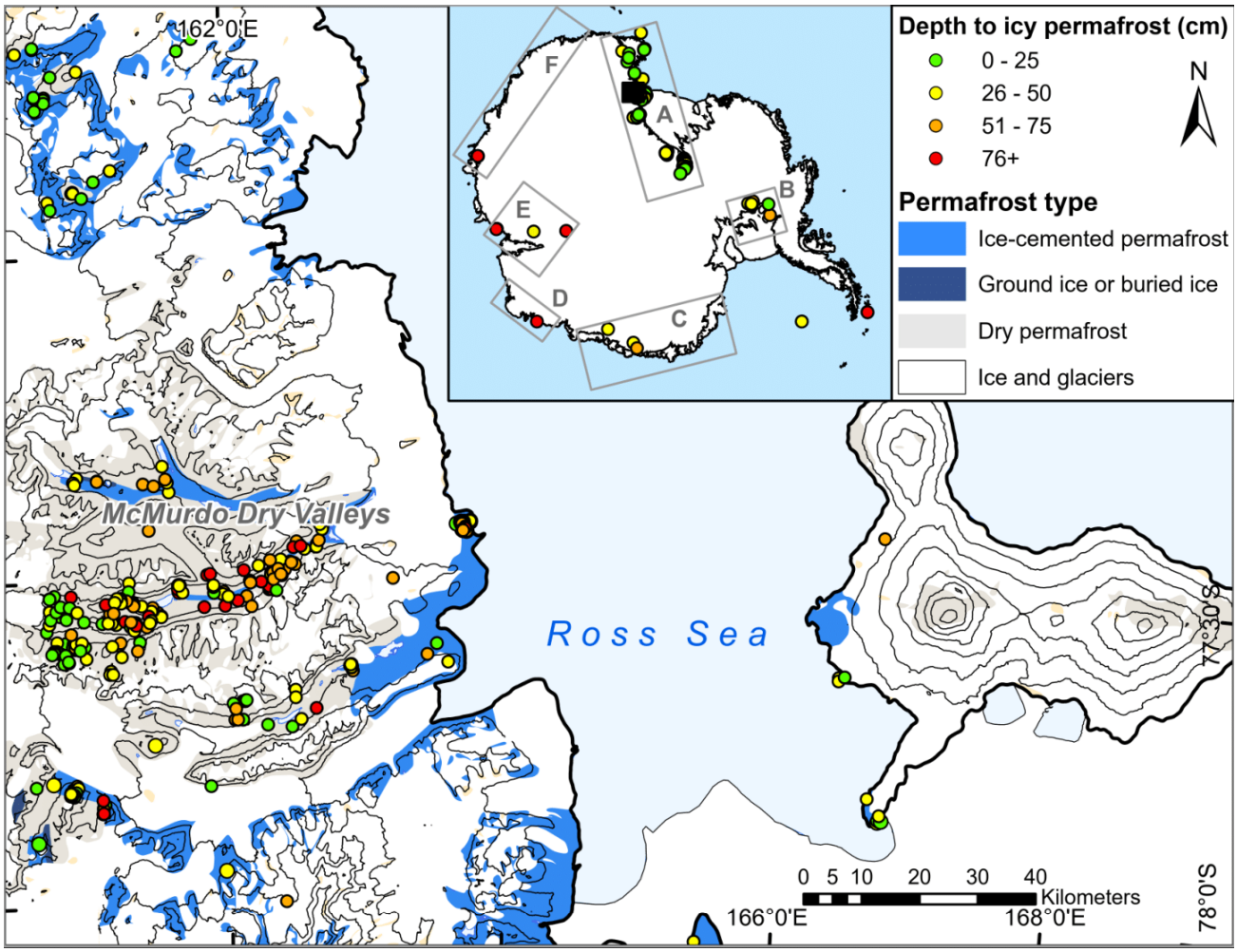

Figure 1. Predicted distribution of ground ice (modified from Bockheim et al. 2007) with compilation of depths to icy permafrost measurements in different sectors of Antarctica: A. Transantarctic Mountains (Campbell and Claridge 1964–1999; Denton et al. 1986; Dickinson and Rosen 2003; Lacelle et al. 2013; Marchant et al. 2002; McLeod et al. 2004–2007; Verret et al. 2021), B. Ellsworth Mountains (Campbell and Claridge 1964–1999; McKay et al. 2019), C. Queen Maud Land (Lacelle et al. in press; Matsuoka et al. 1990; Vtyurin 1986), D. Enderby Land (Alekseev and Abakumov,2020; MacNamara 1969), E. MacRobertson Land (Alekseev and Abakumov 2020; Li et al. 2003) and F. Wilkes Land (Alekseev and Abakumov 2020). The depth to icy permafrost corresponds to the thaw depth and active layer depth in the coastal thaw zones but represents a sublimation unconformity in stable upland sites.

depth of the 0 °C isotherm; the boundary with the underlying permafrost is termed the permafrost table (Brown and Kupsch 1974). In Antarctica, the thickness of the active layer estimated from soil thermistors varies from zero to a few centimeters in the coldest high elevations of the Transantarctic Mountains, and up to > 5 m in bedrock sites of the Antarctic Peninsula (Hrbáček et al. 2023). As a general trend, active layer thickness decreases with increasing elevation and continentality (Adlam et al. 2010; Hrbáček et al. 2023). Marchant and Head III (2007) define three climatic zones which can be applied to Antarctic permafrost: (1) the coastal thaw zone (CTZ), where temperatures regularly exceed 0 °C resulting in seasonal melt, (2) the intermediate mixed zone (IMZ), where temperatures may rise above 0 °C only for short periods resulting in the periodical presence of liquid water and (3) the stable upland zone (SUZ), where maximum air temperatures do not exceed 0 °C resulting in little or no melting of snow and/or ice. The absence of vegetation and surface organic matter, and lack of snow cover and/or moist active layer (e.g., Fountain et al. 2010) result in a small to negligible surface offset (i.e., mean annual ground temperature ~ mean annual air temperature; Lacelle et al. 2016).

Permafrost has also been defined as ground that remains frozen for two or more consecutive year (Muller 1945). Under this definition, the active layer corresponds to the near-surface soils that seasonally thaw and freeze and its depth equals or exceeds that defined by the 0 °C isotherm, the difference is caused by the soil water salinity and the associated freezing point depression (Anderson and Morgenstern 1973; Brown and Kupsch 1974). However, in

Antarctica, the cryotic soils above the icy permafrost are often dry and the soil water salinity cannot explain this difference. Considering that the Arctic-centric perspective of frozen ground did not translate to regions with dry permafrost, terms like “dry-frozen permafrost” (Muller 1945) and “dry and wet shell” (Ward et al. 1969) were introduced to describe permafrost in hyper-arid regions, and the term “ice table” was introduced to define the boundary between dry and icy permafrost (first introduced in lunar and planetary science; Gold 1962; Smoluchowski 1968). Thus, when using the thermal definition of the active layer in Antarctica, the depth to the ice table (icy soils) can exceed that of the 0 °C isotherm, the two being separated by dry permafrost. The depth to the ice table varies from a few centimeters to more than two meters (e.g., Campbell and Claridge 1964–1999; Figure 1). As a general trend, the ice table is observed mainly in the stable, high elevation, SUZ and corresponds to a sublimation unconformity; in the CTZ, the depth to icy permafrost mainly corresponds to the thaw depth. The depth of the ice table in the SUZ is set by the water vapour density gradient between the ground surface and the ice-bearing ground (Fisher et al. 2016; McKay et al. 1998), although it can be recharged periodically by snowmelt (Hagedorn et al. 2010; Marinova et al. 2013). Fisher et al. (2016) developed a numerical model (REGO) to predict the depth of the ice table based on ground surface temperature and humidity as the boundary conditions, along with damping of diurnal and annual temperature cycles within sandy soils. The measurements from three sites fit well the predicted ice table depth for the surface relative humidity or difference in frost point values between the surface and ice table (Figure. 2).

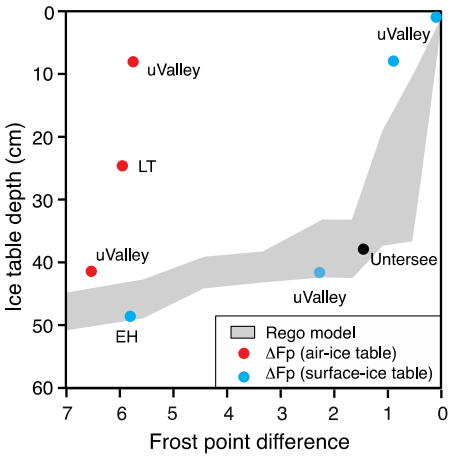

Figure 2. Measured ice table depths at sites with known frost point differences in the Transantarctic Mountains (University Valley) and Queen Maud Land (Untersee Oasis), along with *Linnaeus Terrace* and *Ellsworth Mountains* compared with those predicted by the REGO model.

2.1 Depth of ice table and diameter of polygons

Geophysical approaches (i.e., ground-penetrating radar) have been used to attempt to identify the presence of ground ice in Antarctic permafrost, but they have only been successful at identifying thick bodies of massive ice (Drake 2015; Winsor et al. 2020). Polygonal terrains are features visible from satellite imagery and could allow for an efficient method to map ground ice in areas where data are lacking. Mellon et al. (2014) observed a relationship between the depth to the ice table and the diameter of polygons, and numerical modeling of seasonal stress in permafrost showed that the ice table depth is the main parameter that controls the diameter of polygons. Much like the polygons studied in University and Farnell valleys within the upper MDV (Mellon et al. 2014), data on polygon size from Pritzker Valley in Untersee Oasis and other MDV locations—such as McKelvey Valley, Andrew Ridge, Taylor Valley, Barwick Valley and Victoria Valley—reveals a consistent positive correlation between the size of the polygons and the depth of the ice table. In fact, the sizes and depths of the 14 surveyed sites align closely with the predictions made by Mellon et al. (2014) in their study (Figure 3).

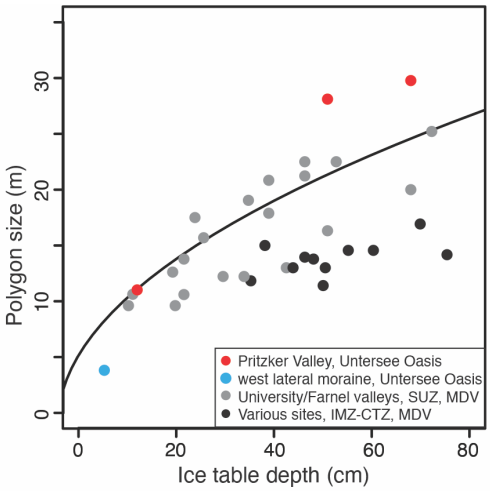

Figure 3. Relationship between polygon diameter and ice table depth at various Antarctic sites: University and Farnell valleys (Mellon et al. 2014), Pritzker Valley (Lacelle et al. in press) and various MDV sites, where ice table depths are obtained from Campbell and Claridge (1964–1999) and average polygon diameter are measured using Lidar data from Fountain et al. (2017).

2.2 A transient layer in Antarctic permafrost?

The transient layer has been defined as the zone in which the active layer thickness experiences interannual fluctuations over decadal to centennial time-scale (Shur et al. 2005). The transient layer is often ice-rich and described as essential to permafrost’s long-term stability. Shur et al. (2005) suggested that interannual variations in active layer thickness over decadal timescales could be assessed from the maximum variation (%) as a function of average active layer thickness. We examined whether the year-to-year changes in the thickness of the active layer in Antarctica are comparable to those in the Arctic. We used data on active layer thickness from the Circumpolar Active Layer Monitoring (CALM) Programme dataset, focusing on sites with over a decade of measurements. The data show that

the relative changes in active layer thickness can vary widely, ranging from 4% to 114% (Figure 4). With the exception of Mount Fleming (1697 m a.s.l. and a very shallow active layer thickness), the range in variations is within those calculated for sites in the Arctic, and like in the Arctic, a negative relationship is observed with increase mean active layer thickness (i.e., Shur et al. 2005). Shur et al. (2005) suggested that % variations in active layer thickness are affected by climate and soil types and are greater in organic soils. The latter can be ruled out for Antarctica given the absence of a surface organic layer. As such, future work should explore environmental parameters that might affect the % variations in active layer thickness (depth to ice table, thickness of dry permafrost, soil types, soil moisture).

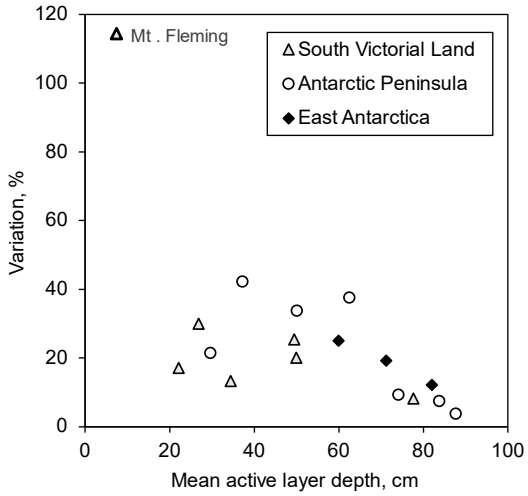

Figure 4. Variations of active layer thickness and average active layer thickness. Monitoring period is minimum 10 years. Data retrieved from the Circumpolar Active Layer Monitoring (CALM) Programme.

3 VERTICAL DISTRIBUTION OF GROUND ICE

Antarctica's earliest and most extensive survey for permafrost and ground ice was the *Dry Valleys Drilling Project* (DVDP), where cores were retrieved from the three main valleys (Taylor, Wright and Victoria valleys). Ground ice was found in all three valleys and up to depths of 320 m in Taylor Valley (Stuiver et al. 1976). Subsequently, the boreholes of the *Coring for microbial records of Antarctic climate* (COMRAC) project (5–20 m) from Taylor Valley, Miers Valley, Mount Feather and Beacon Valley were all drilled in icy permafrost and had ice contents in 25 to 50 wt% (i.e., gravimetric water content expressed in weight%) range immediately below the dry permafrost layer (Gilichinsky et al. 2007). More recently, the Table Mountain drill cores (Dickinson et al. 2012), the Friis Hills Drilling Project (FHDP; Verret et al. 2021) and a University of Washington-led drilling project in Beacon Valley (Cuozzo et al. 2020) reached depths of 5 m, 50 m and 30 m respectively and the cores were mostly ice-cemented, with discrete ice lenses (20 to 80 wt%).The Friis Hills cores showed interesting ice content trends with depth with icy permafrost down to 5 m depth, followed by near-dry permafrost (5–20 m depth), and, again, ice-poor to ice-rich permafrost with distinct thin ice layers below 20 m depth (Figure 5). Overall, below the dry permafrost, the distribution and content of ground ice in Antarctic permafrost is similar to that in the Arctic (e.g., Lacelle et al. 2022).

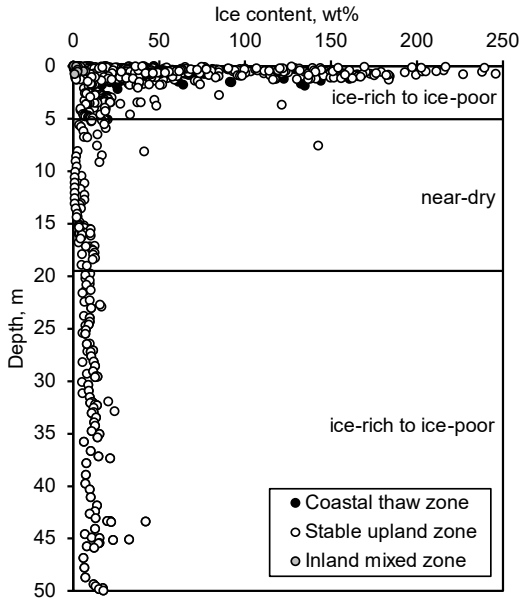

Figure 5. Ice content at different sites from the three different climatic zones in the McMurdo Dry Valleys (defined by Marchant and Head III 2007): the coastal thaw zone (n = 366 from 66 sites), the inland mixed zone (n = 16 from 3 sites) and the stable upland zone (n = 966 from 98 sites). Data from Campbell and Claridge (1964–1999), Dickinson and Rosen (2003), Lacelle et al. (2013), Lapalme et al. (2017) and Verret et al. (2021).

4 ORIGIN OF GROUND ICE

The CTZ harbours ice emplacement mechanisms similar to those found in the Arctic (French 2017). Thus, the following sections will focus on the origin of ground ice in the SUZ. Early investigations of permafrost and models describing ground ice in Antarctica suggested that that ground ice should persist for only a few thousand years as sublimation would eventually remove it from the ground (e.g., Hagedorn et al. 2007; Hindmarsh et al. 1998; McKay et al. 1998; Schorghofer and Aharonson 2005). Yet, in sediments dating back to the mid-Miocene (Dickinson and Rosen 2003; Verret et al. 2021), ground ice was found in abundance at shallow depths (30 to 70 cm). This suggests that there may either be an error in the boundary layer of the model parameters—specifically, using air-based parameters instead of those at the ground surface—or that there has been a recent deposition of ice in the soils. The latter mechanism has been found to be of marginal importance, since a recent study using meteoric Beryllium-10 as a tracer for water infiltration concluded that minimal liquid water has penetrated the ground for at least a few million years at the high-elevation sites of the MDV (Schiller et al. 2019; Verret et al. 2023). In addition, the most recent

modeling studies show that the depth of the ice table can be explained using the ground surface as the boundary layer (Fisher et al. 2016). There are three known mechanisms of ice emplacement in SUZ permafrost: (1) episodic freezing of snow meltwater, (2) diffusion of water vapour and (3) burial of glacier ice.

4.1 Freezing of snow meltwater

Although instances of wedge ice have been observed in Northern Victoria Land (Raffi and Stenni 2011), two main types of ground ice originate from the freezing of liquid water in the SUZ: segregated ice and pore ice (e.g., Dickinson and Rosen 2003; Lacelle et al. 2013; Marchant et al. 2002; Verret et al. 2021). These types of ice are widely present in the Arctic (French and Shur 2010); however, their presence in Antarctic permafrost at sites where mean annual air temperatures remain below < 0 °C have raised questions about mechanisms of ice emplacement and the source of water. A number of studies have inferred the source of liquid water for ground ice in the near-surface of hyper-arid sites using stable water isotopes coupled with soluble ions in the ice (Cuozzo et al. 2020; Dickinson and Rosen 2003; Hagedorn et al. 2010; Lacelle et al. 2013; Verret et al. 2021). Stable isotope depth profiles displayed a higher isotopic composition near the surface throughout these studies. This trend results from the infiltration of highly evaporated (up to 95%) snowmelt (Cuozzo 2021; Lacelle et al. 2013; Verret et al. 2021). Ice that forms from evaporated snowmelt is usually characterized by high solute load (on the order of 1 to 10 mg g^{-1} dry soils), enriched $\delta^{18}O$ and δD values plotting well below the local meteoric water line (LMWL; $\delta D = 7.9\delta^{18}O+0.8$; Figure 6). In fact, D-excess values are amongst the lowest reported on Earth (–105.8‰; Lacelle et al., in press). This process has been observed in both low and high elevations of the MDV sector (Victoria Valley, 450 m a.s.l.; Friis Hills, 1200–1500 m a.s.l; University Valley, 1600–1800 m a.s.l; Table Mt) and it most likely also occurs in other regions, such as in Pritzker Valley (800–1100 m a.s.l.), situated in Queen Maud Land (Figure 6).

The snow meltwater that enters the icy permafrost may then be redistributed along thermal and stress fields. Fisher et al. (2020) employed a model to track the migration of unfrozen water in icy permafrost, aiming to estimate how ground ice content profiles change over time. This movement of unfrozen water leads to ice-rich and ice-poor zones forming at specific depths over time, primarily influenced by the thermal diffusivity, water chemistry and soil type of the icy permafrost. Evidence of this process was found in the Friis Hills Drilling Project cores, where nearly dry permafrost across 5–20 m depth originated from the redistribution of unfrozen water (Figure 5).

4.2 Vapour diffusion

In the SUZ of Antarctic permafrost, where ground temperatures remain cryotic year-round and little surface melt occurs, ground ice was found to originate from the diffusion of water vapour into the soils. Vapour diffusion creates closed-cavity ice, which is indifferentiable structurally to pore ice. All sites showed similar ground ice profiles, including a shallow and narrow ice-rich horizon at 5–10 cm depth (> 50% excess ice content), that then progressively decreased with depth. All these sites yielded δD-$\delta^{18}O$ regression slope values similar to the LMWL but with low D-excess values such that the data plot well below the LMWL. The very low D-excess values suggest that the source of water vapour is either from direct condensation of atmospheric moisture in the soils, which would plot along the LMWL but with D-excess near -35‰ and/or from transient frost that forms just at and under the ground surface in winter (Fisher et al. 2016). This mechanism of ground ice accumulation in sediments within cold–dry settings can still result in overfilled pore ice (excess ice), even without the presence of liquid water, following repeated thermal cycling in the icy soils.

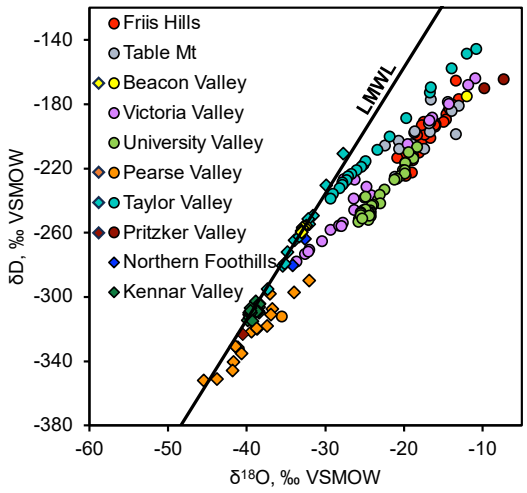

Figure 6. Stable isotope composition for selected buried ice (diamonds) and pore/segregated ice (circles) in Antarctic permafrost: Friis Hills (77°45′S 161°28′E; Verret et al. 2021), Table Mountain (77°57'S, 161°57'E; Dickinson and Rosen 2003), Beacon Valley (77°50'S, 159°30'E; Marchant et al. 2002), Victoria Valley (77°22'S, 161°35'E; Cuozzo 2021; Hagedorn et al. 2010), University Valley (77°52'S, 163°45'E; Lacelle et al. 2013; Lapalme et al. 2017), Pearse Valley (77°42'S, 161°36'E; Heldmann et al. 2012; Swanger et al. 2010), Taylor Valley (77°37′S, 163°00′E; Gardner et al. 2022; Levy et al. 2011; Toner and Sletten 2013), Pritzker Valley in Queen Maud Land (71°17'S, 13°43'E; Lacelle et al. in press), Northern Foothills in Northern Victoria Land (74°44′S 163°55′E; Guglielmin and French 2004) and Kennar Valley (Swanger 2017). Note: we use the LMWL from the MDV (Lacelle et al. 2011), which encompasses most sites, unless specified otherwise.

4.3 Buried glacier ice

Buried ice is a sub-group of ground ice, where ice, such as glacier ice, is preserved in permafrost (emplacement conditions and mechanisms dicussed in Harris and Murton 2005). Two types of buried glacier ice have been found, debris-covered (or basal) glacial ice and surface (firn-derived) glacial ice. Debris-covered glacial ice has been observed in multiple locations in Antarctica, particularly in

the MDV sector, where ice from Ross Sea ice sheet and other glaciers have been preserved for thousands of years (e.g., Lacelle et al. 2013; Swanger 2017; Swanger et al. 2019), and even > 1 million years in the case of Beacon Valley (Yau et al. 2015), Ong Valley (Bergelin et al. 2022) and Allan Hills (Yan et al. 2019). Buried surface glacial ice typically has low dissolved ion concentrations and meteoric isotopic signatures (Figure 6).

5 GROUND ICE IN A WARMING CLIMATE

This review has highlighted the widespread presence of ground ice in Antarctica. We will now explore advancements related to ground ice in the context of a warming climate.

5.1 Relict ground ice to predict future Antarctic terrestrial climate

Relict ground ice which has preserved its original meteoric water can be used to reconstruct paleo air temperatures (Porter and Opel 2020). In Antarctica, particularly in the MDV, air temperatures have remained cold enough to sustain continuous permafrost since the mid-Miocene (Verret et al. 2021). Subsequent alteration of ground ice by vapour diffusion through diurnal and annual temperature cycles is only possible to a certain depth that can be modeled (Fisher et al. 2016). Additionally, ground ice accumulation rate decrease following an e-folding function following decrease in porosity as ice accumulates (Fisher et al. 2020). This implies that drilling deep (>30 m; depending on the ground's thermal properties) into Antarctic permafrost could potentially uncover meteoric ground ice that kept its original isotopic signature, like the ice found at the bottom of the Friis Hills cores (Verret et al. 2021). This finding offers the potential to use meteoric ground ice as a paleotemperature proxy dating back to the early Miocene, which extends beyond the oldest ice core record (currently 800,000 yrs at EPICA Dome C; Wolff et al. 2010). Buried glacier ice, which represents long-term archives of glacial ice, could be used to reconstruct past glacial advances (Swanger et al. 2019).

However, paleoclimate inferences from ground ice stable isotope records remain a mostly underutilized due to the lack of dating methods for relict ice. Meteoric Beryllium-10 has been used as a tracer for water infiltration (along with other cosmogenic nuclide dating methods), which allows one to constrain the timing of the emplacement of the ground ice (Verret et al. 2023). However, this indirect dating method relies on a complete understanding of the periglacial history for interpretation. Development of a suitable isotope methods for dating old ice will be required to make more direct interpretations. Ground ice may, however, offer rare glimpses of the terrestrial climate systems during intervals that are simply not captured by any other terrestrial archives. This may become critical to our understanding of future climate change.

5.2 Role of ground ice in Antarctic terrestrial ecosystems

Antarctic ground ice has long been considered stable. However, recent studies suggest accelerated thermokarst formation driven by increased insolation in coastal areas (Levy et al. 2013). Under mild 1–2 °C warming conditions in the MDV sector, active layer could increase up to 20 cm (Levy et al. 2013), potentially reaching ice table depths at certain sites. Increasing moisture availability in hyper-arid sites would have significant impacts on soil ecosystems (Andriuzzi et al. 2018; Wlostowski et al. 2018). Moreover, recent studies using lipid biomarkers, have suggested that legacy carbon locked-in at depth in permafrost has been bioavailable under past warmer climate (Verret et al., in prep). Carbon being one of the key physiochemical factors in the development of soil microbial communities (Cary et al. 2010), future climate warming could lead to considerable changes in the structure and function of ecosystems in the MDV.

5.3 Transient layer in degrading Antarctic permafrost

The impact of Antarctic ground ice on the ground's thermal regime is not yet fully understood. Ice-rich permafrost in the transient layer at many coastal thaw zone locations could serve as a thermal buffer by releasing latent heat during phase change, similar to phenomena observed in the Arctic (Shur et al. 2005). Conversely, an increase in water content in the stable upland zone, which has a layer of dry permafrost, could also significantly influence the ground thermal regime in the transient layer. Dry permafrost acts as a short-term buffer, as dry soils have a lower thermal conductivity than moist soils, mitigating the effects of rising ground temperatures (Andersland and Ladanyi 1994). In summary, the distribution and content of ground ice and the presence of unfrozen water are key variables for understanding the terrestrial Antarctic environment and its response to a warming climate.

6 ACKNOWLEDGEMENTS

We would like to highlight the pioneering work of Dr Iain Campbell and Dr Graeme Claridge, their colleagues, and the Manaaki Whenua – Landcare Research for making their Antarctic soil dataset publicly available. The Friis Hills Drilling Project (austral summer 2016–2017) led by R. Levy and T. Naish was funded by the Past Antarctic Climate Programme. Funding support was provided by the New Zealand Ministry of Business, Innovation and Employment through contracts C05X1001 and ANTA1801. Fieldwork was made possible with the logistical support of Antarctica New Zealand. We also extend our gratitude to the TAWANI Foundation and the Trottier Family Foundation for their support of research at Untersee Oasis, as well as to our fellow field team members for their invaluable assistance during numerous Antarctic expeditions.

7 REFERENCES

Adlam, L.S., Balks, M.R., Seybold, C.A., and Campbell, D.I. 2010. 'Temporal and spatial variation in active layer depth in the McMurdo Sound Region, Antarctica', *Antarctic Science 22*(1), pp. 45–52.

Alekseev, I. and Abakumov, E. 2020. 'Permafrost table depth in soils of Eastern Antarctica oases, King George and Ardley Islands (South Shetland Islands)', *Czech Polar Reports* 10(1), pp. 7–22.

Andersland, O.B. and Ladanyi, B. 1994. 'Physical and thermal properties', in O.B. Andersland and B. Ladanyi (eds.), *An Introduction to Frozen Ground Engineering*. Boston, Massachusetts, United States: Springer, pp. 23–63. Available at: https://doi.org/10.1007/978-1-4757-2290-1_2.

Anderson, D.M. and Morgenstern, N. 1973. 'Physics, chemistry and mechanics of frozen ground: A review', *Proceedings of the Second International Conference on Permafrost* (North American Contribution), pp. 257–288.

Andriuzzi, W., Adams, B., Barrett, J., Virginia, R., and Wall, D. 2018. 'Observed trends of soil fauna in the Antarctic Dry Valleys: early signs of shifts predicted under climate change', *Ecology* 99(2), pp. 312–321.

Bergelin, M., Putkonen, J., Balco, G., Morgan, D., Corbett, L.B., and Bierman, P.R. 2022. 'Cosmogenic nuclide dating of two stacked ice masses: Ong Valley, Antarctica', *The Cryosphere* 16(7), pp. 2793–2817.

Bockheim, J.G., Campbell, I.B., and McLeod, M. 2007. 'Permafrost distribution and active-layer depths in the McMurdo Dry Valleys, Antarctica', *Permafrost and Periglacial Processes* 18(3), pp. 217–227.

Brown, R. and Kupsch, W. 1974. 'Permafrost terminology', *National Research Council of Canada* Technical Memorandum 111. Available at: https://doi.org/10.4224/20378592.

Campbell, I.B. and Claridge, G.G. 1964–1999. 'Ross Sea region soils', *Manaaki Whenua - Landcare Research* Report pre 2005.Available at: https://soils.landcareresearch.co.nz/topics/soil-data/antarctic-soil-data/reports-pre-2005/ (Accessed: 03.08.2023).

Campbell, I.B., Claridge, G.G., Campbell, D.I., and Balks, M.R. 1998. 'The soil environment of the McMurdo Dry Valleys, Antarctica', in J.C. Priscu (ed.), *Ecosystem dynamics in a polar desert: the McMurdo Dry Valleys, Antarctica*. Antarctic Research Series vol. 72, pp. 297–322.

Cary, S.C., McDonald, I.R., Barrett, J.E., and Cowan, D.A. 2010. 'On the rocks: the microbiology of Antarctic Dry Valley soils'. *Nature Reviews Microbiology* 8(2), pp. 129–138.

Cuozzo, N. 2021. *Novel studies of McMurdo Dry Valleys ice-cemented permafrost cores document chemical weathering in permafrost and the timing of Plio-Pleistocene glaciations*. PhD thesis, University of Washington, Seattle, Washington, United States.

Cuozzo, N., Sletten, R.S., Hu, Y., Liu, L., Teng, F.-Z., and Hagedorn, B. 2020. 'Silicate weathering in antarctic ice-rich permafrost: Insights using magnesium isotopes', *Geochimica et Cosmochimica Acta* 278, pp. 244–260.

Denton, G., Bockheim, J., Wilson, S., and Schlüchter, C. 1986. 'Late Cenozoic history of Rennick Glacier and Talos dome, northern Victoria Land, Antarctica', *Geological investigations in northern Victoria Land* 46, pp. 339–375.

Dickinson, W.W. and Rosen, M.R. 2003. 'Antarctic permafrost: An analogue for water and diagenetic minerals on Mars', *Geology* 31(3), pp. 199–202.

Dickinson, W.W., Schiller, M., Ditchburn, B.G., Graham, I.J., and Zondervan, A. 2012. 'Meteoric Be-10 from Sirius Group suggests high elevation McMurdo Dry valleys permanently frozen since 6 Ma', *Earth and Planetary Science Letters* 355, pp. 13–19.

Drake, A. 2015. *Mapping of Massive Ground Ice Using Ground Penetrating Radar Data in Taylor Valley, McMurdo Dry Valleys of Antarctica.* MSc thesis, Uppsala University, Uppsala, Sweden.

Fisher, D.A., Lacelle, D., and Pollard, W. 2020. 'A model of unfrozen water content and its transport in icy permafrost soils: Effects on ground ice content and permafrost stability'. *Permafrost and Periglacial Processes* 31(1), pp. 184–199.

Fisher, D.A., Lacelle, D., Pollard, W., Davila, A., and McKay, C.P. 2016. 'Ground surface temperature and humidity, ground temperature cycles and the ice table depths in University Valley, McMurdo Dry Valleys of Antarctica', *Journal of Geophysical Research: Earth Surface* 121(11), pp. 2069–2084.

Fountain, A.G., Fernandez-Diaz, J.C., Obryk, M., Levy, J., Gooseff, M., Van Horn, D.J., Morin, P., and Shrestha, R. 2017. 'High-resolution elevation mapping of the McMurdo Dry Valleys, Antarctica, and surrounding regions', *Earth System Science Data* 9(2), pp. 435–443.

Fountain, A.G., Nylen, T.H., Monaghan, A., Basagic, H. J., and Bromwich, D. 2010. 'Snow in the McMurdo Dry Valleys, Antarctica', *International Journal of Climatology: A Journal of the Royal Meteorological Society* 30(5), pp. 633–642.

French, H. 2017. 'Ground Ice and Cryostratigraphy', in H. French (ed.), *The Periglacial Environment 4e*. John Wiley & Sons, Ltd., pp. 111–137.

French, H. and Shur, Y. 2010. 'The principles of cryostratigraphy', *Earth-Science Reviews* 101(3-4), pp. 190–206.

Gardner, C.B., Diaz, M.A., Smith, D.F., Fountain, A.G., Levy, J.S., and Lyons, W.B. 2022. 'Isotopic signature of massive, buried ice in eastern Taylor Valley, Antarctica: Implications for its origin', *Arctic, Antarctic, and Alpine Research* 54(1), pp. 335–345.

Gilichinsky, D., Wilson, G., Friedmann, E., McKay, C., Sletten, R., Rivkina, E., Vishnivetskaya, T., Erokhina, L., Ivanushkina, N., and Kochkina, G. 2007. 'Microbial populations in Antarctic permafrost: biodiversity, state, age, and implication for astrobiology', *Astrobiology* 7(2), 275-311.

Gold, T. 1962. 'Processes on the lunar surface', *Proceeding of the 14th International Astronomical Union Symposia*, pp. 433-440.

Guglielmin, M. and French, H.M. 2004. 'Ground ice in the Northern Foothills, northern Victoria Land, Antarctica', *Annals of Glaciology* 39, pp. 495–500.

Hagedorn, B., Sletten, R.S., and Hallet, B. 2007. 'Sublimation and ice condensation in hyperarid soils: modeling results using field data from Victoria Valley, Antarctica', *Journal of Geophysical Research: Earth Surface* 112(F3).

Hagedorn, B., Sletten, R.S., Hallet, B., McTigue, D.F., and Steig, E.J. 2010. 'Ground ice recharge via brine transport in frozen soils of Victoria Valley, Antarctica: Insights from modeling δ18O and δD profiles', *Geochimica et Cosmochimica Acta* 74(2), pp. 435–448.

Harris, C. and Murton, J.B. 2005. 'Interactions between glaciers and permafrost: an introduction', in C. Harris and J.B. Murton (eds.), *Cryospheric systems: glaciers and permafrost*. Geological Society of London, Special Publications, 242, pp. 1–9.

Harris, S.A., French, H.M., Heginbottom, J.A., Johnston, G.H., Ladanyi, B., Sego, D.C., and van Everdingen, R.O. 1988. 'Glossary of Permafrost and Related Ground-Ice Terms', *National Research Council of Canada* Technical Memorandum 142.

Heldmann, J., Marinova, M., Williams, K., Lacelle, D., McKay, C., Davila, A., Pollard, W., and Andersen, D. 2012. 'Formation and evolution of buried snowpack deposits in Pearse Valley, Antarctica, and implications for Mars', *Antarctic Science* 24(3), pp. 299–316.

Hindmarsh, R., Van der Wateren, F., and Verbers, A.L. 1998. 'Sublimation of ice through sediment in Beacon Valley, Antarctica', *Geografiska Annaler: Series A, Physical Geography* 80(3-4), pp. 209–219.

Hrbáček, F., Oliva, M., Hansen, C., Balks, M., O'Neill, T. A., de Pablo, M.A., Ponti, S., Ramos, M., Vieira, G., and Abramov, A. 2023. 'Active layer and permafrost thermal regimes in the ice-free areas of Antarctica', *Earth-Science Reviews*, 104458.

Kotze, C. and Meiklejohn, I. 2017. 'Temporal variability of ground thermal regimes on the northern buttress of the Vesleskarvet nunatak, western Dronning Maud Land, Antarctica', *Antarctic Science* 29(1), pp. 73–81.

Lacelle, D., Davila, A. F., Fisher, D., Pollard, W.H., DeWitt, R., Heldmann, J., Marinova, M.M., and McKay, C.P. 2013. 'Excess ground ice of condensation–diffusion origin in University Valley, Dry Valleys of Antarctica: Evidence from isotope geochemistry and numerical modeling', *Geochimica et Cosmochimica Acta* 120, pp. 280–297.

Lacelle, D., Davila, A.F., Pollard, W.H., Andersen, D., Heldmann, J., Marinova, M., and McKay, C.P. 2011. 'Stability of massive ground ice bodies in University Valley, McMurdo Dry Valleys of Antarctica: Using stable O–H isotope as tracers of sublimation in hyper-arid regions', *Earth and Planetary Science Letters* 301(1–2), pp. 403–411.

Lacelle, D., Fisher, D.A., Verret, M., and Pollard, W. 2022. 'Improved prediction of the vertical distribution of ground ice in Arctic-Antarctic permafrost sediments', *Communications Earth & Environment* 3(1), p. 31.

Lacelle, D., Lapalme, C., Davila, A.F., Pollard, W., Marinova, M., Heldmann, J., and McKay, C.P. 2016. 'Solar radiation and air and ground temperature relations in the cold and hyper-arid Quartermain Mountains, McMurdo Dry Valleys of Antarctica', *Permafrost and Periglacial Processes* 27(2), pp. 163–176.

Lacelle, D., Verret, M., Faucher, B., Fisher, D., Gaudreau, A., Pellerin, A., Ecclestone, M., and Andersen, D. (in press). 'Permafrost and ground ice conditions in the Untersee Oasis, Queen Maud Land, East Antarctica', *Antarctic Science*.

Lapalme, C., Lacelle, D., Pollard, W., Fisher, D., Davila, A., and McKay, C.P. 2017. 'Distribution and origin of ground ice in University Valley, McMurdo Dry Valleys, Antarctica', *Antarctic Science* 29(2), pp. 183–198.

Levy, J.S., Fountain, A.G., Dickson, J.L., Head, J.W., Okal, M., Marchant, D.R., and Watters, J. 2013. 'Accelerated thermokarst formation in the McMurdo Dry Valleys, Antarctica', *Scientific reports* 3(1), 2269.

Levy, J.S., Fountain, A.G., Gooseff, M.N., Welch, K.A., and Lyons, W.B. 2011. 'Water tracks and permafrost in Taylor Valley, Antarctica: Extensive and shallow groundwater connectivity in a cold desert ecosystem', *GSA Bulletin* 123(11–12), pp. 2295–2311.

Li, X., Liu, X., Ju, Y., and Huang, F. 2003. 'Properties of soils in Grove Mountains, East Antarctica', *Science in China Series D: Earth Sciences* 46, pp. 683–693.

MacNamara, E. 1969. 'Biological research opportunities at the Soviet antarctic station Molodezhnaya', *Antarctic Journal of the United States* 4(3), pp. 8–12.

Marchant, D., Lewis, A.R., Phillips, W.M., Moore, E., Souchez, R., Denton, G.H., Sugden, D., Potter Jr, N., and Landis, G.P. 2002. 'Formation of patterned ground and sublimation till over Miocene glacier ice in Beacon Valley, southern Victoria Land, Antarctica', *Geological Society of America Bulletin* 114(6), pp. 718–730.

Marchant, D.R. and Head III, J.W. 2007. 'Antarctic Dry Valleys: Microclimate zonation, variable geomorphic processes, and implications for assessing climate change on Mars', *Icarus* 192(1), pp. 187–222.

Marinova, M.M., McKay, C.P., Pollard, W.H., Heldmann, J.L., Davila, A.F., Andersen, D.T., Jackson, W.A., Lacelle, D., Paulsen, G., and Zacny, K. 2013. 'Distribution of depth to ice-cemented soils in the high-elevation Quartermain Mountains, McMurdo Dry Valleys, Antarctica', *Antarctic Science* 25(4), pp. 575–582.

Matsuoka, N., Moriwaki, K., Iwata, S., and Hirakawa, K. 1990. 'Ground temperature regimes and their relation to periglacial processes in the Sør Rondane Mountains, East Antarctica', *Proceedings of the National Institute of Polar Research Symposium on Antarctic Geosciences* 4, pp. 55–66.

McKay, C.P., Balaban, E., Abrahams, S., and Lewis, N. 2019. 'Dry permafrost over ice-cemented ground at Elephant Head, Ellsworth Land, Antarctica', *Antarctic Science* 31(5), pp. 263–270.

McKay, C.P., Mellon, M.T., and Friedmann, E.I. 1998. 'Soil temperatures and stability of ice-cemented ground in the McMurdo Dry Valleys, Antarctica', *Antarctic Science* 10(1), pp. 31–38.

McLeod, M., Balks, M., and Bockheim, J.G. 2004–2007. 'Antarctic Soils Database', *Manaaki Whenua - Landcare Research* Reports post 2005. Available at: https://soils.landcareresearch.co.nz/topics/soil-data/antarctic-soil-data/reports-post-2005/ (Accessed 03.08.2023).

Mellon, M.T., McKay, C.P., and Heldmann, J.L. 2014. 'Polygonal ground in the McMurdo Dry Valleys of Antarctica and its relationship to ice-table depth and the recent Antarctic climate history', *Antarctic Science* 26(4), pp. 413–426.

Muller, S.W. 1945. *Permafrost, Or Permanently Frozen Ground: And Related Engineering Problems*. Army map service, US Army.

Pewe, T.L. 1959. 'Sand-wedge polygons (tesselations) in the McMurdo Sound region, Antarctica; a progress report', *American Journal of Science* 257(8), pp. 545–552.

Porter, T.J. and Opel, T. 2020. 'Recent advances in paleoclimatological studies of Arctic wedge-and pore-ice stable-water isotope records' *Permafrost and Periglacial Processes* 31(3), pp. 429–441.

Raffi, R. and Stenni, B. 2011. 'Isotopic composition and thermal regime of ice wedges in northern Victoria Land, East Antarctica' *Permafrost and Periglacial Processes* 22(1), pp. 65–83.

Schiller, M., Dickinson, W., Iverson, N., and Baker, J. 2019. 'A re-evaluation of the Hart Ash, an important stratigraphic marker: Wright Valley, Antarctica', *Antarctic Science* 31(3), pp. 139–149.

Schorghofer, N. and Aharonson, O. 2005. 'Stability and exchange of subsurface ice on Mars', *Journal of Geophysical Research: Planets* 110(E5).

Shur, Y., Hinkel, K.M., and Nelson, F.E. 2005. 'The transient layer: implications for geocryology and climate-change science', *Permafrost and Periglacial Processes* 16(1), pp. 5–17.

Smoluchowski, R. 1968. 'Mars: Retention of ice', *Science* 159(3821), pp. 1348–1350.

Stuiver, M., Yang, I.C., and Denton, G.H. 1976. 'Permafrost oxygen isotope ratios and chronology of three cores from Antarctica', *Nature* 261(5561), pp. 547–550.

Swanger, K.M. 2017. 'Buried ice in Kennar Valley: a late Pleistocene remnant of Taylor Glacier', *Antarctic Science* 29(3), pp. 239–251.

Swanger, K.M., Babcock, E., Winsor, K., and Valletta, R.D. 2019. 'Rock glaciers in Pearse Valley, Antarctica record outlet and alpine glacier advance from MIS 5 through the Holocene', *Geomorphology* 336, pp. 40–51.

Swanger, K.M., Marchant, D.R., Kowalewski, D.E., and Head III, J.W. 2010. 'Viscous flow lobes in central Taylor Valley, Antarctica: origin as remnant buried glacial ice', *Geomorphology* 120(3–4), pp. 174–185.

Toner, J.D. and Sletten, R.S. 2013. 'The formation of Ca-Cl-rich groundwaters in the Dry Valleys of Antarctica: Field measurements and modeling of reactive transport', *Geochimica et Cosmochimica Acta* 110, pp. 84–105.

Verret, M., Dickinson, W., Lacelle, D., Fisher, D., Norton, K., Chorley, H., Levy, R., and Naish, T. 2021. 'Cryostratigraphy of mid-Miocene permafrost at Friis Hills, McMurdo Dry Valleys of Antarctica', *Antarctic Science* 33(2), pp. 174–188.

Verret, M., Trinh-Le, C., Dickinson, W., Norton, K., Lacelle, D., Christl, M., Levy, R., and Naish, T. 2023. 'Late Miocene onset of hyper-aridity in East Antarctica indicated by meteoric beryllium-10 in permafrost', *Nature Geoscience* 16, pp. 492–498.

Vtyurin, B. 1986. 'A geocryological account of the Schirmacher Oasis', *Polar Geography* 10(3), pp. 200–212.

Ward, S.H., Jiracek, G.R., and Linlor, W.I. 1969. 'Some factors affecting electromagnetic detection of lunar subsurface water', *IEEE Transactions on Geoscience Electronics* 7(1), pp. 19–27.

Winsor, K., Swanger, K.M., Babcock, E., Valletta, R.D., and Dickson, J.L. 2020. 'Rock glacier characteristics serve as an indirect record of multiple alpine glacier advances in Taylor Valley, Antarctica', *The Cryosphere* 14(1), pp. 1–16.

Wlostowski, A., Gooseff, M., McKnight, D., and Lyons, W. 2018. 'Transit times and rapid chemical equilibrium explain chemostasis in glacial meltwater streams in the McMurdo Dry Valleys, Antarctica', *Geophysical Research Letters* 45(24), pp. 13,322–313,331.

Wolff, E., Barbante, C., Becagli, S., Bigler, M., Boutron, C., Castellano, E., De Angelis, M., Federer, U., Fischer, H., and Fundel, F. 2010. 'Changes in environment over the last 800,000 years from chemical analysis of the EPICA Dome C ice core', *Quaternary Science Reviews* 29(1–2), pp. 285–295.

Yan, Y., Bender, M.L., Brook, E.J., Clifford, H.M., Kemeny, P.C., Kurbatov, A.V., Mackay, S., Mayewski, P.A., Ng, J., and Severinghaus, J.P. 2019. 'Two-million-year-old snapshots of atmospheric gases from Antarctic ice', *Nature* 574(7780), pp. 663–666.

Yau, A.M., Bender, M.L., Marchant, D.R., and Mackay, S.L. 2015. 'Geochemical analyses of air from an ancient debris-covered glacier, Antarctica', *Quaternary Geochronology* 28, pp. 29–39.

Experimental study on the freezing/thawing characteristic curves of sand/clay mixtures

Quoc-Hung Vu, Anh-Minh Tang & Jean-Michel Pereira

Laboratoire Navier, École des Ponts, Université Gustave Eiffel, CNRS, Marne-la-Vallée, France

ABSTRACT

The soil freezing characteristic curve (SFCC), relating temperature and unfrozen water content, is essential in modelling hydro-thermal processes in permafrost. In this study, the SFCC of sand/clay mixtures, with clay content varying from 0 to 20%, was determined. Compacted soil samples were first subjected to a freezing path (temperature decreasing from 0 °C to -3 °C) followed by a subsequent thawing path (temperature increasing from -3 °C to 0 °C). During this freezing/thawing cycle, volumetric unfrozen water content was measured as a function of soil temperature. The results show a significant hysteresis of the relationship between these two parameters. This finding is important because the hysteresis of SFCC is rarely considered in the modelling of hydro-thermal processes in permafrost. In addition, clear effects of clay content on the thawing curve were identified. At a given temperature, volumetric unfrozen water increases with clay content. Finally, a model predicting the SFCC of sandy soils was introduced, considering the effect of clay content.

1 INTRODUCTION

More than 20% of the world's land surface is underlain by permafrost, particularly in Russia, Canada and China (French 2007). With diverse human activities in cold regions such as mining, oil exploitation, construction, etc., freezing-thawing processes in frozen soils cause geotechnical engineering problems including damage to pavements and existing foundation structures, etc.

Frozen soil consists of mineral particles, liquid water, ice and gases (air and water vapour). The freezing process, when a fraction of liquid water solidifies into ice at temperatures sufficiently below 0 °C (Andersland and Ladanyi 1994), causes significant modifications of the physical-hydraulic-mechanical properties of soils (Andersland and Ladanyi 2004). The freezing-thawing process is usually the main cause of frost heave and thaw settlement inducing damages to infrastructure in permafrost of cold regions (Russo et al. 2015; Han et al. 2016; Zhang et al. 2016a; Yu et al. 2020). Interested readers are referred to Bordignon (2020) for a scientometric review of permafrost research with a focus on infrastructure vulnerability.

The Soil Freezing Characteristic Curve (SFCC) represents the relationship between the temperature and the quantity of liquid water in the soil. It is one of the most essential data in studying the hydro-thermal behaviour of permafrost. In general, the SFCC can be described using empirical models or derived from the Soil Water Retention Curve (SWRC) or a thermodynamic approach. In the first approach, different empirical models have been determined experimentally using power, piecewise or exponential functions (Anderson and Tice 1972; Tice et al. 1976; Ye et al. 2007; Kozlowski 2007; Ge et al. 2011; Kozlowski and Nartowska 2013; He et al. 2020; Teng et al. 2021). The second approach is based on the theoretical similarity between freezing-thawing and drying-wetting processes that is illustrated by Clausius-Clapeyron equation (Zhang et al. 2007, 2016b; Dall'Amico 2010; Sheshukov and Nieber 2011; Liu and Yu 2013; Zhou et al. 2019; Teng et al. 2020; Li and Vanapalli 2023). The two approaches capture the effects of supercooling, hysteresis, pore blocking, capillarity, free energy barriers, contact angles and electrolytes (Bittelli et al. 2003; Li et al. 2020). However, aside from a few models (e.g., Zhou et al. 2019), most of the existing SFCCs consider a unique relationship between unfrozen water content and temperature and ignore hysteresis effects (i.e., different paths between freezing and thawing).

SFCC can be determined in the laboratory by subjecting a soil specimen to a freeze-thaw cycle. Different methods can be used to measure unfrozen water content at negative temperatures such as dilatometry (Koopmans and Miller 1966; Patterson and Smith 1981), gas dilatometry (Spaans and Baker 1995), adiabatic calorimetry (Kolaian and Low 1963; Anderson and Tice 1973), isothermal calorimetry (Tice et al. 1976), differential scanning calorimetry (Yong et al. 1979; Kozlowski 2003, 2004), X-ray diffraction (Anderson and Hoekstra 1965; Anderson and Morgenstern 1973), time/frequency domain reflectometry (TDR/FDR; Stähli and Stadler 1997; Zhou et al. 2014; Schafer and Beier 2020) and pulsed nuclear magnetic resonance (P-NMR; Tice et al. 1981; Watanabe and Mizoguchi 2002; Li et al. 2020).

It is found that the shape of SFCC depends on several factors, including liquid limit (Tice et al. 1976), stress condition (Mu et al. 2019), salt content and solute types (Ming et al. 2020), initial water content or degree of saturation (Jia et al. 2019), types of soil (Zhang et al. 2020), and fines content (Tian et al. 2014). Among these factors, fines content can influence others (liquid limit, pore-size distribution and types of soil). As far as fines content is concerned, by determining the unfrozen water content of several clays, a silt and a gravel, Tice et al. (1976) observed significantly different unfrozen water contents at the same temperature below 0 °C. Tian et al. (2014) carried out tests on three soils corresponding to three clay contents and found that the unfrozen water degree of saturation also changed in different ways in both freezing and thawing processes. For soils containing higher clay fraction, unfrozen water degree of saturation was higher at any given

https://doi.org/10.52381/ICOP2024.223.1

temperature below the freezing point and the hysteresis loop was smaller.

The present study aims to investigate the effects of clay content on the SFCC of sandy soils. Sandy soils with clay content of 0, 5, 10, 15, and 20% were compacted and saturated. The specimens were then subjected to freezing and thawing paths in undrained conditions. During this freezing-thawing cycle, the soil's temperature and unfrozen water content were measured.

2 MATERIALS AND EXPERIMENTAL METHODS

2.1 Materials

Fontainebleau sand and Speswhite kaolin clay (physical properties shown in Table 1) were mixed in a dry state, using an automatic mixer, to obtain five sand/clay mixtures with different clay contents varying from 0 to 20%. The two materials were chosen because their hydro-mechanical properties have been widely investigated (Boussaid 2005). Figure 1 shows the grain size distribution curves of the five mixtures: S0, S5, S10, S15, and S20 (e.g., S10 corresponds to 10% of clay and 90% of sand in dry mass). Then, distilled water was added to the mixtures to reach their optimum water content, as determined from the Standard Proctor compaction curve obtained for the same soil compositions (Boussaid 2005). Wet soil was finally left to equilibrate in a plastic bag for at least 24 hours before compaction in a cylindrical cell using a Proctor rammer to the maximum dry density. The tested soil properties are shown in Table 2.

Table 1. Physical properties of Speswhite kaolin clay and Fontainebleau sand (Boussaid 2005).

Property	Speswhite kaolin clay	Fontainebleau sand
Median grain size, D_{50} (mm)	-	0.21
Uniformity coefficient, C_U	-	1.52
Minimum void ratio, e_{min}	-	0.54
Maximum void ratio, e_{max}	-	0.94
Particle density, ρ_{soslid} (Mg/m³)	2.65	2.65
Minimum dry density, $\rho_{d,min}$ (Mg/m³)	-	1.37
Maximum dry density, $\rho_{d,max}$ (Mg/m³)	1.45	1.72
Liquid limit, LL (%)	55	-
Plastic limit, PL (%)	30	-
Plasticity index, PI	25	-
Specific surface area (m²/g)	0.94	-
Particles diameter < 0.002 mm (%)	79	-
Particles diameter > 0.01 mm (%)	0.5	-

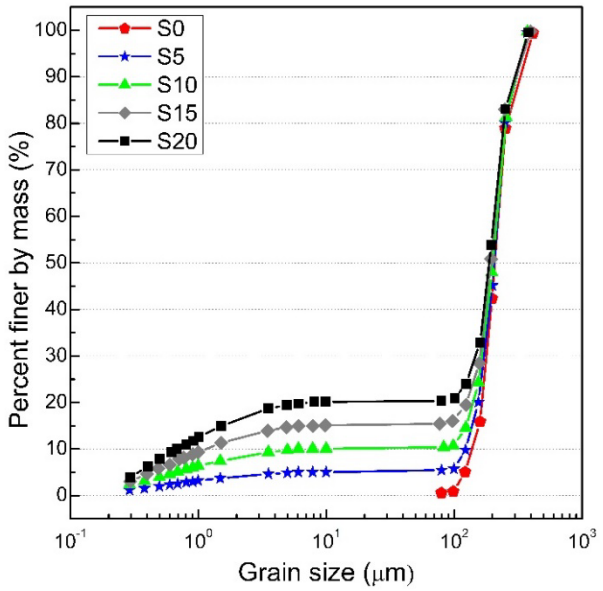

Figure 1. Grain size distribution curves of the five mixtures.

Table 2. Physical properties of tested soils.

Test No.	Clay content (%)	Water content at compaction (%)	Dry density, ρ_d (Mg/m³)	Porosity, n (-)
S20	20	11.2	1.98	0.25
S15	15	9.1	1.99	0.25
S10	10	8.0	1.91	0.28
S5	5	7.0	1.78	0.33
S0	0	5.6	1.67	0.37

2.2 Experimental setup and procedure

The experimental setup is shown in Figure 2. A soil specimen was confined in a rigid metallic cylindrical cell (150 mm in height and 150 mm in diameter). Four sensors (properties in Table 3) measuring the soil thermal conductivity (KD2-Pro), suction (T5x), temperature (PT100) and water content (ThetaProbe ML2x) were installed. The cell was submerged in a temperature-controlled bath (F38-EH JULABO with ±0.03 °C in accuracy). As Thetaprobe sensor measures soil apparent dielectric constant (K_a) which is the ratio of the dielectric permittivity of a substance to that of vacuum, soil volumetric unfrozen water content (θ_w) was estimated from the measured K_a by using empirical Equation 1 (Smith and Tice 1988) and Equation 2 (Topp et al. 1980) for frozen and unfrozen soils, respectively. Equation 1 was used where ice is expected to exist in soil (i.e., after the occurrence of freezing and before the completion of thawing). Equation 2

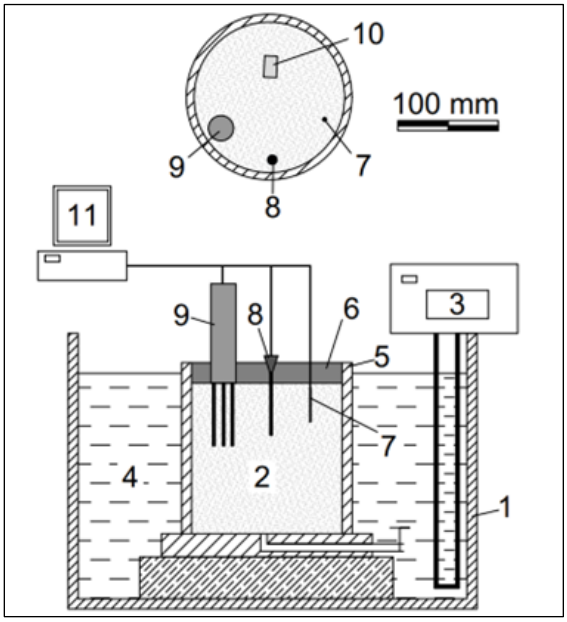

Figure 2. Schematic view of the experimental setup (Vu et al. 2022).

Table 3. Properties of sensors used in the experiments.

Measured variable	Method	Accuracy	Range
Temperature	Resistance temperature detector	±0.03 °C	-200 to 400 °C
Volumetric unfrozen water content	Time domain reflectometry (dielectric constant)	0.01 m^3/m^3	0.01 to 1 m^3/m^3

was used only for the initial state (before any freezing) and for the final state where thawing is complete.

$$\theta_u = -0.1458 + 3.868 \times 10^{-2} \times K_a - 8.502 \times 10^{-4} \times K_a^2 + 9.92 \times 10^{-6} \times K_a^3 \quad (1)$$

$$\theta_u = -5.3 \times 10^{-2} + 2.92 \times 10^{-2} \times K_a - 5.5 \times 10^{-4} \times K_a^2 + 4.3 \times 10^{-6} \times K_a^3 \quad (2)$$

After the installation of the sensors, an insulating cover made of expanded polystyrene was placed over the experimental setup to avoid heat exchange with ambient air. Then, the soil specimen was saturated by injecting water from the bottom of the specimen for 0.5 to 2 days depending on the clay content (a longer duration was required for samples with higher clay content and thus lower hydraulic conductivity). The whole system was then transferred inside the temperature-controlled bath (Figure 2). The bath temperature was first set at a temperature between 0 °C and -1 °C (slightly higher than the expected spontaneous nucleation temperature which marks the freezing process). The start of each test began with a temperature decrease from -1 °C towards -3 °C, before a temperature increase later in the test. The bath temperature was decreased in steps of 0.1 °C to freeze the soil pore water. Each temperature ramp took less than one hour to stabilize and it was held constant for several hours. Once the freezing was triggered, the temperature continued to be decreased in steps of 0.2 °C until -2 °C or -3 °C to observe the change of liquid water content during further cooling. Afterwards, during the warming path, the bath temperature was increased in steps of 0.2 °C until 0 °C to thaw the frozen soil. During both cooling and warming paths, the bath temperature was changed to the subsequent step only when soil temperature and volumetric unfrozen water content had reached an equilibrium state, considered achieved when these two quantities did not change (< 0.05 °C for temperature and < 1% for water content) during at least 2 h.

3 EXPERIMENTAL RESULTS

As an example, the results of test S10 are shown in Figure 3 where soil temperature and unfrozen water content are plotted versus elapsed time for the whole freezing and thawing path.

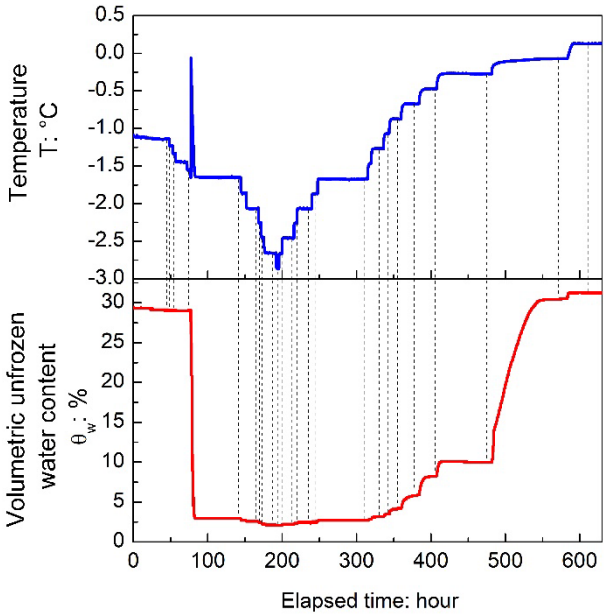

Figure 3. Soil temperature and volumetric unfrozen water content versus elapsed time of test S10.

From -1.2 °C, soil temperature was decreased in steps of 0.1 °C down to -1.6 °C. During this stage, soil temperature was controlled through the bath's temperature, and volumetric water content remained constant. When soil

temperature reached -1.6 °C, soil freezing started inducing abrupt changes in the soil temperature. The latter increased abruptly to -0.1 °C before a progressive decrease and reached the imposed temperature (-1.6 °C) again while soil water content decreased to 3%. These results are representative of the freezing process because transformation of liquid water to ice releases latent heat (Vu et al. 2022). After the freezing process, a decrease in temperature induced a slight decrease in volumetric unfrozen water content. During the warming path, temperature was increased by steps of 0.2 °C from -2.8 °C to 0 °C. It induced thawing of frozen water (corresponding to a gradual increase of unfrozen water content when compared to the freezing case).

From the results shown in Figure 3, volumetric unfrozen water content obtained at the end of each step is plotted versus the corresponding soil temperature for test S10 in Figure 4. The hysteresis, which is clearly shown in Figure 4, is significant in the temperature range of -0.1 °C to -1.6 °C.

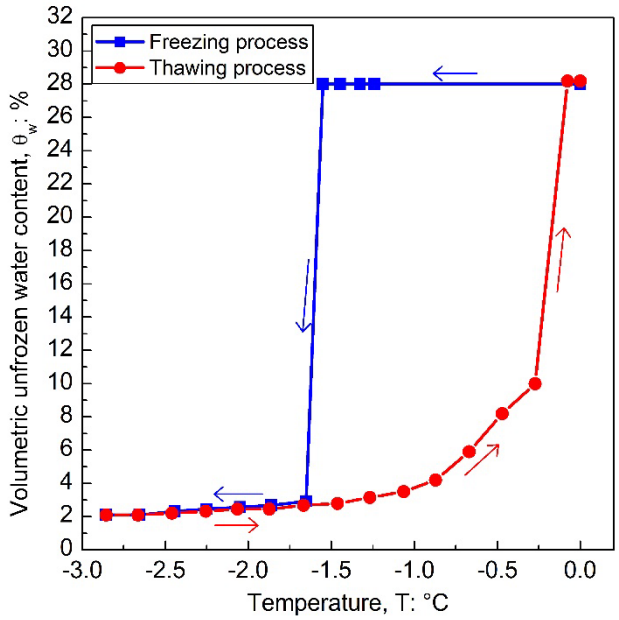

Figure 4. Soil freeing characteristic curve determined from test S10.

SFCC of all soils are plotted in Figure 5 where unfrozen water degree of saturation is plotted as a function of temperature for the thawing path. The freezing path is not analysed in this study because it depends on other factors (besides clay content) such as the test procedure. The results show that the unfrozen water degree of saturation increased gradually with thawing.

4 SFCC MODEL OF SANDY SOILS

Van Genuchten's model, which is initially proposed for the water retention curve in unsaturated unfrozen soil, allows relating cryogenic suction (s) to unfrozen water content in frozen soil as shown in Equation 3 (van Genuchten 1980; Nishimura et al. 2009):

$$S_w = \left[1 + \left(\frac{s}{\rho_r}\right)^{\frac{1}{1-\lambda_r}}\right]^{-\lambda_r} \quad (3)$$

where:

- S_w is the unfrozen water degree of saturation.
- λ_r is a fitting parameter which relates to the curvature at temperatures close to 0 °C.
- ρ_r is a fitting parameter (kPa) corresponding to the soil suction at which the residual unfrozen degree of saturation is reached. For larger values of suction, the unfrozen degree of saturation changes insignificantly.
- s is the soil suction (kPa).

To relate the temperature and soil suction, the Clausius-Clapeyron equation was used to estimate suction during thawing as follows:

$$s = L_f \rho_w \frac{T - T_f}{T_f} \quad (4)$$

where $\rho_w = 1000$ kg/m^3 is the density of water, $L_f = 334$ kJ/kg is the latent heat of fusion, $T_f = 273.15$ K is the freezing point of water, T is the soil temperature in Kelvin.

Based on the results from the thawing path in tests S0 to S20, van Genuchten model for SFCC for different soils was calibrated as shown in Figure 5. The two fitting parameters for each soil are shown in Table 4. The effect of clay content on fitting parameters of van Genuchten's model is shown in Figure 6.

Table 4: van Genuchten's model parameters.

Materials	Fitting parameter λ_r(-)	Fitting parameter ρ_r(kPa)
S0	0.46	30
S5	0.46	98
S10	0.44	126
S15	0.37	140
S20	0.33	150

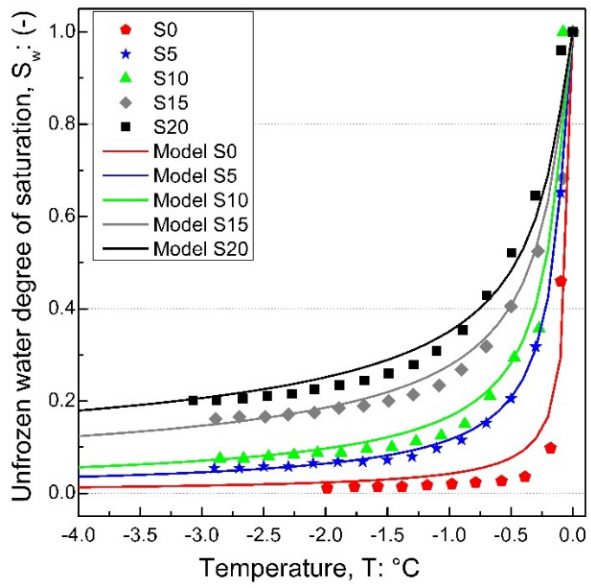

Figure 5. van Genuchten hydraulic model fitted to experimental SFCC (thawing path).

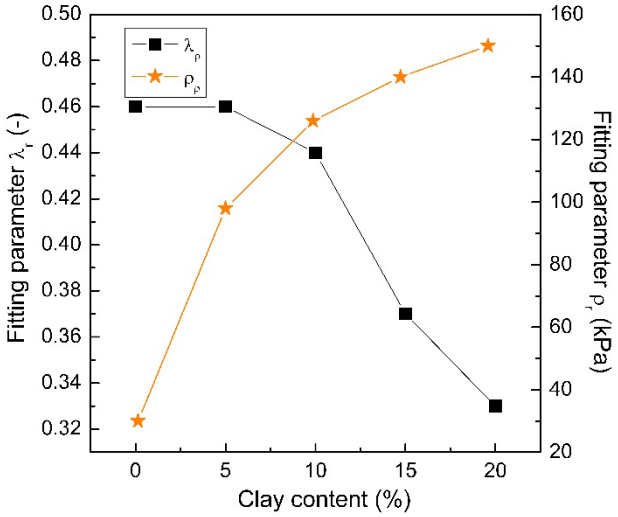

Figure 6: Effect of clay content on fitting parameters of van Genuchten's model.

5 DISCUSSION

In this study, to determine the relationship between unfrozen water content and temperature during a freezing-thawing cycle, large soil specimens (150 mm in height and 150 mm in diameter) were prepared to embed several sensors within the soil mass without interference between sensors. To minimise thermal and any other gradients, soil temperature was changed by small steps and equilibrium was checked at the end of each step prior the subsequent step. At equilibrium, the soil temperature and unfrozen water content were thus supposed to be homogeneous within the specimen.

The measurement of unfrozen water content in the present study was obtained from the measurement of the apparent dielectric constant, K_a, which is strongly dependent of temperature (Wraith and Or 1999; Haynes 2016). In this study, Topp's empirical model (Equation 2) is used for its better compatibility with unfrozen soils in comparison to the existing models in the literature (Topp et al. 1980; Roth et al. 1990; Stähli and Stadler 1997; Schafer and Beier 2020). For frozen soils, Smith and Tice (1988) proposed a model based on a comparison of unfrozen water content for 25 soils covering a wide range of specific surface areas. For this reason, in the present work, the model of Smith and Tice (1988; equation 1), which provides an accuracy of ±3%, compared to experimental data, was used for frozen soils.

Residual unfrozen water degree of saturation (value corresponding to lowest temperature in Figure 5) was observed to increase with clay content. Increasing clay content induces an increase in the amount of specific surface of soils (Tian et al. 2014). When freezing is triggered, only free water is frozen (Bing and Ma 2011). Residual unfrozen water should then correspond to bound water. According to Tian et al. (2014), the amount of bound water in soils is proportional to the thickness of the electric double layer and the specific surface area. In the present study, a higher clay content corresponds to a higher specific surface area and an associated increase in bound water.

Hysteresis of SFCC (difference between the freezing and the thawing curves) is usually attributed to the same factors inducing hysteresis in SWCC, such as the effect of electrolytes, pore geometry, pore blocking, effect of contact angle and change in pore structure (Ren and Vanapalli 2019). In this study, the hysteresis was observed only above the temperature of spontaneous nucleation (at -1.6 °C for the test S10). Supercooling, the process of lowering the temperature of a liquid below its freezing point without phase change, could mainly contribute to hysteresis due to the absence of electrolytes.

Figure 5 demonstrates a significant effect of clay content on the thawing path of SFCC. Actually, at a given temperature, a higher unfrozen water degree of saturation was obtained at a higher clay content. These results are consistent with the findings of previous works (Tice et al. 1976; Tian et al. 2014; Zhang et al. 2020; Li et al. 2020). Following these studies, Gibbs-Thompson equation which presents the thermodynamic treatment of the solid/liquid transition in confined pores can be used to relate the pore size distribution and the thawing path of SFCC; a lower temperature corresponds to a smaller pore (Vu et al. 2023). In this study, soil having higher clay content would have a larger volume of micropores (inter-aggregates and intra-aggregates pores) and consequently a lower volume of macropores (space between sand particles).

van Genuchten model with two parameters corresponding to the residual unfrozen water degree of saturation and the curvature at temperatures close to 0 C can predict well the SFCC of sandy soils with varying clay content in the thawing path. However, the hysteresis could not be captured by the model as well as the existing models in literature due to the abrupt decrease of unfrozen water degree of saturation at freezing temperature along the freezing path.

The results of this work reveal the role of fines content on soil freezing characteristic curve. Results shown in Figure 6

would help to better choose parameters of van Genuchten's model when clay fines content is known.

6 CONCLUSIONS

The results obtained in this study show that clay content in sandy soils significantly influenced the SFCC along the thawing path. The freezing path was not presented because it is influenced by other factors such as the test procedure. Based on the investigation of five levels of clay content (varying from 0 to 20%), the following conclusions can be drawn:

- The hysteresis of SFCC in sandy soils is mainly due to supercooling.
- The SFCC along a thawing path is significantly influenced by clay content.
- The SFCC along the thawing path of five soils with increasing clay content from 0% to 20% can be well predicted by van Genuchten model. The model could not capture SFCC in freezing path due to an abrupt change of unfrozen water content at freezing temperature.

7 REFERENCES

Andersland, O.B. and Ladanyi, B. 1994. 'An Introduction to Frozen Ground Engineering', in *An Introduction to Frozen Ground Engineering*. Springer Science & Business Media.

Andersland, O.B. and Ladanyi, B. 2004. *Frozen Ground Engineering*. John Wiley & Sons.

Anderson, D.M.and Hoekstra, P. 1965. 'Migration of interlamellar water during freezing and thawing of Wyoming bentonite', *Soil Science Society of America Journal* 29(5), pp. 498–504. doi:10.2136/sssaj1965.03615995002900050010x.

Anderson, D.M. and Morgenstern, N.R. 1973. 'Physics, chemistry, and mechanics of frozen ground: a review', in *Permafrost: North American Contribution [to The] Second International Conference*. Washington, DC, United States.

Anderson, D.M. and Tice, A.R. 1972. 'Predicting unfrozen water contents in frozen soils from surface area measurements', *Highway Research Record* 393(2), pp. 12–18.

Anderson, D.M. and Tice, A.R. 1973. 'The unfrozen interfacial phase in frozen soil water systems', in A. Hadas, D. Swartzendruber, P.E. Rijtema, M. Fuchs and B. Yaron (eds.), *Physical aspects of soil water and salts in ecosystems*. Heidelberg, Germany: Springer-Verlag Berlin Heidelberg, pp. 107–124.

Bing, H. and Ma, W. 2011. 'Laboratory investigation of the freezing point of saline soil', *Cold Regions Science and Technology* 67(1–2), pp. 79–88. doi:10.1016/j.coldregions.2011.02.008.

Bittelli, M., Flury, M., and Campbell, G.S. 2003. 'A thermodielectric analyzer to measure the freezing and moisture characteristic of porous media', *Water Resources Research* 39(2).

Bordignon, F. 2021. 'A scientometric review of permafrost research based on textual analysis (1948–2020)', *Scientometrics* 126, pp. 417–436. doi:10.1007/s11192-020-03747-4.

Boussaid, K. 2005. *Sols intermédiaires pour la modélisation physique : application aux fondations superficielles*. PhD thesis, École Centrale de Nantes et Université de Nantes.

Dall'Amico, M. 2010. *Coupled water and heat transfer in permafrost modeling*. PhD thesis, Faculty of Engineering, University of Trento.

French, H.M. 2007. *The periglacial environment*. Third Edition. John Wiley & Sons.

Ge, S., McKenzie, J., Voss, C., and Wu, Q. 2011. 'Exchange of groundwater and surface-water mediated by permafrost response to seasonal and long term air temperature variation', *Geophysical Research Letters* 38(14), pp. 1–6. doi:10.1029/2011GL047911.

Van Genuchten, M.Th. 1980. 'A Closed-form Equation for Predicting the Hydraulic Conductivity of Unsaturated Soils', *Soil Science Society of America Journal* 44(5), pp. 892–898. doi:10.2136/sssaj1980.03615995004400050002x.

Han, L., Ye, G., Li, Y., Xia, X., and Wang, J. 2016. 'In situ monitoring of frost heave pressure during cross passage construction using ground-freezing method', *Canadian Geotechnical Journal* 53(3), pp. 530–539. doi:10.1139/cgj-2014-0486.

Haynes, W.M. (ed.) 2016. *CRC Handbook of Chemistry and Physics*. 97th edition. Boca Raton, Florida, United States: CRC press.

He, Z., Teng, J., Yang, Z., Liang, L., Li, H., and Zhang, S. 2020. 'An analysis of vapour transfer in unsaturated freezing soils', *Cold Regions Science and Technology* 169(68), 102914. doi:10.1016/j.coldregions.2019.102914.

Jia, H., Ding, S., Wang, Y. et al. 2019. 'An NMR-based investigation of pore water freezing process in sandstone', *Cold Regions Science and Technology* 168, 102893. doi:10.1016/j.coldregions.2019.102893

Kolaian, J.H. and Low, P.F. 1963. 'Calorimetric determination of unfrozen water in montmorillonite pastes', *Soil Science* 95(6), pp. 376–384.

Koopmans, R.W.R. and Miller, R.D. 1966. 'Soil freezing and soil water characteristic curves', *Soil Science Society of America Journal* 30(6), pp. 680–685.

Kozlowski, T. 2003. 'A comprehensive method of determining the soil unfrozen water curves', *Cold Regions Science and Technology* 36(1–3), pp. 71–79. doi:10.1016/S0165-232X(03)00007-7.

Kozlowski, T. 2004. 'Soil freezing point as obtained on melting', *Cold Regions Science and Technology* 38(2–3), pp. 93–101. doi:10.1016/j.coldregions.2003.09.001.

Kozlowski, T. 2007. 'A semi-empirical model for phase composition of water in clay–water systems', *Cold Regions Science and Technology* 49(3), pp. 226–236. doi:10.1016/j.coldregions.2007.03.013.

Kozlowski, T. and Nartowska, E. 2013. 'Unfrozen Water Content in Representative Bentonites of Different Origin Subjected to Cyclic Freezing and Thawing', *Vadose Zone Journal* 12(1). doi:10.2136/vzj2012.0057.

Li, Z., Chen, J., and Sugimoto, M. 2020. 'Pulsed NMR Measurements of Unfrozen Water Content in Partially Frozen Soil', *Journal of Cold Regions Engineering* 34(3), 04020013. doi:10.1061/(ASCE)CR.1943-5495.0000220.

Liu, Z. and Yu, X. 2013. 'Physically Based Equation for Phase Composition Curve of Frozen Soils', *Journal of the Transportation Research Board* 2349(1), pp. 93–99. doi:10.3141/2349-11.

Li, Y. and Vanapalli, S.K. 2023. 'Equations for soil freezing characteristics curves based on the thermodynamics principles', *Geoderma* 439, 11644. doi:10.1016/j.geoderma.2023.116644

Ming, F., Chen, L., Li, D. and Du, C. 2020. 'Investigation into freezing point depression in soil caused by NaCl solution', *Water* 12, 2232. doi:10.3390/w12082232

Mu, Q.Y., Zhou, C., Ng. C.W.W., and Zhou, G.G.D. 2019. 'Stress effects on soil freezing characteristic curve: equipment development and experimental results', *Vadose Zone Journal* 18(1), pp. 1–10. doi:10.2136/vzj2018.11.0199

Nishimura, S., Gens, A., Olivella, S., and Jardine, R.J. 2009. 'THM-coupled finite element analysis of frozen soil: Formulation and application', *Geotechnique* 59(3), pp. 159–171. doi:10.1680/geot.2009.59.3.159.

Patterson, D.E. and Smith, M.W. 1981. 'The measurement of unfrozen water content by time domain reflectometry: results from laboratory tests', *Canadian Geotechnical Journal* 18(1), pp. 131–144. doi:10.1139/t81-012.

Ren, J. and Vanapalli, S.K. 2019. 'Comparison of Soil-Freezing and Soil-Water Characteristic Curves of Two Canadian Soils', *Vadose Zone Journal* 18(1), pp. 1–14. doi:10.2136/vzj2018.10.0185.

Roth, K., Schulin, R., Fluhler, H., and Attinger, W. 1990. 'Calibration of time domain reflectometry for water content measurement using a composite dielectric approach', *Water Resources Research*, 26(10), pp. 2267–2273.

Russo, G., Corbo, A., Cavuoto, F., and Autuori, S. 2015. 'Artificial Ground Freezing to excavate a tunnel in sandy soil. Measurements and back analysis', *Tunnelling and Underground Space Technology* 50, pp. 226–238. doi:10.1016/j.tust.2015.07.008.

Schafer, H. and Beier, N. 2020. 'Estimating soil-water characteristic curve from soil-freezing characteristic curve for mine waste tailings using time domain reflectometry', *Canadian Geotechnical Journal* 57(1), pp. 73–84. doi:10.1139/cgj-2018-0145.

Sheshukov, A.Y. and Nieber, J.L. 2011. 'One-dimensional freezing of nonheaving unsaturated soils: Model formulation and similarity solution', *Water Resources Research* 47(11), pp. 1–17. doi:10.1029/2011WR010512.

Smith, M.W. and Tice, A.R. 1988. 'Measurement of the unfrozen water content of soils: comparison of NMR and TDR methods', *Cold Regions Research and Engineering Laboratory* CRREL Report 88-18.

Spaans, E.J.A and Baker, J.M. 1995. 'Examining the use of time domain reflectometry for measuring liquid water content in frozen soil', *Water Resources Research* 31(12), pp. 2917–2925. doi:10.1029/95WR02769.

Stähli, M. and Stadler, D. 1997. 'Measurement of water and solute dynamics in freezing soil columns with time domain reflectometry', *Journal of Hydrology* 195(1–4), pp. 352–369. doi:10.1016/S0022-1694(96)03227-1.

Teng, J., Kou, J., Yan, X., Zhang, S., and Sheng, D. 2020. 'Parameterization of soil freezing characteristic curve for unsaturated soils', *Cold Regions Science and Technology* 170(68), 102928. doi:10.1016/j.coldregions.2019.102928.

Teng, J., Zhong, Y., Zhang, S., and Sheng, D. 2021. 'A mathematic model for the soil freezing characteristic curve: the roles of adsorption and capillarity', *Cold Regions Science and Technology* 181(68), 103178. doi:10.1016/j.coldregions.2020.103178.

Tian, H., Wei, C., Wei, H., and Zhou, J. 2014. 'Freezing and thawing characteristics of frozen soils: Bound water content and hysteresis phenomenon', *Cold Regions Science and Technology* 103, pp. 74–81. doi:10.1016/j.coldregions.2014.03.007.

Tice, A.R., Anderson, D.M., and Banin, A. 1976. 'The prediction of unfrozen water contents in frozen soils from liquid limit determinations', *Cold Regions Research and Engineering Laboratory* CRREL Report 76-8.

Tice, A.R., Anderson, D.M., and Sterrett, K.F. 1981. 'Unfrozen water contents of submarine permafrost determined by nuclear magnetic resonance' *Engineering Geology* 18(1–4), pp. 135–146.

Topp, G.C., Davis, J.L., and Annan, A.P. 1980. 'Electromagnetic determination of soil water content: Measurements in coaxial transmission lines', *Water Resources Research* 16(3), pp. 574–582.

Vu, Q.H., Pereira, J.M., and Tang, A.M. 2022. 'Effect of fines content on soil freezing characteristic curve of sandy soils', *Acta Geotechnica* 17(11), pp. 4921–4933. Springer Berlin Heidelberg. doi:10.1007/s11440-022-01672-9.

Vu, Q.H., Pereira, J.M., and Tang, A.M. 2023. 'Water retention curve of clayey sands determined from pore structure by using various methods', *E3S Web of Conferences* 382, 09006. Available at: https://doi.org/10.1051/e3sconf/202338209006.

Watanabe, K. and Mizoguchi, M. 2002. 'Amount of unfrozen water in frozen porous media saturated with solution', *Cold Regions Science and Technology* 34(2), pp. 103–110. doi:10.1016/S0165-232X(01)00063-5.

Wraith, J.M. and Or, D. 1999. 'Temperature effects on soil bulk dielectric permittivity measured by time domain reflectometry: Experimental evidence and hypothesis development', *Water Resources Research* 35(2), pp. 361–369.

Ye, M., Pan, F., Wu, Y.-S., Hu, B.X., Shirley, C., and Yu, Z. 2007. 'Assessment of radionuclide transport uncertainty in the unsaturated zone of Yucca Mountain', *Advances in Water Resources* 30(1), pp. 118–134. doi:10.1016/j.advwatres.2006.03.005.

Yong, R.N., Cheung, CH., and Sheeran, D.E. 1979. 'Prediction of Salt Influence on Unfrozen Water Content in Frozen Soils', *Engineering Geology* 13(1–4), pp. 137–155.

Yu, W., Zhang, T., Lu, Y., Han, F., Zhou, Y., and Hu, D. 2020. 'Engineering risk analysis in cold regions: State of the art and perspectives', *Cold Regions Science and Technology* 171(December 2019), 102963. doi:10.1016/j.coldregions.2019.102963.

Zhang, H., Zhang, J., Zhang, Z., Zhang, M., and Cao, W. 2020. 'Variation behavior of pore-water pressure in warm frozen soil under load and its relation to deformation', *Acta Geotechnica* 15(3), pp. 603–614.doi:10.1007/s11440-018-0736-4.

Zhang, S., Sheng, D., Zhao, G., Niu, F., and He, Z. 2016a. 'Analysis of frost heave mechanisms in a high-speed railway embankment', *Canadian Geotechnical Journal* 53(3), pp. 520–529. doi:10.1139/cgj-2014-0456.

Zhang, S., Teng, J., He, Z., Liu, Y., Liang, S., Yao, Y., and Sheng, D. 2016b. 'Canopy effect caused by vapour transfer in covered freezing soils', *Géotechnique* 66(11), pp. 927–940. doi:10.1680/jgeot.16.P.016.

Zhang, X., Sun, S.F., and Xue, Y. 2007. 'Development and Testing of a Frozen Soil Parameterization for Cold Region Studies', *Journal of Hydrometeorology* 8(4), pp. 690–701. doi:10.1175/JHM605.1.

Zhou, X., Zhou, J., Kinzelbach, W., and Stauffer, F. 2014. 'Simultaneous measurement of unfrozen water content and ice content in frozen soil using gamma ray attenuation and TDR', *Journal of the American Water Resources Association* 5(3), 2–2. doi:10.1111/j.1752-1688.1969.tb04897.x.

Zhou, Y., Zhou, J., Shi, X., and Zhou, G. 2019. 'Practical models describing hysteresis behavior of unfrozen water in frozen soil based on similarity analysis', *Cold Regions Science and Technology* 157, pp. 215–223. doi:10.1016/j.coldregions.2018.11.002.

Assessing recent thaw and subsidence of peatland permafrost in coastal Labrador, northeastern Canada

Yifeng Wang[1], Robert G. Way[1], Antoni G. Lewkowicz[2], Rosamond Tutton[1], Jordan Beer[1], Victoria Colyn[1] & Anika Forget[1]

[1]*Northern Environmental Geoscience Laboratory, Department of Geography and Planning, Queen's University, Kingston, Ontario, Canada*

[2]*Department of Geography, Environment and Geomatics, University of Ottawa, Ottawa, Ontario, Canada*

ABSTRACT

Ground temperatures have been monitored since 2014 in four shallow boreholes (up to 5.7 m deep) drilled in palsas along the southeastern Labrador Sea coastline. This borehole network is critical for monitoring the effects of climate change on the terrestrial cryosphere and includes some of the southernmost coastal permafrost in the Northern Hemisphere. In this region, there are very few published measurements of active layer thickness, permafrost thickness, and permafrost temperatures. Mean annual ground temperatures of -1.7 to -0.7 °C at 1 m depth were surprisingly low at the beginning of the study period, given the relatively thin bodies of permafrost present (< 3 m thick). Statistically significant increases in ground temperatures were observed from 2015 to 2022 at some but not all depths in the four boreholes, despite decreases in permafrost thickness observed at all sites. Permafrost thaw resulted from both increased thaw penetration and thaw from the base of permafrost. Thaw penetration relative to the original ground surface increased by 24 to 92% due to a combination of active layer thickening and ground subsidence. Permafrost thaw at these sensitive locations may be driven by changes in mean annual air temperature, vegetation, snow dynamics, hydrology, and human disturbance. These data provide novel insights into the sensitivity of permafrost in this understudied region and can be used to validate predictive thermal modelling under future climate scenarios.

1 INTRODUCTION

Permafrost is typically present at high latitudes and/or at high elevations where mean annual air temperatures (MAAT) are usually below 0 °C. Monitoring of ground temperatures in boreholes is fundamental to understanding changes in permafrost conditions (Noetzli et al. 2021; Isaksen et al. 2022). For the past several decades, permafrost temperatures have been compiled within the Global Terrestrial Network for Permafrost, and analyses of long-term permafrost borehole records have identified global increases in mean annual ground temperatures (MAGT; Biskaborn et al. 2019). These temperature records are critical for understanding permafrost change, which can have impacts on related social, hydrological, and ecological systems (Walvoord and Kurylyk 2016; Schuur and Mack 2018; Gibson et al. 2021; Hjort et al. 2022).

Permafrost distribution in Labrador (Figure 1), northeastern Canada, ranges from continuous at high elevations and latitudes to discontinuous and isolated patches farther south (Heginbottom et al. 1995). Recent investigations identified high densities of permafrost peatlands in lowland locations along the Labrador Sea coastline that contain palsas or peat plateaus (Wang et al. 2023). They extend as far south as 51.4°N and represent some of the most equatorward occurrences of coastal permafrost globally (Dionne 1984; Wang et al. 2023). Recent unmanned aerial vehicle-based analyses have revealed that these palsas and peat plateaus are small, fragmented, and highly vulnerable to thaw (Beer et al. 2023), and this is supported by historical aerial photograph analyses that show a rapid decline of peatland permafrost area in the region (Wang et al. 2024a).

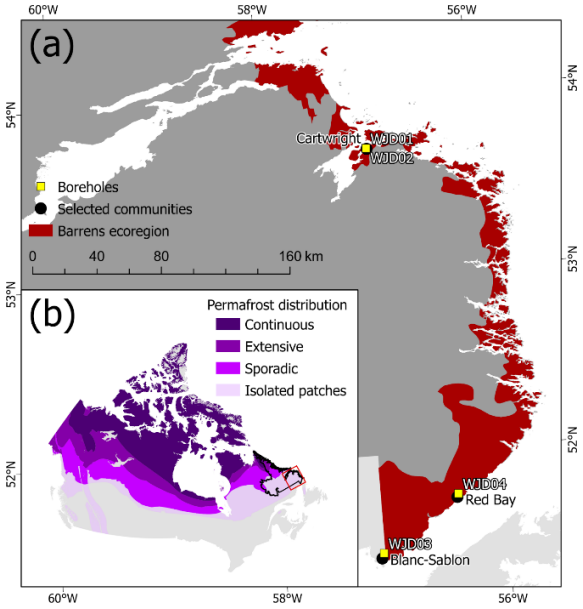

Figure 1. (a) Locations of palsa boreholes, selected communities, and the barrens ecoregion in southeastern coastal Labrador (Government of Newfoundland and Labrador 2020). (b) Inset map showing distribution of permafrost across Canada (Heginbottom et al. 1995) and location of Labrador.

Despite advances in characterizing peatland permafrost in coastal Labrador, there remains a paucity of information on ground thermal conditions and permafrost thicknesses. To reduce these observational gaps, ground temperature monitoring was started in 2014 at four palsas located

https://doi.org/10.52381/ICOP2024.155.1

between 51.5°N and 53.7°N, forming part of the only active permafrost borehole monitoring network in Labrador (Figure 1). This paper summarizes the trends observed in thaw penetration and permafrost thickness and offers the first quantification of change in ground temperatures in permafrost environments in Labrador. This paper contributes to the advancement of knowledge on permafrost as an Essential Climate Variable for the Global Climate Observing System (Smith and Brown 2009).

2 STUDY AREA

Coastal Labrador experiences long, cold winters and short, cool summers and is strongly influenced by the cold Labrador Sea current that runs south along the coast (Banfield and Jacobs 1998; Roberts et al. 2006). MAATs generally decrease with latitude from 0.6 °C at Blanc Sablon to 0.0 °C at Cartwright, and to -2.5 °C at the northernmost community of Nain, Nunatsiavut (56.5°N; 1981–2010 climate normal; Environment and Climate Change Canada 2023), and have increased by ~1.5 °C since 1881 (Way and Viau 2015). Coastal Labrador is also characterized by high amounts of precipitation (~1000 mm/year; Hare 1950; Banfield and Jacobs 1998) with snow fractions of 0.37 for Blanc-Sablon, 0.43 for Cartwright, and 0.51 for Nain (1981–2010 climate normal; Environment and Climate Change Canada 2023). Maximum snow depths occur in March, but high winds lead to significant snow redistribution across the coast's varying topography (Way and Lewkowicz 2018). Ecologically, much of coastal Labrador is classified as coastal barrens (Roberts et al. 2006), an ecosystem where trees are sparse due to a combination of both climatic and physiographic limitations (Figure 1). Wetlands are common (Mahdianpari et al. 2021), and peat thicknesses locally exceed 2 m (Séguin and Dionne 1992; Way et al. 2018). Peatland permafrost is especially concentrated in coastal lowland locations between 53°N and 55°N, where post-glacial marine incursion led to the deposition of fine-grained glaciomarine sediments (Hagedorn 2022; Wang et al. 2023). The region includes coastal portions of the Labrador Inuit Settlement Area (Nunatsiavut) in the north, a land claims agreement-in-principle by the Innu Nation in central Labrador, and areas claimed by the NunatuKavut Community Council in the south that correspond to the region examined in this study.

The four monitoring boreholes are all on small palsas (Figure 2; Table 1). WJD01 and WJD02 are within the same peatland in the community of Cartwright. The palsas measured 0.49 and 0.52 m tall in 2021, and vegetation cover is intact and up to 30 and 3 cm high, respectively (Beer et al. 2023). This peatland is subject to high levels of human disturbance, as persistent snow drifting away from the palsa mounds has led to community members storing komatiks (Inuit style sleds) on palsa surfaces through the winter and over the summer. WJD03 is the southernmost borehole and is located in a 1.24 m high palsa near the community of Blanc-Sablon, Québec. Vegetation cover at this palsa is up to 12 cm high and is largely intact, with some patches of exposed peat found in lower parts of the mound (Beer et al. 2023). WJD04 is positioned on a 0.82 m high palsa near the community of Red Bay. Peat is exposed on the majority of the palsa and vegetation, where present, is up to 4 cm high (Beer et al. 2023).

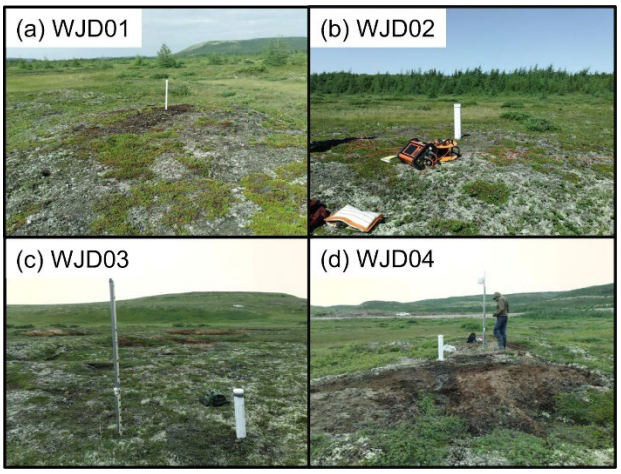

Figure 2. Field photos of the study boreholes and their surrounding conditions at the time of installation in 2014: (a) WJD01, (b) WJD02, (c) WJD03, and (d) WJD04.

Table 1. Characteristics of the coastal Labrador palsa boreholes.

Borehole	Latitude (°N), Longitude (°W), Elevation (m asl)	Mean annual air temperature (°C)[1]	Sensor depths (m)[2]	Logger type[3]	Date established (YYYY-MM-DD)
WJD01	53.71, -57.01, 11	0.5	0.25, 0.5, 1, 2.15	iB	2014-07-23
WJD02	53.71, -57.01, 14	0.5	0.5, 1.0, 2.0, 3.0, 4.25, 5.7	Hobo	2014-07-23
WJD03	51.46, -57.12, 115	0.7	0.25, 0.5, 1.0, 2.0, 3.0, 4.2	Hobo	2014-08-05
WJD04	51.76, -56.41, 75	1.1	0.25, 0.5, 1.0, 2.0, 3.0, 4.25	Hobo	2014-08-06

[1]Mean annual air temperatures were aggregated from bi-hourly measurements taken by Hobo Pro v2 Temperature/Relative Humidity U23-001 loggers from adjacent meteorological monitoring stations. Mean annual air temperatures were calculated over hydrological years (October 1-September 30) from 2015-2016 to 2021-2022 (n=7).
[2]Note that sensor depths are relative to the ground surface at the time of installation in 2014.
[3]Hobo = Hobo V2 U23-003 loggers; iB = DS1922L High Resolution Thermochron F5 iButtons.

3 METHODS

The four boreholes were drilled using the water jet technique in 2014, and the base of permafrost was reached and exceeded at three of the four locations (not at WJD01; Way et al. 2018). Boreholes were cased with PVC pipe immediately after drilling and were instrumented at four to six depths with either Hobo V2 U23-003 loggers (accuracy ± 0.2 °C; resolution ± 0.02 °C at 22 °C but > 0.02 °C at 0 °C), recording ground temperatures every 2 hours, or DS1922L High Resolution Thermochron F5 iButtons (accuracy ± 0.5 °C; resolution ± 0.0625 °C), recording ground temperatures every 4 hours (Table 1). Ground temperature records were interpolated to hourly increments using a spline and then aggregated to daily, monthly, and annual metrics for comparison between sites. Short data gaps in the ground temperature record at 5.7 m at WJD02 were infilled using cross-correlation between records from different depths in the same borehole (Way et al. 2018), but longer data gaps exist where loggers failed. Ground temperatures measured for one full hydrological year post-drilling were excluded to reduce the thermal impacts of disturbance during establishment (Way et al. 2018).

Thaw penetration depths were estimated by linearly extrapolating maximum annual ground temperatures to the depth corresponding to 0 °C using measurements from two depths within the active layer over each hydrological year (October 1 to September 30; Riseborough 2003, 2008). WJD02 lacked the two measurement depths in the active layer necessary for extrapolation, so measurements from a 0.25 m depth ground temperature logger located at an adjacent palsa monitoring station (AMET13) was used together with the existing 0.5 m measurement. The 0.25 m depth measurement from AMET13 were linearly scaled to better match WJD02 local site conditions using an equation ($y=1.3836x-0.2585$; $R^2=0.96$) derived from overlapping ~50 cm depth measurements at AMET13 and WJD02 over 2015–2016. Thaw penetration relative to the initial ground surface was considered instead of thaw depth from the current ground surface to account for the impacts of both active layer thickening and ground subsidence (O'Neill et al. 2023), which can occur simultaneously in ice-rich landforms, including palsas. Total subsidence at the borehole locations from the time of initial installation in Summer 2014 to the most recent field visit in Summer 2023 was calculated from the difference in the depths of the shallowest logger within the borehole casing relative to the ground surface between the two summers. The depths corresponding to the zero annual amplitude were identified from linear interpolation from minimum annual and maximum annual temperature curves, calculated over hydrological years (October 1 to September 30), where the range in minimum and maximum annual temperatures was less than 0.1 °C. The depths corresponding to the base of permafrost were defined as the greatest depth where the maximum annual temperature curve, calculated over hydrological years (October 1 to September 30), intersected with 0 °C (± 0.04 °C to account for decreased logger resolution near 0 °C).

4 RESULTS

4.1 Changes in thaw penetration and permafrost thickness

Thaw penetration in 2015–2016 was less than 1 m at all borehole locations, ranging from 0.53 to 0.85 m (Table 2; Figure 3). The depth of the base of permafrost exceeded 2.15 m and ranged up to 3.53 m, giving permafrost thicknesses of up to 2.92 m. Thaw penetration increased at all locations over the monitoring period (almost doubling at WJD01 and WJD02 to 1.01 and 1.02 m, respectively), and permafrost thicknesses decreased (to as little as 0.50 m at WJD01; Table 2). The increase in thaw penetration represented 42 to 59% of the change in permafrost thickness at the sites. Thaw from the base of permafrost also accounted for a substantial proportion of the change in permafrost thickness (41 to 58%; Table 2). Total subsidence observed at the boreholes was 5 to 50 cm (Table 2), accounting for at least 10% of the increase in thaw penetration (O'Neill et al. 2023).

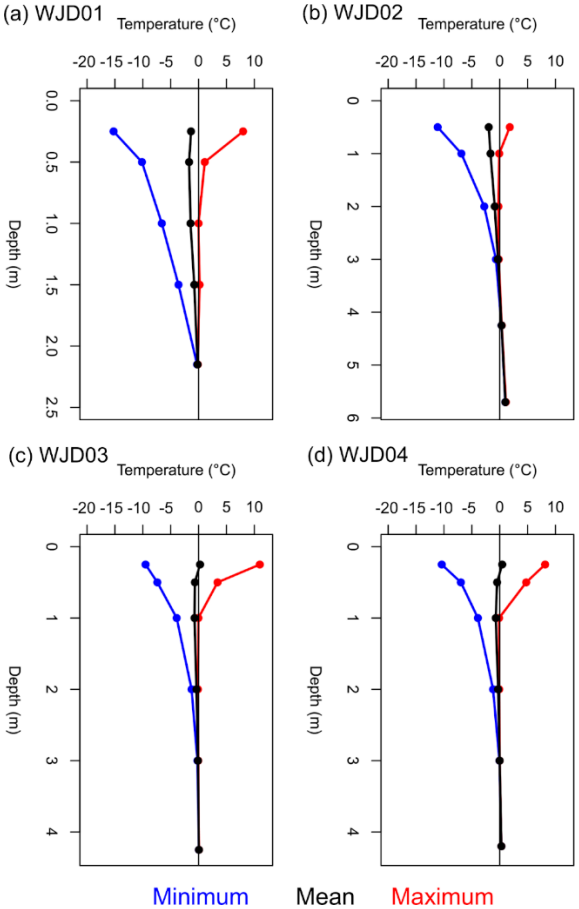

Figure 3. Minimum, mean, and maximum ground thermal profiles for (a) WJD01, (b) WJD02, (c) WJD03, and (d) WJD04 for October 2015 to September 2016 (Oct–Sept). Note that the depths on the y axes are scaled according to the depth of each borehole.

Table 2. Summary of permafrost characteristics at the palsa boreholes for the earliest (2015–2016) and most recent hydrological years of record (2021–2022). Depths of thaw penetration, base of permafrost, and zero annual amplitude are relative to the initial ground surface at the time of installation in 2014.

Borehole	2015-2016				2021-2022				2014-2023
	Thaw penetration depth (m)	Depth of base of permafrost (m)	Permafrost thickness (m)	Depth of zero annual amplitude (m)	Thaw penetration depth (m)	Depth of base of permafrost (m)	Permafrost thickness (m)	Depth of zero annual amplitude (m)	Subsidence (m)
WJD01	0.54	>2.15	>1.61	>2.15	1.01	1.51	0.50	2.09	0.05
WJD02	0.53	3.39	2.86	4.11	1.02	3.05	2.03	2.88	0.50
WJD03	0.61	3.53	2.92	3.44	1.00	3.26	2.26	1.92	0.12
WJD04	0.85	3.30	2.45	2.90	1.05	3.04	1.99	2.30	0.40

4.2 Changes in ground thermal regime

Considering the thin permafrost present at the borehole sites, mean ground temperatures in 2015–2016 were surprisingly low, varying from -0.7 °C at a depth of 1 m at WJD04 to -1.7 °C at a depth of 1 m at WJD02 (Figure 3). The range in ground temperatures was up to ~25 °C at the shallowest depth of 0.25 m (Figure 3), but decreased rapidly with depth at all sites, with depths of zero annual amplitude declining from 4.1 m in 2015–2016 to 2.9 m in 2021–2022 (Table 2).

Mean ground temperatures increased through the monitoring period (Figure 4), but not monotonically (Figure 5). Exceptionally high ground temperatures were observed at all locations in 2020–2021 in response to anomalously warm air temperatures, which were 2.2–2.5 °C warmer than the annual average for 2015–2020. Supra-permafrost taliks were not observed at any of the sites, and ground conditions cooled slightly in the following year (2021–2022) (Figure 4; Figure 5). Statistically significant ground temperature warming was observed within the permafrost at WJD01, at all depths at WJD02, beneath the permafrost at WJD03, and both above and beneath the permafrost at WJD04 (Figure 6).

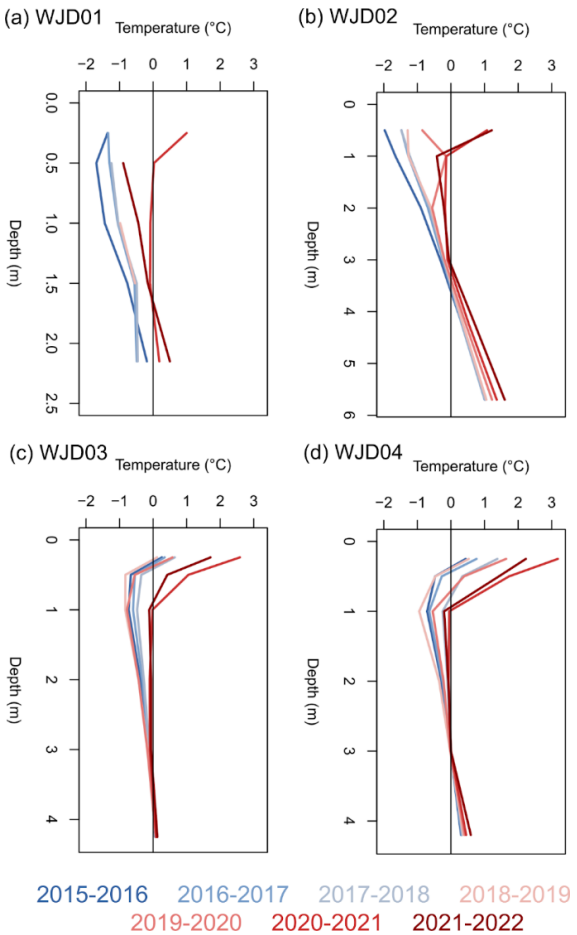

Figure 4. Mean annual ground temperature profiles at (a) WJD01, (b) WJD02, (c) WJD03, and (d) WJD04 from 2015–2016 to 2021–2022. Mean annual ground temperatures were calculated over hydrological years (October 1–September 30). Note that the depths on the y axes are scaled according to the depth of each borehole.

5 Discussion

5.1 Thaw and subsidence of peatland permafrost in coastal Labrador

The coastal Labrador palsa monitoring network has helped to characterize the thermal conditions of thin, yet surprisingly cold, bodies of permafrost along the southeastern Labrador Sea coastline. The combination of relatively low temperatures but limited permafrost thickness has been attributed to lateral heat flow from the surrounding non-permafrost area, possibly combined with advective heat fluxes due to groundwater flow beneath the mounds (Osterkamp 2003; Way et al. 2018).

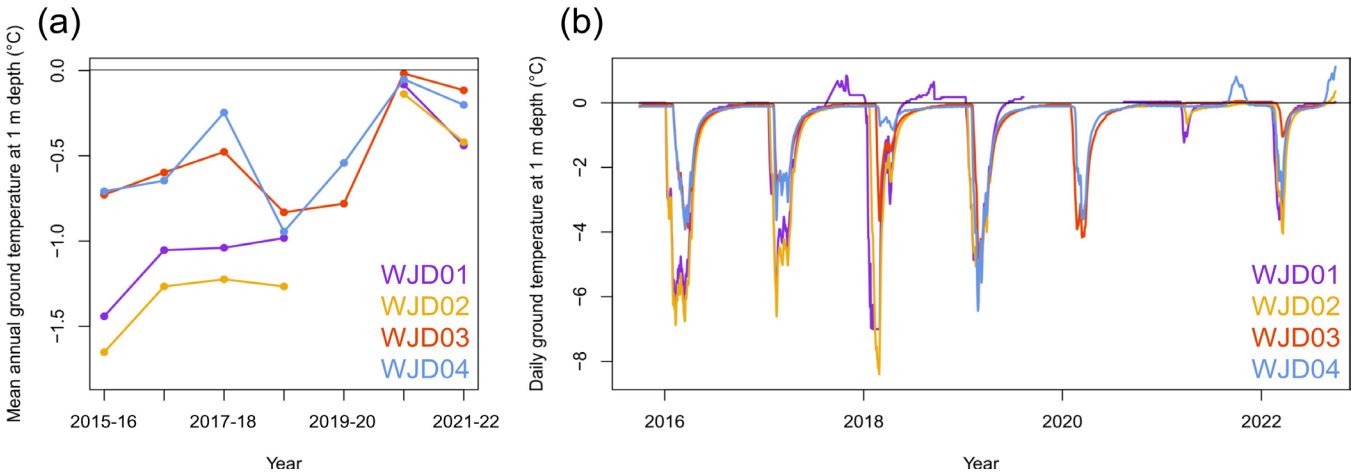

Figure 5. Mean (a) annual and (b) daily ground temperatures at a depth of 1 m at WJD01, WJD02, WJD03, and WJD04 from 2015–2022. Horizontal black lines represent 0 °C.

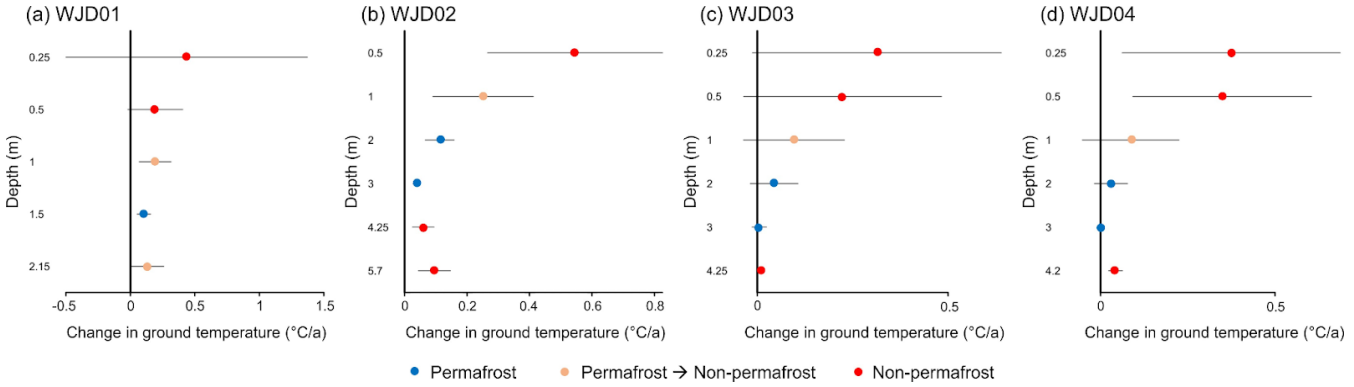

Figure 6. Summary of linear trends in mean annual ground temperatures at (a) WJD01, (b) WJD02, (c) WJD03, and (d) WJD04 from 2015–2016 to 2021–2022. Mean annual ground temperatures were calculated over hydrological years (October 1–September 30). Horizontal black lines represent 95% confidence intervals.

Monitoring of ground temperatures at the four boreholes shows increasing thaw penetration and permafrost thaw since installation in 2014. Warming occurred at all sites, but rates were not statistically significant at all depths in all boreholes. Inter-borehole differences may be attributed to variations in site characteristics, including vegetation cover, peat thickness, underlying sediment type and texture, hydrological connectivity, and human disturbance (Thie 1974; Allard and Rousseau 1999; Zuidhoff and Kolstrup 2005). For example, higher vegetation heights at WJD01 and the placement of komatiks by community members near WJD01 and WJD02, could lead to greater snow trapping and reduced energy escape from the ground in winter, while the thicker snow could also increase surface moisture during snowmelt. At WJD04, vegetation cover has mostly disappeared through processes of degradation and deflation, such that the top of the palsa is mostly characterized by exposed peat. As a result, the palsa at WJD04 likely has a lower albedo and different moisture characteristics compared to the other three sites.

Mechanisms of permafrost thaw were similar across all four locations, with a combination of thaw from both the bottom and top of permafrost. Thaw from the base of permafrost, which occurred by 27 to 64 cm, was likely caused by increased energy fluxes from the warmer surrounding unfrozen wetland and by water around and/or beneath the thin bodies of permafrost (Osterkamp 2003). Thaw from the top of permafrost is more complicated, as increases in thaw penetration occurred as a result of both active layer thickening and ground subsidence (O'Neill et al. 2023). By taking measurements of the borehole sensor depths relative to the surrounding ground surface in Summer 2023, the amount of subsidence could be estimated for each borehole since 2014 (Figure 7). In the absence of more precise measurement techniques, such as using a differential GPS to measure changes in the elevation of the ground surface from year to year, this comparative technique provides a reasonable approximation of the subsidence that occurred in the surrounding palsa at each borehole. This estimate then allowed us to differentiate between the proportion of thaw penetration as subsidence (5 to 50 cm, 11 to 200%) versus the proportion of thaw penetration as active layer thickening. This varied between sites, with 11% occurring as subsidence and 89% occurring as active layer thickening at WJD01 and 31% occurring as subsidence and 69% occurring as active layer thickening at WJD03. This likely reflects differences in ground ice content between the landforms at WJD01 and WJD03, as

permafrost with higher ground ice content is expected to have greater potential for subsidence as it thaws, while permafrost with lower ground ice content may experience change in a more subtle manner (Kokelj and Jorgenson 2013; Olefeldt et al. 2016). At WJD02 and WJD04, the amount of subsidence measured in Summer 2023 relative to Summer 2014 exceeded the total thaw penetration that was calculated for the study period. This may reflect potential changes in buoyancy within the wetland (Seppälä 1994), frost heave and jacking of the borehole casing itself, or limitations in using loggers (i.e., accuracy, resolution) when monitoring permafrost temperatures close to 0 °C.

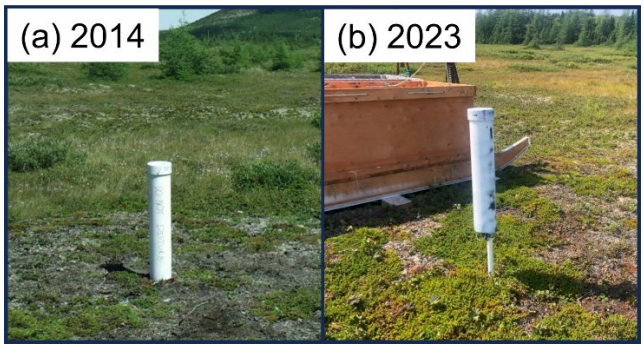

Figure 7. Field photos of WJD02 in (a) 2014 and (b) 2023. Since 2014, residents of the nearby community of Cartwright have parked a komatik on the WJD02 palsa. There was also visually evident subsidence at this site between 2014 and 2023.

Enhanced thaw, manifested as both active layer thickening and subsidence, occurred in Summer 2021, following an exceptionally warm winter (+5 °C higher than the baseline average for 1961–1990; Environment and Climate Change Canada 2021) in coastal Labrador in 2020–2021. Summer 2021 was the first time that ground temperatures at a nominal depth of 1 m at WJD03 and WJD04 exceeded 0 °C, while ground temperatures at 1 m depth at WJD01 and WJD02 were right at the point of thaw (Figure 5), thus we hypothesize that most of the observed ground subsidence occurred that year. Ground temperatures returned to slightly lower values in Winter 2021–2022. Continued monitoring of these landforms will be critical to understanding the long-term impacts of extreme winter events like 2020–2021 on peatland permafrost in the region.

5.2 Possible limitations

Differences in patterns and mechanisms of permafrost thaw between WJD01 and the other three palsa boreholes, especially with WJD02 located only 60 m away, may be potentially due to the sensitivity and accuracy of the data loggers that were used. As WJD01 is instrumented with less accurate DS1922L High Resolution Thermochron F5 iButtons (accuracy ± 0.5 °C; resolution ± 0.0625 °C) compared to Hobo V2 U23-003 loggers (accuracy ± 0.2 °C; resolution ± 0.02 °C at 22°C but > 0.02 °C at 0 °C), it is possible that ground temperatures at WJD01 are lower than recorded and that permafrost is thicker than presented here (Table 2). Additional investigations, such as geophysical surveys (Way et al. 2018), may help resolve the interpretation of permafrost thickness at this location.

Estimates of thaw penetration were especially challenging for WJD02 due to the arrangement of the temperature loggers at this borehole. While it was possible in this case to estimate the ground temperature at 25 cm at WJD02 for 2015–2016 based on an overlapping record at an adjacent monitoring location (AMET13), a closer spacing of thermistors at the boreholes, especially within the active layer, will be needed to assess ongoing and future changes in thaw penetration.

5.3 Other boreholes in the region

The only other palsa borehole in this region of northeastern Canada is located ~5 km north of WJD03 at 51.50°N, 57.15°W. Ground temperatures at this borehole from 2004–2005 to 2011–2012 were near 0 °C (MAGT of -0.46 °C at 1 m), and temperature records showed consistent active layer thicknesses just under 1 m and a base of permafrost deeper than 10 m throughout the study period (Centre d'études nordiques 2013). This borehole experienced statistically significant warming at 4 m by 0.02 °C/year from 2004 to 2012 and simultaneous statistically significant cooling at 5, 6, 9, and 10 m by up to -0.29 °C/year. This temperature record unfortunately does not overlap temporally with our four borehole records, and it does not reflect significant changes in air temperature, vegetation, and snow that have occurred in the region since 2012 (Barrette et al. 2020; Wang et al. 2024a). The continued monitoring of existing permafrost landforms and the expansion and installation of new boreholes in other peatland permafrost landforms in the region will be essential for characterizing permafrost change in the context of a warming climate.

6 Conclusions

Borehole records reveal progressive thaw at four palsa sites in coastal Labrador from 2015 to 2022. Thermal changes were subtle, as is characteristic of permafrost that is close to 0 °C (Smith et al. 2005), but when coupled with apparent physical changes, these data show ongoing increases in thaw penetration and declines in permafrost thickness. Permafrost thickness decreased by 18 to 69%, while thaw penetration increased by 24 to 92%. Thaw penetration was found to be attributed to a combination of active layer thickening and ground subsidence, and differences in the proportion of active layer thickening versus ground subsidence may reflect variations in ground ice content between palsas. Six additional boreholes, drilled in palsas (n=4) and peat plateaus (n=2) from 2015 to 2022 via water jet or percussive drilling techniques, will supplement this existing dataset and provide additional context for ground thermal conditions in peatland permafrost landforms found as far north as 56.6°N in coastal Labrador. The ground temperature data that support this study are publicly available in the Nordicana D data repository (Wang et al. 2024b).

7 ACKNOWLEDGEMENTS

The coastal Labrador peatland permafrost borehole monitoring network is located across the traditional lands of Labrador Inuit, Innu, and Kallunângajuit. Research permits for work conducted at WJD01-04 were granted by the NunatuKavut Community Council Research Advisory Committee, and we are grateful to Bryn Wood, George Russell Jr., Charlene Kippenhuck, and Meredith Purcell, as well as the residents of Cartwright and Red Bay, for their support. We are also grateful to George Russell Jr., Lloyd Pardy, and Gary Bird for meaningful and insightful conversations about peatland permafrost change in southeastern coastal Labrador that helped to motivate this research. Funding for this research was provided by the Natural Sciences and Engineering Research Council of Canada, the Northern Scientific Training Program, Queen's University, the University of Ottawa, the Weston Family Foundation, and the Association of Canadian Universities for Northern Studies. We thank Sharon Smith and Brendan O'Neill for helpful discussions about thaw penetration, and we thank the editor and two anonymous reviewers for their helpful and constructive commentary on this manuscript.

8 REFERENCES

Allard, M. and Rousseau, L. 1999. 'The international structure of a palsa and a peat plateau in the Rivière Boniface region, Québec: Inferences on the formation of ice segregation mounds', *Géographie physique et Quaternaire* 53(3), pp. 373–387. doi:10.7202/004760ar.

Banfield, C.E. and Jacobs, J.D. 1998. 'Regional patterns of temperature and precipitation for Newfoundland and Labrador during the past century', *The Canadian Geographer/Le Géographe canadien* 42(4), pp. 354–364. doi:10.1111/j.1541-0064.1998.tb01351.x.

Barrette, C., Brown, R., Way, R.G., Mailhot, A., Diaconescu, E.P., Grenier, P., Chaumount, D., Dumont, D., Sévigny, C., Howell, S., and Senneville, S. 2020. 'Nunavik and Nunatsiavut regional climate information update (Chapter 2)', in P. Ropars, M. Allard, and M. Lemay (eds.), *Nunavik and Nunatsiavut: From science to policy, an integrated regional impact study (IRIS) of climate change and modernization*, second iteration. Québec City, Québec, Canada: p. 62.

Beer, J., Wang, Y., Way, R.G., Forget, A., and Colyn, V. 2023. 'Uncrewed aerial vehicle-based assessments of peatland permafrost resiliency along the Labrador Sea coastline, northern Canada' (Preprint), *EarthArXiv*. doi:10.31223/X5610M.

Biskaborn, B.K., Smith, S.L., Noetzli, J., Matthes, H., Vieira, G., Streletskiy, D.A., Schoeneich, P., Romanovsky, V.E., Lewkowicz, A.G., Abramov, A., Allard, M., et al. 2019. 'Permafrost is warming at a global scale', *Nature Communications* 10(1), p. 264. doi:10.1038/s41467-018-08240-4.

Centre d'études nordiques 2013. 'Données environnementales de la station Blanc-Sablon, Québec, Canada', v. 1.0 (1990–2012). *Nordicana D5*. doi:10.5885/45111SL-B5D073186F274136.

Dionne, J.-C. 1984. 'Palses et limite méridionale du pergélisol dans l'hémisphère nord : Le cas de Blanc-Sablon, Québec', *Géographie physique et Quaternaire* 38(2), pp. 165–184. doi:10.7202/032550ar.

Environment and Climate Change Canada 2021. *Winter 2020/2021, Climate trends and variations bulletin*. Available at: https://publications.gc.ca/collections/collection_2021/eccc/En81-23-2021-1-eng.pdf.

Environment and Climate Change Canada 2023. *Canadian climate normals*. Available at: https://climate.weather.gc.ca/climate_normals/index_e.html.

Gibson, C., Cottenie, K., Gingras-Hill, T., Kokelj, S.V., Baltzer, J.L., Chasmer, L., and Turetsky, M.R. 2021. 'Mapping and understanding the vulnerability of northern peatlands to permafrost thaw at scales relevant to community adaptation planning', *Environmental Research Letters* 16(5), 055022. doi:10.1088/1748-9326/abe74b.

Government of Newfoundland and Labrador 2020. *Labrador ecoregions*. Available at: https://geohub-gnl.hub.arcgis.com/datasets/labrador-ecoregions/explore.

Hagedorn, G.W. 2022. 'Preliminary delineation of marine sediments in east-central Labrador: Parts of NTS map areas 13F, -G, -I, -J, -K, -N AND –O', *Government of Newfoundland and Labrador, Department of Industry, Energy and Technology Current Research* 22(1), pp. 189–201. Available at: https://www.gov.nl.ca/iet/files/CurrentResearch_Hagedorn_2022.pdf.

Hare, F.K. 1950. 'Climate and zonal divisions of the boreal forest formation in eastern Canada', *Geographical Review* 40(4), p. 615. doi:10.2307/211106.

Heginbottom, J.A., Dubreuil, M.A., and Harker, P.T. 1995. 'Canada, Permafrost. National Atlas of Canada', *Natural Resources Canada, Geomatics Canada*. Available at: https://doi.org/10.4095/294672.

Hjort, J., Streletskiy, D., Dore, G., Wu, Q., Bjella, K., and Luoto, M. 2022. 'Impacts of permafrost degradation on infrastructure', *Nature Reviews Earth & Environment* 3, pp. 24–38. doi:10.1038/s43017-021-00247-8.

Isaksen, K., Lutz, J., Sørensen, A.M., Godøy, Ø., Ferrighi, L., Eastwood, S., and Aaboe, S. 2022. 'Advances in operational permafrost monitoring on Svalbard and in Norway', *Environmental Research Letters* 17(9), 095012. doi:10.1088/1748-9326/ac8e1c.

Kokelj, S.V. and Jorgenson, M.T. 2013. 'Advances in thermokarst research', *Permafrost and Periglacial Processes* 24(2), pp. 108–119. doi:10.1002/ppp.1779.

Mahdianpari, M., Brisco, B., Granger, J., Mohammadimanesh, F., Salehi, B., Homayouni, S., and Bourgeau-Chavez, L. 2021. 'The third generation of pan-Canadian wetland map at 10 m resolution using multisource earth observation data on cloud computing platform', *IEEE Journal of Selected Topics in Applied Earth Observations and Remote Sensing* 14, pp. 8789–8803. doi:10.1109/JSTARS.2021.3105645.

Noetzli, J., Arenson, L.U., Bast, A., Beutel, J., Delaloye, R., Farinotti, D., Gruber, S., Gubler, H., Haeberli, W., Hasler, A., Hauck, C., Hiller, M., Hoelzle, M., Lambiel, C., Pellet, C., Springman, S.M., Vonder Muehll, D., and Phillips, M. 2021. 'Best practice for measuring permafrost temperature in boreholes based on the experience in the Swiss Alps', *Frontiers in Earth Science* 9, 607875. doi:10.3389/feart.2021.607875.

Olefeldt, D., Goswami, S., Grosse, G., Hayes, D., Hugelius, G., Kuhry, P., McGuire, A.D., Romanovsky, V.E., Sannel, A.B.K., Schuur, E.A.G., and Turetsky, M.R. 2016. 'Circumpolar distribution and carbon storage of thermokarst landscapes', *Nature Communications* 7(1), 13043. doi:10.1038/ncomms13043.

O'Neill, H.B., Smith, S.L., Burn, C.R., Duchesne, C., and Zhang, Y. 2023. 'Widespread permafrost degradation and thaw subsidence in northwest Canada', *Journal of Geophysical Research: Earth Surface* 128(8), e2023JF007262. doi:10.1029/2023JF007262.

Osterkamp, T.E. 2003. 'A thermal history of permafrost in Alaska', in *Proceedings of the 8th International Conference on Permafrost*. Zurich, Switzerland: July 21–25, 2003, pp. 863–868.

Riseborough, D.W. 2003. 'Thawing and freezing indices in the active layer', in *Proceedings of the 8th International Conference on Permafrost.* Zurich, Switzerland: July 21–25, 2003, pp. 953–958.

Riseborough, D.W. 2008. 'Estimating active layer and talik thickness from temperature data: Implications from modelling results', in D.L. Kane and K.M. Hinkel (eds.), *9th International Conference on Permafrost*. Fairbanks, Alaska, United States: June 29–July 3, 2008, pp. 1487–1492.

Roberts, B.A., Simon, N.P.P., and Deering, K.W. 2006. 'The forests and woodlands of Labrador, Canada: Ecology, distribution and future management', *Ecological Research* 21(6), pp. 868–880. doi:10.1007/s11284-006-0051-7.

Schuur, E.A.G. and Mack, M.C. 2018. 'Ecological response to permafrost thaw and consequences for local and global ecosystem services', *Annual Review of Ecology, Evolution, and Systematics* 49(1), pp. 279–301. doi:10.1146/annurev-ecolsys-121415-032349.

Séguin, M.K. and Dionne, J.C. 1992. 'Modélisation géophysique et caractérisation thermique du pergélisol dans les palses de Blanc-Sablon, Québec'. *Geological Survey of Canada* Current Research, E(1), pp. 207–216. doi:10.4095/133575.

Seppälä, M. 1994. 'Snow depth controls palsa growth', *Permafrost and Periglacial Processes* 5(4), pp. 283–288. doi:10.1002/ppp.3430050407.

Smith, S.L. and Brown, J. 2009. 'Assessment of the status of the development of the standards for the Terrestrial Essential Climate Variables: Permafrost and seasonally frozen ground', *Global Terrestrial Observing System*. Available at: https://globalcryospherewatch.org/bestpractices/docs/GTOS62.pdf.

Smith, S.L., Burgess, M.M., Riseborough, D., and Mark Nixon, F. 2005. 'Recent trends from Canadian permafrost thermal monitoring network sites', *Permafrost and Periglacial Processes* 16(1), pp. 19–30. doi:10.1002/ppp.511.

Thie, J. 1974. 'Distribution and thawing of permafrost in the southern part of the discontinuous permafrost zone in Manitoba', *ARCTIC* 27(3), pp. 189–200. doi:10.14430/arctic2873.

Walvoord, M.A. and Kurylyk, B.L. 2016. 'Hydrologic impacts of thawing permafrost—A review', *Vadose Zone Journal* 15(6), pp. 1–20. doi:10.2136/vzj2016.01.0010.

Wang, Y., Way, R.G., and Beer, J. 2024a. 'Multi-decadal degradation and fragmentation of palsas and peat plateaus in coastal Labrador, northeastern Canada', *Environmental Research Letters* 19(1), 014009. doi:10.1088/1748-9326/ad0138.

Wang, Y., Way, R.G., Beer, J., Forget, A., Tutton, R., and Purcell, M.C. 2023. 'Significant underestimation of peatland permafrost along the Labrador Sea coastline in northern Canada'. *The Cryosphere* 17(1), pp. 63–78. doi:10.5194/tc-17-63-2023.

Wang, Y., Way, R.G., Lewkowicz, A.G., Beer, J. 2024b. 'Ground temperature records from a peatland permafrost borehole monitoring network in coastal Labrador, v. 1.0 (2014–2023)', *Nordicana D126*. doi:10.5885/45876XD-C1F55FCD3B95415D.

Way, R.G. and Lewkowicz, A.G. 2018. 'Environmental controls on ground temperature and permafrost in Labrador, northeast Canada', *Permafrost and Periglacial Processes* 29(2), pp. 73–85. doi:10.1002/ppp.1972.

Way, R.G., Lewkowicz, A.G., and Zhang, Y. 2018. 'Characteristics and fate of isolated permafrost patches in coastal Labrador, Canada', *The Cryosphere* 12(8), pp. 2667–2688. doi:10.5194/tc-12-2667-2018.

Way, R.G. and Viau, A.E. 2015. 'Natural and forced air temperature variability in the Labrador region of Canada during the past century', *Theoretical and Applied Climatology* 121(3–4), pp. 413–424. doi:10.1007/s00704-014-1248-2.

Zuidhoff, F.S. and Kolstrup, E. 2005. 'Palsa development and associated vegetation in northern Sweden', *Arctic, Antarctic, and Alpine Research* 37(1), pp. 49–60. doi:10.1657/1523-0430(2005)037[0049:PDAAVI]2.0.CO;2.

From science to story: Communicating permafrost concepts with data comics

Zezhong Wang[1], Stephan Gruber[2], Michelle Levy[3] & Sheelagh Carpendale[1]

[1]*Department of Computing Science – Simon Fraser University, Vancouver, British Columbia, Canada*

[2]*Department of Geography and Environmental Studies – Carleton University, Ottawa, Ontario, Canada*

[3]*Department of English – Simon Fraser University, Vancouver, British Columbia, Canada*

ABSTRACT

We are creating data comics that use graphics, narratives and visualization to explain permafrost and its interaction with climate change. Despite the increasing attention to permafrost change due to its local impacts and interactions with global climate, many people without scientific background or lived experience related to permafrost do not understand what permafrost is or why it is important. This knowledge gap reduces public consideration and risk perception. We are exploring new ways to present this information to a wider audience, including policymakers, scientists from other fields, school teachers, and the general public. A major communication challenge we face is that many scientific articles are not easily comprehensible and understanding concepts such as permafrost thaw and its effect on land use and infrastructure can be challenging. To address this challenge, we are developing new ideas in creating data comics, a new format that integrates data visualization and storytelling to deliver insights from data in a new format. We are exploring the use of relatable examples and analogies to make scientific information more comprehensible to the public. We are creating data comics collaboratively with experts in data visualization, narrative construction, data comics, and permafrost science. The data comics are designed to be both scientifically informed and verified, using the best and most current scientific information available. We prioritize data transparency, working towards more understandable and engaging presentations of scientific concepts.

1 INTRODUCTION

In this paper, we harness the data-driven storytelling genre of data comics (Segel and Heer 2010; Bach et al. 2017) to convey the definition and thawing trends of permafrost to a general audience. Data comics blend narrative storytelling with data visualizations, providing an innovative approach to communicating insights from data.

Permafrost thaw matters to people globally because thawing causes the release of greenhouse gases such as carbon dioxide and methane, thereby exacerbating climate change, and to people in cold regions because of the impacts it causes locally and regionally (Pörtner et al. 2019).

Despite its growing urgency, climate change remains a divisive issue, often muddled by cultural, political, and ideological divides (Hulme 2009; Hornsey et al. 2016). The scientific literature, while rigorous, is usually not designed for consumption by those without specific scientific training. Moreover, misinformation and oversimplified messages propagated through media contribute to public confusion and inaction (Cook et al. 2017; Treen et al. 2020).

Our project explores the potential of data comics as an outreach tool. Initially popularized in the field of information visualization, data comics combine graphics, narrative, and data visualization to explain complex data-based messages in an accessible and engaging way (Zhao et al. 2015; Bach et al. 2017; Wang et al. 2019). Previous work, such as Frozen-Ground Cartoons by Bouchard et al. (2018) which focus on fieldwork and interactions with local communities, demonstrates the effectiveness of comics in communicating permafrost science through localized narratives. We extend this approach by incorporating data visualizations into comics and render the information in a digestible way, thereby bridging the gap between scientific research and public comprehension. Our interdisciplinary team—comprising experts in literature and narrative, data visualization, and permafrost science—works collaboratively to create a data comic that distills essential aspects of permafrost science, including its definition, geographic distribution, temperature trends, and the impact of often-overlooked physical phenomena on the interpretation of the temperature trends in thawing permafrost. The comic is available at: https://dc4cc.github.io/permafrost.html.

The story employs the genre of creative nonfiction to weave scientific data and historical news events into the narrative of a family hiking trip in Banff National Park (Alberta, Canada), a region with mountain peaks underlain by permafrost, and frequented by millions of visitors annually (Gruber et al. 2015). Science and data visualizations are embedded and illustrated within the comic. For example, characters draw charts on the snow (Figure 1), and explain the physical phenomena of latent heat by observing the temperature of ice and snow melting in a camping pot (Figures 2 and 3). Through these examples, we aim to make the explanations fun and engaging to the audience.

In the ensuing sections, we outline our creation process and design rationales and delve into the opportunities and challenges of using data comics for science communication, providing valuable insights gleaned from our experience.

https://doi.org/10.52381/ICOP2024.157.1

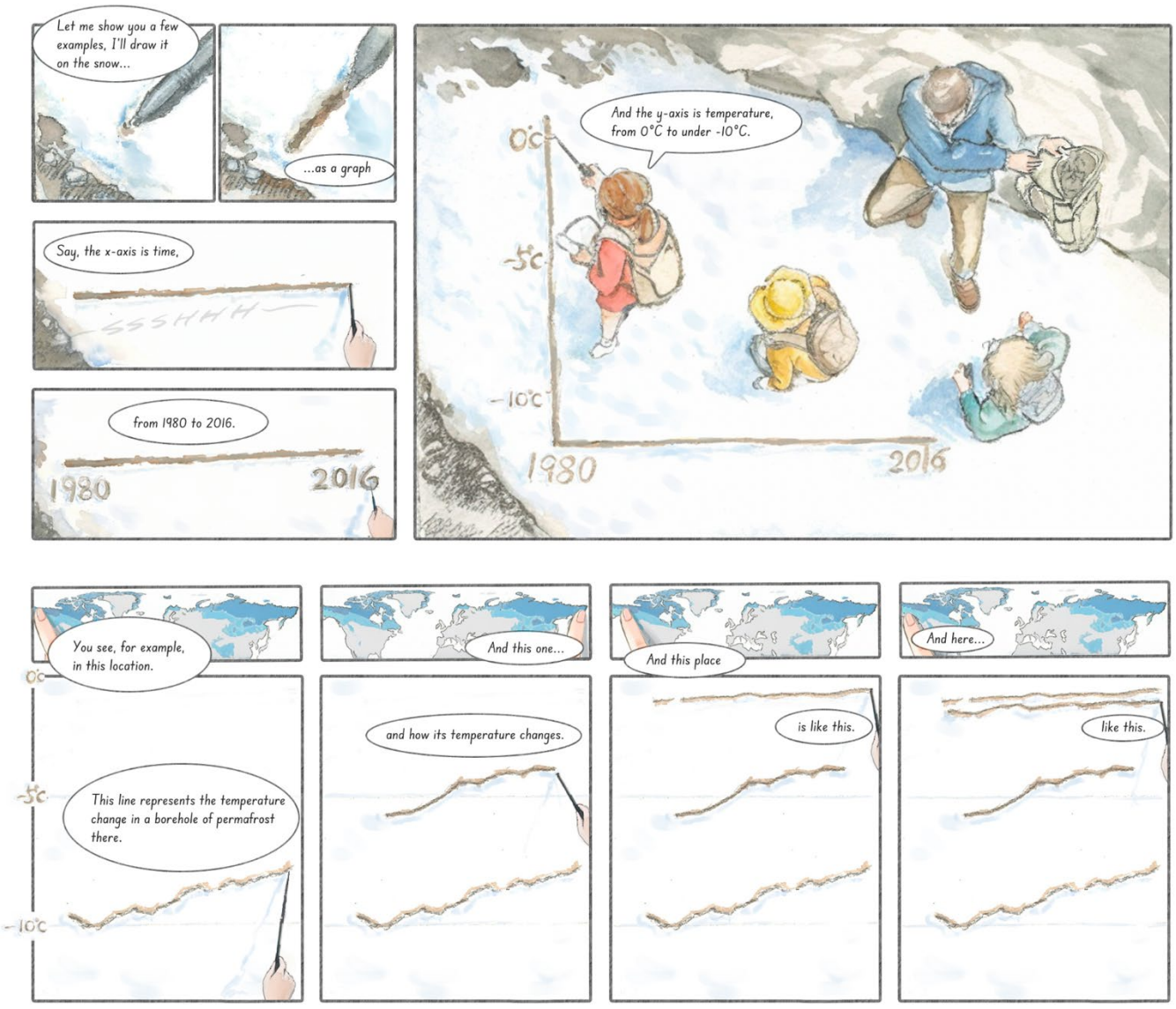

Figure 1. Snippet from page 4 of the data comic; the girl is drawing a line chart on the snow to show her family the temperature of permafrost in different locations in the world.

1.1 Background

1.1.1 Comics and Data Comics

Comics, also referred to as graphic novels or graphic stories, represent a distinctive medium that conveys narratives through an integration of visual imagery and text (Cohn 2005; Kukkonen 2013). With the powerful and expressive ability for communication, comics have been valued for their ability to promote public engagement and used as educational tools for teaching science (Tatalovic 2009; Lin et al. 2015; Farinella 2018).

Inspired by comics, data comics aim to communicate insights with data visualizations. Data comics support data-driven storytelling by making use of peoples' familiarity with reading and understanding comics along with the particular qualities of the medium (Zhao et al. 2015; Bach et al. 2017; Wang et al. 2019); they have recently gained attention in diverse areas, ranging from improving data visualization literacy (Wang et al. 2020; Boucher et al. 2023) to environmental and climate education (Hasan et al. 2022; Lc et al. 2022), and medical science (Alamalhodaei et al. 2020). The data comic we create for permafrost will incorporate *four essential components* (Bach et al. 2017): contextualize the *data visualizations* within a compelling *flow* of *narration* rather than a dry presentation of facts and employ various visual and narrative design patterns (Bach et al. 2018) to combine *words-and-pictures*.

1.1.2 Comics about Climate Change

The communication of climate change science presents a unique set of challenges and opportunities. On one hand,

the diffuse, abstract nature of climate change as well as the invisibility and lack of immediacy of some climate phenomena can create barriers to public understanding (Moser 2010). On the other, the immediacy and urgency of climate change issues require public engagement for effective action (Corner et al. 2014). By fostering a deeper and more enduring engagement with the scientific subject matter, comics contribute to a richer, more nuanced public discourse on climate change and its implications. By incorporating maps, charts, and scientific diagrams, comics are found to create more understanding of climate change (Reumont et al. 2023), to engage with environmental problems and determine attitudes (Topkaya 2016; Munawwaroh et al. 2018; Maggiulli 2022), and to promote a willingness to take actions to protect the climate (Theodorou et al. 2019).

Several works inspired the design of our data comic, for example, an anthology of comic strips about climate change and animal extinction (Goodenough 2021). Regarding examples involving data, a 9-page comic in the journal Nature demonstrates the history of global policy around climate change (Monastersky et al. 2015), and a set of stories with visualizations to show alternative realities of environment (Lc et al. 2022). The use of comics for educating the public about permafrost has proven successful. For example, Frozen-Ground Cartoons by Bouchard et al. (2018)—a collaborative initiative between artists, science communicators, and permafrost researchers—uses everyday language in dialogue and short narratives to clarify the basics of permafrost. By further incorporating interactive elements like augmented reality and board games, this initiative has succeeded in captivating a broad audience, including school children, educators, and the public at large. Our work sits in the genres of data comics and science comics to engage non-specialist individuals and focuses on elucidating the science and data about permafrost.

2 METHODOLOGY

Our methodology for developing the data comic consisted of four primary phases: 1) establishing communication objectives, 2) formulating data visualizations and a script, 3) producing an initial draft of the data comic, and 4) refining through iterative design. Below, we delve into each phase to elucidate our approach.

2.1 Creation Team

The creation team was initiated by three members. A post-doctoral researcher whose research focuses on data-driven storytelling with data comics took the main role in designing the data comic. A professor whose primary research areas are information visualization and interaction design mentored the creation process of this project. A professor whose research focuses on permafrost and related phenomena in high-latitude and high-elevation environments provided resources of scientific explanation, i.e., publications and empirical experience, and made sure the science was properly explained. Two members, a professor, and a M.A. student in literature, later joined to help iterate the story. The team met every second week to discuss the progression and decisions.

2.2 Communication Goals

A clear articulation of communication objectives is fundamental in shaping the language and design of our data comic. Unlike more commonly understood climate concepts such as fossil fuels and greenhouse gases, the term ‘permafrost’ is less familiar to the general public and is often shrouded in misconceptions. As such, we opted to focus on imparting basic knowledge about permafrost and dispelling prevalent myths. Since groups with an interest in permafrost will keep growing and changing (Gruber et al. 2023), we created this comic aiming to be understandable and engaging to a diverse range of people.

2.3 Story Development

Since the data comic designer investigated this project as a novice about permafrost, they brought a non-expert perspective. To familiarize themselves with the subject matter, the designer engaged in discussions with the team’s permafrost scientist, focusing on key questions such as: 1) What foundational knowledge is crucial for comprehending the role of permafrost in climate change? 2) What are the prevalent misconceptions surrounding permafrost? 3) What research methods are commonly employed in permafrost studies, including techniques for data collection? By addressing these inquiries, the designer aimed to gain an in-depth understanding of permafrost and its significance, as well as to identify the key concepts that should be incorporated into the data comic. The designer then formulated a list of key messages to be conveyed according to the discussion and scientific publications and afterward, drafted an initial story script, supplemented by relevant data and visualizations. We initially conceived three alternative storylines imparting the same targeted messages. After extensive team discussions, we decided on one and refined the script before advancing to subsequent visual design phases.

The story employed the notion of *faction*, combining elements of fact and fiction to make verifiable and justifiable claims to truth and simultaneously engage readers (Bruce 2019), and *creative nonfiction* that provides information about a variety of subjects, enriched by relevant thoughtful ideas and personal insight, without exaggerating or making up facts and embellishing details (Gutkind 2012). Our story is a melange of real-world scientific data such as data on global permafrost warming (Biskaborn et al. 2019), historical events such as the demolition of Abbot Pass Hut (Parks Canada 2023), and imagined activities during a hypothetical family hiking trip, aiming to weave multifaceted, accessible factual information into an emotionally resonant story.

2.4 Visual Design Process

Initial drafts created as rough sketches enabled swift changes based on feedback from the team. The comic was then colored with watercolor, its transparency and fluidity being aesthetic features that provide a unique condition for

illustrating the graphics of thawing permafrost. After the coloring stage, the comic was scanned to facilitate digital editing. Adobe Photoshop was used for the bulk of the digital work such as color correction, fine-tuning graphics to ensure accuracy in maps and data visualization, and text insertion. Stable Diffusion was then used to fine-tune the details of characters.

To iterate the data comic, external feedback was obtained from four permafrost scientists. The reviewers were generally positive about the comic's effectiveness in communicating permafrost-related concepts and provided specific suggestions including clarification in certain panels, word choice for increased precision, and minor adjustments to graphical elements for enhanced comprehension.

3 Story and Data Comic Design

The story unfolds during a family hiking trip along the boundary of Banff National Park in Alberta and Yoho National Park in British Columbia. After setting the scene and introducing the characters, the family encounters a plaque that talks about the Abbot Pass Hut, a historic base for mountaineers, which had to be demolished in June 2022 due to permafrost-induced landslides (Parks Canada 2023). This event prompts a conversation about the role of thawing permafrost in the hut's demise.

In a novel twist, we subvert the usual parent-child dynamic: the children, not the parents, offer informed explanations to engage proactively in environmental issues, including permafrost. The son's query about the existence of permafrost in southern Canada opens the door for a discussion about what permafrost is and where it is found. The father's misconceptions serve as teachable moments. He incorrectly equates snow and glaciers with permafrost, and his daughter corrects him.

The story is moved forward as the daughter corrects her father by referring to a fictional brochure named *Mountain, Climate and Ice: Understanding and Seeing Impacts of Climate Change Above and Below Ground on Your Hike*, then by drawing line charts of temperature change of permafrost (Figure 1) in the snow. The *Multiple-Explanations* data comic design pattern is employed by presenting the process of drawing the chart to guide the audience through the mapping of locations to the lines on the chart. In accordance with the recommendations from Kosslyn (2006) and Harold et al. (2016) to include only essential information for the intended communication purpose, we have chosen to highlight four key lines from the original chart presented by Biskaborn et al. (2019). The central message is that while the temperature of permafrost is generally rising, the patterns of increase vary. Specifically, permafrost locations with lower temperatures are experiencing a dramatic rise in temperature, whereas those closer to zero degrees Celsius are seeing a more modest increase. Interpreting these differing trends requires counter-intuitive thinking and knowledge about phase change as context.

To address her father's skepticism, the daughter seizes the opportunity to offer a hands-on explanation, embodying the principle that a small experiment, instead of a long explanation, is a good educational tool. As the father begins

to scoop snow into a camping pot for cooking pasta, she places a thermometer in the snow to monitor its temperature (Figure 2). Concurrently, she sketches another line chart in the snow (Figure 3). This exercise serves to illustrate the concept of latent heat, explaining why the temperature might hover around zero degrees Celsius during phase changes, such as during the thawing of permafrost. The father's doubt is shattered when, in a moment of dramatic tension, a bus-sized rock falls nearby, underlining the immediacy and unpredictability of permafrost-related hazards. The story concludes with a family discussion about the need for immediate action, leaving the audience with both a greater understanding of permafrost and a sense of urgency regarding its environmental impact.

Figure 2. Measuring the temperature of melting snow with a thermometer to illustrate the concept of latent heat, which is not reflected in temperature changes.

4 Discussion

4.1 Data Visualization in Narration

Data visualizations, such as temperature-depth profiles, scatter plots, and heat maps, are abstract by nature and demand a certain level of data and visualization literacy for interpretation. Given that the comic is designed for the general public, it is essential to select visualization techniques comprehensible for the audience with limited data and visualization literacy. A notable example is

'warming stripes' by Ed Hawkins for the 2018 IPCC report, which uses colored stripes to intuitively depict temperature changes over time (Hawkins 2018). In our data comic, basic line charts serve to illustrate various aspects of permafrost temperature changes, both annually and across different locations, as well as the temperature dynamics of melting snow. To ease the reader into the visual language, we introduce visual mapping and components gradually by breaking the chart into many comic panels.

Incorporating data visualizations naturally into a hiking narrative posed a challenge. We overcame this by utilizing elements within the story's setting—for example, using a visitor brochure or drawing on snow with a hiking stick. While some visualizations, like the layered underground diagram, were not integrated through story-specific materials, they were directly overlaid on the comic panels, serving a function similar to a voice-over.

Using analogy and metaphor is integral to scientific thinking (Ortony 1993). Metaphorical concepts are 'those which are understood and structured not merely on their own terms, but rather in terms of other concepts' (Lakoff et al. 1980, p. 195). Ortony (1993, p. 450) outlines six principles for analogical reasoning we found also applicable to the use of visual metaphor in data comics. In our work, we employ the metaphor of cooking frozen meatballs to represent the hidden transformations occurring within permafrost—an ongoing process yet not immediately visible. Similarly, we use the melting process of snow as an analogy for the thawing of permafrost to explain the latent heat. Although two bases (i.e., snow and meatballs) are employed to map permafrost, each focuses on separable aspects. We think involving data visualizations and visual metaphors in the comic can support scientific explanations, and benefit audiences by improving their data and visual literacy. Presenting science diagrams and data visualizations in an artistic way (e.g., hand-drawn line chart on snow) could make the story fun and engaging.

4.2 Promoting Credibility

Trust is a key factor in gaining public acceptance for risk assessments and policy recommendations (Poortinga et al. 2003). The information deficit model, which views the public

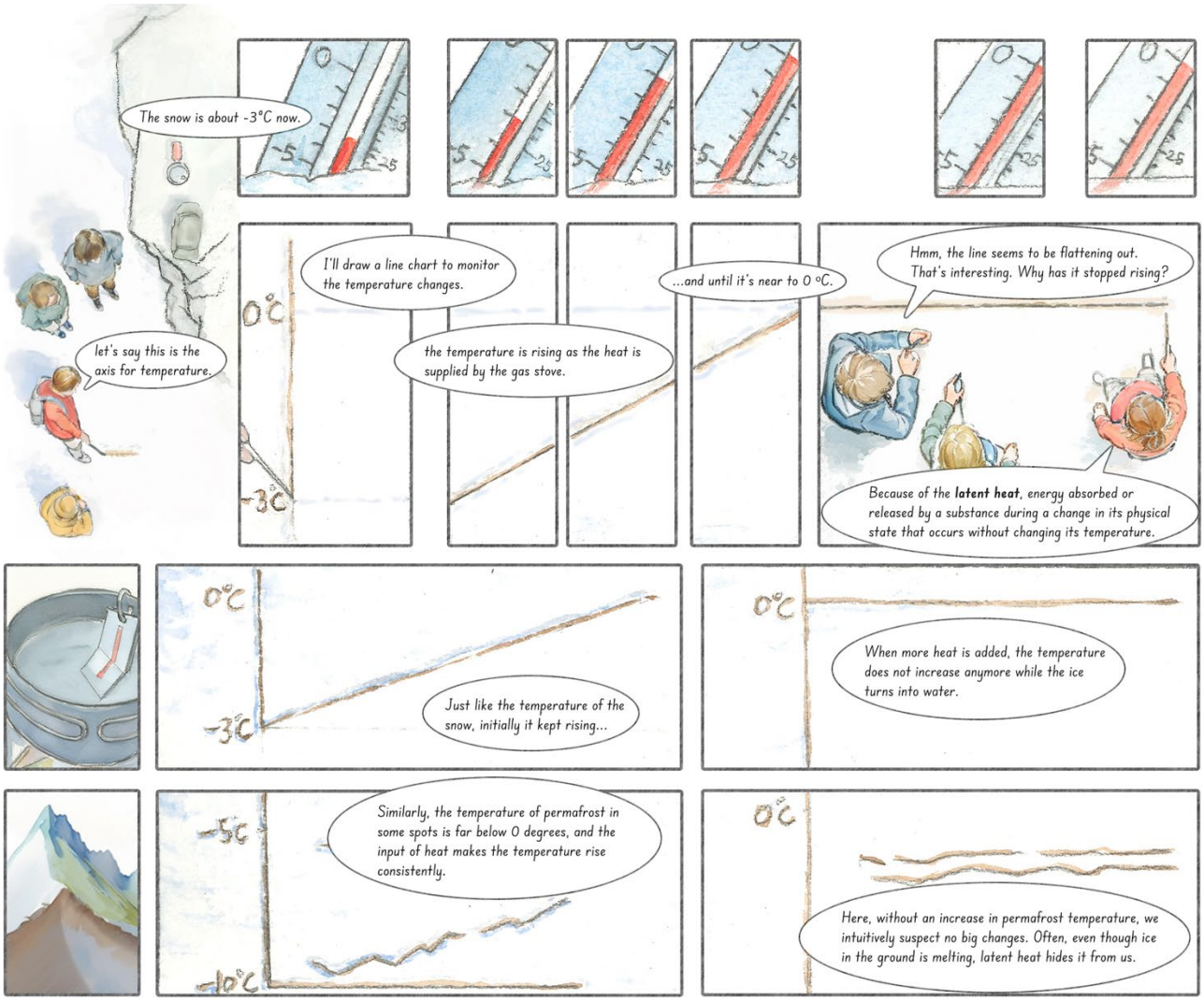

Figure 3. The daughter explains the physical phenomena of latent heat by drawing a line chart demonstrating temperature change of snow melting and compares that with thawing process of permafrost.

as generally lacking in knowledge and needing education, is increasingly giving way to a more nuanced understanding of a public that is informed, engaged, and scientifically literate (Miller 2001; Sturgis et al. 2004). While we recognize that trust is shaped by various complex factors such as ideology, cultural background, and political affiliations, as well as information sources, simply providing credible data is not enough to ensure belief. However, the deficit model continues to be a cornerstone in science communication, featuring prominently in various climate change communication efforts (Davies 2008; Suldovsky 2017). Our data comic aims to uphold the principles of authenticity, accessibility, and transparency. All data used in the comic are sourced from peer-reviewed scientific publications and the comic was verified by the team's permafrost scientist and other four permafrost researchers for accuracy. We intend to regularly update the comic to ensure that it remains current, relevant, and unambiguously correct for readers with diverse backgrounds and perspectives.

4.3 Engaging Collaboration

Crafting data comics necessitates a blend of interdisciplinary expertise, including storytelling, data analysis, visualization, visual design, and illustration. When the subject matter involves specialized domain knowledge like permafrost, effective teamwork across various roles becomes both a challenge and an opportunity for integrating diverse perspectives to overcome communication barriers. Utilizing an ethnographic approach to incorporate local stories into data comics can further connect scientists and local communities.

5 Conclusion

In this paper, we detail our process of crafting a data comic that serves as an educational tool for introducing permafrost (https://dc4cc.github.io/permafrost.html). We outline our design rationale and discuss how data comics offer a promising avenue for effective communication by seamlessly intertwining data visualizations with scientific knowledge and narrative techniques.

6 Acknowledgements

We thank our colleagues and reviewers for their thoughtful comments. This research was funded in part by NFRFE-2022-00856 (Data Comics for Climate Change), and the Canada Research Chair CRC-2019-00368.

7 References

Alamalhodaei, A., Alberda, A.P., and Feigenbaum, A. 2020. 'Humanizing Data through 'Data Comics': An Introduction to Graphic Medicine and Graphic Social Science', in M. Engebretsen and H. Kennedy (eds.) *Data Visualization in Society*, Amsterdam: Amsterdam University Press, pp. 347–366. doi:10.1515/9789048543137-025.

Bach, B., Riche, N.H., Carpendale, S., and Pfister, H. 2017. 'The Emerging Genre of Data Comics', *IEEE Computer Graphics and Applications* 37(3), pp. 6–13. doi:10.1109/MCG.2017.33.

Bach, B., Wang, Z., Farinella, M., Murray-Rust, D., and Henry Riche, N. 2018. 'Design Patterns for Data Comics', in *Proceedings of the 2018 CHI Conference on Human Factors in Computing Systems*, Association for Computing Machinery, Montreal QC, Canada, pp. 1–12.

Biskaborn, B.K., Smith, S.L., et al. 2019. 'Permafrost is Warming at a Global Scale', *Nature Communications* 10(1), p. 264. doi:10.1038/ s41467-018-08240-4.

Bouchard, F., Sansoulet, J., Fritz, M., Malenfant-Lepage, J., Nieuwendam, A., Paquette, M., Rudy, A.C.A., Siewert, M.B., Sjöberg, Y., Tanski, G., Habeck, J.O., and Harbor, J. 2018. '"Frozen-Ground Cartoons": Permafrost comics as an innovative tool for polar outreach, education, and engagement', *Polar Record* 54(5–6): pp. 366–372. doi:10.1017/S0032247418000633.

Boucher, M., Bach, B., Stoiber, C., Wang, Z., and Aigner, W. 2023. 'Educational Data Comics: What Can Comics Do for Education in Visualization?', in *2023 IEEE VIS Workshop on Visualization Education, Literacy, and Activities (EduVis)*, Melbourne, Australia, pp. 34–40. doi:10.1109/EduVis60792.2023.00012.

Bruce, T. 2019. 'The Case for Faction as a Potent Method for Integrating Fact and Fiction in Research', in S. Farquhar and E. Fitzpatrick (eds), *Innovations in Narrative and Metaphor: Methodologies and Practices*. Singapore: Springer. Available at: https://doi.org/10.1007/978-981-13-6114-2_5.

Cohn, N. 2005. '"Un-Defining "Comics": Separating the Cultural from the Structural in "Comics"', *International Journal of Comic Art* 7(2), pp. 236–248.

Cook, J., Lewandowsky, S., and Ecker, U.K.H. 2017. 'Neutralizing Misinformation Through Inoculation: Exposing Misleading Argumentation Techniques Reduces Their Influence', *PLoS One* 12(5), e0175799. Available at: https://doi.org/10.1371/journal.pone.0175799.

Corner, A., Markowitz, E., and Pidgeon, N. 2014. 'Public Engagement with Climate Change: The Role of Human Values', *Wiley Interdisciplinary Reviews: Climate Change* 5(3), pp. 411–422. Available at: https://doi.org/10.1002/wcc.269.

Davies, S.R. 2008. 'Constructing Communication: Talking to Scientists about Talking to the Public', *Science Communication* 29(4), pp. 413–434. Available at: https://doi.org/10.1177/1075547008316222.

Farinella, M. 2018. 'The Potential of Comics in Science Communication', *Journal of Science Communication* 17(1), Y01. Available at: https://doi.org/10.22323/2.17010401.

Goodenough, P. 2021. The Most Important Comic Book on Earth: Stories to save the world. New York, New York, United States: Dorling Kindersley. Available at: https://www.penguin.co.nz/books/the-most-important-comic-book-on-earth-9780241513514.

Gruber, S., Burn, C.R., Arenson, L., Geertsema, M., Harris, S., Smith, S., Bonnaventure, P., and Benkert, B. 2015. 'Permafrost in Mountainous Regions of Canada', in *Proceedings of the 68th Canadian Geotechnical Conference, 7th Canadian Permafrost Conference*, Canadian Geotechnical Society. Québec City, Québec, Canada.

Gruber, S., Hayley, J., Karunaratne, K., King, J., MacLean, T., Marshall, S., and Moore, D. 2023. 'Considerations Toward a Vision and Strategy for Permafrost Knowledge in Canada', *Arctic Science* 9(4). Available at: https://doi.org/10.1139/as-2023-0016.

Gutkind, L. 2012. *You Can't Make This Stuff Up: The Complete Guide to Writing Creative Nonfiction–From Memoir to Literary Journalism and Everything in Between*. Philadelphia, Pennsylvania, United States: Da Capo Press.

Harold, J., Lorenzoni, I., Shipley, T.F., and Coventry, K.R. 2016. 'Cognitive and Psychological Science Insights to Improve Climate Change Data Visualization', *Nature Climate Change* 6(12), pp. 1080–1089. Available at: https://doi.org/10.1038/nclimate3162.

Hasan, M.T., Wolff, A., Knutas, A., Pässilä, A., and Kantola, L. 2022. 'Playing Games through Interactive Data Comics to Explore Water Quality in a Lake: A Case Study', in *Extended Abstracts of the 2022 CHI Conference on Human Factors in Computing Systems*. New Orleans, Louisianna, United States, pp. 1–7.

Hawkins, E. 2018. *Show Your Stripes*. Available at: https://showyourstripes.info/ (Accessed: 1 Dec 2023).

Hornsey, M.J., Harris, E.A., Bain, P.G., and Fielding, K.S. 2016. 'Meta-Analyses of the Determinants and Outcomes of Belief in Climate Change', *Nature climate change* 6, pp. 622–626. Available at: https://doi.org/10.1038/nclimate2943.

Hulme, M. 2009. *Why We Disagree About Climate Change: Understanding Controversy, Inaction and Opportunity*. New York, New York, United States: Cambridge University Press.

Kosslyn, S.M. 2006. *Graph Design for the Eye and Mind*. New York, New York, United States: Oxford University Press Inc.

Kukkonen, K. 2013. *Studying Comics and Graphic Novels*. West Sussex, United Kingdom: John Wiley & Sons Ltd.

Lakoff, G. and Johnson, M. 1980. 'The Metaphorical Structure of the Human Conceptual System', *Cognitive Science* 4(2), pp. 195–208. Available at: https://doi.org/10.1207/s15516709cog0402_4.

Lc, R., Song, Z., Sun, Y., and Yang, C. 2022. 'Designing Narratives and Data Visuals in Comic Form for Social Influence in Climate Action', *Frontiers in Psychology* 13. Available at: https://doi.org/10.3389/fpsyg.2022.893181.

Lin, S.-F., Lin, H.-s., Lee, L., and Yore, L.D. 2015. 'Are Science Comics a Good Medium for Science Communication? The Case for Public Learning of Nanotechnology', *International Journal of Science Education, Part B* 5(3), pp. 276–294. Available at: https://doi.org/10.1080/21548455.2014.941040.

Maggiulli, K. 2022. 'Teaching Invasive Species Ethically: Using Comics to Resist Metaphors of Moral Wrongdoing Build Literacy in Environmental Ethics', *Environmental Education Research* 28(9), pp. 1391–1409. Available at: https://doi.org/10.1080/13504622.2022.2085247.

Miller, S., 2001. 'Public Understanding of Science at the Crossroads', *Public Understanding of Science* 10(1), pp.115–120.

Monastersky, R. and Sousanis, N. 2015. ' The fragile framework', *Nature* 527 pp. 427–435. Available at: https://doi.org/10.1038/527427a.

Moser, S.C. 2010. 'Communicating Climate Change: History, Challenges, Process and Future Directions', WIREs Climate Change, 1(1), pp. 31–53. Available at: https://doi.org/10.1002/wcc.11.

Munawwaroh, E.L., Priyono, B., and Ningsih, M.R. 2018. 'The Influence of Science Comic Based Character Education on Understanding the Concept and Students' Environmental Caring Attitude on Global Warming Material', *Journal of Biology Education* 7(2), pp. 167–173. Available at: https://doi.org/10.15294/jbe.v7i2.24257.

Ortony, A. 1993. *Metaphor and Thought*. New York, New York, United States: Cambridge University Press.

Parks Canada 2023. Abbot Pass Refuge Cabin National Historic Site. Available at: https://parks.canada.ca/pn-np/bc/yoho/culture/abbot/info (Accessed: 21 Aug 2023).

Poortinga, W. and Pidgeon, N.F. 2003. 'Exploring the Dimensionality of Trust in Risk Regulation', *Risk Analysis: An International Journal* 23(5), pp. 961–972. Available at: https://doi.org/10.1111/1539-6924.00373.

Pörtner, H.-O., Roberts, D.C., Masson-Delmotte, V., Zhai, P., Tignor, M., Poloczanska, E., and Weyer, N.M. (eds.). 2019. *IPCC special report on the ocean and cryosphere in a changing climate*. New York, New York, United States: Cambridge University Press.

Reumont, F. von and Budke, A. 2023. 'Learning About Climate Change with Comics and Text: A Comparative Study', *Sustainability Science*. Available at: https://doi.org/10.1007/s11625-023-01398-x.

Segel, E. and Heer, J., 2010. 'Narrative Visualization: Telling Stories with Data', *IEEE Transactions on Visualization and Computer Graphics* 16(6), pp. 1139–1148. Available at: https://doi.org/10.1109/TVCG.2010.179.

Sturgis, P. and Allum, N. 2004. 'Science in Society: Re-evaluating the Deficit Model of Public Attitudes', *Public Understanding of Science* 13(1), pp. 55–74. Available at: https://doi.org/10.1177/0963662504042690.

Suldovsky, B. 2017. 'The Information Deficit Model and Climate Change Communication', *Oxford Research Encyclopedia of Climate Science*. Available at: https://doi.org/10.1093/acrefore/9780190228620.013.301.

Tatalovic, M. 2009. 'Science Comics as Tools for Science Education and Communication: a Brief, Exploratory Study', *Journal of Science Communication* 8(04) A02. Available at: https://doi.org/10.22323/2.08040202.

Theodorou, P., Vratsanou, K.C., Nastoulas, I., Kalogirou, E.S., and Skanavis, C. 2019. 'Climate Change Education Through DST in the Age Group "10–13" in Greece', in W. Leal Filho, B. Lackner, and H. McGhie (eds.) *Addressing the Challenges in Communicating Climate Change Across Various Audiences*. Springer Link, pp. 317–337. Available at: https://doi.org/10.1007/978-3-319-98294-6_20.

Topkaya, Y. 2016. 'The Impact of Instructional Comics on the Cognitive and Affective Learning About Environmental Problems', *TED Egitim ve Bilim*, 41(187). Available at: https://doi.org/10.15390/EB.2016.5713.

Treen, K.M.d., Williams, H.T., and O'Neill, S.J. 2020. 'Online Misinformation about Climate Change', *Wiley Interdisciplinary Reviews: Climate Change*, 11(5), e665. Available at: https://doi.org/10.1002/wcc.665.

Wang, Z., Sundin, L., Murray-Rust, D., and Bach, B. 2020. 'Cheat Sheets for Data Visualization Techniques', in *Proceedings of the 2020 CHI Conference on Human Factors in Computing Systems*, Association for Computing Machinery, Honolulu, Hawaii, United States, pp. 1–13.

Wang, Z., Wang, S., Farinella, M., Murray-Rust, D., Riche, N.H., and Bach, B. 2019. 'Comparing Effectiveness and Engagement of Data Comics and Infographics', in *Proceedings of the 2019 CHI Conference on Human Factors in Computing Systems*. Glasgow, Scotland United Kingdom: pp. 1–12.

Zhao, Z., Marr, R., and Elmqvist, N. 2015. *Data Comics: Sequential Art for Data-Driven Storytelling*. Technical Report.

Capture zone uncertainty and the dynamics of well vulnerability as permafrost thaws – Whatì, NWT, Canada

Andrew J. Wiebe[1], Isabelle de Grandpré[2] & Jeffrey M. McKenzie[3]

[1]*Department of Earth and Environmental Sciences, University of Waterloo, Waterloo, Ontario, Canada*

[2]*Water Monitoring and Stewardship Division, Government of Northwest Territories, Yellowknife, Northwest Territories, Canada*

[3]*Department of Earth and Planetary Sciences, McGill University, Montreal, Québec, Canada*

ABSTRACT

Thawing permafrost modifies the conditions of the ground and can impact groundwater connectivity, quantity, and quality. These changes may increase the contaminant threats to drinking water for communities relying on nearby production wells. This study evaluated possible changes in vulnerability for a community well in Whatì (Northwest Territories, Canada), located in a discontinuous permafrost region beside Lac La Martre, the third largest lake of the Northwest Territories. The community well was installed in a talik at a depth of around 12 m. Where present, the permafrost in the area is warm (> -2 °C) and can be found starting at depths between two and five meters. A two-dimensional analytical method was used to visualize possible theoretical well capture zones for a wedge-shaped aquifer representing the peninsula on which the community is located. Average well pumping rates and aquifer hydraulic conductivity values were employed. Two scenarios simulated stages of likely permafrost thaw based on observations within the community in the 1980s and 1990s and recent field studies at the edge of the community. Results indicate that the well capture zone may initially have underlain a portion of community but that it has likely expanded due to permafrost thaw, now possibly including areas of the land surface with previously unlikely contaminant threats such as more heating fuel storage tanks, the landfill, and wastewater disposal sites. This study highlights the importance of assessing the vulnerability of wells located in permafrost zones in the context of climate change.

1 INTRODUCTION

Permafrost thaw due to climate change may increase the active layer thickness as well as the number and the size of taliks in discontinuous permafrost, thereby enhancing groundwater recharge and flow. This thaw may also increase threats of contamination to groundwater wells in permafrost regions by increasing the connectivity between surface water bodies and groundwater supply aquifers (Lamontagne-Hallé et al. 2018), by eroding the protective low-permeability permafrost layer beneath unlined landfills (INAC 2007; Kent et al. 2003; Wiebe et al. 2023), and by decreasing subsurface travel times during which contaminants might biodegrade or disperse. Climate change is occurring at a rapid rate at northern latitudes (warming at two to three times the global average – IPCC 2022; Zhang et al. 2019) and discontinuous permafrost regions are especially susceptible to thaw and progressive degradation over time (e.g., Devoie et al. 2019).

The use of groundwater as a drinking water source varies across northern Canada from greater than 90% in the Yukon (Government of Yukon 2017) to around 3% in the Northwest Territories (NWT Bureau of Statistics 2022) to ~0% in Nunavut. Groundwater use for drinking water is also common in Alaska, providing around 40% of the combined public and domestic supply (Dieter et al. 2018). Groundwater may be more protected than surface water from certain types of contaminants, especially where there exist low-permeability layers such as clayey confining units or permafrost to limit vertical flow within the footprint of a community. Three communities in the Northwest Territories (NWT; i.e., Fort Liard, Nahanni Butte, and Whatì) have groundwater wells that supply drinking water, and all three are located in the discontinuous permafrost region (Heginbottom et al. 1995). In addition to issues related to permafrost thaw, northern communities may face groundwater management challenges such as limited knowledge regarding their groundwater resources, subsurface properties, permafrost extent, and contamination occurrences (e.g., spills of gasoline and diesel heating fuel). A typical groundwater management approach to protecting wells from contamination is to delineate each well's groundwater contribution area ("capture zone") and then take subsequent steps to safeguard water quality and recharge rates in these areas.

1.1 Well capture zones

Delineating a well capture zone involves estimating the region of the subsurface that contributes water to a well within a specified amount of time (e.g., several decades). The delineation ranges in complexity from a simple calculated fixed radius approach (if the regional water table is relatively flat; BCMOE 2000) to approaches that include regional flow via Darcy's Law (e.g., Ceric and Haitjema 2005) to fully distributed numerical models that account for detailed stratigraphic information and regional boundary conditions (e.g., HydroGeoSphere – Aquanty 2015; Yin 2023). Capture zone delineation in northern Canada is complicated by the fact that many communities are located adjacent to surface water bodies. These pose a challenge for simple approaches because such methods do not account for surface water features. The application of fully distributed, three-dimensional (3-D) models is not always

https://doi.org/10.52381/ICOP2024.204.1

feasible because of data requirements, modelling expertise availability, and the time required to construct a site-specific model and perform simulations. Analytical models capable of accounting for surface water features offer a middle road in terms of model development and complexity while maintaining rapid run times.

1.2 Study site

The community of Whatì, NWT, Canada (117'16"19.9°W, 63'8"38.3°N; Figure 1) has a population of approximately 550 people (NWT Bureau of Statistics 2022) and the community's drinking water supply system consists of one production well screened in highly fractured dolostone bedrock (Stanley Associates 1987). The well is located near the tip of the peninsula on which the community is located, adjacent to Lac La Martre, the third largest lake in the NWT.

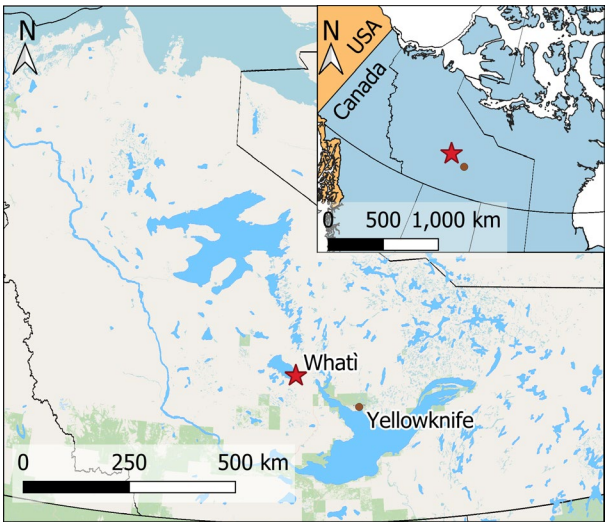

Figure 1. Location of Whatì, NWT (country boundaries: Sandvik 2009; province/territory boundaries: Government of Northwest Territories 2023; basemap: ©OpenStreetMap, 2023).

Whatì is located within a zone of discontinuous permafrost (Daly et al. 2022; Heginbottom et al. 1995), where permafrost is likely to be present in lower permeability soils underlying forests (Stantec 2017) and associated with low-lying peatlands or wetlands. Geotechnical studies (Hardy 1991; Thurber 1981) reported permafrost at depths between 2 and 5 m beneath the community in previous decades, while Daly et al. (2022) collected recent field data regarding permafrost presence or absence in areas largely outside the community (Figure 2). Permafrost thaw is evident from structural damage to some of the buildings within the community. It is likely that permafrost has thawed substantially due to climatic warming since measurements in the 1980s and 1990s.

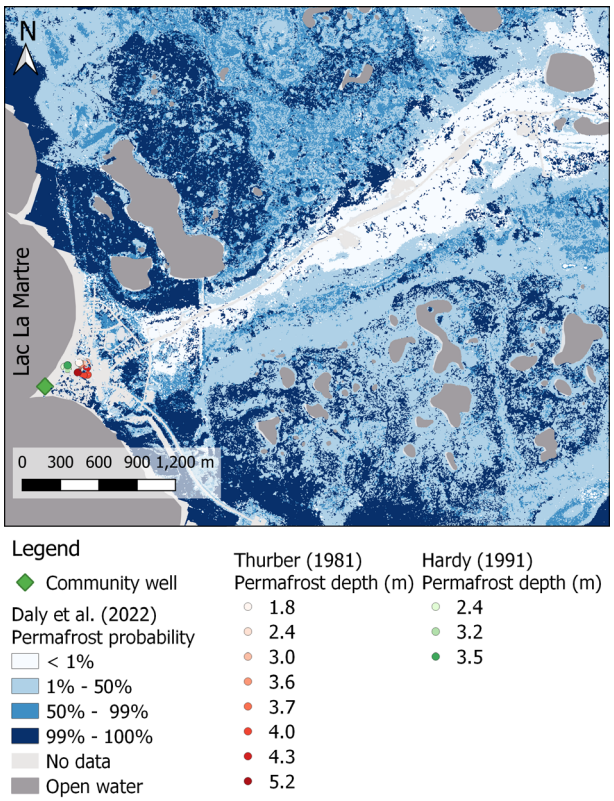

Figure 2. Estimates of permafrost presence (after Daly et al. 2022; S.V. Daly, pers. comm. 2023; Hardy 1991; Thurber 1981).

The local, near-surface geology of the Whatì area consists of glacial overburden and lacustrine sediments overlying dolostone bedrock, the upper surface of which is highly weathered and fractured (Reid Crowther and Bernard 1984). Bedrock has been encountered at depths of about 10 m in multiple boreholes within the community (Reid Crowther and Bernard 1984; Hardy 1991; Stanley Associates 1987; Thurber 1981). Till, lacustrine deposits, and organic deposits are present elsewhere nearby (Figure 3; Ednie et al. 2014).

The current conceptual model for groundwater flow at the site is that shallow, local flow is directed toward Lac La Martre from the upland area immediately east of the lake, but that deeper regional flow is toward the east. This is based on local scale (several hundred metres) and regional scale (tens of kilometres) topography. The land generally rises toward the east away from the lake for several kilometres, but there is a sharp decline in ground surface elevation of over 50 m near La Martre Falls (Natural Resources Canada 2017), which is located about 20 km east of Whatì. The relevant spatial scale of the flow system for the relatively small pumping rate at the community well is the local scale. The "regional" hydraulic gradient that is later discussed in association with the analytical solutions is in fact the shallow, local flow system discussed here.

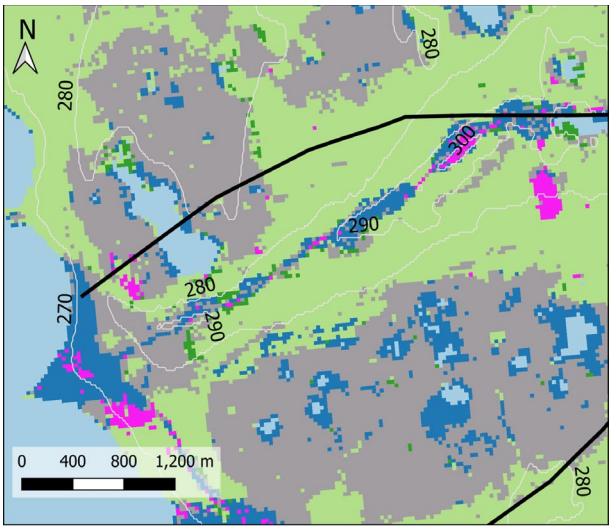

Legend

- Bedrock
- Lacustrine deposits
- Till undifferentiated
- Till veneer
- Organic deposits
- Water
- Meltwater channels or drumlinoid ridges
- Elevation contour (metres above sea level)

Figure 3. Surficial geology (after Ednie et al. 2014; Government of Canada 2017). The validity of the bedrock location predictions is unknown and may not be accurate for these predictions based on remote sensing.

Possible groundwater contaminants include petroleum hydrocarbons, landfill leachate, and wastewater. There is a diesel power plant within the community, and houses and buildings have fuel tanks for winter heating. The community's landfill locations are about 2 and 4 km NE from the well. Wastewater is stored in household tanks that are emptied regularly, and waste is transported by truck to a sewage lagoon that is about 4 km from the well (Community Government of Whatì 2017). Figure 4 shows the locations of potential contaminant sources. Each building on the map was assumed to have associated heating fuel and wastewater tanks.

The Whatì production well is located about 30 m from the lake and screened in fractured dolostone over an effective interval from 10.35 m to 12.77 m below ground surface (Stanley Associates 1987). A 24-hour pumping test by Stanley Associates (1987) at this well yielded a transmissivity estimate of 0.19 m^2/s, but a Cooper-Jacob composite analysis using the pumping test data from Stanley Associates (1987) for the production, test, and standby wells yielded a transmissivity of 0.15 m^2/s. The latter suggests a hydraulic conductivity of about 0.017 m/s, assuming an initial saturated aquifer thickness of 9 m.

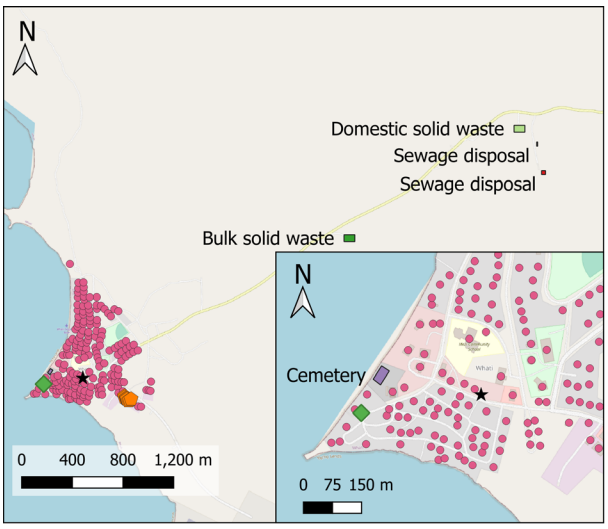

Legend

- Community well
- Cemetery
- Bulk solid waste landfill
- Domestic solid waste landfill
- Sewage disposal
- Diesel power plant
- Gas station tank farm
- Potential and known fuel tanks

Figure 4. Potential contaminant sources (building locations and basemap: © OpenStreetMap 2023; solid waste disposal and sewage disposal locations: Community Government of Whatì 2017). Note: not all potential sources (fuel and wastewater tanks) may be identified at the eastern edge of the community.

1.3 Objectives

The objectives of this study are to investigate how the capture zone of the Whatì community well might change in response to progressive permafrost thaw, and whether this might increase threats to well water quality. Capture zone boundaries are calculated using an analytical approach that approximates constant head boundary conditions based on an imposed gradient. Threats to water quality are evaluated based on known potential sources of contamination within the community. The present study builds on unpublished work by the authors regarding a groundwater vulnerability assessment for the community of Whatì that is based on discussions with community members and review of relevant literature and available data.

2 Methodology

2.1 Analytical capture zone calculations

A 2-D analytical method inspired by Nagheli et al. (2020) and similar to the one by Holzbecher (2005) was used to estimate capture zone boundaries for the Whatì community well under steady-state conditions for two snapshots of permafrost thaw evolution. A 3-D numerical model was not used to estimate capture zones because uncertainty in the stratigraphy and boundary conditions due to data availability would greatly exceed the complex model's usefulness. Hydraulic heads have not been reported except in the immediate vicinity of the community well during initial aquifer tests (Stanley Associates 1987). The analytical

method has the advantages of having short run-times and incorporating surface water features that can reasonably be represented as constant hydraulic head boundaries. The method is briefly outlined as follows.

A wedge aquifer shape was selected to represent the peninsula on which the community of Whatì is located. Parameters such as the saturated thickness and hydraulic conductivity of the aquifer underlying the community were obtained from borehole logs and pumping tests, respectively (Stanley Associates 1987). Hypothetical values were specified for the magnitude and direction of the regional hydraulic gradient because of insufficient data (discussed below). The location of the frozen/unfrozen soil interface was specified as explained below. The x and y axes of the coordinate system were rotated from east and north, respectively, to match the geometry of the Whatì peninsula more closely.

The method employed used image well theory (Strack 1989) and the complex potential for a system consisting of multiple wells and a regional gradient within a homogeneous unconfined aquifer with defined hydraulic conductivity. Superposition of the potentials related to recharge, a regional gradient, and real and image wells was accomplished by adapting the solution of Holzbecher (2005) for two-dimensional groundwater flow in the presence of two isopotential lines (lake shorelines, here) at an angle α, resulting in Eq. 1:

$$\Phi(z) = \Phi_{rech}(z) - (Q_{x0} - iQ_{y0})\, z + (Q_{well}/2\pi)\,[\ln(z^{\pi/\alpha} - z_{well}{}^{\pi/\alpha}) - \ln(z^{\pi/\alpha} - \mathrm{conj}(z_{well})^{\pi/\alpha}) - \ln(z^{\pi/\alpha} - z_{pf}{}^{\pi/\alpha}) - \ln(z^{\pi/\alpha} - \mathrm{conj}(z_{pf})^{\pi/\alpha})], \quad [1]$$

where $\Phi(z)$ is the complex discharge potential, z is the complex coordinate, $\Phi_{rech}(z)$ is the potential related to uniform recharge, $-(Q_{x0} - iQ_{y0})z$ is the complex potential for uniform flow related to the regional gradient (Strack 1989), Q_{well} is the pumping rate of the well, z_{well} specifies the real and imaginary coordinates of the well, $conj(z)$ is the complex conjugate of z, and z_{pf} specifies the coordinates for an optional image well (extraction) that enforces the permafrost boundary on the upland side of the aquifer. The image well was determined (through trial and error) to be located at a distance from the real well of 4 times the perpendicular distance between that well and the permafrost boundary line, along that line. Q_{x0} and Q_{y0} are the x and y- flow components per unit aquifer width, where Q_{x0} was calculated via Eq. 2 (Strack 2017):

$$Q_{x0}(z) = -\partial\Phi(z)/\partial x \approx -\Delta\Phi_{j,k}/\Delta x = -K(h^2_{j,k+1} - h^2_{j,k})/(2\Delta x), \quad [2]$$

where K is the hydraulic conductivity, h is the hydraulic head, and (j,k) specifies the cell coordinates – (imaginary, real) = (row, column). Q_{y0} was calculated similarly, except that the difference was between squared heads in adjacent rows rather than columns. The domain was divided into 0.5 m by 0.5 m grid cells for the calculations ($\Delta x = \Delta y$). Recharge was incorporated by solving the Poisson equation ($\nabla^2\Phi = -b$; e.g., Strack 2017) to represent shallow unconfined flow with a uniform recharge rate of b (50 mm/yr). This was accomplished using a numerical technique outlined by Barba and Forsyth (2017) to solve for the complex discharge potential at each cell within the wedge-shaped aquifer, with boundary conditions specifying a potential of zero along and outside the lake boundaries, and potential values at the inland edges of the aquifer set to adjacent values. Discharge potential for each grid cell (j,k) was calculated iteratively via Eq. 3 (Barba and Forsyth 2017):

$$\Phi^t_{j,k} = (2[\Delta x^2 + \Delta y^2])^{-1}([\Phi^t_{j+1,k} + \Phi^t_{j-1,k}]\Delta y^2 + ([\Phi^t_{j,k+1} + \Phi^t_{j,k-1}]\Delta x^2 - b^t_{j,k}\Delta x^2\Delta y^2) \quad [3]$$

where t is the timestep, and $b^t_{j,k}$ is the recharge rate (uniform in time and space, here). A total of 100 timesteps were employed to calculate the potential related to recharge.

Cubic Hermite interpolation (Van Loan 2000) was used to create a background regional flow field (in the absence of pumping and recharge) by specifying the gradient of the water table as zero at the lake boundaries and as a fixed vector at points along a radius of 1000 m from the peninsula tip. The resulting background flow field (Figure 5) was used for all simulations. Locations along curves starting at points along a radius of 1000 m from the origin that terminated at the lake boundaries, and associated hydraulic head values, were calculated for 21 splines, with one as the centreline bisecting the peninsula, and the other ten pairs of curves mirrored across it (Figure 5). Head values along the outer arc were also calculated with a spline. The head values were interpolated across the grid, subsampled, and then smoothed with a cubic interpolation method. The head values in adjacent cells were used to calculate Q_{x0} via Eq. 2, and Q_{y0} via an analogous equation.

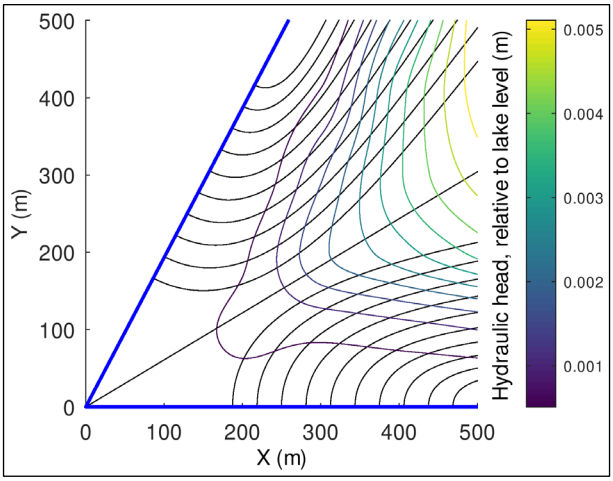

Figure 5. Contour map of background regional flow field hydraulic head (water table). The blue lines are the lake boundaries, and the black lines indicate the splines used to calculate the hydraulic head values.

A sequential contouring approach (Holzbecher 2018) was used to line up the streamlines on either side of a branch cut resulting from the discontinuity in the complex logarithm of the solution. Streamlines along the branch cut were

manually removed in QGIS. Stagnation points were identified using a gradient ascent method search of the *real(Φ(z))* field. Hydraulic heads, $h_{j,k}$, were calculated from the complex potential via Eq. 4 (Strack 2017):

$$h_{j,k} = \text{sqrt}(2 [\text{real}(\Phi_{j,k}) - C_u] / K), \quad [4]$$

where K is the hydraulic conductivity and C_u is a constant (a negative C_u was used to ensure real values of $h_{j,k}$). The sequential contouring step was performed using a modified version of the R (R Core Team 2022) code by Wiebe and McKenzie (2022). The remainder of the method was coded in the scientific computation program GNU Octave (Eaton et al. 2020). All code is available at https://github.com/ajwiebe77/ICOP24.

2.2 Scenario analysis

Two scenarios were employed to assess the changes in capture zone size and shape for the community at Whatì based on hypothesized locations of the interface between frozen and unfrozen soil beneath the community. Scenario 1 assumed that the presence of the interface was located 500 m away from the community well along the two arms of the wedge-shaped aquifer. This scenario sought to represent the interface as a continuous no-flow line, whereas the actual situation is likely more complex because of the discontinuous nature of the permafrost. The location of the permafrost boundary was based loosely on the results of Thurber (1981) and Hardy (1991) and represents conditions where unfrozen soil is present only near the tip of the peninsula. Both scenarios assumed regional flow toward the tip of the peninsula, with a tapering of the slope of the water table to zero at the lake boundaries (Figure 5).

Scenario 2 assumed no permafrost presence and simply employed a semi-infinite boundary along the third side of the wedge. This second scenario represents complete permafrost thaw at some point in the future, or at least such extensive thaw that permafrost does not represent a major barrier to groundwater flow. Table 1 lists the parameters employed during the scenario analysis.

3 Results

Figure 6 shows the results of Scenario 1, which assumed a permafrost boundary located at x = 500 m. The groundwater flow lines are essentially perpendicular to the lake boundaries, as expected for constant head lines. One flow line unrealistically shows flow from the lake around the outside of the capture zone, which is a byproduct of the image well used to represent the permafrost interface. The results visualize that the capture zone for the Whatì production well may initially have encompassed only part of the community footprint. Permafrost may thus have provided some initial protection to the well in terms of potential contamination by limiting the region from which groundwater recharge could convey pollutants, although the cemetery and approximately 50 heating fuel and wastewater tanks are within the capture zone.

Table 1. Summary of capture zone simulation parameters.

Parameter	Scenario 1	Scenario 2
Pumping rate, Q_{well} (L/s)	0.59*	0.59*
Hydraulic conductivity, K (m/s)	0.017	0.017
Saturated aquifer thickness (m)	9†	9†
Magnitude of regional gradient at radius of 1000 m (m/m)	1×10^{-5}	1×10^{-5}
Direction of regional gradient (° clockwise from north; after shape rotation)	246	246
Aquifer radius from well or distance to permafrost along x-axis (m)	500‡	500
Aquifer angle at point of peninsula (°)	63	63
Aquifer rotation angle to align x-axis with south side of peninsula (° counterclockwise from east)	-7	-7
Boundary type on inland side of aquifer	Impermeable	Semi-infinite

* Based on Community Government of Whatì (2021).
† Based roughly on Stanley Associates (1987).
‡ Based on Thurber (1981) and Hardy (1991).

Figure 7 shows the results of Scenario 2, which assumed no permafrost. The results suggest a larger capture zone area that extends throughout the aquifer wedge and beyond the 500 m radius of the calculation region. Most of the heating fuel and wastewater tanks in the community could potentially be within the well capture zone, in addition to the cemetery and the diesel power plant, although groundwater would be expected to flow into the lake rather than toward the well near shoreline areas at some point beyond the 500 m radius shown. The sewage lagoon and landfill are located outside of the community toward the east and may possibly also be within the capture zone for Scenario 2, although groundwater flow directions may be more nuanced with flow toward wetland areas south of these features rather than directly toward the peninsula.

4 Discussion

The results visualize an expansion of the capture zone as permafrost thaws. The diesel power plant is likely within the long term (no permafrost) capture zone, although it is uncertain whether the gas station tank farm is likely to be because of expected flow toward the lake farther from the well and near the shoreline. Additional data such as hydraulic head measurements would improve the analysis.

Limitations of the study include: 1) the use of steady-state snapshots instead of transient scenarios to explore changes in the capture zone, 2) the representation of permafrost as an impermeable region of the subsurface, 3) assumptions of homogeneous aquifer conditions and fully penetrating wells, 4) the assumption that the surface

water boundaries continue beyond the calculation domain, 5) unknown bedrock topography, and 6) neglect of dispersion. Despite the capture zone illustrated for Scenario 1, overland flow downslope toward the lake or supra-permafrost groundwater flow within the active layer could convey contaminants from outside the estimated capture zone into the contributing recharge area. In terms of representing permafrost as an impermeable boundary resulting from an image well, this approach failed to generate a truly impermeable boundary because of the regional gradient, and conceptually does not incorporate the discontinuous nature of local permafrost. It is therefore somewhat unrealistic but conceptualizes the likely initial capture zone as restricted to the unfrozen region. The assumptions of the analytical approach limit the investigation to simplistic scenarios.

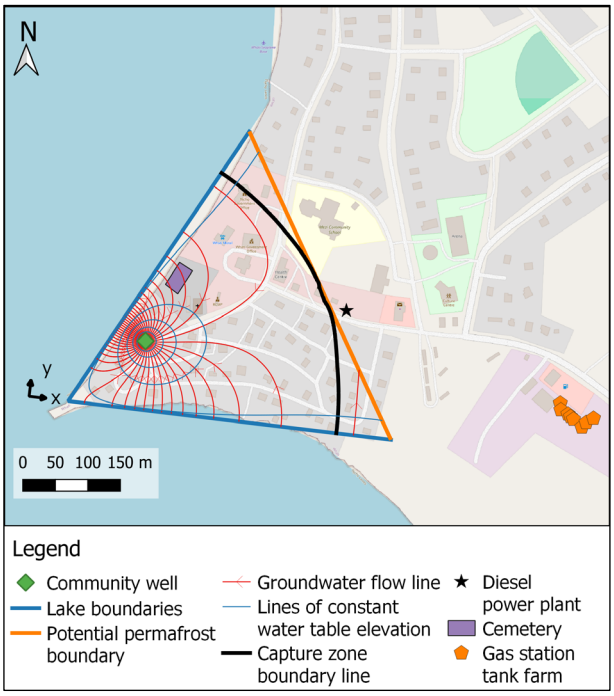

Figure 6. Possible steady-state capture zone for Scenario 1 (basemap: © OpenStreetMap 2023; well location: Stanley Associates 1987). Head contour interval (water table): 2×10^{-5} m; flow line contour interval: 1.31×10^{-5} m^3/s. The capture zone is present throughout nearly the entire unfrozen region of the peninsula.

Despite the limitations listed above, analytical solutions offer certain advantages to capture zone estimates for northern regions. Many wells in northern regions are located near surface water features, and permafrost boundaries may exist near some of these wells. The ability to incorporate surface water and permafrost features represents a distinct advantage over simpler capture zone estimation methods, and the rapid run times and ability to test different parameter combinations quickly has advantages over fully distributed, process-based models.

Analytical approaches could be helpful in assessing possible climate change impacts on well capture zones if boundary conditions can be represented reasonably.

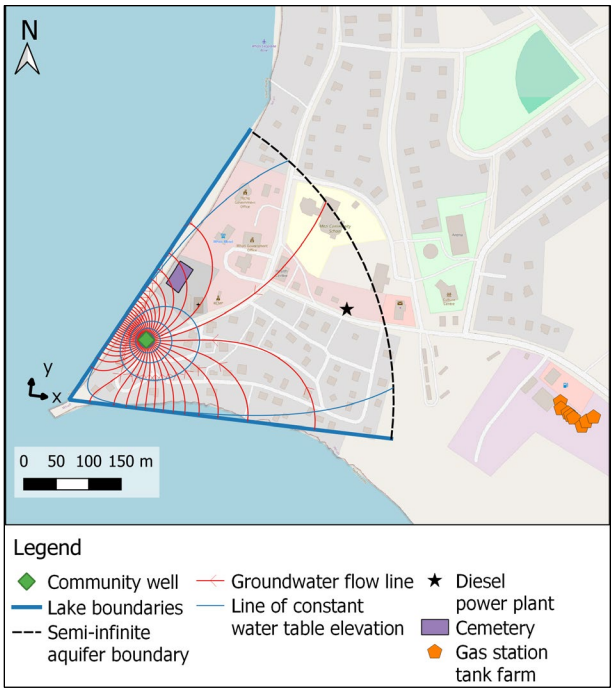

Figure 7. Possible steady-state groundwater flow lines and equipotential lines for Scenario 2 (basemap: © OpenStreetMap 2023; well location: Stanley Associates 1987). Head contour interval: 2×10^{-5} m; flow line contour interval: 1.31×10^{-5} m^3/s. No capture zone boundary is present within the calculation region and the capture zone extends from the peninsula toward the east.

5 CONCLUSIONS

The analytical simulations visualize the evolution of the capture zone shape and area for the Whatì community well over time due to permafrost thaw. The initial capture zone around the 1990s was likely small in extent and confined to the unfrozen region near the tip of the peninsula, due to the presence of permafrost within several hundred metres of the well. Such a capture zone would include multiple household fuel and wastewater tanks but not the diesel power plant, nor the gasoline tank farm, landfill, or sewage lagoon. If permafrost thaws completely, the capture zone could expand to include a larger area and many more potential contaminant sources. Additional data from an observation well network would assist vulnerability assessment and constrain the uncertainty, especially regarding groundwater flow near the lake shoreline. Analytical solutions may offer a relevant approach to estimate capture zones for other wells near surface water features and permafrost in northern regions in the context of climate change, but special care must be taken when representing boundary conditions.

6 ACKNOWLEDGEMENTS

Funding from the Canada First Research Excellence Fund (CFREF) Global Water Futures (GWF) program is gratefully acknowledged. The authors wish to thank the Elders, translator, and other community members from Whatì who participated in the 2022 *What's Happening Under the Land?* workshop. S.V. Daly kindly shared GIS files for the permafrost probability map.

7 REFERENCES

Aquanty Inc. (Aquanty). 2015. *HGS Reference Manual. Manual for HydroGeoSphere code*. Waterloo, Ontario, Canada: Aquanty, Inc. Available at: https://www.aquanty.com/ (Accessed: 12 February 2018).

Barba, L.A. and Forsyth, G.F. 2017. *12 Steps to Navier-Stokes*. Available at: https://nbviewer.org/github/barbagroup/CFDPython/blob/master/lessons/13_Step_10.ipynb (Accessed: 3 January 2024).

British Columbia Ministry of the Environment (BCMOE) 2000. *Well Protection Toolkit. Step 2: Define the Well Protection Area*. Available at: http://www.env.gov.bc.ca/wsd/plan_protect_sustain/groundwater/wells/well_protection/wellprotect.html (Accessed: 22 July 2021).

Ceric, A. and Haitjema, H. 2005. 'On using simple time-of-travel capture zone delineation methods', *Groundwater* 43(3), pp. 408–412. doi:10.1111/j.1745-6584.2005.0035.x.

Community Government of Whatì 2017. *Sewage Disposal: Operation and Maintenance Manual, Version 1.1*. Whatì, Northwest Territories, Canada: Community Government of Whatì, Updated 26 June 2017. Available at: https://mvlwb.com/registry/W2017L3-0002 (Accessed: 7 July 2023).

Community Government of Whatì 2021. *Municipal water licence annual report. Reporting Year: 2020*. Whatì, Northwest Territories, Canada: Community Government of Whatì, Updated 16 Aug 2021. Available at: https://mvlwb.com/registry/W2017L3-0002 (Accessed: 6 March 2023).

Daly, S.V., Bonnaventure, P.P., and Kochtitzky, W. 2022. 'Influence of ecosystem and disturbance on near-surface permafrost distribution, Whatì, Northwest Territories, Canada'. *Permafrost and Periglacial Processes* 33(4), pp. 339–352. doi:10.1002/ppp.2160.

Devoie, E.G., Craig, J.R., Connon, R.F., and Quinton, W.L. 2019. 'Taliks: A tipping point in discontinuous permafrost degradation in peatlands', *Water Resources Research* 55, pp. 9838–9857. doi:10.1029/2018WR024488.

Dieter, C.A., Maupin, M.A., Caldwell, R.R., Harris, M.A., Ivahnenko, T.I., Lovelace, J.K., Barber, N.L., and Linsey, K.S. 2018. 'Estimated use of water in the United States in 2015', *United States Geological Survey* US Geological Survey Circular 1441.doi:10.3133/cir1441.

Eaton, J.W., Bateman, D., Hauberg, S., and Wehbring, R., 2020. *GNU Octave version 6.4.0 manual: A high-level interactive language for numerical computations*. Available at: https://docs.octave.org/v6.4.0/index.html (Accessed: 3 Jan 2024).

Ednie, M., Kerr, D.E., Olthof, I., Wolfe, S.A., and Eagles, S. 2014. 'Predictive Surficial Geology derived from LANDSAT 7, Marian River, NTS 85-N, Northwest Territories', *Geological Survey of Canada* Open File 7543, zip file. doi:10.4095/294923.

Government of Canada 2017. *Elevation in Canada - CanVec Series - Elevation Features*. Available at: https://open.canada.ca/data/en/dataset/64aad38d-f692-4ab6-bf2c-f938586c1249 (Accessed: 11 August 2021).

Government of Northwest Territories 2023. *Provincial Admin. Accessed within QGIS 3.16.9*. Available at: https://www.apps.geomatics.gov.nt.ca/arcgis/services/GNWT_Basemaps/GNWTBasemapLCC/MapServer/WMSServer.

Government of Yukon 2017. *Yukon Observation Well Network: 2017 Report*. Available at: https://yukon.ca/en/yukon-observation-well-network-2017-report (Accessed: 3 August 2023).

Hardy BBT Ltd. (Hardy) 1991. *Geotechnical investigation: Proposed Community Office, Lac La Martre, NWT*. Yellowknife, Northwest Territories, Canada: Government of Northwest Territories Department of Public Works, Architectural Division, March 1991.

Heginbottom, J.A., Dubreuil, M.A., and Harker, P.T. 1995. 'Canada, permafrost', in *The National Atlas of Canada, 5th edition*. Natural Resources Canada, Geomatics Canada, MCR 4177, 1 sheet. doi:10.4095/294672.

Holzbecher, E. 2005. 'Analytical solution for two-dimensional groundwater flow in presence of two isopotential lines', *Water Resources Research* 41, W12502. doi:10.1029/2005WR004583.

Holzbecher, E. 2018. 'Streamline visualization of potential flow with branch cuts, with applications to groundwater', *Journal of Flow Visualization and Image Processing* 25(2), pp. 119–144. doi:10.1615/JFlowVisImageProc.2018025918.

Indian and Northern Affairs Canada (INAC) 2007. *Giant Mine remediation plan.*, Yellowknife, Northwest Territories, Canada: Department of Indian Affairs and Northern Development Giant Mine Remediation Project, 260 p. Available at: http://reviewboard.ca/upload/project_document/EA0809-001_Giant_Mine_Remediation_Plan_1328900464.pdf (Accessed: 14 November 2022).

Intergovernmental Panel on Climate Change (IPCC) 2022. *IPCC Special Report on the Ocean and Cryosphere in a Changing Climate*. Cambridge, United Kingdom and New York, New York, United States: Cambridge University Press, 755 p. doi:10.1017/9781009157964.

Kent, R., Marshall, P., and Hawke, L. 2003. *Background report for updating the guidelines for the planning, design, operations and maintenance of modified solid waste sites in the Northwest Territories*. Yellowknife, Northwest Territories, Canada: Department of Municipal and Community Affairs, Government of the Northwest Territories, prepared by FSC Architects & Engineers. Available at: https://www.enr.gov.nt.ca/sites/enr/files/reports/background_updating_the_solidwaste_guidelines.pdf (Accessed: 14 November 2022).

Lamontagne-Hallé, P., McKenzie, J.M., Kurylyk, B.L., and Zipper, S.C. 2018. 'Changing groundwater discharge dynamics in permafrost regions', *Environmental Research Letters* 13, 0840017. doi:10.1088/1748-9326/aad404.

Nagheli, S., Samani, N., and Barry, D.A. 2020. 'Capture zone models of a multi-well system in aquifers bounded with regular and irregular inflow boundaries', *Journal Hydrology X* 7, 100053. doi:10.1016/j.hydroa.2020.100053.

Natural Resources Canada 2017. *CanVec Elevation Features*. Available at: https://atlas.gc.ca/toporama/en/index.html (Accessed: 7 January 2023).

Northwest Territories (NWT) Bureau of Statistics 2022. *Population Estimates By Community*. Available at: https://www.statsnwt.ca/population/population-estimates/bycommunity.php (Accessed: 20 July 2023).

OpenStreetMap 2023. *Basemap*. Accessed within QGIS 3.1.2 software. Data available under Open Database License https://www.openstreetmap.org/copyright.

R Core Team 2022. *R: A language and environment for statistical computing*. Vienna, Austria: R Foundation for Statistical Computing. Available at: https://www.R-project.org/ (Accessed: 17 March 2022).

Reid Crowther & Partners Ltd., and D.W. Bernard Groundwater Consultants Ltd. (Reid Crowther and Bernard) 1984. *Groundwater Exploration and Well Development Study - 4 Communities in Fort Smith Region, N.W.T.* Yellowknife, Northwest Territories, Canada: Department of Local Governments, Government of the Northwest Territories, March 1984.

Sandvik, B. 2009. *World borders dataset*. GIS digital mapping data. Available at: http://thematicmapping.org/downloads/world_borders.php (Accessed: 27 June 2022).

Stanley Associates Engineering Ltd. (Stanley Associates) 1987. *Lac La Martre - Well Construction, Draft Report*. Yellowknife, Northwest Territories, Canada: Government of Northwest Territories, Engineering Division, Department of Public Works and Highways, 23 March 1987.

Stantec Consulting Ltd. (Stantec) 2017. *Geotechnical report, road alignment, proposed Tlicho all-season road, Northwest Territories*. Ottawa, Ontario, Canada: Tlicho Engineering and Environmental Services Ltd., 10 November 2017.

Strack O.D.L. 1989. *Groundwater Mechanics*. Englewood Cliffs, New Jersey, United States: Prentice-Hall.

Strack, O.D.L. 2017. *Analytical groundwater mechanics*. Cambridge, United Kingdom: Cambridge University Press. doi:10.1017/9781316563144.

Thurber Consultants Ltd. (Thurber) 1981. *Lac La Martre School: Geotechnical Investigation*. Edmonton, Alberta, Canada: Department of Public Works, Government of the Northwest Territories, 9 March 1981.

Van Loan, C.F. 2000. *Introduction to Scientific Computing*. 2nd Edition. Upper Saddle River, New Jersey, United States: Prentice-Hall.

Wiebe, A.J. and McKenzie, J.M. 2022. 'An Open-Source Web Tool for Visualizing Estimates of Well Capture Zones Near Surface Water Features', in *AGU Fall Meeting 2022,* Poster presentation. Chicago, Illinois, United States: 12–16 December 2022. doi:10.22541/essoar.167267811.10671930/v1.

Wiebe, A.J., McKenzie, J.M., Hamel, E., Rudolph, R., Mulligan, B., and de Grandpré, I. 2023. 'Groundwater vulnerability in the Yukon and Northwest Territories, Canada', *Hydrogeology Journal*. doi:10.1007/s10040-023-02720-8.

Yin, H. 2023. *Influence of Dynamic River Stage on the Vulnerability of Water Wells and Structure Foundations in Cold Regions*. Waterloo, Ontario, Canada: MSc. Thesis, University of Waterloo. Available at: http://hdl.handle.net/10012/19605.

Zhang, X., Flato, G., Kirchmeier-Young, M., Vincent, L., Wan, H., Wang, X., Rong, R., Fyfe, J., Lil, G., and Kharin, V.V. 2019. 'Changes in Temperature and Precipitation Across Canada', in E. Bush and D.S. Lemmen (eds), *Canada's Changing Climate Report*, pp 112–193. Available at: https://changingclimate.ca/CCCR2019/ (Accessed: 16 August 2023).

Comparative study of seismic resilience between PC and steel-concrete bridges in a permafrost region on the Qinghai-Tibet Plateau

Zhihua Xiong[1], Jiaqi Li[1], Jianbing Chen[2], Jinping Li[2] & Dongpeng Zhu[2]

[1]*College of Water Resources and Architectural Engineering, Northwest A&F University, Yangling, Shaanxi, China*

[2]*CCCC First Highway Consultants Co. Ltd., Xi´an, Shaanxi, China*

ABSTRACT

The process of the damage accumulation of bridges is studied under the extreme environment of the Qinghai-Tibet Plateau, and an evaluation scheme of the resilience of bridges is proposed, which aims for the cold region with high seismic risk. The objective of the study is to evaluate the robustness of the Prestressed Concrete (PC) bridge in service on the Qinghai-Tibet Plateau and the steel-concrete composite bridge. Based on the theoretic and statistical analysis of the existing data, the pile foundation settlement, fatigue and freeze-thaw damages during the service of concrete bridge and steel-concrete composite bridge were studied respectively. The loss function of bridge before earthquake was constructed. With implementation of bridge vulnerability, the post-earthquake recovery function of bridge system was developed. On the basis of these relationships, the variation functions of the PC and steel-concrete bridges under service are obtained. The critical maintenance and reinforcement date before earthquake are proposed, and the seismic resilience of the two types of bridges are evaluated.

1 INTRODUCTION

The Qinghai-Tibet Engineering Corridor is located in the high-altitude permafrost region, where the bridges in service are subjected to the combined influences of the frozen soil environment and seismic activities. In order to reduce the economic losses caused by earthquakes, the seismic design philosophy of bridges has been extended to include post-earthquake structural functionality restoration and rapid repair. This poses higher requirements for the seismic performance of bridges in permafrost regions with high seismic risk. To explore the post-earthquake recoverability and ease of repair of bridges, the concept of resilience has been introduced into the research related to the seismic design of bridges.

The definition of resilience by Bruneau et al. (2003), which refers to "the ability of social units to reduce disaster risks, control the impacts of disaster occurrence in terms of minimizing community disruptions and reducing future consequences while conducting recovery activities," has been widely accepted. Shinozuka et al. (2000) improved upon Bruneau's approach and developed a new method for measuring resilience. They used the cumulative exceedance probability of functional losses under different seismic motions as an indicator of resilience. Manyena (2006) defined seismic resilience as the inherent ability of a system to adapt, survive, and self-repair by changing its non-essential attributes when subjected to predetermined disturbances. Cimellaro et al. (2010) further studied seismic resilience by analyzing a hospital building, providing a new framework for quantitative research on seismic resilience and proposing various models for post-earthquake structural functionality recovery. Decò et al. (2013) assessed the probability of bridge damage through earthquake vulnerability analysis and derived a sinusoidal function with six parameters as a bridge's functional recovery function. Then they proposed an evaluation method for bridge seismic resilience, which considers the uncertainties of expected damage, recovery, and reconstruction costs. Ikpong et al. (2015) used various performance indicators to evaluate the bridge resilience under the influence of climate, and this evaluation method had been applied to many bridges in Canada. Chandrasekaran et al. (2016) studied the resilience of bridges reconstructed with column jackets of different materials under various disasters such as earthquakes and floods, and proposed a variety of different optimization schemes. Kilanitis et al. (2018) pointed out that measuring the seismic performance of bridges using a single indicator is not sufficiently accurate. They proposed resilience evaluation indicators based on various factors such as vehicle mileage, providing insights for simulating the sequence of seismic strengthening and the post-earthquake recovery process of bridges in a specific region. Vishwanath et al. (2019) took the reinforced concrete bridge deteriorated by chloride corrosion as the research object, analyzed its vulnerability through numerical simulation, and further evaluated the resilience. The results showed that the resilience of the bridge decreased with the aging of the bridge. Li et al. (2020) proposed a framework for long-term resilience and loss assessment of highway bridges under multiple independent natural hazards, providing a reference for the design of bridges under extreme conditions. Mitoulis et al. (2021) established a recovery model of bridges after flooding, and evaluated and quantified the resilience of flood-critical bridges.

The Qinghai-Tibet Engineering Corridor is situated in a high-altitude permafrost zone, which is also characterized by high seismic intensity. Unlike urban bridges, the Corridor faces distinct challenges due to the unique combination of high altitude, low temperature, and intense seismicity. And now, there is still a lack of suitable seismic resilience evaluation methods for bridges in permafrost region with high seismic risk. Based on the author's previous research (Xiong et al. 2018), it is found that currently, the thaw settlement, overloading, and freezing-thawing phenomena are quite common in bridges along the Qinghai-Tibet highway. The accumulation of these unfavorable

https://doi.org/10.52381/ICOP2024.79.1

environmental factors makes the functional performance of bridges more susceptible to degradation. Taking the existing PC girder bridge and the proposed steel-concrete composite girder bridge in permafrost region with high seismic risk as the research object, this paper comprehensively considers the three functional damage factors of the bridge, such as freeze-thaw damage, fatigue damage and uneven settlement of pile foundation, and combined with the analysis of the seismic vulnerability of the bridge, the functional change of the bridge's life cycle is studied. Based on this, the critical maintenance and reinforcement years of bridges are proposed, and the seismic resilience of bridges during their whole life cycle are evaluated, which can provide a reference for seismic design, post-disaster maintenance and repair of bridges in permafrost regions with high seismic risk on the Qinghai-Tibet Plateau.

2 BRIDGE LOSS FUNCTION CONSTRUCTION

2.1 Time-varying Effect of Freeze-thaw Damage

In cold regions, the freeze-thaw cycle can result in physical damage to concrete, affecting its strength, elastic modulus, and the anchoring performance of internal steel bars. Consequently, the durability of the structure is compromised. This study employs the variation of the concrete's relative dynamic elastic modulus under freeze-thaw conditions to represent the functional changes in the bridge system. Based on this, the loss function for freeze-thaw damage of bridges is constructed.

According to the indoor rapid freeze-thaw test (Zheng et al. 2018), the relative dynamic elastic modulus of concrete decreases with the increase of the number of freeze-thaw cycles. The relationship between the relative dynamic elastic modulus of C50 concrete and the number of freeze-thaw cycles can be obtained by fitting the data of the indoor test, as shown in Eq. 1.

$$P = \exp(-0.0034 - 1.7505\times10^{-4}N - 1.9097\times10^{-6}N^2) \quad [1]$$

In the formula, P is the relative dynamic elastic modulus of C50 concrete; N is the cumulative number of freeze-thaw cycles.

Due to the difference of indoor and outdoor environments, the freeze-thaw damage of concrete in indoor environments cannot be equated with that in outdoor environments. According to the research of Li et al. (2000), the expected value of the ratio of the number of freeze-thaw cycles between indoor and outdoor is 1:12 for the currently prescribed rapid freeze-thaw test methods. In this paper, the annual average number of freeze-thaw cycles of Xining, a representative city in Northwest China, is taken as the annual average number of freeze-thaw cycles of the research site, that is, 118 times per year. The loss function of freeze-thaw damage $Q_1(t)$ of concrete is fitted, as shown in Eq. 2.

$$Q_1(t) = \exp(-0.0034 - 1.7213\times10^{-3}t - 1.8466\times10^{-4}t^2) \quad [2]$$

In the formula, $Q_1(t)$ is the loss function of the bridge system under the freeze-thaw cycles, which is a dimensionless quantity in [0, 1]; t is the service time of the bridge.

2.2 Time-varying Effect of Fatigue Damage

In practical engineering, except for static load, bridges resist the repeated action of vehicle load, which causes irreversible fatigue damage of concrete. The fatigue failure of concrete is mainly due to the repeated action of vehicle load, and the internal damage of concrete material leads to the decline of its strength, resulting in the decline of the bearing capacity and durability of the bridge, and the loss of the function of the bridge system. The fatigue deformation modulus of concrete can reflect the degradation of concrete performance under the repeated action of load. According to the research of Xiong et al. (2022), the residual function of the bridge system under fatigue damage is quantified by the reduction coefficient of fatigue deformation modulus, and the calculation formula is shown in Eq. 3.

$$Q_2(t) = 0.93503 - 0.01456\ln(t + 0.01154) \quad [3]$$

In the formula, $Q_2(t)$ is the loss function of the bridge system under the fatigue load, which is a dimensionless quantity in [0, 1]; t is the service time of the bridge.

2.3 Time-varying Effect of Pile Settlement Damage

Under the background of global warming, the annual average air temperature of the Qinghai-Tibet Plateau has been increasing, which has caused the permafrost to thaw continuously, the permafrost table to deepen, and the permafrost mechanical parameters to change constantly. These factors make the settlement of the pile foundation of the bridge more and more serious, and affects the traffic capacity of bridge.

In this study, the finite element software ABAQUS was used to model the bridge pile foundation, and C3D8R elements were used for both the pile foundation and the surrounding soil. The loads considered including the dead weight of the bridge superstructure, the dead weight of the substructure, and the live load. The changes of the permafrost table and the mechanical parameters of permafrost caused by the temperature change were considered in different models, and numerical simulation was carried out on the bridge pile foundation with different service time. The changes of the permafrost limitable and the mechanical parameters of permafrost were referred to the research of Xiong et al. (2022). The finite element model is shown in Figure 1. Through the analysis, the changes of pile foundation settlement of the PC girder bridge and the steel-concrete composite girder bridge versus service time were obtained.

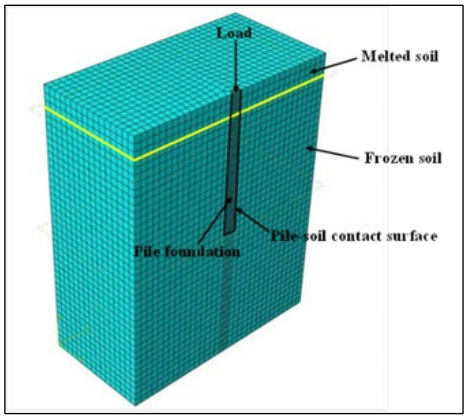

Figure 1. Finite element model.

According to the mechanical performance requirements of the bearing in "Highway Bridge Plate Rubber Bearing" (JT/T-2019), the measured rotation angle tangent value of the plate rubber bearing is tanθ⩾1/300, and the allowable rotation angle tangent value of the bearing is taken as 1/300 in this paper. Considering the most unfavorable effect, the unilateral pile foundation settlement is regarded as the uneven settlement of the bridge pile foundation, and the service range is taken as the tangent value of the bearing's rotation angle from 0 to 1/300, to quantify the loss function of pile foundation settlement by nonlinear fitting of the data. The loss function of the PC girder bridge and the steel-concrete composite bridge is shown in Eq. 4 and Eq. 5, and the fitting curve is shown in Figure 2.

$$Q_3(t) = 0.95283 - 0.01091e^{\frac{t}{44.1677}} \quad [4]$$

$$Q'_3(t) = 0.9598 - 0.0093e^{\frac{t}{44.1677}} \quad [5]$$

In the formula, $Q_3(t)$ and $Q'_3(t)$ are the loss functions of the bridge system under the pile foundation settlement, which are dimensionless quantities in [0, 1]; t is the service time of the bridge.

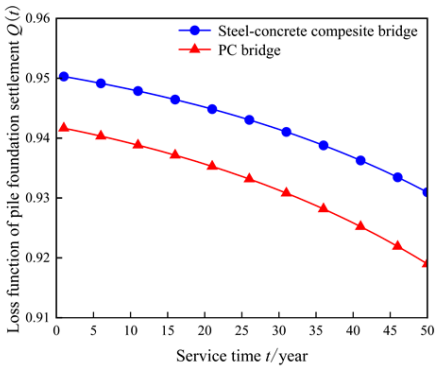

Figure 2. Loss function of pile foundation settlement of the PC bridge and the steel-concrete composite bridge.

2.4 Loss Function

2.4.1 PC Girder Bridge

For the PC girder bridge, as shown in Figure 3, the loss function can be constructed by superimposing the three damage factors of concrete freeze-thaw damage, concrete fatigue damage, and pile foundation settlement.

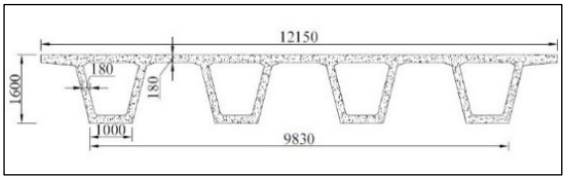

Figure 3. Schematic diagram of the PC bridge.

2.4.2 Steel-concrete Composite Girder Bridge

For the steel-concrete composite girder bridge, as shown in Figure 4, assuming that the freeze-thaw damage mechanism of concrete is similar to the fatigue damage, and both are mainly aimed at the concrete part of the superstructure of the steel-concrete composite girder bridge. Therefore, after linearly superimposing the damage amount of the two factors, it is reduced according to the mass of the concrete part of the superstructure. Considering the most unfavorable situation, the reduced freeze-thaw damage and fatigue damage are superimposed with the pile foundation settlement damage to construct the loss function $Q(t)$ of the steel-concrete composite girder bridge, as shown in Eq. 6.

$$Q(t) = 1 - \begin{bmatrix} (1-Q_1(t)) + (1-Q_2(t)) \times 0.87 \\ + (1-Q'_3(t)) \times 0.87 \end{bmatrix} = Q_1(t) + 0.87Q_2(t) + 0.87Q'_3(t) - 1.74 \quad [6]$$

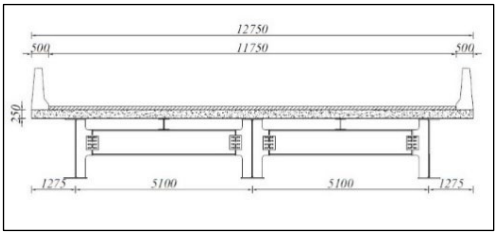

Figure 4. Schematic diagram of the steel-concrete composite bridge.

3 Seismic Resilience Assessment for Bridges

3.1 Vulnerability Analysis

In order to obtain the vulnerability of the bridge system, usually according to the first-order reliability theory, the upper and lower limits of the vulnerability of the bridge system can be obtained from the vulnerability of the vulnerable components, and the actual vulnerability of the

bridge system is between the upper and lower limits. The average value of the upper limit and the lower limit can be taken as the vulnerability of the bridge system, and the upper and lower limits of the vulnerability of the bridge system in a certain damage state can be determined by Eq. 7.

$$\max_{i=1}^{m}\left[P(F_i)\right] \le P\left(F_{system}\right) \le 1-\prod_{i=1}^{m}\left[1-P(F_i)\right] \quad [7]$$

In the formula, $P(F_{system})$ is the exceeding probability of the bridge system reaching a certain damage state; $P(F_i)$ is the exceeding probability of the i-th component reaching a certain damage state; m is the number of vulnerable components.

Xiong et al. (2023) studied the component vulnerability of the PC girder bridge and the steel-concrete composite girder bridge with the same site, span, design level and other conditions in permafrost region with high seismic risk. In this paper, with reference to this study, the system vulnerability of the PC girder bridge and the steel-concrete composite girder bridge is obtained through component vulnerability, as shown in Figures 5 and 6.

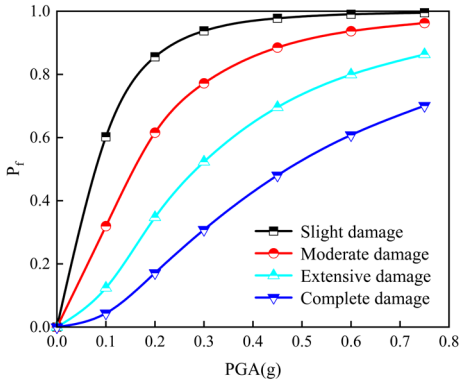

Figure 5. Vulnerability of the PC bridge.

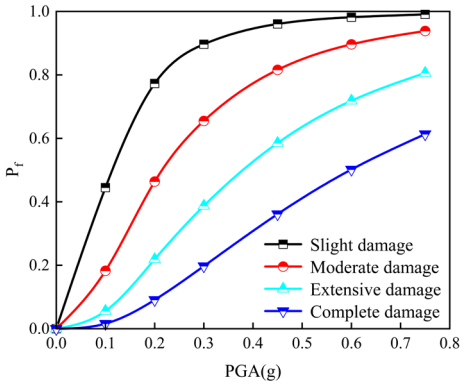

Figure 6. Vulnerability of the steel-concrete composite bridge.

3.2 Earthquake Loss Function

The loss of the bridge system under earthquake action includes two types: direct loss and indirect loss. This paper only considers the impact of direct loss. For a bridge, the direct loss caused by the event E can be expressed by the dimensionless quantity L_D, which is expressed as the ratio of the repair cost C_{rE} to the replacement cost C, which reflects the expected value of the loss. The calculation formula is shown in Eq. 8 (Venkittaraman et al. 2014).

$$L_D = \frac{C_{rE}}{C} = \sum_k P_E\left(F_j|IM\right) \times r_k \quad [8]$$

where C_{rE} represents the repair cost; C represents the replacement cost; k represents the damage state of the bridge; $P_E(F_j|IM)$ is the probability of the bridge being damaged at the damage state k in the earthquake event E, which can be obtained from the fragility curves at all levels of damage states; IM is the earthquake intensity index; r_k is the damage ratio corresponding to the damage state k.

3.3 Post-earthquake Recovery Function

According to HAZUS (Zhou et al. 2010), the average and standard deviations of the bridge system recovery time under different damage states are obtained. The expected value of recovery time under different intensities of earthquakes is defined as the sum of the average value of the recovery time under different damage states and the product of the probability of occurrence of the corresponding damage state, which reflects the expected value of the recovery time. The calculation formula is shown in Eq. 9.

$$T = \sum_k P\left(F_j|IM\right) \times \mu_k \quad [9]$$

T is the expected value of the recovery time; k represents the damage state of the bridge system; $P(F_j|IM)$ is the probability of the bridge system occurring at the damage state j; μ_k is the average recovery time corresponding to the damage state j.

Fitting the loss L_D under different intensities of earthquakes with the expected value of recovery time T, from which *PC* girder bridge's loss function can be obtained.

3.4 Critical Repair and Reinforcement Time Analysis

The critical time when the functionality of the bridge is lower than the critical state is defined as the critical maintenance and reinforcement period. For the bridge system, maintenance and reinforcement must be carried out at this time to ensure the continued opening to traffic.

In this paper, a number of different peak ground accelerations (PGAs) were selected for research, and the schematic diagram of the critical maintenance and reinforcement period and the state of temporary maintenance of traffic of the PC girder bridge and the steel-concrete composite girder bridge is shown in Figure 7 and Figure 8.

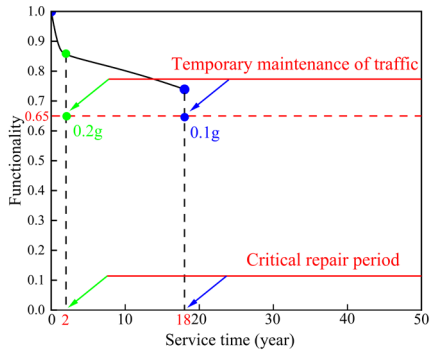

Figure 7. Critical maintenance and reinforcement period of the PC Bridge under different PGA.

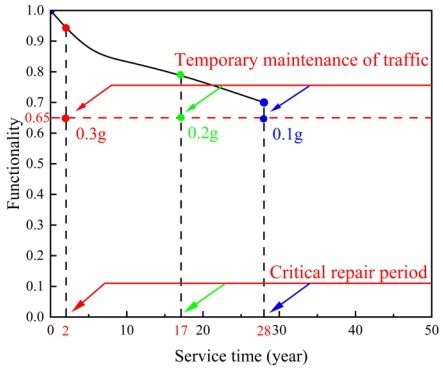

Figure 8. Critical maintenance and reinforcement period of the steel-concrete Bridge under different PGA.

As shown in Figure 7, for the PC girder Bridge, when the PGA is 0.1 g and 0.2 g, the critical maintenance and reinforcement period of the bridge system are 18 years and 2 years, respectively. When the PGA is greater than 0.3 g, the vibration reduction and isolation device must be considered in the bridge design scheme.

As shown in Figure 8, for the steel-concrete composite girder bridge, when the PGA is 0.1 g, 0.2 g and 0.3 g, the critical maintenance and reinforcement period of the bridge systems are 28 years, 17 years and 2 years, respectively.

4 DISCUSSION

In the assessment of the seismic resilience of bridges, in order to quantitatively evaluate the seismic resilience, the integral formula including bridge functionality $Q(t)$ is usually used to calculate the seismic resilience (Soleimani 2022), as shown in Eq. 10.

$$R = \frac{1}{\Delta t}\int_{t_0}^{t_0+\Delta t} Q(t)\mathrm{d}t \qquad [10]$$

When the PC girder bridge has been in operation for 20 years and an earthquake occurs, the recovery curves of the bridge under different PGAs are shown in Figure 9. The recovery time and resilience are shown in Figure 10. It can be seen from Figure 9 that when the PGA is 0.2 g and 0.4 g, the bridge needs to be repaired and the recovery time of the bridge system is 31 and 98 days, respectively. It can be seen from Figure 10 that the recovery time of the bridge system increases with the increase of PGA, and the resilience decreases with the increase of PGA; when the PGA is 0.2 g, 0.3 g, and 0.4 g, the resilience is 0.593, 0.553, and 0.511 respectively.

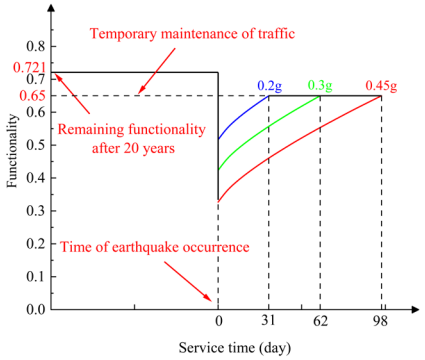

Figure 9. Function curves of the PC bridge under different PGAs.

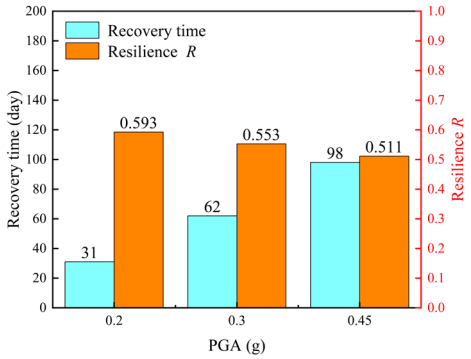

Figure 10. Recovery time and resilience of the PC bridge under different PGAs.

Similarly, when the steel-concrete composite girder bridge has been in operation for 20 years and an earthquake occurs, the bridge needs to be repaired and reinforced to achieve the state of temporary maintenance of traffic. When the PGA is 0.2 g and 0.4 g, the recovery time of the bridge system is 3 and 57 days respectively, and the corresponding resilience is 0.641 and 0.559 respectively.

As shown in Figure 11, the recovery time of the two bridges with a service time of 20 years are compared. It can be seen that under different PGAs, the recovery time of the steel-concrete composite girder bridge is significantly shorter than the PC girder bridge.

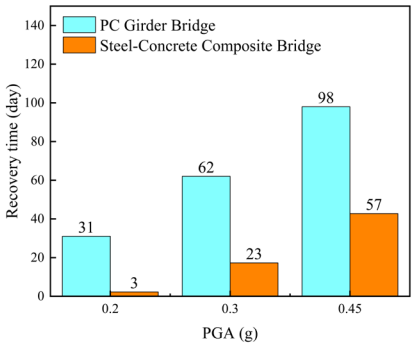

Figure 11. Comparison of recovery time between the PC bridge and the steel-concrete composite bridge.

5 CONCLUSIONS

(1) The loss function of the active PC girder bridge and the proposed steel-concrete composite girder bridge in the Qinghai-Tibet Plateau area is studied. The result shows that the pile settlement damage of the steel-concrete composite bridge is smaller.

(2) The critical repair and reinforcement period before the earthquake of the PC girder bridge and the steel-concrete composite girder bridge in the Qinghai-Tibet Plateau are studied. When the PGA is 0.1 g, 0.2 g and 0.3 g, the critical maintenance and reinforcement period of the steel-concrete composite bridge are 28 years, 17 years and 2 years, and the critical maintenance and reinforcement period of the PC bridge are 18 years and 2 years, and when the PGA is greater than 0.3 g, the vibration reduction and isolation device must be considered in the PC bridge.

(3) A seismic resilience evaluation method for bridges in permafrost region with high seismic risk is proposed, and the seismic resilience comparative evaluation was carried out between the PC girder bridge and the steel-concrete composite girder bridge in the Qinghai-Tibet Plateau. The results show that under the same intensity earthquake, compared with the PC girder bridge, the seismic resilience of the steel-concrete composite girder bridge is higher, and the repair time is shorter.

6 ACKNOWLEDGEMENTS

The research is partly supported by State Key Laboratory of Road Engineering Safety and Health in Cold and High-altitude Regions (No. YGY2020KYPT-06).

7 REFERENCES

Bruneau, M., Chang, S.E., Eguchi, R.T., Lee, G.C., O'Rourke, T.D., Reinhorn, A.M., Shinozuka, M., Tierney, K., Wallace, WA., and Winterfeldt, D.V. 2003. 'A Framework to Quantitatively Assess and Enhance the Seismic Resilience of Communities', *Earthquake Spectra* 19(4), pp. 733–752. doi:10.1193/1.1623497.

Cimellaro, G.P., Reinhorn, A.M., and Bruneau, M. 2010. 'Framework for Analytical Quantification of Disaster Resilience', *Engineering Structures* 32(11), pp. 3639–3649. doi:10.1016/j.engstruct.2010.08.008.

Chandrasekaran, S. and Banerjee, S. 2016. 'Retrofit Optimization for Resilience Enhancement of Bridges under Multihazard Scenario', *Journal of Structural Engineering* 142(8), C4015012. doi:10.1061/(ASCE)ST.1943-541X.0001396.

Decò, A., Bocchini, P., and Frangopol, D.M. 2013. 'A Probabilistic Approach for the Prediction of Seismic Resilience of Bridges', *Earthquake Engineering & Structural Dynamics* 42(10), pp. 1469–1487. doi:10.1002/eqe.2282.

Kilanitis, I. and Sextos, A. 2018. 'Integrated Seismic Risk and Resilience Assessment of Roadway Networks in Earthquake Prone Areas', *Bulletin of Earthquake Engineering* 17, pp. 181–210. doi:10.1007/s10518-018-0457-y.

Ikpong, A. and Bagchi, A. 2015. 'New Method for Climate Change Resilience Rating of Highway Bridges', *Journal of Cold Regions Engineering* 29(3), 04014013. doi:10.1061/(ASCE)CR.1943-5495.0000079.

Li, J.Y., Peng, X.P., Deng, Z.G., Cao, J.G., Guan, Y.S., Lin, L., Tian, J.T., Li, F., Wang, A.Q., Wang, Z.G., Peng, T., Cai, H.Z., and Zhang, X.M. 2000. 'Quantitative Design of Concrete Frost Resistance', *Concrete* 12, pp. 61–65. (in Chinese).

Li, J.Q., Xiong, Z.H., and Liu, C. 2023. 'Review on the Toughness Index of Bridges in Strong Earthquake Area of Permafrost', in *WTC2023 Proceedings*, pp. 715–719. doi:10.26914/c.cnkihy.2023.019338. (in Chinese).

Li, Y., Dong, Y., Frangopol, D.M., and Gautam, D. 2020. 'Long-term Resilience and Loss Assessment of Highway Bridges under Multiple Natural Hazards', *Structure and Infrastructure Engineering* 16(4), pp. 626–641. doi:10.1080/15732479.2019.1699936.

Manyena, S.B. 2006. 'The Concept of Resilience Revisited', *Disasters*, 30(4), pp. 434–450. doi:10.1111/j.0361-3666.2006.00331.x.

Mitoulis, S.A., Argyroudis, S.A., Loli, M., and Imam, B. 2021. 'Restoration Models for Quantifying Flood Resilience of Bridges', *Engineering structures* 238, 112180. doi: 10.1016/j.engstruct.2021.112180.

Shinozuka, M., Feng, M.Q., Lee, J., and Naganuma, T. 2000. 'Statistical Analysis of Fragility Curves', *Journal of Engineering Mechanics* 126(12), pp. 1224–1231. doi:10.1061/(ASCE)0733-9399(2000)126:12(1224).

Soleimani, F. and Hajializadeh, D. 2022. 'Bridge Seismic Hazard Resilience Assessment with Ensemble Machine Learning', *Structures* 38, pp. 719–732. doi:10.1016/j.istruc.2022.02.013.

Venkittaraman, A. and Banerjee, S. 2014. 'Enhancing Resilience of Highway Bridges Through Seismic Retrofit', *Earthquake Engineering & Structural Dynamics* 43(8), pp. 1173–1191. doi:10.1002/eqe.2392.

Vishwanath, B.S. and Banerjee, S. 2019. 'Life-cycle Resilience of Aging Bridges under Earthquakes', *Journal of Bridge Engineering* 24(11), 04019106. doi:10.1061/(ASCE)BE.1943-5592.0001491.

Xiong, Z.H., Chen, J.B., Zhu, D.P., and Fu, J. 2018. 'Review of Design Method and Experiment on Bridge Pile Foundation in Permafrost Regions', *Low Temperature Architecture Technology* 40(08), pp. 84–87. doi:10.13905/j.cnki.dwjz.2018.08.026. (in Chinese).

Xiong, Z.H., Chen, J.B., Liu, C., Li, J.P., and Li, W.W. 2022. 'Bridge's Overall Structural Scheme Analysis in High Seismic Risk Permafrost Regions', *Civil Engineering Journal* 8(7), pp. 1316–1327. doi:10.28991/CEJ-2022-08-07-01.

Zhou, Y.W., Banerjee, S., and Shinozuka, M. 2010. 'Socio-economic Effect of Seismic Retrofit of Bridges for Highway Transportation Networks: a Pilot Study', *Structure and Infrastructure Engineering* 6(1–2), pp. 145–157. doi:10.1080/15732470802663862.

Zheng, S.S., Li, Q.Q., Qin, Q., Gan, C.L., Liu, W. and Dong, L.G. 2018. 'Restoring Force Model of Freezing-thawing Damaged Squat Reinforced Concrete Shear Walls', *Journal of Building Structures* 39(03), pp. 111–119. doi:10.14006/j.jzjgxb.2018.03.014. (in Chinese).

Permafrost protection by thermosyphon under the paved road in West Mongolia

Jambaljav Yamkhin[1], Namdag Choibalsan[2], Tsogt-Erdene Gansukh[3] & Ulambayar Ganbold[3]

[1]*Geocryo LLC, Ulaanbaatar, Mongolia*

[2]*Newcon LLC, Ulaanbaatar, Mongolia*

[3]*Permafrost Department of Institute of Geography and Geoecology, Ulaanbaatar, Mongolia*

ABSTRACT

According to the results of field studies, asphalt pavement increases the absorption of solar radiation and the accumulation of snow or water in the channels on both sides of the road, accelerating the thawing of permafrost under it, and due to this process, waves form on the asphalt surface and driving on it at normal speed becomes dangerous. Field measurements show that the rate of permafrost thawing under natural conditions is 0.5–2.0 cm per year, and permafrost thawing under paved roads is 5–10 times faster than under natural conditions. In 2021–2022, in close cooperation with construction companies, government officers, and permafrost experts, a road with a thermosyphon embankment was built in an ice-rich permafrost area along the western road corridors at six selected road sections. On December 1, 2022, the ground temperature dropped to -14 °C and -20 °C at the evaporator, while in the ground between the thermosyphons dropped to -8 °C or -9 °C. These temperatures increased to +1.6 °C and -0.7 °C at the evaporator and to -0.9 °C and -2.2 °C between thermosyphons. In Mongolia, the thermosyphon works very well, but under the paved road above the evaporators, it is necessary to install pretty good insulation.

1 INTRODUCTION

Permafrost can be understood as a mixture of frozen ground and ice. Under natural conditions, ice contents are different along the permafrost profile. Due to climate warming, permafrost degrades differently, and it degrades faster in Mongolia because Mongolian permafrost is characterized by sensible permafrost with a temperature close to zero degrees (Sharkhuu et al. 2011; Jambaljav et al. 2013, 2017; Ishikawa et al. 2018; Yamkhin et al. 2022).

More than 1,400 km of Mongolian roads pass through the permafrost regions (Figure 1), and some parts of these roads on ice-rich permafrost are damaged.

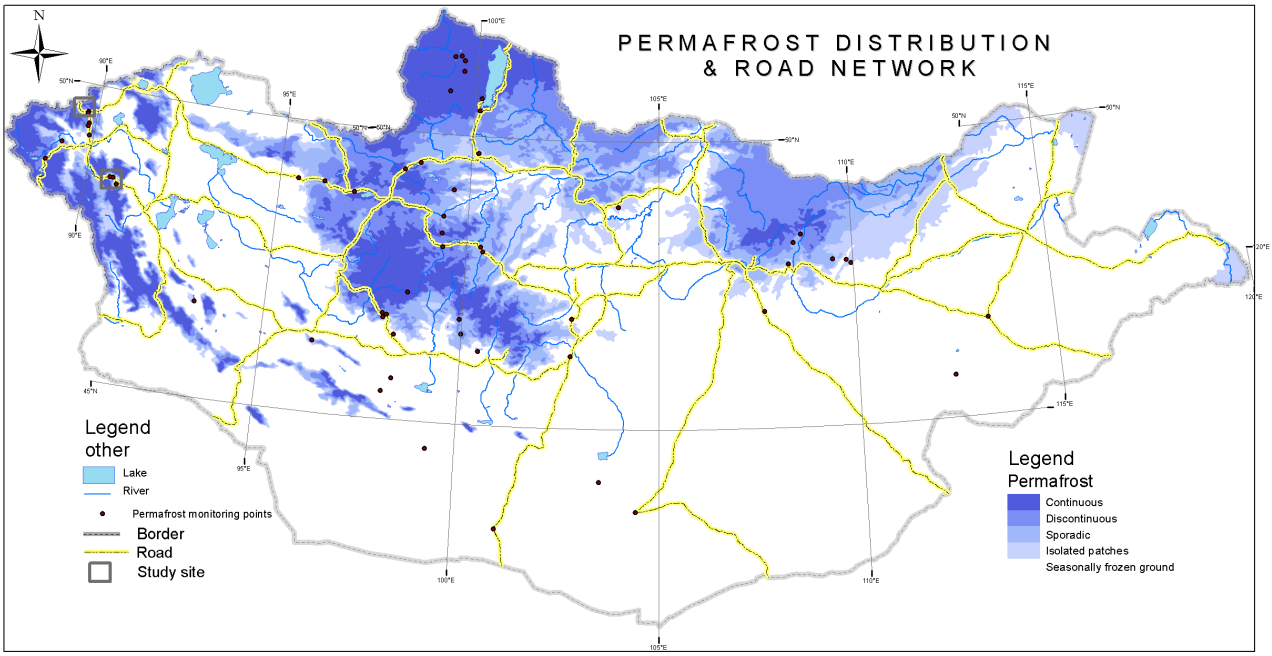

Figure 1. Permafrost distribution and road network over Mongolia.

https://doi.org/10.52381/ICOP2024.186.1

Jambaljav et al. (2019) reported on the state of permafrost along the roads of Mongolia, and as a result of this study, permafrost degrades 5–10 times faster under a paved road compared to permafrost degradation in natural conditions.

According to the results of field studies, asphalt pavement increases the absorption of solar radiation and the accumulation of snow or water in the channels on both sides of the road, accelerating the thawing of permafrost under it, and due to this process, waves form on the asphalt surface and driving on it at normal speed becomes dangerous. Seventy-five percent of traffic accidents occur on countryside roads, and one of the reasons for these accidents is the subsidence of the road surface due to the thawing of permafrost (mrtd.gov.mn).

The permafrost temperature is requested to be cooled down under asphalt-paved roads for warm permafrost regions (Cheng et al. 2008). There are several methods of embankment bed cooling to prevent the permafrost thaw. Here we discuss permafrost studies using electrical resistivity tomography (ERT) along the road in the western regional corridor of Mongolia between Russia and China and monitoring results of ground temperature under roads with thermosyphon cooling and without thermosyphon cooling.

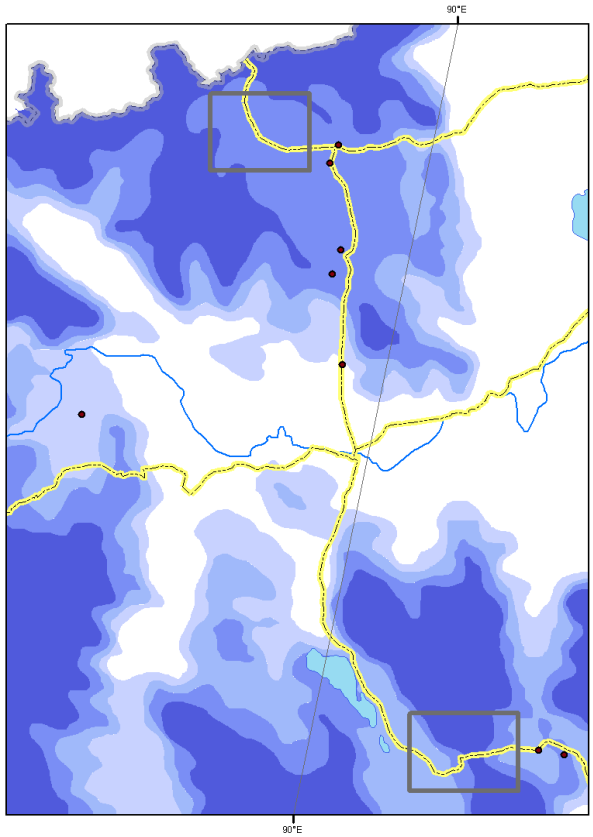

Figure 2. Location of study sites, legend is same as in Figure 1

1.1 Study sites

Our study sites are located in the far west along the western road corridor of Mongolia between Russia and China (Figure 2).

The first site is located at Buraat Pass with an elevation of 2370–2560 m asl. The second site is located between an intermountain valley with an elevation of 2280 m asl, near the Mongolian and Russian border. Both sites have permafrost from discontinuous to continuous distribution.

Cryogenic phenomena such as pingo-like mounds, thermokarst lakes, dog holes in intermountain depressions, and valleys are widely developing.

Ground materials are lacustrine sediments in intermountain depressions, and gravels with sandy fill are typical sediments in intermountain valleys and mountain food slopes. Ice contents are more than 50% along this road in some parts.

Permafrost monitoring has been carried out in boreholes near these study sites since 2009. Permafrost temperature is -0.42ºC at a depth of 10 m in borehole “Hongor-Olon", near site 1, and -0.5ºC at a depth of 10 m in borehole “Tsagaannuur-2”, near site 2. The active layer thickness increases by 0.5–2.0 cm annually (Sharkhuu et al. 2011).

In site 1, we installed inclined thermosiphons on three sections and looped thermosyphons on one section of the paved road following the formation of waves on the road surface in 2021–2022. In 2022–2023, during the construction of the road, inclined thermosyphons were installed on three sections of the paved road in site 2.

In site 1, permafrost studies were conducted after 2 years of road construction, and in site 2, permafrost studies were conducted before one year of road construction. Here, permafrost study and monitoring results are reported for site 2.

2 METHODS

ERT surveys have been conducted along or across roads to study permafrost under paved roads after and before construction. Temperature measurements under roads were made using a thermistor string and data loggers from Onset Computer Corporation.

2.1 Electrical Resistivity Tomography (ERT)

Electrical resistivity surveys have been used for many decades in hydrological, mining, and geotechnical investigations. More recently, it has been used for environmental surveys. The resistivity measurements are commonly made by injecting current into the ground through two current electrodes and measuring the resulting voltage difference at two potential electrodes (Loke 2001). The Ground resistivity is related to various geological parameters such as the mineral and fluid content, porosity, and degree of water saturation. The enormous contrast between groundwater (10–100Ωm) and underground ice (> 1000 Ωm) provides an excellent opportunity to determine frozen and unfrozen layers from the surface surveys. Here, we used the Syscal R1+ with Wenner or Wenner-

Schlumberger arrays. Our measurements were carried out along and across the road with a distance between electrodes of 1–5 m and with 48, 64, and 80 electrodes (Figure 3). Penetration depth depends on the configuration of arrays. Maximum penetration depth was 80 m.

Figure 3. ERT survey across the road, Wenner-Schlumberger array with 1 m spacing

2.2 Temperature measurements

Under paved roads, inclined holes were drilled at an angle of 30 degrees with a distance of 3 m between them, into which iron pipes with a diameter of 50 mm (thermosyphon evaporators) and a PVC tube with a diameter of 15 mm were inserted. Some 15 mm PVC tubes have thermistors and data loggers to monitor the temperature under the paved road (Figure 4).

In addition, we record the temperature under paved roads without thermosyphons to compare the cooling effects.

Figure 4. Monitoring box: temperature sensors are installed in white PVC tubes at the end of the evaporator tube and between the thermosyphons.

3 RESULTS

3.1 ERT survey results at site 2

There are three sections, 200 m long (k13+600:k13+800), 160 m long (k14+360:k14+500), and 140 m long (k15+160:k15+300), on which inclined thermosyphons with a spacing of 3 m were place on site 2 in 2022. At all three sites, surface cuts were made before the ERT survey for the next phase of road construction. Waves of thawing permafrost formed on the surface.

3.1.1 Section 1 (k13+600:k13+800)

The section has a total length of 200 m towards the Russian-Mongolian border and is located in the foothills with short vegetation covering the eastern part of the mountain range. In the excavation, subsidence is observed on the surface due to permafrost thawing along the road. Here, 4 ERT measurements were carried out, and boreholes were drilled at certain points on the electrodes of these ERT profiles. We placed one profile with a distance between electrodes of 5 m along the road and 3 more profiles with a distance between electrodes of 1 m crossed the road. The first profile has a length of 400 m and a penetration depth of > 75 m, and the remaining 3 profiles have a length of 64 m and a penetration depth of 13 m. We set the electrical resistivity value from 50 Ω*m to > 14595 Ω*m to make the profiles visible. It is visible that below the active layer, there is a layer of permafrost 12–15 m deep with a variety of ice (Figure 5).

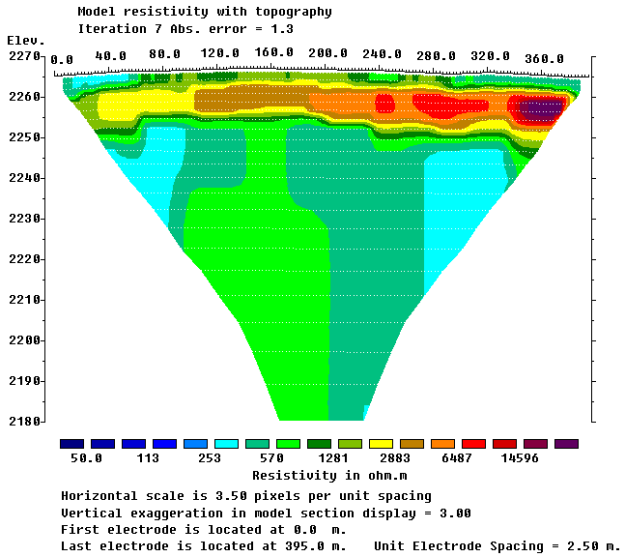

Figure 5. ERT profile along the road section k13+600:k13+800. The depth of penetration is > 75 m. The value of electrical resistivity ranged from 50Ω*m to > 14595Ω*m.

Another 3 profiles have a similar pattern of electrical resistivity images. Therefore, we provide here a description of all profiles together. The profiles received the numbers k13-2, k13-3 and k13-4. Boreholes were also drilled on electrodes No. 32 of profile k13-2, No. 32 of profile k13-3, and No. 56 of profile k13-4. Boreholes K13-2-32 and K13-3-32 are located in the center of the profiles, and borehole k13-2-56 was drilled on the side of the road, located in pristine natural conditions.

As a result of drilling boreholes, soil samples were taken for bulk density, moisture, excess ice, free settlement after thawing, and grain size. The core is dominated by gravel with yellowish sand. Soil density is 1.1–1.76 g/cm^3, moisture is 26.51–76.92%, and 0.5 cm is thaw settlement when thawing a 6 cm layer. In these boreholes and other boreholes of the site, as well as by ERT profiles, the thickness of the active layer is 2–3.1 m. It is visible that the thickness of the active layer is 2–3 m, and some permafrost thawing on both sides of the main direction of the road (Figure 6).

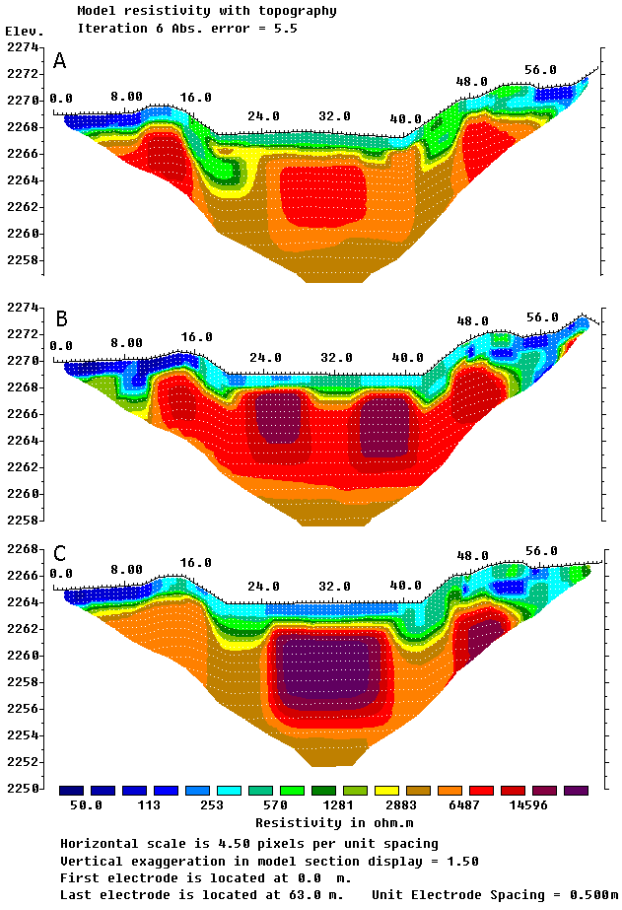

Figure 6. Transverse ERT profiles of the road in section 1 of site 2. The resistivity value is the same as in Figure 2.

3.1.2 Section 2 (k14+360:k14+500)

Electrical resistivity tomography profile k14-1 is located along the road, and ERT profile k14-2 is located across the excavations. The borehole was drilled on electrode no. 24 of ERT profile k14-2. The ERT profile layout and soil materials from the borehole are similar to the previous section 1 regarding soil composition, active layer thickness, and permafrost conditions. The difference is that the resistivity values are lower below the permafrost on both ERT profiles compared to section 1, and lower resistivity values appeared under the main road, but it is around 4324.88 Ω*m. We hypothesized that the lower resistivity beneath the permafrost may be due to lacustrine sediments. The main direction surface has waves and a permafrost thawing bowl on both sides of the main road (Figures 7 and 8).

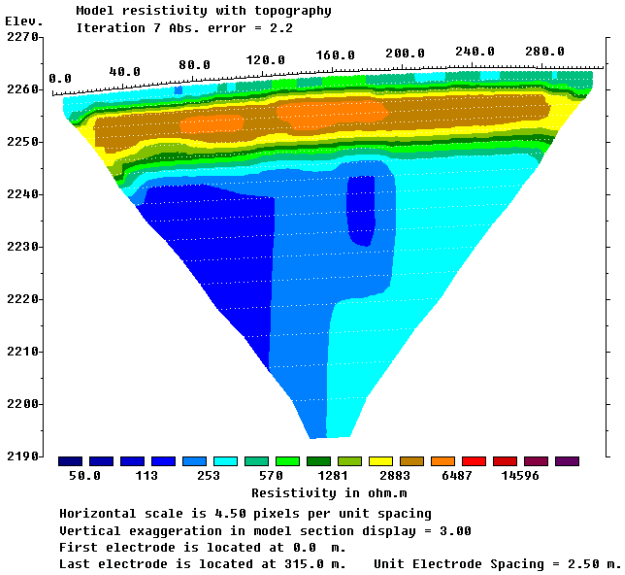

Figure 7. ERT profile along the road at section 2. The penetration depth, profile length, and resistivity value are the same as in Figure 2.

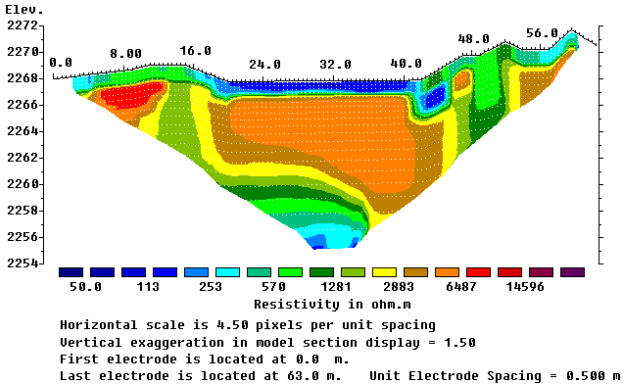

Figure 8. Transverse ERT profile of the road in section 2 of site 2. The penetration depth and resistivity value are the same as in Figure 3.

3.1.3 *Section 3 (k15+160:k15+300)*

There are 2 ERT profiles across the excavations (Figure 9).

The boreholes were drilled on electrode No. k15-1-36 and on electrode No. k15-2-20. Core samples and the pattern of ERT profiles are similar to section 1. The thickness of the active layer is from 2 to 3 m. Permafrost has a high ice content.

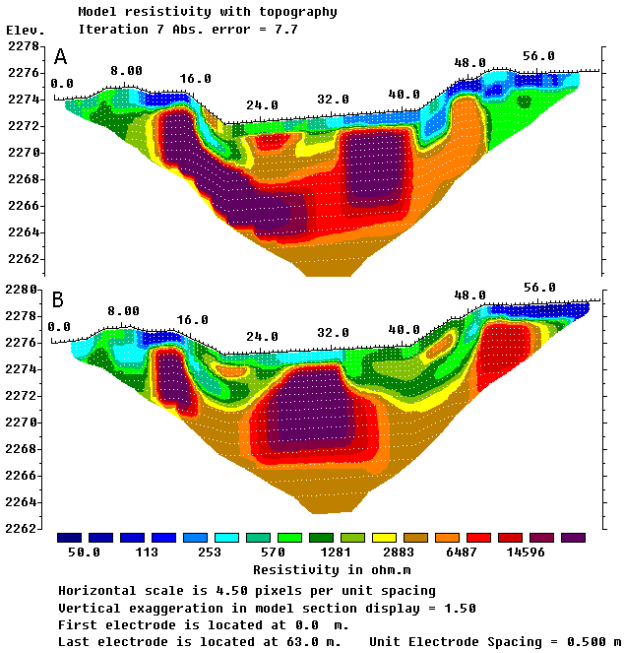

Figure 9. Transverse ERT profiles of the road in section 3 of site 2. The resistivity value is the same as in Figure 3. A-k15-1 profile, B-k15-2 profile

3.2 Ground temperature under the road

In each section, we have installed one monitoring system that records the temperature at the bottom of the evaporator and in the ground under the road between the thermosyphons since December 2022. Also, starting in 2022, the ground temperature under the road is recorded in a section without a thermosyphon. Due to the collapse of the borehole wall, temperature sensors were installed at different depths from the surface.

3.2.1 *Section 1 (k13+600:k13+800)*

In section 1, to monitor the cooling effect of the thermosyphon, the temperature sensor was installed at a depth of 3.0 m from the road surface on the evaporator pipe, and to control the freezing radius between the thermosyphons, the temperature sensor was installed at a depth of 3.75 m from the road surface.

The thermosyphon operates until early May 2023, and until mid-February 2023, the ground cooled to -14 °C. After this, the ground temperature warmed and rose to -0.4 °C on August 1, 2023. Between thermosyphons, the ground temperature dropped to -8.0 °C until early March 2023 and rose to -2.1 °C in early August 2023 (Figure 10).

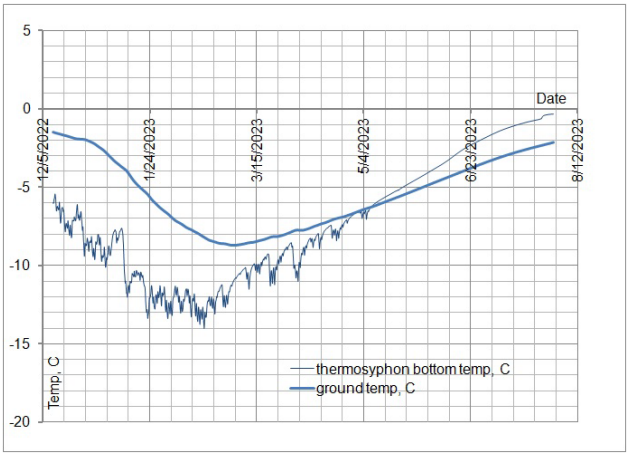

Figure 10. Theromsyphon bottom and ground temperature under the road at section 1, site 2

3.2.2 *Section 2 (k14+360:k14+500)*

In section 2, to monitor the cooling effect of the thermosyphon, the temperature sensor was installed at a depth of 2.3 m from the road surface on the evaporator pipe, and to control the freezing radius between the thermosyphons, the temperature sensor was installed at a depth of 3.0 m from the road surface.

Thermosyphon's operation period is similar to section 1, and until mid-February 2023, the ground cooled down to -20 °C. After this, the ground temperature warmed and rose to +1.6 °C on August 1, 2023. Between thermosyphons, the ground temperature dropped to -9.0 °C until the end of February 2023 and rose to -0.9 °C in early August 2023 (Figure 11).

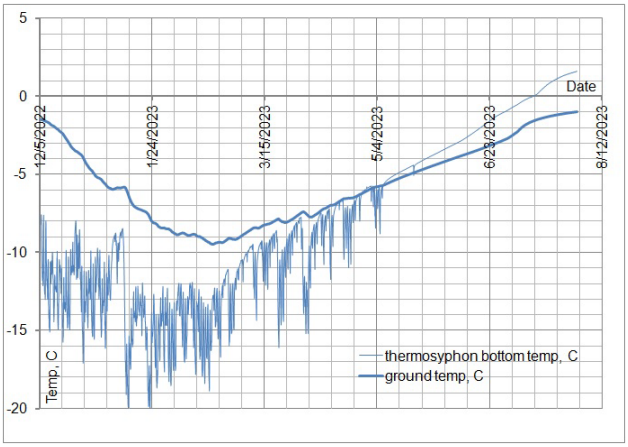

Figure 11. Thermosyphon bottom and ground temperature under the road at section 2, site 2

3.2.3 *Section 3 (k15+160:k15+300)*

In section 3, to monitor the cooling effect of the thermosyphon, the temperature sensor was installed at a depth of 3.0 m from the road surface on the evaporator pipe, and to control the freezing radius between the

thermosyphons, the temperature sensor was installed at a depth of 3.75 m from the road surface.

Thermosyphon's operation period is similar to in section 1, and until mid-February 2023, the ground cooled down to -16 °C. After this, the ground temperature warmed and rose to -0.7 °C on August 1, 2023. Between thermosyphons, the ground temperature dropped to -8.0 °C until the end of February 2023 and rose to -2.2 °C in early August 2023 (Figure 12).

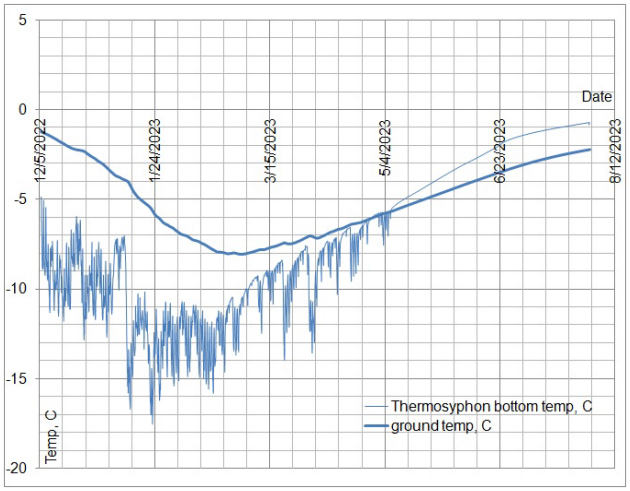

Figure 12. Thermosyphon bottom and ground temperature under the road at section 3, site 2

To compare the soil temperature under a road with and without a thermosyphon, we installed a temperature sensor at a depth of 3.8 m from the road surface on a section of the road without a thermosyphon. By the end of March 2023, the temperature dropped to -3.2 °C. After this, the ground temperature warmed, and on August 1, 2023, it rose to -0.9 °C (Figure 13).

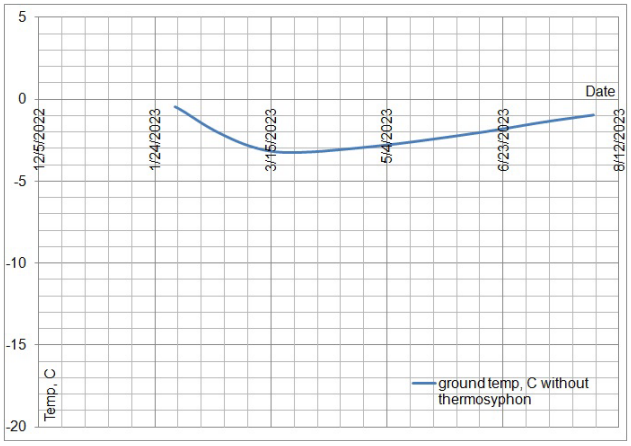

Figure 13. Ground temperature under road without thermosyphon.

4 DISCUSSION

For permafrost studies, ERT surveys were used widely (Lewkowicz et al. 2011; Etzelmuller et al. 2006; Ishikawa et al. 2005, 2001; Hauck et al. 2004), but the use of ERT surveys was relatively less, especially for the study of permafrost under the road (Saruulzaya et al. 2018). Thus, the current study was purposed to investigate the permafrost condition by ERT surveys and monitor the ground temperature under paved roads with thermosyphon and the ground temperature without thermosyphon. The cooling effect of thermosyphon under paved roads was also quantitatively investigated.

4.1 ERT survey

Our ERT profiles showed good contrasts between frozen and unfrozen layers, even in coarse sediments along the road (Figures 5–9). The thickness of the permafrost (approximately 15 m) and the active layer, as well as ice contents, are visible from our ERT profiles. We confirmed them by drilling boreholes in some electrode locations along the ERT lines. For instance, Lewkowicz et al. (2011) and Etzelmuller et al. (2006) suggested that ERT surveys are not a panacea and require additional investigation, such as drilling boreholes, temperature measurement in boreholes, and probing.

The results of ERT surveys indicated that in the upper layer of permafrost, changes begin immediately after the destruction and cutting of the surface layers, and the thawing bowl under the road forms several years later (Jambaljav et al. 2019).

Depending on the ground materials, a thawing bowl forms directly under the road due to the high adsorption of the asphalt pavement and along the sides of the road where the coarse material is located. A thawing bowl forms directly under the road in areas where the ground contains less infiltration material (clay, silt) and directly under the road and along the roadsides where the ground is a good infiltration material (coarse ground). Thus, two distinct thawing events occurred: the first due to increased solar adsorption and the second due to the infiltration and concentration of rain and snowmelt water in the roadside channels.

4.2 Ground temperature

The thermosyphon cools the temperature underground as much as it is cold enough outside.

This finding is supported by several international scholars who indicate the method of cooling the roadbed and thermosyphon cooling, confirmed empirically and by modeling methods (Haynes et al. 1988; Cheng et al. 2006).

Since our monitoring began at the beginning of December 2022, the thermosyphon works to cool the subgrade until the beginning of May 2023. The cooling capacity of a thermosyphon varies along the length of the evaporator pipe. The minimum temperature at the evaporator pipe was -20 °C at 2.3 m from the road surface and -14 °C or -16 °C at a depth of 3.0 m from the road surface. At the end of the summer of 2023, these temperatures were +1.6 °C, -0.9 °C, and -2.1 °C, respectively.

The time shift of temperature fluctuations to a minimum value is half a month for the temperature in the evaporator pipe and between the thermosyphons. Moreover, for the temperature at the evaporator pipe and the temperature without a thermosyphon, this time is 1.5 months.

4.3 Thermal performance of thermosyphon

Thermosyphons can effectively extract heat from the ground without any additional power supply, and they have been widely used to prevent the thawing of permafrost in foundations for many decades (Yarmak et al. 2002; Cheng et al. 2008). They cooled the ground under the infrastructure quite well.

The thermosyphon reduces the ground temperature under the road with a thermosyphon by more than 4 times when comparing the ground temperature under the road without a thermosyphon. The minimum ground temperature was -14 °C or -20 °C under the road with a thermosyphon, and under the road without a thermosyphon, it was -3.2 °C during the monitoring period.

Near site 2, the minimum temperature is -2.45 °C and the maximum is +1.34 °C at a depth of 3 m from the ground surface in the monitoring borehole. Moreover, these temperatures were 5.5 or 6 times colder under paved roads than the temperature from the monitoring borehole at a depth of 3 m. Under a paved road, the maximum temperature is 1.49 times lower than the temperature at a depth of 3 m in the monitoring borehole.

In the warm season, the paved surface heats the underground materials more strongly, and the thermosyphon cools quite well in the cold season.

In Mongolia, the thermosyphon works very well, but installing pretty good insulation above the evaporators under the paved road is necessary.

The present study has limitations. The first limitation is the short monitoring period and air and road surface temperature data, which are limited. However, from 2023, we begin to record these data. Another major limitation is that we focused on construction and monitoring, but we should have considered modeling. We invite anyone to cooperate in modeling thermosyphon cooling for a long period.

5 CONCLUSIONS

1. There are two types of permafrost thawing under and along the paved road. Due to increased solar adsorption, a permafrost thawing bowl is formed under a paved road, and due to the accumulation of rain and melted snow water, permafrost thawing is observed on both sides of the road.

2. Thawing of permafrost begins immediately after the destruction or cutting of the earth's surface, and a permafrost thawing bowl forms several years later.

3. Field measurements show that the rate of permafrost thawing under natural conditions is 0.5–2.0 cm per year, and permafrost thawing under paved roads is 5–10 times faster than under natural conditions.

4. The thermosyphon reduces the ground temperature under a paved road with a thermosyphon by more than 4 times compared to a paved road without a thermosyphon.

6 ACKNOWLEDGEMENTS

The Asian Development Bank financially supported this project under the Western Regional Road Corridor Investment Program (Tranche 2).

We are happy to express our thanks to all of the project participants who worked on this project. Special thanks go to B. Bayan-Amgalan, project coordinator, Ram Prakash, engineer-cum-Team Leader of the Consultant, Ch. Enkhjargal, from an ICT consulting company, and B. Muratbek, from a local road company.

7 REFERENCES

Cheng, G. 2005. 'A roadbed cooling approach for the construction of Qinghai–Tibet Railway', *Cold Regions Science and Technology* 42(2), pp. 169–176, ISSN 0165-232X. Available at: https://doi.org/10.1016/j.coldregions.2005.01.002.

Guodong Cheng, G., Sun, Z. and Niu, F. 2008. 'Application of the roadbed cooling approach in Qinghai–Tibet railway engineering', *Cold Regions Science and Technology* 53(3), pp. 241–258, ISSN 0165-232X. Available at: https://doi.org/10.1016/j.coldregions.2007.02.006.

Etzelmüller, B., Heggem, E.S.F., Sharkhuu, N., Frauenfelder, R., Kääb, A. and Goulden, C. 2006. 'Mountain permafrost distribution modelling using a multi-criteria approach in the Hövsgöl area, northern Mongolia', *Permafrost and Periglacial Processes* 17(2), pp. 91–104. Available at: https://doi.org/10.1002/ppp.554.

Hauck, C., Isaksen, K., Vonder Mühll, D. and Sollid, J.L. 2004. 'Geophysical surveys designed to delineate the altitudinal limit of mountain permafrost: an example from Jotunheimen, Norway', *Permafrost and Periglacial Processes* 15(3), pp. 191–205. Available at: https://doi.org/10.1002/ppp.493.

Haynes F.D. and Zarling J.P. 1988. 'Thermosyphons and foundation design in cold regions', *Cold Regions Science and Technology*, 15(3), pp. 251–259, ISSN 0165-232X. Available at: https://doi.org/10.1016/0165-232X(88)90072-9.

Ishikawa M, Jamvaljav Y, et al. 2018. 'Thermal states, responsiveness and degradation of marginal permafrost in Mongolia', *Permafrost and Periglacial Processes* 29(4), pp. 271–282. Available at: https://doi.org/10.1002/ppp.1990.

Ishikawa, M., Sharkhuu, N., Zhang, Y., Kadota, T. and Ohata, T. 2005. 'Ground thermal and moisture conditions at the southern boundary of discontinuous permafrost, Mongolia', *Permafrost and Periglacial Processes* 16(2), pp. 209–216. Available at: https://doi.org/10.1002/ppp.483.

Ishikawa, M. and Hirakawa, K. 2000. 'Mountain permafrost distribution based on BTS measurements and DC resistivity soundings in the Daisetsu Mountains, Hokkaido, Japan', *Permafrost and Periglacial Processes* 11(2), pp. 109–123. Available at: https://doi.org/10.1002/1099-1530(200004/06)11:2<109::AID-PPP343>3.0.CO;2-O.

Jambaljav, Y. 2017. *Permafrost distribution and changes over Mongolia*. Ulaanbaatar, Mongolia: Colorful Ochir Press. ISBN 978-99978-1-862-1. 78 p. (in Mongolian).

Jambaljav, Y., Saruulzaya, A., et al. 2013. *Establishment of permafrost monitoring network over Mongolia*. Ulaanbaatar, Mongolia: Scientific report of the project funded by Mongolian Science and Technology (in Mongolian).

Jambaljav, Y., Saruulzaya, A., Tsogt-Erdene, et al. 2019. *Permafrost study along some road*. Ulaanbaatar, Mongolia: Scientific report of the project funded by Mongolian Science and Technology (in Mongolian).

Lewkowicz, A.G., Etzelmüller, B. and Smith, S.L. 2011. 'Characteristics of Discontinuous Permafrost based on Ground Temperature Measurements and Electrical Resistivity Tomography, Southern Yukon, Canada', Permafrost Periglacial and Processes 22(4), pp. 320–342. Available at: https://doi.org/10.1002/ppp.703.

Loke, Meng 2001. *Tutorial: 2-D and 3-D Electrical Imaging Surveys*. Available at: www.geoelectrical.com.

Saruulzaya, A., Jambaljav, Y., Gansukh, Y., et al. 2018. 'High-resolution Electrical Resistivity Tomography (ERT) measurements along the paved roads in permafrost regions of Mongolia', in *5th European Conference on Permafrost*, Universite Savoie Mont Blanc, Chamonix, France, 23 June–1 July, 2018.

Sharkhuu, N. and Anarmaa, S. 2011. 'Long-term monitoring of permafrost in Mongolia', in *Extended abstracts of international second symposium on mountain and arid land permafrost*, OOP LLC, Ulaanbaatar, Mongolia, pp. 59–61.

Ministry of Road and Transport Development 2022. *Statistical data of Mongolia for 2022*. Available at: mrtd.gov.mn.

Yamkhin, J., Yadamsuren, G., Khurelbaatar, T., et al. 2022. 'Spatial distribution mapping of permafrost in Mongolia using TTOP', *Permafrost and Periglacial Processes* 33(4), pp. 386–405. doi:10.1002/ppp.2165.

Yarmak, E., Jr. and Long, E.L. 2002. 'Recent developments in thermosyphon technology', in K.S. Merrill (ed.), *Proceedings of the 11th International Conference on Cold Regions Engineering*. Anchorage, Alaska, United States. pp. 656–662.

Cover photo: *Lake in ice-rich terrain in tundra uplands northwest of Inuvik, Northwest Territories. Ice wedge polygons are visible adjacent to the lake (Photo: Rae Landriau).*

12TH INTERNATIONAL CONFERENCE ON PERMAFROST

2024

XII

WHITEHORSE YUKON

INTEGRATING PERSPECTIVES OF PERMAFROST THAW, CHANGE, AND ADAPTATION